
# The Sixth Asian School-Conference on Physics and Technology of Nanostructured Materials

**Vladivostok, Russia, April 25 – 29, 2022**

# PROCEEDINGS

**Vladivostok**
**Far Eastern Federal University**
**2022**

**Sixth Asian School-Conference on Physics and Technology of**

**Nanostructured Materials**: Proceedings. – Vladivostok, Dalnauka, 2022. – 388 p.

ISBN 987-5-8044-1716-2



The Proceedings include extended abstracts of invited talks and contributed papers of the school-conference. The abstracts reflect the new results and scientific achievements in the field of new materials, nanotechnology and surface science. This proceedings volume is intended for scientist, teachers and post-graduate students.

# The Sixth Asian School-Conference on
# Physics and Technology of Nanostructured Materials

***Organizers***

**Institute of Automation and Control Processes FEB RAS**

**Far Eastern Federal University**

***Sponsor***

**«NT-MDT» Limited Liability company**

**The school-conference official website**

http://ntc.dvo.ru/conf/nanomat2022/

## Chair of ASCO-NANOMAT 2022

Professor **Nikolay GALKIN** (Institute of Automation and Control Processes FEB RAS and Far Eastern Federal University, Vladivostok, Russia)

### INTERNATIONAL PROGRAMME COMMITTEE

**Co-Chair:** Corr. Memb. RAS A.A. Saranin (Vladivostok, Russia)

**Co-chair:** Dr. Sci. A.S. Samardak (Vladivostok, Russia)

Academician MAS E. Arushanov (Chisinau, Moldova)
Prof. Bakhtizin R.Z. (Ufa, Russia)
Prof. A.A. Bogdanov (Moscow, Russia)
Prof. V.E. Borisenko (Minsk, Belarus)
Academician RAS Yu.A. Chaplygin (Moscow, Russia)
Prof. A. Chuvilin (San Sebastian, Spain)
Corr. Memb. RAS A.V. Dvurechenskii (Novosibirsk, Russia)
Prof. V.G. Dubrovskii (S.-Petersburg, Russia)
Prof. A.V. Filimonov (S.-Petersburg, Russia)
Academician BAS S.V. Gaponenko (Minsk, Belarus)
Prof. S.A. Gavrilov (Moscow, Russia)
Corr.-member RAS S.V. Gnedenkov, (Vladivostok, Russia)
Prof. S. Hasegawa (Tokyo, Japan)
Prof. Y.K. Kim (Seoul, Korea)
Prof. V.V. Khovaylo (Moscow, Russia)
Academician RAS G.Y. Krasnikov (Moscow, Russia)
Academician RAS A.V. Latyshev (Novosibirsk, Russia)
Prof. S. Makarov (S.-Petersburg, Russia)
Prof. D. Migas (Minsk, Belarus)
Prof. A.A. Naberezhnov (S.-Petersburg, Russia)
Prof. Y. Nakamura (Osaka, Japan)
Dr. Sci. A.V. Ognev (Vladivostok, Russia)
Prof. S.G. Ovchinnikov (Krasnoyarsk, Russia)
Prof. B. Pecz (Budapest, Hungary)
Prof. V.S. Plotnikov (Vladivostok, Russia)
Prof. O.P. Pchelyakov (Novosibirsk, Russia)
Corr.-member RAS R.V. Romashko, (Vladivostok, Russia)
Prof. A. Rogach (Hong-Cong, Peoples R China)
Prof. T.S. Shamirzaev (Novosibirsk, Russia)
Prof. G. Shao (Bolton, UK)
Academician ASM A.S. Sidorenko (Chisinau, Moldova)
Prof. D.V. Shtansky (Moscow, Russia)
Prof. S.M. Shivaprasad (Bangalore, India)
Prof. T. Suemasu (Tsukuba, Japan)
Prof. H. Tatsuoka (Hamamatsu, Japan)
Prof. Y. Terai (Kyushu, Japan)
Prof. S.P. Timoshenkov (Moscow, Russia)
Prof. S.B. Vakhrushev (S-Petersburg, Russia)
Prof. H. Udono (Ibaraki, Japan)
Prof. A.V. Zotov, Corr. member RAS (Vladivostok, Russia)

## ORGANIZING COMMITTEE

**Chair**: Prof. N.G. Galkin (IACP FEB RAS, FEFU)

**Vice-chair**: Dr. Sci. D.L. Goroshko (IACP FEB RAS, FEFU)

**Vice-chair:** PhD. K.N. Galkin (IACP FEB RAS)

**Secretary**: Ph.D. S.V. Chusovitina (IACP FEB RAS)

Dr. Sci. A.V. Ognev (FEFU)

PhD. S.O. Gurbatov (IACP FEB RAS and FEFU)

PhD. K.V. Ignatovich (IACP FEB RAS)

PhD S.G. Krasitskaya (FEFU)

PhD. A.A. Kuchmijak (IACP FEB RAS and FEFU)

PhD. D.S. Shtarev (FEFU)

PhD E.Yu. Subbotin (IACP FEB RAS)

Mr. I.M. Chernev (IACP FEB RAS)

Ms. V.Yu. Ermachenko (FEFU)

Mr. O.V. Kropachev (IACP FEB RAS)

## PUBLISHING COMMITTEE

**Chair:** Prof. N.G. Galkin, (Vladivostok, Russia)

Prof. D.G. Gromov (Moscow, Russia)

Dr. Sci. D.L. Goroshko (Vladivostok, Russia)

Prof. D.B. Migas (Minsk, Belarus)

Dr. Sci. A.V. Ognev (FEFU)

Prof. Y. Terai (Kyushu, Japan)

Prof. T. Suemasu (Tsukuba, Japan)

Prof. T.S. Shamirzaev (Novosibirsk, Russia)

PhD. A.A. Kuchmijak (Vladivostok, Russia)

# Contents

## Plenary lectures



## I. Physics of nanostructures and interfaces, self-organization processes, two-dimensional materials

## II. Physics of semiconducting nanostructures and heterostructures, including silicide, 4th group material's alloy, $A_3B_5$ and $A_2B_6$ heterostructures:experiment, calculations and technolog

## III. Ferromagnetic and ferroelectric materials, including nanomaterials, a spintronics

## IV. Nanostructured coverages, nanocomposites, functional hybrid materials: formation, structure and properties

## V. Laser nanofabrication, all-dielectric materials, nanomaterials: fundamentals and applications

## VI. Photonic and electronic devices: integrated circuits, solar cells, nanophotonics, biophotonics

# Plenary lectures

# Linear and nonlinear physics of bound states in the continuum

K. Koshelev[1,2], S. Kruk[1], E. Melik-Gaykazyan[1,3], Jae-Hyuck Choi[4], A. Bogdanov[*,2], Hong-Gyu Park[4], Yu. Kivshar[1,2]

[1] Nonlinear Physics Center, Australian National University, Canberra ACT 2601, Australia.
[2] School of Physics and Engineering, ITMO University, St. Petersburg 197101, Russia
[3] Faculty of Physics, Lomonosov Moscow State University, Moscow 119991, Russia
[4] Department of Physics, Korea University, Seoul 02841, Republic of Korea

*e-mail: a.bogdnov@metalab.ifmo.ru

**Abstract.** Subwavelength optical resonators made of high-index dielectric materials provide efficient ways to manipulate light at the nanoscale through mode interferences and enhancement of both electric and magnetic fields. Such Mie-resonant dielectric structures have low absorption, and their functionalities are limited predominantly by radiative losses. We implement a new physical mechanism for suppressing radiative losses of individual nanoscale resonators to engineer special modes with high quality factors: optical bound states in the continuum (BICs). We demonstrate that an individual subwavelength dielectric resonator hosting a BIC mode can boost nonlinear effects increasing second-harmonic generation efficiency. Our work suggests a route to use subwavelength high-index dielectric resonators for a strong enhancement of light–matter interactions with applications to nonlinear optics, nanoscale lasers, quantum photonics, and sensors.

## 1. Introduction

Subwavelength high-index dielectric structures emerged recently as a new platform for nanophotonics [1]. They benefit from low material losses and provide a simple way to realize magnetic response in the visible and near infrared ranges which enables efficient flat-optics devices reaching and even outperforming the capabilities and functionalities of bulk components. Yet, the enhancement of near-field effects for individual subwavelength resonators is strongly limited by low quality factor (Q factor) of the fundamental resonances governing the optical response.

Recently, a novel theoretical approach [2] suggested to achieve high-Q resonances in individual subwavelength resonators in the regime of *supercavity mode*, by employing the physics of genuine nonradiative states – optical *bound states in the continuum* (BICs) [3]. Supercavity modes attracted a lot of attention, but they have never been observed experimentally in individual resonators. This year, we reported on the first experimental observation of the supercavity modes in individual subwavelength dielectric resonators [4] and also demonstrated the record-high efficiency of the second-harmonic generation predicted earlier [5].

## 2. Experiment

First, we observe the supercavity modes in the near-infrared frequency range. We consider cylindrical resonators with height 635 nm made of AlGaAs (permittivity of 11) placed on a silica substrate with an additional highly doped 300 nm ITO layer playing a role of epsilon-near-zero material. This layer provides an additional enhancement of the Q factor due to the interaction between the resonator and the substrate. To engineer the supercavity mode, we vary the resonator diameter between 890 nm and 980 nm to induce strong coupling between a pair of Mie modes [4]. For an efficient excitation, we employ a tightly focused azimuthally polarized vector beam with the wavelength varying from 1500 nm to 1700 nm.

## 3. Results and discussions

The measured Q factor (see Figure) is about 190, which is more than one order of magnitude higher than for conventional dipolar Mie modes. The right panel in the figure shows the simulated near- and far-field pattern of the electric field of the supecavity mode, also confirmed recently in microwave experiments.

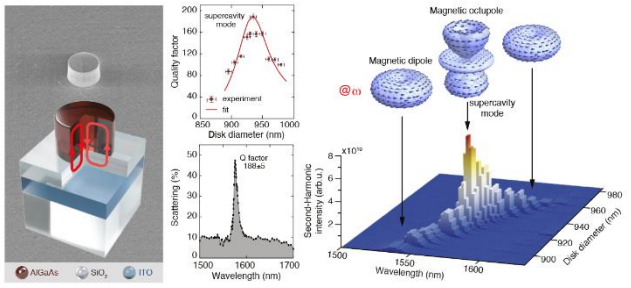


***Figure**. Left: SEM micrograph (top) and schematic (bottom) of an individual dielectric nanoresonator on an engineered substrate supporting supercavity modes. Top center: Mode quality factor depends on the particle diameter and reaches maximum for the supercavity mode condition. Bottom center: Measured backward-scattering spectrum of the supercavity mode. Right: Measured second-harmonic intensity map vs. particle diameter and incident wavelength excited with a structured pump. The top inset shows the resonant mode far-field profiles at the pump frequency.*

## 4. Conclusions

Our study reveals that supercavity modes are formed due to strong interaction of two leaky modes, which interfere destructively resulting in strong suppression of radiative losses. This clearly confirms that the supercavity modes are governed by the physics of bound states in the continuum. We believe that our work opens novel opportunities for subwavelength dielectric metaphotonics and nonlinear nanophotonics.

**Acknowledgements**

This work was supported by Russian Science Foundation (grant number 18-72-10140). A. B. acknowledges the "BASIS" Foundation. This research was supported by Priority 2030 Federal Academic Leadership Program.

**References**

[1] A.I. Kuznetsov et al. Science **354**, aag2472 (2016).
[2] M.V. Rybin et al. Phys. Rev. Lett. **119**, 243901 (2017).
[3] K. Koshelev et al. Science Bulletin **64**, 836 (2019).
[4] K. Koshelev et al. Science **367**, 288-292 (2020).
[5] L. Carletti et al. Phys. Rev. Lett. **121**, 033903 (2018).

# Halide perovskite based nanophotonics: from fundamentals to applications

S.V. Makarov*
ITMO University, Lomonosova 9, Saint Petersburg 191002, Russia

*e-mail: s.makarov@metalab.ifmo.ru

**Abstract.** Nanophotonics and meta-optics based on optically resonant all-dielectric structures is a rapidly developing research area driven by its potential applications for low-loss efficient metadevices. Recently, the study of halide perovskites has attracted enormous attention due to their exceptional optical and electrical properties. As a result, this family of materials can provide a prospective platform for modern nanophotonics and meta-optics, allowing us to overcome many obstacles associated with the use of conventional semiconductor materials. Here, we review the recent progress in the field of halide perovskite nanophotonics starting from single-particle light-emitting nanoantennas and nanolasers to the large-scale designs working for surface coloration, anti-reflection, and optical information encoding.

## 1. Introduction

Lead halide perovskites is a rapidly developing class of semiconductors, which can be synthesized both by wet-chemistry approaches and by various physical deposition methods. They have been intensively studied due to their outstanding electronic and optical properties, which are extremely prospective for solar photovoltaics, light-emitting devices, photodetectors, and X-ray detectors. In addition, high quantum yield of photo- luminescence and gain of the lead perovskites make them very promising materials for lasers. Moreover, high enough refractive index of the perovskite allows them to support Mie resonances in the visible and near-infrared ranges.

## 2. Discussions

We focus on 3D halide perovskites family of materials with formula $ABX_3$, where "A" is the cation (e.g. $MA^+$, $FA^+$, or $Cs^+$), "B" is usually lead ($Pb_2^+$), and "X" is the anion (e.g. $I^-$, $Br^-$, or $Cl^-$). Halide lead perovskites can be considered as direct band-gap materials resembling GaAs. But they have some advantages that make them a very perspective material for nanophotonics. One of such advantages is high optical gain being higher than $10^3$ $cm^{-1}$ at room temperature owing to strong interband transition.

Due to the relatively high refractive index of halide perovskites, it is possible to utilize them for the creation of nanoparticles that support Mie resonances. The resulting enhancement of optical field inside the nanoparticle further augments the exceptional properties of perovskites. In particular, this approach was used to enhance the photoluminescence, second harmonic generation, Raman scattering, amplified spontaneous emission and optical cooling. Importantly, perovskite nanoparticles can be produced by relatively simple fabrication methods, such as laser ablation and chemical synthesis and do not require multi-stage lithography processes. One of the first demonstrations of Mie-resonant perovskite nanoparticles was achieved using laser ablation. The quasi-spherical perovskite nanoparticle was studied as an active optical nanoantenna which allows for a significant enhancement of the photoluminescence and control of the emission directivity. Another aspect of the interaction of light with perovskite nanoparticles arises due to the pronounced exciton resonance of perovskite at room temperature. When a narrow exciton resonance couples to a broader cavity resonant mode, interference effects, manifested as the characteristic Fano lineshape in the spectrum, are expected.

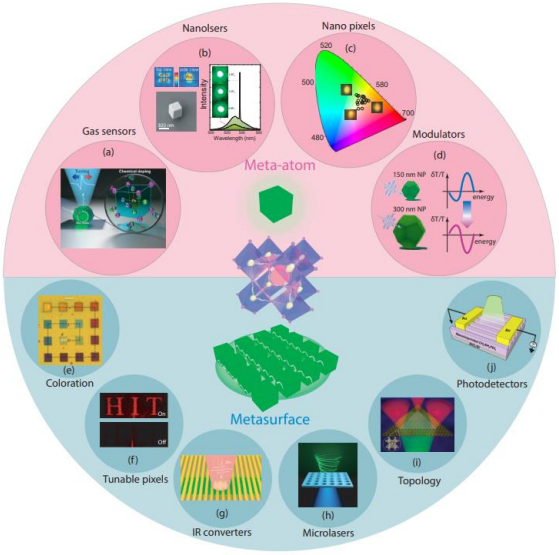


***Fig. 1.*** *Applications of perovskite particles and metasurfaces. (a) The concept of gas sensor based on Fano resonant nanoparticle. Adopted from Ref. [1]. (b) SEM image of a cubic perovskite nanoparticle with a linear size of 310 nm supporting third-order Mie resonance and its lasing spectrum. Adopted from Ref. [2]. (c) CIE 1931 color diagram with shown colors of nanocubes with the sizes in the range of 310-560 nm. Adopted from Ref. [2]. (d) The illustration of an ultrafast nanomodulator based on Fano resonance. Adopted from Ref. [3]. (e) Coloration of metasurfaces assembled from particles of different size. [4] (f) Holographic image "HIT" in with "ON" and "OFF" states corresponding to MAPbBr3 perovskite metasurface and converted MAPbI3 perovskite metasurface. Adopted from Ref. [5]. (g) Infrared converters based on perovskite metasurface enhancing multiphoton photoluminescence. Adopted from Ref. [6]. (h) Vortex microlaser based on perovskite metasurface. Adopted from Ref. [7]. (i) The concept of the topological metasurface functionalized with perovskite nanocrystals. (j) Perovskite metasurface-based photodetector. Adopted from Ref. [8].*

Despite the wide range of applications for single nanoparticles, the creation of a metasurface from meta-atoms can significantly expand their scope. However, due to the random distribution of nanoparticle size and location when using laser printing and various chemical synthesis methods, it is difficult to create highly ordered arrays of

nanoparticles. Thereby, methods such as nanoimprint lithography, electron beam lithography, laser projection lithography, and focused ion beam lithography, are engaging for the fabrication of metasurfaces based on halide perovskites. As a result, the fabricated metasurfaces were applied for coloration, detectors optimization, vortex beam generation, and enhanced nonlinear photoluminescence (Fig.1).

## 4. Conclusions

To summarize, the above-mentioned recent achievements have shown that nanophotonics and metaoptics concepts can be successfully applied for improvement of perovskite-based photonic and optoelectronic devices. In our works, we demonstrate deep connection between fundamental properties of halide perovskites and nanophotonics with such applications as lasers, solar cells, and nonlinear optical frequency converters.

## Acknowledgements

This research was supported by Priority 2030 Federal Academic Leadership Program.

References

[1] E.Y. Tiguntseva, D.G. Baranov, A.P. Pushkarev, B. Munkhbat, F. Komissarenko, M. Franckevicius, A. A. Zakhidov, T. Shegai, Y. S. Kivshar, S. V. Makarov. Nano Letters **18**(2018)5522.

[2] E. Tiguntseva, K. Koshelev, Furasova A., Tonkaev P., Mikhailovskii V., Ushakova E. V., Baranov D. G., Shegai T., Zakhidov A. A., Kivshar Y., et al. ACS Nano **14**(2020)8149.

[3] P. Franceschini, L. Carletti, Pushkarev, A. P.; Preda, F.; Perri, A.; Tognazzi, A.; Ronchi, A.; Ferrini, G.; Pagliara, S.; Banfi, F., et al. ACS Nano **14**(2020)13602.

[4] B. Gholipour, G. Adamo, D. Cortecchia, Krishnamoorthy, H. N.; Birowosuto, M. D.; Zheludev, N. I.; Soci, C. Advanced Materials **29**(2017).

[5] C. Zhang, S. Xiao, Y. Wang, Gao, Y.; Fan, Y.; Huang, C.; Zhang, N.; Yang, W.; Song, Q. Laser & Photonics Reviews **13**(2019)1900079.

[6] Y. Fan, P. Tonkaev, Y. Wang, Song, Q.; Han, J.; Makarov, S. V.; Kivshar, Y.; Xiao, S. Nano Letters **21**(2021)7191.

[7] C. Huang, C. Zhang, S. Xiao, Wang, Y.; Fan, Y.; Liu, Y.; Zhang, N.; Qu, G.; Ji, H.; Han, J., et al. Science **367**(2020)1018.

[8] H. Wang, R. Haroldson, Balachandran, B.; Zakhidov, A.; Sohal, S.; Chan, J. Y.; Zakhidov, A.; Hu, W. ACS Nano 10(2016)10921.

# Collective effects in Si based quantum dot nanomaterials to tune functionality of nano nanoelectronic and nanophotonic components

A.V. Dvurechenskii*, A. Yakimov, A. Zinovieva, V. Zinovyev, A. Bloshkin, A. Nenashev, V. Kirienko
Rzhanov Institute of Semiconductor Physics, Russian Federation

*e-mail: dvurech@isp.nsc.ru

**Abstract.** The approaches to obtain high-performance of infrared photodetectors and luminescent structure based on Ge/Si QDs silicon nanoheterostructures coupled with metasurfaces and photonic crystals are considered.It was shown that composite metasurface consisted of a two-dimensional regular array of silicon pillars and subwavelength holes array in a periodically perforated gold film on top of the detector active region displays about 15 times peak responsivity enhancement at a wavelength of 4.4 μm relative to the bare detector. The planar Ge/Si QDs photodetector coupled with plasmonic structure consisted of a two-dimensional regular array of Al nanodisks is able to increase the photodetectors efficiency by about 40 times at λ=1,2 μm and by 15 times at λ= 1,55 μm with an appropriate choice of the array periodicity and the size of the Al nanodisks. The other idea of the approach is to use photonic crystals in processes of optical absorption in thin layers of quantum dots embedded in photonic crystals. We found that the incorporation of Ge/Si quantum dot layers into a two-dimensional photonic crystal leads to multiple (up 34 times) enhancement of the photocurrent in the near infrared range. The results are explained by the excitation of planar photonic crystal modes by the incident light wave propagating along the Ge/Si layers and effectively interacting with interband transitions in quantum dots. The photoluminescence of the combined Ge/Si QDs heterostructures consisted of a combination of large (200–250 nm) GeSi nanodisks and layered stacks of compact groups of smaller (30 nm) quantum dots grown by site controlled nucleation in the strain fields of nanodisks show the multiple increase in the photoluminescence intensity. The main channels of radiative recombination correspond to spatially direct optical transitions.

The work was funded by Russian Scientific Foundation (grant 19-12-00070).

Sixth Asian School-Conference on Physics and
Technology of Nanostructured Materials
Vladivostok, Russia, 25 – 29 April, 2022

**Plenary 10**

# New ternary magnetic films of MAX phases

I.A. Tarasov*[,1], I.A. Yakovlev[1], M. Visotin[1], M.V. Rautskii[1], A.S. Tarasov[1,2], S.A. Lyaschenko[1], O.A. Maksimova[1,2], S.N. Varnakov[1], T.A. Andryushchenko[3], S.G. Ovchinnikov[1,2]

[1] Kirensky Institute of Physics, Krasnoyarsk Scientific Center, Siberian Branch, Russian Academy of Sciences, 660036 Russia

[2] Siberian Federal University, Krasnoyarsk, 660041 Russia

[3]Reshetnev Siberian State University of Science and Technology, Krasnoyarsk, 660037Russia

*e-mail: tia@iph.krasn.ru

MAX-phase materials ($M_{n+1}AX_n$, n = 1, 2 or 3) [1] are a family of nano-layered hexagonal compounds. In these materials, M is an early transition metal, A is an element of the main group, and X is C or N (n = 1-3). These systems have an atomic-layered structure (figure 1 and figure 2) consisting of m-XM (M2X) layers alternating with the atomic layers of the A-element. The atomic layers are stacked along the C axis. the Layered highly anisotropic crystal structure leads to mechanical properties usually associated with ceramics. MAX-phases combine both ceramic and metal characteristics, providing resistance to high-temperature oxidation, self-healing ability and resistance to thermal shock. Such outstanding mechanical properties have made them interesting materials, for example, for treatable, heat-resistant refractories, heating elements or coatings for electrical contacts. In terms of applications, MAX-phase materials have shown very promising properties for batteries and ultra-high-frequency devices [2]. In addition, MAX-phase materials serve as "raw materials" for the synthesis of dilaminated two-dimensional transition metal carbides (MXenes) [3].

It has long been believed (since the 1960s) that the layered structure of MAX can only be obtained by using early transition metals as the main component of the m layers, which essentially leads to the formation of only paramagnetic compounds. The first MAX phase (Cr0.75Mn0.25)2GeC with long-range magnetic order was synthesized as an epitaxial thin film on MgO(111) in 2013 [4]. Subsequent studies have found several triple and quarter MAX-phases based on Mn with competing ferro - and antiferromagnetic (intra - and interplane) interactions leading to a common complex magnetic response, depending on the field and temperature. Recently, a detailed study of the magnetic properties of $Mn_2GaC$ led to the discovery of the first magnetocaloric MAX-phase with a high ordering temperature and inversion of the magnetostriction and magnetoresistance sign at the phase transition [5]. These new material properties offer new functionality for smart sensors and actuators that are in demand for the “Internet of things”.

Despite the abundance of work on the synthesis and research of thin films of MAX-phases, the systematic study of MAX materials demonstrating ferromagnetic properties is still in its infancy [5]. Since MagMAX materials can contain 4 or more elements, a combination of high-performance deposition and detailed structural, compositional, magnetic and spectroscopic analysis methods is required to find new compounds and the best composition. In addition, the problem of the crystalline quality of the films, as well as the presence of accompanying phases of carbides and intermetallics, remains unsolved.

Most of the first work on the synthesis of thin films of MAX-phases was performed using physical vapor deposition from the gas phase, mainly by magnetron sputtering, as well as using cathode-arc evaporation [9]. The synthesis of thin MAX-phase films using sputtering methods can be divided into three main approaches: joint sputtering with three elementary targets, sputtering with complex targets, and solid-phase synthesis of reactions by spraying an amorphous multilayer material [9]. Sputtering from M, A, and graphite targets is the most common method for laboratory synthesis of MAX carbide thin films. The main advantage of using three elementary targets is flexibility in individual control of element flows [9]. The initial values of the deposition parameters are based on some estimates or calibrations, and then the usual optimization procedure is performed to achieve the desired MAX phase of stoichiometry [10]. Using this approach, the synthesis of thin films of different phases was successfully demonstrated [11, 12]. Reactive spray deposition has been relatively little studied for the synthesis of carbides and nitrides of MAX phases, mainly due to the fact that the technological interval (relative to the partial pressure of the chemically active gas) for the deposition of single-phase or high-purity MAX phases is extremely narrow [9]. Sputtering from complex targets is sometimes preferable for reasons of simplicity and reproducibility [13]. However, the general problem remains that the composition of the film can be very different from the nominal composition of the target.

In this talk we make a review of the main characteristics of magnetic MAX – phases, experimental and theoretical approaches. We also propose and will discuss a pure crystallogeometrical approach proposed [6] to predict orientation relationships (ORs), habit planes, and atomic structures of the interfaces between MAX-phases and various substrates and as well consideration of buffer layers possible between them. Preliminary results are given for the case of the $Mn_2GaC$ phase on $Al_2O_3$ (Fig.1), MgO, $SrTiO_3$, SiC-3C, SiC-6H, YSZ, $TiO_2$, $SiO_2$, C (diamond), mic, $MgAl2O_4$. GaN, TiN monocrystalline substrates or buffer layers. Lattice stress in epitaxial MAX-phase thin films is carried out with geometric phase analysis and distribution of interplanar and angular distances obtained with XRD and TEM [7] (Fig.1 lower). Additionally, the application of the method to the analysis of the formation of concurrent phases in epitaxial system Cr2GaC on MgO(111) will be discussed. We study thermodynamic favourability of competing phases (CPs) and $Cr_2GaC$ MAX-phase

depending on the chemical composition of the atomic flow (Fig.1 middle) [8]. The density of near-coincidence sites [6] for interfaces between MAX-phases, thermodynamically favourable CPs, and MgO(111) surface is considered to show a role of the interface in the determination of the structural quality of the MAX-phase thin film grown on MgO(111). The NCS-density is also used to predict the faceting of the competitive phase inside the matrix of the MAX-phase.

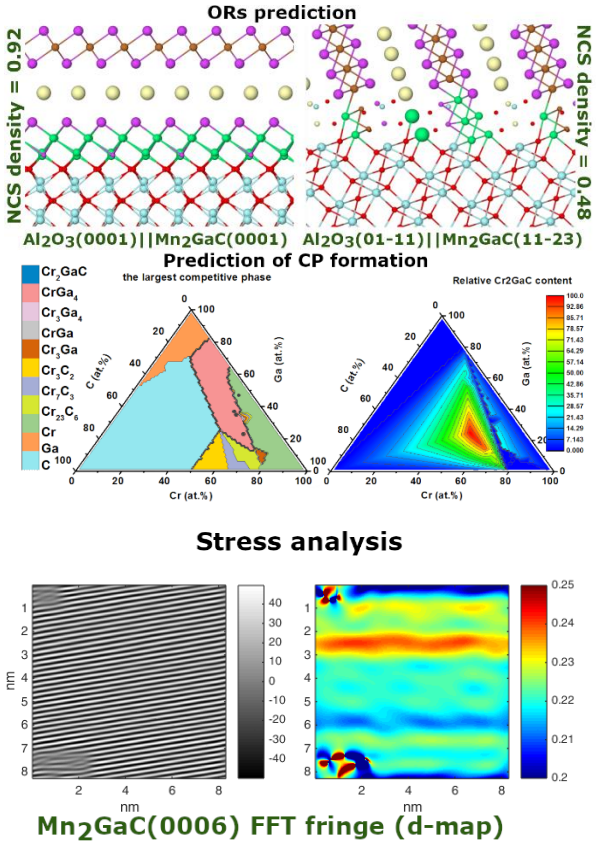


***Fig. 1.*** *Summary illustrating some results for prediction of the ORs, formation of CPs and stress analysis.*


## Acknowledgements

The research is carried out with the financial support of the Russian Foundation for Basic Research, the Government of the Krasnoyarsk Territory, the Krasnoyarsk Regional Science Foundation in the framework of the scientific project No. 20-42-240012, the Government of the Russian Federation in the framework of the grant for the creation of world-class laboratories (agreement No. 075-15-2019-1886).


## References


[1] M. Sokol, V. Natu, S. Kota and M. W. Barsoum, Trends in Chemistry 1 (2), 210-223 (2019).

[2] M. R. Lukatskaya, S. Kota, Z. Lin, M.-Q. Zhao, N. Shpigel, M. D. Levi, J. Halim, P.-L. Taberna, M. W. Barsoum, P. Simon and Y. Gogotsi, Nature Energy 2, 17105 (2017).

[3] N. K. Chaudhari, H. Jin, B. Kim, D. San Baek, S. H. Joo and K. Lee, J Mater Chem A 5 (47), 24564-24579 (2017).

[4] Novoselova, I.P., et al., Sci Rep, 2018. 8(1): p. 2637.; R. Salikhov, A. S. Semisalova, A. Petruhins, A. S. Ingason, J. Rosen, U. Wiedwald and M. Farle, Materials Research Letters 3 (3), 156-160 (2015).

[5] F. M. Römer, U. Wiedwald, T. Strusch, J. Halim, E. Mayerberger, M. W. Barsoum and M. Farle, RSC Advances 7 (22), 13097-13103 (2017).

[6] Visotin MA, Tarasov IA, Fedorov AS, et al (2020) Acta Crystallogr Sect B Struct Sci Cryst Eng Mater 76:469–482.

[7] Novoselova IP, Petruhins A, Wiedwald U, et al (2018) Scientific reports 8:2637. doi:10.1038/s41598-018-20903-2

[8] Tarasov IA, Visotin MA, Kuznetzova T V., et al (2018) J Mater Sci 53:7571–7594

[9] A.S. Ingason, A. Petruhins, J. Rosen, Mater. Res. Lett. 4 (2016) 152–160.

[10] O. Wilhelmsson, J.-P. Palmquist, T. Nyberg, U. Jansson, Appl. Phys. Lett. 85 (2004) 1066–1068

[11] O. Wilhelmsson, J.-P. Palmquist, E. Lewin, J. Emmerlich, P. Eklund, P.O.Å. Persson, H. Högberg, S. Li, R. Ahuja, O. Eriksson, L. Hultman, U. Jansson, Deposition and characterization of ternary thin films within the Ti–Al–C system by DC magnetron sputtering, J. Cryst. Growth. 291 (2006) 290–300.

[12] I.C. Schramm, C. Pauly, M.P. Johansson Jõesaar, P. Eklund, J. Schmauch, F. Mücklich, M.

[13] Odén,165, Acta Mater. 129 (2017) 268–277.

# Topological features of quantum magnetotransport in $Bi_{1-x}Sb_x$ ($0 \leq x \leq 0.2$) bicrystals

Fiodor Muntyanu[1], V. Chistol[2], E. Condrea[1] and A. Sidorenko[*,1,2]

[1] Institute of Electronic Engineering and Nanotechnologies, Chisinau, 2028, Moldova
[2] Technical University of Moldova, Chisinau, 2004 Republic of Moldova

*e-mail: anatoli.sidorenko@kit.edu

**Results and discussions**

Unusual topological features related to the interface Dirac electrons [1, 2] have been revealed: the longitudinal Hall quasi-plateaus, along with minima in magnetoresistance; the manifestation of Umkehr effect, non- allowed by the crystal symmetry; two new harmonics of quantum transport from interface layers, which characterizes larger than cross-sectional areas of the FS of crystallites; the magnetoresistance peculiarities, indicating both the occurrence of a small group of the infinitely moving electrons and the electronic phase transitions of the semiconductor–semimetal type in magnetic field. A high-field behaviour of αii(B) has been identified (it linearly increases in magnetic field without saturation, the sign changes from negative to positive, the nontrivial π-Berry phase is observed, etc.) in CIs layers, specifying the signature of 3D topological semimetal at 3D Dirac point forming (x ~ 0.04). In addition, it has been found that the bicrystals of Bi1-xSbx ($0.07 \leq x \leq 0.2$) alloys exhibit peculiarities typical of 3D TI: αii(B) undergoes saturation in magnetic field or smoothly increase, the Landau level index n in all CIs layers linearly depend on 1/Bn and extrapolated to –0.5 if $1/Bn \rightarrow 0$.

**References**

[1] Fiodor M.Muntyanu, Andrzej Gilewski, Andrzej J. Zaleski, Vitalie Chistol, Viorel Munteanu, Krzysztof Rogacki and Anatolie Sidorenko, A.Sidorenko (Ed.), Functional Nanostructures and Metamaterials for Superconducting Spintronics, Springer International Publishing AG, 2018, pp.247-263 part of Springer Nature., Resp. ed. A. Sidorenko (Chapter 12).

[2] F. M. Muntyanu, A. Gilewski, A.J. Zaleski, V. Chistol, K. Rogacki, Physics Lett. A 381(2017) 2040.

# I. Physics of nanostructures and interfaces, self-organization processes, two-dimensional materials

Sixth Asian School-Conference on Physics and
Technology of Nanostructured Materials
Vladivostok, Russia, 25 – 29 April, 2022

I.i.01

# Pb-based low-dimensional structures on silicon

D.V. Gruznev*[,1], L.V. Bondarenko[1], A.Y. Tupchaya[1], Y.E. Vekovshinin[1,2], A.N. Mihalyuk[1,2], A.V. Zotov[1], A.A. Saranin[1]

[1] Institute of Automation and Control Processes FEB RAS, Vladivostok 690041, Russia
[2] Far Eastern Federal University, Vladivostok 690950, Russia

*e-mail: gruznev@iacp.dvo.ru

**Abstract.** Single-atomic layers of lead (Pb) demonstrate many intriguing phenomena such as superconductivity at the ultimate atomic scale. Its modification by other elements with the formation of binary alloys and Pb-based 2D compounds is a natural expansion of the list of materials with potential advanced properties. Here we discuss novel Pb-based surface reconstructions, formed by incorporating into the Pb/Si(111) layer a light element with small electronegativity (Mg) and a rare-earth f-element (Ce). Crystal and electronic structures are discussed based on experimental results of scanning tunneling microscopy, angle-resolved photoelectron spectroscopy, and DFT calculations.

## 1. Introduction

Single-atomic layers of lead (Pb) demonstrate several intriguing phenomena, such as 2D superconductivity [1], Rashba-type spin-splitting of the surface states [2], etc. It not only renders them a promising 2D material for future electronic and spintronic applications but also allows using them as a playground to probe the influences of various effects on superconductivity and related phenomena at the ultimate atomic scale. A remarkable effect of disorder on superconductivity was demonstrated with Pb/Si(111) monolayers [3]. 2D topological superconducting domains with chiral in-gap edge states were created by incorporating magnetic Co-based islands beneath the Pb layer on Si(111) [4]. Yu-Shiba-Rusinov (YSR) bound states were observed after individual magnetic atoms were embedded into the Pb/Si(111) layer [5].

Many novel Pb-based compound 2D structures with fascinating electron properties were synthesized in recent years. The (Pb, Bi)/Si(111) surface reconstruction with quasi-1D spin-polarized electron channels [6], the superconducting (Tl, Pb) structures on Si(111) and Ge(111) substrates [7], and many others.

In this report, we discuss several compound surface reconstructions on Si(111) surface created by the incorporation of foreign atoms (Mg and Ce) into the superconducting single-atomic layer of Pb on the Si(111). Results of scanning tunneling microscopy (STM), angle-resolved photoelectron spectroscopy (ARPES), and DFT calculations are presented.

## 2. Results and discussions

First, we discuss the synthesis and characterization of a new 2D compound layer consisting of a Mg layer sandwiched between a Pb layer and Si(111) substrate. A moiré pattern produced by the lattice mismatch between the Si(111) surface and the Mg sheet, results in the formation of unique structure, where Mg atoms form a giant honeycomb network covered with a layer of Pb atoms, and voids of the lattice are filled with a single Pb layer (Fig. 1). ARPES data revealed the close similarity of its electronic structure with that typical for the Pb/Si(111) system. As a result of Mg intercalation, which is a light element with relatively small electronegativity, 0.45 eV bending of surface-state bands takes place due to electron doping from Mg (1.27 electron per atom). The electron-phonon coupling constant λ is enhanced (2.54±0.1) compared to the pristine Pb/Si(111) monolayer (0.58±0.1) as derived from temperature-dependent ARPES measurements of the lifetime broadening. However, the superconducting transition temperature Tc, which depends on electron-phonon coupling, rises insignificantly (1.15 K compared to 1.1 K for the case of pristine Pb/Si(111) system) as revealed by four-point probe transport measurements (Fig. 1).

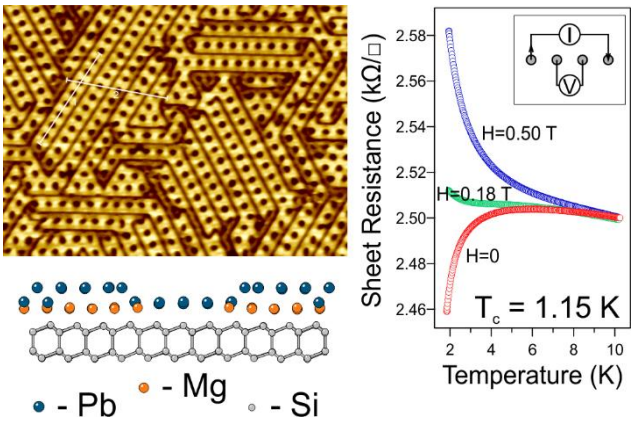


***Fig. 1.*** *STM image (60×45 nm$^2$), atomic model (side view) and results of transport measurements for the (Mg, Pb)/Si(111) system.*

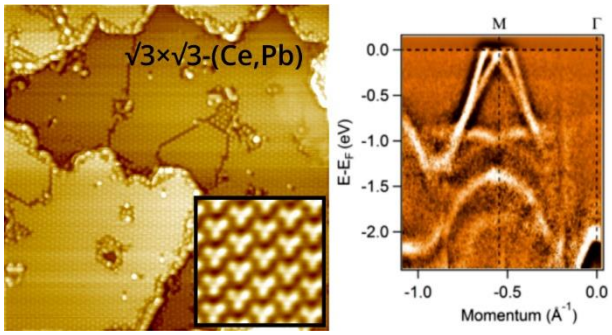


***Fig. 2.*** *STM image (40×40 nm$^2$, inset shows high-resolution empty-state 3×3 nm$^2$ image) and ARPES spectrum of the Si(111)√3×√3-(Ce, Pb) reconstruction.*

Another interesting example of a Pb-based 2D system is obtained by adsorption the rare-earth *f*-element Ce onto the Pb/Si(111) layer. In the bulk form, the $CePb_3$ is a heavy-fermion antiferromagnet that becomes superconducting in high magnetic fields [8]. The first experimental realization

of a two-dimensional heavy-fermion system ($CeIn_3$) was achieved recently [9], but a synthesis of such materials on the Si(111) surface is still challenging. For exploring the possibility of $CePb_3$ synthesis as a 2D layer on a silicon surface, we studied the Ce adsorption onto the Pb/Si(111) layer and found a new compound Si(111)$\sqrt{3}\times\sqrt{3}$-(Ce, Pb) reconstruction.

STM images of the surface are shown in Fig. 2. The structural model proposed based on STM data and DFT calculations includes three Pb atoms per unit cell forming a kagome-type lattice and one Ce atom in the hexagonal voids. This atomic configuration repeats an isolated (111) atomic plane of a bulk $CePb_3$ placed onto Si(111) surface and compressed. The electronic structure features a Rashba-type spin splitting around the M point with a band-crossing point very close to the Fermi level (Fig. 2). DFT calculations also predict the presence of dispersionless heavy states formed by Ce *f*-electrons in the band structure, which is typical for heavy-fermion systems.

**Acknowledgments**

The work was supported by the RSF Grant 22-12-00174. The calculations were conducted using the equipment of Shared Resource Center "Far Eastern Computing Resource" IACP FEB RAS (https://cc.dvo.ru).

**References**

[1] T. Zhang, *et al*., Nature Physics 6 (2010) 104.
[2] K. Yaji, *et al*., Nature Comm. 1 (2010) 17.
[3] C. Brun, *et al*., Nature Physics 10 (2014) 444.
[4] G.C. Ménard, *et al*., Nature Comm. 8 (2017) 2040.
[5] G.C. Ménard, *et al*., EPJ-Special Topics 227 (2019) 2303.
[6] A.N. Mihalyuk, *et al*., Phys. Rev. B 104 (2021) 125413.
[7] T. Nakamura, *et al*., Appl. Surf. Sci. 479 (2019) 679.
[8] C.L. Lin, *et al*., J. Magn. Magn. Mater. 54–57 (1986) 379.
[9] H. Shishido, *et al*., Science 327 (2010) 980.

# Ultrafast Charge Carrier dynamics of topological insulators

Mahesh Kumar[*,1,2], Prince Sharma[1,2], Saurabh K. Siani[1,2], V.P. S. Awana[1,2]
[1] CSIR-National Physical Laboratory, Dr. K.S. Krishnan Marg, New Delhi-110012, INDIA
[2] Academy of Scientific and Innovative Research (AcSIR), Ghaziabad, 201002, INDIA

*e-mail: mkumar.npl@nic.in

**Abstract.** Topological insulators are a new class of quantum matter. And are being widely explored for their exotic properties. We present here the ultrafast charge carrier dynamics of the various topological insulators grown in the form of large single crystals to understand their charge carrier and phonon dynamics both at room temperature and at low temperature. The single crystalline phase is identified by XRD and the structural information is gathered by secondary electron microscopy.

Sixth Asian School-Conference on Physics and
Technology of Nanostructured Materials
Vladivostok, Russia, 25 – 29 April, 2022

**I.i.03**

# Single layer nickel disilicide on surface and as embedded layer

L.V. Bondarenko[1], A.Y. Tupchaya[1], Y.E. Vekovshinin[1,2], D.A. Olyanich[1], A.V. Matetskiy[1], N.V. Denisov[1], S.V. Eremeev[3,4], A.N. Mihalyuk[1,2], Yu.P. Ivanov[1,2,5], D.V. Gruznev[1], A.V. Zotov[1], A.A. Saranin[1]

[1] Institute of Automation and Control Processes FEB RAS , 5 Radio St., Vladivostok 690041, Russia
[2] Far Eastern Federal University, 8 Sukhanova St., Vladivostok 690950, Russia
[3] Institute of Strength Physics and Materials Science SB RAS, 634021 Tomsk, Russia
[4] Tomsk State University, 634050 Tomsk, Russia
[5] University of Cambridge, Cambridge CB3 0FS, U.K.

*e-mail: bondarenko@dvo.ru

**Abstract.** Single monolayers of various materials (e.g. graphene, silicene, bismuthene, plumbene, etc) have recently become fascinating and promising objects in modern condensed-matter physics and nanotechnology. However, growing a monolayer of non-layered material is still challenging. In the present report, it will be shown that single monolayer $NiSi_2$ can be fabricated at Si(111) surface stabilized by either Tl, Pb or In monolayers. Nickel atoms were found to intercalate the stabilizing metal layers upon deposition and to reside in the interstitial sites inside the first silicon bilayer of bulk-like-terminated Si(111)1×1 surface. The interstitial positions almost coincide with the bulk $NiSi_2$ atomic positions thus forming $NiSi_2$ single layer. Atomic and electronic structure of formed systems is described in detail by means of a set of experimental techniques, including low-energy electron diffraction, scanning tunneling microscopy, angle-resolved photoemission spectroscopy and also first-principles density-functional-theory calculations. Quality of formed single monolayer $NiSi_2$ was additionally confirmed by *in situ* four-probe transport measurements that show that single monolayer $NiSi_2$ preserves a metallic-type conductivity down to 2.0 K. Moreover it was found that delta-type structure with atomic sheet of $NiSi_2$ silicide embedded into a crystalline Si matrix can be fabricated using room-temperature overgrowth of a Si film onto the Tl stabilized $NiSi_2$ surface layer. Confinement of the $NiSi_2$ layer to a single atomic plane has been directly confirmed by high-resolution transmission electron microscopy.

## 1. Introduction

Among transition metal silicides, $NiSi_2$ has exceptional fluorite structure (along only with $CoSi_2$) with remarkably close lattice matching to crystal silicon, such that it displays perfect epitaxial growth on Si surfaces with an atomically abrupt interface [1, 2]. More importantly, nickel disilicide is a 'good' metal and known to be metallic down to 1 K [3]. In 1983, Tung et al [1] showed that $NiSi_2$ layers can be grown epitaxially on Si(111) and Si(100) surfaces, which has generated considerable interest in the subject due to its importance for semiconductor microelectronics. In subsequent years the formation process of epitaxial $NiSi_2$ layers on silicon surface has been studied and it was shown that thick $NiSi_2$ films can be controllably formed in two possible orientations [2]: type-A (Si lattice planes continue through the interface) and type-B (180° rotated). However, it was also shown that single or double monolayer $NiSi_2$ cannot be formed [4]. Its formation remains a desirable task because single monolayers of various materials (e.g. graphene, silicine, bismuthene, plumbene, etc) have recently become fascinating and promising objects in modern condensed-matter physics and nanotechnology. At the same time, growing a monolayer of non-layered material is still challenging.

## 2. Results and discussions

Figure 1 illustrates the growth procedure that was used to fabricate a single monolayer nickel disilicide. In the first step, Tl/Si(111)1×1 surface was prepared (figure 1(a)), which is known to contain 1.0 ML of Tl atoms occupying every $T_4$ site on the bulk-like-terminated Si(111) surface (fig.2 (a)). To form the $NiSi_2$ layer, nickel was deposited onto the Tl/Si(111) surface with postannealing at 300°C. As it was proven by angle-resolved photoemission spectroscopy and first-principles density-functional-theory calculations, adsorbed Ni atoms penetrate through the Tl layer to form $NiSi_2$ monolayer sheet beneath it [5].

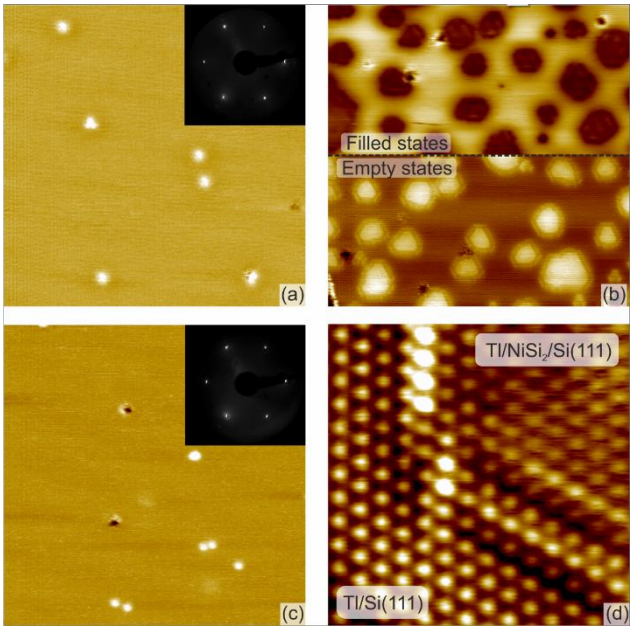


***Fig. 1.*** *Formation of the Tl/$NiSi_2$/Si(111) system. 50×50 nm² STM images of (a) the initial Tl/Si(111) surface (empty states), (b) the surface at the intermediate stage with 0.2 ML of Ni deposited onto Tl/Si(111) surface at RT followed by 300°C annealing; (c) final Tl/$NiSi_2$/Si(111) surface with 1.0 ML of Ni deposited (filled states). The upper inserts in (a) and (c) show corresponding LEED patterns ($E_p$ = 54 eV). (c) - 5 × 5 nm² high-resolution STM image of the border area between Tl/$NiSi_2$/Si(111) and Tl/Si(111).*

Figure 1(b) illustrates the intermediate stage, when about 0.2 ML of Ni was deposited and the surface contains

patches of Tl/$NiSi_2$/Si(111) surrounded by areas of Tl/Si(111). A high-resolution STM image shown at figure 1(d) demonstrates border area between Tl/$NiSi_2$/Si(111) and Tl/Si(111). When 1.0 ML of Ni is deposited followed by annealing at 300°C, a homogeneous highly-ordered Tl/$NiSi_2$/Si(111) surface forms (fig. 1(d)). The same formation routine can be used with Pb [6] and In monolayers as stabilizers of $NiSi_2$ layer.

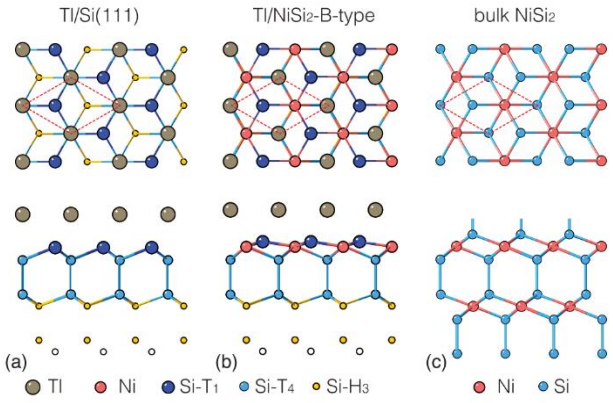


***Fig. 2.*** *Atomic ball-and-stick models of (a) initial Tl/Si(111) surface, (b) Tl/$NiSi_2$/Si(111) surface and (c) $NiSi_2$ bulk crystal. Tl atoms are shown by gray balls, Ni atoms by red balls and Si atoms by balls and circles of different sizes and colors (dark blue, light blue, yellow and white) depending on the site and atomic layer. The 1×1 unit cells are outlined by dashed red rhombuses.*

Nickel atoms were found to intercalate Tl layer upon deposition and to reside in the interstitial sites inside the first silicon bilayer of bulk-like-terminated Si(111)1×1 surface (fig.2 (b)). The interstitial positions almost coincide with the bulk $NiSi_2$ atomic positions thus forming $NiSi_2$ single layer (fig.2 (c)).

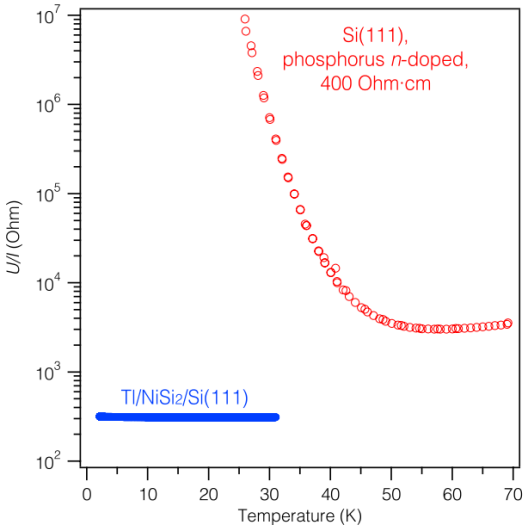


***Fig. 3.*** *Temperature dependence of sheet resistance of the Tl/$NiSi_2$/Si(111) sample (blue diamonds) in comparison with that of the bare Si(111) substrate (red circles).*

Angle-resolved photoemission spectroscopy show that formation of $NiSi_2$ single layer enhance metallicity of the surface regardless of the stabilizing element (Tl, Pb or In). Metallic character was also confirmed by the *in situ* transport measurements with four-point-probe technique, whose results are presented in figure 3. It can be seen that in contrast to the bare Si(111) substrate, the Tl/$NiSi_2$/Si(111) sample demonstrates a metallic-type conductivity down to 2.0 K.

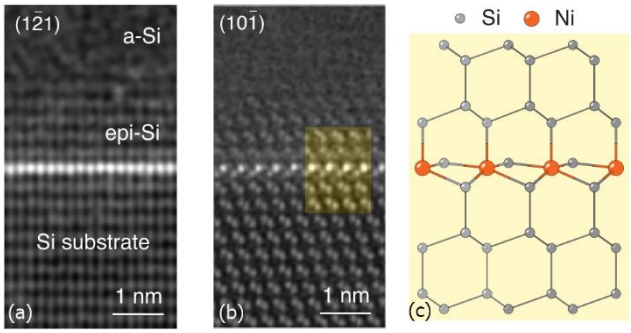


***Fig. 4.*** *High-resolution transmission electron microscopy characterization of the formed Si/$NiSi_2$/Si(111) delta-structure: (a) - (12$\bar{1}$) cut cross-section sample, (b) - (10$\bar{1}$) cut cross-section sample. (c) - ball-and-stick model of the $NiSi_2$ delta-layer.*

Finally room temperature Si deposition onto Tl-stabilized surface monolayer $NiSi_2$ was found to facilitate formation of embedded by Si crystalline matrix monolayer $NiSi_2$, or in other words $NiSi_2$ delta layer in silicon [7]. Figure 4 contain high-resolution transmission electron microscopy images of two different cross-sections (a) and (b) of formed delta layer along with atomic model (c). Such $NiSi_2$ delta-layer demonstrates advanced values of conductivity and carrier mobility (as was shown by *ex situ* low-temperature conductivity and Hall measurements) and highly stable in air making it almost ideal model system for exploring transport through a single-atomic-layer metal.

## 4. Conclusions

Single layer $NiSi_2$ was fabricated on Si(111) surface and as embedded delta-type layer inside Si crystal matrix for the first time. Tl, In or Pb monolayers were essential elements required for its formation and stabilization. *Ex situ* and *in situ* low-temperature conductivity measurements and angle-resolved photoemission spectroscopy show that single layer $NiSi_2$ exhibits metallic properties.

## Acknowledgements

The work was supported by the RSF Grant 19-12-00101-П. The calculations were conducted using the equipment of Shared Resource Center “Far Eastern Computing Resource” IACP FEB RAS (https://cc.dvo.ru).

## References

[1] R. T. Tung, J. M. Gibson, and J. M. Poate. Phys. Rev. Lett. 50(1983)429.
[2] [H. von Känel. Mater. Sci. Rep. 8(1992)193 – 269.
[3] J. C. Hensel, R. T. Tung, J. M. Poate, and F. C. Unterwald. Appl. Phys. Lett. 44(1984)913.
[4] Y. Hoshino, T. Nishimura, Y. Taki, Y. Asami, K. Sumitomo and Y. Kido. Surf. Sci. 511(2002)112.
[5] L.V. Bondarenko, et al. 2D Materials. 7(2020)025009.
[6] L.V. Bondarenko et al. Surface Science,716(2022)121966.
[7] L.V. Bondarenko et al., ACS Nano 15, 12(2021) 19357-19363.

Sixth Asian School-Conference on Physics and
Technology of Nanostructured Materials
Vladivostok, Russia, 25 – 29 April, 2022

**I.o.01**

# Morphological transformations on Si(111) surface induced by (√3×√3)-Sn reconstruction formation

A.S. Petrov*[,1,2], A.I. Vergules[1,2], D.I. Rogilo[1], D.V. Sheglov[1], A.V. Latyshev[1,2]

[1] Rzhanov Institute of Semiconductor Physics of SB RAS, 13 pr. Lavrentieva, Novosibirsk 630090, Russia
[2] Novosibirsk State University, 2 Pirogova St., Novosibirsk 630090, Russia

*e-mail: alexey_petrov@isp.nsc.ru

**Abstract.** We report *in situ* ultrahigh vacuum reflection electron microscopy and *ex situ* atomic force microscopy study of mass transport and morphological transformations on the Si(111) surface induced by the adsorption of ~1/3 ML Sn surfactant layer forming (√3×√3)-Sn reconstruction. The formation of pure (√3×√3)-Sn structure during Sn deposition at T<650°C leads to Si ilands nucleation, while the formation of a mosaic phase of (√3×√3)-Sn structure with a mix of Sn and Si atoms at T>650°C provides Sn/Si(111) interface with wide atomically flat terraces. The increased Si mass transport within the disordered Sn layer during desorption/electromigration-induced "1×1"-Sn ⇒ (√3×√3)-Sn phase transition entails strong roughening of the surface morphology.

## 1. Introduction

Being in the same group with Si and Ge elemental semiconductors, tin is one of the most widely used metals in present Si- and Ge-based epitaxial technologies. The adsorbed on the Si(111) surface 1/3 ML Sn coverage (1 ML = $7.8\times10^{14}$ cm$^{-2}$) acts as a surfactant layer: it enhances surface diffusion and suppresses 2D island nucleation during Ge/Si [1] or Si/Si [2] epitaxial growth. Sn surfactant layer on the Si(111) surface forms by direct 1/3 ML Sn deposition inducing (7×7) ⇒ (√3×√3)-Sn structural transition [3] or by annealing of pre-deposited 1 ML Sn coverage with following desorption-induced "1×1"-Sn ⇒ (√3×√3)-Sn structural transition [4]. However, impurity-induced structural transitions also lead to roughening of the growth interface during the redistribution of Si surface atoms [5]. Therefore, the formation of Sn/Si(111) interfaces optimal for the following epitaxial growth requires detailed information about the atomic processes during Sn-induced structural transitions, especially in the temperature range 300–700°C being typical for Ge/Si and Si/Si epitaxy [1,2,6]. Recently, we have reported that (7×7) ⇒ (√3×√3)-Sn structural transition at T > 700°C is followed by monatomic step shift, while Sn electromigration induces "1×1"-Sn ⇔ (√3×√3)-Sn due to Sn coverage redistribution [7]. In this work, using *in situ* ultrahigh vacuum reflection electron microscopy (UHV REM) and *ex situ* atomic force microscopy (AFM) we reveal morphological transformations on the Si(111) surface after the formation of (√3×√3)-Sn surfactant layer induced by Sn deposition, desorption, and electromigration at substrate temperatures 600–850°C.

## 2. Experiment

The experiments on Sn deposition were carried out by *in situ* UHV REM. Specimens with 8×1.0×0.4 mm dimensions were cut from phosphorus-doped Si(111) wafers with 0.01°–0.3° miscut angles and 0.3Ω×cm resistivity. To remove a native oxide layer and obtain an atomically clean surface, the samples were annealed at 1300°C for about 5 min by AC (50 Hz) passing before the experiments. The sample surface morphology with step bunches, straight steps, and terraces of moderate width (up to 10 μm) was created in UHV REM using step bunching by DC (electric field strength U = 70 V/cm) resistive heating at 1050–1300°C. Sn was deposited from an embeddable evaporator (tungsten filament wetted with molten Sn and heated by DC) at substrate temperatures 500–850°C. All morphological transformations on the Sn/Si(111) surface were observed and recorded by *in situ* REM technique. Due to a small angle of electron beam incidence onto the sample surface, REM images are foreshortened by ~50 times along beam incidence which distorts the shape of all surface morphology features. Following analysis of Sn/Si(111) morphology was carried out by *ex situ* AFM technique in air.

## 3. Results and discussions

At temperatures up to 650°C the (7×7) ⇒ (√3×√3)-Sn structural transition induced by 1/3 ML Sn deposition is followed by nucleation of two-dimensional (2D) growth islands (Fig. 1b). These 2D islands are assumed to be formed from Si adatoms that appeared on the Si(111) surface after (7×7) reconstruction destruction. The top layer of the initial Si(111)-(7×7) surface contains 102 atoms per (7×7) unit cell, but the formation of √3-Sn reconstruction requires the redistribution of the Si(111) substrate top layer atoms under Sn adsorption layer to the (1×1) bulk termination with 98 atoms per the area of (7×7) unit cell. This means that four Si atoms per (7×7) unit cell (or ≈ 0.08 ML) are released to the terraces during the (7×7) ⇒ (√3×√3)-Sn structural transition. Further AFM analysis of the Si(111)-(√3×√3)-Sn surface has shown that nucleated 2D islands cover 4% of the terrace area, which exactly corresponds to 0.08 ML Si coverage. 2D island nucleation does not occur on the <1 mkm width terraces, where Si atoms can reach the step edges during diffusion on the terraces at temperatures up to 650°C.

At temperatures above 650°C, Sn deposition onto Si(111)-(7×7) surface leads to an increase with temperature monatomic step shift in the step-up direction (Fig.1c–d). The temperature dependence Si atoms released on the terrace after step shift correlates with the reduction of Sn coverage required for (√3×√3)-Sn reconstruction formation at a temperature increase. Si atoms detached from steps mix with deposited Sn atoms and form mosaic phase of (√3×√3)-Sn reconstruction [7]. At T>650°C, in presence of Sn coverages ≤1/3 ML the adsorbed Si atoms diffuse to the longer distance and without nucleation of 2D islands can attach to the nearest step edges: vacancy islands (indicated

by black arrows in Fig. 1c) vanished after (7×7) ⇒ (√3×√3)-Sn structural transition. Thus, an Sn/Si(111) interface with >1 mkm atomically flat terraces can be obtained at the mosaic (√3×√3)-Sn phase formation.

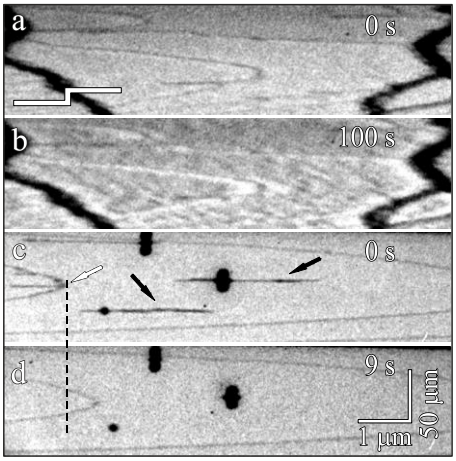


***Fig. 1.*** *In situ REM images of the Si(111) surface before and after (7×7) ⇒ √3-Sn structural transition induced by Sn deposition at (a,b) 600°C and (c,d) 800°C.*

The morphology changes on the Si(111) surface are most pronounced at (√3×√3)-Sn ⇔ "1×1"-Sn phase transitions, especially at T≥800°C in conditions of Sn desorption and DC-induced electromigration. With further Sn deposition up to 1.1 ML (Fig.2b) monatomic step shift was observed during the (√3×√3)-Sn ⇒ "1×1"-Sn structural transition and upon its completion: step 1 noticeably shifted towards the overlying step bunch and partially attach to it. In the absence of an external Sn flux, a reverse "1×1"-Sn ⇒ (√3×√3)-Sn structural transition being a result of electromigration and desorption occurs [7]. After this transition, only step 3 shifted to the overlying step bunch is observed on the surface (Fig.2c), while steps 2 and 4 were attached to the ascending and descending step bunches respectively. This indicates a strong mass transport within the disordered "1×1"-Sn layer not only of Sn atoms but also of Si atoms. In addition, during all stages of formation and disappearance of the disordered "1×1"-Sn phase, a successive decrease of the step bunches width occurs due to the clustering of atomic steps within them.

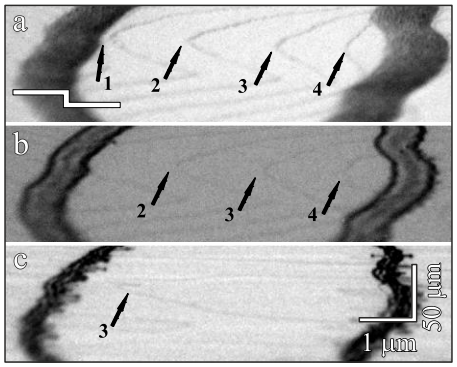


***Fig. 2.*** *(a) Clear Si(111)-(7×7) surface, (b) Si(111)-"1×1"-Sn surface with 1.1 ML Sn coverage, (c) Si(111)-(√3×√3)-Sn surface after Sn desorption and electromigration. Step-down DC heating, T=800°C.*

Fig. 3 shows AFM image of the Si(111)-(√3×√3)-Sn surface after (√3×√3)-Sn ⇔ "1×1"-Sn phase transitions and further quenching to the room temperatures. The step edges have a torn structure different from the $[\bar{1}\bar{1}2]$-type faceting of the step edges on the clean Si(111)-(7×7) surface. There are a lot of 2D islands near the steps (1 in Fig. 3), which are assumed to be part of the steps before Sn-induced structural transitions, and there are vacancy islands on the terraces (2 in Fig. 3). The presence of surfactant coverage is considered to reduce energy barriers for atoms to attach/detach to the step edge [8]. The "1×1"-Sn domains displacing under DC-induced electromigration entail detaching of Si atoms from the step, which disorders and ruins the step edge and leads to their shift in step-up direction. The Si atoms migrating over the surface within "1×1"-Sn disordered phase can further attach to the steps, which causes the shift of some monatomic steps in the step-down direction.

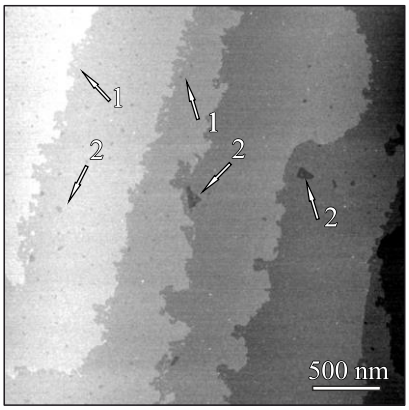


***Fig. 3.*** *AFM image of Si(111)-(√3×√3)-Sn surface after electromigration-induced "1×1"-Sn ⇒ (√3×√3)-Sn phase transition.*

## 4. Conclusions

In this work, we have presented the study of the Si(111)-(√3×√3)-Sn surface formation suitable for further Sn-induced surfactant epitaxy. Our observations show that the formation of atomically flat Si(111)-(√3×√3)-Sn interface with wide atomically flat terraces requires Sn deposition at T>650°C, while at lower temperatures 2D island nucleation occurs. Increased Si mass transport during reverse "1×1"-Sn ⇒ (√3×√3)-Sn phase transition strongly roughen the final Si(111)-(√3×√3)-Sn surface and make it unsuitable for further growth of thin epitaxial layers.

## Acknowledgements

This work was performed on the equipment of CKP "Nanostruktury" and was supported by Russian Science Foundation [grant number 19-72-30023].

## References

[1] A. E. Dolbak, B. Z. Olshanetsky. Cent. Eur. J. Phys. **6**(2008)634.
[2] S. Iwanari, K. Takayanagi. Thin Solid Films **119**(1992)229.
[3] T. Ichikawa. Surf. Sci. **140**(1984)37.
[4] C. Törnevik, M. Gijthelid, M. Hammar, U. O. Karlsson, Surf. Sci. **314**(1994)179.
[5] S. Hasegawa, R. G. Ryland, E. D. Williams. Appl. Phys. Lett. **65**(1994)2609.
[6] A. S. Petrov, D. I. Rogilo, D. V. Sheglov, A. V. Latyshev, J. Cryst. Growth, **531**(2020)125347.
[7] D. I. Rogilo, S. V. Sitnikov, E. E. Rodykina, A. S. Petrov, S. A. Ponomarev, L. I. Fedina, A. V. Latyshev. Crystallogr. Reports. **66**(2021)570.
[8] I. Markov. Surf. Sci. **429**(1999)102.

Sixth Asian School-Conference on Physics and
Technology of Nanostructured Materials
Vladivostok, Russia, 25 – 29 April, 2022



# Surface conductivity study of ultrathin Li layers on the reconstructed Si(111) surface

D.A. Tsukanov*[,1,2], M.V. Ryzhkova[1]

[1] Institute of Automation and Control Processes FEB RAS , 5 Radio St., Vladivostok 690041, Russia
[2] Far Eastern Federal University, 8 Sukhanova St., Vladivostok 690950, Russia

*e-mail: tsukanov@iacp.dvo.ru

**Abstract.** In this work the properties of the reconstructed Si(111) surface after lithium deposition were studied. The new surface reconstructions have been discovered that represent two-dimensional alloys that are composed of adsorbed lithium and parent species. For the two-dimensional ordered as well as disordered metallic layers the surface conductivity measurements were conducted before and after lithium dosing. It was shown that using the surface reconstruction as an intermediate layer between the Si(111) substrate and adsorbed lithium enables to control the growth mode of ultrathin films on the surface.

## 1. Introduction

Last time the study of the interaction of alkali atoms with metal and semiconductor surfaces has been of great interest [1-6]. This interaction occurs through charge transfer between the adsorbed atoms and the substrate surface and is caused by the low electronegativity of alkali metal atoms, which in this case play the role of an electron donor. From this point of view, the study of the surface conductivity of the interacting adsorbate-substrate system will make it possible to estimate changes in the electrical conductivity of the near-surface region of the substrate caused by charge transfer effects, which are strongly related to the structure of the initial substrate surface and its electronic states. Thus, by forming a suitable initial surface reconstruction of the substrate, as well as by controlling the concentration of adsorbed atoms, it becomes possible to modify the structural and electronic properties of both the substrate surface and its near-surface layer.

In this work, the possibility of controlled changes in the surface conductivity of a Si(111) substrate with surface reconstructions and adsorbed lithium measured by the in situ four-probe method, together with the use of low energy electron diffraction to observe the crystal structure of the surface is investigated.

## 2. Experiment

The experiments were carried out in a RIBER DEL-300 ultrahigh vacuum chamber with a base pressure of ~$10^{-10}$ Torr. The chamber is equipped with low energy electron diffraction (LEED) and a four-probe head for electrical measurements. The head is placed on a retractable manipulator with four tungsten probes located at the corners of a square with an inter-probe distance of 0.6 mm. The surface conductivity of the samples was measured under ultrahigh vacuum conditions at room temperature. Four-terminal measurements were performed using a Keithley 6221 DC and AC current source and a Keithley 2182A nanovoltmeter. To suppress contribution from thermopower sources, for each data point, the DC current was set in one direction and then inverted. The samples were rectangular silicon wafers 15 × 5 × 0.45 $mm^3$ in size, doped with phosphorus, with a resistivity of 300–1700 Ω cm. The surface of the sample was cleaned by flash heating up to 1250°C by passing an alternating current. Lead and gallium were evaporated from a tantalum cell, gold was evaporated from resistively heated tungsten filament, and a getter dispenser from SAES Getters was used as a source of lithium. The deposition rate of the adsorbed material was calibrated using LEED patterns from a reconstructed surface with a known concentration of adsorbate atoms (one monolayer (ML) corresponds to an atomic concentration of $7.8\times10^{14}$ $cm^{-2}$ for a non-reconstructed Si(111) surface). In the case of lithium deposition onto the Au/Si(111) surface the Si(111)√3×√3-Au reconstruction was used as a template for the study of structural and electrical changes. In the experiment for lithium deposition onto the Pb/Si(111) surface as a bared surface reconstructions the Si(111)1 × 1-Pb and the Si(111)√3×√3-Pb stripped incommensurate (SIC) phases were used. In the case of lithium deposition onto the Ga/Si(111) surface there are two bared surface reconstructions have been chosen: Si(111)√3×√3-Ga (gallium coverage 0.3 ML) and Si(111)6.3√3×6.3√3-Ga (gallium coverage 1 ML).

## 3. Results and discussions

Adsorption of about 0.1 ML of lithium onto the Si(111)√3×√3-Au reconstructed surface have been found to induce pronounced changes in structural and electrical properties of the sample. Li deposition on this surface held at room temperature results in gradual destruction of the initial surface structure while after heating at about 350°C this surface developes into the so-called homogeneous (highly ordered) *h*-√3×√3-(Au,Li) surface. The new surface reconstructions have been found in the (Pb,Li)/Si(111) and the (Ga,Li)/Si(111) systems, which are ordered two-dimensional alloys of lithium and lead or gallium atoms. Thus, according to the data obtained using LEED, the deposition of submonolayer doses of lithium on the SIC-Pb surface leads to the formation of a 4 × 1 surface structure (at a Li dose of up to ~0.25 ML), and then a 3√3 × 3√3 structure (at a Li dose of about ~0.3 ML). Further deposition of Li leads to the appearance of a 2 × 2 surface structure. In the case of lithium deposition onto the Ga/Si(111) surface several new surface reconstruction were observed: √31×√31 (at a Li dose of 0.3-1.2 ML and 400°C heating) (Fig. 1), 8×8 (1.2 ML Li and 200-300°C heating) and others. These results were summarized in the phase diagrams constructed separately for each submonolayer system studied.

It is shown that such changes in the surface structure well correlate with changes of the surface conductivity of the substrate. For example, Li deposition on Si(111)7x7

and Si(111)β-√3×√3-Au surfaces held at room temperature results in slight changes in the surface conductance while after heating at about 350ºC this surface develops into the *h*-√3×√3-(Au,Li) surface with high conductance (Fig. 2). As was reported earlier [2,7] during alkali adsorption electronic filling of surface state band is occurring leading to the surface conductivity increasing. In such manner, electrical measurements reveal a strong dependence of initial reconstruction on the behavior of conductance. These results are connected with peculiarities in structural and electronic properties of observed reconstruction and will be discussed in the paper. The report presents the results of conductivity measurements after adsorption of the lithium atoms on the reconstructed surfaces Si(111)1x1-Pb, Si(111)√3x√3-Pb (Pb coating 0.33 ML) and Si(111)√3x√3-Pb (SIC) at both room and elevated temperatures. In addition, the effect of lithium dosing of a disordered lead metal film on the Si(111)7x7 surface is considered.

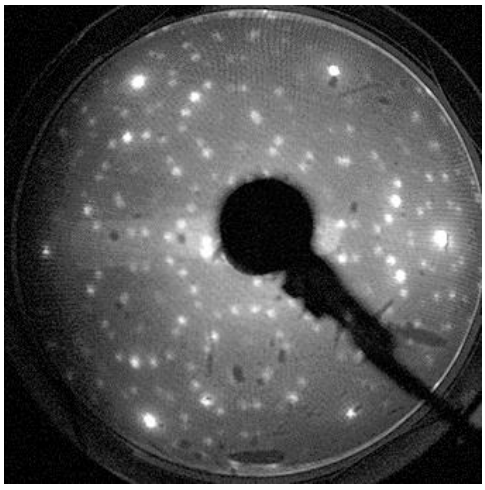

***Fig. 1.*** *LEED √31×√31 pattern at 56 eV from 0.6 ML of Li on Si(111) √3×√3-Ga surface deposited at 400ºC.*

The report discusses possible mechanisms of interaction of lithium atoms with surface reconstructions on Si(111), depending on the initial surface structure and concentration of adsorbed alkali metal atoms, as well as the transport of charge carriers in such structures. In the course of the experiments, it was found that the adsorption of lithium on a semiconductor surface has little effect on the electrical conductivity of the substrate, while several stages of interaction of adsorbed atoms with the film are clearly observed on the metal surface: first, a decrease in electrical conductivity is observed due to the formation of dipoles on the surface, then at more than 1 monolayer of adsorbed lithium is coated, a metal film with high electrical conductivity is formed. It should be noted that the use of surface reconstructions as an intermediate layer between the Si(111) substrate and deposited lithium makes it possible to control the growth style of the lithium metal film, layer by layer or island, and determines the optimal conditions for the formation of such structures.

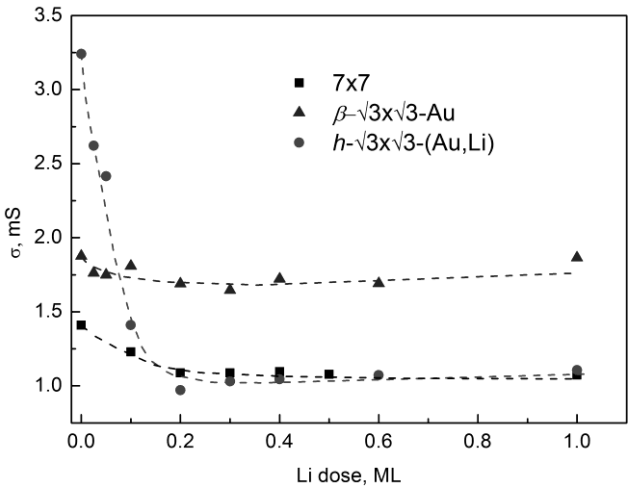


***Fig. 2.*** *Changes in surface conductance after Li-dosing of Si(111)7×7 (squares), Si(111)β-√3×√3-Au (triangles) and Si(111)h-√3×√3-(Au,Li) surface reconstructions at room temperature.*

## 4. Conclusions

Structural and electrical properties of the reconstructed Si(111) surface after lithium deposition were studied. The new surface reconstructions have been discovered that represent two-dimensional alloys that are composed of adsorbed lithium and parent species. For the two-dimensional ordered as well as disordered metallic layers the surface conductivity measurements were conducted before and after lithium dosing. It was shown that using the surface reconstruction as an intermediate layer between the Si(111) substrate and adsorbed lithium enables to control the growth mode of ultrathin films on the surface

## Acknowledgements

This work was done due to financial support from Russian Foundation for Basic Research (grant No. 20-02-00497).

## References

[1] M. Caragiu, S. Finberg. Journal of Physics: Condensed Matter **17**(2005)R995.
[2] S.V. Eremeev, E.N. Chukurov, D.V. Gruznev, A.V. Zotov, A.A. Saranin. Journal of Physics: Condensed Matter **27**(2015)305003.
[3] M. Gurnett, L.J. Holleboom, H.M. Zhang, L.S.O. Johnsson. Surf. Sci. **603**(2009)727.
[4] C. Weindel, H. J. Jänsch, G. Kirchner, H. Kleine, J. J. Paggel, J. Roth, H. Winnefeld, and D. Fick. Physical Review B **71**(2005)115318.
[5] R. D. Diehl, R. McGrath. Journal of Physics: Condensed Matter **9**(1997)951.
[6] T. Aruga, Y. Murata. Progress in Surface Science **31**(1989)61.
[7] L.V. Bondarenko, A.V. Matetskiy, A.A. Yakovlev, A.Y. Tupchaya, D.V. Gruznev, M.V. Ryzhkova, D.A. Tsukanov, E.A. Borisenko, E.N. Chukurov E.N., A.V. Zotov, A.A. Saranin. Journal of Physics: Condensed Matter **26**(2014)055009.

# Application of convolutional neural networks for the study of spin models

A.O. Korol[1,2], A.E. Rybin[1,2], D.Yu. Kapitan[1,2], E.V. Vasiliev[1,2], M.A. Padalko[1,2], A.V. Perzhu[1], R.A. Volotovskiy[1,2], A.G. Makarov[1,2], Yu.A. Shevchenko[1,2], K.S. Soldatov[1,2], V.Yu. Kapitan[*,1,2], K.V. Nefedev[1,2]

[1] Far Eastern Federal University, FEFU Campus, 10 Ajax Bay, Russky Island, Vladivostok, 690922, the Russian Federation
[2] Institute of Applied Mathematics, Far Eastern Branch, Russian Academy of Science, Vladivostok, 690041, 7 Radio St., the Russian Federation

*e-mail: kapitan.vyu@dvfu.ru

**Abstract.** The authors describe a method for determining the critical point of a second order phase transitions using a convolutional neural network based on the Ising model on a square lattice. Data for training and analysis were obtained using Monte Carlo simulations. The neural network was trained on the data corresponding to the low-temperature phase, that is a ferromagnetic one and high-temperature phase, that is a paramagnetic one, respectively. After training, the neural network analyzed input data from the entire temperature range: from 0.1 to 5.0 (in dimensionless units J) and determined the Curie point $T_c$.

## 1. Introduction

Nowadays, methods and techniques Deep Learning are being used in various scientific areas. They help to automatize calculations without losing in quality [1]. In this paper the applying of convolutional neural network was considered in frame of problems from statistical physics and computer simulation of magnetic films. A convolutional neural network (CNN) was used to determine critical Curie point for Ising model on 2D square lattice. Obtained results were compared with classical Monte-Carlo methods and exact solution. Systems of various lattice sizes and the influence of the size effect on the results' accuracy were considered.

## 2. Research description

The Ising model is the simplest of the mathematical models of statistical physics used to study phase transitions and critical points with an exact solution: $\frac{T_c}{J} = \frac{2}{ln(1+\sqrt{2})} = 2.269$, with which the data obtained by other methods were compared. We used the Hamiltonian for a square Ising spin lattice with four nearest neighbors and periodic boundary conditions. This mathematical model is a set of discrete variables (values of the magnetic moments of atomic spins), which can take one of two values: $S_i = \pm 1$, corresponding to one of two states. The Ising spin system has the size $N = L \times L$ and the Hamiltonian:

$$H = -J \sum_{<i,j>} S_i S_j \quad (1)$$

We used configurations of spin systems obtained at different simulation parameters for the training and subsequent classification of them in a neural network. To date, the most accurate analysis results are demonstrated by neural networks based on convolutional architecture. We used the TensorFlow library to create a convolutional neural network and to classify our spin systems to different phases.

In our research, we have reduced the problem of determining the phases of spin systems to the problem of image classification - in fact, to the main problem area in which neural networks are used. For recognising images, CNN accepts them in the RGB format as a three-dimensional matrix. In our case, the convolutional neural network received as input a three-dimensional array representing the components of a spins.

Different sets of input data of the neural network obtained with different parameters of the Metropolis algorithm for systems of 10×10 and 20×20 Ising spins were used. The obtained data will be used to select the optimal simulation parameters, which will be further used in the study of more complex spin systems. A comparative analysis is carried out with the results of MC modelling and the exact solution of Onsager.

## 3. Conclusion

In paper, we described a method for determining the critical point of a second order phase transitions using the convolutional neural network based on the Ising model on a square lattice.

The application of convolutional neural networks to determine the critical temperature of a second-order phase transition in comparison with performed MC simulations and known solutions. As it was shown above CNN could be successfully used to such problems by reducing them to the problem of classifying spin states at different temperatures. The dependence on the number of Monte Carlo steps and the sample size for the accuracy of training the network and its subsequent application is shown in comparison with the Metropolis algorithm. Systems of various sizes and the influence of the size effect on the accuracy of the results are considered.

## Acknowledgements

This work was supported by a grant from the President of the Russian Federation for State Support of Leading Scientific Schools of the Russian Federation No. NSh-2559.2022.1.2.

## References

[1] G. Carleo et al., Reviews of Modern Physics. 91(4), 045002 (2019).

Sixth Asian School-Conference on Physics and
Technology of Nanostructured Materials
Vladivostok, Russia, 25 – 29 April, 2022



# The axial next-nearest neighbor 2D Ising model polynomial solution

M.A. Padalko[*,1,2], K.V. Nefedev[1,2]

[1] Institute of Applied Mathematics, Far Eastern Branch, Russian Academy of Science, 690041 Vladivostok, Russia
[2] Far Eastern Federal University, 8 Sukhanova St., Vladivostok 690950, Russia

*e-mail: padalkoma1992ofacc@gmail.com

**Abstract.** The exact polynomial solution of the axial next-nearest neighbor 2D Ising model (ANNNI) is obtained. The underlying method is based on the Vdovichenko approach of loops building. The spin representation reduces to the loop representation and a polynomial exact solution is constructed. The method can be applied in the sphere of the machine learning, the spin glass theory.

## 1. Introduction

In the ANNNI model the nearest spins and the 2d-order spins along one diagonal interact. The scheme of the interaction of ANNNI model is given in Fig. 1. The ANNNI model can describe materials with components interacting via competing short-range attractive and long-range repulsive interactions [1].

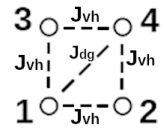


allowed bonds:
spin 1 - spin 2, spin 3 - spin 4, spin 1 - spin 3,
spin 2 - spin 4, spin 1 - spin 4

***Fig. 1.*** *The ANNNI model.*

## 2. The Method

To obtain an exact solution, it is necessary to transfer from the partition function in the spin representation to the loop representation [2]:

$$Z(T)=\sum_{\{\sigma_1,\ldots,\sigma_N\}}\left(\prod_{<i,j>_{vh}}^{N_{bond,vh}}\left(\exp\left(\frac{-J_{vh}\sigma_i\sigma_j}{T}\right)\right)\cdot\prod_{<k,l>_{dg}}^{N_{bond,dg}}\left(\exp\left(\frac{-J_{dg}\sigma_k\sigma_l}{T}\right)\right)\right)$$

$$Z(T)=2^N ch\left(\frac{J_{vh}}{T}\right)^{N_{bond,vh}}\cdot ch\left(\frac{J_{dg}}{T}\right)^{N_{bond,dg}}\cdot\sum_C\left(th\left(\frac{-J_{vh}}{T}\right)^{l_{vh}(C)}\cdot th\left(\frac{-J_{dg}}{T}\right)^{l_{dg}(C)}\right)$$

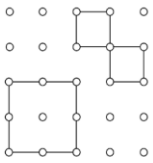

***Fig. 2.*** *The reducing to the loop representation. Here N – a number of spins, Nbond,vh – a number of vertical and horizontal bonds, Nbond,dg – a number of digonal bonds, T – temperature, Jvh – vertical and horizontal coupling constant, Jdg – diagonal coupling constant.*

For *Z(T)* one can get the follow expression [3]:

$$Z(T)=2^N ch\left(\frac{J_{vh}}{T}\right)^{N_{bond,vh}} ch\left(\frac{J_{dg}}{T}\right)^{N_{bond,dg}}\sqrt{det(I-U)},$$

where *U* is the *6N* x *6N* matrix *U* is given in the Table I and Table II, *I* is the unity matrix.

***Table I.*** *Elements of the 6N x 6N matrix with elements Uiv,jμ where i and j run over N spins, v and μ over possible directions. We have 6 possible directions in the ANNNI model.*

| $\nu$ | corresp. direc-tion | $\mu$ | corresp. direc-tion | $U_{i\nu,j\mu}$ |
|---|---|---|---|---|
| 3 | ← | 4 | ↓ | $\delta_{x_i,x_j}\delta_{y_i-1,y_j}\cdot e^{\frac{i\pi}{4}}\cdot th(\frac{J_{ver}}{T})$ |
| 1 | → | 4 | ↓ | $\delta_{x_i,x_j}\delta_{y_i-1,y_j}\cdot e^{-\frac{i\pi}{4}}\cdot th(\frac{J_{ver}}{T})$ |
| 6 | ↙ | 4 | ↓ | $\delta_{x_i,x_j}\delta_{y_i+1,y_j}\cdot e^{\frac{i\pi}{8}}\cdot th(\frac{J_{ver}}{T})$ |
| 5 | ↗ | 4 | ↓ | $\delta_{x_i,x_j}\delta_{y_i+1,y_j}\cdot e^{-\frac{i3\pi}{8}}\cdot th(\frac{J_{ver}}{T})$ |
| 1 | → | 5 | ↗ | $\delta_{x_i+1,x_j}\delta_{y_i+1,y_j}\cdot e^{\frac{i\pi}{8}}\cdot th(\frac{J_{diag}}{T})$ |
| 3 | ← | 5 | ↗ | $\delta_{x_i+1,x_j}\delta_{y_i+1,y_j}\cdot e^{-\frac{i3\pi}{8}}\cdot th(\frac{J_{diag}}{T})$ |
| 4 | ↓ | 5 | ↗ | $\delta_{x_i+1,x_j}\delta_{y_i+1,y_j}\cdot e^{\frac{i3\pi}{8}}\cdot th(\frac{J_{diag}}{T})$ |
| 2 | ↑ | 5 | ↗ | $\delta_{x_i+1,x_j}\delta_{y_i+1,y_j}\cdot e^{-\frac{i\pi}{8}}\cdot th(\frac{J_{diag}}{T})$ |
| 3 | ← | 6 | ↙ | $\delta_{x_i-1,x_j}\delta_{y_i-1,y_j}\cdot e^{\frac{i\pi}{8}}\cdot th(\frac{J_{diag}}{T})$ |
| 1 | → | 6 | ↙ | $\delta_{x_i-1,x_j}\delta_{y_i-1,y_j}\cdot e^{-\frac{i3\pi}{8}}\cdot th(\frac{J_{diag}}{T})$ |
| 2 | ↑ | 6 | ↙ | $\delta_{x_i-1,x_j}\delta_{y_i-1,y_j}\cdot e^{\frac{i3\pi}{8}}\cdot th(\frac{J_{diag}}{T})$ |
| 4 | ↓ | 6 | ↙ | $\delta_{x_i-1,x_j}\delta_{y_i-1,y_j}\cdot e^{-\frac{i\pi}{8}}\cdot th(\frac{J_{diag}}{T})$ |
| 1 | → | 3 | ← | 0 |
| 2 | ↑ | 4 | ↓ | 0 |
| 3 | ← | 1 | → | 0 |
| 4 | ↓ | 4 | ↑ | 0 |
| 5 | ↗ | 5 | ↙ | 0 |
| 6 | ↙ | 6 | ↗ | 0 |

We can consider models either with all different values *Jver*, *Jhor*, *Jdiag* or with *Jver*=*Jhor*=*Jvh*. Elements of the matrix U store information about all possible rotations of loops in all possible positions in the lattice.

Determinant can be computed for polynomial time (for example LU-method). So, we can compute statistical sum numerically for polynomial time as well. Knowing the partition function one can get the thermodynamic averages and phase diagrams.

## 4. Conclusions

The polynomial time algorithm has been developed for the ANNNI model. The important problem is the construction of the exact solution for the 2nd order Ising model. But in this case in the loop representation, we face the problem of the self-intersection of diagonal bonds. At least we can try to build any approximate solution.

***Table II.*** *Elements of the 6N x 6N matrix with elements Uiv,jμ where i and j run over N spins, v and μ over possible directions. We have 6 possible directions in the ANNNI model.*

| $\nu$ | corresp. direc-tion | $\mu$ | corresp. direc-tion | $U_{i\nu,j\mu}$ |
|---|---|---|---|---|
| 1 | $\rightarrow$ | 1 | $\rightarrow$ | $\delta_{x_i+1,x_j}\delta_{y_i,y_j} \cdot th(\frac{J_{hor}}{T})$ |
| 2 | $\uparrow$ | 2 | $\uparrow$ | $\delta_{x_i,x_j}\delta_{y_i+1,y_j} \cdot th(\frac{J_{hor}}{T})$ |
| 3 | $\leftarrow$ | 3 | $\leftarrow$ | $\delta_{x_i-1,x_j}\delta_{y_i,y_j} \cdot th(\frac{J_{ver}}{T})$ |
| 4 | $\downarrow$ | 4 | $\downarrow$ | $\delta_{x_i,x_j}\delta_{y_i-1,y_j} \cdot th(\frac{J_{ver}}{T})$ |
| 5 | $\nearrow$ | 4 | $\nearrow$ | $\delta_{x_i+1,x_j}\delta_{y_i+1,y_j} \cdot th(\frac{J_{diag}}{T})$ |
| 6 | $\swarrow$ | 4 | $\swarrow$ | $\delta_{x_i-1,x_j}\delta_{y_i-1,y_j} \cdot th(\frac{J_{diag}}{T})$ |
| 4 | $\downarrow$ | 1 | $\rightarrow$ | $\delta_{x_i+1,x_j}\delta_{y_i,y_j} \cdot e^{\frac{i\pi}{4}} \cdot th(\frac{J_{hor}}{T})$ |
| 2 | $\uparrow$ | 1 | $\rightarrow$ | $\delta_{x_i+1,x_j}\delta_{y_i,y_j} \cdot e^{-\frac{i\pi}{4}} \cdot th(\frac{J_{hor}}{T})$ |
| 6 | $\swarrow$ | 1 | $\rightarrow$ | $\delta_{x_i+1,x_j}\delta_{y_i,y_j} \cdot e^{\frac{i3\pi}{8}} \cdot th(\frac{J_{hor}}{T})$ |
| 5 | $\nearrow$ | 1 | $\rightarrow$ | $\delta_{x_i+1,x_j}\delta_{y_i,y_j} \cdot e^{-\frac{i\pi}{8}} \cdot th(\frac{J_{hor}}{T})$ |
| 1 | $\rightarrow$ | 2 | $\uparrow$ | $\delta_{x_i,x_j}\delta_{y_i+1,y_j} \cdot e^{\frac{i\pi}{4}} \cdot th(\frac{J_{ver}}{T})$ |
| 3 | $\leftarrow$ | 2 | $\uparrow$ | $\delta_{x_i,x_j}\delta_{y_i+1,y_j} \cdot e^{-\frac{i\pi}{4}} \cdot th(\frac{J_{ver}}{T})$ |
| 5 | $\nearrow$ | 2 | $\uparrow$ | $\delta_{x_i,x_j}\delta_{y_i+1,y_j} \cdot e^{\frac{i\pi}{8}} \cdot th(\frac{J_{ver}}{T})$ |
| 6 | $\swarrow$ | 2 | $\uparrow$ | $\delta_{x_i,x_j}\delta_{y_i+1,y_j} \cdot e^{-\frac{i3\pi}{8}} \cdot th(\frac{J_{ver}}{T})$ |
| 2 | $\uparrow$ | 3 | $\leftarrow$ | $\delta_{x_i-1,x_j}\delta_{y_i,y_j} \cdot e^{\frac{i\pi}{4}} \cdot th(\frac{J_{hor}}{T})$ |
| 4 | $\downarrow$ | 3 | $\leftarrow$ | $\delta_{x_i-1,x_j}\delta_{y_i,y_j} \cdot e^{-\frac{i\pi}{4}} \cdot th(\frac{J_{hor}}{T})$ |
| 5 | $\nearrow$ | 3 | $\leftarrow$ | $\delta_{x_i-1,x_j}\delta_{y_i,y_j} \cdot e^{\frac{i3\pi}{8}} \cdot th(\frac{J_{hor}}{T})$ |
| 6 | $\swarrow$ | 3 | $\leftarrow$ | $\delta_{x_i-1,x_j}\delta_{y_i,y_j} \cdot e^{-\frac{i\pi}{8}} \cdot th(\frac{J_{hor}}{T})$ |

## References


[1] Y. Hu, P. Charbonneau. Resolving the two-dimensional axial next-nearest-neighbour Ising model using transfer matrices. Phys. Rev. B **103** (2021) 094441.

[2] N. Vdovichenko. A calculation of the partition function for a plane dipole lattice, Sov. Phys.-JETP 20 (1965) 477–479.

[3] L. Saul, M. Kardar, The 2D +/-J Ising spin glass exact partition functions in polynomial time, Nuclear Physics **B 432** [FS], (1994) 641-667.

# *In situ* imaging of van der Waals epitaxy and sublimation of the $Bi_2Se_3$(0001) surface

S.A. Ponomarev[1,2], D.I. Rogilo[*,1], N.N. Kurus[1], L.S. Basalaeva[1], K.A. Kokh[1], A.G. Milekhin[1], D.V. Sheglov[1], A.V. Latyshev[1,2]

[1] Rzhanov Institute of Semiconductor Physics SB RAS, Acad. Lavrent'ev ave. 13, Novosibirsk 630090, Russia
[2] Novosibirsk State University, Pirogov Str. 2, Novosibirsk 630090, Russia

*e-mail: rogilo@isp.nsc.ru

**Abstract.** We have first visualized van der Waals epitaxy and sublimation of the $Bi_2Se_3$(0001) surface by *in situ* reflection electron microscopy. When $Bi_2Se_3$(0001) surface was exposed to a Se molecular beam (up to 0.1 nm/s) and heated to ~400°C, atomic steps on the surface move in the ascending direction, which corresponds to a congruent $Bi_2Se_3$ sublimation. We have found that, during the sublimation, grooves made by probe lithography act as sources of atomic steps and trigger self-organization of regularly-spaced zigzag atomic steps having 1 nm height on the $Bi_2Se_3$(0001) surface. The deposition of Bi onto the $Bi_2Se_3$(0001) surface at constant Se flux reversed the step flow direction. The deposition of other metals (In or Sn) under Se overpressure at $Bi_2Se_3$ temperatures of about 400°C led to van der Waals growth of a layered selenide ($In_2Se_3$ or $SnSe_2$) via 2D island nucleation followed by the screw-dislocation-driven formation of 3D islands.

## 1. Introduction

Layered 2D metal chalcogenides are promising materials for microelectronics, photonics, and photovoltaics [1], and nanostructures based on these materials have proved their outstanding performance as infrared photodetectors [2]. To grow high-quality heterostructures and superlattices, molecular beam epitaxy is used [3], but various defects are generated during the growth: point defects [4], twin domain boundaries [5], antiphase boundaries caused substrate's atomic steps [6]. This puts a demand for *in situ* microscopy investigation of surface processes and growth mechanisms [7].

## 2. Experiment

We used *in situ* reflection electron microscope (REM) equipped with two separate evaporators for Se and a metal (Bi, In, or Sn). Samples were prepared from $Bi_2Se_3$ single crystal by cleavage along (0001) plane into ~0.2 mm slabs that were cut into 8×3 mm pieces. Samples were heated resistively by passing a direct electric current. A detailed description of the REM experimental setup for $Bi_2Se_3$ substrates is described elsewhere [8].

*Ex situ* analysis of surface morphology was carried out by atomic force microscopy (AFM, Bruker Multimode 8). The same equipment was used for the creation of 15–30-nm-deep grooves by probe lithography. The crystal phase analysis of grown films was realized by *ex situ* Raman scattering measurements (XploRa Plus, Horiba, 532 nm laser).

## 3. Results and discussions

Figure 1a shows an *in situ* REM image of a $Bi_2Se_3$(0001) surface exposed to a Se molecular beam at ~400°C. The bright-contrast regions correspond to singular (0001) terraces separated by dark-contrast atomic steps. Figures 2b,c have been obtained at the same conditions 22 and 44 seconds later; the images show that the atomic steps move in ascending direction (to the left). We have observed neither change of terrace contrast nor three-dimensional (3D) Bi island nucleation after 30 nm sublimation and conclude thus that the $Bi_2Se_3$ surface does not decompose, and the observed sublimation is congruent. After *in situ* experiments, the samples were cooled to room temperature while Se deposition stopped at ~200°C. *Ex situ* AFM investigation of the $Bi_2Se_3$(0001) surface morphology shows that the wide contrast of the atomic steps is caused by their zigzag shape (figure 2). One can see in figure 2 1-nm-deep 2D vacancy islands that nucleated mostly at surface regions where step separation is great enough.

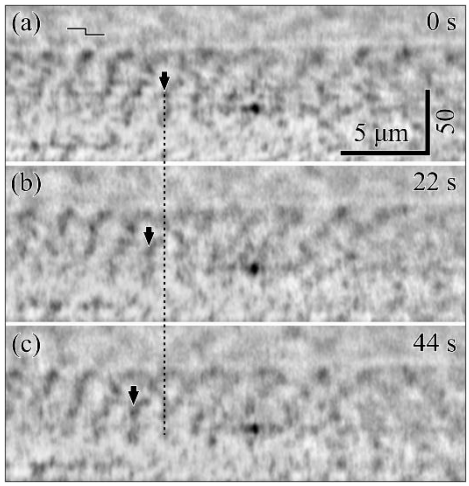


***Fig. 1.*** *REM images of the ascending step flow on the $Bi_2Se_3$(0001) surface during sublimation with a 0.022 nm/s rate.*

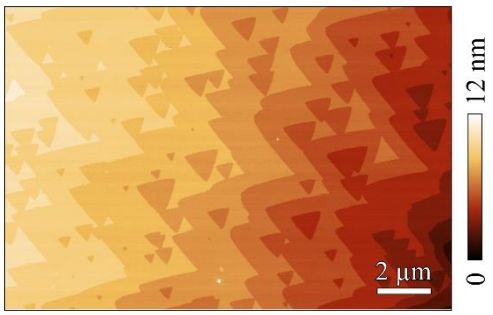


***Fig. 2.*** *AFM image of the $Bi_2Se_3$(0001) surface after sublimation.*

Figure 3a shows a REM image of a groove (a black vertical line) formed by probe lithography and a dark-contrast impurity particle serving as an immovable reference point. During $Bi_2Se_3$ sublimation at ~400°C, the

groove widens while many 2D vacancy islands nucleate, grow, and coalesce on the terraces (speckled black-and-white contrast marked with a white arrow in figure 3b) analogously to periodic island nucleation observed on a silicon surface during epitaxial growth [9] and etching [10]. After sublimation of 10 $Bi_2Se_3$ layers, one can see that the groove annealing has formed atomic steps and step bunches aligned along the groove (dark-contrast zigzag lines in figure 3c). The center of the groove remains visible in REM images and acts as a source of atomic steps: the groove deepens and generates new atomic steps that move in the ascending direction away from the source and attach to the step bunches. The ascending motion of the step bunches is accompanied by their decomposition into regularly-spaced 1-nm-high atomic steps at the distance of ~50–100 μm from the groove center. We used this phenomenon to create self-organized regular zigzag atomic steps on the $Bi_2Se_3$(0001) surface.

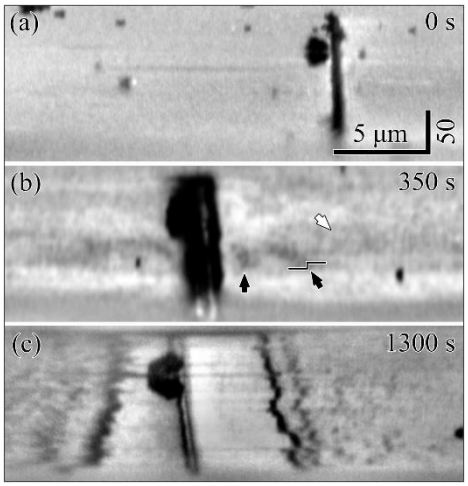


***Fig. 3.*** *Annealing of a groove on the $Bi_2Se_3$(0001) surface. 1-nm-high atomic steps and a region of vacancy island nucleation are marked with black and white arrows, respectfully.*

To study van der Waals epitaxy by *in situ* REM, a patterned $Bi_2Se_3$(0001) surface was exposed to Se molecular beam (≲0.1 nm/s) and heated to ~400°C. During this annealing, lithographically preformed grooves generated atomic steps that moved in ascending direction with a velocity corresponding to ~0.001 nm/s sublimation. After Bi deposition onset ($10^{-4}$–$10^{-2}$ nm/s in different experiments), the steps moved in descending direction. We observed no change in REM contrast of terraces and steps during this growth, and the reflection high-energy electron diffraction (RHEED) pattern remained the same, which authenticates that this layer-by-layer $Bi_2Se_3$ growth is epitaxial.

A similar experimental setup was used for *in situ* REM investigation of van der Waals heteroepitaxy. The deposition of In or Sn was carried out under Se overpressure (In:Se = 1:6–1:3, Sn:Se = 1:20–1:10) at substrate temperatures of about 400°C, which led to van der Waals growth of $In_2Se_3$ or $SnSe_2$, respectfully. The growth began with the nucleation of 2D islands and, at 3–5 nm film thickness, continued with a screw-dislocation-driven formation of 3D islands (figure 4). *Ex situ* Raman scattering measurements of the grown layers have shown vibrational modes that originate from the β-$In_2Se_3$, and $SnSe_2$ crystal phases.

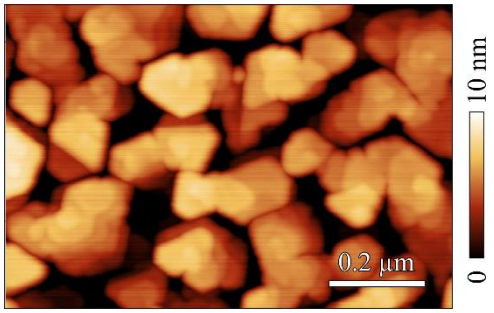


***Fig. 4.*** *AFM image of a 20-nm-thick $In_2Se_3$ film on the $Bi_2Se_3$(0001) surface.*

## 4. Conclusions

We have first visualized morphological transformations of the $Bi_2Se_3$(0001) surface by *in situ* REM during sublimation and van der Waals epitaxy. When $Bi_2Se_3$(0001) surface is exposed to Se molecular beam and heated to ~400°C, congruent sublimation triggers ascending motion of atomic steps. During the sublimation, 15–30 nm deep grooves preformed by probe lithography increase in all dimensions and act as sources of atomic steps having 1 nm height on the $Bi_2Se_3$(0001) surface. Simultaneous deposition of Se and metal (Bi, In, or Sn) at ~400°C induced van der Waals growth. *In situ* REM shows that the $Bi_2Se_3$ homoepitaxy with rates below ~0.01 nm/s proceed via descending step flow while the growth of layered β-$In_2Se_3$ and $SnSe_2$ on the $Bi_2Se_3$(0001) surface start with 2D island nucleation. Despite $Bi_2Se_3$ van der Waals epitaxy proceeds in layer-by-layer mode, the growth of $In_2Se_3$ and $SnSe_2$ switched to the formation of 3D islands after 3–5 nm film thickness. These results show that *in situ* REM technique can be applied to study real-time surface dynamics of the layered 2D materials during sublimation, adsorption, and van der Waals epitaxy.

## Acknowledgements

This research was financially supported by Russian Science Foundation [grant number 19-72-30023] and was performed on the equipment of CKP “Nanostruktury”.

## References

[1] X. Li, L. Tao, Z. Chen, et al. Appl. Phys. Rev. **4**(2017)021306.
[2] F. Wang, Y. Zhang, Y. Gao, et al. Small **15**(2019)1901347.
[3] S. Vishwanath, X. Liu, S. Rouvimov, et al. J. Mater. Res. **31**(2016)900.
[4] C. Callaert, M. Bercx, D. Lamoen, et al. Acta Crystallogr. Sect. B Struct. Sci. Cryst. Eng. Mater. **75**(2019)717.
[5] J. Kampmeier, S. Borisova, L. Plucinski, et al. Cryst. Growth Des. **15**(2015)390.
[6] S. Borisova, J. Kampmeier, M. Luysberg, et al. Appl. Phys. Lett. **103**(2013)081902.
[7] Z. Yang, J. Hao. Adv. Mater. Technol. 4(2019)1900108.
[8] S. A. Ponomarev, D. I. Rogilo, N. N. Kurus, et al. J. Phys. Conf. Ser. **1984**(2021)012016.
[9] D. I. Rogilo, L. I. Fedina, S. S. Kosolobov, et al. J. Cryst. Growth **457**(2017)188.
[10] D. I. Rogilo, L. I. Fedina, S. A. Ponomarev, et al. J. Cryst. Growth **529**(2020)125273.

# Valley polarization of trions in TMDC interfaced with iron garnet

V. Kravtsov[1], T. Ivanova[1], A.N. Abramov[1], P.V. Shilina[2,9], P.O. Kapralov[3], D.N. Krizhanovskii[1,4], V.N. Berzhansky[5], V.I. Belotelov[3,5,6], I.A. Shelykh[1,7], A.I. Chernov[*,2,3,8], I.V. Iorsh[1]

[1] Department of Physics and Engineering, ITMO University, Saint Petersburg 197101, Russia
[2] Center for Photonics and 2D Materials, Moscow Institute of Physics and Technology, National Research University, Dolgoprudny 141700, Russia
[3] Russian Quantum Center, Skolkovo Innovation City, Moscow 121353, Russia
[4] Department of Physics and Astronomy, University of Sheffield, Sheffield S3 7RH, United Kingdom
[5] Vernadsky Crimean Federal University, Simferopol 295007, Russia
[6] Photonic and Quantum Technologies School, Lomonosov Moscow State University, Moscow 119991, Russia
[7] Science Institute, University of Iceland, Dunhagi-3, IS-107 Reykjavik, Iceland
[8] NTI Center for Quantum Communications, National University of Science and Technology MISiS, Moscow 125009, Russia
[9] HSE University, Moscow 101000, Russia

*e-mail: chernov.ai@mipt.ru

**Abstract.** An intrinsic valley degree of freedom in thin van der Waals semiconductors can be controlled by interfacing with magnetic substrates. In this work we study circularly polarized photoluminescence in heterostructures of transitional metal dichalcogenides and thin films of ferrimagnetic bismuth iron garnet (BIG). We observe strong emission from charged excitons with circular polarization and demonstrate contrasting response to left and right circularly polarized excitation. The peculiar properties depend on the type of the BIG magnetization.

## 1. Introduction

Transition metal dichalcogenides (TMDs) in their monolayer form are attractive candidates for integration into future on-chip opto-electronic devices as atomically thin and air-stable materials that support strongly bound excitons [1]. One of the promising approaches to control the TMD excitonic valley properties is via interfacing the layer with magnetic materials [2].

Iron garnets, in particular yttrium iron garnet (YIG), have attracted much attention as promising magnetic substrates for TMD-based heterostructures. These heterostructures provide an opportunity to study valley physics of charged excitons in TMDs, as it was demonstrated in recent reports on trion valley polarization in $MoS_2$/YIG [3] and $WS_2$/YIG samples.

## 2. Experiment

The samples consisted of a monolayer $MoSe_2$ interfaced with thin (3 μm) bismuth iron garnet (BIG) films on 500 μm thick GGG ($Gd_3Ga_5O_{12}$) substrates (Fig. 1). Magnetic films were grown by liquid phase epitaxy. Specifically, two types of the garnet composition were used: $(BiY)_3(FeScAl)_5O_{12}$ with in-plane magnetic anisotropy and $(BiLuEu)_3(FeGaAl)_5O_{12}$ with an easy axis along the out-of-plane direction. The magneto-optic characterization of the latter is depicted in Fig. 1. High-quality flakes of $MoSe_2$ monolayers were mechanically exfoliated from a commercial bulk crystal (HQ Graphene) with Nitto tape. TMD/BIG structures were assembled via dry transfer of $MoSe_2$ onto BIG films with viscoelastic polydimethylsiloxane stamps. Spectroscopic measurements were performed with samples mounted in a closed-cycle ultralow-vibration cryostat (Advanced Research Systems) and maintained at a controlled temperature in 6– 50 K range, at 633 nm excitation wavelength.

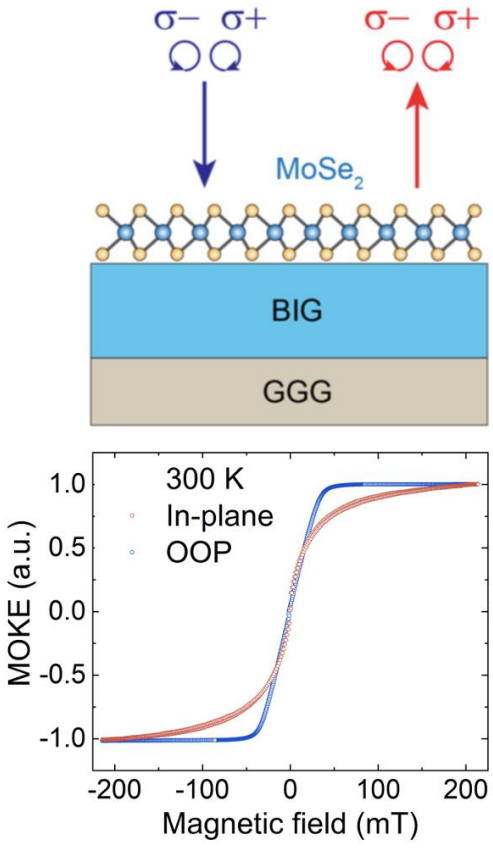


***Fig. 1.*** *Top image is the principal scheme of the sample, consisting of monolayer $MoSe_2$ transferred onto thin film of bismuth iron garnet (BIG) on gadolinium gallium garnet (GGG) substrate, and types of different excitation/detection with circular polarization. Bottom image is the magneto-optic Kerr effect (MOKE) measurements for easy-axis BIG sample: field reversal in the plane of the sample (red symbols) and perpendicular to the sample plane (blue symbols).*

## 3. Results and discussions

Figure 1 depicts the hysteresis loops, which were obtained in BIG films with out-of-plane easy axis via magneto-optic Kerr effect measurements with field reversal along two directions: in the sample plane (red symbols) and perpendicular to the sample plane (blue symbols). The extracted Ms values of the film are circa 0.20 T for the in-plane and 0.05 T for out-of-plane configurations. Similar experiment, but for a sample with easy plane anisotropy resulted in the extracted Ms values of 0.001 T and 0.04 T, respectively. Further, $MoSe_2$ monolayers were placed on these magnetic films. Figure 2 represents the photoluminescence (PL) spectra for both types of magnetic films.

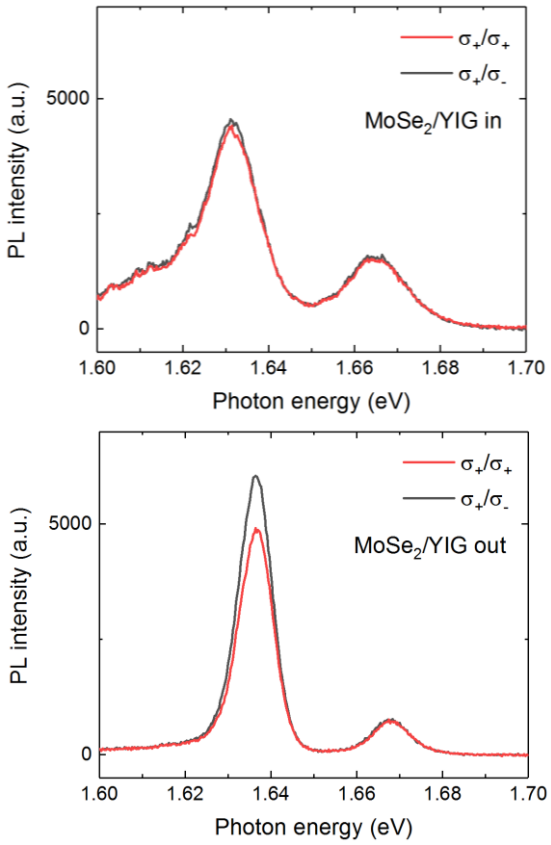


***Fig. 2.*** *Low temperature photoluminescence spectra from the $MoSe_2$ monolayer positioned on the magnetic films. The spectra are taken in co- (RR, red curves) and cross- (RL, black curves) polarized detection channels with right circularly polarized laser excitation. Top image is for the case of the magnetic film with in-plane anisotropy, and the bottom one is for the out-of-plane easy axis film.*

The spectra contain two peaks that correspond to emission from the neutral (X) around 1.67 eV and charged (T, trion) exciton complexes. The trion PL is enhanced while the neutral exciton PL is significantly suppressed, which is due to doping from BIG films. The important feature is the significant difference in PL intensity of the trion peak for co- and cross-polarized detection of the TMD layer placed on the magnetic film with the out-of-plane easy axis (Fig. 2 bottom image). We quantify the corresponding contrast with the degree of circular polarization (DOCP) defined as DOCP = (Ico − Icross)/(Ico + Icross), where Ico , Icross are PL intensities in the co- and cross-polarized channels, respectively. The DOCP value characterizes the degree of valley polarization in the two valleys K/K′ of the $MoSe_2$ monolayer and is estimated for the trion PL peak as ∼ −7%. The negative DOCP value implies that, following excitation in a certain valley, the resulting population of trions becomes higher in the opposite valley. An inverted trion valley polarization response depends crucially on temperature and excitation energy. It is most pronounced at low temperatures and pump energy close to the B exciton. The mechanism is clarified in detail in [4].

The values of the Fermi energy and electron Zeeman splitting in the conduction band have been estimated, and the value of the induced effective magnetic field B was found to be ∼ 2.5 T, which is much larger than the saturation magnetization field of BIG (see Fig. 1 bottom image). Such large value of the effective field points to the presence of proximity effects in the $MoSe_2$/BIG hetero-structure.

## 4. Conclusions

We have investigated circularly polarized PL of trions in monolayer $MoSe_2$ interfaced with ferrimagnetic BIG films. Magnetic properties of the BIG film significantly influence the optical response of the 2D monolayer. We detect the PL intensity increase of trions in the monolayer, when interfaced with BIG. The experimentally observed negative trion DOCP and contrast in co-polarized PL for the right and left circularly polarized excitation are found for the BIG films with out-of-plane easy axis. The saturation magnetization for out-of-plane configuration is 0.05 T. However, we extract the large effective magnetic field of ∼2.5 T for $MoSe_2$/BIG structures, which allows lifting the valley degeneracy of trions. The ability to controllably invert the valley polarization of trions in TMDs without applying high external magnetic fields opens new routes for the development of valleytronic devices.

## Acknowledgements

The authors acknowledge funding from the Ministry of Education and Science of the Russian Federation through Megagrant No. 14.Y26.31.0015. Optical measurements were funded by the Russian Science Foundation, project No. 19-72-00146. Magnetic properties investigation was supported by RSF project No. 21-12-00316. V.K. acknowledges support by the Government of the Russian Federation through the ITMO Fellowship and Professorship Program.

## References

[1] K.F. Mak, J. Shan, Nat. Photonics **10** (2016) 216–226.
[2] Q. Zhang, S.A. Yang, W. Mi, Y. Cheng *et al.*, Adv. Mater. **28** (2016) 959–966.
[3] B. Peng *et al.*, ACS Nano **11** (2017) 12257–12265.
[4] V. Kravtsov, T. Ivanova, A.N. Abramov *et al.*, 2D Materials, **9** (2022) 015019.

Sixth Asian School-Conference on Physics and
Technology of Nanostructured Materials
Vladivostok, Russia, 25 – 29 April, 2022



# DFT study of the hole states charge density in Ge/Si structures

M.S. Aleshin*[,1], A.N. Chibisov[1,2]

[1] Laboratory for Modelling of Quantum Processes, Pacific National University, 136 Tikhookeanskaya St., Khabarovsk, 680035, Russia
[2] Computing Center, Far Eastern Branch of the Russian Academy of Sciences, 65 Kim Yu Chen St., Khabarovsk, 680000, Russia

*e-mail: max@pnu.edu.ru

**Abstract.** This paper presents the results of computer modeling of the charge density in a thin slab of crystalline germanium enclosed between layers of silicon. The simulations have been performed using the Quantum Espresso software [1] for Si/Ge/Si interfaces in the crystallographic planes (001) and (105). We analyzed changes in the crystal lattice parameters during relaxation of both types of surfaces and showed that the formation of hole states in the germanium layer is more likely to occur for interface (105).

## 1. Introduction

Recently, more and more attention has been paid to quantum computing, which has already proven effective in solving specialized problems, which cannot be produced by classical computing machines. Various systems are being studied to produce quantum dots used as qubits. Recent studies have shown that holes in semiconductors have a spin-orbit interaction, so not only the filled states of the conduction band, but also the vacant states of the valence band are promising for the implementation of spin qubits [2]. We pay special attention to structures based on germanium, which has the highest hole mobility at room temperature among all semiconductors. Among such systems the most promising are germanium nanowires (HW) produced on the surface of silicon (001) by molecular beam epitaxy, having a triangular cross-section with planes (105), bounded from above also by a silicon layer [3].

## 2. Model

Supercells representing an interface of alternating Si/Ge/Si layers, each of which contained the same number of atoms (in the ratio 1/3 : 1/3 : 1/3), were considered. Two types of interfaces were simulated, which correspond to the crystallographic planes (001) and (105), respectively. The latter, according to the experimental data [2], plays a key role in the formation of hole states. As a result of relaxation calculations the change in the volume of cell (001) was less than 1%, cell (105) - 25%, there was a significant compression (parameters are given in Table I).

***Table I.*** *Evolution of Si/Ge/Si structures parameters as a result of relaxation.*

| Structure | a (Å) | b (Å) | c (Å) | α (°) | β (°) | γ (°) |
|---|---|---|---|---|---|---|
| (001) before | 5.431 | 5.431 | 31.93 | 90.0 | 90.0 | 90.0 |
| (001) after | 5.443 | 5.443 | 31.93 | 90.0 | 90.0 | 88.6 |
| (105) before | 14.499 | 5.687 | 26.65 | 90.0 | 90.0 | 90.0 |
| (105) after | 10.783 | 5.710 | 26.65 | 90.0 | 90.0 | 90.7 |

## 3. Results and discussions

Hole states were simulated for the following interfaces: Si/Ge/Si (001) included 96 atoms placed in a cell with the 10.886 × 10.886 × 31.932 Å$^3$ volume and Si/Ge/Si (105) included 168 atoms in a cell with the 21.566 × 11.420 × 26.653 Å$^3$ volume. The electronic density in the structures was calculated by introducing an excess positive charge corresponding to the presence of one hole. The density of the neutral structure was then subtracted from the obtained distributions. During calculation of the Si/Ge/Si system electronic density, for the (001) plane model we used a special 4 × 4 × 1 k-points set, for the (105) plane model – 2 × 4 × 1 k-points set. Cut-off energy of plane waves was set to 680 eV in both cases

The analysis of the hole electron density distribution in the Ge layer showed that the hole formation probability for the Ge (105) orientation is at least one order of magnitude higher than for Ge (001).

## 4. Conclusions

The proposed model agrees with the experimental data [4] and will make it possible to analyze the change in the distribution of hole states in the Ge/Si structure under the action of the applied electric field. It will also allow us to reveal the regularity of the magnetic moment change due to the presence of holes in Ge.

## Acknowledgements

The work was supported by the Ministry of Science and Higher Education of the Russian Federation (project No. 0818-2020-0005) using resources of the Shared Services «Data Center of the Far-Eastern Branch of the Russian Academy of Sciences».

## References

[1] P. Giannozzi, O. Andreuss, T. Brumme, O. Bunau, M. B. Nardelli, M. Calandra, R. Car, C. Cavazzoni, D. Ceresoli, M. Cococcioni. J. Phys.: Condens. Matter **29**(2017)465901.
[2] C. Kloeffel, D. Loss. Annu. Rev. Condens. Matter Phys. Annual Reviews **4**(2013)51.
[3] J. J. Zhang, G. Katsaros, F. Montalenti, D. Scopece, R. O. Rezaev, C. Mickel, B. Rellinghaus, L. Miglio, S. De Franceschi, A. Rastelli, O. G. Schmidt. Phys. Rev. Lett. **109**(2012)085502
[4] F. Gao, J. H. Wang, H. Watzinger, H. Hu, M. J. Rančić, J. Y. Zhang, T. Wang, Y. Yao, G. L. Wang, J. Kukučka, et al. Adv. Mater. **32**(2020)1906523.

Sixth Asian School-Conference on Physics and
Technology of Nanostructured Materials
Vladivostok, Russia, 25 – 29 April, 2022

**I.p.02**

# Dipole superspin ice on a trimerized triangular lattice

M.A. Chesnokov*[,1], I.N. Nalivaiko[1], K.S. Soldatov[1,2], V.S. Strongin[1,2], K.V. Nefedev[1,2]

[1] Far Eastern Federal University, Vladivostok, Russky Island, 10 Ajax Bay, 690922, Russian Federation
[2] Institute of Applied Mathematics, Far Eastern Branch, Russian Academy of Science, Vladivostok, Radio 7, 690041, Russian Federation

*e-mail: chesnokov.ma@students.dvfu.ru

**Abstract.** We are doing the research on the thermodynamic properties and phase transitions of two-dimensional arrays which consist of dipole coupled Ising-type nanomagnets located at the vertices of a triangular lattice called a trimerized triangular lattice. The Metropolis method is used to investigate phase transitions depending on the lattice parameter, frustrations, and the influence of an external field on the system.

## 1. Introduction

Artificial spin ice is a nanomagnetic, multiferroic, artificial material consisting of nanoparticles of elongated shape. The magnetic moment of a particle consists of many spins, therefore it is called a superspin or macrospin. The behavior of the magnetic moment of nanoparticles makes it possible to use the Ising model, since there are only two possible mutually exclusive orientations for it – "up" or "down". Initially, artificial spin ice was understood as two-dimensional artificial analogues of spin ice on a pyrochlore lattice. Currently, research on artificial spin ice is relevant. Thermodynamic properties of systems are investigated. Theoretical work is usually aimed at confirming experimental observations. However, the most fundamental issue is the development of algorithms that could allow calculating a complete group of events based on a sample from the state space. Currently, there are no theories and, consequently, technical, software capabilities for accurate calculation of the statistical sum of a large number (>40) of interacting particles of a fully connected model. Therefore, interest in the topic of artificial spin systems is constantly growing.

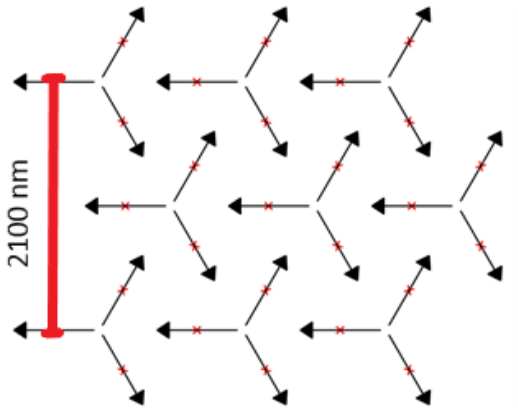


***Fig. 1.*** *Trimerized triangular lattice.*

The paper will investigate the properties of a trimerized triangular lattice which combines elements of two systems - an artificial kagome lattice and triangular spin ice. The nanomagnetic vertices (or trimmers) in it are located periodically at an angle of 60 °. The resulting array is shown in Fig. 1.

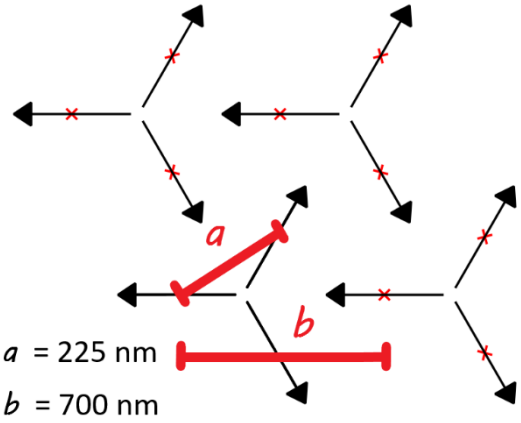


***Fig. 2.*** *Lattice parameters a and b [1].*

The thermodynamic properties will be strongly influenced by the lattice parameters a and b (Fig. 2) since the physical properties of the system directly depend on them. The smaller the b, the closer the trimmers are to each other, and the greater the competitive interaction between the dipoles in the system. From certain values of b competitive interactions reduce to zero, and the system becomes an array of subsystems [1].

## 2. Formalism and model

The energy of the dipole-dipole interaction of a system of dipoles on a trimerized lattice is calculated using the formula (2.1):

$$E_{ij} = \frac{(\vec{m}_i \vec{m}_j)}{|\vec{r}_{ij}|^3} - 3\frac{(\vec{m}_i \vec{r}_{ij})(\vec{m}_j \vec{r}_{ij})}{|\vec{r}_{ij}|}, \qquad (2.1)$$

where **i**, **j** - the numbers of the interacting dipoles, **r** is the vector between the centers of the magnetic moments of the interacting dipoles, **m** is the value of the magnetic moment vector.

To determine the thermodynamic properties of the system under study we used The Metropolis method. The main idea of this method is the equal formation of a sample of the state space with a given probability of the distribution of states. At each step of the sampling process, a configuration with a given probability is accepted (or rejected):

$$P(E_i \rightarrow E_j) = min\left(\frac{P(E_i)}{P(E_j)}, 1\right). \qquad (2.2)$$

When numerically calculating the temperature behavior of the system, the probability of the configuration energy is determined according to the canonical Gibbs distribution:

$$P(E_i) = min\left(\frac{e^{-E_i/k_BT}}{Z}\right). \quad (2.3)$$

Combine equations (2.1) and (2.2), we get

$$\begin{aligned} P(E_i \to E_j) &= min\left(\frac{e^{-E_j/k_BT}}{e^{-E_i/k_BT}}, 1\right) \\ &= min\left(exp\left[-\frac{E_j - E_i}{k_BT}\right], 1\right) \\ &= min\left(exp\left[-\frac{\Delta E}{k_BT}\right], 1\right), \end{aligned} \quad (2.4)$$

where $\Delta\mathbf{E}$ is the change in the energy level of the system as a result of configuration change, **T** is the absolute temperature. In the process of sampling, a certain characteristic (order parameter or spin excess) is determined for each selected configuration. Based on the obtained characteristics, the standard deviation and the mathematical mean are determined, based on which the thermodynamic quantities are calculated [2].

### 3. Research plan

It is expected that a system with relatively low values of parameter b will be able to phase transition. It is necessary to determine from which b and by which dynamics the system loses this opportunity as b increases. To do this, the heat capacity of the system will be determined, so it can be used to judge the presence of a phase transition. The heat capacity directly depends on the energy of the system obtained by the Metropolis method, and can be found by the formula:

$$C(T) = -\frac{\langle E^2\rangle - \langle E\rangle^2}{k_BT^2}. \quad (3.1)$$

The most important task in the study of artificial spin systems is to find the ground state of the system: a configuration in which the total energy of the system is minimal. It is necessary to try to find the minimum energy by the Metropolis method for various b, compare with the already available results and use other methods (e.g. a greedy algorithm) to search for lower-energy configurations or an exact solution by parallel full search, if possible.

After that, it is planned to conduct the same studies using an external magnetic field, as well as to address the issue of frustrations in the system: at which b the system displays the greatest number of frustrations, and how the degeneracy of the ground state depends on **b**.

### Acknowledgements

This work was financially supported by the state task of the Ministry of Science and Higher Education of the Russian Federation №0657-2020-0005.

### References

[1] Hofhuis K. et al. Geometrical frustration and competing orders in the dipolar trimerized triangular lattice //Physical Review B. – 2021. – Т. 104. – №. 1. – С. 014409.

[2] Шевченко Ю. А. Термодинамические свойства фрустрированных спиновых систем. – 2017.R.

Sixth Asian School-Conference on Physics and
Technology of Nanostructured Materials
Vladivostok, Russia, 25 – 29 April, 2022

**I.p.03**

# Low energy and ground states of trimerized dipole spin ice

M.A. Chesnokov*[,1], I.N. Nalivaiko[1], K.S. Soldatov[1,2], V.S. Strongin[1,2], K.V. Nefedev[1,2]

[1] Far Eastern Federal University, Vladivostok, Russky Island, 10 Ajax Bay, 690922, Russian Federation
[2] Institute of Applied Mathematics, Far Eastern Branch, Russian Academy of Science, Vladivostok, Radio 7, 690041, Russian Federation

*e-mail: chesnokov.ma@students.dvfu.ru

**Abstract.** We are doing the research on the ground state and density of states of two-dimensional arrays consisting of dipole-coupled Ising-type nanomagnets located at the vertices of a triangular lattice, called a trimerized triangular lattice. The complete enumeration method is used to investigate of possibilities of phase transitions and frustrations depending on the lattice parameters.

## 1. Introduction

Artificial spin ice is a nanomagnet, multiferroic, an artificial nanomaterial consisting of nanoparticles of elongated shape. The magnetic moment of a particle consists of many atom spins; therefore, it is called a superspin or macrospin. The behavior of the magnetic moment of a nanoparticle makes it possible to use the Ising model, since due to the shape anisotropy energy, there are only two possible mutually exclusive moment orientations - "up" or "down". Initially, artificial spin ice was understood as two-dimensional artificial analogues of spin ice on a pyrochlore lattice. Currently, research on artificial spin ice is relevant. The thermodynamic properties of the systems are investigated. Theoretical work is usually aimed at confirming experimental observations. Important questions are the search for the ground state of the system, low-energy states - configurations with the lowest energy of interaction in the system of dipoles, and the multiplicity of their degeneracy. The question of calculating the probability density of all possible states (configurations) has great fundamental and theoretical significance due to the fact, that it also allows to obtain information about the degree of frustration in the system. Currently, there are no theories and, consequently, technical, software capabilities for accurate calculation of the statistical sum of a large number (>40) of interacting particles of a fully connected model. Therefore, interest in the topic of artificial spin systems is constantly growing.

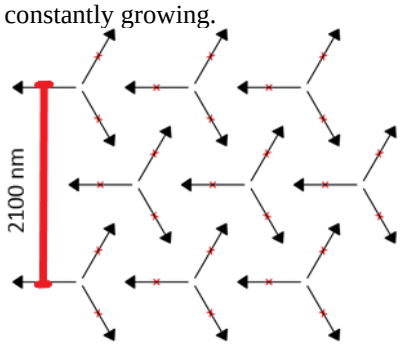


***Fig. 3.*** *Trimerized triangular lattice.*

The paper will investigate the properties of a trimerized triangular lattice which combines elements of two systems - an artificial kagome lattice and triangular spin ice. The nanomagnetic vertices (or trimmers) in it are located periodically at an angle of 60 °. The resulting array is shown in Fig. 1

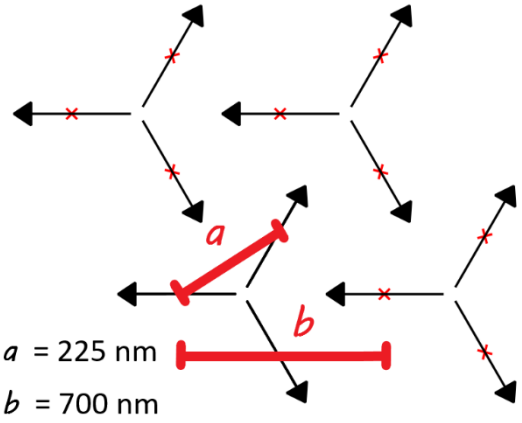


***Fig. 4.*** *Lattice parameters a and b [1].*

The thermodynamic properties will be strongly influenced by the lattice parameters *a* and *b* (Fig. 2) since the physical properties of the system directly depend on them. The smaller the *b*, the closer the trimmers are to each other, and the greater the competitive interaction between the dipoles in the system. From certain values of *b* competitive interactions reduce to zero, and the system becomes an array of subsystems [1].

## 2. Formalism and model

The energy of the dipole-dipole interaction of dipoles *i* and *j* on a trimerized lattice is calculated using the formula (2.1):

$$E_{ij} = \frac{(\vec{m}_i \vec{m}_j)}{|\vec{r}_{ij}|^3} - 3\frac{(\vec{m}_i \vec{r}_{ij})(\vec{m}_j \vec{r}_{ij})}{|\vec{r}_{ij}|^5}, \qquad (2.1)$$

where $\vec{r}_{ij}$ is the vector between the centers of the magnetic moments of the interacting dipoles, $\vec{m}_i$ is the value of the magnetic moment vector.

The brute force method was used for the calculations which is the only way to get accurate results, since it considers each of the possible lattice configurations. However, this method suffers from an exponential increase in computational time as N increases, and is only efficient in small systems (N<40). It can be used to obtain accurate results and then scale them up for comparison with results obtained with approximate methods for larger systems.

To speed up the algorithm, the CUDA computing architecture was used, which makes it possible to reduce the computation time due to the use of a large number of simultaneous threads on the GPU. The use of CUDA and

the resources of supercomputer clusters makes it possible to achieve a significant acceleration of calculations.

### 3. Results and discussions

It was expected that a system with relatively low values of the parameter *b* would be able to phase transition. The larger the *b* parameter, the farther the trimers are from each other, which in turn affects the interaction energy of many parts. The ground state was searched and the density of states was calculated by using brute force method for a small lattice.

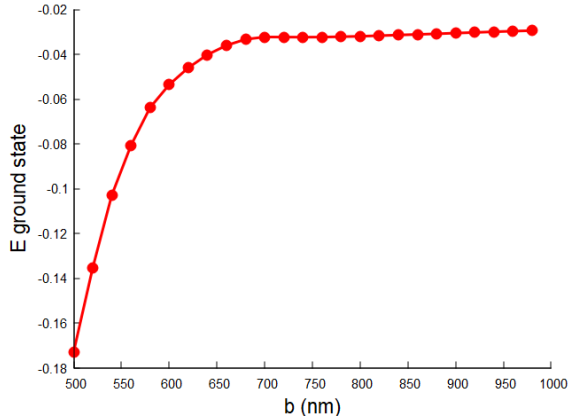


***Fig. 3.*** *Dynamics of change in the energy of the ground states depending on b.*

Figure 3 shows the dynamics of changes in the energy of the ground state for of the same sized and shaped lattices with different parameters b. As can be seen, from certain values of b, the system is divided into subsystems, the total interaction energy of which tends to zero. In such states, the system is not capable to phase transition.

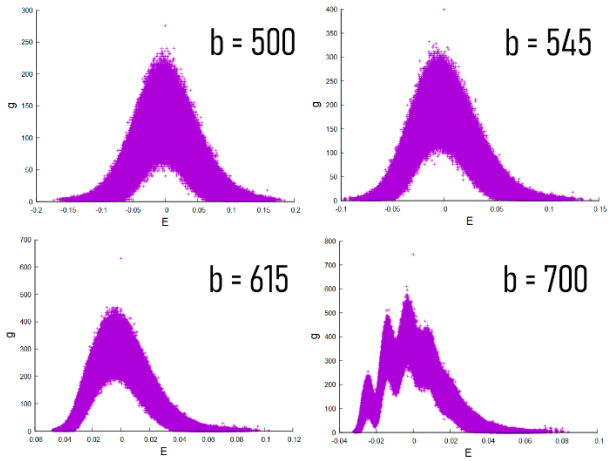


***Fig. 4.*** *Density of states for various b.*

Also, the density of states was calculated for lattices of the same size and shape with different parameters *b*. The same values of *b* were used as in Article 1. The change in the shape of the graphs as *b* increases not only shows the change in the minimum energy, but also indicates a disproportionate distribution of states with different *b*. This means that the systems have different frustration rates, which is consistent with the results from Article 1.

### Acknowledgements

The research results connected with model samples preparation and physical experiments were obtained within the framework of the state task of the Ministry of Science and Higher Education of the Russian Federation of Russia (No. 0657-2020-0005). The research results connected with algorithms elaboration, program coding end implementation of parallel scheme of calculation obtained at the expense of the grant of the President of the Russian Federation for state support of the leading scientific schools of the Russian Federation (NSh-2559.2022.1.2)

### References

[1] Hofhuis K. et al. Geometrical frustration and competing orders in the dipolar trimerized triangular lattice //Physical Review B. – 2021. – Т. 104. – №. 1. – С. 014409.

Sixth Asian School-Conference on Physics and
Technology of Nanostructured Materials
Vladivostok, Russia, 25 – 29 April, 2022



# Investigation of changes in the composition of anodic $TiO_2$ nanotubes at different stages of formation by AES and ToF SIMS methods

D.A. Dronova*, A.S. Gavrilov, A.A. Dronov
National Research University of Electronic Technology, Zelenograd 124498, Russia

*e-mail: demetpatakai@gmail.com

**Abstract.** The article discusses the complex research of chemical composition and morphology of nanotubular anodic $TiO_2$ layers at the initial stages of the porous structure nucleation, by means of scanning electron microscopy (SEM), Auger spectroscopy (AES) and time-of-flight secondary ion mass spectrometry (ToF SIMS). Such complex research aimed to show the profile distribution of chemical elements and reaction products at each of the initial stages of the anodic oxide growth in fluorine-containing ethylene glycol-based electrolytes, which will help expand the understanding of pore formation mechanisms in anodic titanium oxide.

## 1. Introduction

Nanostructured titania currently represents a major research interest due to its possible application in the storage of energy sources [1-3], photocatalysis [4,5], and solar cells [6-9].

One of the promising nanostructured modifications of titanium oxide is nanotube anodic titanium oxide ($TiO_2$ NTs). The anodic formation process makes it possible to create not only a highly ordered $TiO_2$ NTs array on a titanium substrate, which facilitates the formation of electronic structures based on them but also allows very precise control of geometric parameters during growth, in contrast to classical powder nanomaterials based on $TiO_2$ [10].

Despite the extensive studies of how the properties of structures based on $TiO_2$ NTs and material composition, the mechanisms of pore nucleation and formation is still not fully clear.

This article discusses complex research of the chemical composition and morphology of $TiO_2$ nanotubes at the first stages of the nucleation of a porous structure, such as scanning electron microscopy (SEM), Auger spectroscopy (AES) and time-of-flight secondary ion mass spectrometry (ToF SIMS). Such complex research aims to show the profile distribution of chemical elements and reaction products at each of the initial stages of the growth of anodic oxide in fluorine-containing electrolytes, which will help expand the understanding of the mechanism of pore formation in titanium oxide.

## 2. Experiment

$TiO_2$ NTs were formed on titanium foil (0.89 mm thick, 99.7% metal basis, Alfa Aesar). Prior to anodization, substrates were chemically polished in $HNO_3$:HF solution during 120 s, then washed in deionized water and dried in an argon stream.The electrochemical growth of titanium oxide was carried out in a potentiostatic mode (60 V) and a temperature of 20 ˚C. A platinum grid was used as a counter electrode. Anodizing has carried out in ethylene glycol 98 vol.% $C_2H_5O_2$ with the addition of 0.3 vol.% $NH_4F$ and 2 vol.% $H_2O$.

The anodizing time corresponds to the points marked in Figure 1- A, B, C, D. After anodizing, the samples were washed in ethyl alcohol and dried in a stream of air. Subsequently, ready samples were not subjected to heat treatment and remained in the amorphous state.

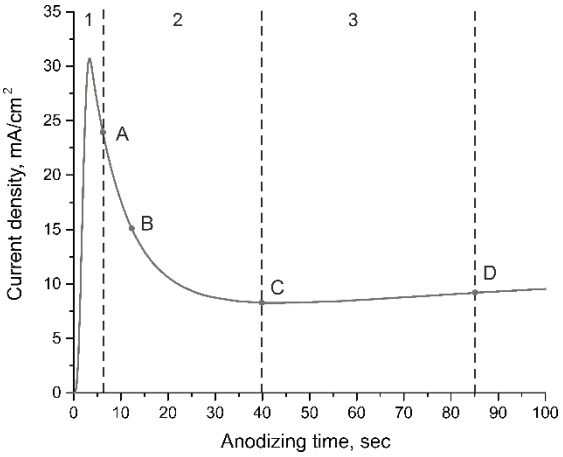


***Fig. 1.*** *Growth kinetics of porous titanium oxide.*

The graph shows a typical curve of the growth process of the $TiO_2$ layer in a model with marked formation stages and points of critical current density Fig. 1. These critical points, together with the intermediate point B, were selected for the analysis of the chemical distribution over depth in order to visualize the development of each stage of the formation of the $TiO_2$.

## 3. Results and discussions

### Point A

In the first 6 seconds of anodization, a textured dense oxide layer.

The graph of the distribution of the elemental composition over depth, obtained by the method of Auger electron spectroscopy (Fig. 2), shows two peaks of carbon, one of which is a hydrocarbon contamination ($C_{surf}$) and is almost always found on the surface of the samples, the other corresponds to the carbide peak of carbon in the volume of the oxide film ($C_{film}$). Surface contamination disappears almost completely at about a depth of 10 nm, while the signal of carbon carbide begins to drop noticeably only at a depth of about 20 nm.

The presence of fluorine atoms in the structure is associated with the use of fluoride electrolytes, the anions of which are incorporated into the film during growth.

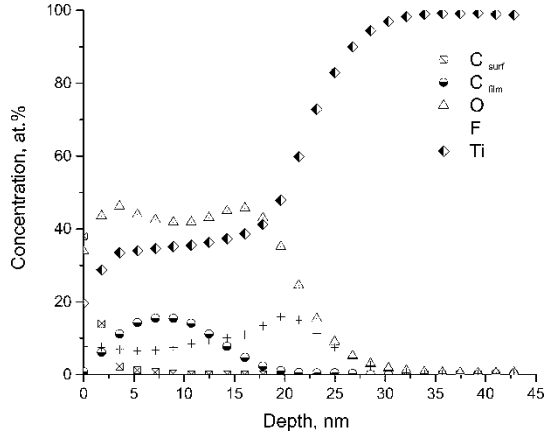


*Fig. 2. AES profile analysis of anodized Ti surface at point A.*

To establish chemical bonds of fluorine and carbon with other elements in the oxide, ToF SIMS was used.

From the results of the profile SIMS analysis (Fig. 3), it can be seen that on the oxide surface (about 5 nm) there is an increased intensity of contamination represented by the ionic fragment $CH_3O^-$, which gradually decreases to 15 nm and is more likely associated with the residues of the reaction products from the electrolyte.

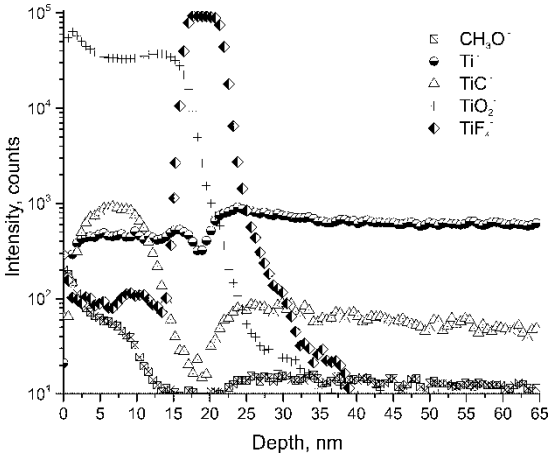


*Fig. 3. ToF-SIMS profile of anodized Ti surface at point A.*

The ionic fragment of $TiC^-$, $TiF_4^-$ repeats the shape of the distribution from $C_{film}$ and fluorine in the AES method.

**Point D**

At point D, the pores already develop deep into the titanium foil and the process of further growth becomes equilibrium. In the previous work [11], we showed that a single TiO2 nanotube has a three-layer structure, in which is located exclusively in the inner layer of the tube, but here we see a similar distribution of with fluorine due to the larger analysis area and the already developed structure of the array. In the profile analysis of SIMS (Fig. 4) it can be seen that the ionic fragments $CH_3O^-$ have a stable intensity from 100 to 500 nm, which indicates the presence of reaction products from the electrolyte in the array of tubes.

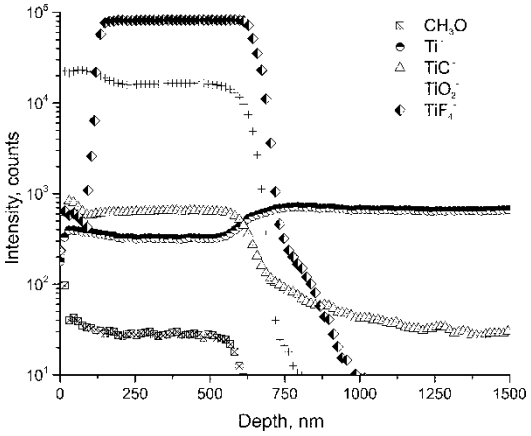


*Fig. 4. ToF-SIMS profile of anodized Ti surface at point D.*

The time-of-flight mass spectrometry showed that at the near-surface layer (approx. 100 nm) there is a layer that differs in composition from the array of nanotubes, that presumably formed during the initial stage of anodic oxidation at high electric field strengths.

## 4. Conclusions

In the present study, it was found that during the anodic oxidation process not only oxidized forms of titanium are formed, but also the incorporation of carbon-containing impurities occurred into the nanotube structure, because of the interactions with an ethylene glycol-based electrolyte. It is also shown that the composition of the near-surface layer differs from that of the underlying nanotube layer, which presumably formed during the initial stage of anodic oxidation at high electric field strengths.

## Acknowledgements

This work was partially supported by the Ministry of Science and Higher Education of the Russian Federation in the framework of State assignment № FSMR-2020-0018 and RFBR grant № 19-33-90287.

## References

[1] Z.-D. Gao, X. Zhu, Y.-H. Li, X. Zhou, Y.-Y. Song, P. Schmuki, Chemical Communications. **51**(2015)7614–7617.
[2] N.A. Kyeremateng, N. Plylahan, A.C.S. dos Santos, L.V. Taveira, L.F.P. Dick, T. Djenizian, Chem. Commun. **49**(2013)4205–4207.
[3] J.-Y. Eom, S.-J. Lim, S.-M. Lee, W.-H. Ryu, H.-S. Kwon, Journal of Materials Chemistry A. **3**(2015)11183–11188.
[4] L.L. Costa, A.G.S. Prado, Journal of Photochemistry and Photobiology A: Chemistry. **201**(2009)45–49.
[5] H. Liang, X. Li, Applied Catalysis B: Environmental. **86**(2009)8–17.
[6] Y.-C. Nah, I. Paramasivam, P. Schmuki, ChemPhysChem. **11**(2010)2698–2713.
[7] M. Yang, D. Kim, H. Jha, K. Lee, J. Paul, P. Schmuki, Chem. Commun. **47**(2011)2032–2034.
[8] K. Lee, P. Schmuki, Electrochemistry Communications. **25**(2012)11–14.
[9] T.-J. Whang, H.-Y. Huang, M.-T. Hsieh, J.-J. Chen, International Journal of Molecular Sciences. **10**(2009)4707–4718.
[10] K. Lee, A. Mazare, P. Schmuki, Chemical Reviews. **114**(2014)9385–9454.
[11] A. Dronov, I. Gavrilin, E. Kirilenko, D. Dronova, S. Gavrilov, Applied Surface Science. **434**(2018)148–154.

Sixth Asian School-Conference on Physics and
Technology of Nanostructured Materials
Vladivostok, Russia, 25 – 29 April, 2022

**I.p.05**

# Crystal structure of cobalt films and nanostrips grown on a stepped Si(111)-5.55×5.55-Cu surface

K.S. Ermakov*, V.N. Kharitonov, A.V. Davydenko, A.V. Ognev, A.S. Samardak
Institute of High Technologies and Advanced Materials, Far Eastern Federal University, Vladivostok 690950, Russia

*e-mail: ermak_ph@mail.ru

**Abstract.** The technological conditions of the growth of a 2-phase (fcc and hcp) epitaxial thin Co film and an array of single-crystal hcp-Co nanostrips on a stepped Si(111)-5.55×5.55-Cu surface with a Cu (111) buffer layer are shown. The crystal structure of the epitaxial thin Co films and single-crystal Co nanostrips are studied by the RHEED method.

## 1. Introduction

Low-dimensional structures and nanostructured materials are the most relevant and dynamically developing areas of modern physics. Interest in this area is associated with the prospects of creating completely new devices and nanosystems with broad functionality. The study of nanomagnetism is associated with the possibility of varying the properties of low-dimensional structures and creating solid-state devices with controlled parameters on their basis. In this work, using electron diffraction, the structures of epitaxial Co film and nanostrips with a width of 39 ± 3 nm were studied. We show that Co film consists of alternating area with hcp and fcc structure, and nanostripes have hcp structure.

## 2. Experiment

Film growth and self-organization of Co nanostrips were carried out by molecular beam epitaxy (MBE) at a pressure of $5\times10^{-10}$ Torr. $Cu_2Si$ and Cu buffer layers were formed by the MBE method on a stepped Si(111)-5.55×5.55-Cu surface. The growth of Co films was carried out by thermal deposition at normal temperature, and the self-organization of Co nanostrips was carried out by thermal deposition of the material at an angle of 20° to the surface of a stepped substrate with a Cu buffer layer. The Cu and Co deposition rates were 0.84 and 3.6 nm/min, respectively. The thickness of the $Cu_2Si$ buffer layer is 1.4 nm. The thickness of the Cu buffer layer is 2 nm.

The crystal structure of the samples was studied by reflection high-energy electron diffraction (RHEED). The surface morphology was studied by atomic force microscopy (AFM), scanning tunneling microscopy (STM) and scanning electron microscopy (SEM).

## 3. Results and discussion

The thickness of the epitaxial Co films and single-crystal Co nanostripes on the stepped Si(111)-5.55×5.55-Cu surface was 10 nm. The width of the Co nanostripes was ≈ 40 nm.

Surface studies by AFM, STM, and SEM showed that Co films with a Cu buffer layer repeat the stepped structure of the Si(111)5.55×5.55-Cu surface. Co nanostripes are formed along the steps of the Si(111)5.55×5.55-Cu substrate.

An analysis of the RHEED patterns showed that the stepped surface of the Cu buffer has an fcc lattice and is oriented by the (111) plane on the modified Si(111)5.55×5.55-Cu surface: Cu(111)‖Si(111) and <112>Cu‖ <110>Si.

Deposition of Co at a right angle to the plane of the stepped surface of the Si(111)5.55×5.55-Cu substrate with a Cu(111) buffer layer leads to the formation of a 2-phase epitaxial Co film with an fcc and hcp lattice.

An analysis of the RHEED pattern from an epitaxial Co film on a Cu(111) buffer layer showed that the reciprocal lattice consists of two superimposed lattices, Co fcc - (211) and Co hcp - (0001). This indicates the presence of two phases (fcc and hcp) in the epitaxial Co film.

The fcc Co film has the same orientation as the Cu buffer layer: Co(111)/Cu(111)-R30°/Si(111)-5.55×5.55-Cu and <112>Co‖<110>Si. The lattice of the hcp Co film is oriented by the plane Co(-23-10)/Cu(111)-R30°/Si(111)-5.55×5.55-Cu and [0001]Co‖<110>Si.

Deposition of Co at an angle of 20° to the plane of the stepped surface leads to the formation of an ordered array of Co single-crystal nanostrips.

Repeatability of the diffraction pattern is observed through 180°. This indicates the second-order crystal symmetry (L2 is the rotational axis) of single-crystal Co nanostrips.

Analysis of the diffraction pattern of the Co nanostrips showed that they have an hcp lattice, which is oriented on the steps of the Cu/Si(111)5.55×5.55-Cu surface by the (-23-10) plane.

## 4. Conclusion

The study of the crystal structure of the epitaxial thin films and single-crystal Co nanostrips on a stepped Si(111)-5.55×5.55-Cu surface with a Cu(111) buffer layer showed:

- on a stepped Si(111)-5.55×5.55-Cu surface with a Cu(111) buffer layer, when Co is deposited at a normal angle, a 2-phase (hcp and fcc) epitaxial thin film of Co with the thickness of 10 nm is grown;

- on a stepped Si(111)-5.55×5.55-Cu surface with a Cu(111) buffer layer during an oblique Co deposition, an array of single-crystal hcp-Co nanostrips with orientation (-23-10)[0001]Co‖(111)<112 is formed >Cu‖(111)<110>Si;

## Acknowledgements

The authors thank the Russian Ministry of Science and Higher Education for state support of scientific research conducted under the supervision of leading scientists in Russian institutions of higher education, scientific foundations, and state research centers (Project No. 075-15-2021-607) and for the state task (Project No. 0657-2020-0013).

Sixth Asian School-Conference on Physics and
Technology of Nanostructured Materials
Vladivostok, Russia, 25 – 29 April, 2022

**I.p.06**

# External pressure effect on the structure and magnetization of 2D Ge with hole qubits

A.V. Goncharov*[,1], A.N. Chibisov[1,2]

[1] Pacific National University, 136 Tikhookeanskaya St., Khabarovsk 680033, Russia
[2] Computing Center, Far Eastern Branch of the Russian Academy of Sciences, 65 Kim Yu Chen St., Khabarovsk, 680000, Russia

*e-mail: 008809@pnu.edu.ru

**Abstract.** In this paper the Ge {105} structure of the hut-wire type was constructed. It has been optimized by means of DFT calculation using full-relativistic ultrasoft pseudopotential. The electronic structure of the system at external pressure from -1 GPa to 1 GPa with hole qubit was calculated.

## 1. Introduction

Research in the field of quantum computing elements is one of the priority direction in solid-state nanoelectronics at present. Quantum qubits based on germanium hut wire structures are a promising quantum computing element [1]. A distinctive feature of such structures is the use of hole-hole centers as the basis of a quantum transistor. A hole-hole interaction strength in this systems can reach 20 μRy [2]. The special structure of the Ge hut wire provides them a combination of quantum well and quantum filament properties. The limited free path in the plane, as well as the presence of a compression strain in the structure [2] lead to the dominance of heavy holes in the germanium structure. In Ge quantum threads with cylindrical shape, there is a mixing of heavy and light holes, that cause an increased dephasing time, reaching 200 ns. For the hut wire {105} structure with pyramid shape and an angle at the base equal to 11.5°. but the dephasing time is 72-130 ns.

## 2. Methods and Approaches

In this work, a model of the Ge {105} structure was constructed with subsequent optimization by the DFT method. The hole effect on the total energy and spin-magnetization of the system was studied. To study the mechanism of hole interaction within the framework of the model an external pressure in the range from -1 GPa to 1 GPa was applied and hole localization in the structure was investigated. At the first stage of the work it was necessary to obtain for the germanium cell a surface bounded by the group of crystallographic planes {105} in the germanium cell.

The testing of the full-relativistic ultrasoft Ge pseudopotential [3] was performed on a unit cell [4] with homogeneous 6x6x6 k-point grid, constructed according to the Monkhorst-Pack technique . For calculation of the {105} slab structure 2x3x1 k-points were used. The cutoff energy of the plane wave basis was 50 Ry.

## 3. Results and discussions

Figure 1 shows the initial structure (a) and the resulting geometry optimization in the Quantum Espresso [5] code (b). The total energy of the resulting system was -657.54 Ry.

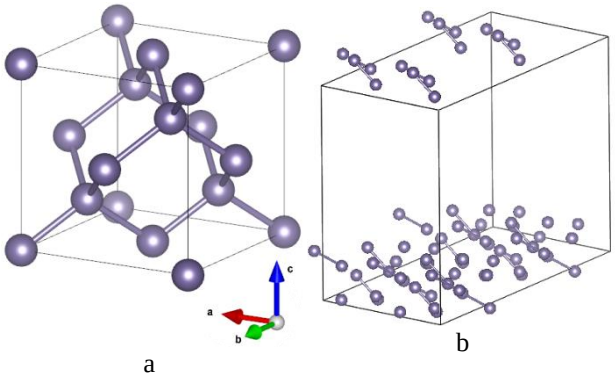


***Fig. 1.*** *Initial bulk Ge structure (a) and optimized {105} structure of hut-wire Ge (b).*

At pressure of -1 GPa the total energy of the system increased by 0.05 Ry, and at 1 GPa by 0.03 Ry. When the hole was introduced into the structure, we also observed an increase in the total energy of the system by 0.09 Ry for the system without external pressure. At external negative pressure this increase is 0.06 Ry, and at positive pressure is 0.07 Ry.

Next, the change in the direction of the system total spin was studied yin the presence of the hole and external pressure. It was found, that the spin varies from 0 to 0.99 in both cases, the zenith angle varies from 0° to -1.52° for negative pressure and from 0 to -1.55° for positive pressure. The azimuthal angle varies from 0° to 1.19° for negative pressure, and from 0 to -1.57° for positive pressure. Figure 2 shows the change in the total spin direction with hole at negative (a) and positive (b) external pressure.


***Fig. 2.*** *Magnetization direction with negative (a) and with positive external pressure (b) in the Ge {105} system with hole qubit.*

## 4. Conclusions

The Ge {105} structure with the hut wire type was calculated using density functional theory. It was found that the external positive and negative pressure, , leads to the direction change in the system spin. The total energy of structure with hole is increased by 0.09 Ry. In the absence of external pressure and the presence of a hole, the spin-magnetization of the system is also equal to zero.

## Acknowledgements

The work was supported by the Ministry of Science and Higher Education of the Russian Federation (project No. 0818-2020-0005) using resources of the Shared Services «Data Center of the Far-Eastern Branch of the Russian Academy of Sciences».

## References

[1] J. Kukucka, “Implementation of a hole spin qubit in Ge hut wires and dispersive spin sensing,” IST Austria, 2020.
[2] Zero Field Splitting of Heavy-Hole States in Quantum Dots Georgios Katsaros, Josip Kukučka, Lada Vukušić, Hannes Watzinger, Fei Gao, Ting Wang, Jian-Jun Zhang, and Karsten Held Nano Letters 2020 20 (7), 5201-5206 DOI: 10.1021/acs.nanolett.0c01466.
[3] Dal Corso, A. Pseudopotentials Periodic Table: From H to Pu. Computational Materials Science 2014, 95, 337-350.
[4] Hom T, Kiszenick W, Post B Accurate lattice constants from multiple reflection mesurements II. lattice constants of germanium, silicon and diamond. Journal of Applied Crystallography 8 (1975) 457-458.
[5] P. Giannozzi, O. Andreuss, T. Brumme, O. Bunau, M. B. Nardelli, M. Calandra, R. Car, C. Cavazzoni, D. Ceresoli, M. Cococcioni. J. Phys.: Condens. Matter **29**(2017)465901.

Sixth Asian School-Conference on Physics and
Technology of Nanostructured Materials
Vladivostok, Russia, 25 – 29 April, 2022



# A neural networks approach to the thermodynamic averages calculation of the Edwards-Anderson spin glass model

D.Yu. Kapitan*[,1,2,3], P.D. Andriushchenko[1], A.E. Rybin[2,3], A.O. Korol[2,3], E.V. Vasiliev[2,3], M.A. Padalko[2,3], A.V. Perzhu[2,3], R.A. Volotovskiy[2,3], A.G. Makarov[2,3], Yu.A. Shevchenko[2,3], K.S. Soldatov[2,3], V.Yu. Kapitan[2,3], K.V. Nefedev[2,3]

[1] ITMO University, Kronverksky Pr. 49, bldg. A, St. Petersburg, 197101, Russian Federation
[2] Institute of Applied Mathematics, Far Eastern Branch, Russian Academy of Science, Vladivostok, 690041, 7 Radio St., Russian Federation
[3] Far Eastern Federal University, 8 Sukhanova St., Vladivostok 690950, Russian Federation

*e-mail: madgfess@gmail.com

**Abstract.** We study the dependence of neural network architecture on the prediction accuracy of the values of basic thermodynamic characteristics. The object of the study is the Edwards-Anderson model on a square lattice of Ising spins. We compare the results of trained fully connected neural networks and networks with custom architectures that mimic the structure of the spin lattice.

## 1. Introduction

One of the most popular approaches to studying systems with complex interactions in recent decades has been the Monte Carlo method. At the same time, this approach is evolving and improving due to modern advances in computing technologies and new computational approaches, such as machine learning and neural networks. The application of machine learning to statistical physics began relatively recently but is rapidly evolving. For example, in [1,2,3] approaches to calculate the critical temperature from Monte Carlo-generated spin configurations were shown. In [4] a similar approach is shown which allows recognizing different phases of spin systems depending on parameters such as DMI and external magnetic field $H_z$ using a neural network. In this research, we will focus on the study of the ability of different neural network architectures to predict the main thermodynamic characteristics of the Edwards-Anderson spin glass models.

## 2. Model

Object of our research is the spin glass model, considered by Edwards and Anderson in 1975 [5]. This model is a square lattice of interacting Ising spins, characterized by frustrations which could be described as the occurrence of strong competition between ferromagnetic and antiferromagnetic interactions. The interaction $J_{ij}$ between each neighbor's spin pair $(ij)$ can be +1 either -1, and changes during the transition from one pair to another. The Hamiltonian is expressed as:

$$E = \sum_{\langle i,j \rangle} J_{ij} S_i S_j, \quad (1)$$

where $S_i, S_j$ – spins of the lattice, $< i,j >$ denotes the summation over pairs of interacting spins in a system with size $N$, $N$ – system linear size.

## 3. Results and discussions

We studied the effect of neural network architecture on the quality of predictions. We compared the results of fully connected neural networks with different number of hidden layers and custom neural networks with different number of layers and different approaches for linking neurons of different layers.

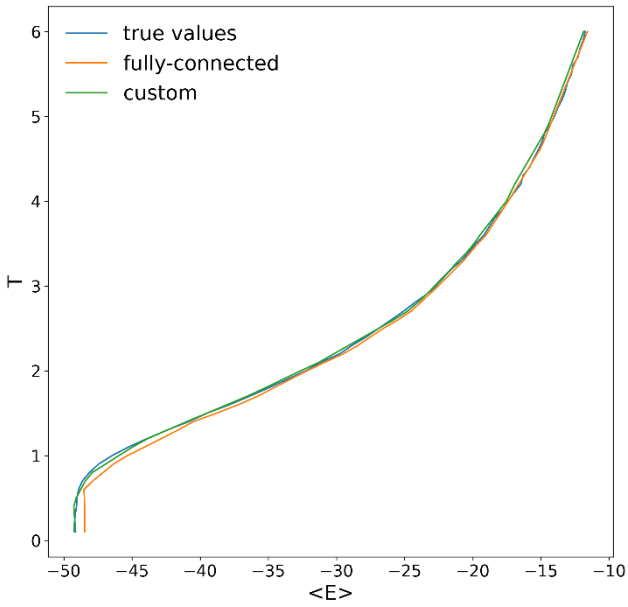


***Fig. 1.*** *Comparison of the prediction quality of a fully connected neural network and a custom neural network with the exact solution.*

We fed link configurations and temperature to the input of the neural networks and predicted average energy and magnetization on the output. Using Monte Carlo simulations, the average energy and magnetization of 41000 different 6x6 spin glass configurations were calculated for 60 different temperature each (from 0.1 T to 6.0 T). We were start from spin glass configuration, where all interaction $J_{ij} = 1$(ferromagnetic case) and then we added different numbers of negative interaction to the system. The number of configurations for each distribution was proportional to value of $C_n^k$, where n – amount of all bonds, and k – number of negative bonds.

In addition to the full-link neural network architecture, other architectures were considered. Since each input corresponded to the connection of $i$ with $j$ spins, we considered a network architecture where the second layer

represented spins ($N^2$ nodes), and each node of the second layer was connected to 4 corresponding input nodes.

An example of prediction of energy values for a particular test configuration is shown in Fig. 1. One can see that a network with a custom architecture shows more accurate energy prediction results for the test systems.

Both networks were compared on 150 unique spin configurations. Due to results on test dataset shown in Table 1, custom neural network shows more accurate predictions rather than fully-connected network. As an error metric we used root mean square error.

***Table I.*** *Accuracy comparison on test dataset.*

| | Fully connected | Custom |
|---|---|---|
| *RMS error* | 0.3497 | 0.0270 |

## 4. Conclusions

In this work we have demonstrated the possibility of using neural networks to calculate the basic thermodynamic characteristics of the Edwards-Anderson spin glass models. We also compared the accuracy results of neural network implementations of different architectures. On average, the custom neural network architecture showed more accurate results compared to the full-link architecture.

## Acknowledgements

The research was supported by RSF (project No. 21-72-00157).

## References

[1] Carrasquilla, J., & Melko, R. G. (2017). Machine learning phases of matter. Nature Physics, 13(5), 431-434.
[2] Shiina, K., Mori, H., Okabe, Y., & Lee, H. K. (2020). Machine-learning studies on spin models. Scientific reports, 10(1), 1-6.
[3] Korol, A. O., & Kapitan, V. Y. E. (2021). Neural Network for Prediction of Curie Temperature of Two-Dimensional Ising Model. Dal'nevostochnyi Matematicheskii Zhurnal, 21(1), 51-60.
[4] Kapitan, V., Vasiliev, E., Perzhu, A., Kapitan, D., Rybin, A., Korol, A., ... & Shevchenko, Y. (2021). Numerical simulation of magnetic skyrmions on flat lattices. AIP Advances, 11(1), 015041.
[5] S. F. Edwards, P. W. Anderson. Phys. F: Metal Phys. 5 (1975).

Sixth Asian School-Conference on Physics and
Technology of Nanostructured Materials
Vladivostok, Russia, 25 – 29 April, 2022

**I.p.08**

# Monte Carlo simulation of magnetic skyrmions

A.V. Perzhu[1], E.V. Vasiliev[1,2], M.A. Padalko[1,2], A.O. Korol[1,2], A.E. Rybin[1,2], D.Yu. Kapitan[1,2], R.A. Volotovskiy[1,2], A.G. Makarov[1,2], Yu.A. Shevchenko[1,2], K.S. Soldatov[1,2], V.Yu. Kapitan[*,1,2], K.V. Nefedev[1,2]

[1] Far Eastern Federal University, FEFU Campus, 10 Ajax Bay, Russky Island, Vladivostok, 690922, the Russian Federation
[2] Institute of Applied Mathematics, Far Eastern Branch, Russian Academy of Science, Vladivostok, 690041, 7 Radio St., the Russian Federation

*e-mail: kapitan.vyu@dvfu.ru

**Abstract.** Magnetic two-dimensional films, in which magnetic vortex textures - skyrmions appear because of competition between the direct Heisenberg exchange and the Dzyaloshinskii-Moriya interaction, were studied using the Monte-Carlo simulation technique. The process of nucleation of skyrmions with increasing of the external magnetic field was studied, various phases into which the Heisenberg spin system transitions were recognized using by a convolutional neural network for data analysis.

## 1. Introduction

Skyrmions are formed in magnets in which spin interactions favor a magnetic structure with chiral symmetry, such as a vortex. In such a system, the strongest interaction between the spins is direct exchange. The energy of this interaction, which contributes to the collinear alignment of neighboring spins and controls the ordering in the system, is determined by the Heisenberg exchange. A much weaker interaction favoring the perpendicular orientation of neighboring spins exists in some magnets in which electrons have a strong spin-orbit coupling. The energy of this interaction is described by the Dzyaloshinskii-Moriya (DM) interaction and leads to the fact that the spins in the magnet deviate from the parallel orientation, which naturally leads to a chiral structure.

In our paper, the conditions for the nucleation and stable existence of magnetic skyrmions in two-dimensional magnetic films were considered in the frame of the classical Heisenberg model. We studied several types of flat lattices with DMI and the direct exchange between spins:

1. a honeycomb lattice with 3 nearest neighbours (NN),
2. a square lattice with 4 NN,
3. a hexagonal or triangular lattice with 6 NN.

## 2. Research description

The Metropolis algorithm, being a Monte Carlo method, is a general method, suitable for high-performance computing, for studying the thermodynamic properties of substances consisting of interacting individual particles and dynamics in external magnetic fields. In this study, we used the Metropolis algorithm for the simulation of magnetic skyrmions in the frame of the classical Heisenberg model, taking into account direct short-range exchange and Dzyaloshinsky-Moriya interaction. The influence of the DM interaction on the spin system in frame of the Heisenberg model was analysed. We used the next Hamiltonian in our research [1]:

$$H = H_J + H_{DMI} + B + A \quad (1)$$

$$H_J = -J \sum_r S_r \cdot \left(S_{r+\hat{x}} + S_{r+\hat{y}} + S_{r+\hat{z}}\right), \quad (2)$$

$$H_{DMI} = -D \sum_r S_r \times S_{r+\hat{x}} \cdot \hat{x} + S_r \times S_{r+\hat{y}} \cdot \hat{y} + S_{r+\hat{z}} \cdot \hat{z} \quad (3)$$

$$B = -B_z \sum_r S_r \quad (4)$$

$$A = A_z \sum_r S_r^2 \quad (5)$$

The ferromagnetic-exchange interaction (the first term), the Dzyaloshinskii-Moriya interaction (the second term), the Zeeman coupling (the third term), magnetic anisotropy (the fourth term) are considered.

## 3. Conclusion

In the frame of the classical two-dimensional Heisenberg model, a spin system with direct short-range exchange was modelled, and a study of its competition with the Dzyaloshinski i-Moriya interaction was carried out. For the analysis of the data obtained during the Monte Carlo simulation, a convolutional neural network (CNN) was used for the recognition of different phases of the spin system, depending on simulation parameters such as DMI and the external magnetic field ($H_z$). Based on these data, the phase diagrams ($H_z$,D) for different lattices were plotted. It is known that one of the features of the practical application of skyrmions is that they are usually stable in a narrow region of low temperatures and external magnetic fields. Therefore, based on the data from the phase diagrams, we can select appropriate parameters that significantly affect the properties of spin systems and lead to the formation of various phases that provide different functionalities for use in spintronics.

## Acknowledgements

This work has been supported by the state task of the Ministry of Science and Higher Education of Russia No. 0657-2020-0005.

## References

[1] Belemuk, S. Stishov, Physical Review B **95** (22) (2017) 224433.

Sixth Asian School-Conference on Physics and
Technology of Nanostructured Materials
Vladivostok, Russia, 25 – 29 April, 2022



# Self-assembled growth of $C_{60}$ monomolecular layers at $Tl/NiSi_2$ atomic sandwich on Si(111)

V.V. Mararov[1], T.V. Utas[1], L.V. Bondarenko[1], A.Y. Tupchaya[1], Y.E. Vekovshinin[1,2], D.V. Gruznev[1], A.N. Mihalyuk[1,2], A.V. Zotov[1], A.A. Saranin[*,1]

[1] Institute of Automation and Control Processes FEB RAS , 5 Radio St., Vladivostok 690041, Russia
[2] Far Eastern Federal University, 8 Sukhanova St., Vladivostok 690950, Russia

*e-mail: saranin@iacp.dvo.ru

**Abstract.** Self-assembled growth of $C_{60}$ layers at the $Tl/NiSi_2/Si(111)$ atomic sandwich has been studied as a function of the density of the Tl atomic layer. It has been found that fullerenes form hexagonal close-packed arrays. Inside $C_{60}$ layer, fullerenes can form together with Tl atoms three distinct configurations which are reflected by difference of the $C_{60}$ brightness — dim, normal and bright, — at the STM images. It was found out that the brightness level directly depends on the amount of thallium under fullerenes. Using additional Tl deposition, it is possible to change the relative fractions of the dim, normal and bright fullerenes, in particular to fabricate the homogeneous $C_{60}$ layers consisting exclusively of the fullerenes of a single type.

## 1. Introduction

The molecular self-assembly, which is one of the basic approaches for creating nanoscale structures, has been extensively investigated owing to its great potential for a wide range of applications. Due to its spherical shape and high symmetry, $C_{60}$ has been considered an ideal molecule for studying self-assembly process on crystalline surfaces. As examples, one can remind growth of the 2D fullerene quasi-crystals on the $Pt_3Ti(111)$ crystal intentionally terminated by the two layers of Pt [1], fabrication of the molecular arrays almost exclusively built of the magic clusters on the In-modified Au/Si(111) surface [2], self-assembled $C_{60}$ ordering into the unusual "trilliumene" structures on Si(111) and Ge(111) surfaces covered by monolayers of Tl or Pb [3]. The discovery of graphene has caused a strong increase of the interest in 2D materials having a thickness of one atomic layer. These materials are considered as promising candidates for the synthesis of supramolecular systems, including those containing $C_{60}$ fullerenes [4,5]. This served as an additional motivation for considering in this study the self-assembly of $C_{60}$ on the $Tl/NiSi_2/Si(111)$ atomic sandwich [6]. The upper atomic layer is represented in this sandwich by a Tl monolayer, which can be transformed into a tallene [7]. Also, this work is related to our past studies on the $C_{60}/Tl/Si(111)$ system, where the formation of trilliumens was discovered [4]. Although Tl monolayers on a pure Si(111) surface and on top of a single-layer $NiSi_2$ on Si(111) look very similar, their structural properties are not identical. In the Tl/Si(111) system, a decrease in Tl coverage of 1.0 ML leads to the appearance of other reconstructions, 3×1-Tl and √3×√3-Tl [8], while in the $Tl/NiSi_2/Si(111)$ system, Tl coverage can decrease to ~0.6 ML. Using the possibility of changing the Tl coating, the effect of the Tl atomic density on the structure of the $C_{60}$ layers was investigated.

## 2. Experiment

Our experiments were performed with the UHV Omicron MULTIPROBE system operating in an ultrahigh vacuum (~$2.0 \times 10^{-10}$ Torr). Atomically-clean Si(111)7 ×7 surfaces were prepared *in situ* by flashing to 1280 °C after the samples were first outgassed at 600 °C for several hours. Thallium was deposited from a Ta tube, Ni from an electron beam evaporator and fullerenes from a resistively heated Ta boat. DFT calculations were conducted using VASP code, with core electrons represented by PAW potentials. The GGA-PBE to the exchange-correlation functional is employed for structure relaxation. To simulate the $C_{60}$ superstructure on $Tl/NiSi_2/Si(111)$ surface we used a slab consisting of 5 BLs of the substrate with the PBE-optimized bulk Si lattice constant. The atomic positions of $C_{60}/Tl/NiSi_2$ atoms and atoms of Si layers within the two BLs of the slab were optimized.

## 3. Results and discussions

Fig. 1 shows STM images illustrating the growth stages of the $C_{60}$ layer on the $Tl/NiSi_2/Si(111)$ surface with gradual metered deposition of Tl. As can be seen, hexagonal arrays of fullerenes contain "holes" arranged in the √3×√3 lattice inside a monomolecular fullerite layer. This coincides with the periodicity of √21×√21 in the lattice constants Si(111), $a_{Si}$ = 0.384 nm, since the $C_{60}$ layer has a periodicity of √7×√7.

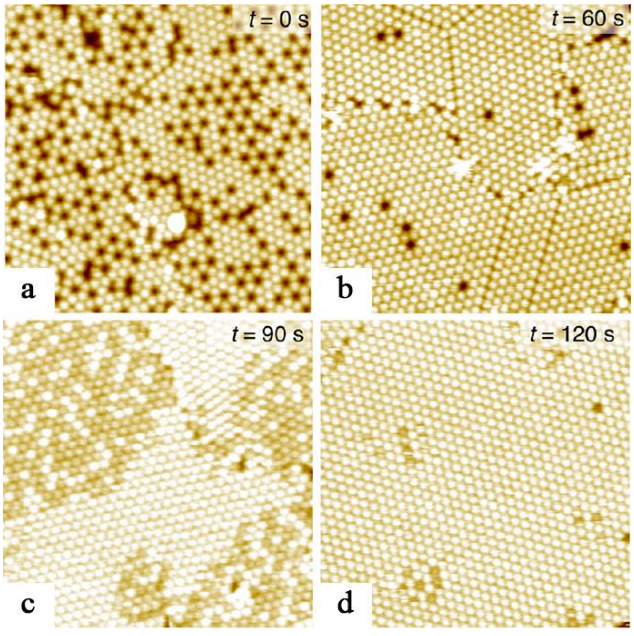


***Fig. 1.*** *A set of 30×30 nm² STM images illustrating the evolution of the surface structure after each step of Tl deposition for 30 s. at a rate of 0.14 ML/min onto the $C_{60}$ monolayer grown on the $Tl/NiSi_2/Si(111)$ surface with 0.73 ML of Tl.*

At a glance, it might seem that the new structure is similar to the trilliumene from the $C_{60}$/Pb/Si(111) system [3]. However, if in the case of trilliumene the "holes" are real vacancies, in the current case the "holes" are fullerenes located lower than their neighbors. We called such molecules "dark", and the molecules around them with normal brightness — "normal". Deposition of Tl at RT on this surface led to a gradual decrease in the density of dark fullerenes and after total deposition for 60 s. the dark molecules completely disappeared and the arrays began to consist only of normal fullerenes (Fig. 1(b)). With further deposition of thallium, "bright" fullerenes begin to appear, their number increases in proportion to the dose of Tl, eventually all regions consist only of such bright molecules (Fig. 1(d)). It can be concluded that there are three different height levels that fullerenes can occupy on the Tl/$NiSi_2$/Si(111) substrate, and with increasing atomic density of the Tl monolayer, fullerenes gradually become higher. Conducting calibration experiments to convert the deposition time of Tl into coating gave an understanding of the origin of dark, normal and bright fullerenes. The difference in the brightness of $C_{60}$ molecules is related to the number of Tl atoms under an individual fullerene. Using DFT calculations, structural models of $C_{60}$ on Tl/$NiSi_2$/Si(111), which adsorption sites and orientation of $C_{60}$ fullerenes were varied, as well as the number of Tl atoms under them, were tested. It was found that $C_{60}$ occupy $T_4$ positions, which are preferable over the $T_1$ and $H_3$ positions, and are oriented with a hexagon upwards. As for the number of Tl atoms, the single model that corresponds to the available experimental data is shown in Fig. 2.

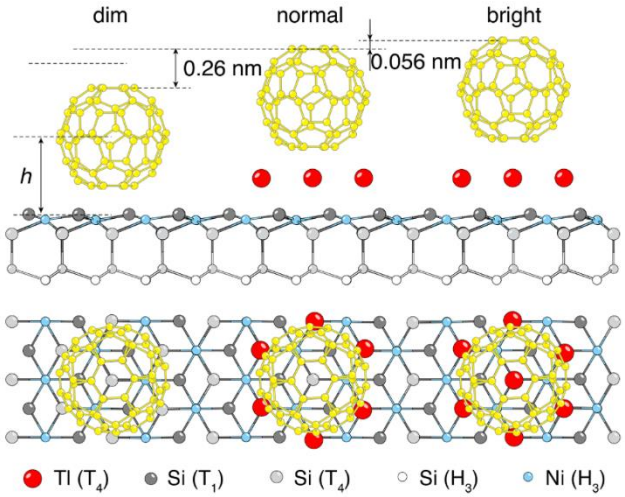


***Fig. 2.*** *Structural models for the dim, normal and bright $C_{60}$ fullerenes on the Tl/Si(111) surface (side and top views). The corresponding legend in the lower panel indicates color designations of various atoms and the sites occupied by atoms of each type.*

It was concluded that there are completely lack Tl atoms under dark fullerene, one thallium atom is missing under normal fullerene, and all 7 atoms sit in their places under bright fullerene. Accordingly, it was calculated that normal fullerenes are 0.26 nm above the dark and 0.056 nm below the bright. Using information about the number of Tl atoms under each of the fullerenes, STM images were processed to assess the Tl coating at each stage of Tl deposition. The obtained results coincided with the calibration data, thereby confirming the reliability of the calculated models.

## 4. Conclusions

In conclusion, using STM observations and DFT calculations we have examined self-assembled formation of $C_{60}$ monomolecular layers on the surface of the atomic Tl/$NiSi_2$/Si(111) sandwich. Deposited $C_{60}$ fullerenes form hexagonal close-packed arrays. Within the $C_{60}$ layer, the fullerenes display three distinct types of contrast in the STM images — dim, normal and bright. It has been elucidated that the bright fullerenes reside atop a completed Tl monolayer, in the case of the normal fullerenes one Tl atom directly beneath the given fullerene is missing, while under the dim fullerenes no Tl atoms are left. The fraction of fullerenes of each type can be changed in controllable way using Tl deposition onto the $C_{60}$/Tl/$NiSi_2$/Si(111) sample. In particular, one can fabricate the homogeneous $C_{60}$ layers consisting exclusively of the fullerenes of a single type, normal or bright depending on the desire. Bearing in mind that single-layer $NiSi_2$ possesses advanced metallic properties [6], elucidating the effects produced by Tl overlayers of various atomic densities and $C_{60}$ layers with various separations from a single-layer $NiSi_2$ are of interest for examine the peculiarities of the electronic transport in the layered atomic structures. Possibility for growing thick $C_{60}$ films as protective layers for the buried atomic sandwich [9] allows to conduct *ex situ* transport measurements, the topic of interest for both fundamental research and the advancement of electronic applications.

## Acknowledgements

The work was supported by the Russian Foundation for Basic Researches under Grant 19-32-90010. The calculations were conducted using the equipment of Shared Resource Center Far Eastern Computing Resource IACP FEB RAS (https://cc.dvo.ru).

## References

[1] M. Paßens, S. Karthäuser. Acta Cryst. A **875**(2019)41–49.
[2] D.V. Gruznev, A.V. Matetskiy, L.V. Bondarenko, O.A. Utas, A.V. Zotov, A.A. Saranin, J.P. Chou, C.M. Wei, M.Y. Lai, Y.L. Wang. Nat. Commun. **4**(2013)1679–7.
[3] A.V. Zotov, D.A. Olyanich, V.V. Mararov, T.V. Utas, L.V. Bondarenko, A.Y. Tupchaya, D.V. Gruznev, A.N. Mihalyuk, C.V. Wei, Y.L. Wang, A.A. Saranin. J. Chem. Phys. **149**(2018)034702–7.
[4] M. Švec, P. Merino, Y.J. Dappe, C. González, E. Abad, P. Jelínek, J.A. Martín-Gago. Ph. Rev. B **86**(2012)121407.
[5] H. Guo, A. Martínez-Galera, J. Gomez-Rodrıguez. Nanotechnology **32**(2020)025711.
[6] L.V. Bondarenko, A.Y. Tupchaya, A.N. Mihalyuk, S.V. Eremeev, A.V. Matetskiy, N.V. Denisov, Y.E. Vekovshinin, A.V. Slyshkin, D.V. Gruznev, et al. 2D Mater. **7**(2020)025009–9.
[7] D.V. Gruznev, L.V. Bondarenko, A.Y. Tupchaya, A.N. Mihalyuk, S.V. Eremeev, A.V. Zotov, A.A. Saranin. 2D Mater. **7**(2020)045026–7.
[8] V.G. Kotlyar, A.A. Saranin, A.V. Zotov, T.V. Kasyanova. Surf. Sci. **543**(2003)L663–L667.
[9] D.A. Olyanich, V.V. Mararov, T.V. Utas, L.V. Bondarenko, A.Y. Tupchaya, A.V. Matetskiy, N.V. Denisov, et al. Appl. Surf. Sci. **501**(2020)144253.

Sixth Asian School-Conference on Physics and
Technology of Nanostructured Materials
Vladivostok, Russia, 25 – 29 April, 2022



# Trident macrospin ice

I.N. Nalivaiko*,1, M.A. Chesnokov[1], K.S. Soldatov[1,2], V.S. Strongin[1,2], K.V. Nefedev[1,2]

[1] Far Eastern Federal University, Vladivostok, Russky Island, 10 Ajax Bay, 690922, Russian Federation
[2] Institute of Applied Mathematics, Far Eastern Branch, Russian Academy of Science, Vladivostok, Radio 7, 690041, Russian Federation

*e-mail: nalivaiko.in@students.dvfu.ru

**Abstract.** We are doing the research on the thermodynamic properties and phase transitions of two-dimensional arrays which consist of dipole coupled Ising-type nanomagnets located at the vertices of a triangular lattice called a trident lattice. The Metropolis method is used to investigate phase transitions depending on the lattice parameter, frustrations, and the influence of an external field on the system.

## 1. Introduction

Artificial square ice [1], consisting of dipole-interacting nanoparticles with Isingian-type moments lithographically arranged on a two-dimensional square lattice, was introduced as a two-dimensional analogue of pyrochlore spin ice [2] and provided prospects for direct investigation of the physics of geometric frustrations. Despite the presence of competing interactions, square dipole ice does not show macroscopic degeneracy, which is observed in spin ice on the pyrochlore lattice. Macroscopic degeneracy of the ground state leads to many interesting physical phenomena. Several concepts have been proposed to search for systems where this phenomenon is observed, in particular kagome ice, where a spin-liquid phase can be observed. Nevertheless, the implementation of the lattice, which at the same time would be technically simple, would be suitable for direct visualization of thermal fluctuations in real time remains, and most importantly would show macroscopic degeneracy of the ground state, remains questionable [3].

In [4], the results of a study of a new trident lattice were presented, which has similarities with the square geometry of ice, but at the same time demonstrates a higher degree of geometric frustrations. The building blocks in such a lattice are three nanomagnets (tridents) periodically arranged orthogonally (Fig. 1). The lattice parameters a and b allow you to change the strength of the interaction between the dipoles.

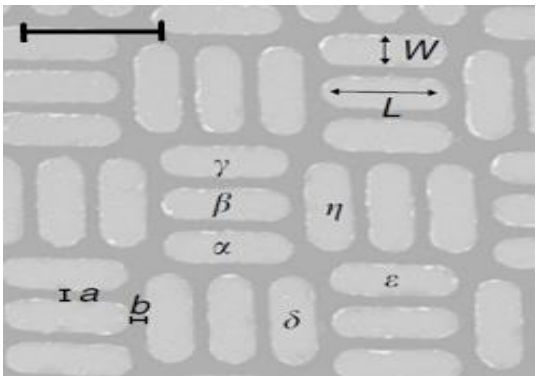


***Fig. 5.*** *Trident lattice [4].*

The paper presents the results of experiments conducted on the trident lattice. For example, a system of dipoles was heated to a certain temperature, after which its behavior during thermal relaxation was monitored. Also, the experiments investigated cases with a = b and with different b. By changing the distance between the tridents, the authors of the article were able to influence the balance of competing interactions in the lattice, and, as a result, the number of frustrations in the system [1].

## 2. Formalism and model

The energy of the dipole-dipole interaction of a system of dipoles on a trimerized lattice is calculated using the formula (2.1):

$$E_{ij} = \frac{(\vec{M}_i \vec{M}_j)}{|\vec{r}_{ij}|^3} - 3\frac{(\vec{M}_i \vec{r}_{ij})(M_j \vec{r}_{ij})}{|\vec{r}_{ij}|^5}, \qquad (2.1)$$

where *i, j* - the numbers of the interacting dipoles, $\vec{r}_{ij}$ is the vector between the centers of the magnetic moments of the interacting dipoles, $\vec{M}_i$ is the value of the magnetic moment vector.

It should be noted that since the lattice geometry requires taking into account the relative elongation of the nanostructures, instead of one large magnetic moment, i.e. superspin, we will use three co-directional moment vectors, which, in accordance with the Ising model, will change the direction coherently under the influence of thermodynamic fluctuations.

To determine the thermodynamic properties of the system under study we used The Metropolis method. The main idea of this method is the equal formation of a sample of the state space with a given probability of the distribution of states. At each step of the sampling process, a configuration with a given probability is accepted (or rejected):

$$P(E_i \rightarrow E_j) = min\left(\frac{P(E_i)}{P(E_j)}, 1\right). \qquad (2.2)$$

When numerically calculating the temperature behavior of the system, the probability of the configuration energy is determined according to the canonical Gibbs distribution:

$$P(E_i) = min\left(\frac{e^{-E_i/k_B T}}{Z}\right). \qquad (2.3)$$

Combine equations (2.1) and (2.2), we get

$$\begin{aligned} P(E_i \rightarrow E_j) &= min\left(\frac{e^{-E_j/k_B T}}{e^{-E_i/k_B T}}, 1\right) \\ &= min\left(exp\left[-\frac{E_j - E_i}{k_B T}\right], 1\right) \\ &= min\left(exp\left[-\frac{\Delta E}{k_B T}\right], 1\right), \end{aligned} \qquad (2.4)$$

where $\Delta E$ is the change in the energy level of the system as a result of configuration change, $T$ is the absolute

temperature. In the process of sampling, a certain characteristic (order parameter or spin excess) is determined for each selected configuration. Based on the obtained characteristics, the standard deviation and the mathematical mean are determined, based on which the thermodynamic quantities are calculated [2].

### 3. Research plan

It is supposed to repeat the experiments described in the article with the help of computer computational methods to confirm the practical results and study frustration in this system.

By analogy with article [5], an increase in the exponent b in this lattice should affect the possibility of a phase transition. For large values of b, the system is divided into subsystems. To do this, the heat capacity of the system will be determined, so it can be used to judge the presence of a phase transition [5]. The heat capacity directly depends on the energy of the system obtained by the Metropolis method, and can be found by the formula (3.1):

$$C(T) = \frac{1}{N}\frac{\langle E^2\rangle - \langle E\rangle^2}{k_B T^2}. \quad (3.1)$$

Magnetic susceptibility:

$$\chi(T) = \frac{1}{N}\frac{\langle |\vec{M}|^2\rangle - \langle |\vec{M}|\rangle^2}{k_B T}. \quad (3.2)$$

Correlation function:

$$G(T) = \frac{1}{N}\langle \sum \vec{M}_i \vec{M}_j \rangle - \frac{1}{N}\langle \left|\vec{M}\right| \rangle^2. \quad (3.3)$$

The most important task in the study of artificial spin systems is to find the ground state of the system: a configuration in which the total energy of the system is minimal. It is assumed to use the Metropolis algorithm, the hybrid Metropolis algorithm, or other methods, such as, for example, a greedy algorithm or an exact solution by a parallel exhaustive enumeration algorithm for relatively small systems. After that, it is planned to conduct a study of the external magnetic field.

### Acknowledgements

The research results connected with model samples preparation and physical experiments were obtained within the framework of the state task of the Ministry of Science and Higher Education of the Russian Federation of Russia (No. 0657-2020-0005). The research results connected with algorithms elaboration, program coding end implementation of parallel scheme of calculation obtained at the expense of the grant of the President of the Russian Federation for state support of the leading scientific schools of the Russian Federation (NSh-2559.2022.1.2)

### References

[1] Wang, R. F. et al. Artificial ‘spin ice’ in a geometrically frustrated lattice of nanoscale ferromagnetic islands. Nature 439, 303–306 (2006).

[2] 2. Bramwell, S. T. & Gingras, M. J. P. Spin ice state in frustrated magnetic pyrochlore materials. Science 294, 1495–1501 (2001).

[3] Perrin, Y., Canals, B. & Rougemaille, N. Extensive degeneracy, Coulomb phase and magnetic monopoles in artificial square ice. Nature 540, 410–413 (2016).

[4] Farhan, A., Petersen, C.F., Dhuey, S. et al. Nanoscale control of competing interactions and geometrical frustration in a dipolar trident lattice. Nat Commun 8, 995 (2017).

[5] Hofhuis K. et al. Geometrical frustration and competing orders in the dipolar trimerized triangular lattice //Physical Review B. – 2021. – Т. 104. – №. 1. – С. 014409.

Sixth Asian School-Conference on Physics and
Technology of Nanostructured Materials
Vladivostok, Russia, 25 – 29 April, 2022



# Molecular dynamics study of the influence of free volume and orientation of the crystallization front on its velocity in nickel

G.M. Poletaev*[,1], I.V. Karakulova[1], R.Yu. Rakitin[2]

[1] Polzunov Altai State Technical University, 46 Lenin Av., Barnaul 656038, Russia
[2] Altai State University, 61 Lenin Av., Barnaul 656049, Russia

*e-mail: gmpoletaev@mail.ru

**Abstract.** The molecular dynamics method was used to study the influence of free volume and orientation of the crystallization front relative to the growing crystal on the front velocity in nickel. According to the data obtained, the crystallization velocity with an increase in the undercooling temperature does not increase monotonically, but has a maximum at 0.7 of the melting point, after which it gradually decreases. Crystallization proceeds faster with the orientation of the front plane (100), slower – with the (110) and (111) orientations. When free volume was introduced into the computational cell, the concentration of free volume occurred, as a rule, at the last stage of crystallization, where the completion of the crystal construction took place.

## 1. Introduction

Solidification and the accompanying crystallization of metals and alloys are technologically widespread and important processes that have a significant impact on the final structure of the material. Despite the great attention to the crystallization process and its long-term study, there are still unresolved questions even for pure metals, and this applies not only to the kinetics of a relatively more complex homogeneous crystallization mechanism [1, 2] associated with the nucleation of crystalline nuclei, but also heterogeneous [3, 4], when the process is accompanied by the movement of the crystallization front.

This work is devoted to the study of the influence of free volume and orientation of the crystallization front relative to the growing fcc crystal on the front velocity in nickel. Three front orientations were considered: (100), (110) and (111). Nickel was chosen as a typical fcc metal, for which a fairly large set of experimental data has been collected, and there are well-tested interatomic interaction potentials.

## 2. Description of the model

Modeling was carried out using computational cell in the form of an elongated parallelepiped with a square cross section. The computational cell contained about 107 thousands atoms, was 5.8 nm high and wide, and 37.5 nm long. At the ends of the parallelepiped (along the Z axis), the crystal structure was fixed, which imitated the starting position of the crystallization front. Along another axes X and Y, periodic boundary conditions were imposed.

To describe interatomic interactions in nickel, the many-particle potentials of Cleri and Rosato [5] were used. Potentials of this type have been repeatedly used in molecular dynamics models and have been tested for a large number of characteristics. The experience of their application shows that with their help it is possible to describe the various properties of metals and alloys. The time integration step in the molecular dynamics method was 2 fs. The temperature in the model was set through the initial velocities of the atoms according to the Maxwell-Boltzmann distribution, taking into account the thermal expansion of the computational cells. To keep the temperature constant during the simulation, a Nose-Hoover thermostat was used.

At the first stage, the computational cell was melted by holding it at a temperature significantly higher than the melting point. Then the thermostat was turned on, and holding was carried out at a given constant temperature. During the molecular dynamics experiment, the crystallization front moved from the ends of the computational cell to its center.

## 3. Results and discussions

Front velocity was determined as the average speed of the left and right fronts:

$$\upsilon = \frac{\Delta l_1 + \Delta l_2}{2\Delta t} \quad , \qquad (1)$$

where $\Delta l_1$ and $\Delta l_2$ are distances travelled by the crystallization front in the upper and lower parts of the computational cell during the time $\Delta t$ (Fig. 1). In most cases, the position of the front was clearly visible visually. The determination error did not exceed, as a rule, two atomic planes.

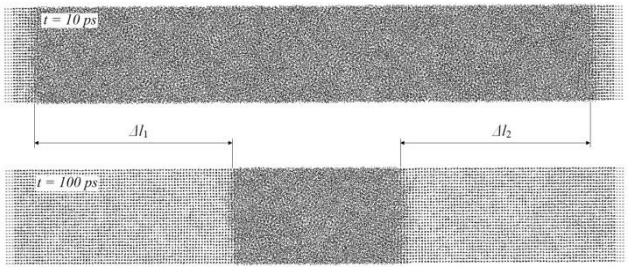


***Fig. 1.*** *To the method of calculating the velocity of the crystallization front movement.*

Fig. 2 shows the temperature dependences of the crystallization velocity obtained in this work for three different orientations of the front relatively growing fcc crystal: (100), (110) and (111). According to the data obtained, the crystallization velocity with an increase in the undercooling temperature does not increase monotonically, but has a maximum at 0.7 of the melting point, after which it gradually decreases.

Such behavior in the region of super-high values of supercooling is well described by the Wilson-Frenkel model with diffusion limitation [1, 3]:

$$\upsilon(T) = A\exp\left(-\frac{E}{kT}\right)\left[1-\exp\left(-\frac{\Delta\mu}{kT}\right)\right] \qquad (2)$$

Here $A$ is the preexponential factor, $E$ is the activation energy of the migration of an atom in the liquid phase, $k$ is the Boltzmann constant, $T$ is the temperature, $\Delta\mu$ is the difference between the free energies of the liquid and crystalline states.

In our case, the main factor responsible for the effect of temperature on the velocity of the crystallization front is the value of $E$ in formula (2), i.e. diffusion mobility of atoms in the amorphous phase. With a decrease in temperature, this mobility decreases exponentially, and at a certain temperature (at $0.7 \cdot T_m$ in our case), this decreasing contribution begins to prevail over the increasing contribution of the second factor in formula (2).

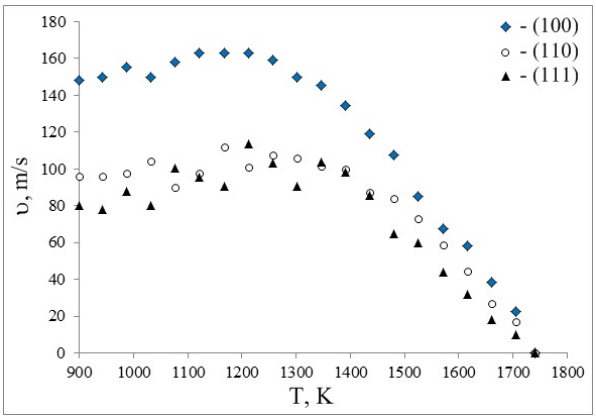


***Fig. 2.*** *Dependences of the crystallization front velocity on the temperature for three different front orientations.*

As can be seen from Fig. 2, crystallization proceeds faster with the front orientation (100), slower – with the (110) and (111) orientations. To explain the anisotropy of the crystallization velocity, one should obviously pay attention to the second factor in formula (2) and the value of $\Delta\mu$, which is usually defined as the difference between the free energies of the liquid and crystalline states. However, near the liquid-crystal interface, it is not the difference in energies within the volumes of the crystal and the liquid is of greater importance, but the difference in the free energies of an atom near the interface in the liquid phase and of an atom built-in into the boundary of a growing crystal. If the value of $\Delta\mu$ is determined in this way, it ceases to be constant and becomes dependent on the orientation of the liquid-crystal interface. This energy can be compared with the energy of an adatom on the corresponding free surface of the crystal, or with the activation energy of its migration over a given surface. For example, in [6], the activation energies of surface self-diffusion were obtained for nickel: 0.33 eV over the free (111) surface and 0.63 eV over the (100) surface.

The maximum values of the crystallization velocity obtained in our work at $0.7 \cdot T_m$ coincide with the values given in [7] for nickel, where they were obtained by modeling using another potential: 150 m/s for (100) orientation and 100 m/s for (110) orientation.

The free volume was introduced by removing atoms from the starting computational cell. During crystallization, the concentration of free volume occurred, as a rule, at the last stage of crystallization, where the completion of the crystal construction took place (Fig. 3). In addition, it was noted that in the presence of excess free volume, twins were formed comparatively more often. As the free volume increased, the crystallization front velocity decreased.

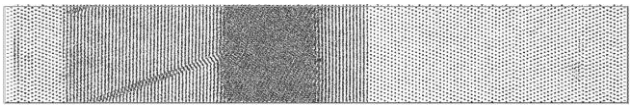

***Fig. 3.*** *Concentration of free volume at the final stage of crystallization.*

## 4. Conclusions

The molecular dynamics method was used to study the influence of free volume and orientation of the crystallization front relative to the growing crystal on the front velocity in nickel. The obtained dependences coincided within the limits of error with the experimental data, which indicate of the adequacy of the model and the chosen interatomic potential. According to the data obtained, the crystallization velocity with an increase in the undercooling temperature does not increase monotonically, but has a maximum at 0.7 of the melting point, after which it gradually decreases. This decrease in the crystallization velocity can be explained by a decrease in the diffusion mobility of atoms in the amorphous phase.

Crystallization proceeds faster with the orientation of the front plane (100), slower – with the (110) and (111) orientations. The anisotropy of the crystallization velocity is associated with the difference between the free energies of an atom near the boundary in the liquid phase and of an atom built-in into the boundary of a growing crystal, which depends on the orientation of the boundary and, in particular, correlates with the energy of an adatom on the corresponding free surface of the crystal.

When free volume was introduced into the computational cell, the concentration of free volume occurred, as a rule, at the last stage of crystallization, where the completion of the crystal construction took place. As the free volume increased, the crystallization front velocity decreased.

## References

[1] P.K. Galenko, V. Ankudinov, K. Reuther, M. Rettenmayr, A. Salhoumi, E.V. Kharanzhevskiy. Philosophical Transactions of the Royal Society A: Mathematical, Physical and Engineering Sciences **377**(2019)20180205.
[2] S.K. Jha, S. Karthika, T.K. Radhakrishnan. *Resource-Efficient Technologies* **3**(2017)94.
[3] V.I. Mazhukin, A.V. Shapranov, V.E. Perezhigin, O.N. Koroleva, A.V. Mazhukin. Mathematical Models and Computer Simulations **9**(2017)448.
[4] G. Sun, J. Xu, P. Harrowell. Nature Materials **17**(2018)881.
[5] F. Cleri, V. Rosato. Physical Review B **48**(1993)22.
[6] C.L. Liu, J.M. Cohen, J.B. Adams, A.F. Voter. Surface Science **253**(1991)334.
[7] H.Y. Zhang, F. Liu, Y. Yang, D.Y. Sun. Scientific Reports **7**(2017)10241.

Sixth Asian School-Conference on Physics and
Technology of Nanostructured Materials
Vladivostok, Russia, 25 – 29 April, 2022



# Quantum-mechanical study of the substitution and adsorption of P atoms on silicene

A.V. Prokhorenko*[,1], A.A. Gnidenko[2], A.N. Chibisov[3], M.A. Chibisova[3]

[1] Pacific National University, Khabarovsk, 136 Tikhookeanskaya St., Khabarovsk 680035, Russia
[2] Institute of Material Science of Khabarovsk Scientific Centre, Far Eastern Branch of the Russian Academy of Sciences, 153 Tikhookeanskaya St., Khabarovsk 680000, Russia
[3] Computing Center, Far Eastern Branch of the Russian Academy of Sciences, 35 Kim Yu Chena St., Khabarovsk 680000, Russia

*e-mail: aimpva@pnu.edu.ru

**Abstract.** The behavior (substitution and adsorption) of the phosphorus atom on the surface of silicene has been studied using quantum mechanical calculations. The most favorable positions, binding energies and the value of the activation barrier for phosphorus diffusion have been established. The change in the local magnetic moment on the phosphorus atom is described depending on its position and the positions of the surrounding silicon atoms.

## 1. Introduction

Silicene is of great interest for fundamental physics and practical applications. It has a stronger spin-orbit interaction [1], in contrast to graphene, which will make it possible to observe the spin Hall effect at not too low temperatures [2]. Theoretical studies have also reported such unique properties as a mechanically adjustable band gap [3] and a metal phase with valley polarization [4]. Experimental observations and synthesis of silicene [5–9] showed the prospects of nanosized materials that can be easily functionalized chemically or mechanically and introduced into modern electronics [10]. The study of the interaction of phosphorus atoms with the surface of silicene, presented in this work, may be of interest in the prospect of creating qubits for quantum computers based on this material, by analogy with crystalline silicon doped with phosphorus.

## 2. Experiment

The Quantum Espresso software package [11] based on the density functional theory and the pseudopotential method was used to perform quantum mechanical calculations. The calculations were performed taking into account the spin-orbit non-collinear interaction. Fully relativistic pseudopotentials for silicon and phosphorus were selected from the Quantum Espresso program library [12]. The cutoff energy of the plane wave basis was 476 eV. Calculations of Si:P structures were carried out with a homogeneous grid of k-points 9×9×1, constructed according to the Monkhorst-Pack scheme. The analysis of the values of charges on atoms was carried out using the Bader partitioning method.

## 3. Results and discussions

To study substitution, one silicon atom in the silicene structure was replaced by phosphorus. The binding energy is calculated as follows:

$$E_B = E_{system} - [E_{silicene}\,(N_{Si} - 1)/N_{Si} + E_P] \qquad (1)$$

where $E_{system}$ is the total energy of the P-doped silicene, $E_{silicene}$ is the total energy of the perfect silicene, $N_{Si}$ is the number of Si atoms in a supercell of pristine silicene, $E_P$ is the total energy of an isolated P atom. The binding energy of the resulting system is -3.34 eV. To study adsorption, key variants of the location of the phosphorus atom were considered (Fig. 1).

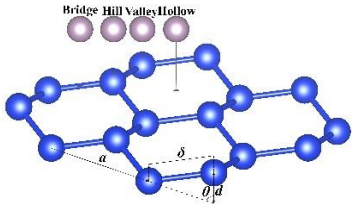


***Fig. 1.*** *Structure of silicene and possible sites of adsorption of the phosphorus atom.*

Binding energy for adsorption:

$$E_B = E_{system} - (E_{silicene} + E_P) \qquad (2)$$

The most favorable is *Hill* site with a binding energy of -3.84 eV. The local magnetization and charge on the phosphorus atom is determined by the silicon environment – the number of neighboring silicon atoms, the distances to them. The magnetic moment of the phosphorus atom in the *Bridge* site is 0.210 $\mu_B$/cell and decreases to 0.020 $\mu_B$/cell in the *Hill* position. The charge value varies in the range from -1.20 *e* in the case of substitution to -0.83 *e* in the *Hollow* site. The magnitude of the charge on the phosphorus atom does not correlate with the magnitude of the magnetization. The Nudged Elastic Band (NEB) method was used to determine the energy barrier when a phosphorus atom moves over the silicene surface from the *Hill* position through the hexagonal ring to the next *Hill* position. The activation energy to overcome the barrier, which is located between the *Hill* and *Hollow* sites, was 1.51 eV.

The adsorption of a phosphorus atom onto a silicene surface already containing either one substituting (Fig. 2a) or one adsorbed (Fig. 2b) phosphorus atom was considered.

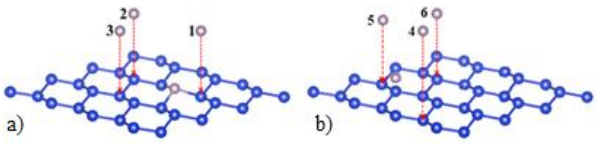


***Fig. 2.*** *Options for the location of the adsorbed P atom next to a) a substituting one; b) absorbent.*

In the 2nd and 3rd cases, in the region of adsorption of the second phosphorus atom, shifts occur in the arrangements of neighboring silicon atoms, similar to the *Hill* and *Valley* sites considered earlier; in this case, the binding energies become lower, the *Hill* site (-4.17 eV) is the most favorable. In the case of two adsorbing atoms, according to the binding energies, configuration 5 can be distinguished as the most favorable (-4.23 eV), the location of the second phosphorus atom near the first reduces its binding energy in configuration 4, and in configuration 6 leads to a spontaneous displacement from the already existing adsorbed atom. The charge on phosphorus atoms deviates insignificantly from the previously considered cases of single substitution or absorption of a phosphorus atom on silicene. Local magnetic moments on phosphorus atoms are not expressed.

## 4. Conclusions

A complex of quantum mechanical calculations made it possible to determine the optimal positions of one and two phosphorus atoms on the silicene surface. Adsorption has been shown to be more beneficial than substitution; the energy gain is 0.5 eV. The binding energy during the absorption of the second P atom decreases while maintaining the distance between the phosphorus atoms; the formation of dimers from phosphorus atoms is energetically unfavorable. The dependences of the local magnetization on phosphorus atoms on the silicon environment are established. Using the NEB method, the activation energy for the transfer of an adsorbed P atom over the silicene surface was determined.

## Acknowledgements

The work was carried out within the framework of the subject of the Laboratory for the Simulation of Quantum Processes of the Pacific National University in accordance with the State assignment for research work implementation from the Ministry of Science and Higher Education of the Russian Federation (project № 0818-2020-0005).

## References

[1] Liu, C.C., Jiang, H., Yao, Y. Low-energy effective Hamiltonian involving spin-orbit coupling in silicene and two-dimensional germanium and tin. Physical Review B 84(2011)195430.
[2] Liu, C.C., Feng, W., Yao, Y. Quantum Spin Hall Effect in Silicene and Two-Dimensional Germanium. Physical Review Letters 107(2011)076802
[3] Topsakal, M., Ciraci, S. Elastic and plastic deformation of graphene, silicene, and boron nitride honeycomb nanoribbons under uniaxial tension: A first-principles density-functional theory study. Physical Review B 81(2010)024107.
[4] Ezawa, W. Valley-Polarized Metals and Quantum Anomalous Hall Effect in Silicene. Physical Review Letters 109(2012)055502.
[5] Padova, P.D., Quaresima, C. et al. Evidence of graphene-like electronic signature in silicene nanoribbons. Physical Review Letters 96(2010)261905.
[6] Padova, P.D., Leandri, C. et al. Burning Match Oxidation Process of Silicon Nanowires Screened at the Atomic Scale. Nano Letters 8(2008)2299.
[7] Vogt, P., Padova, P.D. et al. Silicene: Compelling Experimental Evidence for Graphenelike Two-Dimensional Silicon. Physical Review Letters 108(2012)155501.
[8] Lin, C.-L., Arafune, R. et al. Structure of silicene grown on Ag (111). Applied Physics Express 5(2012)045802.
[9] Jamgotchian, H., Colignon, Y. et al. Growth of silicene layers on Ag(111): Unexpected effect of the substrate temperature. Journal of Physics Condensed Matter 24(2012)172001.
[10] Fleurence, A., Friedlein, R. et al. Experimental Evidence for Epitaxial Silicene on Diboride Thin Films. Physical Review Letters 108(2012)245501.
[11] Giannozzi, P., Baroni, S. et al. QUANTUM ESPRESSO: A Modular And Open-Source Software Project For Quantum Simulations Of Materials. Journal of Physics: Condensed Matter 21(2009)395502.
[12] Dal Corso, A. Pseudopotentials Periodic Table: From H to Pu. Computational Materials Science 95(2014)337.

Sixth Asian School-Conference on Physics and
Technology of Nanostructured Materials
Vladivostok, Russia, 25 – 29 April, 2022



# Silicon growth and etching by oxygen and selenium: evolution of Si(111)-7×7 surface structure and morphology

D.I. Rogilo*[,1], S.V. Sitnikov[1], S.A. Ponomarev[1,2], D.V. Sheglov[1], L.I. Fedina[1], A.V. Latyshev[1,2]

[1] Rzhanov Institute of Semiconductor Physics SB RAS, Acad. Lavrent'ev ave. 13, Novosibirsk 630090, Russia
[2] Novosibirsk State University, Pirogov Str. 2, Novosibirsk 630090, Russia

*e-mail: rogilo@isp.nsc.ru

**Abstract.** Using *in situ* reflection electron microscopy and *ex situ* atomic force microscopy, we have studied the morphological stability of large-scale (~10–100 μm) Si(111)-7×7 terraces during silicon growth and etching by oxygen and selenium. On the large-scale terraces, silicon growth proceeds in multilayer mode that we have divided into three regimes based on RMS surface roughness scaling analysis. Surface etching by selenium is characterized by 2.65 eV activation energy that limits etching kinetics in a low-temperature range when the whole surface is converted to a disordered "1×1"-Se phase. The etching of the singular Si(111)-7×7 surface by selenium preserves flat surface morphology, while oxygen-induced etching leads to the slow development of multilayer morphology due to hindered diffusion of oxygen adatoms. On the step-bunched surface, the silicon or selenium adatom diffusion to the step bunches leads to the self-organization of pyramidlike or valley-like morphology during silicon growth or selenium-induced etching, respectively.

## 1. Introduction

Si-based electronics downscales gradually to 1 nm where next-generation devices will require the production of ultrathin films and superlattices with atomically sharp interfaces and, potentially, self-ordered 3D nanostructures promising for a range of applications [1–3]. Therefore, single monatomic steps always existing on crystalline substrates become a significant object of surface engineering [4], and the investigation of wafer-scale surface treatments (e.g. growth, etching, metal adsorption) fosters the control over substrate surface morphology at the monatomic step level to improve the properties of overlying films.

## 2. Experiment

*In situ* experiments were carried out in an ultrahigh vacuum reflection electron microscope (UHV REM) equipped with several interchangeable evaporators: a resistively heated single crystal silicon, a crucible loaded with commercial selenium pellets with 99.9996% purity, and a barium peroxide in a perforated metal shell that releases oxygen when heated to ~500°C. We used specimens with 8×1×0.38 mm dimensions cut from n-type (0.3 Ω×cm) Si(111) wafers with a miscut angle of <0.1°. The detailed descriptions of the UHV REM experimental setup for silicon growth [5], oxygen [6], and selenium [7] treatments of the Si(111) surface are presented elsewhere. The exact shape of steps and 2D islands as well as their distribution on the surface was analyzed using atomic force microscopy (AFM, Bruker Multimode 8).

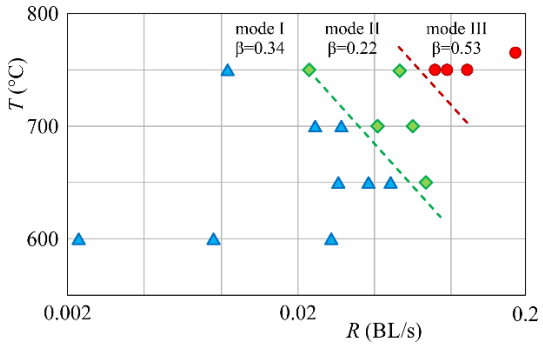


***Fig. 1.*** *R–T map of morphological instability modes.*

## 3. Results and discussions

Figure 1 shows the *R–T* map of surface morphologies discovered from the analysis of topographic AFM images after Si growth on extremely wide Si(111) terraces. According to this map, the main parameter controlling the surface morphology evolution of a growing Si film is deposition rate *R*. At low *R* (triangles in figure 1), the Si growth gradually switches from periodic 2D island nucleation and growth to multilayer mode with root-mean-square surface roughness scaling with coverage $W \propto \Theta^{0.34}$ (figure 2a). The scaling exponent β≈0.34 authenticates that ascending/descending Si fluxes governing surface morphology evolution are imbalanced by effective diffusion along step edges [8] (figure 2b).

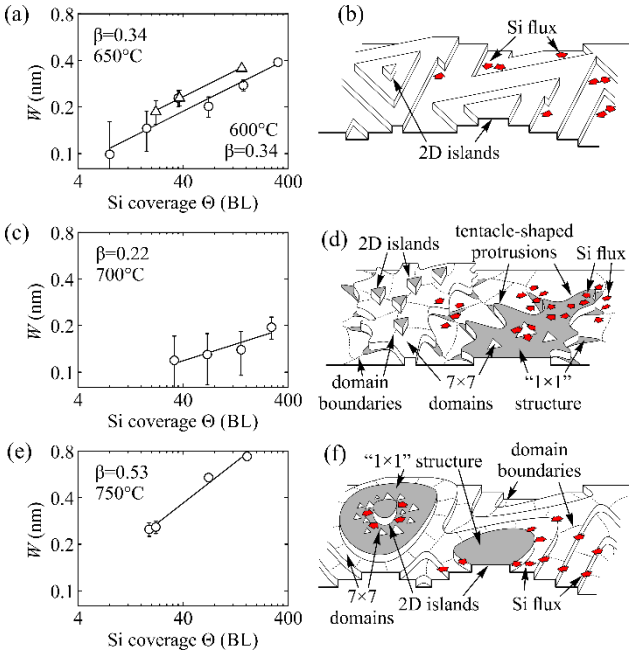


***Fig. 2.*** *(a,c,e) Dependences of RMS roughness W on the Si coverage Θ deposited at (a) 600°C and 0.03 BL/s (circles), 650°C and 0.043 BL/s (triangles), (c) 700°C and 0.067 BL/s, (e) 750°C and 0.09 BL/s. Error bars show the magnitude of W oscillations caused by submonolayer coverage variations. (b,d,f) Surface processes under the conditions of different instability modes: (b) I, (d) II, (f) III. Red arrows denote destabilizing Si surface fluxes.*

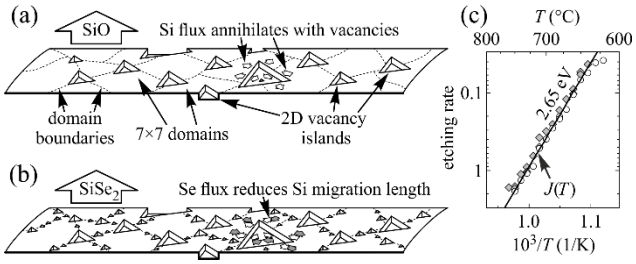


***Fig. 3.*** *Processes on the Si(111) surface during etching by (a) oxygen and (b) selenium. White and grey arrows denote Si and Se fluxes, respectively. (c) Temperature dependence of Si etching rate J(T). Grey diamonds (white circles) correspond to incomplete (complete) Si(111) surface coverage by the "1×1"-Se phase.*

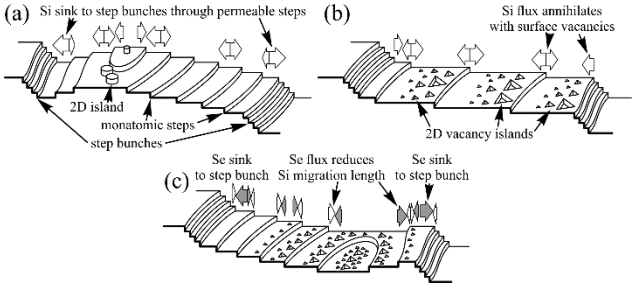


***Fig. 4.*** *Main processes on the step-bunched Si(111) surface during (a) Si growth, (b) etching by oxygen, (c) etching by selenium. White and grey arrows denote Si and Se fluxes.*

At higher deposition rates ~0.07 BL/s (1 BL = $1.56\times10^{15}$ cm$^{-2}$) and enhanced temperatures ~700°C (diamonds in figure 1), Si(111) terraces are covered by numerous randomly arranged regions with disordered "1×1" phase. This growth mode displays slow ($W\propto\Theta^{0.2}$, figure 2c) build-up of dendritic-like mounds (figure 2d). When taking into account the oscillations of RMS surface roughness $W$ during each period of 2D island nucleation (error bars in figure 2c), one can note that this instability II may be a growth mode transient from layer-by-layer to surface mounding and having no definite scaling exponent.

At high deposition rates (≳0.1 BL/s) and temperatures around 750°C (circles in figure 1), Si growth shows strong surface mounding ($W\propto\Theta^{0.53}$, figure 2e). This growth mode is controlled by net uphill adatom flux caused by persisting "1×1" phase regions at the top of each mound (figure 2f).

The etching of the Si(111) surface in a low-pressure oxygen atmosphere triggers a weak morphological instability—incomplete disappearance of the previous (upper) layer when next-layer 2D vacancy islands have been nucleated and grown (figure 3a). Despite the Si(111) surface looks very similar when etched in an oxygen atmosphere and during exposure to selenium molecular beam, the weak instability does not develop during selenium-induced etching. AFM surface morphology analysis has shown that small vacancy islands nucleate only at the upper terrace (until it disappears) due to preferred nucleation at 7×7 domain boundaries (figure 3b). This explains the enhanced morphological stability of the selenium-induced etching of the singular Si(111) surface in comparison with the oxygen-induced etching.

Using *in situ* REM data, we have measured Si(111) surface etching rate as a function of substrate temperature at fixed selenium coverage corresponding to full surface conversion to impurity-induced "1×1"-Se phase (figure 3c). The Arrhenius-type approximation yields 2.65 eV activation energy that we attribute to the activation energy of $SiSe_2$ molecule formation and its desorption, which agrees with the published binding energy $E_b$=2.7 eV/atom [9]. It is important to note that, unlike oxygen atoms, Se adatoms have a reasonable energy barrier for surface diffusion (about 1.2 eV [10]), which puts a significant surface diffusion of Se adatoms into the physical picture of surface processes. The surface Se flux interferes with Si adatom mass transport via their involvement in the formation of the volatile $SiSe_2$ molecules.

To study the effect of the atomic steps always existing on the substrate surface, we have investigated the morphological evolution of the step-bunched Si(111)-7×7 surface during Si growth and etching. When the Si deposition rate was high enough to realize layer-by-layer 2D island nucleation and growth in 600–750°C interval, we always observed gradual self-organization of pyramidlike waves—prolonged stepped mounds between the step bunches (figure 4a) [5,11]. During the etching of the step-bunched Si(111) surface, its evolution depended on the etchant type (oxygen or selenium). In oxygen atmosphere, we observed only ascending step flow and periodic vacancy island nucleation on wide terraces (figure 4b). On the contrary, the etching by Se molecular beam lead to the self-organization of stepped valley-like surface morphology caused by the excavation of the regions between the step bunches (figure 4c) [7]. In ref. [12], we have related the formation of pyramidlike and valley-like surface morphologies to the effective surface transfer of Si and Se adatoms, respectively, from terraces towards step bunches.

## 4. Conclusions

We have shown that the interplay of local structural transitions and complex surface mass transfer governs the non-trivial morphological evolution of the Si(111)-7×7 surface exposed to a Si molecular beam, an oxygen atmosphere, or a Se molecular beam. During Si growth, the appearance of disordered high-atom-density "1×1" phase changes Si mass transport routes and causes transitions between different mounding modes. When Si(111) surface is etched in a vacuum, diffusion of Se adatoms stabilizes the *singular* Si(111) surface but excavates the *step-bunched* surface by creating multilevel valley-like morphology analogously to the formation of the pyramidlike waves triggered by Si adatom diffusion during Si growth.

## Acknowledgements

This research was financially supported by Russian Science Foundation [grant number 19-72-30023] and was performed on the equipment of CKP "Nanostruktury".

## References

[1] F. Grillot, et al. Nanophotonics (2020)20190570.
[2] S. Pandya, et al. Sci. Rep. **6**(2016)26075.
[3] D. Diaz-Fernandez, et al. Appl. Surf. Sci. **455**(2018)227.
[4] Henryk Turski, et al. Appl. Surf. Sci. **484**(2019)771.
[5] D. I. Rogilo, et al. J. Cryst. Growth **457**(2017)188.
[6] S. V. Sitnikov, A. V. Latyshev, S. S. Kosolobov. J. Cryst. Growth **457**(2017)196.
[7] D. I. Rogilo, et al. J. Cryst. Growth **529**(2020)125273.
[8] M. V. Ramana Murty, B. H. Cooper. Phys. Rev. Lett. **83**(1999) 352.
[9] A. C. Papageorgopoulos, M. Kamaratos. Surf. Sci. **504**(2002)L191.
[10] S. Q. Wu, et al. Chem. Phys. **382**(2011)41.
[11] D. I. Rogilo, et al. // Phys. Rev. Lett. **111**(2013)036105.
[12] D. Rogilo, et al. Appl. Surf. Sci. **540**(2021)148269.

# Parallel hybrid multispin Monte-Carlo method for the Edwards-Anderson spin glass model

A.E. Rybin*[,1,2], D.Yu. Kapitan[1,2,3], K.V. Nefedev[1,2], E.V. Vasiliev[1,2], M.A. Padalko[1,2], A.V. Perzhu[1,2], R.A. Volotovskiy[1,2], A.G. Makarov[1,2], Yu.A. Shevchenko[1,2], A.O. Korol[1,2], K.S. Soldatov[1,2], V.Yu. Kapitan[1,2], P.D. Andriushchenko[1]

[1] Institute of Applied Mathematics, Far Eastern Branch, Russian Academy of Science, Vladivostok, 690041, 7 Radio St., Russian Federation
[2] Far Eastern Federal University, 8 Sukhanova St., Vladivostok 690950, Russian Federation
[3] ITMO University, Kronverksky Pr. 49, bldg. A, St. Petersburg, 197101, Russian Federation

*e-mail: rybin.ae@dvfu.ru

**Abstract.** We study the effectiveness of parallel hybrid multispin Monte-Carlo method by calculating ground states. The object of the study is the Edwards-Anderson model on a square lattice of Ising spins. We compare the results to the other Mc methods, and brute force method on small lattices.

## 1. Introduction

During the 1960s, it was revealed that some magnetic alloys have unusual magnetic properties. This discovery led to the development of spin glass models, which are used to study complex disordered systems. Spin glasses are characterized by two main characteristics that strongly distinguish these systems from others: disorder in the position of magnetic atoms in the alloy and the occurrence of strong competition between ferromagnetic and antiferromagnetic interactions.

## 2. Model

*In this paper, the authors consider the two-dimensional Edwards-Anderson model [1], with the exchange integral $J_{ij}$ as a random function and the average value of $J_{ij}$ is zero. In such a system, at one-half of the spins the interaction with each other is ferromagnetic, and at the other - antiferromagnetic. The interaction $J_{ij}$ between the spin pair (ij) changes during the transition from one pair to another. The Hamiltonian is expressed as:*

$$H = -\sum_{<i,j>} J_{ij} S_i S_j - h \sum_{i=1}^{N} S_i$$

$S_i$, $S_j$ – spins of the lattice, <i,j> denotes the summation over pairs of interacting spins in a system with size $N$, $h$ is the external magnetic field.

## 3. Results and discussions

One of the actual problems for the Edwards-Anderson model is the search for the ground state. We proposed parallel modification for multispin Monte Carlo algorithm. [2]. To speed up the calculations it was proposed to use parallel computing using the OpenMP library. The number of clusters should be equal to the number of threads. Our method allows one to search for low-energy states or even ground states. We are based on the assumption that minimization of the energy of subsystems should lead to the minimization of the energy of the whole system.

We calculated ground states of considered model with lattice size of 36, 100, 400 and 900 spins using various methods (Table 1). The proposed method showed efficiency at the level of exact solution at small lattice sizes, and the lowest ground state value at large lattices, remaining the calculation speed on Monte Carlo level.

***Table I.*** *Comparison of the values of the main states of the system obtained by different methods.*

| Lattice size | Exact solution | Replica-exhange Monte Carlo | Hybrid Monte Carlo | Parallel hybrid Monte Carlo |
|---|---|---|---|---|
| 6x6 | -1.50 | -1.27 | -1.33 | -1.50 |
| 10x10 | -1.40 | -1.24 | -1.32 | -1.40 |
| 20x20 | - | -0.98 | -1.06 | -1.34 |
| 30x30 | - | -0.76 | -0.79 | -1.34 |

## 4. Conclusions

In this work, we have demonstrated that the parallel hybrid MC method showed greater efficiency, then various variations of regular Monte Carlo methods.

## Acknowledgements

The research results connected with model samples preparation and physical experiments were obtained within the framework of the state task of the Ministry of Science and Higher Education of the Russian Federation of Russia (No. 0657-2020-0005). The research results connected with algorithms elaboration, program coding end implementation of parallel scheme of calculation obtained at the expense of the grant of the President of the Russian Federation for state support of the leading scientific schools of the Russian Federation (NSh-2559.2022.1.2)

## References

[1] S. Edwards, P. Anderson, Theory of spin glasses, Journal of Physics F: Metal Physics 5 (5) (1975) 965–974.
[2] K. V. Makarova, A. G. Makarov, M. A. Padalko, V. S. Strongin, K. V. Nefedev, “Multispin Monte Carlo Method”, Dal'nevost. Mat. Zh., 20:2 (2020), 212–220.

# Structures and electrical conductance at the initial stages of magnesium growth on Si(111)-Pb surface

M.V. Ryzhkova*[,1], D.A. Tsukanov[1,2]

[1] Institute of Automation and Control Processes FEB RAS , 5 Radio St., Vladivostok 690041, Russia
[2] Far Eastern Federal University, 8 Sukhanova St., Vladivostok 690950, Russia

*e-mail: lavric@iacp.dvo.ru

**Abstract.** In the present work, using low-energy electron diffraction (LEED) and four-point-probe method (4PP), we have studied the growth of Mg on Si(111) surface modified by Pb. New surface phases with magnesium and lead have been obtained: √7x√7 and √19x√3. Electrical conductance has investigated after formation of magnesium layers at room temperature until 6-8 monolayers (ML). It was concluded that growth of magnesium layers depends both, on the structure of Pb layer and on the deposition manner of magnesium flux.

## 1. Introduction

Metal adsorption onto semiconductor surfaces has incredible interest not only from a physical point of view, but also it is useful in various technological applications. We have been studying a number of Pb/Si(111) surface phases in terms of their affect the growth of the Mg films, because the Pb/Si(111) system has a relatively well studied atomic structure and the reconstruction mechanisms depending on the coverage of metal and deposition temperature [1-3]. In this work, Mg was grown at room temperature on Pb-rich surface structures: δ(7x7)-Pb, β-√3x√3-Pb, 1x1-Pb, and their ordering and properties have been studied.

## 2. Experiment

The experiments were performed in the ultrahigh vacuum chamber at a base pressure $2 \cdot 10^{-10}$ Torr. Mg was deposited from heated Ta tube at a rate 0.6 ML/min. The Mg amount was calibrated by the formation of 4x4-(Pb, Mg) and 6x6-(Pb, Mg) surface phases, which were formed at 0.3 ML and 0.8 ML of Mg dose, respectively [4]. Pb was deposited from heated Ta tube at a rate 0.4 ML/min. Pb was calibrated by formation of 1x1-Pb structure with 1 ML of Pb coverage. All samples were *n*-type (P-doped) with the electrical resistivity 20-1700 Ω·cm. The sizes of specimen were 15x5x0.45 $mm^3$ with Si(111) orientation of surface. (Pb,Mg)/Si(111) systems were investigated by LEED and 4PP method. The measuring head consists of four probes with a distance of 0.6 mm from each other arranged in square cones.

## 3. Results and discussions

On the Si(111)1x1-Pb surface deposition of Mg up to 1 ML leads to the consistent transformation of the surface structure that is accompanied with changes in electrical conductance (fig.1). At 0-0.5 ML of Mg dose electrical conductance decreases and the 4x4-(Pb,Mg) surface phase forms. The next 6x6-(Pb,Mg) structure demonstrates relatively high conductance due to metallic layer formation but at the next stage their properties depend on deposition manner. At large portions of the order of 1-2 ML the LEED pattern shows 4x4 periodicity, while at little portions of the order of 0.2-0.5 ML the LEED pattern shows 2x2 periodicity and low electrical conductance (fig.1). Deposition of Mg on δ(7x7)-Pb leads to decrease of the electrical conductance after 1 ML as well as deposition on β-√3x√3-Pb by little portions results in low conductance and destruction of surface order according to LEED observations. The growth of Mg layer by the large portions takes place with characteristic ring on the LEED pattern. Moreover, new surface phase √7x√7-(Pb,Mg) have been formed. Mg growth on this surface has demonstrated 1x1 periodicity at 2.6 ML but at 7 ML the polycrystal film grows accompanied with high conductance.

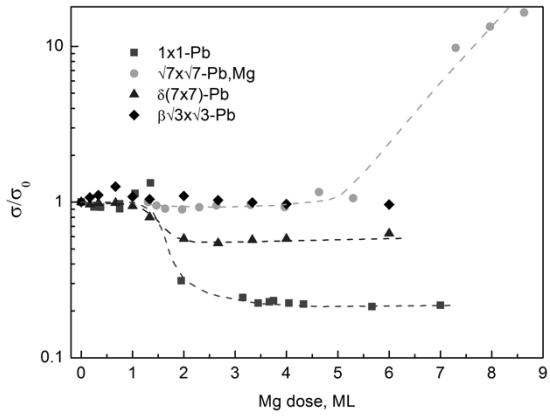


***Fig. 1.*** *Electrical conductance of surface structures at formation of magnesium films.*

## 4. Conclusions

In summary, new surface phases √7x√7, √19x√3 with coadsorbed Mg and Pb have been obtained. It was concluded that growth of Mg films depends on the structure of Pb/Si(111) surface and on the deposition manner. For these films electrical conductance has been investigated.

## Acknowledgements

This work is supported by Russian Foundation for Basic Research (grant No. 20-02-00497).

## References

[1] O. Kubo, A.A. Saranin, A.V. Zotov, J.-T. Ryu, H. Tani, T. Harada, M. Katayama, V.G. Lifshits, K. Oura. Surface Science **415** (1998) L971–L975.
[2] D. Lee, G. Lee, S. Kim, Ch. Hwang, Ja-Y. Koo, H. Lee. J. Phys.: Condens. Matter **19** (2007) 266004.
[3] Mustafa M. Ozer and Hanno H. Weitering. Phys.Rev.B **88** (2013) 045415.
[4] A.Y.Tupchaya, L.V. Bondarenko, A.A. Yakovlev, A.N. Mihalyuk, D.V. Gruznev, N.S. Denisov, A.V. Matetskiy, A.Yu. Aladyshkin, A.V. Zotov, A.A. Saranin (in press)

# High-quality GaSb(111) film on the Si(111)√3×√3-B surface

A.V. Slyshkin[1], D.V. Gruznev[1], A.Y. Tupchaya[1], L.V. Bondarenko[1], A.N. Mihalyuk[1,2], A.V. Zotov[1], A.A. Saranin[1]

[1] Institute of Automation and Control Processes FEB RAS , 5 Radio St., Vladivostok 690041, Russia
[2] Far Eastern Federal University, 690950 Vladivostok, Russia

*e-mail: zsanichz@gmail.com

**Abstract.** Experimental and calculated studies of the formation process of GaSb(111) films on the Si(111) surface with the √3×√3-B reconstruction are presented. A reduced formation of silicide and the growth of atomically smooth unstressed films are shown.

## 1. Introduction

When the Si (111) substrate is heavily doped with B atoms (0.001 Ω cm), the segregation of B atoms during high-temperature annealing leads to the formation of the √3×√3-B reconstruction. This reconstruction has proven to be a stable inert surface suitable for the formation of organic nanostructures and supramolecular ensembles [1]. Due to the absence of unsaturated dangling bonds, such a surface is also suitable for changing the growth mode of some metals [2]. In addition, hole doping of the near-surface layer leads to changes in some physical properties of 2D structures formed on such substrates. For example, an unexpected phase transition in the Sn layer [3] and induced superconductivity in the Si(111)√3×√3-Sn reconstruction [4].

This paper discusses the possibility of using the √3×√3-B reconstruction to form low-dimensional structures, particularly GaSb, whose formation on a "clean" silicon surface is challenging due to the high chemical activity of its constituent elements. The results of experimental studies by scanning tunneling microscopy (STM), low-energy electron diffraction (LEED) are presented.

## 2. Experiment

Our experiments have been performed with a variable-temperature Omicron VT-STM operating in an ultrahigh vacuum (~$2.0\times10^{-10}$ Torr). Si(111)√3×√3-B reconstruction has been prepared from Si (111) substrate, which is heavily doped with B atoms, by annealing to 900°C for one hour. Ga and Sb have been deposited from the Ta tube. Ga and Sb deposition rate has been calibrated using STM.

## 3. Results and discussions

A change in the growth mode of GaSb films on the Si(111) surface with the √3×√3-B reconstruction is shown. This problem has high practical importance for applications in electronic and optoelectronic devices. Nowadays, the growth of A3B5 on Si is carried out mainly using numerous buffer layers; without them, an Sb wetting layer is formed, on which dome-shaped GaSb islands of various orientations are located [5].

This work shows that introducing the Si(111)√3×√3-B reconstruction into the interface changes the growth mode from island to pseudo-layer one (Fig. 1) with a smooth surface and high crystalline quality of the film. STM analysis of the surface reconstructions (2×2 and 2√3×2√3, Fig. 2) showed that a Ga-terminated film is formed.

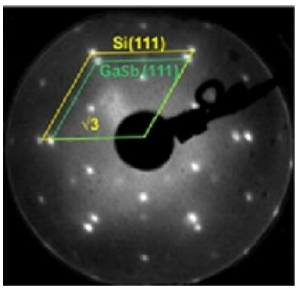


***Fig. 1.*** *LEED image (unit cells of Si(111) and GaSb(111) lattices are highlighted).*

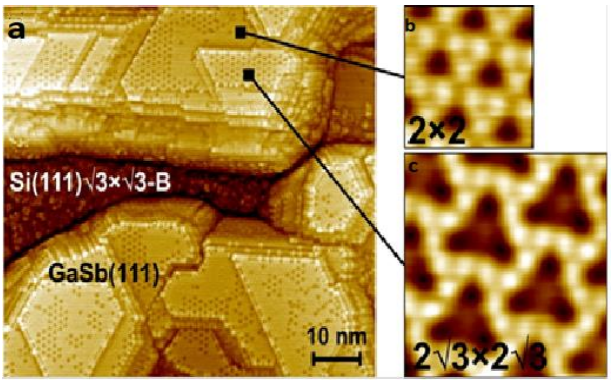


***Fig. 2.*** *STM images of the film with two Ga reconstructions, (b)2×2 and (c)2√3×2√3 (50×50 nm²).*

## 4. Conclusions

On the Si(111)√3×√3-B reconstruction, the high-quality GaSb(111) film can be formed with two different reconstructions, 2×2 and 2√3×2√3. The structure and growth processes were studied by using STM and LEED.

The work was supported by the Russian Foundation for Basic Research under Grant 20-02-00497.

## References

[1] Y. Makoudi, J. Jeannoutot, F. Palmino, F. Chérioux, G. Copie, C. Krzeminski, F. Cleri, B. Grandidier. Surf. Sci. Rep., 72, 316 (2017).
[2] K. Nagase, R. Ushioda, K. Nakatsuji, T. Shirasawa, H. Hirayama. Appl. Phys. Express, 13, 085506 (2020).
[3] F. Ming, D. Mulugeta, W. Tu, T. Smith, P. Vilmercati, G. Lee, Y. Huang, R. Dieh, P. Snijders, H. Weitering. Nat. Comm., 8, 14721 (2017).
[4] X. Wu, F. Ming, T. Smith, G. Liu, F. Ye, K. Wang, S. Johnston, H. Weitering, K. Oyoshi, D. Lenssen, R. Carius, S. Mantl. Phys. Rev. Lett. 125, 117001 (2020).
[5] S. Hara. J. J. Appl. Phys. 50, 08LB03 (2011).

Sixth Asian School-Conference on Physics and
Technology of Nanostructured Materials
Vladivostok, Russia, 25 – 29 April, 2022



# Solving a long-standing problem regarding atomic structure of Si(100)2×3-Ag

A.N. Mihalyuk[1,2], V.G. Kotlyar[1], O.A. Utas[1], T.V. Utas[1], L.V. Bondarenko[1], A.Y. Tupchaya[*,1], D.V. Gruznev[1,2], A.V. Zotov[1], A.A. Saranin[1]

[1] Institute of Automation and Control Processes FEB RAS , 5 Radio St., Vladivostok 690041, Russia
[2] Far Eastern Federal University, 8 Sukhanova St., Vladivostok 690950, Russia

*e-mail: tupchaya@iacp.dvo.ru

**Abstract.** The atomic structure of the Si(100)2×3-Ag reconstruction has remained unknown for more than 25 years since its first observation with scanning tunneling microscopy, despite a relatively small unit cell and seeming abundance of the available experimental data. We propose a structural model of the Si(100)3×2-Ag reconstruction which comfortably fits all the principal experimental findings, including our own and those reported in the literature. The model incorporates 3 Si atoms and 4 Ag atoms per the 2×3 unit cell forming linear atomic chains along the $3a_{Si}$-periodic direction. A peculiar feature of the Si(100)2×3-Ag structure is the occurrence of the inner Si dimers in the second atomic layer from the top of the Si(100) substrate. The reconstruction is proved to possess semiconducting properties.

## 1. Introduction

Low-dimensional systems composed of atomically thin metal films on semiconductor surfaces have attracted great attention due to their intriguing electronic properties and potential prospects for applications in atomic-scale devices. In particular, the metal-induced surface reconstructions on silicon are known to display a set of fascinating phenomena, including single-atomic-layer superconductivity, giant Rashba-type spin-splitting of metallic bands, exhibition of the exotic properties of the quantum spin Hall insulators, etc. Breakthrough in assessing the prospects of a given reconstruction has typically been trigged out by the conclusive determination of its atomic arrangement. Sometimes it takes decades to reach this goal. The Ag/Si(100) system can serve as an example. Though onset of the extensive study of the system dates back to the mid-1990s [1], atomic arrangement of its surface reconstructions still remains unknown with the only fresh exception; namely, the atomic structure of the Si(100)2×2-Ag reconstruction forming at room temperature (RT) has very recently been determined. The advanced key idea that has allowed the authors to get a success was to adopt an Ag tetramer as a reconstruction building block instead of a more habitual Ag dimer.

In the present study, we have addressed the Si(100)3×2-Ag reconstruction that is formed in the Ag/Si(100) system at elevated temperatures and whose structure was examined in a number of experimental works [2]. In spite of a relatively small unit cell and abundance of the experimental data, including high-resolution STM images in both polarities, evaluation of the reconstruction composition, established registry of the STM protrusions with respect to the Si(100) substrate, and determined electronic band structure, no convincing structural model has been so far proposed for the Si(100)2×3-Ag reconstruction. Thus, up to now elucidating the Si(100)2×3-Ag structure has still remained a challenging task.

## 2. Results and discussions

Optimal procedure to produce a surface completely covered by the 2×3-Ag reconstruction included RT deposition of about 1.0 ML of Ag followed by annealing at 500°C for a few minutes. Formation of the 2×3-Ag phase involves a considerable surface Si mass transport which manifests itself in developing the two-level system of the two-dimensional one-atomic-layer-high (0.136 nm) islands on terraces, as one can see in the large-scale STM image (Fig. 1c). Its formation indicates that the Si content in the 2×3-Ag reconstruction differs from 1.0 ML in the top layer of original intact Si(100)2×1 surface. From the quantitative analysis of the Si redistribution, one can determine the coverage of Si atoms incorporated in the 2×3-Ag reconstruction. Present evaluation yields the value of 0.49±0.03 ML which coincides with that of 0.52±0.04 ML determined earlier [3]. Thus, it is safe to conclude that Si(100)2×3-Ag incorporates 1/2 ML of Si (i.e., 3 Si atoms per 2×3 unit cell).

At the atomic scale, the reconstruction shows up as the array of the $2a_{Si}$-wide rows running along the [011] direction and having the $3a_{Si}$ periodicity along the rows [$a_{Si}$ = 3.84 Å, the Si(100)1×1 lattice constant] (Fig. 1d). Concerning the $3a_{Si}$ periodicity, one can notice the occurrence of numerous two-dimensional stacking faults with respect to the neighboring rows, as well as within a given row (Fig. 1d). As a result, in the 2×3 LEED patterns the half-order spots are sharp and bright, while the third-order spots are faint and streaky (Fig. 1a). The high-resolution STM images (Fig. 1d) demonstrate the well-defined characteristic features which strongly depend on the bias polarity. In order to find a proper structural model of the Si(100)2×3 reconstruction, we employed the AIRSS (Ab Initio Random Structure Searching) technique basing on the available information on its composition. In particular, 3 Si atoms per 2×3 unit cell incorporated in the reconstruction was believed to be a reliable value, as shown above. In contrast, the accurate Ag coverage remained a debated subject. It was generally believed to be 1/2 ML (i.e., 3 Ag atoms per 2×3 unit cell). However, the other Ag coverages were also reported, i.e., between 1/2 and 2/3 ML or even ~ 0.3 ML. The doubt regarding 3 Ag atoms per 2×3 unit cell was expressed in the paper devoted to the Si(100)2×3-Ag electronic structure [4]. Therefore, in our study the AIRSS technique was applied to the three possible cases, in which the number of Ag atoms was either 3, 4, or 5 per 2×3 unit cell, while the number of Si atoms

was always 3. Evaluation revealed that the structure with four Ag atoms is clearly the most favorable one.

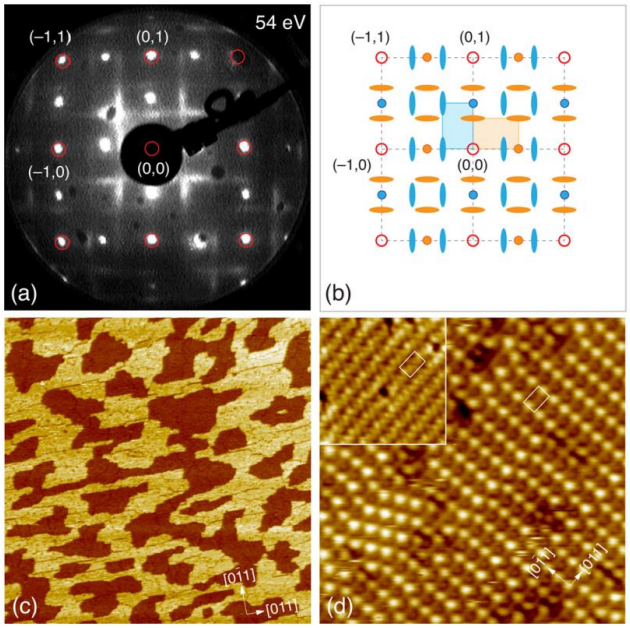


***Fig. 1.*** *(a) LEED pattern of the double-domain Si(100)2×3-Ag surface and (b) its schematic presentation, where integer-order reflections are shown by open red circles, the sharp ½ fractional-order reflections by small filled circles, and the streaky 1/3 fractional-order reflections by ovals of orange and blue colors for 2×3 and 3×2 domains, respectively. The corresponding 2×3 and 3×2 unit cells are hatched in orange and blue, respectively. (c) Large-scale (380×380 nm$^2$) and (d) high-resolution (17×17 nm$^2$) empty-state STM images. The inset in (d) shows the filled-state (7×7 nm$^2$) STM image of the Si(100)2×3-Ag surface. The 3×2 unit cell in (d) is outlined by a white frame.*

Figure 2a shows a ball-and-stick model of the Si(100)2×3-Ag structure with 2/3 ML of Ag and 1/2 ML of Si yielded by the AIRSS as having the lowest formation energy. The structure consists of the Ag (shown by yellow balls) and Si (shown by light blue balls) atomic chains aligned along the $3a_{Si}$-periodic direction. The Si chain is almost straight, and the Ag chain is slightly meandering. The underlying top layer (the first layer in Figure 2) of the Si(100) substrate is dimerized with dimers being oriented along the $2a_{Si}$-periodic direction. In the second Si(100) layer, there are also Si dimers (shown by a pair of orange balls in Figure 2a and to be referred hereafter as the inner Si dimers). Occurrence of such dimers appears to be very important for stabilization of the Si(100)2×3-Ag reconstruction. It lowers the formation energy by 630 meV, as compared to that of a similar structure having the same atomic arrangement of the top Ag and Si chains but without the inner Si dimers (Fig. 2b).

The electronic band structure calculated for the Si(100)2×3-Ag reconstruction model with the inner Si dimer shows semiconducting properties with an indirect band gap of ~ 0.8 eV (Fig. 3).

## 3. Conclusions

We have proposed a structural model of the Si(100)2×3-Ag reconstruction, thus solving a long-standing problem. The model incorporates 3 Si atoms and 4 Ag atoms per 2×3 unit cell, forming linear atomic chains running along the $3a_{Si}$-periodic direction of the reconstruction. The essential feature of the Si(100)2×3-Ag structure is the occurrence of the inner Si dimer in the second atomic layer from the top of Si(100) substrate. The model properly fits the principal experimental findings, including our own and those reported before.

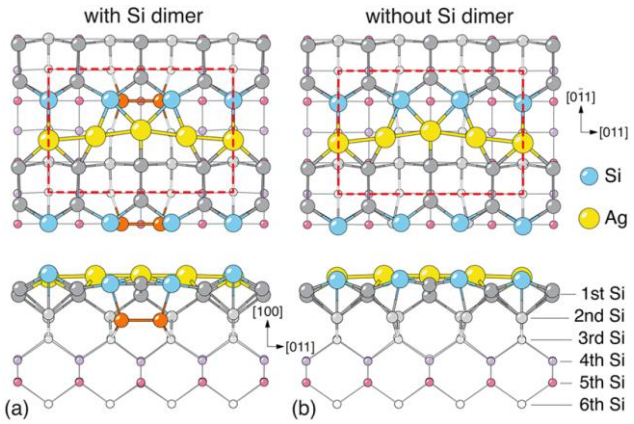


***Fig. 2.*** *Ball-and-stick models of the Si(100)2×3-Ag reconstruction (top and side views) (a) with and (b) without the inner Si dimer (shown by pair of orange balls) in the second layer of the Si(100) substrate. Ag atoms are shown by yellow balls, Si atoms incorporated in the 2×3-Ag reconstruction in the form of atomic chain by light-blue balls, Si atoms of the complete Si(100) layers from the first down to the third by the gray balls, whose size and contrast diminish for the deeper layers, Si atoms in the fourth, fifth, and sixth layers by the light purple, pink, and white circles, respectively.*

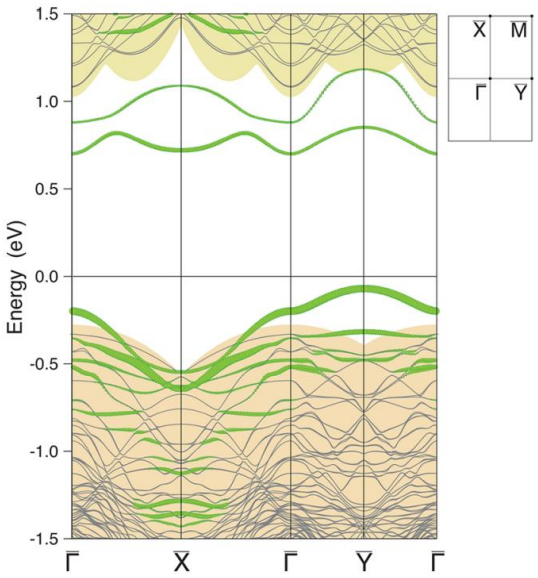


***Fig. 3.*** *Electronic band structure of the Si(100)2×3-Ag structure calculated within the 2×3 surface Brillouin zone (shown in the inset with the indication of the high-symmetry points).*

## Acknowledgements

The work was supported by the RSF Grant 21-72-00127.

## References

[1] K. Huang, W. S. Huxter, C. V. Singh, J. Nogami. J. Phys. Chem. Lett. **9**(2018)6275 − 6279.
[2] X. F. Lin, K. J. Wan, J. Nogami. Phys. Rev. B: Condens. Matter Mater. Phys. **49**(1994)7385 − 7393.
[3] R. M. Tromp, T. Michely. Nature **373**(1995)499 − 501.
[4] H. W. Yeom, I. Matsuda, K. Tono, T. Ohta. Phys. Rev. B: Condens. Matter Mater. Phys. **57**(1998)3949 − 3954.

# Investigation a possibility of modeling skyrmions using the Monte Carlo method in flat lattices with various geometries

E.V. Vasiliev*[,1,2], A.V. Perzhu[1,2], A.O. Korol[1,2], D.Yu. Kapitan[1,2], A.E. Rybin[1,2], M.A. Padalko[1,2], R.A. Volotovskiy[1,2], A.G. Makarov[1,2], Yu.A. Shevchenko[1,2], K.S. Soldatov[1,2], V.Yu. Kapitan[1,2], K.V. Nefedev[1,2]

[1] Far Eastern Federal University, 8 Sukhanova St., Vladivostok 690950, Russia
[2] Institute of Applied Mathematics, Far Eastern Branch, Russian Academy of Science, Vladivostok, 690041, 7 Radio St., Russian Federation

*e-mail: vasilev.eva@dvfu.ru

**Abstract.** The work aims to investigate the possibility of modeling skyrmions with the Metropolis algorithm of the Monte Carlo method in various spin systems. Examples of such systems can be both ferromagnetic and antiferromagnetic materials, as well as different types of flat gratings: triangular, square or hexagonal. The conditions of occurrence of various phase states in such systems are studied, as well as the possibilities of the origin, stable existence and movement of magnetic skyrmions.

## 1. Introduction

Over the last few decades, there has been a growing increasing interest in the study of magnetic vortices - skyrmions in order to use them in data storage and transmission devices. Skyrmions can be used to store data in new spin electronic devices, because they, as well as magnetic domains, can take values of 0 and 1, and the advantage is that the skyrmions are topologically stable, have a small size and are easy to control by acting on them with electric current and an external magnetic field. Direct control over the movement, size and shape of magnetic vortices allow them to be used as information carriers in a new type of magnetic media - racetrack memory [1]. From the point of view of practical application of magnetic materials, thin magnetic films are of particular interest. This is due to the fact that at the interface of a thin film, individual skyrmions can be stabilized using the Dzyaloshinsky – Moriya interaction (DMI).

## 2. Computational experiment

The numerical Monte Carlo method, namely one of its examples, the Metropolis algorithm [2], is well suited for computer simulation of magnetic spin systems. It allows one to study both the behavior and the critical properties of systems with complex Hamiltonians in a wide range of temperatures and other external parameters.

In this paper, the results of numerical simulation of the classical Heisenberg spin model are considered. Plane lattices with direct exchange and DM-interaction between spins were studied and the influence of the lattice type on the behavior of spin systems was studied. The following types of lattices have been studied: a hexagonal lattice of the "honeycomb" type with 3 nearest neighbors (NN), a square lattice with 4 NN and a hexagonal or triangular lattice with 6 NN.

$$H = H_j + H_{DMI} + H_B, \quad (1)$$

$$H_j = -J_{ij} \sum_{\langle i,j \rangle} S_i S_j, \quad (2)$$

$$H_{DMI} = -D \sum_{\langle i,j \rangle} S_i \times S_j, \quad (3)$$

$$H_B = B \sum_i S_i^{\hat{z}} \quad (4)$$

## 3. Results and discussions

In a spin system, various phases are observed depending on different parameters, for example, temperature (T), DMI (D) and external magnetic field (B): helical, skyrmionic, ferromagnetic and their mixed states. For a more detailed consideration of the skyrmion state, the study of its stability, methods of creating and manipulating it, it is necessary to clearly understand the conditions of vortices appearance in different crystal lattices.

The data from the Monte Carlo simulation were analyzed using a convolutional neural network to recognize different phases of the spin system depending on the simulation parameters. From these data, phase diagrams were constructed.

As a result, we found that depending on the type of crystal lattice, not only the position of the main phase changes, but also their sizes. Also, it should be noted that the stability of the skyrmion, its minimum size and the temperature of its existence depend on the type of lattice.

## 4. Conclusions

We studied skyrmions of various types and determined the values of external and internal modeling parameters required to create and stabilize skyrmions in magnetic two-dimensional ferromagnetic films with different geometries. We showed that the switching between different stable states of the spin system depends not only on external and internal parameters, such as the DMI value or the external magnetic field, but also on the lattice type (discretization type) of the magnetic film. It was also shown that the lattice structure affects parameters such as the number, size, and temperature stability of the skyrmions.

## Acknowledgements

The research was carried out within the RSF's project No. 21-72-00058.

## References

[1] R. Tomasello, E. Martinez, R. Zivieri, L. Torres, M. Carpentieri, G. Finocchio. Scientific reports **4**(2014)1.
[2] S. Buhrandt, L. Fritz. Physical Review B **88**(2013)195137.

Sixth Asian School-Conference on Physics and
Technology of Nanostructured Materials
Vladivostok, Russia, 25 – 29 April, 2022



# Nanoscale patterns in the mixed Pb and Tl atomic layer on $NiSi_2$/Si(111)

Y.E. Vekovshinin*[,1], L.V. Bondarenko[1], A.Y. Tupchaya[1], A.N. Mihalyuk1[,2], A.V. Zotov[1], A.A. Saranin[1]

[1] Institute of Automation and Control Processes FEB RAS , 5 Radio St., Vladivostok 690041, Russia
[2] Far Eastern Federal University, Vladivostok 690950, Russia

*e-mail: vekovsh981@gmail.com

**Abstract.** In the present work we report on the results of a comprehensive study of electronic and atomic structures of $NiSi_2$/Si(111) sandwiched between Si(111) substrate and a mixture of Pb and Tl atoms.

## 1. Introduction

The formation of two-dimensional (2D) metallic compounds based on heavy elements on different substrates sparked enormous interest not only due to the possibility of their existence but owing to unique properties which have been observed. Among them, 2D superconductivity [1], Rashba-type splitting of surface states [2] and quantum spin Hall effect [3] are of great interest from the viewpoint of further applications in new spintronics devices. Being the heaviest elements of III and IV groups, Tl and Pb contribute to strong spin-orbit coupling in surface structures, leading to the emergence of interesting properties. For example, the (Tl, Pb)/Si(111) system transforms into the superconducting state at 2.25 K, followed by the Berezinskii-Kosterlitz-Thouless mechanism [4].

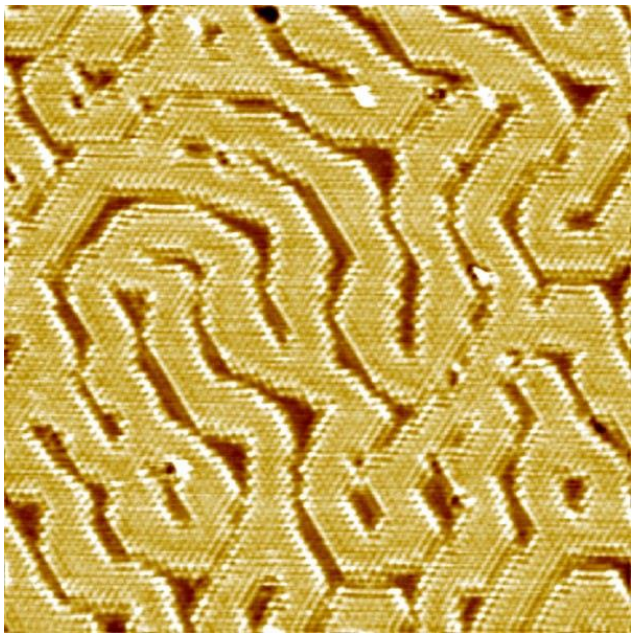

***Fig. 1.*** *STM image 50×50 nm$^2$, +1.5V. The bright stripes are Pb segments separated by dark areas of Tl ones.*

In the present paper, Pb atoms were used to modify a single monolayer $NiSi_2$ sandwiched between Si(111) substrate and a capping Tl layer [5]. Single-layer $NiSi_2$ was formed by Ni adsorption onto the initial Si(111)1×1-Tl surface at room temperature with subsequent anneal at 300°C. When the disilicide was grown, Pb atoms were deposited at room temperature. It resulted in partial replacement of Tl atoms by Pb ones and formation of two regions within the same atomic layer, both having 1×1 periodicity. The structural and electronic properties were characterized using a set of experimental techniques, including low-energy electron diffraction, scanning tunneling microscopy (STM), angle-resolved photoelectron spectroscopy, and first-principles density-functional theory calculations.

In contrast to the (Pb, Tl)/Si(111) system, where several compound surface reconstructions are formed, Pb and Tl atoms on the NiSi2 monolayer are separated and create a mixture of discrete Pb/$NiSi_2$ and Tl/$NiSi_2$ structures. This mixture demonstrates an unusual ordering where elongated Pb- and Tl-based stripes with an average width of about 7.14 nm intertwine, forming nanoscale Turing-like pattens.

When Pb coverage approaches about 1 ML, low-energy electron diffraction and angle-resolved photoelectron spectroscopy obtained at 78 K revealed that Pb regions coalesce and undergo a structural transition with the formation of surface reconstructions with greater periodicities [6].

## Acknowledgements

The work was supported by the Russian Foundation for Basic Research under Grant 20-02-00510.

## References

[1] T. Zhang, P. Cheng, W.-J. Li, Y.-J. Sun, G. Wang, X.-G. Zhu, K. He, L. Wang, X. Ma, X. Chen, Y. Wang, Y. Liu, H.-Q. Lin, J.-F. Jia, and Q.-K. Xue. Nat. Phys. 6, 104 (2010).T. Suemasu, T. Fujii, K. Takakura, F. Hasegawa. Thin Solid Films **381**(2001)209.

[2] K. Yaji, Y. Ohtsubo, S. Hatta, H. Okuyama, K. Miyamoto, T. Okuda, A. Kimura, H. Namatame, M. Taniguchi, and T. Aruga. Nat. Commun. 1, 17 (2010)

[3] C.-H. Hsu, Z.-Q. Huang, C.-Y. Lin, G. M. Macam, Y.-Z. Huang, D.-S. Lin, T. C. Chiang, H. Lin, F.-C. Chuang, and L. Huang. Phys.Rev.B 98, 121404(R) (2018).

[4] A. V. Matetskiy, S. Ichinokura, L. V. Bondarenko, A. Y. Tupchaya, D. V. Gruznev, A. V. Zotov, A. A. Saranin, R. Hobara, A. Takayama, and S. Hasegawa. Phys. Rev. Lett. 115, 147003.

[5] L.V. Bondarenko, A.Y. Tupchaya , A.N. Mihalyuk, S.V. Eremeev, A.V. Matetskiy, N.V. Denisov, Y. E. Vekovshinin, A.V. Slyshkin, D.V. Gruznev, A.V Zotov, A.A. Saranin. 2D Materials. 7 (2020) 025009.

[6] L.V. Bondarenko, A.Y. Tupchaya, Y.E. Vekovshinin, D. V. Gruznev, A.N. Mihalyuk, N.V. Denisov, A.V. Matetskiy, A.V. Zotov, A.A. Saranin. Surface Science, 2022, Vol.716, P.121966-6.

Sixth Asian School-Conference on Physics and
Technology of Nanostructured Materials
Vladivostok, Russia, 25 – 29 April, 2022



# Modeling of thermodynamic properties of spin ice on a rhombic lattice

R.A. Volotovskiy*[,1,2], Yu.A. Shevchenko[1,2], E.V. Vasiliev[1,2], D.Yu. Kapitan[1,2], A.E. Rybin[1,2], M.A. Padalko[1,2], A.G. Makarov[1,2], K.S. Soldatov[1,2], K.V. Nefedev[1,2], A.V. Perzhu[1,2]

[1] Institute of Applied Mathematics, Far Eastern Branch, Russian Academy of Science, Vladivostok, 690041, 7 Radio St., Russian Federation

[2] Far Eastern Federal University, 8 Sukhanova St., Vladivostok 690950, Russian Federation

*e-mail: volotovskii.ra@dvfu.ru

**Abstract.** In our work, we wondered whether the arrangement of spins and their proximity to each other affect the thermodynamic properties (heat capacity, entropy, magnetic susceptibility) in the model of spin ice on a rhombic lattice.

## 1. Introduction

All magnetic materials have at least two thermodynamic phases — order and disorder, which determine the second-order phase transition. The peak in the temperature behavior of the specific heat, which diverges for infinite systems, is an indirect confirmation of the presence of a phase transition. For example, frustrated spin-ice lattices, have an additional phase transition, determined by the presence of long-range order [1,2]. In this work, we decided to consider a two-dimensional rhombic lattice at its different tilt angles $\varphi$ between system spins and to study the effect of such systems on phase transitions.

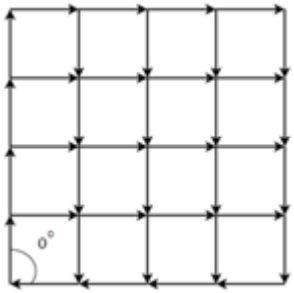


***Fig. 1.*** *Lattice of spins of the 2D Ising model slope parameter φ = 0.*

## 2. Model

Is there any if the location of the spins and their proximity to each other affect, for this we will consider a rhombic lattice, the spins of which at different angles $\varphi$ change the direction of the magnetic moment and the location in a two-dimensional lattice. In this study, we use the canonical Metropolis algorithm. The Metropolis algorithm was used to calculate the temperature behavior of heat capacity. The interaction between the spins is dipole-dipole and is determined as:

$$E_{ij} = \frac{\vec{m}_i \vec{m}_j}{|\vec{r}_{ij}|^3} - 3\frac{(\vec{m}_i \vec{r}_{ij})(\vec{m}_j \vec{r}_{ij})}{|\vec{r}_{ij}|^5} \qquad (1)$$

where $\vec{m}$ – vector of magnetic moment, $\vec{r}$ – radius vector between a pair of spins. In the frame of model, we considered a system of Ising-like dipoles, where $\vec{m}_i$ is replaced by $s_i \vec{m}_i'$, and $\vec{m}_i'$ – is a fixed value, with length $|\vec{m}_i'| = 1$. The value $s_i = \pm 1$ determines the direction of the vector. Each possible configuration of the arrangement of spins corresponds to the energy H obtained from the interaction of spins determined by the radius:

$$r = \sqrt{(S_i x - S_{i+1} x)^2} + \sqrt{(S_i y - S_{i+1} y)^2} \qquad (2)$$

The initial lattice configuration is determined in accordance with the conditions:

On the x-axis, the first line of spins is fixed, the rest shift depending on the angle phi. On the Y axis, there is not only displacement but also rotation of spins.

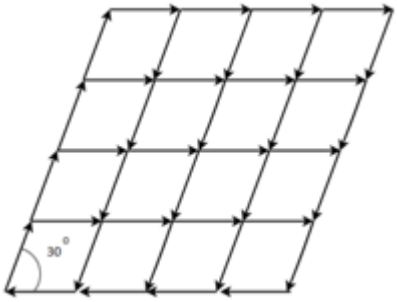


***Fig. 2.*** *Lattice of spins of the 2D Ising model slope parameter φ = 30.*

## 3. Conclusions

The result of numerical studies of the rhombic lattice will be the heat capacity graphs, the analysis of which will help to reveal the influence of the rhombus parameters on the characteristics of the graphs and on the presence of phase transitions.

## References

[1] Shevchenko, Y. A., Makarov, A. G., Andriushchenko, P. D., & Nefedev, K. V. (2017). Journal of Experimental and Theoretical Physics, 124(6), 982-993.

[2] Chern, G. W., Morrison, M. J., & Nisoli, C. (2013). Physical review letters, 111(17), 177201.

Sixth Asian School-Conference on Physics and
Technology of Nanostructured Materials
Vladivostok, Russia, 25 – 29 April, 2022



# Epitaxial growth of $Mn_5Ge_3$ on Si(111)

I.A. Yakovlev*, I.A. Tarasov
Kirensky Institute of Physics, Federal Research Center KSC SB RAS, Akademgorodok 50, bld. 38, Krasnoyarsk 660036, Russia

*e-mail: yia@iph.krasn.ru

**Abstract.** The structure of $Mn_5Ge_3$ films deposited with and without different buffer layers on Si(111)7×7 substrates at a temperature of 390 °C are investigated by reflection high energy electron diffraction. It is shown that the 200 nm single-crystal germanide film is formed using two buffer layers with a slight manganese deficiency in the structure. But when deposition is without buffer layers, the thickness of a single-crystal film does not exceed 15 nm.

## 1. Introduction

The high energy consumption of various household and industrial appliances is a one of the problems of modern and the near future. The creation of new materials and technologies that will allow the development of devices with lower power consumption is an urgent task for the scientific community. The transition to spintronics devices that use the spin freedom degrees of electrons in working is a one of the ways to solve problem. It makes possible to reduce overall energy consumption, improve the speed of computer RAM and expand data processing capabilities [1-3].

The $Mn_5Ge_3$ is an example of such materials. This is a ferromagnetic metal with Tc = 296 K, which has a high spin polarization, and the effects of spin injection and detection into a semiconductor have already been demonstrated for it [4-5]. There are many works on the synthesis of this germanide epitaxial films on semiconductor Ge substrates, on Ge epitaxial buffer layers, and also on GaAs(111) [6–8]. And there were no works on the synthesis of single-crystal ferromagnetic manganese germanides on silicon. The creation of a technology for the epitaxial thin films synthesis of this material on silicon with controlled and reproducible properties in the future will make it possible to obtain microdevices necessary for the implementation of semiconductor spintronics technology compatible with silicon CMOS.

## 2. Experiment

The experiment was carried out with ultrahigh vacuum molecular-beam epitaxy "Angara" set-up [9], equipped with a system of reflection high-energy electron diffraction (RHEED). The base pressure in the growth chamber was $6.5\times10^{-8}$ Pa. The 15mm*20 mm n-Si(111) substrates were used and prepared by special treatment [9] including annealing in vacuum. The component materials were evaporated from Knudsen effusion cells with BN-cricible.

The $Mn_5Ge_3$ films were prepared by molecular-beam epitaxy technique with simultaneous deposition of Mn and Ge on Si(111) 7×7 at 390 °C at different ratio of materials including stochiometric $Mn_5Ge_3$. The thickness of the films was in the range of 30-200 nm. The structure formation was monitored *in situ* by RHEED. In all experiments, the germanium deposition rate was 0.32 nm/min, and the manganese deposition rate varied from 0.28 to 0.30 nm/min. This rate range includes a flow ratio mode for obtaining a stoichiometric $Mn_5Ge_3$, which is V(Mn)/V(Ge)=0.926. In this work, a single-layer film of manganese germanide with the $Mn_5Ge_3$ stoichiometry was obtained, as well as two films with different Mn-Ge buffer layers close to $Mn_5Ge_3$ stoichiometry.

## 3. Results and discussions

A single-crystal film with an island morphology is formed at the initial deposition stages of a single-layer $Mn_5Ge_3$ film on Si(111)7×7 at a temperature of 390 °C. The film acquires a smoother surface at 6 nm thickness, while the crystal structure is transformed to polycrystalline at 15 nm the layer thickness (Fig. 1).

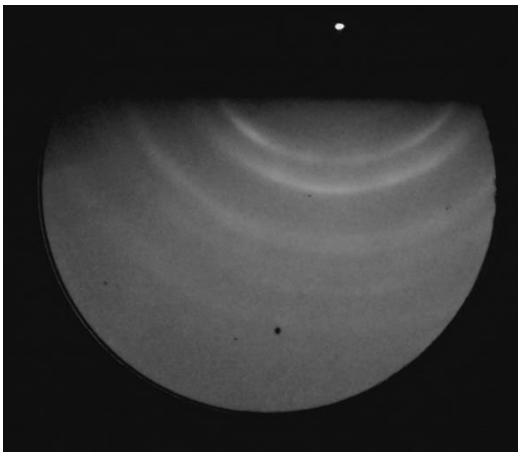

***Fig. 1.*** *RHEED pattern of 30 nm $Mn_5Ge_3$/Si(111)7×7 without buffer layer.*

The single-crystal $Mn_5Ge_3$ film with 26 nm thickness was formed after deposition of 3 nm $Mn_{[5\text{-}0.3]}Ge_3$ buffer layer on Si(111)7×7 at a temperature of 390 °C. However, a textured polycrystal begins to form with further deposition (Fig. 2).

The film of stoichiometric $Mn_5Ge_3$ grows with a single-crystal structure up to 200 nm after deposition of two buffer layers in succession with stoichiometry $Mn_{[5\text{-}0.3]}Ge_3$ and $Mn_{[5\text{-}0.15]}Ge_3$ and with 5 and 12 nm thicknesses, respectively. Fig. 3 shows the RHEED pattern from surface the 200 nm thick $Mn_5Ge_3$ film obtained with two buffer layers.

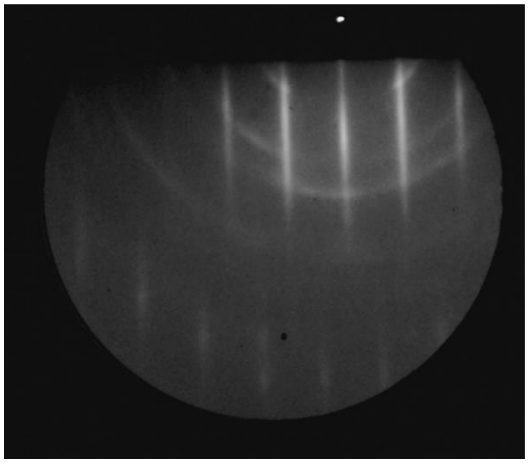

***Fig. 2.*** *RHEED pattern of 30 nm $Mn_5Ge_3$/buff/Si(111)7×7 with 3 nm $Mn_{5-0,3}Ge_3$ buffer layer.*

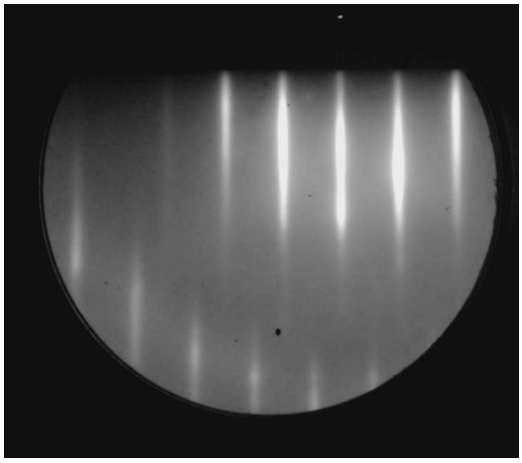

***Fig. 3.*** *RHEED pattern of 200 nm $Mn_5Ge_3$/2buff/Si(111)7×7 with two buffer layers.*

## 4. Conclusions

The experimental results on the synthesis of epitaxial single-crystal $Mn_5Ge_3$ films on Si(111) 7×7 substrates are presented. It has been established that the crystal structure of a single-layer film of stoichiometric germanide $Mn_5Ge_3$ transforms from a single-crystal to a polycrystall at 15 nm thickness. The use of two buffer layers with a reduced amount of manganese in the composition makes it possible to compensate for the mismatch between the crystal lattices of the substrate and the film, which leads to epitaxial growth of a single-crystal film up to a 200 nm thickness.

## References

[1] I. Zutic, J. Fabian, S. Das Sarma, Rev. Mod. Phys. 76 (2) (2004) 323–41.
[2] R. Jansen, Nature Materials. V.11. P. 400–408 (2012).
[3] A. Hirohata, et al. JMMM 509 (2020) 166711.
[4] J. Tang, et al. Nano Lett. 13 (9) (2013) 4036–4043.
[5] A. Spiesser, et al. PRB 90, 205213 (2014).
[6] Olive-Mendez S, et al 2008 Thin Solid Films 517 191
[7] S. Bechler et al Semicond. Sci. Technol. 33 (2018) 095008
[8] Dung et al. J. Appl. Phys. 114, 073906 (2013)
[9] I.A. Yakovlev, S.N. Varnakov, B.A. Belyaev et al. JETP letters 99(9), 527 (2014).

Sixth Asian School-Conference on Physics and
Technology of Nanostructured Materials
Vladivostok, Russia, 25 – 29 April, 2022 **I.p.22**

# Investigation of the Ga films grown on Si(111)-√3x√3-Ga reconstruction

V.S. Zhdanov*, D.A. Olyanich, T.V. Utas, A.N. Mihalyuk, N.V. Denisov, A.V. Matetskiy, A.V. Zotov, A.A. Saranin

Institute of Automation and Control Processes FEB RAS , 5 Radio St., Vladivostok 690041, Russia

*e-mail: vzhdanov@iacp.dvo.ru

**Abstract.** Using scanning tunneling microscopy (STM) the Ga thin films grown on the Si(111)-√3x√3-Ga template have been investigated. The first Ga layer exhibits structure with 4×√13 periodicity and contains 1.81 ML of Ga. The proposed model of this structure contains 29 Ga atoms per 4×√13 cell. The second Ga layer reveals an ordered array of trimers with √7×√7 periodicity and coverage equal to 4.14ML. The low temperature four-point probe measurement doesn't show the superconductivity.

## 1. Introduction

The formation of thin superconducting metal films on the silicon surfaces have attracted intense interest both for practical application in microelectronic devices and for fundamental research. One of the promising materials is gallium (Ga), because bulk Ga has several metastable phases. Thus, stable α-Ga passes into the superconductivity state at temperatures Tc<1.2 K, while the metastable β-Ga has a critical temperature Tc = 6.04(5) K [1]. In this work, we studied the growth of gallium films on the Si(111)-√3×√3-Ga surface. The resulting structures were studied by scanning tunneling microscopy at room temperatures (RT), as well as by the 4 point probe method for superconductivity at temperatures down to 2 K.

## 2. Experiment

Our experiments were carried out in a variable-temperature Omicron VT-STM operating in an ultrahigh vacuum (~$2.0\times10^{-10}$ Tor). Atomically-clean Si(111)-7×7 surfaces were prepared in situ by flashing to 1280°C after the samples were first outgassed at 600°C for several hours. Gallium was deposited from a tantalum basket with a rate of 0.2 ML/min. To prepare the Si(111)-√3x√3-Ga surface, the 1/3 ML of Tl was deposited onto Si(111)-7×7 with subsequent annealing at 550°C. Transport measurements at low temperature were carried out on a UNISOKU USM-1500 LT STM system. Our calculations were based on DFT as implemented in the Vienna ab initio simulation package VASP [3] using a planewave basis set.

## 3. Results and discussions

Initially, the Si(111)-√3×√3-Ga surface phase was formed on the Si(111)-7×7 surface by depositing ⅓ ML of gallium on the surface followed by annealing at 550°C. The subsequent deposition of gallium was performed on the Si(111)-√3×√3-Ga surface at room temperature (RT). From STM observations, the deposition of gallium on Si(111)-√3×√3-Ga at RT leads to the formation of flat disordered islands of irregular shape. Increasing Ga coverage leads to increases in the area of the islands, and when the coverage of gallium reaches 1.81 ML, the islands merge into a continuous disordered flat film. The fact that such a layer of gallium has no long-range order was also established using the low energy electron diffraction (LEED) method. Mild heating of the gallium film at a temperature of 50°C leads to the ordering of gallium atoms into a structure with 4×√13 periodicity. A gallium film with the same periodicity was observed by M.L. Tao et al [2]. In this work, the authors deposited gallium on a heated Si(111)-√3×√3-Ga surface at 50°C. Further deposition of gallium both on an ordered film with 4×√13 periodicity and on a disordered one (before heating) leads to the formation of flat islands of the second gallium layer. As the coverage increases, the islands merge into a flat film at 4.14 ML Ga. The flat film looks like an ordered array of trimers with √7×√7 periodicity. Using numerical calculations employing the VASP software package, models were established for structures with a periodicity of 4×√13 and √7×√7. Each of these structures contains 29 gallium atoms per 4×√13 and per √7×√7 cells, respectively. For gallium structures with 4×√13 and √7×√7 periodicity, the temperature dependence of the film conductivity was measured. It was found that as the temperature decreases down to 2K, no superconducting transition is observed.

## 4. Conclusions

In this work, we studied the growth of gallium films on the Si(111)-√3x√3-Ga surface reconstruction. The deposition of 1.81 ML Ga leads to the formation of a flat disordered layer. Annealing of such a layer at 50°C forms a flat structure with 4×√13 periodicity containing 29 atoms per cell. Further deposition of gallium produces the next layer looking like an ordered array of trimers with √7×√7 periodicity. Low-temperature measurements down to 2K did not reveal superconducting transitions.

## Acknowledgements

The work was supported by the RSF Grant 19-12-00101-П.

## References

[1] D. Campanini, Z. Diao, A. Rydh. Physical Review. B 97(2018)184517.
[2] M. L. Tao , Y. B. Tu, K. Sun, Y. L. Wang, Z. B. Xie, L. Liu, M. X. Shi, J.Z. Wang. 2D Materials 5(2018)035009.
[3] G. Kresse, J. Hafner, Ab initio molecular dynamics for liquid metals, Phys. Rev. B 47 (1993) 558.

# II. Physics of semiconducting nanostructures and heterostructures, including silicide, 4th group material's alloy, $A_3B_5$ and $A_2B_6$ heterostructures: experiment, calculations and technology

Sixth Asian School-Conference on Physics and
Technology of Nanostructured Materials
Vladivostok, Russia, 25 – 29 April, 2022



# Structural features and quantum confinement effects in thin films of $Mg_2Si$ and $Ca_2Si$

A.Yu. Alekseev[1], D.B. Migas[*,1,2], A.B. Filonov[1], N.V. Skorodumova[3]

[1] Belarusian State University of Informatics and Radioelectronics, P. Browka 6, 220013 Minsk, Belarus
[2] National Research Nuclear University MEPhI (Moscow Engineering Physics Institute), Kashirskoe shosse 31, 115409 Moscow, Russia
[3] Department of Materials and Engineering, Royal Institute of Technology (KTH), SE-10044 Stockholm, Sweden

*e-mail: migas@bsuir.by

**Abstract.** We used *ab initio* techniques to investigate the effects of quantum confinement on the band-gap values of semiconducting $Mg_2Si$ and $Ca_2Si$ thin films. Thus, thin films of cubic $Mg_2Si(111)$ are found to be dynamically stable for thicknesses ($d$) larger than 0.3 nm and possess no surface states near the band-gap energy region. We show that quantum confinement effects sizably affect the band gap of $Mg_2Si(111)$ with $d < 6$ nm and can be fairly well described by the simple effective mass approximation. Even though the bulk cubic phase of $Ca_2Si$ is higher in energy that the orthorhombic one, the cubic $Ca_2Si(111)$ thin films are more stable than any orthorhombic thin film for $d < 3$ nm. We show that significant structural distortions occurring in $Ca_2Si$ thin films with $d < 3$ nm cause the appearance of surface states at the top/bottom of the valence/conduction band and result in an odd behaviour of the band gap, which cannot be explained by quantum confinement effects.

## 1. Introduction

Since the common silicon technology is well-developed, it is worthwhile to search for new materials that are compatible to it and can open a feasible way to fabrication of new-generation electronic devices. In addition to that, implementation of nanostructures is a nice possibility to drastically change material properties with respect to a bulk counterpart due to the increase of surface/volume ratio, where quantum confinement effects and surface properties are expected to dominate, and due to unavoidable structural and symmetry changes. In this respect silicides both in the bulk and nanostructured forms attract much attention and can be viewed as potential candidates to be used in various electronic devices [1].

Recently, we have theoretically predicted the stability of two-dimensional (2D) alkali-earth metal silicides, germanides, and stannides ($Me_2X$, where Me = Mg, Ca, Sr, Ba and X = Si, Ge, Sn) which display semiconducting properties [2]. The aim of this paper is to theoretically trace changes in structure and electronic properties of thin films of $Mg_2Si$ and $Ca_2Si$ with respect to a film thickness (from 2D to several nm) in order to reveal whether it is really necessary to experimentally grow 2D (or a few monolayer) structures to get unique properties or it is quite sufficient to relatively easy form thin films with nm thickness because of marginal changes in properties with respect to 2D structure.

## 2. Details of calculations

$Ca_2Si$ and $Mg_2Si$ thin films with different surfaces have been considered as periodic arrangement of slabs separated by 10 Å of vacuum. Each slab is characterized by two equal surfaces and the $Mg_2Si$ or $Ca_2Si$ stoichiometry. We have investigated the slabs with thicknesses starting from ~0.2 nm (corresponds to the 2D structure) up to 17 nm. All of the atoms in the slab were allowed to relax. We investigated orthorhombic $Ca_2Si(100)$, (010), and (001) thin films as well as cubic $Mg_2Si$ and $Ca_2Si$ thin films with the (111) and (110) orientations.

The full structural optimization of the investigated thin films and the calculation of their band structures were performed by the *ab-initio* projector augmented-wave method [3] within the generalized gradient approximation [4].

## 3. Results and discussions

Results of our *ab initio* investigation on structure and electronic properties of the cubic $Mg_2Si(111)$ thin films indicate that there is no sizable changes in the in-plane lattice parameters and interlayer distances with respect to the bulk ones when moving down in the film thickness from 17 nm to 0.5 nm. It is also found that the thinnest cubic $Mg_2Si(111)$ thin film ($d$ = 0.5 nm) is dynamically stable against the phonon excitation while the phase transition occurs in order to observe 2D $Mg_2Si$ in the orthorhombic distorted phase ($d$ = 0.2 nm). Analysis of the corresponding band structures of the cubic $Mg_2Si(111)$ thin films shows these nanostructures to be the indirect band-gap materials displaying almost the same dispersion of the bands near the gap region like in the bulk. Moreover, their band gaps decrease from 1.18 eV ($d$=0.5 nm) to 0.63 eV (bulk) is observed as a consequence of the influence of the quantum confinement effects and no surface states have been detected in the gap region and in the top/bottom of the valence/conduction band. The absence of the surface states in the gap region and small changes in the structural parameters allow for applying the simple effective mass approximation to fairly well predict the band-gap variation with $d$ in the cubic $Mg_2Si(111)$ thin films.

In the $Ca_2Si$ thin films we have found the cubic phase to be more stable in the total energy then the orthorhombic one at $d < 3$ nm. Contrary to the cubic $Mg_2Si(111)$ thin films, the cubic $Ca_2Si(111)$ and orthorhombic $Ca_2Si(100)$, $Ca_2Si(010)$, $Ca_2Si(001)$ thin films possess sizable changes in the structural parameters especially at small thicknesses, however their band structures inherit the same dispersion of bands close to the gap region as in the parent bulk materials. We have also revealed the appearance of the surface states, which are located 0.03 eV above the top of the valence band of the bulk (cubic $Ca_2Si(111)$ thin films) and 0.15 eV below the bottom of the conduction band of the bulk (orthorhombic $Ca_2Si(001)$ thin films). For the orthorhombic $Ca_2Si(100)$ and $Ca_2Si(010)$ thin films the

formation of the surface states, which only appear $d < 5$ nm, are due to sizable structural distortion. The influence of the surface states and changes in the structural parameters on the band-gap value for the cubic $Ca_2Si(111)$ thin films is traced pointing out the importance of simultaneous considering quantum confinement effects and the presence of the surface states. We predict that for the orthorhombic $Ca_2Si(100)$ and $Ca_2Si(010)$ thin films the odd behavior of the band-gap variation with $d$ (at $d < 2$ nm) is attributed to crucial changes in their structural parameters. Thus, for $Ca_2Si$ thin films the simple effective mass approximation is not appropriate choice to predict their band gaps.

**Acknowledgements**

This work has been supported by the Belarusian National Research Programs "Materials science, new materials and technology", Belarusian Republican Foundation for Fundamental Research (grant No. F20R-003) and MSCA-RISE-2018 Project (grant No. 823728 DiSeTCom). The computations were enabled by resources provided by the Swedish National Infrastructure for Computing (SNIC) at High Performance Computing Center North and National Computer Center at Linköping University partially funded by the Swedish Research Council (grant agreement no. 2018-05973). D. B. Migas acknowledges the support of the MEPhI Program Priority 2030.

**References**

[1] Y.-Ch. Lin, Y. Chen, Y. Huang. Nanoscale **4**(2012)1412.
[2] A. Y.Alekseev, D. B.Migas, A.B. Filonov, V.E. Borisenko, N.V. Skorodumova. Jpn. J. Appl. Phys. **59** (2020) SF0801.
[3] G. Kresse, D. Joubert. Phys. Rev. B. **59**(1999)1758.
[4] J. P. Perdew, K. Burke, M. Ernzerhof. Phys. Rev. Lett. **77**(1996)3865.

Sixth Asian School-Conference on Physics and
Technology of Nanostructured Materials
Vladivostok, Russia, 25 – 29 April, 2022



# Synthesis of Si-based nanostructures from $CaSi_2$ crystals using metal chloride powder, vapor and aqueous solution

H. Tatsuoka*,[1], S. Ito[1], K. Tanaka[2]*, and Y. Shimura[1,3]

[1] Graduate School of Integrated Science and Technology, Shizuoka University, 3-5-1 Johoku Naka-ku Hamamatsu 432-8561, Japan
[2] Faculty of Engineering, Shizuoka University, 3-5-1 Johoku, Naka-ku, Hamamatsu, 432-8561, Japan
[3] Research Institute of Electronics, Shizuoka University, 3-5-1 Johoku Naka-ku Hamamatsu 432-8011, Japan

*e-mail: tatsuoka.hirokazu@shizuoka.ac.jp

**Abstract.** Based on the synthesis of nanosheet bundle structures, fabrications of low dimensional hybrid structures were examined. Si-based nanowires were synthesized with the formation of the Si-based nanosheet bundles. To synthesize the nanosheet bundles, vapor phase reaction of $CaSi_2$ crystals under metal chloride vapors at elevated temperatures was employed. The formation mechanisms of the nanowires were discussed based on the reaction process of the nanosheet bundles. On the other hand, Ru or Cu nanodots-interspersed nanosheets were fabricated using metal chloride aqueous solution. The structural and morphological properties of the nanowire/nanosheet and nanodot/nanosheet hybrid complex structures were examined.

## 1. Introduction

Two-dimensional (2D) nanosheets have attracted much interest because of their enhanced or modified optical, electronic, and mechanical properties compared to those of the bulk materials [1]. In addition, nanostructured 2D layered semiconductors are generally considered important building blocks for next generation electronics/ optoelectronics [2], and the assembly of nanosheets as building blocks into ordered layered structures, such as complex heterostructures, is also of great importance [3]. In the same manner, nanosheet bundles are potential structures for practical technological applications [4], especially large-volume and large-area devices such as thermoelectric batteries, Li-ion batteries, and solar cells. In addition, for the functional modifications of the nanosheets, a variety of derivatives has been synthesized [5], and doped nanosheets were also synthesized [6]. It was reported that the structural property of the nanosheets and their functionality were modified in order to synthesize their derivatives to be bound to organic molecules [7].

To synthesize nanosheets, the topological synthesis technique has been widely used [8]. As one example, $CaSi_2$ is used for the formation of Si-based 2D nanosheets. Zintl-$CaSi_2$ has a layered crystal structure, which consists of corrugated extended puckered Si layers similar to the crystalline Si{111} layers linked by ionically-bonded planar monolayers of Ca atoms. One of the polymorphs, tr6 stacking $CaSi_2$, has a trigonal crystal structure (R3 m, No.166) with the lattice constants of a = 0.386 and c = 3.061 nm [9].

The development of fabrication techniques for these desired materials is important for not only the synthesis of elemental semiconductor nanosheets, but also the structural modification to form a variety of compound nanosheets, which is expected to provide further applications of the nanosheets. A variety of silicon, silicide, and silicate nanosheet bundles has been synthesized. Si-based nanosheet bundles were formed by Ca atom extraction from the $CaSi_2$ crystals by thermal treatment using $CrCl_2$ [10], $FeCl_2$, $FeCl_3$, $NH_4Cl$, and $MgCl_2$ [11]. $Mg_2Si$ and $Mg_2SiO_4$ nanosheet bundles were synthesized by thermal treatment using $MgCl_2$/Mg mixed vapor and using the $MgCl_2$/Mg mixed vapor with the appropriate $O_2$ and/or $H_2O$ content, respectively [12,13]. On the other hand, Si and Ge nanosheet bundles were synthesized using $CaSi_2$ and $CaGe_2$, respectively, by Ca atom extraction from the powders using inositol hexakisphosphate (IP6) [14, 15].

It is expected to further modify the structural and morphological control of the nanosheet bundles Thus far, simple nanowires or simple nanosheets, and their complex or further sophisticated three-dimensional (3D) superstructures with the assembly of variety of nanowires and/or nanosheets have been developed to provide a wider range of functionalities and improve device performance [16]. It was also practically pointed out that one option to realize the 3D superstructure is to manipulate the 2D nanomaterials such that individual 2D nanosheets could be bound together to construct 3D architectures, thus avoiding the aggregation of the individual 2D nanosheets [17]. The bottom-up growth of nanosheet-nanowire heterostructures and nanosheet-nanowire network complexes have been reported [18, 19]. Further sophisticated 3D architectures containing nanowires and nanosheets have been also constructed for applications tin thermoelectric devices, lithium-ion batteries, supercapacitors, hydrogen evolution, stretchable conductors, etc [20 – 25]. A nanosheet bundle is also one of the important structures to construct the 3D architectures for technological applications.

On the other hands, nanodots-interspersed nanosheets [26], nanodot-coupled nanosheets [27] or quantum dot/nanosheets hybrids [28] have been also developed to provide a wider range of functionalities and improve device performance with the assembly of nanodots and nanosheets or nanotubes. In the same way, their bundle structure would also be expected to be one of complex hybrid structures. For example, recently, synthesis of Cu nanoparticles, nanodots or nanoparticle [29 – 31], and the synthesis of Ru nanodots was also reported [32, 33].

In this study, silicide-based nanowire/nanosheet bundle structures, which consist of nanosheets connected with Si-based nanowires, were synthesized. In addition, as preliminary work for future fabrication of nanodots/

* High school student of Future Scientists' School in Shizuoka University, Global Science Campus supported by Japan Science and Technology Agency.

nanosheets bundle structures, Cu and Ru nanodots-interspersed nanosheets bundles were synthesized using metal chloride aqueous solution.

## 2. Experiment

Commercially available $CaSi_2$ crystal powders were used as the source material. The $CaSi_2$ and $MnCl_2/NH_4Cl$ mixed powders with the molar ratio of $CaSi_2$ : $MnCl_2$ : $NH_4Cl$ = 10:1:20 were placed in a container inside a sealed stainless-steel cell under an Ar atmosphere with the detected oxygen level of less than 0.1%. On the other hand, the $CaSi_2$ and $MnCl_2$ mixed powders with the molar ratio of $CaSi_2$:$MnCl_2$=1:1 were placed in a crucible under air atmosphere. The cell or crucible was heated to the thermal annealing temperature of 500 °C – 800 °C and maintained for 0 – 5 h. The heaters were then turned off, and the cell or crucible was naturally cooled. The temperature profile of the thermal annealing is shown elsewhere [11], and it is noted here that the "0min" of the duration time of the highest thermal annealing temperature means the heaters were immediately turned off when the cell or crucible temperature reached the annealing temperature. After the thermal annealing process, the prepared nanosheet bundles were washed in ethanol a few times for a few minutes to remove any residual chloride compounds.

In addition, Cu or Ru nanodot/Si-based nanosheet bundle structures were synthesized by chemical extraction of Ca atoms from the $CaSi_2$ powders. The commercially available raw $CaSi_2$ powders were simply immersed for about ten min in $CuCl_2$ or $ReCl_3$ aqueous solutions. After the treatment, the products were filtered, then dried at room temperature.

The morphological and structural properties of the bundle structures were characterized by field-emission scanning electron microscopy (FE-SEM), conventional transmission electron microscopy (TEM), high-resolution TEM (HRTEM) with fast Fourier transform (FFT), and scanning transmission electron microscopy (STEM) with energy-dispersive X-ray spectroscopy (EDS). For the TEM sample preparation, the products were dispersed in a small amount of ethanol, then transferred onto a lacey-carbon-coated copper grid and dried.

## 3. Results and discussions

First, the synthesis of nanowire/nanosheet bundle structures is shown as follows. For the case of the products synthesized using the sealed stainless-steel cell, the image of the side wall of the product shows that the nanosheet bundle structure was formed with a collection of nanosheets stacked each other with a void space [Fig. 1(a)]. The products were synthesized in a powder form, which kept the dimensions of the original $CaSi_2$ powders. The observed nanosheets were exfoliated into thinner nanosheets. The small void space was formed by the volume reduction caused by the Ca-atom extraction. In addition, dense Si nanowires were randomly grown around the nanosheets. The Si nanowires were not straight but twisting curly Si nanowires were distributed on the side walls of the nanosheet bundles, as shown in Fig.1(a).

On the other hand, for the case of the products synthesized using a crucible thermally treated under air atmosphere, the nanowires, which were stuck on the surfaces, were observed as shown in Fig.2(b). The nanowires were more straightly formed, and the formation of $Ca_2SiO_3Cl_2$ wires are possible.

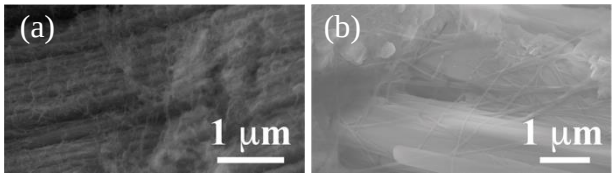


***Fig. 1.*** *SEM images of nanowire/nanosheet bundle structures with (a) Si nanowires thermally annealed at 800 °C for 0 min in the sealed cell and (b) $Ca_2SiO_3Cl_2$ nanowires thermally annealed at 700 °C for 5 h in the crucible.*

As already mentioned, the Si-based nanowire/ nanosheet bundle structures were constructed by the thermal annealing under $MnCl_2/NH_4Cl$ vapors. The process of nanosheet bundle formation is dominantly governed by the thermal annealing in $NH_4Cl$ vapor. In contrast, the nanowire formation process is dominantly governed by the thermal annealing in the $MnCl_2$ vapor. It is considered that Si chlorides are formed by the reaction of $MnCl_2$ and Si, and they are transported to the nanowire formation sites.

On the other hand, $Ca_2SiO_3Cl_2$ was formed in the nanowire morphology. The compound was formed under air environment. It is noted that Cl atoms preferentially react with Ca or Si from $CaSi_2$ with O atoms, not Mn in this thermal treatment conditions.

Then, synthesis of the nanodot/nanosheet bundle structures is shown. Ru dots were formed around the surfaces exfoliated new surface of the powders as shown in Fig.2(a). On the other hand, Cu nanodots with a diameter of several nm were distributed on the Si-based nanosheet as shown in Fig.2(b).

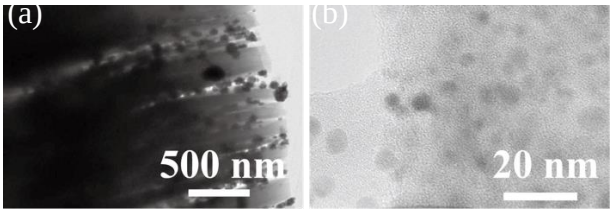


***Fig. 2.*** *(a) cross-sectional TEM image of the Si-based nanosheet bundles with Ru dots distributed around nanosheet surfaces, (b) plan-view TEM image of the Si-based nanosheet with Cu nanodots distributed on the nanosheet.*

## 4. Conclusions

A variety of Si, silicide, and silicate nanosheet bundles have been synthesized by Ca extraction from $CaSi_2$ crystal powders. For further modification of the bundle properties, in addition to the formation of layered materials, nanowire/nanosheet bundle structures and nanodot/ nanosheet bundle structures were fabricated. Si and $Ca_2SiO_3Cl_2$ nanowire growth took place under appropriate thermal treatment condition with the formation of the nanosheet bundles. The nanowires are distributed randomly on the sidewalls of the nanosheet bundles and the sheet surfaces. On the other hand, nanodot growth took place in metal chloride aqueous solution. Ru and Cu nanodots are distributed around the new surfaces formed by the exfoliation process. It is expected that the simple fabrication of the low-dimensional hybrid complex structures leads the further improvements of the bundle properties, and open wide range of applications

**Acknowledgements**

A part of this study was supported by JSPS KAKENHI Grant No. 20K04560, and the Cooperative Research Project of Research Center for Biomedical Engineering.

**References**

[1] W. L. B. Huey and J. E. Goldberger, Chem. Soc. Rev. 47, 6201 (2018).
[2] G. Liu, Z. Li, X. Chen, W. Zheng, W. Feng, M. Dai, D. Jia, Y. Zhou, and P. Hu, Nanoscale 9, 9167 (2017).
[3] M. Zeng, Y. Xiao, J. Liu, K. Yang, and L. Fu, Chem. Rev. 118, 6236 (2018).
[4] H. Tatsuoka, W. Li, E. Meng, and D. Ishikawa, ECS Trans. 50, 3 (2012).
[5] H. Nakano, H. Tetsuka, M. J. S. Spencer, and T. Morishita, Sci. Technol. Adv. Mater. 19, 76 (2018).
[6] H. Nakano, T. Mitsuoka, M. Harada, K. Horibuchi, H. Nozaki, N. Takahashi, T. Nonaka, Y. Seno, and H. Nakamura, Angew. Chemie Int. Ed. 45, 6303 (2006).
[7] H. Itahara and H. Nakano, Jpn. J. Appl. Phys. 56, 05DA02 (2017).
[8] X. Xiao, H. Wang, P. Urbankowski, and Y. Gogotsi, Chem. Soc. Rev. 47,8744 (2018).
[9] G. Vogg, M. S. Brandt, M. Stutzmann, and M. Albrecht, J. Cryst. Growth 203, 570 (1999).
[10] X. Meng, H. Imagawa, E. Meng, H. Suzuki, Y. Shirahashi, K. Nakane, H. Itahara, and H. Tatsuoka, J. Ceram. Soc. Jpn. 122, 618 (2014).
[11] X. Meng, P. Yuan, Y. Hayakawa, K. Sasaki, K. Tsukamoto, S. Kusazaki, Y. Saito, Y. Kumazawa, and H. Tatsuoka, E-J. Surf. Sci. Nanotechnol. 16, 218 (2018).
[12] T. Koga, R. Tamaki, X. Meng, Y. Numazawa, Y. Shimura, N. Ahsan, Y. Okada, A. Ishida, and H. Tatsuoka, Jpn. J. Appl. Phys. 60, SBBK07 (2021).
[13] Y. Numazawa, S. Itoh, Y. Ono, Y. Huang, Y. Shimura, Y. Hayakawa, and H. Tatsuoka, Jpn. J. Appl. Phys. 59, SFFD02 (2020).
[14] X. Meng, K. Sasaki, K. Sano, P. Yuan, and H. Tatsuoka, Jpn. J. Appl. Phys.56, 05DE02 (2017).
[15] V. Saxena, N. Atsumi, Y. Shimura, and H. Tatsuoka, Jpn. J. Appl. Phys. 59, SGGK08 (2020).
[16] 4) D. Zhang, S. Wang, Y. Ma, and S. Yang, J. Energy Chem. 27, 128 (2018).
[17] X. Cao, Z. Yin, and H. Zhang, Energy Environ. Sci. 7, 1850 (2014).
[18] U. N. Maiti, K. K. Chattopadhyay, S. Karan, and B. Mallik, Scr. Mater. 62, 305 (2010).
[19] C. Li, Y. Yu, M. Chi, and L. Cao, Nano Lett. 13, 948 (2013).
[20] J. R. Szczech, J. M. Higgins, and S. Jin, J. Mater. Chem. 21, 4037 (2011).
[21] O. Caballero-Calero and M. Mart n-Gonz lez, Scr. Mater. 111, 54 (2016).
[22] C. Tang, Q. Zhang, M. Q. Zhao, J. Q. Huang, X. B. Cheng, G. L. Tian, H. J. Peng, and F. Wei, Adv. Mater. 26, 6100 (2014).
[23] J. Shen, Y. Zhu, H. Jiang, and C. Li, Nano Today 11, 483 (2016).
[24] S. Peng, N. Li, X. Han, W. Sun, M. Srinivasan, S. G. Mhaisalkar, F. Cheng, Q. Yan, J. Chen, and S. Ramakrishna, Angew. Chem. Int. Ed. 53, 12594 (2014).
[25] M. Chen, L. Zhang, S. Duan, S. Jing, H. Jiang, and C. Li, Adv. Funct. Mater. 24, 7548 (2014).
[26] Z. Xiao, Z. Li, P. Li, X. Meng, and R. Wang, ACS Nano 13, 3608 (2019).
[27] X. Wu, W. Zhong, H. Ma, X. Hong, J. Fan, H. Yu, J. J. Colloid Interface Sci. 586, 719 (2021).
[28] T.H. Chen, Z.S. Liu, Mater. Lett. 236, 248 (2019).
[29] D. Ni, H. Shen, H. Li, Y. Ma, T. Zhai, Appl. Surf. Sci., 409, 241 (2017).
[30] J.-X. Feng, J.-Q. Wu, Y.-X. Tong, and G.-R. Li, J. Am. Chem. Soc., 140, 610 (2018).
[31] Q. Wu, L. Liu, H. Guo, L. Li, X. Tai, J. Alloys Compd. 821, 153219 (2020).
[32] J. H. Yoon, K. M. Kim, M. H. Lee, S. K. Kim, G. H. Kim, S. J. Song, J. Y. Seok, and C. S. Hwanga, Appl. Phys. Lett. 97, 232904 (2010).
[33] A. Biswas, S. Paul and A. Banerjee, J. Mater. Chem. A, 3, 15074 (2015).

Sixth Asian School-Conference on Physics and
Technology of Nanostructured Materials
Vladivostok, Russia, 25 – 29 April, 2022



# Structure and optical properties of germanium nanowires subjected to thermal post-treatment

A.V. Pavlikov[1], A.M. Sharafutdinova[1], I.M. Gavrilin[2,3], V.B. Zaytsev[1], A.A. Dronov[*,2], S.A. Gavrilov[2]

[1] Faculty of Physics, M.V. Lomonosov Moscow State University, Leninskie Gory, Moscow, 119991, Russia
[2] National Research University of Electronic Technology – MIET, Bld. 1, Shokin Square, Zelenograd, 124498, Russia
[3] Frumkin Institute of Physical Chemistry and Electrochemistry Russian Academy of Sciences,31, bld.4, Leninsky prospect, Moscow, 119071, Russia

*e-mail: dronov.alexey@org.miet.ru

**Abstract.** This work is dedicated to the heat treatment effect on structural and optical properties of germanium nanowires obtained by electrochemical deposition from an aqueous solution. Raman spectroscopy showed an increase in the initial crystalline fraction in the sample annealed at 600 ºC compared to that annealed at 300 ºC. As-prepared sample was amorphous and crystallized under the action of probe laser radiation. The intensity of specular reflection at the boundary of the IR and visible ranges dropped which indicates an increase in the contribution of diffuse reflection and absorption. A detailed study of diffuse reflection in the visible range showed higher absorption at 633 nm than at 488 nm, which is consistent with the obtained estimates of the crystallization threshold values.

## 1. Introduction

Germanium nanowires (Ge NW) have a wide range of application due to their electrophysical and optical properties. It has been demonstrated that Ge NW may be used in Li- and Na- ion batteries, thermoelectricity, photodetectors and sensors. The most commonly used technique for the fabrication of semiconducting Ge NW is vapor deposition. However, vapor–liquid–solid methods require high- energy density and rather toxic reagents and complex equipment. Recently, the possibility of electrochemical deposition of Ge NW from aqueous solutions using particles of low- melting metals (Ga, In etc.) at nearly room temperature has been demonstrated.[1, 2] In this case liquid metal nanodroplets have been used as an electrode for reduction of Ge-containing ions at the electrode surface, followed by dissolving and crystallizing the melt at the substrate interface. The growth mechanism, which was called in literature as electrochemical liquid–liquid–solid (ec- LLS) crystal growth, is similar to vapor–liquid–solid method.[1] The structures obtained by this method showed excellent electrochemical characteristics in Li- and Na- ion batteries. Along with this, in our recent studies of such Ge NW by Raman spectroscopy, irreversible changes in the spectral line shape were demonstrated, indicating a structural transformation due to intense exciting radiation.[3, 4] This structural change can be associated with strong heating of Ge NW due to their low thermal conductivity. Heat treatment can change and stabilize the structures under investigation.

## 2. Experiment

Electrochemical deposition of Ge NW was performed in a three-electrode cell. Titanium (Ti) foil was used as the substrate. Indium nanoparticles were deposited on a Ti foil as described in previous works.[16, 17] A platinum ring was used as a counter electrode, a standard silver chloride electrode was used as the reference one. The solution contained 0.05 M of germanium (IV) oxide, 0.5 M of potassium sulfate and 0.5 M of succinic acid. The solution temperature was controlled using fluid thermostat. Deposition was performed at 0,2 $mAcm^{-2}$ at a solution temperature of 20 ºC. The current density was set using. The prepared samples were washed in deionized water and were dried in an argon flow.

The obtained samples were annealed at 300ºC and 600ºC in vacuum oven at a residualpressure of the atmosphere below $3\times10^{-5}$ Torr for 30 min (Table I).

***Table I.*** *Conditions of annealing.*

| Sample | Annealing |
|---|---|
| *1* | as-prepared |
| *2* | 300 ºC in vacuum |
| *3* | 600 ºC in vacuum |

Backscattered Raman spectra were measured under excitation with focused laser radiation using a Horiba HR800 micro-Raman spectrometer. In our experiments we used He-Ne laser (wavelength 632.8 nm, maximal power 6 mW) and Ar laser (wavelength 488.0 nm, maximal power 6 mW).

Measurements of specular reflection spectra of infrared radiation were performed on a Bruker IFS 66v/S Fourier transform IR spectrometer in the near (5000–13000 $cm^{-1}$) region with a 2 $cm^{-1}$ resolution. Measurements were carried out at room temperature on an attachment with an alternating angle of incidence.

Diffuse reflection in visible range of spectrum was studied with the help of PerkinElmer LS-55 spectrometer. The diffuse reflection was measured in the geometry, when the angle between the incident and diffusely reflected rays is 90º . At the incident angle from 45º to 75º, the intensity of the scattered beam practically did not change. And at the incident angle of 15 , the intensity of the scattered light drops by about 20 times. The incident angle of about 60 was selected for the measurements.

## 3. Results and discussions

In Figure 1 SEM images of the samples under investigation are presented. The Ge NW have mean diameter of 20-40 nm and form rather dense layers about 500 nm thick. Annealing does not change the morphology or thickness.

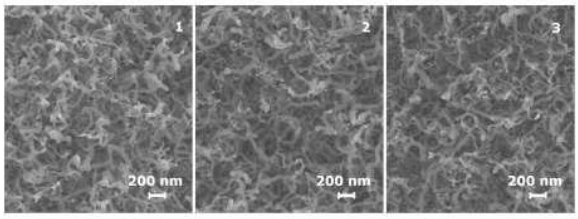


***Fig. 1.*** *SEM images of Ge NW samples 1-3.*

After Raman spectra were obtained with an exciting He-Ne laser, sample 1 did not demonstrate any evidence of crystalline fraction at the beginning of the measurements. After heating with the maximum intensity of laser radiation, a crystalline fraction with nanocrystals 2 nm in size appeared in sample 1. The size of the nanocrystals of sample 2 was around 1.5 nm before the beginning of Raman measurements cycling and they grew to become up to 2 nm in size at the end of cycling. Thus, the cross-section ratio parameter y was estimated to be around 1 for samples 1 and 2 during the whole cycle of measurements. As for the sample 3, parameter y was found to be around 1.5 at the beginning and 2.5 at the end of cycling. Samples 2 and 3 were subjected to annealing, as a result of which the crystalline volume fraction in the entire layer increased, in contrast to the action of laser excitation, when crystallization occurred locally. For sample 3, the calculation showed an almost constant volume fraction of about 80%, for sample 2 it increased from 60% at the beginning of the cycle to 80% at the end, and for sample 1 the volume fraction increased from zero to about 70%.

According to estimates based on diffuse reflection, the absorption coefficient of sample 1 at wavelength of 488 nm is 1.7 times lower than at a wavelength of 633 nm. To better see the differences in the reflection coefficient of samples 2 and 3 compared to sample 1, shows the relative change in reflection. It can be seen that after annealing at 300 ºC, the diffuse reflection of light from the sample 2 near the wavelength of 633 nm practically did not change compared to the sample 1 (the change is within 5%), and therefore the absorption at this wavelength did not change. Near the wavelength of 488 nm, the reflection increased by about 20% for sample 2. The change in reflection at a wavelength of 488 nm observed after annealing at 300 ºC corresponds to a 1.5-fold decrease in the absorption coefficient. The diffuse reflection of sample 3 changed slightly at wavelengths near 488 nm compared to the sample 2 but the reflection at wavelengths near 633 nm increased by about 60-70% compared to the samples 1 and 2, which means that the absorption coefficient in this wavelength region has sharply decreased.

A rough estimate in accordance with obtained data shows that for the observed increase in diffuse reflection coefficient near the wavelength of 633 nm, and the absorption coefficient in this spectral region should be 2.5–3 times less. It was stated that, such an increase of reflection may be explained by formation of polycrystalline fraction. A decrease in the absorption coefficient makes Ge NW more resistant to the thermal effects of a He-Ne laser.

## 4. Conclusions

The heat treatment effect on structural and optical properties of germanium nanowires obtained by electrochemical deposition from an aqueous solution was studied. As-prepared samples were amorphous and crystallized under the action of probe laser radiation. The crystallization thresholds for the as-prepared sample were found to be 10 W*cm-2 at 633 nm and 375 W*cm-2 at 488 nm. Specular reflection in the near IR and visible ranges decreases with decreasing wavelength due to the increasing contribution of diffuse reflection and absorption in the Ge NW layer. According to our estimates, the absorption coefficient of as-prepared sample at a wavelength of 488 nm is 1.7 times lower than at a wavelength of 633 nm. This results in stronger heating when excited with a He-Ne laser and a lower crystallization threshold. The estimated crystalline volume fraction demonstrates, that annealing in a vacuum oven at 300 ºC and 600 ºC leads to partial crystallization of Ge NW which retain their morphology. However, annealing at 600 ºC made the studied nanostructures more resistant to the thermal effect of probe laser radiation. Annealing at a temperature of 600 ºC leads to lower red-light absorption in Ge NW as compared to annealing at 300 ºC, as a result of which the crystalline volume fraction practically does not change during the entire time of the He-Ne laser probing. The obtained results will be useful for the development of various devices (metal-ion batteries, photodetectors, sensors, etc.) based on Ge NW obtained by the ec-LLS method. For example, electric currents flowing in metal-ion batteries during operation, especially at high charging/ discharging rates and operating in hot climate can cause their strong heating. The heating of the Ge NW can lead to irreversible effects in the structure and, as a consequence, to a change of the electrochemical characteristics. In turn, annealing at 600 ºC can make the studied nanostructures more resistant to heat.

## Acknowledgements

The work was supported by the Russian Science Foundation (project no. 20-19-00720).

## References

[1] E. Fahrenkrug, S. Maldonado, Accounts of Chemical Research **48**(2015)7.
[2] I. Gavrilin, D. Gromov, A. Dronov, S. Dubkov, R. Volkov, A. Trifonov, N. Borgardt, S. Gavrilov, Semiconductors, **51**(2017)8.
[3] S. Gavrilov, A. Dronov, I. Gavrilin, R. Volkov, N. Borgardt, A. Trifonov, A. Pavlikov, P. Forsh, P. Kashkarov, Journal of Raman Spectroscopy **49**(2018)5.
[4] A. Pavlikov, P. Forsh, P. Kashkarov, S. Gavrilov, A. Dronov, I. Gavrilin, R. Volkov, N. Borgardt, S. Bokova-Sirosh, E. Obraztsova, Journal of Raman Spectroscopy **51(**2020)4.

Sixth Asian School-Conference on Physics and
Technology of Nanostructured Materials
Vladivostok, Russia, 25 – 29 April, 2022



# Pressure induced $Mg_2Ge$ symmetry modifications — DFT evolutionary search results

Yu.V. Luniakov*
Institute of Automation and Control Processes FEB RAS , 5 Radio St., Vladivostok 690041, Russia

*e-mail: luniakov@iacp.dvo.ru

**Abstract.** The search of minimal enthalpy structures of magnesium germanide $Mg_2Ge$ under pressure has been performed using the software suite USPEX implementing the evolution algorithm combined with the density functional theory (DFT) approach. It is shown that in the pressure range P≤25 GPa the triclinic P1 and P-1, monoclinic $P2_1/c$, orthorhombic Amm2 and trigonal P3m1 structures can coexist besides the well-known cubic Fm3m, orthorhombic Pnma and hexagonal $P6_3/mmc$ ones. The new discovered structures are unstable. They can transform into orthorhombic Pnma or hexagonal $P6_3/mmc$ structure at pressures P ≥ 14 GPa.

## 1. Introduction

$Mg_2Ge$ germanide is one of magnesium compounds most extensively studied in recent years [1-4], along with $Mg_2Si$ silicide [2, 3] and $Mg_2Sn$ stannide [2-6]. In connection with relatively high melting temperature T= 1390 K [7] and high electrical conductivity, $Mg_2Ge$ germanide is suited for application as thermoelements in industrial production [8, 9]. Like many oxides and sulphides of rare-earth metals, $Li_2O$, $Na_2S$, $K_2S$, $Li_2S$, and $Rb_2S$, $Mg_2Ge$ germanide at normal conditions has a simple cubic structure of the type of antifluorite with symmetry Fm3m. The first experiments [10] performed in 1964 showed that the magnesium silicide $Mg_2Si$ with the antifluorite structure is characterized by the following structural phase transitions under pressure: antifluorite (Fm3m) → anticottunite (Pnma) → hexagonal $Ni_2In$-type structure ($P6_3/mmc$). Yu [11] simulated the behavior of $Mg_2Ge$ germanide under hydrostatic pressures $0 \le P \le 100$ GPa and obtained the following values of the phase transition pressures in a generalized gradient approximation. For the antifluorite →anticottunite phase transition, P = 8.71 GPa; for the anticottunite → $Ni_2In$-type structure phase transition, P = 33.28 GPa. In 2017, similar study was performed in [12] by M. Guezlane et al., where, for the antifluorite →anticottunite phase transition, pressure P= 7.85 GPa was obtained in generalized gradient (GGA) approximation and P= 4.88 GPa, in a local density approximation (LDA). For the pressure of the anticottunite → $Ni_2In$-type structure phase transition, they obtained P = 29.77 GPa in GGA and P = 63.45 GPa, in the LDA.

The aim of this work is to perform similar calculations for $Mg_2Ge$ germanide at high pressures using the evolutionary search methods and to compare the results with the results of other studies [11, 12], including the results available in the Material Project database [13]. Recent theoretical studies predicted new crystal structures of $Mg_2Si$ [14] and $Mg_2Sn$ [15] isomorphs under pressure $P \ge 5$ GPa, giving us a hope to discover some new structures of $Mg_2Ge$.

## 2. Calculation details

The optimal structures with minimum enthalpy were determined using contemporary methods of evolutionary search implemented in the software suite Universal Structure Predictor; Evolutionary Xtallography (USPEX) [16–18]. During the evolutionary search, we produced more than 20 generations: each of the generation contained 24 structures, except for the first generation that contained 140 structures. Convergence was considered to be attained, if the most energetically advantageous structure remains unchanged for twenty generations in succession. The obtained structures were geometrically optimized by the conjugate gradient method implemented in the VASP software [19] with an energy precision of up to 0.1 meV per cell. In this case, the cutoff energy of the plane-wave basis was $E_{cut}$ = 520 eV (for comparison with the data from database in [18]); the exchange correlation potential was chosen in the Perdew–Burke–Ernzerhof parametrization [20] in the approximation.. The enthalpy at a zero temperature was determined using relationship $F = E + PV$, where $E$ is the total energy, $P$ is the external pressure, and $V$ is the primitive cell volume. The external hydrostatic pressure was taken in the range $0 \le P \le 25$ GPa.

***Table I.*** *Symmetry of the most advantageous structures at different pressures. Second row in Table 1 enumerate the structure according to International Tables for Crystallography [21]. In the third row the Hermann–Mauguin notation of the corresponding structure is given.*

| Pressure, GPa | 0.0001 | 5 | 10 | 15 | 20 | 25 | 30 |
|---|---|---|---|---|---|---|---|
| Structure | 38 | 1 | 2 | 14 | 62 | 156 | 1 |
| symmetry | Amm2 | P1 | $P\bar{1}$ | $P2_1/c$ | Pnma | P3m1 | *P1* |

## 3. Results and discussions

Table 1 demonstrates symmetries of the most energetically favourable structures at the pressures $P \le 25$ GPa with step 5 GPa. We can see that at the ambient pressure condition the most favorable structure is orthorhombic Amm2 (38 space group). $Mg_2Ge$ in known to crystallize in the cubic anti-fluorite structure with symmetry Fm3m (225 space group). The application of FINDSYM utility [22] to the resulting orthorhombic Amm2 identified this structure as Fm3m one if the atomic displacement tolerance parameter is set to be high enough $\sigma \ge 0.01$ Å. The energy difference between Fm3m and Amm2 structures is less than 0.5 meV.

If we apply the FINDSYM utility [22] to all of the best structures shown in Table 1, we can obtain space group symmetry of these structures — 2, 11, 14, 62, 63 and 194, depending on the given tolerance $0.001 \le \sigma \le 0.1$ Å. To exclude the influence of precision in symmetry determination all the obtained structures were fully

optimized after re-determination of symmetry with different tolerance σ. The results are collected in fig.1, where the pressure dependence of the difference of enthalpies between the most advantageous structures and the reference one which is chosen to be orthorhombic Pnma with 62 space group. Besides the enthalpy of the calculated structures fig.1 also collects the enthalpies of the structures available on database [13]. The last ones were calculated for all pressures under investigation $0 \le P \le 25$ GPa. The enthalpy difference for all structures with close symmetries is within the precision of calculations. For example the enthalpies of P-1 and $P2_1/c$ structures differ less than 2.5 meV, the enthalpies of P1 and Pnma structures differ less than 1.3 meV and the enthalpies of P-1 and Pnma structures differ less than 0.8 meV in all pressure range. The enthalpy of P3m1 structure is almost identical to the enthalpy of hexagonal structure mp-1018794 from database [13].

The observed ambiguity of the structures obtained in these calculations can be illustrated by the artifact phase transition from P1 to $P6_3/mmc$ structure that is seen in fig. 1. The P1 to $P6_3/mmc$ transition was not observed by the other calculations [12, 13] and can be associated by the instability of the non-symmetrical structure P1, defined to be optimal at pressures $P \ge 5$ GPa. To check it out we perform full optimization of the non-symmetrical structure P1 including the cell optimization and atomic relaxations with increased accuracy. The resulted structure relaxed into the Pnma one at pressures $P \le 15$ GPa and it relaxed into the $P6_3/mmc$ one at pressures $P \ge 16$ GPa as we can see in fig. 1. There are no the discontinuities in the first derivatives of the thermodynamic potential, i. e. the volume as a function of pressure. Two first order phase transitions are characterized by change of the volume as a function of pressure and observed in Fig.1 at pressures P= 5.88 GPa and P = 24.81 GPa. The first value corresponds to the Fm3m → Pnma structure transition and agrees with the data P =7.85 GPa obtained by M. Guezlane et al. [13] and P = 8.71 GPa obtained by Yu et al. [12]. The second phase transition pressure Pnma → $P6_3/mmc$ P = 24.81 GPa agrees with value P = 18.4 GPa obtained by Yu et al. [12] and value P = 29.77 GPa obtained by M. Guezlane et al. [13], taking into account that in the LDA approximation M. Guezlane et al. obtained the twice higher value P = 63.45 GPa. This discrepancy in the Pnma → $P6_3/mmc$ transition value can be related to the complexity of the potential relief of the Pnma and $P6_3/mmc$ structures.

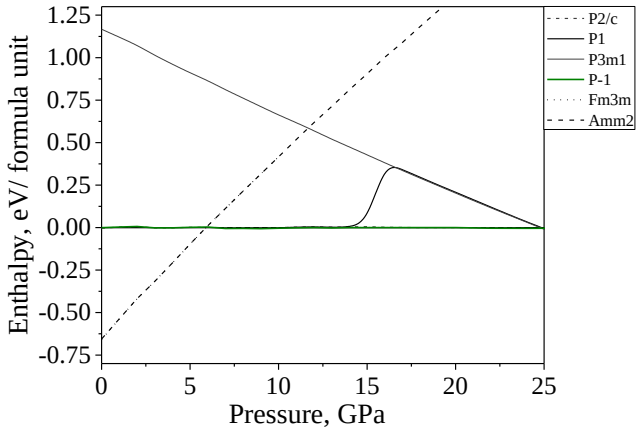


***Fig. 1.*** *Enthalpy of different $Mg_2Ge$ structures versus pressure.*

## 4. Conclusions

Evolutionary search allow to reproduce the antifluorite, anticottunite and $Ni_2In$-type structure of $Mg_2Ge$ and predict the unknown structures of 2, 11, 14, 62, 63 and 194 space group symmetries at pressures P > 5 GPa. The last structures are unstable due to a complex potential relief at high pressures.

## Acknowledgements

The calculations were carried out using IACP FEB RAS Shared Resource Center «Far Eastern Computing Resource» equipment (https://cc.dvo.ru).

## References

[1] J.Tani, M.Takahashi, and H. Kido, J. Alloys Compd. 485 (2009) 764.
[2] M.Cahana and Y.Gelbstein, Intermetallics 120 (2020) 106767.
[3] G. Murtaza, A. Sajid, M. Rizwan, Y. Takagiwa, H. Khachai, M. Jibran, R. Khenata, S. Bin Omran, Mater. Sci. Semicond. Process 40 (2015) 429.
[4] G.Castillo-Hernandez, M. Yasseri, B.Klobes, S. Ayachi, E.Müller, J. Boor, J. Alloys Compd. 845 (2020) 156205.
[5] Y.Zhu, Zh.Han, F.Jiang, E.Dong, B.-P.Zhang, W.Zhang, W.Liu, Mater. Today Physics 16 (2021) 100327.
[6] H.T. Chen and Zh.-Z.Shi, Mat. Let. 281 (2020) 128648.
[7] A. A. Nayeb-Hashemi, J. B. Clark, Bull. of Alloy Phase Diagrams 5 (1984) 466.
[8] A.M. Iida, T. Nakamura, K. Fujimoto, Y. Yamaguchi, R. Tamura, T. Iida, and K. Nishio, RS Advances 1.60 (2016) 3971.
[9] M.Akasaka, T.Lida, A.Matsumoto, K.Yamanaka, Y.Takanashi, T.Imai, N.Hamada, J. Appl. Phys. 104 (2008) 13703.
[10] P. Cannon, E.T. Conlin, Science 145 (1964) 487.
[11] F. Yu, J.-X. Sun, T.-H. Chen. Physica B 406, 1789 (2011).
[12] M. Guezlane. H. Baaziz, Z. Charifi, A. Belgacem-Bouzida, Y. Djaballah. J. Sci. Adv. Mater. Devices 2, 105 (2017).
[13] A. Jain, S.P. Ong, G. Hautier, W. Chen, W.D. Ri-chards, S. Dacek, Sh. Cholia, D. Gunter, D. Skinner, G. Ceder, K.A. Persson. APL Mater. 1, 011002 (2013).
[14] Yu. Luniakov, Physics of the Solid State, 62 (2020) 783
[15] Yu. Luniakov, Physics of the Solid State, 63 (2021) 452
[16] A.R. Oganov and C.W. Glass, J. Chem. Phys.124 (2006) 244704.
[17] C.W. Glass, A.R. Oganov, and N. Hansen, Comput. Phys. Commun. 175 (2006) 713.
[18] A.R. Oganov, A.O. Lyakhov, M.Valle, Acc. Chem. Res. 44 (2011) 227.
[19] G. Kresse and J. Furthmuller, Phys. Rev. B 54, 11169 (1996).
[20] J.P. Perdew, K. Burke, M. Ernzerhof, Phys. Rev.Lett. 77 (1996) 3865.
[21] International Tables for Crystallography A (2006) 720
[22] T. Hahn, U. Shmueli, J. W. Arthur, International tables for crystallography 1 (1983) 182.
[23] S.T. Stokes, D.M. Hatch, B.J. Campbell, Isotropy Software Suite, iso.byu.edu.

Sixth Asian School-Conference on Physics and
Technology of Nanostructured Materials
Vladivostok, Russia, 25 – 29 April, 2022



# Semipolar GaN layers on nanostructured silicon: the technology,the properties

V.N. Bessolov, E.V. Konenkova*, S.N. Rodin
Ioffe Institute, 26 Politekhnicheskaya st., St. Petersburg, 194021 Russia

*e-mail: lena@triat.ioffe.ru

**Abstract.** It has been studied the epitaxial growth of AlN and GaN layers using the method of metal-organic chemical vapor deposition on nano-structured Si(100) or Si(113) substrates, respectively, with a V-shaped or U–shaped surface profile. It is shown that during the formation of a semipolar AlN layer at the initial stage of epitaxy, coalescence surfaces are formed from semipolar planes that form GAN(10-11) and GaN(11-22) layers with half-widths of the X-ray diffraction curve $\omega_\Theta$ ~ 30 arcmin for structures on Si(100) or Si(113) substrates, respectively.

## 1. Introduction

The attempts to synthesize hexagonal III-nitride layers on the most widely used Si(100) substrate in electronics have shown that hexagonal layers of 6-point symmetry originate on a silicon surface with 4-point symmetry with a large difference in lattice constants and the layers grow in two crystallographic orientations.

Recently, there has been a proposal to use the inclined face of Si(111) for synthesis on Si(100), Si(113), and in our experiments nanostructures with the size of elements on the surface <100 nm were formed (Fig.1a). This work is devoted to the development of the technology of semi-polar layers GaN(10-11) and GaN(11-22) on V-shaped and U-shaped nanostructured substrates Si(100) and Si(113), respectively.

## 2. Experiment

The nano-structure was formed as a result of a two-stage process described in [1]. The GaN layers on the substrates were grown by the metal-organic chemical vapor deposition (MOCVD) on a modified EpiQuip installation with a horizontal reactor. Hydrogen was used as a carrier gas, and ammonia, trimethylgallium and trimethylaluminium as precursors. The structures consisted of an AlN layer ~20 nm thick and GaN layer ~ 1 μm thick. X-ray diffraction analysis showed that the GaN layers have a half-width of the X-ray diffraction curve $\omega_\Theta$ ~ 30 arcmin for the structures GaN(11-22)/NP-Si(113) and GaN(10-11)/NP-Si(100).

## 3. Results and discussions

### Semipolar GaN(10-11)/NP-Si(100) structures:

SEM images of the cross-section of AlN layer shows that a layer about 20 nm thick is formed in the form of crystallites, in which the faces of AlN(10-11), AlN(0001) can be distinguished. It can be seen that the layer has "grooves" with a size of about 10 nm and a depth of about 20 nm with faces and AlN(10-11) and AlN(0001) (Fig.1b), which, with further growth, form a corrugated surface consisting of two semipolar AlN(10-11) with opposite "*c*" axes.

During further epitaxy of GaN layers on NP-Si(100) with symmetrical nanochannels, their growth occurs in the semipolar direction, as evidenced by the XRD data and the typical asymmetric character of the semipolar GaN(10-11) blocks (Fig.1 c).

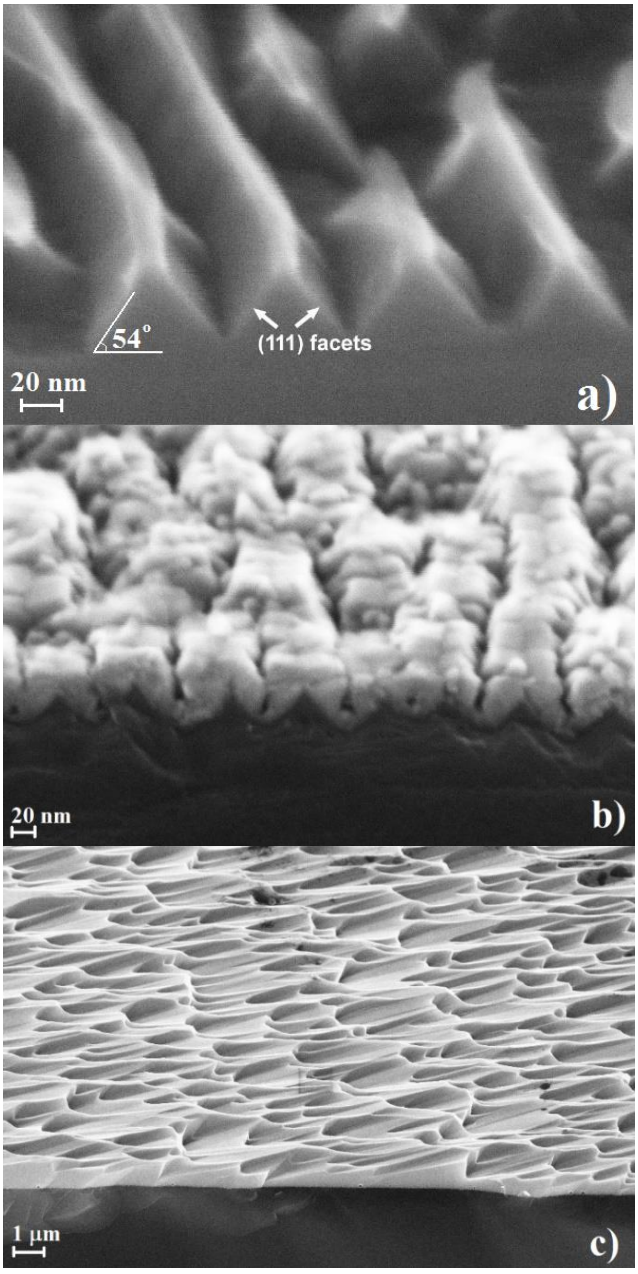


***Fig. 1**. SEM images of the cross-section of the NP-Si(100) substrate (a), AlN/NP-SI(100) structure at the initial stage of growth(b) and the surface of the GAN(10-11)/AlN/NP-Si(100) structure (c).-*

The formation of a semipolar GaN(11-11) occurs due to the asymmetric properties of the NP-Si(100) substrate after the N.ions treatment, as described [2]. It should be noted that when the scanning is carried out in the direction perpendicular to the grooves, the distance between the peaks of the grooves in the GaN layer (10-11) was 3 -5mkm and significantly differs from the similar distance set by the NP-Si(100) substrate - less than 100 nm (Fig. 1).

**Semipolar GaN(11-22)/NP-Si(113) structures:**

The two samples were grown during the technological experiment in the same temperature-time regimes – insular or continuous semipolar layers of GaN on NP-Si(113).

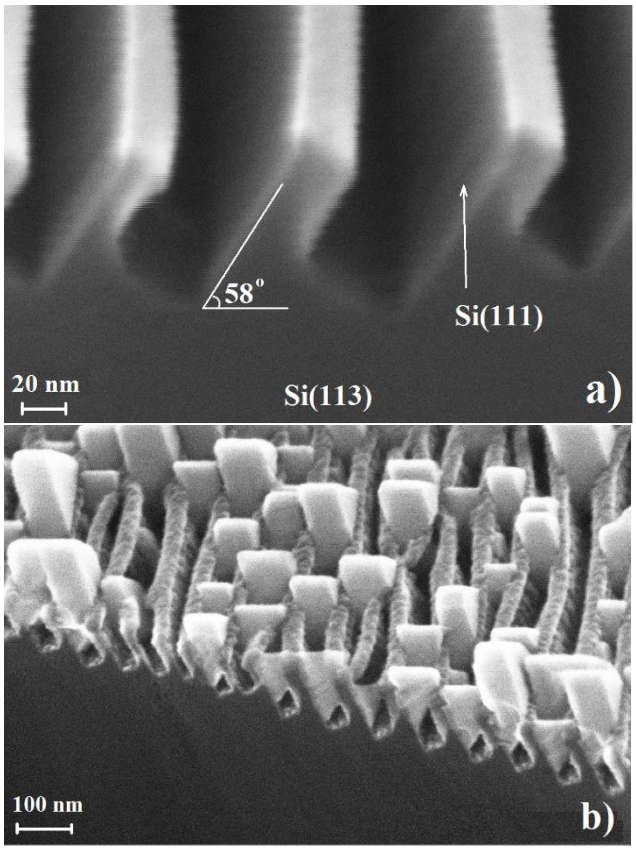


***Fig. 2.*** *SEM image of the cross-section of the NP-Si(113) substrate(a) and GaN/AlN/NP-SI(113) structure at the initial stage of growth (b).*

Initially, a buffer layer AIN with a thickness of 20 nm was grown on all structures in a hydrogen atmosphere. Then, an insular layer of GaN(11-22) with dimensions of ~ 0.05-0.2 μm or continuous layers with a thickness of ~ 0.6-1 μm GaN(11-22) was grown on the buffer layer. After anisotropic chemical etching, two parallel faces are formed in the grooves with an angle of inclination of 58° with respect to the surface, where one face (111) faces up and the other (111) faces down. Another face (011) is formed at the bottom of each groove. SEM images showed that the surface of inclined nanogrooves, including amorphous nitride nanowires on their tops, after epitaxy of the buffer layer is covered with a continuous even AlN layer with a thickness of about 20 nm (Fig.2a), despite the complex nature of the surface of the structured Si(113) substrate. We believe that the continuity of the buffer layer is achieved by the fact that the nucleation of AlN occurs under conditions when the free path of the adatom Al over the surface of Si becomes comparable to the size of the face of Si(111) in one of the directions. It is necessary to ensure the nucleation density during the nucleation of AlN for the "quasi-two-dimensional" growth of the layer, so that the individual nuclei are separated by a distance less than twice the distance of the diffusion length of the Al-adatom. Otherwise, adatoms migrating along the surface will increase the possibility of secondary nucleation with the appearance of cavities between the nucleus. Indeed, the diffusion length of the adatom on the Si(111) surface is about 40 nm [3], and in our experiments the length of the edge of Si(111) is 75 nm. The nucleation of the GaN layer occurs on the surface of the AlN/Si(111) face, and at first an island layer is formed with clearly defined faces (Fig.2b), and then a solid layer of GaN (11-22) is appeared with a half-width X-ray diffraction curve $\omega_\theta$ ~30 arcmin. Selective growth of GaN(11-22) on NP-Si(113) by HVPE is accompanied by the formation of voids in the region of the bottom of the nanogrooves, which provides stress relaxation in the GaN layer and it has been opened up the prospect of separation of thick GaN layers by the VAS method (Void Assisted Separation).

## 4. Conclusions

Thus, the use of a nanoscale structured substrate allows for the "quasi-two-dimensional" epitaxial growth of thin 20 nm AlN layers on nano-structured NP-Si(100) and NP-Si(113) substrates, and to ensure the formation of semipolar GaN(10-11) and GaN(11-22) layers with half-widths of X-ray diffraction curves $\omega_\theta$ ~ 30 arcmin, respectively.

## Acknowledgements

V.N.Bessolov and E.V.Konenkova, thank for the support the Russian Foundation for basic research (project № 20-08-00096). The authors thank V.K.Smirnov for providing nano-structured Si(100) substrates.

## References

[1] V.K. Smirnov, D.S. Kibalov. Proc.21st Int. Conf. on Ion-Surface Interactions (Yaroslavl, Russia), **1**(2013),62.

[2] Bessolov V.N., Konenkova E.V., Rodin S.N., Kibalov D.S., Smirnov V.K., Semicond., **55**(2021)471.

[3] C.Bayram, J.A.Ott, K.-T.Shiu, Ch.-W.Cheng, Y.Zhu, J.Kim, M.Razeghi, D.K.Sadana,, Adv. Funct. Mater. **24**(2014)4492.

Sixth Asian School-Conference on Physics and
Technology of Nanostructured Materials
Vladivostok, Russia, 25 – 29 April, 2022



# Low-temperature hysteresis of β⇔β' phase transition in $In_2Se_3$/Si(111) films

S.A. Ponomarev[*,1,2], D.I. Rogilo[1], A.Y. Mironov[1], N.N. Kurus[1], A.G. Milekhin[1], D.V. Sheglov[1], A.V. Latyshev[1]

[1] Institute of Semiconductor Physics of SB RAS, 13 pr. Lavrentieva, Novosibirsk 630090, Russia
[2] Novosibirsk State University, 2 Pirogova St., Novosibirsk 630090, Russia

*e-mail: s.ponomarev1@g.nsu.ru

**Abstract.** Electronic properties of layered $In_2Se_3$ films grown on the Si(111) surface have been studied. We have measured the layered $In_2Se_3$ film temperature dependence of the resistance and Raman spectra during the cooling to 77 K and subsequent heating to the room temperature. There is a reversible phase transition β-$In_2Se_3$ ⇔ β'-$In_2Se_3$ observed by STM [ACS Nano 2 (2019) 10 6774–6782]. At the temperature of about 140 K, the film's resistance decreases sharply by ~$10^4$ times. The reverse transition occurs during heating to a temperature above 180 K. This hysteresis corresponds to the β-$In_2Se_3$ ⇔ β'-$In_2Se_3$ phase transition. We have measured the Raman spectra of the $In_2Se_3$ film during the cooling to the 77 K and subsequent heating to the room temperature and have observed the same hysteresis, that corresponds to the β-$In_2Se_3$ ⇔ β'-$In_2Se_3$ phase transition. During the cooling at the temperature of about 140 K we have observed the disappearance of the peak at 175 $cm^{-1}$ with the subsequent appearance of the peaks at 155, 170, and 188 $cm^{-1}$. The peak at 175$cm^{-1}$ returns at the heating to 180 K and upper.

Keywords —layered In2Se3, *in situ* reflection electron microscopy, resistance, layered materials, van-der-Waals epitaxy, Raman

## 1. Introduction

At the beginning of the XXI century layered two-dimensional (2D) materials have become promising candidates for future microelectronics, photonics, and photovoltaics due to the fact that this class of materials includes semiconductors, metals, and dielectrics [1]. layered $In_2Se_3$ is of interest for the development of solar photocells, photodetectors operating in the range from UV to near IR, and memory devices.

Recently, about ten $In_2Se_3$ phases have been experimentally discovered and theoretically predicted [2,3]. When taking into account the stability of the phases under normal conditions and their known electrophysical properties, only α-, β-, γ-$In_2Se_3$ phases attract attention as candidates for technological application, the rest of the $In_2Se_3$ phases are unstable or do not exist under normal conditions [4,5]. There is a reversible phase transition between α- and β-$In_2Se_3$ phases in the region 200–250°C [5]. The switching between the phases makes this material promising for information storage devices [6]. However, the investigation of $In_2Se_3$ controllable van-der-Waals growth with a given phase and its electronic properties is a current research topic for potential applications in the fields of modern electronics [7,8].

## 2. Experiment

Growth experiments were carried out using in situ reflection electron microscopy. This technique makes use of a 100 keV electron beam reflecting from the substrate surface at Bragg angle to provide a high sensitivity to surface morphology, as well as a possibility of analyzing the surface structure by reflection high-energy electron diffraction (RHEED). Also, this method allows obtaining in situ images of the processes on the substrate surface in real time with monatomic-step-level resolution [9].

We used Si(111) specimens with 8×1×0.38 mm dimensions cut from n-type (0.3 Ω·cm) Si(111) wafers with a miscut angle of about 0.1 deg. The substrate was heated resistively by passing an electric current through it. The surface of this substrate was cleaned by annealing at 1300°C for 5 minutes. The selenium flow was calibrated against the etching rate of the Si(111) surface [10]. The In deposition rate was calibrated by the appearance of a √3×√3 superstructure on the Si(111) surface at 450°C [11]. The In/Se flux ratio was selected in the 1/6–1/3 range. Within this flux ration range, $In_2Se_3$ grows with a lower concentration of defects [12]. Next, the surface was annealed at 600°C to obtain an atomically clean Si(111) surface with a 1×1 structure. Then the surface was cooled below 100°C, passivated with selenium atoms by deposition of 1/2 selenium monolayer (1 ML=$7.8\times10^{14}$ $cm^{-2}$), and then heated to 100°C to remove the amorphous layer of excess selenium. Next, 2 ML of indium was deposited simultaneously with selenium to grow 1-nm-thick amorphous $In_2Se_3$ film. Then the film was rapidly heated to the temperature of layered $In_2Se_3$ growth (about 450°C) [12]. This procedure leads to the growth of single-phase β-$In_2Se_3$ film [7]. The growth of the layered $In_2Se_3$ phase was confirmed by the RHEED patterns observed after this heating. The layered growth mode of $In_2Se_3$ film continued until the formation of three-dimensional (3D) islands, after which the experiment was terminated. The nucleation of 3D islands occurred when $In_2Se_3$ films reached 3–5 nm thickness. We used a 3He/4He Oxford Instruments dilution refrigerator and a two-contact technique to measure the temperature dependence of the electrical resistance. The temperature dependence of Raman spectra was measured by using the Horiba XploRa Plus with the 10°C steps during the cooling to 77 K and then heating to the room temperature, the wavelength of the laser was 532 nm.

## 3. Results and discussions

Fig. 1 shows the temperature dependence of the electrical resistance of an 8-nm-thick $In_2Se_3$ film. One can see a smooth resistance hysteresis in the 20–40 K range without abrupt changes. The second hysteresis is found in the 140–180 K range. When the sample was cooled from room temperature, we have first observed an abrupt decrease in the resistance by ~$10^4$ times around 140 K. The

reverse transition occurred when the temperature rose above 180 K.

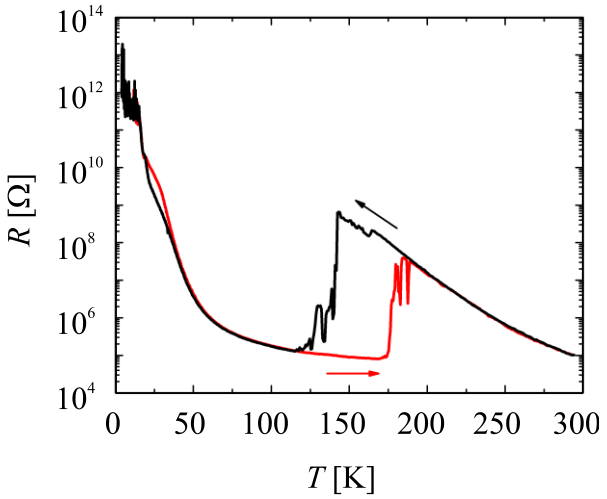


***Fig. 1.*** *Dependence of 8-nm-thick $In_2Se_3$ film resistance on temperature. The red plot is heating, the black plot is cooling.*

A similar jump in conductivity by 3 orders of magnitude was found at about 323–473 K, corresponding to the phase transition from the α-$In_2Se_3$ phase to the β-$In_2Se_3$ phase [5]. In our case, the hysteresis has the conductivity jump at much lower temperatures (140–180 K). In this temperature range, a transition from the β-phase to a β'-phase has been recently discovered by scanning tunneling microscopy [7]. It was theoretically predicted that the β'-$In_2Se_3$ has a wider bandgap than the β-$In_2Se_3$. Since we have found much lower resistance for the low-temperature phase, we suggest that this phase is β'-$In_2Se_3$ has a high concentration of structural defects that increase film's conductivity through the generation of shallow donors or acceptors after the β-$In_2Se_3$ ⇒ β'-$In_2Se_3$ structural transition.

A film with a thickness of about 70 nm was obtained by the *in situ* REM on the Si(111) surface for measuring the Raman spectra. Raman spectra were measured (Fig. 2) during cooling to 77 K and subsequent heating to room temperature in steps of 10 K. During the cooling with the 10 K steps to the temperatures about 140 K we observed the disappearance of the peak at 175 $cm^{-1}$, and the subsequent appearance of three peaks at 155, 170, and 188 $cm^{-1}$ that correspond to the β'-$In_2Se_3$. Moreover, when the film was heated to a temperature of about 180 K, we observed the reappearance of a peak at 175 $cm^{-1}$ that corresponds to the β-$In_2Se_3$.

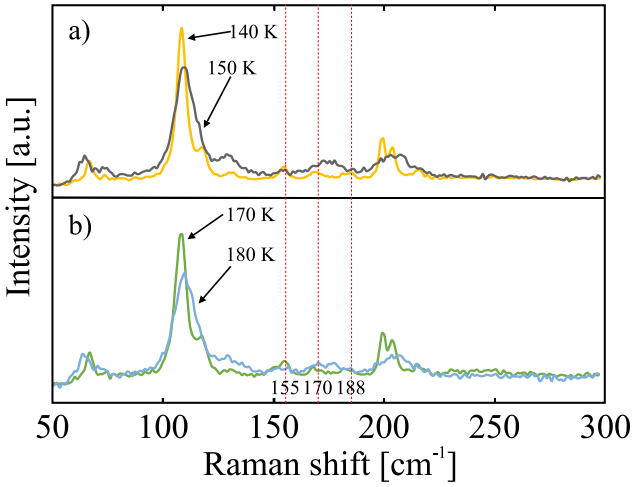


***Fig. 2.*** *a) Raman spectra of $In_2Se_3$ film during the cooling. At 140 K shows the appearance of the peaks at 155, 170, and 188 $cm^{-1}$ b) Raman spectra during the heating. At 180 K shows the disappearance of peaks at 155, 170, and 188 $cm^{-1}$.*

## 4. Conclusions

We have measured the Raman spectra of the $In_2Se_3$ film during the cooling to the 77 K and subsequent heating to the room temperature and have observed the hysteresis, which corresponds to the β-$In_2Se_3$ ⇔ β'-$In_2Se_3$ phase transition. During the cooling at the temperature of about 140 K we have observed the disappearance of the peak at 175 $cm^{-1}$ with the subsequent appearance of the peaks at 155, 170, and 188 $cm^{-1}$. The peak at 175$cm^{-1}$ returns at the heating to 180 K and upper. We have first observed an abrupt decrease in the resistance by ~$10^4$ times around 140 K. The reverse transition occurred when the temperature rose above 180 K.

## Acknowledgments

This research was performed on the equipment of CKP "Nanostruktury".

## References

[1] S. Vishwanath, X. Liu, S. Rouvimov, L. Basile, N. Lu, A. Azcatl. K. Magno, R. Wallace, M. Kim, J. Idrobo, J. Furdyna, D. Jena, H. Xing. J. Mater. Res. **31**(2016)900.
[2] W. Li, F. Sabino, F. Crasto de Lima, T. Wang, R. Miwa, A. Janotti. Phys. Rev. B **98**(2018)165134.
[3] X. Tao, Y. Gu. Nano Lett. **13**(2013)3501
[4] F. Zhang, Z. Wang, J. Dong, A. Nie, J. Xiang, W. Zhu, Z. Liu, C. Tao. ACS Nano, vol. **13**(2019)8004.
[5] C. Julien, M. Eddrief, M. Balkanski, E. Hatzikraniotis, K. Kambas. **88**(1985)687
[6] J. Igo, M. Gabel, Z. Yu, L. Yang, Y. Gu. ACS Nano. **2**(2019)6774.
[7] S. Rathi, D. Smith, J. Drucker. Cryst. Growth Des. **14**(2014)4617.
[8] M. Claro, J. Grzonka, N. Nicoara, P. Ferreira, S. Sadewasser. Adv. Opt. Mater. **9**(2021)2001034.
[9] A. V. Latyshev, A. L. Aseev, A. B. Krasilnikov, S. I. Stenin. Surf. Sci. **213**(1989)157
[10] D. Rogilo, L. Fedina, S. Ponomarev, D. Sheglov, A. Latyshev. J. Cryst. Growth **529**(2020)125273.
[11] A. Zotov, A. Saranin, O. Kubo, T. Harada, M. Katayama, K. Oura. Appl. Surf. Sci. **159**(2000)237.
[12] B. Thomas, Appl. Phys. A Solids Surfaces. **54**(1992)293.
[13] T. Suemasu, T. Fujii, K. Takakura, F. Hasegawa. Thin Solid Films **381**(2001)209.

# Black magnesium germanide: from Ge surface texturing to optical properties evaluation

A.V. Shevlyagin*[,1], V.M. Il'yaschenko1, A.A. Kuchmizhak[1,2], E.V. Mitsai[1], D.V. Pavlov[1], A.V. Gerasimenko[3]

[1] Institute of Automation and Control Processes FEB RAS , Vladivostok, 690041, Russia
[2] Pacific Quantum Center, Far Eastern Federal University, Vladivostok, 690922, Russia
[3] Institute of Chemistry FEB RAS, Vladivostok, 690022, Russia

*e-mail: shevliagin@mail.ru

**Abstract.** Narrow band gap of germanium (Ge) opens possibility of optical platform with efficient near-infrared optical properties to be developed. Providing surface texturing protocol one can expect black Ge demonstration with wider spectral antireflection compared to black silicon. In order to further enhance its light-trapping performance and extend its "blackness" toward middle-infrared range, we propose (i) a simple and scalable method of wet chemical texturing of Ge substrates (text-Ge) resulting in the formation of randomly distributed massive of Ge pyramids and (ii) vacuum deposition of magnesium germanide ($Mg_2Ge$) film as cover layer atop text-Ge. The results of crystal structure, phase composition and optical measurements confirmed successful formation of the $Mg_2Ge$/text-Ge heterostructure called black magnesium germanide with 10-times lower averaged in (450-3000) nm wavelength range optical reflectance (~4.2%) compared with pristine flat Ge surface (40.2%).

## 1. Introduction

Since exploring of the butterfly wing phenomenal structure [1] and first demonstration of the Vantablack® substance [2], there is an ongoing quest for the synthesis and applications of the ultra-black materials. The most intensive investigations aim for an extending of the spectral "blackness" from visible (VIS) to infrared (IR) wavelength ranges with continuous improvements in antireflection and light-trapping properties keeping in mind simplicity and scalability of the any newly discovered black material. For instance, black silicon (b-Si) delivers a platform for VIS applications, while its decorating and coating resulted in the near-infrared (NIR) performance enhancement [3-8]. The latter effects are mainly originated from narrow band gap material adding ($E_g < E_g^{Si}$ =1.12 eV) atop b-Si nanocones or nanospikes geometry. Thus, turning researchers' eyes on germanium (Ge) substrate instead of Si is a feasible way to obtain black NIR material due to Ge band gap of 0.67 eV. Historically, it was Ge substrate reactive ion etching (RIE), which resulted in first demonstration of the semiconducting black texture [9]. However, RIE is a high-cost technology. Metal-assisted chemical etching and other wet chemical processes are alternative solutions successfully used for Si surface texturing. Unfortunately, Ge surface chemistry differs a lot from that of Si [10].

This work proposes a simple wet chemical etching protocol resulted in pyramid-type texturing of Ge (001) substrate using well-known Piranha solution with optimized etchants both concentration and temperature. In addition, a magnesium germanide ($Mg_2Ge$) coating deposited by vacuum evaporation technique was approved for further extending of the antireflection properties deeper to MIR region owing to its band gap of ~ 0.25-0.6 eV [11-13].

## 2. Experiment

The $Mg_2Ge$/textured Ge (black magnesium germanide or b-$Mg_2Ge$) samples were prepared as follows: first, the (001) oriented Ge substrates were immersed into Piranha solution containing 10 ml of 30% concentrated $H_2O_2$ and 10 ml of 49% concentrated $H_2SO_4$ maintanning at 60°C for 10 minutes followed by dipping in de-ionzed water. Then, substrates were loaded into turbomolecular pumped vacuum chamber with $1\times10^{-6}$ Torr base pressure equipped with Mg vapor source (K-cell, 5N purity), quartz crystal microballance sensor and rotating sample's holder with resistive heating. After substrate outgassing at 600°C, 100 nm-thick Mg layer was deposited at room temperature followed by annealing at 380°C for 10 minutes, so-called solid phase epitaxy (SPE). Pristine flat, textured and $Mg_2Ge$ covered samples were investigated by X-ray diffraction (XRD) and Raman spectroscopy to evaluate crystallinity and phase composition, while scanning electron microscopy (SEM) was used to check evolution of the Ge flat surface after texturization and covering steps. Optical reflectance was recorded in 0.4-3 μm range to verify antireflection properties.

## 3. Results and discussions

Fig. 1(a) shows morphology evolution of the initially flat Ge (001) surface after texturing and $Mg_2Ge$ covering examined with planar SEM images. Pyramidal structure can be clearly seen after Ge dipping into heated Piranha solution. Ge pyramids have random surface distribution with average base width of 2 μm. Solid phase synthesis of the $Mg_2Ge$ layer atop pyramids results in base broadening and appearance of considerable relief on pyramid facets, which suggests $Mg_2Ge$/text-Ge heterostructure to be of core-shell-like one.

Next, structural and elemental analyses of the flat, textured and covered Ge surfaces were investigated and summarized in Fig. 1(b) and (c). XRD and Raman data assume that texturing step resulted in Ge oxidizing in addition to Ge pyramids formation. One can see diffraction and Raman peaks, which correspond to quartz-$GeO_2$ crystal structure [14]. Tentatively, this effect can be associated with well-known Ge surface damaging and $H_2O_2$ promoted fast oxidation [10]. Nevertheless, it is more likely to be that text-Ge outgassing at 600°C under vacuum conditions is favorable for an artificial Ge oxide removing in contrast to naturally oxidized one [15]. As a result, after $Mg_2Ge$ SPE step there are no $GeO_2$ related features on both XRD and Raman spectra, whereas all observed features can be

ascribed as Ge (2Θ ≈ 31,6°, 66°; TO Raman-active mode at 301 $cm^{-1}$) and $Mg_2Ge$ (2Θ ≈ 24°, 27°, 40°, 47°; TO Raman-active mode at 256 $cm^{-1}$) contributions [16].

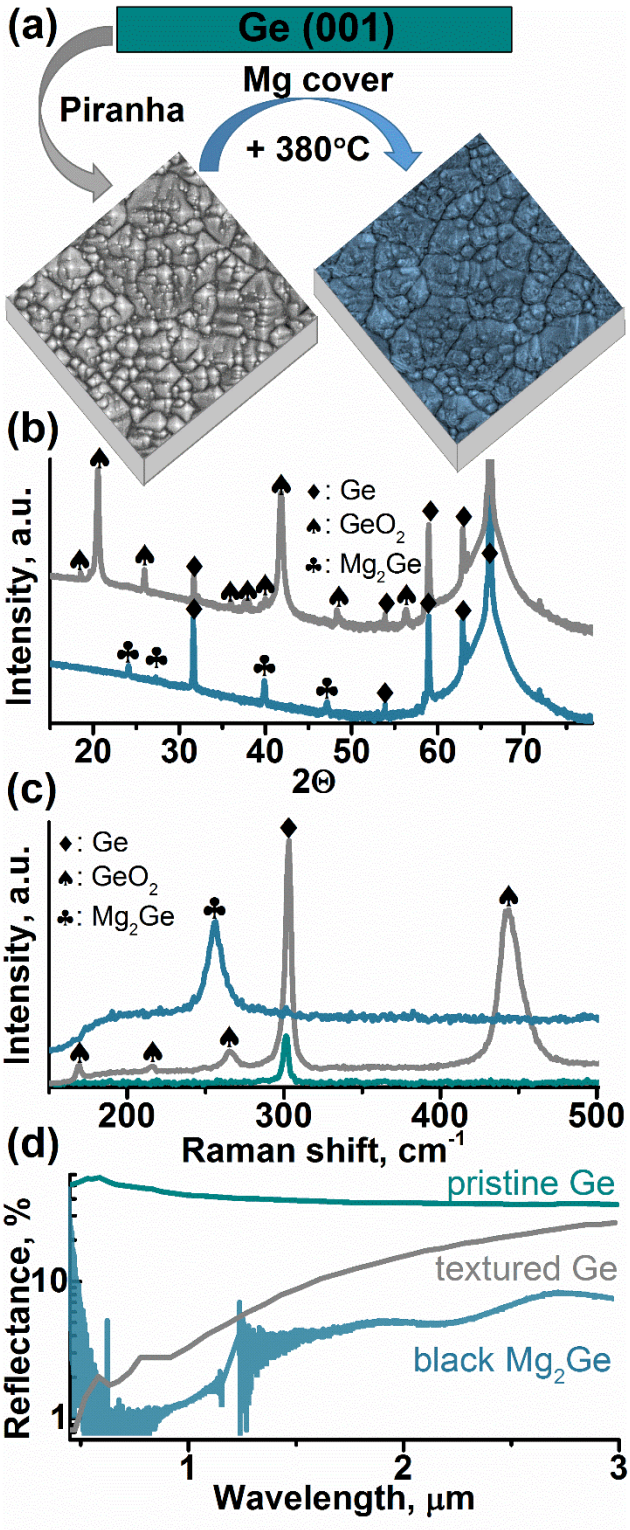


***Fig. 1.*** *Summary of the b-$Mg_2Ge$ R&D. (a) Sketch demonstrates step-by-step preparation of the b-$Mg_2Ge$ with surface morphology changes examined by planar SEM images (30×30 $\mu m^2$). (b) XRD and (c) Raman data representing material balance and phase composition after Ge surface texturing and $Mg_2Ge$ covering. (d) Wideband optical reflectance reduction in passing from flat to textured and covered Ge substrates.*

Verification of the black magnesium germanide antireflection properties is demonstrated in Fig. 1(d). Marked decrease in total optical reflectance in wide spectral range is observed, first, for text-Ge sample compared to pristine flat Ge, as well as for $Mg_2Ge$/text-Ge sample in comparison with uncovered one. In terms of bare facts, pyramid-like Ge surface and $Mg_2Ge$ covered pyramids have averaged over (450-3000) nm optical reflection of 12.2% and 4.2%, respectively, whereas flat Ge does 40.2%. Thus, 10-fold enhancement of antireflection properties is demonstrated for the proposed black-$Mg_2Ge$ material. We attribute this effect to narrow band gap semiconducting $Mg_2Ge$ cover layer, which preserves Ge pyramids morphology and can effectively absorb incident MIR photons scattered by Ge pyramids.

## 4. Conclusions

In summary, we successfully fabricated both textured and $Mg_2Ge$ covered Ge samples. The latter was named as black magnesium germanide. Ge pyramids formation as well as $Mg_2Ge$ formation were confirmed by SEM, XRD and Raman data. The average reflectance of the b-$Mg_2Ge$ was found to be 10-times lower in comparison with flat Ge substrate. Thus, a simple and low cost method of both Ge surface texturing and its "blackness" spectral extending to MIR region are approved. Results obtained promise solar cells and wideband photodetection applications.

## Acknowledgements

This research was supported by the Russian Science Foundation under Grant No. 20-72-00006.

## References

[1] Z. Han *et al.* Nanoscale **4** (2012) 2879.
[2] P. Ball. Nature Mater. **15** (2016) 500.
[3] J. Lu *et al.* J. Phys. Chem. C **125** (2021) 2733.
[4] K. Isakov, A. Perros, A. Shah, H. Lipsanen. Nanotechnology, **29** (2018) 335303.
[5] Y. Song *et al.* J. Mater. Sci.-Mater. El. **31** (2020) 4696.
[6] K. Wang *et al.* J. Mater. Sci.-Mater. El. **32** (2021) 11503.
[7] A. Sarkar, S. Mukherjee, A. Das, S. Ray. Nanotechnology **30** (2019) 485202.
[8] A. Shah *et al.* Sci. Rep. **6** (2016) 25922.
[9] L. Gilbert, R. Messier, R. Roy. Thin Solid Films **54** (1974) 149.
[10] A. Dutta, S. Mollick, P. Maiti, T. Som. Sol. Energy **221** (2021) 185.
[11] D. Goroshko *et al.* Solid State Phenomena **247** (2016) 66.
[12] C. Mead. J. Appl. Phys. **35** (1964) 2460.
[13] G. Grosch, K. Range. Physica B **235** (1996) 250.
[14] M. Madon, Ph. Gillet, Ch. Julien, G. D. Price. Phys. Chem. Minerals **18** (1991) 7.
[15] K. Prabhakarana *et al.* Surf. Sci. **316** (1994) L1031.
[16] L. Hou *et al.* Mater. Res. Express **6** (2019) 086459.

Sixth Asian School-Conference on Physics and
Technology of Nanostructured Materials
Vladivostok, Russia, 25 – 29 April, 2022



# Coordination of atomic and electronic structure at chemically passivated *n*-InP(100) surfaces

M.V. Lebedev*[,1], T.V. Lvova[1], A.N. Smirnov[1], V.Yu. Davydov1, A.V. Koroleva[2], E.V. Zhizhin[2], S.V. Lebedev[2]

[1] Ioffe Institute, 26 Politekhnicheskaya St., St. Petersgurg 194021, Russia
[2] Saint-Petersburg State University, 7–9 Universitetskaya Nab., St. Petersburg 199034, Russia

*e-mail: mleb@triat.ioffe.ru

**Abstract.** Photoluminescence, Raman spectroscopy and x-ray photoelectron spectroscopy are employed to study *n*-InP(100) surfaces modified with different sulfide solutions. Sulfide treatment results in removal of the native oxide layer and formation at the *n*-InP(100) surface of the passivating coat consisting of In–S chemical bonds with solution composition-dependent atomic structure and surface dipole. At the same time, the photoluminescence intensity of *n*-InP(100) increases indicating surface electronic passivation, while the surface depletion layer reduces. The efficiency of the *n*-InP(100) surface electronic passivation depends on the composition of the sulfide solution and correlates with the arrangement of the sulfur atoms in the passivating coat.

## 1. Introduction

Indium phosphide (InP) is the important III–V semiconductor material used in nanostructured electronic and optoelectronic devices. Surfaces of III–V semiconductors are chemically reactive and contain states within the bandgap resulting in non-radiative surface recombination. Therefore, surface modification becomes unavoidable for surface chemical stabilization, as well as for elimination of the surface recombination and accompanying optical and electronic losses in nanostructured devices [1]. One of the most widely used methods for III–V surface modification is the treatment with sulfide solutions that involves removal of the native oxide layer and formation of passivating coat eliminating surface recombination. Composition of the sulfide solution affects in a great extent the efficiency of the III–V surface electronic passivation due to activation of different chemical reactions at the semiconductor/solution interface modifying atomic structure of the passivated surfaces.

In the present study the *n*-InP(100) surfaces treated with different sulfide solutions are studied by photoluminescence (PL), Raman spectroscopy and x-ray photoelectron spectroscopy (XPS) in order to relate electronic passivation efficiency with the surface atomic and electronic structure.

## 2. Experiment

The samples were cleaved from *n*-InP(100) wafers with the doping densities of $6\times10^{17}$ or $2\times10^{18}$ cm$^{-3}$ called as low-doped and highly-doped samples, respectively. The samples were treated with one of the different $(NH_4)_2S$ solutions. As solutions, a standard commercial aqueous $(NH_4)_2S$ solution with the concentration of about 44%, as well as aqueous or alcoholic solutions prepared by dilution of a standard one by water or 2-propyl alcohol (2PA) to the concentration of about 4% were used.

The micro-photoluminescence (μPL) and micro-Raman (μRaman) studies were performed in air at room temperature using a T64000 (Horiba Jobin-Yvon, Lille, France) spectrometer equipped with a confocal microscope. The excitation was provided by the 442 nm line of a He–Cd laser. The XPS measurements were performed on an Escalab 250Xi photoelectron spectrometer equipped with an AlKα radiation source (photon energy of 1486.6 eV).

## 3. Results and discussions

After passivation with any sulfide solution, the PL intensity of the low-doped *n*-InP(100) increased essentially [**2**] (Table I). The highest PL intensity and thus more efficient electronic passivation was observed after short treatment with the alcoholic $(NH_4)_2S$ solution for 1 min.

***Table I.*** *Parameters of Treated n-InP(100) Samples.*

| Sample treatment | PL increase ($6\times10^{17}$ cm$^{-3}$) | PL increase ($2\times10^{18}$ cm$^{-3}$) |
|---|---|---|
| As is (untreated) | 1 | 1 |
| $(NH_4)_2S_{aq}$ (4%) | 4.2 | — |
| $(NH_4)_2S_{aq}$ (44%) | 5.75 | — |
| $(NH_4)_2S$ + 2PA, 10 min | 7.9 | 0.75 |
| $(NH_4)_2S$ + 2PA, 1–2 min | 10.9 | 1.25 |

On the other hand, the short treatment with alcoholic solution of the highly-doped *n*-InP(100) surface results in rather small PL increase, while the longer treatment deteriorates the PL intensity (Table I).

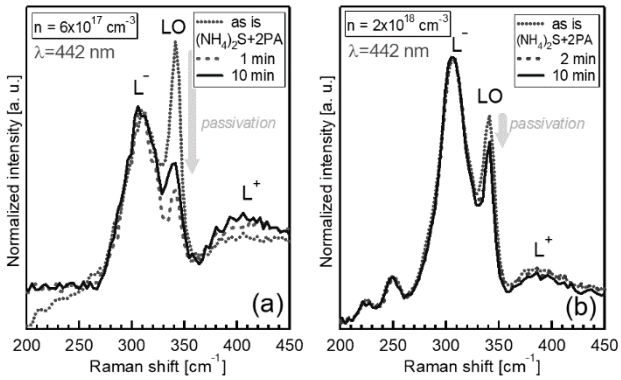


***Fig. 1.*** *Portions of the Raman spectra of low-doped (a) and highly-doped (b) n-InP(100) before and after passivation with $(NH_4)_2S$+2PA solution for different time. Spectra are normalized to the intensity of $L^-$ phonon-plasmon mode.*

After passivation, the Raman spectra change considerably showing narrowing of the surface depletion layer (Fig. 1). Indeed, the intensity of the LO peak related to the scattering in the surface depletion layer decreases both in low-doped (Fig. 1a) and in highly-doped (Fig. 1b) *n*-InP(100). In particular, after passivation with the alcoholic $(NH_4)_2S$ solution, the surface depletion layer of low-doped *n*-InP(100) decreases from ~155 to 65 Å [2], whereas in the highly-doped *n*-InP(100) the depletion layer decreases from 65 to 55 Å. Moreover, the calculated values of the depletion layer width correlate with the PL intensity increase for the passivated low-doped *n*-InP(100) surfaces if the surface band bending remains intact [2].

XPS data shows that even brief treatment of the native-oxide-covered *n*-InP(100) results in complete removal of the native oxide layer and formation of a thin passivating coat consisting of indium sulfide. The surface band bending of about 0.15–0.20 eV usually remains unchanged after passivation. However, in some cases, the surface band bending increases after passivation by 0.10–0.15 eV. It means that the total band bending at the chemically modified *n*-InP(100) surfaces is a superposition of the band bending derived from surface states and potential of interface dipoles formed by In–S chemical bonds.

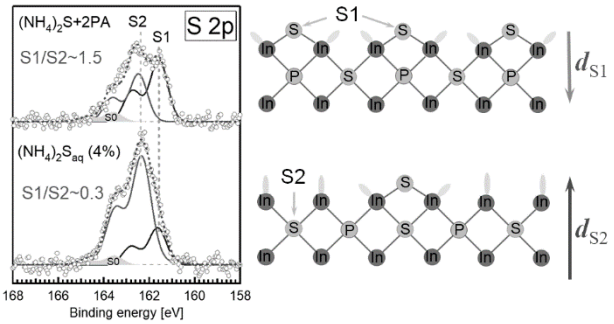


***Fig. 2.*** *Examples of the S 2p core level spectra of n-InP(100) surfaces passivated with different sulfide solutions and the schematic atomic structure models of the corresponding passivated surfaces.*

The dependence of In–S interface dipole on the solution composition can be explained using the analysis of the S 2p core level spectra, which can be fitted with three components associated with S atoms bridge-bonded to surface In atoms (S1), S atoms substituting P-vacancies in the second layer (S2), as well as excess sulfur (S0), respectively (Fig. 2). The ratios of S1 and S2 components in the spectra measured after treatment with various sulfide solutions can be different (Fig. 2). The data obtained indicates that the higher S1/S2 ratio causes more efficient electronic passivation [2].

The In–S–In surface bridge bonds (state S1), as well as In–S–In bonds in which sulfur occupies phosphorous sites in the second atomic layer (state S2) should have a dipole moment. The dipole $\boldsymbol{d}_{S1}$ corresponding with the state S1 and the dipole $\boldsymbol{d}_{S2}$ associated with the state S2 should have an opposite direction. In general, they can have a different value as well. Therefore, the interface dipole component related to interface In–S bonds formed after sulfide treatment should depend on the S1/S2 ratio that characterizes relative amount of sulfur atoms occurring in the states S1 and S2. Once the majority of sulfur atoms are in the S1 state, the direction of this interface dipole component should be the same as $\boldsymbol{d}_{S1}$ (Fig. 2). On the other hand, the interface dipole will be inverted when the majority of sulfur atoms is in the S2 state (Fig. 2). Thus, the direction and the value of the interface dipole component should depend on the surface atomic structure of the sulfide layer, which will be determined by peculiarities of the chemical process of surface passivation.

At the same time, prevailing of the S2 state in the fitting of the S 2p core level spectrum results in increase in the surface band bending by 0.10–0.15 eV, as observed, *e.g.* after treatment of the low-doped *n*-InP(100) surfaces with diluted aqueous $(NH_4)_2S$ solution. In this case, the increase in PL intensity after passivation is not as large as can be expected from the narrowing of the surface depletion layer [2]. Similar effect was observed after treatment of the highly doped *n*-InP(100) surface with alcoholic $(NH_4)_2S$ solution.

It should be noted that the low-doped and highly-doped untreated *n*-InP(100) surfaces exhibited different In/P atomic ratios (1.7 and 1.1, respectively), which can also affect the atomic arrangement of sulfur atoms in the passivating coat after treatment with a certain sulfide solution.

So, the electronic passivation of the *n*-InP(100) surface with sulfide solutions is related to removal of the indium phosphate layer and formation of the In–S bonds at the surface. Such a modification causes changing of the surface dipole so that the depletion layer width decreases essentially. Variation of the sulfide solution composition by changing solvent or sulfide ions concentration causes modification of the sulfur atoms arrangement, which opens up the possibilities for controlling electronic structure of the InP surface.

## 4. Conclusions

Electronic and atomic structure of *n*-InP(100) surfaces modified with different sulfide solutions was investigated by photoluminescence and Raman spectroscopy, as well as by x-ray photoelectron spectroscopy. After sulfide treatment the photoluminescence intensity of *n*-InP(100) increases indicating surface electronic passivation, while the surface depletion layer reduces. The efficiency of the *n*-InP(100) surface electronic passivation depends on the composition of the sulfide solution. Treatment with any of the sulfide solutions results in removal of the native oxide layer from the *n*-InP(100) surface and the formation of the passivating coat consisting of In–S chemical bonds with different atomic structure depending on the solution composition and possessing thus a different dipole moment. Variation of the surface dipole causes modification in the shape of the near-surface band potentials and thereby in the surface electronic structure.

## Acknowledgements

This work was supported in part by Russian Foundation for Basic Research (project number 20-03-00523).

## References

[1] P. R. Narangan, J. D. Butson, H. H. Tan, C. Jagadish, S. Karuturi. Nano Lett. **21**(2021)6967.

[2] M. V. Lebedev, T. V. Lvova, A. N. Smirnov, V. Yu. Davydov, A. V. Koroleva, E. V. Zhizhin, S. V. Lebedev. J. Mater. Chem. **C 10**(2022)2163 https://doi.org/10.1039/D1TC03493F.

Sixth Asian School-Conference on Physics and
Technology of Nanostructured Materials
Vladivostok, Russia, 25 – 29 April, 2022



# Transport and thermoelectric properties of FeVSb-based half-Heusler alloys

A. El-Khouly*[,1,2], A.M. Adam[3], I. Serhiienko[1], E. Chernyshova[1], A. Ivanova[1], V.L. Kurichenko[1], A. Sedegov[1], D. Karpenkov[4], A. Novitskii[1], A. Voronin[1], V. Khovaylo[1]

[1] National University of Science and Technology MISIS, Moscow 119049, Russian Federation.
[2] Damanhour University, Faculty of Science, Physics Department, 22516 Damanhour, Egypt.
[3] Faculty of Engineering, King Salman International University, Sinai, Egypt
[4] Moscow State University, 119991 Moscow, Russian Federation.

*e-mail: menaim.elkhouly@yahoo.com

**Abstract.** This work studies the thermoelectric properties of $FeV_{1-x-y-z}Hf_xTi_yNb_zSb$ half-Heusler alloys as functions of temperature from 300 to 800 K. Transition heavy elements such as Hf, Ti and Nb were used as dopants to both modify carrier concentration for enhancing the electrical properties and to enhance the phonon scattering aiming at reducing the material's lattice thermal conductivity, which may lead to significant improvement in the thermoelectric efficiency. The power factor significantly increased, whereas a reduction in the thermal conductivity was achieved with increasing doping elements. The $FeV_{0.24}Nb_{0.4}Hf_{0.16}Ti_{0.2}Sb$ compound showed the lowest lattice thermal conductivity with a value of (1.81± 0.1 $Wm^{-1}K^{-1}$) at room temperature with a reduction of ~82% compared with FeVSb compound, due to point defect scattering enhancement introduced by Hf-Ti-Nb triple-doping. The $FeV_{0.24}Nb_{0.4}Hf_{0.16}Ti_{0.2}Sb$ compound showed the highest power factor value of (19.5 ± 1.7) μW $cm^{-1}$ $K^{-2}$ at 800 K and a maximum figure of merit value of ~ (0.44 ± 0.07) has been obtained at 725 K.

## 1. Introduction

Most of input energy is lost as waste heat in exhaust and industrial systems. In recent years, thermoelectric (TE) materials have attracted great attention due to their ability in waste heat conversion into electricity, which make them good candidates as new and environmentally friendly sources of energy [1, 2]. Efficient TE material is required to possess high electrical conductivity to achieve high power factor (S2σ), where S and σ are the Seebeck coefficient and the electrical conductivity, respectively. Simultaneously, it should exhibit low thermal conductivity (κtot), which can be expressed as the summation of the electronic, κe, and the lattice, κl, thermal conductivity.

Over the recent years, half-Heusler (HH) materials have been considered as a novel class of TE materials for mid-high temperature due to their high-temperature stability and the huge promise in the field of TE efficiency [3]. With the advantages of being ecofriendly and being thermally and mechanically stable, half-Heusler (HH) compounds are promising materials for exhibiting good TE performances for medium to high temperature applications [4]. Due to their high electrical transport properties, FeVSb- half-Heusler alloys are of huge interest for TE applications. However, lower performance is reported due to the high thermal conductivity [5, 6]. Therefore, the focus in the study of FeVSb-based HH alloys is the reduction of their thermal conductivity, while maintaining good electronic properties, which results in an enhanced TE efficiency. The material's TE efficiency is mainly determined by the dimensionless figure of merit $zT = S^2\sigma T/(\kappa_e+\kappa_l)$, where $T$ is the absolute temperature.

## 2. Experiment

The ingots with nominal composition of $FeV_{1-x-y-z}Hf_xTi_yNb_zSb$ were synthesized from the pure Fe, V, Hf, Ti, Nb and Sb elements at various composition ratios by arc melting followed by induction melting under argon atmosphere. The prepared ingots were annealed at 923 K for 48 h in an evacuated quartz tube, followed by quenching in cold water. Then, the resultant ingots were crushed into powder and then ball milled under argon atmosphere at 450 rpm for 1 hours. The obtained powders were loaded into the graphite dies of 12.7 mm diameter and compacted under vacuum atmosphere using SPS at 1023 K under a uniaxial pressure of 65 MPa for 15 minutes. The obtained disk-shaped specimens were sealed in an evacuated quartz tube and annealed at 923 K for 3 days to reduce any impurity phase and improve microstructure. Disk-shaped samples, with a diameter of 12.7 mm and ~ 1.5mm thickness, were used for thermal diffusivity measurements. Then, the pellets were cut into bars with dimensions of about 10 mm × 2.5 mm × 1.5 mm for the electrical transport properties measurements.

***Table I.*** *Room-temperature values of σ, S, n for the concerned samples.*

| Sample | $S$ (μV $K^{-1}$) | $\sigma$ ($10^2$ $\Omega^{-1}cm^{-1}$) | $n$ ($10^{20}$ $cm^{-3}$) |
|---|---|---|---|
| FeVSb | -110 | *7.5* | 0.099 |
| $FeV_{0.9}Hf_{0.1}Sb$ | 127 | *4.4* | 0.71 |
| $FeV_{0.64}Hf_{0.16}Ti_{0.2}Sb$ | 93 | *12* | 5.5 |
| $FeV_{0.24}Nb_{0.4}Hf_{0.16}Ti_{0.2}Sb$ | 128 | *5.8* | 11.1 |

## 3. Results and discussions

Fig. 1 shows the XRD patterns of the as-pressed samples. All the diffractions peaks are well-matched with the FeVSb HH phase (PDF#25-1134) as the dominant phase with a cubic MgAgAs-type crystal structure (space group $F\bar{4}3m$). The main peak shifting to the left side was observed, which suggests the successful substitution of host atom by dopants (see Fig. 1).

The SEM analysis are used to identify the microstructure and surface morphology after treating the samples with the SPS system and annealing processes (see Fig. 2). SEM images of the $FeV_{0.24}Nb_{0.4}Hf_{0.16}Ti_{0.2}Sb$ sample showed high

densification of the sample, with no visible cracks or voids.

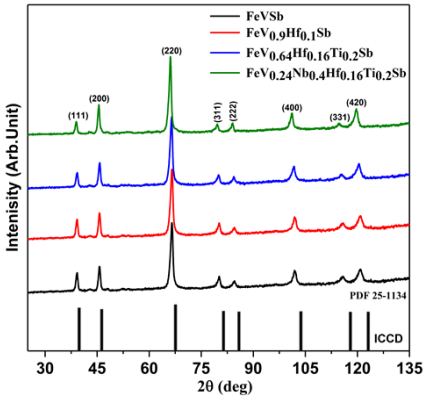


***Fig. 1.*** *XRD patterns of $FeV_{1-x-y-z}Hf_xTi_yNb_zSb$ samples.*

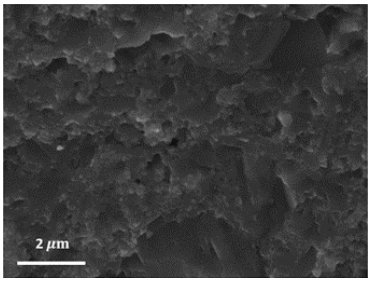


***Fig. 2.*** *The SEM image of the fractured surface of the polished surface for the FeV0.24Nb0.4Hf0.16Ti0.2Sb sample.*

Fig. 3 represents the power factor, *PF*, of the examined samples, which was calculated using the equation $PF = S^2\sigma$. The power factor increases as the temperature increases reaching a maximum point and then decreases, except for the $FeV_{0.24}Nb_{0.4}Hf_{0.16}Ti_{0.2}Sb$ compound, which shows increasing behaviour with temperature. This can be ascribed to the behaviours of the Seebeck coefficient and the electrical conductivity. As a result, a maximum $PF = 19.5 \pm 1.7$ μW cm$^{-1}$ K$^{-2}$ was observed for the $FeV_{0.24}Nb_{0.4}Hf_{0.16}Ti_{0.2}Sb$ compound at 800 K.

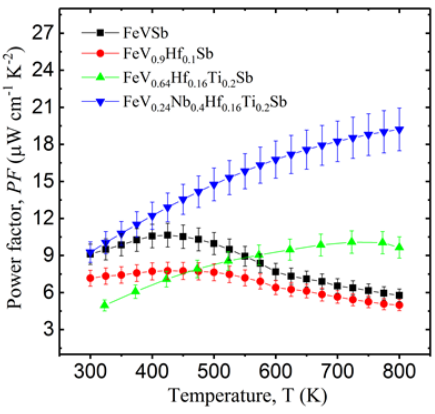


***Fig. 3****. Temperature dependence of power factor for FeV1-x-y-zHfxTiyNbzSb samples.*

The temperature dependence of the thermoelectric figure of merit *zT* of samples is shown in Fig. 4. Generally, *zT* increased with increasing temperature, exhibits a maximum value of 0.44 at 725 K for the $FeV_{0.24}Nb_{0.4}Hf_{0.16}Ti_{0.2}Sb$ compound. This enhancement with *zT* can be ascribed to the more significant improvement in power factor and suppression of the total thermal conductivity.

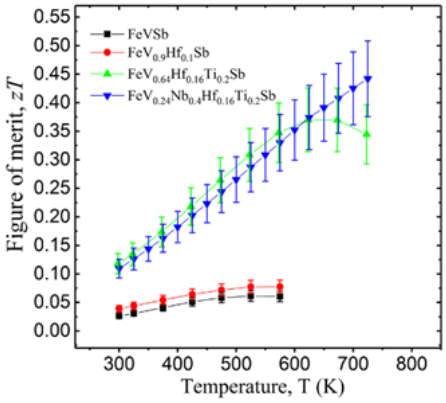


***Fig. 4.*** *Temperature dependences of the thermoelectric figure of merit for the FeV1-x-y-zHfxTiyNbzSb system.*

## 4. Conclusions

The concerned alloys were successfully synthesized by arc/induction melting followed by mechanical alloying (MA) and treated with the spark plasma sintering (SPS) system. The power factor significantly increased, whereas a reduction in the thermal conductivity was achieved with increasing doping content. A maximum power factor value of $(19.5 \pm 1.7)$ μW cm$^{-1}$ K$^{-2}$ at 800 K and figure of merit (*zT*) value of 0.44 were recorded at 725 K for $FeV_{0.24}Nb_{0.4}Hf_{0.16}Ti_{0.2}Sb$ compound.

## Acknowledgements

The work at NUST "MISiS" was supported by the Russian Science Foundation (project No. 21-12-00405).

## References

[1] A.M. Adam, A. El-Khouly, A.K. Diab, alloys, J. Alloys Compd. 851 (2021) 156887.
[2] A.M. Adam, A. El-Khouly, A.P. Novitskii, E.M.M. Ibrahim, A.V. Kalugina, D.S. Pankratova, A.I. Taranova, A.A. Sakr, A. Trukhanov, M.M. Salem, V. Khovaylo, J PHYS CHEM SOLIDS, 138 (2020) 109262.
[3] Xie, W.; Weidenkaff, A.; Tang, X.; Zhang, Q.; Poon, J.; Tritt, T, Nanomaterials 2012, 2 (4), 379–412.
[4] El-Khouly, A., Adam, A.M., Ibrahim, E.M.M., Nafady, A., Karpenkov, D., Novitskii, A., Voronin, A., Khovaylo, V. and Elsehly, E.M, *Journal of Alloys and Compounds* (2021): 161308.
[5] El-Khouly, A.; Novitskii, A.; Adam, A. M.; Sedegov, A.; Kalugina, A.; Pankratova, D.; Karpenkov, D.; Khovaylo, V, J. Alloys Compd. 2020, 820, 153413.
[6] Fu, C.; Xie, H.; Zhu, T. J.; Xie, J.; Zhao, X. B, J. Appl. Phys. 2012, 112 (12), 124915.

# Thermoreflectance method for thermal conductivity measurements of low dimensional objects

I.L. Tkhorzhevskiy*[,1,2], P.S. Demchenko[1,2], A.S. Tukmakova[1,2], A.D. Sedinin[2], A.V. Asach[2], A.V. Novotelnova[2], M.K. Khodzitskiy[2]

[1] Tydex LLC Domostroitelnaya 16, 194292 St. Petersburg, Russia
[2] ITMO University, Kronverksky Pr. 49, bldg. A, St. Petersburg, 197101, Russia

*e-mail: Tkhorzhevskiy.ivan.l@gmail.com

**Abstract.** A design of a set up for non-contact measurements of thermal conductivity in bulk, thick films and low dimensional materials is proposed. The performed method is based on the so-called steady-state thermoreflectance (SSTR) technique[1] that utilizes a pump-probe approach. SSTR can significantly improve and speed up measurements of cross-plane thermal conductivity.

## 1. Introduction

During the measurement, the specimen absorbs radiation from the pump source. That results in a steady sample heating and temperature rise. Energy is delivered by the means of relatively long laser pulses (tenths of seconds). Probe source and balance detector are used for the evaluation of reflectance alterations from the sample interface (originated from the sample temperature rise).

## 2. Experiment

The set up calibration has been done using the Si reference samples and by a finite element method simulation. Further measurements have been performed on PCB FR4 samples. The results of the measurements have been compared with the results obtained by laser flash method[2] measurements. This measurement have been carried out on the commercial LFA-457 (Netzsch) setup.

The measurement set up proposed in this work can be modified and utilised for numerous types of materials with the wide range of thermal conductivity values.

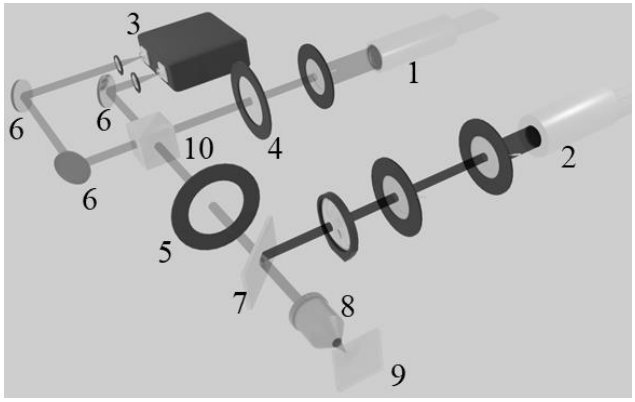


***Fig. 1.*** *The scheme of the proposed set up. 1 – Probe laser, 2 – pump laser, 3 – lock-in amplifier, 4,5 – half- and quarter- wave plated, 6 – mirrors, 7 – hot mirror, 8 – 20x objective lens, 9 – sample, 10 – polarizing beam splitter.*

## Acknowledgements

The research is funded by the RSF project #22-22-00597.

## References

[1] Braun J. L. et al. A steady-state thermoreflectance method to measure thermal conductivity //Review of Scientific Instruments. – 2019. – Т. 90. – №. 2. – С. 024905.

[2] Parker W. J. et al. Flash method of determining thermal diffusivity, heat capacity, and thermal conductivity //Journal of applied physics. – 1961. – Т. 32. – №. 9. – С. 1679-1684.

Sixth Asian School-Conference on Physics and
Technology of Nanostructured Materials
Vladivostok, Russia, 25 – 29 April, 2022



# InGaAs/InGaAlAs and InGaAs/GaAsN superlattice based long wavelength VCSEL

A.Yu. Egorov*[,1], S.A. Blokhin[2], A.A. Blokhin[2], E.V. Pirogov[1], D.V. Denisov[3], L.Ya. Karachinsky[1,4], A.V. Babichev[1], I.I. Novikov[1], A.G. Gladyshev[5], E.S. Kolodeznyi[4], S.S. Rochas[4], V.N. Nevedomskii[2], K.O. Voropaev[6], V.E. Bougrov[4], V.M. Ustinov[7]

[1] Alferov University, 8-3 Khlopina str., St. Petersburg 194021, Russia
[2] Ioffe Institute, 26 Politekhnicheskaya str., St. Petersburg 194021, Russia
[3] Saint Petersburg Electrotechnical University "LETI", 5 Prof. Popova str., 197022 St. Petersburg, Russia
[4] ITMO University, 49 Kronverksky pr. St. Petersburg, 197101 Russia
[5] Connector Optics LLC, 16 lit B Domostroitelnaya str., St. Petersburg 194292, Russia
[6] JSC OKB-Planeta, 13a Bolshaya Moskovskaya str., Veliky Novgorod 173004, Russia
[7] Submicron Heterostructures for Microelectronics, Research & Engineering Center RAS, 26 Politekhnicheskaya str., St. Petersburg 194021, Russia

*e-mail: egorov@spbau.ru

**Abstract.** The paper presents the results of the study of 1550-nm edge-emitters and 1300-nm wafer-fused vertical-cavity surface-emitting lasers based on InGaAs/InGaAlAs superlattice active region and study of InGaAs/GaAsN superlattice enable for the creation of 1300-nm monolithic vertical-cavity surface-emitting lasers.

## 1. Introduction

One of the promising areas of modern semiconductor optoelectronics is the creation of semiconductor vertical-cavity surface-emitting lasers (VCSEL) of the spectral range of 1300-1550 nm for fiber-optic communication lines [1]. Traditionally, to obtain effective optical radiation at wavelengths of 1300-1550 nm, heterostructures of solid solutions InAlGaAsP, which are grown on the InP substrate, are used. However, distributed Bragg reflectors (DBR) based on these solid solutions have a low refractive index contrast and poor thermal conductivity compared to GaAs/AlGaAs DBR. One way to solve this problem is the hybrid integration of GaAs/AlGaAs DBR with an optical resonator based on InAlGaAsP/InP materials. The hybrid integration can be done by the wafer fusion technology, which is applicable for materials based on InP and GaAs. Additionally, the use of buried tunnel junction (BTJ) technology, in the creation of such VCSEL, allows to effectively ensure current and optical limitation due to the formation of mesa structures and their subsequent regrowing, including the method of molecular beam epitaxy (MBE). In VCSEL, the efficiency of overlapping the active region, which amplifies light, is reduced by a standing light wave in the cavity compared to edge lasers. This leads to an increase in the densities of threshold currents, at which the saturation effect of optical amplification is already observed in quantum wells. The increasing of the gain is possible when using several quantum wells (QW), or when using a short-period superlattice (SL) consisting of 20-30 pairs of thin layers, which allows the most efficient use of cavity space to amplify light due to the formation of a miniband. The miniband increases the width of the effective part of the active area by increasing the overlap of a standing light wave with an active region that amplifies light [2]. This paper presents the results of the study of 1550-nm edge-emitters and 1300-nm wafer-fused VCSEL based on SL active region and study of InGaAs/GaAsN SL enable for the creation of 1300-nm monolithic vertical-cavity surface-emitting lasers.

## 2. Experiment

Edge-emitters and VCSELs heterostructures were grown at Connector Optics LLC using molecular-beam epitaxy Riber49 setup. For 1300 nm VCSELs the active region was a 24-period superlattice $In_{0.57}Ga_{0.43}As$ (0.8nm)/$In_{0.53}Al_{0.27}Ga_{0.20}As$(2.0nm) on InP substrate. Distributed Bragg reflectors were grown on GaAs substrates and made of 35.5 and 21 pairs of $Al_{0.91}Ga_{0.09}$ As/GaAs quarter-wave layers for the bottom and top DBR, respectively. Double wafer fusion of the active region with the top DBR and the bottom DBR was carried out on an EVG 510 bonding machine under high vacuum conditions at a temperature of 600°C at JSC OKB-Planeta. Heterostructures with an InAs/GaAsN superlattice on a GaAs substrate were grown at Alferov University using plasma assisted molecular-beam epitaxy Veeco GenIII setup. TEM studies were conducted at the Ioffe Institute on a transmission electron microscope JEM 2100F JEOL, at an accelerating voltage of 200 kV.

## 3. Results and discussions

The effect of gain saturation was investigated in 1550-nm InGaAs/InAlAs/InP edge-emitting lasers. The lasers with active region based on 7-10 QW and 29 periods InGaAs/InGaAlAs superlattice were under investigation. Figure 1 shows the optical gain-current density characteristics of 1550-nm InGaAs/InAlAs/InP edge-emitting lasers with QW and SL. Figure 2 shows optical amplification derivative by injection current density. One can see, that the lasers with 29 periods superlattice shown lowest transparency current density and gain characteristics comparable with 10 QW sample. Thus, one can try to replace the QW VCSEL active region by superlattice. The results of the study of 1300-nm VCSELs with an active region based on superlattice shows below.

The 1300-nm wafer-fused VCSELs with an active region based on InGaAs/InGaAlAs superlattice demonstrate extremally higher output optical power and low threshold current. The current-voltage and current - output optical power (LIV) characteristics of the studied

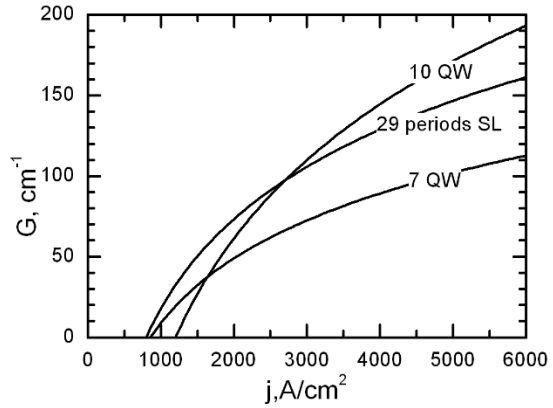


***Fig. 1.*** *Gain-current density characteristics of 1550-nm InGaAs/InAlAs/InP edge-emitting lasers with an active region based on 7-10 QW and 29 periods InGaAs/InGaAlAs superlattice.*

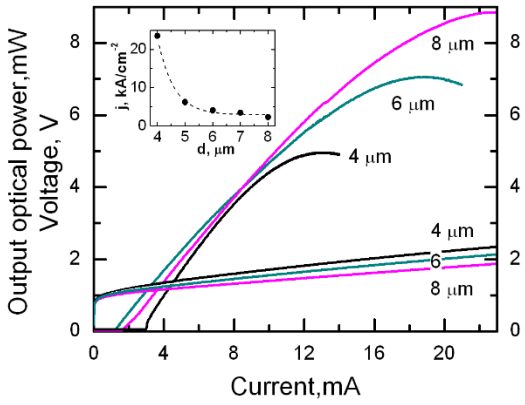


***Fig. 3.*** *LIV characteristics of the 4–8 μm BTJ 1300-nm wafer-fused VCSEL with an active region based on InGaAs/InGaAlAs superlattice. The insertion shows the dependence of the BTJ size on the threshold current density.*

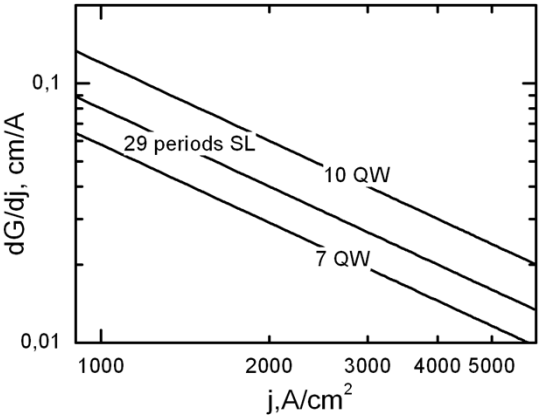


***Fig. 2.*** *Optical amplification derivative by injection current density1550-nm InGaAs/InAlAs/InP edge-emitting lasers with an active region based on QW and superlattice.*

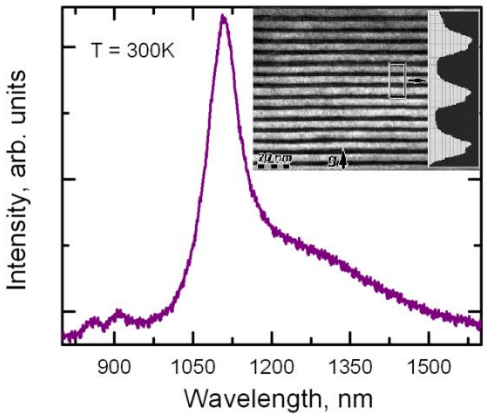


***Fig. 4.*** *Photoluminescence spectra (300K) and TEM image of sample with InAs/GaAs$_{0.979}$N$_{0.021}$ super lattice matched to GaAs. There is a red shift of the peak position with increasing of temperature.*

VCSELs with different diameters of the BTJ at temperatures of 20°C are shown in Figure 3. The maximum output optical power increases with an increase in the BTJ diameter and reaches a value of 8.8 mW at 20°C for the 8 μm BTJ devices. 6 μm BTJ devices demonstrate the minimum threshold current. The insertion in Figure 3 shows the dependence of the BTJ size on the VCSEL threshold current density. The threshold current density increases with decrease of BTJ diameter. VCSELs with a 4 μm BTJ diameter have the highest threshold currents, more than 20 kA/cm$^2$.

In order to investigate the possibility of creating a monolithic VCSEL heterostructure with an active region based on an InAs/GaAsN superlattice on a GaAs substrate we have grown the series of samples containing superlattices consisting of alternating layers of InAs and GaAsN. All samples were grown by the plasma assisted MBE. The insertion in Figure 4 shows the sample TEM dark-field image under two-beam conditions with an active reflection vector g=(002), the contrast of which reflects changes in chemical composition. The insert shows the intensity profile of the image. It can be seen that there are no extended defects in the crystal. In the sample annealing process at 700°C interdiffusion occurs between the InAs and GaAsN layers and InAs(0.3nm)/GaAsN(7nm) heterostructure converts to a InGaAsN(2.1)/GaAsN(5.2 nm) heterostructure.

The photoluminescence spectrum of that heterostructure with a superlattice consisting of 54 pairs of alternating layers InAs/GaAsN with a total thickness of 394 nm recorded at room temperature is shown in Figure 4. The sample emits at a wavelength of 1100 nm, with the crystal lattice constant coinciding with GaAs. A further increase in the radiation wavelength to 1300 nm can be achieved by reducing the thickness of the GaAsN layer to 5 nm and increasing the nitrogen concentration therein to 0.03.

## 4. Conclusions

Thus, the possibility of fabrication higher efficiency 1300-nm wafer-fused VCSEL with active region based on InGaAs/InGaAlAs superlattice have been demonstrated. The next step is the fabrication of monolithic 1300-nm VCSEL with active region based on of InAs/GaAsN superlattice.

## Acknowledgements

This work was supported by the Russian Science Foundation, project no. 21-19-00718.

## References

[1] Koyama, F., Journal of Lightwave Technology 24(12) (2006).
[2] Karachinsky, L.Y., et al., Optics and Spectroscopy 127(6) (2019).

Sixth Asian School-Conference on Physics and
Technology of Nanostructured Materials
Vladivostok, Russia, 25 – 29 April, 2022



# Investigation of thermal properties and crystallization kinetics of chalcogenide semiconductors compounds for the phase change memory application

A.V. Babich, A.S.Bozhedomova*, A.A. Sherchenkov, D.D. Glebova
National Research University of Electronic Technology Bld. 1, Shokin Square, Zelenograd, Moscow 124498, Russia

*e-mail: bozhedomova98@gmail.com

**Abstract.** The aim of this work was to investigate thermal properties and crystallization kinetics of the $Ge_2Sb_2Te_5$ thin films for the phase change memory application. The most suitable method for these studies is the differential scanning calorimetry. Based on the data obtained, we considered three phase transitions, and also calculated the heat of melting and heat capacity of the material. Kinetic parameters were determined by the previously developed technique based on the joint application of model-free and model-fitting methods. Using this method, three kinetic parameters were calculated: a model of the reaction of the crystallization process, preexponential factor and activation energy of crystallization. It was found that the initial effective activation energy of crystallization was about 1.8 eV and slightly decreased to about 1.6 eV. Obtained results correlate with the model, according to which crystallization takes place in two stages: nucleation and growth of nuclei.

## 1. Introduction

At present, information technologies are developing rapidly, which requires the development of new information carriers with a large capacity and speed. An important requirement for modern types of drives is non-volatility. One of the most promising new types of storage devices is considered to be phase change memory, which claims to be universal, combining the advantages of non-volatile and high-speed dynamic memories.

The current stage in the development of phase change memory technology is associated with the use of thin film chalcogenides of the Ge-Sb-Te system lying on the quasi-binary line $GeTe$-$Sb_2Te_3$ [1].

The most studied compound is $Ge_2Sb_2Te_5$, which is highly stability at room temperature. However, the crystallization process in $Ge_2Sb_2Te_5$ thin films, which determines operation speed of phase change memory cells, is poorly understood.

In this regard, the purpose of this work was to study the features of the crystallization kinetics for thin films of the $Ge_2Sb_2Te_5$ material.

## 2. Experiment

Thin films were obtained by magnetron deposition of a stoichiometric $Ge_2Sb_2Te_5$ polycrystalline target at room temperature.

The composition of the films was analyzed by Auger spectroscopy (PerkinElmer PHI-660). Structural features of thin films were studied using X-ray phase analysis (Rigaku Smart Lab).

The optimal method for studying thermal properties and crystallization kinetics is the method of differential scanning calorimetry. In this work, we used a differential scanning calorimeter DSC-50 (Shimadzu). In order to be able to estimate the crystallization kinetics, the measurements were carried out at six different heating rates from 2 to 30 °C/min in nitrogen atmosphere. Temperature range of the measurements is from room temperature to 620 °C.

Reaction kinetics was studied by previously developed technique based on joint application of model-free and model-fitting methods. Ozawa-Flynn-Wall model-free and Coats-Redfern model-fitting methods were used [2].

In the cases when some thermal effects are superimposed on each other not allowing to estimate their parameters with high accuracy, we used the decomposition of the peaks by Gaussian distributions.

## 3. Results and discussions

The results of studying the composition of deposited thin films showed that the deposited thin films are close in composition to $Ge_2Sb_2Te_5$.

The deposited films were shown to be amorphous.

Three phase transitions were found on the obtained DSC curves, which correlates with the literature data. n the temperature range 150-190 °C, a crystallization peak is observed. The transition from the metastable cubic phase to the stable hexagonal phase is present in the temperature range 230-250 °C. The temperature of the onset of the melting peak above 600 °C was also determined. We were primarily interested in the crystallization peak.

Using peak processing and mathematical calculations, the conversion (the degree of reacted material), the effective activation energy of crystallization, and the reaction model were obtained.

According to the calculations obtained, it can be noted that at the initial stage of crystallization, the effective activation energy is 1.8 eV and somewhat decreases to 1.6 eV during the reaction, which may indicate that crystallization most likely proceeds in two stages: the first stage nucleation with an effective activation energy of 1.8 eV and the second stage of nucleation growth with an effective activation energy of 1.6 eV.

## 4. Conclusions

Thus, in this work, we investigated the thermal properties and estimated the crystallization kinetics of the $Ge_2Sb_2Te_5$ thin films. In the future, the obtained kinetic parameters can be used to calculate the crystallization time, which will make it possible to estimate the operating time of the final memory device.

## Acknowledgements

This work was supported by a grant from the President of the Russian Federation (project number MK-5457.2021.4).

**References**

[1] A. Yakubov, A. Sherchenkov, A. Babich, J Therm Anal Calorim., (2020) 142.
[2] A. Babich, A. Sherchenkov, S. Kozyukhin, J Therm Anal Calorim., (2017) 127.

# Formation and models of $Mg_2Si$ seed layers on Si with (111), (100), and (110) orientations for $Ca_2Si$ sacrificial epitaxy

S.A. Dotsenko*, K.N. Galkin, E.Yu. Subbotin, O.V. Kropachev, and N.G. Galkin
Institute of Automation and Control Processes FEB RAS , 5 Radio St., Vladivostok 690041, Russia

*e-mail: docenko@iacp.dvo.ru

Calcium semi-silicide ($Ca_2Si$) is a stable semiconductor compound [1] in the silicon-calcium system with a direct band gap according to first-principle theoretical calculations [2,3]. The growth of epitaxial calcium half-silicide films on silicon with different orientations is a non-trivial task, taking into account their different crystal structures. Calcium semi-silicide has an orthorhombic structure [2], while silicon, as is well known, has a cubic structure. To grow $Ca_2Si$ on Si(111), a low-temperature technology was used to form a sacrificial $Mg_2Si$ layer, which was transformed into a thin layer of $Ca_2Si$ in a weak calcium flow [4]. The $Ca_2Si$ seed layer formed in this way was further used for molecular beam epitaxy of a thick $Ca_2Si$ film during the co-deposition of Ca and Si atoms with an optimal ratio. It is of interest to use silicon substrates with different orientations to create sacrificial magnesium silicide layers with their subsequent transformation into thin $Ca_2Si$ seed layers and subsequent formation of $Ca_2Si$ epitaxial films. This issue remained unresolved.

In this paper, we compare the formation of $Mg_2Si$ sacrificial layers on silicon substrates with (111), (100), and (110) orientations according to low energy electron diffraction (LEED) data. Modeling of ordered growth and construction of conjugation models are carried out, which are compared with experimental data.

Magnesium silicide ($Mg_2Si$) films were grown on Si(111), Si(110), and Si(100) substrates in an ultrahigh vacuum (UHV) chamber of an OMICRON Compact setup with a base vacuum of $1\times10^{-10}$ Torr. Mg was deposited using a Knudsen cell consisting of a boron nitride crucible with a heating coil and a tantalum screen with small holes. The deposition rate of Mg for the formation of $Mg_2Si$ was constant and amounted to 0.1 nm/min. The substrate temperature during magnesium deposition was 150°C. After the formation of $Mg_2Si$ two-dimensional layers, LEED patterns were recorded at various electron beam energies from 17 eV to 68 eV.

Reactive epitaxy of magnesium on Si(111)7×7 revealed orienting growth of $Mg_2Si$ with epitaxial relations $Mg_2Si(111)\|Si(111)$, $Mg_2Si[11\bar{2}]\|Si[1\bar{1}0]$, and $Mg_2Si[1\bar{1}0]\|Si[11\bar{2}]$. It has been established that in this case, the reconstruction of $Mg_2Si(111)$"1×8" is observed on the surface. The best matching of the $Mg_2Si$ and Si lattices on the Si(111) surface is achieved at the $Mg_2Si$ lattice constant a=0.62718 nm. In this case, the $Mg_2Si$ lattice is compressed by 1.9% compared to the relaxed lattice (a=0.6391 nm). The model LEED image constructed for this value for the surface reconstruction of $Mg_2Si(111)$"1×8" is in good agreement with the LEED image from the $Mg_2Si$ film.

Reactive epitaxy of magnesium on Si(001) revealed oriented growth of $Mg_2Si$ with epitaxial relations $Mg_2Si(111)\|Si(001)$, $Mg_2Si[11\bar{2}]\|Si[010]$, and $Mg_2Si[1\bar{1}0]\|Si[100]$. The best matching of the $Mg_2Si$ and Si lattices on the Si(001) surface is achieved at the $Mg_2Si$ lattice constant a=0.665 nm. In this case, $Mg_2Si[11\bar{2}]=2\times Si[010]$, and the length $4\times Mg_2Si[1\bar{1}0]$ is less than the length $7\times Si[100]$ by 1.03%, while the $Mg_2Si$ lattice is stretched by 4.05% compared to the relaxed lattice. Using epitaxial relations, a model of a 2D $Mg_2Si$ cell on Si(001) was constructed taking into account the $Mg_2Si$ lattice constant stretched by 4.05%, which is in good agreement with the experimental data.

On the LEED image from the $Mg_2Si$ film grown on the Si(110) surface, instead of the point reflections that were on the Si(001) surface, dashes and arcs are visible located at the vertices of two hexagons rotated by 90° relative to each other. The presence of hexagonal symmetry in the LEED image from the $Mg_2Si$ film means that in this case we are also dealing with the $Mg_2Si(111)$ surface. Two types of epitaxial grains were found in the $Mg_2Si$ film. For type 1 $Mg_2Si$ grains on Si(110), the following epitaxial relations hold: $Mg_2Si(111)\|Si(110)$, $Mg_2Si[11\bar{2}]\|Si[1\bar{1}0]$, and $Mg_2Si[1\bar{1}0]\|Si[001]$. The best lattice matching of type 1 $Mg_2Si$ grains and Si grains on the Si(110) surface is achieved at the $Mg_2Si$ lattice constant a=0.62718 nm. Since in this case $Mg_2Si[11\bar{2}] \sim 2\times Si[1\bar{1}0]$, and the length of $3\times Mg_2Si[1\bar{1}0]$ is less than the length of $5\times Si[001]$ by 1.99%. For type 2 $Mg_2Si$ grains on Si(110), the following epitaxial relations hold: $Mg_2Si(111)\|Si(110)$, $Mg_2Si[11\bar{2}]\|Si[00\bar{1}]$ and $Mg_2Si[1\bar{1}0]\|Si[1\bar{1}0]$. The best lattice matching of $Mg_2Si$ grains of the 2nd type and Si on the Si(110) surface is achieved at the $Mg_2Si$ lattice constant a=0.665 nm, since in this case $Mg_2Si[11\bar{2}]=3\times Si[00\bar{1}]$ (i.e., good the $Mg_2Si$ and Si lattices agree), and the length $4\times Mg_2Si[1\bar{1}0]$ is less than the length $5\times Si[1\bar{1}0]$ by 2.03%. Crystal lattices are constructed for both types of grains and compared with the experimental ones. Correspondence with the experimental picture of LEED has been obtained.

**Acknowledgements**

This work was financially supported by the RFBR grant - BRFFR No. 20-52-00001_Bel_a.

**References**

[1] H. Tatsuoka, et.al. Thin Solid Films **461**(2004)57.
[2] D.B. Migas, L. Miglio, et.al. Phys. Rev. B **67**(2003)205203.
[3] S. Lebegue, B. Arnaud, M. Alouani. Phys. Rev. B **72**(2005) 085103.
[4] N.G. Galkin, K.N. Galkin, S.A. Dotsenko, S.A. Pyachin, I.A. Astapov. Mat. Sci. in Sem. Proc. **113**(2020)105036.

Sixth Asian School-Conference on Physics and
Technology of Nanostructured Materials
Vladivostok, Russia, 25 – 29 April, 2022



# Chaotic potential of charged dislocations in III-nitride heterojunctions at high temperatures

V.B. Bondarenko[1], A.V. Filimonov[*,1], E.Yu. Koroleva[2], Ravi Kumar[3]

[1] Peter the Great St. Petersburg Polytechnic University, 195251, Polytechnicheskaya 29, St. Petersburg, Russia
[2]Ioffe Institute, 194021 Saint-Petersburg, Russia
[3] Indian Institute of Technology-Madras (IIT Madras), Chennai, 600036, India

*e-mail: filimonov@rphf.spbstu.ru

**Abstract.** The paper investigates the high-temperature structure of the chaotic potential in heterojunctions of Group III nitrides, induced by the electrostatic field of charged dislocations. The amplitude of the chaotic potential in the junction plane was found taking into account the spatial dispersion of the dielectric response of two-dimensional electron gas. We have uncovered the dependence of the chaotic potential parameters on the parameters of the system. If two-dimensional non-degenerate gas is present in III-nitride heterojunctions, with the dislocation densities up to and over $10^{10}$ cm$^{-2}$, the magnitude of the chaotic potential amplitude exceeds that of the thermal energy.

## 1. Introduction

Heterojunctions based on nitrides of Group III elements (Al, Ga, In) are finding increasing applications in solid-state devices used as high-power microwave sources. While these systems offer a number of obvious advantages over the structures based on $A^{III}B^{V}$ compounds, certain drawbacks remain due to the specifics of the synthesis technology, affecting, for example, the parameters of high-electron-mobility transistors (HEMT). The parameter fluctuations detected for the devices are likely due to the initial defects in the materials and heterointerfaces forming. Lattice mismatch in III-nitrides and substrates used is known to generate initial misfit/threading dislocations, turning out to be electrically charged in many cases. Electron scattering by charged dislocations in the 2D channel of the HEMT produces a certain decrease in electron mobility. The chaotic potential causes tails to appear in the density of electronic states, with part of the carriers localized to the conducting channel in HEMT. The goal of this study consisted in determining the parameters of the chaotic potential of charged dislocations in heterojunctions of nitride semiconductor compounds at high temperatures.

## 2. Charged dislocation field

To be definite, we consider an indium-containing structure, InAlN/GaN, remaining stable at record high temperatures up to 1000 °C. Misfit dislocations with the surface density $N_{\text{disl}}$ are represented by linear defects that are normally oriented to the junction plane. If the spatial arrangement of these extended defects is uncorrelated, their number follows a Poisson distribution with the parameter $\langle N\rangle = N_{\text{disl}}S$ determining the mean number of these defects in the near-junction region with an area $S$. Since the channel layer is formed from undoped (or compensated) GaN, the space charge in the near-junction region with band bending is generated primarily by charged dislocations. These extended defects within the space charge region can be assumed to be uniformly charged at large band bending, with a certain linear density taking the maximum value λ. If a delocalized surface charge is present in the heterojunction, the electrostatic image method can be used at a high density of surface states $D_s$ (over $10^{14}$ cm$^{-2}$eV$^{-1}$) to establish the parameters of a chaotic field. We determine the field of an arbitrarily chosen dislocation in a cylindrical coordinate system, where ρ is the radial coordinate measuring the distance from the dislocation in the junction plane. The magnitude of the field strength for a charged dislocation is obtained by a simple calculation in the form

$$F_i(\rho) = \frac{2\lambda}{\varepsilon}\left(\frac{1}{\rho} - \frac{1}{\sqrt{\rho^2 + L_0^2}}\right) \quad (1)$$

Here ε is the dielectric constant of the medium where the $i$th dislocation is located, $L_0$ is the width of the space charge region. Assuming that 2DEG is strongly degenerate, let us now turn to analysis of expression (1), focusing on the nature of the dislocation distribution. The mean value of (1) in an area of radius $R$ is found from the expression

$$\langle F_i \rangle (R) = \frac{4\lambda}{\varepsilon R^2}\left(R - \sqrt{R^2 + L_0^2} + L_0\right) \quad (2)$$

As a matter of fact, Eq. (2) determines the mean contribution of one charged dislocation to the field strength. Considering the distribution of charged dislocations, we can also represent the mean fluctuations in their number in the corresponding surface region with an area $S = \pi R^2$ in the form

$$\delta N(R) = R\sqrt{\pi N_{\text{disl}}} \quad (3)$$

The product of (2) by (3) gives an estimate for the characteristic scale of the inhomogeneities in the surface field strength. The resulting function (4) is monotonically decreasing, reaching its maximum at $R << L_0$.

$$\delta F(R) = \frac{4\lambda}{\varepsilon R}\sqrt{\pi N_{\text{disl}}}\left(R - \sqrt{R^2 + L_0^2} + L_0\right) \quad (4)$$

Calculating the exact upper bound of this expression (in the limit $R \to 0$), we obtain the amplitude of the chaotic field:

$$\delta F = \frac{4\lambda\sqrt{\pi N_{disl}}}{\varepsilon} \quad (5)$$

These high densities of surface states allow to directly estimate the magnitude of the chaotic potential amplitude in the 2DEG plane. The magnitude of potential inhomogeneities can be found under these conditions in the Thomas–Fermi approximation:

$$\delta\sigma = eD_s \cdot \delta U \quad (6)$$

It is assumed here that the potential perturbation is small in comparison with the mean electron energy in the surface zone, while the variation in the density of states is neglected. Next, taking into account the linear dependence of the surface charge on the field strength $F = 4\pi\sigma/\varepsilon$, as well as expressions (5) and (6), we can relate the quantity $\delta U$ with the parameters of the system:

$$\delta U = \frac{\lambda}{eD_s} \cdot \sqrt{\frac{N_{disl}}{\pi}} \qquad (7)$$

### 3. Case of low density of electron states

The case when the densities of electron states in a heterojunction are relatively low deserves more detailed analysis of the potential fluctuations emerging, using the dielectric response function of the surface subsystem. The potential energy of a surface electron in the field of a charged dislocation without a reaction of the medium takes the form

$$V_i(\rho) = e\lambda \cdot ln\frac{\sqrt{\rho^2 + L_0^2} + \rho}{\rho} \qquad (8)$$

In view of the Fourier–Bessel transformation (8) in the space of wave vectors $q$, we have

$$V_i(q) = \frac{e\lambda}{q^2} \cdot \left[1 - exp(-qL_0)\right] \qquad (9)$$

The dielectric response function has the following form in the high-temperature region (i.e., for classical statistics of two-dimensional electron gas):

$$\varepsilon(q) = \frac{\varepsilon_1 + \varepsilon_2}{2} \cdot \left(1 + \frac{q_s(q)}{q}\right) \qquad (10)$$

Here $\varepsilon_1$ and $\varepsilon_2$ are the dielectric constants of contacting semiconductors, $q_s(q)$ is the screening parameter in a two-dimensional electronic system. The relation $q << q_s$ also holds true with large band bends for most of the harmonics; in this case, the dielectric response function (10) can be approximately represented as:

$$\varepsilon(q) \approx \frac{2\pi e^2 n_s}{kT \cdot q} \qquad (11)$$

Using the form of the initial potential (9), the inverse Fourier–Bessel transform, and the expression for the dielectric response of system (11), we obtain the potential electron energy in the surface plane accounting for screening:

$$U_i(\rho) = \frac{\lambda kT}{2\pi e n_s} \cdot \left(\frac{1}{\rho} - \frac{1}{\sqrt{\rho^2 + L_0^2}}\right) \qquad (12)$$

The functional dependence on the radial coordinate in (12) coincides with a similar dependence in (1), allowing to repeat the previous calculation algorithm for directly finding the amplitude of the chaotic potential:

$$\delta U = \frac{\lambda kT}{en_s} \cdot \sqrt{\frac{N_{disl}}{\pi}} \qquad (13)$$

The resulting expression may not be final, requiring in some cases to additionally find the 2DEG density in terms of the chaotic potential parameters, i.e., to establish the functional dependency $n_s = n_s(\delta U)$.

The corresponding density of electron states $D(E)$ can be obtained for a specific form of the potential energy distribution for a surface electron, characterized by the probability density $p(U)$. Since the density of surface states is initially constant if dispersion follows a parabolic law, this density takes the following form in the presence of a chaotic potential:

$$D(E) = D_s \int_{-\infty}^{E} p(U)dU \qquad (14)$$

Calculating the integral in (14) for a Gaussian distribution with the standard deviation parameter equal to $\delta U$ yields the result known from probability theory via the error function:

$$D(E) = \frac{D_s}{2} \cdot \left[1 + erf\left(\frac{E}{\delta U\sqrt{2}}\right)\right] \qquad (15)$$

The density of 2DEG in the junction is determined by integration over all occupied states:

$$n_s = \int_{-\infty}^{+\infty} D(E)\, f(E)dE \qquad (16)$$

The Boltzmann distribution law $f(E) \approx exp[\mu - E)/kT]$ should be chosen here for the high-temperature limit, where $\mu$ is the chemical potential measured from the bottom of the unperturbed surface band of electron states. In view of the form that perturbed density (15) takes, we obtain from expression (16):

$$n_s = D_s kT \cdot exp\left[\frac{\mu}{kT} + \frac{1}{2}\left(\frac{\delta U}{kT}\right)^2\right] \qquad (17)$$

Thus, to determine the magnitude of the chaotic potential amplitude, we should solve the transcendental equation obtained by substituting (17) into (13):

$$\delta U = \frac{\lambda}{eD_s} \cdot \sqrt{\frac{N_{disl}}{\pi}} \cdot exp\left[-\frac{\mu}{kT} - \frac{1}{2}\left(\frac{\delta U}{kT}\right)^2\right]. \qquad (18)$$

### 4. Conclusions

Summarizing the analysis carried out, we should note that the expression for the characteristic values of surface potential inhomogeneity at high temperatures (13) could be obtained from Eq. (7) by substituting the density of states $D_s$ with the ratio $n_s/kT$. Estimating the values that $\delta U$ takes for the chaotic potential parameters in heterojunctions based on III-nitrides, we adopt the effective electron mass in the surface zone $m^* \approx 0.2m$ ($m$ is the electron rest mass) and the corresponding unperturbed density of surface states $D_s \approx 10^{14}$ cm$^{-2}$eV$^{-1}$. Then, assuming that the dislocation density at the interface is of the order of $10^{10}$ cm$^{-2}$, carrying the maximum charge per unit length of about 0.01 ESU, $\delta U$ values in non-degenerate 2DEG exceed the thermal energies $kT$ in a wide range of negative values of the chemical potential (or electrochemical potential, if a blocking voltage is applied to the transistor gate). The chaotic potential amplitude can reach over 100 meV in HEMP operating modes close to the cutoff, even at significantly lower dislocation densities. The corresponding 2DEG densities decrease from the initial levels (about $10^{13}$ cm$^{-2}$) by one or two orders of magnitude.

Sixth Asian School-Conference on Physics and
Technology of Nanostructured Materials
Vladivostok, Russia, 25 – 29 April, 2022



# Formation of thin films of $Mg_2Si$ on Si (111) and investigation of their electronic properties

D.V. Fomin*[,1], I.A. Astapov[2], A.V. Polykov[1]

[1] Amur State University, Ignatievskoe shosse, 21, Blagoveshchensk, 675027, Russia
[2] Kosygin Institute of Tectonics and Geophysics, FEB RAS, Khabarovsk, 680000, Russia

*e-mail: e-office@yandex.ru

**Abstract.** Under ultrahigh vacuum conditions, two samples were formed by the SPE method on Si(111) substrates: the first by co-deposition of Si and Mg at room temperature, and the second by layer-by-layer deposition of Si and Mg at a substrate temperature of 195 °C. The Si and Mg deposition process was controlled in-situ by Auger electron spectroscopy (AES) method. By the X-ray Phase Analysis method, after the formation of films, it was found that Mg is part of the film of only the second sample, while it has changed lattice parameters.

## 1. Introduction

The study of magnesium silicide in its bulk state made it possible to establish that this silicide is a narrow-band semiconductor with band gap values in the range of 0.6-0.8 eV, having photoconductivity, which allows $Mg_2Si$ to be considered as a promising material for optoelectronics [1]. A study of its photovoltaic properties has shown that the photoresponse is observed up to wavelengths of 1800-2100 nm [2], and the photosensitivity at 1310 nm reaches several tens of mA/W with a small reverse bias [3]. The use of $Mg_2Si$ is no less attractive when creating thermoelectric converters [4].

In the laboratory of surface physics of the Scientific and Educational center of AmSU, $Mg_2Si$ films are grown by solid-phase epitaxy in the Varian ultrahigh vacuum chamber (UHV) of the PHI-590 device with a base pressure of $1.3*10^{-7}$ Pa, equipped with a two-span energy analyzer of the "cylindrical mirror" type. This laboratory already has experience in the formation of thin films of silicides on silicon [5-6].

## 2. Experiment

The silicon substrate for the samples was cut from an industrial KEF–100 Si (111) n-type conductivity wafer with a resistivity from 2 to 15 Ω*cm. The source of magnesium (Mg) was Mg chips with a purity of 99.999%, placed in a tantalum tube with a puncture.

Si (111) substrates were subjected to RCA cleaning before loading into the chamber, and after loading, they were heated at T = 600°C for 1 hour and at T= 1250°C for 3 seconds 3 times with intervals of 10 minutes.

The deposition rate of Mg and Si was measured using a quartz sensor in the UHV chamber connected to a Sycon Instruments device, the rate was 4 nm/min for Mg and 0.24 nm/min for Si when deposited on the first sample; 2.6 nm/min for Mg and 0.35 nm/min for Si when deposited on the second sample.

All samples were formed by the SPE method. The temperature of the substrates was different: for the first sample – room temperature, and for the second - T=195°C.

The first step was to form a buffer layer of silicon with a thickness of 60 mm on both Si (111) substrates.

Further, the experiment was carried out in different ways for each sample. For the first sample, a 1.5 nm thick Mg seed layer was deposited on the silicon buffer layer and then Mg and Si were co-deposited with a velocity ratio of 16:1. For the second sample, layers of magnesium and silicon with a thickness of 15 and 5 nm were alternately deposited on the buffer layer, respectively. The deposition of these layers was repeated three times. As a result, a thin film with a thickness of 100 nm was formed for the first sample, and 60 nm for the second.

## 3. Results and discussions

Control over the formation of films was carried out *in situ* by Auger electron spectroscopy (AES) and electron energy loss spectroscopy (EELS). At the beginning, the formed films were examined by the AES method. The AES spectra obtained at all stages of the formation of the first sample are shown in Figure 1.

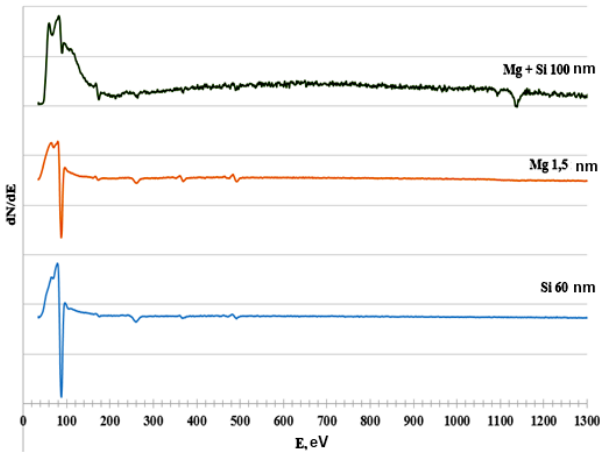


***Fig. 1.*** *Spectra of Auger electrons of the first sample.*

In Figure 1, the AES peak of high intensity with energy of 92 eV belonging to Si is observed. At the stage of co-deposition of Mg and Si (upper spectrum), a peak with energy of 1186 eV is observed, indicating the presence of Mg atoms in the composition of the sample surface. Figure 2 shows the AES spectra obtained at all stages of the formation of the second sample. It also clearly shows a AES peak with energy of 92 eV, corresponding to pure silicon. At the formation stage of the first magnesium layer, the sample has a peak of high intensity at 45 eV and low intensity peak at 92 eV, belonging to Mg and Si, respectively. At the formation stage of the second layer (Si with a thickness of 5 nm), only the AES peak of high intensity at 92 eV belonging to Si is noticeably observed.

At the formation stage of the third layer (Mg with a thickness of 15 nm), one AES peak of high intensity at 45 eV, belonging to Mg, is visible. A similar patterns of Auger electron spectra is preserved for subsequent layers.

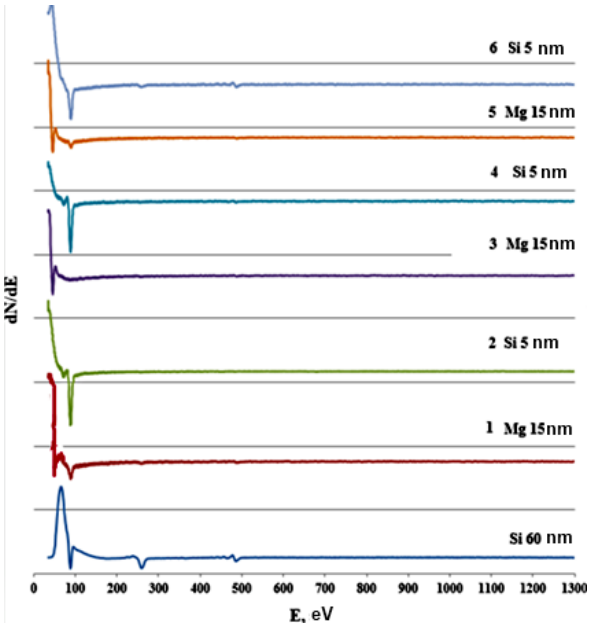


***Fig. 2.*** *Spectra of Auger electrons of the second sample.*

Further, the formed samples, after extraction from the growth chamber, were examined by X-ray phase analysis. The X-ray diffraction patterns (XRD) of the samples are shown in Figures 3 and 4

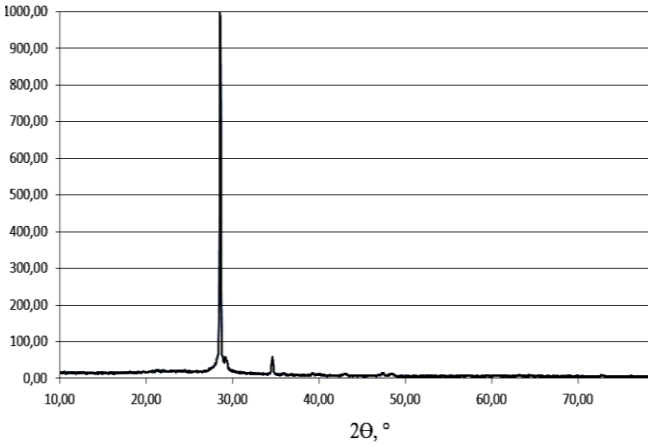


***Fig. 3.*** *Diffractogram of the first sample.*

On the XRD spectra of both samples, the peak of the highest intensity (2Θ=28°, which corresponds to the interplane distance d = 3.12 Å) belongs to the substrate material - Si (111).

Magnesium silicides were not detected in the XRD spectrum of the first sample with known diffraction data ($Mg_2Si$, $Mg_5Si_6$, $Mg_6Si_3$ or $Mg_9Si_5$). In the spectrum of the second sample, in addition to silicon, another reflex was noted (2Θ=35.8°, which corresponds to the interplane distance d = 2.504 Å). This peak does not belong to the $Mg_2Si$ phase. It can be attributed to the $Mg_5Si_6$ compound (with oriented growth along one crystallographic direction), but it is more likely that it is Mg with strained lattice parameters.

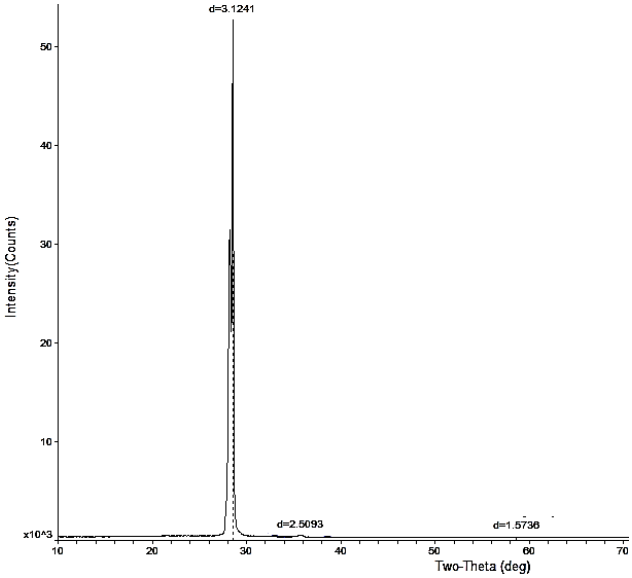


***Fig. 4.*** *Diffractogram of the second sample.*

## 4. Conclusions

Thus, as a result of the growth experiments carried out, two samples were formed by the SPE method: the first by co-deposition of Si and Mg at room temperature, and the second by layer-by-layer deposition of Si and Mg at a substrate temperature of 195°C. The Si and Mg deposition process was controlled in-situ by AES and EELS methods. By the X-ray Phase Analysis method, after the formation of films, it was found that Mg is part of the film of only the second sample, while it has changed lattice parameters.

## References

[1] J. E. Mahan, A.Vantomme, and G. Langouche. Physical Review B **54**(1996)16 965.
[2] H.Udono, Y.Yamanaka, M.Uchikoshi, M. Isshiki. J. Phys. Chem. Solids **74**(2013)311.
[3] T Akiyama, N.Hori, S. Tanigawa, D.Tsuya, H.Udono. JJAP Conf. Proc. **5**(2017)011102.
[4] V.K. Zaitsev, M.I. Fedoro , E.A.Gurieva, I.S. Eremin, P.P. Konstantinov, A.Y. Samunin, M.V. Vedernikov. Thin Solid Phys. Rev. B **74**(2006)045207.
[5] N.G. Galkin, D.V. Fomin, V.L. Dubov, S.A. Pyachin, A.A. Burkov. Defect and Diffusion Forum **386**(2018)48.
[6] D.L. Goroshko, N.G. Galkin, D.V.Fomin, A.S. Gouralnik, S.V. Vavanova. Journal of Physics Condensed Matter **21**(2009)435801.

# The electronic structure and optical properties of $Ca_2Si$ films grown on silicon different oriented substrates and calculated from first principles

K.N. Galkin*[,1], O.V. Kropachev[1], A.M. Maslov[1], I.M. Chernev[1], E.Yu. Subbotin[1], N.G. Galkin[1], A.Yu. Alekseev[2] and D.B. Migas[2]

[1] Institute of Automation and Control Processes FEB RAS , 5 Radio St., Vladivostok 690041, Russia
[2] Belarusian State University of Informatics and Radioelectronics, 6 P. Browka St., 220013 Minsk, Belarus

*e-mail: galkinkn@iacp.dvo.ru

In the calcium-silicon system, at least six silicides are formed [1], including calcium semi-silicide ($Ca_2Si$), which has semiconductor properties [2]. Since calcium silicides are formed from environmentally friendly and widely distributed elements in the Earth's crust, they are of considerable interest for silicon electronics and optoelectronics. $Ca_2Si$, the most well-known and obtained in the form of films, has been mainly studied on silicon with the (111) orientation [3], while studies of its structure and optical properties on other surfaces (Si(100) and Si(110)) have not yet been carried out.

This work is devoted to approbation of two methods for growing $Ca_2Si$ on silicon with orientations (111), (100), and (110) by molecular beam epitaxy (MBE) using a sacrificial $Mg_2Si$ layer. The electronic structure and optical properties of the grown films were studied and compared with the data of first-principles calculations of the optical functions of $Ca_2Si$ from its electronic structure.

The growth of $Ca_2Si$ films was carried out in an ultrahigh vacuum (UHV) chamber of an OMICRON Compact setup with a base vacuum of $1\times10^{-10}$ Torr, equipped with a LEED and AES/EELS analyzer, a block of silicon (Si) and calcium (Ca) molecular beam sources for Ca deposition, Mg and Si on silicon substrates. $Ca_2Si$ films were grown on all substrates by co-deposition of Si and Ca at a temperature of 250°C on a preliminarily formed $Mg_2Si$ sacrificial layer, which was transformed into $Ca_2Si$ upon deposition of Ca atoms on the substrate at 250°C. The deposition rates (Ca, Mg, and Si) were calibrated using a quartz thickness sensor.

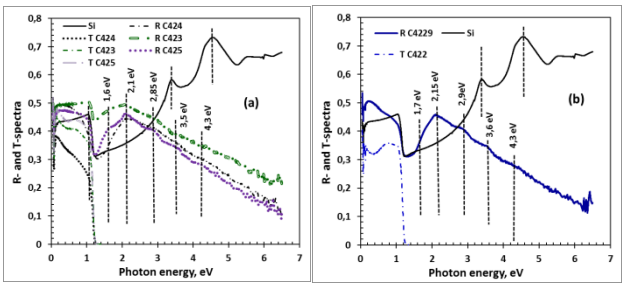


***Fig. 1.*** *Reflectance and transmittance spectra of $Ca_2Si$ films on Si(111) (a) and Si(110) (b) substrates.*

The reflectance (R) and transmittance (T) spectra of the grown $Ca_2Si$ samples (Fig. 1) were recorded within one day after unloading at room temperature in the photon energy range of 0.05–6.20 eV on a Hitachi U-3010 spectrophotometer and a Bruker Fourier spectrometer Vertex 80v. The calculations of the electronic band structure and optical functions were also performed using the FLAPW method in its scalar-relativistic version using the WIEN2k package [4].

The main features for the selected samples with $Ca_2Si$ films were transparency in the photon energy range of 0.05 – 1.2 eV. Comparison with the data of theoretical reflection spectra for three planes of $Ca_2Si$ single crystals shows a good agreement in terms of peaks in $Ca_2Si$, which corresponds to the main interband transitions in $Ca_2Si$ single crystals. Calculations from the R- and T-spectra of the absorption coefficients ($\alpha$) for the grown films showed for $Ca_2Si$ the existence of a direct interband transition at 1.07 eV. The absorption edge, according to the calculation data, is at an energy of about 0.72 - 0.82 eV, depending on the polarization of the incident radiation. The strongest interband transition begins at energy of about 1.2 eV [5]. High-energy interband transitions in $Ca_2Si$ films, determined from the reflection spectra (Fig. 1) in the energy range 1.6 – 6.5 eV, satisfactorily agree with the data in the reflection spectra calculated from the band structure: 1.8 eV, 2.0 eV, 2.8 eV and 3.8-4.2 eV.

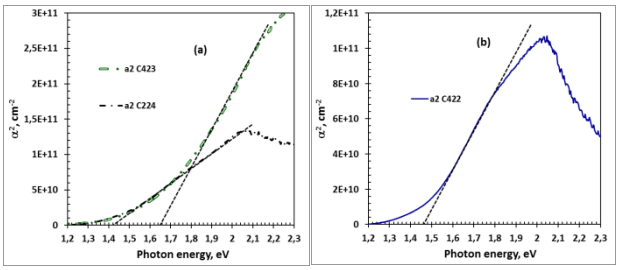


***Fig. 2.*** *Dependence of the square of the absorption coefficient on the photon energy. The dashed lines indicate a strong direct interband transition to $Ca_2Si$.*

Calculations from the reflection spectra by the Kramers-Kronig method showed the presence in $Ca_2Si$ films on silicon of strong direct interband transitions with energies of 1.42 - 1.47 eV and 1.65 eV, depending on the presence of an additional phase, for example, CaSi.

## Acknowledgements

This work was financially supported by the RFBR grant - BRFFR No. 20-52-00001_Bel_a.

## References

[1] P. Manfrinetti, et.al. Intermetallics. **8**(2000)223.
[2] S. Lebegue, et.al. Phys. Rev. B **72**(2005)085103.
[3] N.G. Galkin, et.al. Mat. Sci. in Sem. Proc. **113**(2020)105036.
[4] P. Blaha, et.al. (Karlheinz Schwarz, Tech. Universität Wien, Vienna, 2001).
[5] D.B. Migas, et.al. Jpn. J. Appl. Phys. **54**(2015)07JA03.

Sixth Asian School-Conference on Physics and
Technology of Nanostructured Materials
Vladivostok, Russia, April 25 - 29, 2022



# Comparison of the crystal structure and electronic interband transitions of $Ca_2Si$ thin semiconductor films on $Al_2O_3$(0001) and Si(111) substrates

N.G. Galkin*, K.N. Galkin, O.V. Kropachev, I.M. Chernev, D.L. Goroshko, E.Yu. Subbotin and S.A. Dotsenko

Institute of Automation and Control Processes FEB RAS , 5 Radio St., Vladivostok 690041, Russia

*e-mail: galkin@iacp.dvo.ru

Calcium silicides form six compounds $Ca_2Si$, CaSi, $Ca_5Si_3$, $Ca_3Si_4$, $Ca_{14}Si_{19}$ and $CaSi_2$ [1]) with different crystal structure and composition and have a wide range of properties from semiconductor [2] to semimetallic [3]. Semiconductor silicides with different band gaps include ($Ca_2Si$, $Ca_3Si_4$, $Ca_5Si_3$ and $Ca_{14}Si_{19}$) [2,3], among which $Ca_2Si$ is currently attracting the main attention [4]. According to ab initio theoretical calculations, $Ca_2Si$ is a direct-gap semiconductor with a band gap from 0.30 - 0.36 eV [5] to 1.02 eV [6]. However, the direct band structure has not yet been confirmed by experimental data. Semiconductor epitaxial $Ca_2Si$ films on a Si(111) substrate have recently been grown through the formation of a two-dimensional sacrificial $Mg_2Si$ layer [7-19, 20] and its transformation into $Ca_2Si$, followed by growth to thick $Ca_2Si$ films by molecular beam epitaxy at 250°C [8]. For grown thick epitaxial $Ca_2Si$ films, the first direct interband transition was determined at energy of 1.095 eV, which, however, is not fundamental due to the high density of defect states at 0.5–1.0 eV. To establish the nature of the fundamental interband transition in $Ca_2Si$ films at photon energies below 1.0 eV, it is necessary to grow them on a transparent substrate, for example, sapphire ($Al_2O_3$(0001)).

In this work, we tested an original technique for growing $Ca_2Si$ epitaxial films on sapphire; we grew $Ca_2Si$ epitaxial films on Si(111) silicon with different ratios of calcium and silicon fluxes. For all $Ca_2Si$ films on sapphire and silicon, the crystal and phonon structures are studied, the optical functions at room temperature are determined, the fundamental interband transition is identified, and the dependences of the main interband transitions in the transparency region of $Ca_2Si$ films on temperature on single-crystal sapphire are studied and analyzed.

The crystal structure of the grown $Ca_2Si$ films was studied by X-ray diffraction. It has been established that one peak from $Ca_2Si$(400) is observed in the sample on sapphire, which refers to the epitaxial ratio $Ca_2Si$(100) // $Al_2O_3$(0001), and for films on silicon, two epitaxial ratios are established: $Ca_2Si$(111)/Si(111) and $Ca_2Si$(110)/Si(111) at a high calcium to silicon deposition rate ratio of 7.69 – 9.26. At lower deposition rate ratios of 4.4–6.5, one epitaxial ratio was found: $Ca_2Si$(111)/Si(111). The identification of Raman peaks for films on both substrates and their comparison with the previously published experimental data for epitaxial $Ca_2Si$ films [8] confirmed the predominant contribution of the $Ca_2Si$ phase to the structure of the grown films and their high crystalline quality.

Recording the transmission and reflection spectra showed that the transparency of the $Ca_2Si$ film on sapphire is observed up to photon energies of about 2.5 eV, while the transparency of $Ca_2Si$ films on silicon is limited by the substrate transparency to 1.2 eV. Calculations of the refractive index (n), extinction coefficient (k) for both types of films, carried out from a two-layer model [9] based on the transmission and reflection spectra of the film-substrate system, and then the absorption coefficient and its square showed the following results. In $Ca_2Si$ films on sapphire, a fundamental direct interband transition was detected at an energy of $E_g$=0.88±0.01 eV. The second direct interband transition is observed at an energy of $E_2$=1.16±0.01 eV, and the third direct interband transition is observed at an energy of $E_3$=1.49±0.01 eV. For $Ca_2Si$ films on Si(111), extrapolation of the linear portions of the dependence of the square of the absorption coefficient on the photon energy gave a certain spread in the values of the direct interband transition from 1.08 eV to 1.10 eV, which does not coincide with the data for $E_2$ = 1.16 ± 0.01 eV in $Ca_2Si$ films on sapphire in terms of due to the underestimation of the interband transition energy in $Ca_2Si$ due to strong absorption in silicon at photon energies above 1.2 eV. At photon energies of 0.7–0.9 eV, in $Ca_2Si$ films on Si(111), as well as in $Ca_2Si$ films on $Al_2O_3$(0001), there should be a fundamental transition, which is difficult to identify due to high absorption at defect levels (Urbach edge [10]) and light scattering on the roughness of the film and the film-substrate interface, which are not taken into account within the framework of the ideal two-layer model [9].

**Acknowledgements**

This work was financially supported by the RFBR grant - BRFFR No. 20-52-00001_Bel_a.

**References**

[1] P. Manfrietti, M.L. Fornasini, A. Palenzona, Intermetallics **8**(2000)223.
[2] S. Lebegue, Phys. Rev. B. **72**(2005)085103.
[3] O. Bisi, L. Braikovich, et.al. Phys. Rev. B. **40**(1989)10194.
[4] C. Wen, T. Nonomura, et.al. Physics Procedia **11**(2011)106.
[5] D.B. Migas, et.al. Jpn. J. Appl. Phys. **54**(2015)07JA03.
[6] S. Lebegue, et.al. Phys. Rev. B **72**(2005)085103.
[7] S.A. Dotsenko, et.al. Physics Procedia **11**(2011)95.
[8] N.G. Galkin, K.N. Galkin, S.A. Dotsenko, et.al. Mat. Sci. Sem. Proc., **113**(2020)105036.
[9] N.G. Galkin, A.M. Maslov and A.V. Konchenko, Thin Solid Films **311**(1997)230.
[10] J.I. Pankov, (Dover Books on Physics), 2nd Revised ed. edition (November 18, 2010), New York, p. 448.

Sixth Asian School-Conference on Physics and
Technology of Nanostructured Materials
Vladivostok, Russia, April 25 - 29, 2022



# Formation, structure and photoelectric properties of $Ca_2Si$/Si-n and $Ca_2Si$/Si-p diode structures

D.L. Goroshko*, K.N. Galkin, I.M. Chernev, O.V. Kropachev, A.B. Cherepakhin and N.G. Galkin
Institute of Automation and Control Processes FEB RAS , 5 Radio St., Vladivostok 690041, Russia

*e-mail: goroshko@iacp.dvo.ru

It is known that calcium semi-silicide ($Ca_2Si$) is a semiconductor with a band gap from 0.3–0.36 eV [1,2] to 1.02 eV [3] according to theoretical data, and according to optical data, its thin epitaxial films have the first direct interband transition with an energy of about 1.095 eV [4]. In this case, the fundamental transition is masked by absorption at defects in the photon energy range from 0.6 eV to 1.0 eV. An additional way to check the sensitivity of $Ca_2Si$ films is to create diode structures on silicon with various types of conductivity and their photospectral measurements.

To test the photosensitivity of semiconductor $Ca_2Si$, two structures were grown on n- and p-type silicon. $Ca_2Si$ films were formed by the previously developed sacrificial-seed layer method [4]. The film thickness in both samples was 80–100 nm. Device mesa structures with deposited and annealed contacts to the silicide film and silicon were created on one of the parts with dimensions of 5x6 $mm^2$. The contact to the substrate was made directly to the chip package through the silver conductive paste. To control the conductivity and photocurrent in the $Ca_2Si$ film, an aluminum contact was attached to it using ultrasonic welding. A photo of a standard device mesa structure is shown in Fig. 1.

***Fig. 1.*** *Photo of diode structure in the chip package.*

On working diode structures, studies were carried out at room temperature of the current-voltage characteristics (I-V) for C422 samples on a Si-p substrate and a C424 sample (Si-n substrate). On p-type silicon (sample C422), a linear I–V characteristic with a very weak sensitivity to white light was found. This corresponds to the formation of a heterojunction with a low barrier, and the low sensitivity to light is also determined by the small thickness of the $Ca_2Si$ film. On the C424 sample, the I-V(s) were recorded with different top contacts. In the case of using the upper contact to the gold pad (Au) and the rear ohmic contact, non-linear I-V characteristics were observed both without illumination (dark) and with illumination (light). A short circuit current (0.1–0.2 mA) and an open circuit voltage (0.2–0.25 V) were observed. These facts correspond to the formation of the $Ca_2Si$/Si-n heterojunction and the separation of the generated carriers by the heterojunction.

To study the spectral photoresponse, a C424 mesa-diode was chosen, for which photo-emf spectra were recorded at room temperature in the range from 400 to 1300 nm, which are shown in Fig. 2. As a reference, a mesa diode was used, formed on the basis of a silicon wafer with a built-in p-n junction. The characteristics are quite similar. The maximum contribution of the $Ca_2Si$/Si-n heterostructure is observed in the wavelength range of 850 -1200 nm. This is due to the fact that the $Ca_2Si$ film is quite thin (up to 100 nm), so the main generation in it is noticeable only at energies above the band gap in $Ca_2Si$ with strong absorption of radiation with energies of 1–1.45 eV. Taking into account that the fundamental transition in $Ca_2Si$, in accordance with our data on sapphire, begins at 0.88 eV, but the oscillator strength is insignificant, the film thickness should be at least 1 μm for intense absorption. In this case, one can expect a noticeable generation of electron-hole pairs with energies from 0.88 to 1.5 eV and obtain their efficient separation by the $Ca_2Si$/Si-n heterojunction. In the case when the direct contact to the $Ca_2Si$ film through the Al wire is used to record the photocurrent signal, the photocurrent signal is significantly reduced and becomes smaller than in the case of contact to the gold pad. It is assumed that in this case, during ultrasonic compression of the aluminum wire to the $Ca_2Si$ film, the film can be pierced, and in this case, a signal from the Al/Si-n Schottky barrier is recorded.

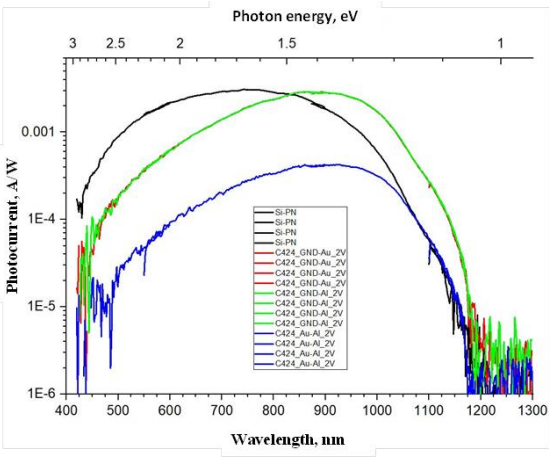


***Fig. 2.*** *Spectral photocurrent dependences of $Ca_2Si$/Si-n and Si-pn diodes.*

## Acknowledgements

This work was financially supported by the RFBR grant - BRFFR No. 20-52-00001_Bel_a.

## References

[1] D.B. Migas, V.O. Bogorodz, A.B. Filonov, et.al. Phys. Rev. B **67**(2003)205203.
[2] J. Hu, A. Kato, T. Sadoh, Y. Maeda, e. Int. J. Mod. Phys. B **24**(2010)4639
[3] S. Lebegue, et.al. Phys. Rev. B **72**(2005)085103.
[4] N.G. Galkin, K.N. Galkin, et.al. Mat. Sci. in Sem. Proc. **113**(2020)105036.

Sixth Asian School-Conference on Physics and
Technology of Nanostructured Materials
Vladivostok, Russia, 25 – 29 April, 2022



# Raman and photoluminescence investigation of temperature stability of germanium nanowires obtained by electrochemical deposition

D.L. Goroshko*[,1], E.A. Chusovitin[1], A.A. Dronov[2], I.M. Gavrilin[2]

[1] Institute of Automation and Control Processes FEB RAS , 5 Radio St., Vladivostok 690041, Russia
[2] National Research University of Electronic Technology, Bld. 1, Shokin Square, Zelenograd, Moscow 124498, Russia

*e-mail: goroshko@iacp.dvo.ru

Germanium nanowires (NWs) obtained by cathodic deposition from aqueous solutions of germanium oxide are a promising material for a new elemental base of electronic devices, since, compared to silicon, it has a higher charge carrier mobility, a smaller band gap, and a lower processing temperature [1]. Also of great interest is the use of Ge NWs in lithium-ion batteries [2, 3]. In addition, they are an interesting example of nanosized structures in which quantum effects associated with size limitation can be observed [4, 5].

The possibility of electrochemical deposition of Ge NW from aqueous solutions using particles of low-melting metals (Ga, In, etc.) at nearly room temperature has been demonstrated [6,7]. In this case, liquid metal nanodroplets have been used as an electrode for reduction of Ge-containing ions at the electrode surface, followed by dissolving and crystallizing the melt at the substrate interface. The growth mechanism, which is known as electrochemical liquid–liquid–solid (ec-LLS) crystal growth, is similar to the vapor–liquid–solid method [6].

It was shown in a series of works [8–10] that successive laser annealing of Ge NWs obtained by this method lead to the recrystallization of samples and the appearance of Ge nanocrystals (NCs) of different sizes from 1.5 to 5 nm, and the behavior of the samples varies greatly depending on the presence or no vacuum annealing. In this paper, we analyze the effect of preliminary vacuum annealing of germanium nanowires obtained by cathodic deposition from aqueous solutions of germanium oxide on the change in their temperature stability.

Electrochemical deposition of Ge NWs was carried out in a three-electrode cell. Fifty micrometer thickness titanium foil was used as the substrate. Indium nanoparticles were deposited on a Ti foil, as described in previous work [8]. The solution contained 0.05 M of germanium (IV) oxide $GeO_2$, 0.5 M of potassium sulfate $K_2SO_4$, and 0.5 M of succinic acid. Deposition was carried out at 0.2 mA×cm$^{-2}$ at a solution temperature of 20 °C. The prepared samples were washed in deionized water and were dried in an argon flow. Some of the obtained samples were annealed at 600 °C in vacuum oven at a residual pressure below $3\times10^{-5}$ Torr for 30 min.

Photoluminescence (PL) measurements and backscattered Raman spectra were registered under excitation with focused laser radiation using a NTEGRA Spectra II micro-Raman spectrometer. We used diode-pumped solid-state laser (wavelength 473 nm, maximal power 50 mW, and minimal spot radius 2 μm) for Raman experiments. Photoluminescence spectra were registered under 405 nm excitation. The laser power was attenuated by means of neutral filters with different optical densities.

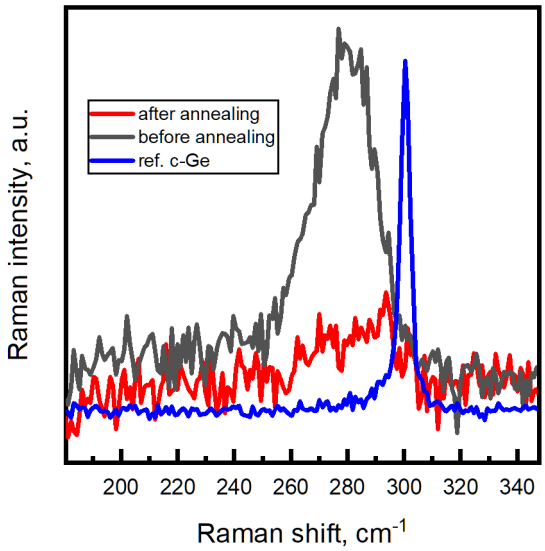


***Fig. 1.*** *Raman spectra registered before and after laser annealing. c-Ge Raman spectrum is scaled to fit the graph.*

Raman (Fig. 1) and PL (Fig. 2) spectra were recorded at the same points of the sample before and after laser annealing. Annealing was performed at a power density of 100 kW/cm$^2$ for 5 s, and control spectra were recorded at 4.4 kW/cm$^2$. This mode of registration of control spectra did not lead to irreversible changes in the sample.

After laser annealing, there is a significant decrease in the intensity of the TO peak and its shift to the high-frequency region at a position of 294.2 cm$^{-1}$, as well as the appearance of a long low-frequency shoulder. For comparison, Figure 1 shows the position of the TO phonon in crystalline germanium.

Estimation of the shift in the position of the Raman peak, taking into account the deformation of the crystal lattice and the heating of the sample under the laser beam relative to the position of the crystalline germanium peak, makes it possible to estimate the size of the Ge nanocrystals (NCs) before and after annealing. As a result, it turned out that in the process of recrystallization under the action of high temperature during laser annealing, the size of the Ge NCs increased from 1.3 to 5 nm. Since such annealing was carried out in ambient conditions, part of the nanocrystals was completely oxidized, which led to a decrease in the intensity of the Raman signal.

In such samples, the effect of size limitation can lead to the appearance of PL in the infrared range (with an energy of the order of the band gap of germanium), since the Bohr radius of a direct-gap exciton in Ge is 20–30 nm (depending

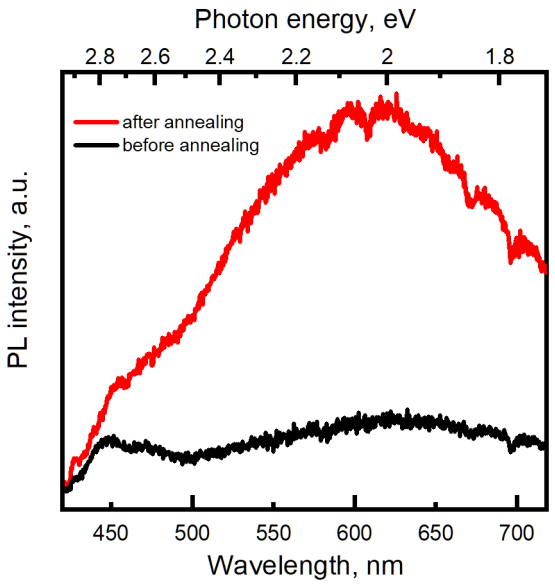


***Fig. 2.*** *Photoluminescence spectra registered before and after laser annealing of sample with germanium nanowires.*

on the conditions and calculation technique [9–10]) and thus can be several times greater than the actually achievable size of a germanium nanocrystal or NW diameter. In this case, the emission of a photon with an energy of 1.3-2.67 eV is expected. The convincing presence of IR PL in Ge nanowires was demonstrated in [11], but, as the authors point out, quantum confinement effects are unlikely to be involved in this, since the NW diameter is 40 nm and exceeds the exciton Bohr radius. The effect of oxidation on the edge PL of Ge NW was studied in [12], where it was shown that the intensity of indirect transitions is unambiguously related to increasing oxidation of the wires and is explained by the passivation of nonradiative recombination centers initially present on the nanowire surface by oxide.

As for PL in the visible and UV ranges, at present, most authors are inclined to believe that its source is the $Ge/GeO_x$ or $GeO_x$ interface states. Similar conclusions are reached by studying freestanding $Ge/GeO_2$ core-shell NCs with varying sizes and shell thicknesses. Strong photoluminescence peaks in the visible and UV region are attributed to $Ge/GeO_2$ interface defect states [13] or Ge–O bonded material, i.e., $GeO_x$s [14].

In our case, we did not register a PL signal from samples with Ge nanowires in the IR wavelength region. This is probably due to the high concentration of indium contained in the samples and the passivation of the $Ge/GeO_2$ interface states, which, as shown above, are the source of PL in the IR range. However, the PL signal was detected in the visible region of the spectrum (Fig. 2).

It is clearly seen that the weak PL of Ge NWs in the initial state increases in intensity by a factor of about 3 after laser annealing. This changes the shape of the spectrum, as well as the position of the maximum. The evolution of the PL spectra shown in Figs. 2 is explained by the transformation of germanium oxide phases in the sample. The synthesis of Ge nanowires took place under oxygen-deficient conditions; therefore, the PL spectrum contains a high-energy peak with a position of 2.77 eV. After laser annealing, the formation of the tetragonal phase of germanium oxide occurs, since annealing took place under ambient conditions in the presence of a sufficient amount of oxygen. As a result, a 2–3-fold increase in the luminescence intensity and the predominance of a peak with an energy of 2.05 eV are observed in the spectrum. Also, after annealing, the spectrum exhibits a well-defined shoulder at an energy of 2.7 eV, which refers to the initial trigonal phase. Its presence is explained by the rather high temperature stability of alpha-$GeO_2$, which, according to [15], transforms into a tetragonal phase at 800–1000 °C.

In turn, vacuum annealing of a sample with Ge NWs at 600 °C significantly affects the result of laser annealing. In this case, the change in the intensity of both the Raman and PL spectra is significantly less, which indicates an increase in the resistance against thermal oxidation. This phenomenon is analyzed and explained taking into account the formation mechanisms of germanium oxides under different conditions and the influence of indium on the oxidation process.

**Acknowledgements**

This research was financially supported by the Russian Science Foundation (Project no. 20-19-00720)

**References**

[1] C. Claeys, E. Simoen, Germanium-Based Technologies: From Materials to Devices, Elsevier, 2011.
[2] S. Liu, J. Feng, X. Bian, Y. Qian, J. Liu, H. Xu, Nano Energy **13** (2015) 651–657.
[3] H. Tian, F. Xin, X. Wang, W. He, W. Han, Journal of Materiomics **1** (2015) 153–169.
[4] M. Bruno, M. Palummo, A. Marini, R. Del Sole, V. Olevano, A.N. Kholod, S. Ossicini, Phys. Rev. B **72** (2005) 153310.
[5] G. Gu, M. Burghard, G.T. Kim, G.S. Düsberg, P.W. Chiu, V. Krstic, S. Roth, W.Q. Han, Journal of Applied Physics **90** (2001) 5747–5751.
[6] E. Fahrenkrug, S. Maldonado, Acc. Chem. Res. **48** (2015) 1881–1890.
[7] I.M. Gavrilin, D.G. Gromov, A.A. Dronov, S.V. Dubkov, R.L. Volkov, A.Yu. Trifonov, N.I. Borgardt, S.A. Gavrilov, Semiconductors **51** (2017) 1067–1071.
[8] A.V. Pavlikov, P.A. Forsh, P.K. Kashkarov, S.A. Gavrilov, A.A. Dronov, I.M. Gavrilin, R.L. Volkov, N.I. Borgardt, S.N. Bokova-Sirosh, E.D. Obraztsova, Journal of Raman Spectroscopy **51** (2020) 596–601.
[9] Y. Maeda, Phys. Rev. B **51** (1995) 1658–1670.
[10] [Y.-H. Kuo, Y.-S. Li, Phys. Rev. B **79** (2009) 245328.
[11] [Y. Kawamura, K.C.Y. Huang, S.V. Thombare, S. Hu, M. Gunji, T. Ishikawa, M.L. Brongersma, K.M. Itoh, P.C. McIntyre, Phys. Rev. B **86** (2012) 035306.
[12] F.S. Minaye Hashemi, S. Thombare, A.F. i Morral, M.L. Brongersma, P.C. McIntyre, Appl. Phys. Lett. **102** (2013) 251122.
[13] P.K. Giri, S. Dhara, Journal of Nanomaterials **2012** (2012) 1–5.
[14] G. Kartopu, S.C. Bayliss, R.E. Hummel, Y. Ekinci, Journal of Applied Physics **95** (2004) 3466–3472.
[15] C.B. Finch, G.W. Clark, American Mineralogist **53** (1968) 1394–1398.

Sixth Asian School-Conference on Physics and
Technology of Nanostructured Materials
Vladivostok, Russia, 25 – 29 April, 2022



# Raman investigation of amorphous and nanocrystalline SiSn alloys

S.A. Kitan'*, S.A. Dotsenko, D.L. Goroshko, K.N. Galkin, E.A. Chusovitin, N.G. Galkin
Institute of Automation and Control Processes FEB RAS , 5 Radio St., Vladivostok 690041, Russia

*e-mail: kitan@iacp.dvo.

**Abstract.** A nanocrystalline $Si_{1-x}Sn_x$ films with a small content of amorphous phase were grown by simultaneous deposition of tin from a Knudsen effusion cell and silicon from a Si sublimation source at a co-deposition and/or solid-phase crystallization temperature of about 250-350 $^0$C on a Si(100) and $SiO_2$/Si(100) substrates. Raman/mapping spectroscopy shows the absence of Sn segregation and the successful substitutional incorporation of Sn into the Si lattice of nanocrystalls. A significant difference between the co-deposition on these substrates is the formation, respectively, of a continuous $Si_{1-x}Sn_x$ film consisting of a mixture of nanocrystalline and amorphous phases, and a film consisting of $Si_{1-x}Sn_x$ nanocrystallites forming a dentridoid structure on the surface of an amorphous Si.

## 1. Introduction

The silicon-tin (SiSn) alloy is a promising candidate material for the next-generation group-IV semiconductors.

First of all, the optical band gap of SiSn depends on the concentration of Sn and can be optimized by the corresponding content. Many previous studies indicate that an indirect-direct band-gap crossover of SiSn is theoretically expected as Sn fraction increases 25% [1,2].

Based on the above, SiSn is expected for near-infrared optical device applications [3] what cannot be realized using pure Si.

Secondly, the dramatic phonon scattering is caused by Sn atoms incorporated in the Si lattice and therefore the values of thermal conductivity for SiSn is very low [4]: this means the feasibility of high-performance thermoelectric device for "internet of things" on the basis of the thermoelectric figure of merit $ZT = S^2\sigma T/\kappa$, where S is the Seebeck coefficient, σ is the electrical conductivity, T is the absolute temperature, and κ is the thermal conductivity.

Thirdly, by selecting the appropriate Sn content and annealing temperature, SiSn-based alloys can be transformed from an amorphous phase into a nanocrystalline one with controlled nanocrystallite sizes. This controlled transformation is very important for the production of solar cells based on nanocrystalline silicon.

The purpose of this work was to determine by methods of Raman spectroscopy and AFM the dependence of the degree of crystallinity of $Si_{1-x}Sn_x$ films for x=0.0; 0.1; 0.15; 0.2 on the heating and/or annealing temperature and the substrate surface (face (100) of single-crystal Si and natural oxide on Si (100)), as well as the crystallization temperature.

## 2. Experiment

Si-Sn alloy films with Sn concentration of 0 – 20% were formed by co-deposition of Si and Sn onto substrates with various surfaces in an ultrahigh vacuum chamber with a base pressure of $10^{-9}$ Torr. The samples *A, B, C* had an atomically clean silicon surface Si(100) 2×1. The surface of the *D* was covered with a film of natural oxide, and - *E* had excessive roughness (RMS=30 nm). During co-deposition all samples were indirectly heated by Sn and Si sources between 150-300 °C. During the co-deposition of Si and Sn, samples *D* and *E* were additionally heated by passing a direct current and after - they were annealed for 20 s at T≈360 °C.

Details of sample cleaning, calibration of deposition rates and a choice of the Si and Sn deposition rate ratio are described in [6].

The surface topography of the grown films was studied by AFM using a Solver P47 instrument. Raman spectra were measured by the DXR Thermo Science and NT-MDT NTEGRA Spectra instruments using a lasers with a wavelengths correspondenly of 514 nm for *A*, *B* and *C* and 473 nm for *D, E* samples.

***Table I.*** *Parameters of samples.*

| Sample | Substrate | Tsub, °C | Sn content [%] | Film thickness [nm] | RMS [nm] |
|---|---|---|---|---|---|
| *A* | Si(100)2×1 | 200-280 | 0 | *220* | 1 |
| *B* | Si(100)2×1 | 100-180 | 10 | *240* | 0.3 |
| *C* | Si(100)2×1 | 200-280 | 15 | *260* | 0.4 |
| *D* | $SiO_2$/ Si(100) | 300-380 | 20 | *160* | 4.4 |
| *E* | Si(100) | 300-380 | 20 | *160* | 3-8 |

## 3. Results and discussions

The fitting in Fig. 1 (a), (b) shows three phonon bands typical of all our $Si_{1-x}Sn_x$ having an amorphous fraction: 2TA+LA (maxima between 294-333 cm$^{-1}$), LO (392-427 cm$^{-1}$) and TO (463-480 cm$^{-1}$), including film with x=0. For x>0 a new TO phonon band appears (350-373 cm$^{-1}$) corresponding to the Si-Sn bond vibrations. On the spectra *C, D, E* there are two additional phonon bands with centers of fit peak between 493-499 cm$^{-1}$ and 503-518 cm$^{-1}$. Both TO bands are associated with Si-Si bond vibrations in the Si or SiSn crystalline fraction. The crystallites size, substitution Sn content, residual stress, grain boundaries structure, Si and SiSn structure determine the peak positions of these modes. In addition, some spectra have a 520 cm$^{-1}$ peak from the c-Si substrate.

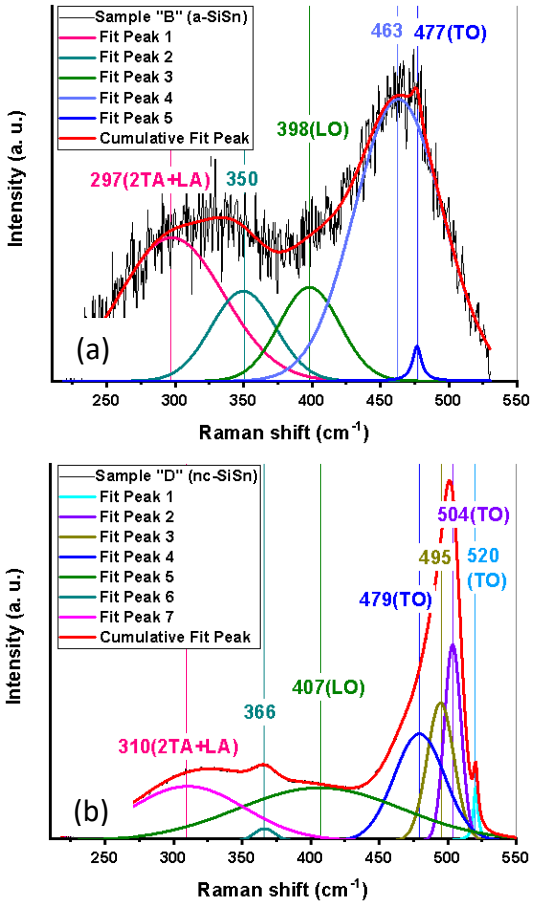


***Fig. 1.*** *RAMAN spectra and their decomposition by Lorentz (peak 520 cm$^{-1}$) and Gauss functions (all peaks except 520 cm$^{-1}$) from amorphous (a) and nanocrystalline SiSn (b) films grown, respectively, on Si(100)2×1 at T≤180 °C (sample B) and at SiO2/Si(100) at T≈350 °C (sample D).*

AFM images of samples *B* and *D* are shown in Fig. 2. It can be seen that the SiSn islands are distributed nearly uniform over the surface. Samples *B* and *D* have average grain sizes of 15 and 20 nm and mean square surface roughness of 0.3 and 4.4 nm, respectively. The morphology of the sample *D* indicates dendritic crystallization.

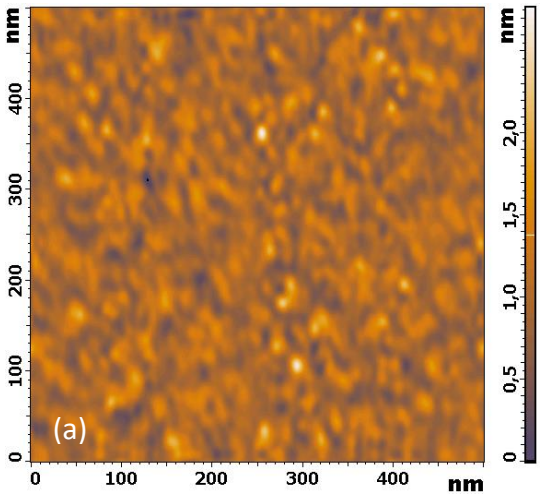


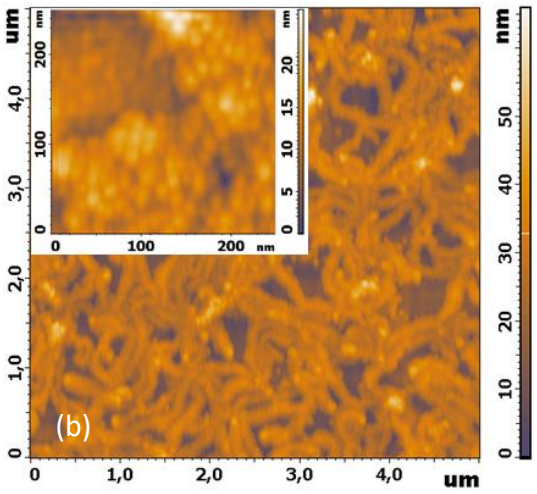


***Fig. 2.*** *AFM images of the samples B (a) and D (b).*

AFM and Raman data, as a calculated data of amorphous and crystalline volume fraction, substitution tin content and nanocrystallite sizes will be presented in the report.

## 4. Conclusions

Simultaneous deposition of Si and Sn on both Si(100)2×1 and $SiO_2$/Si(100) allows to obtain sufficiently smooth ($\sigma_{rms}$ = 0.4-4.4 nm) Si-Sn nanocrystalline films with a thickness of 160-260 nm and a Sn content of 10-20%. A significant difference between the co-deposition on these substrates are the formation, respectively, of a continuous SiSn film consisting of a mixture of nanocrystalline and amorphous phases, and a film consisting of SiSn nanocrystallites forming a dentridoid structure on the surface of amorphous Si. Additional annealing up to 380°C of partially amorphized SiSn films significantly reduces the content of the amorphous fraction without Sn segregation. The crystallization temperature of the SiSn alloy can be reduced by increasing the initial concentration of Sn. The choice of the initial Sn concentration, temperature and substrate surface allows controlling the size of nanocrystallites.

## References

[1] Y. Nagae, M. Kurosawa, S. Shibayama, M. Araidai, M. Sakashita, O. Nakatsuka, K. Shiraishi, S. Zaima, Jpn. J. Appl. Phys. 55, 08PE04 (2016).
[2] J. Tolle, A. Chizmeshya, Y. Fang, J. Kouvetakis, V. D'Costa, C. Hu, J. Menendez, and I. Tsong, Appl. Phys. Lett. 89(23), 231924 (2006).
[3] M. Kurosawa, Y. Inaishi, R. Tange, M. Sakashita, O. Nakatsuka, and S. Zaima, Jpn.J. Appl. Phys. 58, SAAD02 (2019).
[4] M. Tomita, M. Ogasawara, T. Terada, and T. Watanabe, Jpn. J. Appl. Phys. 57, 04FB04 (2018).
[5] V. Neimash, A. Goushcha, P. Shepeliavyi, V. Yukhymchuk, V. Dan'ko, V. Melnyk, A. Kuzmich, Ukr. J. Phys.Vol. 59, No. 12 (2014).
[6] S.A. Dotsenko, D.L. Goroshko, E.A. Chusovitin, S.A. Kitan, K.N. Galkin, N.G. Galkin, Defect and Diffusion Forum, Vol. 386, pp 95-101 (2018).

Sixth Asian School-Conference on Physics and
Technology of Nanostructured Materials
Vladivostok, Russia, 25 – 29 April, 2022



# Structural properties of cadmium arsenide magnetron films on different substrates

A.V. Kochura[1], Zaw Htet Aung[1], V.S. Zakhvalinskii[2], E.A. Pilyuk[2]
[1] South West State University, 50 years of October St, Kursk, 305040, Russia
[2] Belgorod State University, Belgorod, 308015, Russia

*e-mail: alex_dop@mail.ru

**Abstract.** Cadmium arsenide ($Cd_3As_2$) is a well-known material with very high carrier mobility at the room temperature. We present a structure study of the $Cd_3As_2$ thin magnetron films. They were obtained by radio frequency magnetron sputtering on silicon, sapphire and strontium titanate substrates. The structure and morphology of the surface were studied by atomic force microscopy, Raman spectroscopy, electron microscopy and X-Ray diffraction. The composition of the films has been shown to correspond to the $Cd_3As_2$ stoichiometry. All films were nanostructured with a strong texturing after annealing.

## 1. Introduction

Topological materials currently attract wide interest related to the existence of Dirac nodes in their electron spectrum and related nontrivial topological characteristics of both bulk and surface states [1]. Theoretical and experimental studies have established that $Cd_3As_2$ belongs to a special class of topological insulators - Dirac semimetals, in which charge carriers - Dirac fermions have zero effective mass and obey relativistic laws of motion [2]. It has recently been discovered low-temperature superconductivity in cadmium arsenide films prepared by different methods. [3, 4]. The nature of this phenomenon is not completely clear and can have different reasons, for example, a sharp increase in the number of topologically protected states can occur, both due to an increase in internal stresses in polycrystalline films [3], and due to a weak, but sufficient for the appearance of the effect fine tuning of the band structure in the presence of a slight excess of cadmium and violation of stoichiometry [5]. This stimulates more detailed studies of the structure and composition of synthesized films. In this work, we study changes in the structural properties and morphology of cadmium arsenide films on various substrates, depending on the conditions for their production by reactive magnetron sputtering.

## 2. Experiment

Cadmium arsenide thin films were obtained by radio frequency magnetron sputtering in an argon atmosphere at a pressure of $8\times10^{-3}$ mbar without heating the substrate. The sputtering rate at the supplied power of 10 W and the target substrate distance was about 1 nm/min. The powder target was made from pre-synthesized $Cd_3As_2$ single crystals. Monocrystalline polished oriented silicon p-Si (111), sapphire $\alpha$-$Al_2O_3$ (001) and strontium titanate $SrTiO_3$ (100) were used as substrates. After deposition part of the film was annealed in an argon atmosphere at the temperature of 520 K. The structure and morphology of the thin films were studied by atomic force microscopy (AFM) (AIST Smart SPM, Horiba), Raman spectroscopy (RS) (OmegaScope, Horiba), electron microscopy (EM) (JEOL 6610LV) and X-Ray diffraction (XRD) (GBC EMMA) at the room temperature.

## 3. Results and discussions

The typical X-Ray diffraction patterns of the $Cd_3As_2$ magnetron films on different substrates with the crystal structures of α (sp. Gr. $I4_1cd$) and α' (sp. Gr. $P4_2/nbc$) polimorfic modifications found earlier in Ref. 3, 6. XRD of As-growth films had complex structure with small amorfization. After annealing all obseved diffraction peaks we can correspond to the (112) family crystal planes (Fig. 1). This is typical because the (112) plane is the cleavage plane of cadmium arsenide.

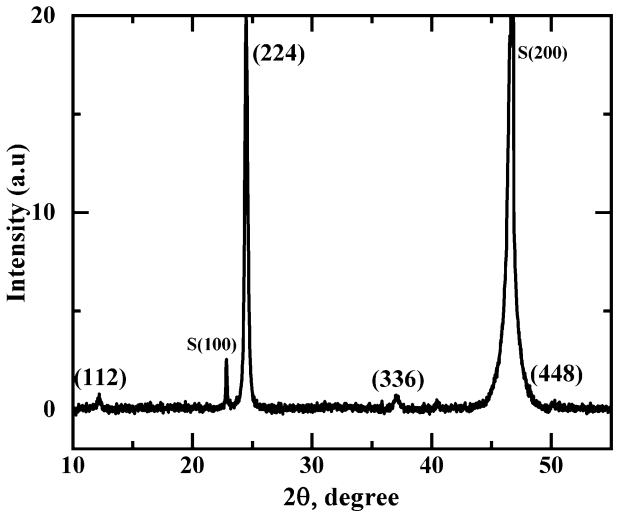


***Fig. 1**. X-ray diffraction patterns of annealed thin $Cd_3As_2$ film grown by magnetron sputtering on $SrTiO_3$ substrate (labeled by «S»).*

In addition, AFM results demonstrates (Fig. 2) that the films are continuous with a granular structure with an average granule size within 20 - 40 nm for annealed samples. Their thickness was about 50 nm – 60 nm.

It is clearly seen that the films exhibit Stranski-Karstanov growth, with initial deposition of a homogeneous thin layer and subsequent growth with intense nucleation. The composition of the film corresponded to the stoichiometric within the measurement error and was uniform, as is observed on the maps of the distribution of Cd and As atoms by EM.

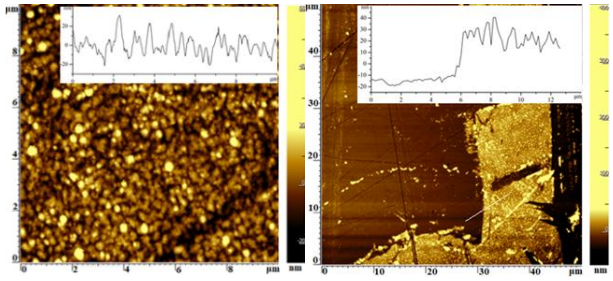

***Fig. 2**. AFM images with profiling of annealed $Cd_3As_2$ film on $Al_2O_3$ substrate in the center (on left) and near edge (on right).*

The study of thin films using RS in the far IR region confirms that the films are formed from cadmium arsenide. Two broad peaks with a position of about at at 193.2 and 247.7 $cm^{-1}$, whose nature is not associated with the classical mechanism of inelastic light scattering, are often used to characterize nanostructures containing $Cd_3As_2$ single crystals and films. Figure 3 shows the Raman spectra measured in individual regions of the crystal for the sample. For the α-$Cd_3As_2$ crystal structure, the experimental Raman spectra in the region above 100 $cm^{-1}$ contained only three strong vibrational modes located near 140, 195 and 250 $cm^{-1}$. Unfortunately, due to the peculiarities of the Raman equipment used, the spectra were measured only at $\omega > 140$ $cm^{-1}$, so one can see only two pronounced peaks and some a weak peak formed by the combination of the basic phonon modes with $\omega < 100$ $cm^{-1}$. Since the general form of the spectra of single-crystal and film samples are similar, it can be concluded that the films after annealing have a high degree of crystallinity with a tetragonal structure similar to bulk crystals of α-$Cd_3As_2$.

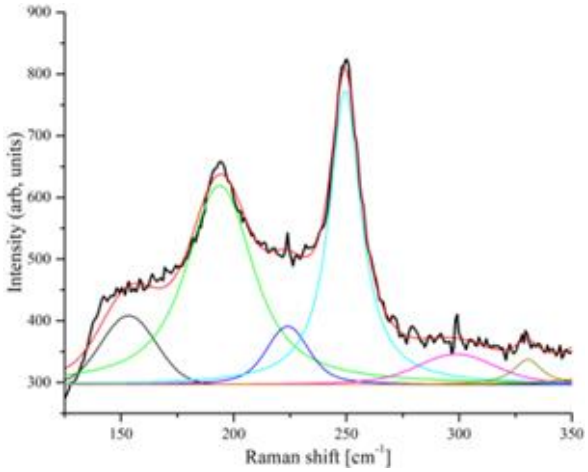


***Fig. 3**. Raman spectra of the annealed $Cd_3As_2$ film grown on $Al_2O_3$ substrate.*

## 4. Conclusions

Cadmium arsenide films were grown by RF magnetron sputtering on different substrates. The composition and structural properties of this nanostructured films have been studied by X-ray analysis, scanning electron microscopy combined with energy-dispersive analysis, and Raman spectroscopy. The films are continuous with stoichiometric content and had a granular structure. After annealing they After the films are annealed, their crystallinity increases and they become textured with the (112) texture axis.

## Acknowledgements

This work was supported by the Ministry of Education and Science of the Russian Federation (grant number 0851–2020–0035).

## References

[1] N.P. Armitage, E.J. Mele, A. Vishwanath. Rev. Mod. Phys. 90(2018)015001.
[2] I. Crassee, R. Sankar, W.-L. Lee, A. Akrap, M. Orlita M. Phys. Rev. Mat. 2(2018)120302.
[3] A. V. Suslov, A. B. Davydov, L. N. Oveshnikov, L. A. Morgun, K. I. Kuge, V. S. Zakhvalinskii, E. A. Pilyuk, A. V. Kochura, A. P. Kuzmenko, V. M. Pudalov, B. A. Aronzon. Physical Review B. 99(2019)094512.
[4] L.N. Oveshnikov, A.B. Davydov, A.V. Suslov, A.I. Ril', S.F. Marenkin, A.L. Vasiliev, B.A. Aronzon. Scientific reports. 10(2020)4601.
[5] N. Kovaleva, L. Fekete, D. Chvostova, A. Muratov. Metals. 10(2020)1398.
[6] A. V. Kochura, V. S. Zakhvalinskii , Aung Zaw Htet, A. I. Ril', E. A. Pilyuk, A. P. Kuz'menko, B. A. Aronzon, S. F. Marenkin. Inorganic Materials. 55(2019) 933.

# Formation, structure, and optical properties of textured CaSi and epitaxial $CaSi_2$ films on silicon substrates grown by MBE and RDE methods

K.N. Galkin[1], O.V. Kropachev[*,1], I.M. Chernev[1], A.M. Maslov[1], E.Yu. Subbotin[1], N.G. Galkin[1], A.Yu. Alekseev[2] and D.B. Migas[2]

[1] Institute of Automation and Control Processes FEB RAS , 5 Radio St., Vladivostok 690041, Russia
[2] Belarusian State University of Informatics and Radioelectronics, 6 P. Browka St., 220013 Minsk, Belarus

*e-mail: chernobez@gmail.com

Calcium silicides are environmentally friendly materials and occupy a special place among alkaline earth metal silicides. This is primarily due to a wide range of properties of calcium silicides from semiconducting [1] to semimetallic [2]. This may lead to their widespread use in various fields of technology and electronics. However, the growth of single-phase films of semimetallic monosilicide (CaSi) and calcium disilicide ($CaSi_2$) on silicon and the study of their optical properties are complicated due to the presence of at least 6 silicides of different compositions in the Ca-Si system [3] and the lack of methods for separating the preferred orientation during growth silicon silicides.

This work is devoted to approbation of new methods for growing CaSi and $CaSi_2$ on silicon with (111) orientation. The structure and optical properties of the grown films are studied and compared with the data of first-principles calculations of optical functions from the electronic structure of CaSi and $CaSi_2$.

The growth of Ca silicide films was carried out in an ultra-high vacuum (UHV) chamber of the OMICRON Compact setup with a base vacuum of $1\times10^{-10}$ Torr, equipped with a LEED and AES/EELS analyzer, a block of silicon (Si) and calcium (Ca) molecular beam sources for Ca deposition, Mg and Si on silicon substrates. The growth of a CaSi film on a Si(111) substrate was carried out by MBE at 300–500°C on a CaSi seed layer preliminarily transformed from $Mg_2Si$. For the growth of $CaSi_2$, the MBE method was also used during the co-deposition of Ca and Si on an atomically clean silicon surface at temperatures of 640–680 °C. The deposition rates of Ca, Mg and Si, calibrated with quartz thickness sensor, ranged from 0.1 nm/nm and 8.5–9.5 nm/min for Ca, 0.7 nm/min for Mg, and 0.28–0.65 nm/min for Si in different experiments.

The reflection spectra (R-spectra) and transmission spectra (T-spectra) of the grown samples were recorded within one day after unloading at room temperature in the photon energy range of 0.05–6.50 eV on a Hitachi U-3010 spectrophotometer with an integrated sphere and a Bruker Fourier spectrometer Vertex 80v. The optical functions were calculated in the transparency region from the T- and R- spectra, as well as from the integral Kramers-Kronig relations. The structure of Ca monosilicide films was studied on a RIGAKU SmartLab diffractometer (9 kW rotating anode, CuKα radiation, parallel beam, 2θ/ω mode, incident beam size 0.1 mm), using a silicon sample holder with zero background and HyPix-3000 detector (1D measurement mode). The diffraction pattern was recorded in the range of 2θ angles from 5° to 80°, with a 2θ step of 0.01°. Calculations of the electronic band structure and optical functions were also performed using the method of self-consistent full-potential linearized augmented plane waves (FLAPW) in its scalar-relativistic version using the WIEN2k package [4].

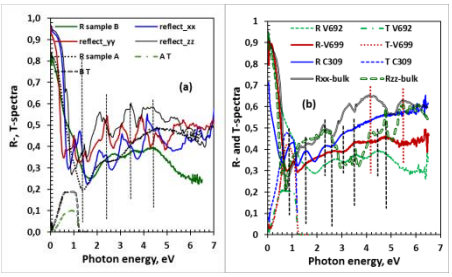


***Fig. 1.*** *Reflection (R) and transmission (T) spectra of CaSi (a) and $CaSi_2$ (b) films in samples and the results of calculating the reflection spectra of a CaSi and $CaSi_2$ single crystals for different planes: xx, yy, zz.*

After the samples were unloaded from the growth chambers, the transmission and reflection spectra were recorded in the photon energy range from 0.05 eV to 6.5 eV. The main features for the CaSi and $CaSi_2$ films were the partial transparency of both films in the photon energy range of 0.2–1.1 eV and the plasma minimum in reflection, which was previously observed for $CaSi_2$ films [5] with semimetallic properties. In this case, the transparency of $CaSi_2$ films (Fig. 1a) is slightly higher than the transparency of CaSi (Fig. 1b). Comparison with the data of theoretical reflection spectra for three planes of a single crystal of CaSi (Fig. 1a) and $CaSi_2$ shows good agreement in the position of the plasma minimum for both silicides, which is associated with the contribution of two types of carriers, according to the calculations performed in this work. The reflection spectra also agree in magnitude and position of the main peaks in the photon energy range of 1.5 – 6.5 eV, which corresponds to the main interband transitions in CaSi and $CaSi_2$ single crystals.

## Acknowledgements

This work was financially supported by the RFBR grant - BRFFR No. 20-52-00001_Bel_a.

## References

[1] S. Lebegue, et.al. Phys. Rev. B 72(2005)085103.
[2] O. Bisi, et. al. Phys. Rev. B. 40(1989)10194.
[3] P. Manfrinetti, et.al. Intermetallics 8(2000)223.
[4] P. Blaha, et.al. (Karlheinz Schwarz, Tech. Universität Wien, Vienna, 2001).
[5] N.G. Galkin, et.al. J. All. Comp. **770**(2019)710.

# III. Ferromagnetic and ferroelectric materials, including nanomaterials, a spintronics

Sixth Asian School-Conference on Physics and
Technology of Nanostructured Materials
Vladivostok, Russia, 25 – 29 April, 2022

**III.o.01**

# Complex magnetostatic interactions in Fe-Au barcode nanowire arrays

A.Yu. Samardak*[,1], Y.S. Jeon[2], A.G. Kozlov[1], K.A. Rogachev[1], A.V. Ognev[1], E. Jeong[3], G.W. Kim[3], M.J. Ko[3], A.S. Samardak[1], Y.K. Kim[2,3]

[1] Institute of High Technologies and Advanced Materials, Far Eastern Federal University, 8 Sukhanova St., Vladivostok 690950, Russia
[2] Institute of Engineering Research, Korea University, Seoul 02841, Republic of Korea
[3] Department of Materials Science and Engineering, Korea University, Seoul, 02841, Republic of Korea

*e-mail: samardak.aiu@dvfu.ru

**Abstract.** One of the most important things scientists should consider while designing high-density magnetic media is magnetostatic interactions between elements. Densely packed magnetic memory cells induce strong stray fields, which affecting the magnetic properties of each element drastically, resulting in modified hysteresis behaviour and domain structure compared to non-coupled elements. In this work we focus on the detailed investigation of magnetostatic interactions in Fe-Au barcode nanowire arrays with alternating magnetization of Fe- and Au-rich segments, embedded in porous alumina template. Using experimental and simulation approaches we study the influence of the segment length on the overall magnetic behavior and the character of magnetostatic interactions in the nanowire array. We demonstrate that depending on the segment length magnetic interactions can be of three types. We show that a preferable type of interaction depends on the geometric parameters of the Fe- and Au-rich segments and the interwire distance.

## 1. Introduction

Barcode nanowires have wide range of possible magnetic, electrical, mechanical, and biomedical applications [1-4]. Single bath electrodeposition [5] is allowing precise control over number of segments in nanowire, their composition and length.

The magnetic properties of the barcode nanowires arrays are highly dependent on the composition of each segment, yet other works usually consider barcode nanowires electrodeposited from a single bath as a set of magnetic and non-magnetic cylinders, and the possibility of synthesis of the alloy consisting of both elements presented in bath is not considered [6,7]. In this work, we investigate the element distribution in segments to prove their composition as Fe-Au alloy with different concentrations depending on the synthesis conditions.

To investigate complex magnetostatic interactions in the array of barcode nanowires first order reversal curve (FORC) diargam method was implemented, together with magnetic force microscopy and micromagnetic simulations.

## 2. Experiment

Barcode nanowires were synthesized by electrodeposition from a single bath into the porous alumina template with 200-300 nm diameter of the pores. The electrolyte consisted of a mixture of deionized water and solutions of iron (II) sulfate heptahydrate (FeSO4 7H2O, 0.10 M) as a source of Fe ions, and potassium dicyanoaurate (KAu (CN)2, 0.015 M) as a source of Au ions. To deposit segments with different compositions, pulses with different current density (10 mA $cm^{-2}$ and 0.01 mA $cm^{-2}$) were fed to the electrochemical cell. Fe-rich segments grew during high density current, Au-rich segments grew during low density current, and length of the segments was controlled by the time of the deposition with corresponding current density.

Barcode nanowires morphologies were studied with ultrahigh resolution field-emission scanning electron microscopy (UHR–SEM, Hitachi, SU–70) and dual–beam scanning electron microscopy (SEM, ThermoFisher Scios 2 DualBeam). Furthermore, the microstructure was analyzed by transmission electron microscopy (TEM, JEOL, JEM–2100F) and X–ray diffraction (XRD, Rigaku, D/MAX–2500V/PC). The sample composition was probed by SEM and TEM energy dispersive X–ray spectroscopy (EDX, HORIBA, X–MAXn and EDX, EDAX team).

Magnetic properties were studied using a vibrating sample magnetometer (LakeShore 7410 VSM). The FORC diagram method was used to investigate the irreversible processes in the barcode nanowires arrays and the influence of interaction fields on the magnetic behavior. Magnetic force microscopy (MFM NT–MDT Ntegra Aura system) was used to study the micromagnetic structure of the barcode nanowires. Finally, micromagnetic simulations were performed using MuMax3 software for a detailed study of spin configuration in segments with a different composition.

## 3. Results and discussions

SEM studies (see Fig. 1) showed the diameters of nanowires about 250 nm, length ~ 5 μm and sharp borders between segments. EDX analysis confirmed sharp borders between segments and showed that Fe-rich segments consist of $Fe_{90}Au_{10}$ alloy and Au-rich segments – of $Fe_{45}Au_{55}$ alloy. According to the literature, the magnetic moment of Fe-rich segments ~ 800 G and 20-100 G in Au-rich segments.

Hysteresis loop measurements showed that samples with Fe-rich segment length L=100 nm are almost isotropic, with minor differences in magnetic behavior depending on the direction of an external magnetic field. The anisotropy of the Fe(200)Au(x) samples is much more visible and manifests itself in a clear difference in the hysteresis loops measured in different directions of the external magnetic field. Most pronounced anisotropy in the Fe(200)Au(30) sample decreases with increasing Au-rich segment length.

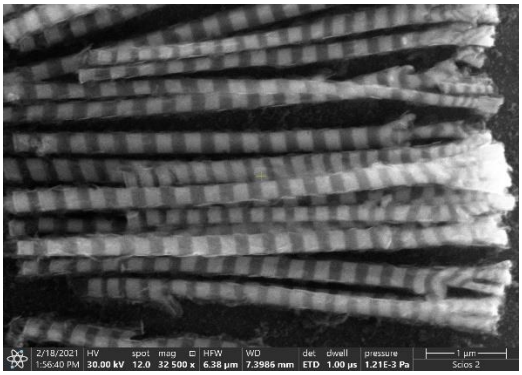

***Fig. 1.*** *SEM image of the Fe(200)Au(200) nanowires etched from the alumina template.*

In contrast to magnetic hysteresis loops, FORC diagrams differ greatly depending on the direction of the applied external field. In the longitudinal direction of the field, all samples showed the distribution of switching processes induced by the interaction fields, with distribution along the interaction field $H_u$ axis, while in the perpendicular direction of the field, FORC diagrams showed absence of the reversible processes, which is due to coherent rotation in such geometry of the field. With an increase in the Au-rich segment's length, the distribution of the interaction induced switching $H_u$ in the FORC diagrams, obtained with an external magnetic field applied along the barcode nanowires, is broadening for Fe(200)Au(x) samples. In contrast, for the Fe(100)Au(x) series, $H_u$ remains at the same level.

In the absence of an external magnetic field, the MFM contrast was not visible for all samples. When the longitudinal external magnetic field was applied, an alternating contrast of black and white poles became visible in the MFM picture. When the picture of the distribution of the elemental composition on the MFM images of the MFM was superimposed, it was revealed that black and white poles are formed strictly at the boundaries between Fe-rich and Au-rich segments. With a perpendicular to the long axis of the barcode nanowires external magnetic field, the poles of the stray field are rotated to 90° and localized exclusively in the Fe-rich segments at the edges of the nanowire. Micromagnetic simulation of stray fields showed good overlap between experimental MFM results and simulation data. The vortex state of the magnetization was confirmed by simulation for all samples.

Detailed analysis of interactions showed that depending on the segment lengths 3 types of interactions are presented in the barcode nanowires array: interactions between opposite magnetic pole of the adjacent segment in the same nanowire (type I), opposite magnetic pole of the same segment (type II) and closest poles in the segments of the neighboring nanowires in the array (type III). The dominating type of enclosed magnetic flux depends only on the geometric parameters of the sample: length of the Au-rich segment (30–200 nm) for type I, length of the Fe-rich segment (100 and 200 nm) for type II, and interwire distance in the array (~200 nm) for type III.

## 4. Conclusions

This study carried out a detailed study of the structure and magnetic properties of arrays of barcode nanowires electrodeposited into an alumina oxide matrix. We found that the barcode nanowires fabricated by electrodeposition from one solution consist of Fe-Au alloy with different concentrations of Fe and Au. Hysteresis loop measurements showed that the effective magnetic anisotropy depends on the length of the Fe- and Au-rich segments. We found out that the observed magnetostatic interactions can be of three types: interactions between the opposite poles of the adjacent Fe-rich segments in the same barcode nanowire, coupling of poles of the same Fe-rich segment, and interaction of Fe-rich segments in the neighboring barcode nanowires in array with their strength varying on the geometrical parameters of barcode nanowires.

## Acknowledgements

This work was supported by the Russian Ministry of Science and Higher Education (State Task No. 0657-2020-0013).

## References

[1] S. Min, Y. S. Jeon, H. J. Jung. Advanced Materials., **32** (2020)2004300.
[2] S. Min, Y.S. Jeon. H. Choi. Nano Letters **20**(2020)7272–7280.
[3] S. Bochmann, A. Fernandez-Pacheco and M. Mačković. Rsc Advances **60**(2017)37627-37635.
[4] J.A Moreno, H. Mohammed, and J. Kosel, Journal of Magnetism and Magnetic Materials., **484**(2019)110-113.
[5] J. G. Fernández, V. V. Martínez, A. Thomas. Nanomaterials **8** (2018).
[6] L. Clime, S.Y Zhao, P. Chen, F. Normandin, H. Roberge, T. Veres. Nanotechnology. **43**(2007)435709.
[7] S. Moraes, D. Navas, F. Beron, M. P.Proenca, K. R. Pirota, C. T. Sousa, J.P. Araujo. Nanomaterials **8**(2018)490.

Sixth Asian School-Conference on Physics and
Technology of Nanostructured Materials
Vladivostok, Russia, 25 – 29 April, 2022

**III.o.02**

# Field-induced heterophase state in $PbZrO_3$ thin films

R.G. Burkovsky*[,1], G.A. Lityagin[1], A.F. Vakulenko[1], A.E. Ganzha[1], R. Gao[2], A. Dasgupta[2], Bin Xu[3], A.V. Filimonov[1], L.W. Martin[2]

[1] Peter the Great Saint-Petersubrg Polytechnic University, 29 Politekhnicheskaya, 195251, St.-Petersburg, Russia
[2] Department of Materials Science and Engineering, University of California, Berkeley, California 94720, United States
[3] School of Physical Science and Technology, Soochow University, Suzhou 215006, China

*e-mail: roman.burkovsky@gmail.com

## 1. Introduction

Antiferroelectric epitaxial thin films demonstrate a complex behavior with regard to their structural phase transition, including the electric-field-induced switching between the antiferroelectric and ferroelectric phases. We use in-situ x-ray diffraction with such films to demonstrate that the reaction of the material to relatively weak fields includes the formation of the ferrielectric-like phase, which forms inside the antiferroelectric matrix. The structure of the field-induced phase is peculiar and needs new approaches in modeling to be understood. Especially remarkable is the energy of heterophase boundaries that appear to define the specific structure.

## 2. Experiment

Epitaxial thin film $PbZrO_3$ samples were grown using pulsed laser deposition technique at UC Berkeley. The field has been applied using Cr-Au top electrodes. The bottom electrode was from $SrRuO_3$, which was the buffer layer between $PbZrO_3$ film and $SrTiO_3$ substrate. The in-situ x-ray characterization was done using SuperNova single crystal diffractometer.

## 3. Results and discussions

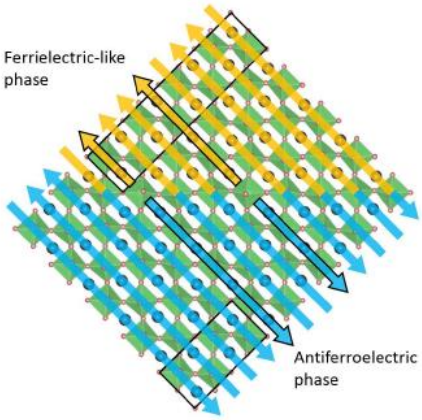


***Fig. 1.*** *Schematic depiction of a heterophase boundary, which shows that some layers of lead-ion displacements propagate the boundary intact, while the others are "broken", which costs energy. Accounting for this energy allows reproducing the experimentally observed structure.*

An unusual new structure grows in volume continuously on the increase of electric field, implying the presence of two-phase state with moving boundary. We have developed a simple energy model for the material in question, which includes not only a bulk part, but also the part related to the heterophase boundaries between the host and guest phases. The model is empirical (parametrized), but its parameter values are determined with the help of ab-initio calculations. The energy due to heterophase boundaries is modeled with the use of a notion of antiferroelectric field, which is being cast onto the guest phase by the host phase. Figures 1 and 2 show, respectively, the scheme of heterophase boundary and the phase diagram obtained with the model.

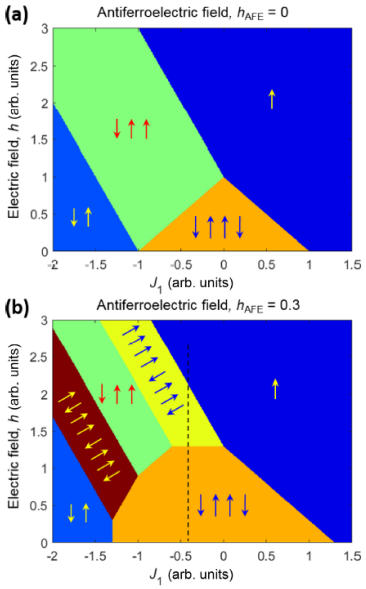


***Fig. 2.*** *Model phase diagram of PbZrO3 material in the presence of both electric and antiferroelectric fields. The diagram shows the tendency towards the formation of the ferrielectric-like phase (yellow) between the antiferroelectric and ferroelectric phases upon the electric field increase when there is only a mild-magnitude antiferroelectric field present. This suggests a defining role of heterophase boundaries in choosing the structure that forms experimentally.*

## 4. Conclusions

The work demonstrates an unusual experimental observation together with a novel approach required for its qualitative explanation. The ferrielectric-like phase combines a relatively long period, similar to the ones of incommensurate phases in these materials, with the commensurateness induced by the heterophase contact. The findings pave the way for creating sophisticated structures in antiferroelectrics, which can be potentially useful in dense memories and other electronics. Further information can be found in the forthcoming publication [1].

## Acknowledgements

M. Alexe and A. K. Tagantsev are acknowledged for useful discussions. R.G.B, G.L., and A.G. acknowledge the

support of the Russian Science Foundation (Grant No. 20-72-10126) for the experimental work (apart from thin film synthesis) and interpretation (apart from first-principles analysis). B.X. acknowledges financial support from National Natural Science Foundation of China under Grant No. 12074277 and Natural Science Foundation of Jiangsu Province (BK20201404) for performing first-principles analysis. Thin film samples were synthesized at UC Berkeley. R.G. acknowledges support from the National Science Foundation under Grant No. DMR-2102895. A.D. acknowledges support from the National Science Foundation under Grant No. DMR-1708615. L.W.M. acknowledges support from the Army Research Office under Grant No. W911NF-21-1-0118.

**References**

[1] R. Burkovsky et al., Field-induced heterophase state in $PbZrO_3$ thin films, Phys. Rev. B, in press.

Sixth Asian School-Conference on Physics and
Technology of Nanostructured Materials
Vladivostok, Russia, 25 – 29 April, 2022

**III.o.03**

# Magnetoresistance of MIS structure based on PbSnTe:In crystalline topological insulator film

A.E. Klimov*[,1,2], I.O. Akhundov[1], V.A. Golyashov[1,3], D.V. Gorshkov[1], D.V. Ishchenko[1], N.S. Pashchin[1], G.Yu. Sidorov[1], S.P. Suprun[1], A.S. Tarasov[1], E.V. Fedosenko[1], O.E. Tereshchenko[1,3]

[1] Rzhanov Institute of Semiconductor Physics of SB of RAS, 13, Lavrentieva ave., Novosibirsk, Russia, 630090
[2] Novosibirsk State Technical University, 20, Karl Marx ave., Novosibirsk, Russia, 630073
[3] Novosibirsk State University, 1, Pirogova st., Novosibirsk, Russia, 630090

*e-mail: klimov@isp.nsc.ru

**Abstract.** For the first time in the world, on the basis of MBE-grown PbSnTe:In epitaxial films, MIS structures of the transistor type (MIST) with a thin-film $Al_2O_3$ gate dielectric were created and studied at helium temperatures. The dependences of the MIST channel current on the drain-source voltage and gate voltage, temperature, and magnetic field were explored. The results obtained are qualitatively explained in terms of the injection nature of the channel current with current limitation by the space charge in the presence of various types of traps, including surface traps.

## 1. Introduction

Lead and tin tellurides form a $Pb_{1-x}Sn_xTe$ solid solution in the range of $x = (0 – 1)$. At $x_{inv} \sim 0.35$, the bands become inverted, and $E_g = 0$. At low temperatures, the fundamental absorption edge $\lambda_r \sim (5.5 – 12)$ micron corresponds to $x \sim (0 – 0.20)$, with parameters of PbSnTe necessary for creation of *p-n* junctions and photodiodes with properties suitable for practical use in thermal imaging technology. The PbSnTe surface attracted considerable interest in the 1970s mainly because of the problem of surface leakage currents in photodiodes. Large values of $n_0$ (or $p_0$) and high static permittivity ($\varepsilon > 400$ for PbTe, up to $\varepsilon \sim 1000 \div 4000$ and more with increasing $x$) prevented the use of MIS structures and the field effect for solving these problems. Moreover, in a comparative analysis of two materials for IR technology, namely HgCdTe and PbSnTe, the large $\varepsilon$ of the latter was indicated as a disadvantage that prevented the use of MIS technologies for photodetectors. In the late 1970s, it was found [1, 2] that the introduction of In at concentrations up to several at.% sharply reduces $n_0$ ($p_0$) in PbSnTe:In of composition $x \sim (0.18 – 0.27)$, bringing it up to an insulating state near $T = 4.2$ K. However, despite the large number of publications on the properties of PbSnTe:In, MIS structures based on it have not been studied at all. In the last decade, special interest in PbSnTe is attracted due to the fact that compositions with $x \sim x_{inv}$ and higher exhibit the properties of a topological crystalline insulator (TCI) [3]. In this case, the effects conditioned in TCI by Dirac surface states can manifest themselves against the backdrop of other properties of PbSnTe:In associated with the surface. The aim of this work was to create MIS structures based on PbSnTe:In and to study their properties related to the surface, including galvanomagnetic phenomena.

## 2. Experiment

A fairly detailed description of the world's first PbSnTe:In MISFET structure was given in [4]. Using photolithography, MISFETs were fabricated on 1 to 2 micron thick PbSnTe:In films, grown on (111) $BaF_2$ substrates with molecular beam epitaxy (see, for example, [5]). The MISFET channel had a width of near 10 micron and a length $L$ about 6 to 18 micron. The drain and source of $n^+$-type of conductivity were formed with vacuum deposition of a thin indium layer followed by diffusion annealing. The gate $Al_2O_3$ dielectric 72 nm thick was formed with atomic layer deposition. The titanium gate was also fabricated using vacuum deposition. The leakage current through $Al_2O_3$ did not exceed $10^{-12}$ A at the gate voltage $|U_{gate}| < 10$ V. Modulation of the channel current $I_{ds}$ with the $U_{gate}$ voltage was observed in the range $T = (0.1 – 22)$ K, and under certain conditions it exceeded $10^3$ times. Static current-voltage characteristics $I_{ds} = f(U_{ds})$, dependences $I_{ds} = f(U_{gate})$ with stepwise and sawtooth changes in $U_{gate}(t)$ and different $U_{ds}$, dependences of $I_{ds}$ versus magnetic field ($I_{ds}=f(B)$) at different $U_{ds}$ were explored for different values of $U_{gate}$. At the field $B < 12$ T, the change in $I_{ds}$ attained more than $10^3$ times at a certain combination of $U_{ds}$, $U_{gate}$ and $T$. Some of the results obtained on MISFET with $L = 6$ micron at $T = 4.2$ K are given below.

## 3. Results and discussions

Pieces of curves $I_{ds} = f(t)$ with a stepwise change in $U_{gate}(t)$, for $U_{ds} = 0.4$ V and $B = 0$, 3.68 T, and 7.35 T are shown in Fig. 1 for the temperature $T = 4.2$ K. The magnetic field is directed normally to the PbSnTe:In surface. The dotted lines show the curves of approximation of sections $I_{ds}(t)$ in the functional form of

$$I_1(t) = I_{01}(t) + \Delta I_1 \cdot e^{-\frac{t-t_s}{\tau_1}}$$

and

$$I_2(t) = I_{02}(t) + \Delta I_2 \cdot (1 - e^{-\frac{t-t_s}{\tau_2}})$$

for the falling and growing curve sections, respectively. Here $t_s = 80$, 100, and 120 s are the $U_{gate}$ switching times. The falling sections are those in the interval $\Delta t = 100 \div 120$ s and the middle (red) curve at $t > 120$ s. The fitting parameters of $\tau_1$ or $\tau_2$ are shown near the dotted curves. It can be seen that the magnetic field strongly affects both the magnitude of the relative change in $I_{ds}$ upon switching (from less than a factor of 10 to more than a factor of 100) and the characteristic time constants, which change in a magnetic field by a factor of 15 – 30. The magnetic field can also change the apparent behavior of relaxation. So, for

example, in the region $t > 120$ s, at $B = 0$ or 7.35 T, the current $I_{ds}$ increases, while at $B = 3.68$ T, it decreases.

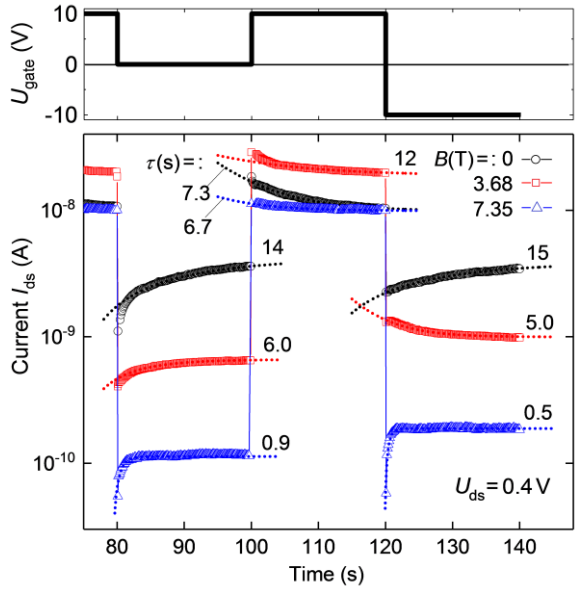


***Fig. 1.*** *Dependences* $I_{ds}(t)$ *for 3 values of* B *(below, figures and solid lines) for a stepwise change in* $U_{gate}$*, and approximation of* $I_{ds}$ *by exponential functions (dotted lines).* $U_{ds}$ *= 0.4 V,* T *= 4.2 K. The time constants* τ *are indicated near the curves. The* $U_{ds}(t)$ *plot is shown at the top.*

The dependences $I_{ds} = f(U_{gate})$ for a sawtooth change in $U_{gate}(t)$ with a period of 36 s for three values of $B$ and $U_{ds} = 0.4$ V are shown in Fig. 2.

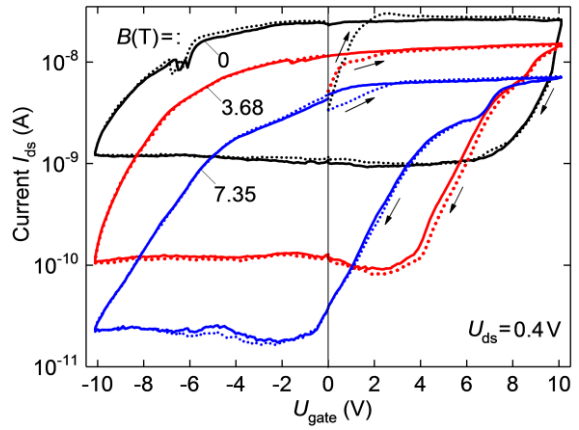


***Fig. 2.*** $I_{ds}$ *versus* $U_{gate}$ *characteristics of MISFET for constant* $U_{ds}$*=0.4 V and three values of* B *(shown in the figure).* T *= 4.2 K. The* $U_{gate}(t)$ *was swept in sawtooth waveform with period of 36 s. The sweep direction is indicated by arrows.*

For each value of $B$, two dependences are shown, measured one after another: the first one is dotted and the second one is solid. The directions of change in $U_{gate}(t)$ are shown by arrows. It can be seen from the figure that quite a good reproducibility for the two successive curves is observed with a pronounced hysteresis due to the recharging of the traps. The maximum relative change in $I_{ds}$ caused by $U_{gate}$ is close to 300 (at $B = 7.35$ T).

At a qualitative level, the presented results can be described as follows. First of all, for $I_{ds}$, the space charge limited current (SCLC) mode is supposed. In this case, the electrons injected from the $n^+$ source not only contribute to the current transport but are also captured by relatively "slow" traps, including those at the surface. At $U_{gate} > 0$, a negative charge is gradually accumulated on such traps, which causes the "dips" in $I_{ds}$ in Fig. 1 after switching $U_{gate}$ at $t = 80$ and 120 s, as well as a rapid decrease in $I_{ds}$ in Fig. 2 as $U_{gate}$ begins to decrease back after it reaches +10 V. And vice versa, the rapid increase in $I_{ds}$ with increasing $U_{gate}$ near $U_{gate} = -10$ V is qualitatively explained by the accumulation of a positive charge on surface traps (due to the ejection of electrons from them) at $U_{gate} < 0$. Numerous features on the curves in Fig. 2 are explained by the presence of traps of various types with a complex energy spectrum [6]. The degree of their population is important in the SCLC mode and changes differently with $U_{gate}$. Parameters of these traps can strongly depend on $B$, and the ionization energy of different traps grows differently with increasing $B$ [7]. This may be the reason why $B$ so strongly affects the shape of curves in Fig. 2 and the relaxation dependences in Fig. 1.

## 4. Conclusions

The channel current of the first created MISFET structure based on PbSnTe:In depends in a complex way on the magnetic field and, under certain conditions, can vary up to $10^3$ times in fields up to $B = 12$ T. The obtained results are qualitatively explained within the framework of a model that assumes the predominance of space charge-limited currents in the MISFET channel in the presence of various types of traps, including surface traps.

## Acknowledgements

This work was supported in part by the Russian Foundation for Basic Research, grant no. 20-02-00324.

## References

[1] B. A. Akimov, N. B. Brandt, S. A. Bogoslovskii, L. I. Ryabova, S. M. Chudinov. JETP Lett. **29**(1979)9.
[2] B. M. Vul, I. D. Voronova, G. A. Kalyuzhnaya, T. S. Mamedov, T. Sh. Ragimova. JETP Lett. **29**(1979)18.
[3] S.-Y. Xu et al. (21 co-authors). Nat. Commun. **3**(2012)1192(11).
[4] A. E. Klimov, V. A. Golyashov, D. V. Gorshkov, E. V. Matyushenko, I. G. Neizvestnyi, G. Yu. Sidorov, N. S. Pashchin, S. P. Suprun, O. E. Tereshchenko. Fiz.Tekhn.Polupr. **56**(2022)243
[5] A. E. Klimov, D. V. Krivopalov, I. G. Neizvestnyi, V. N. Shumsky, N. I. Petikov, M. A. Torlin, E. V. Fedosenko. Appl. Surf. Sci. **78**(1994)413.
[6] A. E. Klimov, V. N. Shumsky. Physica B **404**(2009)5028.
[7] A. N. Akimov, V. S. Epov, A. E. Klimov, V. V. Kubarev, N. S. Paschin. J. Phys.: Conf. Ser. **946**(2018)012016(8).

Sixth Asian School-Conference on Physics and
Technology of Nanostructured Materials
Vladivostok, Russia, 25 – 29 April, 2022

**III.o.04**

# Dependence of the Dzyaloshinskii-Moriya interaction and chiral damping effect on the roughness of the lower Pd layer in the Pd/Co/Pd system

A.V. Davydenko*, N.N. Chernousov, A.A. Turpak, A.G. Kozlov, A.S. Samardak
Laboratory of Spin-Orbitronics, Institute of High Technologies and Advanced Materials, Far Eastern Federal University, Vladivostok 690922, Russia

*e-mail: avdavydenko@gmail.com

**Abstract.** Domain wall propagation in the creep regime was studied in Pd($d_{Pd}$)/Co(0.7 nm)/Pd(3 nm) epitaxial structures in simultaneously applied in-plane and out-of-plane magnetic fields. The thickness of the bottom Pd layer varied from 3 to 10 nm. An increase in the thickness of the bottom Pd layer led to an increase in the interface roughness in the samples, while the distribution of the strains in the Co layers was not affected. Therefore, we investigated the influence of the roughness of the interfaces on the magnetic parameters of the samples. The Dzyaloshinskii-Moriya interaction field increased with increasing of the interface roughness from 17 ± 2 to 31 ± 3 mT but remained lower than domain wall anisotropy field. The chiral damping weight demonstrated a maximum of 0.994 with a thickness of the Pd bottom layer of 5 nm. The roughness of interfaces strongly influenced the asymmetry of domain-wall propagation in the combination of in-plane and out-of-plane magnetic fields.

## 1. Introduction

The Dzyaloshinskii-Moriya interaction (DMI) is an intriguing phenomenon that has recently attracted significant interest due to the possibility of using it in racetrack memory devices [1]. The DMI has a predominant contribution from the interfaces in multilayered heavy metal-ferromagnetic structures because the inversion symmetry is broken in the interface layers (interfacial DMI). The net interfacial DMI in symmetric multilayered systems should be absent because the effective contributions to the DMI from the bottom and top interfaces should compensate each other. However, non-zero DMI is observed in symmetrical systems, which is often explained by different properties of the lower and upper interfaces, such as deformations, structural quality, roughness, and sharpness [2].

In this paper, we investigate a series of Pd/Co/Pd samples with a constant Co thickness of 0.7 nm and a variable Pd bottom layer thickness since the interface roughness strongly depends on the thickness of the Pd bottom layer. We try to find out the influence of interface roughness on the creep of domain walls (DWs) and DMI. The experimental data are fitted by the extended dispersive stiffness theoretical model. The obtained results are discussed and analyzed.

## 2. Experiment

The samples were evaporated in an Omicron ultrahigh vacuum system, which consisted of a molecular beam epitaxy chamber and an analysis chamber interconnected with each other. Si(111) was used as the substrate, which was washed with isopropyl alcohol and distilled water before being loaded into the chamber. The substrates were then heated in situ at 800 K by indirect heating for 12 h. Immediately before deposition, the substrates were subjected to instantaneous direct current heating at 1400 K seven times for 5 s and slowly cooled down to 300 K. All the metals were evaporated from high temperature effusion cells.

The deposition rates were monitored by a quartz crystal microbalance, which was calibrated by means of reflection high energy electron diffraction (RHEED). The lattice period of the metal layers during growth and their structure were analyzed using RHEED. Epitaxial Pd($d_{Pd}$)/Co(0.7 nm)/Pd(3 nm) trilayers were grown on a Si/Cu(2 nm) surface. The thickness of the bottom Pd layer $d_{Pd}$ was varied from 3 to 10 nm. The roughness of the lower Pd layer was evaluated by scanning tunneling microscopy.

The magnetic hysteresis loops of the samples were measured using a vibrating sample magnetometer with applied magnetic fields of up to 2.2 T. The magnetic structure was investigated by a magneto-optical Kerr effect (MOKE) microscope. The MOKE microscope was equipped with a handmade coil that applied out-of-plane (OOP) magnetic fields and an in-plane (IP) electromagnet. The OOP coil was used in pulse mode and produced magnetic fields with an amplitude of up to 60 mT and a width down to 2 ms. The scheme for the measurement of the DW velocity was as follows. Using focused ion etching, an artificial defect was made on the surface of the sample, on which a circular domain was stably nucleated. A constant IP magnetic field was switched on. The pulse of the OOP magnetic field of the calibrated time-length was applied. The distance at which the DW propagated was measured from a snapshot of differential magnetic contrast made by the Kerr microscope. The velocities of the left and right DWs were measured separately, after which the results were averaged.

## 3. Results and discussions

The RHEED streaks confirm the well-ordered crystalline structure of the layers. The bottom Pd layer demonstrates a volume lattice parameter at the thickness of 3 nm that does not change with further increasing of the Pd bottom layer thickness up to 10 nm. The Co layers grown on top of the lower Pd layers are strained. As the Co layers grow, the strains partially relax. Because the thickness of the Co layers was only 0.7 nm, the lattice parameter at the top of the Co layers is not restored to the volume lattice parameter of Co. The root-mean-square (RMS) roughness of the bottom Pd layer increases from 0.24 to 0.8 nm in the thickness interval of the Pd bottom layer from 3 to 10 nm (Fig. 1).

As the of Pd of the bottom layer thickness increases, the perpendicular magnetic anisotropy field increases nearly linearly from 1.24 to 1.32 T, which may be explained by an increase in roughness and, hence, a decrease in the demagnetizing coefficient along the normal surface of the samples. A saturation magnetization remains nearly the same in the whole series of samples.

The $v(H_x)$ curves demonstrate strong asymmetry. The velocity curves of the samples were approximated by an extended dispersion stiffness model [3]. The fitting parameters were a DMI field $H_{DMI}$, a DW anisotropy field $H_B$, a correlation length $\xi$, a chiral damping weight $\chi^*$, and a characteristic velocity $v_0^*$ . A fitting program searched for the minimal residual dispersion by means of variation of the fitting parameters. The dependence of the DMI field on the thickness of the lower Pd layer is shown in Fig. 2. It monotonously increases with increasing of the interface roughness from 17 ± 2 to 31 ± 3 mT. The DMI field near doubles at the extreme points of the $\mu_0 H_{\mathrm{DMI}}(d_{\mathrm{Pd}})$ dependency. This result confirms the conclusions of our recent article in which we observed an increase in DMI in sputtered systems with increasing interface roughness [4]. Nevertheless, the absolute values of the DMI fields remain lower than those of the anisotropy fields regardless of the interface roughness, which indicates that the DWs have a transient Bloch-Neel structure in the investigated system.

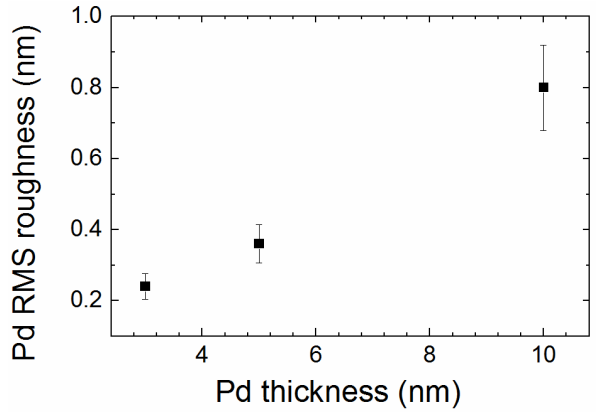


***Fig. 1.*** *Dependence of the RMS roughness of the Pd bottom layer on the thickness of the Pd bottom layer.*

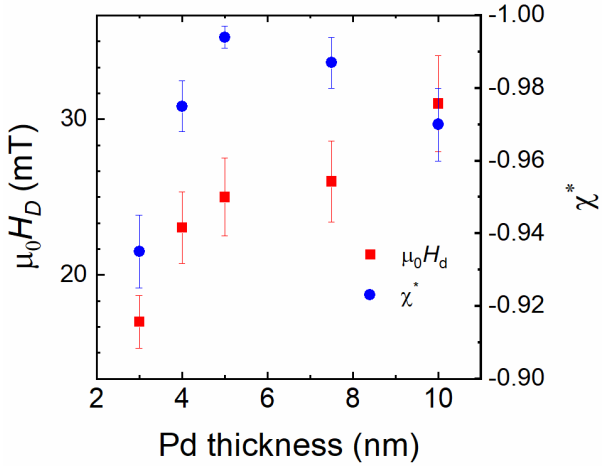


***Fig. 2.*** *Dependencies of the DMI field and chiral damping weight on the thickness of the Pd bottom layer in the Pd/Co/Pd epitaxial system.*

As the thickness of the lower Pd changes from 3 to 5 nm, the absolute value of the chiral damping weight increases and then, with further increasing of the thickness of the bottom layer of Pd, decreases as shown in Fig. 2. Strictly speaking, the physical nature of the asymmetry of the curves $v(H_x)$ is a subject of discussion. In some studies, this effect is called induced chirality, or additional asymmetry. Relatively low changes of the chiral damping coefficient strongly influence the behavior of $v(H_x)$ curves and increase the asymmetry between parts of the $v(H_x)$ curves measured in positive and negative IP magnetic fields.

## 4. Conclusions

We investigated the creep of DWs in the combination of in-plane and out-of-plane magnetic fields in a series of epitaxial Cu(2 nm)/Pd(3–10 nm)/Co(0.7 nm)/Pd(3 nm) samples. The thickness of the Pd bottom layer defines the roughness of the interface in this system. The measured velocity curves, $v(H_x)$, are fitted with an extended dispersive elasticity model. The Dzyaloshinskii-Moriya interaction (DMI) field increases with increasing interface roughness from 17 ± 2 to 31 ± 3 mT. The absolute value of the chiral damping coefficient increases from 0.935 to 0.994 with an increase of the thickness of the Pd bottom layer from 3 to 5 nm, and then decreases to 0.97 at the thickness of the Pd bottom layer of 10 nm.

## Acknowledgements

We acknowledge the Russian Ministry of Science and Higher Education for state support of scientific research conducted under the supervision of leading scientists in the Russian Institution of Higher Education, scientific foundation, and state research centers (Project No. 075-15-2021-607) and the state task (Project No. 0657-2020-0013).

## References

[1] S. Parkin, S. H. Yang. Nat. Nanotech. **10** (2015) 195.
[2] A. W. J. Wells, P. M. Shepley, C. H. Marrows, T. A. Moore. Phys. Rev. B **95** (2017) 054428.
[3] A.V. Davydenko, A.G. Kozlov, M.E. Stebliy, A.G. Kolesnikov, N.I. Sarnavskiy, I.G. Iliushin. Phys. Rev. B **103** (2021) 094435.
[4] A. S. Samardak, A.V. Davydenko, A.G. Kolesnikov, A.Yu. Samardak, A.G. Kozlov, Bappaditya Pal, A.V. Ognev, A.V. Sadovnikov, S.A. Nikitov, A.V. Gerasimenko, I.H. Cha, Y.G. Kim, G.W. Kim, O.A. Tretiakov, Y. K. Kim. NPJ Asia Materials **12** (2020) 51.

Sixth Asian School-Conference on Physics and
Technology of Nanostructured Materials
Vladivostok, Russia, 25 – 29 April, 2022

**III.o.05**

# Magnetoplasmonic structures with nanostructured layers of bismuth-substituted iron garnets

T.V. Mikhailova*,1, S.D. Lyashko[1], E.V. Skorokhodov[2], S.V. Osmanov1, A.V. Karavainikov[1], A.L. Kudryashov[1], A.S. Nedviga[1], S.A. Gusev[2], and A.N. Shaposhnikov[1]

[1] V.I. Vernadsky Crimean Federal University, 4 pr. Vernadskogo, Simferopol 295007, Russia
[2] Institute for Physics of Microstructures of the Russian Academy of Sciences (IPM RAS), 7 Academicheskaya St., Nizhny Novgorod 603087, Russia

*e-mail: taciamikh@gmail.com

**Abstract.** Structural, optical and magneto-optical characteristics of $Bi_{2.3}Dy_{0.7}Fe_{4.2}Ga_{0.8}O_{12}$ / Au magnetoplasmonic structures formed on the pre-structured substrate of gadolinium gallium garnet in the form of one-dimensional arrays of nanostrips and two-dimensional arrays of nanoholes were considered. An increase in the initial period of structuring during the sequential formation of layers and resonance features of the structures in the wavelength range from 400 to 950 nm were demonstrated.

## 1. Introduction

More recently it has been shown that optical, magneto-optical and optomagnonic effects not previously observed in continuous nanoscale films present in structured iron garnets (metasurfaces of iron garnets) and its quite promising for photonics and spintronics applications [1-3]. Research and development of possible experimental methods for the formation of metasurfaces of iron garnets are actual tasks in these field in addition to comprehensive modeling and experimantal studies of the influence of structural parameters to their properties. This investigation presents the analysis of morphology and structural parameters, optical and magneto-optical properties of nanostructured films of bismuth-substituted dysprosium iron garnet with nominal composition $Bi_{2.3}Dy_{0.7}Fe_{4.2}Ga_{0.8}O_{12}$ (BiDyIG) and magnetoplasmonic structures on their basis. It was proposed to carry out the structuring of film by synthesizing them on structured substrate of gadolinium gallium garnet (GGG).

## 2. Experiment

One-dimensional and two-dimensional gratings in the form of nanosrips and nanoholes on GGG surface were formed by electron beam lithography, ion and plasma chemical etching. A positive high-resolution PMMA 950 C2 resist and special multilayer masks of metal V, Cu and Ta films were used in lithography to create the necessary grating periods and etching thicknesses. We studied the dynamics of crystallization of BiDyIG layers with nanosized thicknesses from 30 to 110 nm on GGG substrates without nanostructuring before the formation of iron garnet on the surface of structured GGG. As a result, a BiDyIG film thickness of about 60 nm was chosen for the formation of a meander type structure, since the initial surface structuring has a period $P$ from 400 to 800 nm for structures in the form of stripes array and from 800 to 1000 nm for structures in the form of nanoholes array. The depth of GGG surface structuring is 70 nm. The deposition of BiDyIG layer on nanostructured GGG was carried out on a URM 3-279.014 setup in an oxygen-argon mixture using an ion-beam source "Kholodok-1". BiDyIG was crystallized by annealing in air at atmospheric pressure and a temperature of 700°C. The duration of crystallization annealing was 60 min. The sample were heated and cooled at a temperature rate of about 5°C/min during annealing process. Metal layer of structure GGG / BiDyIG / Au was synthesized using the magnetron sputtering method. The thickness of layers, structure and topology of the surface of synthesized samples were studied using the INTEGRA scanning probe microscope (NT-MDT) and the equipment of the Central Collective Use Center "Physics and Technology of Micro- and Nanostructures" (electron microscope SUPRA 50 VP with a hardware-software complex ELPHY PLUS electronic lithography, NEON 40 two-beam system, etc.). Semicontact atomic force microscopy (AFM) was applied to measure surface parameters: root mean square roughness *rms* and polycrystalline size *Z*. The measurements were carried out by cantilevers of HA_HR ETALON. To visualize the optical response of structures in nanoscale the scanning near-field optical microscopy (SNOM) were used [4]. The structures were examined by linearly polarized ligth with a wavelength of 630 nm from the bottom side of substrate using aspherical lens with a low numerical aperture $NA$ = 0.3. The ligth was collected in the near field zone from the sample surface through the nanosized aperture of the probe SNOM_NC and objective lens ($NA$ = 0.7, 100x).

Spectra of transmittance and rotation angle of polarization plane (optical and magneto-optical) were measured by handmade automated spectropolarimeter in the field 2 kOe at normal incidence. The rotation angle of polarization plane was fixed by compensation of the transmittance to minimal values using fixed analyzer and rotating polarizer.

Faraday rotation $\theta_F$ were determined as half-difference of two values $\theta_F(+H)$ and $\theta_F(-H)$ obtained for two opposite directions of magnetic field:

$$\theta_F = \frac{\theta_F(+H) - \theta_F(-H)}{2}. \quad (1)$$

Rotation difference $\theta_R$ due to magnetization reversal in opposite fields were determined as half of the sum of two values $\theta_F(+H)$ and $\theta_F(-H)$:

$$\theta_R = \frac{\theta_F(+H) + \theta_F(-H)}{2}. \quad (2)$$

## 3. Results and discussions

Figure 1 shows AFM images of synthesized metasurfaces with different geometric parameters and structuring type. The crystallized BiDyIG layer deposited

the first in GGG / BiDyIG / Au structure has a pronounced polycrystalline structure with a large average grain size *AGS* = 136 nm. In this case, iron garnet layer repeats the nanostructure on the surface of GGG substrate retaining the original topology. A similar situation occurs after the synthesis of Au layer. However, an increase in the average value of period *P* of the structure is observed with successive deposition of layers. Thus, the value of *P* is 645 nm at slot width *W* = 290 nm in the case of BiDyIG sedimentation and 640 nm (*W* = 300 nm) in the case of Au sedimentation for nanostructure on GGG as an array of nanostrips with *P* = 600 nm (*W* = 242 nm).

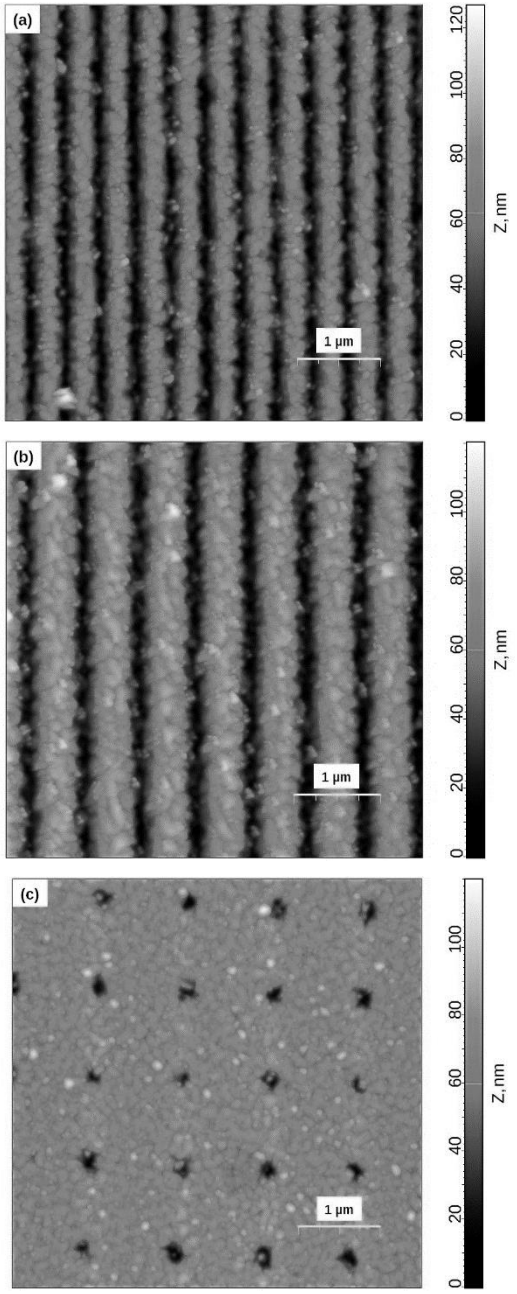


***Fig. 1.*** *AFM images of surface of BiDyIG layer on different structured areas of GGG substrate with P of 400 nm (a), 600 nm (b) and 1000 nm (c).*

According to SNOM-investigation of structures and structured GGG substrate without deposited layers, the highest intensity of electromagnetic light field is observed for the slit regions. The intensity distribution weakly depends on the polarization position of the incident light on the structure.

Figure 2 shows the relative transmission spectrum and rotation spectra of the structure with *P* = 600 nm in comparison with the same data for the unstructured region of the sample. Three characteristic resonances can be distinguished in the spectra at 634, 675 and 815 nm. The most pronounced resonance is at 675 nm with a 20% increase in transmittance and the appearance of a significant difference in rotations in opposite fields.

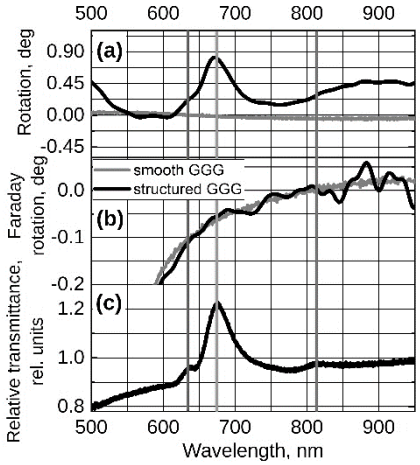


***Fig. 2.*** *Rotation angels spectra* $\theta_R$ (*a*) *and* $\theta_F$ (*b*) *of the structure with P = 600 nm (black lines) in comparison with the same data for unstructured region of the sample (gray lines) and its relative transmittance spectrum (c).*

## 4. Conclusions

Formation features of iron garnet metasurface of meander-type and magnetoplasmonic structure based on it were studied using scanning probe microscopy methods. An increase in the initial period of structuring during the sequential formation of layers were demonstrated. An enhancement in the rotation of polarization plane of light at the resonant wavelength of the structure was found.

## Acknowledgements

The development of technique of electron beam lithography in order to obtain one-dimensional and two-dimensional gratings on the surface of GGG substrates was carried out using technological and analytical equipment of the Common Research Center "Physics and Technology of Micro- and Nanostructures" of the Institute for Physics of Microstructures RAS.

The authors acknowledge support by Russian Science Foundation (project no. 19-72-20154).

## References

[1] D. O. Ignatyeva, D. Karki, A. A. Voronov, M. A. Kozhaev, D. M. Krichevsky, A. I. Chernov, M. Levy, V. I. Belotelov. Nature communications **11**(2020)1.

[2] P. E. Zimnyakova, D. O. Ignatyeva, D. Karki, A. A. Voronov, A. N. Shaposhnikov, V. N. Berzhansky, M. Levy, V. I. Belotelov. Nanophotonics **11**(2022)119.

[3] D. Ignatyeva, V. Ozerov, M. Hamidi, A. Chernov, V. Belotelov. AIP Conference Proceedings **2300**(2020)020045.

[4] Yu. E. Vysokikh, T. V. Mikhailova, S. Yu. Krasnoborodko, A. S. Kolomiytsev, O. I. Ilin, A. N. Shaposhnikov, V. N. Berzhansky, M. F. Bulatov, D. V. Churikov, V. I. Shevyakov. Journal of Magnetism and Magnetic Materials **543**(2021)168167.

Sixth Asian School-Conference on Physics and
Technology of Nanostructured Materials
Vladivostok, Russia, 25 – 29 April, 2022

**III.o.06**

# Features of magnetic and magneto-optical properties of lanthanum manganite microparticles

R.D. Ivantsov*,[1], M.M. Mikhailov[2], I.S. Edelman[1], G.Y. Yurkin[3]

[1] Kirensky Institute of Physics SB RAS, Krasnoyarsk, 660036, Russia
[2] Tomsk State University of Control System & Radioelectronics, Tomsk, 634050, Russia
[3] Siberian Federal University, Svobodny Av., 79, Krasnoyarsk, 660041, Russia

*e-mail: ird@iph.krasn.ru

**Abstract.** For $La_{1-x}Sr_xMnO_3$ powders prepared by the solid-phase reaction method using various thermal regimes and x values, the temperature dependences of magnetization, circular magnetic dichroism (MCD), and diffuse reflectance spectra were studied. The powders synthesis at temperatures of 800–900 °C for 2 h leads to the formation of a multiphase state. The higher temperatures and duration of synthesis lead to the formation of two predominant magnetic phases with the Curie temperature ($T_C$) of about 250 and 360 K. Correlation is established between magnetic states of the powder and the shape of the diffuse reflection spectra. The strong red shift of the MCD spectrum for the $La_{1-x}Sr_xMnO_3$ powder is revealed comparing to the MCD spectra of $La_{1-x}Sr_xMnO_3$ films available in literature.

## 1. Introduction

The manganite $R_{1-x}M_xMnO_3$, where R is the trivalent lanthanide and M is the divalent alkaline earth metal attracts considerable attention because of chemical stability, strong correlation between magnetism and transport properties and have potential for such applications as magnetic field sensors, giant magnetoresistive (GMR) elements in spintronic devices, and for creation of thermal stabilized coatings. In Ref. [1], strong changes were revealed of the $La_{1-x}Sr_xMnO_3$ diffusion spectrum shape in visible region in dependence on the synthesis conditions. As this material possesses ferromagnetic order, it is interesting to consider the correlations between the revealed optical peculiarities and the powder magnetic properties which are formed by the different technological regimes and x-values. The magneto-optical MCD and Kerr effect in dependence on the light wave energy and temperature were investigated here alongside with the magnetization dependences on temperature and an external magnetic field to obtain additional information about the samples magnetic phases.

## 2. Experiment

Two series of $La_{1-x}Sr_xMnO_3$ powders were fabricated by solid-state reaction method [1] from the mixture of $La_2O_3$, $MnCO_3$ and SrCO at different synthesis parameters. For the first series of samples with fixed x=0.175, the synthesis temperature changed from 900 to 1200 °C, for the second series two-stage annealing of the samples at 800 and 1200 degrees was used, while x varied from 0.15 to 0.25.

## 3. Results and discussions

For all samples, the effect of the synthesis thermal regimes and Sr concentration on the dependences of magnetization on temperature M(T) and external magnetic field M(H) were established, these results substantially supplemented the XRD data. In the derivative of magnetization with respect to temperature, M(T)/dT, curves (Fig.1.), the peak was observed for all samples at 42 K which was in the total agreement with XRD patterns and corresponded $Mn_3O_4$ phase. The synthesis temperatures exceeding 1000 °C in the one-stage regime and synthesis in two-stage regime lead to formation of two coexisting magnetic phases (1) with x close to 0.185 and Curie temperature of about 250 K and (2) with x close to 0.4 and Curie temperature of about 360 K.

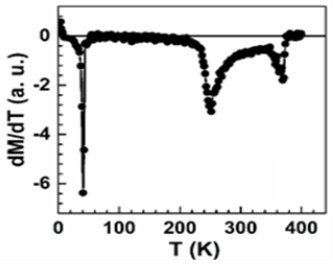


***Fig. 1.*** *Derivative of magnetization with respect to temperature for sample x=0.175 1200 °C, 6 h.*

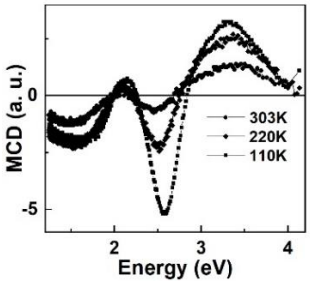


***Fig. 2.*** *MCD spectra at different temperatures for sample x=0.175, 800 °C, 2 h +1200 °C, 2 h.*

For all samples obtained, correlation between M(T) dependences and diffuse reflection spectra was observed. Magnetic circular dichroism (MCD) was studied for the manganite powder samples for the first time. In all cases, the character of the spectral dependence of the MCD (Fig. 2) coincides in shape with the MCD literature data of a thin La0.7Sr0.3MnO3 film, but the entire spectrum is rigidly shifted to lower energies by about 0.5 eV. The most intense maxima of the MCD spectrum in the region of 2.2 and 3.3 eV are assigned to spin-allowed and spin-forbidden electronic transitions in Mn3+ and Mn4+ ions. It should be noted that the MCD data confirmed the assumption of the coexistence of several magnetic phases in the samples under study.

## References

[1] M. Mikhailov, V. Vlasov, T. Utebeko et.al., Mater. Res. Bull. **89** (2017) 154.

Sixth Asian School-Conference on Physics and
Technology of Nanostructured Materials
Vladivostok, Russia, 25 – 29 April, 2022



# Investigation of the dependence of current induced magnetization switching in the W-CoTb-Ru structure

Zh.Zh. Namsaraev*, M.A. Bazrov, M.E. Letushev, M.E. Stebliy
Laboratory of Spin-Orbitronics, Institute of High Technologies and Advanced Materials, Far Eastern Federal University, Vladivostok 690922, Russia

*e-mail: namsaraev.zhzh@dvfu.ru

**Abstract.** The study of ferrimagnets is an important direction in the development of spintronics since these materials can combine the advantages of ferromagnetic and antiferromagnetic materials. Of particular interest is the compensation point – the state with zero net magnetization. In this work effect of spin-polarized current on the magnetic structure has been investigated in the W/CoTb/Ru ferrimagnetic system. It is shown that using current pulses it is possible to reversibly switch the orientation of the magnetization in the structure. The effectiveness of such an impact depends on the thickness of the ferrimagnet layer and the position of the compensation point.

## 1. Introduction

Local control and detection of the magnetization orientation by the means of electric current in magnetically ordered media is an important fundamental area of research with the possibility of practical application. A promising medium for such research is ferrimagnets (FIM): multicomponent materials with antiparallel ordered magnetic sublattices formed by different atoms. Zero resulting magnetic moment can be achieved in a such system, which makes it possible to combine the advantages of ferromagnets (FM) and antiferromagnet (AFM): high stability and high dynamics of the antiferromagnet [1], and ease of states registration by means of magnetotransport methods, as in a ferromagnet, even under the condition of zero magnetization, due to the different nature of the magnetic moments in the atoms of rare earth and ferromagnetic elements. Thus, the study of the mechanisms of FIM remagnetization under the action of a spin-polarized current can give important theoretical and practical results for the development of spintronics.

## 2. Experiment

The compensation point can be obtained as a result of changing one of the three parameters, with other fixed: the mutual concentration of atoms in the CoTb alloy [2]; 2) sample temperature [3]; 3) FIM layer thickness [4]. In a number of works, it is stated that in the vicinity of the compensation point, the maximum ratio of the effective magnetic field induced by the current to the conduction current density can be achieved [5]. In such works, the state of compensation is achieved by changing the composition of the alloy. In this work, the effect of current-induced magnetization reversal is considered in the case when the compensation state is achieved by changing the thickness of the FIM layer. A series of samples of the composition W(4)/$Co_{56}Tb_{44}$(x)/Ru(2 nm), x from 1.5 to 7 nm, was prepared by magnetron sputtering on $Si/SiO_2$ substrates, Fig.1a. To study the magnetic transport properties the Hall bar structures were prepared by photolithography and ion-plasma etching, Fig. 1b.

## 3. Results and discussions

A study of the magnetic properties showed that with the specified composition, the compensation state corresponds to a thickness of 4 nm, Fig. 1d. Decreasing thickness brings the sample to the Co-rich state: the magnetic moments of Co atoms are oriented along the external field, while Tb is antiparallel. An increase in thickness, on the contrary, to the Tb-rich state. The passage of current pulses through the Hall bar structure in the presence of a constant in-plane field Bx leads to a reversible switching of the magnetization orientation in the structure from the up-state to the down, Fig. 1c, because of the spin-orbit torque effect [6]. Switching current Ic was noted as a parameter indirectly corresponding to the efficiency of current-induced magnetization reversal. In Fig.1d dependences of the magnetic moment and switching current on the FIM layer thickness are compared. The lower switching current corresponds to the minimum thickness of the FIM layer.

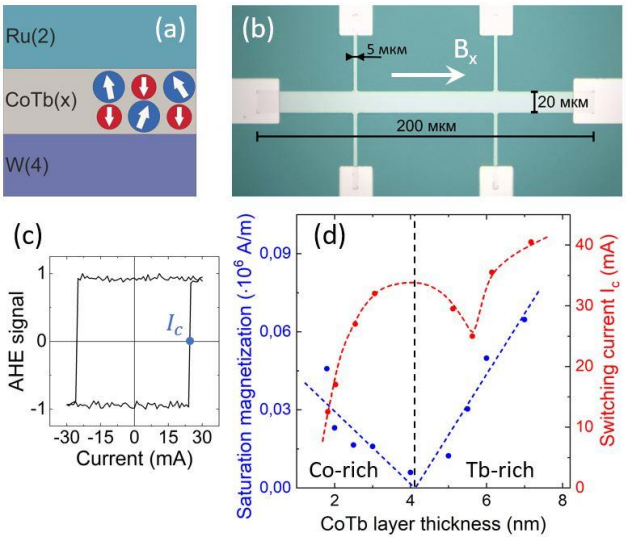


**Fig. 1.** (a) Composition of the investigated structure, thickness in nm. (b) Image of the Hall bar structure with orientation of the in-plane external field. (c) Hysteresis loop obtained by current propagation through the Hall bar structure. (d) Saturation magnetization and switching current versus CoTb layer thickness.

However, there is a local minimum on the dependence, which does not coincide with the compensation point, as might be expected. The displacement can be explained by the heating of the Hall structure in the process of current. Upon heating, the magnetic moment of Tb atoms decreases, which leads to a shift in the compensation point to the region of large thicknesses. In the research, several

additional studies have been carried out and the obtained results have been interpreted.

## 4. Conclusions

The effect of current-induced magnetization reversal of the W/CoTb/Ru structure is studied as a function of the thickness of the ferrimagnet layer. It is shown that the efficiency of current exposure has a complex dependence, determined both by the thickness of the FIM layer and by the value of the saturation magnetization, which changes during the passage of current as a result of heating. The maximum efficiency corresponds to the minimum thickness, however, the dependence of the switching current has a local minimum in the region of the compensation current.

## Acknowledgements

This work has been supported by the grants the Russian Science Foundation, RSF 21-72-00138, a grant of the Government of the Russian Federation for state support of scientific research conducted under supervision of leading scientists in Russian institutions of higher education, scientific foundations, and state research centers of the Russian Federation (Project No. 075-15-2021-607), and the Russian Ministry of Science and Higher Education (State Task No. 0657-2020-0013).

## References

[1] Sala, G., Krizakova, V., Grimaldi, E. et al. Real-time Hall-effect detection of current-induced magnetization dynamics in ferrimagnets. Nat Commun 12, 656 (2021).
[2] Joseph Finley, Luqiao Liu, Spin-Orbit-Torque Efficiency in Compensated Ferrimagnetic Cobalt-Terbium Alloys. Phys. Rev. Applied 6, 054001 (2016).
[3] Yuushou Hirata, Teruo Ono, Correlation between compensation temperatures of magnetization and angular momentum in GdFeCo ferrimagnets. Phys. Rev. B 97, 220403 (2018).
[4] Birgit Hebler, Alexander Hassdenteufel, Manfred Albrecht, Ferrimagnetic Tb–Fe alloy Thin Films: composition and Thickness Dependence of Magnetic Properties and all-Optical switching. Frontiers in Materials (2016).
[5] Yunzhuo Wu, Xiaoxue Zeng, Jiangwei Cao, Spin–orbit torque-induced magnetization switching in Pt/Co–Tb/Ta structures. Appl. Phys. Lett. 118, 022401 (2021).
[6] A. Manchon, I. M. Miron, P. Gambardella, Current-induced spin-orbit torques in ferromagnetic and antiferromagnetic systems. Rev. Mod. Phys. 91, 035004 (2019).

Sixth Asian School-Conference on Physics and
Technology of Nanostructured Materials
Vladivostok, Russia, 25 – 29 April, 2022

**III.o.08**

# Effects of constant, pulse and pulse-reverse current modes on the electrodeposition of NiFe films

A.N. Kotelnikova*, T.I. Zubar, T.I. Usovich, M.I. Panasyuk, V.A. Fed'kin, O.D. Kanafiev, A.V. Trukhanov

SO "SPC NAS of Belarus for Materials Science", 220072, Minsk, Petrusya Brovki street, 19, Belarus

*e-mail: anna.kotelnikova.98@mail.ru

**Abstract.** The effect of current modes on composition, crystal structure and microstructure was investigated in this work. For this purpose, NiFe films were obtained using stationary, pulsed and pulse-reversed electrodeposition. The films composition, crystal structure and surface microstructure were studied. It has been shown that films obtained in direct current have less concentration of Fe (36.4%) then films obtained in pulse current (42.15%). And the sample obtained in pulse-reversed mode have the Fe concentration of 27.5%. It has been shown that all the samples have a Ni face-centered cubic lattice. Direct current and pulse current films have a smooth surface, while a pulse-reverse current film surface is covered by volumetric cauliflower-like microstructure. The model of saccharin adsorption effect on film growth mechanism in direct and alternating current modes was described in this work.

## 1. Introduction

Electrodeposited NiFe alloys are widely used in microelectronics due to their magnetic softness. In particular, they are used to create magnetic recording heads and hard disk media. The main advantage of the electrodeposition method is the ability to apply thin films (both nano- and micro-dimensional) on parts of any shape. The use of different compositions of electrolytes, as well as changes in the technological parameters of deposition (such as the mode of current supply, current density, etc.) make it possible to obtain alloys with different compositions and different microstructure of films, which accordingly affects the magnetic properties of materials [1–4].

## 2. Experiment

In this study NiFe films were electrochemically deposited from an electrolyte of the following composition: $NiSO_4 \cdot 7H_2O$ — 210 g/L, $NiCl_2 \cdot 6H_2O$ — 20 g/L, $H_3BO_3$—30 g/L, $MgSO_4 \cdot 7H_2O$ — 60 g/L, $FeSO_4 \cdot 7H_2O$ — 15 g/l, $KNaC_4H_4O_6 \cdot 4H_2O$ (Rochelle salt) —30 g/l, ascorbic acid — 2 g/l, saccharin — 2 g/l. The films were deposited on polished steel substrates at 35 °C and a solution pH of 2.3. The current density was 25 mA/cm2, which, under these conditions, corresponds to a deposition rate of 25 μm/h for synthesis at a constant current. The films were deposited in direct current, pulsed current, and pulse-reverse current modes. The deposition parameters are presented in Table 1.

***Table I.*** *Technological parameters for obtaining NiFe films at constant, pulse and pulse-reverse current*

| Sample | Pulse duration, s | Pause duration, s | Reverse pulse duration, s | Total deposition time, min |
|---|---|---|---|---|
| *DC* | 3600 | - | - | 60 |
| *PC* | 0.1 | 0.1 | - | 120 |
| *PRC* | 0.1 | 0.095 | 0.005 | 126 |

Deposition time was chosen as follows to obtain fims with almost the same thikness. DC film was deposited for 60 minutes. PC film was deposited for 120 minutes (as current flowed only during ½ of all time) so effective deposition time was 60 minutes. Full deposition time for pulse-reverse mode was calculated by the Equation 1:

$$t_{FD} = t_{ED} \times \frac{t_C + t_A + t_{Off}}{t_C - t_A} \quad (1)$$

Where $t_{FD}$ is full deposition time, s; $t_{ED}$ is effective deposition time, s; $t_C$ is duration of cathodic pulse, s; $t_A$ is duration of anodic pulse, s; $t_{Off}$ is duration of pause, s.

## 3. Results and discussions

The percentage of iron obtained from the analysis of energy-dispersive X-ray spectra is presented in the Table 2. There is an increase in the concentration of Fe during the transition from stationary mode (36.4%) to pulse mode (42.15%). The reason for the increase in the Fe content is the feature of the initial stages of sedimentation. In the early stages of deposition, the widely described anomalous deposition of iron is observed, accompanied by the formation of iron-rich layers [5–6]. The pulse mode is a special case of the stationary one. It consists of repeated initial stages of a stationary mode, which means that layers enriched with iron are formed not only at the beginning of deposition, but throughout its entire length.

There is a decrease in the Fe content during the transition to pulse-reversed mode (27.5%). This is due to the difference in the dissolution rates of nickel and iron. Pulse-reversed mode includes stage of the films short-term dissolution when the polarity of the current is reversed. Iron has a lower electrode potential (-0.44 V) than nickel (-0.24 V), which means iron is more prone to oxidation and dissolves faster under the action of the reverse current. Thus, the iron content in the film is reduced.

Figure 1 and Table 2 demonstrate results of XRD investigations of the NiFe films obtained by the different modes. The number of well-distinguished peaks can be observed on the XRD patterns. The most intense and characteristic peaks are 42-43 deg. (corresponding to the Ni atomic plane (111) and 50-51 deg. (corresponding the Ni atomic plane (200). This indicates that these alloys have a face-centered cubic lattice. Consequently, at the initial stage of electrodeposition of the Ni – Fe alloy, nickel adatoms are the first to be deposited. They determine the type of the formed crystal lattice of the alloy. Iron atoms replace the latter at the nodes of the crystal lattice, causing internal stresses. Broadened peaks in the diffraction

patterns indicate a small grain size and high internal stresses in the lattice. A decrease in the intensity and increase in the width at the half- height of the (111) peak was observed for PRC sample, while there are no significant differences for DC and PRC samples. Increase in the intensity of the (200) peak was observed for PRC sample. Width at the half- height of the (200) peak decreases from DC through PC to PRC sample. Table 2 shows that the CSR was 6 nm for both DC and PRC samples. Then, an increase in CSR to 7 nm was observed for sample PC. Crystal lattice parameters a and V are almost the same for all samples

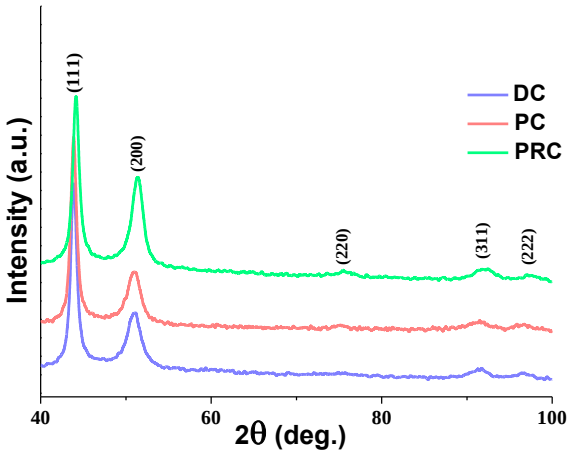


***Fig. 1.*** *X-ray diffraction data of NiFe films deposited in DC, PC and PRC modes.*

***Table II.*** *Technological parameters for obtaining NiFe films at constant, pulse and pulse-reverse current.*

| Sample | at. Fe, % | CSR, nm | a, Å | V, Å |
|---|---|---|---|---|
| *DC* | 36.40 | 6±1 | 3.570 | 45.50 |
| *PC* | 42.15 | 7±1 | 3.571 | 45.54 |
| *PRC* | 27.51 | 6±1 | 3.577 | 45.77 |

The surface microstructure of NiFe films, examined by SEM, is shown in Figure 2. The PT sample has a smooth surface with a large number of pores. The surface of sample PC0.1 is slightly less smooth, but does not contain pores. The surface of the PRC0.005 sample is covered with volumetric structures in the form of "cauliflower" [7].

Such a dramatic modification of the surface microstructures is due to the difference in the saccharin adsorption during electrodeposition in direct and alternating current modes. In case of DC or PC deposition saccharine is well adsorbed at the sample surface and it inhibits vertical grain growth. As result smooth and bright deposit forms. Whereas in PRC deposition, anodic pulses lead to faster saccharine desorption in the bulk of electrolyte leading to decrement of its vertical growth inhibitor activity. Thus, grains vertical growth was increased and contributed to the development of volumetric microstructures on the deposit surface [8].

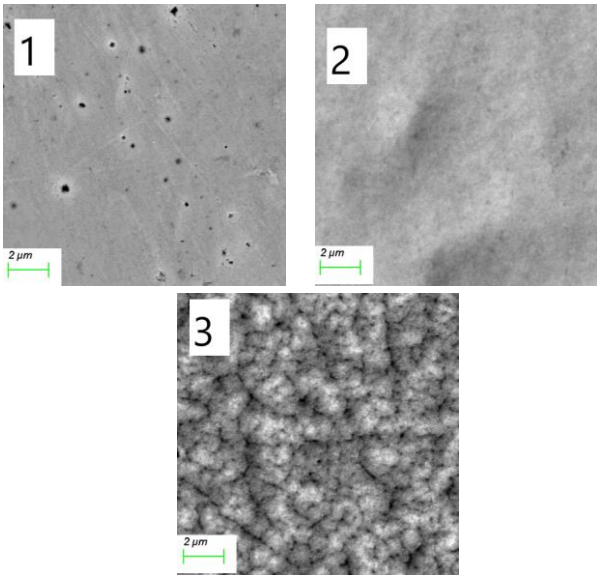


***Fig. 2.*** *Microstructure of the surface of NiFe films, investigated using SEM: 1-DC, 2-PC, 3-PRC.*

## 4. Conclusions

A set of NiFe alloy films was obtained using direct, pulse and pulse-reverse electrodeposition. The samples had a composition from 27.5 to 42.15 at % Fe, with differences caused by change in current modes. The PC film had a higher Fe content (42.15 at %) as compared to DC film (36.40 at %), what is the result of more anomalous character of codeposition in PC mode. The PRC film Fe content, on the contrary, was lower than those of the DC and PC films. The reason for this is the faster Fe oxidation and dissolution during anodic pulses. XRD studies of the crystal structure have shown that the most intense and characteristic peaks are corresponds to Ni atomic planes for all samples. The unit cell parameter is almost the same for DC and PC samples, but increases from 3.571 to 3.577 Å and from 45.54 to 45.77 Å3 with transition from pulse to pulse-reverse electrodeposition. The reason for the extension of the crystal lattice can be the effect of the chemical composition. The microstructure was investigated using SEM. DC and PC samples had a smooth surface while PRC sample had surface covered by volumetric microstructures. Such a radical change in the surface is probably caused both by a change in the current supply mode and by changes in the adsorption of saccharin during cathodic and anodic pulses.

## References

[1] D. Flynn [et al.]. IEEE Trans. Magn. **46**(2010)979.
[2] T. I. Zubar [et al.]. J. Electrochem. Soc. **166** (2019)173.
[3] Y. Sknar [et al.]. East.-Eur. J. Enterp. Technol. **4**(2017)4.
[4] H. L. Seet [et al.]. J. Alloys Compd. **449**(2008)279.
[5] H. Nakano[et al.]. Nippon Kinzoku Gakkaishi/Journal Japan Inst. Met. **69**(2005)548.
[6] M. J. Nicol [et al.]. J. Electroanal. Chem.**70**(1976)233.
[7] H. Dahms [et al.]. J. Electrochem. Soc. **112**(1965)771.
[8] M. Ramasubramanian [et al.]. J. Electrochem. Soc. **143**(1996)2164.

Sixth Asian School-Conference on Physics and
Technology of Nanostructured Materials
Vladivostok, Russia, 25 – 29 April, 2022



# Magnetic properties of epitaxial Pd/Co(d)/CoO/Pd structures promising for spin-orbitronics

G.S. Suslin*, O.E. Ayanitov, E.V. Tarasov, A.V. Davydenko, D.O. Yushchenko, P.S. Nazarova, A.S. Samardak, A.V. Ognev, A.G. Kozlov

Laboratory of Spin-Orbitronics, Institute of High Technologies and Advanced Materials, Far Eastern Federal University, Vladivostok 690922, Russia

*e-mail: suslin_gs@dvfu.ru

**Abstract.** Many studies in the field of spintronics are focused on new materials with precisely controlled magnetic properties. We are showing how to control the magnetic parameters of Pd/Co/CoO/Pd films, such as the effective anisotropy coefficient, saturation magnetization, and coercive force, by changing the Co thickness.

## 1. Introduction

Research in spintronics is aimed to create new devices that will be both cheaper and faster. For this purpose, it is necessary to have a way to control the magnetic properties of the spin-orbitronic materials. In this work we study the influence of the Co layer thickness dependent interface parameters on the effective anisotropy (Keff), coercive force (Hc), and the oxidation process in epitaxial Pd/Co(d)/CoO/Pd systems. Since Pd and Co have different lattice parameters (the mismatch is ~9.7%), elastic stresses appear at the interfaces, which contribute to the perpendicular magnetic anisotropy (PMA) energy [1].

## 2. Experiment

The epitaxial Pd/Co/CoO/Pd films were grown by molecular beam epitaxy in an ultrahigh vacuum chamber. After deposition of the ferromagnetic layer, the films were oxidized in a dry oxygen atmosphere to form a CoO layer. The change in lattice parameters was measured by reflectivity high-energy electron diffraction (RHEED). Magnetic parameters were studied by a vibrating-sample magnetometer (VSM) measuring hysteresis loops, and a Kerr microscope visualizing a magnetic domain structure.

## 3. Results and discussions

The saturation magnetization ($M_s$) of Pd/Co/CoO/Pd samples was determined from the dependences found for Pd/Co/Pd; therefore, the dependence of $M_s$ on the magnetic moment per unit area ($M_s(m_s/S)$) was built for nonoxidized samples:

$$M_s = \frac{(M_s^{Co} * d_{Co} + 2M_s^{Pd\ pol} * d_{Pd}^{pol})}{d_{Co}} \quad (1)$$

where $d_{Pd}^{pol} = 0.2$ nm, $M_s^{Pd\ pol} = 3.1 * 10^5\ A/m$ – parameters of polarized Pd layer [2, 3], and $M_s^{Co} = 1.42 * 10^6\ A/m$.

The $M_s$ value for the prepared series of nonoxidized samples was calculated in the absence of one interface:

$$M_s = \frac{(M_s^{Co} * d_{Co} + M_s^{Pd\ pol} * d_{Pd}^{pol})}{d_{Co}} \quad (2)$$

Approximated values for nonoxidized samples were used to determine $M_s$ from $m_s/S$ values of the oxidized samples.

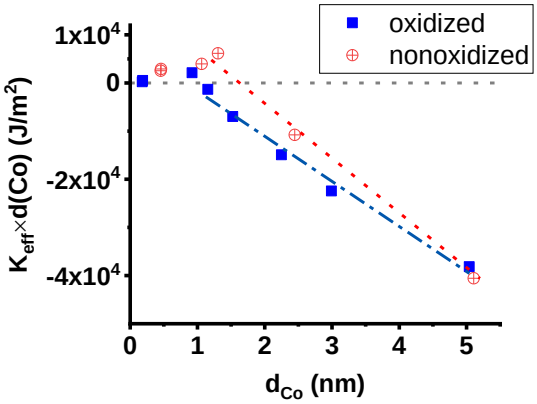


***Fig. 1.*** *$K_{eff}$× $d_{Co}$ depending on the thickness of Co.*

Increasing the thickness of the cobalt layer with a fixed oxidation dose leads to a decrease in the coercive force and the anisotropy field. The Keff×dCo values for oxidized and nonoxidized samples differ not only in magnitude, but also in slopes, Fig.1.

## 4. Conclusions

Magnetic properties of Pd/Co/CoO/Pd films were investigated. The dependences of the magnetic parameters on the thickness of the ferromagnetic layer (coercive force, effective magnetic anisotropy, magnetic moment, saturation magnetization) were defined.

We found that with the increasing thickness of Co, the coercive force the effective anisotropy decrease. The saturation magnetizations of Pd/Co/CoO/Pd samples were determined.

## Acknowledgements

The authors thank the Russian Ministry of Science and Higher Education for state support of scientific research conducted under the supervision of leading scientists in Russian institution of higher education, scientific foundation, and state research centers (Project No. 075-15-2021-607).

This study was partially funded by the Council of the President's Grants of the Russian Federation (Project No. MK-1384.2021.1.2), the Russian Ministry of Science and Higher Education (the state task 0657-2020-0013), Russian Science Foundation [Project No. 21-42-00041].

**References**

[1] K. Oyoshi, D. Lenssen, R. Carrius, S. Mantl. Thin Solid Films **381**(2001)194.
[2] T. Suemasu, T. Fujii, K. Takakura, F. Hasegawa. Thin Solid Films **381**(2001)209.
[3] R. Bayazitov, R. Batalov, R. Nurutdinov, V. Shustov, P. Gaiduk, I. Dezsi, E. Kotai. Nucl. Instr. Meth. **B 24**(2005)224.
[4] K. Oyoshi, D. Lenssen, R. Carius, S. Mantl. Thin Solid Films **381**(2001)202.
[5] J. Chrost, J. J. Hinarejos, E. G. Michel, R. Miranda. Surf. Sci. **330**(1995)34.

Sixth Asian School-Conference on Physics and
Technology of Nanostructured Materials
Vladivostok, Russia, 25 – 29 April, 2022

**III.o.10**

# All-dielectric metasurface with tunable magneto-optical response

D.O. Ignatyeva[*,1,2,3], D.M. Krichevsky[2,4], P.E. Zimnyakova[2,4], S. Xia[5], L. Bi[5], V.I. Belotelov[1,2,3]

[1] Physics and Technology Institute, Vernadsky Crimean Federal University, 295007 Simferopol, Russia
[2] Russian Quantum Center, 121353 Moscow, Russia
[3] Lomonosov Moscow State University, 119991 Moscow, Russia
[4] Moscow Institute of Physics and Technology (MIPT), 141700 Dolgoprudny, Russia
[5] National Engineering Research Center of Electromagnetic Radiation Control Materials, University of Electronic Science and Technology of China, Chengdu 610054, China

*e-mail: ignatyeva@physics.msu.ru

**Abstract.** All-dielectric magnetic metasurfaces enable efficient interaction of photons and spins in a specially designed nanopatterned materials with subwavelength thickness. Here we show that a hybrid metasurface containing a smooth Ce:YIG layer and a Si nanodisk pattern on its top provides sharp optical resonances corresponding to excitation of the guided modes. These resonances are accompanied by the Fano-type resonances of the Faraday effect. Compared to its plasmonic counter-parts, such all-dielectric metasurface have low optical losses and thus provide high-Q optical and magneto-optical resonances of several nanometers linewidth. The position of the magneto-optical resonance is extremely sensitive to the metasurface parameters, including the materials permittivities which can be easily tuned by the external stimulus. We show that that the magneto-optical Faraday response of all-dielectric metasurface could be efficiently controlled using the thermal heating.

## 1. Introduction

All-dielectric metasurfaces attract much attention nowadays for their unusual properties which can be achieved by the design of forming them nano-elements, so-called ‘meta-atoms’. Recently all-dielectric magnetic metasurfaces were shown to enable efficient interaction of photons and spins leading to the significant enhancement of the known magneto-optical effects, such as Faraday effect [1,2], for example, and appearance of the new magneto-optical effects, such as transverse magnetophotonic intensity effect [3]. It was also demonstrated that transverse magneto-optical Kerr effect (TMOKE) and longitudinal magneto-optical Kerr effect (LMOKE), which are close to zero in a transparent dielectric films and crystals, can experience several orders increase in all-dielectric magnetic metasurfaces [4-7]. Most of these studies consider the ‘static’ metasurfaces with only the magnetic field direction changing.

Here we exploit the concept of metasurface tunability arising from the sensitivity of its optical, and, consequently, magneto-optical properties on the parameters of the materials forming it. We show that the magneto-optical response of the magnetic metasurface itself could be tuned via external stimulus. Here we consider the most straightforward way of such a control using a thermal heating. However, this approach can also exploit additional external magnetic field, acoustic pulses, electric currents and many other phenomenon to achieve the tunability of the all-dielectric magnetic metasurface magneto-optical response.

## 2. Experiment

We consider a hybrid all-dielectric magnetic metasurface containing a smooth Ce:YIG layer of 200 nm thickness and a Si nanodisk pattern on its top. The height of the Si disk is 117 nm, and radius of the disk is 140 nm. The metasurface is schematically shown in Fig.1 (see inset). The parameters of the metasurface were chosen to provide prominent optical resonances corresponding to excitation of the hybrid Mie-coupled guided modes of TM polarization at 900 nm and TE type at 1000 nm, correspondingly (see [6] for the detailed resonance analisys). Fig. 1 shows the transmittance spectra of the structure exhibiting two dips, which are associated with these modes.

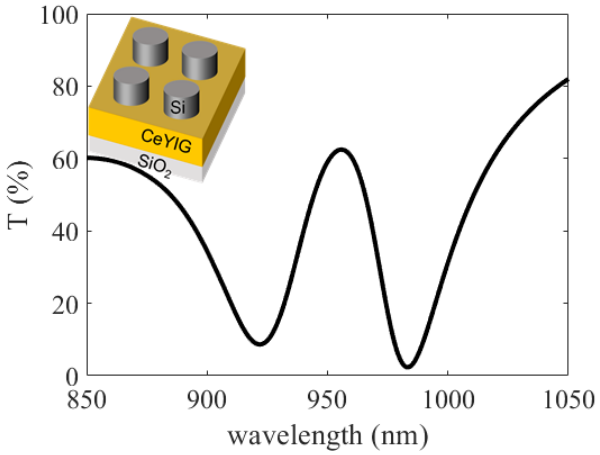


***Fig. 1.*** *Transmittance spectra of hybrid CeYIG-Si magneto-optical metasurface (see scheme in the inset).*

Due to the peculiar character of the displamenet currents induced in the CeYIG film by the optical fields under optical mode excitation, Faraday rotation is significantly enhanced in the vicinity of the TE-type resonance. Faraday rotation spectra (see Fig. 2) show that it has a Fano-type shape due to the presence of the non-resonance contribution of the smooth film and resonant contribution arising from the excitation of the optical modes. One may see that the latter is very strong causing the Faraday rotation even to change its sign in the vicinity of the resonance. Faraday rotation of all-dielectric metasurface increases 4 times compared to the same film without Si disk pattern.

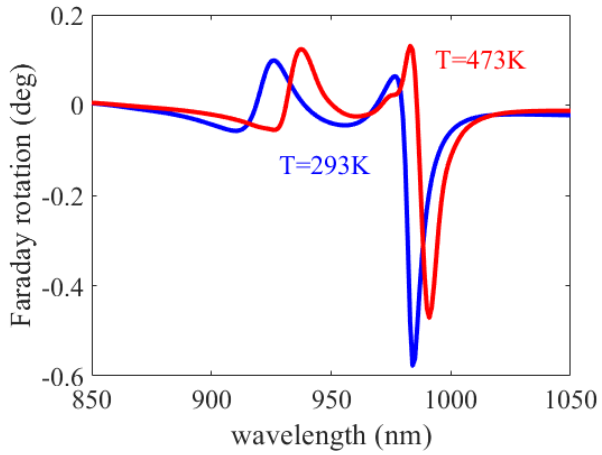


***Fig. 2.*** *Faraday rotation spectra of the hybrid CeYIG film + Si disks magneto-optical metasurface for the temperatures 293K (blue line) and 473K (red line).*

A bare CeYIG film exhibits a smooth wavelength Faraday rotation dependence in this spectral region. It is clearly seen from Fig. 2 that the magneto-optical signal of the metasurface has a sharp resonance with a high derivative of 0.02deg/nm in the vicinity of the resonance.

## 3. Results and discussions

It is important that the position of this resonance is determined by the metasurface parameters, and, therefore, could be efficiently controlled using the external stimulus. Here we consider a thermal heating as such a stimulus.

Refractive index of a material is sensitive to the heating process. Even higher sensitivity is a achieved in a metasurface, which gives rise to thermonanophotonics [8]. The shift of the mode position in optical spectra that is achieved due to the heating process leads the shift of a sharp Fano resonance curve. Fig.2 shows that for a fixed wavelength of 982 nm the considered all-dielectric metasurface exhibits Faraday rotation of -0.3 deg at a room temperature. If the structure is heated to 473 K, the Faraday rotation at this wavelength changes it sign and is equal to +0.1 deg.

Therefore, Faraday rotation in the considered metasurface is efficiently controlled by its temperature. Variation of the temperature in the range of 180 K makes it possible to achieve Faraday rotation values at a fixed wavelength in the full range between -0.3 deg and +0.1 deg. These changes are compared and even exceed the Faraday rotation angle of a smooth film, which was measured as -0.1 deg at the same wavelength.

Such approach gives rise to a novel type of tunable magneto-optical metasurfaces which magneto-optical response is not fixed after the structure fabrication, but can be tuned in a wide range via the external stimulus. It is important that thermal heating can be performed locally at the spots of ~1um diameter using focused laser pulses of diode lasers or any other laser types. In this case, the magneto-optical response can be tuned locally by the proper selection of the local temperature in the area of several microns. Thus one may obtain the inhomogeneous Faraday rotation distributions across the metasurface by creation of the laser beam patterns with the desired intensity profiles.

## 4. Conclusions

A hybrid metasurface containing a smooth Ce:YIG layer and a Si nanodisk pattern on its top provides sharp optical resonances. These resonances are accompanied by the Fano-type resonances of the Faraday effect, which position is extremely sensitive to the metasurface parameters. Here we exploit the concept of metasurface tunability arising from this sensitivity.

We show that the magneto-optical response of the magnetic metasurface itself could be tuned via external stimulus. The most straightforward way of such a control using a thermal heating was considered. It was demonstrated that Faraday rotation of the metasurface could be efficiently tuned between -0.3 deg and +0.1 deg values by the variation of the metasurface temperature.

## Acknowledgements

This work was financially supported by Russian Science Foundation, Grant No. 21-72-10020.

## References

[1] P.E. Zimnyakova, D.O. Ignatyeva, D. Karki, A.A. Voronov, A.N. Shaposhnikov, V.N., Berzhansky, M. Levy, V.I. Belotelov. Nanophotonics. **11** (2022)119.
[2] F. Royer, B. Varghese, E. Gamet, S. Neveu, Y. Jourlin, and D. Jamon. ACS Omega **5**(2020)2886.
[3] D.O. Ignatyeva, D. Karki, A.A. Voronov, M.A. Kozhaev, D.M. Krichevsky, A.I. Chernov, M. Levy, and V.I. Belotelov, Nature Communications. **11**(2020)1.
[4] A.A. Voronov, D. Karki, D.O. Ignatyeva, M.A. Kozhaev, M. Levy, and V.I. Belotelov. Optics Express. **28**(2020)17988.
[5] L. Bsawmaii, E. Gamet, F. Royer, S. Neveu, and D. Jamon. Optics Express. **28**(2020)8436.
[6] D.M. Krichevsky, S. Xia, M.P. Mandrik, D.O. Ignatyeva, L. Bi, and V.I. Belotelov. Nanomaterials. **11**(2021)2926
[7] L. Bsawmaii, E. Gamet, S. Neveu, D. Jamon, F. Royer. Optical Materials Express. **12**(2022)513.
[8] G.P. Zograf, M.I. Petrov, S.V. Makarov, Y.S. Kivshar. Advances in Optics and Photonics. **13**(2021)643.

Sixth Asian School-Conference on Physics and
Technology of Nanostructured Materials
Vladivostok, Russia, 25 – 29 April, 2022



# Factor of nanohomogeneity in the formation and application of electronic properties of structurally disordered metal oxide materials

S.D. Khanin*
Military Telecommunications Academy, 3 Tikhoretsky Pr; Saint Petersburg, 194064, Russia

*e-mail: sd_khanin@mail.ru

**Abstract.** The results of studies of the electronic properties of noncrystalline oxides of d-elements of variable valence (tantalum and niobium) are presented, indicating a significant role in the formation of their electronic properties of nanohomogeneity of the structure. Based on the developed model concepts, productive methods have been developed for improving the functional properties and non-destructive quality control of oxide capacitors

## 1. Introduction

The electronic properties of noncrystalline metal oxide materials have been and remain the subject of extensive research, which is due to the scientific interest in processes in disordered systems with a strong localization of charge carriers and the expanding scope of these materials. The latter covers today not only the creation of capacitors with record specific characteristics, but also the basic elements of integrated circuits - field-effect transistors with an ultrashort channel, non-volatile memory elements, etc., which allows us to speak about the formation and development of metal oxide electronics as a significant direction [1].

In this paper, we present the results of studies of representative for noncrystalline variable valence d-elements oxides, amorphous oxides of tantalum and niobium, obtained on the metal surface by electrochemical oxidation [2].

The basis for the concepts of nanohomogeneity, along with general images of the conjugation of structural disorder with nonhomogeneity [3], is the nonstoichiometry of the composition inherent in the material under study in a wide range of homogeneity, which manifests itself in the presence of defects such as dangling bonds, which creates conditions for the formation of regions of local rarefaction.

## 2. Results and discussions

The presence of nanohomogeneity is indicated by the fact that at a smaller, according to X-ray diffraction analysis, metal-oxygen distance and a higher coordination number of the metal atom than in a metal oxide crystal similar in the short-range order, the density of the amorphous oxide is lower than that of the crystalline one.

Based on the structural data and guided by the laws of thermodynamics and kinetics, it can be assumed that the structure of the oxide in the regions of nanohomogeneity is similar to the crystalline one.

These concepts underlie the calculation of the density of electronic states in the metal oxides under study [4], which is represented as a superposition of the densities of state of the amorphous and crystalline components with the corresponding short-range order parameters.

The calculation results show that with an increase in the volume content of crystal-like regions, the concentration of localized states in the band gap of the oxide increases. As the concentration of nonstoichiometry defects such as oxygen vacancies increases, the localized states are filled with electrons. The latter is consistent with X-ray photoelectron spectroscopy data on the appearance of an emission band in the band gap during the reductive heat treatment of oxides.

The nanoheterogeneity of the structure largely determines the patterns of charge carrier transport in amorphous metal oxides [5]. An expressive manifestation of this is the presence at a positive potential on the base metal of the effect of a decrease in non-ohmic conductivity in strong electric fields, which precedes its exponential growth, which indicates a rearrangement of the current flow paths. It is important to note that this effect manifests itself starting from the time of loading, when the sizes of the cluster of states, along which the charge carrier is transported, reach a value on the order of ten nanometers.

At a negative potential on the base metal, when protons are injected into the oxide dielectric of the capacitor and electrochemical reduction of the oxide occurs, leading to a sharp increase in current [6], the presence of nanohomogeneity creates conditions for intense ion transport. This is manifested in the experimentally established significant increase in the proportion of current flowing through areas of increased conductivity.

It is important to note that, as the results of X-ray diffraction analysis show, when a significant current level is reached, thermal crystallization of the oxide takes place under these conditions. Significant here can be a crystal-like structure in the regions of local rarefaction, just as it takes place during the formation of glass ceramics.

Nanoheterogeneity is also significantly manifested in the electrically stimulated crystallization that occurs during long-term loading of capacitor structures [7], creating channels for long-range diffusion of oxygen from the working capacitor electrolyte to the metal-oxide interface, from where the growth of field crystals begins. The indicated mechanism of the process of electrically stimulated crystal growth is evidenced by the obtained experimental data on the distribution profile of labeled atoms ($O^{18}$ isotope) and the dependences of the current during crystal growth and the degree of crystallinity on time.

Based on the developed concepts, practical recommendations have been developed for improving the functional properties of oxide capacitors by modifying the dielectric formation technology. It is shown that the

stabilization of the highest oxidation state of the metal in them, aimed at increasing the homogeneity of the structure of amorphous oxides, can significantly reduce the leakage current at both voltage polarities and increase the resistance of properties to long-term electrothermal loading.

In order to characterize metal oxide materials on the subject of determine the degree of their nonhomogeneity, a number of methods have been proposed based on non-destructive measurement of parameters and characteristics that are informative in the considered aspect. As such, the following are defined and substantiated: the value and behavior of static conductivity in strong electric fields [8], the cutoff frequency of the multiplet hopping conductivity on alternating current [8,9], the rate of current growth with time at a negative potential on the base metal [10], the magnitude and nature of the frequency dependence of the dielectric loss tangent in the infrasound region, spectral density of low-frequency excess noise [11].

**4. Conclusions**

The results of the study show that in the analysis of the physical nature and functional application of the electronic properties of non-crystalline oxides of d-elements of variable valence, one should take into account the nanohomogeneity of their structure.

**References**

[1] A.L. Pergament, G.B. Stefanovich, A.A. Velichko, S.D. Khanin. Electronic Switching and Metal-Insulator Transitions in Compounds of Transition Metals. Condenced Matter at the Leading Edge (Nova Science Publishes, 2006).
[2] L.L. Odynets, V.M. Orlov. Anodic oxide films. (Leningrad.: Nauka, 1991).
[3] T.V. Bocharova, G.O. Karapityan, A.M. Mironov, K.G. Karapityan. Physics of nanoscale structures. Formation of nanoscale regions in glassy materials (Saint Petersburg: Polytechnic University Press, 2008).
[4] S.D. Khanin, A.L. Ivanovskii. Phys. Stat. Sol. (b). **174** (1992) 449.
[5] S.D. Khanin. Physics of disordered and nanostructured metal oxides and chalcogenides (Saint Petersburg: A.I. Herzen RGPU Press, 2011).
[6] G.M. Gusinsky, L.G. Karpukhina, V.M. Muzhdaba, V.O. Naidenov, G.F. Tomilenko, S.D. Khanin. Solid State Physics. 29 (1987) 3253.
[7] S.D. Khanin. Materials Science Forum. **185-188** (1994) 573.
[8] S.D. Khanin. Materials Science Forum. **185-188** (1994) 563.
[9] H. Böttger, VV Bryksin. Hopping Conduction in Solids (VCH, 1985).
[10] S.D. Khanin. Relaxation charge injenction and charge transport (The Dielectric Soc.Ann.Meeting: Canterberry, 1991).
[11] S.D. Khanin. Problems of Electrophysics of Metal Oxide Capacitor Dielectrics Reviews in Electronic Engineering. (Moscow, 1990).

Sixth Asian School-Conference on Physics and
Technology of Nanostructured Materials
Vladivostok, Russia, 25 – 29 April, 2022

**III.o.12**

# Effect of Si(001)2×1 surface wetting by Cu monolayers on granulation process and ferromagnetic properties of nanofilms consisting of Cu, Co and/or Fe layers

N.I. Plusnin*[,1,2], E.V. Blinkova[2]

[1] Institute of Automation and Control Processes FEB RAS , 5 Radio St., Vladivostok 690041, Russia
[2] Academy of Telecommunications, Tikhoretsky pr., 3, St. Petersburg, 194064

*e-mail: plusnin@iacp.dvo.ru

**Abstract.** Nanofilms and multilayers of Fe, Cu and Co were studied by the methods of LEED, AES, EELS, AFM and MOKE when growing on a clean surface of Si(001)2×1 and on wetting layers of Cu (Cu-WL) on Si (001) after their deposition and annealing. Studies have shown that pseudolayer growth of nanofilms occurs on a clean Si(001)2×1 surface. However, the presence of Cu-WL increases the agglomeration and ferromagnetism of these nanofilms.

## 1. Introduction

In recent years, the focus has been on the development of multilayer metal-semiconductor nanostructures for nanoelectronics and spintronics devices. The interest in studying layered nanostructures based on multi-layers of transition metals, such as Fe, Co, Cu, is due to the fact that they can differ significantly from their bulk counterparts in crystal structure, electronic and magnetic properties.

## 2. Experiment

Fe nanofilms, as well as multi layers of Cu/Fe/Cu/Co and Cu/Co/Cu/Fe were deposited at room temperature of the substrate and reduced vapor temperature. Samples of A, B and C - type were obtained, which were deposited on a pure Si(001)2×1 substrate, on a Cu/Si(001) interlayer and before and after annealing at 250 °C. The temperature in the sources during the deposition of Cu (1-5 ML), Fe (10-25 ML) and Co (10 ML) had a reduced (as in [1-5]) value and was 900, 1250 and 1130 °C, respectively. The thickness of the Cu interlayer corresponded to the thickness of the copper wetting layer (Cu-WL) on Si (001) [5] and was within 1-2 ML.

## 3. Results and discussions

LEED and AES studies of at the initial stage of growth (WL stage) have shown that in all cases the rate of attenuation of reflexes in the images of LEED (complete attenuation after 1 ML) and the rate of disappearance of the interband satellite of the Auger peak L23VV of the Si substrate corresponds to a pseudo-layered or multi-point growth mechanism. At the same time, in the case of a ferromagnetic metal (Co, Fe), the appearance of a new interband satellite of the L23VV peak at 2 ML and the preservation of its structure with subsequent growth after 3 ML indicates Si segregation. With that, the shift of the plasma satellite of the L23VV peak after 3 ML indicates the enrichment of the film composition with metal.

In the B - and C-type samples, relative to the A-type samples, and in the A-type sample, relative to the theoretical layer-by-layer growth model, a slower growth of the Co or Fe Auger peak was observed. However, in the A-type sample, a slower attenuation of the Si Auger peak was also observed. This shows agglomeration of films during growth in B - and C-type samples and mixing of Co or Fe layers with Si from the substrate in an A-type sample. This conclusion was also confirmed by the EELS study, which showed a faster formation of volume plasmon loss peaks in B - and C-type samples compared to A-type samples.

AFM data confirmed agglomeration in B - and C-type samples: they showed that the average relief height was higher than that in A-type samples and that with a total metal thickness of 2.0-3.0 nm, the average relief height in B - and C-type samples reached 3.5-4.5 nm. At the same time, the lateral grain size in the B - and C-type samples was also higher, but them number was smaller. Assuming that the grain morphology of the entire film repeats the morphology of the first ferromagnetic layer (Co, Fe), we can conclude that the presence of Cu-WL leads to agglomeration of this first layer in the form of islands. With further growth of the layers, the influence of Cu-WL consists in additional agglomeration, with a decrease in the continuity of the layers and the formation of grains of similar sizes.

Thus, our studies have shown that, in the case of growth on a buffer layer of non-magnetic metal (NM), as for B-and C-type samples, FM nanofilms and NM/FM2/NM/FM1 multilayers become more friable, consist of larger islands, and have a more pronounced relief. Moreover, if NM is a noble metal (Cu) and if it is not annealed, the nanofilms are more strongly compressed into 3D islands. As a result, after deposition of the NM buffer WL (NM-WL) and its annealing, ferromagnetism (coercive force and magnetization) in the obtained nanofilms is stronger than without the interlayer.

The found phenomena have the following explanations. When a metal nanofilm is deposited (on a clean silicon surface - without a buffer layer), the growth mechanism is the usual: WL growth, growth of metastable, then stable bulk silicide of this metal, and growth of bulk metal [3-5]. In this case, unreacted Si is segregated both during the growth of WL and during subsequent phase transitions. And at the last stage of growth, segregated Si is dissolved in the growing metal film. Therefore, without the interlayer, the formation of silicide, segregation and dissolution of Si in the FM film inhibits it has ferromagnetism.

In the presence of buffer NM-WL, a multi-island growth of the FM nanolayer occurs without mixing with silicon, but with a small agglomeration. However, when NM-WL is annealed, NM silicide is formed, which has a

higher wettability than NM itself. Annealing of this buffer layer collects NM silicide near the steps of the substrate. This leads to the fact that multi-island growth is concentrated near the steps and the film becomes less continuous. In both cases, growth proceeds according to the Folmer-Weber mechanism, and the FM nanofilm gathers more strongly in islands than when growing on a clean surface of a silicon substrate.

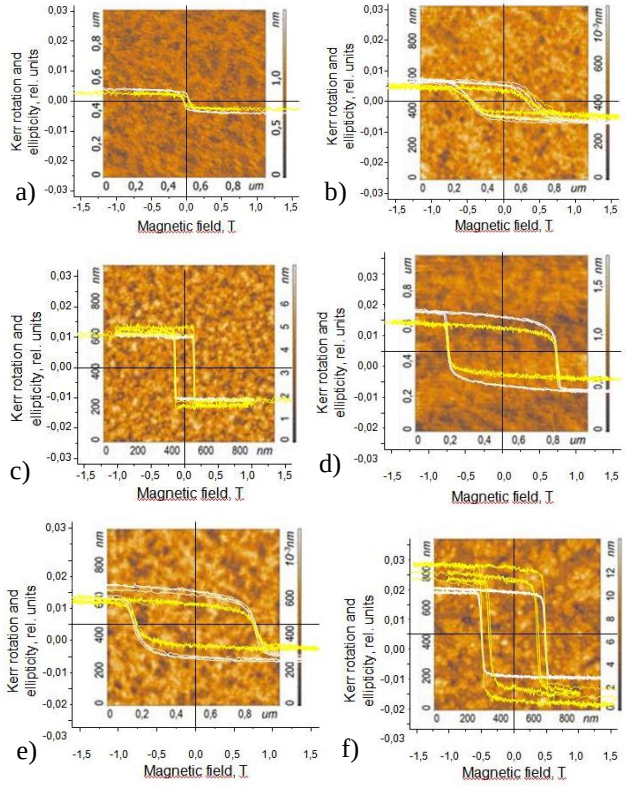


***Fig. 1.*** *Kerr longitudinal rotation and ellipticity (yellow), as well as AFM image (1000 × 1000 nm2) in Fe (a, b, d, e) and Cu/Fe/Cu/Co (c, f) nanolayers grown on Cu-WL/Si(001): without pre-annealing Cu - WL – (a, b, c, e, f) and with annealing - (d). Thickness: Cu-WL: (a, d) -1 ML and (b, c) - 2 ML; Fe – ~ 10 ML; Cu/Fe/Cu/Co-35÷40 ML.*

Nevertheless, the growth of the next NM layer occurs according to the Van Der Merwe mechanism, since the NM layer wets the FM1 agglomerates well and spreads evenly over their surface. This encourages the formation of a round (spherical) shape of agglomerates. In this case, the substrate surface is partially exposed between the agglomerates. The subsequent growth of FM2 also occurs according to the Van Der Merwe mechanism, but mainly between FM1 agglomerates. And the growth of the last NM layer again leads to NM spreading on FM2 agglomerates and stabilizes their round (or spherical) shape.

As for the ferromagnetic properties, the stronger the agglomeration of the nanofilm, the higher the thickness of the agglomerates and the more ferromagnetism is manifested in it (see, for example, [6]). In addition, this ferromagnetism is expressed by a rectangular hysteresis loop, if the agglomerates of ferromagnetic metal acquire a round or spherical shape. In the case of a multi-layer film, the agglomerates FM1 and FM2 are adjacent through an ultra-thin (< 5 ML) interlayer. This leads to the exchange interaction between them and to the formation of the smallest coercive force among these two FMs (in the case of Fe and Co, the coercive force of Co).

## 4. Conclusions

The role of wetting Cu layers in the formation of the structure and ferromagnetic properties of single-layer and multilayer nanofilms of ferromagnetic metals (Co, Fe) on a silicon substrate is shown.

## References

[1] N. Plusnin, V. Il'yashenko, S. Kitan', S. Krylov. Appl. Surf. Sci. **253** (2007) 7225.
[2] N. Plyusnin, V. Ilyashchenko, S. Kitan, and S. Krylov. Letters to ZhTF. **33** (2007) 79 (RUS).
[3] N. Plusnin, V. Il'iashchenko, S. Kitan', S. Krylov. Journal of Physics: Conference Series. **100** (2008) 052094.
[4] N. Plyusnin, V. Ilyashchenko, S. Kitan, and S. Krylov. Surface. X-ray, synchrotron, and neutron studies. No. **9** (2009) 86 (RUS).
[5] N. Plyusnin, V. Ilyashchenko, S. Kitan, and N. Tarima. Surface. X-ray, Synchrotron, and Neutron Studies. No. **9** (2011) 29 (RUS).
[6] Z. Qiu , S. Bader. Journal of magnetism and magnetic materials. **200** (1999) 664.

Sixth Asian School-Conference on Physics and
Technology of Nanostructured Materials
Vladivostok, Russia, 25 – 29 April, 2022



# Structure and magnetic properties of Fe-, Co-enriched composite titania coatings

M.V. Adigamova*, I.V. Lukiyanchuk, V.P. Morozova, I.A. Tkachenko
Institute of Chemistry, Far-Eastern Branch, Russian Academy of Sciences, 159, Pr. 100-letya Vladivostoka, Vladivostok 690022, Russia

*e-mail: adigamova@ich.dvo.ru

**Abstract.** Fe+Co/$TiO_2$/Ti composites exhibiting ferromagnetic properties were formed by plasma-electrolytic oxidation in electrolyte with colloidal particles of iron and cobalt hydroxides. It has been established that the main contribution to the magnetic behavior of the samples is made by micro- and nanosized formations with an increased iron and cobalt contents, which were found at the bottom and walls of the pores.

## 1. Introduction

Composites "ferromagnetic oxide coating/paramagnetic metal" can be used as absorbers of electromagnetic radiation as absorbers of electromagnetic radiation, materials in microelectronics and design of microwave waveguides. Recently, a direction has been developed associated with the formation of such composites by the method of plasma electrolytic oxidation (PEO), using electrolytes containing colloidal particles of iron, cobalt, or nickel hydroxides. During PEO treatment, electrolyte components are incorporated into the $M_xO_y$ layer growing on the substrate metal. In this case, the metals from the electrolyte are distributed unevenly over the coating surface, concentrated in defective areas of the surface, including pores and cracks.

In the pores, metals are concentrated in the composition of crystallites, which, apparently, are metal particles surrounded by oxide-hydroxide shell. The experimental data previously obtained for such systems suggest that it is the crystallites that make the main contribution to the magnetic characteristics of the formed composites. In this work, Fe+Co/$TiO_2$/Ti composites have been formed, and their magnetic characteristics have been studied in relation to their composition and structure, including those at the microlevel.

## 2. Experiment

Fe-, Co-containing PEO coatings have been formed on an anode-polarized VT1-0 titanium sample at an effective current density of 0.1 A/$cm^2$ for 5 min in PBWFeCo electrolyte, containing (mol/L): 0.066 $Na_3PO_4$ + 0.034 $Na_2B_4O_7$ + 0.006 $Na_2WO_4$ + 0.015 $Fe_2(C_2O_4)_3$ + 0.04 $Co(CH_3COO)_2$. Surface images and data on the elemental composition, including individual surface components (crystallites in pores, pore bottoms and walls) were obtained using a Hitachi S5500 high-resolution scanning electron microscope (Japan) with a Thermo Scientific energy-dispersive analysis attachment (USA). Magnetic measurements were carried out on a SQUID MPMS 7 magnetometer (USA) at a temperature of 300 K. During the measurements, the samples were placed parallel to the direction of the magnetic field. When calculating the magnetization, the measured magnetic moment was normalized to the mass of the coated sample.

## 3. Results and discussions

The use of electrolyte-sol with dispersed particles of iron and cobalt hydroxides allows obtaining the coatings with ferromagnetic characteristics on titanium substrate. The value of the coercive force at 300 K is 179 Oe. Iron and cobalt from the electrolyte are concentrated in pores in the composition of spherical formations with characteristic dimensions of ~70 nm, combined into agglomerates. Fig. 1 shows SEM image of crystallites in the pores of PEO coating. The particles contain (at.%): 15.9 Fe, 25.7 Co, 37.1 Ti, 11.2 O, 7.8 P, 2.3 W, while the surface composition of the coatings is as follows (at.%): 22.9 C, 64.2 O, 4.6 Na, 4.4 P, 0.4 Fe, 2.3 Ti, and 1.2 Co. Elevated concentration of iron and cobalt and a lack of oxygen for the formation of their stoichiometric oxides may indicate the presence of reduced metals in the composition of crystallites localized at the bottom and walls of the pores. The crystallites apparently consist of a mixture of reduced Fe or Fe + Co metal cores, surrounded by oxide-hydroxide shell.

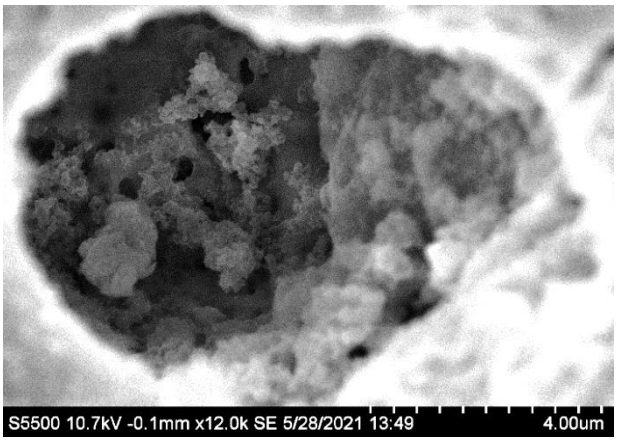


***Fig. 1.*** *SEM image of crystallites in the pore of the formed coating.*

## 4. Conclusions

Using plasma-electrolytic treatment of titanium in an electrolyte containing simultaneously colloidal particles of Fe(III) and Co(II) hydroxides makes it possible to form Fe+Co/$TiO_2$/Ti ferromagnetic composites. The Co- and Fe-enriched crystallites in the pores of the coatings are apparently responsible for the ferromagnetism of the formed composites.

**Acknowledgements**

The work was carried out within the Institute of Chemistry FEBRAS State Order (project No 0205-2021-0003).

**References**

[1] V. Rudnev, I. Lukiyanchuk, M. Adigamova, et. al. Surf. Coat. Technol. **269**(2015)23.
[2] V. Rudnev, M. Adigamova, I. Lukiyanchuk, et. al. Surf. Coat. Technol. **381**(2020)125180.

Sixth Asian School-Conference on Physics and
Technology of Nanostructured Materials
Vladivostok, Russia, 25 – 29 April, 2022



# Field dependence of the Griffith phase in a dilute ferromagnet

A.K. Chepak*[,1,2], L.L. Afremov[1]

[1] Far Eastern Federal University, 8 Sukhanova St., Vladivostok 690950, Russia
[2] Institute of Chemistry FEB RAS, prosp. 159th anniversary of Vladivostok, Vladivostok, 690022

*e-mail: chepak.ak@mail.ru

**Abstract.** In this work, within the framework of the Ising model, a study was made of the influence of a magnetic field on the concentration phase transition in a dilute ferromagnet at a temperature $T \to 0$. It is shown that, in a face-centered cubic lattice, a random substitution of magnetic atoms for non-magnetic ones leads to a transition from a ferrimagnetic state to a paramagnetic state through an intermediate phase, the Griffiths phase. In this case, the magnetic field compresses this phase due to the displacement of the paramagnetic point of the phase transition closer to the ferromagnetic one.

## 1. Introduction

To date, many modern works are devoted to the study of spin and cluster glasses, and materials with ordering similar to the Griffith phase [1-6]. Among these systems, double perovskites Re2CoMnO6 (Re = rare earth ions) attract special attention due to the manifestation of semimetallic, semiconductor, magnetic, and piezoelectric properties [6], which are associated with the Griffith phase. In such a phase, both long-range and short-range orders can exist simultaneously, which will be responsible for various types of magnetic ordering. In the classical view, the Griffith phase is considered as a set of ferromagnetic clusters of various shapes and sizes distributed in a paramagnetic matrix [7].

In this paper, we report that the anomalous behavior of the magnetic susceptibility observed by us in Monte Carlo simulations of a diluted Ising ferromagnet indicates the presence of the Griffith phase.

## 2. Research methodology

The presence of a phase transition was determined from the position of the maximum of the magnetic susceptibility $\chi$ calculated from the well-known formula (1) and the behavior of the magnetization $M$ (2):

$$\chi = \frac{N}{t}[\langle M^2\rangle - \langle M\rangle^2], \quad (1)$$

$$\mathrm{M_{ma}} = \frac{1}{\mathrm{N}}\left[\langle\sum_{\mathrm{i}}^{\mathrm{N_m}} \mathrm{s_i}\rangle\right], \quad (2)$$

here $N$ is the number of nodes in the lattice; $t = (k_B T)\,/\,J$ – relative temperature; $k_B$ is the Boltzmann constant; brackets $\langle\ \rangle$ and [ ] denote averaging over $10^4$ Monte Carlo steps and $2 \cdot 10^2$ different lattice configurations, respectively. The calculation was carried out at a temperature close to absolute zero $t = 0.01$. The Hamiltonian was determined by expression (3), where $J = 1$ is the exchange integral, and $h = H/J$ is determined by the magnetic field in the range from 0 to 5 T.

$$\mathcal{H} = -J\left(\frac{1}{2}\sum_{\{i,j\}} c_i c_j s_i s_j + h\sum_i c_i s_i\right), \quad (3)$$

$\boldsymbol{s_i}$ is the spin variable of the magnetic moment at the $\boldsymbol{i}$-th site of the lattice, and $\boldsymbol{c_i} = \mathbf{0}$ or $\mathbf{1}$ if the site is occupied by a non-magnetic or magnetic atom.

## 3. Results and discussions

The anomalous behavior of the magnetic susceptibility, which manifests itself in two maxima (Figure 1), is interpreted by us as a manifestation of two successive phase transitions. Similar anomalies are observed both in the magnetization [1-3], and in the susceptibility [2-4] and heat capacity [5] of real systems. Thus, we believe that the high-concentration peak $\boldsymbol{p_{c,h}}$ corresponds to the transition from the ferromagnetic phase to the Griffith phase, and the low-concentration $\boldsymbol{p_{c,l}}$ from the Griffith phase to the paramagnetic phase. In the region between $\boldsymbol{p_{c,h}}$ and $\boldsymbol{p_{c,l}}$, a state is observed in which the magnetization remains high due to the existence of large ferromagnetic clusters.

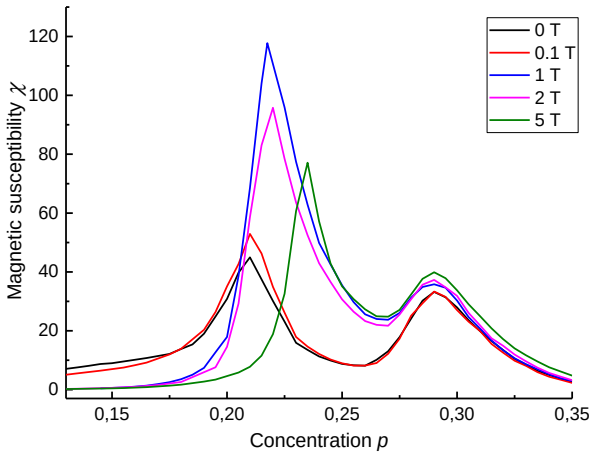


***Fig. 1.*** *Dependence of the magnetic susceptibility $\chi$ on the concentration of magnetic atoms p in various magnetic fields $H$.*

It should be noted that the high-concentration peak does not change its position with an increase in the magnetic field. This is explained by the fact that the transition from the ferromagnetic state to the Griffith phase is accompanied by the rupture of an infinite cluster and the appearance of unbound large clusters. And although there is no interaction between them, the ferromagnetic order is preserved within each individual cluster. At lower concentrations, such clusters are already much smaller, and the Griffith phase in the low-concentration region is represented mainly by the

spin glass phase. It is known that in such a state the magnetic field can shift the equilibrium state, which explains the displacement of the paramagnetic point. Such a behavior at the boundaries of the Griffith phase corresponds to the experimental data [2].

## 4. Conclusions

Nonmagnetic dilution of the ferromagnetic Ising model leads to two successive phase transitions: ferromagnet – Griffith phase and Griffith phase – paramagnet. Two such phase transition points can be considered as ferrimagnetic and paramagnetic, where the paramagnetic point, as expected, depends on the magnetic field. In this case, the ferromagnetic point (into the Griffith phase) remains unchanged at different fields. This confirms that the Griffith phase in the region of high concentrations is represented by cluster glass.

### Acknowledgements

The work was carried out within the framework of the state task of the Ministry of Science and Higher Education of the Russian Federation No. 0657-2020-0005.

## References

[1] Y.Xin, L. Shi, J.Zhao, X.Yuan, Sh.Zhou, Li Hou, L.Yang, Journal of Alloys and Compounds **893**(2022)162222.
[2] K. Anand, M. Alam, A. Pal, P. Singh, S. Kumari Amish G.Joshi, A. Das, A.Mohan, S. Chatterjee, Journal of Magnetism and Magnetic Materials 528(2021)167697.
[3] Romualdo S. Silva Jr, J. Fernando D. Fontes, Nilson S.Ferreira, Rafael S.Gonçalves, Marcelo E.H. Maia da Costa, P. Barrozo, Journal of Magnetism and Magnetic Materials, 546(2022)168851.
[4] R. Revathy, M. R. Varma, K. P. Surendran, Physica status Solidi (B), 258(2021)2000341.
[5] S. Kitani, M. Tachibana, H. Kawaji, Solid state communications 179(2014)16.
[6] V. P. Kumar, Bulletin of Materials Science 44(2021)1.
[7] R. B. Griffiths, Physical Review Letters 23(1969)17.

Sixth Asian School-Conference on Physics and
Technology of Nanostructured Materials
Vladivostok, Russia, 25 – 29 April, 2022



# Magnetic properties of amorphous alloys in a random field model

V.I. Belokon, O.I. Dyachenko*, R.V. Lapenkov
Far Eastern Federal University,10 Ajax Bay, Russky Island, Vladivostok 690922, Russia

*e-mail: dyachenko.oi@dvfu.ru

**Abstract.** In this study, an attempt was made to sequentially calculate the Curie temperature of iron-containing alloys based on the theory of random fields of exchange interaction. This method makes it possible to determine the conditions for the occurrence of ferromagnetism in an amorphous alloy depending on the concentration of exchange-interacting ions, their Holschmidt radius, and the type of crystal lattice of the transition metal.

## 1. Introduction

Despite many publications on the research topic [1-5], there are gaps in the explanation of some magnetic properties of amorphous metal alloys, including the behaviour of the Curie point depending on the concentration and type of metalloids. From general considerations, the Curie point of an amorphous iron-based alloy should be lower than that of a crystalline analogue since the number of neighbours in the first and second coordination spheres, which make the main contribution to the field of exchange interaction in the bcc lattice, is greater than in objects with random close packing, for which the average coordination number is z*≈12 [6]. In this study, an attempt was made to sequentially calculate the Curie temperature of iron-containing alloys based on the theory of random fields of exchange interaction [7-8].

## 2. The method of random fields of exchange interaction

Following [9], we considered a system of interacting particles randomly distributed over the volume. The projection of the field $H_i$ on the $z$ axis (the axis of symmetry in the Ising model), created at the origin by one arbitrary particle located at a point with coordinate $r_i$ with a magnetic moment $\boldsymbol{m}_i$, can be determined by means the law:

$$H_i = \varphi(r_i, \boldsymbol{m}_i). \quad (1)$$

Given the known distribution of particles over $r_i$ and $\boldsymbol{m}_i$, the distribution density of the interaction field on a particle located at the origin of coordinates is a δ-function of the form:

$$\delta[H_i - \textstyle\sum_i \varphi(r_i, \boldsymbol{m}_i)]. \quad (2)$$

Considering the probability of particle distribution over volume and magnetic moment, the distribution density of the random interaction field $H$ can be represented as

$$W(H) = \frac{1}{\sqrt{\pi}\,B} \exp\left(-\frac{\left(H - H_0(\alpha-\beta)\right)^2}{B^2}\right). \quad (3)$$

$$H_0 = n \int \varphi(\boldsymbol{r})\ \mathrm{d}V,\ \ B^2 = 2n \int \varphi^2(\boldsymbol{r})\,\mathrm{d}V. \quad (4)$$

where value $n=N/v$ is the "effective" number of particles per unit volume, $\alpha$ and $\beta$ are the relative number of particles oriented "up" and "down".

Similar relationships for crystalline ferromagnets are as follows:

$$H_0 = p \textstyle\sum \varphi_k,\ B^2 = 2p(1 - m^2 p) \sum \varphi_k^2, \quad (5)$$

where $p$ is the concentration of exchange-interacting ions at the sites of the crystal lattice. Near the Curie point, $B^2 \approx 2p \sum \varphi_k^2$.

Thus, the main characteristics of the distribution function $H_0$ and $B$ are interconnected through the interaction law $\varphi(\boldsymbol{r})$. As for the exchange interaction of two particles, its energy can be determined as follows: $E_{ij} = -m_i m_j J_{ij} = -m \cdot mJ(r_{ij}) = -m\,\varphi(r_{ij})$.

The Curie point is determined by the relation:

$$\frac{H_0}{B} \tanh\left(\frac{mB}{k_B T_c}\right) = 1. \quad (6)$$

Obviously, the relation $\frac{H_0}{B}$ must be greater than 1. And the condition $\frac{H_0}{B} = 1$ determines the critical concentration $p_c$ of exchange-interacting ions. In the case of a crystalline ferromagnet and interaction between particles of only the first coordination sphere, $\varphi_k = f = \mathrm{const}$. From here,

$$\gamma = \frac{H_0}{B} = \frac{p_c\, z\, f}{f\sqrt{2 p_c\, z}} = 1, \quad (7)$$

$$p = \frac{2}{z}, \quad (8)$$

where $z$ is the number of nearest neighbours.

## 3. Magnetic phase transition in an amorphous alloy

The greatest difficulty for calculating the exchange interaction fields in an amorphous alloy is the calculation of the exchange integral $J$ between neighbouring atoms (ions) as a function of the distance between them. Perhaps the only exact result was obtained when calculating the exchange interaction energy of an ionized hydrogen molecule [10]. The exchange energy, up to sign, is proportional to the exchange integral and has the form

$$E_0 \sim \frac{1}{r_0}\left(1 - \frac{2}{3} {r_0}^2\right) \exp(-r_0), \quad (9)$$

where $r_0 = \frac{a}{c}$, $c$ is the radius of the first Bohr orbit, and $a$ is the distance between the nuclei.

We consider the Bette–Slater dependence of the exchange integral $J$ on the ratio of the distance between ion a to the diameter of the unfilled shell $2r$, which qualitatively correctly reflects the dependence of the exchange integral on the distance. Ferromagnetic elements Fe, Co, and Ni have the highest value of the exchange integral. Based on such a scheme, it is possible to explain not only the ferromagnetism of Fe, Co, and Ni but also the antiferromagnetism of alloys, and so forth.

We tried to approximate the Bette–Slater curve based on formula (9). Assuming the dependence of the exchange

integral on the ratio of the distance between ions a to the diameter of the unfilled shell $2r$ in the form:

$$J(x) = \frac{e^{-2x}(-1+\frac{4x^2}{9})}{x}, \quad (10)$$

where $x = \frac{a}{2r} = \frac{a}{d}$.

Using the approach described above, consider an amorphous alloy containing iron in an amount of 70% of the total composition. The volume of the crystal cell in accepted units is $V = x^3 = \left(\frac{a_0}{d}\right)^3 = 7.26$. The volume occupied by two ions is $NV_0 = 2\frac{4}{3}\pi\left(\frac{r_g}{r}\right)^3 = 4.93$, where $r_g = 0.124 \cdot 10^{-9}\, m$ is the Holschmidt radius and $r = 74 \cdot 10^{-12}\, m$ is the iron ion radius. The volume fraction occupied by ions is defined as $\frac{NV_0}{V} = \frac{4.93}{7.26} = 0.68$. Thus, the effective density can be found as $n = 0.7\frac{NV_0}{V}\left(1 + 0.7\frac{NV_0}{2V}\right) = 0.59$.

Using formula (4), we determine the moments of the distribution function by integrating over volume: $H_0 = 444.9\, T$, $B = 230.2\, T$.

From Eq. (6), one can determine the Curie temperature of an amorphous alloy with an iron concentration of 70% and a magnetic moment of iron ions, $m = 1.9\mu_B$. We considered that the average magnetic moment of bulk iron changes to $1.9\mu_B$ when passing from a crystalline compound to its amorphous counterpart. We find that the Curie temperature in the case of an amorphous alloy was $T_c \approx 513K$, which is consistent with the result shown in [11].

Therefore, the result obtained can be considered approximate. Using the values $H_0$ and $B$ obtained by us, we can estimate the "effective number of nearest neighbours" $z$ of iron ions for an amorphous alloy using the ratio $z = \left(\frac{H_0}{B}\right)^2\frac{2}{p}$. Then, $z = 12.66$, which also agrees with the result obtained experimentally in [11].

## 4. Conclusion

Thus, the method of random fields of exchange interaction makes it possible to determine the conditions for the occurrence of ferromagnetism in an amorphous alloy depending on the concentration of exchange-interacting ions, their Holschmidt radius, and the type of crystal lattice of the transition metal.

The Curie point can significantly depend on the magnetic moment of iron ions, which in turn, is determined by the concentration and type of metalloids that make up the alloy. The data known to us indicate that in alloys with an iron ion concentration of 70%–80%, the magnetic moment per atom ranges from $1.2\,\mu_B$ to $1.9\,\mu_B$. The effective number of the nearest neighbours at an iron ion concentration of 70% during amorphization turns out to be approximately 12.66, which corresponds to the experimental data.

## Acknowledgements

The research results presented in section 2 were obtained within the framework of the state task of the Ministry of Science and Higher Education of the Russian Federation of Russia (No. 0657-2020-0005). The research results presented in section 3 were obtained at the expense of the grant of the President of the Russian Federation for state support of the leading scientific schools of the Russian Federation (NSh-2559.2022.1.2)

## References

[1] M.E. McHenry, M.A. Willard, D.E. Laughlin. Amorphous and nanocrystalline materials for applications as soft magnets. Prog. Mater. Sci. **44**(1999)291.

[2] K. Błoch. Magnetic properties of the suction-cast bulk amorphous alloy: $(Fe_{0.61}Co_{0.10}Zr_{0.025}Hf_{0.025}Ti_{0.02}W_{0.02}B_{0.20})_{96}Y_4$ . J. Magn. Magn. Mater. **390** (2015) 118.

[3] H.R. Lashgari, D. Chu, S. Xie, H. Sun, M. Ferry, S. Li Composition dependence of the microstructure and soft magnetic properties of Fe-based amorphous/nanocrystalline alloys: a review study J. Non-Cryst. Solids **391** (2014)61.

[4] A. Inoue. Bulk amorphous and nanocrystalline alloys with high functional properties Mater. Sci. Eng. A **304–306** (2001)1.

[5] A. Makino, A. Inoue, T. Mizushima. Soft magnetic properties of Fe-based bulk amorphous alloys. Mater. Trans., JIM **41** (2000)147.

[6] G. A. Petrakovskiĭ. Amorphous magnetic materials. Soviet Physics Uspekhi **24(6)**(1981)511.

[7] V. Belokon, R. Lapenkov, E. Chibiriak, O. Dyachenko. Magnetic susceptibility of systems with different types of interactions: The random interaction fields method. Journal of Magnetism and Magnetic Materials **512**(2020)167051.

[8] V. Belokon, A. Trofimov, O. Dyachenko. Oguchi's method and random interaction fields' method: Investigation of properties of ferromagnetic materials. Journal of Magnetism and Magnetic Materials **471**(2019)501.

[9] V. Belokon, K. Nefedev. Distribution function for random interaction fields in disordered magnets: Spin and macrospin glass. Journal of Experimental and Theoretical Physics **93 (1)** (2001)136.

[10] A. Sokolov. Quantum mechanics. Moscow: Uchpedgiz (1962)591.

[11] N. Ilin, V. V. Tkachev, A. N. Fedorets, A. Tsesarskaya, V. Ivanov, A. Kuchma, A. Frolov, V. Dolzhikov, G. Kraynova, V. Plotnikov. Magnetic Properties of Amorphous Nanocrystalline Alloys Based on Iron with Different Contents of Nobium in Structural Relaxation Processes. Bulletin of the Russian Academy of Sciences Physics **82(7)** (2018) 860-863.

Sixth Asian School-Conference on Physics and
Technology of Nanostructured Materials
Vladivostok, Russia, 25 – 29 April, 2022



# The effect of high-speed nonequilibrium on morphologic and magnetic properties of melt-spun $Co_{58}Ni_{10}Fe_5Si_{11}B_{16}$ alloys

A.M. Frolov*[,1], T.A. Pisarenko[1,2], G.S. Kraynova[1], N.V. Ilin[1], A.Yu. Ralin[1]
[1] Far Eastern Federal University, 8 Sukhanova St., Vladivostok 690950, Russia
[2] Institute of Automation and Control Processes FEB RAS , 5 Radio St., Vladivostok 690041, Russia

*e-mail: froloff5@yandex.ru

**Abstract.** In this work we present the study of the morphologic and magnetic properties of the melt-spun $Co_{58}Ni_{10}Fe_5Si_{11}B_{16}$ alloy, depending on the production conditions such as the high-speed non-equilibrium of a melt-spinning process. It is shown the amorphous states of different disorder degree may be formed by varying spinning parameters. A correlation was established between the structural and magnetic properties at the level of the hierarchical mesoscale structure (from atomic scales to the morphologic scale of the ribbon surface). It was found that the fractally ordered hierarchical mesoscale structure of the alloy affects the character of the magnetic interaction: the higher the fractal dimension, the more pronounced the soft magnetic properties of the melt-spun $Co_{58}Ni_{10}Fe_5Si_{11}B_{16}$ alloy.

## 1. Introduction

Amorphous metal alloys (AMA) are of great scientific interest in the study of the physical properties of disordered system. Soft magnetic AMA fabricated by the rapid quenching melt have a high magnetic permeability, as a result, one may be successfully applied for the manufacture of magnetic heads, magnetic shields, and secondary power supplies [1-4]. These alloys have high strength and corrosion resistance, which is important when operating in aggressive environments. This class of material also includes multicomponent soft magnetic amorphous alloys based on cobalt.

The aim of this work is to identify the structural-morphological ordering and magnetic ordering in cobalt-based AMA produced by spinning the melt on a cooling roller at different speed condition. It is interesting to trace the correlations of production conditions, surface morphology, and physical properties. Since, on the one hand, disordered media are characterized by the collective behavior of defects, which form a hierarchical system having a fractal structure in the configuration space [5], and, on the other hand, it is well known that magnetic properties are structure-sensitive [4-7].

## 2. Experiment

In this work, we investigate the melt-spun $Co_{58}Ni_{10}Fe_5Si_{11}B_{16}$ alloy fabricated by melt-spinning technique on a cooling roller in the equipment MeltSpinner SC. Several samples of this alloy were produced, parameterized by the melt-spinning conditions. The technological and geometric parameters of the samples are given in Table I. As can see from the Table I, in this sample series, the cooling roller speed is the most interesting parameter that affects the non-equilibrium of the melt-spinning process. The analysis of atomic ordering was performed by X-ray diffraction (using Bruker D8 Advance diffractometer, Fe-Kα-radiation). The morphology analysis was carried out by use of HRTEM images produced by the transmission electron microscopy (FEI TITAN 300). Using the specialized software "Complex for spectral analysis of the electron-optical imaging" [8], the Fraunhofer diffraction patterns were obtained based on FFT algorithm. Then, the power spectra were calculated as a result of the angular convolution of the diffraction pattern. Moreover, the images were parameterized by fractal dimension using the fracton analysis of structural ordering [5]. The hysteresis loops were measured by an automated vibromagnetometer for all Samples.

***Table I.*** *Parameters of Samples.*

| Sample | *V(m/s)* | *P1 (mbar)* | *P2 (mbar)* | *t (μm)* |
|---|---|---|---|---|
| *A* | 22,0±0,1 | 50±5 | 200±5 | 21,1±4,5 |
| *B* | 25,1±0,1 | 50±5 | 250±5 | 22,9±1 |
| *C* | 28,3±0,1 | 50±5 | 350±5 | 22,8±1 |
| *D* | 31,4±0,1 | 50±5 | 350±5 | 19,3±0,5 |
| *E* | 37,7±0,1 | 60±5 | 400±5 | 16,1±1 |

where *V* is the linear speed of cooling roller, *P1* is the pressure in the chamber, *P2* is the pressure in the crucible, *t* is the ribbon thickness.

## 3. Results and discussions

X-ray diffraction analysis revealed that the rapidly quenched $Co_{58}Ni_{10}Fe_5Si_{11}B_{16}$ alloy remains X-ray amorphous at all production conditions [9], and the X-ray diffraction patterns practically coincide when superimposed. The diffraction patterns present a single diffuse peak at angles of $2\theta = (57 \div 59)^o$, which corresponds to the short-range order period of (0.203÷0.197) nm, while there are no crystal peaks. The study of the fractograms obtained by antiplane deformation of the $Co_{58}Ni_{10}Fe_5Si_{11}B_{16}$ ribbon had identified a hierarchical structure in the range over from 20 nm to (1–2) μm looking the coral-like and cellular structures [9]. It is shown that the coral-like structure, as well as the solidification process, begins from the contact ribbon surface. Figure 1 shows a fragment of a HRTEM image of the hierarchical mesoscale structure for the Sample A, to which the fracton analysis was applied.

In this work the parameters sensitive to high-speed nonequilibrium are the fractal dimension ($D_f$) and the coercive force ($H_c$), Fig. 2. According to the kinetics of fractal dimension, two classes of a hierarchical

subordination were distinguished with fractal dimensions greater and less than 2, Fig. 2. In both cases, a fractal percolation cluster is formed near the percolation threshold.

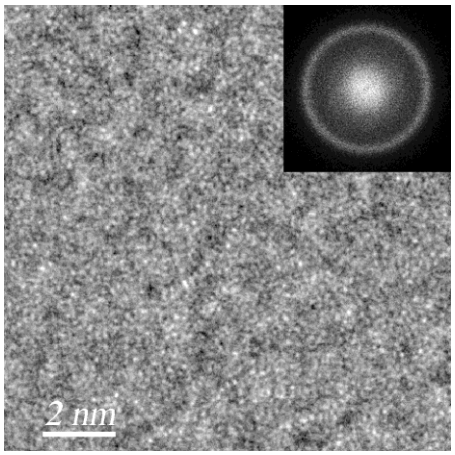


***Fig. 1.*** *TEM subimage of the melt-spun $Co_{58}Ni_{10}Fe_5Si_{11}B_{16}$ alloy (Sample A). The inset shows the Fraunhofer diffraction pattern.*

However, in the first case, the deterministic component prevails in the subordination character; as a result, a spatial connected cluster is formed [10], which provides a minimum coercive force. Whereas in the second case, the subordination character is dominated by the stochastic component, which leads to the formation of a frustrated fractal cluster [10], which significantly reduces the magnetic interaction, as a result the coercive force of these Samples increases.

The sharp change of coercive force from the minimum value to the maximum, Fig. 2, is caused by a change in the ordering of the hierarchical mesoscale structure from nanocrystalline state, in which fractaltally ordered nanocrystals dissolve in an amorphous matrix [4], generating connected cluster, to a homogeneous glassy state, in which both structural and magnetic percolation cluster are strongly stochastic [6], which are represented as an infinite number of non-intersecting fragments [10].

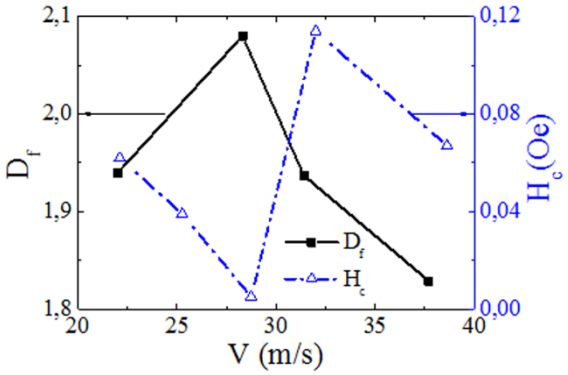


***Fig. 2.*** *Dependences of the fractal dimension and of the coercive force of the $Co_{58}Ni_{10}Fe_5Si_{11}B_{16}$ alloy on the cooling roller speed.*

Based on the obtained results, it can be assumed that the fractally ordered hierarchical mesoscale structure of ribbon effects on the magnetic splitting. As a result, the hierarchical mesoscale structure of morphological inhomogeneities, which is characterized by fractal dimension as a quantitative measure of the order-disorder induced by high-speed nonequilibrium, determines the spatial distribution of the magnetic percolation cluster, starting from the short-range order scale (atomic scale) to hierarchical (nano)cluster structure. Due to dualism, both hierarchical structures are fractal, but not identical. Therewith, the melt-spun $Co_{58}Ni_{10}Fe_5Si_{11}B_{16}$ alloy is the more magnetically soft, the higher the fractal dimension. Thus, the obtained fractal characteristics of the hierarchical mesodefect system of rapidly quenched $Co_{58}Ni_{10}Fe_5Si_{11}B_{16}$ alloy agree with their magnetic parameters.

## 4. Conclusions

In this work, a systematic analysis of the structural and magnetic properties of the melt-spun $Co_{58}Ni_{10}Fe_5Si_{11}B_{16}$ alloy, made at different spinning conditions, has been carried out. High-speed nonequilibrium leads to the amorphization of the $Co_{58}Ni_{10}Fe_5Si_{11}B_{16}$ alloy at all conditions; however, the disordering character in these alloys is significantly different. It is shown that the amount of order-disorder in an amorphous medium can be characterized by fractal dimension. The maximum of the fractal dimension is caused by the fractal ordering of the hierarchical structure of morphological inhomogeneities look a spatial connected cluster, which provides a minimum coercive force. Thus, the study of the functional properties of melt-spun alloys using fractal analysis increases the efficiency of developing technical conditions for the formation of soft magnetic materials fabricated by the rapid quenching melt.

## Acknowledgements

The work was supported by the state task of the Ministry of Science and Higher Education of the Russian Federation under Grant № 0657-2020-0005.

The experimental results were obtained on the equipment of the Centre of Collective Usage of the Far Eastern Federal University, registration No. 200556 (Vladivostok).

## References

[1] L. Hawelek, T. Warsk, P. Wlodarczyk, M. Polak, P. Zackiewicz, W. Maziarz, A. Wojcik, M. Steczkowska-Kempka, A. Kolano-Burian. Materials **14**(2021)10.
[2] Y. Han, J. Ding, F.L. Kong, A. Inoue, S.L. Zhu, Z. Wang, E. Shalaan, F. Al-Marzouki. J. of Alloys and Compounds **691**(2017)36.
[3] C. Liu, A. Inoue, F.L. Kong, E. Zanaeva, A. Bazlov, A. Churyumov, S.L. Zhu, F. Al-Marzouki, R.D. Shull. J. of Non-Crystalline Solids 554(2021)120606.
[4] G. Herzer. Acta Mater. **61**(2013)718.
[5] T.A. Pisarenko, A.M. Frolov, G.S. Kraynova. Solid State Phenom. **215**(2014)190.
[6] S.V. Komogortsev, R.S. Iskhakov, V.A. Fel'k. Journal of Experimental and Theoretical Physics **128**(2019)754.
[7] A.N. Kotvitckii, G.S. Krainova, A.M. Frolov, V.S. Pechnikov. Bulletin of the Russian Academy of Sciences: Physics. **77**(2013)1206.
[8] B.N. Grudin, and V.S. Plotnikov, Processing and simulating of microscopic images, Dal'nauka, Vladivostok, 2010.
[9] Pustovalov E.V., Modin E.B., Frolov A.M., et. al. Journal of Surface Investigation: X-ray, Synchrotron and Neutron Techniques **13**(2019)600.
[10] B.B. Mandelbrot, The fractal geometry of nature, Freeman, New York, 1982.

Sixth Asian School-Conference on Physics and
Technology of Nanostructured Materials
Vladivostok, Russia, 25 – 29 April, 2022



# Dependence the metastability magnetic states of core/shell nanoparticles from interfacial exchange interaction

L.L. Afremov[1,2], I.G. Iliushin[*,1,2]

[1] Laboratory of Spin-Orbitronics, Institute of High Technologies and Advanced Materials, Far Eastern Federal University, Vladivostok 690922, Russia
[2] Far Eastern Federal University, 10 Ajax Bay, Russky Island, Vladivostok 690922, Russia

*e-mail: iliushin.ig@dvfu.ru

**Abstract.** In this article, we present the model of core/shell nanoparticle with random orientation of the axes of magnetic anisotropy of magnetic phases. The results of calculation are presented: the total energy of the core/shell nanoparticle, which includes the energies of crystallographic and surface anisotropy, interfacial exchange interaction, and Zeeman energy. The resulting expression for the total energy makes it possible to study the effect of geometric parameters (phase size, its elongation, and orientation long axes) and interfacial exchange interaction on the metastability of magnetic states core/shell nanoparticles.

## 1. Introduction

Wide practical use of magnetic core/shell nanoparticles in biomedicine, electronics, catalysis and composite materials has given rise to numerous studies on the effects of various factors on their magnetic properties. Decreasing the size of the core/shell nanoparticles leads to a decrease of the coercive field, the saturation magnetisation, the remanent saturation magnetisation $M_{rs}$ and the blocking temperature. Furthermore, decreasing the size of the nanoparticles lowers the potential barriers which separate different magnetic states. A decrease of the potential barriers results in an increase of thermal fluctuations, which can cause the system of core/shell nanoparticles to undergo a transition into the superparamagnetic state. In this work, we present the results of our theoretical study of the dependence of the metastability magnetic states of core/shell nanoparticles from interfacial exchange interaction [1].

## 2. Model of core/shell nanoparticle

We will use the model described in detail in [2]. The main features of this model are as follows:

1. We consider a uniformly magnetised ellipsoidal nanoparticle (phase (1)) of volume V with an elongation *Q* and minor semiaxis *B* containing a uniformly magnetised ellipsoidal core (phase (2)) of volume $v = \varepsilon V$ and elongation *q* and minor semiaxis *b*. The long axes of both phases are oriented along the axis Oz (see. Fig. 1).
2. We assume the crystallographic anisotropy axes to be parallel to the long axes of the ferromagnetic nanoparticle and the core.
3. The spontaneous magnetisation vectors of both phases $M_s^{(1)}$ and $M_s^{(2)}$ are located in the plane $xOz$ containing the long axes of the magnetic phases and make the angles $\vartheta^{(1)}$ and $\vartheta^{(2)}$ with the axis $Oz$, respectively.
4. An external magnetic field *H* is applied along the axis *Oz*.

The assumption that the distribution of the magnetic moment is uniform in the shell leads to a limitation of its thickness. The shell thickness cannot be greater than the width of the domain wall.

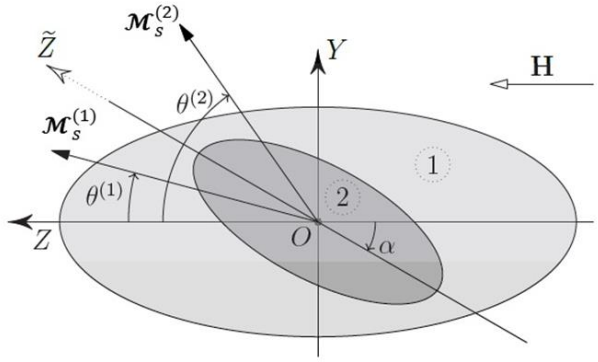


***Fig. 1.*** *Model of core/shell nanoparticle.*

## 3. Results and discussions

The energy of a nanoparticle *E* located in an external field *H* can be represented as the sums of the energy crystallographic anisotropy $E_A$, the energy of the demagnetizing field $E_m$, the energy of interfacial exchange interaction $E_{ex}$, and the Zeeman energy $E_H$:

$$E = E_A + E_m + E_{ex} + E_H =$$
$$= \left\{ -\frac{(\mathcal{M}_s^{(1)})^2}{4}\mathcal{K}^{(1)}\cos 2(\vartheta^{(1)} - \delta^{(1)}) - \right.$$
$$-\frac{(\mathcal{M}_s^{(2)})^2}{4}\mathcal{K}^{(2)}\cos 2(\vartheta^{(2)} - \delta^{(2)}) +$$
$$+\mathcal{M}_s^{(1)}\mathcal{M}_s^{(2)}[-\mathcal{U}_1 \sin\vartheta^{(1)}\sin\vartheta^{(2)} + \mathcal{U}_2\cos\vartheta^{(1)}\cos\vartheta^{(2)}$$
$$+\frac{1}{2}\varepsilon\, k_N^{(2)}\sin 2\alpha \sin\left(\vartheta^{(1)} + \vartheta^{(2)}\right) -$$
$$\left. -H\left[(1-\varepsilon)\ \mathcal{M}_s^{(1)}\cos\vartheta^{(1)} + \ \varepsilon\ \mathcal{M}_s^{(2)}\cos\vartheta^{(2)}\right]\right\}V \qquad (1)$$

Here, $\mathcal{K}^{(1,2)}$ are the effective anisotropy constants, $\delta^{(1,2)}$ are the position of effective axes of the core and the shell, $\mathcal{U}_1$ and $\mathcal{U}_2$ are interfacial interaction constants. Its are defined by the following expressions:

$$\mathcal{K}^{(1)} = \sqrt{\left((1-\varepsilon)k_A^{(1)} + (1-2\varepsilon)k_N^{(1)} + \varepsilon k_N^{(2)}\cos 2\alpha\right)^2 + \left(\varepsilon k_N^{(2)}\sin 2\alpha\right)^2}, \qquad (2)$$

$$tg(2\delta^{(1)}) = -\frac{\varepsilon k_N^{(2)} \sin 2\alpha}{(1-\varepsilon)k_A^{(1)} + (1-2\varepsilon)k_N^{(1)} + \varepsilon k_N^{(2)} \cos 2\alpha}, \quad (3)$$

$$\mathcal{K}^{(2)} = \varepsilon\sqrt{\left(k_A^{(2)}\right)^2 + \left(k_N^{(2)}\right)^2 + 2k_A^{(2)}k_N^{(2)}\cos 4\alpha}, \quad (4)$$

$$tg(2\delta^{(2)}) = -\frac{k_N^{(2)} - k_A^{(2)}}{k_N^{(2)} + k_A^{(2)}} tg\, 2\alpha,$$

$$\mathcal{U}_1 = \varepsilon\left(\frac{\left(k_N^{(1)} - k_N^{(2)}\right)}{3} + \frac{2sA_{in}}{v\,\delta\,\mathcal{M}_s^{(1)}\,\mathcal{M}_s^{(2)}}\right), \quad (5)$$

$$\mathcal{U}_2 = \varepsilon\left(\frac{2\left(k_N^{(1)} - k_N^{(2)}\right)}{3} - \frac{2sA_{in}}{v\,\delta\,\mathcal{M}_s^{(1)}\,\mathcal{M}_s^{(2)}}\right).$$

Here in the equations (2) – (5) $k_A^{(1,2)} = K_1^{(1,2)}/\left(\mathcal{M}_s^{(1,2)}\right)^2$, $k_N^{(1,2)}$ are dimensionless constants of crystallographic anisotropy and shape anisotropy core (2) and shell (1). $K_1^{(1,2)}$ are first phase anisotropy constants, $s$ is surface area of the separating phase, $\delta$ is transition area width having the order of the lattice constant, $A_{in}$ is interfacial exchange interaction constant. Note that the shape anisotropy constant $k_N = 2\pi\,(1-3N_z)$is expressed in terms of the demagnetizing coefficient along the long axis. It expressed in terms of the demagnetizing factor along the long axis $N_z = \left[q\ln\left(q+\sqrt{q^2-1}\right) - \sqrt{q^2-1}\right]/(q^2-1)^{3/2}$. It depends only on the elongation of the ellipsoid q.

The magnetic states can depend on the surface anisotropy. As was shown in [1], adding to the energies listed above the energy of surface anisotropy is equivalent to replacing $k_N^{(1,2)}$ to $k_N^{(1,2)} + 2\pi k_S^{(1,2)} b_{(1,2)}^2 \xi\left(q_{(1,2)}\right)$.

Energy minimization (1) with respect to $\vartheta^{(1)}$ and $\vartheta^{(2)}$together with the minimum conditions

$$\frac{\partial E}{\partial \vartheta^{(1)}} = 0, \quad \frac{\partial E}{\partial \vartheta^{(2)}} = 0; \quad \frac{\partial^2 E}{\partial \vartheta^{(1)2}} > 0$$
$$\frac{\partial^2 E}{\partial \vartheta^{(1)2}}\frac{\partial^2 E}{\partial \vartheta^{(2)2}} - \left(\frac{\partial^2 E}{\partial \vartheta^{(1)}\partial \vartheta^{(2)}}\right)^2 > 0 \quad (6)$$

leads to a system of equations that allows one to determine the ground and metastable states of the magnetic moments of the nanoparticle phases.

## 4. Result

We used the diagram $\{b, q\}$, each point of which is associated with a nanoparticle (with given values $B$ and $Q$) containing a core with semi-minor axis $b$ and elongation $q$ (see Fig. 2). The dot nanoparticles are fell into the dark region can be in one of the four basic or metastable states listed above. The light area corresponds to nanoparticles in basic equilibrium states.

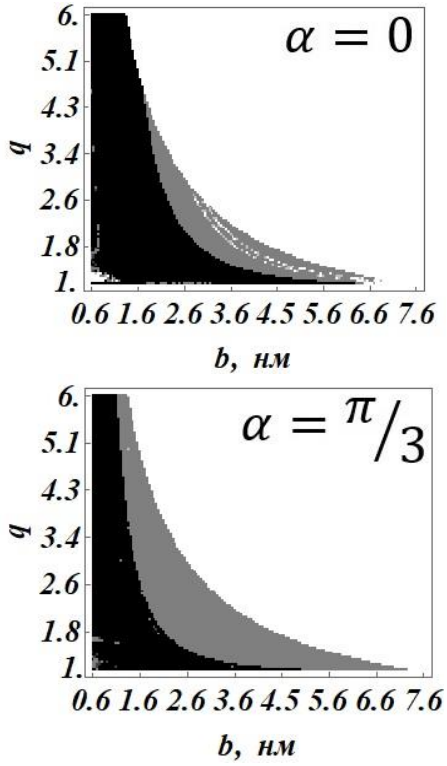


***Fig. 2.*** *Diagrams $\{b, q\}$ of magnetic states of nanoparticles $Fe_3O_4 - Fe_{2.44}Ti_{0.56}O_4$ for different angles $\alpha$ between the long axes of the cores and nanoparticle.*


## Acknowledgements

This study was supported by the grant of the Government of the Russian Federation for state support of scientific research conducted under supervision of leading scientists in Russian institutions of higher education, scientific foundations and state research centres of the Russian Federation (Project No. 075-15-2021-607).


## References


[1] G.C. Lavorato, E. Lima Jr, D. Tobia, D. Fiorani, H.E. Troiani, R.D. Zysler, E.L. Winkler Nanotechnology, **25** (2014), p. 355704.

[2] L. Afremov, S. Anisimov, I. Iliushin. Journal of Magnetism and Magnetic Materials **447,** (2018) 88–95.

Sixth Asian School-Conference on Physics and
Technology of Nanostructured Materials
Vladivostok, Russia, 25 – 29 April, 2022



# Tuning of magnetic behavior of Cu/Co barcode nanowires for 3D-memory applications

V.N. Kharitonov*[,1], A.Yu. Samardak[1], M.Yu. Pavliuk[1], E.V. Tepnin[1], A.V. Ognev[1], D.R. Khairetdinova[2,3] , I.M. Doludenko[2].

[1] Far Eastern Federal University, FEFU
[2] Federal State Institution "Federal Research Center "Crystallography and Photonics" of the Russian Academy of Sciences
[3] Moscow Steel and Alloys Institute

*e-mail: kharitonov.vn@dvfu.ru

**Abstract.** In this paper, we consider the magnetic properties of segmented Cu/Co nanowires grown in track membranes with cylindrical channels by electrochemical deposition. The study of switching processes resulting from the magnetization reversal of such heterostructures using computer simulation methods will simplify the search for the most appropriate parameters of substances that can be used as the basis for 3D memory elements. The study of the magnetic characteristics of nanowires can improve the energy efficiency and effectiveness of the electronic devices in which they are used.

## 1. Introduction

Since the publication of Kelly et al. [1], the development of composite materials has become a topic of interest. Due to the emergence of composite nanomaterials in recent years, and due to their interesting structure and numerous physical properties, this has promoted the research of multifunctional macroscopic engineering materials and made progress in growth of nanocomposites. materials [2]. Now, it is hardly a surprising fact that the multilayer and sandwich nanostructures have gained considerable attention, both in industrial and scientific communities, owing to their excellent properties. Recently, a lot of researchers have pointed out the significance of multilayer magnetic/nonmagnetic nanostructures, and it became a topic of research for theoretical and experimental studies. Due to the noteworthy magnetic exchange interaction and giant magnetic resistance phenomena observed in such nanostructures (i.e., NWs) they have many desirable properties.
applications in magnetic barcoding systems, electrical switching devices, magnetic sensors, dense storage medium, and giant magnetoresistance (GMR) hard drives.

Numerous synthesis methods were used for the formation of heterostructured NWs for device applications [4-9]. After the synthesis of barcode metallic NWs by Pen et al. [10], electrodeposited multi-segmented NWs were used.

Studies of such systems are carried out to analyze the interaction of nanowires in such disordered systems, which can be chaotic or completely exclude interactions in the array.

Segmented nanowires are distinguished by unusual types of interaction [3]. The magnetic flux in them, depending on the length of the segments, is divided into interactions between adjacent segments in a wire, between poles in one segment, and between segments in neighboring nanowires. Therefore, in the case of a random distribution of the distance between nanowires, the magnitudes of these interactions will change strongly, which can lead to unusual magnetic effects.

## 2. Experiment

Track membranes were made from polymer films by bombarding their surface with high-energy accelerated ions which create the latent tracks. During subsequently etching the through pores could be formed. During this process, it is possible to accurately control the pore diameters, from 50 nm to 5 microns, depending on the etching time. These membranes with through pores (of cylindrical shape) could be used as a templates for the growth of one-dimensional nanostructures (nanowires) by electrochemical deposition.

Using the electrodeposition method (with the single bath which contained Co and Cu ions), segmented (layered) Co/Cu nanowires could be obtained in the pores of track membranes. The elemental composition of the segments was controlled by the deposition potential (0.5 V for copper and 1,5 V for cobalt), while the length of the segments was controlled by the passed charge. For furhter microscopic investigation (SEM) of polymer membrane a conductive copper layer about 20 nm thick was deposited on the surface of membrane in a molecular beam deposition facility to obtain higher quality images. SEM images of nanowires were obtained after removing of host polymer matrix. The list of samples studied is presented in Table I.

***Table I.*** *Parameters of Samples.*

| Sample | Pore diameter(nm) | Nanowire length(μm) | Segment length(nm) |
|---|---|---|---|
| Cu20_Co200 | 100 | 2.2 | 20 Cu, 200 Co |
| Cu50_Co200 | 100 | 2.5 | 50 Cu, 200 Co |
| Cu100_Co200 | 100 | 2.5 | 100 Cu, 200 Co |
| Cu200_Co200 | 100 | 2.5 | 200 Cu, 200 Co |

The magnetic properties of all samples were studied on a LakeShore VSM 7410 vibrating magnetometer in the useful range from -7 kOe to 7 kOe.

Micromagnetic modeling in the MuMAX3 package was used to analyze the micromagnetic structure. The geometry of the nanostructures was set by processing SEM images using the Fiji software package, where each pore was taken as containing a ferromagnetic nanowire and translated over a distance of 2 μm. The cell size in the simulation was assumed to be close to the value of the exchange constant for Co and amounted to 5 nm. The magnetic parameters were set as for bulk Co with a 10% correction for the polycrystalline structure and the possible presence of impurities in the composition of the nanowires. To achieve

reliable model, simulated results were compared to experimental ones.

### 3. Results and discussions

As SEM investigation showed, the porous matrix does not have long-range order, and the interpore distance varies from 50 nm to 500 nm. It should also be noted that porous agglomerates consisting of combinations of pores of various shapes.

The results of micromagnetic modeling for the Cu20_Co200 sample along the long axis of the nanowire are shown in Figure 1. The spin configuration of nanowires in an external magnetic field along the main axis of nanowires equal to 2500 Oe and -2500 Oe are shown in the Figures 1(a) and 1(b), respectively. Figures 1(c) and 1(d) shows the spin configuration of the sample at zero external field in longitudinal and transverse sections, respectively. As one can see, vortex state is preferable configuration for such nanosystems, and the switching occurs by the vortex core switching and coherent rotation of the rest of the vortex after the external field. In the remnant state, skyrmion-like winding of the vortex is presented.

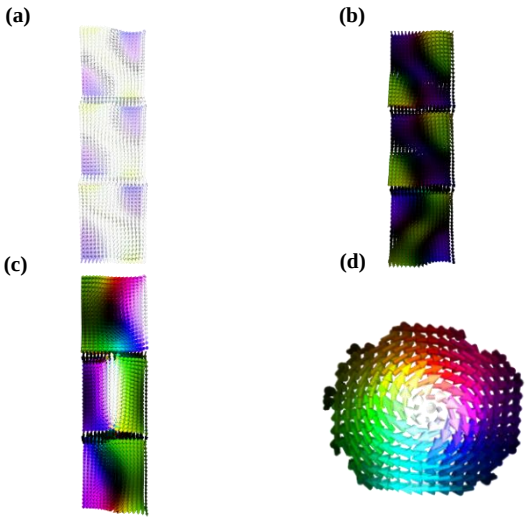


***Fig. 1.*** *Spin configuration of the Cu20_Co200 sample in an external field corresponding to 2500Oe(a), -2500Oe(b) and 0Oe in longitudinal(c) and transverse(d) sections.*

The magnetic hysteresis loops obtained in the results of micromagnetic modeling were compared with experimental data and showed a good correspondence between the developed model and the studied samples.

### 4. Conclusions

As a result of the work, one-dimensional ferromagnetic nanostructures prepared by electrodeposition into porous track membranes of different diameters were investigated. Studies of the structural properties have shown that track pores have a uniform diameter distribution, but due to the chaotic nature of pore formation, their agglomerates are often found, which upon electrodeposition will contain structures that differ from cylindrical nanowires. On the basis of experimental data, a micromagnetic model was constructed, which was used to analyze the domain structure and magnetization reversal processes occurring in the system.

### Acknowledgements

We acknowledge the Russian Ministry of Science and Higher Education for state support of scientific research conducted under the supervision of leading scientists in the Russian Institution of Higher Education, scientific foundation, and state research centers (Project No. 075-15-2021-607) and the state task (Project No. 0657-2020-0013).

The sample growth was supported by State Task of FRSC «Crystallography and photonics» of RAS.

### References

[1] Kelly, A. Composite materials after seventy years. J. Mater. Sci. 2006, 41, 905–912.
[2] Thostenson, E.; Li, C.; Chou, T. Nanocomposites in context. Compos. Sci. Technol. 2005, 65, 491–516.
[3] Da-Shuang Wang, Aiman Mukhtar, Kai-Ming Wu, Liyuan Gu and Xiaoming Cao, Multi-Segmented Nanowires: A High Tech Bright Future, Materials · November 2019.
[4] Bicelli, L.P.; Bozzini, B.; Mele, C.; D′Urzo, L. A review of nanostructural aspects of metal electrodeposition Int. J. Electrochem. Sci. 2008, 3, 356–408.
[5] Hyun, J.K.; Zhang, S.; Lauhon, L.J. Nanowire heterostructures. Annu. Rev. Mater. Res. 2013, 43, 451–479.
[6] Li, Y.; Qian, F.; Xiang, J.; Lieber, C.M. Nanowire electronic and optoelectronic devices. Mater. Today. 2006, 18-27.
[7] Yan, R.; Gargas, D.; Yang, P. Nanowire photonics. Nat. Photonics. 2009, 3, 569.
[8] Lu, W.; Lieber, C.M. Semiconductor nanowires. J. Phys. D Appl. Phys. 2006, 39, R387.
[9] Yuan, J.; Xu, Y.; Mueller, A.H. One-dimensional magnetic inorganic–organic hybrid nanomaterials. Chem.
[10] Nicewarner-Pena, S.R.; Freeman, R.G.; Reiss, B.D.; He, L.; Peña, D.J.; Walton, I.D.; Cromer, R.; Keating, C.D.; Natan, M.J. Submicrometer metallic barcodes. Science 2001, 294, 137–141.
[11] Rojo, M.M.; Calero, O.C.; Lopeandia, A.F.; Rodriguez-Viejo, J.; Martín-Gonzalez, M. Review on measurement techniques of transport properties of nanowires. Nanoscale 2013, 5, 11526–11544.

# Magnetic anisotropy and Dzyaloshinskii-Moriya interaction in ultrathin Pd/Co/Ta films

M.A. Kuznetsova*, P.S. Nazarova, A.F. Shishelov, G.S. Suslin and A.G. Kozlov
Institute of High Technology and Advanced Materials, Far Eastern Federal University, Vladivostok 690922, Russia

*e-mail: kuznetcova.mal@students.dvfu.ru

**Abstract.** In this research, we investigated an ultrathin epitaxial heavy metal1(HM1)/ferromagnetic (FM)/heavy metal2(HM2) films. The main magnetic parameters such as thickness of transition from perpendicular magnetic anisotropy (PMA) to in-plane magnetic anisotropy (IMA), value of dead magnetic layer on the Co/Ta interface and thicknesses dependence of coercivity were studied Existence of Dzyaloshinskii-Moriya interaction and chiral dumping effect were showed.

## 1. Introduction

Development of Spintronics demand a search of new nanostructure materials with opportunity to use one in controllable magnetic processes for creation skyrmionium racetrack memory, logic devices etc. Trilayer magnetic structures HM1/FM/HM2 are perspective for development of spintronics devices. directions. Ultrathin epitaxial magnetic films (~1nm) have expressed anisotropy properties, which lead to series of interface effects: enhancement of perpendicular magnetic anisotropy (PMA), interfacial DMI (iDMI), spin-Hall effect etc. [1]. These effects are used for formation, stabilization and controlling spin textures

## 2. Experiment

In our work we prepared a series of thin Pd(111)/Co/Ta films with different value of Co thickness at the room temperature, using ultrahigh vacuum system (Omicron Nanotechnology) which consisted of a molecular beam epitaxy chamber and an analysis chamber interconnected with each other. We used previously chemically and temperature cleaned monocrystalline Si(111) as substrates with Cu (2nm) buffer layer to prevent a silicide formation and avoid of mismatch Si and Pd crystallography structure. Using parameters: Pd thickness – 2nm, Ta flux – 260mA, time of Ta sputtering – 10 min. magnetic parameters were studied by hysteresis loops measured with vibrating sample magnetometer (7410 VSM, LakeShore). Hysteresis loops M(H) were measured in two external field directions: in-plane and out-of-plane. We studied the main magnetic parameters such as magnetic moment, saturation magnetization, anisotropy field, coercivity and energy of magnetic anisotropy depending on ferromagnetic Co thickness.

## 3. Results and discussions

As a result, we determine the value of Co thickness for transition perpendicular magnetic anisotropy to in-plane magnetic anisotropy (~1,5nm) and the value of magnetic dead layer of Co/Ta interface (~0,48nm). (Fig.1) The value of polarized Pd/Co interface we took based on the previous data [2].

Domain structure visualization was carried out with Kerr microscopy (Evico Magnetics). To investigation of iDMI, we studied the velocity curves for samples with PMA. Curves describe the domain wall propagation at the combination of an in-plane and out-of-plane magnetic field by creep law. Non-zero value of $H_{min}$ (~ 300 Oe) indicates of DMI existence, and asymmetrical shape relative the minimum shows the chiral damping contribution (Fig.2).

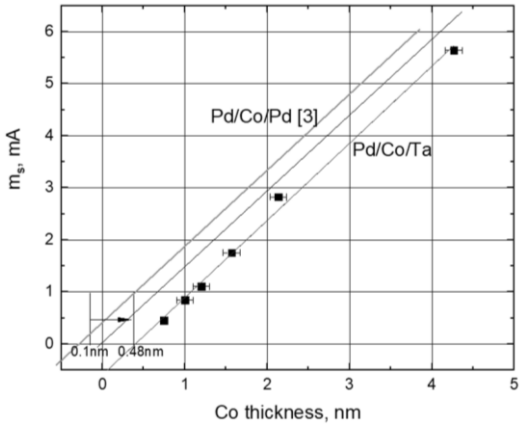


***Fig. 1.*** *Determination of dead layer in Co/Ta interface*

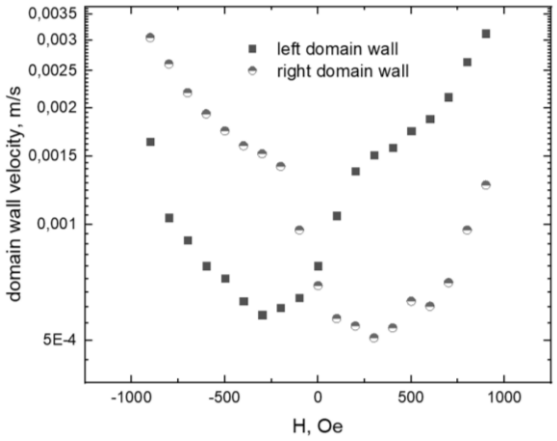


***Fig. 2.*** *Domain walls velocity curves.*

## 4. Conclusions

In this study, we found that the behavior of all studied magnetic parameters is consistent with theoretical concepts. We determine values of transition IMA to PMA (~1,5nm) and dead layer of Co/Ta interface for Pd/Co/Ta magnetic films (~0,48nm). Also, our results show on existence of DMI and damping contribution.

**Acknowledgements**

This research was supported by the Grant Program of the Russian President (Grant No. MK1384.2021.1.2), a grant of the Government of the Russian Federation for state support of scientific research conducted under supervision

of leading scientists in Russian institutions of higher education, scientific foundations, and state research centers of the Russian Federation (Project No. 075-15-2021-607), and the Russian Ministry of Science and Higher Education (State Task No. 0657-2020-0013).

**References**

[1] A.G. Kolesnikov, et. al – Appl. Surf. Sci. Vol.543, (2021), 148720.
[2] A. V. Davydenko, et. al Phys. Rev. B 103, 094435 (2021).
[3] A. V. Davydenko, et. al Phys. Rev. B 95, 064430 (2017).

Sixth Asian School-Conference on Physics and
Technology of Nanostructured Materials
Vladivostok, Russia, 25 – 29 April, 2022



# Magnetic susceptibility and other properties of artificial dipole ice on a hexagonal lattice

A.G. Makarov*[,1,2], K.V. Makarova[1,2], Yu.A. Shevchenko[1,2], V.Yu. Kapitan[1,2], K.S. Soldatov[1,2], K.V. Nefedev[1,2]

[1] Far Eastern Federal University, 10 Ajax Bay, Russky Island, Vladivostok 690922, Russia
[2] Institute of Applied Mathematics, Far Eastern Branch, Russian Academy of Science, 7 Radio St., Vladivostok 690041, Russia

*e-mail: makarov.ag@dvfu.ru

**Abstract.** For calculation properties for artificial dipole ice on a hexagonal lattice we apply the Hybrid Multispin Monte Carlo method. The method is based on combining a random selection of a set of spins (cluster) using the Monte Carlo with a complete enumeration of all states of the selected cluster. The method works only for Ising models with a restricted radius of interaction.

## 1. Introduction

To calculate the properties of a system of interacting magnetic moments (spins) at a given temperature in thermodynamic equilibrium, it is necessary to know the partition function, i.e. it is necessary to have information about all possible states of the system, such as internal energy, magnetic moment, etc. However, in practice, the exact calculation of the partition function is possible only in very rare cases, only for a limited number of models. This is due to the exponentially large state space. In addition, there are practically no ideal systems in nature, in addition, the law of interaction of particles and the geometry of the system can be very complex. Computing a complete group of events from a portion of independent samples from a probability distribution is an important computational problem. There are various approaches to the calculation of statistical thermodynamics, each with its own advantages and disadvantages. In this paper, we applied the Hybrid Monte Carlo method of our own design [1], in which, instead of a single spin flip, we use a complete enumeration of all spin states within a small cluster that interact only with boundary spins.

## 2. Formalism and model

"Artificial spin ice" (ASI) is an artificial analogue of natural spin ice - geometrically frustrated magnetic pyrochlores that mimic the ordering of water proton spins, and also a convenient basis for developing, testing and verifying the accuracy of theoretical models of many interacting bodies and new statistical methods.

We use point Ising dipoles located on the edges of a two-dimensional hexagonal lattice with periodic boundary conditions. The magnetic moment of the dipole *i* is defined as $\boldsymbol{m}_i$ and is directed along the edges, see details in [1,2]. An example of a dipole hexagonal lattice is shown in Fig. 1.

For the operation of the Hybrid Monte Carlo method, we limited the radius of the dipole-dipole interaction to three coordination spheres according to the results [3]. Each cluster spin has 14 nearest neighbors, see Fig. 2.

It is also necessary to determine the clusters and boundaries to which each hexagon belongs. The hexagon itself acts as a cluster, and the nearest neighbors of the hexagon spins are the boundary that interacts with the cluster and separates it from all other spins.

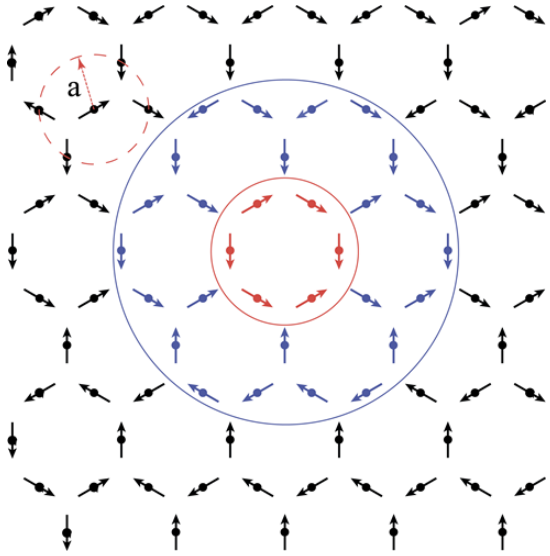


***Fig. 1.*** *An example of hexagonal lattice with Ising-like point dipoles (spins). Cluster spins are marked in red (small circle) and border spins in blue color (big circle), which are used as subsystems in the Hybrid Monte Carlo method.*

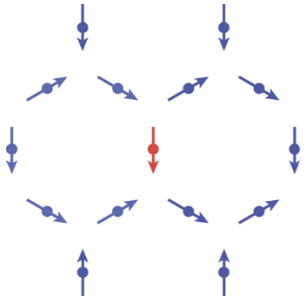

***Fig. 2.*** *The cluster spin and interacting dipole–dipole neighbors up to the third coordination sphere.*

The cluster is shown by red arrows in Fig. 1 and consists of six spins. The cluster boundary is shown by blue arrows and consists of 24 nearest neighboring spins. In total, the cluster and the boundary block contain 30 spins, the states of which can be easily enumerated by a complete enumeration. In the future, this block will be used for the operation of the Hybrid Monte Carlo method.

To calculate the energy, it is necessary to determine the neighbors for each spin. Due to the fact that the boundary

conditions are periodic, all elements in the system have the same number of neighbors (Fig. 2).

The energy of dipole–dipole interaction between ASI spins in system is defined as

$$E = Da^3 \sum_{i<j} \frac{(\boldsymbol{m}_i \boldsymbol{m}_j)}{|\boldsymbol{r}_{ij}|^3} - 3\frac{(\boldsymbol{m}_i \boldsymbol{r}_{ij})(\boldsymbol{m}_j \boldsymbol{r}_{ij})}{|\boldsymbol{r}_{ij}|^5}, \quad (1)$$

where $D = \mu^2/a^3$ is the dipole coupling constant, $a = \sqrt{3}/2$ is the lattice parameter (Fig. 1), and $\boldsymbol{r}_{ij}$ is the radius vector between spins *i* and *j*.

### 3. Results

For systems with different numbers N of spins, we calculated the specific heat capacity C(T) per spin in the absence of an external magnetic field and the magnetic susceptibility χ(T) per spin at |H| → 0 depending on temperature

$$C(T) = \frac{1}{N}\frac{\langle E^2\rangle - \langle E\rangle^2}{k_b T^2}, \quad (2)$$

$$\chi(T)|_{|H|\to 0} = \frac{1}{N}\frac{\langle |M|^2\rangle - \langle |M|\rangle^2}{k_b T}, \quad (3)$$

where $\langle E\rangle$ and $\langle |M|\rangle$ the average thermodynamic quantities, $k_b$ – Boltzmann coefficient, *T* - temperature.

By using our method, we obtain the specific heat (Fig. 3) and magnetic susceptibility at $|H| \to 0$ (Fig. 4) for the hexagonal spin ice consisting of different number of spins.

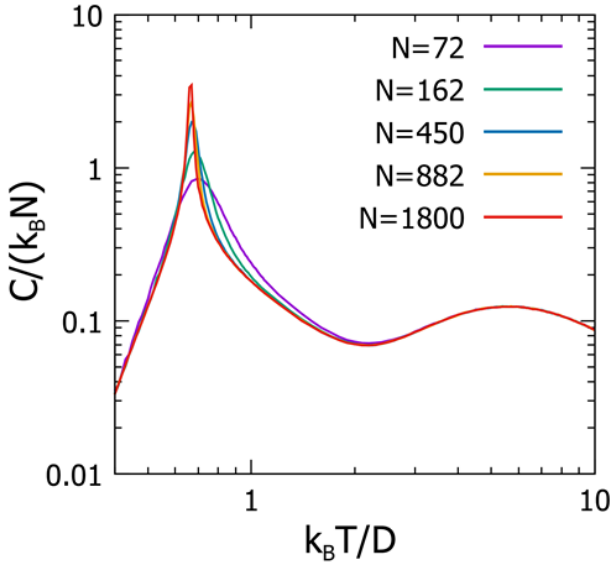


***Fig. 3.*** *The temperature behavior of the specific heat for different number of spins on the hexagonal lattice, calculated by the Hybrid Monte Carlo method.*

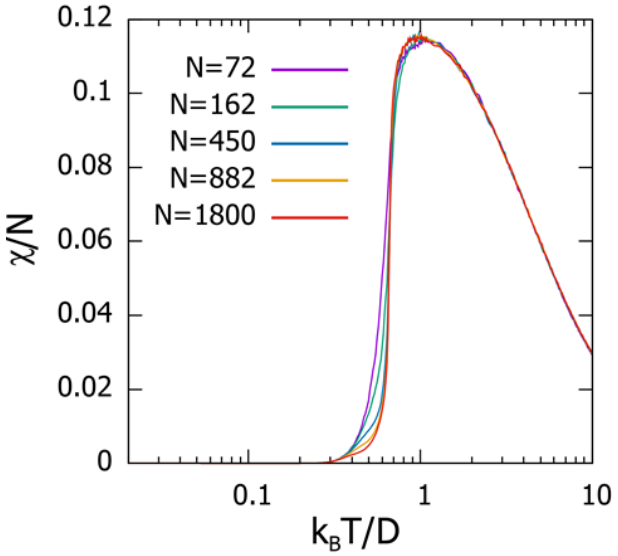


***Fig. 4.*** *The temperature behavior of the magnetic susceptibility at |H|→0 for different number of spins on the hexagonal lattice, calculated by the Hybrid Monte Carlo method.*

The temperature behavior of the heat capacity has two peaks. An increase in one of the heat capacity peaks with an increase in the size of the system may indicate the presence of a phase transition. The temperature behavior of the magnetic susceptibility at $|H| \to 0$ of hexagonal spin ice has no features, and the height of the peak does not change with an increase in the size of the system.

### Acknowledgements

The research results connected with model samples preparation and physical experiments were obtained within the framework of the state task of the Ministry of Science and Higher Education of the Russian Federation of Russia (No. 0657-2020-0005). The research results connected with algorithms elaboration, program coding end implementation of parallel scheme of calculation obtained at the expense of the grant of the President of the Russian Federation for state support of the leading scientific schools of the Russian Federation (NSh-2559.2022.1.2).

### References

[1] A. Makarov, et al. JETP Letters **110**(2019)702.
[2] K. Makarova, et al. Physical Review E **103**(2021)042129.
[3] P. Andriushchenko. Journal of Magnetism and Magnetic Materials **476**(2019)284.

Sixth Asian School-Conference on Physics and
Technology of Nanostructured Materials
Vladivostok, Russia, 25 – 29 April, 2022



# Magnetic susceptibility and other properties of artificial dipole ice on the Cairo lattice

K.V. Makarova*[,1,2], A.G. Makarov[1,2], Yu.A. Shevchenko[1,2], V.Yu. Kapitan[1,2], K.S. Soldatov[1,2], K.V. Nefedev[1,2]

[1] Far Eastern Federal University, 10 Ajax Bay, Russky Island, Vladivostok 690922, Russia
[2] Institute of Applied Mathematics, Far Eastern Branch, Russian Academy of Science, 7 Radio St., Vladivostok 690041, Russia

*e-mail: makarova.kv@dvfu.ru

**Abstract.** In our paper, we calculated the thermodynamics in frame short-range interaction model on the pentagonal Cairo lattice. We used a hybrid multispin Monte Carlo method for lattices with N=80, N=500 and 980 dipoles.

## 1. Introduction

Systems of artificial spin ice with a variable, not fixed, variable coordination number [1,2] are of particular interest. It is usually assumed that a change in the lattice parameters can significantly affect the degree of degeneracy of the energy levels and, accordingly, the low-temperature properties of spin ice. Exact calculation of the properties even for a classical Ising spin glass on a 2D lattice with the interaction of neighbors of the nearest environment is a computationally difficult problem and is of fundamental and practical interest.

## 2. Formalism and model

The Cairo lattice is sometimes called the "pentagonal lattice" [3] or "Cairo pentagonal lattice" [4-6]. In this paper, we consider the thermodynamics of samples of a finite number of Ising-like point dipoles on the Cairo lattice, since the sizes of nanoislands were below the critical single-domain threshold, and the shape anisotropy selects the direction for the magnetic moment. The dipoles were placed at the centers of the lattice faces (see Fig. 1). The lattice parameters were $a$=472, $b$=344, $c$=376 nm.

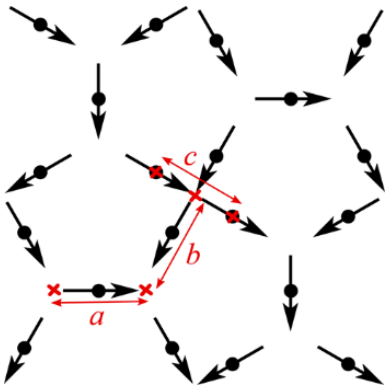


***Fig. 1.*** *An example of Cairo lattice with Ising-like point dipoles (spins) and relevant parameters a, b, and c.*

To implement the hybrid multispin Monte Carlo method [7], which makes it possible to calculate the necessary properties, a cluster was chosen, the size of which, together with the boundary, was 29 dipoles (Fig. 2).

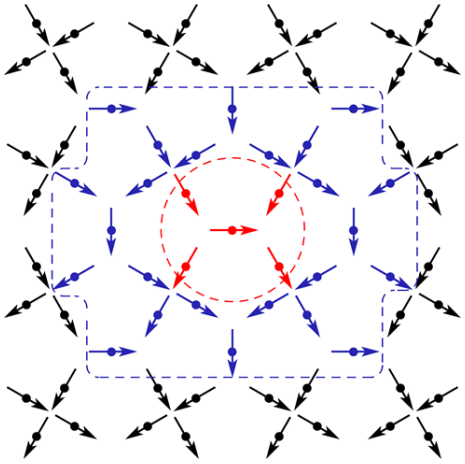

***Fig. 2.*** *Cluster spins are marked in red (small circle) and border spins in blue color (big rectangle), which are used as subsystems in the Hybrid Monte Carlo method.*

Figure 3 shows the restriction of the interaction of dipoles to 13 neighbors.

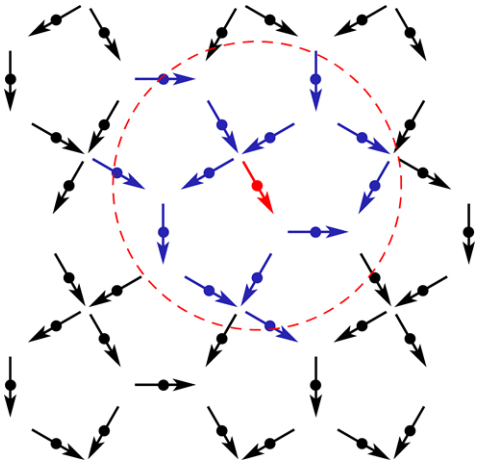

***Fig. 3.*** *The cluster spin and interacting dipole–dipole neighbors.*

The energy of the dipole-dipole interaction in the Cairo lattice was calculated using the following well-known formula:

$$E_{dip}^{ij} = \frac{(\boldsymbol{m}_i \boldsymbol{m}_j)}{|\boldsymbol{r}_{ij}|^3} - 3\frac{(\boldsymbol{m}_i \boldsymbol{r}_{ij})(\boldsymbol{m}_j \boldsymbol{r}_{ij})}{|\boldsymbol{r}_{ij}|^5}, \quad (1)$$

where $\boldsymbol{m}$ is the dipole magnetic moment; $\boldsymbol{r}_{ij}$ is radius vector connecting $i$ and $j$ dipoles.

## 3. Results

For systems with different numbers N of spins, we calculated the specific heat capacity C(T) per spin in the absence of an external magnetic field and the magnetic susceptibility χ(T) per spin at |H| → 0 depending on temperature

$$C(T) = \frac{1}{N}\frac{\langle E^2\rangle - \langle E\rangle^2}{k_b T^2}, \quad (2)$$

$$\chi(T)|_{|H|\to 0} = \frac{1}{N}\frac{\langle |M|^2\rangle - \langle |M|\rangle^2}{k_b T}, \quad (3)$$

where $\langle E\rangle$ and $\langle |M|\rangle$ the average thermodynamic quantities, $k_b$ – Boltzmann coefficient, $T$ - temperature.

By using our method [7], we obtain the specific heat (Fig. 4) and magnetic susceptibility at $|H| \to 0$ (Fig. 5) for the pentagonal Cairo spin ice consisting of different number of spins.

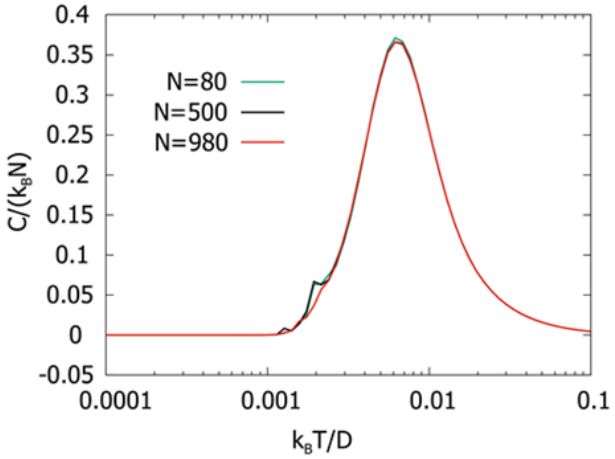


***Fig. 4.*** *The temperature behavior of the specific heat for different number of spins on the pentagonal Cairo lattice, calculated by the Hybrid Monte Carlo method.*

As can be seen from the Fig. 4, with an increase in the number of dipoles on the Cairo lattice of spin ice, no increase in heat capacity is observed in the model with a limited interaction radius. The absence of size effects in the temperature behavior of the heat capacity, i.e. the finite height of the heat capacity peak, which is the same for all studied N = 80, 500 and 980, indicates the absence of a phase transition in the nearest neighbor model.

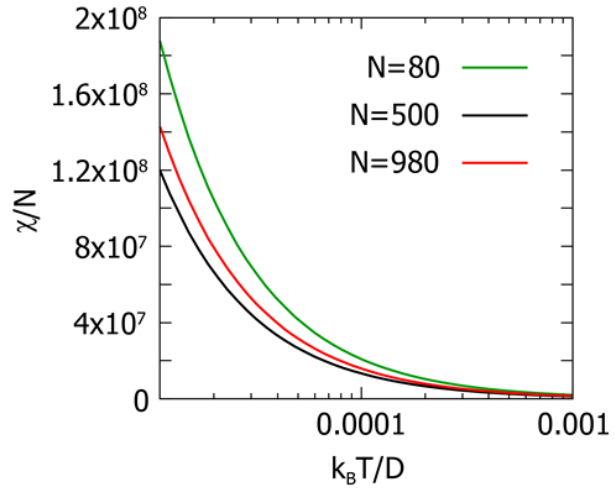


***Fig. 5.*** *The temperature behavior of the magnetic susceptibility at |H|→0 for different number of spins on the pentagonal Cairo lattice, calculated by the Hybrid Monte Carlo method.*

The unusual behavior of the magnetic susceptibility plot requires further study, and it is also necessary to study the influence of an external magnetic field.

## Acknowledgements

The research results connected with model samples preparation and physical experiments were obtained within the framework of the state task of the Ministry of Science and Higher Education of the Russian Federation of Russia (No. 0657-2020-0005). The research results connected with algorithms elaboration, program coding end implementation of parallel scheme of calculation obtained at the expense of the grant of the President of the Russian Federation for state support of the leading scientific schools of the Russian Federation (NSh-2559.2022.1.2). To perform the calculations, we used the computational resources provided by the Shared Facility Center "Data Center of FEB RAS" [8].

## References

[1] I. Gilbert, et al. Nature Physics **10**(2014)670.
[2] C. Nisoli, et al. Reviews of Modern Physics **85**(2013)1473.
[3] R. Moessner, et al. Physical Review B **63**(2001)224401.
[4] V. Urumov. Journal of Physics A: Mathematical and General **35**(2002)7317.
[5] A. Ralko. Physical Review B **84**(2011)184434.
[6] E. Ressouche, et al. Physical review letters **103**(2009)267204.
[7] A. Makarov, et al. JETP Letters **110**(2019)702.
[8] A. A. Sorokin, et al. Scientific and Technical Information Processing **44**(2017)302.

# Magneto-ellipsometry for optically anisotropic structures

O.A. Maximova*[,1,2], S.A. Lyaschenko[1], S.N. Varnakov[1], S.G. Ovchinnikov[1,2]

[1] Kirensky Institute of Physics, Federal Research Center KSC Siberian Branch Russian Academy of Sciences, bld. 38, 50 Akademgorodok, Krasnoyarsk 660036, Russia

[2] Siberian Federal University, 79 Svobodny pr., Krasnoyarsk 660041, Russia

*e-mail: maximo.a@mail.ru

**Abstract.** This article is devoted to the data analysis of magneto-optical ellipsometry data when they are collected from structures with uniaxial optical anisotropy. The magneto-optical parameter, being a part of an off-diagonal tensor elements of dielectric permittivity, was deduced through Maxwell equations consideration. The way of carrying out an experiment is also dicsussed.

## 1. Introduction

Magneto-ellipsometry is a method used for materials characterization due to its high sensitivity and possibility to use in situ without destroying the sample. However the mathematical apparatus is quite complex and requires many measurements which prevents wide use. That is why it is appreciated to develop the methodology of magneto-ellipsometry to ease the ways of carrying out experiments and processing the obtained data.

Very often the materials have uniaxial optical anisotropy [1-3]. When magneto-optical properties of such a structure are considered, in addition to existing optical anisotropy, it is necessary to take into account induced anisotropy [4, 5] associated with the application of an external magnetic field, which inevitably complicates the calculation and analysis of the total dielectric tensor:

$$[\varepsilon]=\begin{bmatrix} \varepsilon_{xx} & -i\varepsilon_{zz}Q & 0 \\ i\varepsilon_{zz}Q & \varepsilon_{zz} & 0 \\ 0 & 0 & \varepsilon_{zz} \end{bmatrix} \quad (1)$$

where $Q=Q1-iQ2$ is a complex magneto-optical parameter proportional to the magnetization lying in the plane of the film. The tensor is written for the case of the transverse geometry (Fig.1) when the magnetization M lies in the plane of the sample.

## 2. Results and discussions

By solving Maxwell equations for the chosen geometry we found out how the reflection coefficients change when anisotropy is taken into account, which allowed to obtain the magneto-optical parameter [6]:

$$Q=\frac{(N_0\cos\varphi_{tp})^2-(N_z\cos\varphi_0)^2}{2N_0N_z\sin\varphi_{tp}\cos\varphi_0\left(1-\left(1-\frac{N_z^2}{N_x^2}\right)\cos^2\varphi_{tp}\right)}\times \quad (2)$$
$$\times\left(\delta\Delta-i\frac{\delta\psi(1+\tan^2\psi_0)}{\tan\psi_0}\right)$$

As it can be seen from the obtained expression (2), to calculate all components of the dielectric tensor, it is sufficient to have information about

- the angle of incidence of light $\varphi 0$,
- the refractive index of the external medium N0,
- the refractive indices of the anisotropic structure in the plane of the sample Ny = Nz and perpendicular to it Nx,
- ellipsometric parameter $\psi 0$, measured without the application of a magnetic field,
- magneto-ellipsometric parameters $\delta\psi = \psi(+H) - \psi(-H)$, $\delta\Delta = \Delta(+H) - \Delta(-H)$, measured in the transverse configuration of the magneto-optical Kerr effect, where ±H is the external magnetic field on the sample.

This gives us a simple scheme for carrying out magneto-ellipsometric measurements to obtain all components of the dielectric tensor of a uniaxial anisotropic material, for example, MAX-phases.

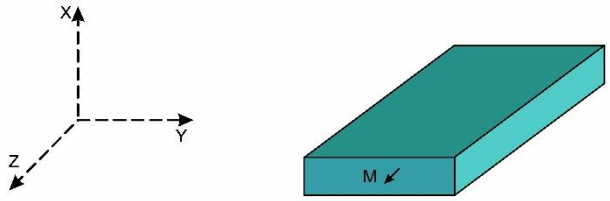


***Fig. 1.*** *Geometry of the transverse magneto-optical Kerr effect.*

## 3. Conclusions

Thus, we considered the interface between the external medium and the sample with optical uniaxial anisotropy, taking into account the magneto-optical response in the geometry of the transverse magneto-optical Kerr effect. The magneto-optical parameter Q was analytically calculated for the transverse geometry of the experiment.

## Acknowledgements

This work was supported by the grant from the Russian Science Foundation No. 21-12-00226, http://rscf.ru/project/21-12-00226/ .

## References

[1] J. Gomis-Bresco, D. Artigas, and L. Torner, Nat. Photon.**11**, (2017) 232.
[2] K. Chaudhuri, Z. Wang, M. Alhabeb, et al., in 2D Metal Carbides and Nitrides (MXenes), Ed. by B. Anasori and Y. Gogotsi (Springer, Cham, 2019), p. 327.
[3] K. Hantanasirisakul and Y. Gogotsi, Adv. Mater. **30**, (2018) 1804779.
[4] A. V. Sokolov, Optical Properties of Metals (GIFML, Moscow, 1961; Am. Elsevier, New York, 1967).
[5] H. Fujiwara, Spectroscopic Ellipsometry Principles and Applications (Wiley, Chichester, 2007).
[6] O. A. Maksimova, Cand. Sci. (Phys. Math.) Dissertation (Krasnoyarsk Sci. Center Sib. Branch RAS, Krasnoyarsk, 2020).

Sixth Asian School-Conference on Physics and
Technology of Nanostructured Materials
Vladivostok, Russia, 25 – 29 April, 2022



# Magnetic properties and MCD spectroscopy of $Co_xZn_{1-x}Fe_2O_4$ nanoparticles synthesized with a citrate precursor method

D.A. Petrov*[,1], A. Thakur[2], P. Thakur[2], S.M. Zharkov[1,3], A.L. Suhachev[1], I.S. Edelman[1]

[1] Kirensky Institute of Physics, 50/38 Akademgorodok St., Krasnoyarsk 660036, Russia
[2] Amity University Haryana, Gurugram, Haryana 122413, India
[3] Siberian Federal University, 79 Svobodny Ave., Krasnoyarsk 660041, Russia

*e-mail: irbiz@iph.krasn.ru

**Abstract.** $Co_xZn_{1-x}Fe_2O_4$ (x=0.0–0.5) nanoparticles (NPs) were studied with transmission electron microscopy, energy dispersive elemental mapping, vibrating sample magnetometer, and optical magnetic circular dichroism (MCD). NPs were synthesized with the citrate precursor method. The sample A was composed of $ZnFe_2O_4$. In the samples B, C, and D, Co was distributed evenly. At higher Co doses, iron oxide NPs and NPs with high Co concentration were observed alongside with main the main $Co_xZn_{1-x}Fe_2O_4$ phase. The samples magnetization behavior was rather complicated. Magnetization dependence on magnetic field indicated the ferromagnetic behavior of NPs with hysteresis. At the same time, the saturation magnetization increased strongly with decreasing temperature what is characteristic of superparamagnetic NPs. This behavior can be associated with a large size dispersion of NPs. The main contribution in MCD is associated with the $ZnFe_2O_4$ phase at x=0.0–0.2, and the $CoFe_2O_4$ phase at x=0.3–0.5.

## 1. Introduction

$CoFe_2O_4$ is a hard magnetic ferrite with moderate saturation magnetization and high coercive field [1], it has a great demand in electronic industry [2]. At the same time $ZnFe_2O_4$ is a soft magnetic oxide which is chemically stable, paramagnetic in bulk and ferromagnetic in nanocrystalline form [3], it plays an important role in many applications like magnetic recording, magnetic storage. The replacement of $Zn^{2+}$ by $Co^{2+}$ in zinc ferrite causes changes in lattice parameter and expands range of applications of these materials. Cobalt-zinc ferrites are useful in high frequency applications due to their high value of electrical resistivity and low dielectric losses [4].

Resistivity and dielectric properties of cobalt substituted zinc ferrite nanoparticle (NPs) of the series $Co_xZn_{1-x}Fe_2O_4$ prepared by citrate precursor technique were described in the article [3], and this work is devoted to their magnetic and magneto-optical properties of these NPs.

## 2. Experiment

$Co_xZn_{1-x}Fe_2O_4$ NPs (x = 0.0, 0.1, 0.2, 0.3, 0.4, 0.5, samples A-F, correspondingly) were prepared by technique described in [1]. At first, stoichiometric amount of $Zn(NO_3)_2 \cdot 6H_2O$, $Co(NO_3)_2 \cdot 6H_2O$, and $Fe(NO_3)_3 \cdot 9H_2O$ were dissolved in 125 mL distilled water. Then 5g of citric acid was added into the solution containing metal nitrates and kept for stirring at 80 ˚C to get a homogeneous solid solution. After that, the samples were pre-sintered at 700˚C for 3 h, followed by cooling to room temperature. The resultant samples were pelletized by adding 2% polyvinyl alcohol as a binder. Final sintering was done at 800˚C for 3 h.

The morphology, microstructure and local elemental composition of the nanoparticles were investigated using transmission electron microscope (TEM) JEM-2100 (JEOL Ltd.) operating at the accelerating voltage of 200 kV. The microscope was equipped with an energy dispersive spectrometer (EDS), Oxford Instruments, which was used to control the elemental composition of the samples. Selected-area electron diffraction (SAED) was used to determine the structure of NPs.

The field dependences of the magnetization of the samples were studied using a vibrating sample magnetometer VSM 8604 (LakeShore Cryotronics, USA).

MCD was measured in the normal geometry. The modulation of the light wave polarization state from the right-hand to the left-hand circular polarization relatively to the magnetic field direction was used for the MCD measurements. The MCD value was measured as the difference between the sample optical density for the right and left polarized light waves.

## 3. Results and discussions

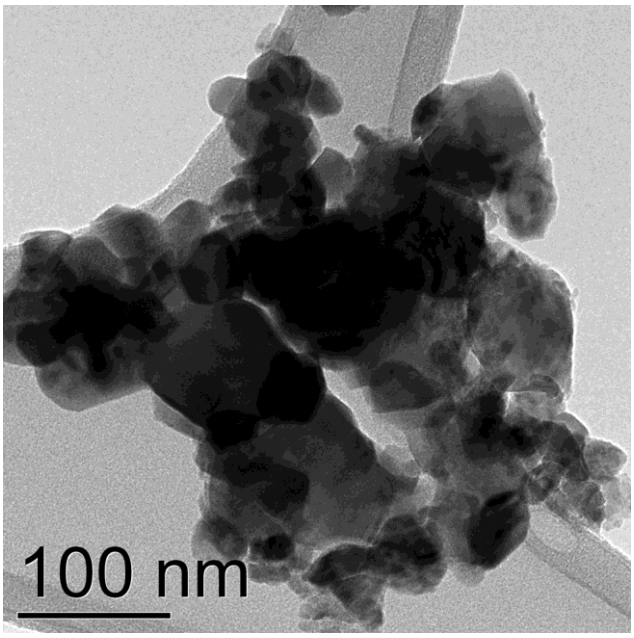


***Fig. 1.*** *Bright-field TEM image of the $Co_{0.4}Zn_{0.6}Fe_2O_4$ nanoparticles.*

TEM image of $Co_{0.4}Zn_{0.6}Fe_2O_4$ nanoparticles is shown in fig. 1. The images for the rest of the samples look pretty much the same. Irregular nanoparticles have a size of 5–

200 nm. According to analysis of SAED patterns, the main crystal phase in all samples was $ZnFe_2O_4$ (Fd-3m, a=8.441 Å, PDF 4+ card #00-022-1012). HRTEM images also correspond to $ZnFe_2O_4$.

The analysis of EDS data showed that the sample A was composed of $ZnFe_2O_4$, In the samples B, C, and D, Co distributed evenly. At higher Co doses, iron oxide NPs and NPs with high Co concentration were observed alongside with main $Co_xZn_{1-x}Fe_2O_4$ phase.

The field dependences of magnetization indicated the ferromagnetic behavior with hysteresis of all samples. At room temperature, the coercivity of the samples was 10–20 Oe. At T = 100 K, it smoothly increased with Co content increase up to 70 Oe for the sample D and up to 220 Oe for sample E. At the same time, the saturation magnetization increased by 4–5 times with decreasing temperature in samples A–D and 2.5 times in sample E what is characteristic of superparamagnetic NPs. This behavior of the samples magnetization can be associated with a large size dispersion of NPs.

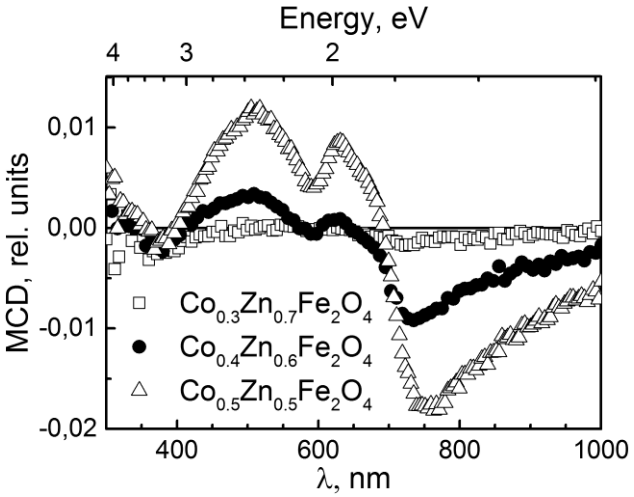


***Fig. 2.*** *MCD spectra of samples* D, E *and* F.

Fig. 2 demonstrates the MCD spectra of samples D–F. An increase in the signal amplitude with a Co content increase in the samples was observed. The temperature decrease also caused significantly amplitude increases. For samples A and B the MCD signal slightly differs from zero. In the sample C at room temperature a noticeable signal appears near 400 nm. With temperature decrease it changed the sign and increased significantly. Another peak near 750 nm also appeared and increased, as in samples D-F. At temperature below 200 K, the feature like butterfly was manifested near 600 nm. The sample D demonstrated similar temperature behavior, but with a more pronounced peak near 500 nm. MCD spectra of samples D–F were in qualitative agreement with the spectra of $CoFe_2O_4$ nanoparticles presented in the work [5].

## 4. Conclusions

Morphology, magnetic and magneto-optical properties of $Co_xZn_{1-x}Fe_2O_4$ NPs prepared by citrate precursor technique were studied. Irregular nanoparticles have a size of 5–200 nm. No dependence of particle morphology on their composition was found. Substitution of Zn with Co leads to transition from the $ZnFe_2O_4$ phase to the $Co_xZn_{1-x}Fe_2O_4$ phase. For high Co doses, iron oxide phase and NPs with high Co concentration were observed also

The field and temperature dependences of magnetization indicated the coexistence of ferromagnetic and superparamagnetic phases in the samples what was associated with wide dispersion of the NPs size. MCD spectra are predominantly associated with the $CoFe_2O_4$ phase.

## Acknowledgements

Electron microscopic studies were carried out in the electron microscopy laboratory of the Central Collective Use Center of the Siberian Federal University, which functions with the support of the state order of the Ministry of Science and Higher Education of the Russian Federation (scientific topic code FSRZ-2020-0011). Magnetic measurements were carried out on a vibrating magnetometer of the Krasnoyarsk Regional Center for Collective Use of the Federal Research Center of the Krasnoyarsk Scientific Center of the Siberian Branch of the Russian Academy of Sciences.

## References

[1] S.G.C. Fonseca, L.S. Neiva, M.A.R. Bonifácio, P.R.C. dos Santos, U.C. Silva, J.B.L. de Oliveira, Materials Research. **21.3**(2018)e20170861.

[2] T.L. Phan, N. Tran, D.H. Kim, N.T. Dang, D.H. Manh, J. Electron. Mater. **46**(2017)4214

[3] D. Chahar, S. Taneja, P. Thakur, A. Thakur, J. Alloys Comp. **843**(2020)155681.

[4] A. Khan, M.A. Bhuiyan, G. Dastegir al-quaderi, K.H. Maria, K.S. Choudhury, A. Hossain, S. Akther, d.K. Saha, J. Bangladesh Acad. Sci. **37**(2013)73e82.

[5] Y.A. Gromova, V.G. Maslov, M.A. Baranov, R. Serrano-García, V.A. Kuznetsova, F. Purcell-Milton, Y.K. Gun'ko, A.V. Baranov, and A.V. Fedorov, J. Phys. Chem. C (2018)11491−11497.

# Micromagnetic Modeling of the Superparamagnetic Fraction of Composites $Fe_3O_4$–$Fe_{3-x}Ti_xO_4$

A.Yu. Ralin*[,1], P.V. Kharitonskii[2], N.A. Zolotov[2,3], K.G. Gareev[2], Yu.A. Anikieva[2]

[1] Far Eastern Federal University, 10 Ajax Bay, Russky Island, Vladivostok 690922, Russia
[2] Saint Petersburg Electrotechnical University «LETI», 5 Professora Popova St., Saint Petersburg 197022, Russia
[3] Institute of Precambrian Geology and Geochronology of RAS, 2 Makarova emb., Saint Petersburg 199034, Russia

*e-mail: ralin.ayu@dvfu.ru

**Abstract.** Modeling of the hysteresis characteristics of $Fe_3O_4$–$Fe_{3-x}Ti_xO_4$ composites was performed using the "magnetic rectangles" method. Their magnetic properties are well explained within the model of an ensemble of magnetostatically interacting chemically inhomogeneous particles. It is shown that taking into consideration the contribution of the superparamagnetic fraction makes it possible to agree the theoretical and experimental magnetic characteristics of the samples.

## 1. Introduction

Theoretical works devoted to the study of ensembles of superparamagnetic particles often use the "non-interacting particles" approximation and the assumption of their chemical homogeneity. The authors [1, 2] studied $Fe_3O_4$–$Fe_{3-x}Ti_xO_4$ composites, in which the presence of a significant fraction of superparamagnetic particles was found. It was shown that the magnetic properties of the studied samples cannot be explained without taking into consideration the chemical inhomogeneity of individual particles and the magnetostatic interaction between them. The same factors should be taken into consideration when modeling the magnetic properties of the superparamagnetic fraction.

## 2. Experiment

Synthesis of composites based on the $Fe_mO_n$–$TiO_2$ system was carried out by magnetite precipitation in suspension of $TiO_2$ powder [1, 2]. 4 g of $FeCl_3 \cdot 6H_2O$ and 2 g of $FeSO_4 \cdot 7H_2O$ (molar ratio 2:1) were dissolved in 100 mL of distilled water. Samples T05L, T10L, and T20L were obtained by dispersing $TiO_2$ powder (0.5, 1.0, and 2.0 g, respectively) into solution, followed by hydrothermal treatment (240°C, 50 MPa) for 4 hours. Sample T05H was treated as well, but under different conditions (470°C, 42 MPa). Sample T20R was not subjected to temperature treatment.

Titanium-containing iron oxides (magnetite, maghemite, hematite, etc.) are a series of solid solutions $Fe^{2+}(Fe^{3+}, Fe^{2+}, Ti)_{\sim 2}O_4$, called titanomagnetites and commonly denoted as $Fe_{3-x}Ti_xO_4$. According to the experimental data [1, 2], titanomagnetites are formed in very small quantities under the specified conditions. Significant content of hematite is detected, indicating significant oxidation of the samples during processing. The lattice period of 0.8362–0.8367 nm is intermediate between the constants of the lattice of maghemite (0.8339 nm) and magnetite (0.8397 nm).

Table I shows the characteristics of the studied samples [1, 2]: $M_s$ is the saturation magnetization and $M_{rs}$ is the saturation remanent magnetization, $\mu_0 H_c$ is the coercive force and $\mu_0 H_{cr}$ is the remanence coercivity.

***Table I.*** *Hysteresis characteristics of the samples.*

| Sample | $M_s$, ($Am^2/kg$) | $M_{rs}$, ($Am^2/kg$) | $\mu_0 H_c$, (mT) | $\mu_0 H_{cr}$, (mT) |
|---|---|---|---|---|
| T05L | 26.37 | 2.95 | 5.62 | 14.92 |
| T10L | 19.53 | 2.06 | 4.77 | 12.61 |
| T20L | 14.11 | 1.92 | 5.97 | 13.77 |
| T05H | 23.79 | 4.15 | 8.78 | 18.32 |
| T20R | 28.95 | 0.35 | 0.51 | 1.90 |

For the first four samples, the ratios of $M_{rs}/M_s$ values are in the range of 0.1–0.2 and $H_{cr}/H_c$ in the range of 2–3. For sample T20R, these ratios are approximately equal to 0.01 and 4, respectively. According to magnetic granulometry data [3], it can be assumed that the first group of samples is dominated by single- and low-domain particles, while in sample T20R by superparamagnetic particles.

## 3. Theoretical modeling

For the modeled samples [1, 2], the presence of three groups of particles was assumed: 1) the fraction of chemically inhomogeneous two-phase particles (magnetite/maghemite – titanomagnetite), 2) the weakly magnetic fraction (mainly hematite), and 3) superparamagnetic particles of the first two fractions. Since the spontaneous magnetization $I_{s1}$ of the first fraction is two orders of magnitude higher than that of the weakly magnetic fraction ($I_{s2}$), the two-phase particles make the main contribution to the saturation remanent magnetization of $M_{rs}$ samples.

The first fraction is an ensemble of cubic two-phase particles with an infinitely thin boundary between the phases [4]. Each phase is a homogeneously magnetized crystallographically uniaxial ferrimagnetic (magnetite/maghemite and titanomagnetite). The characteristic size of particle $a$ ranged from 20 to 80 nm, and the relative thickness of the second phase $\varepsilon$ ranged from 0.05 to 0.20.

To find the magnetic states and critical fields of remagnetization, the free energy was minimized, including magnetocrystalline, magnetostatic, and Zeeman energies. The magnetostatic energy was calculated considering the constancy of surface magnetic charge densities of mutually parallel and mutually perpendicular rectangles – the

"magnetic rectangles" method [4, 5]. In this case, the two-phase particle can be in four states: the magnetic moments of the phases are parallel to each other (along or against the external magnetic field *H*) or antiparallel to each other.

In the case of non-interacting particles in the absence of an external field, it is possible to determine their relative number in the *m*-th state:

$$n_m|_{H=0} = A\exp(-E_m/(kT)), \quad (1)$$

where $A$ is found from the normalization condition, in which the sum of $n_m$ equals one.

Then the magnetization of the ensemble of two-phase ferrimagnetic particles is [4]:

$$M(\varepsilon,H) = C_1[I_{s\,sm}(1-\varepsilon)(n_1-n_2+n_3-n_4) + \\ +I_{s\,wm}\varepsilon(n_1-n_2-n_3+n_4)]. \quad (2)$$

Here $C_1 = N{\cdot}v/V$ is the volume concentration of the first fraction ($N$ and $v$ are the number and average volume of two-phase particles, $V$ is the sample volume), and $I_{s\,sm}$ and $I_{s\,wm}$ are the effective spontaneous magnetizations of the first and second phases, respectively.

If we assume that the random fields of magnetostatic interaction $H_i$ are uniformly distributed in the interval from $-H_{max}$ to $+H_{max}$, the calculation of the magnetization of the fraction of two-phase particles with the same $\varepsilon$ in the first approximation is reduced to the case of non-interacting particles with a shift of the critical fields by $-H_{max}$ [4].

During modeling, the saturation remanent magnetization in the first approximation was provided by the strongly magnetic two-phase particles and the weakly magnetic fraction. However, it was possible to agree the theoretical values of the saturation magnetization with the experimental data only in the assumption of the presence of a large number of superparamagnetic particles in the samples.

Then for the first four samples (Table I)

$$M_s = M_{s1} + M_{s2} + M_{s\,sp}, \quad M_{rs} = M_{rs1} + M_{rs2}, \quad (3)$$

where $M_{s1}$ and $M_{rs1}$, $M_{s2}$ and $M_{rs2}$, $M_{s\,sp}$ are the magnetizations of the corresponding three fractions.

Judging by the hysteresis characteristics (Table I), the fifth sample (T20R) contains mainly superparamagnetic particles. Therefore, the average particle size of this sample varied in the range of 20–30 nm (for spherical magnetite grains, the single-domain size is 29–36 nm [6]). The contribution of all particles to the saturation magnetization was taken into consideration, and only the particles blocked due to the magnetostatic interaction were included in the remanence. In this case, the two-phase particle model was also used for the strongly magnetic fraction.

Magnetostatic interaction results in that a particle with the volume $v > v_b(H_i)$ can contribute to the remanent magnetization. Here $v_b(H_i)$ is the critical volume of a particle whose magnetic moment remains stable when the particle is exposed to the interaction field $H_i$ [7]. For superparamagnetic interacting particles, the time-averaged nonzero magnetic moment contributing to the remanent magnetization is [7]:

$$m = vI_s\tanh[v_b(H_i)I_s|H+H_i|/kT] = vI_{s\,sp}, \quad (4)$$

where $I_{s\,sp}$ is the effective spontaneous magnetization of two-phase superparamagnetic particles blocked due to magnetostatic interaction, which coincides with $I_s = I_{s1}$, in the saturation field, while the calculation of the saturation remanent magnetization is tens of times smaller.

Then for the superparamagnetic sample T20R

$$M_s = M_{s1\,b} + M_{s2\,b} + M_{s\,nb}, \quad M_{rs} = M_{rs1\,b} + M_{rs2\,b}, \quad (5)$$

where $M_{s1\,b}$ and $M_{rs1\,b}$, $M_{s2\,b}$ and $M_{rs2\,b}$ correspond to the blocked particles and $M_{s\,nb}$ to the unblocked particles.

## 4. Results and discussions

Having calculated the critical fields of remagnetization $H_0$ of the strongly magnetic fraction using the two-phase particle model and assuming that $H_0 = H_{cr1}$, we estimated the coercive force of this group of particles $H_{c1}$.

Then, using the experimental values (Table I), we fitted $H_{cr2}$ and $H_{c2}$. Taking into consideration the shares of the fractions, the average theoretical values of $H_c$ and $H_{cr}$ of the samples coincided with the experimental ones.

Table II shows the calculated magnetization values, which in total are equal to the experimental $M_s$ and $M_{rs}$ of the samples (Table I).

***Table II.*** *Theoretical values of magnetizations.*

| Sample | $M_{s1}$ | $M_{s2}$ | $M_{s\,sp}$ | $M_{rs1}$ | $M_{rs2}$ |
|---|---|---|---|---|---|
| | | | (Am²/kg) | | |
| T05L | 10.07 | 0.26 | 16.04 | 2.89 | 0.06 |
| T10L | 7.26 | 0.24 | 12.03 | 2.02 | 0.04 |
| T20L | 6.20 | 0.30 | 7.61 | 1.84 | 0.08 |
| T05H | 22.14 | 0.60 | 1.05 | 3.79 | 0.36 |
| Sample | $M_{s1\,b}$ | $M_{s2\,b}$ | $M_{s\,nb}$ | $M_{rs1\,b}$ | $M_{rs2\,b}$ |
| | | | (Am²/kg) | | |
| T20R | 23.74 | 0.51 | 4.70 | 0.23 | 0.12 |

## 5. Conclusions

The hysteresis characteristics of the simulated composites are well explained within the model of an ensemble of magnetostatically interacting two-phase particles. The superparamagnetic fraction largely determines the magnetic properties of the samples and its consideration makes it possible to agree their theoretical and experimental characteristics.

## References


[1] P. Kharitonskii, S. Kirillova, K. Gareev *et al.* IEEE Trans. Magn. **56**(2020)7200209.

[2] P. Kharitonskii, A. Kosterov, A. Gurylev *et al.* Phys. Solid State **62**(2020)1527.

[3] J. L. Kirschvink, D. S. Jones, B. J. MacFadden. Magnetite Biomineralization and Magnetoreception in Organisms. A New Biomagnetism. Plenum Press, New York (1985).

[4] L. Afremov, A. Ralin, P. Kharitonsky. Izv. Phys. Solid Earth **31**(1996)533.

[5] P.V. Kharitonskii, A.M. Frolov. Izv. vuzov. Fizika (in Russian) **3/2**(2010)197.

[6] D.J. Dunlop. J. Geophys. Res. **78**(1973)1780.

[7] P. Kharitonskii, K. Gareev, S. Ionin *et al.* J. Magn. **20**(2015)221.

# Magnetic properties of CoFe alloy nanosprings depending on the coil thickness

K.A. Rogachev*[,1], A.Yu. Samardak[1], A.G. Kozlov[1], V.N. Kharitonov[1], M.E. Stebliy[1], M.E. Letushev[1], M.A. Bazrov[1], Y.S. Jeon[2], E. Jeong[3], A.V. Ognev[1], A.S. Samardak[1], Y.K. Kim[3]

[1] Institute of High Technologies and Advanced Materials, Far Eastern Federal University, Vladivostok 690950, Russia
[2] Institute of Engineering Research, Korea University, Seoul 02841, Republic of Korea
[3] Department of Materials Science and Engineering, Korea University, Seoul 02841, Korea

*e-mail: kirpers26@gmail.com

**Abstract.** Magnetic nanosprings are novel magnetic materials with uncommon properties, caused by a combination of strong shape anisotropy of a one-dimensional wire with its helical curling. The high magnetic moment of the CoFe alloy conducts strong interactions between the coils and neighbors in the arrays, resulting in a complex micromagnetic structure. Due to their properties, such nanostructures can be implemented as sensors of magnetic fields, actuators of nanorobots, and containers for drug delivery. We investigated the remagnetization process, domain structure, and features of interaction fields induced by modulation of the thickness of the coil of nanosprings, embedded in the porous alumina matrix.

## 1. Introduction

One-dimensional nanostructures such as nanotubes and nanowires, because of their strong differences in the magnetic behavior compared to bulk magnetic materials and thin magnetic films are the point of high interest for modern material science and for application. The high aspect ratio of these nanostructures usually induced a strong uniaxial magnetic anisotropy in the direction of the long axis, with strong interactions between neighbors in the arrays [1].

With the development of one-dimensional nanostructure synthesis techniques, a facile method was developed to prepare helical-shaped nanostructures [2]. Although we have observed the dynamics of magnetization reversal behavior about nanospring and nanowire array with micromagnetic simulation [3], nanospring is still considered as one-dimensional nanostructures as well, and can show a completely different magnetic behavior due to their complex helical shape. In this study, we investigated the changes of magnetic properties in dependence on the three dimensional nanostructures like controlling the coil thickness. The possibility of controlling the motion of such nanostructures by external magnetic fields [4] provides many potential applications in nanorobotics [5] and biomedicine [6]. The low remanent magnetic moment of nanosprings can be useful for the design of agents for target delivery of drugs, since low remanence will prevent the formation of agglomerates due to the absence of strong magnetic poles.

## 2. Experiment

Nanosprings were synthesized by electrodeposition in a commercial porous alumina template (Whatman, Anodisc) with 200 nm diameter of the pores under galvanostatic conditions. The electrolyte contained cobalt sulfate ($CoSO_4 \cdot 7H_2O$), iron sulfate ($FeSO_4 \cdot 7H_2O$) and was modified with vanadium oxide sulfate ($VOSO_4 \cdot H_2O$) and ascorbic acid ($C_6H_8O_6$) to define the helical shape of the nanospring. The diameter of the coil was controlled by the current density of the electrodeposition.

Surface morphology was studied by scanning electron microscopy (SEM, ThermalScientific SCIOS 2). For visualization the nanosprings were etched out of AAO template using $H_3PO_4$ (6 wt%) and $H_2CrO_4$ (1.8 wt%) solution and NaOH. Elemental composition was studied using energy-dispersive X-ray spectroscopy (EDX, EDAX TEAM).

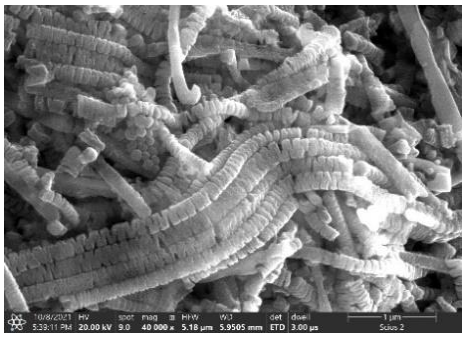

***Fig. 1.** SEM image of nanosprings without alumina template.*

The magnetic properties of the CoFe nanosprings were carried out by vibration magnetometry (LakeShore VSM 7410). First-order reversal curve (FORC) diagram method was used to study the complex distribution of interaction and coercive fields in the nanosprings array. The domain structure was investigated using magnetic force microscopy (MFM, NT-MDT NTEGRA Aura).

For visualization the magnetic structures and defining the magnetostatic interactions the micromagnetic package MuMax3 was used. To achieve trustworthy model, experimental data (hysteresis loops and MFM images) were compared with simulation results.

## 3. Results and discussion

Investigation of geometric parameters using SEM showed that the nanosprings are 200 nm in diameter and approximately 14 μm in length. The coil thickness varied from 38 to 95 nm. EDX analysis showed that all samples consisted of the $Fe_{49}Co_{51}$ alloy.

Hysteresis measurements showed that all samples have a slight anisotropy of magnetic properties in the longitudinal direction, which can be explained by shape anisotropy of the nanospring. Samples with the smallest coil thickness have strong differences from the thicker samples, which can be explained by changes in the

magnetization reversal processes occurring in the structures with changing the diameter of the coil.

The FORC diagram showed that irreversible switching occurs mostly in the external fields, perpendicular to the main axis of the nanosprings, which is uncommon for one-dimensional nanostructures. The results obtained by the FORC diagram method are presented in Table 1 ($H_u$ – interaction fields, $H_c$ – coercive force, (⊥) and (||) indicate the perpendicular and longitudinal directions of the external magnetic field relative to the helix axis, respectively). As one can see, the coercive force of the samples with the smallest diameter of the coil is six times larger than the median of the rest of the samples. This can be explained by a possible single domain configuration and the presence of high amounts of impurities and defects in the samples.

***Table I.*** *The results of the FORC diagram measurement.*

| Sample | $H_c$(\|\|), (Oe) | $H_c$(⊥), (Oe) | $H_u$(\|\|), (Oe) | $H_u$(⊥), (Oe) |
|---|---|---|---|---|
| *1* | 648 | 145 | 170 | 178 |
| *2* | 100 | 100 | 156 | 250 |
| *3* | 82 | 214 | 156 | 266 |
| *4* | 149 | 142 | 164 | 177 |
| *5* | 132 | 158 | 135 | 180 |

Micromagnetic simulation has shown that the magnetization of nanosprings occurs differently and depends on the direction of the external magnetic field. If the field is applied in the longitudinal direction of the main axis of the nanosprings, then the magnetic moment smoothly rotates along with the field. In the transverse direction of the field, switching is due to the formation and annihilation of domain walls. The remnant states obtained in both directions of the field are shown in Fig. 3.


***Fig. 2.*** *Simulated domain structure in the remanent state of sample with 38 nm thickness of the coil after saturation in (a) longitudinal and (b) transverse direction of the external magnetic field.*

## 4. Conclusions

In this work, we have studied the magnetic properties of nanosprings with different coil thicknesses.

We are showing that with an increase of the coil thickness from 36 nm to 50 nm, the coercive force $H_c$ and its distribution in the field applied along the nanospring axis decrease dramatically. The same behavior is observed for interaction fields $H_u$ in the longitudinal direction. Considering the behavior of the samples under the transverse application of the field, a peak is observed for $H_u$ and $H_c$ at a diameter of about 62 nm. Different thicknesses of the coils of the nanosprings result in changing of the magnetic properties of the array due to the change of the magnetic processes occurring in them. The behavior of samples with a larger coil thickness is closer to that of nanotubes (samples 4, 5). In turn, in thinner nanosprings, the magnetic interaction between neighboring coils is observed. The cardinal differences in the magnetic properties of the sample with the smallest coil thickness can be explained by a change in the magnetization reversal process.

## Acknowledgements

This work was supported by the Russian Ministry of Science and Higher Education (State Task No. 0657-2020-0013)

## References

[1] L. Elbaile, R. D. Crespo, V. Vega, J. A. Garcıa. Journal of Nanomaterials **2012** (2012)198453.
[2] Y. S. Jeon, B. C. Park, M. J. Ko, J. H. Moon, E. Jeong, Y. K. Kim, Nano Today **42**(2022)101348.
[3] D. Y. Nam, A. Yu. Samardak, Y. S. Jeon, S. H. Kim, A. V. Davydenko, A. V. Ognev, A. S. Samardak, Y. K. Kim. Nanoscale **10**(2018)20405-20413.
[4] J. Li, S. Sattayasamitsathit, R. Dong, W. Gao, R. Tam, X. Feng, S. Ai and J. Wang. Nanoscale **6**(2014)9415–9420.
[5] K. I. Morozov, A. M. Leshansky. Nanoscale **6**(2014)1580–1588.
[6] X.-Z. Chen, M. Hoop, F. Mushtaq, E. Siringil, C. Hu, B. J. Nelson, S. Pané, Appl. Mater. Today **9**(2017), 37–48.

# Structure and magnetic properties of Nd-(Fe,Co)-B hard magnetic powders with and without Cu doping

V.Yu. Samardak, V.N.Kharitonov, A.A. Belov, O.O. Shichalin, E.K. Papynov, A.S. Samardak, A.V. Ognev

Institute of High Technologies and Advanced Materials, Far Eastern Federal University, Vladivostok 690922, Russia

*e-mail: vadimsamardak@gmail.com

**Abstract.** Hard magnetic Nd-(Fe,Co)-B powders prepared by ball milling from melt-spun ribbons are investigated. The effect of doping by 1 wt% Cu on magnetic properties is shown. Furthermore, the thermal stability of the Nd-(Fe,Co)-B powder with Cu doping is studied. The structure and morphology of the powders are observed. The contribution of the $Nd_2(Fe, Co)_{14}B$ and α-(Fe,Co) phases to magnetic properties is determined using temperature dependences of AC susceptibility in the range of 17 to 847 °C. The reversal magnetization and energy product of the Nd-(Fe,Co)-B powders with and without Cu doping are investigated and discussed.

## 1. Introduction

The development of modern technologies for robotics, automobile transport, small aircraft, electric transport, clean energy, and other areas requires strong and compact permanent magnets, which are used in electric drives and generators [1]. Composites from polymer materials with magnetic powders (magnetoplastics) are also used in numerous applications, including electromagnetic drives for micropumps [2]. Intensive research has focused on new methods for synthesis and optimal microstructure formation since the discovery of superior $Nd_2Fe_{14}B$ hard magnetic alloys [3].

Bonded Nd-Fe-B magnets or magnetic elastomers require magnetic powders. These powders can be obtained by milling ingots of melt-spun Nd-Fe-B ribbons or via hydrogen dispersion-desorption-recombination (HDDR) alloys treated. The fabrication of magnetic powders is the most important technological task that requires understanding the processes of structure transformation during milling and developing methods to stabilize the magnetic properties. During fast consolidation of nanostructured powders using the Spark Plasma Sintering (SPS) technique, the magnetic properties of $Nd_2Fe_{14}B$ can change. Transition or rare-earth metal additives (Tb, DyCo, Cu + DyCo, and Al + DyCo) can be added to avoid the reduction of the parameters

The aim of this work is to investigate the influence of the Cu additive on the structure and magnetic properties of powders, which was obtained from the melt-spun of ribbons of the Nd-(Fe,Co)-B alloy. Copper was incorporated by mechanical synthesis during powder milling. The influence of a relatively high concentration of Cu (1 wt%) on the structure, reversal magnetization, and energy product of Nd-(Fe,Co)-B neodymium magnets were investigated.

## 2. Experiment

Hard magnetic powders were obtained by ball milling of the commercial rapidly quenched Nd-(Fe,Co)-B alloy (product No. 04821610, Jovi International, China) using a Tencan XQM-0.4A planetary ball mill (China), regime: 700 rpm in one 6-hour cycle in an inert gas atmosphere (argon) and acetone. Powder samples with Cu incorporation were synthesized by adding 1 wt% of Cu powder in the initial alloy before ball milling. Furthermore, powders without additives and with 1 wt% Cu incorporation were annealed at 750 °C for 10 minutes for thermal stability investigation. Such heat treatment is traditionally used for the compaction of nanocrystalline powders via the hot-pressing technique.

## 3. Results and discussions

The XRD of the initial powder of Nd-(Fe,Co)-B alloy and its milled form, as well as after doping with 1 wt% of Cu, are shown in Figure 1. The composition of the powder phase and the lattice parameters of the phases are presented in Table 1. The main phase of the powders is the tetragonal phase $Nd_2Fe_{14}B$ (2-14-1) with the spatial symmetry group P42/mnm. Miller indices of the phase are shown in Figure 1a. The lines of the (2-14-1) phase are very broad, which allows for an estimate of the coherent scattering regions (CSRs) size of about 30 nm. The grain deformation of the initial powder is 0.1%, and after milling it increases several times.

The XRD diffractograms of the initial powder of the Nd alloy (Fe, Co) -B before and after annealing qualitatively coincide. However, the XRD diffractograms of milled powders before and after annealing are significantly different. Intensive lines of NdO oxide and α-phase Fe-Co phases appear in XRD diffractograms for milled powders after annealing. This explains the decrease in $H_c$ for the powders.

***Table I.*** *XRD results for powders before and after milling.*

| Nd-(Fe,Co)-B powders | XRD | Phases volume (%) | Parameter | | CSR (nm) | Deformation (%) |
|---|---|---|---|---|---|---|
| | | | *a* (Å) | *c*(Å) | | |
| Initial powder | 2-14-1<br>α-Fe | 99<br>~1 | 8.789<br>2.847 | 12.197<br>- | 26<br>- | Initial powder |
| Powder after milling | 2-14-1<br>α-Fe | 99<br>~1 | 8.790<br>2.847 | 12.199<br>- | 32<br>- | Powder after milling |
| Powder after milling with 1 wt% Cu | 2-14-1<br>α-Fe | 99<br>~1 | 8.790<br>2.847 | 12.199<br>- | 30<br>- | Powder after milling with 1 wt% Cu |

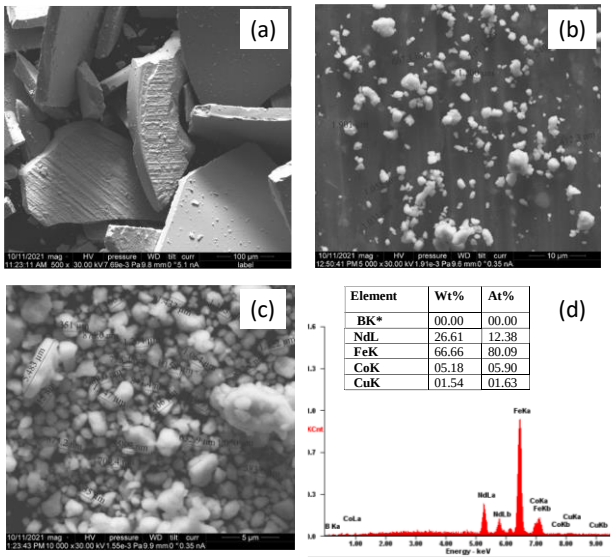


***Fig. 1.*** *SEM images of the morphology of the Nd- (Fe, Co) -B alloy particles in the initial state (a), after being milled without copper (b) and morphology (c) and results of the EDX analysis (d) of the Nd- (Fe, Co) -B alloy with the 1 wt% Cu additive.*

Figure 1a shows SEM images of the initial powder of Nd-(Fe,Co)-B alloy. The powder particles are plate-shaped with sharp edges. The thickness of the particles is about 20 μm with an average in-plane size of about 370 μm. Figures 1b and c show SEM images of the powder of the Nd-(Fe,Co)-B alloy after milling. These powders contain agglomerates, as well as individual particles of different sizes and irregular shapes. The average grain size is 2 μm. Figure 1d shows the data of the EDX results for the powder alloy Nd-(Fe,Co)-B with the 1 wt% Cu additive. The content of Nd, Fe, and Co does not change for all samples. The composition of individual particles of the Nd-(Fe,Co)-B powder alloy differs significantly from the average composition of the large area.

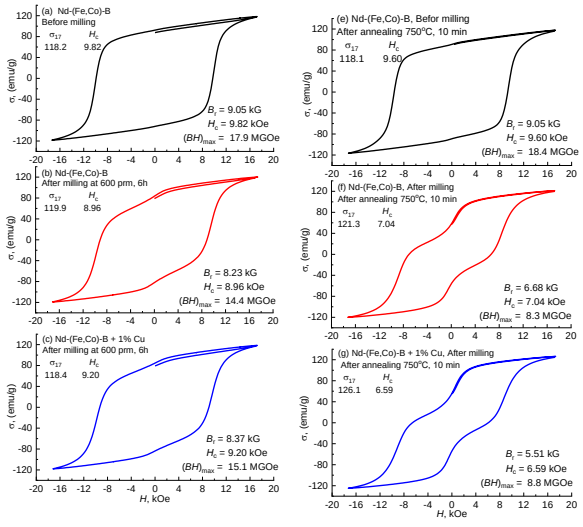


***Fig. 2.*** *Hysteresis loops of the initial Nd-(Fe,Co)-B alloy powders (a), after milling (b), with 1% wt Cu additive (c), and the same powders after annealing at 750°C for 10 minutes (e, f, g).*

Figure 2 shows the magnetic hysteresis loops for Nd-(Fe,Co)-B alloy powders measured by a vibrating magnetometer. Each figure shows the values of the maximum specific magnetization $\sigma_{17}$ measured in a magnetizing field with a strength of 17 kOe, the coercive force $H_c$, the residual induction $B_r$, and the maximum energy product $(BH)_{max}$ that was calculated assuming that the alloy density ρ is 7.87 g/cm$^3$. To get an idea of the influence of high annealing temperatures on the powder coercivity of the Nd-(Fe,Co) -B alloy and the same milled powders without and with the 1 wt% Cu additive, these powders were annealed at 750°C for 10 minutes.

Figure 2 e-g shows hysteresis loops of annealed powders. The magnetic characteristics of the initial powders did not change significantly after annealing (Fig. 2a, e). The coercivity decreased considerably for milled powders, indicating significant powder contamination after milling and increased contributions of surface effects. The coercivity and energy product are higher for samples with 1 wt.% Cu additive than for those without Cu. This trend persists even after annealing. The improvement in magnetic characteristics for Nd-(FeCo)-B alloy powders with the 1 wt% Cu additive is probably due to the segregation of Cu in the intergranular phase region and the stabilization of the magnetically stiff phase.

## 4. Conclusions

In the study, it was found that the initial fast quenched Nd-(Fe,Co)-B alloy powder has a composition of approximately 28 Nd, 66 Fe, 5 Co, 1 B (wt%). The main phase of the alloy is the $Nd_2Fe_{14}B$ structure. The high powder coercivity up to 9.82 kOe is due to the presence of nanocrystalline grains of about 30-60 nm inside the powder particles with an average size of about 370 μm. The particle size of the powder is reduced to an average size of approximately 2 μm after milling. The coercivity for the milled powders decreases slightly but remains at a fairly high level (8.96 and 9.20 kOe). The addition of 1 wt% of Cu leads to an increase in coercivity and energy ratio compared to the powder without Cu.

## Acknowledgements

The research was carried out with the support of the Russian Science Foundation (project 19-72- 20071). S.A.S. thanks the Russian Ministry of Science and Higher Education for support under the state task (0657-2020-0013) in a part of the surface morphology study. S.V.Yu. was supported by the grant of the Government of the Russian Federation for state support of scientific research conducted under the supervision of leading scientists in Russian institutions of higher education, scientific foundations, and state research centers of the Russian Federation (Project No. 075-15-2021-607) in a part of VSM measurements.

## References

[1] Coey, J.M. Magnetism in future / J.M. Coey // J. Magn. Magn. Mater. - 2001. - V. 226–230. - P. 2107–2112.
[2] A PMMA valveless micropump using electromagnetic actuation / C. Yamahata, C. Lotto, E. Al-Assaf, M.A.M. Gijs // Microfluid. Nanofluidics. - 2005. - V. 1. - P. 197
[3] New material for permanent magnets on a base of Nd and Fe (invited) / M. Sagawa, S. Fujimura, N. Togawa, H. Yamamoto, Y. Matsuura // J. Appl. Phys. - 1984. - V. 55. - P. 2083–2087.

# Magnetic properties of $[Pd/Co/CoO]_n$ superlattices

V.S. Shatilov*, G.S. Suslin, E.V. Tarasov, K.L. Karimov, A.V. Ognev, A.G. Kozlov and A.S. Samardak

Institute of High Technologies and Advanced Materials, Far Eastern Federal University, 690922, 10 Ajax bay, Vladivostok, Russia

*e-mail: shatilov.vs@dvfu.ru

**Abstract.** Results of research on the magnetic properties of multilayered ferromagnetic epitaxial films with oxidized top interfaces of the ferromagnetic layer are shown. Experimental data demonstrate the presence of PMA in $[Pd/Co/CoO]_n$ films, as well as an increase in the coercivity and magnetic moments from the number of layers.

## 1. Introduction

Thin magnetic films are valuable for studying them as a material for new types of logical devices for storage, reading/writing, and information processing. Precise driving of the parameters of magnetic materials is required for the development of such devices. The Dzyaloshinskii-Moriya Interaction (DMI) and PMA are the most important properties of such systems. Interfacial DMI appears due to symmetry breaking at the interface of ultrathin films, which leads to asymmetric spin rotation, and in combination with strong PMA allows one to stabilize the topological structures as chiral domain walls and skyrmions.

The experiment was based on the Co/Pd(111) epitaxial system since it is characterized by good thermal stability and strong PMA, the origin of the former being well described in the work of Davydenko A. V. et al [1]. Further studies of similar systems, specifically Pd/Co/Pd(111), demonstrated that such a symmetrical structure can lead to the formation of DMI [2]. However, if the symmetry is broken by oxidizing the ferromagnetic layer, the magnetic parameters are preserved and become more stable [3].

In our samples $[Pd/Co/CoO]_n$ films, both DMI and PMA appear. Meanwhile, with an increasing number of film layers (n), the crystal structure is preserved. To determine operating parameters such as layer thicknesses and oxidation parameters - time and pressure, the magnetic properties of single-layer samples were previously studied.

## 2. Experiment

The Omicron ultrahigh-vacuum complex was used to obtain multilayer films $[Pd/Co/CoO]_n$. The samples were grown by molecular-beam epitaxy at pressure ≈10-10 Torr, A Si(111) substrates were prepared by chemical cleaning before loading into the chamber. The samples were then degassed by indirect heating for 13 hours and at a temperature of 600 C°, and the substrates were annealed bya direct current at the temperature of 1200 C° by short pulses to clean the surface of silicon oxide and form a 7x7 surface reconstruction. After annealing, a layer of Cu (21 Å thick) was deposited as the buffer layer. Each ferromagnetic layer (Co) was oxidized for 3 minutes in a dry oxygen atmosphere. The structure of a single film with 3 layers (trilayers) is presented as Pd(20Å)/Co(10Å)/CoO. The deposition of each new layer was controlled by recording the reflective high energy electron diffraction pattern. Preservation of the crystalline order with an increase in the layers of the film was observed.

The final layer of Pd (50 Å thick) was sputtered, to prevent subsequent oxidation of the film.

The magnetic properties of the samples were studied using a vibrating sample magnetometer (VSM). Investigation of the domain structure was carried out by a magneto-optical Kerr microscope (MOKE).

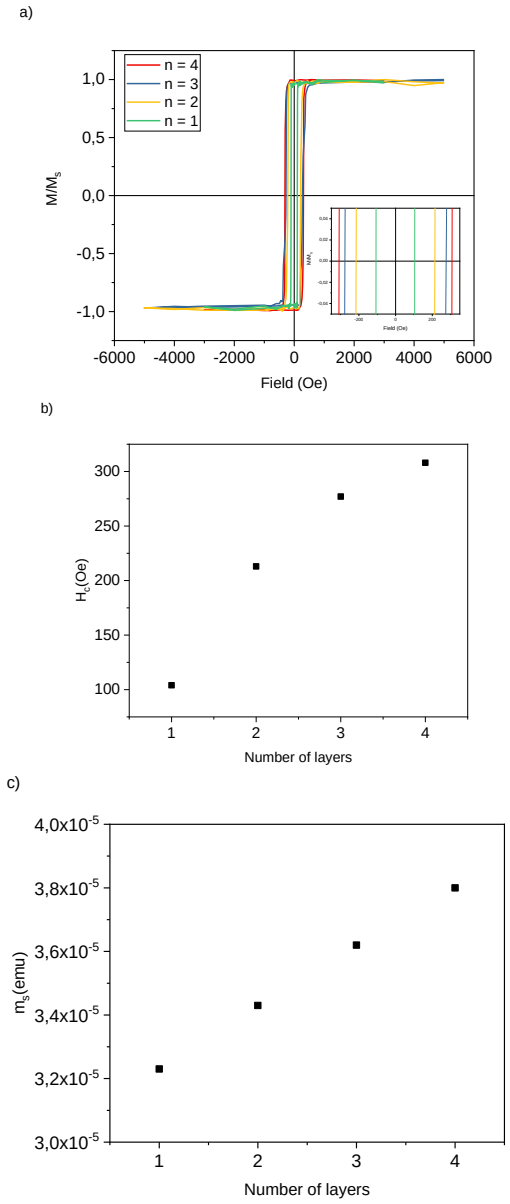


***Fig. 1.*** *a) The hysteresis loops for $[Pd/Co/CoO]_n$ films; b) Dependence of the coercive force on the number of layers (n); c). Dependence of the magnetic moment on the number of layers (n).*

### 3. Results and discussions

Hysteresis loops taken perpendicularly to the plane of the sample indicate the easy magnetization axis in this orientation, which indicates the presence and preservation of PMA on each layer. (Fig 1. a). The growth of the coercive force and magnetic moment with an increasing number of trilayers was shown (Fig 1. b and c.).

The domain structure of the samples was studied by MOKE-microscopy (Fig 2). A magnetic field was applied in the range from ±100 to ±500 Oe. The structure of the labyrinth domains was observed in a demagnetized state.

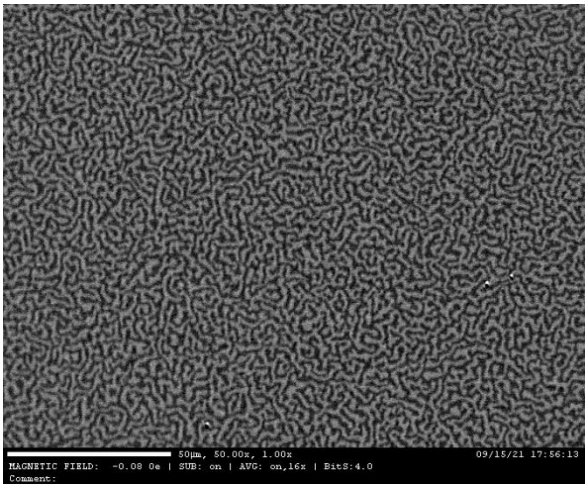


***Fig. 2.*** *Labyrinth domain structure in the [Pd/Co/CoO]$_4$ film.*

### 4. Conclusions

The dependences of the coercive force and magnetic moment on the number of layers of a [Pd/Co/CoO]$_n$ multilayer thin film were studied. The labyrinthine domain structure of the sample was observed. The ability to control the coercive force and magnetic moment will potentially allow the use of top-interface oxidation as a mechanism for controlling magnetic parameters. In addition, the presence of PMA in the samples reinforces the interest in further research. Determining the characteristics makes it possible to further use films as a material for a new type of magnetic memory.

### Acknowledgements

This research was funded by the Russian Ministry of Science and Higher Education (State Task No. 0657-2020-0013) and the Russian President Grant Program of the x (Grant No. MK1384.2021.1.2). Authors acknowledge the Russian Ministry of Science and Higher Education for state support of scientific research conducted under the supervision of leading scientists in Russian institution of higher education, scientific foundation, and state research centers (Project No. 075-15-2021-607).

### References

[1] Davydenko A. V., et al., Phys. Rev. B, Vol. 95, 064430 (2017).
[2] A. V. Davydenko, et al., Phys. Rev. B, Vol. 103, 094435 (2021)
[3] J. Feng et al., Phys. Rev. Applied, Vol. 13.4, 044029 (2020).

# Synthesis and magnetic properties of electrodeposited Ni nanowires with a high aspect ratio

M.I. Sobirov*, A.Yu. Samardak, S.A. Azon, A.S. Samardak, A.V. Ognev
Institute of High Technologies and Advanced Materials, Far Eastern Federal University, 10 Ayax., Vladivostok 690090, Russia

*e-mail: sobirov.mi@dvfu.ru

**Abstract.** The synthesis of anodic aluminum oxide templates and the preparation of Ni nanowires by electrodeposition in a two-stage anodizing mode are considered. Ni nanowires with the length from 1.5 to 4 μm are prepared. The magnetic and morphological properties of the Ni nanowires are studied.

## 1. Introduction

Magnetic nanomaterials can be used for media with high recording density, for new types of magnetoresistive memory, and highly sensitive sensors [1]. Currently, porous anodic aluminum oxide is used as a template to prepare nanocrystals, nanotubes, nanofibers, quantum dots, in filter production, in instrumentation, in biomedicine, and optoelectronics [2]. The parameters of the templates depend on characteristics and the type of electrolyte, and current density during anodization. [3]. The electrodeposition method allows one to prepare metallic nanowires inside an Al2O3 template. Using pattern electrodeposition methods, various one-dimensional nanostructures are obtained, in particular: nanowires, nanotubes, nanosprings, segmented nanowires with different compositions and crystal structures [4]. The application of such ferromagnetic nanostructures is not limited by IT and sensors; they can be used for biomedical applications, for example, to destroy cancer cells by hyperthermia and mechanical destruction of tumors, targeted drug delivery, magnetic resonance contrast agents, and sources of secondary irradiation in radio treatment of tumors [5]. We are shown the results of technology optimization for electrodeposition of Ni nanowires (NWs). The magnetic properties of NWs were characterized by the first-order reversal curve (FORC) diagram method.

## 2. Experiment

Porous $Al_2O_3$ templates were synthesized using the two-step anodization method [6]. The anodization was carried out in mild potentiostatic mode at 40V in 2-3°C and 20-23 ° C oxalic acid for 3 hours for the first anodization and 15 hours for the second anodization using the Agilent 6030A power supply. After the porous membrane was achieved, Al was dissolved with 0.08M of $CuCl_2$+8% HCl in 20°C at 1h, and the barrier layer on one side of the pores was etched with 1,0M of $H_3PO_4$ acid at 40-60m. After that, a thick conducting layer of Cu was deposited on the top side of the porous membrane to avoid the formation of dendrites during the growth of the nanowires. Templates were checked by scanning electron microscope (SEM). ThermoScientific SCIOS2.

The nanowires were electrodeposited from a Watts solution containing $NiSO_4$, NiCl2, and $H_3BO_3$ into prepared templates in galvanostatic mode at a current density of 250 mA/cm for 10 and 30 minutes. The Keithley 2460 power source was used. The geometrical properties and elemental composition of synthesized nanowires were investigated and analyzed by SEM. ThermoScientific SCIOS2 with EDX module.

Magnetic properties were studied using a LakeShore VSM 7410 vibration magnetometer. The FORC diagram method was used to study the distribution of coercive force and magnetostatic interactions in the arrays of Ni nanowires

## 3. Results and discussions

SEM images of the templates are shown in Figure 1. The medium pore diameter for samples with matrices synthesized at 2-3°C was 60-80 nm, the length is up to 50 μm with high porosity, high level of hexagonal ordering and uniform round pores. Meanwhile, templates synthesized at room temperature had a lesser diameter 40-60 nm with broken long-range order and nonround pores.

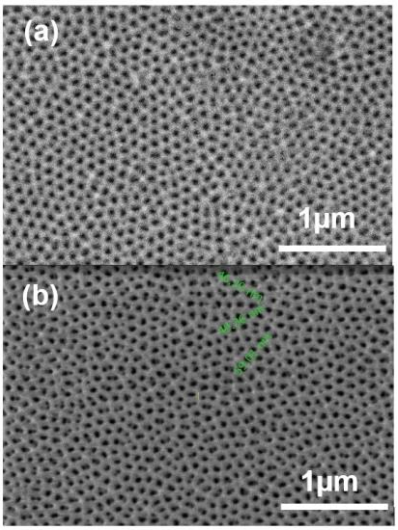


***Fig. 1.*** *SEM image of a porous alumina on the top of (a) a porous alumina template synthesized at 2-3°C, (b) a porous alumina template synthesized at 20-23°C.*

Ni nanowires etched out from templates are presented in Figure 2. The diameter of the nanowires was equal to the diameter of the pores for all samples. The length was controlled by the time of the deposition and was approximately 1.5 μm, with a growth rate of approximately 150 nm/s. EDX analysis confirmed that the nanowires consist of Ni.

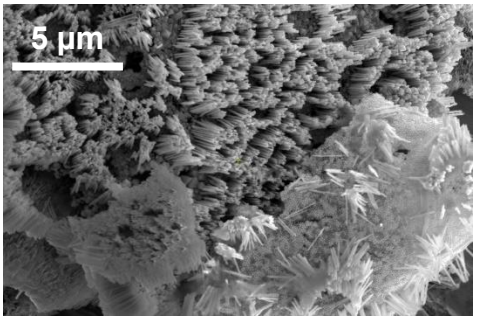


***Fig. 2.*** *Ni nanowires etched from a porous alumina template synthesized at 2-3°C.*

Nanowires have a strong uniaxial anisotropy in the direction of the main axis of nanowires. The coercive force $H_c$ and the ratio of the residual magnetic moment to the magnetic moment of saturation $M_r/M_s$ were determined from the hysteresis loops. Value of $H_c$~950 Oe (out of plane) and $H_c$~550 Oe (in plane). Value of $Mr/Ms$ ~0,92 (out of plane) and $M_r/M_s$~0,29 (in plane). On the basis of the results obtained from the values of $H_c$ and $M_r/M_s$, it can be judged that the nanowires are in a single-domain state. The FORCs diagram showed the distribution of $H_c$ in the range of 600 to 1300 Oe, with strong interactions between the nanowires with $H_u$ up to 1000 Oe. The coercive force for a sample with an electrodeposition time of 10 minutes (l = 1,5 µm) is 800 Oe, but for a sample with an electrodeposition time of 30 minutes, $H_c$ = 1000 Oe.

## 4. Conclusions

As a result, the optimal conditions for aluminum oxide templates synthesizes are established. The nickel nanowires were obtained by electrochemical deposition. The geometry, elemental composition, and magnetic properties of nanowires were investigated.

## Acknowledgements

This work was supported by the Russian Ministry of Science and Higher Education (State Task No. 0657-2020-0013).

## References

[1] S.P. Gubin, Y. I. Spichkin, G. Yu. Yurkov, A. M. Tishin. Russian Journal of Inorganic Chemistry **47**(2002) S32–S67.
[2] J.M. Vargas, L.M. Socolovsky, M. Knobel, D. Zanchet, Nanotechnology **16** (2005) S285.
[3] H. Masuda, K. Kanezawa, K. Nishio. Chemical Letters **31**(2002)1218.
[4] A.N. Belov., S.A. Gavrilov., V.I. Shevyakov. Технические науки **9**(2015)170.
[5] E. Sinibaldi, V. Pensabene, S. Taccola, S. Palagi, A. Menciassi, P. Dario, V. Mattoli. Journal of Nanotechnology in Engineering and Medicine **1.2** (2010) 021008.
[6] A. Mukhtar, K. Wu, X. Cao, l. Gu Nanotechnology **31**(2020)433001.

# Temperature studies of magnetic properties of Pd/Co/CoO epitaxial films

E.V. Tarasov*[,1,2], H.S. Suslin[1], A.V. Gerasimenko[2], I.A. Tkachenko[2], A.G. Kozlov[1]

[1] Far Eastern Federal University, 8 Sukhanova St., Vladivostok 690950, Russia
[2] Institute of Chemistry, Far Eastern Branch of the RAS, 159 Prospect 100 Letiya Vladivostok, Vladivostok 690022, Russia

*e-mail: tarasov.ev@dvfu.ru

**Abstract.** An exchange bias has been found in $[Pd/Co/CoO]_n$ epitaxial films with different oxidation depths and different repetition numbers (n) characterized by perpendicular magnetic anisotropy. The oxidation parameters and the number of bilayers affect the exchange bias. The Néel temperature depends on the thickness of the Co oxide and does not depend on the number of bilayers.

## 1. Introduction

Exchange bias is one of the phenomena associated with the exchange anisotropy that occurs at the interface between ferromagnetic (FM)/antiferromagnetic (AFM) materials. It arises when nanostructures of the FM/AFM type are cooled in the presence of a constant magnetic field to a temperature $T<T_N$, and $T_N<T_C$, manifests itself, as a rule, in a shift of the magnetic hysteresis loop in the opposite direction relative to the field applied during cooling. This phenomenon appears in different materials such as: microparticles, thin films, inhomogeneous materials. However, from the point of view of practical application, thin films are the most promising. in these systems, the interface can be controlled and characterized quite effectively. Due to the increased coercive force, exchange biased materials can be used as materials for permanent magnets and high-density magnetic memory devices [1,3]. Of particular interest are systems of ultrathin epitaxial films with an exchange bias directed perpendicular to the FM/AFM interface, since they are less susceptible to thermal noise and are well suited for a large class of spintronic devices [2]. The use of the method of molecular beam epitaxy (MBE) to obtain such structures will make it possible to grow ultra-thin, extra-pure films with sharp interfacial boundaries.

In this work, we studied the structure and magnetic properties, including the exchange bias, in ultrathin Pd/Co/CoO epitaxial films with different Co and $[Pd/Co/CoO]_n$ oxidation doses, where n is the number of repetitions. Single-crystal silicon (111) wafers were used as the substrate. The films were obtained by molecular-beam epitaxy on an Omicron ultra-high-vacuum complex with a base pressure of $3 \times 10^{-11}$ Torr. Data on the structure of the samples were obtained using reflective high-energy electron diffraction during sample deposition. The magnetic properties of the samples were studied experimentally using a SQUID magnetometer, PPMS, and VSM. In the SQUID and PPMS experiments, an external magnetic field was applied perpendicular to the plane of the sample.

## 2. Results

Epitaxial Pd(2nm)/Co(1nm) films were obtained by MBE, after that the procedure of controlled oxidation in dry oxygen was carried out. During the oxidation process, the thickness of CoO increased due to the decrease in the thickness of cobalt. As a result of the analysis of the magnetic hysteresis loops obtained at temperatures of 300, 100, (70K for multilayer systems), 50 and 4K, the values of the exchange bias $H_{Eb}$ (Fig. 1) were determined for samples with different thicknesses of cobalt. It has been established that the exchange bias depends on the degree of Co oxidation, and it begins to appear at a temperature equal to or below 100 K for a sample with an oxidation time of 5 minutes and increases with decreasing temperature. A sample with a residual cobalt thickness of 0.55 nm was chosen as the base sample for obtaining a series of samples with different numbers of repetitions Pd/Co/CoO. The dependences of the magnetization on the external magnetic field studied at different temperatures for samples with n = 1, 2, 3 made it possible to establish that the exchange bias begins to manifest itself at temperatures below 100 K, and a decrease in temperature leads to an increase in the exchange bias (Fig. 2). It is known that the size factor significantly affects the magnetic properties of a substance, for example, the transition temperature to a magnetically ordered state. In this regard, it would be reasonable to study the influence of the oxidation depth on the magnetic characteristics of such structures with temperature. We studied the temperature dependences of the magnetization of all fabricated samples. Based on the data obtained, it was found that the Neel temperature depends on the thickness of cobalt oxide and does not depend on the number of bilayers (Fig. 3).

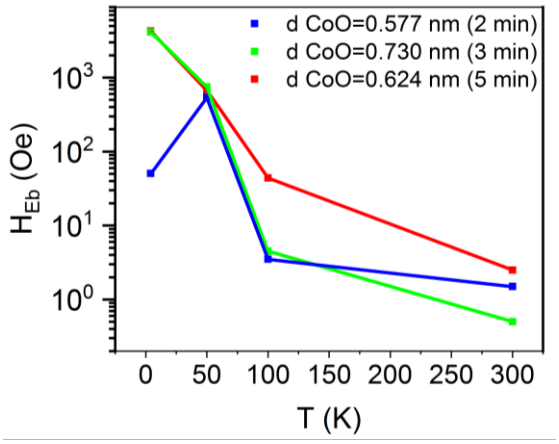


***Fig. 1.*** *Temperature dependences of the exchange bias for samples with different Co oxidation times.*

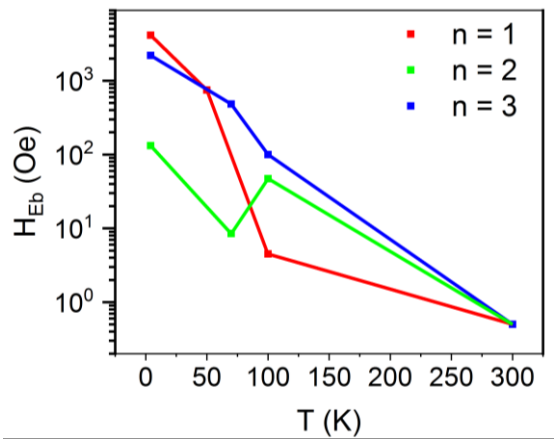


***Fig. 2.*** *Temperature dependences of the exchange bias for samples with different numbers of repetitions Pd/Co/CoO.*

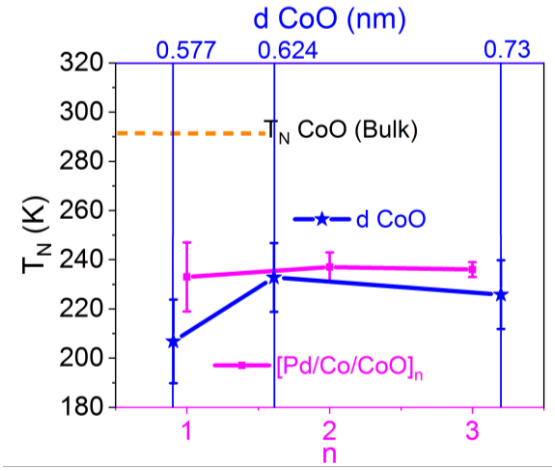


***Fig. 3.*** *Dependence of the Néel temperature on the thickness of CoO (d) and the number of repetitions (n).*

### 3. Conclusions

The possibility of the existence of an exchange bias perpendicular to the film plane in Pd/Co/CoO epitaxial structures with different degrees of Co and $[Pd/Co/CoO]_n$ oxidation, which are characterized by perpendicular magnetic anisotropy, has been shown. It was found that the exchange bias depends on the oxidation parameters and on the number of bilayers. The Neel temperature depends on the thickness of the Co oxide and does not depend on the number of repetitions.

### Acknowledgements

The work was carried out within the framework of the state assignment of the Institute of Chemistry, Far Eastern Branch of the RAS No. 0205 2021 0001.

The work was supported by the Ministry of Science and Higher Education of the Russian Federation (State Assignment No. 0657 2020 0013) and Project No.075-15-2021-607) and by Council for Grants of the President of the Russian Federation (project – MK-1384.2021.1.2).

### References

[1] T.J.Moran, J. M. Gallego and I. K. Schuller Increased exchange anisotropy due to disorder at permalloy/CoO interfaces// J. Appl. Phys. (1995) V.78 No.3. – P.1887-1891.

[2] Kim, Gideok, et al. Physical Review Materials 3.8 (2019) 084420.

[3] Nogues J., Schuller I. K. Exchange bias //J. Magn. Magn. Mater. (1999) – 192 №. 2. – pp. 203-232.

# IV. Nanostructured coverages, nanocomposites, functional hybrid materials: formation, structure and properties

# The role of low-dimensional effects in electrochemical synthesis of nanomaterials

S.A. Gavrilov*
National Research University of Electronic Technology – MIET, Bld. 1, Shokin Square, Zelenograd, Moscow, Russia

*e-mail: pcfme@miee.ru

New approaches to the use of electrochemical deposition and etching for the synthesis of nanostructures are considered in the present work. A brief review of the known methods for obtaining nanostructures is given, classified into two types: self-organized and the use of template deposition into porous materials. Porous silicon and porous anodic alumina are considered as the most studied examples of self-organized structures.

Special attention is paid to the methods of deposition of filamentous structures into nanosized pores of oxides. Approaches to the optimization of deposition regimes based on the combined consideration of the conditions (charge carrier transport at the electrode/electrolyte interface; the kinetics of electrochemical reactions at the interface; the thermodynamics of chemical transformations and the hydrodynamics of mass transfer in nanometer pore channels) are presented. The features of the electrodeposition of metals into pores based on the application of asymmetric voltage pulses are considered in detail. Using the Cd-S-$H_2O$ system as an example, a method for creating CdS whisker nanocrystals in the pores of anodic alumina in the direct current mode, based on the analysis of thermodynamic equilibrium conditions in a multicomponent system, is demonstrated.

The focus of the work is on new methods for the synthesis of filamentous nanostructures in aqueous solutions, based on the use of molten metals as an interface that isolates the reducing metal ions from hydration. This makes it possible to deposit nanocrystals of elements, the deposition of which is possible only in non-aqueous electrolytes. Given that the temperature range in which aqueous solutions remain in a liquid state is limited by the boiling point, the choice of metals that can be used to implement such a process is thermodynamically justified. On the basis of theoretical estimates, it is shown that metals with a melting point significantly higher than the boiling point of aqueous solutions can be used as a molten interface. This possibility is explained on the basis of the dependence of the melting temperature on the dimension of film structures and structures in the form of nanosized particles.

Experimental confirmation of the proposed theoretical approaches is presented by the example of cathode deposition of Ge on In nanocrystals. The main dependences of the deposition kinetics on the sizes of In nanoparticles and the electrolyte temperature are presented. The reasons for the observed increased solubility of In in Ge nanocrystals are also discussed.

In conclusion, a brief review of the areas of application of Ge nanocrystals in lithium-ion and sodium-ion batteries (LIB and SIB) is presented. The prerequisites for maintaining the efficiency of LIB at low temperatures on the basis of the high diffusion coefficient of Li in Ge are discussed.

**Acknowledgements**

The work is supported by the State assignment 2020-2022 № FSMR-2020-0018.

**References**

[1] K. Oyoshi, D. Lenssen, R. Carrius, S. Mantl. Thin Solid Films **381**(2001)194.
[2] T. Suemasu, T. Fujii, K. Takakura, F. Hasegawa. Thin Solid Films **381**(2001)209.
[3] R. Bayazitov, R. Batalov, R. Nurutdinov, V. Shustov, P. Gaiduk, I. Dezsi, E. Kotai. Nucl. Instr. Meth. **B 24**(2005)224.
[4] K. Oyoshi, D. Lenssen, R. Carius, S. Mantl. Thin Solid Films **381**(2001)202
[5] J. Chrost, J. J. Hinarejos, E. G. Michel, R. Miranda. Surf. Sci. **330**(1995)34.

# Formation of Group-IV polycrystalline alloys by crystallization control

Y. Shimura*[,1,2], M. Okado[1], J. Utsumi[1], and H. Tatsuoka[1]

[1] Graduate School of Integrated Science and Technology, Shizuoka University, 3-5-1 Johoku Naka-ku Hamamatsu 432-8561, Japan

[2] Research Institute of Electronics, Shizuoka University, 3-5-1 Johoku Naka-ku Hamamatsu 432-8561, Japan

*e-mail: shimura.yohsuke@shizuoka.ac.jp

Polycrystalline group-IV alloys, such as $Si_{1-x}Ge_x$, $Ge_{1-x}Sn_x$, and $Si_{1-x-y}Ge_xSn_y$, have attractive benefits for thermoelectric generators which can directly convert heat energy into electricity with less environmental impact. Grain boundaries in the polycrystalline material can successfully reduce thermal conductivity which is essential to operate the thermoelectric devices under temperature difference [1]. Besides, mass differences between component elements of the alloy contribute to modulate phonon characteristics [2].

In terms of the synthesis of the polycrystalline group-IV alloys, it has been challenging to realize crystallization, which typically needs high temperature annealing, simultaneously with controlling composition, especially Sn content which is limited by low solid solubility into Ge and Si as 1 at.% and 0.1 at.%, respectively, under equilibrium condition [3].

As one of the solutions to obtain the polycrystalline group-IV alloys having high Sn content, using crystalline Sn nanodots as nuclei is effective for the growth of crystalline alloys at low temperature. The low temperature growth, which is the growth far away from the equilibrium, enables introduction of Sn more than its solubility limit [4].

Amorphous Sn layer deposited on $SiO_2$ substrate can be easily transformed into crystalline Sn nanodots by just applying an annealing in vacuum. We demonstrated the formation of polycrystalline $Ge_{1-x}Sn_x$ and $Si_{1-x}Sn_x$ alloys by deposition of Ge and Si on the Sn nanodots at the substrate temperature of 150 °C and 225 °C, respectively [5,6]. However, we found that Ge preferentially reacts with Sn nanodots when Si and Ge are simultaneously deposited on the Sn nanodots. In this case, Si remains as amorphous, meaning the effect of nucleus for the low temperature crystallization is not effective for Si if Ge exists. This result suggests that Si has to be crystallized prior to Ge.

One can notice that the polycrystalline $Si_{1-x}Sn_x$ can be formed by the Sn nanodots mediated formation process as mentioned above. Therefore, we have proposed the 2-step formation process consisting of poly-$Si_{1-x}Sn_x$ crystallization and Ge alloying with the poly-$Si_{1-x}Sn_x$ which can be considered as a virtual substrate [6]. Using the 2-step formation process, whole deposited region was successfully crystallized with alloying Si, Ge, and Sn. The estimated Si and Sn content in the as-grown polycrystalline $Si_{1-x-y}Ge_xSn_y$ layer were as high as 10.8% and 3.5%, respectively. Impact of introduction of Sn on phonon characteristics is also planned to be discussed at the presentation.

**Acknowledgements**

This work was supported by JSPS KAKENHI Grant Number JP18K13786 and 21K04137 from the Japan Society for the Promotion of Science.

**References**

[1] S. Bathula, M. Jayasimhadri, N. Singh, A. K. Srivastava, J. Pulikkotil, A. Dhar, and R. C. Budhani, Appl. Phys. Lett. **101**(2012)213902.
[2] S. N. Khatami and Z. Aksamija, Phys. Rev. Appl. **6**(2016)014015.
[3] F. A. Trumbore, Bell Syst. Tech. J. **39**(1960)205.
[4] Y. Shimura, N. Tsutsui, O. Nakatsuka, A. Sakai, S. Zaima, Thin Solid Films, **518**(2010)S2.
[5] J. Utsumi, T. Ishimaru, Y. Hayakawa, and Y. Shimura, Semicond. Sci. Technol. **33**(2018)124004.
[6] Y. Shimura, M. Okado, T. Motofuji, and H. Tatsuoka, Jpn. J. Appl. Phys. **61**(2022)SC1008.

Sixth Asian School-Conference on Physics and
Technology of Nanostructured Materials
Vladivostok, Russia, 25 – 29 April, 2022

**IV.o.01**

# Anomalous optical and magnetic properties in nanocrystalline $LaCoO_3$ and $GdCoO_3$

A.E. Sokolov[1, 2], V.A.Dudnikov[1], Yu.S. Orlov[1, 2], N.P. Shestakov[1], and S.G. Ovchinnikov[*,1,2]

[1] Kirensky Institute of Physics, Federal Research Center KSC SB RAS, 660036 Krasnoyarsk, Russia
[2] Siberian Federal University, 660041 Krasnoyarsk, Russia

*e-mail: sgo@iph.krasn.ru

**Abstract.** Bulk polycrystalline samples of $LnCoO_3$ (Ln = La, Gd) were synthesized from nanosized crystallites. For the $LaCoO_3$ compound in the temperature range of 2–300 K, the field and temperature dependences of the magnetic moment were measured, , and a comparative analysis of the magnetic properties at different synthesis temperatures was carried out, with the bulk $LaCoO_3$. Significant differences in the magnetic properties associated with the presence of ferromagnetism in nanostructured $LaCoO_3$ are found. An unusual temperature dependence of the infrared absorption spectra of rare-earth cobalt oxides $LaCoO_3$ and $GdCoO_3$ in the temperature range 3.2–550 K has been studied experimentally and theoretically. It is shown that the observed strong softening of the optical phonon mode is due to the electron-phonon interaction quadratic in the lattice shift and fluctuations in the multiplicity of Co3+ ions.

## 1. Introduction

$LaCoO_3$ is the basic representative of a number of rare earth cobaltites with the formula $Ln^{3+}Co^{3+}O_3^{2-}$. Transitional and rare earth (REM) elements exhibit the same valency equal to three. In the LaCoO3 compound, the cobalt ion is surrounded by a slightly distorted oxygen octahedron, forming $CoO_6$ complexes. The 3d shell of the $Co^{3+}$ ion contains six electrons that can form the HS (S=2), LS (S=0), and IS -intermediate spin (S=1) terms. The 10Dq crystal field is so strong that the main term is the LS singlet, and HS and IS are excited with low excitation energies [1]. As a result, starting from 100 K and above, the population of magnetic terms is significant, which forms the complex and unusual electrical, magnetic, and structural properties of $LaCoO_3$ and other rare earth cobaltites. When La is replaced by another rare-earth element Ln the same phenomena are observed as in $LaCoO_3$, but the maxima in the temperature dependences of the anomalies of thermal expansion and magnetic susceptibility shift to high temperatures, which is associated with an increase in the spin gap due to lanthanide contraction and an increase in chemical pressure with a decrease in the ionic radius of the rare earth element. Stabilization of the high-spin state can lead to the appearance of ferromagnetic ordering, which was observed experimentally on the surface of a $LaCoO_3$ single crystal [2], in grain boundaries [3] and in thin films on stretchable substrates [4].

So far, very little experimental information has been obtained both on the density of phonon states and on the dispersion laws of phonons in rare-earth cobalt oxides. Phonon dispersion in $LaCoO_3$ was studied by inelastic neutron scattering in the temperature range from 10 to 200 K in [5] and from 10 to 536 K in [6]. Estimates show that the scale of temperature variations in phonon frequencies near the boundary of the Brillouin zone is almost an order of magnitude greater than the lattice contribution associated with thermal expansion. It is allows to assume a significant electron-phonon interaction. The study of ferromagnetism in nanocrystalline LaCoO3 samples and unusual temperature dependences of the infrared absorption spectra of rare-earth cobalt oxides LaCoO3 and GdCoO3 is the aim of this work.

## 2. Experiment

High-purity oxides $Ln_2O_3$ (99.99%) (Ln = La, Gd) and $Co_3O_4$ (99.7%) in a stoichiometric amount were carefully mixed in an agate mortar with the addition of ethanol, annealed in air at 1373 K in an alundum crucible for 24 h with a triple grinding cycle - calcination. After tablet pressing and annealing at a temperature of 1373 K, the synthesized samples were ground in ethanol in a Pulverisette 7 premium line planetary micromill (Fritsch GmbH, Germany, glass and balls from 96.2% ZrO2) to a particle size of less than 100 nm. After evaporation, some of the obtained aggregates were ground in an ultrasonic bath for measurements on an electron microscope (SEM with a JEOL JSM-7001F electron microscope, TEM with a Hitachi HT7700) and optical studies. The IR spectroscopy measurements were carried out with the vacuum Fourier Transformation IR spectrometer Vertex 80v equipped with an RT-DLaTGS detector. Cryogenic measurements were carried out with a cryostat-type OptistatAC-V12 and Temperature Controller ITC503s from Oxford Instruments in the range 3.2–296K, a Variable Temperature Cell 147/QV High Stability Temperature Controller 4000 Series TM from Specac Ltd were used for the temperature region 297–523 K. The other part was ground and pressed into tablets for sintering and studying magnetic properties (PPMS-9, Quantum Design (USA).

## 3. Results and discussions

Transmission electron microscope images indicate that the particle sizes lie in the nano range (Fig. 1) . At the same time, the absence of a clear cut indicates that these particles are aggregates that formed from smaller particles during the evaporation of alcohol.

The behavior of the magnetic susceptibility $\chi(T)$ for a nanopowder and a nanostructured sample synthesized at 1023 K is similar. In the region of helium temperatures, one can see the beginning of the formation of a bend characteristic of the “classical” $LaCoO_3$ (Fig. 2, inset). At the same time, the value of $\chi(T)$ at T = 2 K for nanopowder is 15 times higher than the similar value for a bulk and single crystal samples.

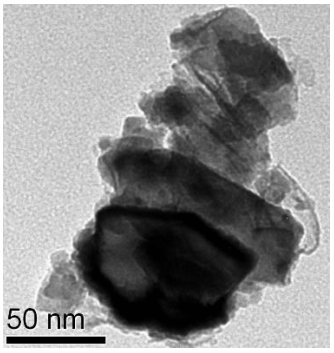


***Fig. 1.*** *Characteristic TEM images of ground $LnCoO_3$ powders after evaporation and grinding in an ultrasonic bath.*

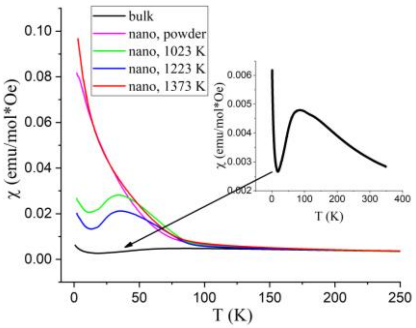


***Fig. 2.*** *Temperature dependences of the magnetic susceptibility obtained in the ZFC mode in the temperature range 2–300 K for samples $LaCoO_3$ synthesized at different temperatures.*

Recrystallization of samples as a result of synthesis at higher temperatures (1223 K, 1373 K) leads to a change in the course of the χ(T) curve with the formation of a maximum at temperatures below 50 K. The field dependences of nanostructured samples indicate the presence of ferromagnetic ordering (Fig. 3)

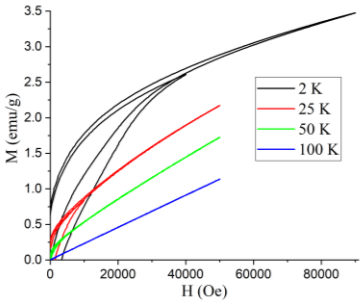


***Fig. 3.*** *Part of the hysteresis loop of nanostructured $LaCoO_3$ synthesized at 1023 K.*

The high-energy part of the phonon spectrum (0.04 – 0.08 eV), in which the breathing (compression) vibronic mode is located, is shown in Fig. 4. Well-resolved vibrational excitations are seen in the high-energy part of the phonon spectrum, similar to those observed in [7]. The highest energy maximum in the absorption spectrum, which we attribute to the excitation of the respiratory mode, shifts to lower energies with increasing temperature. The shift for La is noticeably stronger than for Gd (Fig. 5a), and we attribute it to the population of the HS state of $Co^{3+}$ ions with increasing temperature. Figure 5(b) shows the calculated temperature dependence of the position of the maximum in the IR absorption spectrum corresponding to the excitation of the breathing (compression) mode of crystal lattice vibrations for two compounds.

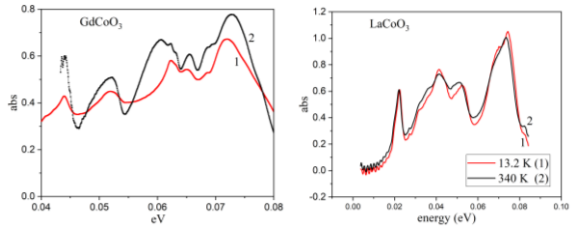


***Fig. 4.*** *Absorption spectrum of $LaCoO_3$ (right) and $GdCoO_3$ (left) at T = 3.2 and 550 K in the energy range 0.04 – 0.08 eV.*

As the temperature increases, the absorption maximum shifts to lower frequencies, which corresponds to the experimental data obtained (Fig. 5a).

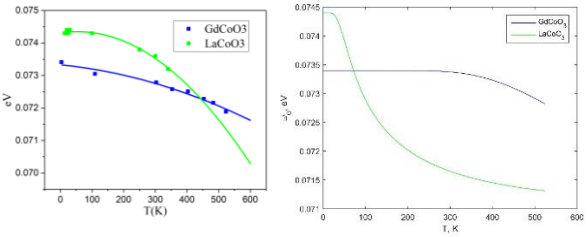


***Fig. 5.*** *(left) Experimentally obtained temperature dependence of the breathing mode energy in $LaCoO_3$ and $GdCoO_3$. (right) Calculated temperature dependence of the breathing mode frequency of $CoO_6$ octahedra. The calculations were performed for the following values of the spin gap $\Delta_S$: $\Delta_{GdCoO3}$ = 2300 K, $\Delta_{LaCoO3}$ = 150 K.*

## 4. Conclusions

The study of nanostructured $LaCoO_3$ magnetic properties showed the presence of ferromagnetic ordering, which can be associated with the stabilization of the high-spin state of $Co^{3+}$ ions at the grain boundaries. The study of the temperature dependences of the infrared absorption spectra of $LaCoO_3$ and $GdCoO_3$ revealed a strong softening of the optical phonon mode, which is due to the quadratic electron-phonon interaction in the lattice shift and fluctuations in the multiplicity of $Co^{3+}$ ions.

## Acknowledgements

This work was supported by the Russian Science Foundation grant 18-02-00022.

## References

[1] J. B. Goodenough. J. Phys. Chem. Sol. **6** (1958) 287.
[2] J. Q. Yan, J. S Zhou, J. B. Goodenough. Phys. Rev. B **70** (2004) 014402.
[3] A. Fujii, T. Kondo, T. Taniguchi, T. Sakaya. American Mineralogist **96** (2011) 329.
[4] A. Harada, T. Taniyama, Y. Takeuchi, T. Sato, T. Kyômen, M. Itoh. Phys. Rev. B **75** (2007) 184426
[5] Y. Kobayashi, T. S. Naing, M. Suzuki, M. Akimitsu, K. Asai, K. Yamada, J. Akimitsu, P. Manuel, J. M. Tranquada, G. Shirane, Phys. Rev. B **72** (2005) 174405.
[6] A. V. Rybina, V.V. Efimov, P.A. Alekseev, I.O. Troyanchuk, A.S. Ivanov, V. V. Sikolenko, E.S. Clementyev. Journal of Surface Investigation X-ray, Synchrotron and Neutron Techniques **5(6)** (2011) 1140.
[7] N. O. Lipari, C. B. Duke, L. Pietronero. J. Chem. Phys. **65** (1976) 1165.

Sixth Asian School-Conference on Physics and
Technology of Nanostructured Materials
Vladivostok, Russia, 25 – 29 April, 2022



# Features of the formation of nanoparticles and binary nanoalloys during thermal evaporation and condensation on an inert surface in vacuum

D.G. Gromov*[,1,2], S.V. Dubkov[1], S.A. Gavrilov[1]

[1] Institute of Advanced Materials and Technologies, National Research University of Electronic Technology, 124498 Zelenograd, Russia

[2] I.M. Sechenov First Moscow State Medical University, 119435 Moscow, Russia

*e-mail: gromadima@gmail.com

**Abstract.** The several features of the formation of nanoparticles Ag, Au and binary nanoalloys Ag-Cu, Au-Cu, Cu-Rh by thermal evaporation, condensation and heating on an inert surface in vacuum are shown. Rapid changes in the initial Ag array take place at an unusually low temperature of 75-100 0C, and after the array enters a metastable state. The impact of the electron beam of a transmission electron microscope on the initial condensate is demonstrated to lead to the migration of nanoparticles and their fusion despite their crystalline state. The difference in the formation of Ag-Cu, Au-Cu and Cu-Rh nanoalloys is also demonstrated. The considered features of the formation of nanoparticles and nanoalloys are associated with the size effect of lowering the melting temperature.

## 1. Introduction

Nanoparticles of metals and alloys are actively studied for various applications due to their observed extraordinary properties. In particular, they can be used in biomedical [1,2], catalytic [3,4], sensor [5,6], electronic [7,8] and other applications. There are physical and chemical methods for the formation of nanoparticles on a solid-phase surface. Physical methods include thermal evaporation and condensation on an inert surface in vacuum. This technique makes it possible to obtain arrays of metal nanoparticles with a controlled average size depending on the amount of evaporated substance [наши]. In this work, we consider the features that arise in the implementation of this technique both in the formation of particles of elemental metals and particles of binary alloys.

## 2. Decreasing the melting temperature with a decrease in the size of nanoobjects

We believe that the main reason for the formation and behavior of metal nanoparticles is the effect of decreasing the melting temperature, which intensifies with a decrease in the size of nanoparticles or other nanoobjects.

It follows from the conditions of equilibrium thermodynamics that for a system bounded by a surface, the melting temperature decreases in accordance with the expression

$$T = T_\infty \left( \frac{\Delta H(T)}{\Delta H(T_\infty)} + \frac{\sigma_L A_L - \sigma_S A_S}{V \Delta H(T_\infty)} \right) \quad (1)$$

where T is the phase transition temperature of a system bounded by a surface, in particular, a nanosystem, $T_\infty$ is the phase transition temperature of a macrosystem, σ is the surface energy, A is the surface area, V is the volume, ΔH(T) is the change in enthalpy as a result of the phase transition at temperature T. Comparison of the calculations of the melting temperature of gold nanoparticles depending on their size with the known experimental data [9] shows that this expression gives a very good agreement [10].

A comprehensive analysis of model calculations based on this expression allows to reveal a number of features of the phenomenon of heterogeneous melting of a decrease in the melting temperature:

• the reason for the downward shift of the melting temperature with decreasing size is the surface energy σ, whose contribution to the total energy of the object increases with decreasing size;

• the "trigger" of the process of heterogeneous melting is the difference between the surface energies of the liquid and solid phases $\sigma_L$-$\sigma_S$. However, the magnitude of this difference does not significantly affect the decrease in temperature;

• a decrease in the melting heat ΔH(T), which becomes smaller at lower temperatures, strongly affects the lowering of the melting point.

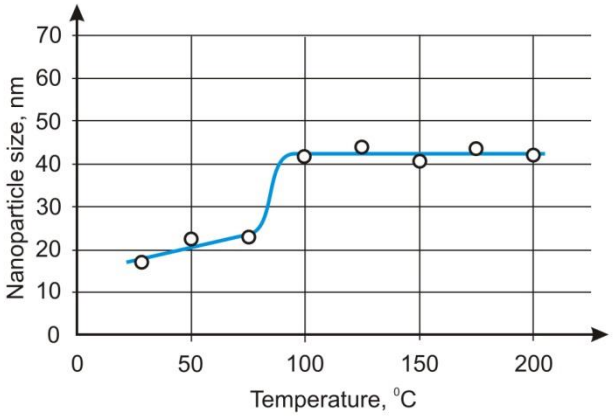


***Fig. 1.*** *Dependence of the average lateral size of nanoparticles on temperature of in-situ heating during atomic force microscope measurement.*

## 3. Instability of a metal condensate formed on an unheated substrate

Interesting results were obtained in the study of the evolution of an array of silver nanoparticles on the surface of $SiO_2$ by atomic force microscopy during in-situ heating up to 200 $^0$C [11]. The initial silver condensate is an array of disks and is unstable. Even a slight change in temperature by 20-30 $^0$C leads to coarsening of particles, change in their number per unit surface and change in their shape, which becomes closer to spherical. Rapid changes in

the array take place at an unusually low temperature of 75-100 $^0$C, as can be seen in Fig.1. As a result of these changes, the array enters a metastable state, which persists at least up to 200 $^0$C.

We observed a similar instability for the gold condensate. In particular, the impact of the electron beam of a transmission electron microscope on the initial condensate leads to the migration of nanoparticles and their fusion, as can be seen in Fig. 2. It should be noted that the nanoparticles are in a crystalline form, but at the same time, when merged, they change shape, acquiring a more spherical shape.

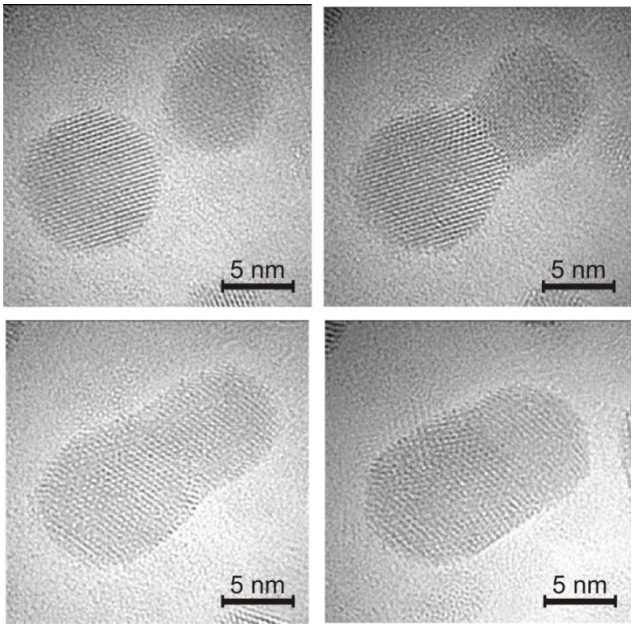


***Fig. 2.*** *TEM time-lapse storyboard of the process of combining two silver nanoparticles on an amorphous carbon surface.*

### 4. Formation of nanoparticles of binary alloys

Among binary nanoalloys, systems of the Ag-Cu eutectic type, a continuous series of Au-Cu solid solutions, and with the decomposition of a solid solution in the Cu-Rh solid phase were studied. The results of studies of the Au-Cu system show that solid solution nanoparticles are easily formed during deposition and low heating with a smoothly controlled composition and crystal lattice parameter ranging from pure copper to pure gold [12]. Interestingly, in the Cu-Rh system, the decomposition of the solid solution in the solid phase was not observed, and the formation of a nanoalloy with a continuous solid solution series was also observed [13]. This contradicts the Cu-Rh phase diagram and thus is a typical size effect. At the same time, in the Ag-Cu system, the formed nanoparticles were always composite: a part from a solution enriched with copper and a part from a solution enriched with silver [14].

### 5. Conclusions

We attribute the unusual behavior of nanoparticles on the surface of a solid to the size effect of lowering the melting point of the material. This, among other things, determines that for nanoalloys there is a serious deviation from the phase diagram of the bulk material. Ultimately, this allows us to form nanoparticles and nanoalloys of a specific composition and structure.

### Acknowledgements

The work was supported by the Russian Science Foundation (Project No. 21-19-00761).

### References

[1] Erathodiyil, J.Y. Ying. Acc. Chem. Res. **44** (2011) 925.
[2] B. Klębowski, J. Depciuch, M. Parlińska-Wojtan, J. Baran. J. Mol. Sci. **19** (2018) 4031.
[3] L. Liu, A. Corma. Chem. Rev. **118** (2018) 4981.
[4] G. Chang, Z. Cai, H. Jia, Z. Zhang, X. Liu, Z. Liu, R. Zhu, Y. He. Int. J. Hydrogen Energy. **43** (2018) 12803.
[5] S. Zeng, D. Baillargeat, H.-P. Ho, K.-T. Yong. Chem. Soc. Rev. **43** (2014) 3426.
[6] Q. Zhou, L. Xu, A. Umar, W. Chen, R. Kumar. Sens. Actuators B Chem. **256** (2018) 656.
[7] K. Liu, Y. Bai, L. Zhang, Z. Yang, Q. Fan, H. Zheng, Y. Yin, C. Gao. Nano Lett. **16** (2016) 3675.
[8] Y. Sonnefraud, A. Leen Koh, D.W. McComb, S.A. Maier. Laser Photon. Rev. **6** (2012) 277.
[9] Ph.Buffat, J.-P. Borel, Physical Review A, 13 (1976) 2287.
[10] D.G.Gromov, S.A.Gavrilov. In Thermodynamics; J.C.Piraján-Moreno, Ed.; IntechOpen: Rijeka, Croatia, (2011) 157.
[11] D.G.Gromov, S.V.Dubkov, G.S.Eritsyan, A.I.Savitsky, V.A.Bykov, Yu.A.Bobrov. Russian Microelectronics. **49** (2020) 485.
[12] S.Dubkov, D.Gromov, A.Savitskiy, A.Trifonov, S. Gavrilov. Mater. Res. Bull. **112** (2019) 438.
[13] L.Sorokina, A.Savitskiy, O.Shtyka, T.Maniecki, M.Szynkowska-Jozwik, A.Trifonov, E.Pershina, I.Mikhaylov, S.Dubkov, D.Gromov. J. All. Com. **904** (2022) 164012.
[14] S.V.Dubkov, A.I.Savitskiy, A.Yu.Trifonov, G.S.Yeritsyan, Yu.P.Shaman, E.P.Kitsyuk, A.Tarasov, O.Shtyka, R.Ciesielski, D.G.Gromov. Optical Materials: X. **7** (2020) 100055.

# Mesoporous $Na_2Ti_3O_7$ materials with a coral-like hierarchical architecture constructed by nanotubes: synthesis and properties

A.I. Neumoin*, D.P. Opra, S.L. Sinebryukhov, A.B. Podgorbunsky, S.V. Gnedenkov
Institute of Chemistry FEB RAS, 159 Pr. 100-letiya Vladivostoka, Vladivostok 690022, Russia

*e-mail: anton_neumoin@ich.dvo.ru

Due to valuable physical and chemical properties, the scope of using materials based on titanium oxides is almost unlimited. They have found wide application in such areas as paint and varnish branches, micro/nanoelectronics (since recently), photocatalysis, food and hygiene products, biomedical technologies, etc. Demand for them has also arisen in the energy sector: solar cells, hydrogen production, and batteries. Regarding the latter much attention has recently been paid to the development of next-generation systems and technologies, such as sodium-ion batteries. This dictates the need to search for new materials with improved characteristics, as well as ways to obtain them that meet the requirements of scalability. One of the ways to solve these problems can be the creation of nanomaterials that often have a complex of physicochemical properties that radically differ from the characteristics of their counterparts in the micro- or macroscopic state. At the same time, it is important to control the texture (specific surface area, porosity), morphology, and topology of such materials. Functional materials with hierarchical micro/nano architecture, constructed by unique aggregates of constituent elements and possessing a porous structure have great prospects. In view of the above, among other methods, the hydrothermal technique seems to be suitable because of it is allowed to control of a wide range synthesis conditions and parameters.

In the present study, a method for preparation of mesoporous nanostructured sodium trititanate ($Na_2Ti_3O_7$) with a hierarchical architecture was developed. Mesoporous $Na_2Ti_3O_7$ microparticles consist of nanotubes were obtained through hydrothermal treatment of $TiO_2$ P25 (99.7%, Sigma-Aldrich) in a highly alkaline medium (10 M NaOH solution) at a temperature of 130 °C for 36 hours. To characterize the product, a number of scientific techniques were involved, including scanning and transmission electron microscopy, low-temperature nitrogen adsorption-desorption, X-ray diffraction, X-ray photoelectron spectroscopy, energy-dispersive X-ray analysis, UV-vis diffuse reflection spectroscopy, electrochemical impedance spectroscopy, etc.

The results showed that the material exhibits a complex hierarchically-organized two-layer architecture. At the first level of hierarchy, the material is represented by particles, similar to corals having a roughness surface with a diameter of one to ten microns. An in-depth analysis shows that these microparticles consist of elements of a smaller scale – ultrathin one-dimensional nanotubes with a diameter of 6–9 nm. The wall thickness of nanotubes is 3–4 nm.

According to the adsorption measurements, the BET specific surface area for the sample is about 300 $m^2/g$ and the BJH pore volume reaches 0.5–0.6 $cm^3/g$. Next, the formation of a mesoporous structure with a narrow pore size distribution of near 5–6 nm is proved. The specific surface area and porosity are important characteristics of functional materials, which determine the possibilities and areas of their practical application.

The phase composition of the synthesized product is represented by $Na_2Ti_3O_7$, crystallizing in the monoclinic system (sp. gr. $P2_1/m$) with an impurity of anatase titanium dioxide. The obtained data correlate with the results of energy-dispersive X-ray microanalysis and X-ray photoelectron spectroscopy.

According to the UV-Vis spectroscopy, the material absorbs UV rays and has a high reflectance in the region $\lambda > 400$ nm, which is typical for $Na_2Ti_3O_7$. The band gap of the sample calculated by Tauc method for indirect allowed transitions (taking into account the Kubelka–Munk model) is 3.37 eV, which agrees with the results of theoretical calculations (3.28 eV) and experimental measurements (3.4–3.85 eV) by other authors. Electrochemical impedance spectroscopy data show that the resulting coral-like hierarchical $Na_2Ti_3O_7$ nanotube-constricted architecture has a sufficiently high electrical conductivity of at least $4.97 \cdot 10^{-3}$ S/cm.

This work was financially supported by the Russian Science Foundation (grant № 22-23-00912). Electron-microscopic studies and energy-dispersive X-ray analysis were carried out using the core facilities available at the A.V. Zhirmunsky National Scientific Center of Marine Biology FEB RAS and Institute of Chemistry FEB RAS (researches within the budget theme No. 0205-2021-0004 of the state assignment).

Sixth Asian School-Conference on Physics and
Technology of Nanostructured Materials
Vladivostok, Russia, 25 – 29 April, 2022



# On the issue of obtaining heterostructures based on copper molybdates by solid-phase synthesis

M.S. Gurin, M.D. Ostrikov, D.V. Gritcuk, A.O. Lembikov, M.I. Balanov, D.S. Shtarev*
Far Eastern Federal University, 10 Ajax, Russky Island, Vladivostok 690922, Russia

*e-mail: shtarev.ds@dvfu.ru

**Abstract.** In this work, we study the possibility of obtaining heterostructures based on copper molybdates of various compositions by solid-phase synthesis from oxide precursors. It is shown that this method can be effectively used for the controlled synthesis of heterostructures that include both copper molybdates of various compositions and initial oxide precursors. A number of the most promising heterostructures have been identified, the properties of which have not yet been described and which can be synthesized by the proposed method.

## 1. Introduction

Copper molybdates are promising materials, often exhibiting catalytic and photocatalytic properties. The most studied representative of this class of compounds is $CuMoO_4$. It is known that it can act as an effective catalyst for soot afterburning [1,2], be used for oxidation [3,4] or reduction [4] of various organic compounds, and exhibit the properties of an electrocatalyst in the oxygen evolution reaction [5] or $CO_2$ reduction [6]. The properties of other copper molybdates, $Cu_3Mo_2O_9$ and $Cu_6Mo_5O_{18}$, have also been studied. The first of them is proposed to be used either as a catalyst for afterburning carbon monoxide or soot [2], or as a photocatalyst [7–9], or for lithium storage and supercapacitor performance [10]; the second - as an effective electrode for electrochemical water splitting [11]. The above list of works covers almost all stable phases of copper molybdates formed from copper and molybdenum oxides in higher oxidation states in air and presented in the corresponding phase diagram [12].

To increase the activity of copper molybdates, as a rule, a standard approach is used to obtain heterostructures based on them. In this case, zinc oxide ($CuMoO_4$/ZnO nanocomposites [13]) or its molybdate ($CuMoO_4$/$ZnMoO_4$ nanoflowers [14]), or, for example, titanium dioxide ($CuMoO_4$/$TiO_2$ [15]), can be used as the second element of heterostructures.

However, recently [16], using the example of strontium bismuthates, another promising way was proposed for obtaining heterostructures with increased photocatalytic activity. It consists in obtaining heterostructures from two strontium bismuthates of different compositions, located next to each other in the phase diagram. This is achieved by choosing a nonstoichiometric ratio of precursors for further solid-phase synthesis. With this approach, the resulting components of the heterostructure are sufficiently close in chemical composition and properties, which ensures the permeability of the interface for photocarriers and manifests itself in an increase in photocatalytic activity. Also, the indisputable advantage of this approach is the simplicity of its implementation.

In this work, an attempt is made to extrapolate the method proposed in [16] for obtaining heterostructures to copper molybdates.

## 2. Experiment

For solid-phase synthesis, commercial powders of copper oxides CuO and molybdenum $MoO_3$ were used without additional processing. The precursors were mixed in molar ratios of CuO:$MoO_3$ from 1:9 to 9:1 with a step of 10 mol.% and homogenized in a planetary mill. After that, the mixtures of powders were annealed in air at temperatures of 675-800 $^0$C for 4 hours.

The phase composition of the synthesized samples was analyzed by XRD. For this, a Bruker D8 Advance X-ray diffractometer with Cu-Kα radiation at a voltage of 40 kV and a current of 15 mA was used. The shooting range was 10-56 $^0$, the accumulation time was 0.1 s, the step was 0.006 $^0$ (2Θ). The X-ray patterns were recorded with a Vantec linear detector. Phase analysis was carried out in the Eva program, semi-quantitative analysis was carried out in the Qual-X program.

## 3. Results and discussions

The phase composition of all objects of study is presented in Table I. It can be seen that the phase composition of the obtained samples of heterostructures based on copper molybdates is mainly determined by the ratio of copper and molybdenum in the precursors. The annealing temperature generally has a smaller effect on the phase composition of the final samples.

However, the cases in which the molar ratio of metals in the precursors is close to equal should be considered separately. Thus, at a molar ratio of metals of 5:5, upon annealing at 675 $^0$C, the formation of copper molybdate $CuMoO_4$ and a significant amount of excess, unreacted molybdenum oxide $MoO_3$ are observed. With an increase in the synthesis temperature to 700 $^0$C, the picture changes dramatically: copper and molybdenum oxides react completely, without residue, while more actively forming copper molybdate $Cu_3Mo_2O_9$ (its fraction reaches 63%) and slightly less actively - copper molybdate $CuMoO_4$ (37%). With a further increase in the synthesis temperature to 750 $^0$C, it is accompanied by an increase in the proportion of $Cu_3Mo_2O_9$ up to 84%.

Also, the influence of the annealing temperature on the ratio between the components of the heterostructure is observed at a molar copper and molybdenum ratio of 4:6. Thus, at an annealing temperature of 675 $^0$C, the heterostructure consists of 64% molybdenum oxide and 36% $CuMoO_4$. At 700 $^0$C, the ratio of components is opposite: the sample consists of 74% $CuMoO_4$ and only 26% of $MoO_3$. Unfortunately, a further increase in the synthesis temperature is accompanied by sample melting.

***Table I.*** *Phase composition and content of components of heterostructures based on copper molybdates depending on the ratio of precursors and annealing temperature.*

| The CuO : $MoO_3$ molar ratio | Phase (content, %) | | |
|---|---|---|---|
| Temp., $^0C$ | 675 | 700 | 725 |
| *9:1* | CuO/55<br>$Cu_3Mo_2O_9$/45 | CuO/58<br>$Cu_3Mo_2O_9$/42 | CuO/58<br>$Cu_3Mo_2O_9$/42 |
| *8:2* | $Cu_3Mo_2O_9$/69<br>CuO/31 | $Cu_3Mo_2O_9$/71<br>CuO/29 | $Cu_3Mo_2O_9$/69<br>CuO/31 |
| *7:3* | $Cu_3Mo_2O_9$/85<br>CuO/15 | $Cu_3Mo_2O_9$/86<br>CuO/14 | $Cu_3Mo_2O_9$/84<br>CuO/16 |
| *6:4* | $Cu_3Mo_2O_9$/95<br>CuO/5 | $Cu_3Mo_2O_9$/97<br>CuO/3 | $Cu_3Mo_2O_9$/96<br>CuO/4 |
| *5:5* | $CuMoO_4$/59<br>$MoO_3$/41 | $Cu_3Mo_2O_9$/63<br>$CuMoO_4$/37 | $Cu_3Mo_2O_9$/63<br>$CuMoO_4$/37 |
| *4:6* | $MoO_3$/64<br>$CuMoO_4$/36 | $CuMoO_4$/74<br>$MoO_3$/26 | Melted |
| *3:7* | $MoO_3$/61<br>$CuMoO_4$/39 | $MoO_3$/82<br>$CuMoO_4$/18 | Melted |
| *2:8* | $MoO_3$/90<br>$CuMoO_4$/10 | $MoO_3$/88<br>$CuMoO_4$/12 | Melted |
| *1:9* | $MoO_3$/92<br>$CuMoO_4$/8 | $MoO_3$/90<br>$CuMoO_4$/10 | Melted |
| Temp., $^0C$ | 750 | 775 | 800 |
| *9:1* | CuO/54<br>$Cu_3Mo_2O_9$/46 | CuO/57<br>$Cu_3Mo_2O_9$/43 | CuO/57<br>$Cu_3Mo_2O_9$/43 |
| *8:2* | $Cu_3Mo_2O_9$/63<br>CuO/37 | $Cu_3Mo_2O_9$/67<br>CuO/33 | $Cu_3Mo_2O_9$/67<br>CuO/33 |
| *7:3* | $Cu_3Mo_2O_9$/85<br>CuO/15 | $Cu_3Mo_2O_9$/85<br>CuO/15 | $Cu_3Mo_2O_9$/84<br>CuO/16 |
| *6:4* | $Cu_3Mo_2O_9$/95<br>CuO/5 | $Cu_3Mo_2O_9$/94<br>CuO/6 | $Cu_3Mo_2O_9$/95<br>CuO/5 |
| *5:5* | $Cu_3Mo_2O_9$/84<br>$CuMoO_4$/16 | Melted | Melted |
| *4:6* | Melted | Melted | Melted |
| *3:7* | Melted | Melted | Melted |
| *2:8* | Melted | Melted | Melted |
| *1:9* | Melted | Melted | Melted |

## 4. Conclusions

The studies performed have shown that, by varying the parameters of solid-phase synthesis (the ratio of components and the annealing temperature), one can effectively control the composition of heterostructures based on copper molybdates and the ratio of components in them. The application of this approach makes it possible to obtain three types of heterostructures — $Cu_3Mo_2O_9$/CuO, $CuMoO_4$/$MoO_3$, and $Cu_3Mo_2O_9$/$CuMoO_4$ — the properties of which have not been described previously.


## Acknowledgements

The research was carried out at the expense of a grant from the Russian Science Foundation (project No. 19-73-10013).


## References


[1] P. G. Chigrin, N. V. Lebukhova, A. Y. Ustinov. Reaction Kinetics, Mechanisms and Catalysis **113**(2014)1.

[2] E. V. Soltys, K. K. Urazov, T. S. Kharlamova, O. V. Vodyankina. Kinetics and Catalysis **59**(2018)58

[3] X. Yu, H. Liu, Q. Wang, W. Jia, H. Wang, W. Li, J. Zheng, Y. Sun, X. Tang, X. Zeng, F. Xu, L. Lin. ACS Sustainable Chemistry and Engineering **9**(2021)13176

[4] H.O. Hassani, M. Akouibaa, S. Rakass, M. Abboudi, B. El Bali, M. Lachkar, F. Al Wadaani. Journal of Science: Advanced Materials and Devices **6**(2021)501

[5] A.A. Yadav, Y.M. Hunge, S.-W. Kang. Surfaces and Interfaces **26**(2021)101425

[6] A. Rahmani, H. Farsi. RSC Advances **10**(2020)39037

[7] N.F. Dummer, Z. Sodiq-Ajala, D.J. Morgan, T.E. Davies. Catalysis Communications **163**(2022)106414

[8] T. Akiyama, R. Sei, S. Takenaka. Catalysis Science and Technology **11**(2021)5273

[9] Z. Xia, J. Min, S. Zhou, H. Ma, B. Zhang, X. Tang. Ceramics International **47**(2021)12667

[10] H. Liu, L. Liu, C. Ding. Journal of Alloys and Compounds **867**(2021)159061

[11] S.P. Keerthana, B. J. Rani, R. Yuvakkumar, G. Ravi, Y. Shivatharsiny, E. S. Babu, H. S. Almoallim, S. A. Alharbi, D. Velauthapillai. International Journal of Hydrogen Energy **46**(2021)7701

[12] K. Nassau, J. W. Shiever. Journal of The American Ceramic Society **52**(1969)36

[13] R. Syah, A. H. Altajer, O. F. Abdul-Rasheed, F. A. Tanjung, A. M. Aljeboree, N. A. Alrazzak, A. F. Alkaim. Journal of Nanostructures **11**(2021)73

[14] A.B. Appiagyei, J. O. Bonsu, J. I. Han. Journal of Materials Science: Materials in Electronics **32**(2021)6668

[15] N. V. Lebukhova, V. S. Rudnev, E. A. Kirichenko, P. G. Chigrin, I. V. Lukiyanchuk, N. F. Karpovich, M. A. Pugachevsky, V. G. Kurjavyj. Surface and Coatings Technology **261**(2015)344

[16] D. S. Shtarev, A. V. Shtareva, M. S. Molokeev, A. V. Syuy, E. O. Nashchochin. Key Engineering Materials **806**(2019)161

Sixth Asian School-Conference on Physics and
Technology of Nanostructured Materials
Vladivostok, Russia, 25 – 29 April, 2022



# Influence of phenol red in Earl's solution on the corrosion properties of coated and uncoated Mg alloy

A.I. Pleshkova[*,1,2], M.A. Piatkova[1,2], K.V. Nadaraia[1], A.B. Podgorbunsky[1], S.L. Sinebryukhov[1], S.V. Gnedenkov[1]

[1] Institute of Chemistry FEB RAS, 159 Pr. 100-letiya Vladivostoka, Vladivostok, 690022, Russia
[2] Far Eastern Federal University, 8 Sukhanova St., Vladivostok 690950, Russia

*e-mail: othariadna@gmail.com

**Abstract.** Metallic biomaterials are widely used for clinical purposes due to their excellent mechanical properties and good strength. Inspired by the functional surface of natural biological systems, many new designs and concepts have recently emerged to create multifunctional surfaces with great potential for biomedical applications. In present study, bioactive coatings were formed on Mg alloy by plasma electrolytic oxidation (PEO). Morphological features and composition of formed layers were studied by SEM and EDS. It was revealed that PEO-coatings have Ca and P, as well as hydroxyapatite in their composition, which increases the biocompatibility. Moreover, obtained coatings demonstrated high corrosion properties: corrosion current density substantially decreased compared to bare alloy.

## 1. Introduction

Currently, the development of technologies makes it possible to create safe implants that are biocompatible with the human body. The development of new materials for bone implants requires a deep knowledge of the chemical, physical and mechanical properties of natural bone tissue, the qualitative and quantitative characteristics of implant materials. Recently, the possibility of natural regeneration has been actively studied, when the implant material biodegrades and dissolves in body fluids, and the process of healing of damaged tissues occurs with the replacement of the implant with the body's own tissue. This property of bioresorption is possessed by magnesium and magnesium alloys. Early clinical studies, as well as in vivo and in vitro studies show that magnesium-based implants are highly biocompatible. It has also been reported that magnesium-based implants can stimulate the development of calluses at fracture sites [1].

The unique mechanical properties of Mg alloys also make them desirable solid-state implants. Magnesium has been tested as non-allergenic and stimulates new bone formation in vivo and in vitro [1].

However, the high electrochemical activity of magnesium and low wear resistance of this material can lead to early failure of the implant, which in turn can significantly affect to the patient's recovery [2]. As result, magnesium needs additional protection to improve corrosion resistance and reduce wear. One of the possible ways to solve this problem is formation of coating on the surface of a magnesium implant by the method of plasma electrolytic oxidation (PEO) [3]. Note that, the possibility of creating surface layers of a given structure and composition by this method, the use of PEO makes it possible to form coatings similar in composition to human bone tissue [1,4].

## 2. Experiment

Bioactive coatings were formed on MA8 Mg alloy by plasma electrolytic oxidation (PEO). Morphological features and composition of formed layers were studied by SEM and EDS.

The electrochemical parameters of the samples were studied by potentiodynamic polarization using VersaSTAT MC electrochemical system (Princeton Applied Research, USA) in accordance with the technique described in [3].

The measurements were carried out in a three-electrode cell at a temperature of 37° C in Earl's solution with and without phenol red, which are solutions similar in ionic composition to human blood plasma (Table I).

***Table I.*** *Ion concentration (mmol/L) in saline and human blood plasma.*

| Ion concentration, mmol/L | Human blood plasma | Earle's solution |
|---|---|---|
| $Na^+$ | 142 | 143.5 |
| $Cl^-$ | 103 | 123.5 |
| $HCO^{3-}$ | 27 | 26.2 |
| $K^+$ | 5.0 | 5.4 |
| $Ca^{2+}$ | 2.5 | 1.8 |
| $Mg^{2+}$ | 1.5 | 0.8 |
| $PO4^{3-}$ | 1.0 | 0.9 |
| $SO4^{2-}$ | 0.5 | 0.8 |
| *Glucose, g/L* | 1.1 | 1.0 |

## 3. Results and discussions

Potentiodynamic polarization data indicate an improvement in the corrosion properties of the samples after coatings formation on their surface. Based on the analysis of the polarization curves, it can be conclude that the corrosion current density $i_{corr}$ decreased after application of PEO-coating on Mg alloy surface (Table II).

***Table II.*** *Electrochemical Parameters of Samples in Earle's solution with and without Phenol Red.*

| Electro-chemical parameters | Earle's solution without phenol red | | Earl's solution with phenol red | |
|---|---|---|---|---|
| | Bare magnesium alloy | With PEO-coating | Bare magnesium alloy | With PEO-coating |
| $E_{corr}$ *(V vs. SCE)* | -1.75 | -1.62 | -1.82 | -1.63 |
| $i_{corr}$ *(A/cm$^2$)* | $8.6\times10^{-6}$ | $6.7\times10^{-6}$ | $1.01\times10^{-5}$ | $6.8\times10^{-6}$ |

| | | | | |
|---|---|---|---|---|
| $\beta_a$ *(mV/Decade)* | 271.7 | 217.8 | 232.2 | 200.20 |
| $\beta_c$ *(mV/Decade)* | 270.88 | 188.35 | 197.94 | 180.95 |
| *Rp* *(Ω × cm²)* | $6.78\times10^3$ | $6.53\times10^3$ | $4.59\times10^3$ | $6.0\times10^3$ |

Note that there is differences between corrosion current density values for Earle's solution with and without phenol red (Fig. 1).

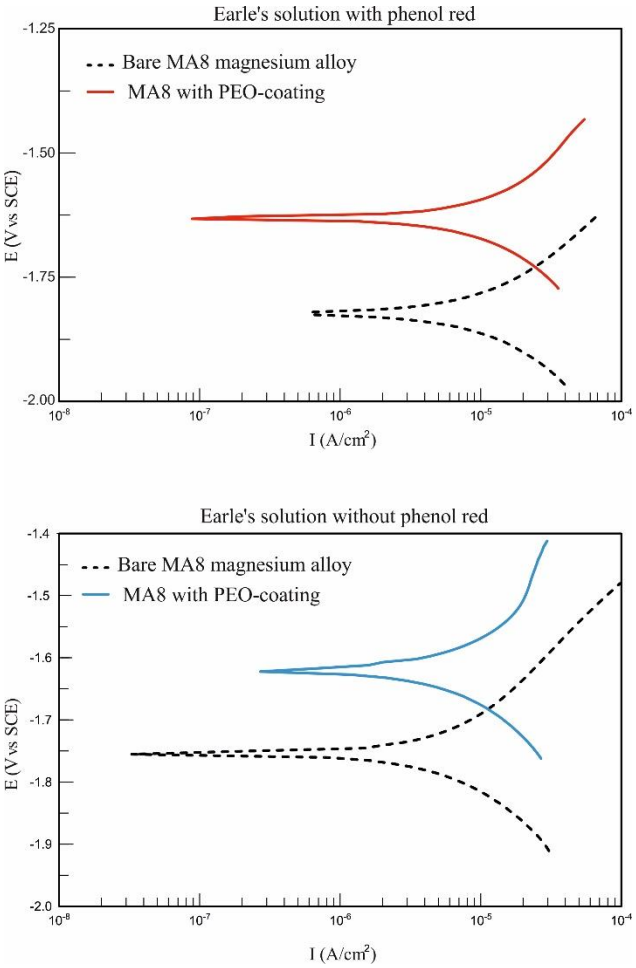


***Fig. 1.*** *Polarization curves for samples with different types of surface treatment.*

During chemical reactions, a layer is formed at the interface, which slightly decrease the electrochemical corrosion. This probably the result of alkalization of the adjacent substrate surface due to the interaction of magnesium ions released at the beginning of corrosion and phenol red in Earle's solution.

It was revealed that PEO-coatings have Ca and P, as well as hydroxyapatite in their composition, which increases the biocompatibility. Moreover, obtained coatings demonstrated high corrosion properties: corrosion current density substantially decreased compared to bare alloy.

## 4. Conclusions

Coatings, containing Ca/P, were obtained on Mg alloy by plasma electrolytic oxidation. Obtained coatings have high corrosion resistance compared to bare alloy. Moreover, differences in the results of electrochemical studies showed that the phenol red in Earl's solution affects the course of reactions on the surface of the studied samples. Further research will take this fact into account.

## Acknowledgements

This work has been supported by the grants the Russian Science Foundation, RSF 22-23-00915. The results of SEM and EDS were carried out under the government assignments of Ministry of Science and Higher Education of the Russian Federation (project No. FWFN-2021-0003).

## References

[1] N. Nassif, I. Ghayad. Advances in Materials Science and Engineering **2013** (2013).
[2] A.S. Gnedenkov, S.V. Lamaka, S.L. Sinebryukhov, D.V. Mashtalyar, V.S. Egorkin, I.M. Imshinetskiy, M.L. Zheludkevich, S.V. Gnedenkov. Corros. Sci. **182** (2021).
[3] G. Barati Darband, M. Aliofkhazraei, P. Hamghalam, N. Valizade. Journal of Magnesium and Alloys. **5** (2017)74–132.
[4] P. Roach, D. Eglin, K. Rohde, C. C. Perry. Journal of Materials Science: Materials in Medicine. **18** (2007)1263–1277.

# Thermal management to control the combustion behavior of Al-CuO multilayer thermites

M.E. Shiryaev[1], A.V. Sysa[2], R.M. Ryazanov[2], E.A. Lebedev[*,1,2]

[1] National Research University of Electronic Technology, Shokin Sq., H. 1, Zelenograd, 124498, Moscow, Russia
[2] Scientific-Manufacturing Complex "Technological Centre", Shokin Sq., H. 1, Bld. 7, Zelenograd, 124498, Moscow, Russia

*e-mail: dr.beefheart@gmail.com

Nanothermite materials are the most promising energy compositions, which in the near future can play a major role in the development of pyrotechnics, which has been stagnating over the past decades, and open up fundamentally new areas of their application. The main fundamental problem is related to the construction of nanothermite materials according to the “bottom-up” principle, from the scale of a single particle to the final object. And here new effects will appear, for example, when initiating reactions or material combustion, the influence of the substrate (the so-called thermal management) and macro-dimensional restrictions or 3D design (when restrictions are imposed in one or several directions, i.e. the formation of one-dimensional nanothermites (fibers, threads, columns, etc.) or two-dimensional (thin films and coatings) objects).

Traditionally, thermal management is understood as the design of microelectronic devices and devices in order to maximize heat dissipation and minimize local heating. Within the framework of this project, it is planned to develop and solve the inverse problem related to the understanding and controllable tune of heat dissipation in the course of a self-propagating reaction in multilayer energy (including thermite) materials

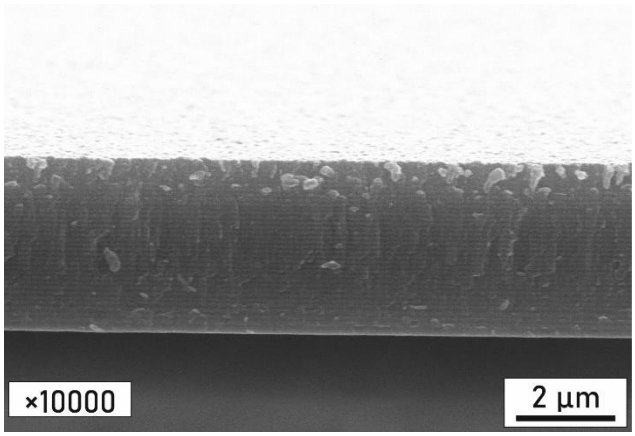


***Fig. 1.*** *SEM image of Al-$CuO_x$ multilayer structures cross-sections with 75 nm bilayer thickness.*

Within the framework of this work, the features of the formation of Al-$CuO_x$ multilayer thermite materials by the magnetron sputtering method were studied (SEM image of a multilayer structure is shown in Fig. 1). The dependences of the deposition rate and the composition of materials on the composition of the atmosphere and the sputtering power have been determined.

The dependences of the propagation velocity of the wave combustion front and the overall thermal effect of the reaction in Al-$CuO_x$ multilayer materials on the size effect, the substrate material, and the composition of energy materials have been comprehensively studied.

The results of experimental studies of the effect of thermal storage or barriers at the "energy material - substrate" interface on the propagation velocity of the wave combustion front have been obtained (Storyboards of Al-$CuO_x$ multilayer structures combustion process is presented on Fig. 2).

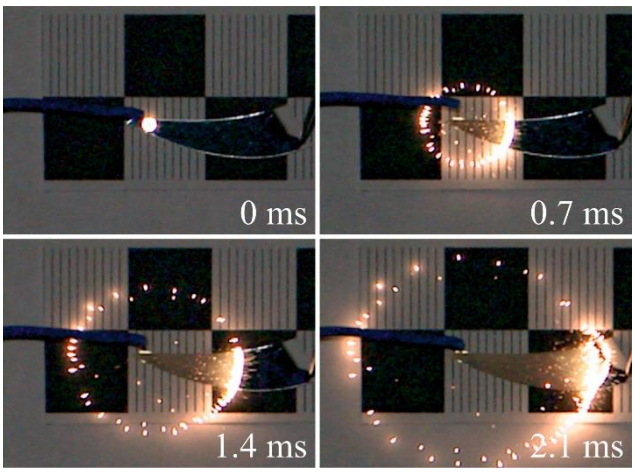


***Fig. 2.*** *Storyboards of Al-$CuO_x$ multilayer structures combustion process.*

The developed integrated energy microsystems with controlled properties can later be used as local heat sources for joining of various surfaces, incl. heterogeneous. Further development of this direction will make it possible to create integral miniature safety actuators, initiators of secondary reactions, gas generators and getters.

**Acknowledgements**

The study was supported by the Russian Science Foundation grant No. 22-29-01177, https://rscf.ru/project/22-29-01177/.

Sixth Asian School-Conference on Physics and
Technology of Nanostructured Materials
Vladivostok, Russia, 25 – 29 April, 2022



# Modification of the PEO-coating on MA8 Mg alloy using layered double hydroxide: electrochemical behavior, protective properties

A.D. Nomerovskii*, A.S. Gnedenkov, S.L. Sinebryukhov, S.V. Gnedenkov
Institute of Chemistry FEB RAS, 159 prospect 100-letiya Vladivostoku, Vladivostok 690022, Russia

*e-mail: nomerovskii.ad@outlook.com

**Abstract.** In this work, a coating containing layered double hydroxide (LDH) in the form of lamellar formations was obtained, and impregnated with a corrosion inhibitor. The electrochemical behavior of coatings, their phase and elemental composition, and morphology were investigated. The LDH structure makes it possible to improve the corrosion protection of magnesium alloy in a corrosive environment.

## 1. Introduction

Magnesium and its alloys are lightweight materials having density about 1.8 g/cm$^3$, which is lower than aluminum (about 2.7 g/cm$^3$), titanium (about 4.5 g/cm$^3$) and steel (about 7.8 g/cm$^3$). Magnesium alloys attracted significant interest of researchers owing to good specific strength, lightness, high damping capacity and good recyclability [1, 2].

Magnesium alloys do not have a protective oxide layer on their surface, in contrast to stainless steel, aluminum and titanium alloys. Intensive corrosion of Mg alloys appears in the marine atmosphere [2, 3]. Plasma electrolytic oxidation (PEO) is one of the well-known methods of applying protective coatings to metals and their alloys. This method is based on the polarization of the material in electrolyte solutions at voltages that cause flow of microdischarges on the surface of treated metals and their alloys [4].

For better protection of alloys and metals against corrosion the "smart coatings" are used. This type of coating has the property of self-healing due to gradual release of the corrosion inhibitors when damaged. In this paper, we consider the design and application of layered double hydroxides (LDH) for the protection of the MA8 magnesium alloy.

## 2. Experiment

The following coatings were obtained on the MA8 magnesium alloy: PEO-coating, PEO-coating containing LDH, and PEO-coating containing LDH and impregnated with an inhibitor.

PEO treatment [4] was carried out for 10 min in a bipolar mode (anodic phase: 30–300 V, cathode phase: –30 V) in an electrolyte containing 15 g/L $Na_2SiO_3 \cdot 5H_2O$ and 5 g/L NaF.

The sample with PEO-coating was treated to synthesize LDH [5] in a solution containing 50 g/L EDTA-Na, 40 g/L NaOH, and 5 g/L Al (aluminum were previously dissolved in sodium hydroxide). The samples were placed in the solution and kept for 48 h at 60°C.

The inhibitor treatment was carried out by immersion of sample in a solution containing 0.1 M sodium oleate for 24 h.

To control the weight of the samples, a Shimadzu AUW120D analytical balance was used. The coating thickness was measured using a VT-201 eddy current coating thickness gauge. SEM images and element distribution maps were obtained using a Zeiss EVO 40 electron microscope. X-ray diffraction analysis was performed on a Bruker D8 Advance diffractometer. Electrochemical measurements were carried out using a VersaSTAT MC electrochemical station (Princeton Applied Research, USA) in a 3.5 wt. % NaCl solution in a three-electrode cell with the Ag/AgCl electrode as a reference electrode.

## 3. Results and discussions

The thickness of the obtained coatings for all samples was 15 ± 2 μm. The surface area was 10.4 cm$^2$. The weight gain for the sample containing the LDH was 0.8 mg, and for the sample impregnated with the inhibitor, the weight gain was 0.4 mg. For samples with a PEO-coating containing LDH, a change in the color was noted (the initial PEO-coating was white, the PEO-coating with LDH was yellow). The color of coatings did not change during treatment with an inhibitor.

According to the XRD data and EDX maps of the elements distribution, one can unequivocally judge the formation of the layered double hydroxide phase $(Mg_{0.667}Al_{0.333})(OH)_2(CO_3)_{0.167}(H_2O)_{0.5}$. The element composition on the sample surface is as follows (at. %): O – 50.6; C – 22.0; Mg – 19.5; Si – 4.8; Al – 2.1; Na – 1.0.

The SEM image (Figure 1) of the sample containing LDH shows a lamellar structure, which corresponds to the LDH phase, in the space between solid areas.

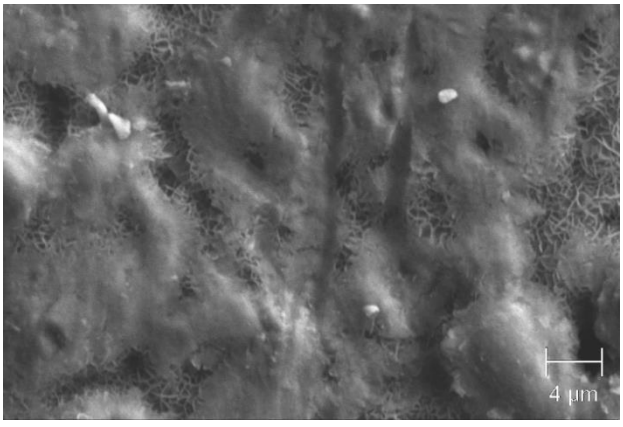


***Fig. 1.*** *SEM image of a PEO-coating containing LDH.*

The analysis of the obtained impedance spectra and potentiodynamic curves indicates the positive effect of LDH in the corrosion protection of magnesium alloy. The

electrochemical performance of Mg alloy sample with and without protective coatings are presented in Table I. The impedance modulus at 0.1 Hz, $|Z|_{0.1Hz}$, increases from the uncoated sample to sample with a PEO-LDH coating impregnated with corrosion inhibitor.

Corrosion current density, $I_c$, decreased and corrosion potential, $E_c$, increased after the treatment with an inhibitor.

***Table I.*** *Characteristics of obtained coatings.*

| *Sample* | $\|Z\|_{0.1Hz}$, $\Omega \cdot cm^2$ | $I_c$, $A/cm^2$ | $E_c$, $V$ | $R_p$, $\Omega \cdot cm^2$ |
|---|---|---|---|---|
| *MA8* | $6{,}7 \cdot 10^2$ | $1{,}7 \cdot 10^{-5}$ | *-1,512* | $8{,}7 \cdot 10^2$ |
| *MA8-PEO* | $8{,}4 \cdot 10^3$ | $4{,}1 \cdot 10^{-7}$ | *-1,411* | $7{,}4 \cdot 10^4$ |
| *MA8-PEO-LDH* | $1{,}7 \cdot 10^4$ | $3{,}5 \cdot 10^{-7}$ | *-1,422* | $1{,}4 \cdot 10^5$ |
| *MA8-PEO-LDH-oleat* | $2{,}1 \cdot 10^5$ | $2{,}6 \cdot 10^{-7}$ | *-1,389* | $6{,}4 \cdot 10^4$ |

## 4. Conclusions

1. Layered double hydroxide was formed on the PEO-coating containing MgO and $Mg_2SiO_4$.

2. The obtained LDHs have a positive effect on the stability of the coating obtained by the PEO method in the corrosive environment. The impedance modulus measured at lowest frequency (0.1 Hz) increased, and the corrosion current density decreased after “smart coating” formation on MA8 Mg alloy.

3. Inhibitor treatment also improves the corrosion resistance of the protective coating.

## Acknowledgements

The study of material`s structure and composition were supported by the Grant of Russian Science Foundation, Russia (project no. 20-13-00130, https://rscf.ru/en/project/20-13-00130/). Electrochemical measurements and coating formation were supported by the Grant of Russian Science Foundation, Russia (project no. 21-73-10148, https://rscf.ru/en/project/21-73-10148/).

## References

[1] F. Nazeer, J. Long, Z. Yang, C. Li. Journal of Magnesium and Alloys (2021).
[2] W. Xu, N. Birbilis, G. Sha, Y. Wang, J.E. Daniels, Y. Xiao, M. Ferry. Nature Materials **14**(2015)1229.
[3] L. Guo, W. Wu, Y. Zhou, F. Zhang, R. Zeng, J. Zeng. Journal of Materials Science & Technology **34**(2018)1455.
[4] A. S. Gnedenkov, S. L. Sinebryukhov, D. V. Mashtalyar, S. V. Gnedenkov. Corrosion Science **102**(2016)348.
[5] C.-Y. Li, L. Gao, X.-L. Fan, R.-C. Zeng, D.-C. Chen, K.-Q. Zhi. Bioactive Materials **5**(2020)364.

Sixth Asian School-Conference on Physics and
Technology of Nanostructured Materials
Vladivostok, Russia, 25 – 29 April, 2022



# Core-shell $Fe_3O_4$@C nanoparticles for magneto-mechanical destroy of Ehrlich ascites carcinoma cells

A.E. Sokolov*[,1,2], O.S. Ivanova[1,2], E.S. Svetlitsky[1,2], K.A. Lukyanenko[3], A.V. Shabanov[1], N.P. Shestakov[1], Ying-Zhen Chen[4], Yaw-Teng Tseng[4], Chun-Rong Lin[4]

[1] Kirensky Institute of Physics, FRC KSC SB RAS, 50 Akademgorodok St., Krasnoyarsk 660036, Russia
[2] Siberian Federal University, 79 Svobodny Ave., Krasnoyarsk 660041, Russia
[3] Federal Research Center "Krasnoyarsk Science Center of the Siberian Branch of the Russian Academy of Science", 660036 Krasnoyarsk, Russia;
[4] Department of Applied Physics, National Pingtung University, Pingtung City 90003, Taiwan

*e-mail: alexeys@iph.krasn.ru

**Abstract.** The core-shell magnetic nanoparticles, $Fe_3O_4$@C, were synthesized and surface aptamer-functionalized to use them as destroyers of living cancer Ehrlich's ascitic carcinoma cells. The morphology and features of the structural and magnetic properties of the obtained hybrid nanoparticles are studied.

## 1. Introduction

The unique properties of magnetite nanoparticles (NPs) have been used in various technical applications. Two relatively recent applications of magnetic NPs – water purification due to the adsorption of pollutants by the surface of NPs and magneto-mechanical destroy of cancer cells created many research challenges. The ease of magnetic separation of the adsorbed material and a high adsorption capacity are significant advantages of using magnetite NPs in the first case [1], and the NPs biocompatibility with living organisms is an attractive circumstance for using magnetite NPs in the second case [2].

It is known that the ability of magnetite NPs to adsorb substancies of various nature is due to both the presence of hydroxyl groups on their surface and to coordinatively unsaturated $Fe^{3+}$ and $Fe^{2+}$ ions. Depending on the nature and structure of the adsorbate molecules, they are easily retained on the active centers of the magnetite surface due to electrostatic, donor-acceptor, hydrophobic interactions and/or the formation of hydrogen bonds. And in the process of covalent immobilization, strong covalent bonds are formed between the modifier and the oxide surface. For these reasons, magnetite NPs are very convenient objects for covering them with various shells, creating core-shell structures, and functionalizing their surface.

The ability to attach certain molecules to themselves, and the high magnetic moment which makes it possible to control magnetite NPs behavior by a gradient magnetic field, create prerequisites to use these particles as candidates for the mechano-magnetic destruction of living cells.

In the present work, we studied the structural and magnetic properties of the core-shell $Fe_3O_4$@C NPs, functionalized their surface for attaching aptamers to them, and investigated the possibility of using them for the magneto-mechanical destruction of Ehrlich ascitic carcinoma cell cultures.

## 2. Experiment

Magnetite $Fe_3O_4$ NPs (0.2 g) obtained with the thermal decomposition reaction of the iron-oleate were mixed with glucose (1 g) in distilled water (30 ml) by sonication for 15 min. Then solution was placed in an autoclave for 12 h at 200°C. After cooling to room temperature, the black products were separated by an external magnetic field and washed several times with water and ethanol. Next, the NPs $Fe_3O_4$@C were dried at 60°C for 6 hours.

The synthesized NPs were examined with X-ray diffraction (XRD), transmission electron microscope (TEM), Fourie rtransform infrared spectroscopy (FTIR), vibrating sample magnetometer (VSM), magnetic circular dichroism spectroscopy (MCD).

To use the obtained $Fe_3O_4$@C NPs in experiments with living cells, a stage-by-stage functionalization of their surface was carried out.

To form –COOH functional groups, carbon-coated magnetite NPs were treated with a solution of nitric acid (1 normal) at 60°C for 3 hours with stirring under temperature control. The reaction product was washed several times with deionized water and once with ethanol.

Then 1 mg of NPs were placed in 1.5 ml a buffer solution (PBS) (filtered solution of $Ca^{2+}$ and $Mg^{2+}$, pH=7.4) containing: 1-ethyl-3-(3-dimethylaminopropyl) carbodiimide (1 mg) N-hydroxysuccinimide (1 mg ) for 30 minutes. This solution should activate the carboxyl group, which is capable to form an amide bond with the amino group of the biomolecule as a receptor molecule. At this stage, the so-called carboxylated NPs were obtained. Immobilization of $Fe_3O_4$@C nanoparticles with the aptamer was carried out by placing them in a PBS containing the aptamer (with the amino group AmPrcom5) in the concentration of the aptamer in the buffer solution was 10 mM

Finally, after incubation at room temperature, the aptamer-functionalized nanoparticles were washed with deionized water and mixed with cancer cells, Ehrlich's ascitic carcinoma. The samples were placed in an alternating magnetic field $H_{max}$= 100 Oe for 20 min. Photographs were taken with a Levenhuk M1400 PLUS microscope camera at 10x magnification 2 hours after exposure to a magnetic field. To visualize the destruction of the cells, they were originally tinted by trypan blue, so in the photo the whole cells are clearly visible as thin blue shells, and the destroyed cells are visible as a blue spots, due to the mixing of the dye from the shell with the internal contents of the cell during destruction. A typical picture observed through a microscope is shown in Fig. 1

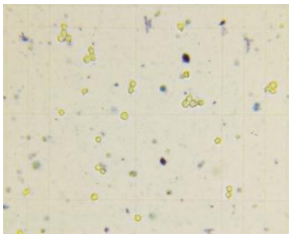

***Fig. 1.*** *The typical picture observed under a microscope for counting living and destroyed cells.*

### 3. Results and discussions

Figure 2 shows the $Fe_3O_4$ NPs morphology: well-dispersed spherical NPs of about 15 nm in diameter are seen. XRD patterns showed that the magnetic core of both $Fe_3O_4$ and $Fe_3O_4$@C NPs have a spinel-ferrite crystal structure with the parameters of the most intense peaks corresponding to the $Fe_3O_4$ phase (PDF Card # 04-005-4319). The high values of saturation magnetization – 79 emu/g, in the magnetite NPs and 64 emu/g in the carbon-coated NPs, measured in H=15 kOe, close to the saturation magnetization of bulk magnetite (84 emu/g), also confirm this fact.

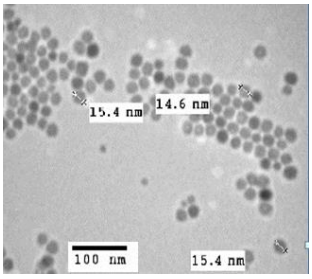


***Fig. 2.*** *TEM image of the initial $Fe_3O_4$ NPs.*

The FT-IR spectra showed the appearance of new bands during the transition: magnetite $Fe_3O_4$, core-shell $Fe_3O_4$@C and core-shell NPs after treatment in nitric acid $Fe_3O_4$@C–COOH, which indicates appearance of chemical bonds. In the spectrum of pure $Fe_3O_4$ NPs, an intense band at 580 $cm^{-1}$ is due to Fe-O stretching vibrations. This band is observed in the spectra of all samples. In the carbon-coated particles, C-O and O-R bonds appear at 1050 $cm^{-1}$, the $CH_2$-O-$CH_2$ group was indicated by the appearance of a wide band in the region of 1150-1100 $cm^{-1}$. In the nanoparticles treated in acid, the carboxyl group is clearly identified by the 1475 $cm^{-1}$ band and $CH_2COOH$ by the 1475 $cm^{-1}$ band. A slightly noticeable band at 798 $cm^{-1}$ is characteristic of pendulum oscillations of the NH3 group. Thus, IR spectra confirmed the coating of nanoparticles with carbon and its further carboxylation for bio-functionalization of the surface.

The percentage of dead ascitic cells in the test samples was statistically assessed by 5 independent samplings from the samples. Fig. 3 shows the average results of cell death. To confirm the joint antitumor effect of magnetite NPs immobilization with aptamers and magnetic field action on the mortality of the model cancer cells - Ehrlich's ascites carcinoma, four cases were considered: 1) a control sample of cells; 2) cells with aptamer-functionalized NPs without magnetic field application; 3) cells with aptamer-functionalized NPs after exposure to a magnetic field and 4) a mixture of cells with NPs without aptamers after exposure to a magnetic field.

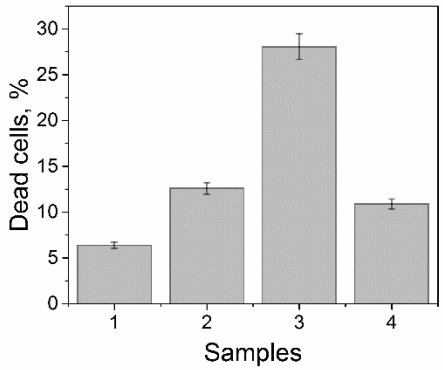


***Fig. 3.*** *The results of statistical processing of the count of living and destroyed cells - 1) control cells; 2) cells with aptamer-functionalized $Fe_3O_4$@C NPs without field application; 3) cells with aptamer-functionalized $Fe_3O_4$@C NPs after exposure to a magnetic field and 4) cells with NPs without aptamers after exposure to a magnetic field.*

The analysis of the results suggests that the use of magnetic NPs increases the number of the destroyed cancer cells. An increase in mortality during the interaction of aptamers- functionalized NPs with cells without exposure to an external magnetic field indicates their successful attachment to cells. And exposure to an alternating gradient field leads to the destruction of even more cell membranes under the influence of the chaotic movement of magnetic NPs in magnetic field.

### 4. Conclusions

In this study, core-shell magnetic nanoparticles, $Fe_3O_4$@C, were synthesized and then aptamer-functionalized to use them as destroyers of living cancer Ehrlich's ascitic carcinoma cells. XRD data showed the magnetic core of the particles to have the magnetite $Fe_3O_4$ crystal structure, transmission electron microscopy showed predominantly round shape NPs with the average size of 15 ± 2 nm in the initial $Fe_3O_4$ powder sample. The FT-IR spectra confirmed the appearance of the chemical bonds between the carbon shell and magnetic core of NPs as well between the carbon and carboxylated groops. The magnetic measurements revealed high saturation magnetization close to value of the bulk magnetite crystal.

Thus, the results described above allow us to conclude that the bio-functionalization of the surface of $Fe_3O_4$@C particles is successful and that these particles can be used for magneto-mechanical destruction of cancer cells.

### Acknowledgements

The work was supported financially by Ministry of Science and Technology of Taiwan, Grants MOST № 108-2923-M-153-001-MY3 and № 109-2112-M-153-003-The electron microscopy investigations were conducted in the Krasnoyarsk Regional Center of Research Equipment of Federal Research Center «Krasnoyarsk Science Center SB RAS».

### References

[1] J. Gómez-Pastora, E. Bringas, I. Ortiz. Chemical Engineering Journal **256**(2014)187.
[2] Magnetite biomineralization and magnetoreception in organizms. A new biomagnetism. Edited by J. Kirschvink, Plenum press New York and London (1985) p.704.

Sixth Asian School-Conference on Physics and
Technology of Nanostructured Materials
Vladivostok, Russia, 25 – 29 April, 2022



# Technology for the fabrication of thermoelectric legs by screen printing

I.A. Voloshchuk*, D.Yu. Terekhov, A.V. Babich, A.O. Yakubov, A.A. Sherchenkov
National Research University of Electronic Technology, 1 Shokin Square., Moscow, Zelenograd 124498, Russia

* e-mail: voliriand@gmail.com

**Abstract.** In this work, technology for the formation of legs of n- and p-type thermoelements by screen printing using aqueous alkaline sodium silicate solution as binders was developed. Thermoelectric properties of thick films were investigated. Technology has been developed for obtaining branches with an optimized composition by introducing a highly conductive carbon additive C45 into the suspension. Based on the research results, a thick-film flexible TEG was simulated in order to optimize the design parameters.

## 1. Introduction

Today, the development of flexible thermoelectric generators (TEG) is of particular interest, since the use of such TEGs can become both a serious addition and an alternative to batteries used today in portable microelectronics. The main advantage of flexible TEGs compared to classical ones is the ability to take the necessary shape within certain limits, which makes it possible to use such devices on heat exchangers with a developed surface, for example, to convert the heat of a living organism, including the human body, which emits on average from 100 to 400 Watts of thermal energy depending on physical activity. Such generators can be useful in the field of energy-saving technologies, in addition, it is worth noting their environmental friendliness in relation to the batteries used today.

The most promising technology for the formation of flexible TEGs is the technology of flexible thick-film TEGs, namely the method of screen printing from suspensions, the advantages of which are relative cheapness, simplicity, and the ability to produce TEGs of unlimited sizes.

At present, the technology of thick-film flexible thermoelectric generators formed from suspensions hasn't been developed in the world as a whole. In addition, a significant problem of this technology is the low electrical conductivity of the resulting thermoelectric material. Thus, the purpose of this work is to develop a technology for fabricating a flexible thermoelectric generator by screen printing.

## 2. Experiment

Experimental samples were made using low-temperature thermoelectric materials: Bi2Te2.8Se0.2 (n-type) and Bi0.5Sb1.5Te3 (p-type). To obtain a thermoelectric suspension, the thermoelectric material was crushed to a powder state and mixed with a binder (an aqueous alkaline solution of sodium silicate). The samples were formed by screen printing through a stainless steel mask with a geometric window size of 5x10x0.6 mm3, after which they were dried at room temperature for 24 hours. To study the electrophysical and thermoelectric properties of the obtained samples, electrical contacts were formed by the method of electrochemical deposition. Ni and Cu were used as deposited materials, Ni was used as a diffusion barrier layer.

Before the investigation of electrophysical and thermoelectric parameters, the fabricated samples were subjected to two-stage annealing: 4 hours at 110℃ and 15 minutes at 200℃. To investigate the thermoelectric characteristics of the fabricated samples, 2 measurements were carried out; in the first case, the temperature dependence of the Seebeck coefficient was investigated at a temperature difference (ΔT) at the ends of the sample from 2 to 40 K. In the second case, the measurements were carried out in the temperature range from room temperature to 350 K with temperature difference ΔT=40. The study of electrophysical properties was carried out in the temperature range from room temperature to 200℃ with a heating rate of 5℃/min.

Samples with a modernized composition of the suspension were also made by introducing a highly conductive carbon additive C45. Studies of electrophysical and thermoelectric parameters have been carried out.

## 3. Results and discussions

Table 1 shows results obtained for thick film samples fabricated from suspensions.

***Table I.*** *Parameters of Thermoelectric legs.*

| Conduc-tivity type | α (mV/K) | κ (W/mK) | Conduc-tivity, ($Ohm^{-1}$ $cm^{-1}$) |
|---|---|---|---|
| *n* | 225 | 0.94 | 14.28 |
| *p* | 250 | 0.94 | 20.00 |

The obtained values for the samples made from suspensions on the basis of aqueous alkaline sodium silicate solution are lower than for the synthesized material. However, the developed technique for the formation of thermoelectric legs can be used for fabricating portable thermoelectric generators.

## 4. Conclusions

This paper presents a technology for the formation of thermoelement legs by screen printing from suspensions using an aqueous alkaline solution of sodium silicate. This binder is a widely used material, safe for human beings, and relatively cheap. Experimental samples were made using low-temperature thermoelectric materials: Bi2Te2.8Se0.2 (n-type) and Bi0.5Sb1.5Te3 (p-type). The electrical contacts were formed by electrochemical deposition. The electrical conductivity of the obtained legs was 20.00 and

14.00 Ohm-1·cm-1 for p- and n-type, respectively, and the Seebeck coefficient was more than 225 μV/K for both types of conductivity.

Technology has been developed for obtaining thermoelectric legs with an optimized composition by introducing a highly conductive carbon additive C45 into the suspension.

**Acknowledgements**

This work was supported by Russian Science Foundation (project number 21-19-00312).

Sixth Asian School-Conference on Physics and
Technology of Nanostructured Materials
Vladivostok, Russia, 25 – 29 April, 2022



# Electrodeposited functional Bi films for shielding applications against ionizing radiation

D.I. Tishkevich
SSPA "Scientific and Practical Materials Research Centre of NAS of Belarus", 220072 Minsk, P. Brovki str. 19, Belarus

*e-mail: dashachushkova@gmail.com

**Abstract.** Bismuth is a promising material for radiation shielding applications. The problem of dense films obtaining is a key factor that needs improvement. In this regard two electrodeposition regimes were proposed for the formation of Bi films with microstructural characteriastics and density values meeting the requirements for radiation shielding materials. Scanning electron microscopy, X-ray energy dispersive analysis and Archimedes' principle were used for the Bi samples characterization. The optimal electrodeposition conditions in galvanostatic and pulse regimes were suggested for the Bi films formation with the best microstructure parameters and relative density.

## 1. Introduction

Modern micro- and nanoelectronics is due to the rapid development of functional devices which are used in various fields. In this regard, one of the important requirements is the ways to increase their stability of functioning not only under normal, but also under extreme conditions (temperature, humidity, exposure to ionizing radiation (IR), etc.). So, for example, electronic devices used in aviation, aerospace, nuclear industry operate in critical conditions, being exposed to radiation effects of natural and artificial origin (electrons, gamma radiation, heavy charged particles, etc.). Often, failures of onboard control systems, navigation, communication, information processing, etc. in real conditions are determined by the emerging radiation effects in the electronic components during irradiation. As a rule, components with radiation resistant properties or shielding methods are used to improve the reliability of operation and to eliminate failures [1].

The danger of IR also exists in medicine. Many diagnostic installations work using IR (X-rays, gamma, electrons, etc.). However, there is equipment that uses IR to treat cancer, such as radiation therapy or radiotherapy. These two classes are united by one thing – the need to protect not only the elements of devices that are particularly sensitive to radiation, but also medical personnel and patients. is important not only to accurately determine the radiation dose that the patient will receive during treatment, but also to protect the body parts that are not affected by tumor formations shielding methods.

Lead is the most common material used for radiation shielding. However, despite the fact that it is inexpensive, one should not forget about its main disadvantage – high toxicity. Its application creates significant difficulties for the environmental situation in the production and disposal of radiation protection products. In February 2003 the European Union developed a directive (RoHS), which aims to limit the use of hazardous substances, which should ensure the protection of human health and the environment [2]. On the list of hazardous substances, lead was placed first, which is why RoHS is often referred to as the "lead-free directive". Thus, the scientific community around the world does not stop work aimed at finding new lead-free materials that could find worldwide use in many areas of human life. An alternative to lead can be bismuth, which is located nearby in the periodic table and has the same high density values. Bismuth is non-toxic and has a low cost, and the wide technological possibilities of its production make it very relevant to use as a material for radiation protection. In this work, studies of the influence of the Bi electrodeposition conditions on the films microstructural parameters are presented. It is shown that the use of Bi-based films as a material for radiation shields is promising.

## 2. Experiment

Bi films were electrodeposited onto Cu substrate (thickness 70 μm). The copper substrates were treated in a Viennese lime mixture, consisting of CaO and MgO (1v:1v). Then, the degreased surface of the copper substrates was polished in the ammonium persulfate solution (120 g/L (NH4)2S2O8 + 20 g/L H2SO4) within 30 s for the removal of an oxide film from the Cu surface. Bi electrochemical deposition was carried out from the perchlorate electrolyte with following solution compositions: Bi2O3 – 40 g/l, concentrated 65% HClO4 – 400 ml/l, distilled H2O – up to 1 l, temperature – (20-25) °C, mixing with 400 rpm speed. All chemicals used were commercial reagents with analytical purity. Samples were prepared at two regimes: galvanostatic and pulse. Bi samples obtained in galvanostatic regime were electrodeposited at 10-25 mA/cm2 current density, in pulse regime – 15 mA/cm2. The pulse duration was varied in the following ranges: short pulse – 20 μs, medium pulse – 20 ms, long pulse – 1 s. The duration of the pulses during such electrodeposition was equal to the pauses duration. The thickness of Bi films for all samples was 20±2 μm. Bismuth rods with 8 mm diameter, containing 97.5% Bi and up to 2.5% PbO2, were used as anodes. The Bi electrodeposition was performed using a potentiostat/galvanostat P45-X.

Bi films surface morphology and chemical composition study was realized with the scanning electron microscope (SEM) Carl Ziess EVO10 at an accelerating voltage of 20 kV in conjaction with Oxford energy-dispersive X-ray (EDX) detector. A relative density was calculated on the basis of Archimedes' principle.

## 3. Results and discussions

Figure 1 presents the SEM images of the Bi films obtained in galvanostatic regime. It has been seen that the everage grain size increases and the morphology changes with the current density value rising from 10 to 25 mA/cm$^2$. Bismuth grains obtained in galvanostatic regime have a

granular sharp shape. The layered granular structure is especially noticeable during deposition at a current density of 20-25 mA/cm$^2$. The films have a rough structure. Thus, when the current density doubles from 10 to 20 mA/cm$^2$, the average grain size increases almost 2.5 times from 1-3 μm to 4-7 μm. The grains have a clear texture which is characteristic for electrodeposited Bi films [4]. Explanation for the occurrence of texturing may be the presence of an accommodative enlargement of grains (subgrains) of the main texture component. The enlargement occurs due to their coalescence. Further, due to the coalescence of the neighboring Bi grains of the main and other texture components and with the disappearance of the boundaries separating them, the electrodeposited film is formed. This mechanism may explain the formation of the texture of a coarse-grained film, in which large grains consist of subgrain blocks (Fig. 1 C and D). The EDX results confirm the absence of impurities in the Bi films (Fig. 1D). The calculations of the relative density showed that the densest Bi films are obtained during electrodeposition at a current density of 10 mA/cm2. The relative density increases from 96.8 to 98.6% with the current density rising. However, the deposition rate at the 10 mA/cm$^2$ is significantly lower than at 25 mA/cm$^2$ due to the limitation by kinetic processes during the synthesis. From the practical point of view the most optimal conditions for obtaining dense films is a current density of 15 mA/cm$^2$ when Bi films with a grain size of 4-7 μm and a relative density of 97.9% are formed.

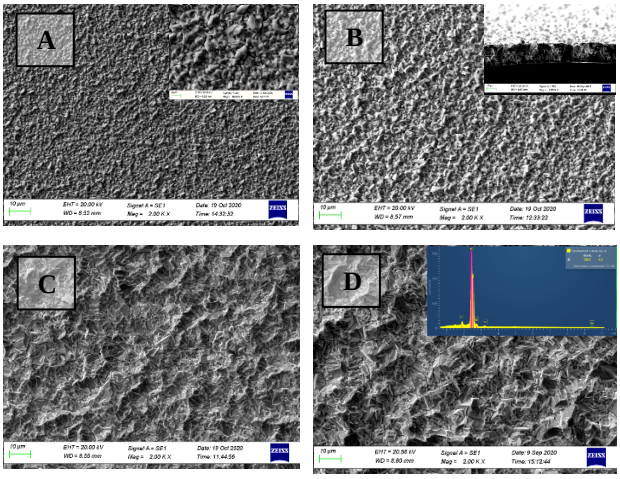


***Fig. 1*** *SEM images of the Bi films surface electrodeposited from perchlorate electrolyte in galvanostatic regime at 10 (A), 15 (B), 20 (C) and 25 (D) mA/cm$^2$ current density. Inserts – inlarge SEM image of Bi film (A), SEM image of the Bi film cross-section (B), EDX spectra of the Bi film (D).*

A current density of 15 mA/cm$^2$ was chosen to study the effect of pulsed deposition on the microstructure of Bi films and three main modes were studied: short pulse, medium pulse, and long pulse (Fig. 2). The effective deposition time was calculated based on the value of the current density, the pulse and pause durations. The thickness of the Bi films was also equal to 20±2 μm. The SEM results show that with a decrease in the pulse duration from 1 s to 20 μs, a significant change in the average grain size and microstructure of the films is observed. Bi films have low roughness and fine-grained microstructure.

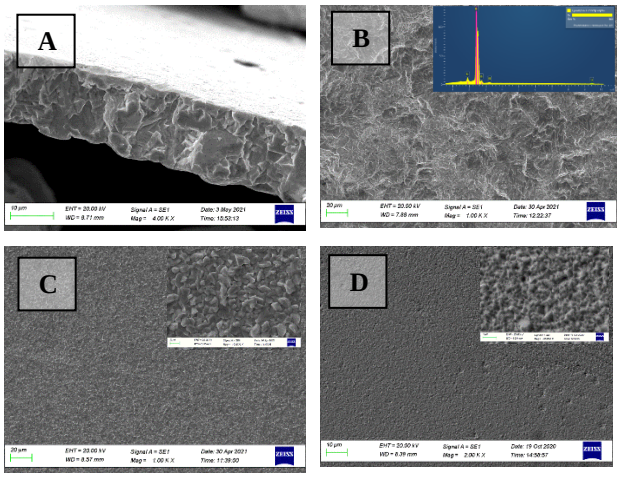


***Fig. 2.*** *SEM images of the Bi films cross section (A) and surface electrodeposited at 15 A/cm$^2$ current density and following pulse regimes: long pulse (B), medium pulse (C), short pulse (D). Inserts – EDX spectra of the Bi film (B), enlarge SEM images of Bi films (C and D).*

Bi films with an average grain size of 0.4-2 μm are obtained during electrodeposition with a pulse duration of 1 s. The average grain size becomes 300-700 nm when the pulse value decreases to a short range (20 μs). Attention is drawn to the fact that the relative density of the Bi films increases from 97.9-99.1% with the pulse duration decreasing from 1 s to 20 μs.

Thus, it has been shown that by varying the electrodeposition regimes it is possible to obtain Bi films with a controlled microstructure and relative density, which is most important for the manufacture of radiation shields where the density is a key parameter.

## 4. Conclusions

Bi films with thickness of 20±2 μm were obtained via electrochemical deposition. It has been shown that Bi films obtained in galvanostatic regime have grains with granular sharp shape. The relative density calculations revealed that the densest Bi films are obtained during electrodeposition at a current density of 10 mA/cm$^2$. The relative density increases from 96.8 to 98.6% with the current density rising. It has been demonstrated that in pulse regime with a decrease in the pulse duration from 1 s to 20 μs, a significant change in the average grain size and microstructure of the films is observed. Thus, during electrodeposition with pulse duration of 1 s Bi films with an average grain size of 0.4-2 μm are obtained. The average grain size becomes 300-700 nm when the pulse value decreases to a short range (20 μs). From the practical point of view the most optimal conditions for obtaining dense films as follows: galvanostatic regime – current density of 15 mA/cm$^2$ when Bi films with a grain size of 4-7 μm and a relative density of 97.9% are formed; pulse regime – current density of 15 mA/cm$^2$ and short pulse with duration of 20 μs when the Bi films with a grain size of 300-700 nm and relative density of 99.1% are formed.

## References

[1] D.I. Tishkevich [et al.] IOP Conf. Ser.: Mater. Sci. Eng. 848 (2020) 012089.

[2] https://ec.europa.eu/environment/topics/waste-and-recycling/rohs-directive_en.

Sixth Asian School-Conference on Physics and
Technology of Nanostructured Materials
Vladivostok, Russia, 25 – 29 April, 2022



# Electron paramagnetic resonance of zinc ferricyanide and their polyethylenimin-based nanocomposites

V.P. Polishchuk*, A.M. Ziatdinov
Institute of Chemistry FEB RAS, 159, Pr-t 100-letiya Vladivostoka, Vladivostok, 690022, Russia

*e-mail: polishchuk.vr@students.dvfu.ru

**Abstract.** The zinc ferricyanide ($Zn_3[Fe(CN)_6]_2$) and its nanocomposite with polyetherimide (PEI) have been studied by the EPR method. The presence of $Fe^{3+}$ clusters (dimers) in them was established. In the PEI/$Zn_3[Fe(CN)_6]_2$ nanocomposite, along with dimers, single $Fe^{3+}$ ions are also present. Consequently, some $Fe^{3+}$ dimers are destroyed by PEI. The crystalline fields acting on single $Fe^{3+}$ ions have a significant rhombic component. When PEI/$Zn_3[Fe(CN)_6]_2$ is illuminated with ultraviolet light, nitrogen containing radicals are reversibly formed in it.

## 1. Introduction

True to its name, a single molecular magnet (SMM) is a molecule that behaves like a nanoscale magnet. Due to their small size, SMMs exhibit many interesting quantum properties, such as macroscopic quantum tunneling of magnetization, Berry phase interference, etc [1, 2]. SMMs are promising materials for high-density data storage, molecular spintronics, cryogenic magnetic cooling, etc [3-5]. One of the main tools for studying SMM is the electron paramagnetic resonance (EPR) method. This paper presents the results of EPR studies of potential SMM of zinc hexacyanoferrate ($Zn_3[Fe(CN)_6]_2$) and its nanocomposite with polyethylenimine (PEI).

## 2. Experiment

$Zn_3[Fe(CN)_6]_2$ was synthesized by coprecipitation method at stoichiometric ratio of the components. PEI/$Zn_3[Fe(CN)_6]_2$ was synthesized via the same rote as described in [6] for PEI/$Zn_2[Fe(CN)_6]$ composite.

The EPR spectra of the samples were recorded on a JES-X330 spectrometer (JEOL, Japan) in the X-range of operating frequencies. The power of the microwave field during the recording of the spectra was 2.00 mW, the constant magnetic field (B) was deployed in the range of 0–500 mT and modulated at a frequency of 100 kHz. Temperature-dependent measurements were carried out in a continuous flow of nitrogen gas using a standard variable temperature unit ES-13060 DVT5 (JEOL, Japan). The samples were illuminated directly in the cavity of the EPR spectrometer using standard equipment for irradiating ES-USH500 with light from a mercury lamp using infrared and ultraviolet filters.

## 3. Results and discussions

At room temperature, the EPR spectrum of $Zn_3[Fe(CN)_6]_2$ is dominated by a broad asymmetric resonance with a less intense resonance in its high-field wing (Fig. 1). The effective *g*-factors of these resonances, determined from the low-field peaks of the first derivative of their absorption lines, are ~5.1 and ~3.2, respectively. As the temperature decreases, the peak intensity of the main resonance increases, the effective value of its *g*-factor decreases, and the smaller resonance merges with the main one and ceases to be observed (Fig. 1).

The EPR spectrum of the PEI/$Zn_3[Fe(CN)_6]_2$ nanocomposite at all temperatures contains three characteristic components (Fig. 2): a wide asymmetric resonance with an effective value of *g*~85, which has a significant intensity even at zero magnetic fields, a narrow asymmetric resonance with *g*~4.36, and an unresolved

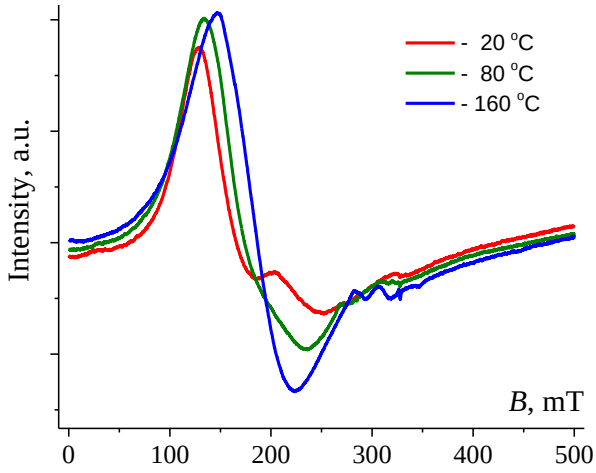


***Fig. 1.*** *EPR spectra of $Zn_3[Fe(CN)_6]_2$ at various temperatures.*

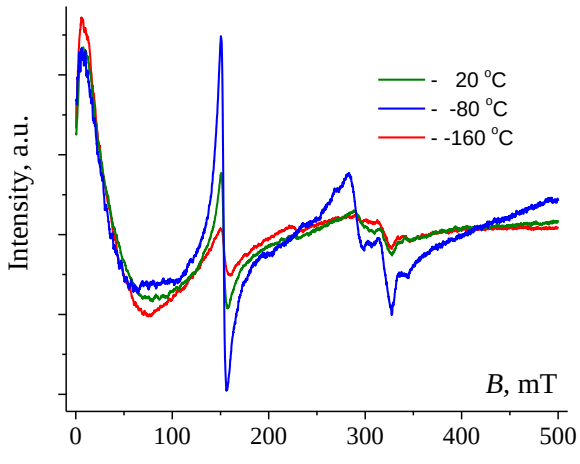


***Fig. 2.*** *EPR spectra of the PEI/$Zn_3[Fe(CN)_6]_2$ nanocomposite at various temperatures.*

two-component resonance with *g*~2.26 and ~2.05. As the temperature decreases, the peak intensity of the weak-field component of the spectrum slightly increases, while the peak intensities of the other two components of the spectrum increase synchronously and significantly. The temperature has little effect on the effective values of the *g*-factors of all components of the spectrum (Fig. 2).

When the PEI/$Zn_3[Fe(CN)_6]_2$ nanocomposite is illuminated with ultraviolet light at -160 °C, new resonances appear in the EPR spectrum (Figs. 3 and 4), the most intense of them is characterized by the value $g$=2.003. The remaining components of the spectrum do not change significantly when the sample is illuminated with ultraviolet (Fig. 3).

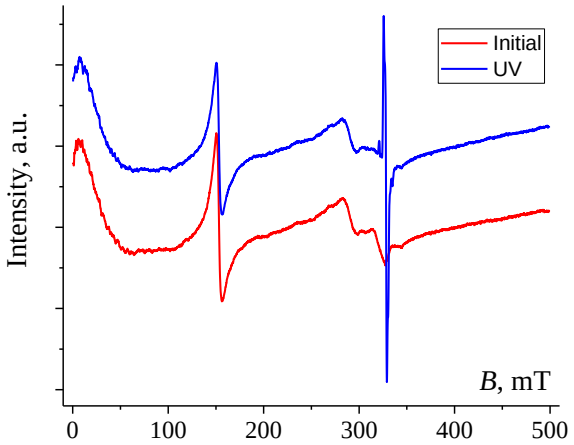


***Fig. 3.*** *Changes in the EPR spectrum of the PEI/$Zn_3[Fe(CN)_6]_2$ nanocomposite under ultraviolet irradiation.*

The time of relaxation of the EPR spectrum to its original form after UV illumination depends both on the sample illumination time and on the chosen temperature for studying the spectrum reconstruction process. For example, after 20 minutes of irradiation at -160 °C, the spectrum at the same temperature returns to its original form in ~10 hours, and at room temperature, relaxation is completed after ~10 minutes. UV illumination does not change the EPR spectrum of $Zn_3[Fe(CN)_6]_2$.

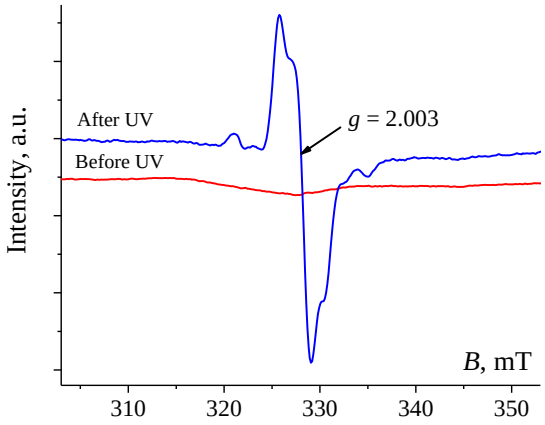


***Fig. 4.*** *Change in the fragment of the EPR spectrum of the PEI/$Zn_3[Fe(CN)_6]_2$ nanocomposite under ultraviolet irradiation.*

In SMM, paramagnetic ions are combined into clusters. In compounds of the $Zn_3[Fe(CN)_6]_2$ type, $Fe^{3+}$ ions ($3d^5$, S=5/2, I=0), in principle, can form the simplest cluster - a dimer [7]. Possible spin states of such dimer: S = 5, 4, 3, 2, 1, 0. In general, the EPR spectrum of the $Fe^{3+}$ dimer is complex and unpredictable. Nevertheless, the observation of resonances with $g$ ~5.13 and ~3.22 in the EPR spectrum of $Zn_3[Fe(CN)_6]_2$ at room temperature (Fig. 1) allows us to consider them as transitions between spin sublevels of dimers.

A resonance similar to the main resonance of the EPR spectrum of $Zn_3[Fe(CN)_6]_2$ is also present in the EPR spectrum of PEI/$Zn_3[Fe(CN)_6]_2$, although it is observed at much lower magnetic fields (Fig. 2). From the fact of its significant intensity even at a zero value of the magnetic field, it follows that it belongs to the transition between spin sublevels, the energy interval between which in a zero magnetic field is close to the energy of an electromagnetic field quantum, i.e. 0.3 $cm^{-1}$. An intense asymmetric signal with $g$ ~4.36 is characteristic of $Fe^{3+}$ ions in crystalline fields with a significant rhombic component [8]. The symbatic change with temperature of the intensities of this signal and the unresolved two-component signal with $g$~2.26 and $g$~2.05 indicate that the latter also belongs to single $Fe^{3+}$ ions.

The characteristic shape of the multicomponent EPR spectrum that appears when PEI/$Zn_3[Fe(CN)_6]_2$ is illuminated with ultraviolet light (Fig. 4) makes it possible to attribute it to the nitrogen containing radicals.

## 4. Conclusions

Thus, the data of EPR studies of $Zn_3[Fe(CN)_6]_2$ indicate the presence of $Fe^{3+}$ clusters (dimers) in it. In the PEI/$Zn_3[Fe(CN)_6]_2$ nanocomposite, along with them, there are also single $Fe^{3+}$ ions. Consequently, some $Fe^{3+}$ dimers are destroyed by PEI. The crystal fields acting on single $Fe^{3+}$ ions in PEI/$Zn_3[Fe(CN)_6]_2$ have a significant rhombic component. When the PEI/$Zn_3[Fe(CN)_6]_2$ nanocomposite is illuminated with ultraviolet light, nitrogen containing radicals are reversibly formed in it. UV illumination does not change the EPR spectrum of $Zn_3[Fe(CN)_6]_2$.

## Acknowledgements

The authors are grateful to N.S. Saenko for recording some EPR spectra and D.V. Balatskiy and I.A. Malakhova for the synthesis of $Zn_3[Fe(CN)_6]_2$ and PEI/$Zn_3[Fe(CN)_6]_2$.

## References

[1] D. Gatteschi, R. Sessoli. Angew. Chem., Int. Ed. **42**(2003)268.
[2] L. Thomas, F. Lionti, R. Ballou, D. Gatteschi, R. Sessoli, B. Barbara, Nature, London. **383**(1996)145.
[3] L. Bogani and W. Wernsdorfer, Nature Mater. **7**(2008)179.
[4] N. Domingo, E. Bellido, D. Ruiz-Molina. Chem. Soc. Rev. **41**(2012)258.
[5] M. Evangelisti, O. Roubeau, E. Palacios, A. Camón, T. N. Hooper, E. K. Brechin, J. J. Alonso. Angew. Chem. Int. Ed. **50**(2011)6606.
[6] Malakhova, I.; Parotkina, Y.; Palamarchuk, M.; Eliseikina, M.; Mironenko, A.; Golikov, A.; Bratskaya, S. Composite Zn(II) Ferrocyanide/Polyethylenimine Cryogels for Point-of-Use Selective Removal of Cs-137 Radionuclides. Molecules **26**(2021)4604.
[7] A. Lunghi, F. Totti. Inorganics **4**(2016) 28.
[8] I. Kokorin, R. Amal, W.Y. Teoh, A.I. Kulak. App. Magn. Reson. **48**(2017)447.

Sixth Asian School-Conference on Physics and
Technology of Nanostructured Materials
Vladivostok, Russia, 25 – 29 April, 2022

**IV.o.12**

# Cluster analysis of atomic structures in amorphous alloys

D.S. Dilla*, E.V. Pustovalov, A.N. Fedorets
Far Eastern Federal University FEFU Campus 10 Ajax Bay, Russky Island Vladivostok 690922, Russia

*e-mail: dilla.d@dvfu.ru

**Abstract.** Scientific breakthroughs are built on the successful visualization of objects that are invisible to the human eye; as a result, the physicochemical properties of amorphous and amorphous-crystalline alloys are distinct, attracting the attention of researchers in the search for new materials. The functional properties of alloys are determined by the composition as well as the atomic structure with a lower degree of order. However, finding an effective approach to investigation tools for studying the atomic-scale structure and properties remains one of the remaining challenges for both theory and experiment. As a result, the need for an efficient and modern approach to studying electron microscopy image processing and simulations has become a critical component of current research.

We present an extensive review of developed software and experimental results on amorphous and amorphous-crystalline alloy specimen electron microscopy image processing in this paper. We also discuss the experimental results and the application of our developed software tools for calculating atomic-scale structure.

## 1. Introduction

For amorphous and amorphous-crystalline alloys possess a unique set of physicochemical properties, which attracts the attention of researchers to the search for new materials. The atomic structure with a reduced degree of order, as well as the composition, largely determines the functional properties of the alloys. The absence of long-range order in the atomic structure presupposes the presence of many realizations of the topological and compositional local atomic environment [5]. This causes the presence of many stable configurations of the structure, local minima of the total energy of the system, but which are energetically less favorable than an ordered, crystalline structure of the same composition. This is associated with the degradation of properties with time and with external influences, for example, heating. Often, small changes in the structure lead to significant changes in the physicochemical characteristics of the material. Electron microscopic images of structures are used to determine local order in both materials' science and biological objects. Despite many studies, the authors fail to present universal characteristics of atomic order, as well as a sufficiently complete theory of ordering processes in an amorphous structure. The difficulties are caused by the large number of variants of the disordered atomic structure, the absence of long-range order and the impossibility of describing the local order by crystallographic groups, and the large number of computational resources required for simulating macroscopic measurable volumes of material. In this study, based on the analysis of electron microscopic images of an amorphous structure, a method is proposed for studying local atomic ordering with any kind of symmetry, including non-crystallographic one. It is shown that under thermal action, by the example of the structure of amorphous alloys CoP, CoNiP, NiW, there is a 30% change in the density of atomic clusters with an ordered structure of 1–2 nm in size. It has been shown that, upon heating, both an increase in the degree of order and a decrease occurs.

## 2. Experiment

Samples of CoP, CoNiP, NiW amorphous alloys were prepared by electrochemical deposition. We investigate atomic structure of the samples by means of high resolution transmission electron microscopy on FEI Titan 80-300 at 300 and 80 kV with abberation correction. Samples placed on standart cupper grid have thickness from 2 to 10 nm. Small thickness of the samples allows us to investigate the local atomic structure and show different level of ordering. Series of HRTEM images were obtained at temperatures from 20°C to 300°C.

HRTEM image processing perfomed by GPU software to have cross-correlation with double-core: $H_{\varphi,r_0}(x,y) = h(x,y) \cdot \sum_{\varphi} h(x - r_0 \cdot sin\varphi, y - r_0 \cdot cos\varphi)$, where $h(x,y) = sinc(\rho/\rho_0) - h_0$. We select $r_0$ =0.25 nm, $\rho_0$ = 0.15nm. Parameter $h_0$ selected from following condition: $\sum_{x,y} h(x,y) \approx 0$. [6]

## 3. Results and discussions

We created a software program that can compute large amounts of information in our datasets in order to simulate electron microscopic image studies. The developed app calculates the distance between two points in the Euclidean 2D plane using the electron microscope image pixels as coordinate points[1]. We now need to calculate the distance between two points, so we use Pythagoras' Theorem, which is nothing more than the Euclidean distance [2]. Distance, assume point $p$ have Cartesian coordinates $(p_1, p_2)$ and let q have coordinate $(q_1, q_2)$. Then the distance between p and $q$ is given by [1-4].

$$d(p,q) = \sqrt{(q_1 - p_1)^2 + (q_2 - p_2)^2}$$

and finds the nearest neighbor for each point in a dataset within a radius of $r$=2 nm. Following the determination of nearest neighbors for each point, the program sorts the neighbors in ascending order and prepare the data points for plotting an undirected 2D graph using the nearest neighbor graph algorithm.

**The algorithm is as follows:**

**Input:** check to see if the file exists output text or create an empty file.

Input filename read from a file if the file exists; otherwise, return if the file does not exist.

If a file exists, read the x and y coordinates from it and convert them to a two-dimensional vector.

Define k as well as a distance metric (typically Euclidean distance).

Find the nearest k points to each data point in a dataset with a given radius.

**Output:** write the nearest neighbors to each data point in a dataset into a file as shown below
Initial point: (250.167,11.167)
Distance = 11.353, position = 51, the point = (241.5,18.5)

Distance = 11.751, Position = 30, the point = (261.667,13.583)

All nearest neighbors (NN) are calculated for the nearest neighbor search on a two-dimensional Euclidean plane with a specific radius r. After locating the initial coordinate point x, y, the process computes the Euclidean distance for all coordinate points in the dataset. After computing the distance between two points, the program compares the calculated distances while taking the given radius r into account for each point's computed results and writes the output to a file the nearest points with their coordinates, the distance between the points, and the positions of the coordinates within the given parameter radius. This procedure is repeated for all of the coordinate points in a dataset.

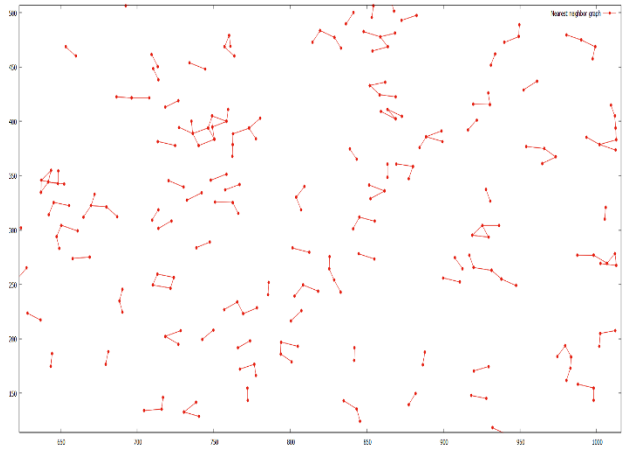

***Fig. 1.*** *A nearest neighbor graph of 2997 points in the Euclidean plane100- 50 interval.*

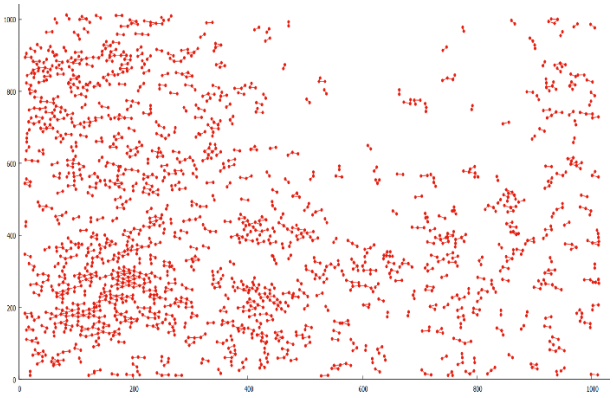

***Fig. 2.*** *A nearest neighbor graph of 2997 points in the Euclidean plane.*

A directed graph defined for a set of points in a metric space, particularly the Euclidean distance in the plane, is known as the nearest neighbor graph. Every point in the NNG has a vertex, and whenever q is a nearest neighbor of p, that is, a point whose distance from p is the smallest among all the given points other than p itself, a directed edge from p to q is formed [4].

In our applications of these graphs, the edge orientations are ignored, and the NNG is instead specified as an undirected graph.

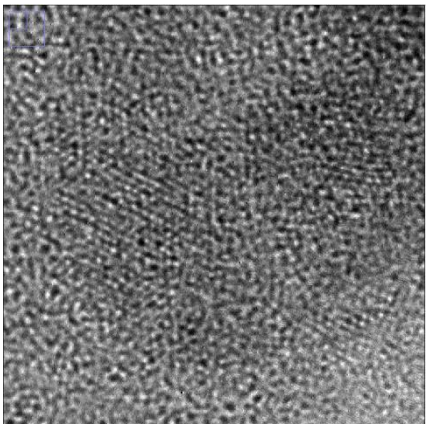

***Fig. 3.*** *HRTEM images of Amorphous alloy samples from series4 00001.dm3.*

## 4. Conclusions

The results of this study demonstrated the accuracy of the nearest neighbor search algorithm within a given radius using various distance metrics. Experiments were conducted using large datasets derived from electron microscopy images of amorphous and amorphous – crystalline alloy specimens. This allows us to conduct detailed research on the properties of amorphous and amorphous-crystalline alloys. Researchers are still looking for ways to use modern computing software to determine the atomic structure and physicochemical properties of amorphous alloys.

We can provide accurate information with much less execution time and resources by using an effective and modern approach to study Cluster analysis of atomic structures in amorphous alloys. More research and innovation are required to fully comprehend the physicochemical properties of amorphous alloys.

## References


[1] Andoni, A., Indyk, P. and Razenshteyn, I., 2019. Approximate Nearest Neighbor Search In High Dimensions. Proceedings of the International Congress of Mathematicians (ICM 2018),.

[2] Dokmanic, I., Parhizkar, R., Ranieri, J. and Vetterli, M., 2015. Euclidean Distance Matrices: Essential theory, algorithms, and applications. IEEE Signal Processing Magazine, 32(6), pp.12-30.

[3] Li, W., Zhang, Y., Sun, Y., Wang, W., Li, M., Zhang, W. and Lin, X., 2020. Approximate Nearest Neighbor Search on High Dimensional Data — Experiments, Analyses, and Improvement. IEEE Transactions on Knowledge and Data Engineering, 32(8), pp.1475-1488.

[4] Liu, J., 2021. Advances and Applications of Atomic-Resolution Scanning Transmission Electron Microscopy. Microscopy and Microanalysis, 27(5), pp.943-995.

[5] Miller, M., Rodriguez, M. and Cox, I., n.d. Audio fingerprinting: nearest neighbor search in high dimensional binary spaces. 2002 IEEE Workshop on Multimedia Signal Processing.,.

[6] Pustovalov E.V. et al., 2019, Effect of the Process Conditions for the Preparation of CoNiFeSiB Amorphous Alloys on Their Structure and Properties. Journal of Surface Investigation: X-ray, Synchrotron and Neutron Techniques, Vol. 13, No. 4, pp. 600–608.

[7] Svatiuk, O., 2016. Contrast of Electron Microscopy Images of Amorphous Objects. Journal of Nano- and Electronic Physics, 8(1), pp.01005-1-01005-7.

Sixth Asian School-Conference on Physics and
Technology of Nanostructured Materials
Vladivostok, Russia, 25 – 29 April, 2022



# Influence of halloysite nanotubes incorporation on the properties of PEO layers formed on MA8 alloy

I.M. Imshinetskiy*[,1], V.V. Kashepa[1,2], K.V. Nadaraia[1], D.V. Mashtalyar[1], S.L. Sinebryukhov[1], S.V. Gnedenkov[1].

[1] Institute of Chemistry FEB RAS, 159 Pr. 100-letiya Vladivostoka, Vladivostok 690022, Russia
[2] Far Eastern Federal University, 10 Ajax Bay, Russky Island, Vladivostok 690922, Russia

*e-mail: igorimshin@gmail.com

**Abstract.** The properties of coatings formed on the MA8 magnesium alloy by the plasma electrolytic oxidation (PEO) in electrolytes containing halloysite nanotubes were investigated. Obtained coatings reduce corrosion current density by nearly half compared to the base PEO-layer (from $1.1\times10^{-7}$ A/cm$^2$ for base PEO layer to $5.6\times10^{-8}$ A/cm$^2$ for coatings with nanoparticles). It has been found that the presence of halloysite nanotubes in the composition of coating has a beneficial effect on their hardness (this parameter has increased from 4.5±0.4 GPa to 7.3±0.5 GPa).

## 1. Introduction

The interest of many researchers in magnesium alloys has grown since its potential use as biodegradable material has been founded. However, modern implantology faces the problem of magnesium application as orthopedic medical device material due to its low corrosion resistance and hardly controllable biosorption [1]. The plasma electrolytic oxidation (PEO) process figures prominently in the surface modification of metals and combines corrosion resistance improvement with functional properties development [2, 3]. PEO became widely disseminated due to a broad range of adjustable process parameters and the possibility of coatings properties management.

The ceramics formed by the PEO method can be improved by nanoparticles incorporation. The PEO-coatings with various nanoscaled additives demonstrate anti-corrosive, biocompatible, and biodegradable properties, as well as coatings morphology features and substances encapsulation ability, which has gained special importance in the recent decade [2-5]. Halloysite nanotubes (HNT) are naturally formed nanoparticles that have been developed lately as an entrapment system for loading, storage, and controlled release of active molecules [6, 7] such as drugs, corrosion inhibitors, proteins, etc. The low-alloy magnesium implants with PEO-coating containing halloysite nanotubes are of great scientific interest since their lightness, biocompatibility, bioresorbability, corrosion and wear resistance along with active molecules delivery capability.

In this paper, the formation of the protective multifunctional coatings by the PEO method with the halloysite nanotubes incorporation on the MA8 alloy is investigated. The electrochemical and mechanical properties of the obtained PEO layers are represented.

## 2. Experiment

Plates made of MA8 magnesium alloy (Mn 1.30; Ce 0.15; Mg bal. (wt.%)) were used as a substrate. The size of specimens was 20 mm × 15 mm × 2 mm. The solution, containing sodium fluoride (5 g/l) and sodium silicate (20 g/l), was chosen as a base electrolyte. In this work, we used halloysite nanotubes (CAS № 1332-58-7; Sigma Aldrich, USA) with a length of 1-3 μm, an outer diameter of 50-70 nm, and a lumen diameter of 15-30 nm. Nanoparticles were dispersed in the base electrolyte in concentrations of 0, 10, 20, 30, and 40 g/l (Table I.). Concentrations of the base electrolyte components remained unchanged. The process of coatings formation was carried out using a plasma electrolytic oxidation unit. Coatings morphology was studied with optical laser profilometry and scanning electron microscopy (SEM). The elemental composition was determined by energy dispersive spectroscopy (EDS). Electrochemical properties of the coatings were investigated by electrochemical impedance spectroscopy and potentiodynamic polarization. The study of the mechanical properties of the coatings was carried out with microhardness and scratch testing.

***Table I.*** *Composition of the used electrolytes.*

| Samples | The concentration of the electrolyte components, g/l | | | |
|---|---|---|---|---|
| | $Na_2SiO_3{\cdot}5H_2O$ | NaF | $NaC_{12}H_{25}SO_4$ | HNT |
| H0 | 20 | 5 | 0 | 0 |
| H10 | 20 | 5 | 0.25 | 10 |
| H20 | 20 | 5 | 0.25 | 20 |
| H30 | 20 | 5 | 0.25 | 30 |
| H40 | 20 | 5 | 0.25 | 40 |

## 3. Results and discussions

Halloysite nanotubes present the chemical formula of $Al_2Si_2O_5(OH)_4{\cdot}nH_2O$ and consist of remarkably stable siloxane groups (Si-O-Si) along with aluminol groups (Al-OH) [8] that supposedly dehydrate under plasma discharge temperature and turn into the chemically stable, hard, and wear-resistant $Al_2O_3$. Hence, halloysite nanotubes are expected to improve the chemical stability and mechanical properties of the coatings. Moreover, an increase of specific surface area due to nanoparticles agglomerates' presence on the surface of the samples is expected.

The SEM images of surfaces show significant differences in surfaces structure among samples. Samples obtained in electrolytes with a high concentration of the halloysite nanotubes have a more rugged and irregular surface (Fig. 1). Higher concentration factors contribute to better nanoparticles incorporation. Incorporation is statistically more likely to happen in electrolytes enriched with nanoparticles, thus clusters and aggregates are especially clearly visible for H20, H30, H40 samples.

A typical volcano-like or crater-like structure can be observed over all samples.

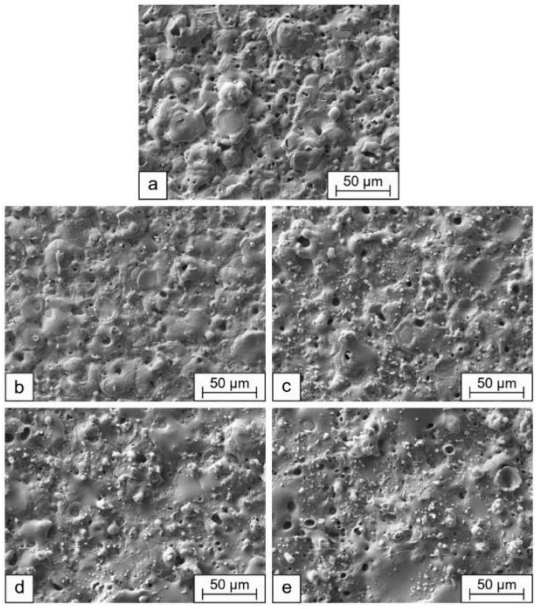


***Fig. 1.*** *SEM images of the coatings surfaces: H0 (a), H10 (b), H20 (c), H30 (d), H40 (e).*

According to surface topography results, halloysite nanoparticles agglomerates existence is verified by increasing roughness parameters over the samples (Table II). Agglomerates prevalence rising with halloysite nanotubes content, as well the surface roughness. It is plain to see, that thickness of the layers is in direct proportion to halloysite nanotubes concentration as well, it grows with the content of nanoparticles.

***Table II.*** *Thickness and roughness parameters of the studied samples*

| Sample | $R_a$, μm | $R_z$, μm | $S_a$, μm | Thickness, μm |
|---|---|---|---|---|
| H0 | 1,7±0,4 | 9,6±2,2 | 3,04±0,1 | 51.4±1.3 |
| H10 | 2,0±0,3 | 10,8±2,8 | 3,4±0,3 | 53.8±1.0 |
| H20 | 2,5±0,6 | 12,2±2,9 | 4,6±0,1 | 55.0±1.5 |
| H30 | 3,0±0,7 | 15,5±2,9 | 5,8±0,1 | 68.6±2.0 |
| H40 | 3,4±0,7 | 16,5±3,1 | 6,1±0,4 | 78.8±1.5 |

The change in corrosion properties of coatings containing halloysite nanotubes compared to the base PEO-coating is clearly evident on the represented polarization curves (Fig. 2).

All curves of the samples containing halloysite nanotubes (2, 3, 4), except curve 5 for the H40 sample, represent small corrosion rates and high polarization resistance compared to the base PEO-layer (curve 1). Furthermore, all samples containing nanoparticles demonstrated a decrease in the corrosion current density in contrast to the base PEO layer. Distinguishing H10 and H30 samples corrosion current density fall to half of the same value for base PEO-coating.

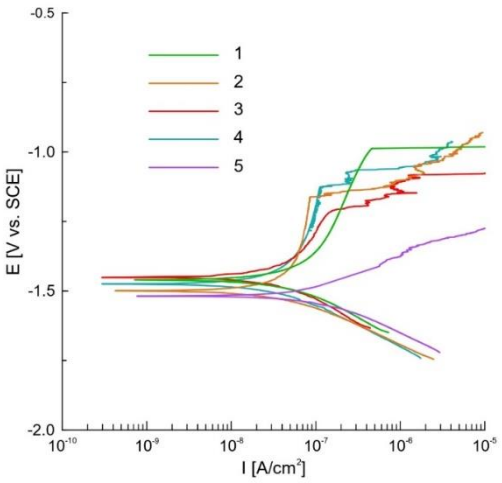


***Fig. 2.*** *Polarization curves for the H0 (1), H10 (2), H20 (3), H30 (4), H40 (5) samples.*

## 4. Conclusions

It has been established that PEO-coatings formed on the MA8 magnesium alloy in electrolytes containing halloysite nanotubes have improved electrochemical characteristics in comparison with the surface layers obtained without the use of nanoparticles. Based on obtained results it has been concluded that the coating formed in an electrolyte with a 20 g/l nanoparticles concentration has the highest protective properties in the corrosive medium not only for the first 2 hours of exposure but also after the further 24 hours of exposure. However, the highest adhesion to the substrate was demonstrated by the H30 sample coating. The incorporation of nanoparticles led to an increase in the microhardness of the surface layers by 1.5 times, and its highest magnitudes were observed for the H10 and H20 samples. Formed coatings are perspective for biomedical applications, especially in implantology due to their biocompatibility and corrosion resistance.

## Funding

Formation of coatings, their morphological and structural features, electrochemical properties were carried out within the framework of the Grant of the Russian Science Foundation, project No. 22-23-00937. The SEM results were collected under the government assignments from Ministry of Science and Higher Education of the Russian Federation, Russia (project no. 0205-2021-0003)

## References

[1] D. Zhao, F. Witte, F. Lu, J. Wang, J. Li, L. Qin. Biomaterials **112**(2017)287.
[2] D. Mashtalyar, S. Sinebryukhov, I. Imshinetskiy, A. Gnedenkov, K. Nadaraia, A. Ustinov. Appl. Surf. Sci. **503**(2020)144062.
[3] D. Mashtalyar, K. Nadaraia, S. Sinebryukhov, S. Gnedenkov J. Mater. Sci. Technol. **33**(2017)661.
[4] M. Molaei, K. Babaei, A. Fattah-Alhosseini, J. Magnes. Alloy. **9**(2021)1164.
[5] E. Parfenov, L. Parfenova, G. Dyakonov, K. Danilko, V. Mukaeva, R. Farrakhov, E. Lukina, R. Valiev. **357**(2019)669
[6] A. Santos, C. Ferreira, F. Veiga, A. Ribeiro, A. Panchal, Yu. Lvov, A. Agarwal. **257**(2018)58.
[7] K. Zahidah, S. Kakooei, M. Ismail, P. Raja. Prog. Org. Coatings **111**(2017)175.
[8] T. Bates, F. Hildebrand. Am. Mineral. **35**(1950)463.

Sixth Asian School-Conference on Physics and
Technology of Nanostructured Materials
Vladivostok, Russia, 25 – 29 April, 2022



# Effect of tungsten disc electrode rotation rate on the growth of anodic $WO_x$ and its photocatalytic properties

Y. Nazarkina[1], V. Benu[1], E. Grigoryeva[1], E. Eganova[2]

[1] National Research University of Electronic Technology (MIET), Bld. 1 Shokin Square, Zelenograd, Moscow 124498, Russia

[2] Institute of Nanotechnology of Microelectronics of the Russian Academy of Sciences (INME RAS), 32A Leninsky Prospekt, Moscow 119991, Russia

*e-mail: engvel@mail.ru

**Abstract.** Porous $WO_x$ films were synthesized in 0,1 M $NH_4NO_3$: ethylene glycol: 1% $H_2O$ electrolyte. RDE system was carried out to control the hydrodynamical conditions. It was found that tungsten RDE rotation rate influences the $WO_x$ morphology, affording to obtain regular nanotubular structures with the pores of around 100 nm in diameter. The photocatalytic properties of such nanostructures were investigated. It was determined that the highest value of the degradation constant is achieved when using samples obtained at a rotation speed of 500-750 rpm. The results correlate with the morphology analysis data, where it was estimated that these tungsten oxide films had the largest porous layer thickness with an average pore diameter of 75±5 nm.

## 1. Introduction

Due to the high electron mobility, the short diffusion length of charge carriers, and nontoxicity, tungsten oxide is a promising material for use as a photocatalyst. Since the efficiency of a photocatalyst depends on its effective surface area, it is promising to obtain nanostructured tungsten oxide.

Anodic oxidation enables the synthesis of nanostructured $WO_x$ films of various morphologies, depending on the technological parameters of anodization. Unfortunately, at the moment, there is practically no information on the effect of hydrodynamic conditions on the anodic formation of tungsten oxide. In this work, we investigated the influence of the rotation speed of a tungsten rotating disc electrode (RDE) on the morphology of the resulting tungsten oxide structures and their photocatalytic properties.

## 2. Experiment

The samples were formed by anodization in the electrolyte, containing 0,1 M $NH_4NO_3$: ethylene glycol (EG) : 1% $H_2O$. A platinum electrode served as the cathode. The process was carried out at a temperature of 40°C. The platinum electrode and the tungsten anode were placed at a fixed height. The electrode rotation rate was set in the range 0 - 1000 rpm.

The fabricated samples were subjected to the heat treatment in a PL 20 muffle furnace (220 V, power 3 kW) at a temperature of 500°C for 2 hours in the air. The samples were then slowly cooled down.

The morphology of nanostructured $WO_x$ samples was investigated by field-emission scanning electron microscope (FESEM) Helios NanoLab 650.

The photocatalytic properties of the obtained samples of nanostructured tungsten oxide were explored using a xenon lamp with a power of 150 W. (Newport, mod. 6255). Annealed samples of nanostructured anodic tungsten oxide were immersed in an aqueous solution of methylene blue (MB) with a concentration of 7.815 μmol/L and time dependences of MG concentration in the presence of the nanostructured $WO_3$ layers were measured, and the MB decomposition rate constants were estimated. To take into account the effect of MB adsorption on the surface of the samples, the samples were preliminarily kept in the MB solution in the dark.

## 3. Results and discussions

Table 1 represents the geometrical and photocatalytic properties of the samples obtained at the different tungsten RDE rotation velocities.

***Table I.*** *Parameters of Samples.*

| Rotation speed, rpm | Reynolds number | Pore diameter, nm | Pore diameter, “burning”, nm | MB decomposition rate constant |
|---|---|---|---|---|
| 0 | 0 | 17±4 | - | 0,0009 |
| 150 | 60 | 23±5 | 51±2 | 0,0031 |
| 500 | 200 | 40±5 | 76±5 | 0,0075 |
| 750 | 300 | 35±5 | *78*±5 | 0,0061 |
| 1000 | 400 | 38±7 | 79±6 | 0,0020 |

By scanning electron microscopy, at rotational speeds of 150-1000 rpm, "burning points" were detected. At low rotation speeds of the electrode, points are localized in a small area, but they penetrate the depth of the sample, causing through-thickness etching. With the rotation speed increasing, “burning points” spread over larger areas (of the order of several tens of microns[2]). But “burning” becomes more controllable and through-etching of the foil does not occur. In the “non-burning” areas, the tungsten oxide is porous, but pores are randomly branched. With the increase in the rotation speed, the pores acquire a more cylindrical shape, and their diameter increases. In the burning areas, the pores are ordered, located normally to the substrate, have a clear cylindrical shape. Pores are approximately twice larger than in non-burning areas. With increasing rotation velocity, the pore diameter increases due to the pore wall thinning, and at 1000 rpm the structure becomes brittle and partially fractures.

It has been established that the highest value of degradation constants is achieved when using samples obtained at rotation speeds of 500-750 rpm. At such electrode rotation speeds, a large portion of the sample surface is covered with burning points, while neither W foil

overetching, nor $WO_x$ destruction due to thinning of the walls of the porous oxide occurs, and the pore diameter at the non-burning areas is the largest (around 40 nm).

## 4. Conclusions

Porous $WO_x$ films were synthesized in 0,1 M $NH_4NO_3$: ethylene glycol: 1% $H_2O$ electrolyte. It was found the RDE rotation velocity increasing support to the formation of mildly “burning” areas, where the ordered cylindrical shape oxide with the pore diameter of around 75 nm forms. The investigation of the MB decomposition in the presence of the nanostructured $WO_3$ layers showed that such ordered cylindrical $WO_3$ structures can effectively decompose organic contaminations.

## Acknowledgements

This work was supported by State assignment 2020-2022 № FSMR-2020-0018 (Proposal mnemonic code 0719-2020-0018), Agreement № 075-03-2020-216.

Sixth Asian School-Conference on Physics and
Technology of Nanostructured Materials
Vladivostok, Russia, 25 – 29 April, 2022



# Structure and mechanical properties of electrodeposited nanostructured Ni-Fe films

T.I. Zubar*
SSPA "Scientific and Practical Materials Research Centre of NAS of Belarus", 220072 Minsk, P. Brovki str. 19, Belarus

*e-mail: fix.tatyana@gmail.com

**Abstract.** Nanostructured NiFe film was obtained via pulsed electrodeposition and annealed at a temperature from 100 to 400 °C in order to study the effect of heat treatment on the surface microstructure and mechanical properties. The mechanical properties of the NiFe films have been investigated by nanoindentation. The results showed the opposite effect of heat treatment on the mechanical properties in the near-surface layer and in the material volume. An explanation of this phenomenon was found in the complex effect of changing the ratio of grain volume/grain boundaries and increasing the concentration of thermally activated diffuse gold atoms from the sublayer to the NiFe film.

## 1. Introduction

Soft magnetic NiFe films are used in a wide range of applications due to the optimal balance of electric, magnetic and mechanical properties. Permalloy has applications in areas, such as low frequency magnetic shielding and transformer cores, as functional magnetic materials in magnetic field sensors (since they demonstrate the effects of giant and amorphous magnetoresistance), magnetic recording devices, as spintronic material and as electromagnetic shields to protect functional electronics from permanent magnetic fields and electromagnetic radiations [1-3]. Ni-Fe alloys show good adhesion to various types of the substrates, and excellent mechanical characteristics (hardness in macro- and nanoscale, elastic modulus, wear and crack resistance, as well as resistance to plastic deformation) [4,5]. Thanks to this, permalloys or Ni-rich alloys are an attractive material for use as a functional coating that provides both mechanical protection and protection from the electromagnetic and magnetic fields. Electrodeposited films are promising, due to high economic viability of the electrodeposition process. The ability to deposit thin films and coatings via electrodeposition on puff-shaped substrates should also be noted among the main advantages of the method. This is especially important for using magnetic films as shields from electromagnetic interference, when it is necessary to cover parts. Internal stresses are greater, the thicker the film and the more complex the shape of the substrate. Residual stresses in the film and coating can lead to a decrease in the magnetic and electrical properties and, of course, mechanical characteristics.

In this work, we studied the effect of heat treatment on the microstructure and mechanical properties of nanostructured NiFe films that are deposited on a Si wafer. Critical changes in the mechanical and magnetic properties occur in 100 to 400 °C temperature range [6-7]. Heat treatment at higher temperatures leads to changes in the crystal lattice [7], for example, polymorphic transformations. We have shown that even relatively low temperatures can have a beneficial effect on the hardness, Young's modulus, and resistance to the elastoplastic deformation. In addition, we studied differences in the behavior of the surface layer and the internal volume of the material and found explanations for their opposite response to an increase in heat treatment temperature.

## 2. Experiment

Pulsed electrodeposition was used to form a nanostructured NiFe film. A short pulse duration (10−3 s) leads to the formation of a material with a small grain size. All technological parameters are given in [8]. Heat treatment was carried out at temperatures of 100, 200, 300, and 400 °C in air. The samples were heated at a rate of 100 °C/h, and then kept at maximum temperature for 1 h and naturally cooled to room temperature. The measurement of the micromechanical parameters and surface microstructure investigation were studied using the nanoindenter Hysitron 750 Ubi by penetration of the Berkovich diamond pyramid with continuous registration of the deformation curves (indentation load (P) vs. indentation depth (h)). The materials were loaded according to the scheme "10-10" (10 s of loading, 10 s of unloading). At least 25 measurements were carried out for each value of the maximal indentation depth and for each sample. Each deformation curve included 2–4 thousand measurements. The maximal values of the indentation depth were 10 nm (for the near-surface layer investigation) and 50 nm (for the investigation of the material in bulk). The penetration of the indenter to a depth of more than 10% of the film thickness might not correctly reflect the mechanical properties, since the influence of the substrate increases during increasing the indentation depth.

## 3. Results and discussions

The coalescence process is completed when the heat treatment temperature reaches 200 °C. Figure 1e shows distinct individual grains that are not clustered. The most probable grain size is 13 nm. The dispersion width increases with an increasing grain size, as can be seen in Figure 1f. With a further increase in temperature to 300 °C, the second stage of coalescence begins, which will be completed between 300 and 400 °C. The formation of multigrain clusters is also characteristic of the second stage of coalescence, as well as of the first. The presence of a large number of smooth sections around the clusters suggests that the second stage of grain association is close to completion. Smooth areas with a homogeneous surface are likely to become grains, the boundaries of which will be at the place of clusters. The grain size approaches 200 nm for the sample that was subjected to heat treatment at 300 °C (we mean grains inside the clusters, since it is difficult to determine the boundaries of large smooth

grains). An increase in the temperature to 400 °C leads to a significant increase in the most probable size of grains to 580 nm. Obviously, the coalescence is complete and the surface looks uniform in this sample. The evolution of the grain microstructure, including two stage of the grain coalescence, are presented schematically in Figure 1.

The mechanical tests were carried out at two depths—10 nm (black squares) and 50 nm (red circles). Thus, we tried to compare the behavior of the surface and volume of a NiFe film under the influence of heat treatment (figure 2). The results of nanoindentation show that heat treatment has an opposite effect on the surface layer and the internal volume of the material. Analysis of graphs in Figure 3a,b allows for us to conclude that the hardness and Young's modulus of the as-prepared sample on the surface and in the bulk are quite close $H_{10nm}$ = 8.64 ± 0.43 GPa, $H_{50nm}$ = 7.51 ± 0.32 GPa and $E_{10nm}$ = 183.6 ± 7.0 GPa, $E_{50nm}$ = 196.8 ± 5.4 GPa. An increase in heat treatment temperature leads to a nonlinear increase in Young's modulus to 256.1 ± 8.3 GPa (for 400 °C) and hardness to 11.1 ± 0.98 GPa on the surface (black squares) and a simultaneous decrease in these parameters in the film volume (red circles), $E_{50nm}$ = 165.1 ± 9.3 GPa, and $H_{50nm}$ = 5.88 ± 0.58 GPa. The relatively high measurement error (in some cases more than 10%) is due to a significant difference in the mechanical response of the material when the indenter hits the boundary or center of the grain.

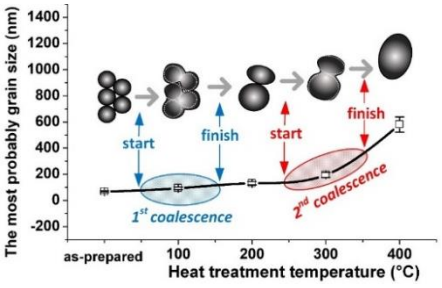


***Fig. 1*** *An increase in the most probable grain size upon heat treatment during two stages of coalescence.*

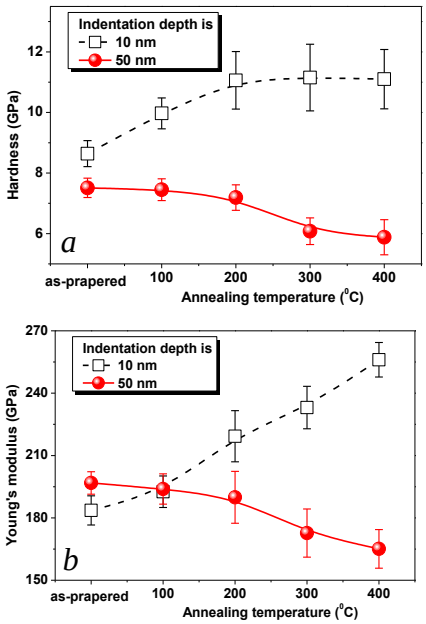


***Fig. 2.*** *Mechanical properties of the Au/NiFe nanostructured system with indentation depth of 10 nm and 50 nm after heat treatment investigated using nanoindentation. (a) Dependence of the hardness, (b) Young's modulus.*

The ratio H/E or resistance to the elastoplastic deformation during elastoplastic deformation inside the material (h = 50 nm) tends to nonlinearly decrease. The ratio remains almost unchanged during heat treatment not higher than 200 °C (H/E = 0.037–0.038), and then decreases to 0.035. The surface layer during heat treatment at 100 °C has an increase in deformation resistance from 0.047 to 0.051, and a decrease to 0.043 with an increase in temperature to 400 °C.

Probably, the opposite behavior of the mechanical properties is associated with the difference in the processes activated by heat treatment, both in the material volume and on the surface. We concluded that three complex processes significantly affect the mechanical properties of the system after analyzing the investigation results and literature [9]:

1. An increase in grain size, which is always accompanied by a decrease in the number of grain boundaries.
2. The formation of oxide on the surface.
3. Thermally activated diffusion of gold atoms from the sublayer into the film.

## 4. Conclusions

It has been established that an increase in grain size with a simultaneous decrease in the number of grain boundaries leads to a decrease in the number of barriers to the distribution of dislocations during mechanical deformation. Consequently, the mechanical properties decrease with increasing grain size, especially in the volume of the material, since the surface as a whole is characterized by an incomparably greater defectiveness, and other mechanisms act because of this.

Heat treatment in air activates surface oxidation. The oxidation process was studied step by step with increasing temperature while using an analysis of deformation curves. The thickness of the oxide layer increases from about 5 to 20 nm with an increasing temperature of heat treatment. It was found that when the oxide thickness hox is less than the indentation depth (hox < h), the hardness value includes two components: hardness of oxide and NiFe. This is true for the range from the as-prepared sample to the sample after treatment at 200 °C. Hardness increases from 8.6 to 11.0 GPa in this range. When hox > h, (after treatment at 300 and 400 °C), the hardness value remains constant at about 11.0 GPa, since the indentation takes place inside the oxide layer. It was also found that surface oxidation does not significantly affect the mechanical properties of the internal volume of the NiFe film.

The third process, which is activated by heat treatment, is the diffusion of Au atoms from the sublayer into the NiFe film. Diffusing atoms are point defects, which facilitate the propagation of deformation and soften NiFe. The gold concentration for each temperature at the investigated indentation depth (10 and 50 nm) was calculated using I Fick's law and the Arrhenius equation. Consequently, it was found that a relative concentration of more than 0.02 is a critical point, after passing through which a decrease in hardness, elastic modulus, and resistance to elastoplastic deformation begins.

## References

[1] K.S. Dijith [et al.] Mater. Chem. Front. 2 (2018) 1829–1841.
[2] [S. Evanczuk [et al.] Electron. Prod. 56 (2014) 11.
[3] J. Park [et al.] Thin Solid Films 677 (2019) 130–136.

[4] D.V. Kumar [et al.] Mater. Chem. Phys. 201 (2017) 26–34.
[5] J.D. Giallonardo [et al.] Philos. Mag. Abingdon (Abingdon) 91 (2011) 4594–4605.
[6] G.Y. Deng [et al.] Int. J. Mech. Sci. 155 (2019) 267–285.
[7] G. Lee [et al.] J. Alloys Compd. 613 (2014) 164–169.
[8] T. I. Zubar [et al.] J. Alloys Compd. 748 (2018) 970–978.
[9] W. Ge [et al.] Coatings. 10 (2020) 332.

# Effects of group IV–VII elements doping on $TiO_2$ electrochemical lithium storage performance

A.A. Sokolov*, D.P. Opra, S.L. Sinebryukhov, V.V. Zheleznov, A.B. Podgorbunsky, S.V. Gnedenkov

Institute of Chemistry FEB RAS, 159 Pr. 100-letiya Vladivostoka, Vladivostok 690022, Russia

*e-mail: alexsokol90@mail.ru

Titanium dioxide is widely used in the chemical industry, for example, in the production of white pigment, medicines, cosmetics, sensors, photocatalysts, etc. Some time ago, the object of attention was the use of titanium dioxide as an anode material for lithium-ion batteries (LIBs) capable of operating in the fast-charge mode and over a wide temperature range. However, the slow diffusion of lithium ions ($10^{-15}$ $cm^2$ $s^{-1}$) and low electrical conductivity ($10^{-12}$ S $cm^{-1}$) act as limiting factors for the use of $TiO_2$ in LIBs. A promising way to improve the characteristics of $TiO_2$ is modification due to cationic and anionic substitution in the $Ti^{4+}$ and $O^{2-}$ positions.

Within the scopes of present work, nanostructured $TiO_2$(anatase) doped with group IV–VII elements (such as hafnium, zirconium, nitrogen, and fluorine) was investigated as anode materials for LIBs. All samples were synthesized by a template sol-gel method on a carbon fiber.

According to the scanning and transmission electron microscopy investigations, as-synthesized $TiO_2$-based materials have a tubular microstructure (length: 5–300 μm; outer diameter: 2–5 μm). Tubes have a nanostructured surface and assembled by nanoparticles with an average size of 10–25 nm.

According to the Raman spectroscopy studies, the incorporation of doping elements into titania crystal structure leads to distortion in crystal lattice, increasing the unit cell volume, due to the difference in $Zr^{4+}$ (0.72 Å), $Hf^{4+}$ (0.71 Å), and $Ti^{4+}$ (0.604 Å) ionic radii. At the same time, according to the ultraviolet–visible spectroscopy and electrochemical impedance spectroscopy, the doping of $TiO_2$ with nitrogen and fluorine narrows of the band gap of anatase from 3.24 eV to 2.58 eV (Fig. 1) and increases its electrical conductivity. In particular, the conductivity of (Zr, N, F) co-doped $TiO_2$ reaches $1.22 \cdot 10^{-5}$ S $cm^{-1}$, that is higher than for only Zr-doped ($1.19 \cdot 10^{-6}$ S $cm^{-1}$) and undoped $TiO_2$ ($0.9 \cdot 10^{-6}$ S $cm^{-1}$). In addition, the presence of fluorine stabilizes anatase, shifting the temperature of the anatase–rutile phase transition.

The as-synthesized $TiO_2$ as anode material was tested in half-cell with a lithium counter electrode in the voltage range of 1–3 V. After the galvanostatic charge/discharge cycling at a current density of 33.5 mA $g^{-1}$ the reversible capacities of 60 mA $g^{-1}$ (undoped $TiO_2$), 155 mA $g^{-1}$ (Hf-doped $TiO_2$), and 140 mA $g^{-1}$ (Zr-doped $TiO_2$) were achieved. Meanwhile, for titanium dioxide doped with zirconium, fluorine, and nitrogen, a storage capacity of 160 mAh $g^{-1}$ was found at a current load of 335 mA $g^{-1}$.

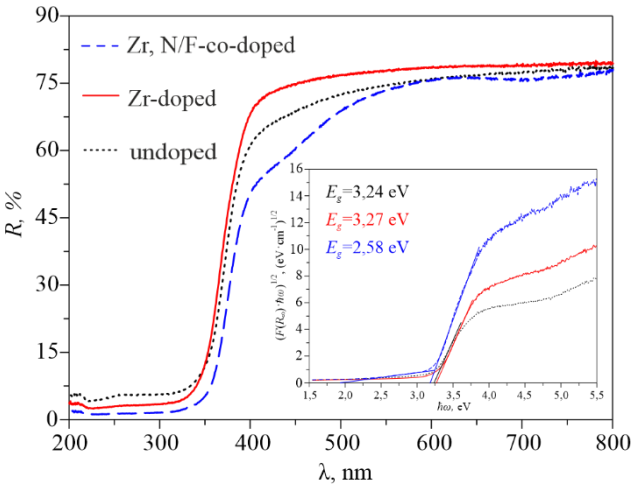


***Fig. 1.*** *UV-Vis diffuse reflectance spectra for undoped, Zr-doped, and (Z, F, N) co-doped $TiO_2$ samples (inset represents corresponding Kubelka–Munk plots).*

Thus, it was established that the doping of titanium dioxide with group IV–VII elements has a beneficial effect on its performance as an anode material for LIBs. The main reasons are as follows: i) increased volume of unit cell as a result of titanium substitution by hafnium or zirconium; ii) improved conductivity and decreased proportion of rutile due to co-modification with nitrogen and fluorine.

This work was supported by funding from the Russian Science Foundation (grant № 19-73-10017).

Sixth Asian School-Conference on Physics and
Technology of Nanostructured Materials
Vladivostok, Russia, 25 – 29 April, 2022

**IV.o.17**

# Effect of a metal oxides interlayers on the properties of silver nanoparticles in porous silicon for SERS spectroscopy

K. Girel[1,2], A. Burko[1,2], S. Zavatski[1,2], S. Dubkov[2], E. Grinakovskiy[2], D.G. Gromov[2], D.V. Novikov[2], H. Bandarenka[*,1,2]

[1] Applied Plasmonics Laboratory, Belarusian State University of Informatics and Radioelectronics, 6 Brovka St., Minsk 220013, Belarus

[2] Institute of Advanced Materials and Technologies, National Research University of Electronic Technology, 1 Shokin sq., Zelenograd, Moscow 124498, Russia

*e-mail: h.bandarenka@bsuir.by

**Abstract.** Porous silicon coated with plasmonic nanostructures of noble metals has been reported to demonstrate an activity in surface enhanced Raman scattering (SERS) spectroscopy providing a detection of organic compounds (e.g. dyes, phospholipids, peptides, proteins, etc.) at extremely low concentrations down to single molecules. The outstanding sensitivity and fabrication compatibility of such SERS substrates with standard silicon technology makes them very attractive for a wide application in analysis by Raman spectroscopy. However, there is a need of imparting additional properties to such substrates, for example, the ability of self-cleaning for multiple use. In this work, we studied how the interlayers of different metal oxides (ZnO, $ZrO_2$ and $TiO_2$) between porous silicon and silver particles affect the properties of SERS substrates.

## 1. Introduction

Surface enhanced Raman scattering (SERS) spectroscopy is now on its way of transferring from research laboratories to practical application for detecting and characterizing various chemical compounds at submolar concentrations to solve tasks arising in biomedical diagnostics, forensic examination, monitoring sanitary-epidemiological conditions, environmental pollution control and so on [1]. As a rule, plasmonic materials made up of noble metal nanoparticles, which act as Raman photon multipliers from analyte molecules pre-adsorbed on their surface, provide a unique sensitivity of SERS method. An implementation of the SERS-spectroscopy strongly depends not only on key performance indicators of SERS substrates but also on a mercantile aspect defined by their cost. Currently available SERS substrates well meet requirements to an enhancement factor and a reproducibility of signal intensity but they are still rather expensive for a routine analysis. In this regard, some efforts have been made to overcome a latter hurdle through the development of reusable SERS substrates [2]. In particular, our approach is to combine a silvered porous silicon fabricated by affordable Si-compatible process that has already proved its effectiveness as a SERS substrate [3] and photocatalytically active metal oxides (e.g. ZnO, $ZrO_2$, $TiO_2$) possessing the self-cleaning upon ultraviolet (UV) light.

## 2. Experiment

Lightly doped p-Si wafer was used as an initial substrate to fabricate macroporous silicon by electrochemical etching in an electrolyte constituted by HF (45%) and dimethyl sulfoxide mixed at 10:46 volume ratio. The current density of 8 mA/cm$^2$ was applied for 7 min. A depth of the macropores varied between 0.7 and 1.5 μm while a diameter was 0.5 – 1.0 μm. Highly doped n-Si wafer was used as an initial substrate to fabricate mesoporous silicon by electrochemical etching in an electrolyte constituted by HF (45%), $C_3H_7OH$ and $H_2O$ mixed at 1:1:3 volume ratio. The current density of 100 mA/cm$^2$ was applied for 85 s. A depth of the mesopores was 5 μm while a diameter was 50 – 70 nm. Next, the porous silicon was coated with ZnO, $ZrO_2$ and $TiO_2$ film of 60 nm thickness by magnetron sputtering. SERS-active coating was formed by thermal evaporation of Ag nanoparticles, which diameter was 5 and 25 nm. After that, some samples were subjected to an additional electroless deposition of silver from a mixture of $AgNO_3$, $C_2H_5OH$, HF and water. Morphological characterization of the samples was carried out with scanning electron microscope (SEM) Hitachi 4800. For the SERS measurements, the obtained substrates were kept in a water solution of $10^{-5}$ M DTNB or $10^{-6}$ M R6G for 2 h and then studied using 3D scanning Raman microscope Confotec NR500 equipped with 473 nm and 633 nm lasers. The self-cleaning feature was tested using SERS substrates with analyte molecules immersed in a Petri dish filled with a distilled water. Two samples were taken for each metal oxide interlayer. One substrate was subjected to UV light (365 nm) for 10 min. After that, the Raman analysis was performed again to check if the substrate remains its SERS activity.

## 3. Results and discussions

In the course of the work, a series of samples of meso- and macroporous silicon were prepared, coated with layers of metal oxides of 60 nm thickness. After that the samples were subjected to deposition of silver particles by thermal evaporation and electroless plating from solution. During the thermal deposition, two types of substrates were formed with particles of 5 and 25 nm in diameter. The type of porous silicon and oxide material did not significantly affect the deposition kinetics and nanoparticle sizes. Electroless deposition resulted in formation of polydisperse particles, which diameter varied from 10 to 200 nm. Fig. 1 presents SEM images of meso- and macroporous silicon coated with titanium oxide and silver particles. The rate of electroless deposition on mesoporous silicon was higher, since its surface is more developed and saturated with dangling bonds than that of macroporous one. Samples with

silver particles of 5 nm diameter showed no SERS activity due to the small amount of plasmonic material and low density of its coating. Substrates with nanoparticles of 25 nm diameter were SERS active only upon excitation with a 473 nm laser, since their plasmon resonance lies at about 470 nm. Polydisperse silver particles were active at 473 and 633 nm lasers due additional higher order plasmon oscillation modes. Those samples were found to demonstrate the most effective enhancement of Raman signal from analyte molecules provided by many hot spots between nearly connected silver particles and the largest silver mass compared to that of evaporated silver nanoparticles.

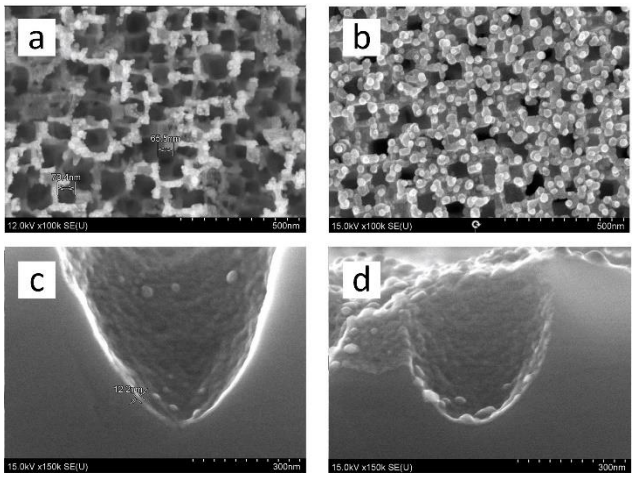


***Fig. 1.*** *SEM top and cross section images of (a, b) meso- and (c, d) macroporous silicon coated with $TiO_2$ layer and thermally evaporated silver nanoparticles with mean diameter (a, c) 5 nm and (b, d) 25 nm.*

The substrates based on mesoporous silicon showed no photocatalytic activity while using macroporous template resulted in a pronounced UV facilitated cleaning when the $TiO_2$ interlayer was used as this can be seen in Fig. 2, d.

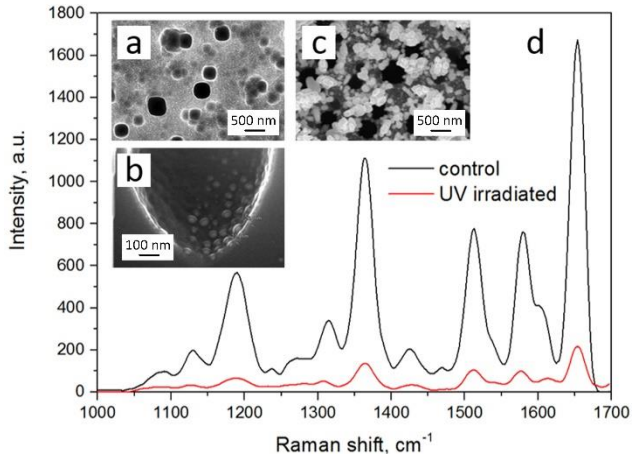


***Fig. 2.*** *SEM images of macroporous silicon/$TiO_2$ after (a, b) evaporation and (c) electroless deposition of silver. SERS spectra of R6G on the control and UV irradiated samples of (c) type.*

Such an effect is due to a larger surface area of photocatalytically active oxide in macropores in contrast to that on mesoporous silicon. Despite $ZrO_2$ interlayer was not found to promote photocatalytic activity it still can be considered as a perspective material for the substrates' cleaning. Its $E_g$ is wider than that of $TiO_2$ and photocatalytic properties are expected to be possessed under excitation of 250 nm. This should be noted that the substrates with the $ZrO_2$ interlayer were revealed to induce higher SERS activity after UV treatment if DTNB analyte is used. The DTNB molecules are dimers containing two monomers connected via disulfide bridge. As a rule, this bond is partly broken in presence of silver or gold nanoparticles leading to anchoring monomer on metal surface through -S. We suppose an external irradiation contributes to the disruption of the S-S bond follow by more effective analyte adsorption.

## 4. Conclusions

Samples based on meso- and macroporous silicon coated with metal oxides' (ZnO, $ZrO_2$, $TiO_2$) interlayers and silver particles with diameters 5 nm, 25 nm and 10 – 200 nm were formed. The obtained nanostructures were tested to reveal an ability to enhance Raman signal from molecules of R6G and DTND adsorbed on their surface. SERS activity was typical for the substrates with silver nanoparticles of 25 nm diameter upon 473 nm excitation and for the polydisperse silver particles at 473 and 633 nm lasers. The latter is caused by contribution of higher order plasmonic modes provided polydispersity. The only macroporous silicon-based substrates with $TiO_2$ interlayer showed UV facilitated cleaning, which is thanks to a larger surface area of oxide in macropores in contrast to that on mesoporous silicon. ZnO and $ZrO_2$ interlayers were not found to promote photocatalytic activity. However, zirconia is expected to be a perspective material for the substrates' cleaning if shorter UV wavelength is applied. The $ZrO_2$ interlayer was revealed to induce higher SERS activity after UV treatment in case of DTNB analyte. The results of this research shows that the modification of the SERS substrates' composition with metal oxides opens an opportunity to tune their properties to achieve reusability and to adapt them for better specific analyte detection avoiding functionalization.

## Acknowledgements

The reported research was supported by the Russian Science Foundation (Project 21-19-00761).

## References

[1] Li C. et al. J. Mater. Chem. C, **9**(2021)11517-11552.
[2] Lai Y.-C. et al. Applied Surface Science, **439**(2018)852-858.
[3] Khinevich N. et al. Microporous and Mesoporous Materials, **323**(2021)111204.

# Electron spectroscopy for in-situ analysis of MAX-phases

T.A. Andryushchenko*[,1], S.A. Lyaschenko[2], I.A. Tarasov[2], S.N. Varnakov[2]

[1] Reshetnev Siberian State University of Science and Technology, 31 Krasnoyarsky Rabochy Av., Krasnoyarsk 660037, Russia

[2] Kirensky Institute of Physics SB RAS, Akademgorodok 50/38, Krasnoyarsk 660036, Russia

*e-mail: tanya.andryuchshenko@mail.ru

**Abstract.** Electron spectroscopy methods allow performing in-situ analysis of the elemental composition of MAX-phase thin films. Auger electron spectroscopy makes it possible to determine the chemical bonds formed during the synthesis. This paper describes the results of using Auger electron spectroscopy for in-situ analysis of $Mn_2GeC$ and $Cr_2GeC$.

## 1. Introduction

MAX-phases ($M_{n+1}AX_n$, where n = 1, 2, 3) are nanolayered, hexagonal transition metal carbides and nitrides. M is a transition metal, A is an element of the main subgroup of the periodic system, X is carbon or nitrogen [1].

MAX materials exhibit many useful properties such as high strength, high thermal and electrical conductivity, corrosion resistance and high temperature stability. These valuable properties of MAX-phases make them promising materials for creating details that can be used in extreme conditions. For example, it can be applied to the manufacture of electrical contacts, heating elements, protective coatings.

The Auger electron spectroscopy method makes it possible to perform in-situ elemental analysis of MAX-phases thin films to determine the formed chemical bonds. This paper describes the application of Auger electron spectroscopy in the synthesis of MAX-phases based on chromium (Cr), manganese (Mn), germanium (Ge) and carbon (C), which are widespread at the present time [1–3].

## 2. Experiment

We have synthesized $Mn_2GeC$ and $Cr_2GeC$ structures by pulsed laser deposition (PLD) technology at high-vacuum chamber pressure $P \leq 2.8 \cdot 10^{-8}$ Torr. We measured the Auger electron spectra using a low energy diffraction and Auger electron analysis system (SPECS) with a retarding field energy analyzer. The primary electron energy was 3000 eV.

## 3. Results and discussions

The Auger spectra of the $Mn_2GeC$ structure contains peaks which positions correspond to the energy of Auger transitions in germanium, carbon and manganese atoms [4]. Figure 1 shows Auger electron spectra after deposition of the $Mn_2GeC$ structure on $Al_2O_3$ substrate.

The shape of the carbon Auger peak is typical to graphite rather than manganese carbide. The intensity of the manganese Auger peaks is specific to the peaks in the composition of the $Mn_5Ge_3$ spectrum, which is described in [5]. These results showed the existence of different from $Mn_2GeC$ phase in the composition of the synthesized thin film.

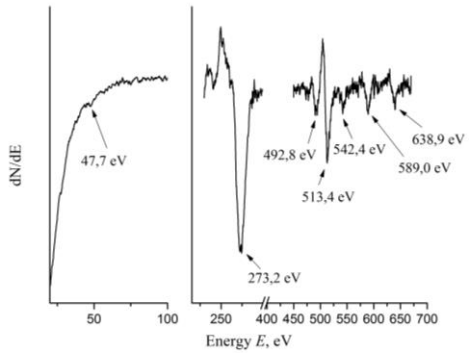


***Fig. 1.*** *Auger electron spectra after deposition of the $Mn_2GeC$ structure on $Al_2O_3$ substrate (after smoothing).*

In the Auger spectra of $Cr_2GeC$ structure we identified peaks that are characteristic to chromium, germanium and carbon atoms.

The carbon peaks have a shape that is specific to carbide, which may indicate the presence of chromium carbide $Cr_2C$.

## 4. Conclusions

It was found that the application of Auger electron spectroscopy makes it possible to determine the elemental composition of thin films and the presence of transition metal carbides in thin polycrystalline or epitaxial films. Which is an additional highly sensitive in-situ method for the identification of MAX-phases in the study of the initial processes of their formation.

## Acknowledgements

The research was supported by the government of the Russian Federation (agreement No. 075-15-2019-1886) and the Russian Science Foundation (grant #21-12-00226, http://rscf.ru/project/21-12-00226/).

## References

[1] M. Sokol, V. Natu, S. Kota, M. W. Barsoum. Trends in Chemistry **1**(2019)210.

[2] A. S. Ingason, M. Dahlqvist, J. Rosen. Journal of Physics: Condensed Matter **28**(2016)4333003.

[3] R. Salikhov, A. S. Semisalova, A. Petruhins, A. S. Ingason, J. Rosen, U. Wiedwald, M. Farle. Materials Research Letters 3(2015)156.

[4] L. E. Davis, N. C. MacDonald, P. W. Palmberg, G. E. Riach, R. E. Weber. Physical Electronics (1976).

[5] M. Petit, M. T. Dau, G. Monier, L. Michez, X. Barre, A. Spiesser, V. L. Thanh, A. Glachant, C. Coudreau, L. Bideux, C. Robert-Goumet. Phys. Status Solidi C 9 **6**(2012)1374.

Sixth Asian School-Conference on Physics and
Technology of Nanostructured Materials
Vladivostok, Russia, 25 – 29 April, 2022



# Special methods for catalysis of molecular crosslinking of composite materials based on polydimethylsiloxane

E.V. Antonov[1], N.D. Prasolov[1,2], I.M. Sosnin[1,3], L.M. Dorogin[*,1]

[1] ITMO University, Kronverkskiy pr., 49, 197101 St.Petersburg, Russia
[2] Ioffe Institute, Politekhnicheskaya str., 26, 194021 St. Petersburg, Russia
[3] Togliatti State University, Belorusskaya Str., 14, 445020, Togliatti, Russia

*e-mail: leonid.dorogin@majorrevision.com

**Abstract.** The fabrication of polydimethylsiloxane involves a curing process at room temperature or external heat. These operations can be inconvenient, for example, in medical applications or in ultra-precision systems requiring local cross-linking or accelerated curing without external heating. In this paper, we consider the optimal methods for catalyzing the process of molecular crosslinking of polydimethylsiloxane and ensuring the possibility of the locality of this procedure. It also describes the testing of a composite material of polydimethylsiloxane with silver nanoparticles to accelerate curing by microwave method, as one of the methods. The resulting composite materials were studied for general properties, from which it can be concluded that the bulk properties are similar to the original polydimethylsiloxane, but the surface properties are different.

## 1. Introduction

Polydimethylsiloxane (PDMS) as a material has a number of worthy properties such as biocompatibility, optical transparency, poor wettability, flexibility, and chemical and thermal stability. Due to this, this substance is used in flexible electronics, microfluidic systems, medical applications, wearable devices [1].

The manufacturing process of solid polydimethylsiloxane is the curing of a liquid prepolymer, which is dimethylsiloxane monomers, by forming perpendicular networks throughout the volume of the body as a result of a chemical reaction. In general, this process takes up to two days or is required in external heating, which can reduce this time to 10 minutes (at 150 °C). However, in some situations it may be necessary to speed up the curing process without external heating, or to allow the material to cure in localized areas.

This area has been actively explored in recent years. Various mechanisms for accelerating the molecular crosslinking of a polymer are being studied using methods such as heating with a bulb [2], exposure to microwave [3], laser [4], and UV [5] radiation (including the Mosquito method), magnetic induction [6], and addition of nano-silica sol [7]. In addition, the possibilities of partial (local) crosslinking of silicone are considered [8].

We proposed to use microwave irradiation for curing. Due to its non-polarity, pure polydimethylsiloxane is ineffectively affected by this irradiation. To correct this, it was proposed to introduce metal nanoparticles into the volume of polydimethylsiloxane. In this work, the possibility of accelerated crosslinking of a composite material based on polydimethylsiloxane with silver nanoparticles (NPs) was tested, and the optical, mechanical, and adhesive properties of the fabricated samples were studied.

## 2. Experiment

A composite material based on polydimethylsiloxane was made using the sylgard 184 elastomeric kit in a ratio of 10:1 base to hardener and silver nanoparticles with a diameter of 35-120 nm, synthesized by the reduction method followed by crystallization. Silver NPs were introduced in the form of an ethanol suspension to ensure uniform distribution, in an amount that provided a concentration of silver NPs in the final material of 0.01%. The total weight of the uncured material was 5 g, while the amount of ethanol was 1.577 g. Mixing was carried out for 40 seconds at 3500 rpm in a SpeedMixer (TM) DAC 150.1 FVZ mixer, during the curing process, the solvents were also subjected to microwave irradiation at a frequency of 3450 MHz at a power of 700 V with a duration of 0-4 hours, which is described in more detail in [9].

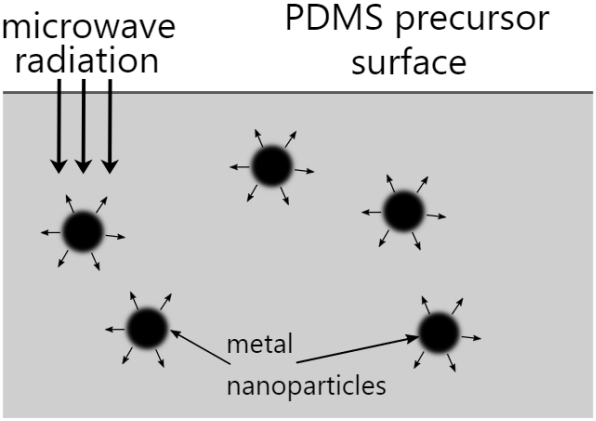


***Fig. 1.*** *Schematics of the physical principles underlying electromagnetic microwave radiation assisted curing of metal nanoparticle filled polydimethylsiloxane (PDMS) prepolymer liquid.*

To evaluate the resulting composite materials, some of the properties shown in Table 1 were studied. The viscoelastic modulus was obtained by dynamic mechanical analysis (DMA) on a Q800 facility by measuring in tensile mode with applied sinusoidal stress under high and low strain conditions. When processing the obtained data, the principle of time-temperature superposition (TTS) was used. Water wettability was studied by measuring advancing and receding contact angles to obtain equilibrium contact angle, adhesive interaction between glass and the fabricated elastomers studied by custom-made Johnson-Kendall-Roberts (JKR) inspired adhesion testing setup. UV/VIS (200-1100 nm) absorption spectra of the PDMS-based materials was obtained by spectrometer instrument Ava-Absorbance (Avantes, Netherlands).

***Table I.*** *Table of fabricated elastomer materials and the main measured properties. The sample label is encoded with the base material, the additional component (if any, via /), as well as microwave curing conditions (if any, via @).*

| Sample | Work of adhesion, J/m$^2$ | Storage modulus (low-strain), MPa |
|---|---|---|
| *PDMS (stock)* | 0.44 | 1.68 |
| *PDMS@1hMW* | 0.41 | 1.73 |
| *PDMS@2hMW* | 0.35 | 1.84 |
| *PDMS@3hMW* | 0.34 | 1.69 |
| *PDMS@4hMW* | 0.28 | 1.84 |
| *PDMS/AgNP* | 1.72 | 1.37 |
| *PDMS/AgNP@1 hMW* | >1.39* | 1.61 |
| *PDMS/AgNP@2 hMW* | 0.88 | 1.52 |
| *PDMS/AgNP@3 hMW* | 0.8 | 1.47 |
| *PDMS/AgNP@4 hMW* | 0.91 | 1.64 |

**) Lower boundary indicated due to the adhesion of the sample being too strong for the used experimental conditions.*

## 3. Results and discussions

As can be seen from the table, the composite materials with silver nanoparticles have a lower viscoelastic modulus, better adhesive properties, and slightly lower transparency, especially in the silver absorption region. Exposure to microwave irradiation during the curing procedure increases the elastic modulus, reduces the adhesion work, and does not affect the optical properties of both the initial PDMS and the composite material based on it.

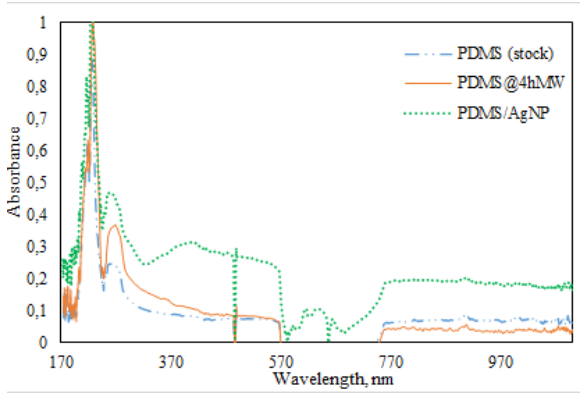


***Fig. 2.*** *Transmittance (absorption) optical spectra of the stock PDMS material, the sample with 4-hours treatment and PDMS material with AgNP.*

## 4. Conclusions

Several methods for curing elastomeric polydimethylsiloxane have been considered. We also tested silver nanoparticles as a reagent for curing polydimethylsiloxane and evaluated the properties of the composite material compared to the original polydimethylsiloxane.

In general, materials with silver turned out to be less elastic and more tenacious to glass and water. The optical absorption also slightly increased with a small peak at 410 nm, corresponding to the absorption peak of silver nanoparticles.

It can be concluded that silver NPs can serve as an internal heater for PDMS elastomers to catalyze crosslinking by microwave irradiation. In this case, the presence of silver in the composite material slightly affects its optical and viscoelastic properties, but significantly changes the surface properties.

## Acknowledgements

This work was supported by the Ministry of Science and Higher Education of the Russian Federation (agreement nr. 075-15-2021-1349).

## References

[1] R. Helgason, A. Banavali, Y. Lai. Med. DEVICES Sens. **2**(2019)e10025.
[2] C. McDonald, D. McGloin. Biomed. Opt. Express **6** **10**(2015)3757.
[3] P. Katare и S. S. Gorthi. Microfluid. Nanofluidics **24** **7**(2020)46.
[4] H. Selvaraj, B. Tan, K. Venkatakrishnan. J. Microelectromechanical Syst. **21** **5**(2012)1071.
[5] V. Argueta и B. Fitzpatrick. International Optical Design Conference 2017. (2017)19.
[6] L. Al-Harbi, M. Darwish, M. Khowdiary, I. Stibor. Polymers. **10**(2018)507.
[7] D. Chen, F. Chen, X. Hu, H. Zhang, X. Yin, Y. Zhou. Compos. Sci. Technol. **117**(2015)307.
[8] H. Yu, G. Zhou, F. S. Chau, и S. K. Sinha. Microsyst. Technol.. **17**(2011)443.

Sixth Asian School-Conference on Physics and
Technology of Nanostructured Materials
Vladivostok, Russia, 25 – 29 April, 2022



# Sol-gel preparation and study photocatalysts ZnS-modified biogenic silica

O.D. Arefieva*[,1,2], M.S. Vasilyeva[1,2], V.V. Tkachev[1]

[1] Far Eastern Federal University, FEFU Campus 10 Ajax Bay, Russky Island, Vladivostok 690922, Russia
[2] Institute of Chemistry, Far Eastern Branch of Russian Academy of Sciences, Prosp. 100-letiya Vladivostoka 159, Vladivostok, 690022, Russia

*e-mail: arefeva.od@dvfu.ru

**Abstract.** Sol gel technology has produced effective and stable ZnS-$SiO_2$ photocatalysts based on wet gel and xerogel of biogenic silica from rice husk. According to electron microscopy data, the microstructure of sulfide photocatalysts does not depend on the type of gel and is a porous $SiO_2$ matrix, which includes faceted ZnS crystals. Both samples exhibit photocatalytic activity in the degradation reaction of methyl orange when exposed to UV, visible and sunlight. The sample had a higher activity, during the preparation of which $SiO_2$ xerogel was used, the degree of degradation of methyl orange in its presence was 88 and 30% when excited by UV and sunlight, respectively. The immobilization of zinc sulfide in the silica matrix led to the stability and photocatalytic activity of this material under various irradiation conditions.

## 1. Introduction

Heterogeneous photocatalysis is considered to be one of the most promising and innovative types of advanced oxidative processes used for wastewater treatment from persistent organic pollutants. Nanoparticles of metal sulfides are of considerable interest as effective photocatalysts. The introduction of such nanoparticles into the silicon dioxide matrix, which has a high specific surface area, makes it possible to protect sulfides from photocorrosion and improve the adsorption properties of photocatalysts [1-3]. To obtain highly active compositions with a high specific surface area, sol-gel technology is the most accessible, which provides high purity, uniformity and control of the structure of synthesized materials [4]. Tetraethylortosilicate (TEOS) [1], ethyl silicate [2], 3-mercaptopropyltrimethoxysilane [3] are used as silicon-containing compounds. The possibilities of using biogenic silica from rice production waste as a silicophilic plant have not been practically investigated.

The aim of the work is to obtain sol-gel technology and to investigate the photocatalytic properties of sulfide photocatalysts with a matrix of biogenic silica from rice husk in the degradation reaction of methyl orange.

## 2. Experiment

In this work, samples of zinc-containing sulfide photocatalysts with a matrix of biogenic silica obtained from rice husk (RH) were obtained. The synthesis of the photocatalyst included 3 stages. At the first stage, sodium orthosilicate was extracted from the RH. For this purpose, alkaline hydrolysis of RH was carried out when heated to 90ºC for 1 h. Next, a concentrated hydrochloric acid solution was added to the sodium orthosilicate solution to pH 6 and a wet gel was obtained. To obtain xerogel, one of the parts of the wet gel was calcined in a muffle furnace. At the last stage, $Zn(CH_3COO)_2 \cdot 2H_2O$, distilled water, thiourea and concentrated ammonia solution were mixed. Then a wet gel or xerogel of $SiO_2$ was added to the resulting mixture. The resulting suspensions were dried and calcined in a muffle furnace. The resulting powders were designated as ZnS-$SiO_{2wg}$, ZnS-$SiO_{2xg}$.

Elemental analysis of photocatalyst samples was performed using the method of energy dispersive X-ray fluorescence analysis on the EDX 800 HS spectrometer (Shimadzu, Japan). To determine the functional groups in the studied samples, IR absorption spectra in the region of 400-4000 $cm^{-1}$ were recorded in potassium bromide on a Vertex 70 Fourier spectrometer (Bruker, Germany). X-ray phase analysis of the samples was performed on a D8 Advance diffractometer (Bruker, Germany). The morphology and elemental composition of the catalyst surface were studied using a high-resolution scanning electron microscope Carl Zeiss Ultra+ (Zeiss AG, Germany).

The photocatalytic activity of the samples was evaluated in the degradation reaction of an organic pollutant - methyl orange (MO) under UV, solar and visible light irradiation. The catalytic process was carried out in a 100 ml cell. 50 ml of MO solution (pH 6.8) and a catalyst were placed in the cell. The loading of the catalyst was 1 g/l. The solution was irradiated with constant stirring on a magnetic stirrer (625 rpm) for 3 hours. The source of UV irradiation was a UV lamp of 100P/F (maximum radiation at 365 nm); the visible one was a xenon irradiator with a nominal lamp power of 35 watts and with radiation maxima in the region of 540-675 nm.

When irradiated with sunlight, the process was carried out under the same conditions on sunny days between 9 and 13 hours in March.

## 3. Results and discussions

According to the results of X-ray fluorescence analysis, the main element for the photocatalysts ZnS-$SiO_{2xg}$ и ZnS-$SiO_{2wg}$ is silicon. Zinc and sulfur are contained in equal amounts (Table I).

***Table I.*** *Chemical composition of sulfide photocatalysts, mass. %*

| Samples | Si | Na | Zn | S | Cl |
|---|---|---|---|---|---|
| ZnS-$SiO_{2wg}$ | 35 | 13 | 28 | 8 | 16 |
| ZnS-$SiO_{2xg}$ | 32 | 19 | 23 | 9 | 18 |

According to IR spectroscopy data, the spectra of the ZnS-$SiO_{2xg}$ and ZnS-$SiO_{2wg}$ photocatalysts are similar to each other and contain absorption bands in the 467-473, 798- 802 and 1103-1109 $cm^{-1}$ regions corresponding to

valence and deformation vibrations of Si-O-Si siloxane bonds. The absorption bands in the region of 3450-3508 and 1628 $cm^{-1}$, characteristic of the vibrations of the O-H bonds, indicate the presence of sorbed water molecules in them. In the spectra of the samples there is a band in the region of 621 $cm^{-1}$, which refers to the valence vibrations of the Me-S bond.

X-ray phase analysis of samples of sulfide photocatalysts showed that they are in an amorphous-crystalline state. The presence of an amorphous phase is indicated by a blurred peak in the region $2\theta$ = ~ 22-25°. A zinc sulfide semiconductor with a band gap of 3.67 eV has been identified in the crystalline phase. In both cases, the photocatalyst samples are loose irregularly shaped particles with sizes from 1 to 30 and more microns (Fig. 1a). The microstructure of sulfide photocatalysts synthesized using wet gel and xerogel has no significant differences and is a porous $SiO_2$ matrix, which includes faceted crystals of various shapes and sizes, presumably ZnS (Fig. 1b).

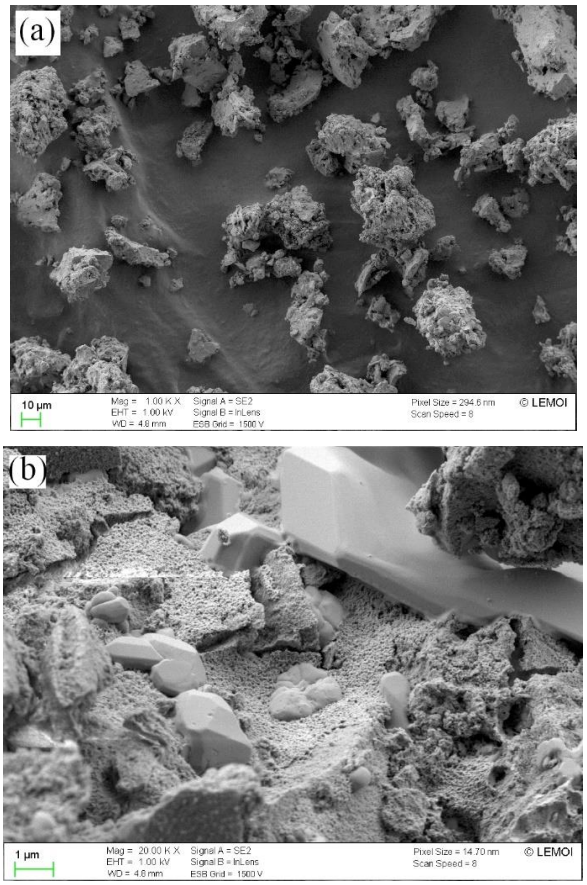


***Fig. 1.*** *SEM-image of the photocatalyst ZnS-$SiO_{2wg}$.*

The results of photocatalytic tests showed that the studied samples showed photocatalytic activity under various types of irradiation. When exposed to UV and sunlight, the sample had a higher activity, in the process of obtaining which $SiO_2$ xerogel was used. Comparing the degree of decomposition of MO when using ZnS-$SiO_{2xg}$ in the dark and when irradiated with visible light, it can be noted that this material does not exhibit photoactivity – a decrease in the concentration of the dye occurs, apparently, due to its sorption. The ZnS-$SiO_{2wg}$ sample obtained on the basis of a wet $SiO_2$ gel demonstrated a response when excited by UV, visible and sunlight, while the efficiency of MO degradation ranged from 11 to 35% (Table II).

***Table II.*** *The degree of degradation of MO under various irradiation conditions using sulfide photocatalysts, %*

| Photocatalyst | Irradiation conditions | | | |
|---|---|---|---|---|
| | Sunlight | UV light | Visible light | In the dark |
| ZnS-$SiO_{2wg}$ | 11± 6 | 35±7 | 15±9 | 1 |
| ZnS-$SiO_{2xg}$ | 30±5 | 88±5 | 16 ± 5 | 13 |

Samples of zinc-containing sulfide photocatalysts are stable in aqueous solutions – the content of $Zn^{2+}$ in the dye solution after decomposition under various irradiation conditions was 0.4 MPC for water bodies for household and drinking purposes.

## 4. Conclusions

Sulfide $SiO_2$-ZnS composite photocatalysts with a matrix of biogenic silica sol-gel method were obtained. The immobilization of zinc sulfide in the silica matrix led to the stability and photocatalytic activity of this material under various irradiation conditions. The materials have a response when excited by sunlight in the degradation reaction of the methyl orange dye.

## Acknowledgements

The work was carried out within the framework of the state task of the Institute of Chemistry of the FEB RAS 0205-2021-0002. The authors are grateful to the Laboratory of Molecular and Elemental Analysis and the Laboratory for X- ray Structural Analysis (Institute of Chemistry, FEB RAS).

## References

[1] Y. Yesu Thangam, R. Anitha. Journal of Research in Nanobiotechnology **1**(2012)14.
[2] M. Tan, W. Cai, L. Zhang. Applied Physics Letters **71**(1997)3697.
[3] B. Pal, T. Torimoto, K. Iwasaki, T. Shibayama, H. Takahashi, B. Ohtani. Journal of Applied Electrochemistry **35**(2005)751.
[4] N. Ugemuge, Y. R.Parauha, S. J.Dhoble. Energy Materials. Fundamentals to Applications Chapter **15**(2021)445.

Sixth Asian School-Conference on Physics and
Technology of Nanostructured Materials
Vladivostok, Russia, 25 – 29 April, 2022



# Application of Mössbauer spectroscopy to characterize iron-containing oxide coatings formed on titanium by plasma electrolytic oxidation

D.V. Balatskiy*[,1,2], Yu.B. Budnikova[1,2], M.S. Vasilyeva[1,2], I.V. Lukiyanchuk[1]

[1] Institute of Chemistry FEB RAS, 159 prospect 100-letiya Vladivostoka, Vladivostok, 690022 Russia
[2] Far Eastern Federal University, FEFU Campus, 10 Ajax Bay, Russky Island, Vladivostok 690922, Russia

*e-mail: denis.balatskiy@bk.ru

**Abstract.** In this work, we report the application of the Mössbauer spectroscopy technique to the study of Fe-containing oxide coatings formed on titanium by plasma electrolytic oxidation (PEO). Several models were used to process the Mössbauer spectrum, and the most suitable model was selected. The results of the Mössbauer spectrum processing showed the presence of both Fe(II) and Fe(III) high-spin states of iron in the samples.

## 1. Introduction

One of the promising methods of surface engineering of valve metals and their alloys is the technology of plasma electrolytic (microarc) oxidation (PEO), which allows obtaining surface oxide layers with a unique set of properties on objects of almost any geometric shape [1].

Iron-containing oxide PEO coatings on metals can have ferromagnetic properties and make it possible to obtain magnetic materials, including constructional ones, for example, 'metal/magnetic film' systems, which can be used as electromagnetic screens, structures absorbing electromagnetic radiation and etc. [2].

The magnetic properties of coatings depend on the valence state, the nearest environment of atoms located not only on the surface, but also in the bulk of the coatings.

Mössbauer spectroscopy is a highly informative method to obtain qualitative and quantitative information about the valence states and the nearest environment of iron. The values of isomeric shifts can indicate the presence of both Fe(II) and Fe(III) and their spin states. Due to the high selectivity of this method, it seems possible to determine the nature of the bonds formed during PEO coatings doping with 3d elements, that which are responsible for ferro- and ferrimagnetism. Similar studies have not yet been carried out for PEO coatings. For the correct interpretation of the Mössbaur spectra, it is necessary to choose the correct model for their processing, which was the task of this study.

## 2. Experiment

Titanium plates of the grade VT1–0 of a size of 2.0×2.0×cm were used in plasma electrolytic oxidation. Prior to anodizing, the samples were mechanically and chemically polished in a mixture of concentrated acids $HF:HNO_3$ (1:3) at 60–80 ºC for 2–3 s and then rinsed in distilled water and dried in air.

PEO process was carried out in polypropylene glass of 1000 mL in volume using thyristor unit TER4-63/460H (Russia) with unipolar pulse current.

The Fe-containing coating on titanium was formed at effective current density 0.1 A/cm$^2$ for 10 min in an aqueous electrolyte containing 0.05 M $Na_3PO_4$ + 0.05 M EDTA + 0.05 M $Fe_2C_2O_4$. After PEO treatment, the PEO-coated sample was rinsed with water and air-dried at 70 ºC.

To obtain Mössbauer spectra Fe-containing PEO coating was removed from the titanium surface and powdered. Mössbauer spectrum of Fe-containing PEO coating (hereinafter, the Fe-containing sample) was obtained at room temperature in transmission geometry on a Wissel spectrometer (Germany). The $^{57}$Co isotope in a rhodium matrix (RITVERZ JSC, Russia) was used as a source of γ-radiation. The velocity scale was calibrated using the spectrum of sodium nitroprusside with further conversion to metallic iron (α-Fe).

## 3. Results and discussion

The Mössbauer spectrum of Fe-containing sample is a wide asymmetric doublet. The broadening and asymmetry of the absorption lines of the Mössbauer spectrum indicate the presence of several different positions of the iron environment in the sample under study, which differ from each other in the type of symmetry.

The value of the isomeric shift of the Mössbauer spectrum indicates the presence of the positions of the iron nuclei in the bivalent high-spin state in the sample under study.

For correct processing of Mössbauer spectrum, it is necessary to determine the processing model. To do this, three models were used, consisting of two, three or four subspectra describing the bivalent high-spin states of iron, Figure 1.

The types of the theoretical spectrum, the distribution curve of the fitting error, and the $\chi^2$ values for different processing models were compared to find the best model. It was established that the model with two subspectra (Figure 1, model A) was not suitable for describing the experimental spectrum ($\chi^2$ = 2.11), the model of three subspectra (Figure 1, model B) had a better value of $\chi^2$ = 1.68. However, the distribution of the error suggested that introduction of one more subspectrum is required for good description of the experimental spectrum. The four-subspectrum model (Figure 1, model C) for describing the divalent high-spin states of iron nuclei had $\chi^2$ = 1.55, but did not completely coincide with the experimental spectrum. The error distribution curve showed that it was necessary to use the subspectrum corresponding to the high-spin trivalent state of iron nuclei (not shown). Parameters of processing by different models of the Mössbauer spectrum presented in Table I.

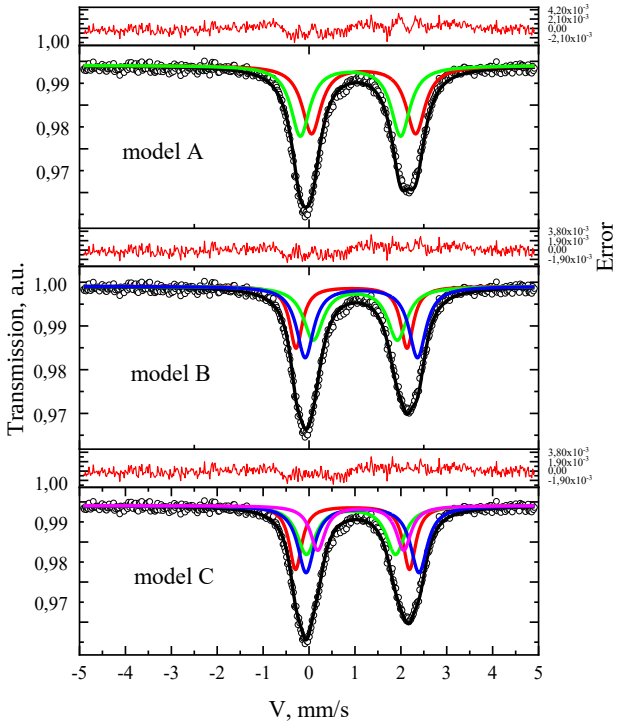


***Fig. 1.*** *Models for processing two valence high-spin states in the Mössbauer spectrum of Fe-containing sample and the values of the fitting errors. The models A, B, and C consist of two, three, and four doublets, respectively.*

***Table I.*** *Parameters of processing by different models of the Mössbauer spectrum**

| Model | $\delta$ (mm/s) | $\Delta$ (mm/s) | Relative area (%) | $\chi^2$ |
|---|---|---|---|---|
| *A* | 1.13 | 1.97 | 58 | 2.11 |
| | 1.18 | 2.53 | 42 | |
| *B* | 0.99 | 2.04 | 25 | 1.68 |
| | 1.18 | 2.71 | 17 | |
| | 1.22 | 2.13 | 58 | |
| *C* | 0.96 | 1.98 | 22 | 1.55 |
| | 1.19 | 2.26 | 33 | |
| | 1.19 | 2.74 | 21 | |
| | 1.21 | 1.85 | 24 | |

**Isomer shift (δ), quadrupole splitting (Δ). Values of δ are reported relative to α-Fe. Fitting error in the values of δ, Δ remained below 0.01 mm/s.*

## 4. Conclusions

A comparison of three models for processing the Mössbauer spectrum of titanium-free Fe-containing PEO coating has enabled one to find the number of subspectra required to describe the bivalent high-spin states of iron in the sample. It was also figured out that addition of subspectrum corresponding to the positions of iron in the trivalent high-spin state was necessary to fit experimental spectrum.

## Acknowledgements

The work was carried out within the framework of the State Order of the Institute of Chemistry of FEB RAS, projects Nos. 0205-2021-0003 (fabrication of PEO coating) and 0205-2021-0002 (Mössbauer spectroscopy investigations).

## References

[1] M. Kaseem, S. Fatimah, N. Nashrah, Y. Gun Ko. Progress in Materials Science **117**(2021)100735.

[2] V.S. Rudnev, A.Yu. Ustinov, I.V. Lukiyanchuk, P.V. Kharitonskii, A.M. Frolov, V.P. Morozova, I.A. Tkachenko, V.I. Sergienko. Doklady Physical Chemistry **428**(2009)189.

Sixth Asian School-Conference on Physics and
Technology of Nanostructured Materials
Vladivostok, Russia, 25 – 29 April, 2022



# A thin-layer hafnium oxide as auxiliary layer obtained by atomic layer deposition onto macroporous silicon for SERS

K. Girel[*,1,2], K. Litvinova[3], A. Burko[1,2], S. Dubkov[2], A.I. Savitskiy[2], D.V. Novikov[2], A. Tarasov[2], H. Bandarenka[1,2]

[1] Belarusian State University of Informatics and Radioelectronics, 6 P.Brovki st., Minsk, 220013, Belarus
[2] Institute of Advanced Materials and Technologies, National University of Electronic Technology, 1 Shokin Sq., Zelenograd, Moscow, 124498, Russia
[3] National University of Science and Technology Leninskiy Prospekt 4, NUST MISIS, Moscow, 119049, Russia

*e-mail: k.girel@bsuir.by

**Abstract.** This paper describes a technique for atomic layer deposition of thin-layer hafnium oxide as auxiliary layer on the external and internal surfaces of macroporous silicon. The silver immersion deposition was used for formation of the plasmon coating for SERS. The SERS activity of the obtained substrates was studied using the Ellman's Reagent as an analyte.

## 1. Introduction

Hafnium oxide (HfOx) is a material having good mechanical, thermal and chemical stability, high dielectric constant and high refractive index [1]. Hafnium oxide as a high-k dielectric opens new prospects not only for micro- and nanoelectronics, but also provides new opportunities for SERS spectroscopy.

At present, SERS spectroscopy solves problems not only of increasing the intensity Raman signal and the sensitivity, but also to improve chemically stability and biocompatibility. Obtaining renewable and reusable SERS-active substrates is difficult but extremely necessary task due to they will be expendable materials for SERS spectroscopy in the future. Various methods are used for the deposition of plasmonic metals on the surface of ordered porous matrices to form plasmonic structures with such properties.

The formation of an auxiliary layers by the atomic layer deposition (ALD) method can make it possible to increase the adsorption capacity of SERS-active substrates which also increases their sensitivity. The ALD provides accurate film thickness and greater area uniformity. The HfOx can be singled out, which has a high melting point and low thermal conductivity, which reduces the thermal effect on the SERS-active substrate under high-power laser radiation and ensures the morphological stability of the structure [2, 3].

## 2. Experiment

Electrochemical anodizing process was used to form a system of highly ordered pores. As initial substrates p-type monocrystalline silicon wafer of (100) orientation and 12 Ohm·cm resistivity was used.

The anodizing process was carried out in an electrolyte containing hydrofluoric acid (45 %) and dimethyl sulfoxide as a wetting agent mixed in a volume ratio of 10:46, respectively, at a current density of 8 mA/cm$^2$. Wafers were thoroughly cleaned from the organic pollution and the native $SiO_2$ before anodization.

A thin layer of the HfOx was deposited on the surface of porous silicon by the ALD method. The HfOx film was deposited at a stage temperature of 250°C and the temperature of the chamber walls was 130°C. The chemisorption process was carried out using the supply of two precursors: TEMAH $Hf[N(CH_2CH_3)(CH_3)]_4$ and $H_2O$. The pulse time for supplying the organometallic precursor and water was 15 s and 0,02 s, respectively. After the TEMAH precursor supply pulse, the reactor chamber was purged with argon for 6 s. The TEMAH temperature was 70 °C. The TEMAH is an organometallic liquid and sticky substance in order to avoid its sticking to the gas pipes the precursor supply pipes were heated. The temperature of the water container was 20°C, the water supply tube was heated to 120°C.

Silver was used as plasmon metal due to its strong plasmon properties. We used the immersion deposition of silver on the surface of macroporous silicon from an aqueous solution of 3 m$MAgNO_3$ and 0,05 M HF for 25 min at room temperature to fabricate a SERS-active substrates.

## 3. Results and discussions

Electrochemical anodizing method allowed to form macroporous silicon with diameter of pores from 500 to 1500 nm and 5 μm thickness. The surface layer of wall pore with a thickness of around 100 nm, which has a microporous structure, was etched in an HF-based solution. This was necessary due to the penetration of reagents during ALD occurred deeper and it leads to the formation of a thicker film of HfOx.

The study of the inner surface of macroporous silicon using TEM showed that oxide penetrates deep into porous silicon and evenly coats the pore walls. The oxide deposition rate was preliminary estimated on planar structures to form a layer 10 nm thick (Fig. 1).

It should be noted that the analysis of the substance distribution at the interface between the HfOx film and the Si substrate showed that the element atoms have a depth distribution and their mutual penetration is observed at the interface. This may be due to both the presence of diffusion processes during film growth and «island» growth with an increase in surface roughness.

On the surface of macroporous silicon coated with a layer of the HfOx a developed structure with silver nanoparticles and silver dendrites was formed. Silver structures were deposited predominantly on the external surface of the macroporous silicon. The silver dendrites were directed both vertically upwards and along the microporous silicon surface. The size of silver branches reached up to 10 μm. The size of particles located on the

surface around pores was varied from 20 nm to 1 μm were formed (Fig.2).

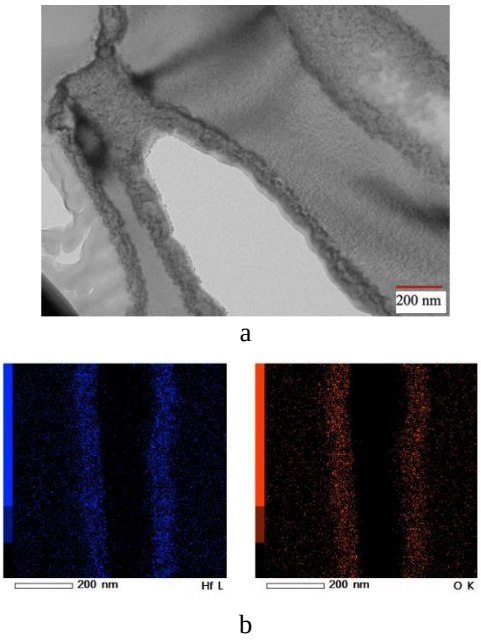


a

b

***Fig. 1.*** *Images of macroporous silicon after deposition of hafnium oxide, obtained using TEM (a) and EDX (b).*

Such a developed structure of silver particles and dendrites contributes to the appearance of a greater number of so-called «hot spots» which is favorable for increasing the Raman signal. Study of SERS-activity was performed by Raman confocal microscope Confotec NR500 (Sol Instruments, Belarus).

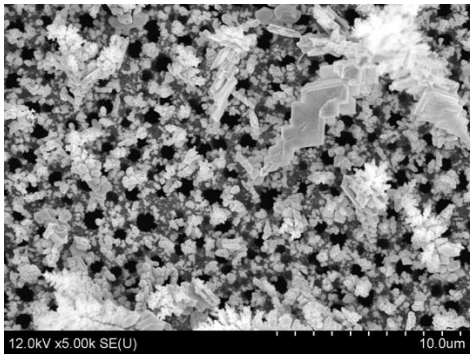


***Fig. 2.*** *SEM image of macroporous silicon /HfOx surface after silver deposition.*

The SERS spectra were recorded using excitation laser radiation with a wavelength of 473 nm. Preliminary study of SERS-activity was showed good and stability Raman signal which has been confirmed using DTNB (Ellman's Reagent (5,5-dithio-bis-(2-nitrobenzoic acid)) as analyte with a concentration of $10^{-5}$ M.

## 4. Conclusions

In the result of this work SERS-active substrates which consist of macroporous silicon, HfOx as auxiliary layer, silver nanoparticles and dendrites were formed.

It is assumed that the presence of an auxiliary layer of hafnium oxide will increase the stability of the Raman signal during the measurement, and will allow reduce the local heating, which this can lead to the destruction of the analyte, which greatly complicates the analysis of its spectrum. We obtained good spectrum corresponding to DTNB at each point of the map taken on an area of 48x48 μm.

## Acknowledgements

The research was supported by BRFFR and RFBR (projects №T21PM-136, №20-58-04016).

## References

[1] M.F. Al-Kuhaili Optical Materials **27**(2004)383–387.
[2] Yang, L., Wei, Y., Song, Y., Peng, Y., Yang, Y., & Huang, Z. Materials and Design **193**(2020)108808.
[3] S. Wang, S. Zoub, S. Yang, H. Wu, J. Jia, Y. Li, Z. Zhang, J. Jiang, M. Chu, X. Wang Sensors and Actuators B **265**(2018)539–546.

# Anti-icing fluoropolymer-containing composite coatings on titanium alloys

E.A. Belov*, K.V. Nadaraia, D.V. Mashtalyar, S.L. Sinebryukhov, S.V. Gnedenkov
Institute of Chemistry FEB RAS, 159 pr. 100-letiya Vladivostoka, Vladivostok 690022

*e-mail: belov_eal@mail.ru

**Abstract.** Composite coatings were formed on titanium alloy, obtained by a combination of the PEO method and the application of polytetrafluoroethylene, providing an anti-icing properties. The use of a commercial suspension F-4d made it possible to obtain coating with a smooth polymer-containing surface, which made it possible to reduce the adhesion strength of ice in comparison with the base PEO layer by more than an order of magnitude. The use of an alcoholic suspension of superdispersed polytetrafluoroethylene made it possible to reduce the adhesion of ice to the surface 6 times compared to the base PEO layer.

## 1. Introduction

Icing is one of the most serious hazards for aviation, marine, and other heavily loaded structures in the Far North [1,2].

Thus, preventing the formation of an ice crust on the surface of an object is one of the important tasks in the development of protective coatings for marine equipment and oil platforms that will operate in the Arctic region [3].

Ice-phobic coatings in most cases are surfaces with a developed structure and superhydrophobic properties. However, due to the destruction of their structure, they are not durable and in conditions of ice fog and supercooled suspension, their morphology, which can be destroyed under these conditions, is the main problem.

Thus, to protect structures made of metal alloys, another direction can be used, in the form of the use of flat surfaces and films that prevent ice fixing.

## 2. Experiment

VT1-0 commercially pure titanium (Ti – 98.6 wt.%, impurities – 1.4 wt.%) was used as the substrate material for the manufacture of samples. The dimensions of the samples were 50×50×1 $mm^3$. Before applying coating, the samples were mechanically processed.

The coating was formed by plasma electrolytic oxidation in a phosphate electrolyte (20 g/L $Na_3PO_4$). The process was carried out in two stages using the potentiodynamic mode of treatment. In the first stage, the potentiodynamic voltage increased from 80 to 300 V during 120 s. In the second stage, the voltage decreased from 300 to 240 V within 580 s. During the process, the temperature was maintained at about 8°C.

The composite coating (CC-3X F-4d) was formed by dipping into an F-4d commercial aqueous suspension at an angle of 75°, holding in the suspension, and removing it at a rate of 60 mm/min. Then, the samples were subjected to heat treatment at 365°C for 20 min.

The second method consisted in vertical immersion of the samples in an alcohol suspension of superdispersed polytetrafluoroethylene (SPTFE) for 10 s, after which they were removed and dried in air. The coated samples (CC-3X – SPTFE) were heat treated in an oven at 315°C for 15 min [4]. This procedure was repeated triple.

To determine the adhesion of ice to the surface, ice column shear studies were carried out. An ice column with a diameter of 30 mm and a volume of 7 ml was formed on the sample surface at a -10°C .

The sample was then fixed and an ice column was subjected to an increasing load parallel to the surface of the sample.

## 3. Results and discussions

***Table I.*** *Results of ice adhesion strength tests for samples with different surface treatment.*

| Coating type | Ice adhesion strength (kPa) |
|---|---|
| *Base PEO-layer* | 653 |
| *CC-3X F-4d* | 5 |
| *CC-3X – SPTFE* | 107 |

The analysis of obtained results showed that the formed smooth coating with the use of F4-d suspension has the smallest adhesion force with an ice. The ice shear force decreased by more than 2 orders of magnitude in comparison with the base PEO-layer. When using SPTFE, the adhesive force also decreased by more than 6 times compared to the PEO-coating. Apparently, this is the result of the less surface free energy of composite coatings in comparison with PEO-layers.

## 4. Conclusions

In the course of work, the obtained composite coatings showed a high decrease in ice adhesion to the surface in comparison with the protective coating due to a decrease in surface free energy and obtaining a more uniform layer.

## Acknowledgements

The formation of composite coatings and testing of the adhesion strength of ice to the coating were carried out within the framework of a grant from the Russian Foundation for Basic Research (No. 19-29-13020).

## References

[1] A. Barabadi, A.H.S. Garmabaki, R. Zaki, Cold Reg. Sci. & Tech. 124 (2016) 77-78.
[2] S. Hildebrandt, Q. Sun, J. of Wind Engin. & Ind. Aerodyn. 219 (2021) 104795.
[3] Z. Zhang, L. Ma, Y. Liu, J. Ren, H. Hu, Cold Reg. Sci. & Tech. 181 (2021) 103196.
[4] D.V. Mashtalyar, K.V. Nadaraia, I.M. Imshinetskiy, E.A. Belov, V.S. Filonina, S.N. Suchkov, S.L. Sinebryukhov, S.V. Gnedenkov, Appl. Surf. Sci. 536 (2021) 14976.

Sixth Asian School-Conference on Physics and
Technology of Nanostructured Materials
Vladivostok, Russia, 25 – 29 April, 2022



# Radiation induced defects of zinc oxide particles star and flower shapes

A.N. Dudin*[,1], V.I. Iurina[1], V.V. Neshchimenko[1,2], Li Chundong[2]
[1] Amur State University, Blagoveshchensk, Russia
[2] Harbin Institute of Technology, Harbin, China

*e-mail: andrew.n.dudin@gmail.com

**Abstract.** The results of modeling a proton beam with energies of 100 keV on zinc oxide particles star and flower shapes in the Geant4 software package are presented. A high ability to accumulate primary defects was demonstrated for star-type particles in comparison with flower-type particles. A comparative analysis of the calculated data on the study of defects as a result of modeling with experimental data is carried out.

## 1. Introduction

Studies of the radiation resistance and optical properties of pigments in thermal control coatings based on the direct-gap semiconductor II-IV of the semiconductor group ZnO have shown that the particle morphology plays an important role in the accumulation of radiation defects [1-2]. Changes in the size and shape of the irradiated particles, in addition to the occurrence of nanoeffects, with characteristic sizes in the nanometer range, in some cases, lead to an increase in the specific surface area of the particles and to a change in the processes of formation of point defects.

## 2. Experiment

Modeling was carried out in the GEANT4 software package, the star-type target geometry is a set of 13 cylinders 0.25 μm in diameter, crossed with each other, with a total swept diameter of 5 μm. The geometry of the flower-type target was half a sphere with a radius of 3 μm with segments of spheres included in it, forming petals with a thickness of 0.05 μm. The particles under consideration were packed into an ensemble sized 35×35×14 μm for star type particles, 36×36×9 μm for flower type particles.

Irradiation was carried out relative to the normal to the target surface by a monoenergetic proton beam with an energy of 100 keV and a fluence of $5\times10^9$ $cm^{-2}$. The threshold displacement energy for the zinc atom was chosen to be 52 eV, for oxygen − 57 eV [3].

When modeling, the processes used in the QGSP_BIG_EMY physics set were taken into account, including: ionization of the medium, multiple scattering, elastic and inelastic scattering of hadrons, bremsstrahlung, etc.

The Frenkel defect concentration calculated in GEANT4 was determined using the modified Kinchin-Pisa formula [4]:

$$FP \sim \frac{E_{dis}}{2.5E_d} \quad (1)$$

where $E_d$ – is the threshold displacement energy, $E_{dis}$ – is the dissipated energy in nuclear collisions.

The comparison was made with synthesized ZnO particles of the star and flower types obtained by the hydrothermal method [5]. The SEM micrographs synthesized particles presented in Fig. 1. The average size of the synthesized star-type particles was 4-7 μm, flower-type particles – 4-8 μm. The average value of the specific surface area for star-type particles is 44.3 ± 2.9 $m^2g^{-1}$, for flower-type particles – 68.4 ± 6.6 $m^2g^{-1}$.

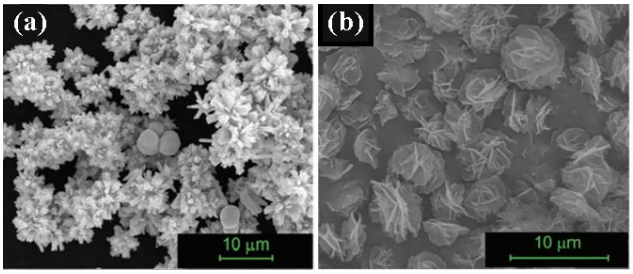


***Fig. 1.*** *SEM images of ZnO star (a) and flower (b) particles.*

The irradiation of the synthesized particles was carried out by protons with an energy of 100 keV with a fluence of $5\times10^{11}$ $cm^{-2}$ in a vacuum $5\times10^{-5}$ Pa, using a space simulator.

## 3. Results and discussions

Visualization of the process of passage of a proton beam with an energy of 100 keV with a fluence $5\times10^9$ $cm^{-2}$, through a particle of the star and flower type, is shown in Fig. 2 and 3, respectively.

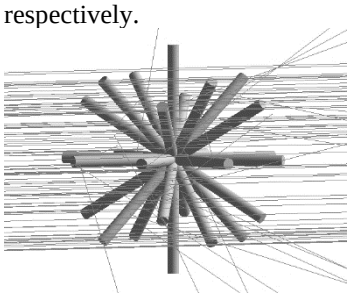

***Fig. 2.*** *The simulation in Geant4 zinc oxide particles star shape irradiated by protons.*

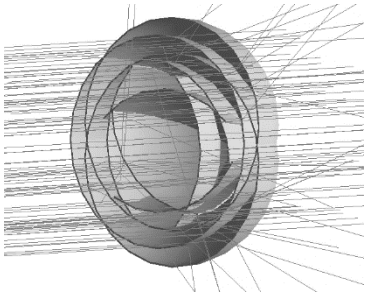

***Fig. 3.*** *The simulation in Geant4 zinc oxide particles flower shape irradiated by protons.*

The results of numerical calculations of the effect of radiation on a star-type particle give the proton mean free path equal to 1.41 Å The total number of primary knocked-on atoms (PKA) is $4.7\times10^6$ $cm^{-3}$. Concentration of formed primary defects (Frenkel pairs) – $1.88\times10^{17}$ $cm^{-3}$. For a particle of the flower type, similar values have the following form: mean free path – 1.65 Å; PKA – $1.3\times10^6$ $cm^{-3}$; concentration of primary defects – $4.82\times10^{16}$ $cm^{-3}$.

The reflectance spectra of the synthesized particles (Fig. 4) show a close match of the main absorption edge. The diffuse reflectance ($\rho_\lambda$) of flower-type particles is higher than that of star-type particles in the wavelength range from the edge of the main absorption to the near infrared (NIR) region. The difference between the spectra of synthesized particles in the near infrared region of the spectrum is due to free electrons and chemisorbed gases.

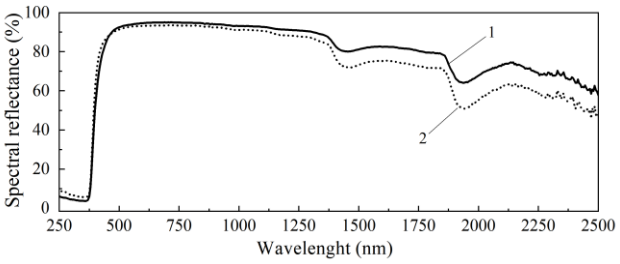


***Fig. 4.*** *Reflection spectra of synthesized particles like a flower (1) and a star (2).*

The induced absorption spectra (Fig. 5) of the synthesized particles, after irradiation with protons, show the main peak in the UV and visible spectral region. The induced absorption bands in the region from 3.5 to 2 eV of synthesized star and flower particles are similar in intensity and have a maximum value of 60%. In the near-IR region, there is a decrease in the induced absorption spectrum for flower-type particles, in comparison with star-type particles. The difference in the intensity of the absorption bands in this region reaches 5%.

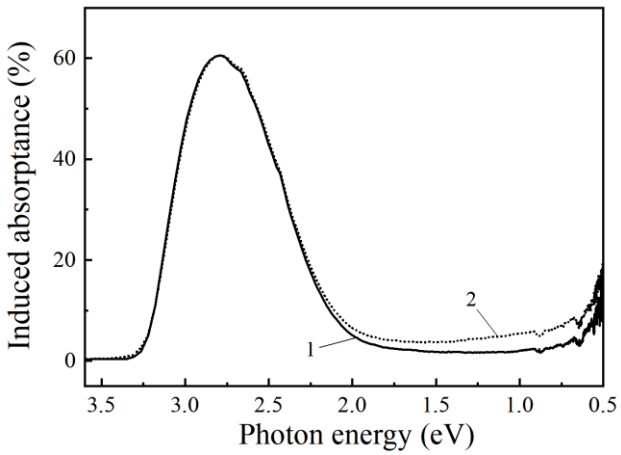


***Fig. 5.*** *Induced absorption spectra of synthesized particles like a flower (1) and a star (2)*

The ratio of intensities between different types of particles is associated with different concentrations of radiation defects $Zn_i$, $V_{Zn}$, $O_i$ and $V_O$ in different charge states, which are absorbed in different parts of the spectrum. The absorption of light quanta in the UV region is due to centers associated with $Zn_i$, but the absorption in the visible region of the spectrum with $V_{Zn}$, $O_i$, $V_O$ and related complexes $V_{Zn}$-$O_i$ and $V_{Zn}$-H, which is formed during the implantation of hydrogen into the crystal lattice of ZnO. Absorption intensity in the near infrared region of the spectra after irradiation increases due to the Urbach tail.

## 4. Conclusions

It has been established that ZnO particles of the flower type have a higher radiation resistance to the action of protons compared to ZnO particles of the star type This is indicated by the calculated values obtained in the simulation, which demonstrate a higher concentration of primary defects for star-type particles – $1.88\times10^{17}$ $см^{-3}$, compared to flower-type particles – $4.82\times10^{16}$ $cm^{-3}$. Also, synthesized flower-type particles demonstrate better reflectivity, which also indicates radiation resistance. The induced absorption spectra of the synthesized particles demonstrate a high concentration of induced defects for star-type particles, which directly correlates with the data obtained from the simulation. In conclusion, we can conclude that ZnO particles of the flower type are more radiation-resistant to the effects of protons compared to ZnO particles of the star type.

## References

[1] N. M. Flores, U. Pal, R. Galeazzi and A. Sandoval, RSC Adv. **4**(2014)41099
[2] A. Dudin, V. V. Neshchimenko, V. Iurina. J. Surf. Invest.: X-Ray, Synchrotron Neutron Tech. **14**(2020)823.
[3] K. Lorenz, E. Alves, E. Wendler, O. Bilani, W. Wesch, M. Hayes. Appl. Phys. Lett. **87**(2005) 191904.
[4] C. Leroy, P.G. Rancoita. WSPC **2**(2016)1344
[5] V. V. Neshchimenko, Chundong Li, M. M. Mikhailov, Jinpeng Lv. Nanoscale **10**(2018)22335.

Sixth Asian School-Conference on Physics and
Technology of Nanostructured Materials
Vladivostok, Russia, 25 – 29 April, 2022



# Characterization of titanium dioxide nanoparticles synthesized by hydrothermal method depending on subsequent cleaning approaches

I.V. Egelskii*, M.A. Pugachevskii, A.P. Kuzmenko
Southwest State University, 50 Let Oktyabrya St., 94, Kursk 305040, Russia

*e-mail: ive1996@yandex.ru

**Abstract.** Titanium dioxide nanoparticles were synthesized by the hydrothermal method at a temperature of 100 °C. The obtained particles are characterized by IR spectroscopy, scanning electron microscopy, X-ray diffractometry, and small-angle X-ray scattering technique. Various methods of treatment with solvents and thermal annealing were investigated to obtain nanoparticles with a given size and a minimum residual content of carbon compounds.

## 1. Introduction

Recently, researchers have been intensively developing new methods for producing titanium dioxide nanoparticles. Due to the unique physicochemical characteristics of this material [1], it can be used in many areas: from solar energy to systems for purification from organic contaminants [2-4].

It is known that there are three polymorphic modifications of titanium dioxide under normal conditions: anatase, brookite, and rutile [5]. The most promising for photocatalysis are the anatase and rutile phases. It has been determined that when the material is heated, anatase irreversibly transforms into a rutile form at temperatures of 450-650 °C [5, 6].

One of the perspective methods for obtaining nanoparticles is the hydrothermal synthesis, which is ordinary and cheap to implement, is suitable for getting a wide range of oxide materials, and allows receiving monodisperse nanopowders with adjusted particle size [7, 8].

It is worth noting that the final characteristics and properties of the synthesized nanoparticles significantly depend on the following methods of purifying the product from the residual components of the hydrothermal reaction. For example, changes in temperature conditions during hydrothermal treatment, as well as the use of various solvents, change the polymorphic modification of the samples [9]. Annealing at different temperatures changes the size, photocatalytic properties, and band gap of nanoparticles [6,10].

The variety of used cleaning methods leads to the need to accurately determine the most optimal treatment scheme from the point of view of obtaining particles with specified characteristics. That is why the purpose of this work is to study the effect of purification approaches on the dimensional characterization, elemental, and phase composition of hydrothermally synthesized titanium dioxide nanoparticles.

## 2. Experiment

Hydrothermal synthesis of titanium dioxide nanoparticles was carried out in an autoclave reactor OLT-PH Xiamen Ollital Technology with a volume of 50 ml, with the possibility of programmable temperature and pressure control. The precursor for TiO2 was Titanium (IV) butoxide, which was mixing with triethanolamine and distilled water. All components were placed in an autoclave bowl and mixing with a magnetic stirrer at 800 rpm for 15 minutes. Then there was gradual heating up to 100 °C for 30 minutes, after which the resulting substance was hold in an autoclave with isothermal mode for 24 hours. The resulting substrate was washed with various polar and non-polar solvents, spinning with a magnetic stirrer. Ethanol, isopropyl, hexane, chloroform were used as solvents, separately and with alternate washing by each one. The samples were drying at different washing steps at a temperature of 100-110 ºC to obtain a dry powder. Some of those samples were also subjected to thermal annealing in a furnace at a temperature of 500 °C.

The chemical composition was getting characterized on a Nicolet iSO50 infrared Fourier spectrometer. The morphology and sizes of TiO2 particles were studied using a JSM-6610LV scanning electron microscope. The phase composition was determined using a GBC EMMA X-ray diffractometer. The size and morphological compound were analyzed using a SAXSess Anton Paar small-angle X-ray diffractometer.

## 3. Results and discussions

According to the results of FTIR spectroscopy, spectra were obtained at each washing step. The spectral analysis results demonstrate the efficiency of substance washing after autoclave for separating organic components from titanium dioxide.

Phase analysis of the synthesized titanium dioxide nanoparticles was carried out. According to X-ray diffractometry results, the titanium dioxide nanoparticles had an anatase structure.

Figure 1 shows a SEM image of a sample after washing with ethanol, isopropyl, and hexane, followed by annealing in an oven at 500 °C. It can be seen from the figure that the synthesized titanium dioxide nanoparticles have a rounded shape and a characteristic average size of 23 nm. During thermal annealing, nanoparticles tend to form agglomerates over 100 nm in size.

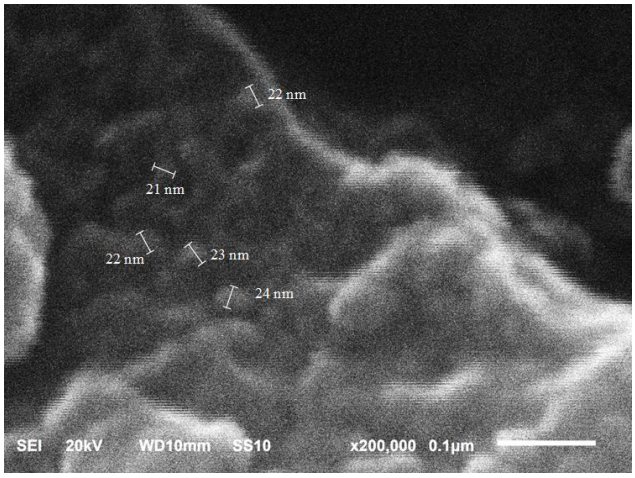


***Fig. 1.*** *Image of titanium dioxide nanoparticles after washing with ethanol, isopropanol, and hexane, followed by annealing in an oven at 500 °C.*

Table I shows the atomic weights of carbon, oxygen, and titanium in the samples before washing and under certain washing conditions with solvents and annealing. Sample N1 without washing and annealing has a 66% atomic mass of carbon. Sample N2 washed with ethanol, isopropanol, and after hexane without annealing contains more than 30% carbon. When using a combination of ethanol and isopropyl and annealing at 500 °C, the carbon content in sample N3 drops to 7.5%. Sample N4 was washed with ethanol, isopropyl, and hexane and then annealed at 500 °C. It has a carbon ratio of about 5%. Sample N5 is identical to N4, except it was filtering in distilled water. As a result, N5 contains closer to 4% of the carbon. Thus, combined washing with polar and non-polar solvents in combination with thermal annealing can significantly improve the process of purifying titanium dioxide powder from carbon compounds.

***Table I.*** *Atomic content (%) of elements in samples.*

| Element | N1 | N2 | N3 | N4 | N5 |
|---|---|---|---|---|---|
| *C* | 68.89 | *30.53* | 7.53 | 4.79 | 4.36 |
| *O* | 30.13 | *52.45* | 61.47 | 61.09 | 54.69 |
| *Ti* | 0.98 | *17.02* | 31.00 | 34.12 | 40.94 |

The results of studies by small-angle X-ray diffractometry show that the synthesized titanium dioxide nanoparticles have a size of 20 nm (according to Guinier SAXS approach for a homogeneous sphere). We also analyzed the distribution functions of paired distances for the samples.

Comparison of the results of Guinier analysis and the distribution function of paired distances indicates the formation of agglomerates of various sizes from the initially synthesized titanium dioxide nanoparticles.

## 4. Conclusions

Titanium dioxide nanoparticles with an average size of 23 nm were obtained by hydrothermal synthesis at low temperatures up to 100 °C. Phase analysis established that the particles have an anatase structure. Their structure remains unchanged during subsequent temperature treatment up to 500 °C. It was proved that combined washing with polar and non-polar solvents in conjunction with thermal annealing leads to a significant decrease in the content of carbon (up to 4%) compounds in the synthesized product.

## Acknowledgements

This study was carried out with the financial support of the Russian Foundation for Basic Research within the framework of scientific project no. 20-02-00599, as well as with the support of the Ministry of Education and Science of the Russian Federation, s/o 2020 no. 0851-2020-0035.

## References

[1] Sungur S Handbook of Nanomaterials and Nanocomposites for Energy and Environmental Applications (Cham: Springer International Publishing) **1**(2020)1-18.
[2] Tasić N et al *Electrochim Acta* **210(**2016)606–614.
[3] Sousa V S et al *Water Res* **109**(2017)1–12.
[4] Pugachevskii M A *Technical Physics Letters* **39**(2013)36-38.
[5] Muscat J *Physical review* **65**(2002)224112.
[6] Pugachevsky M A *Journal of Applied Spectroscopy* **79**(2012)834-837.
[7] Schmidt H Applied Organometallic Chemistry **15**(2001)331–343.
[8] Dubey R S *Mater Lett* **215**(2018)312–317.
[9] Reyes-Coronado D et al *Nanotechnology* **19**(2008)145605.
[10] Huang F et al C Bulletin of the Korean Chemical Society **35**(2014)2512–2518.

Sixth Asian School-Conference on Physics and
Technology of Nanostructured Materials
Vladivostok, Russia, 25 – 29 April, 2022



# *In vitro* corrosion performance of bioresorbable Mg-Ca alloy with hydroxyapatite-containing protective coating

V.S. Filonina*, A.S. Gnedenkov, S.L. Sinebryukhov, A.N. Minaev, S.V. Gnedenkov
Institute of Chemistry FEB RAS, 159 Pr. 100-letiya Vladivostoka, Vladivostok, 690022

*e-mail: filonina.vs@gmail.com

**Abstract.** The paper presents the results of the study of protective properties of hydroxyapatite-containing coatings obtained on the surface of bioresorbable Mg-0.8Ca magnesium alloy using plasma electrolytic oxidation (PEO). Using traditional electrochemical methods (EIS, PDP, OCP) it was established that the PEO treatment of Mg-0.8Ca alloy leads to a significant increase in corrosion resistance of the material. The forming of an oxide layer on a magnesium alloy contributes to a decrease in corrosion current density ($I_C$) more than three times. The increase in the impedance modulus measured on lowest frequency ($|Z|_{f=0.1\ Hz}$) for a coated material was two times compared to an uncoated one.

## 1. Introduction

Features of magnesium degradation process determines its great prospects in application as an implant material. Unfortunately, rapid and heterogeneous corrosion as well as an alkalization of a surrounding media obstruct the expansion of magnesium scope [1],[2]. Improving the corrosion resistance of bioresorbable magnesium-based materials will make it possible to control the degradation process of the material in the human body in order to ensure matching the rates of implant resorption and osteogenesis. The most common way to improve both corrosion resistance and biocompatibility of magnesium is to form protective coatings, containing inorganic components of a human bone – Ca, P, Mg and their compounds, including hydroxyapatite. According to [3], magnesium has a positive effect on the activity of osteoblasts and osteoclasts, and therefore on bone growth. In turn, the release of calcium ions and phosphates from surface layer compounds forms a saturated ionic solution at the interface. In this case there is an ion exchange between the implant material and the patient's bone, some of which will be deposited on the bone matrix, forming new bone tissue.

## 2. Experiment

The experiments were carried out on Mg-0.8Ca alloy samples (wt. %: 0.8 – Ca, balance – Mg) with a size of 15×30×1 mm. Standardization of samples` surface was realized through grinding with Si-C abrasive paper with gradual reduction of a grain size to 14-20 μm (P1000) with following rinsing in isopropyl alcohol and drying in desiccator. Plasma electrolytic oxidation (PEO) coating was formed in a combined bipolar mode with current dencity of ≤ 0.75 A $cm^{-2}$. Duty cycle was equal to 1, total oxidation time reached 120 s. The composition of the formed coating was studied via XRD method using a SmartLab diffractometer (Rigaku, Japan). The measurements were carried out in the range 2θ = 4°–90° with a step of 0.01°. To evaluate the corrosion resistance of formed samples, electrochemical measurements (including potentiodynamic polarization (PDP), electrochemical impedance spectroscopy (EIS) and monitoring of open circuit potential (OCP) change) were realized. Experiments were carried out using a Versa STAT MC electrochemical system (Princeton Applied Research, USA) and the electrolyte was minimal essential medium (MEM) solution (a synthetic cell culture medium).

## 3. Results and discussions

As a result of the PEO process, ceramic-like coatings with high heterogeneity of the surface relief were obtained on the surface of a Mg-0.8Ca bioresorbable magnesium alloy. XRD analysis showed that the main component of the PEO-coating was hydroxyapatite. The other component of protective layer was periclase. According to data obtained by PDP and EIS, the formation of a PEO-layer provides the material an advanced corrosion resistance. The corrosion current density ($I_C$) for a coated sample ($I_C$ = $2.8 \cdot 10^{-6}$ A·$cm^{-2}$) are more than 3 times lower than the ones for an uncoated Mg-0.8Ca ($I_C$ = $9.5 \cdot 10^{-6}$ A·$cm^{-2}$). The results of the analysis of electrochemical impedance spectroscopy data also make it possible to confirm the higher corrosion resistance of the sample with a PEO-coating, compared to the material without a protective layer. The values of the impedance modulus measured at a lowest frequency ($|Z|_{f=0.1\ Hz}$) during exposure in the MEM for a sample with a PEO layer are more than 2 times higher ($|Z|_{f=0.1\ Hz}$ = $1.7 \cdot 10^{4}$ Ω·$cm^{-2}$) than the value for uncoated Mg-0.8Ca ($|Z|_{f=0.1\ Hz}$ = $8.1 \cdot 10^{3}$ Ω·$cm^{-2}$). For the coated sample during 42 h of exposure to MEM there is an increase in the diameter of the half-cycle on Nyquist plot. This is due to the formation of a Ca-P film of corrosion products of the sample (including PEO-layer and substrate material) and components of the MEM, which leads to sealing the pores of the PEO-layer. For comparison, uncoated material is characterized by an increase in these parameters only during the first 30 h of exposure, then protective properties of the surface layer decrease noticeably, which is associated with the intensification of the corrosion process, leading to the destruction of the Ca-P compounds film.

## 4. Conclusions

The way to improve the corrosion resistance of bioresorbable magnesium alloy Mg-0.8Ca was developed. Formation of the hydroxyapatite-containing oxide layers leads to a significant increase in the $I_C$ and a decrease in $|Z|_{f=0.1\ Hz}$. Based on the analysis of the obtained data, the prospects for use of calcium-phosphate PEO-coatings on a bioresorbable magnesium alloy for the needs of implant surgery were established.

**Acknowledgements**

This work was supported by the Grant of Russian Science Foundation (project no. 21-73-10148, https://rscf.ru/en/project/21-73-10148/).

**References**

[1] A. S. Gnedenkov, D. Mei, S. V. Lamaka, S. L. Sinebryukhov, D. V. Mashtalyar, I. E. Vyaliy, M. L. Zheludkevich, S. V. Gnedenkov Corr. Sci **170** (2020)
[2] A.S.Gnedenkov, S.L.Sinebryukhov, V.S.Filonina, V.S.Egorkin, A.Yu.Ustinov, V.I.Sergienko, S.V.Gnedenkov Journal of Magnesium and Alloys (2021) in press.
[3] R. Sammons Hydroxyapatite (HAp) for Biomedical Applications (2015).

Sixth Asian School-Conference on Physics and
Technology of Nanostructured Materials
Vladivostok, Russia, 25 – 29 April, 2022



# Effect of heat treatment on the morphology and composition of Silicon-Germanium nanocomposite

I.M. Gavrilin*,[1], A.A. Dronov[1], N. Grevtsov[2], A.V. Pavlikov[1], E. Chubenko[2], V. Bondarenko[2]

[1] National Research University of Electronic Technology (MIET), Bld. 1, Shokin Square, Zelenograd, 124498, Moscow, Russia

[2] Belarusian State University of Informatics and Radioelectronics, P. Brovki str. 6, Minsk 220013, Belarus

*e-mail: gavrilin.ilya@gmail.com

## 1. Introduction

Film structures based on $Si_xGe_{1-x}$ are widely used in high-temperature thermoelectric converters, which have high stability and high efficiency in the temperature range 800-1100 °C, which provides a wide range of their application. For example, such materials are used to utilize heat removed during various high-temperature processes [1]. Also, $Si_xGe_{1-x}$ films are used in optoelectronic devices [2].

However, given the high cost of crystalline Ge and its gaseous precursors, compounds with a low Ge concentration, which do not have a combination of electrophysical and physicochemical parameters that are optimal for thermoelectric conversion, are usually used to obtain $Si_xGe_{1-x}$ alloys.

In [3], a new approach is proposed to the formation of $Si_{1-x}Ge_x$ films. This approach includes electrochemical processes of the formation of porous silicon (por-Si), electrochemical deposition of low-melting metals, and Ge. When pores are filled with germanium at a given porosity, por-Si allows to control of the ratio of Ge and Si in the initial Si/Ge nanocomposite and, as a consequence, the Ge concentration in the final $Si_{1-x}Ge_x$ alloy after heat treatment at 950°C.

This paper presents the effect of heat treatment on the morphology and composition of Silicon-Germanium nanocomposite.

Por-Si has been obtained by anodizing KES-0.01 (100) plates in a solution consisting of HF (45%), $H_2O$, and isopropanol taken in a volume ratio of 1:3:1. Anodizing has been carried out at a current density of 70 mA/cm$^2$ for 30 s. The electrochemical deposition of indium has been carried out from a solution of $In_2(SO_4)_3$, $H_2O$, and $Na_2SO_4$ taken in a mass ratio of 6:300:1 at 0.5 mA/cm$^2$ for 60 s.

Electrochemical deposition of Ge NWs has been performed in a three-electrode cell, as described in previous work [4]. A platinum ring has been used as a counter electrode; a standard silver chloride electrode has been used as the reference one. The solution has been contained 0.05 M $GeO_2$, 0.5 M $K_2SO_4$, and 0.5 M $C_4H_6O_4$. The deposition process has been performed at a potential of -1.3 V (vs. Ag/AgCl).

To obtain $Si_{1-x}Ge_x$ films, the samples have been annealed at different temperatures and time periods in an argon atmosphere.

The morphology and composition of the samples have been investigated by scanning electron microscopy (SEM), Raman spectroscopy, and X-ray diffraction.

Analysis of the SEM images of the obtained samples has been showing that the porous layer and Ge nanowires are thermally stable up to 950°C for 10 min. However, at a temperature of 950°C, the Ge nanowires located on the surface of the porous layer begin to melt. The results of SEM images of the morphology of the obtained samples after annealing at a temperature of 950°C for various times have been shown the time process of alloying of porous silicon and Ge nanowires under these conditions is about 120 minutes. The results allow the stages of melting to be established. First of all, the Ge nanowires located on the surface of porous silicon begin to melt. Then the Ge nanowires located in the pores of silicon begin to melt and alloy with the porous silicon matrix. With longer annealing, the structures are completely alloyed.

The results of SEM images of the morphology of the obtained samples with a high Ge content have shown that an increase in the amount of Ge reduces the alloying temperature of porous silicon and Ge nanowires. Partial alloying of Ge nanowires with porous silicon occurs already at 750°C.

Thus, the data obtained will make it possible to establish the features of the $Si_{1-x}Ge_x$ alloy formation mechanism, which will facilitate the creation of film structures with a high content of Ge for use in thermoelectric devices.

## Acknowledgments

This research was financially supported by the Russian Science Foundation (Project no. 20-19-00720).

## References

[1] A. Usenko, D. Moskovskikh, M. Gorshenkov, A. Voronin, A. Stepashkin, S. Kaloshkin, D. Arkhipov, V. Khovaylo. Scripta Materialia, 127(2017)63.

[2] C. Kriso, F. Triozon, C. Delerue, L. Schneider, F. Abbate, E. Nolot, D. Rideau, Y.-M. Niquet, G. Mugny, C. Tavernier. Solid-State Electronics. 129(2017)93.

[3] I. Gavrilin, N. Grevtsov, A. Pavlikov, A. Dronov, E. Chubenko, V. Bondarenko, S. Gavrilov. Materials Letters. 13(2022)1.

[4] I. Gavrilin, D. Gromov, A. Dronov, S. Dubkov, R. Volkov, A. Trifonov, N. Borgardt, S. Gavrilov. Semiconductors. 51(2017)1067.

Sixth Asian School-Conference on Physics and
Technology of Nanostructured Materials
Vladivostok, Russia, 25 – 29 April, 2022



# Atomic and electronic structure of the $YFeO_3$ surface with oxygen vacancies

A.A. Gnidenko*, P.G. Chigrin
Khabarovsk Federal Research Center Institute of Materials Science of FEB RAS, 153 Tihookeanskaya St., Khabarovsk 680042, Russia

*e-mail: agnidenko@mail.ru

**Abstract.** The atomic and electronic structure of $YFeO_3$ surfaces at the formation of oxygen vacancies are investigated by the methods of quantum-mechanical calculations. The dependence of the formation energy of surface oxygen vacancy on its concentration and type of surface is shown.

## 1. Introduction

In the last two decades, complex oxides with a perovskite structure ($ABO_3$) have become the subject of intensive research worldwide. The field of application of these materials is very wide: various types of sensors and detectors, solar cells, photocatalysts and solid oxide fuel cells [1-3]. The functional properties of these compounds are mostly determined by stoichiometry and structural changes within $ABO_3$. It was found that the defect formation in the crystal lattice of $ABO_3$ leads to a significant increase in catalytic activity, while the oxygen non-stoichiometry of $YFeO_{3-\delta}$ can reach $\delta = 0.25$. Perovskite compounds can be used as alternative multifunctional catalysts for the neutralizing of diesel gases.

It should be noted that vacancies on the perovskite surface are filled with oxygen from the bulk of the crystal. Thus, the influence of the structural characteristics of perovskite on the mobility, surface/volume reactivity of oxygen, and catalytic activity in carbon oxidation is of great interest for fundamental research. In the present work yttrium orthoferrite ($YFeO_3$) was considered, the atomic and electronic structure of this perovskite at the formation of oxygen vacancies on the surface was studied using modern computer simulation methods.

## 2. Methods and calculation parameters

Quantum Espresso software package [4], based on the density functional theory and the pseudopotential method, was used to perform quantum mechanical calculations. The exchange-correlation contribution to the total energy was described by the generalized gradient approximation (PBE). Cutoff energy of the plane wave basis was 60 Rydberg. Uniform k-point grids were specified by Monkhorst-Pack procedures and varied depending on the size of the supercell. Ultrasoft pseudopotentials for yttrium, iron, and oxygen were taken from the Quantum Espresso pseudopotential database and were tested for a correct description of the properties of the crystal lattices of Y and Fe, as well as of the $O_2$ molecule.

Perovskites $ABO_3$ (where B = Fe) are often antiferromagnets, the equilibrium configuration for $YFeO_3$ corresponds to the *G*-type antiferromagnetic state, which is consistent to the literature data. Hubbard correction (DFT+U) was applied into the calculations for adequate description of strongly localized *3d*-states of Fe.

## 3. Results and discussions

For constructing slab, we took a primitive orthorhombic cell of $YFeO_3$, which contains 4 structural units (20 atoms in total). We considered the facets of the primitive cell, thus we obtained surfaces with indices (001), (010) and (100). We used an asymmetric slab model with fixed lower atomic layers. The vacuum gap in our calculations was about 14 Å. The surface energy was calculated as a difference between the slab energy before ($E_{unrel.slab}$) and after ($E_{rel\_slab}$) atomic relaxation, reduced to a unit of surface area ($S$):

$$E_{surf} = \frac{E_{unrel\_slab} - E_{rel\_slab}}{S} \quad (1)$$

The calculated values of surface energies are given in Table I.

***Table I.*** *Surface energies of $YFeO_3$ (001), (010) and (100)*

| Surface | Area, $m^2$ | Layers number | Surface energy, $J/m^2$ |
|---|---|---|---|
| *001* | $4.36 \cdot 10^{-19}$ | *5* | 0.97 |
| *010* | $3.01 \cdot 10^{-19}$ | *9 ($FeO_2$)* | 1.05 |
| | | *9 (YO)* | 1.31 |
| *100* | $4.11 \cdot 10^{-19}$ | *5* | 1.11 |

For (001) and (100) surfaces it had been shown that the difference in surface energy between 5- and 7-layer slabs is only 0.01 $J/m^2$. The number of layers in the (010) slab is 9, because in this direction, the linear size of the unit cell is larger. For the direction [010], the atomic layers consist of either Fe and O atoms or Y and O atoms. Our calculations showed that the formation of a ($FeO_2$) surface is more favourable, the energy difference is 0.3 $J/m^2$. Further we considered only this type of (010) surface.

In the simplest approximation, taking the chemical potential of oxygen as half of the $O_2$ molecule total energy, the formation energy of a surface vacancy is determined as follows:

$$E_{form} = E_{slab} - E_{slab+vac} + \frac{1}{2}E_{O_2} \quad (2)$$

where $E_{slab}$ is the energy of the $YFeO_3$ slab, $E_{slab+vac}$ is the energy of the slab with oxygen surface vacancy, $E_{O2}$ is the energy of an isolated $O_2$ molecule. The obtained values are shown in Table II.

***Table II.*** *The energies of oxygen vacancy formation for different types of $YFeO_3$ surfaces*

| Surface | Area, $m^2$ | $E_{form}$, eV |
|---|---|---|
| *001* | $4.36 \cdot 10^{-19}$ | 2.40 |
| | $17.45 \cdot 10^{-19}$ | 1.74 |
| *100* | $4.11 \cdot 10^{-19}$ | 1.79 |
| | $16.44 \cdot 10^{-19}$ | 0.81 |
| *010* | $3.01 \cdot 10^{-19}$ | 3.51 |
| | $12.03 \cdot 10^{-19}$ | 3.33 |

For each surface, we considered two cases, which were differed from each other by the cross-section area. In contrast to the description of bulk oxygen vacancies, we cannot operate in terms of oxygen non-stoichiometry; therefore, and here and below we will speak of high and low concentrations of surface oxygen vacancies. Figure 1**Ошибка! Источник ссылки не найден.** shows the atoms forming the surface layer for (001), (100), and (010); the second and third images in each row correspond to high and low vacancy concentrations. To create vacancy on the surface we removed oxygen atom with the highest position in the direction of the slab orientation; for all surfaces it was an oxygen atom from the Fe–O–Fe bridge. Thus, the formation of an oxygen vacancy leads to the formation of a Fe-Fe bond on the surface (its length varies from 2.62 to 2.82 Å)**Ошибка! Источник ссылки не найден.**

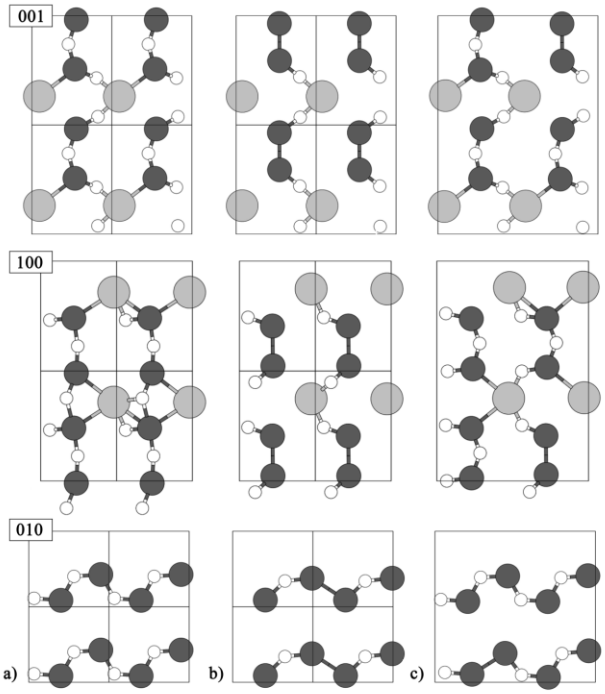


***Fig. 1.*** *Atoms of $YFeO_3$ surface layers: a) without oxygen vacancy; b) one vacancy per unit cell cross-section; c) one vacancy per cell area increased by 4 times.*

It was found that the formation energy of a surface oxygen vacancy decreases with an increase of the cross-section area, i.e. a decrease in the vacancy concentration. Due to the specific arrangement of atoms on the $YFeO_3$(010) surface layer, the formation energies do not differ too much from the previously calculated values for "bulk" oxygen vacancies (3.13-3.79 eV) [5]. However, for the (001) and (100) surfaces, the vacancy formation energies are significantly lower; in the case of low concentration on the (100) surface, the lowest value was obtained, 0.81 eV.

For a more details, we analyzed the density of electronic states (DOS) for all considered cases. The formation of an oxygen vacancy leads to the appearance of levels in the band gap, as well as to a partial delocalization of the *3d* states of Fe, in the case of high concentration this is more pronounced. At the vacancy formation on the $YFeO_3$ (010) surface in addition to the sharp peak corresponding to the *3d* states of bulk Fe atoms, there are distributed states corresponding to the surface Fe atoms. In the case of the (001) and (100) surfaces there is a partial splitting of the peak corresponding to the bulk states, this occurs due to the formation of the Fe-Fe bond when oxygen is removed from the surface and the surface layers are included in the atomic relaxation process.

## 4. Conclusions

Computer simulation methods have been used to study changes in the atomic and electronic structure at the formation of oxygen vacancies on different surfaces of yttrium orthoferrite. It was found that there is a tendency to a decrease in the formation energy with an increase in the surface area, which corresponds to a decrease in the vacancy concentration. The smallest value of 0.81 eV was obtained for the (100) surface, which is approximately four times less than the formation energy of a bulk oxygen vacancy. An analysis of the electronic structure showed a partial delocalization of the *3d* states of Fe atoms at the surface formation process; the formation of an oxygen vacancy, due to the appearance of Fe-Fe bond, enhances this effect.

## Acknowledgements

This research was supported in through computational resources provided by HPC cluster «Akademik V.M. Matrosov» (Irkutsk) [6].

## References

[1] Ch. H. Li, K. Ch. K. Soh, P. Wu. J. Alloys Compd. **372** (2004) 40.
[2] J. Shi, L. Guo. Progress in Natural Science: Materials International **22** (2012) 592.
[3] A. Chroneos, R. V. Vovk, I. Goulatis, L. I. Goulatis. J. Alloys Compd. **494** (2010) 190.
[4] P. Giannozzi, S. Baroni, N. Bonini, M. Calandra M, et al. J. Phys.: Condens. Matter. **21** (2009) 395502.
[5] A.A. Gnidenko, P.G. Chigrin, E.A. Kirichenko. Solid State Phenomena. **312** (2020) 355.
[6] Irkutsk Supercomputer Center of SB RAS, URL: http://hpc.icc.ru

# Structural and physical properties of NbOx thin films deposited by reactive magnetron sputtering

E. Grinakovskiy*,[1], E.A. Lebedev[1], S. Dubkov[1], I. Mikhailov[2], D. Gromov[1]

[1] National Research University of Electronic Technology "MIET", 124498 Moscow, Russia
[2] Federal State Budgetary Institution of Science Institute of Nanotechnologies of Microelectronics of the Russian Academy of Sciences "INME RAS" 119911 Moscow, Russia

*e-mail: theretribution25@gmail.com

**Abstract:** Recently, research has revealed many interesting physicochemical properties of niobium oxide. This work is devoted to the study of the structural and physical properties of thin films of niobium oxide obtained by reactive magnetron sputtering in an oxygen environment. To change the phase of niobium oxide, the oxygen pressure in the vacuum chamber was changed. Auger electron spectroscopy was used to estimate and detect oxygen in the structure. Using this method, unbound oxygen was detected in the structures.

## 1. Introduction

Niobium oxides have many different interesting properties. The presence of a wide range of properties classifies this material as universal. Based on niobium oxides, solid-state electrolytic capacitors, transparent conductive layers, and memristors can be created. However, the understanding of these oxide systems is still clearly insufficient. To date, it is known that niobium oxides are a complex system with many phases inherent in it, as well as polymorphism. Particularly important are the issues of stoichiometric composition. The paper shows studies of thin films of niobium oxide of various stoichiometric compositions. The work is aimed at demonstrating the properties and possible applications of these materials.

## 2. Experiment

Substrates with $SiO_2$ were used to obtain thin-film structures of niobium oxide by reactive magnetron sputtering in oxygen. The silicon substrates were oxidized in a diffusion furnace in a steam atmosphere. The thickness of $SiO_2$ was about 0.6 μm. Next, the formation of niobium oxide films took place on a reactive magnetron sputtering unit. Pure niobium was used as a target. The process parameters are given in Table I. Surface resistance measurements of thin-film structures of niobium oxide were carried out on a CDE ResMap setup. The oxygen concentration in thin films was measured using AES.

***Table I.*** *Parameters of Reactive Magnetron Sputtering.*

| № | Power (W) | Pressure $O_2$ (Torr) | Pressure Ar (Torr) | Time (min) |
|---|---|---|---|---|
| 1 | 1000 | 0 | $3\times10^{-3}$ | 20 |
| 2 | 1000 | $3\times10^{-4}$ | $3\times10^{-3}$ | 35 |
| 3 | 1000 | $9\times10^{-4}$ | $3\times10^{-3}$ | 36 |
| 4 | 1000 | $3\times10^{-3}$ | $3\times10^{-3}$ | 40 |

## 3. Results and discussions

In the course of the experiment, samples of thin-film structures of niobium oxide were obtained using reactive magnetron sputtering in an oxygen environment. Changes in the $O_2$ pressure parameter in the chamber led to different oxygen concentrations in the film composition. As the pressure increased, the percentage of oxygen increased. This can be judged from the resistivity of the films. According to the Auger spectra, it was found out how much oxygen is contained in each sample obtained in percent. The results of measuring the thickness of the samples, resistivity and oxygen concentration are presented in Table II. Since the oxygen concentration and, consequently, the resistance in sample No. 4 is the highest available, it can be assumed that this sample is stoichiometrically close to $Nb_2O_5$. Sample №2 still has conductive properties. When sample №3 was exposed to an electron beam, an increase in the intensity of the Auger signal was recorded, which indicates an increase in the oxygen concentration. Oxygen migrated from the area affected by the beam from the depth of the film. The exact depth could not be determined. The surface of the sample was preliminarily cleaned to remove natural contaminants. The dependence of the signal intensity growth on the etching time is shown in Figure 1.

***Table II.*** *Results of measurements of thickness, resistance and concentration $O_2$.*

| № | h (nm) | Resistance (ohm×cm) | Concentration $O_2$ (%) |
|---|---|---|---|
| 1 | 358 | $2{,}32\times10^{-4}$ | 2 |
| 2 | 636 | $1{,}88\times10^{-5}$ | 38 |
| 3 | 205 | $2{,}05\times10^{-2}$ | 59 |
| 4 | 119 | $1{,}19\times10^{-1}$ | 64 |

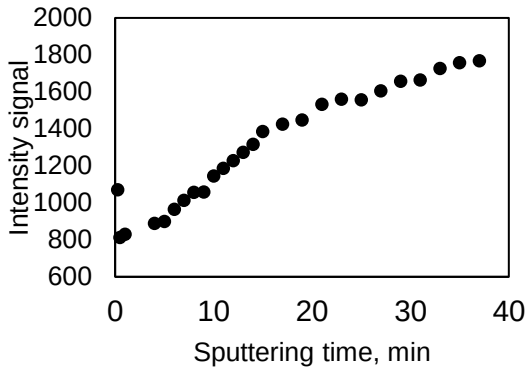


***Fig. 1.*** *Change of intensity signal over time.*

Since the sample was preliminarily cleaned from surface impurities, it can be assumed that oxygen migrates not from the surface of the film, but from its depth.

## 4. Conclusions

The results show that niobium oxide films obtained by reactive magnetron sputtering in an oxygen medium do indeed have interesting properties, one of which is the presence of free oxygen unbound to niobium atoms. The results showed that the energy impact on a thin film of niobium oxide leads to the fact that free oxygen begins to migrate over the volume. This gives prospects for the creation of various devices based on such thin-film structures, in particular, memristors.

## Acknowledgements

This work was supported by the State assignment 2020-2022 № FSMR-2020-0018.

## References

[1] C. Nico, T. Monteiro, M.P.F. Graça. Niobium oxides and niobates physical properties: Review and prospects (2016)3810-193.
[2] D. Bach, H. Störmer, R. Schneider, D. Gerthsen, J. Verbeeck. EELS investigations of different niobium oxide phases. Microsc Microanal (2006)12:416–23.
[3] V. Yuriy, Pershin & Massimiliano Di Ventra. Memory effects in complex materials and nanoscale systems. Advances in Physics(2011)60:2, 145-227.

# Enhancing transport and thermoelectric properties of Heusler based alloys

Mohamed Asran Hassan[*,1,2], A. El-Khouly[1,3], I. Serhiienko[1], E.A. Argunov[1], A. Sedegov[1], D. Karpenkov[1], D. Pashkova[1], M. Gorshenkov[1], A. Novitskii[1], A. Voronin[1], V. Kostishyn[1], V. Khovaylo[1,4]

[1] National University of Science and Technology MISIS, Moscow 119049, Russia
[2] Physics Department, Faculty of Science, Sohag University, 82524 Sohag, Egypt
[3] Physics Department, Faculty of Science, Damanhour University, 22516 Damanhour, Egypt
[4] National Research Belgorod State University, Belgorod 308015, Russia

*e-mail: m.asran@science.sohag.edu.eg

**Abstract.** In this study, we report on structural and thermoelectric properties of novel double half-Heusler compounds $Hf_2FeNiSb_{2-x}In_x$ where (x=0.1,0.2,0.3,0.4) Polycrystalline samples were successfully synthesized by arc melting and melt spinning techniques and consolidated by spark plasma sintering method. The studied compound were found to crystallize in a complex cubic crystal structure, as can be judged by superstructural reflections, clearly seen on X-ray diffraction pattern. Thermal conductivity $K_{tot}$ of the samples was found to be significantly lower than that in the related half-Heusler alloy, TiCoSb. However, rather a high, as compared to modern thermoelectric materials, value of K (4 – 6 W $m^{-1}$ $K^{-1}$) and good electrical properties allowed one to attain a moderate thermoelectric figure of merit, which around ZT ~ 0.3.

Sixth Asian School-Conference on Physics and
Technology of Nanostructured Materials
Vladivostok, Russia, 25 – 29 April, 2022



# Selective adsorption capacity of $Fe_3O_4$@C nanoparticles with respect to organic cationic dyes

O.S. Ivanova*,[1], I.S. Edelman[1], A.E. Sokolov[1], E.S. Svetlitsky[1], Chun-Rong Lin[2], Ying-Zhen Chen[2], Yaw-Teng Tseng[2]

[1] Kirensky Institute of Physics, FRC KSC SB RAS, 50 Akademgorodok St., Krasnoyarsk 660036, Russia
[2] Department of Applied Physics, National Pingtung University, Pingtung City 90003, Taiwan

*e-mail: osi@iph.krasn.ru

**Abstract.** The $Fe_3O_4$ and core-shell $Fe_3O_4$@C magnetic nanoparticles (NPs) with an average size of 15 ± 2 nm were synthesized and characterized. Comparative study of two types of NPs revealed their different sorption capacity of cationic and anionic dyes. The leading role of electrostatic interactions in the dyes adsorption by $Fe_3O_4$@C NPs has been revealed.

## 1. Introduction

In recent years, there has been an avalanche-like increase in the number of publications on the use of the adsorption properties of magnetic nanoparticles (NPs), in particular, magnetite. At the same time, the variety of fields of application is striking in its breadth - chemical, pharmaceutical, food, agricultural, bio-medical, and many others [1].The variety of uses of magnetite nanoparticles is due to the ability to reliably attach various substances to their surface. For this reason, magnetite nanoparticles are attractive objects for creating core-shell structures and modifying their surface in order to create various functional properties. The creation of selective adsorption by NPs is invaluable, in some cases to remove certain substances from solutions, and in other cases, for example, medicine, in order to deliver the necessary substances to certain places. Possession at the same time a large magnetic moment allows you to control the movement of magnetic particles.

The carbon shell is one of the universal coatings for NPs. It provides exceptional chemical stability and protects the magnetic core from oxidation, prevents agglomeration and allows additional functionalization of the carbon surface. High adsorption capacity $Fe_3O_4$@C NPs along with easy magnetic separation and the possibility the multiple use noted in these works stimulates the search for new technological solutions for further improving the characteristics of adsorbents based on these NPs [2].

This work is devoted to a comparative study of the adsorption capacity of cationic (Methylene blue (MB), rhodomine C (Rh C)) and anionic (Congo red (CR), methyl orange (MO) and eosin y (EoY)) dyes by $Fe_3O_4$ and $Fe_3O_4$@C NPs.

## 2. Experiment

Magnetite $Fe_3O_4$ NPs were obtained from the thermal decomposition reaction of iron-oleate complex. After that, the $Fe_3O_4$ NPs were mixed with glucose in distilled water by sonication for 15 min was placed in an autoclave for 12 h at 200°C. After cooling to room temperature, the black products were then separated by an external magnetic field and washed several times with water and ethanol. Next, the NPs $Fe_3O_4$@C were dried at 60°C for 6 hours.

The synthesized NPs were examined with X-ray diffraction (XRD), transmission electron microscope (TEM), Fourie rtransform infrared spectroscopy (FTIR), vibrating sample magnetometer (VSM). Changes in the absorption spectra of the dye solutions were recorded with the UV/VIS circular dichroism spectrometer SKD-2MUF at the wavelength corresponding to the maxima in the spectra of 490 nm for eosin Y, 505 nm for CR, 500 nm for MO and 664 nm for MB. For the experiment, 3 mg of NPs were dispersed in 1.5 ml aqueous dye solution in an ultrasonic bath for 10 minutes. Then magnetic NPs were separated using magnetic field and measured the optical absorption of the remaining solution. Then the solution was again mixed with magnetic particles, and the described procedure repeated several times to obtain kinetic curves. The value of the adsorption capacity of NPs at any point in time, $q_t$ (mg/g) was calculated as follows:

$$q_t = \frac{(C_0 - C_t)V}{m} \quad (1)$$

where $C_0$ and $C_t$ is the initial and concentration of the dye at any time, $V$ is the volume of the solution; and $m$ represents the weight of the adsorbing NPs introduced into solution.

## 3. Results and discussions

The $Fe_3O_4$ NPs were nearly spherical crystals with an average diameter of about 15 nm with a narrow size distribution. The most intense X-ray peaks corresponded to the $Fe_3O_4$ phase (PDF Card # 04-005-4319) in both case. High values of saturation magnetization – 79 emu/g in magnetite NPs and 64 emu/g in carbon-coated NPs, measured at H=15 kOe, close to the saturation magnetization of bulk magnetite (84 emu/g). The $q_t$(t) dependencies for different dyes are shown in Fig. 1 for the $Fe_3O_4$.

The higher values of the adsorption capacity and the short time to reach the equilibrium value for the CR indicate the preferred absorption of anionic dyes by $Fe_3O_4$ NPs. The kinetic curve for CP is well described by the pseudo-first order kinetic model, and the isotherm shape is well described by Brunauer–Emmett–Teller (BET) theory isotherm equation for liquid phase adsorption for Case-3 - polymolecular adsorption model [3]. At the same time, up to a dye concentration of 50 mg/L, nanoparticles adsorbed 90 % of the dye, with an increase in the dye concentration up to 200 mg/L, particles adsorbed up to 60 % of the dye.

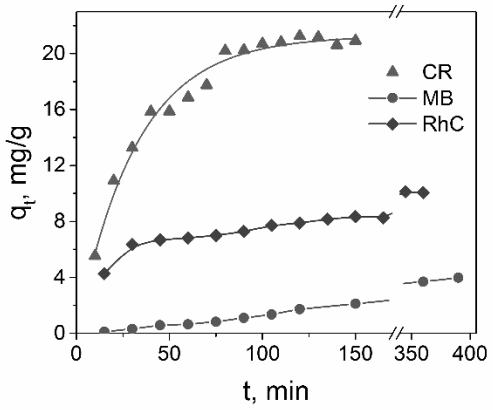


***Fig. 1.*** *The effect of contact time on the dye adsorption for $Fe_3O_4$ NPs. Experimental conditions: $C_0$=60 mg/L, m(NPs)=3 mg, V=1.5 mL.*

The adsorption capacity of the core shell $Fe_3O_4$@C of magnetic NPs has changed dramatically, NPs have expressed complete indifference to anionic dyes. Experiments carried out on three anionic dyes: CR, MO and EoY showed the same results - no adsorption. The ability to adsorb cationic dyes while improving. Figure 2 shows the kinetic curves of the adsorption of cationic dyes. The time to reach the equilibrium state for RhC is 60 min, and for MB approximately 200 min. In this case, the concentration dependences of the equilibrium value of the adsorption capacity are described by the Langmuir equation, showing the formation of a homogeneous adsorbed monolayer, while the adsorbed molecules do not interact with each other.

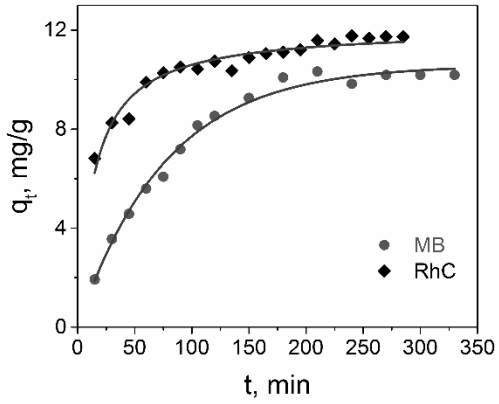


***Fig. 2.*** *The effect of contact time on the dye adsorption for $Fe_3O_4$@C NPs. Experimental conditions: $C_0$=30 mg/L, m(NPs)=3 mg, V=1.5 mL.*

The presented results show that the selective adsorption of certain substances can be obtained by modifying the NP surface. In our case, the coating of particles with carbon led to the selective sorption of cationic dyes. Note that the sorption process is influenced by many factors, pH, ionic strength of an aqueous solution, temperature, and can also significantly affect the efficiency of dye adsorption on NPs by involving various adsorption mechanisms, including electrostatic interactions, hydrogen bonds, Van der Waals forces. The pronounced adsorption ability to absorb cationic dyes and completely not adsorb anionic dyes by carbon-coated NPs confirms the negatively charged surface of $Fe_3O_4$@C NPs and the significant role of electrostatic interaction in our case.

## 4. Conclusions

In this study, $Fe_3O_4$ and core-shell $Fe_3O_4$@C magnetic NPs with an average size of 15 ± 2 nm were synthesized and characterized. Magnetic measurements revealed a high saturation magnetization close to that of the bulk magnetite crystal. A comparative study of the adsorption capacity of cationic and anionic dyes revealed the manifestation of selective sorption of the particles under study. The $Fe_3O_4$ NPs showed predominant adsorption of anionic dyes. The kinetic data are well described by the pseudo first order kinetic model, and the shape of the isotherm by the BET equation for liquid phase polymolecular adsorption. The $Fe_3O_4$@C NPs showed selective sorption of only cationic dyes. The experimental data in this case are approximated by the Langmuir model of adsorption processes, which indicates the predominance of homogeneous and monolayer adsorption in the cases under consideration. Electrostatic interactions play the main role in the dye adsorption by $Fe_3O_4$@C NPs.

## Acknowledgements

The work was supported financially by Ministry of Science and Technology of Taiwan, Grants MOST № 108-2923-M-153-001-MY3 and № 109-2112-M-153-003-

## References

[1] J.S. Beveridge, J.R. Stephens, M.E.Williams. Annu. Rev. Anal. Chem. **4**(2011)251.
[2] M.M. Lima, D.L.P. Macuvele, L. Muller, J. Nones, L.L. Silva, M.A. Fiori, C. Soares, H.G. Riella. J. Adv. Chem. Eng. 7(2017)1000172.
[3] A. Ebadi, J.S. Soltan Mohammadzadeh, A. Khudiev. Adsorption **15** (2009)65.

# Development of eco-friendly self-polishing antifouling coatings

U.V. Kharchenko[1], L.A. Zemnukhova[1], S.B. Yarusova[1], I.A. Beleneva[2], V.S. Egorkin[1], N.V. Chi[3], I.E. Vyaliy[1], N.V. Izotov[*,1,4], S.L. Sinebryukhov[1], S.V. Gnedenkov[1]

[1] Institute of Chemistry, 159 pr. 100-letiya Vladivostoka, Vladivostok 690022, Russia
[2] A.V. Zhirmunsky National Scientific Center of Marine Biology, Far Eastern Branch, Russian Academy of Sciences, Palchevskogo str. 17, Vladivostok, Russia 690041
[3] Russian-Vietnamese Tropical Scientific and Technological Center, 30 Nguyen Thien Thuat, Nha Trang, Vietnam
[4] Far Eastern Federal University, 10 Ayaks village, Russian Island, Vladivostok, 690922, Russia

*e-mail: izotov.nik7@gmail.com

## 1. Introduction

Silicates are a well-known class of chemical compounds that are widely used in various sectors of the national economy. Such a wide range of applications of silicon-containing substances is explained by their chemical inertness, thermal stability, and porosity.

The paint and varnish industry are a promising area for the application of silicon-containing compounds. In polymer and coating technology, it has been shown that the addition of $SiO_2$ or wollastonite to polymer matrices has improved many properties and provided new functions for coatings [1, 2].

## 2. Experiment

In order to find out the respective effect of $SiO_2$ and calcium hydrosilicate (CH) on the physicochemical characteristics of the coating, different paints were compiled according to different types of fillers and their ratio (Table 1). A bacterial organic extract from *Pseudoalteromonas piscicida* 2202 with antifouling and anticorrosion properties served as an antifouling agent.

***Table I.*** *The composition (g) of different paint under study.*

| Component | | Coating | | |
|---|---|---|---|---|
| | | *№1* | *№2* | №3 |
| Binder | Acrylic copolymer | 15 | 15 | 15 |
| | Rosin | 20 | 20 | 20 |
| Pigments | ZnO | 20 | 20 | 20 |
| Antifoulants | Extract (ml) | 10 | 10 | 10 |
| Filler | CaCO, | 10 | | |
| | $SiO_2$-rh | | 10 | |
| | CH | | | 10 |
| Solvent | Xylene (ml) | 100 | 100 | 100 |

Paints were applied to polycarbonate plates with an automatic applicator to determine the physico-chemical properties and by brush to PVC plates to evaluate the antifouling effectivity in field tests. Painted samples were exposed to seawater on a test bench located in Dam Bay (Vietnam) at a depth of 1.5 m for 9 months. The average temperature and salinity of seawater during the experiments were 28 °C and 32 ‰, respectively.

## 3. Results and discussions

The replacement of widely used calcium carbonate with additives of $SiO_2$-rh and calcium hydrosilicate (CH), which make up from 30 to 50 % of the total volume of the filler, has little effect on the water-absorbing properties of the resulting coatings. In this case, the hardness of the coatings increases by more than 1.5 times. Complete replacement of $CaCO_3$ leads to an increase in water absorption by 20–30 % and an increase in the rate of degradation of the coating by 2 times when using $SiO_2$ and by 8 times when using CH. Thus, the partial replacement of $CaCO_3$ by $SiO_2$-rh and CH favorably affects the hardness of coatings without affecting their sensitivity to erosion.

Figure 1 shows a panel with areas painted with different coatings after 4 and 9 months of immersion in seawater. Even after 9 months of exposure, only non-adhesive algal slime remains on the surface of the painted areas, while on the surface that is not pained, a layer of macrofouling is formed, consisting of bryophytes and single balanuses. It should be noted that the area of Coating 2 with CH as a filler is more susceptible to fouling than areas 1, 3 and 4 with $CaCO_3$ and $SiO_2$-rh as fillers.

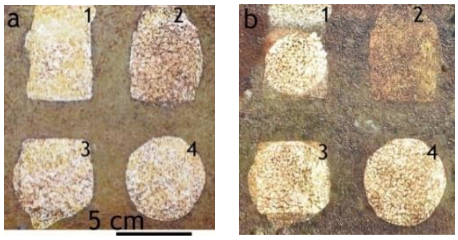


***Fig. 1.*** *Fouling of immersed panels with various paints (1 and 4 with $CaCO_3$, 2 with CH, 3 with $SiO_2$-rh) after 4 months (a) and 9 months (b) field tests.*

## 4. Conclusions

The use of silicate by-products as fillers in antifouling has maintained a balance between antifouling and mechanical strength of the developed coatings. The results of the study showed that the barrier characteristics of coatings can be substantially enhanced by incorporating particles of inorganic filler $SiO_2$-rh and CH by reducing heterogeneity and limiting the diffusion path for water. Incorporating these details into self-polishing coatings also offers environmentally friendly solutions by enhancing the integrity and durability of coatings. Improved antifouling performance has been shown in coatings with $SiO_2$-rh in combination with a bacterial antifouling extract.

## Acknowledgements

The reported study was funded by RFBR, project number 19-29-13020.

## References

[1] Dao PH, Nguyen TV, Dang MH. Vietnam J Sci Technol 56(2018)117-125.
[2] Bui TMA, Nguyen TV, Nguyen TM. Mater Chem Phys 241(2020)122445.

# Influence of SPTFE on the corrosion behavior of composite coatings during salt-spray test

V.S. Egorkin[1], N.V. Izotov[*,1,2], U.V. Kharchenko[1], I.E. Vyaliy[1], A.N. Minaev[1,2], S.L. Sinebryukhov[1], S.V. Gnedenkov[1]

[1] Institute of Chemistry, 159 pr. 100-letiya Vladivostoka, Vladivostok 690022, Russia
[2] Far Eastern Federal University, 10 Ayaks village, Russian Island, Vladivostok, 690922, Russia

*e-mail: izotov.nik7@gmail.com

## 1. Introduction

In order to provide protection against long-term corrosion, aluminum parts are coated with various protection methods: anodizing, painting, and others. Another modern method of corrosion protection is plasma electrolytic oxidation (PEO) [1]. There are also theories that combining some protection methods into a single composite coating can improve properties. One such composite coating is the combination of a paint applied to a PEO-coating. This paper presents a study of electrochemical properties and corrosion resistance of a composite coating obtained by spray painting of the PEO coated sample using the paint with the addition of different concentrations of superdispersed polytetrafluoroethylene (SPTFE) [2, 3].

## 2. Experiment

In this work, a multicomponent electrolyte was used to form the PEO coating as a protective sublayer.

On the formed PEO coating, 5 types of paint and varnish solutions were applied by spraying. Jotun SeaForce 30 was chosen for modification. SPTFE was added to this paint in different concentrations from 0 to 20 mass. % of the total solution. The resulting coatings are shown in Figure 1.

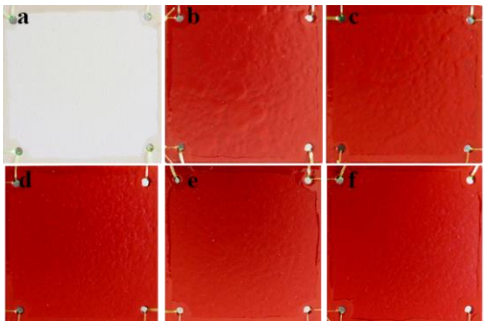


***Fig. 1.*** *Formed protective coatings: a - PEO coating, b - CC without SPTFE, c - CC with 5 % SPTFE, d - CC with 10 % SPTFE, e - CC with 15 % SPTFE, f - CC with 20 % SPTFE.*

Together with electrochemical studies of CC salt spray tests were carried out in a salt spray chamber to assess the protective properties of composite coatings under identical operating conditions. The follwing spray mode was used: 5 % NaC1 solution was sprayed for 15 min every 45 min of exposure. The temperature was kept within 27±2°C. The duration of the test is 10 days with an interim analysis every 4 days of the exposition. After the end of the test all samples were weighed to calculate the weight loss.

## 3. Results and discussions

The application of a paint coating on a PEO coating led to an increase in the coating thickness up to 120±12 μm. An additional dependence of the coating thickness on the content of SPTFE in the paint was obtained with the same method and number of application layers: an increase in the concentration of SPTFE leads to a slight decrease in the thickness of the composite coating.

Analyzis of the samples after the salt spray test led to conclusion that all composite coatings passed the test and do not have any defects on the surface. In turn, an oxide film appeared on the aluminum alloy, and the PEO coating darkens with increasing testing time, which indicates internal oxidation due to the porosity of this coating.

After the samples were rinsed with deionized water and air dried for 120 min, they were reweighed. The mass measurement before and after the salt spray test showed that bare aluminum alloy and PEO-coated samples increased their mass due to oxidation by 0.14 % and 0.07 %, respectively. Composite coatings behaved differently in this experiment: all coatings lose mass. It should be noted that the addition of 10 % SPTFE resulted in the smallest weight loss of 0.04 %. For composite coatings without addition and with 5 % SPTFE, the weight change was the same - 0.05%. And an increase in the concentration of SPTFE to 15 and 20 % leads to an increase in weight loss to 0.07 and 0.11 %, respectively. From the obtained data on weight loss, it follows that the optimal value of the concentration of SPTFE is 10 %, and a further increase leads to a change in the properties of the composite coating.

## 4. Conclusions

A PEO coating has been developed that can serve as a substitute for a primer layer for the formation of composite coatings by applying a paint coating on PEO layers. The formed composite coatings were tested, according to standards, in a salt spray chamber. As a result of the study the optimum concentration of superdispersed polytetrafluoroethylene to a paint was determined and equal to 10 %. The lower concentration value leads to minor changes relative to the original paint. An increase in concentration of more than 10 % leads to a deterioration in the properties of the composite coating.

**Acknowledgements**

The reported study was funded by RFBR, project number 19-29-13020.

## References

[1] V.S. Egorkin, D.V. Mashtalyar, A.S. Gnedenkov. Polymers **13**(2021)3827.
[2] S.V. Gnedenkov, S.L. Sinebryukhov, V.S. Egorkin. Russian Journal of Inorganic Chemistry **62**(2017)1.
[3] V.S. Egorkin, I.E. Vyaliy, N.S. Sviridov. Defect and Diffusion Forum **386**(2018)315.

# Influence of an electrolyte on the electrophysical properties of RuO-carbon nanomaterials based supercapacitors

Yu.I. Kakovkina[1,2], S.S. Isakjanov[2], R.M. Ryazanov[1], E.A. Lebedev[2], E.P. Kitsyuk[*,1]

[1] Scientific-Manufacturing Complex "Technological Centre", 7 Shokina Sq., Zelenograd, Moscow 124498, Russia
[2] National Research University of Electronic Technology – MIET, 1 Shokina Sq., Zelenograd, Moscow 124498, Russia

*e-mail: kitsyuk.e@gmail.com

## 1. Introduction

Active progress in the development of microelectronics leads to a reduction in the size of electronic devices while increasing performance and expanding capabilities. At the same time, energy requirements most often do not decrease, which, taking into account the decrease in the available volume for batteries, requires the development of new approaches to their formation.

One of the most capacious materials for forming the electrochemical capacitance of supercapacitors is ruthenium oxide, which has a theoretical capacitance of 1358 F/g. However, for supercapacitors, an important indicator is also the power, determined by the total area of the electrodes. Here, carbon nanoparticles were used as a matrix with a large surface area, constituting an electrically conductive matrix for ruthenium oxide particles. To fully unlock the potential of the entire system, an electrolyte is needed that can provide sufficient ionic conductivity, neutrality to electrode materials, and good wettability. In this work, the influence of an 1 M KOH, 1 M LiCl and 1 M $H_2SO_4$ electrolytes on the electrophysical properties of RuO-carbon nanomaterials based supercapacitors was studied.

## 2. Experiment

Supercapacitor composite electrodes were created by electrophoretic deposition on the basis of nickel foil. Ruthenium oxide (concentration range 0.05-0.3 mg/ml) and comercially avalible carbon material Super C45 (fixed concentration 0.2 mg/ml) have been proposed as the main electrode components. The suspension with this materials was prepared using a mixture of isopropyl alcohol-acetone in a 1:1 ratio. Dispersion of the resulting solution was carried out using a submersible disperser with stabilized by water cooling system temperature in the range of 15 ± 3 ° C. Nickel substrates (50×20 mm and 0,05 mm thick) before deposition of electrode layer were cleaned by two step process: in acetone:isopropyl alcohol:$H_2O$ = 1:1:1 solution and in an aqueous solution $HNO_3$:$H_2O$ = 1:4. The final stage of cleaning the substrates was washing in deionized water and drying in isopropyl alcohol vapor.

Composite electrode material was deposited in an electrophoretic cell. One electrode (nickel cathode) was partially masked by a rigid sitall mask. As anode was used gold electode. The electric field strength during deposition process varied from 50 to 150 V / cm, deposition was carried out in 1 cycle or 3 cycles of 60 s each with suspension renewal. To determine the sediment on the cathode mass, the samples were weighed before and after the electrophoretic deposition process. After deposition, L-shaped electrodes were cut from the initial substrates. A schematic representation of the electrophoretic deposition process is shown in Figure 1.

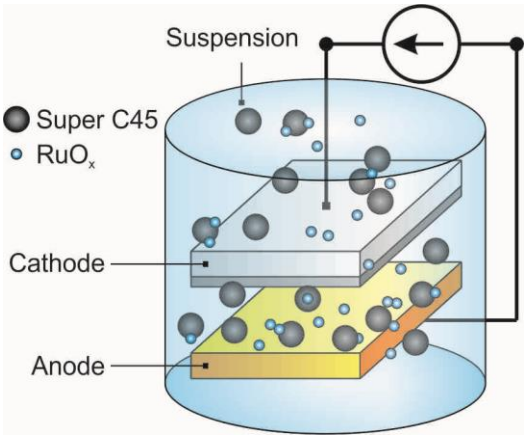


***Fig. 1.*** *Schematic representation of the electrodes preparation process.*

As an electrolytes, one representative of each type was taken – acidic (1 M $H_2SO_4$), alkaline (1 M KOH) and neutral (1 M LiCl).

Registration of cyclic sweeps and charge-discharge curves of electrochemical energy storage devices prototypes was carried out using an Elins-45X potentiostat. Cyclic sweeps were recorded at rates of 10 and 100 mV / s in the cell voltage range from 0 to 1000 mV. The charge-discharge was also carried out in the voltage range from 0 to 1000 mV in the galvanostatic mode, while the current strength was selected in the range from 5 to 100 mA so that the discharge duration was at least 10 seconds.

## 3. Results and discussions

Characteristics of the electrolyte, such as type and size of ions; ion concentration and solvent; interaction between an ion and a solvent; and the interaction between electrolyte and electrode materials, all have a critical influence on capacitance and pseudo capacitance. The dependences of the electrophysical characteristics of supercapacitors based on a composite ruthenium oxide – Super C45 material were studied. The effect of structure wettability, penetration depth, and electrolyte composition on the supercapacitor impedance, device power, and capacity drop with increasing charge-discharge rate is determined.

## Acknowledgements

This work was partially supported by the Ministry of Science and Higher Education of the Russian Federation (project FNRM-2021-0002).

# Composite triazole-containing PEO-coatings as the effective way of corrosion protection of AMg3 aluminum alloy

Ya.I. Kononenko*, A.S. Gnedenkov, S.L. Sinebryukhov, V.S. Filonina, I.E. Vyaliy, S.V. Gnedenkov
Institute of Chemistry of FEB RAS, 159 Pr. 100-letiya Vladivostoka, Vladivostok, 690022, Russia

*e-mail: yana1996i@mail.ru

**Abstract.** This paper discusses the possibility of formation an effective composite PEO-coating containing corrosion inhibitors, 1,2,4-triazole and benzotriazole in various concentrations, to protect the AMg3 aluminum alloy against corrosion. The morphology of the obtained coatings was investigated by SEM; their protective properties was assessed by the electrochemical impedance spectroscopy (EIS).

## 1. Introduction

Aluminum is a structural material with such important properties as lightweight, strength, ductility, etc. It found application in many industries. However, during exploitation, aluminum can contact with the aggressive environment, which results in corrosion degradation.

One of the ways to prevent aluminum corrosion is the formation of protective coatings on it`s surface. Plasma electrolytic oxidation (PEO) is one of the easiest and optimal methods to protect the surface of valve metals (including aluminum and its alloys). In some cases the duration of the corrosion protection of PEO-coatings may be insufficient due to high heterogeneity (including porosity) of obtained surface layers. Corrosion inhibitors are widely used for modification of coatings in order to provide autonomous self-healing properties and prolong the provision of protective ability. The most studied metallic corrosion inhibitors are phosphates, nitrites, molybdates, tungstates, vanadates, borates, rare earth salts and the organic corrosion inhibitors including different types of triazoles [1]. Thus, authors of the article [2] describe an efficiency of a composite coating applied by a sol-gel method, with benzotriazole. It was established that this corrosion inhibitor, in the protective layer, capable of starting the process of healing damage of the coating on AA7075 alloy.

This study is focused on formation of composite coatings on AMg3 alloy with the introduction of inhibitors of the triazole group of various concentrations in the previously formed base PEO-layer with purpose to improve the protective properties of the material.

## 2. Experiment

The experiments were carried out on samples made of AMg3 aluminum alloy with size of 20×30×2 mm. The surface preparation of the samples was realized through wet grinding with SiC paper with a gradual decrease in abrasive grain size from 28-40 to 14-20 μm, followed by washing in isopropyl alcohol and drying in a desiccator. PEO was carried out in a tartrate-fluoride electrolyte in a galvanostatic mode for 40 s. The current density was equal to 1.79 A·cm$^{-2}$ and the duty cycle was equal to 1. To ensure the best filling of coating microtubes with inhibitor, the formed samples were subjected to vacuum impregnation in aqueous solutions of 1,2,4-triazole and benzotriazole at various concentrations (0.05 M and 0.1 M), with the following exposure to inhibitor solutions for 1 h under constant stirring, and then dried in a desiccator at a temperature of 40 °C for 24 h.

The protective properties of the formed coatings was assessed using the electrochemical methods, including electrochemical impedance spectroscopy (EIS) and open circuit potential (OCP) measurements. Experiments were carried out in a three-electrode cell with a silver chloride (Ag/AgCl) electrode as a reference electrode and platinum mesh as a counter electrode using the VersaSTAT MC potentiostat/galvanostat electrochemical system (Princeton Applied Research, USA). 3 wt. % NaCl solution was used as an electrolyte.

For surface morphology analysis, Sigma (Carl Zeiss, Germany) scanning electronic microscope (SEM) was used.

## 3. Results and discussions

As a result of the study the composite inhibitor-containing coatings with a self-healing ability were obtained on the AMg3 aluminum alloy. Coatings consisted of a PEO-layer with a self-organized microtubular structure and inhibitors of the triazole group.

Table 1 shows the results of EIS study for an uncoated aluminum alloy AMg3 (A), a PEO-coated sample (B), and samples with inhibitor-containing layers (C–F) after the exposure for 1 h in a 3 wt. % NaCl solution.

***Table I.*** *The coating specification and electrochemical parameters of samples according to the results of EIS test*

| Samples name | Coating type | $\lvert Z\rvert_{f=0.1\ Hz}$, Ω·cm$^{-2}$ |
|---|---|---|
| *A* | AMg3 uncoated | $2.56\cdot10^4$ |
| *B* | PEO | $4.65\cdot10^6$ |
| *C* | PEO 1,2,4-tr 0.05 M | $6.61\cdot10^7$ |
| *D* | PEO 1,2,4-tr 0.1 M | $6.11\cdot10^6$ |
| *E* | PEO b-tr 0.05 M | $1.63\cdot10^7$ |
| *F* | PEO b-tr 0.1 M | $7.72\cdot10^6$ |

As can be seen from the analysis of the impedance modulus measured at low frequency ($|Z|_{f=0.1\ Hz}$, Table 1) after 1 h of exposure, all samples with composite inhibitor-containing coatings (C–F) perform higher corrosion resistance compared to the uncoated sample (A) and base PEO-layer.

The sample with a PEO-layer impregnated with 1,2,4-triazole at a concentration of 0.05 M (C) is characterized by

the best protective properties. The value of $|Z|_{f=0.1\ Hz}$ for this composite coating is more than one order of magnitude higher than the values for the sample with base PEO-layer (Table 1). An increase in the concentration of inhibitors to 0.1 M leads to a decrease in the $|Z|_{f=0.1\ Hz}$, and, as a consequence, a decrease in corrosion resistance, due to the PEO-layer degradation, which is consistent with the data presented in [2].

## 4. Conclusions

During the study, heterooxide layers with a microtubular structure were obtained on the AMg3 aluminum alloy. The impregnation of corrosion inhibitors into the PEO-coating contributed to a significant increase in the corrosion resistance of the studied material. The sample impregnated with 1,2,4-triazole at a concentration of 0.05 M is characterized by the best protective properties.

## Acknowledgements

The samples preparation, protective coating formation, and electrochemical measurements were supported by the Grant of Russian Science Foundation, Russia (project no. 21-73-10148, https://rscf.ru/en/project/21-73-10148/). The study of coating composition was supported by the Grant of Russian Science Foundation, Russia (project no. 20-13-00130, https://rscf.ru/en/project/20-13-00130/).

## References

[1] Fan Zhang, Pengfei Ju, Mengqiu Pan, Dawei Zhang, Yao Huang, Guoliang Li, Xiaogang Li Corrosion Science **144** (2018) 74-88.

[2] M. Farahani, H. Yousefnia, Z.S. Seyedraoufi, Y. Shajari Ceramics International **45** (2019) 16584–16590.

Sixth Asian School-Conference on Physics and
Technology of Nanostructured Materials
Vladivostok, Russia, 25 – 29 April, 2022



# Applicability assessment of $Fe_3O_4$-$SiO_2$-Au nanoparticles for the radiotherapy for cancer

N.S. Markin*[,1,2], S.I. Ivannikov[2], A.V. Ognev[1], L.L. Afremov[1], A.S. Samardak[1]

[1] Laboratory of Spin-Orbitronics, Institute of High Technologies and Advanced Materials, Far Eastern Federal University, Vladivostok 690922, Russia, 8 Sukhanova St., Vladivostok 690950, Russia
[2] Institute of Chemistry of FEB RAS, 159 Prosp. 100-letya Vladivostoka, Vladivostok 690022, Russia

*e-mail: markkin.ns@gmail.com

**Abstract.** The results of an experimental evaluation of the secondary electromagnetic radiation output during irradiation of $Fe_3O_4$-$SiO_2$-Au nanoparticles with gamma radiation from a source of $^{137}Cs$ radionuclides are presented. Secondary electromagnetic radiation in the range of 40-118 keV is detected. The intensity of secondary radiation is about 0.9 becquerel per kilobecquerel of the initial source. $Fe_3O_4$-$SiO_2$-Au nanoparticles are shown to be a perspective material for use as a cancer radiotherapy radiosensitizer.

## 1. Introduction

To date, radiotherapy is one of the most common methods of cancer treatment. One of the methods to increase the effectiveness of radiation therapy is to increase the absorbed radiation dose in the tumor localization area by infusing nanoparticles with a high atomic number into a given area. The high cross-sections of the interaction of heavy materials with radiation provide a significant output of low-energy secondary electronic and electromagnetic radiation. Secondary radiation leads to a significant increase in absorbed dose near the irradiated nanoparticles [1-3].

The general purpose of this work is to experimentally determine the intensity of secondary electromagnetic radiation of $Fe_3O_4$-$SiO_2$-Au nanoparticles during γ-radiation flux of $^{137}Cs$ irradiation.

## 2. Experiment

The electron microscopy study showed that the $Fe_3O_4$-$SiO_2$-Au nanoparticles had a core-shell structure. The average size of the magnetite core was 227±7 nm, the thickness of the protective shell made of $SiO_2$ was 2 nm, the average size of gold nanoparticles covering the core was 16±0.6 nm.

Since the effective atomic number of this system is 63, it is a promising material for use as a radiosensitizer for cancer radiotherapy.

To estimate the output of secondary electromagnetic radiation during irradiation of the Fe3O4-SiO2-Au nanoparticles, an experimental unit was constructed.

A plastic cuvette (a disk Ø 5.2 cm) with a suspension of nanoparticles in water (concentration of nanoparticles - 140 mg×l$^{-1}$, sample volume - 7ml) was placedat a distance of 40 cm from the detector lid on its axis. A scintillation gamma-ray spectrometer based on a NaI(Tl) 78×78 crystal was used as a detector. The relative efficiency of registration at the $^{137}Cs$ 662 keV line was 25%, and the resolution at the $^{137}Cs$ 662 keV line was 9%. A collimated beam of gamma radiation from $^{137}Cs$ was directed to the cuvette perpendicular to the axis of the spectrometer. The activity of the $^{137}Cs$ radionuclide source was 99 MBq.

To take into account the background component of the obtained data, we measured the energy spectrum of the blank sample. A water sample (volume - 7ml) was used as a blank. The experiment was carried out in 3 series. The measurement time was 18 hours for each series.

## 3. Results and discussions

The spectrum of secondary electromagnetic radiation for each series of measurements was obtained by subtracting the blank sample spectrum from the spectrum of a cuvette with nanoparticles for each channel. The resulting difference was summed up for each of the nine channels:

$$\Delta N_j = \sum_{i=9j-8}^{i=9j} \left(N_i - N_i^{BG}\right)$$

where: $\Delta N_j$ is the number of secondary electromagnetic radiation pulses; $N_i$ is the number of registered pulses from the cuvette with nanoparticles; $N_i^{BG}$ is the number of registered pulses from the blank sample. The summation step was selected according to the resolution of the spectrometer.

The absolute error of the data obtained was determined by the method of calculating the errors of indirect measurements according to the formula:

$$\sigma\left(\Delta N_j\right) = \sqrt{\sum_{i=9j-8}^{i=9j} \left(N_i + N_i^{BG}\right)}$$

where: $\sigma\left(\Delta N_j\right)$ is the absolute error in determining the number of pulses of secondary electromagnetic radiation.

Radionuclides $^{57}Co$, $^{140}La$, $^{238}U$, $^{153}Sm$, $^{137}Cs$, and $^{76}As$ were used as calibration sources. The measurement time of calibration spectra was 15 hours.

The short-lived nuclides $^{140}La$, $^{153}Sm$, $^{76}As$ were detected on a neutron activation analysis unit based on a $^{252}Cf$ radionuclide neutron source [4]. The reactions of neutron radiation capture $^{39}La(n, \gamma)^{140}La$, $^{75}As(n, \gamma)^{76}As$, $^{152}Sm(n, \gamma)^{153}Sm$ were used.

The activity of calibration sources was defined with a semiconductor HPGe detector manufactured by Canberra. The detector energy resolution was 1.8 keV at a radiation energy of 1332 keV, and the relative recording efficiency at the peak of 1332 keV was 10%.

The resulting flux of secondary electromagnetic radiation is calculated using the following formula.

$$\Phi_j = \frac{\langle \Delta N_j \rangle}{\varepsilon_j \cdot t}$$

where: $\langle \Delta N_j \rangle$ is the weighted average of the countability of the secondary electromagnetic radiation signal, $\varepsilon_j$ is the radiation registration efficiency, $t$ is the measurement time.

The intensity of the characteristic radiation is (0.45±0.05) $\frac{Bq}{kBq}$, the total intensity of the secondary electromagnetic radiation in the range of 40-118 keV is (0.89±0.11) $\frac{Bq}{kBq}$.

## 4. Conclusions

As a result, a method was developed to estimate the output of secondary electromagnetic radiation emitted by $Fe_3O_4$-$SiO_2$-Au nanoparticles during $^{137}Cs$ gamma irradiation.

Secondary electromagnetic radiation was detected in the direction perpendicular to the initial gamma ray beam of $^{137}Cs$ in the range 40-118 keV.

The intensity of secondary electromagnetic radiation was (0.89±0.11) $\frac{Bq}{kBq}$.

The predominant mechanism of secondary electromagnetic radiation generation is the photoelectric absorption of the gamma quanta of the primary beam. This leads to a significant emission of photoelectrons, ionization electrons, and the Auger electron, which form significant dose loads near the nanoparticle.

Therefore, $Fe_3O_4$-$SiO_2$-Au nanoparticles are shown to be a promising material for use as a cancer radiotherapy radiosensitizer.

## Acknowledgements

We acknowledge the Russian Ministry of Science and Higher Education. Synthesis and structural studies of nanoparticles were carried out with financial support the Russian Ministry of Science and Higher Education, State Order No. 0657-2020-0013. Radiological studies were carried out with financial support of the Ministry of Russian Ministry of Science and Higher Education, State Order No. 0205-2021-0002

## References

[1] Haume, K., Rosa, S., Grellet, S. et al. Gold nanoparticles for cancer radiotherapy: a review. Cancer Nano 7, 8 (2016). https://doi.org/10.1186/s12645-016-0021-x.
[2] Pallares, R.M., Abergel, R.J. Nanoparticles for targeted cancer radiotherapy. Nano Res. 13, 2887–2897 (2020). https://doi.org/10.1007/s12274-020-2957-8.
[3] Kwatra D, Venugopal A, Anant S. Nanoparticles in radiation therapy: a summary of various approaches to enhance radiosensitization in cancer. Transl Cancer Res 2013;2(4):330-342. doi: 10.3978/j.issn.2218-676X.2013.08.06.
[4] Ivannikov, S.I., Markin, N.S., Zheleznov, V.V. Determination uranium in solutions by the method of Neutron activation analysis with 252Cf radionuclide neutron source. Nuclear Technology and Radiation Protectiont. 36, 12-17 (2021).
[5] https://doi.org/10.2298/ntrp201217005i.

# Effect of thermal annealing on the composition of Ge-Co nanostructure obtained by electrochemical deposition

I.K. Martynova*, I.M. Gavrilin
National Research University of Electronic Technology (MIET), Bld. 1, Shokin Square, Zelenograd, 124498, Moscow, Russia

*e-mail: irina.martynova.miet@gmail.com

**Abstract.** The one-dimension Ge-Co nanostructures have been prepared by electrochemical deposition. Effect of thermal annealing on the composition of Ge-Co nanostructure has been studied. The method of X-ray diffraction analysis has been used to investigate composition changes of Ge-Co. Diffractograms show the presence of $Co_2GeO_4$ catalyst at an annealing temperature of 600 °C. The sample with this annealing temperature shows the best properties as oxygen evolution catalyst.

## 1. Introduction

At present, due to the development of the global energy industry, there is a need to use clean and cheap fuel, including to reduce carbon dioxide emissions.

One of the ways to obtain ecological fuel is the electrolysis of water to produce hydrogen [1]. However, this process has a disadvantage, which is the slow reaction rate on conventional electrodes. To eliminate it, it is necessary to investigate various substances that accelerate electrochemical reactions, which are called catalysts. In this case, catalysts are needed for two processes on two electrodes: the hydrogen evolution reaction and the oxygen evolution reaction (OER) [2].

One of the promising areas of research on effective and stable oxygen evolution catalysts (OECs) are cobalt-based catalysts because of its OER activity and thermal stability [3].

In this work, we report about formation OEC based on the one-dimension nanostructure Ge-Co by electrochemical deposition and investigate effect of thermal annealing on the composition of this structure.

## 2. Experiment

In the syntesis of Ge-Co nanostucture the 50 μm-thickness titanium foil (batch VT 1–00) has been used as a substrate. These titanium samples have been previously cleaned in a mixture of $H_2O_2$:$NH_4OH$:$H_2O$ (1:1:4) at 80 °C for 15 min, and then they have been washed in hot and cold deionized water for 5 min and dried. Then the samples surface has been activated in a mixture of HF:$HNO_3$:$H_2O$ (1:2:6), washed in deionized water and dried again.

After that an array of spherical indium nanoparticles has been deposited by vacuum-thermal evaporation at the residual pressure of $1 \times 10^{-5}$ Torr of material weighed portion of 35 mg from a Mo evaporator, placed at 40 cm from the substrate. After depositing the metals, the samples have been annealed in vacuum at 150 °C for 10 min.

Ge-Co structures have been formed on the substrates by electrochemical deposition in a three-electrode cell. A platinum plate has been used as an counter electrode, and a standard silver chloride electrode has been used as a reference one.

The solution contained 0.05 M of germanium (IV) oxide $GeO_2$, 0.5 M of potassium sulfate $Na_2SO_4$ and 0.1 M of tartaric acid with the addition of 0.05 g $CoCl_2$. The solution pH has been brought to 6.5 by adding $NH_4OH$. The solution temperature has been controlled using a LAUDA Alpha thermostat (LAUDA, Germany).

Deposition has been performed at constant voltage -1,3 V for 1 min at the solution temperature of 85 °C. The voltage has been set using Autolab PGSTAT302N potentiostat/galvanostat (Metrohm, Netherlands).

After deposition, the samples have been annealed at various temperature (300 °C, 450 °C, 600 °C).

The method of X-ray diffraction analysis (XRD) has been used to deteminate the crystalline phases (germanium, cobalt, their oxides, etc.) after the formation of the Ge-Co compound and to investigate the effect of annealing at different temperatures on the composition of Ge-Co.

X-ray diffraction patterns (diffractograms) of synthesized samples have been obtained using the RADIAN DR-02 device with a copper X-ray tube and a nickel filter.

## 3. Results and discussions

The results of X-ray diffraction after annealing germanium nanostructures with cobalt Ge-Co at various temperature are shown in Fig. 1

The sample without annealing has peaks of two phases: crystalline germanium and titanium substrate.

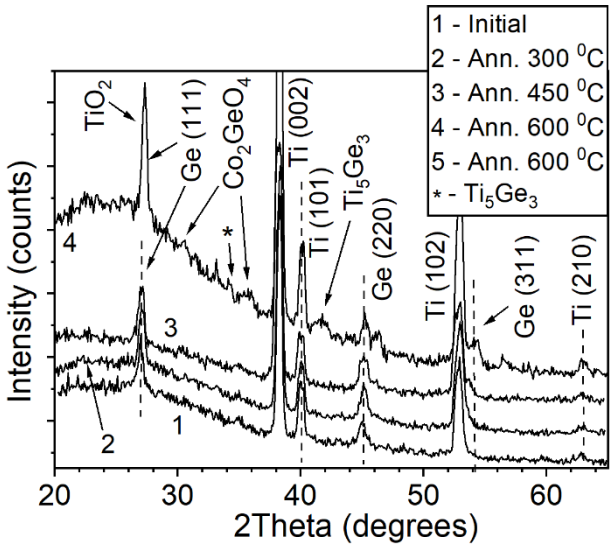


***Fig. 1.*** *X-ray diffractograms of Ge-Co samples after annealing at different temperatures.*

At annealing temperatures of 300 °C and 450 °C, there is an increase in the intensity of germanium peaks,

especially the first peak (27.3°) [4]. With an increase in the annealing temperature, a slight shift of the germanium peaks to the right to the reference values is also noticeable.

However, at an annealing temperature of 600 °C, the diffractogram shows a presence of germanium-cobalt compounds in the nanostructure, particularly cobalt germanate $Co_2GeO_4$ at 30-40° [4], which has not been observed at lower annealing temperatures. A well-marked phase of titanium oxide and a certain amount of the compound $Ti_5Ge_3$ are also visible.

The first peak of germanium becomes indistinguishable due to the presence of titanium oxide, which leads to the overlap of two peaks and its sharp increase.

Additionally obtained Ge-Co samples after annealing and without it have been also tested for the OER activity in a solution of 1 M NaOH. Graphics of current density-voltage curve (CV curve) based on the results of the sample study are shown in Fig. 2. This figure also shows the CV curve of a pure titanium substrate obtained for comparison.

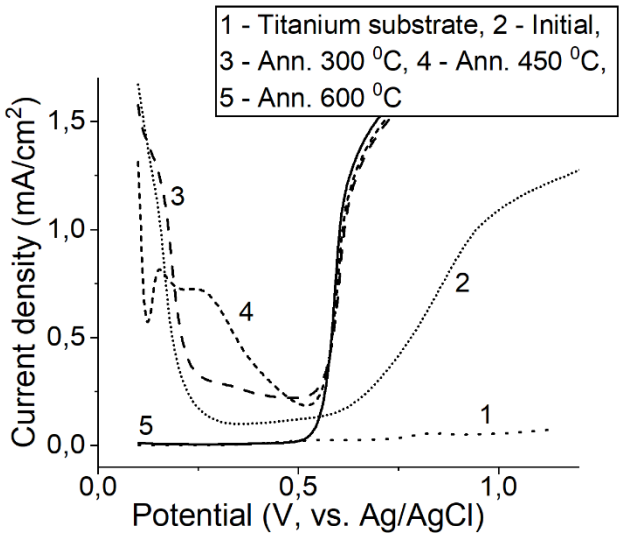


***Fig. 2.*** *CV curve of initial/annealing Ge-Co samples and titanium substrate.*

According to the graph of the titanium substrate, it can be seen that the current density almost does not change in the voltage range, which means that there are practically no electrochemical processes.

The current density for Ge-Co samples (except for the sample after annealing at 600°C) at a potential of 0.2 V to 0.5 V indicates reactions caused with the oxidation of germanium and cobalt. At a potential of 0.5 V, the current density increases due to the beginning of oxygen release. For a sample without annealing, the current density increases more slowly compared to annealing samples, which indicates its lower OER activity.

At the same time, with an annealing at 600 °C, reactions caused only with the release of oxygen are observed on the sample (the current density begins to increase only at a potential of 0.5 V) due to the presence of a cobalt germanate. It can be concluded that the annealing temperature at 600 °C is the most optimal temperature for the formation of an oxygen evolution catalyst based on Ge-Co nanostructure.

## 4. Conclusions

In the present work nanostructures Ge-Co have been prepared by electrodeposition from the aqueous solution. The effect of thermal annealing on the composition of Ge-Co has been investigated.

According to the results of X-ray diffraction, with an increase in the annealing temperature, the crystal phase of germanium decreases and germanium compounds with cobalt are formed. On an annealing temperature at 600 °C, a compound cobalt germanate $Co_2GeO_4$ is found that could be a good oxygen evolution catalyst.

## Acknowledgements

The work is supported by the Grant of the President of the Russian Federation №МК 5839.2021.1.3 and by the State assignment 2020-2022 № FSMR-2020-0018.

## References

[1] X. Chen, C. Li, M. Grätzel, R. Kostecki. Chem. Soc. Rev. **41**(2012)7909.
[2] Z. Seh, J. Kibsgaard, C. Dickens, I. Chorkendorff. Science **355**(2017)6321.
[3] Z. Xu, W. Li, X. Wang, Z. Shi. ACS Applied Materials & Interfaces **10**(2018)30357.
[4] Information on http://www.crystallography.net/cod/.

# Development of a technique for studying trimethylamine oxide solutions using planar SERS structures

D.G. Gromov[1,2], P.Y. Kopylov[2], Af. A. Bestavashvili[2], S.V. Dubkov[1], D.V. Novikov[*,1], H. Bandarenka[3], E.V. Latipov[4], A.I. Savitskiy[5]

[1] Institute of Advanced Materials and Technologies, National Research University of Electronic Technology (MIET), Bld. 1, Shokin Sq., Moscow 124498, Russia
[2] I.M. Sechenov First Moscow State Medical University, Bolshaya Pirogovskaya st., 2, Bld. 4, Moscow 119435, Russia
[3] Belarusian state university of informatics and radioelectronics, 6 P. Brovki St, Minsk 220013, Belarus
[4] Institute of Nanotechnology of Microelectronics of the Russian Academy of Sciences, 32a Leninsky Av., Moscow 119991, Russia
[5] Scientific-Manufacturing Complex «Technological Centre», H. 1, Bld. 7, Shokin Sq., Moscow 124498, Russia

*e-mail: tororo@bk.ru

**Abstract.** In this work, we study the effect of treatment with weak HCl solutions and isopropanol vapor on SERS structures based on metal, dielectric, and Ag nanoparticle layers on the Raman spectra. The influence of the methods of deposition of the analyte on the substrate on the quality of the Raman spectra was studied. TMAO solutions with concentrations of 10 mM, 10 μM, and 10 nM were used as an analyte in the work.

## 1. Introduction

Today, there are many different SERS structures in the world, providing a wide range of sensitivities and operating wavelengths [1]. At the same time, there is a problem that some substances require not only a high sensitivity of the structure, but also certain preparation and measurement parameters in order to obtain their spectra with the greatest efficiency.

One of these substances that interested us is trimethylamine oxide (TMAO) [2]. This substance in human blood serves as a marker of the risk of cardiovascular disease, obesity and stroke. If the concentration exceeds 2.26 μM, the risks increase significantly. In this regard, there is an increased interest in the method of sample preparation and measurement of this analyte for the most effective study.

## 2. Experiment

In this work, solutions were used as analytes: TMAO with a concentration of 10 mM, 10 μM, and 10 nM. SERS structures were treated with HCl solutions mass. 3.5%, deionized water and isopropyl alcohol.

Si (100) at 300 nm with SiO2 was used as the basis for the SERS structure. The adhesive layer Cr 50 nm was deposited by magnetron sputtering. Then, a 100 nm Ag reflective layer was formed on the substrate by vacuum thermal evaporation. After that, the reflective layer was coated with 20 nm SiO2 as an insulator by the method of electron beam evaporation. The final stage was the deposition of 15 nm Ag followed by annealing at 400 ºC for 10 minutes in an air atmosphere.

Before applying the analyte, some of the finished substrates were not processed. The second part was soaked in a weak solution of HCl and washed in a stream of deionized water. The third part was treated with hot vapors of isopropyl alcohol.

The analyte was applied in two ways: by soaking the finished SERS structure in an analyte solution and by a drop from a dispenser. The substrates were soaked in the analyte solution for 5, 30, and 60 minutes. The substrates with the applied analyte dispenser were dried in a fume hood at room temperature. Part of the samples with drops was covered with a cover slip for distribution and preservation in liquid form until the moment of examination..

Samples were examined on a Raman spectrometer based on an inVia confocal microscope from Renishaw. The light spot diameter was 5 μm, the laser power varied from 500 to 0.05 mW, and the exposure time was at least 6 seconds. Various monochromatic lasers have been used.

## 3. Results and discussions

The most significant result was shown by samples treated in acid and washed in deionized water (Fig. 1). Raman spectra of 10 mM TMAO droplets on treated substrates showed a significant increase in peak sharpness, noise reduction, and a 56-fold increase in intensity compared to spectra on untreated substrates.

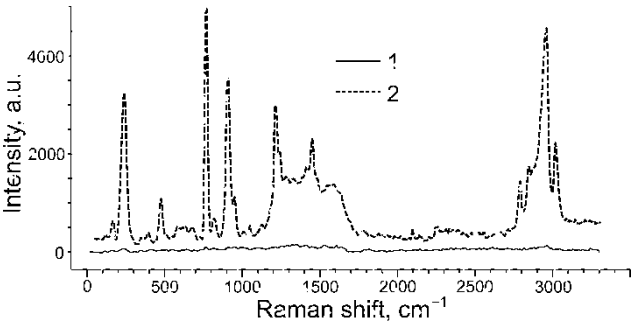


***Fig. 1.*** *Raman spectra of 10 mM TMAO at 532 nm and 5 mW before (1) and after (2) treatment of the substrate by HCl solution, before adding a drop of analyte.*

Pretreatment of the SERS structure in isopropyl alcohol vapor significantly worsened the quality of the spectrum and its intensity. The use of a coverslip led to the appearance of luminescence and the loss of all characteristic TMAO peaks. Soaking the substrates in TMAO solutions showed that the soaking efficiency began to decrease after 30 minutes. When soaking for 60 minutes, the intensity of the spectra increased by only 1.2 times, compared with 30 minutes soaking.

## 4. Conclusions

In the course of the work, it was found that Ag-based SERS structures that underwent atmospheric annealing should be treated for at least 30 seconds in weak HCl solutions and washed in deionized water to remove residual acid. It has been found that keeping samples in solution for more than 30 minutes does not make a significant contribution to the quality of the spectra. It turned out that the use of a laser with a power of more than 5 mW with a light spot area of about 20 $\mu m^2$ leads to the decomposition of TMAO to the state of amorphous carbon.

## Acknowledgements

The work was supported by the Russian Science Foundation (Project No. 21-19-00761).

## References

[1] D. Cialla, A. März, R. Böhme, F. Theil, K. Weber, M. Schmitt, J. Popp. Analytical and Bioanalytical Chemistry **403**(2012)27.
[2] P. Gatarek, J. Kaluzna-Czaplinska. EXCLI JOURNAL **20**(2021)301.

# Tuning $TiO_2$(B) nanobelts through Ni-doping using a hydrothermal approach for metal-ion batteries

D.P. Opra*, S.V. Gnedenkov, S.L. Sinebryukhov, A.A. Sokolov, A.B. Podgorbunsky, A.M. Ziatdinov
Institute of Chemistry FEB RAS, Prospekt 100-letiya Vladivostoka 159, Vladivostok 690022, Russia

*e-mail: dp.opra@ich.dvo.ru

Up until recently, lithium-ion batteries (LIBs) were mainly used for areas demanding moderate characteristics and soft operating standards (e.g., portable electronics, medical equipment, and power tools). At present, they are closely considered for usage in hybrid and electric vehicles, renewable energy, robotics, and standby backup power applications. On the other hand, lithium reserves in the Earth's crust are limited, and the cost of lithium-containing raw materials is growing steadily. In this way, a change to other electrochemical energy storage technologies based on abundant materials, such as sodium-ion batteries (SIBs), is expected in the near future at least for a number of areas. For further progress in both LIBs and SIBs, advanced electrode materials are required. In this way, titanium compounds based on the $Ti^{3+}/Ti^{4+}$ redox couple, including $Li_4Ti_5O_{12}$, $MLi_2Ti_6O_{14}$ (M = Sr, Ba, Na), $Na_2Ti_3O_7$, $TiO_2$, $Na_2Ti_6O_{13}$, $NaTi_2(PO_4)_3$, $ATiOPO_4$ (A = $NH_4$, K, Na) etc. have attracted attention.

Herein, mesoporous belt-like $TiO_2$(B) nanostructures doped with nickel (Ni/Ti atomic ratios of 0.02, 0.05, and 0.08) had been synthesized hydrothermally. Based on electron-microscopic experiments the dimensions of nanobelts are 40–160 nm in width, 3–7 nm in thickness and up to a few micrometers in length. From $N_2$ adsorption/desorption (at 77 K) found that BET specific surface area and BJH pore volume achieve 114 $m^2\ g^{-1}$ and 0.48 $cm^3\ g^{-1}$ (at least 70% of pores are mesocopic with a size of 4.2 nm). According to X-ray diffraction, Ni-doping increases the unit cell volume of $TiO_2$(B) by 4% (Ni/Ti = 0.05), confirming the incorporation of $Ni^{2+}$ ions (with an ionic radius of 0.69 Å) at the $Ti^{4+}$ positions (0.605 Å) with the formation of substitutional solid solution. The generation of localized Ni 3*d* defect states within band gap of $TiO_2$(B) was confirmed by ultraviolet-visible spectroscopy, revealing that band gap energy reduces from 3.28 to 2.70 eV after Ni-doping. Electron paramagnetic resonance studies revealed an oxygen deficiency for Ni-doped $TiO_2$(B). The electrochemical impedance spectroscopy revealed that the conductivity of nickel-containing titanium dioxide increased to $2.24 \times 10^{-8}$ $S \cdot cm^{-1}$ (Ni/Ti = 0.05) exceeding that of the undoped sample ($1.05 \times 10^{-10}$ $S \cdot cm^{-1}$).

Among the tested samples, Ni-containing $TiO_2$(B) nanobelts with a Ni/Ti atomic ratio of 0.05 demonstrated the best battery performance for using as anode material. In lithium cells after 100 cycles, a reversible capacity of 173 $mAh \cdot g^{-1}$ was achieved for Ni-doped $TiO_2$(B) at the current density of 50 $mA \cdot g^{-1}$, whereas unmodified bronze $TiO_2$ electrode maintained 140 $mAh \cdot g^{-1}$. Moreover, Ni-doping enhanced the rate capability of $TiO_2$(B) nanobelts (104 $mAh \cdot g^{-1}$ at the current density of 1.8 $A \cdot g^{-1}$). Concerning the operation in sodium cells, it was found that Ni-containing material exhibited improved cycling with a specific capacity of about 97 $mAh \cdot g^{-1}$ after 50 cycles at the current load of 35 $mA \cdot g^{-1}$. The main factors determining the enhanced electrochemical performance of doped $TiO_2$(B) were (i) increased electronic conductivity, (ii) improved stability of crystal lattice toward guest ion insertion/extraction, and (ii) facilitated transport of $Li^+$ and $Na^+$.

This work was supported by funding from the Russian Science Foundation (grant № 19-73-10017). The authors are grateful to colleagues at the Institute of Chemistry FEB RAS who contributed to research, namely Ph.D. A.V. Gerasimenko, Ph.D. V.G. Kuryavyi, Ph.D. V.Yu. Mayorov, and Sc.D., Prof. A.Yu. Ustinov.

Sixth Asian School-Conference on Physics and
Technology of Nanostructured Materials
Vladivostok, Russia, 25 – 29 April, 2022



# Composite ($SiO_2$-Au) films for magnetophotonics

S.V. Osmanov, T.V. Mikhailova*, A.L. Kudryashov, S.D. Lyashko, A.V. Karavainikov, A.S. Nedviga and A.N. Shaposhnikov

V.I. Vernadsky Crimean Federal University, 4 pr. Vernadskogo, Simferopol 295007, Russia

*e-mail: taciamikh@gmail.com

**Abstract.** Structural and morphological features of layers of composite ($SiO_2$-Au) were experimentally investigated depending on the conditions of formation. It has been demonstrated that the diameter of Au nanoparticles in a $SiO_2$ matrix can vary from 12 to 60 nm. The volume content of Au nanoparticles in the $SiO_2$ matrix in synthesized samples was $f = 0.16$. Taking into account the features of formation of composite and bismuth-substituted iron garnets layers, the magnetophotonic crystal "composite – $SiO_2$ layer – iron garnet – Bragg mirror" was proposed as the most promising from a practical point of view and implementation. Optical and magneto-optical characteristics of the magnetophotonic crystal with different numbers of layers pairs $m$ and the center of photonic band gap $\lambda_0$ of the Bragg mirrors were considered.

## 1. Introduction

Composites are today one of the most promising in practice and the most widespread among modern materials. A large number of investigations in the field of photonics are devoted to them. So, composites based on nanoparticles of gold, silver and copper are used not only as elements of technical devices for electronics and decor, but also as materials with particularly outstanding various properties for use in the chemical industry and medicine. The synthesis of composite thin layers by sputtering methods was considered in [1]. These methods are one of the common methods at the moment [2, 3]. The described technology makes it possible to create the structures of photonic and magnetophotonic crystals (PC & MPC) using composites, that has not been presented before. There are known theoretical works [4], which show that in structures based on composite layers ($SiO_2$-Ag) two types of localized states are possible. These states are Tamm states (Tamm plasmon polaritons) and resonant defect modes. It should be noted that one of the useful properties of such composites is the following. As a result of the imperfection of the particles, the composite itself can work as a polarizer. The longitudinal and transverse components of electromagnetic waves will interact with the structure in different ways, leading to different optical effects for mixed polarizations even at normal incidence [5]. One of the experimental tasks in the implementation of the structure is to achieve the required quality of the composite, namely, to achieve the required sizes of nanoparticles. The sizes of nanoparticles in the matrix should be much smaller than the wavelength, that is, they should not exceed 50 nm. In general, the properties of the composite will also depend on the volume fraction of inclusions (nanoparticles) $f$.

The resonant enhancement of magneto-optical effects due to structure modes arising at the boundary of MPC $[TiO_2 / SiO_2]^m$ / iron garnet / $SiO_2$ / ($SiO_2$-Au), in which the upper layer ($SiO_2$-Au) is a composite layer of $SiO_2$ with metallic Au nanoscale inclusions, and iron garnet is a bi-layer of composition $Bi_{1.0}Lu_{0.5}Gd_{1.5}Fe_{4.2}Al_{0.8}O_{12}$ / $Bi_{2.3}Dy_{0.7}Fe_{4.2}Ga_{0.8}O_{12}$ was discussed in the work [6]. However, the presence of layers with a high bismuth content limits the use of the high annealing temperatures required to form the composite. In this regard, it was proposed to use the reverse order of alternation of layers for the synthesis of structure and to carry out a preliminary analysis of the properties of MPC "composite – $SiO_2$ layer – iron garnet – Bragg mirror".

## 2. Experiment and simulation methods

Considered MPC can be represented by the general formula

$$GGG/(SiO_2\text{-}Au)/SiO_2/G1/G2/\left[SiO_2/TiO_2\right]^m, \quad (1)$$

there GGG is substrate of gadolinium gallium garnet; $[SiO_2/TiO_2]^m$ is Bragg mirror with repetition number $m$; G1 is garnet of composition $Y_3Fe_5O_{12}$; G2 is garnet of composition $Bi_{2.8}Y_{0.2}Fe_5O_{12}$; ($SiO_2$-Au) is composite film.

In order to simulate the optical and magneto-optical characteristics of MPC and numerically solve Maxwell's equations, a software algorithm was implemented using the transfer matrix method 4×4. The software algorithm takes into account the angle of incidence of light on the structure $\theta$, incident light wave polarization state $\Psi$, anisotropy and gyration of structure layers. All layers of the structure were preliminarily synthesized and their structural, optical and magneto-optical properties were determined. The dielectric constant of composite layer was calculated based on the Maxwell-Garnett model. We assumed that the nanoparticles have a spherical shape.

For the synthesis of composite ($SiO_2$-Au), the technology of simultaneous sputtering of Au plates and $SiO_2$ targets was used. To form nanoparticles with lateral dimensions from 10 to 50 nm, the deposited layers were annealed. The sample was sequentially annealed for 30 min at different temperatures from 700°C to 1000°C. Reactive ion beam sputtering was implamented at a URM 3-279.014 setup with ion-beam Kholodok-1 source.

G1 and G2 iron garnet films were synthesized using high-frequency magnetron sputtering at MVU TM MAGNA 09. In order to form the garnet phase, each layer was annealed at the optimum temperature $T_a$ and duration $\tau_a$: $T_a$ = 800°C and $\tau_a$ = 5 min for layer G1 and $T_a$ = 670°C and $\tau_a$ = 25 min for layer G2. Bragg mirror layers were deposited by high-frequency magnetron sputtering at Elim TM 5.

Atomic force microscopy methods (intermittent contact and phase contrast imaging modes) were used to characterize the microstructure. The measurements were carried out by cantilevers of HA_HR ETALON using the INTEGRA scanning probe microscope (NT-MDT).

## 3. Results and discussions

Figure 1 shows an increase in the size of nanoparticles and changes in the optical spectra of composite layer depending on the duration and temperature of annealing. Numerical analysis of optical spectra showed that the composite is characterized by the value $f = 0.16$.

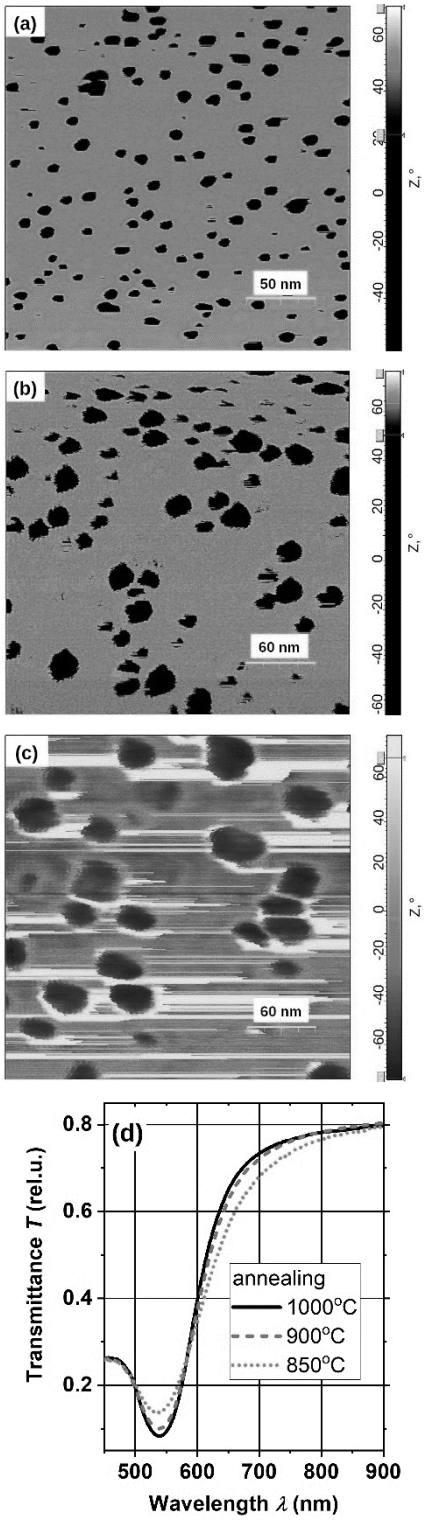


***Fig. 1.*** *AFM images (phase contrast imaging mode) of surface of a ($SiO_2$-Au) layer annealed successively under different conditions: 850°C (a), 900°C (b) and 1000°C (c). Optical spectra of this layer at different stages of the annealing process (d).*

The transmission and Faraday rotation angle spectra of the structure (1) are shown in figure 2. The model parameters of layers were as follows: $m = 3$; the thicknesses of layers of titanium dioxide $h_{(TiO2)} = 52.5 – 70$ nm; silicon dioxide $h_{(SiO2)} = 75.7 – 101$ nm; composite $h_{(SiO2-Au)} = 130$ nm; buffer silicon dioxide $h_{(SiO2)} = 101$ nm; G1 $h_{(G1)} = 67$ nm; and G2 $h_{(G2)} = 335$ nm. At real optical parameters of the composite, only resonance states corresponding to the defect mode are observed in the spectra of structure.

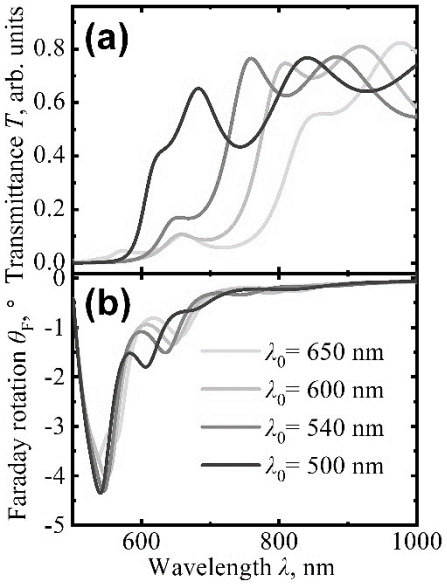


***Fig. 2.*** *Dependences of the spectra of transmittance (a) and Faraday rotation angle (b) of the structure (1) on layer thicknesses in Bragg mirrors (or from the center of photonic bandgap $\lambda_0$) at the volume fraction of inclusions in the composite $f = 0.16$.*

## 4. Conclusions

Modeling of the properties and optimization of conditions for the synthesis of magnetophotonic crystal with composite ($SiO_2$-Au) layer were carried out. It is shown that the highest values of the Faraday rotation can be achieved in the short-wavelength region of the spectrum. A technology has been developed for obtaining composites with desired properties for applications in magnetophotonics.

## Acknowledgements

This work was supported by Russian Science Foundation (project no. 19-72-20154). Structure development and layer analysis were carried out using the equipment of Common Research Center «Physics and Technology of Micro- and Nanostructures» of the Institute for Physics of Microstructures RAS.

## References

[1] R.W. Cohen, G.D. Cody, M.D. Coutts, B. Abeles. Phys. Rew. B **8**(1973)3689.
[2] Zhao Cui-Hua, Zhang Bo-Ping, and Shang Peng-Peng. Chinese Physics B **18**(2009)5539.
[3] J.H. Hsieh, Chua Li, Y.Y. Wu, S.C. Jang. AIP Conference Proceedings **519**(2011)7124.
[4] R.G. Bikbaev, S.Y. Vetrov, I.V. Timofeev. Photonics **5**(2018)22.
[5] Yu. Dadoenkova, I. Glukhov, S. Moiseev, V. Svetukhin, A. Zhukov, I. Zolotovskii. Optics Communications **389**(2017)1.
[6] T.V. Mikhailova, S.V. Osmanov and V.O. Boyko. Journal of Physics: Conference Series **2086**(2021)012156.

# Plasmonic nanopipette for scanning ion-conducting microscopy

S. Dubkov[1], A. Overchenko[*,1], D.V. Novikov[1], V. Kolgmogorov[2], L. Volkova[3], E.V. Latipov[3], T. Grishin[3]

[1] National Research University of Electronic Technology "MIET", 124498 Moscow, Russia
[2] National University of Science and Technology "MISiS", 119049 Moscow, Russia
[3] Institute of Nanotechnology of Microelectronics of the Russian Academy of Sciences "INME RAS", 11934 Moscow, Russia

*e-mail: alexsey7840@mail.ru

**Abstract**. In this work, we report of the successful development of a SERS-active pipette. In the course of the study, various approaches were developed for the formation of particles at the tip of the pipette to enhance the signal. Silver was used as the particle material. The method of vacuum thermal evaporation was used to form an array of nanoparticles. The modified pipettes were captured in a scanning electron microscope. The results of these work allowed us to characterize the morphology of the modified pipette surface using various approaches. The Raman spectra was obtained using these pipettes. Rhodamine in the R6G modification was used as an analyte. Based on the obtained spectra, the most effective technology of particle deposition on a pipette was selected. The SERS pipette can be improved to monitor various intracellular biomarkers.

## 1. Introduction

Reliable analysis of biomarkers from a single cell is a critically important task today. The low concentration of biomarkers and the dynamic nature of living cells make the analysis of the intracellular contents of single cells difficult using traditional analytical methods [1-2]. Despite the fact that modern spectroscopy methods have made great strides in cell analysis, these methods are still difficult to use for accurate monitoring of individual cells. To obtain the most detailed and accurate information about the studied object, people are using SERS substrates. However, SERS has a significant disadvantage due to the complexity and high cost of this technology [3]. A noble metal modified pipette can be used to electrically regulate the delivery of molecules/ions, while simultaneously monitoring changes in real time and in situ measuring measurements caused by exposure to delivered molecules/ions via Raman spectra. With low cost, ease of manufacture and operation, such pipettes will allow SERS experiments to be carried out without having to rely on complex devices.

## 2. Experiment

In the series of experiments carried out, pipettes manufactured at a facility for pulling pipettes from glass based on a CO2 laser (P-2000, SutterInstrumentCo.) from borosilicate glass were used as substrates. The resulting pipettes were manufactured in a length of 45 mm and with an outlet size of about 50-70 nm.

Before carrying out the process of deposition of nanoparticles by vacuum-thermal evaporation, pipette samples underwent standard washing to remove impurities. Washing was carried out sequentially in three solutions. The first was a peroxide-ammonia solution (PAS), the second was deionized water with a temperature of 50 °C, the third was deionized water with a room temperature. The sample was kept in each solution for 5 minutes. At the final stage, the samples were dried.

All the work on the formation of metal nanoparticles was carried out at the vacuum thermal evaporation plant. To fix the pipette on the 3D printer, a special substrate holder was made. To carry out the process, a pressure of $3*10^{-5}$ Torr was created in the working chamber. Then the evaporation of the suspension of the evaporated material was carried out. For the final formation of particles in the same working chamber, samples were annealed at a temperature of 230C ° for 30 minutes and at a pressure of $3\times10^{-5}$ Torr.

All SEM images were obtained from a Helios C4 GX scanning electron microscope. Raman spectra were obtained using a Raman scattering spectrometer based on a confocal microscope (Raman confocal microscope) inVia from the Renishaw campaign. Before the experiment, the analytical substance rhodamine 6G of a millimolar concentration was applied to the pipettes, followed by drying in an air atmosphere for 10 minutes. At the next stage of the experiment, the pipette with the analyte was fixed in the inner space of the chamber of the Raman spectrometer. The laser was aimed at the pipette using a light microscope built into the spectrometer. Two lasers with a wavelength of 405 and 532 nm were used.

## 3. Results and discussions

Using a laser with a wavelength of 405 nm and at all powers, the Raman spectra from all pipettes did not contain any characteristic peaks, but were filled with interference. At a laser wavelength of 532 nm, characteristic peaks of rhodamine 6G were present in the Raman spectra.

The maximum power of the laser used was 500 mW, furher when we will talk about the power as a percentage of the maximum values. In a comparative analysis of Raman spectra, the modified pipette, pure glass and a commercial SERS substrate were coated with rhodamine in modification R6G dye in a millimolar concentration, Spectra were successfully obtained from them at a wavelength of 532 nm. Our goal was to use low laser power to obtain spectra.

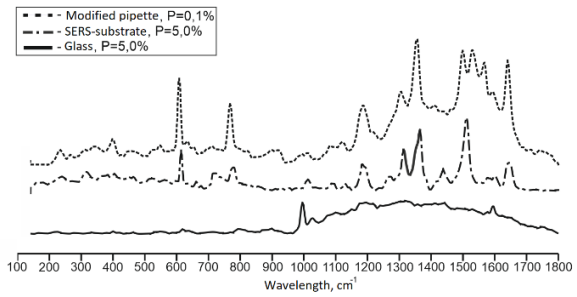


***Fig. 1.*** *Comparative Raman spectra of temperature.*

It is difficult to identify R6G peaks on the spectrum obtained from glass. The spectra of the SERS substrate contain has most of the characteristic peaks that are easy to detect. In the case of a modified pipette, peaks are comparable in quality to a SERS substrate. Also, for pure glass and SERS substrates, the laser power was 5% of the maximum laser power (500 mW), and for pipette they were only 0.1% of the power, while they are in no way inferior to SERS substrates. Potentially, the use of such small capacities will not cause damage to the biomaterial, for example, (TMAO). The calculated enhance factor of the pippette signal is about $10^2$.

## 4. Conclusions

A technique has been developed for applying silver particles to the tip of a pipette. SEM studies have been carried out, it has been shown that the most optimal technique is the method with an array of nanoparticles of the order of 16 nm. Raman spectroscopy studies were carried out, which showed an enhance factor of the order of $10^2$.

## Acknowledgements

This work was supported by the State assignment 2020-2022 № FSMR-2020-0018.

## References

[1] Dittrich, Petra, and Norbert Jakubowski. "Current trends in single cell analysis." Analytical and Bioanalytical Chemistry 406.27 (2014): 6957-6961.

[2] Yuan, Guo-Cheng, et al. "Challenges and emerging directions in single-cell analysis." Genome biology 18.1 (2017): 1-8.

[3] Zou, Sumeng, et al. "Ag Nanorods-Based Surface-Enhanced Raman Scattering: Synthesis, Quantitative Analysis Strategies, and Applications." Frontiers in Chemistry 7 (2019): 376.

Sixth Asian School-Conference on Physics and
Technology of Nanostructured Materials
Vladivostok, Russia, 25 – 29 April, 2022



# Optimization of electrolytic deposition modes of the CoNiP alloy

M.I. Panasyuk[*,1], T.I. Zubar[1,2], T.I. Usovich[1], V.A. Fed'kin[1], O.D. Kanafiev[1], A.N. Kotelnikova[1], A.V. Trukhanov[1,2,3]

[1] SSPA "Scientific and practical materials research centre of NAS of Belarus", 220072, Minsk, P. Brovki str., 19, Belarus
[2] South Ural State University, 454080, Chelyabinsk, Lenin Prospect, 76, Russia
[3] National University of Science and Technology MISiS, 119049, Moscow, Leninsky Prospekt, 4, Russia

*e-mail: maria.panasiuk.99@gmail.com

**Abstract.** Magnetic CoNiP thin film alloys were electrodeposited from chloride and sulphate baths. The effects of solution composition and current density on the magnetic properties and microstructure of electrodeposited CoNiP films were investigated. Solution composition and current density significantly influenced the magnetic properties of CoNiP deposits. These films when deposited from chloride bath showed the maximum coercivity at the level of 500 Oe, whereas from sulphate bath the coercivity has reached 1500 Oe.

## 1. Introduction

Much attention has been paid to magnetic materials in recent years. this can be explained by their wide technological application in industry. A special research study was devoted to solid magnetic materials[1-3]. At present the development of hard magnetic materials is an extremely interesting direction because of potential applications in microelectromechanical systems, such as microactuators, field generators, micromotors etc [4-6]. Triple Co-based films such as CoNiP are of particular interest because of their high coercivity and high anisotropy. However, the researchers faced the problem of a sharp decrease in coercivity with an increase in the thickness of the films. Therefore, the task of obtaining thick hurd magnetic Coni films is still relevant.

In our opinion, the most convenient way to obtain films is electrodeposition. This method has a number of advantages such as low cost, ease of parameter adjustment and the possibility of obtaining the necessary coating properties by changing the deposition conditions.

It is the purpose of the present work to study the effects of electrolyte composition on the magnetic properties of CoNiP thin films.

## 2. Experiment

The CoNiP thin films are electrodeposited on copper wafers using two different electrolytes listed in Table I. The copper substrates are first degreased with Viennese lime followed by immersion in a $(NH_4)_2S_2O_8+H_2SO_4$ bath for 60 seconds to etching. The pH of the solution was adjusted with $H_2SO_4$ and the solution was maintained at 40°C during deposition without any stirring. The experiment was conducted at 20 and 30 mA $cm^{-2}$; nickel sheet was used as a soluble anode.

Magnetic properties were determined using a universal measuring system (automated vibration magnetometer) "Liquid Helium Free High Field Measurement System (Cryogenic LTD", London, UK). Microstructures of CoNiP electrodeposits were examined with a Zeiss EVO 10 scanning electron microscope (SEM) (Zeiss, Oberkochen, Germany). Deposit Co, Ni and P contents were analyzed using AZtecLive Advanced energy dispersive X-ray spectrometer with Ultim Max 40 (Oxford Instruments, Bognor Regis, Great Britain)

***Table I.*** *Bath composition for CoNiP electrodeposits.*

| Electrolyte №1 | | Electrolyte №2 | |
|---|---|---|---|
| Chemical/ conditions | Concentration, g/l | Chemical/ conditions | Concentration, g/l |
| $CoSO_4$ | 150 | $CoSO_4$ | 150 |
| $NiCl_2$ | 100 | $NiSO_4$ | 150 |
| $NiSO_4$ | 50 | $H_3BO_3$ | 30 |
| $H_3BO_3$ | 30 | $Na_2SO_4$ | 60 |
| $NaH_2PO_2$ | 10 | $NaH_2PO_2$ | 8 |
| $pH$ | 2 | $pH$ | 2 |

## 3. Results and discussions

The effects of electrolytes composition on the properties of CoNiP films are investigated. Nickel-sulfate and cobalt-sulfate are used for the metal ions source in both electrolytes. Nickel chloride can decrease anodes passivation. Boric acid was added as pH buffer. Sodium hypophosphite supplies the ions for the cathode and anode reactions.

Figures 1a and 1b shows SEM images of the surface micromorphology of the electrodeposited CoNiP films with a thickness of 35 μm using different current densities (from electrolyte №1). The CoNiP alloy deposited using a higher current density of 30 mA $cm^{-2}$ have a smaller grain size (approximately 250 nm) than materials deposited using a lower current density of 20 mA $cm^{-2}$ (approximately 500 nm). In both cases, the CoNiP alloy has exhibited dendritic, nodular surface morphology.

For the electrolyte №2, CoNiP deposits were smooth. As the deposit thicknesses increases (from 15 to 35) with increasing current density, the deposits become smoother.

Figure 2 shows the hysteresis loops of CoNiP films. Films obtained in electrolyte №2 show a more gradual approach to saturation. In both electrolytes, with an increase in current density from 20 mA $cm^{-2}$ to 30 mA $cm^{-2}$, an increase in coercivity is observed. In electrolyte №1, when the current density increases, the coercivity increases from 420Oe to 500Oe. However, the saturation magnetization decreases from 195emu/g to 160emu/g.

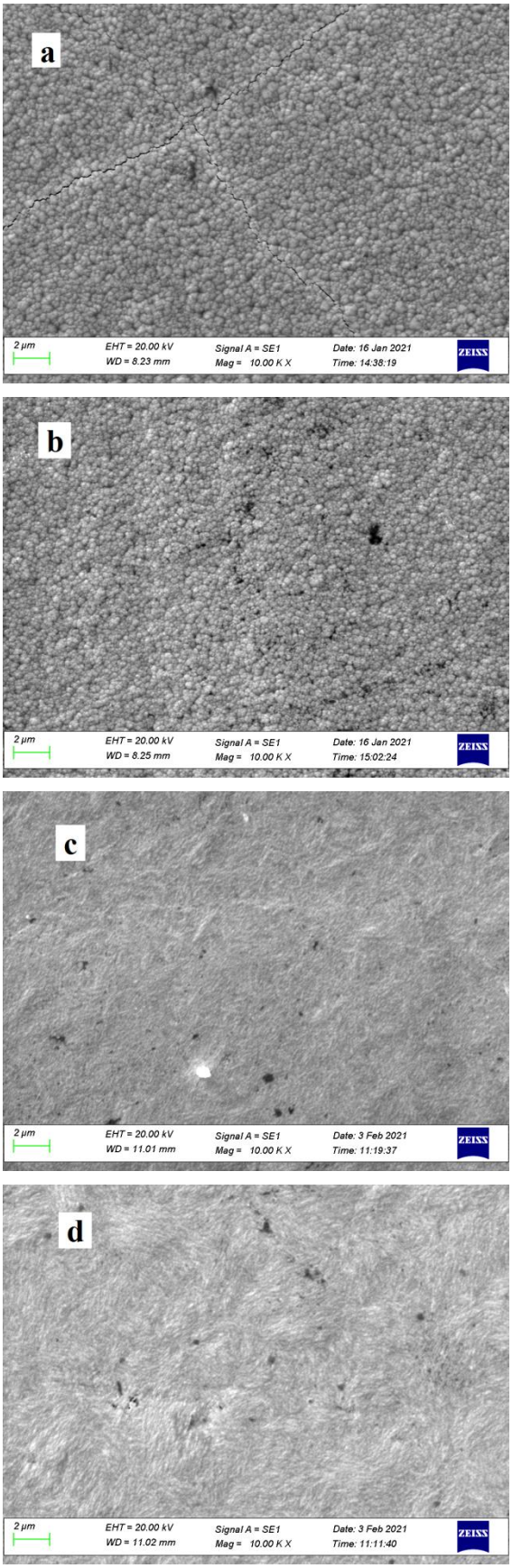


***Fig. 1.*** *SEM images of CoNiP films a) electrolyte №1, 20mA/cm$^2$; b) electrolyte №1, 30mA/cm$^2$; c) electrolyte №2, 20mA/cm$^2$; c) electrolyte №2, 30mA/cm$^2$.*

More impressive values of coercivity are demonstrated by coatings obtained in electrolyte №2. The coercivity reaches values of 1000Oe and 1500Oe at current densities of 20 mA cm$^{-2}$ and 30 mA cm$^{-2}$, respectively. It can also be noted that with an increase in the current density, the saturation magnetization increases almost 2 times: 220emu/g at 30 mA cm$^{-2}$ and 120emu/g at 20 mA cm$^{-2}$.

In both electrolytes, the increase in current density did not affect the composition of the deposits. The film obtained from electrolyte №1 contained 82 at% Co, 14 at% Ni and 4 at%P. The film obtained from electrolyte №1 contained 81 at% Co, 14 at% Ni and 5 at%P.

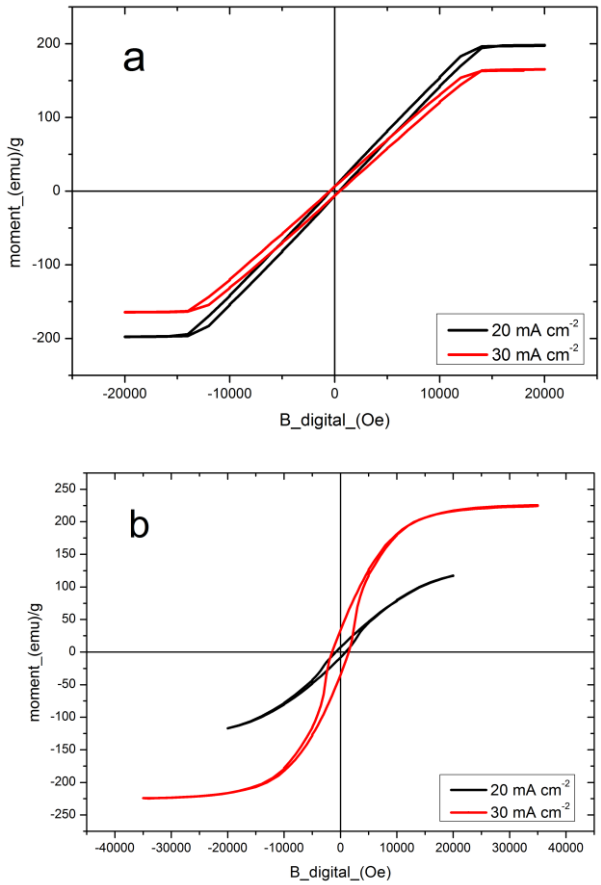


***Fig. 2.*** *Perpendicular hysteresis loops for CoNiP films a) electrolyte №1; b) electrolyte №2.*

## 4. Conclusions

Hard magnetic Co-rich Co–Ni–P films were grown by electrodeposition. Hard magnetic properties were achieved in the as-deposited films and were preserved up to 35 micrometer film thickness.

## References

[1] B. Lochel, A. Maciossek, J. Electrochem. Soc. **143**(1996)3343–3348
[2] T. Wang, A.B. McCandless, R.M. Lienau, K.W. Kelly, D. Hensley, Y. Desta, Z.G. Ling, J. Microelectromech. Syst. **14**(2005)400–409.
[3] S. Guan, B.J. Nelson, J. Microelectromech. Syst. **15**(2006)330–337
[4] T.-S. Chin, J. Magn. Magn. Mater. **209**(2000)75.
[5] J.W. Judy, R.S. Muller, J. Microelectromechanical Sys. **6(3)**(1997) 249.
[6] J.W. Judy, R.S. Muller, H.H. Zappe, J. Microelectromechanical Sys. **4(4)**(1995)162.

# Anodic $TiO_2$ nanotube arrays SILAR modified by $Ag_xO$ for visible light photocatalytic applications

O.V. Pinchuk*,[1], T.P. Savchuk[1], M.F. Kamaleev[1], A.A. Dronov[1], I.I. Tsiniaikin[2,3], A.V. Pavlikov[1,2]
[1] National Research University of Electronic Technology (MIET), 1, sq. Shokin, Zelenograd, Moscow, 124498, Russia
[2] M.V. Lomonosov Moscow State University, Leninskie Gory, Moscow 119991, Russia
[3] MSU QUANTUM TECHNOLOGY CENTRE, 119991, Moscow, Russia

*e-mail: pepsi6382@gmail.com

**Abstract.** To increase the photoactivity of anodic titanium oxide nanotubes in the visible wavelength range, various attempts have been made to increase the absorption spectrum of the material. The heterojunction increases the efficiency of carrier separation and the absorption spectrum of $TiO_2$ in the visible wavelength range. $Ag_xO$ has attracted considerable attention for the creation of heterojunctions between the $TiO_2$ layer due to its narrow band gap (1.2 eV), excellent photocatalytic activity and compatibility with $TiO_2$. In this work, the heterostructures of $TiO_2$ NTs with deposited $Ag_xO$ by the SILAR method were studied. The morphology and composition of the obtained samples were investigated by scanning electron microscopy and Raman spectroscopy. Photoactivity of obtained samples was investigated under solar simulated light 1.5 AM 40 mW/cm$^2$.

## 1. Introduction

Currently, $TiO_2$ is widely studied and used as a photocatalyst for the decomposition of organic pollutants. However, the $TiO_2$ band gap is 3.2 eV, which limits the use of $TiO_2$ in photocatalysis. For photoactivation, $TiO_2$ requires ultraviolet radiation, which is 4% of the total solar spectrum reaching the surface of the planet [1]. To increase the efficiency of a photocatalyst based on $TiO_2$, it is necessary to increase the absorption spectrum of the material. Creation of heterostructures by modification of $TiO_2$ catalyst surface by nanoparticles of semiconductors with smaller band gap than 3 eV can be a promising solution [2, 3]. Silver oxide $Ag_2O$ attracts its attention for making heterojunction with $TiO_2$ due to its band gap (1.2 eV), good compatibility with $TiO_2$ [4]. Using a simple and cheap method as SILAR catalyst's heterostructures can be a perspective way to increase photoactivity of $TiO_2$. However, no data in scientific literature about the effect of the concentration of Ag salt and pH of the solutions on photocatalytic properties of $TiO_2$ NTs/$Ag_2O$ heterostructures are presented. Thus, the purpose of our work is investigation an influence of Ag precursor concentration and pH solutions used in molecular deposition method from the liquid phase on the photocatalytic characteristics of the material.

## 2. Experiment

Samples of $TiO_2$ NTs were obtained by electrochemical oxidation of titanium in ethylene glycol based electrolyte with aded 0.3 wt.% $NH_4F$ and 2 vol.% $H_2O$. Anodizing was carried out in a thermostated cell at 20° C in two stages. The first stage lasted 30 minutes, after that a formed sacrificial nanotubular layer was removed from the foil surface by cathodic polarization in an 5% $H_2SO_4$ solution. The second stage lasted 1 h, after which the sample was washed in ethanol and dried in an air stream. After that, the obtained samples were subjected thermal in a muffle furnace at 450 °C for 1 h for crystallization.

In a standard SILAR process, sample of $TiO_2$ NTs were placed in $AgNO_3$ solution for 5 min to achieve abundant $Ag^+$ adsorption. After that samples were cleaned by deionized water. The sample was transferred to NaOH solution for another 5 min, and then purified again with deionized water. The following concentrations were used in the work: 0.01, 0.05, 0.1, 0.15, 0.2 M $AgNO_3$ and NaOH (12 - 13,3 pH solutions). Designation of samples: TA-0 (0,1 M without heating), TA-1 (0,01 M), TA-2 (0,05 M), TA-3 (0,1 M), TA-4 (0,15 M), TA-5 (0,2 M), pure $TiO_2$ NTs. Each sample was modified by 10 SILAR cycles. After that, the samples were annealed in vacuum at 160 °C for 1 hour.

The morphology and composition of the obtained samples were investigated by scanning electron microscopy and Raman spectroscopy. Photoactivity was studied under solar simulated light by photoelectrochemical techniques in 0,1 M $Na_2SO_4$ solution at 0,5 V vs Ag/AgCl.

## 3. Results and discussions

SEM images of pure and modified $TiO_2$ NTs are presented on Figure 1.

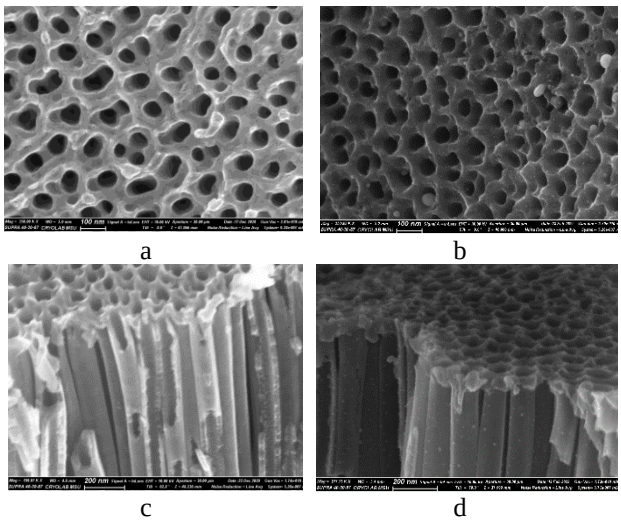


***Fig. 1.*** *SEM images of samples: $TiO_2$ NTs: top view (a) and side view (c); TA-3: top view (b) and side view (d).*

As can be seen, an obtained $Ag_xO$ NPs in various sizes from 2 nm to ~ 40 nm can be observed. Also, nanoparticles are disposed on walls of $TiO_2$ NTs arrays. Influence of concentration precursor or pH solution on size distribution of $Ag_xO$ NPs wasn't observed.

Raman shift spectra of obtained $TiO_2$ NTs samples are presented on Figure 2.

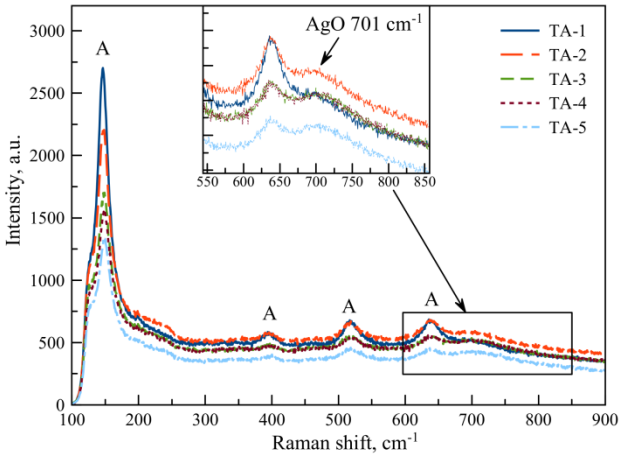


***Fig. 2.*** *Raman spectra of $TiO_2$ NTs modified $AgO_x$ nanoparticles.*

Peaks (146, 393, 517, 638 $cm^{-1}$) corresponding to $TiO_2$ anatase for all samples are observed. As can be seen with increase of concentration of Ag precursor and pH solution a signal intensity from $TiO_2$ peaks decreases. Also, we detect a wide peak at 701 $cm^{-1}$, which can be corresponds to AgO [5].

Figure 3 shows photocurrent transients of obtained samples.

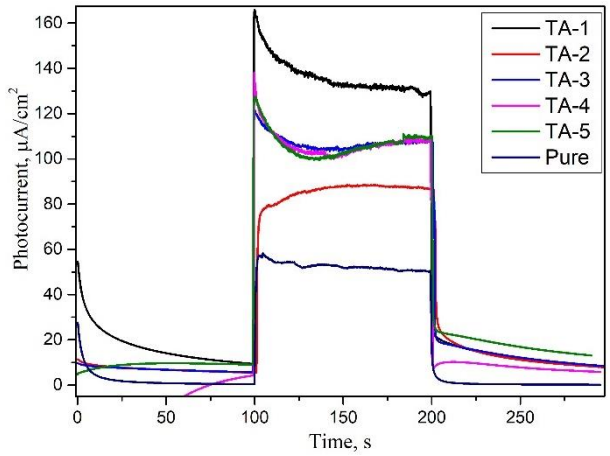


***Fig. 3.*** *Obtained photocurrents of fabricated samples.*

As can be seen, a highest photocurrent attributed for sample TA-1 prepared with 12 pH NaOH solution. An increase of pH and precursor $Ag^+$ concentration don't lead to next enhance of photoactivity of the material. It should be noted that all variants of methodology lead to increase photoactivity under solar simulated light of the material compared to pure TiO2 NTs sample.

## 4. Conclusions

Samples of pure $TiO_2$ NTs and also modified by $Ag_xO$ were obtained. AgO phase was detected by Raman spectroscopy. An influence of Ag+ precursor concentration and pH solutions used in molecular deposition method from the liquid phase on the photocatalytic characteristics of the material was investigated. Can conclude that pH of the solution has most influence on photoactivity of the material. NPs size distribution don't related with concentration of $Ag^+$ precursor change. Obtained data can be a helpful for planning of photoelectrodes with enhances photoactivity based $TiO_2$ NTs modified $Ag_xO$ NPs by SILAR method.

## Acknowledgements

Sample preparation, structural and photoelectrochemical investigation was funded by RFBR grant № 18-29-23038 mk. The research infrastructure of the Interdisciplinary Scientific and Educational School of Moscow State University "Photonic and Quantum Technologies. Digital Medicine" was used for study of obtained samples by scanning electron microscopy. Tsiniaikin I. I. thanks the BASIS Foundation for the Advancement of Theoretical Physics and Mathematics.

## References

[1] Schneider, Jenny, et al. Chemical reviews **114.19**(2014)9919.
[2] Wei, Longfu, et al. Journal of Materials Chemistry A **6.45**(2018)22411.
[3] Bessekhouad, Y., D. Robert, and J-V. Weber. Catalysis today **101.3-4**(2005)315.
[4] Mazierski, Paweł, et al. ACS Catalysis **7.4**(2017)2753.
[5] Waterhouse, Geoffrey IN, Graham A. Bowmaker, and James B. Metson. Physical Chemistry Chemical Physics **3.17**(2001)3838.

Sixth Asian School-Conference on Physics and
Technology of Nanostructured Materials
Vladivostok, Russia, 25 – 29 April, 2022



# Mechanochemical synthesis, characterization and photocatalytic properties of $Bi_2WO_6/SiO_2$ modified biogenic silica

A.I. Pisartseva*,[1], O.D. Arefieva[1,2], M.S. Vasilyeva[1,2], P.I. Mitkina[1], V.V. Tkachev[1]

[1] Far Eastern Federal University, 10 Ajax Bay, Russky Island, Vladivostok 690922, Russia
[2] Institute of Chemistry, FEB RAS, 159, pr. 100-letya Vladivostoka, Vladivostok 690022, Russia

*e-mail: pisarceva_ai@dvfu.ru

**Abstract.** $Bi_2WO_6/SiO_2$ was obtained by mechanochemical activation followed by calcination at 500°C, modified biogenic silica from rice husks. To change the structure of the $Bi_2WO_6/SiO_2$ surface, this sample was etched with 2.5 M NaOH aqueous solution for 0.5; 1; 1.5 hours. According to X-ray phase analysis data, $Bi_2WO_6/SiO_2$ contains reflections of the photoactive phase γ-$Bi_2WO_6$. The photocatalytic activity of the samples in the degradation reaction of indigo carmine under ultraviolet irradiation was studied. It is shown that after etching of the original $Bi_2WO_6/SiO_2$ sample, the photoactivity increases by 5% and ranges from 11.5 to 13.5%.

## 1. Introduction

Purification of industrial effluents from persistent organic substances is an urgent task today. Heterogeneous photocatalysis is considered as a promising technology for industrial wastewater treatment due to its low cost, environmentally friendly process and the absence of secondary pollution [1].

Currently, materials based on tungsten compounds(VI) are being actively studied. Tungsten(VI) oxide is promising for photocatalysis due to its high stability in aqueous solution under acidic conditions, the absence of photocorrosion and a suitable (2.7 eV) band gap for absorption of visible light [2, 3]. However, despite the fact that $WO_3$ absorbs light in the visible region, its photocatalytic activity is very low [4]. Bismuth tungstate ($Bi_2WO_6$) has a narrow band gap (2.8 eV) and low toxicity [5]. There are various ways to obtain a $Bi_2WO_6$ photocatalyst, of which hydrothermal and sol-gel can be distinguished [6, 7]. These materials can also be obtained by mechanochemical activation, which attracts the attention of researchers as a more environmentally friendly process without the use of solvents. Modification of $Bi_2WO_6$ with amorphous silicon dioxide makes it possible to change the morphology of the surface, which affects the photocatalytic activity of the sample [7].

The purpose of this work is to obtain a $Bi_2WO_6/SiO_2$ photocatalyst modified with biogenic silica by mechanochemical activation and to study its photocatalytic activity.

## 2. Experiment

To obtain a sample $Bi_2WO_6/SiO_2$ was mixed $Bi_2O_3$ (analytical grade), $WO_3$ (analytical grade) and $SiO_2$ were mixed in a molar ratio of 1:2:1. Amorphous silicon dioxide samples were obtained from the husk of Dolinnyi brand rice designed in the Federal Scientific Center for Agrobiotechnology of the Far East named after A.K. Chaika (Primorskii Krai, Timiryazevskii settlement, Russia) by oxidative roasting with pre-treatment with 0.1 M hydrochloric acid solution [8].

Photocatalyst $Bi_2WO_6/SiO_2$ was synthesized by mechanochemical activation followed by firing. Mechanochemical processing was carried out at the planetary mill "Pulverisette 6" (Fritsch, Germany) with 35 balls with a diameter of 8 mm with a rotation speed of 600 rpm for 20 minutes. The activated mixture was calcined for 2 hours at 500 °C in a muffle furnace (WiseTherm, South Korea).

The elemental analysis of the photocatalysts samples was performed by energy-dispersive X-ray fluorescence analysis on a Shimadzu EDX 800 HS spectrometer (Japan).

To determine functional groups in the studied samples, IR absorption spectra were recorded in the range 400–4000 $cm^{-1}$ in potassium bromide on a Bruker Vertex 70 Fourier-transform spectrometer (Germany).

X-ray powder diffraction analysis (XRD) of samples was performed in CuKα radiation on a Bruker D8 Advance diffractometer (Germany).

The morphology and elemental composition of catalyst surface was studied using a Carl Zeiss Ultra+ high-resolution scanning electron microscope (SEM) (Zeiss AG, Germany) equipped with a Thermo Scientific add-on unit for energy-dispersive X-ray analysis (Oxford instruments, England).

The resulting sample $Bi_2WO_6/SiO_2$ was subjected to etching with 2.5 M aqueous NaOH solution for 0.5; 1; 1.5 hours (table 1).

The photocatalytic properties of the obtained samples were evaluated using the degradation reaction of indigo carmine in the UV region as an example. The process was carried out in a 100-mL quartz cell filled with 50 mL of MO solution (10 mg/L) and 0.05 g of catalyst. Radiation source was a 100P/F UV lamp (radiation maximum is $\lambda = 365$ nm). The solution was irradiated at constant magnetic stirring (625 rpm) for 3 h. The solution was irradiated with constant stirring on a magnetic stirrer (750 rpm) for 3 hours. Ambient temperature was 25°C.

The optical density of indigo carmine solution was determined by photocolorimetric method on a UNICO-1201 spectrophotometer (United Products & Instruments Inc., USA) at wavelength 610 nm.

## 3. Results and discussions

The results of X-ray fluorescence analysis showed that the $Bi_2WO_6/SiO_2$ sample contains 75% $Bi_2O_3$, 15% $WO_3$ and 9% $SiO_2$. According to the data of X-ray phase analysis, the photocatalyst is in an amorphous-crystalline state have been identified in the crystalline phase orthorhombic γ-$Bi_2WO_6$, tetragonal $Bi_{14}W_2O_{27}$, cubic

$Bi_{12}W_{0.10}O_{18.3+x}$ and cubic δ-$WO_3$. It should be noted that, in general, there are reflections of γ-$Bi_2WO_6$, which has the highest photoactivity.

In the IR spectrum of $Bi_2WO_6/SiO_2$, the absorption bands at 1101 $cm^{-1}$ and 475 $cm^{-1}$ correspond to asymmetric and bending vibrations of the Si–O–Si bond in amorphous silicon dioxide. Absorption band at 1389 $cm^{-1}$, characteristic of the Bi-O bond in bismuth tungstate. In the spectrum of the sample, the absorption bands at 810 and 733 $cm^{-1}$ correspond to the WO and W-O-W bonds in $Bi_2WO_6$. There is also an absorption band at about 847 $cm^{-1}$, which indicates the formation of a Bi-O-Si bond. Bands at 3435 and 1634 $cm^{-1}$ correspond to stretching and bending vibrations of OH groups. This result confirms the formation of $Bi_2WO_6$.

On fig. 1 shows SEM images of photocatalysts. The $Bi_2WO_6/SiO_2$ sample has a smooth structure. After etching, the $Bi_2WO_6/SiO_2$-1 sample becomes looser. Coral branches appear in the structure.

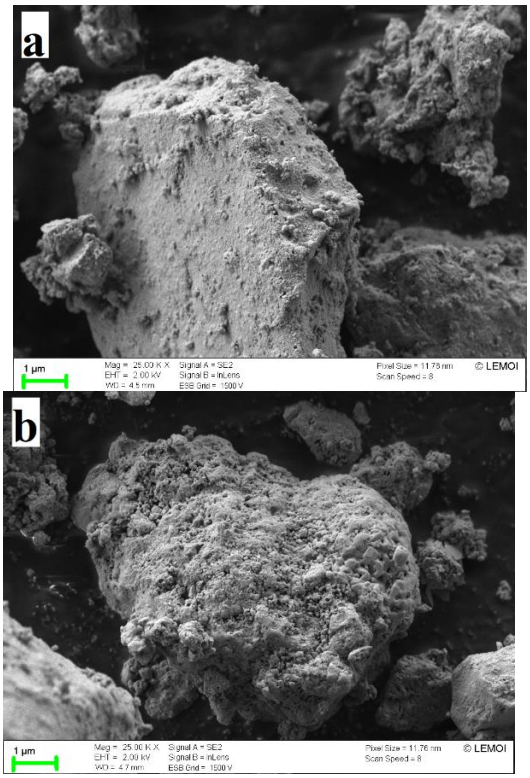


***Fig. 1.*** *SEM images of photocatalysts: a - $Bi_2WO_6/SiO_2$; b - $Bi_2WO_6/SiO_2$-1.*

The results of photocatalytic tests of the initial $Bi_2WO_6/SiO_2$ and etched samples under UV light irradiation in the indigocarmine degradation reaction are shown in table 1.

***Table 1.*** *The degree of decomposition of indigocarmine under UV light irradiation.*

| Sample | χ, % |
|---|---|
| $Bi_2WO_6/SiO_2$ | 8,5 |
| $Bi_2WO_6/SiO_2$-0,5 | 13,0 |
| $Bi_2WO_6/SiO_2$-1 | 13,5 |
| $Bi_2WO_6/SiO_2$1,5 | 11,5 |

Table 1 shows that after etching of the initial $Bi_2WO_6/SiO_2$ sample, the photoactivity increases within 5% and ranges from 11.5 to 13.5%. It should be noted that the etching time does not affect the photoactivity of the sample.

## 4. Conclusions

The $Bi_2WO_6/SiO_2$ photocatalyst modified with biogenic silica from rice husks was obtained by mechanochemical activation. X-ray phase analysis established that the sample contains the photoactive phase γ-$Bi_2WO_6$. The $Bi_2WO_6/SiO_2$ was etched with 2.5 M NaOH aqueous solution for 0.5;1;1.5 hours. It is shown that, after sample etching, the photocatalytic activity increases by ~5%.

## Acknowledgements

The work was carried out within the framework of the state task of the Institute of Chemistry of the FEB RAS 0205-2021-0002. The authors are grateful to the Laboratory of Molecular and Elemental Analysis and the Laboratory for X- ray Structural Analysis (Institute of Chemistry, FEB RAS).

## References

[1] Y. H. Chiu, T. F. M. Chang, C. Y. Chen [et al.]. Catalysts **9**(2019)1.
[2] M. Aslam, I. M. I Ismail, S. Chandrasekaran, A. Hameed. Journal of Hazardous Materials **276**(2014)120.
[3] S. J. Hong, H. Jun, P. H. Borse, J. S. Lee. International Journal of Hydrogen Energy **34**(2009)3234.
[4] K. Sayama, H. Hayashi, T. Arai [et al.]. Applied Catalysis B: Environmental **94**(2010)150.
[5] G. H. He, C. J. Liang, Y. D. Ou [et al.]. Materials Research Bulletin **48**(2013)2244.
[6] F. Amano, K. Nogami, B. Ohtani. Catalysis Communications **20**(2012)12.
[7] S. O. Alfaro, L. C. A. Martínez-De. Applied Catalysis A: General **383**(2010)128.
[8] Zemnukhova L.A., Egorov A.G., Fedorishcheva G.A., Sokol'nitskaya T.A., Barinov N.N., Botsul A.I. Inorganic materials **42**(2006)24.

# Bioresorbable composite materials with controlled resorption rate for bone tissue bioengineering

A.B. Podgorbunsky*[,1], M.V. Sidorova[1], M.S. Gerasimenko[1,2], S.L. Sinebryukhov[1], S.V. Gnedenkov[1]
[1] Institute of Chemistry FEB RAS, 159 pr. 100-letiya Vladivostoka, Vladivostok 690022, Russia
[2] Far Eastern Federal University, 8 Sukhanova St., Vladivostok 690950, Russia

*e-mail: pab@ich.dvo.ru

The experience of the pandemic has shown that it is expected to increase the cost not only for healthcare, but also for developments in the field of medicine to increase the production of competitive medical devices and new generation materials. In China, as the most populous country, has more than 15 million people with limited limb function. More than 3.5 million accidents occur every year in this country, while 70 percent of the injured require bone repair. In the case of osteoporosis in the world, the main risk group includes people of mature and old age. About 200 million people worldwide suffer from osteoporosis and 8.9 million fractures occur each year [1]. By 2050, the number of osteoporotic fractures of the femoral neck is expected to increase to 1 million cases annually in Europe; at the same time, the mortality associated with osteoporotic fractures exceeds oncological ones in most cases. Design of modern tissue-compatible frameworks (scaffolds) imitating the structure of bone tissue, as well as a bioresorbable composite materials allows for complete replacement of the bone defect and preserves the functionality of the limbs [2–6]. Directional synthesis of a composite material combining acceptable elastoplastic properties close to bone (magnesium) and bioactivity of the ceramic component (hydroxyapatite) as an osteointegration basis for the formation of new bone tissue are at the forefront of global research in the field of development of materials for implantology. Since the corrosiveness of magnesium is too high and does not allow the mechanical properties of a temporary implant to be maintained for the period necessary for the bone splicing, its necessary to protect the metal base from destruction, including through forming a coating [7].

This paper presents the results of the multifunctional material design based on magnesium for the needs of implant surgery. An integrated approach has been developed, including: (1) the synthesis of nanoscale hydroxyapatite powder by means of precipitation and microwave aging process; (2) formation of composites based on magnesium and hydroxyapatite powders followed by spark plasma sintering (SPS) technology; (3) formation of a protective/bioactive coating to control the resorption of the composite substrate material.

Pure magnesium (Mg, purity ≥99.9%, size ≤40 μm, Merck) and hydroxyapatite (HAp, ≤80 nm, precipitation-microwave synthesis) powders were used as starting materials for Mg-HAp composition. The resulting mixture was subjected to dispersion in an ethanol medium and subsequent stirring until the solvent evaporated. An oxide coating by the method of plasma electrolytic oxidation (PEO) was applied to the surface of the composites formed by SPS technology. The obtained magnesium-hydroxyapatite mixture as well as sintered SPS composites were analyzed for phase composition, shape and particle size, etc. Morphology of the prepared composites were analyzed by SEM and showed grain size of 20 to 100 μm veined with calcium phosphate ceramic. It is shown that formation of a PEO coating provides protective functions and largely depends on the composition of the substrate. The studied morphology and composition of the substrate–oxide layer interface made it possible to allocate a non-porous magnesium fluoride sublayer formed during plasma electrolytic oxidation at the initial stage near the metal surface. In addition, silicon is uniformly distributed throughout the coating thickness, which suggests the presence of magnesium orthosilicate ($Mg_2SiO_4$) in an amount sufficient for XRD detection. It has been shown that obtained coatings substantially reduce corrosion current density in comparison with bare Mg ($2.54 \cdot 10^{-5} \rightarrow 1.05 \cdot 10^{-8}$ A/cm$^2$). Application of the PEO layer reduces the substrate corrosion rate by more than 6 times (4.21 → 0.65 mm/year). The obtained biodegradable matrices based on magnesium with a significant content of the bioactive component in the volume and on the surface are as close as possible to the properties of bone tissue in terms of morphological structure (porosity that promotes proliferation) and fullness of calcium phosphate compound. Varying the composition of the electrolyte for the formation of a PEO layer makes it possible to regulate the thickness and phase composition of the protective layer by controlling the rate of resorption of the formed material.

**Acknowledgements**

This work was supported by the Russian Science Foundation (grant № 22-23-00915). The authors are grateful to O.O. Shichalin from the Far Eastern Federal University (FEFU, Vladivostok, Russia) for sintering composites by SPS method.

**References**

[1] P. Pisani, M.D. Renna, F. Conversano, E. Casciaro, M. Di Paola, E. Quarta, M. Muratore, S. Casciaro, World J. Orthop., **7** (2016) 171–181.
[2] Y. Li, H. Jahr, J. Zhou, A.A. Zadpoor, Acta Biomater., **115** (2020) 29–50.
[3] N. Sezer, Z. Evis, M. Koç, J. Magnes. Alloy., **9** (2021) 392–415.
[4] M. Haghshenas, J. Magnes. Alloy., **5** (2017) 189–201.
[5] W.S. Al-Arjan, M.U.A. Khan, S. Nazir, S.I.A. Razak, M.R.A. Kadir, Coatings, **10** (2020) 1–17.
[6] X. Wang, L.H. Dong, J.T. Li, X.L. Li, X.L. Ma, Y.F. Zheng, Mater. Sci. Eng. C, **33** (2013) 4266–4273.
[7] M.B. Sedelnikova, Y.P. Sharkeev, T. V. Tolkacheva et al. Materials (Basel)., **13** (2020) 1942.

# Synthesis, structural and electrical properties of nanotubular Ni-doped $Na_2Ti_3O_7$ as a novel functional material

A.B. Podgorbunsky*, D.P. Opra, V.V. Zheleznov, A.M. Ziatdinov, S.L. Sinebryukhov, S.V. Gnedenkov

Institute of Chemistry FEB RAS, 159 pr. 100-letiya Vladivostoka, Vladivostok 690022, Russia

*e-mail: pab@ich.dvo.ru

In recent years, ternary $A_2Ti_nO_{2n+1}$ (A = Li, Na, K; n = 2–9) oxides systems, in particular, sodium trititanate ($Na_2Ti_3O_7$) has received considerable attention due to its potential technological applications in various fields. A large number of titanate nanostructures (i.e., nanotubes, nanowires, and nanobelts) have been widely obtained by a simple hydrothermal treatment of $TiO_2$ particles in NaOH solution. Due to the high-performance ion-exchange properties of $Na_2Ti_3O_7$, it may be used for removal and recovery of heavy metal ions from industrial wastewaters [1], metal-ion batteries and hydrogen storage materials [2,3], as well as photocatalysts, bioactive ceramics and sensors [4–6].

In this work, the effect of nickel doping on the structural and electrical properties of $Na_2Ti_3O_7$ layered ceramics obtained in the form of mesoporous nanotubes is studied by XRD, XPS, SEM, impedance spectroscopy, EPR methods and UV-Vis spectroscopy. Sodium trititanate doped with nickel (1.2–6.9 at.%) was obtained by hydrothermal treatment of titanium(IV) chloride and nickel(II) chloride (25, 75 and 150 mL) in an alkaline medium in the presence of hydrogen peroxide. It was found that the resulting material is nanotubes with a diameter of 30–50 nm and a wall thickness of 3–10 nm (Fig.1a).

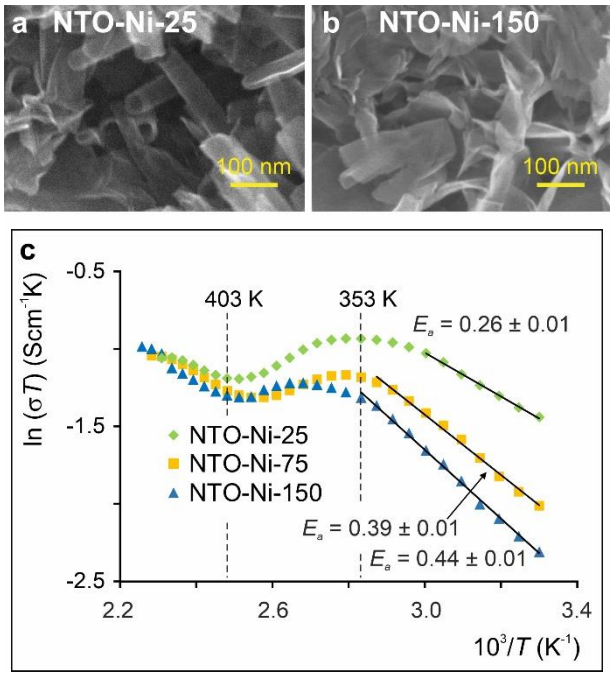


***Fig. 1.*** *SEM images (a, b) and the temperature dependences of the conductivity of Ni-doped $Na_2Ti_3O_7$ (c).*

The nanotubular composition is represented by crystallites 14–12 nm in size, while nickel is successfully incorporated into the sodium trititanate lattice. It is shown that for $Na_{2.09}Ti_{2.89}Ni_{0.16}O_{6.86}$ (nickel alloying 4.6 at.%), a deficiency of oxygen atoms registered. In this case, the most probable location of their location in $Na_2Ti_3O_7$ is the interlayer space. When $Na^+$ ions are replaced by $Ni^+$ ions in low concentrations, the $(Ti_3O_7)^{2-}$ layers tend to bend, rolling into nanotubes; the introduction of a significant amount of nickel leads to a "simplification" of the structure and "unfolding" of nanotubes (Fig. 1b). Temperature dependence of the conductivity for the samples (Fig. 1c) showed the Arrhenius form of the curve only for the range from room temperature to ~350 K. A further increase in temperature leads to a deviation of the curve from the Arrhenius dependence, which can be caused by increasing contribution of interlayer ionic and electronic hopping conduction, which hinders charge transfer. In particular, free oxygen formed when $Ni^{2+}$ is substituted at $Ti^{4+}$ site can be captured by cation vacancies present in the interlayer space.

Thus, the paper presents the results of the synthesis and study of mesoporous materials with a tubular nanostructure based on sodium trititanate doped with nickel. It has been established that doping improves the conductive properties of the material, which is associated with the formation of oxygen vacancies resulting from the charge compensation of the nonisovalent substitution of $Ti^{4+}$ ions by nickel ions.

## Acknowledgements

The synthesis and investigation of composite materials was supported by the Russian Science Foundation (grant № 19-73-10017). Additionally, authors thank Dr. Valery G. Kuryavyi for the SEM analysis.

## References

[1] X. Sun, Y. Li, Chem. - A Eur. J., **9** (2003) 2229–2238.
[2] H. Zhang, X.P. Gao, G.R. Li, T.Y. Yan, H.Y. Zhu, Electrochim. Acta, **53** (2008) 7061–7068.
[3] K. Chiba, N. Kijima, Y. Takahashi, Y. Idemoto, J. Akimoto, Solid State Ionics, **178** (2008) 1725–1730.
[4] N. Miyamoto, K. Kuroda, M. Ogawa, J. Mater. Chem., **14** (2004) 165.
[5] I. Becker, I. Hofmann, F.A. Müller, J. Eur. Ceram. Soc., **27** (2007) 4547–4553.
[6] Y. Zhang, W. Fu, H. Yang, M. Li, Y. Li, W. Zhao, P. Sun, M. Yuan, D. Ma, B. Liu, G. Zou, Sensors Actuators B Chem., **135** (2008) 317–321.

# Structure and electrochemical sodium storage properties of hard carbon doped with molybdenum

N.S. Saenko*, V.V. Zheleznov, D.P. Opra
Institute of Chemistry FEB RAS, 159, Prospekt 100-letiya Vladivostoka, Vladivostok, 690022, Russia

*e-mail: saenko@ich.dvo.ru

Sodium has become a cheap alternative to lithium due to relatively simple production methods and high availability [1, 2]. Hard carbon is the most promising material for use as negative electrodes in sodium-ion chemical current sources, as it comes from natural renewable compounds, has a relatively low cost, and its production has a minimal impact on the environment [3]. However, hard carbon anode material in sodium ion batteries (SIBs) has low capacity at high charging currents [4]. Heteroatomic doping is a widespread way to improve the characteristics of hard carbon materials. For example, simultaneous doping of hard carbon with nitrogen and sulfur leads to an enlarging interlayer distance and an increasing number of defects, which enhances the electrode kinetics and electronic conductivity of SIBs [5, 6]. Several papers report doping hard carbon with molybdenum [7, 8, 9, 10, 11]. However, the complexity of synthesis and the production cost of anode materials primarily determinates their industrial use perspectives for application in SIBs. The paper investigates the structure and electrochemical sodium storage properties of materials prepared by annealing at different temperatures of industrial viscose fibers doped with molybdenum.

There are two broad intensive peaks at ≈24 and 43° in the X-ray diffraction profiles of all materials (fig. 1). Low-intensity peaks corresponding to molybdenum compounds are noticeable in the diffraction profile of material prepared at 630°C. At an annealing temperature of 950°C, there are characteristic reflections of molybdenum oxide $MoO_2$. At higher annealing temperatures (1050 and 1300°C), peaks of molybdenum carbides are registered. The X-ray scattering profiles of all the materials (fig. 1) can be approximated by the sum of Lorentzians and background scattering in the form of a fourth-degree polynomial in 1/2θ, reflecting the contributions to the background scattering profile (due to small-angle scattering, scattering by disordered atoms, scattering by air molecules, and other factors) [12]. In all experimental diffraction patterns, one can distinguish reflections (002), (10), (004), (11) characteristic of turbostratic multilayer nanographenes with maxima near 2θ of 23, 42, 49, and 80°, respectively [13, 14]. Besides, in the approximations of materials prepared at 630 and 950°C, one can distinguish the Lorentzian with a maximum at 2θ ~ 19°, the so-called γ-peak [15, 16, 17]. Additional narrow components at 2θ ~ 26, 32, 37, 40, 62, 75° in the approximation can be attributed to scattering on nanocrystallites of molybdenum oxide and molybdenum carbides.

The interatomic and interlayer spacing, average lateral size and thickness of ordered carbon regions have been estimated using the Debye-Scherrer formula and Bragg's law [14, 18, 19]. The ordered carbon regions in the materials prepared at 630°C have an average lateral size of 1.2 nm. Materials prepared at temperatures higher than 950°C have more extended areas of the ordered carbon network. It should be noted that the distance between ordered carbon layers in all samples significantly exceeds the interlayer distance in turbostratic carbon [20, 21]. This fact may indicate that there are functional groups associated with the carbon network in the interlayer space of these samples [22], or interstitial atoms and molecules [23]. The distance between the carbon layers in the materials decreases in the annealing temperature range from 630 to 1050°C and then increases in the sample annealed at 1300°C. Among all materials, one prepared at 950°C has the maximum number of layers and the maximum distance between the carbon layers in the particles, and therefore it was chosen for testing as a material for negative electrodes in sodium-ion batteries.

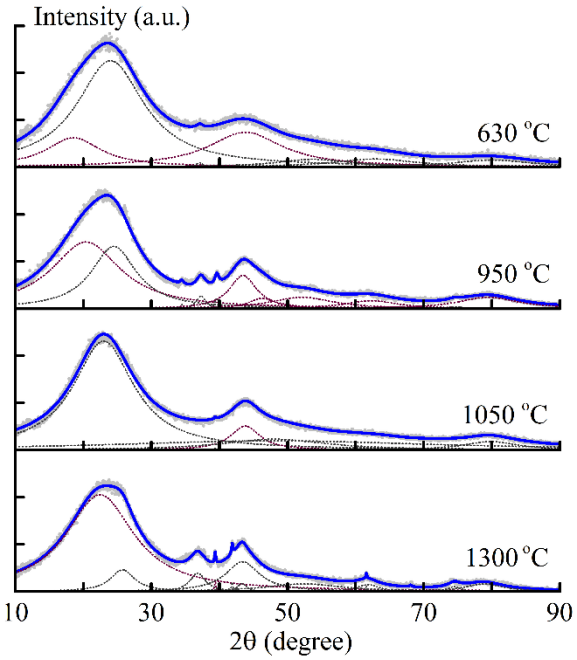


***Fig. 1.*** *Approximation of X-ray diffraction patterns of materials prepared from viscose fiber doped with molybdenum at different annealing temperatures after subtracting the contribution of the background scattering.*

The hard-carbon material has been studied by cyclic voltammetry (CV) and galvanostatic charge-discharge tests. Fig. 2a represents the five initial CV cycles recorded at a potential sweep rate of 0.1 mV/s for a sodium half-cell with working electrode from the hard carbon material annealed at 950°C. There is a pronounced peak near 1.0 V in the cathode region of the first CV curve (fig. 2a). The mentioned peak does not have a corresponding

response in the anode region as well as does not repeated on the curves of subsequent cycles. The origin of this peak is explained by irreversible reactions at the electrode surface and the resultant formation of a solid electrolyte interphase layer [24, 25]. The experimental data are in good agreement with a sodiation mechanism proposed for hard carbon in the literature [26]. In this way, peaks centered near 0.6, 0.1, and 0.01 V correspond to the staged process of sodium accumulation in the anode material. The anode region of all the voltammograms shows a wide peak with a maximum near 0.25 V. It should be noted that by the third cycle, the intensity of this peak increases. Such behavior is typical for hard carbon [27, 28] and is caused by changes in structure and texture during sodium uptake/release. The electrochemical process stabilizes starting from the fourth cycle.

The initial voltage profiles for the sodium half-cell based on hard carbon material annealed at 950°C were obtained at a current density of 25 mA/g (fig. 2). There are several regions on a charge curve indicating a multi-stage electrochemical process. The latter agrees well with the CV data. The corresponding discharge profile shows a pronounced plateau at 0.1 V. The specific capacity values recorded during the first charge and discharge are approximately 455 and 230 mAh/g, respectively, and the irreversible losses are about 225 mAh/g. The subsequent tenfold cycling (fig. 2*b*, inset) reflects the stabilization of the electrochemical process with a reversible capacity of around 240 mAh/g. Thus, the electrochemical measurements have shown the promise of obtained materials as anode materials for sodium-ion batteries.

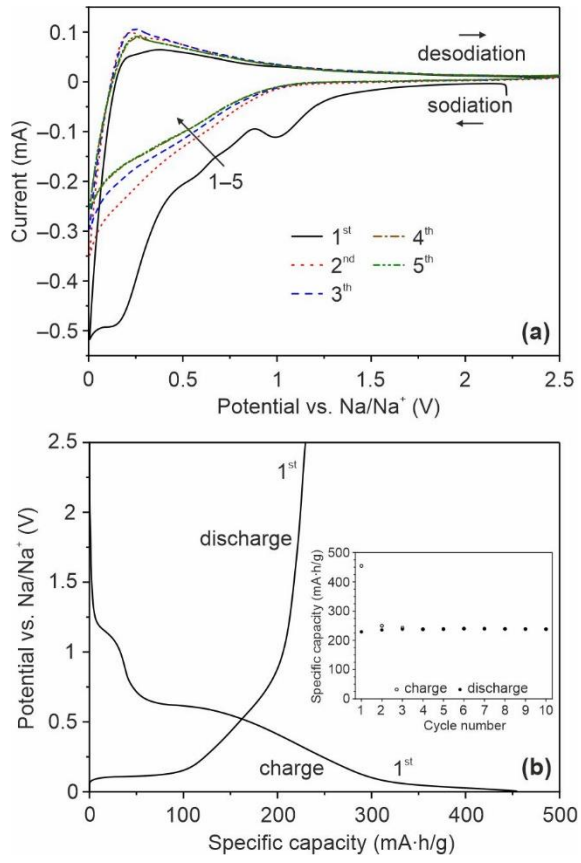


***Fig. 2.*** *(a) Curves of cyclic voltammetry at 0.1 mV/s and (b) charge-discharge profiles of the first cycle at 25 mA/g for hard carbon material (the inset shows the results for ten cycles).*

The study was supported by the Ministry of Science and Higher Education of Russia (state assignment № 0205-2021-0004 and № 0205-2021-0001). Electrochemical studies were carried out within the framework of the grant № 22-23-00912 from the Russian Science Foundation.

## References

[1] F. Xie et al. Prog. Energy **2**(2020)042002.
[2] J. Ma et al. J. Phys. D. Appl. Phys. **54**(2021)183001.
[3] Thompson M., Xia Q., Hu Z., Zhao X.S. Mater. Adv. **18**(2021)5881.
[4] W. Wang et al. J. Mater. Chem. A. **6**(2018)6183.
[5] H. Hou et al. Adv. Energy Mater. **7**(2017)1602898.
[6] D. Xu et al. Adv. Energy Mater. **6**(2016)1501929.
[7] L. David, R. Bhandavat, G. Singh. ACS Nano. **8**(2014) 1759–1770.
[8] C. Zhu et al. Angew. Chemie. **126**(2014)2184.
[9] Q. Xia, Q. Tan. Patent CN №106910884.
[10] L. Zeng et al. Polymers. **12**(2020)2134.
[11] Y. Hao, C. Wang. Molecules **25**(2020)1014.
[12] C. Sisu et al. Dig. J. Nanomater. Bios. **11**(2016)435.
[13] N. Iwashita et al. Carbon **42**(2004)701.
[14] B.E. Warren. Phys. Rev. **59**(1941)693.
[15] R.K. Boruah et al. J. Appl. Crystallogr. **41**(2008)27.
[16] L. Biennier et al. Carbon **47**(2009)3295.
[17] N.S. Saenko, A.M. Ziatdinov. Mater. Today: Proc. **5**(2018)26052.
[18] P. Scherrer. Gottinger Nachrichten Math. Phys. **2**(1918)98.
[19] W.H. Bragg, W.L. Bragg. Proc. R. Soc. London. Ser. A. **88**(1913)428.
[20] J. Biscoe, B.E. Warren. J. Appl. Phys. **13**(1942)364.
[21] A. Oberlin, S. Bonnamy, K. Oshida. Tanso. **224**(2006)281.
[22] A.M. Ziatdinov, N.S. Saenko, P.G. Skrylnik. **65**(2020)133.
[23] M.S. Dresselhaus, G. Dresselhaus. Adv. Phys. **30**(1981)139.
[24] K. Xu et al. Front. Chem. **7**(2019)733.
[25] Z. Zhu et al. J. Mater. Chem. A. **6**(2018)1513.
[26] Z.V. Bobyleva et al. Electrochim. Acta. **354**(2020)136647.
[27] L. Wu et al. ChemElectroChem. **3**(2016)292.
[28] P. Yu et al. J. Colloid Interface Sci. **582**(2021)852.

Sixth Asian School-Conference on Physics and
Technology of Nanostructured Materials
Vladivostok, Russia, 25 – 29 April, 2022



# Electron paramagnetic resonance of nanocrystalline manganese-incorporated bronze titanium dioxide

D.A. Saritsky*, A.M. Ziatdinov, D.P. Opra, A.A. Sokolov, S.L. Sinebryukhov, S.V. Gnedenkov
Institute of Chemistry FEB RAS, 159, Pr-t 100-letiya Vladivostoka, Vladivostok, 690022, Russia

*e-mail: denissaricki@mail.ru

**Abstract.** Herein, manganese-doped bronze titanium dioxide ($TiO_2$(B)) nanoparticles has been studied by the EPR method. The theoretical EPR spectra of particle powders $TiO_2$ containing $Mn^{2+}$ and $Mn^{4+}$ ions in the crystal fields with a strong rhombic distortion are calculated, and their distinguishing features are indicated. Based on the obtained knowledge, a conclusion was drowned about the presence of $Mn^{4+}$ ions in the studied samples and the types of crystal fields acting on them were indicated. The occupancies of two possible positions of impurity $Mn^{4+}$ ions in $TiO_2$(B) are estimated.

## 1. Introduction

The steadily growing needs of modern technology in electrochemical energy storage devices (EESDs) require the improvement of the characteristics for existing systems EESDs, as well as the search for the new redox-active materials for them. One of the promising materials for EESDs is titanium dioxide ($TiO_2$) especially its nanocrystalline forms of bronze polymorph ($TiO_2$(B)). However, because it is a wide-bandgap semiconductor, its poor electronic properties need to be improved before usage as an electrode in EESDs [1]. It was found that electronic structure of $TiO_2$(B) may be modified through doping with some metals and non-metals [2]. Hence, the studying of the structure and properties of doped $TiO_2$(B) have gained a much attention in recent years. In this work, the electron paramagnetic resonance (EPR) method is used to study some aspects of the structure and properties of $TiO_2$(B) doped with manganese ions.

## 2. Experimental

The doping strategy is based on hydrothermal synthesis involved the treatment of commercial anatase nanopowder and manganese(II) nitrate with alkali in presence of ammonium hydrogen fluoride. Hereinafter the obtained material is referred as $TiO_2$(B):Mn.

The EPR spectra of $TiO_2$(B):Mn powders were recorded on a JES-X330 instrument (JEOL, Japan) in the X- and Q-bands of work frequencies. The power of the microwave field during the recording of the spectra was 2.00 mW, the constant magnetic field ($B$) was deployed in the ranges of 0–500 mT (X-band) and 0–1500 mT (Q-band) and modulated at a frequency of 100 kHz. Temperature-dependent measurements were carried out in a continuous flow of nitrogen gas using a standard variable temperature unit ES-13060 DVT5 (JEOL, Japan). The integral intensities and $g$-factors of the EPR lines were calibrated, respectively, by the integral intensity and the value $g$=2.002293±0.000003 of the spin resonance signal at the conduction electrons of Li nanoparticles in the reference LiF:Li sample, which do not change in the range from 2 to 400 K [3].

The experimental spectra were approximated using by the EasySpin – software package for simulation and analysis of EPR spectra written in the MATLAB language.

In the X-band EPR spectra of all samples $TiO_2$(B):Mn are dominated by a broad intense component with a weakly expressed sextet structure characterized by the spectroscopic splitting factor $g$~2.00 (Fig. 1). In the Q-band, the sextet structure of this line is much better expressed Fig. 2). A narrow low-intensity line with

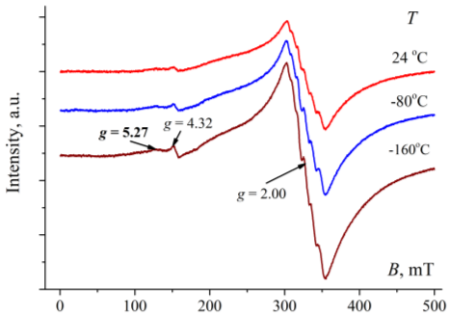


***Fig. 1.*** *EPR powder spectra of $TiO_2$(B), doped with manganese ions, at various temperatures. The X-band.*

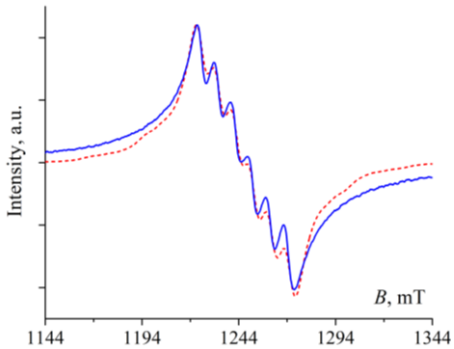


***Fig. 2.*** *Experimental (solid line) and simulated (dotted line) EPR powder spectra of $TiO_2$(B), doped with manganese ions, at room temperatures. The Q-band.*

$g$~4.32 (Fig. 3) is characteristic of ions with a $3d^5$ configuration located in crystalline fields with a significant rhombic component [4]. The spectra of all samples also contain a broad low-intensity component with $g$~5.27 (Figs. 1 and 3), which partially overlaps with a narrow resonance with $g$=4.32. When the samples are cooled, the intensities of EPR lines increase, while their characteristic features become more pronounced (Fig. 1).

## 3. Results and discussions

Naturally occurring manganese is almost practically isotopically-pure element and consisting of the only stable isotope $^{55}$Mn with nuclear spin $I$=5/2. According to this, the main line of in the EPR spectrum of the $TiO_2$(B):Mn powder, with considering its sextet structure in lightly

doped samples, should be attributed to paramagnetic manganese ions. In principle, impurity manganese ions in $TiO_2$(B) can exist in three paramagnetic oxidation states: $Mn^{2+}$ ($3d^5$, $S = 5/2$, $I = 5/2$), $Mn^{3+}$ ($3d^4$, $S = 2$, $I = 5/2$), and $Mn^{4+}$ ($3d^3$, $S = 3/2$, $I = 5/2$). However, only the first and the last of them in solids at room temperature have sufficiently long spin-lattice relaxation times at the room temperature, which making it possible to observe paramagnetic resonance on them [5]. Consequently, the main line of the in EPR spectrum of the $TiO_2$(B):Mn powder belongs either to one of these two ions or is a combination of resonances on them. Measurements of the EPR spectra in the Q-band allows to make a choice between these two possible situations.

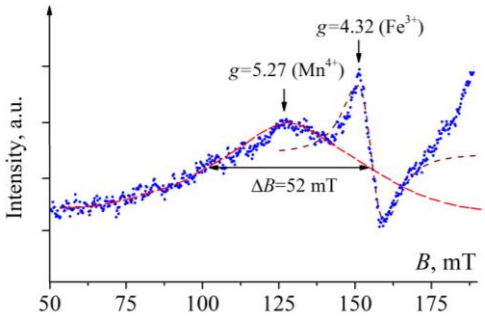


***Fig. 3.*** *Experimental (points) and simulated (dashed lines) EPR powder spectra of $TiO_2$(B) with $Mn^{4+}$ and $Fe^{3+}$ ions in crystal fields with strong rhombic distortion. The X-band.*

Indeed, if the resonances on both manganese oxidation states made an insignificant contribution to the main line of the in EPR spectrum, then, due to a small difference in the values of their $g$-factors ($\Delta g$~0.07 [5]), the transition to a higher frequency range of measurements should have led to some blurring of the sextet structure. In our experiments, conversely, the sextet structure of the main line in the X-band (Fig. 1) is resolved worse than in the Q-band (Fig. 2). This means that only one of the considered oxidation states contributes to the main line in EPR spectrum.

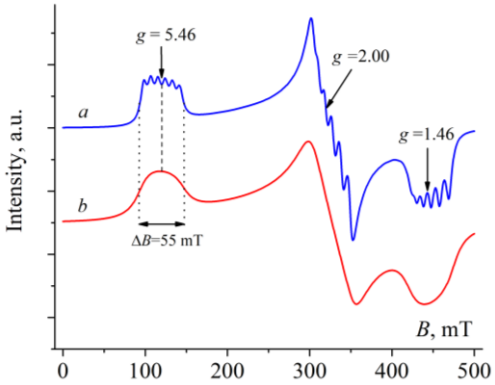


***Fig. 4.*** *Simulated EPR spectra of powder $TiO_2$(B) with $Mn^{4+}$ ions in crystal fields with strong rhombic distortion. Spectra "A" and "B" differ in the width ($\Delta B$) of the HFS lines (see table 1). The X-band.*

In order to establish the origin of the main resonance in the EPR spectra of $TiO_2$(B):Mn powders, we calculated the EPR spectrum of the $Mn^{4+}$ ions in an octahedral crystal field with strong rhombic distortion. The spin Hamiltonian in the calculations had the following form:

$$\hat{H}=g\beta(\vec{\boldsymbol{B}}\cdot\vec{\boldsymbol{S}})+D\left(\hat{\boldsymbol{S}}_z^2-\frac{S(S+1)}{3}\right)+E\left(\hat{\boldsymbol{S}}_x^2-\hat{\boldsymbol{S}}_y^2\right)+A(\vec{\boldsymbol{I}}\cdot\vec{\boldsymbol{S}}), \qquad (1)$$

where $\beta$ is the Bohr magneton, $\vec{\boldsymbol{B}}$ is the applied magnetic field, $g$ is the spectroscopic splitting factor, $\vec{\boldsymbol{S}}$ is the vector of the spin angular momentum of the system, $\hat{\boldsymbol{S}}_x$, $\hat{\boldsymbol{S}}_y$ и $\hat{\boldsymbol{S}}_z$ – spin angular momentum operators along the $x$, $y$, and $z$ axes, respectively, $S$ is the spin value, $D$ and $E$ – axial and rhombic components of the crystal field, $\vec{\boldsymbol{I}}$ – nuclear spin angular momentum vector, $A$ – is the constant of hyperfine structure (HFS). The calculations were performed under the assumption that $E$ and $D >> g\beta|\vec{\boldsymbol{B}}|$ and $0 \le E/D \le 1/3$. The shape of the individual HFS line was Lorentzian. Two spectra calculated under the above assumptions are shown in Figure 4. The parameters of the Hamiltonian (1), with which they were calculated, are given in Table 1.

***Table I.*** *Spin Hamiltonian Parameters Simulated EPR Spectra.*

| Спектр | $g$ | $E/D$ | $A$ (MHz) | $\Delta B$ (mT) |
|---|---|---|---|---|
| *A* | 2.00 | 1/3 | 245 | 5.4 |
| *B* | 2.00 | 1/3 | 245 | 23 |

A comparison of the experimental and calculated spectra allows us to conclude that the EPR spectra in the studied $TiO_2$(B):Mn powders belong to $Mn^{4+}$ ions. Most of them are in crystalline fields with weak rhombic distortion. The presence of a resonance with $g$~5.27 in the experimental spectrum indicates that some of them are in fields with a strong rhombic component (with $E/D$ ~ 1/3).

## 4. Conclusions

The EPR spectra of $TiO_2$(B):Mn powders were studied in two frequency ranges at different temperatures. Based on the results of calculations of the EPR spectra of $Mn^{4+}$ ions in crystal fields with a strong rhombic component, it was concluded that these ions are present in all the samples studied. Most of them are in crystal fields with a small rhombic distortion; their smaller part is affected by crystal fields with a significant rhombic component. The paper indicates the locations of $Mn^{4+}$ ions in $TiO_2$(B) that satisfy various requirements for the configuration of their environment.

## Acknowledgements

The authors are grateful to N.S. Saenko for help in recording some EPR spectra. D.P. Opra acknowledges the Russian Science Foundation (grant No. 19-73-10017).

## References

[1] D.P. Opra, S.V. Gnedenkov, S.L. Sinebryukhov, A.V. Gerasimenko, A.M. Ziatdinov, A.A. Sokolov, A.B. Podgorbunsky, A.Yu. Ustinov, V.G. Kuryavyi, V.Yu. Mayorov, I.A. Tkachenko, V.I. Sergienko. Nanomaterials **11**(2021)1703.
[2] Y. Wang, T. Chen, Q. Mu. J. Mater. Chem. **21**(2011)6006.
[3] F.G. Cherkasov, I.V. Ovchinnikov, A.N. Turanov, S.G. L'vov, V.A. Goncharov, A.Ya. Vitols. Low Temperature Physics **23**(1997)174.
[4] I. Kokorin, R. Amal, W.Y. Teoh, A.I. Kulak. App. Magn. Reson. **48**(2017)447.
[5] J. Weil, J.R. Bolton. Electron Paramagnetic Resonance: Elementary Theory and Practical Applications. Second edition. New Jersey: Wiley_Interscience. 2007. 688 pp.

# Estimation of local and long-range ordering of the structure of $TiO_2$ nanotubes

N.B. Kondrikov, P.L. Titov, S.A. Shchegoleva*, V.V. Korochentcev, I.V. Stepanov
Far Eastern Federal University, 8 Sukhanova St., Vladivostok 690950, Russia

*e-mail: sveta170@bk.ru

**Abstract.** In the article, the study of the SEM (scanning electron microscopy) images of the titanium oxide nanotube array was undertaken. The initial and modified samples were examined before and after annealing. It has been found that the annealing of the modified and unmodified samples results in different degrees of the local ordering. The nanotubular coverings were modified by the nanoparticles Pt formed by the $H_2PtCl_6$ solutions infiltration for change of their electro- and photo-catalytic properties estimated by measuring the photoelectric currents. The influence of the morphology and ordering degree of the nanotubular coverings on the manifestation of their functional properties has been studied.

## 1. Introduction

Nanostructured and microstructured materials, whose principally new physical properties result from the developed surface and quantum-size effects, constitute the group of promising objects of the advanced materials science. Porous titanium oxides are well-known representatives of this type of materials [1]. Recently, adsorption, optical, electrical, catalytic, and photocatalytic properties of $TiO_2$ have attracted a special interest of researchers [2-4].

Up to present, a number of efficient methods of creating nanostructures, including those based on the self-organization principle, have been developed. Self-organization of titanium oxide can be attained by its anodization in acids (for instance, sulfuric or phosphoric), most often, in fluorine-containing electrolytes, since dissolution proceeds there through formation of fluoride complexes. Anodic oxidation of titanium in a fluorine-containing electrolyte enables one to obtain nanostructured coatings consisting of $TiO_2$ nanotubes, whose parameters can be controlled varying the oxidation conditions [5-7].

## 2. Experiment

Anodic oxidation of titanium was performed in a two-electrode electrochemical cell using a B5-49 direct current source. Pt served as an auxiliary electrode, the Ti plate was a working electrode. The electrolyte temperature during anodization was maintained constant and equal to 20 °C using a thermostat. To obtain the nanotubular structure of titanium anodes, an aqueous solution of $NH_4F{\cdot}HF$ with addition of $Na_2SO_4$ and complexing agents was used. Thereafter, for the sake of properties modification, the obtained $Ti/TiO_2$(nano) systems were held in an aqueous solution of $H_2PtCl_6$ of the concentration $3{\cdot}10^{-2}$ $mol{\cdot}l^{-1}$ ($Ti/TiO_2$(nano), Pt) for 1 h, dried, and annealed in a muffle furnace at 500 °C for 4 h (Table I).

***Table I.*** *Modification condition.*

| Sample | Concentration $H_2PtCl_6$, M | Anneal time, h |
|---|---|---|
| *No. 1* | - | - |
| *No. 2* | - | *4* |
| *No. 3* | $3{\cdot}10^{-2}$ | - |
| *No. 4* | $3{\cdot}10^{-2}$ | *4* |

The surface structure was investigated on a Hitachi S-5500 scanning electron microscope (SEM) (Hitachi, Japan).

## 3. Results and discussions

In the SEM-image of the sample No. 1, the nanotubes with well-defined boundaries of a regular form are observed (Fig. 1 a, b).

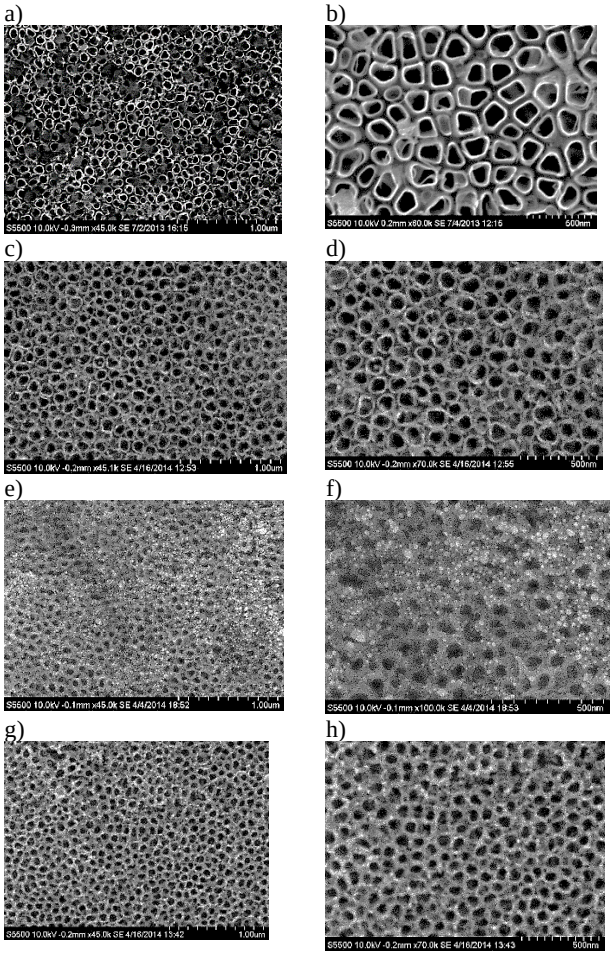


***Fig. 1.*** *SEM images of electrodes surface: a, b – simple No. 1; c, d – simple No. 2; e, f – simple No. 3; g, h – simple No. 4.*

The sufficiently great number of boundaries approximates in the form to convex polygons with well defined directions of sides. For example, one can observe the boundaries in the form of rounded rectangles. It can be

also seen that the boundaries of adjacent nanotubes are separated from each other, i.e. do not form one common boundary. The average diameter of nanotubes is approximately 100 nm. Some defects of the surface can be also seen on the sample.

Considering the local configurations of nanotubes, it can be observed that they are sufficiently similar in nature to the "plate" structure. Because the boundaries of nanotubes have often the marked sides then the nanotubes "contact" along these sides with each other. Therefore, the different types of local ordering arise. Taking heed that the boundaries of nanotubes have no some specific, most frequently repeating form, one cannot identify the preferential type of local ordering. However, sometimes, one can also observe the near correct configurations in the form of square, rectangle and, less frequently, hexagon.

In Figs. 1c, d, it can be observed that, after annealing, the boundaries of nanotubes become blurred and widen. However, one can still identify the boundaries associated with isolated nanotubes. Although the structure gets worse and becomes in whole more uneven, but the short-range local order in the relative positioning of nanotubes is preserved. The same stable configurations in the form of square, rectangle and hexagon can be seen. A part of boundaries of nanotubes "becomes blurred" and the nanotubes themselves block up partly (Fig. 1c).

Let us consider the SEM-image of the sample No. 3 modified by platinum (Fig. 1e, f). In that case, the presence of the additional component changes materially the surface structure. One can distinguish large quantity of platinum nanoparticles; their size mainly is in the order of 10 nm but can also achieve 30 nm. These particles are observed over the whole sample surface, basically, at the boundaries of nanotubes. Using the X-ray photoelectron spectroscopy method, it was shown that Pt nanoparticles on the surface of nanotubes correspond to the non-oxidized and oxidized states.

The nanotubes, in contrast to the sample No. 1, have no individual boundaries. The neighbor nanotubes are separated by common and, at the same time, sufficiently wide boundaries (walls), the thickness of which can be 20-40-50 nm. The inner diameters of nanotubes are commensurate with the wall thickness and equal predominantly 50-60 nm. Because the boundaries between nanotubes are blurred and their width is comparable with their length, one cannot give some specific characteristic of local ordering. It can be said that the structure of the nanotube array is in completely stochastically uniform and, in it, there are only rare "pieces" of regular local configurations of nanotubes.

After annealing, the common structure of the nanotube array acquires a sharpness (Fig. 1e). The boundaries of nanotubes become essentially thinner and, in such case, the inner diameter of nanotubes increases automatically. The image, as compared to the sample No. 3, is more contrast and this is to say that the nanotubes become deeper or open. The observed quantity of the platinum nanoparticles decreases essentially as compared to the sample No. 3. As before, the single particles can be observed at the boundaries of nanotubes. In such case, the walls, as before annealing, are common for the neighbor nanotubes.

Because the walls of nanotubes after annealing become thinner, one can speak to local ordering. Such sharply defined configurations of different types as in the SEM-image of the sample No. 1 are not observed because the boundaries of nanotubes are predominantly round-shaped. Considering the fact that average diameter of nanotubes changes weakly and the sections of nanotubes are tightly packed on the $R^2$ plane, the hexagon should be predominant configuration. This circumstance can turn up evidence in the Fourier spectrum character.

## 4. Conclusions

The titanium oxide nanotubes obtained when using the aqueous solution of $NH_4F{\cdot}HF$ with addition of $Na_2SO_4$ and complexing agents (sample No. 1) have sufficiently well-defined structure, sections reminding in the form the roundish convex polygons as well as boundaries individual for each nanotube.

The modification with platinum (sample No. 3) results in changing the character of the nanotube structure and "coarseness", "adhesion" of the boundaries of nanotubes with disturbance of geometry as well as appearance of large number of the platinum nanoparticles predominantly at the boundaries of nanotubes.

The annealing of these samples leads to different results. For unmodified sample, the form of the nanotube sections became less delineated. The SEM-image "became blurred" and local ordering was less pronounced. On the contrary, the annealing of the modified sample has resulted in the thinning of nanotubes boundaries and manifestation of this structure because it has no well-defied structure in the initial state. Thereby, the short-range order has better manifested in the local configurations of nanotubes if not so sharply as in the sample No. 2.

## References


[1] S.Berger Dissertation (2009) 212.

[2] T.M. Zimina, V.V. Luchinin, J. of Analytical Chemistry. **66, 12** (2011) 1136.

[3] V.A. Moshnikov, I.E. Gracheva, A.S. Lenshin, Y.M. Spivak, M.G. Anchkov, V.V. Kuznetsov, J.M. Olchowik, J. of Non-Crystalline Solids. **358, 3** (2012) 590.

[4] J. Ferre-Borrull, G. Macias, J.Pallares, L. F. Marsal, Materials **7** (2014) 5225.

[5] J. M. Macak, H. Tsuchiya, A. Ghikov. Current opinion in Solid State & Materials Sci. **11** (2007) 3.

[6] O.V. Lozovaya, M.R. Tarasevich, V.A Bogdanovskaya, I.V. Kasatkina, A.I. Shcherbakov. Fizikokhimiya poverkhnosti i zashchita materialov. **47, 1** (2011) 46.

[7] D. Fang, Z. Luo, K. Huang, D.C. Lagoudas. App. Surface S. – **257, 15** (2011) 6451.

Sixth Asian School-Conference on Physics and
Technology of Nanostructured Materials
Vladivostok, Russia, 25 – 29 April, 2022



# Dynamics of guest molecules in pillared zeolites studied by NMR

M.G. Shelyapina*,[1], D. Nefedov[1], R. Yocupicio-Gaxiola[2], V. Petranovskii[2], S. Fuentes[2]

[1] Saint Petersburg State University, 7/9 Universitetskaya nab., Saint Petersburg 199034, Russia
[2] Centro de Nanociencias y Nanotecnología, Universidad Nacional Autónoma de México, Ensenada, B.C., 22860 México

*e-mail: marina.shelyapina@spbu.ru

**Abstract.** Here we report on the results of our $^1$H NMR study of the dynamics of water molecules confined in interlamellar space of pillared mordenite and ZSM-5 zeolites. Analyzing the temperature dependence of the spectral parameters of the lines, it is possible to identify various modes of water behavior in mesopores, as well as to determine the freezing temperature of bulk water (about 180 K). According to spin-lattice relaxation measurement, three different processes with different activation energy can be distinguished: motion of water protons interacting with silanol groups on the zeolite surface and $SiO_2$ pillars, fast rotation of water protons not bound by hydrogen bonds, freezing of bulk water. The latter is in good agreement with the $^1$H NMR spectroscopy measurement.

## 1. Introduction

Layered zeolites are used as precursor for mesoporous catalysts. For the successful development of these materials, knowledge on the surface structure, dynamics of guest molecules and host-guest interaction are highly required. Recent work has demonstrated that water can positively influence reaction rates in zeolite-catalyzed chemistries. Since water molecules have high polarity and ability to form an extensive hydrogen-bonding network among themselves, bulk water, in the both liquid and solid state, exhibits very high internal cohesiveness. In restricted geometries the water molecules can also interact with the surfaces. Due to a competition between the surface-water and water–water interactions new structures of water may appear. Mesoporous silica or zeolites provide spectacular examples of the impact of nanoconfinement on the water structure and behavior.

Both water structure and dynamics can be probed by proton nuclear magnetic resonance [1].

In this contribution we report on the results of our $^1$H NMR study of the dynamics of water molecules confined in interlamellar space of recently synthetized pillared mordenite and ZSM-5 zeolites [2].

## 2. Materials and experimental methods

The samples were synthesized according to the procedure described in our previous work [2]. The preparation method included four steps: (i) preparing of lamellar zeolites by self-assembling method using cetyltrimethylammonium bromide (CTAB) and polyethylene glycol (PEG) as mesopore creating agents in a one-pot synthesis; (ii) introduction of TEOS molecules into the interlamellar space; (iii) hydrolysis and formation amorphous $SiO_2$; (iv) calcination (evacuation of organic molecules). The pillared zeolite with mordenite and ZSM-5 structure are labelled as MOR-P and MFI-P, respectively.

$N_2$ physisorption isotherms were recorded at 77 K using a QuadraSorb SI instrument. Before analysis, the samples were outgassed under secondary vacuum for 6 h at 300 °C. Surface areas were obtained by applying the Brunauer–Emmett–Teller (BET) equation on the linear zone of the BET plot. Thermal gravimetric (TG) analysis was carried out using a Netzsch STA 449 F1 Jupiter. Analysis of the samples was carried out within the temperature range 40–820 °C at a heating rate of 10 °C/min in an argon stream at a rate of 90 mL/min.

$^1$H NMR experiments were done using a Bruker Avance IIITM 400 MHz solid-state NMR spectrometer (operating with Topspin version 3.2) using a double-resonance 4mm low temperature magic angle spinning (MAS) probe. The temperature was changed within a temperature range from 173 to 293 K and controlled with accuracy 0.5 K. In MAS experiment the rotation frequency was equal to 12 kHz. Spin-lattice relaxation times $T_1$ were measured using the inversion-recovery method (180° – τ – 90°). In addition, $T_1$ relaxation times were measured at 90 MHz using Bruker SXP 4-100 spectrometer within a temperature range from 238 to 293 K.

## 3. Results and discussion

Studies of the textural properties of pillared zeolites by nitrogen porometry have shown the presence of both micropores characteristic of 3D zeolites and mesopores. For MOR-P, the main contribution to mesoporosity is made by pores with a diameter of 4 nm, but there are also pores with a diameter of 7 nm. The total pore volume is 0.546 cc/g. The MFIP sample is characterized by a monomodal mesopore size distribution with a pore diameter of about 3.9 nm. The total pore volume is 0.514 cc/g.

According to TG analysis, Figure 1, the MOR-P sample demonstrates a higher water content compared to the MFI-P sample (14.3 and 10.1 wt. %, respectively). At the same time, for the both samples, the peak of water release corresponds to 58 and 52 °C, respectively, and can be associated with the release of water from mesopores. For a sample of pillared mordenite, there is also a small peak (less than 8% of the total intensity) at 102 °C, which may be associated with the release of water from micropores.

To study the mobility of water in mesopores of pillared zeolites, $^1$H NMR studies (MAS and spin-lattice relaxation) were performed. Studies have shown that for both samples, the $^1$H NMR spectrum at room temperature consists of two lines: intense L1 at 2.7 ppm and less intense L2 at 5.2 ppm, which can be attributed to water protons interacting with the surface of the pillared zeolite and bulk water in mesopores, respectively, see Figure 2.

For a deeper study of water mobility $^1$H MAS NMR spectra at $\nu_{rot}$ = 12 kHz were recorded within the temperature range from 173 to 293 K. Both samples exhibit

similar feature of the $^1$H NMR spectra evolution with temperature decreasing. For MFI-P they are shown in Figure 3(a). As one can see, with temperature decreasing the shape of the $^1$H signal changes: (i) decreasing and broadening the signal L1 with simultaneous increasing intensity of the broad line L2; (ii) increasing the line intensity at 0 ppm, whose linewidth $\Delta\nu_{1/2}$ remains 0.4 ppm even at 173 K.

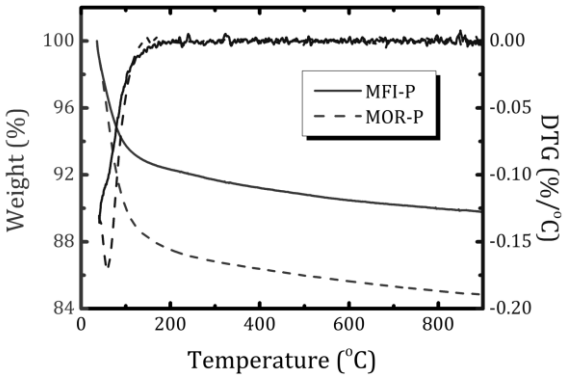


***Fig. 1.*** *TG and DTG curves for the MOR-P and MFI-P samples.*

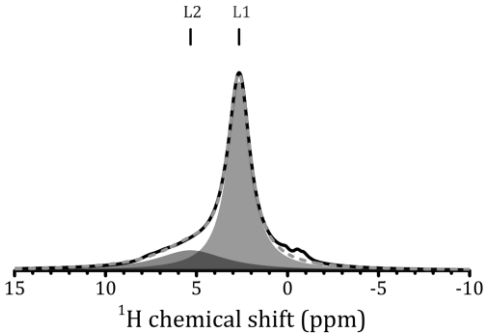


***Fig. 2.*** *$^1$H MAS NMR spectrum for MOR-P at 273K.*

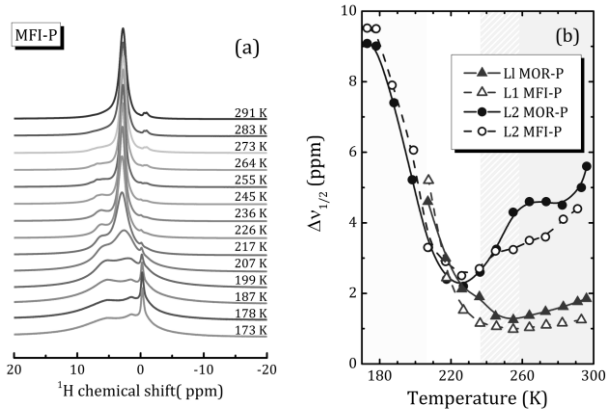


***Fig. 3.*** *$^1$H MAS NMR at various temperature for MFI-P (a); $\Delta\nu_{1/2}$ of the L1 and L2 lines vs temperature in MOR-P and MFI-P (b).*

Analyzing the temperature dependence of the spectral parameters of the lines, it is possible to identify various modes of water behavior in the nanocontainment of pillared zeolites, as well as to determine the freezing temperature of bulk water (about 180 K) and, using the Waugh -Fedin ratio, the activation energy associated with this process (about 28 kJ/mol).

It is known that spin-lattice relaxation is more sensitive to changes in molecular dynamics compared to spectral characteristics. For more careful study of water mobility in pillared zeolites the temperature dependence of the spin-lattice relaxation time $T_1$ of protons has been measured. For the both studied samples the $^1$H magnetization recovery curves exhibit a mono-exponential behavior over the whole studied temperature range. The temperature dependences of the proton spin-lattice relaxation times $T_1$ for the MOR-P and MFI-P samples are shown in Figure 4. They also indicate the complex dynamics of water molecules in the mesopores of pillared zeolites: there are at least three distinct processes with different activation energies. The use of the exchange relaxation model, developed earlier by the authors and successfully applied to the interpretation of proton mobility in heterogeneous media [3], made it possible to separate different types of proton motion and determine the corresponding activation energy and pre-exponential factor in the Arrhenius equation. In particular, for the MOR-P sample, three different processes can be distinguished with the activation energy of 24.5 kJ/mol (motion of waters proton interacting with the silanol groups on the zeolite surface and $SiO_2$ pillars), 8.5 kJ/mol (rapid rotation of water protons not bound by hydrogen bonds) and 31.0 kJ/mol (freezing of bulk water). The latter is in good agreement with the $^1$H NMR spectroscopy measurement. For MFI-P, there are also three processes with motion parameters rater similar to those ones in the pillared mordenite.

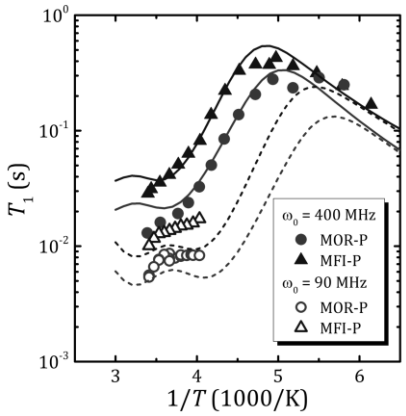


***Fig. 4.*** *$^1$H $T_1$ relaxation times vs 1/T at 400 and 90 MHz in MOR-P and MFI-P. Lines represent fitting within the exchange model.*

## 4. Conclusions

A complimentary $^1$H NMR spectroscopy and relaxation study reveals a complex behavior of nanoconfined water in zeolite with hierarchical porosity: MOR-P and MFI-P. Distinct activation energies can be attributed to different types of water motion. The obtained results will be helpful to understand behavior of other adsorbed molecules in presence of water.

## Acknowledgements

The samples were synthetized at CNyN-UNAM and studied at the Research Park of Saint Petersburg State University (Thermogravimetric and Calorimetric Research Centre, Centre for Diagnostics of Functional Materials for Medicine, Pharmacology and Nanoelectronics).

## References

[1] V.I. Chizhik, Y.S. Chernyshev, A.V. Donets, V.V. Frolov, A.V. Komolkin, M.G. Shelyapina, Magnetic resonance and its applications, Springer International Publishing, Heidelberg, New York, Dordrecht, London, 2014.

[2] M.G. Shelyapina R.I. Yocupicio-Gaxiola I.V. Zhelezniak, M.V. Chislov, J. Antúnez-García, F.N. Murrieta-Rico, D.

Homero Galván, V. Petranovskii. S. Fuentes-Moyado, Molecules **25** (2020) 4678.
[3] V.I. Chizhik, V.S. Kasperovich, M.G. Shelyapina, Y.S. Chernyshev. Int. J. Hydrogen Energy. 36 (2011) 1601

# $TiO_2$-2D mordenite nanocomposites for photocatalytic applications

M.G. Shelyapina*,[1], R. Yocupicio-Gaxiola[2], U. Caudillo-Flores[2], A. Urtaza[3], V. Petranovskii[2]

[1] Saint Petersburg State University, 7/9 Universitetskaya nab., Saint Petersburg 199034, Russia
[2] Centro de Nanociencias y Nanotecnología, Universidad Nacional Autónoma de México, Ensenada, B.C., 22860 México
[3] Escuela Nacional de Estudios Superiores, UNAM, León, Guanajuato 37684, México

*e-mail: marina.shelyapina@spbu.ru

**Abstract.** The new $TiO_2$-2D mordenite nanocomposites were synthetized from lamellar mordenite by introduction of TEOT into the interlamellar space with further hydrolysis and calcination. Anatase nanoparticles of 4 nm in size form pillars separating mordenite layers, creating mesoporosity. The surface area, pore size distribution and total pore volume of the nanocomposites depend on the media in which the hydrolysis TEOT occurs. The band gap width of the synthetized nanocomposites exhibits blue shift as compared to bulk $TiO_2$. The obtained materials may be effective photocatalysts for degradation of organics in water with high mass transfer.

## 1. Introduction

Development of environmentally friendly water treatment technologies is one of the global goals for sustainability. Photocatalytic decomposition of organic pollutants is an important strategy for water treatment.

$TiO_2$ is an n-type semiconductor with a wide energy band gap. Its photocatalytic effectiveness is governed by the crystal phase, particle size and crystallinity. Anatase is generally considered as the most active phase of $TiO_2$. Nanoparticles due to their high surface area-to-volume ratio normally exhibit better efficiency then bulk $TiO_2$. The band gap of $TiO_2$ particles less than 10 nm strongly depends on their size that is attributed to the quantum size effect [1]. One of the drawbacks of such photocatalysts is the mass transfer limitation between solid and liquid phases. Combining $TiO_2$ and zeolites helps overcome it, enhancing the degradation of organics in water [2].

In this contribution we report on the new $TiO_2$-2D mordenite nanocomposites perspective for photocatalytic applications.

## 2. Materials and experimental methods

$TiO_2$-2D mordenite nanocomposites were synthesized from layered mordenite grown by self-organization method in the presence of cetyltrimethylammonium bromide (CTAB) as an organic structure-directing agent [3]. The synthesis included several steps- (i) synthesis of the lamellar mordenite (the sample is labelled as MOR-L); (ii) introduction of titanium tetraetoxide (TEOT) into the interlamellar space of 2D mordenite; (iii) subsequent hydrolysis in water (Ti-W6h) or ethanol (Ti-E6h) for 6 h; and (iv) annealing for 4 h at 550 °C to remove the organic molecules (the samples are labelled as Ti-W6h-C and Ti-E6h-C). Powder X-ray diffraction (XRD) analysis was done on a Bruker D8 DISCOVER diractometer (CuKα).

Diffractograms were recorded in the 2θ range of 5–40°, step width 0.0302°) for the initial layered zeolite (after Step i), where the main characteristic peaks of the mordenite appear, and in the 2θ range of 5–60° for synthetized nanocomposites (after Steps iii and iv) to identify formation of $TiO_2$ nanoparticles. Small angle X-ray scattering (SAXS) patterns were recorded in a scan range from 0.2 to 7.0 2 θ degree, step width 0.01°.

The morphology and elemental analysis of the samples was studied by an optical system integrated into D8 DISCOVER Bruker spectrometer and by scanning electron microscopy (SEM) applying Zeiss Merlin equipped with an Energy Dispersive X-rays (EDX) Oxford Instruments INCAx-act.

$N_2$ physisorption isotherms were recorded at 77 K using a QuadraSorb SI instrument. Before analysis, the samples were outgassed under secondary vacuum for 6 h at 300 °C. Surface areas were obtained by applying the Brunauer–Emmett–Teller (BET) equation on the linear zone of the BET plot. Energy gaps were determined by diffusive reflectance spectroscopy (DRS) using a Simadzu UV-2550 spectrometer.

## 3. Results and discussion

Figures 1 represents the XRD patterns the lamellar zeolite, MOR-L, and the samples Ti-E6h and Ti-E6h-C. As can be seen in Figures 1(b), the sample MOR-L exhibits typical features of the mordenite structure with an amorphous halo (range 2θ between 17-30 degrees). This amorphous halo vanishes after calcination process.

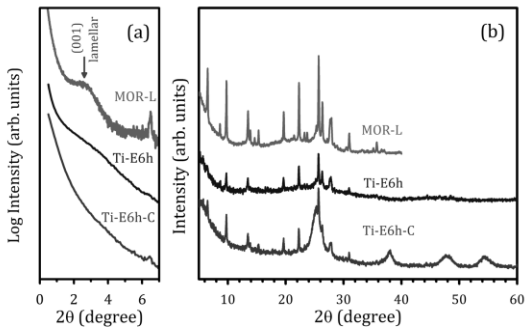


***Fig. 1.*** *Small-angle (a) and full (b) XRD powder patterns for the samples MOR-L, Ti-E6h and Ti-E6h-C.*

SAXS patterns shown in Figures 1(a) unambiguously indicate the formation of lamellar mesophases in MOR-L [1]. For the lamellar sample, the peak at 2θ = 2.7° corresponds to the (001) reflections with interplanar distances $d$ = 3.2 nm. However, the introduction of TEOT with further hydrolysis leads to smoothing this peak and disappearing after calcination. For the calcinated sample additional large peaks that corresponds to the $TiO_2$ anatase nanoparticles appear. The average size of the $TiO_2$ nanoparticles as determined by Scherrer formula from single diffraction peaks of the experimental patterns is

about 4 nm. The nanocomposites, obtained by using hydrolysis in water exhibit the very similar XRD patterns.

The results of the EDX elemental analysis of the lamellar mordenite and the titania loaded and calcinated samples are summarized in Table 1. As one can see for the as synthetized lamellar sample the Si/Al ratios is 8.4; an excess of positive charge (Na/Al > 1) is balanced by Br anions (Br/Al = 0.24). This means that CTAB is present only in its cationic forms, CTA+ balancing the dangling bonds of the zeolite layers.

***Table I.*** *EDS elemental analysis of the as synthetized and Ti loaded samples.*

| Sample | Si/Al | Na/Al | Ti/Al |
|---|---|---|---|
| MOR-L | 8.4 ± 0.3 | 1.14 ± 0.03 | – |
| Ti-W6h-C | 10.3 ± 0.4 | 0.3 ± 0.1 | 25 ± 1 |
| Ti-E6h-C | 10.5 ± 0.6 | 0.3 ± 0.2 | 15 ± 2 |

The pillaring results in a significant dealumination with a simultaneous decrease in the Na content. Despite the rather similar Al content, the Ti loading is very sensitive to the media in which the TEOT hydrolysis occurs: the hydrolysis in water results to an essentially higher Ti content. In addition, it should be noted that all the materials are characterized by a certain inhomogeneity in the distribution of elements: there are regions with higher and lower Si/Al and Ti/Al ratios, which is reflected in a rather large experimental error.

The morphology of the samples was studied by SEM. The $TiO_2$-2D mordenite nanocomposites represent thin plates up to 1-2 μm in size, combined in stacks, see Figure 2. Nanoparticles of about 8 nm dispersed on the surface of the zeolite plates are, presumably, $TiO_2$, that leaks our from interlamellar space.

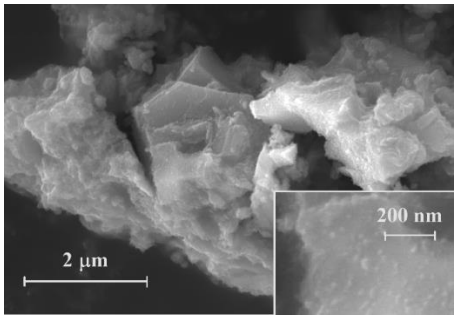


***Fig. 2.*** *SEM image of the Ti-W6h-C sample.*

$N_2$ adsorption/desorption isotherms of calcined samples are shown in Figure 3(a) and exhibit feature typical for hierarchically porous structures with both micro- and mesopores: firstly, a sharp uptake of a gas at low pressure (isotherm I, as classified by IUPAC) and, secondly, another uptake at higher pressures, accompanied with a hysteresis loop (isotherm IV, as classified by IUPAC). The hysteresis loop for the Ti-W6h-C sample corresponds to predominantly inkbottle-shaped pores (type H2) with presence of slit-shaped pores (type H3): the inflection point visible in the desorption curves appears around $P/P_0 = 0.5$, followed by wide hysteresis loop. The $N_2$ adsorption isotherm of Ti-E6h-C shows a characteristic loop for a lower ordered arrangement of mesopores. The determined surface area is 139.547 and 149.368 ml/g for the Ti-W6h-C and Ti-E6h-C samples, respectively. As one can see from Figure 3(b) the hydrolysis in water leads to the formation of mesopores of about 3.8 nm in size with a total mesopore volume of 0.172 cc/g. Hydrolysis in ethanol leads to a bimodal pore size distribution: 4 and 6 nm, with a predominance of the 6 nm diameter fraction. The volume of mesopores is 0.266 cm3/g.

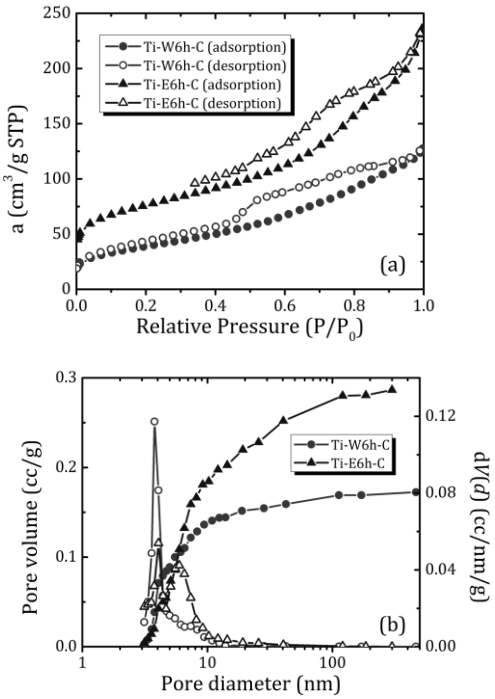


***Fig. 3.*** *Nitrogen adsorption isotherms at 77 K (a) and pore size distribution and pore volume (b) in calcined nanoocomposites.*

According to UV-vis studies the band gap width in $TiO_2$-2D mordenite nanocomposites is 3.45 eV (blue shift as compared to bulk $TiO_2$).

## 4. Conclusions

New $TiO_2$-2D mordenite nanocomposites were successfully synthetized from a lamellar mordenite. Anatase nanoparticles of 4 nm in size form pillars separating mordenite layers, creating mesoporosity. The textural properties depend on the media in which hydrolysis of TEOT occurs. The band gap width of the synthetized nanocomposites exhibits blue shift as compared to bulk $TiO_2$. Altogether it suggests that these new nanocomposites will be effective photocatalysts for degradation of organics in water with high mass transfer.

## Acknowledgements

The samples were synthetized at CNyN-UNAM and studied at the Research Park of Saint Petersburg State University (Centre for X-ray Diffraction Studies, Interdisciplinary Resource Centre for Nanotechnology, Centre for Diagnostics of Functional Materials for Medicine, Pharmacology and Nanoelectronics, Centre for Optical and Laser Materials Research).

## References

[1] L.E. Brus, J. Chem. Phys. **80** (1984) 4403.
[2] S. Fukahori, H, Ichiura, T. Kitaoka, H. Tanaka. Appl. Catal. B Environ. **46** (2003) 453.
[3] M.G. Shelyapina R.I. Yocupicio-Gaxiola I.V. Zhelezniak, M.V. Chislov, J. Antúnez-García, F.N. Murrieta-Rico, D. Homero Galván, V. Petranovskii. S. Fuentes-Moyado, Molecules **25** (2020) 4678.

Sixth Asian School-Conference on Physics and
Technology of Nanostructured Materials
Vladivostok, Russia, 25 – 29April, 2022



# Calcium phosphate oxide coatings formed on a composite resorbable substrate

M.V. Sidorova*, A.B. Podgorbunsky, M.S. Gerasimenko, S.L. Sinebryukhov, S.V. Gnedenkov
Institute of Chemistry FEB RAS, 159 pr. 100-letiya Vladivostoka, Vladivostok 690022, Russia

*e-mail: sidorova-01-02@rambler.ru

**Abstract.** In this work, coatings for the needs of implant surgery were studied, obtained on a magnesium substrate with a different content of a bioactive component – nanosized powder of calcium hydroxyapatite. The biocomposite was formed by spark plasma sintering (SPS). The properties of coatings formed by plasma electrolytic oxidation (PEO) in electrolytes containing calcium compounds were compared.

## 1. Introduction

Over the resent decades implant surgery has made a great leap both in the methodological approach and in the variety of materials used [1]. Vasodilator, orthopedic implants, including plates, prostheses, screws, etc., as well as implants for the dentistry, can radically differ in the requirements for strength characteristics and surface properties [2, 3]. An important role in the orthopedics of cortical bones is played by the implant resorption, which, in the case of restoring the functionality of the bone, excludes repeated surgical intervention to remove it, thereby improving the quality of life and treatment of the patient [2, 4].

Recently, coatings formed on magnesium products with different content of biologically active components, e.g. hydroxyapatite, which is closely resemble of bone and tooth tissues have attracted the greatest interest [5]. The porous coatings applied by the PEO on the surface of a resorbable substrate makes it possible to produce multilayer composite implant materials [6, 7]. Moreover, it could prevents implant rejection, promotes intensive growth of connective tissue and can be used in the osteolysis, osteoporosis treatment. Furthermore, in some cases, there is a need to introduce drugs into the coating that have a long therapeutic effect, which helps *inter alia* to reduce the patient's rehabilitation period.

## 2. Experiment

The samples studied in this work were obtained by spark plasma sintering (SPS) of magnesium powder and nanosized calcium hydroxyapatite in an amount of 3 wt. % and 7 wt. %. A mixture of magnesium powders (purity ≥ 99.9 %, size ≤ 40 μm, Merck) and calcium hydroxyapatite (50–80 nm) obtained by microwave synthesis [7] was subjected to dispersion with ethanol followed by its evaporation in a vacuum oven. The SPS of the samples was carried out on an SPS-515S unit (Dr. Sinter-LABTM, Japan) at a temperature of 823 K under a constant pressing pressure of 25 MPa at a heating rate of 373 K/min. Sintering was carried out in a graphite mold in vacuum (10–5 atm), the samples were held at the maximum temperature for 5 min and then cooled for 45 min to room temperature.

The phase composition of the surface layers was determined on a Rigaku X-ray diffractometer (XRD) (SmartLab, Japan), using $CuK_\alpha$-radiation. During the analysis, a Bragg-Brentano geometry focusing was used in the 2θ angle range from 10° to 80° with a step of 0.02° and an exposure time of 1 s at each point. Adhesive properties were studied on three samples with the same type of coating.

The adhesive properties of the surface layers were investigated by the scratch testing using Revetest Scratch Tester (CSM Instruments, Switzerland). The experiments were carried out at a track length of 5 mm with a gradual increase of the applied load from 1 to 20–30 N for all samples, except Mg–7–H. For the last one, the load reached 50–60 N. Rockwell diamond indenter was used for scratch testing. The load, at which abrasion of the coating to the substrate occurs were determined. The electrochemical tests were carried out using VersaSTAT MC (Princeton Applied Research, USA). Electrochemical impedance spectroscopy and potentiodynamic polarization were performed at room temperature using three-electrode cell Model K0235 Flat Cell (PAR, USA). The samples were studied in 0.9 wt. % NaCl solution. The counter electrode was a niobium grid covered with platinum, reference electrode was saturated calomel electrode (SCE). The area of contact of the sample with electrolyte was 1 $cm^2$.

## 3. Results and discussions

The properties of coatings formed by the PEO method in electrolytes containing osteoinductive components: calcium glycerophosphate and calcium hydroxyapatite were studied in the work (Table 1).

***Table I.*** *Designation of the samples.*

| Ca content in the substrate (wt. %) | Sample | | |
|---|---|---|---|
| | Bare | with PEO | |
| | | Electrolyte with $CaC_3H_7PO_6$ | Electrolyte with $Ca_{10}(PO_4)_6(OH)_2$ |
| 0 | Mg–0 | Mg–0–G | Mg–0–H |
| 3 | Mg–3 | Mg–3–G | Mg–3–H |
| 7 | Mg–7 | Mg–7–G | Mg–7–H |

Using X-ray phase analysis, it was found that the coatings formed in the electrolyte with glycerophosphate contain Mg, MgO, $Ca_5(PO_4)_3F$, $Mg_3(PO_4)_2$, and in the electrolyte with hydroxyapatite – Mg, MgO, $Mg_2SiO_4$.

It has been established that the thickness of the oxide PEO-layers increases with a growth of calcium hydroxyapatite content in the composition of the substrate (Table 2). The adhesive properties of the coatings are represented by the force $L_{C3}$ – the load at which the coating

is rubbed to the metal (Fig. 1). An increase in the thickness of the formed oxide layer is observed with an increase in the content of the calcium-phosphate component in the substrate (Table 2). Comparing the thickness of the PEO-layers and the $L_{C3}$ load, it can be concluded that coatings formed in the electrolyte with hydroxyapatite have higher strength characteristics. It can be explained with the hardness of the components including in the coating. On the Mohs scale, fluorapatite ($Ca_5(PO_4)_3F$) has a hardness of 5, and forsterite ($Mg_2SiO_4$) has a hardness of 7.

***Table II.*** *Mechanical properties of the composite coatings.*

| Sample | $L_{C3}$ (N) | Thickness (μm) |
|---|---|---|
| Mg–0–G | 13.3 ± 0.5 | 73 ± 5 |
| Mg–3–G | 19.3 ± 0.4 | 110 ± 8 |
| Mg–7–G | 19.0 ± 0.3 | 130 ± 10 |
| Mg–0–H | 14.0 ± 0.4 | 47 ± 8 |
| Mg–3–H | 24.4 ± 0.7 | 110 ± 7 |
| Mg–7–H | 37.3 ± 0.9 | 186 ± 12 |

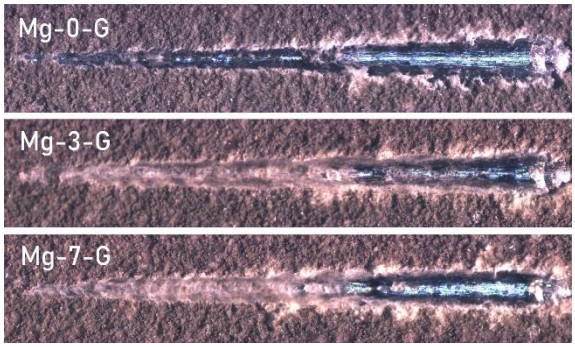


***Fig. 1.*** *The appearance of scratches on the coatings obtained in electrolyte with the calcium glycerophosphate.*

Evaluation of the results of electrochemical studies showed that the curves of the samples Mg–0–G, Mg–7–G on the plot of impedance vs. frequency behave the same at low frequencies, while the Mg–3–G sample shows a greater value of the impedance modulus. The same trend can be traced in the values of the corrosion current density and polarization resistance (Table 3). The coating formed on the substrate containing 3 wt. % hydroxyapatite, demonstrated corrosion resistance. But the coatings obtained in an electrolyte with calcium hydroxyapatite on the Mg–3 substrate, have a higher anticorrosion characteristic of the layers, compared with the coatings formed on the Mg–0 and Mg–7 samples.

***Table III.*** *Corrosion properties of the uncoated/coated samples.*

| Sample | $E_c$ (V vs. SCE) | $I_c$ ($A \cdot cm^{-2}$) | $R_p$ ($\Omega \cdot cm^2$) | $Z$ ($\Omega \cdot cm$) |
|---|---|---|---|---|
| Mg–0 | –1.61 | $1.06 \cdot 10^{-5}$ | $1.61 \cdot 10^{6}$ | $1.77 \cdot 10^{3}$ |
| Mg–3 | –1.55 | $1.21 \cdot 10^{-5}$ | $4.21 \cdot 10^{2}$ | $3.90 \cdot 10^{2}$ |
| Mg–7 | –1.57 | $2.88 \cdot 10^{-5}$ | $5.67 \cdot 10^{2}$ | $8.48 \cdot 10^{2}$ |
| Mg–0–G | –1.58 | $1.25 \cdot 10^{-6}$ | $1.07 \cdot 10^{4}$ | $1.26 \cdot 10^{4}$ |
| Mg–3–G | –1.59 | $9.80 \cdot 10^{-7}$ | $2.29 \cdot 10^{4}$ | $2.96 \cdot 10^{4}$ |
| Mg–7–G | –1.57 | $1.33 \cdot 10^{-6}$ | $1.46 \cdot 10^{4}$ | $1.33 \cdot 10^{4}$ |
| Mg–0–H | –1.54 | $7.37 \cdot 10^{-7}$ | $7.06 \cdot 10^{4}$ | $4.71 \cdot 10^{4}$ |
| Mg–3–H | –1.66 | $1.27 \cdot 10^{-7}$ | $4.05 \cdot 10^{5}$ | $3.32 \cdot 10^{5}$ |
| Mg–7–H | –1.69 | $6.30 \cdot 10^{-7}$ | $1.52 \cdot 10^{5}$ | $1.07 \cdot 10^{5}$ |

## 4. Conclusions

Coatings formed by the PEO on a composite material based on magnesium and hydroxyapatite obtained by spark plasma sintering have been studied. The phase composition of the PEO layers is established, which explains their mechanical properties. The corrosion current density of coatings formed in an electrolyte with calcium glycerophosphate up to 1–2 orders of magnitude than that of bare substrate. Oxidation of composite samples in an electrolyte with calcium hydroxyapatite leads to a decrease in corrosion currents by 2 orders of magnitude, and an increase in polarization resistance and impedance modulus by 2–3 orders of magnitude, against raw samples. It has been established that the best protective properties are exhibited by coatings formed on resorbable substrates with 3 wt. % content of calcium hydroxyapatite in the composition.

## Acknowledgements

This work was supported by the Russian Science Foundation (grant № 22-23-00915). The authors are grateful to O.O. Shichalin from the Far Eastern Federal University (FEFU, Vladivostok, Russia) for sintering composites by SPS method.

## References

[1] D. Hoare, A. Bussooa, S. Neale, N. Mirzai and J. Mercer. Adv. Sci. **6**(2019)1900856.
[2] R. Dhandapani, P. Krishnan, Dharshini, A. Zennifer, V. Kannan, A. Manigandan, M. Arul, D. Jaiswal, A. Subramanian, S. Kumbar, S. Sethuraman. Bioact. Mater. **5**(2020)458–467.
[3] Y. Onuma and P.W. Serruys. Circulation.**123**(2011)779–797.
[4] A. Garimella, G. Awale, R. Parai, S.B. Ghosh and S. Bandyopadhyay-Ghosh. Mater. Technol. **34**(2019)858–866.
[5] M.B. Sedelnikova, Yu.P. Sharkeev, T.V. Tolkacheva, M.A. Khimich, O.V. Bakina, A.N. Fomenko, A.A. Kazakbaeva, I.V. Fadeeva, V.S. Egorkin, S.V. Gnedenkov et al. Material. **13**(2020)1942.
[6] Zykova, Y. et al. Eur. Polym. J. **114**(2019)72–80.
[7] A.B. Podgorbunsky, I.M. Imshinetskiy, D.V. Mashtalyar, A.S. Gnedenkov, S.L. Sinebrukhov and S.V. Gnedenkov. Vestnik of FEB RAS. **5**(2021)43–55 [in russian].

# Polysaccharide micro- and nanoparticles for drug delivery purposes in cancer therapy

V.E. Silant'ev[1,2], L.A. Zemskova[2], L.A. Fatkullina[3], R.A. Shatilov[3], V.S. Egorkin[2], S.V. Gnedenkov[2], V.V. Kumeiko[*,3,4]

[1] Department of Biomedical Chemistry, Far Eastern Federal University, Bldg. M25, FEFU Campus, 10 Ajax Bay, Russky Island, Vladivostok 690922, Russia
[2] Institute of Chemistry, Far Eastern Branch of the Russian Academy of Sciences, 159 100-letiya Vladivostoka Pr., Vladivostok 690022, Russia
[3] Department of Medical Biology and Biotechnology, Far Eastern Federal University, Bldg. M25, FEFU Campus, 10 Ajax Bay, Russky Island, Vladivostok
[4] A.V. Zhirmunsky National Scientific Center of Marine Biology, Far Eastern Branch of the Russian Academy of Sciences, 690041 Vladivostok, Russia

*e-mail: vkumeiko@yandex.ru

Oncological diseases that can affect most of organs and tissues are the first cause of death in industrialized countries and the second in developing countries at the present time.

Various methods of treating neoplasms have been developed and applied in practice, such as radiation therapy, surgical removal of the tumor and chemotherapy. Main disadvantages are lack of selectivity in most of cases and poor susceptibility of some types of neoplasms to these methods [1].

Alternative methods of drug delivery involve targeting of active compounds to the tumor site with controlled time and rate of release. Polymeric materials or composites are generally used for this purpose. Synthetic polymers, such as polylactides, polyalkylcyanoacrylates, polyanhydrides, and composites based on them are characterized by high stability in biological fluids. Unfortunately, their practice applications are faced with toxicological problems [2].

Biopolymers of natural origin can act as alternative to synthetic polymers. Chitosan and pectin are the most promising among them. These polysaccharides are biocompatible, biodegradable and haven't significant toxicity. They are offer advantage by being able to gelling without organic solvents [3, 4]. Chitosan is widely used to produce materials for neoplasm therapy due to its anticancer properties that have been proved by *in vitro* and *in vivo* studies [5]. Pectin is also applied in production of drug delivery systems [6].

Target drug delivery can be carried out by polymers in various forms. Micro- and nanoparticles developed as an alternative to other materials to increase their stability in biological fluids, facilitate their introduction into the body and expand scope of delivery. Particles based on biopolymers are mainly obtained by several methods: desolvation, emulsification, coacervation, and electrospray drying. Complexity of synthesis and usage of organic solvents or oily organic phases lead to significant limitations in the application of these methods. Ionic gelation is the most promising method. Size and stability of nanoparticles are significantly affected by temperature of synthesis, type, concentration and pH of crosslinking agent and concentration of the biologically active substance [7].

This work describes preparation of hydrophilic drug delivery systems for cancer treatment therapy consisting of biopolymer micro- and nanoparticles. Particles based on chitosan and pectin were obtained by ionic gelation. SEM, TEM, AFM and spectral methods were used to investigate physicochemical properties and structure of obtained materials. Abilities of polysaccharide materials to accumulate and release model drugs were studied. Particles were modified with ligands specific to receptors on the surface of particular cancer cell phenotypes for targeted drug delivery.

**Acknowledgements**

This work was supported by the Ministry of Science and Higher Education of the Russian Federation (project 0657-2020-0004).

SEM and TEM studies were performed with support of Far Eastern Center for Electron Microscopy located in A.V. Zhirmunsky National Scientific Center of Marine Biology FEB RAS (Vladivostok, Russia).

**References**

[1] E. Perez-Herrero, A. Fernández-Medarde. Eur. J. Pharm. Bioharm. **93**(2015)52.
[2] S. Sundar, J. Kundu, S.C. Kundu. Sci. Technol. Adv. Mater. **11**(2010)014104.
[3] M. Moslemi Carbohyd. Polym. **254**(2021)117324.
[4] I. Postnova, V. Silant'ev, S. Sarin, Y. Shchipunov. Chem. Rec. **18**(2018)1.
[5] S.M. Asiri, F.A. Khan, A. Bozkurt. Artif. Cell. Nanomed. B. **46**(2018)S1152.
[6] A. Belousov, S. Titov, N. Shved, G. Malykin, V. Kovalev, I. Suprunova, Y. Khotimchenko, V. Kumeiko. Int. Rev. Neurobiol. **151**(2020)111.
[7] S. Racovita, S. Vasiliu, M. Popa, C. Luca. Rev. Roum. Chim. **54**(2009)709.

# Temperature and concentration driven phase transitions in $BiMnO_3$-based ceramics

M.V. Silibin*[,1], D.V. Karpinsky[1,2], D.V. Zhaludkevich[1,2], S.I. Latushka[1,2], V.A. Khomchenko[3], Yu.P. Shaman[1,5], A.V. Sysa[1,5], V.V. Sikolenko[1,4]

[1] National Research University of Electronic Technology "MIET", 124498 Moscow, Russia

[2] Scientific-Practical Materials Research Centre of NAS of Belarus, 220072 Minsk, Belarus

[3] CFisUC, Department of Physics, University of Coimbra, 3004-516 Coimbra, Portugal

[4] Joint Institute for Nuclear Research, 141980 Dubna, Moscow region, Russian Federation

[5] Scientific-Manufacturing Complex "Technological Centre", Zelenograd, Moscow, 124498, Russian Federation

*e-mail: sil_m@mail.ru

**Abstract.** Crystal and magnetic structure of the compounds $(1-x)BiFeO_3$-$(x)BiMnO_3$ has been studied using synchrotron and neutron diffraction. It has been found that increase in Mn content leads to the structural transition from the polar rhombohedral to the antipolar orthorhombic and then to the monoclinic phase via two phase concentration ranges of the adjacent phases in the concentration range $0.25 < x < 0.30$ and $0.60 < x < 0.65$ respectively at room temperature. The compounds having two-phase structural state at room temperature are characterized by irreversible structural transition upon temperature increase which favors a stabilization of high temperature structural phase.

## 1. Introduction

In the last decade, complex oxides of transition metals possessing both magnetic and electrical orders (so called multiferroics) have attracted increased interest of researchers. The most studied single phase multiferroic is bismuth ferrite ($BiFeO_3$), which has high transition temperatures to magnetic (650 K) and ferroelectric (1100 K) phases [1,2]. Bismuth manganite ($BiMnO_3$) is also magnetoelectric material with perovskite monoclinic structure with transition temperature to the magnetically ordered state TC ~ 102 K.

It is known [3], that $BiFeO_3$ and $BiMnO_3$ can form a solid solution in the entire composition range, while Mn-rich compounds can be prepared only by high pressure high temperature synthesis method. Crystal structure and magnetic properties of the compounds $(1-x)BiFeO_3$-$(x)BiMnO_3$ strongly depends on the chemical composition. Thus, structural state of the compounds changes from the polar rhombohedral single phase specific for initial BiFeO3 to the antipolar orthorhombic phase to monoclinic one ($BiMnO_3$) via a stabilization of respective two phase regions [3]. A substitution of $Fe^{3+}$ ions for $Mn^{3+}$ ions in $BiMnO_3$ leads to an increase in the transition temperature to the magnetically ordered state, while the antiferromagnetic component in exchange interactions increase.

## 2. Experiment

Ceramic compounds $(1-x)BiFeO_3$-$(x)BiMnO_3$ were prepared from stoichiometric mixtures of simple oxides $Bi_2O_3$, $Fe_2O_3$, $Mn_2O_3$ using solid state reaction method ($x < 0.5$) and high pressure high temperature technique ($0.5 \leq x < 1$). The high pressure synthesis was performed using a belt-type high pressure apparatus at pressure of 6 GPa and temperature of about 1600 K for 40 min in sealed Pt capsules. After synthesis, the pressure was slowly released, and the samples were quenched at room temperature. The crystal structure of the compounds were analyzed using X-ray diffraction data obtained with a PanAlytical X'pert Pro diffractometer, synchrotron powder diffraction (SPD) data obtained at the KMC-2 beamline (BESSY-II electron storage ring), and neutron diffraction measurements performed with the HRPT diffractometer (PSI). Temperature dependent SPD data were recorded in the range 2θ (10 – 100 °) with a step of 0.014 ° in the range 290 – 970 K at λ ~ 1.77 Å; neutron diffraction data were recorded in the temperature range 290 – 750 K (λ ~1.494 Å). The X-ray and neutron diffraction data were analyzed by the Rietveld method using the FullProf software.

## 3. Results and discussions

Analysis of the laboratory and synchrotron X-ray diffraction patterns of the compounds $BiFe_{1-x}Mn_xO_3$ confirms the changes of crystal structures from the rhombohedral structure (*R3c*) to the orthorhombic (*Pnma*) and then to the monoclinic structure (*C2/c*) with nominal increase in the manganese content which is consistent with available data. The mentioned series of the structural transformations is accompanied by a gradual decrease in the unit cell volume, while the crystal symmetry of the compounds changes non-monotonously. Thus, an increase in the dopant content leads to a stabilization of the orthorhombic structure (s.g. *Pnma*) having large metric as compared to the conventional orthorhombic structure specific for orthoferrites. The large unit cell parameters are caused by additional distortion of the lattice caused by an antipolar ordering of the dipole moments along the c- axis in contrast to the polar order noted for initial compound $BiFeO_3$. In the concentration range of the orthorhombic phase the unit cell parameters change in a different way showing a decrease in the a- and c- parameters, while the c-parameter increases which reflects antipolar distortion of the dipole moments. A stabilization of the monoclinic phase is observed in the concentration range of $0.6 < x < 0.65$ which is accompanied by negligible decrease in the unit cell volume while the metric changes notably, viz. becomes to be $\sqrt{6}ap \cdot \sqrt{2}ap \cdot \sqrt{6}a$ thus leading to a rearrangement in the dipole moments as well as a formation of a new orientation of the magnetic moments.

Temperature increase leads to drastic modification of the crystal structure of the compounds over the entire range

of the solid solution. The compounds with Mn content less than mol. 25 % show temperature induced phase transition similar to that of the initial compound $BiFeO_3$, viz. from the polar active rhombohedral phase to the non-polar orthorhombic phase.

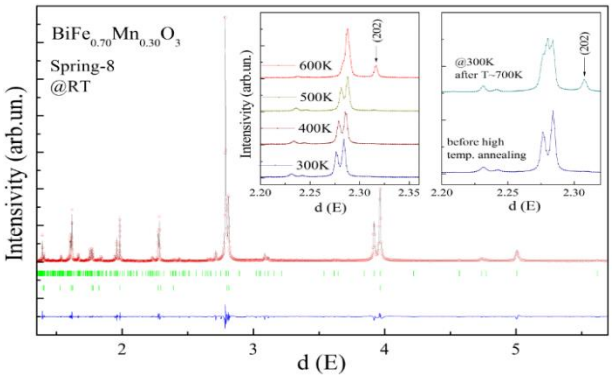


***Fig. 1.*** *SPD pattern recorded for $BiFe_{0.7}Mn_{0.3}O_3$ at room temperature, inset shows temperature evolution of the reflections specific for different structural phases.*

The compounds having two-phase structural state at room temperature show non-monotonous evolution of the structure driven by temperature increase. The temperature dependent diffraction patterns of the compound with x=0.3 having dominant orthorhombic phase at room temperature above T~500 K show a rapid increase in the intensity of the reflections specific for the rhombohedral phase (Figure 1).

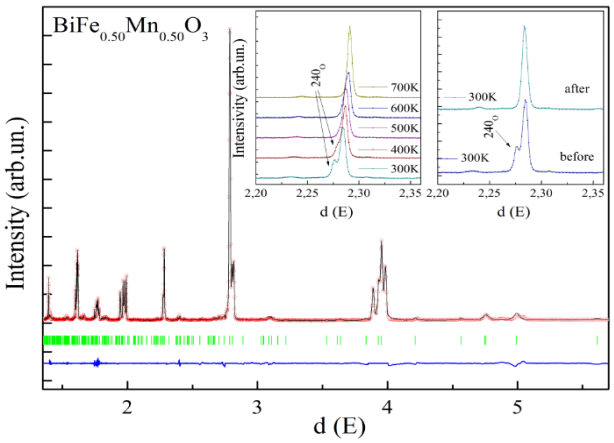


***Fig. 2.*** *SPD pattern recorded for $BiMn_{0.5}Fe_{0.5}O_3$ at room temperature, inset shows temperature evolution of the reflections specific for different structural phases.*

The amount of the rhombohedral phase increase at the expense of the orthorhombic phase but the transition a chemical decomposition of the compound starts.

It should be noted that room temperature pattern of the compound with x=0.3 recorded after heating the sample up to 700 K shows notable changes pointing at the increase in the amount of the rhombohedral phase. Temperature dependent diffraction measurements of the compound with x=0.5 having single phase structural state at room temperature show even more pronounced irreversible structural transformations. In particular, the diffraction patterns at temperatures about 600 K show a formation of new cubic like phase, while this transition is not completed up to 700 K where the chemical decomposition starts. The room temperature pattern recorded for the sample subjected to heating up to 700K shows the stabilization of the two-phase structural state with dominant cubic phase (Figure 2). The compound with x=0.7 is considered to be single phase composition with monoclinic distortion of the unit cell, at room temperature the diffraction pattern is refined assuming the space group *C2/c* which is specific one for the extreme compound $BiMnO_3$.

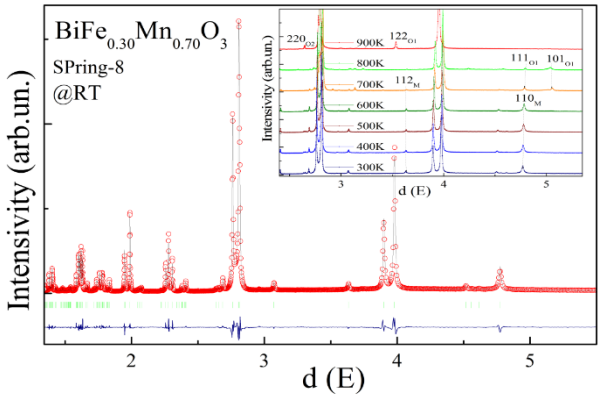


***Fig. 3.*** *SPD pattern recorded for $BiFe_{0.3}Mn_{0.7}O_3$ at room temperature, inset shows temperature evolution of the reflections specific for different structural phases.*

Temperature dependent evolution of the diffraction patterns show a stabilization of the antipolar orthorhombic state above 650 K and the two-phase structural state remains up to 850K and in the narrow temperature range of 820 – 870 K the compound has single phase orthorhombic structure, at temperatures above 870 K a new non polar orthorhombic phase stabilizes and the compound remains to be single phase orthorhombic up to the temperature of chemical decomposition of 950 K. The room temperature pattern recorded for the compound after heating up to 600K shows the stabilization of the two-phase structural state with nearly equal amount of the monoclinic and the antipolar orthorhombic phases (Figure 3).

## 4. Conclusions

The diffraction measurements along allowed to clarify the temperature and concentration driven structural phase transitions. It is determined that concentration driven structural transition from the rhombohedral to the orthorhombic phase is accompanied with a destruction of the modulated antiferromagnetic structure towards non-collinear antiferromagnetic structure ascribed as to weak ferromagnetism and then to orbitally ordered ferromagnetic structure. Annealing of the compounds at high temperatures (above 600K) leads to the irreversible phase transitions favoring a stabilization of the structural phase stable at high temperatures.

## Acknowledgements

This research was funded by RSF (project 21-19-00386).

## References

[1] C. Ederer, N.A. Spaldin. Phys. Rev. B **71**(2005)060401.
[2] I. Sosnowska, W. Schäfer, W. Kockelmann, K.H. Andersen, I.O. Troyanchuk. Appl. Phys. A **74**(2002)1040-1042.
[3] M. Azuma, H. Kanda, A.A. Belik, Y. Shimakawa, M.J. Takano. Magn. Magn. Mater. **310**(2007)1177-1179.

# Excitation of surface plasmon-polaritons in metal-dielectric structures based on opals

A.V. Cvetkov[1], S.D. Khanin[2], Yu.A. Kumzerov[1,3], N.I. Puchkov[1], V.G. Solovyev[*,1,2], A.I. Vanin[1], M.V. Yanikov[1]

[1] Pskov State University, 2 Lenin Sq., Pskov 180000, Russia
[2] S.M. Budienny Military Telecommunications Academy, 3 Tikhorezki Pr., Saint Petersburg 194064, Russia
[3] Ioffe Physico-Technical Institute RAS, 26 Politekhnicheskaya St., Saint Petersburg 194021, Russia

*e-mail: solovyev_v55@mail.ru

**Abstract.** Structure and optical properties of metal-dielectric nanocomposite materials based on opal matrices have been investigated. An anomalous transmission and absorption of light by hybrid plasmon-photonic layered heterostructures, which is apparently associated with excitation of surface plasmon-polaritons, propagating along metal-dielectric interfaces, was revealed.

## 1. Introduction

Surface plasmon polaritons (SPP) propagating at tangential directions along metal-dielectric interfaces [1] allow expanding functionality of photonic crystals [2] that control the flows of electromagnetic (EM) radiation [3].

One of the most common techniques for SPP excitation using phase-matching to SPP can be achieved by grating coupling:

$$\beta = k_x + 2\pi l/a, \qquad (1)$$

where $\beta$ and $k_x$ are tangential projections of wave vectors of SPP and incident photon, respectively, $a$ is the period of grating, $l$ being an integer.

## 2. Experiment

Samples of hybrid plasmon-photonic crystals [5-7] were fabricated by sequential deposition of metal (Ag) and dielectric ($SiO_2$) film coatings of a given thickness on a grating – monolayer (ML) of opal globules [4] made of polymethyl methacrylate by magnetron sputtering on an ATC ORION SERIES SPUTTERING SYSTEM.

A cross-sectional images of the samples (Figs. 1, 2) were obtained after processing them with a ZEISS FIB-SEM GEMINI scanning electron microscope.

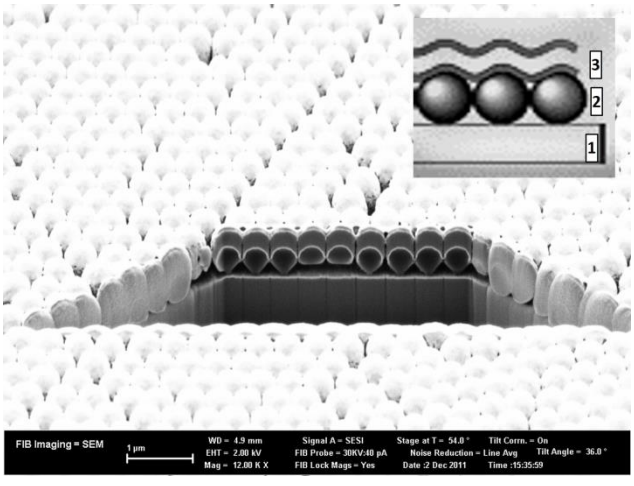


***Fig. 1.*** *Electron microscopic image of a sample of a hybrid plasmon-photonic crystal Ag/$SiO_2$/Ag/ML/Ag. Insert: 1 – glass substrate, 2 – ML of opal globules, 3 - resonator Ag/$SiO_2$/Ag [6].*

The transmission and reflectance spectra of s- and p-polarized light by layered thin-film heterostructures (when the vector of the electric field of the EM wave is perpendicular or parallel to the plane of incidence, respectively) were investigated with angular resolution using an experimental setup based on the OceanOptics QE65000 spectrometer. Ellipsometric measurements complementing results of Bragg spectroscopy were carried out with "Ellipse–1891" spectral ellipsometer.

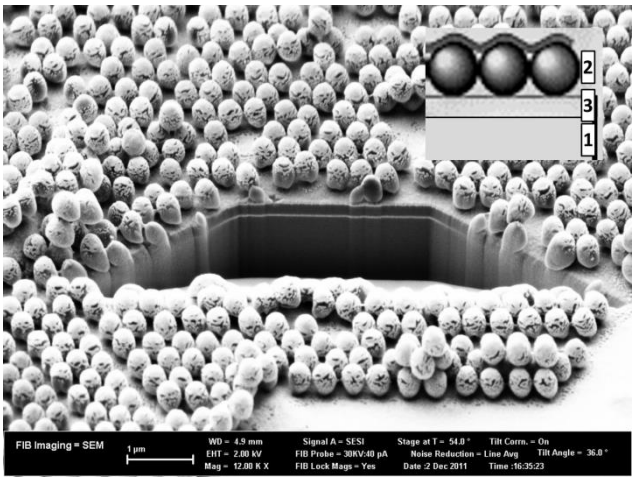


***Fig. 2.*** *Electron microscopic image of a sample of a hybrid plasmon-photonic crystal Ag/ML/Ag/$SiO_2$/Ag. Insert: 1 – glass substrate, 2 – ML of opal globules, 3 - resonator Ag/$SiO_2$/Ag [6].*

## 3. Results and discussions

Both types of hybrid plasmon-photonic crystals under study (Figs. 1 and 2) can be considered as metal-dielectric optical systems consisting of two optical elements (monolayer of opal globules and resonator with transmission coefficients $T_1$ and $T_2$, respectively) connected in serious and located one after another. In the absence of interaction between these "passive" optical elements one can calculate the total transmission coefficient $T$ from the relation $T = T_1 \cdot T_2$, hence, the ratio $r = T/(T_1 \cdot T_2) = 1$. However, experiment confirms this assumption for the hybrid plasmon-photonic crystal *Ag/ML/Ag/$SiO_2$/Ag* with plane surface resonator (Fig. 2), but not for the system *Ag/$SiO_2$/Ag/ML/Ag* (Fig. 1), where the outer surface of a thin layer covering the opal globules retained the shape and spatial periodicity characteristic of the interface between the opal-like film and this layer. In this case, excitation of surface plasmon-polaritons of various types at the interfaces profiled metal layer–monolayer of opal globules takes place. Consequently, the

ratio *r* demonstrates pronounced spectral dependence with maxima at about 489 and 584 nm and minima at 392 and 760 nm (Fig. 3, curve 3).

We attributed these maxima to an extraordinary transmission (EOT) and minima – to an extraordinary absorption (EOA) associated with the excitation of "bright" and "dark" surface plasmon-polaritons, respectively [5-7]. It should be noted that EOT maxima which can be seen in transmission spectrum of a hybrid plasmon-photonic crystal *Ag/SiO₂/Ag/ML/Ag* (Fig. 3, curve 1) correspond to the minima in its reflectance spectrum (Fig. 3, curve 2). At the same time, we emphasize that the spectral positions of EOA (Fig. 3, curve 3) correlate with the minima in the reflectance spectrum of the resonator *Ag/SiO₂/Ag* (Fig. 3, curve 4).

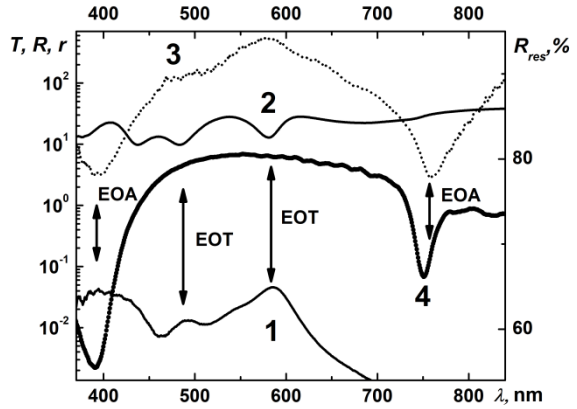


***Fig. 3.*** *Transmission (1) and reflectance (2) spectra of a hybrid plasmon-photonic crystal Ag/ML/Ag/SiO₂/Ag in comparison with the ratio* $r = T/(T_1 \cdot T_2)$ *(3) and reflectance spectrum of resonator Ag/SiO₂/Ag (4). Angle of light incidence* $\theta = 16^o$.

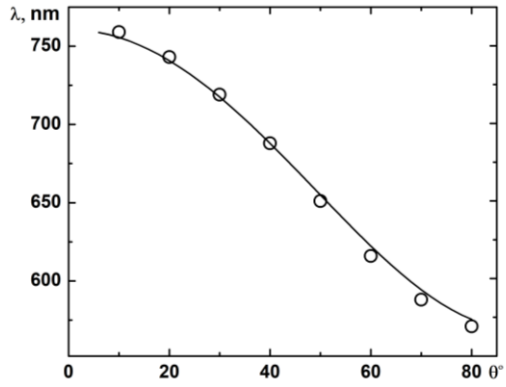


***Fig. 4.*** *Angular dispersion of the long wavelength EOA position and that of the corresponding minimum in the reflectance spectrum of resonator Ag/SiO₂/Ag (circles). Solid line shows angular dependence of the transmission peak of the interference filter* ($\lambda = 2d\sqrt{n^2 - sin^2\theta}$, $d \approx 250\,nm$, $n \approx 1.5$).

We observed this correlation for all the light incidence angles $\theta$ [5], as can be seen from Fig. 4.

At large angles $\theta$ Bragg reflectance spectroscopy may be complemented with spectral ellipsometry due to well-known main ellipsometric equation:

$$tan\Psi \cdot e^{i\Delta} = R_p/R_s, \qquad (2)$$

where $R_p$ and $R_s$ are the reflectance coefficients for two types of light polarisation, $\Psi$ and $\Delta$ being ellipsometric parameters. As can be seen from Fig. 5, experimental results obtained by both optical methods are similar.

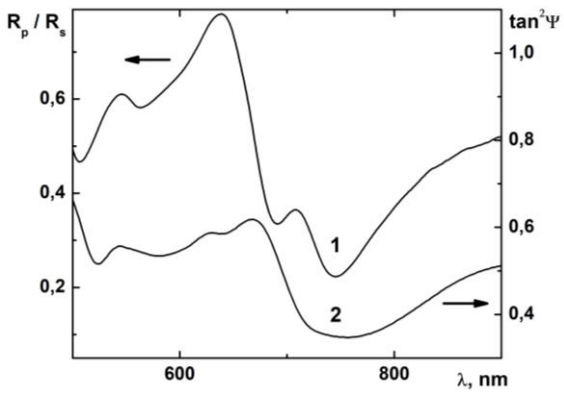


***Fig. 5.*** *Optical spectra of a hybrid plasmon-photonic crystal Ag/ML/Ag/SiO₂/Ag obtained from the ratio of its reflectance coefficients* $R_p/R_s$ *(1) and from ellipscometric parameter* $\Psi$ *(2). Angle of light incidence* $\theta = 50^o$.

## 4. Conclusions

Experimental results suggest that in opal based hybrid plasmon-photonic crystals with a complex architecture, excitation of surface plasmon-polaritons (SPP) is possible when the phase synchronism condition is met.

Two types of surface plasmon-polaritons may be excited in such metal-dielectric structures – "bright" SPP, responsible for extraordinary transmission (EOT), and "dark" SPP causing extraordinary absorption (EOA).

## Acknowledgements

The authors are grateful to U. Peschel and D. Ploss for assistance in conducting experiments. This work was partially supported by the German Academic Exchange Service (DAAD) and by the Russian Foundation for Basic Research (RFBR), project No. 20-32- 90003.

## References

[1] S. A. Maier, Plasmonics: Fundamentals and Applications (Springer, New York, 2007).
[2] S. G. Romanov, A. Korovin, A. Regensburger, and U. Peschel. Adv. Mater. **23**(2011)2515.
[3] J. D. Joannopoulos, R. D. Meade, and J. N. Winn, Photonic Crystals: Molding the Flow of Light (Princeton Univ. Press, Princeton, 2008).
[4] V. G. Balakirev, V. N. Bogomolov, V. V. Zhuravlev, Yu. A. Kumzerov, V. P. Petranovskii, S. G. Romanov, and L. A. Samoilovich. Crystallogr. Rep. **38**(1993)348.
[5] A. I. Vanin, Yu. A. Kumzerov, S. G. Romanov, V. G. Solovyev, S. D. Khanin, A. V. Cvetkov, M. V. Yanikov. Optics and Spectroscopy **128**(2020)2022.
[6] S. D. Khanin, A. I. Vanin, Yu. A. Kumzerov, V. G. Solovyev, A. V. Cvetkov, M. V. Yanikov. Radio communication technology. **4**(2021)89.
[7] A. I. Vanin, A. E. Lukin, S. G. Romanov, V. G. Solovyev, S. D. Khanin, and M. V. Yanikov. Phys. Solid State **60**(2018)774.

# Electrophoretic deposition of $TiO_2$-based photocatalysts with different $CuO_x$ particle contents for $CO_2$ reduction

L.I. Sorokina*[,1,2], A. Kedziora[2], O. Shtyka[2], S.V. Dubkov[1], P.I. Lazarenko[1], M. Szynkowska-Jozwik[2], D.G. Gromov[1]

[1] Institute of Advanced Materials and Technologies, National Research University of Electronic Technology, 124498 Zelenograd, Russia
[2] Institute of General and Ecological Chemistry, Lodz University of Technology, 90–924 Lodz, Poland

*e-mail: larasork@gmail.com

The increase in $CO_2$ emissions is one of the most important problems of our time [1]. Photocatalytically active materials are actively used to solve issues problems of air and water pollution and are also used to generate energy fuel. This paper describes an approach to develop a $TiO_2$-$CuO_x$ based photocatalyst for converting $CO_2$ into energy fuel in visible light. It is known that the modification of a wide-gap semiconductor such as $TiO_2$ by $CuO_x$ nanoparticles significantly improves the photocatalytic activity due to the heterojunction formation [2]. However, it is necessary to determine the optimal ratio between $TiO_2$ and $CuO_x$ to achieve the best results. In this work, photocatalysts with different compositions were formed by electrophoretic deposition of nanoparticles from suspension.

The electrophoretic deposition was performed from a suspension based on isopropyl alcohol, acetone, $TiO_2$, and $CuO_x$ nanopowders in different weight ratios. boron-doped silicon wafer was used as a substrate, stainless steel foil was used as counter electrode. Samples with $CuO_x$ contents of 1.5, 5.5, and 11 wt% were obtained and the band gap of these samples was investigated. The surface morphology, thickness, and stoichiometry of the obtained samples were studied by scanning electronic microscopy and energy dispersive X-ray analysis.

Precise control capability of $TiO_2$-$CuO_x$ nanocomposites composition by changing the suspension content was demonstrated. The optimal mode of the process of $TiO_2$-$CuO_x$ electrophoretic deposition was found. Fig. 1 shows the SEM image of $TiO_2$-$CuO_x$ sample deposited at an applied electric field of 150 V/cm. The bandgap width of the composite containing 11 wt% $CuO_x$ was 2.76 eV compared to pure $TiO_2$ (3.2 eV).

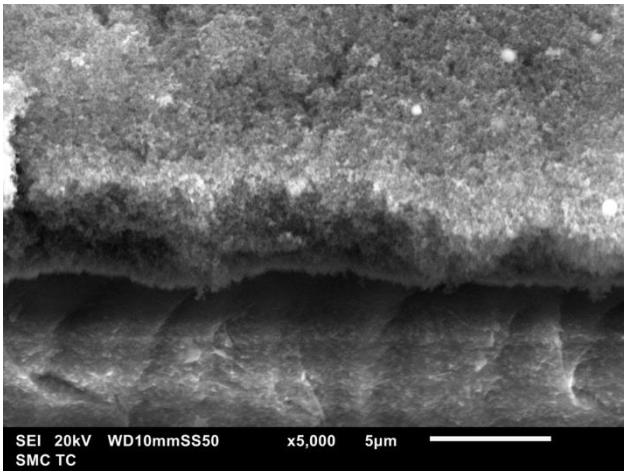


***Fig. 1.*** *SEM image of electrophoretically deposited TiO2-CuOx sample.*

**Acknowledgements**

This work was supported by the State assignment 2020-2022 № FSMR-2020-0018.

**References**

[1] Z. Kovacic, B. Likozar, M. Hus. ACS Catalysis **10** (2020)24.
[2] Y. Wang, J. Tao, X. Wang, Z. Wang, M. Zhang, G. He, Z. Sun. Ceramics International **43**(2017)6.

# How do thermal annealing options influence on size and phase changes in magnetron $TiO_2$ films

A.S. Chekadanov*, M.A. Pugachevskii, Kyaw Aung Hein, A.P. Kuzmenko, A.M. Storozhenko
Southwest State University, Regional Centre of Nanotechnology, 94, 50 let Oktyabrya, Kursk 305040, Russia

*e-mail: alexch17@mail.ru, storogenko_s@mail.ru

**Abstract.** Thin $TiO_2$ films were produced on single-crystal Si-wafers by magnetron sputtering. Subsequently, they were annealed in air at different temperatures. We researched the structure, the phase composition, the morphology, and the dimensional characteristics of the films before and after annealing using X-ray diffraction, energy-dispersive and spectrophotometric analysis, scanning electron microscopy, and small-angle X-ray scattering. The analysis of the influence of annealing parameters on the characteristics of $TiO_2$ films is carried out. The technique for determining the qualitative and quantitative phase composition of $TiO_2$ during its polymorphic transformations at high-temperature heating has been developed. It was found that $TiO_2$ annealing at 400 ºC leads to crystallization of the anatase phase, and annealing at 600 ºC leads to the transformations into the rutile phase. The optical band gap decreases with increasing temperature and with increasing annealing time.

## 1. Introduction

Nano-structured materials are one of the most fast-evolving areas of research. Among all the transition metal oxides, titanium dioxide nano-structures have the largest potential in modern science and technology [1]. $TiO_2$ can be obtained by oxydation of thin Ti films. $TiO_2$ has become famous because of its unique photocatalitic properties [2-4]. Active electron-hole pairs can be generated in the electronic structure of $TiO_2$ due to the absorption of photons with energies above 2.8 eV. When electron-hole pairs emerge on the surface, they participate in redox reactions with the formation of radical complexes. $TiO_2$ crystal exists in three common polymorphs i.e. brookite, anatase (A), and rutile (R) [5]. The photocatalytic activity of anatase is estimated to be higher than that of rutile. However, due to the smaller band gap, rutile can absorb a wider range of sunlight up to 450 nm [6].

It is a daunting task to obtain $TiO_2$ films with suitable characteristics. We took thermal annealing with trial-and-error adjustment of optimal parameters of the processing mode [7]. But equally important is determining the qualitative and quantitative phase composition of $TiO_2$ during its polymorphic transformations at high-temperature heating. That way, our aim was to research the effect of thermal annealing on the morphology and phase composition of magnetron $TiO_2$ films under various processing modes.

## 2. Materials and methods

Thin titanum films were prepared by magnetron sputtering on monocrystalline Si substrates in Ar atmosphere. To get Ti oxide, the ready Ti films were being annealed in air at temperatures 400°C, 600°C, and 800°C for 2, 4, and 6 hours.

Phase composition of the samples was analyzed by X-ray crystallography technique. First, we obtained X-ray diffraction patterns from pure Ti films, then from annealed films.

The morphological features and changes in the surface structure of the films were studied using scanning electron microscope. Line-collimation small-angle X-ray scattering was also used in the characterization of the samples.

To research the optical properties of the annealed films we used a spectrophotometer. The obtained reflection spectrums were converted to the absorption spectrums using Kubelka-Munk equation:

$$\frac{K}{S} = \frac{(1 - R_\infty)^2}{2R_\infty}. \quad (1)$$

Here K and S are absorption and back-scattering coefficients, $R_\infty$ is remission fraction of an infinitely thick layer. Using absorption spectrums we determined the value of band gap.

## 3. Results and discussions

According to scanning electron microscopy (SEM) results, the thickness of the films varied from 0.95 to 1 μm. All our $TiO_2$ films are polydisperse. The grain sizes grow with an increase in annealing time. The minimum grain sizes found on SEM scans are listed in Table 1.

***Table 1.*** *The minimum grain sizes found on SEM scans.*

| Time | Temperature | | |
|---|---|---|---|
| | 400 °C | 600 °C | 800 °C |
| *2 hours* | 25 nm | 25 nm | >100 nm |
| *4 hours* | 35 nm | 30 nm | |
| *6 hours* | 40 nm | 50 nm | |

To provide insight into integral characteristics of $TiO_2$ grains we studied the samples using SAXS. From scattering intensity data, the pair distance distribution functions were plotted (Fig. 1). The configuration of these functions clearly shows that $TiO_2$ grains have irregular shape and different sizes. The Guinier approximation applied at the very beginning of the scattering curves give us the minimum dimension of grains of 20..25 nm.

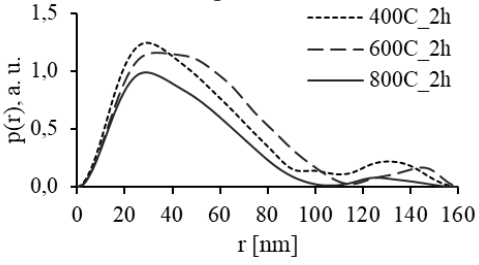


***Fig. 1.*** *SAXS results: pair distance distribution functions.*

The phase composition of the annealed films was determined using powder diffractometer. From the

obtained spectrums one can see that $TiO_2$ anatase phase is formed at a temperature of 400°C, and at 600°C it transforms into a rutile phase (Fig. 2).

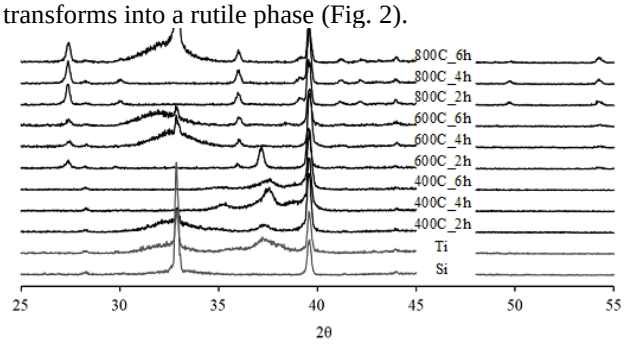


***Fig. 2.*** *Dependence of the band gap value on the annealing time.*

The concept of the coherent scattering region (CSR) was also used to research $TiO_2$ films. CSR size is generally 10-15% smaller than the size of grains identified using electron microscopy, while coherent scattering region corresponds to the inner (ordered) region of grain and does not include severely distorted boundaries [8]. CSR sizes were calculated using the Scherrer equation:

$$D = \frac{k\lambda}{\delta \cos\theta}$$

where k = 0.95 is a dimensionless shape factor; δ is the line broadening at half the maximum intensity; θ is the Bragg angle; λ = 0.154 nm is the X-ray wavelength. The estimation gives the average size of crystallites is from 3 to 11 nm.

In order to research the influence of the size factor on the width of band gap, we studied the optical absorption spectrums of $TiO_2$ nanofilms. We obtained the reflection spectrums of the annealed films and then calculated absorption spectrums using Kubelka-Munk equation (1).

According to quantum-mechanical calculations, in the case of intrinsic absorption of semiconductors and dielectric materials, transitions of electrons from valence band to conduction band are determined through the sum of the probabilities $\alpha_P$ for all states of electrons:

$$\alpha_P = \left(2\frac{m_e m_p}{m_e + m_p}\right)^{3/2} \frac{q_e^2}{ncm_e}\left(h\nu - E_g\right)^{\frac{1}{2}}$$

where $m_e$ and $m_p$ are effective electron and hole masses; $q_e$ is elementary charge; $n$ is refraction coefficient.

For all samples, the band gap $E_g$ was obtained by extrapolating the linear part of the absorption spectrum at α(hν). The dependence of the band gap values on the annealing time at each temperature looks linear (Fig. 3).

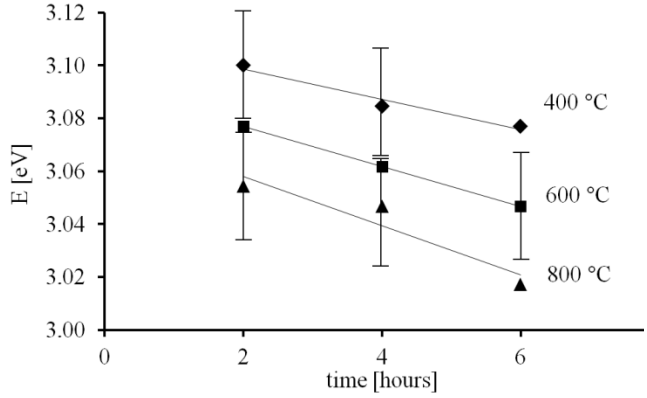


***Fig. 3.*** *Dependence of the band gap value on the annealing time.*

The optical band gap decreases with increasing temperature from 3.10 eV (at 400°C) to 3.02 eV (at 800°C). It also decreases with the annealing time growing. SEM and SAXS data prove that the more the annealing temperature the more the crystallite size, which is accompanied by a decrease in the band gap $E_g$.

## 4. Conclusions

The titanium oxide films were obtained by magnetron Ti sputtering and subsequent annealing in air for 2, 4, and 6 hours at 400 ºC, 600 ºC and 800 ºC. The thickness of the obtained $TiO_2$ films is ~ 1 μm. According to SEM and SAXS data, all studied $TiO_2$ films are polydisperse. The grains have an irregular shape, and their size grows with increasing of temperature and the duration of annealing.

The phase analysis shows that $TiO_2$ annealing at 400 ºC leads to crystallization of the anatase phase, and annealing at 600 ºC leads to the transformations into the rutile phase. According to our estimations of coherent scattering region, the average size of crystallites is in the range from 3 to 11 nm. From optical absorption spectrums we got the band gap for each sample. The value of band gap decreases with increasing annealing time and with increasing temperature. It is 3.10 eV at 400°C and 3.02 eV at 800°C. In summary, one can see that an increase in the annealing temperature leads to an increase in the crystallite size, which is accompanied by a decrease in the band gap.

## Acknowledgements

The study was carried out with the financial support of the Russian Foundation for Basic Research within the framework of scientific project No. 20-02-00599, as well as with the support of the Ministry of Education and Science of the Russian Federation (s/o 2020 no. 0851-2020-0035).

## References

[1] I. Ali, M. Suhail, Z.A. Alothman, A. Alwarthan, RSC Adv. **8** (2018) 30125.
[2] A.L. Linsebigler, G. Lu, J.T. Yates, Chem. Rev. **95** (1995) 735.
[3] E. Cerro-Prada, S. García-Salgado, M.Á., Quijano, F. Varela, Nanomaterials **9** (2019) 1.
[4] Q. Guo, Q. Zhou, Z. Ma, X. Yang, Advanced Materials **31** (2019) 1901997.
[5] J.F. Banfield, B.L. Bischoff, M.A. Anderson, Chem. Geol. **110** (1993) 211.
[6] M. Setvin, C. Franchini, X. Hao, Phys. Rev. Letters **113** (2014) 086402.
[7] M.A. Pugachevskii, V.A. Mamontov, S.N. Nikolaeva, A.S. Chekadanov, V.M. Emelyanov, Proc. of the Southwest State Univ. Series: Engineering and Technologies **11** (2021) 104.
[8] A. I. Gusev, Nanomaterials, nanostructures, and nanotechnologies (in Russian), Fizmatlit, Moscow, 2007.

Sixth Asian School-Conference on Physics and
Technology of Nanostructured Materials
Vladivostok, Russia, 25 – 29 April, 2022



# Dielectric and thermal studies of rubidium nitrate embedded in the aluminum oxide pores

S.V. Baryshnikov[1], A.Yu. Milinskiy[1], E.V. Stukova[*,2], E.V. Charnaya[3]

[1] Blagoveshchensk State Pedagogical University, 104 Lenina St., Blagoveshchensk 675000, Russia
[2] Amur State University, 21 Ignatievskoe highway, Blagoveshchensk, 675027 Russia
[3] St. Petersburg State University, 1 Ulyanovskaya St., St. Petersburg, Peterhof 198504, Russia

*e-mail: lenast@bk.ru

**Abstract.** The temperature dependences of the linear permittivity, third harmonic generation coefficient, and the DTA signal for nanoporous $Al_2O_3$ films with a channel-pore size of 300 nm filled with rubidium nitrate ($RbNO_3$) were studied in comparison with bulk rubidium nitrate. The measurements were carried out while heating and cooling in the range from room temperature to 453 K. A reduction by 3 K of the phase transition temperature (437 K in bulk $RbNO_3$) for the nanocomposite and the emergence of a new phase transition for $RbNO_3$ in the pores of $Al_2O_3$ were found.

## 1. Introduction

A way to obtain nanocomposites with polar properties is to fill mesoporous matrices with ferroelectric materials. Porous glasses, opals, molecular sieves, porous alumina films, etc are used as such matrices.

The properties of particles in pores can differ significantly from the properties of the corresponding bulk materials due to the influence of size effects and the interaction of the embedded materials with the walls of the pores. The largest number of publications on this topic was devoted to nanocomposites with sodium nitrite, Rochelle salt, potassium nitrate, and triglycine sulphate, embedded into pores (see [1–3] and references therein). The experimental data obtained show that the most pronounced influence of restricted geometry is near structural phase transitions. The temperatures of ferroelectric transitions, as a rule, shift relative to the Curie points for bulk materials. Usually, the phase transitions also diffuse.

In this work, we present the results of studies of nanocomposites based on rubidium nitrate $RbNO_3$ embedded in porous $Al_2O_3$ film with a pore size of 300 nm.

## 2. Experiment

Rubidium nitrate is known to have four stable structures at different temperatures. At room temperature, $RbNO_3$ has a trigonal symmetry (phase IV). This phase is stable up to 437 K and according to [4] is pyroelectric with the formation of 180-degree pyroelectric domains. Within the temperature range from 437 to 492 K, rubidium nitrate occurs in the cubic paraelectric phase (phase III). According to [5], at 437 K, the conductivity of $RbNO_3$ increases by two orders in magnitude, and this phase is superionic. Within the range from 492 to 558 K, RbNO3 is in the rhombohedral phase (phase II). This phase is defined as antiferroelectric [6]. Above the phase transition of 558 K, RbNO3 again transfers into a cubic phase (phase I), which exists up to a melting point of 587 K.

To obtain nanocomposites, we used chemically pure $RbNO_3$ and porous $Al_2O_3$ films, manufactured by TopMembranes Technology with a cell size of 450 nm, a pore diameter of 300 nm, and a thickness of 50 μm. A SEM image of the porous $Al_2O_3$ film is shown in Figure 1.

The embedding of rubidium nitrate into the pores was carried out from a heated saturated aqueous solution of $RbNO_3$, after that the samples were dried. The remaining water was removed by heating the samples at a temperature of 420 K during two hours. After repeating the described procedure three times, the degree of pore filling, determined from the change in the weight of the films after filling pores, was no less than 50%. An AND BM-252G balance was used to weigh the samples. Polycrystalline $RbNO_3$ was used as a reference in the form of pellets with a diameter of 10 mm and a thickness of 1.5 mm, obtained by a pressure of $8\times10^3$ kg/cm$^2$.

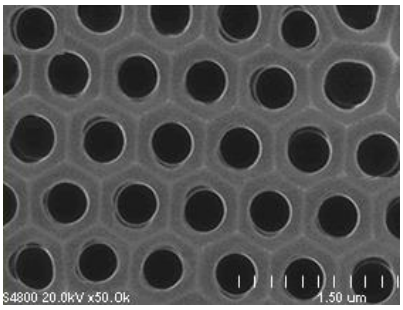


***Fig. 1.*** *SEM image of the surface of porous $Al_2O_3$ films.*

To measure the complex permittivity, an E7-25 digital immitance meter was used. A Linseis STA PT 1600 thermal analyzer was used to record the DTA signal. The possible emergence of the RbNO3 ferroelectric phase was demonstrated by monitoring the generation of the third and second harmonics when an electric field with a frequency of 2 kHz and strength of 50 V/mm was applied to the sample. The technique for studying ferroelectrics by using nonlinear dielectric spectroscopy is described in more detail in [7].

## 3. Results and discussions

The temperature dependences of the permittivity ε'(T) and the third harmonic coefficient $\gamma_{3\omega}$(T) for polycrystalline rubidium nitrate are shown in Figure 2. The clear anomalies of linear permittivity and abrupt change of the third harmonic coefficient are seen at the phase transition with noticeable thermal hysteresis.

The phase transition is observed at a temperature of 437 K upon heating and at 422 K upon cooling. The third harmonic coefficient has a value of the order of 1%.

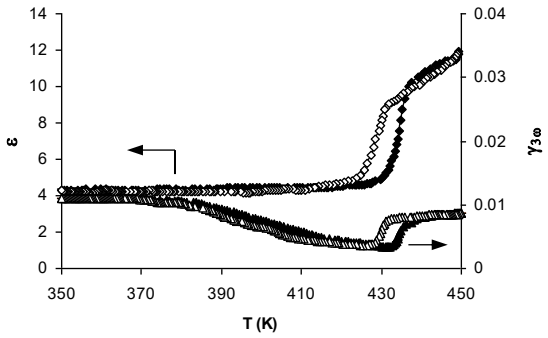


*Fig. 2. Dependences of ε'(T) at a frequency of 20 kHz (diamonds) and the third harmonic coefficient $\gamma_{3\omega}$ (triangles) for $RbNO_3$ at a field strength of 50 V/mm. Closed symbols – heating, open symbols – cooling.*

Figure 3 shows the temperature dependences of the effective permittivity ε*(T) and the third harmonic coefficient $\gamma_{3\omega}(T)$ for $RbNO_3/Al_2O_3$ composite. As it follows from the graphs, the effective permittivity increases for the composite. The third harmonic coefficient also increases by an order of magnitude. In the cooling mode, two phase transitions are observed on the ε*(*T*) curve.

The increase of the third harmonic coefficient for the $RbNO_3/Al_2O_3$ nanocomposite indicates indirectly that limiting the size of $RbNO_3$ particles to the nanometer range leads to the rubidium nitrate transition from the pyroelectric to the ferroelectric state.

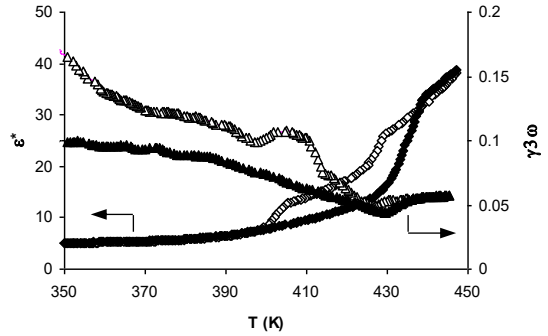


*Fig. 3. Dependences of ε*(T) at a frequency of 20 kHz (diamonds) and the third harmonic coefficient $\gamma_{3\omega}$ (triangles) for an $Al_2O_3$ film, filled with $RbNO_3$ at a field strength of 50 V/mm. Closed symbols – heating, open symbols – cooling.*

The DTA data for polycrystalline $RbNO_3$ and $RbNO_3/Al_2O_3$ composite are shown in Figure 4. For a rubidium nitrate polycrystal, the phase transition is observed at 437 K upon heating and at 423 K upon cooling.

The DTA curves for the $RbNO_3/Al_2O_3$ composite clearly show two phase transitions during heating and cooling. This is apparently due to the fact that part of $RbNO_3$ was not embedded into pores of the alumina film and is located on the surface. Phase transitions at about 437 K upon heating and 423 K upon cooling correspond to rubidium nitrate that was not embedded into pores. For $RbNO_3$ in $Al_2O_3$ pores, the transition temperature decreases down to 434 K upon heating and down to 401 K upon cooling.

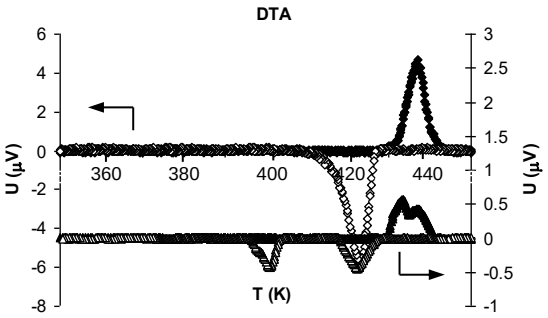


*Fig. 4. A DTA signal for polycrystalline $RbNO_3$ (diamonds) and $Al_2O_3$ film, filled with $RbNO_3$ (triangles). Closed symbols – heating, open symbols – cooling.*

To treat the temperature shift of the polymorph phase transition for nanoparticles under nanoconfinement, as a rule, size effect models developed for isolated particles on the base of the phenomenological Landau theory and the Ising model, are used. These models predict the reduction of the polymorph phase transition temperature with decreasing the particle size if the order parameter (for the Landau theory) or the value of the exchange integral (for the Ising model) at the particle boundaries is smaller than in the bulk.

In conclusion, the studies of the temperature dependences of the dielectric permittivity, the third harmonic coefficient, and the DTA signal show that for nanoporous Al2O3 matrices with a channel-pore size of 300 nm filled with rubidium nitrate, the polymorph phase transition at Tc≈437 K in bulk shifts by 3 K to low temperatures and the thermal hysteresis loop increases from 14 K (for polycrystalline RbNO3) to 33 K (for RbNO3 in nanoporous Al2O3 film).

**Acknowledgements**

This work was supported by the Russian Foundation for Basic Research, Grant No 19-29-03004.

**References**

[1] Ch. Tien, E.V. Charnaya, M.K. Lee, S.V. Baryshnikov. Phys. Status Solidi B **246**, (2009) 2346.
[2] S.V. Baryshnikov, E.V. Stukova, A.Yu. Milinskiy, E.V. Charnaya, C. Tien. Ferroelectrics **396**, (2010) 3.
[3] S.V. Baryshnikov, A.Y. Milinskiy, Y.A. Shatskaya, E.V. Charnaya, C.Tien, D. Michel. Physica B: Condens. Matter **405** (2010) 3299.
[4] P.C. Bury, A.C. McLaren. Phys. Status Solidi **31** (1969) 799.
[5] P.P. Salhotrae, A.C. Subbarao, P.Venkateswarlu. Phys. Status Solidi **31** (1969) 233.
[6] A.Ya. Dantsiger. Soviet Phys. - Solid State **7**, (1966) 1845.
[7] S. Ikeda, H. Kominami, K. Koyama, Y. Wada. J. Appl. Phys. **62** (1987) 3339.

Sixth Asian School-Conference on Physics and
Technology of Nanostructured Materials
Vladivostok, Russia, 25 – 29 April, 2022



# Evaluation of surface free energy of bioactive coatings on magnesium and titanium alloys

S.N. Suchkov*, K.V. Nadaraia, I.M. Imshinetskiy, D.V. Mashtalyar, S.L. Sinebryukhov, S.V. Gnedenkov

Institute of Chemistry FEB RAS, 159 Pr. 100-letiya Vladivostoka, Vladivostok 690022, Russia

*e-mail: snsuchkov@yandex.ru

**Abstract.** Surface free energy (SFE) is crucial for predicting the cell adhesion and as result the osteoconductivity of implantation materials. In this work, the influence of formation of bioactive calcium-phosphate coatings on the value of the SFE of titanium and magnesium implants was studied. Results shows that the formation of bioactive coatings can significantly (by 140% for magnesium and 40% for titanium) increase the SFE of these materials, which in turn should have a positive effect on the adhesion and proliferation of bone tissue cells.

## 1. Introduction

The contact of the implant surface with the body tissues is important for osseointegration [1]. The chemical composition of the implant directly determines biocompatibility with the body; the relief and roughness affect the contact area of the material with the biological medium and cell adhesion [2]. In addition, the adhesion rate of the serum components related to the wettability, which depends on the surface free energy (SFE) [1].

SFE characterizes the energy of the intermolecular interaction of the contacting phases. Many authors note that high-energy surfaces are more desirable to increase osseointegration and osteogenesis [1-3]. One of the reasons is to increase the interaction of biomolecules with the surface of implantation materials, which reduces the risk of scarring and a negative immunological reaction [3].

In this paper, the effect of bioactive coatings formed on pure titanium and magnesium alloy on wettability and the amount of surface energy was investigated.

## 2. Experiment

Rectangular plates (35×25×1.5 $mm^3$) of VT1-0 commercially pure titanium (*Ti*) and Mg-Mn-Ce alloy (*Mg*) (1.3-2.2 wt.% of Mn, 0.15-0.35 wt.% of Ce, Mg to balance) were used as materials. Before wettability measurements, metal surfaces were mechanically treated with sanding papers from #150 to #2500 sequentially, washed with distilled water and degreased with alcohol.

The formation of bioactive PEO coatings is described in [4,5]. Based on the data of X-ray phase and elemental analyses, such coatings include calcium-phosphate compounds prone to the formation of hydroxyapatite in body fluids. In addition to calcium phosphate, the coatings consist of titanium dioxide (in the modification of rutile and anatase) for pure titanium (*Ti-PEO*), magnesium oxide and ortho-silicate for magnesium alloy (*Mg-PEO*).

Surface free energy ($\gamma$) was determined as the sum of the dispersed ($\gamma^d$) and polar ($\gamma^p$) interactions of a liquid droplet with the solid surface, calculated by the OWRK (Owens-Wendt-Rabel-Kaelble) method. Deionized water ($H_2O$) and methylene iodide ($CH_2I_2$) were used as test liquids. The values of the contact angles (CA) were determined by the Young-Laplace method and recorded after reaching a stable wetting state.

## 3. Results and discussions

The measured SFE of the metal surfaces are *Mg* – 33.5 mJ $m^{-2}$ and *Ti* – 43.4 mJ $m^{-2}$, respectively (Table 1), which corresponds to the measurements of other researchers [3]. At the same time, the value of the $\gamma^p$ is small relative $\gamma$; this is common for metal surfaces.

The formation of bioactive PEO coatings (*Mg-PEO*, *Ti-PEO*) significantly increases the wettability and, as a consequence, the SFE of metal implants. For *Mg-PEO* the maximum contact angle that could be registered was no more than 7° and 17° for a drop of water and methylene iodide, respectively. On the *Ti-PEO* surface wettability improved, but worse than for *Mg-PEO* (Table 1).

***Table I.*** *Wettability and components of surface free energy for different surface. The values are averages based on the results of 10 measurements. The statistical error for measuring the contact angle is about 2%, for the SFE no more than 3%.*

| Surface | Contact angle, (°) | | Surface free energy, (mJ $m^{-2}$) | | |
|---|---|---|---|---|---|
| | $H_2O$ | $CH_2I_2$ | $\gamma^p$ | $\gamma^d$ | $\gamma$ |
| *Mg* | 82.6 | 54.9 | 5.2 | 28.3 | 33.5 |
| *Mg-PEO* | 5.4 | 15.7 | 31.4 | 48.9 | 80.3 |
| *Ti* | 75.1 | 43.7 | 5.7 | 37.7 | 43.4 |
| *Ti-PEO* | 41.4 | 50.0 | 25.9 | 34.3 | 60.2 |

Thus, the defined SFE for PEO coatings increased by 140% and 40% for *Mg-PEO* and *Ti-PEO*, respectively, in comparison with the uncoated material.

## 4. Conclusions

Analysis of the conducted studies demonstrates that the SFE for samples with bioactive PEO coatings significantly exceeds the SFE metal surface. An increase in SFE is a positive factor for further *in-vitro* and *in-vivo* studies of these materials, since improved wettability can contribute to better cell proliferation and osteogenesis.

## Acknowledgements

This work was supported by the Russian Science Foundation (project no. 21-73-10148) and the government assignments from Ministry of Science and Higher Education of the Russian Federation (project no. FWFN-2021-0003).

**References**

[1] Schwartz Z., Boyan B. D. J. cell. biochem. **56**(1994)340.
[2] Ferreirós C. M. et al. FEMS microbio. lett. **60**(1989)89.
[3] Baier R. E. J. Mat. Sci.: Mat. Med. **17**(2006)1057.
[4] Mashtalyar D. V. et al. Materials. **13**(2020)4121.
[5] Gnedenkov S. V. et al. Rus. J. In. Chem. **61**(2016)135.

Sixth Asian School-Conference on Physics and
Technology of Nanostructured Materials
Vladivostok, Russia, 25 – 29 April, 2022



# Correlation of structure and strength characteristics of rapidly quenched iron-based alloys

V.V. Tkachev*, A.N. Fedorets, D.A. Polyanski, E.A. Gridasova, A.M. Frolov, G.S. Kraynova, S.V. Dolzhikov, V.S. Plotnikov

Far Eastern Federal University, 8 Sukhanova St., Vladivostok 690950, Russia

*e-mail: tkachev.vv@dvfu.ru

**Abstract.** In this work, microindentation of amorphous metallic alloys of different compositions $Fe_{75}Ni_2Si_{10}B_{13}$, $Fe_{62}Co_{18}Si_6B_{14}$, $Fe_5Co_{58}Ni_{10}Si_{11}B_{16}$ were performed using a cubic angle indenter. Experimental results have shown that alloys containing Co in the initial state have increased microhardness at indenter load P = 0.5N. The amorphous metallic alloys were annealed from 293 K to 773 K. When samples are heated to the temperature of the crystallization initiation, microhardness increases. The investigations by the microindentation and scanning electron microscopy methods made it possible to determine the optimal conditions for obtaining and subsequent heat treatment of the amorphous metallic alloys with high mechanical properties.

## 1. Introduction

Amorphous alloys are often called the materials of the future. The reason for it is their unique properties (mechanical and physical), which are not found in conventional crystalline alloys. One of the main reasons for the amorphous and amorphous-nanocrystalline metallic alloys application is the improvement of product quality due to amorphous alloys use which has superior functional characteristics than traditional crystalline materials, and the possibility of creating new age instruments and devices, which parameters are based on a unique set of their physical, chemical, and mechanical properties [1, 2].

The amorphous and amorphous-nanocrystalline metallic alloys have high strength, wear and corrosion resistance and they are promising as structural materials. Metallic glasses based on cobalt and iron have high initial magnetic permeability and zero magnetostriction that make them suitable materials for magnetic recording heads. Produced from such materials, they have better characteristics than ferrite or permalloy heads. Therefore, the strength problem has a leading place in the nanostructural materials science providing reliable operation and fracture resistance of the amorphous and amorphous-crystalline materials.

It should be noted that today there are no unified ideas about the deformation mechanism of amorphous alloys, which on the one hand is associated with a complex structural model of amorphous alloys, and on the other hand, is associated with a change in their structure and properties during structural relaxation processes [3, 4].

The size reduction of electronic and micromechanical components of nanoelectronics and nanotechnology products has made the application of microindentation method for microhardness determination relevant, which allows to find out behavior patterns of near-surface layers of different materials [5].

## 2. Experiment

The purpose of this work is to determine the microhardness of the rapidly quenched metallic alloys of different iron-based compositions. The study of mechanical properties was carried out on X-ray amorphous metallic alloys of different compositions: $Fe_{75}Ni_2Si_{10}B_{13}$, $Fe_{62}Co_{18}Si_6B_{14}$, $Fe_5Co_{58}Ni_{10}Si_{11}B_{16}$, thickness h ~ 30 μm. The amorphous metallic glasses were prepared by rapidly quenched on a copper wheel in an argon atmosphere.

A microhardness tool (Shimadzu HMV - G) was used for the alloys microindentation. This approach can be used as an indirect estimate of the strength microheterogeneity of the material, which allows analyzing the anisotropy of strength properties. The samples used in our experiments have two surfaces that are distinguishable in morphology: the side of the ribbons which is free from the copper wheel influence has a smoother and bumpy relief than the contact side, whose defects are extended rolling strips and caverns. As a consequence, microindentation was performed on the free side. When the indenter is pressed in, an alloy experiences plastic deformation and to obtain correct results the distance from the indentation center to the sample edge should be more than 2.5d, where d is the length of the indentation diagonal. When studying microhardness, the depth of penetration should not exceed the value of 0.1h, hence the microhardness measurements of the surface layer and control the homogeneity of the obtained samples morphology are carried out in the work.

To calculate the microhardness in the HV units, the following formula was used:

$$\mathrm{HV} = \frac{F}{S} = \frac{0.102 * 2FSin\frac{d}{2}}{d^2} = 0.189\frac{F}{d^2}$$

where F – load value [N], d – length of the indentation diagonal [mm].

Diagonal lengths were measured directly using an integrated optical microscope on the Shimadzu HMV-G microhardness tool and using scanning electron microscopy (SEM) images obtained on a Carl Zeiss Cross Beam 1540XB. Microhardness measurements in this work were carried out at different loads with a load time of 10 sec.

## 3. Results and discussions

The indentation pattern for the rapidly quenched ribbon of $Fe_{75}Ni_2Si_{10}B_{13}$ allows us to conclude that heterogeneous tensile-compression deformations occur during the plastic deformation of this material. The same type of plastic deformation is observed for the ribbon of $Fe_5Co_{58}Ni_{10}Si_{11}B_{16}$ at a load F = 0.5N, Figure 1. Increasing the indenter load up to 5N is indicated by a change in the form of the deformation zone, which becomes radial, it

represents different mechanisms of the plastic deformation and can be associated, for example, with different chemical compositions of the samples. In addition, surfaces of the indentation are concave, hence the material tends to recover its continuity at the embedding point. This means that in the ribbon of $Fe_5Co_{58}Ni_{10}Si_{11}B_{16}$ at F = 5N compression stresses are effective. The observed diffraction contrast, Figure 1, indicates a disclination mechanism of the plastic deformation.

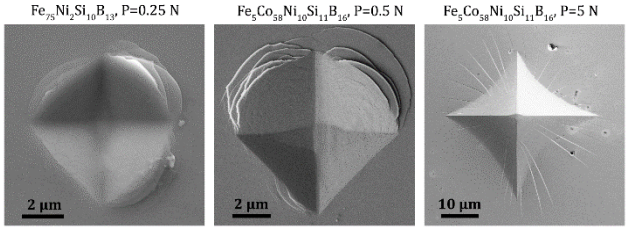


***Fig. 1.*** *SEM images of the indentation patterns obtained on the rapidly quenched ribbons of $Fe_{75}Ni_2Si_{10}B_{13}$ and $Fe_5Co_{58}Ni_{10}Si_{11}B_{16}$ at different loads.*

The mean values of the indentation diagonal lengths and indenter insertion depths indicate the accuracy of the measurements, Table I. The minimum value of microhardness in units of HV (relative error ~ 2 %) has the alloy $Fe_{75}Ni_2Si_{10}B_{13}$. The addition of Co to iron-based alloys leads to microhardness improvements. The highest HV value is for the alloy with a complex chemical composition $Fe_5Co_{58}Ni_{10}Si_{11}B_{16}$.

***Table I.*** *Parameters of Samples.*

| Composition | Diagonal length (μm) | Microhardness (HV) | Indenter insertion depth (μm) |
|---|---|---|---|
| $Fe_{75}Ni_2Si_{10}B_{13}$ | 10.105 | 908.47 | 2.04 |
| $Fe_{62}Co_{18}Si_6B_{14}$ | 9.995 | 929.56 | 2.02 |
| $Fe_5Co_{58}Ni_{10}Si_{11}B_{16}$ | 9.845 | 957.31 | 1.98 |

The rapidly quenched ribbons of $Fe_{75}Ni_2Si_{10}B_{13}$, $Fe_{62}Co_{18}Si_6B_{14}$, and $Fe_5Co_{58}Ni_{10}Si_{11}B_{16}$ were annealed from the room temperature 296 K to 773 K with intervals of 100 K at low and 50 K at high temperatures. The samples were annealed for 30 minutes at each temperature.

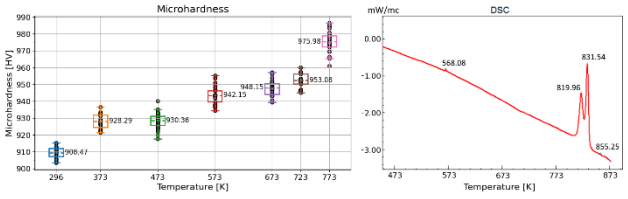


***Fig. 2.*** *The temperature dependence of microhardness and DSC curves of the rapidly quenched ribbons of $Fe_{75}Ni_2Si_{10}B_{13}$.*

Figure 2 shows a graph of the temperature dependence of microhardness of the amorphous alloy of $Fe_{75}Ni_2Si_{10}B_{13}$. The dependence HV = f(T) observed in this temperature range correlates with the differential scanning calorimetry (DSC) curve: the endothermic decay of the curve is caused by structural relaxation of the alloy within the amorphous state and annihilation of the free volume, which is accompanied by an increase in the density of the material. Decreasing the concentration of extra volume significantly influences the mechanical properties and leads to an increase in microhardness. The microhardness increase at the annealing temperature of 773 K is due to the formation of a precursor before the crystallization of the alloy.

Figure 3 shows that the character of the indentation at different annealing temperatures does not change. The analysis of the SEM images demonstrates the presence of a crystal phase of Ni solid solution based on α-Fe at annealed temperature $T_{ann} > 673$ K, which is confirmed by the X-ray diffraction analysis. The major diffusion peak displaces to higher degrees, which corresponds to a decrease in the period of inhomogeneities in the original matrix, and it is associated with the release of extra free volume.

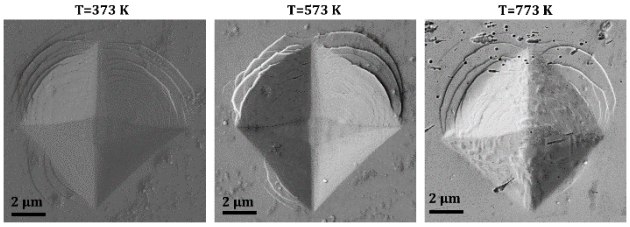


***Fig. 3.*** *SEM images of indenter indentation of the rapidly quenched ribbon of $Fe_{75}Ni_2Si_{10}B_{13}$ at different annealing temperatures.*

## 4. Conclusions

Therefore, for the rapidly quenched alloys the nature of the material reaction to plastic deformation is different, which may be due to the features of phase and structural heterogeneity, as well as the chemical composition of the samples. The microhardness of the samples increases significantly when they are heated to the crystallization temperature. The investigations by the microindentation and scanning electron microscopy methods allowed us to recommend optimal conditions for obtaining amorphous rapidly quenched ribbons with high mechanical properties.

## Acknowledgements

The work was supported by the state task of the Ministry of Science and Higher Education of the Russian Federation under grant № 0657-2020-0005.

The experimental results were obtained on the equipment of the Centre of Collective usage of the Far Eastern Federal University, registration No. 200556 (Vladivostok).

## References

[1] Li F.C., Liu T., Zhang J.Y., Shuang S., Wang Q., Wang A.D., J.G. Wang J.G., Yang Y. Materials Today Advances, 2019, 4,100027.

[2] Tong X., Zhang Y., Wang Y., Liang X., Zhang K., Zhang F., Cai Y., Ke H., Wang G., Shen J., Makino A., Wang W. Journal of Materials Science & Technology, 96, 2022, p. 233–240.

[3] Qiaoa J.C., Wangd Q., Pelletierc J.M., Katoe H., Casalinif R., Crespog D., Pinedag E., Yaoa Y., Y. Yangb Y. Progress in Materials Science, 2019, 104, p. 250–329.

[4] Song J., ZhuW., Wei X. International Journal of Mechanical Sciences, 204, 2021,106570.

[5] Liu C., Inoue A., Kong F.L., Zanaeva E., Bazlov A., Churyumov A., Zhu S.L., Al- Marzouki F., Shull R.D. Journal of Non-Crystalline Solids, 554, 2021, 120606.

# Fe-Cu-Nb-Si-B amorphous metallic alloys nanostructure

V.V. Tkachev*,1, A.N. Fedorets[1], E.V. Pustovalov[1], A.M. Frolov[1], G.S. Kraynova[1], V.S. Plotnikov[1], A.L. Vasiliev[2]

[1] Far Eastern Federal University, 8 Sukhanova St., Vladivostok 690950, Russia
[2] NRC «Kurchatov Institute»

*e-mail: tkachev.vv@dvfu.ru

**Abstract.** In this work, amorphous metallic alloys of different compositions $FeCu_1Nb_5Si_{16,5}B_6$, $FeCu_{0,2}Nb_3Si_{16,5}B_6$, $FeCu_1Si_{16}B_6$ were investigated by methods of transmission electron microscopy (TEM), scanning transmission electron microscopy (STEM), and energy-dispersive X-ray microanalysis. Experimental results have shown that the presence of crystallites from 0.3 nm and other phase inhomogeneities is observed. The presence of inhomogeneity in the elemental distribution of copper in the studied samples is shown.

## 1. Introduction

Magnetically soft amorphous-nanocrystalline metallic alloys obtained by rapid quenching from a melt have a high magnetic permeability, which allows them to be successfully used for the manufacture of magnetic heads, magnetic screens, and secondary power sources [1–4]. Properties of these materials depend on the phase and elemental structure. These alloys have high strength and corrosion resistance, which is important when products made from them are used in aggressive environments, including arctic and tropical maritime climates [5].

## 2. Experiment

The studies were carried out by transmission electron microscopy and scanning transmission electron microscopy on Tecnai Osiris and Tecnai G230ST microscopes at an accelerating voltage of 200 and 300 kV. Some of the samples were prepared by electrochemical etching, the second part was prepared by ion etching in a Gatan Duomill 600 setup at an accelerating voltage of 4 kV at the initial stage and 1.5 kV at the final stage after the hole formation to remove the damaged layer.

## 3. Results and discussions

The dark-field image in Figure 1 indicates the formation of crystallites 0.3–1 nm in size in the $FeCu_1Nb_5Si_{16.5}B_6$ alloy.

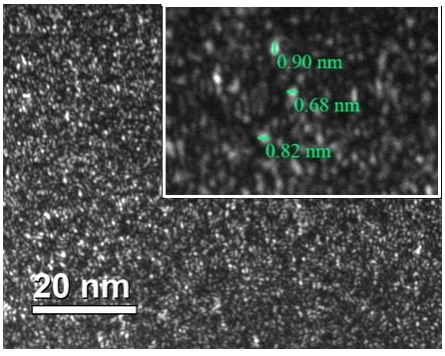


***Fig. 1.*** *Dark-field TEM image, the inset shows an enlarged image with the selected size of crystallites.*

The uniform distribution of iron and silicon is shown. In the copper distribution, there are separate areas with increased content. In the distribution of niobium and boron, there is also an inhomogeneity, but less than in the case of copper (Fig. 2).

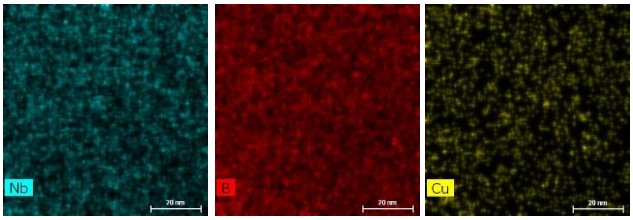


***Fig. 2.*** *Results of elemental mapping of the sample.*

## 4. Conclusions

The microstructure of alloys $FeCu_1Nb_5Si_{16.5}B_6$, $FeCu_{0.2}Nb_3Si_{16.5}B_6$, $FeCu_1Si_{16}B_6$ is polycrystalline with grains size up to 100 nm. In the $FeCu_1Nb_3Si_{16}B_6$ and $FeCu_1Nb_5Si_{16.5}B_6$ alloys, Cu-enriched regions up to 2 nm in size appear. Electron diffraction studies have shown thatthe ordering is present in metallic glass alloys with the formation of two or more coordination spheres.

## Acknowledgements

The work was supported by the state task of the Ministry of Science and Higher Education of the Russian Federation under grant № 0657-2020-0005.

The experimental results were obtained on the equipment of the Centre of Collective usage of the Far Eastern Federal University, registration No. 200556 (Vladivostok).

## References

[1] Willard M.A., Daniil M. Nanocrystalline Soft Magnetic Alloys Two Decades of Progress // Handbook of Magnetic Materials, Volume 21, 2013, p.173-342.
[2] Hawelek L. et al. The Structure and Magnetic Properties of Rapidly Quenched Fe72Ni8Nb4Si2B14 Alloy // Materials, 14, 5, 2021,10p.
[3] Han Y. et al. FeCo-based soft magnetic alloys with high Bs approaching 1.75 T and good bending ductility // Journal of Alloys and Compounds, v.691, 2017, p. 364 – 368.
[4] Liu C. et al. Fe-B-Si-C-Cu amorphous and nanocrystalline alloys with ultrahigh hardness and enhanced soft magnetic properties //Journal of Non-Crystalline Solids, v. 554, 15 February 2021, 120606.
[5] Pustovalov E. V. et al. Effect of the Process Conditions for the Preparation of CoNiFeSiB Amorphous Alloys on Their Structure and Properties // Journal of Surface Investigation: X-ray.

# Exact solution Cairo lattice for nearest neighbors

V. Trukhin*,[1], K.V. Nefedev[1,2]

[1] Far Eastern Federal University, 10 Ayaks St., Vladivostok 690922, Russia
[2] Institute of Applied Mathematics, Far Eastern Branch, Russian Academy of Science, Vladivostok, Radio 7, 690041, Russian Federation

*e-mail: trukhin.vo@dvfu.ru

**Abstract.** In this paper, we propose a new approach to the exact determination of the partition function for a flat lattice of spins in the nearest neighbor approximation. A flat lattice is assembled by successively connecting one-dimensional chains for which the exact solution is known in the Ising model. The resulting algorithm is used to calculate a lattice of complex geometry - the Cairo pentagonal lattice.

## 1. Introduction

Despite the fact that the study of spin ice began in the middle of the last century, active research in this area continues [1, 2]. One of the main problems is the lack of methods for calculating the partition function Z for a relatively large number of spins. The exact solution for at least a small number of spins makes it possible to evaluate the correctness of probabilistic solution methods (such as Metropolis [3]) and can be used in joint methods with them. The main problem in finding an exact solution is the exponential growth in the number of states depending on the size of the system. However, the possibility of a significant reduction in the number of computational cycles by optimizing the enumeration algorithm is noted.

## 2. Numerical solution

Ising's formula for finding the partition function of a one-dimensional chain is as follows:

$$\boldsymbol{Z = \left( e^{\beta} \sqrt{e^{-4\beta} + \frac{1}{4}\,(e^{\beta(-h)} + e^{\beta h})^2 - 1} + \frac{1}{2}\, e^{\beta - \beta h} + \frac{1}{2}\, e^{\beta + \beta h} \right)^n + \left( -e^{\beta} \sqrt{e^{-4\beta} + \frac{1}{4}\,(e^{\beta(-h)} + e^{\beta h})^2 - 1} + \frac{1}{2}\, e^{\beta - \beta h} + \frac{1}{2}\, e^{\beta + \beta h} \right)^n}, \quad (1)$$

where Z – statistical sum, h – external field, n – number of spins in the chain, a $\beta$=1/$kT$ – quantity depending on the Boltzmann constant and temperature.

Let's consider system of three spins. For this system, we get the solution:

$$e^{3\beta-3\beta h} + 3e^{\beta(-h)-\beta} + 3e^{\beta h-\beta} + e^{3\beta+3\beta h}, \quad (2)$$

Adding the second chain of three spins, so as to obtain a flat 2 by 3 lattice, we obtain:

$$\begin{aligned}
&e^{3\beta-3h\beta}\left(e^{3\beta-3h\beta+3\beta} + e^{-\beta-h\beta+\beta} + e^{-\beta-h\beta+\beta} + e^{-\beta-h\beta+3\beta} + e^{-\beta+h\beta-3\beta} + e^{-\beta+h\beta-\beta} + e^{-\beta+h\beta-\beta} + e^{3\beta+3h\beta-3\beta}\right) + \\
&+e^{-\beta-h\beta}\left(e^{3\beta-3h\beta+\beta} + e^{-\beta-h\beta+3\beta} + e^{-\beta-h\beta-\beta} + e^{-\beta-h\beta-\beta} + e^{-\beta+h\beta+\beta} + e^{-\beta+h\beta+\beta} + e^{-\beta+h\beta-3\beta} + e^{3\beta+3h\beta-\beta}\right) + \\
&+e^{-\beta-h\beta}\left(e^{3\beta-3h\beta+\beta} + e^{-\beta-h\beta-\beta} + e^{-\beta-h\beta+3\beta} + e^{-\beta+h\beta+\beta} + e^{-\beta+h\beta-\beta} + e^{-\beta+h\beta-\beta} + e^{-\beta+h\beta+3\beta} + e^{3\beta+3h\beta+\beta}\right) + \\
&+e^{-\beta+h\beta}\left(e^{3\beta-3h\beta-\beta} + e^{-\beta-h\beta+\beta} + e^{-\beta-h\beta+\beta} + e^{-\beta+h\beta-\beta} + e^{-\beta+h\beta+3\beta} + e^{-\beta+h\beta-\beta} + e^{3\beta+3h\beta+\beta}\right) + \\
&+e^{-\beta+h\beta}\left(e^{3\beta-3h\beta-\beta} + e^{-\beta-h\beta-\beta} + e^{-\beta-h\beta+\beta} + e^{-\beta-h\beta+\beta} + e^{-\beta+h\beta-\beta} + e^{-\beta+h\beta-\beta} + e^{-\beta+h\beta+3\beta} + e^{3\beta+3h\beta+\beta}\right) + \\
&+e^{3\beta+3h\beta}\left(e^{3\beta-3h\beta-3\beta} + e^{-\beta-h\beta-\beta} + e^{-\beta-h\beta-\beta} + e^{-\beta-h\beta-\beta} + e^{-\beta+h\beta+\beta} + e^{-\beta+h\beta+\beta} + e^{-\beta+h\beta+\beta} + e^{3\beta+3h\beta+3\beta}\right). \quad (3)
\end{aligned}$$

This approach can be applied not only to rectangular lattices. Let's look at the Cairo lattice of spins.

## 3. Parallel algorithm for calculating the Cairo lattice

At the beginning, all configurations of the chain of spins of two types are bit-encoded: the left part of the "quintuples" and the right part (Fig. 1). Then the energies within the systems are calculated for each elementary chain. The energy of the two combined chains will be as follows:

$$E_{sum} = E_{left} + E_{right} + E_{unif}, \quad (4)$$

where $E_{left}, E_{right}$ are the energies of the left and right chains, respectively, $E_{unif}$ is the unification energy for a given configuration of the left and right chains:

$$E_{unif} = -\sum_{<i,j>}^{z} \sigma_{i,j} J_{i,j} S_{ik}\, S_{jl}, \quad (5)$$

where $S_i$ – the value of the i-th spin variable of the left lattice of *k*-th configuration of boundary, $S_j$ – the value of the j-th spin variable of right lattice of *l*-th configuration, z – a quantity of neibours. $\sigma_{i,j}$ the delta function of the interaction of *i* and *j* spins, $J_{i,j}$ is their exchange integral. The delta function will be equal to 0 if the spins do not interact and 1 if they interact (Fig. 1)

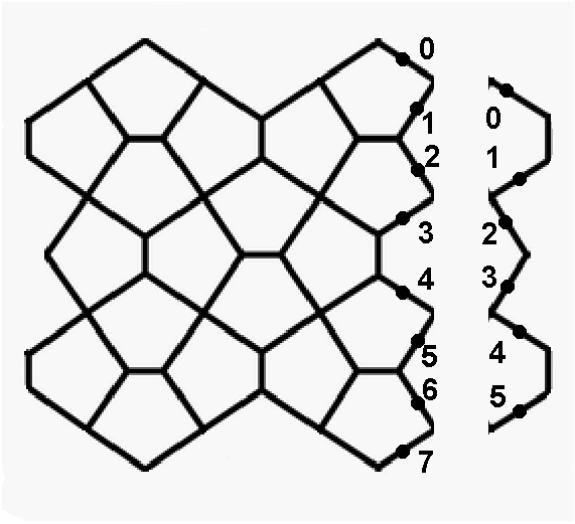


***Fig. 1.*** *Scheme for attaching the next chain to the array of spins of the Cairo lattice.*

The figure shows that, for example, the 2nd spin of the left system interacts with the 1st and 2nd spins of the right lattice but does not interact with the 0th and 3rd.

The pooling energy is calculated according to the following principle: the configurations of the left chain are parallelized by GPU blocks, and the values of the energies of a certain configuration of the left chain are parallelized by threads (Fig. 2).

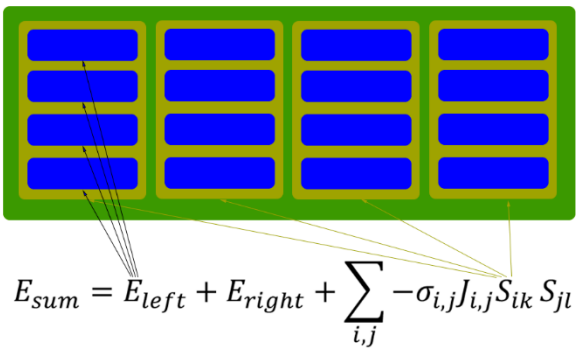


***Fig. 2.*** *Code parallelization scheme using GPU*

## 4. Conclusions

This exact method of calculation gives a significant gain in time for calculating the partition function by exhaustive search and can be effectively used in hybrid methods for finding the heat capacity of a flat Cairo lattice [4,5].

## Acknowledgements

The results of studies related to the development of a theoretical model, samples and physical experiments were obtained within the framework of the state task of the Ministry of Education and Science of Russia (No. 0657-2020-0005). The results of research related to the development of algorithms, programming, coding and implementation of a parallel calculation scheme were obtained at the expense of the grant of the President of the Russian Federation for state support of the leading scientific schools of the Russian Federation (NSh-2559.2022.1.2)

## References

[1] Schiffer P., Nisoli C. Artificial spin ice: Paths forward //Applied Physics Letters. – 2021. – V. 118. – №. 11. – P. 110501.

[2] Caravelli F., Nisoli C. Logical gates embedding in artificial spin ice //New Journal of Physics. – 2020. – V. 22. – №. 10. – P. 103052.

[3] Metropolis N., Ulam S. The monte carlo method //Journal of the American statistical association. - 1949. - V. 44. - №. 247. - P. 335-341.

[4] Makarov A. G. et al. On the numerical calculation of frustrations in the ising model //JETP Letters. – 2019. – T. 110. – №. 10. – C. 702-706.

[5] Makarova K. et al. Low-energy states, ground states, and variable frustrations of the finite-size dipolar Cairo lattices //Physical Review E. – 2021. – T. 103. – №. 4. – C. 042129.

Sixth Asian School-Conference on Physics and
Technology of Nanostructured Materials
Vladivostok, Russia, 25 – 29 April, 2022



# Preparation and study of $TiO_2$-$WO_3$-$ZnWO_4$ film heterostructures on titanium

M.S. Vasilyeva*[,1,2], I.V. Lukiyanchuk[2], A.A. Rybalka[1], Yu.B. Budnikova[1,2], V.G. Kuryavy[2]

[1] Far Eastern Federal University, FEFU Campus, 10 Ajax Bay, Russky Island, Vladivostok 690922, Russia
[2] Institute of Chemistry FEB RAS, Prosp. 100-letiya Vladivostoka 159, Vladivostok, 690022, Russia

*e-mail: vasileva.ms@dvfu.ru

**Abstract.** The composition, morphology, optoelectronic and photocatalytic properties of the $TiO_2$-$WO_3$-$ZnWO_4$ films obtained on titanium by combining the methods of plasma electrolytic oxidation and impregnation followed by annealing in air at temperatures of 500 and 700°C have been studied. This modification leads to the covering of the film surface with individual or melted nanocrystals, which are a homogeneous mixture of $WO_3$ and $ZnWO_4$ semiconductors. As a result, the band gap of the composites decreases and their photocatalytic activity in the degradation of indigo carmine increases.

## 1. Introduction

$ZnWO_4$ and $WO_3$ are important inorganic compounds which extensively studied as heterogeneous photocatalysts for the degradation of organic pollutants [1, 2]. According to [3], the combining them with each other or with other semiconductors can be used to improve their photocatalytic properties and prevent the recombination of charge carriers. As a rule, such materials are obtained in the form of a powders, which requires additional efforts to separate the powder catalyst at the end of the technological cycle. This problem can be solved by depositing a photoactive material on a solid substrate.

A promising method for obtaining films of complex oxide compounds with good adhesion to the substrate is plasma electrolytic oxidation (PEO). PEO is the formation of oxide coatings on metals under electric spark and/or arc discharges at the metal/electrolyte interface [4]. PEO coatings based on tungsten oxides can be obtained on the surface of metals in aqueous electrolytes containing $Na_2WO_4$ with $H_3BO_3$ additives to reduce pH and improve the reproducibility of results [5]. It is known [6] that modification of PEO coatings by impregnation in solutions of active components followed by annealing can be used to obtain nanostructured coatings.

This paper presents the results of a study of Zn-, W-containing coatings on titanium obtained by a combination of PEO in electrolyte containing $Na_2WO_4$ with addition of $H_3BO_3$ and impregnation in solutions containing zinc acetate followed by high-temperature annealing.

## 2. Experiment

Commercially pure VT1-0 titanium plates of a size of 2.0×2.0×0.03 cm were used as substrate in plasma electrolytic oxidation. The procedures for standardization of titanium plates and PEO processing are described in detail in [6].

The W-contining oxide coatings on titanium were formed at effective current density 0.2 A/cm$^2$ for 10 min in aqueous electrolyte containing 0.1 M $Na_2WO_4$ and 0.1 M $H_3BO_3$. The composites obtained (Ti/W) were immersed into alcohol solution of 0.05 M $Zn(CH_3COO)_2$ for 60 min. The rest of the solution was removed from the surface of the composite using filter paper.

Thermal annealing of the impregnating samples was performed in air for 1 h at 500 and 700°C in a muffle furnace. Depending on the annealing temperature, the formed samples were designated as Ti/W/Zn-500 and Ti/W/Zn-700.

The data on morphology and element composition of the surface were obtained using S-5500 scanning electron microscope (Hitachi, Japan) with the system for energy-dispersive X-ray (EDX) analysis.

The phase composition of the films was determined by X-ray diffraction (XRD) analysis.

Diffuse reflection spectra were recorded in the range 200-800 nm using SF-56 spectrophotometer with a PDO-45 diffuse reflection attachment (Russia). The band gap $E_g$ was determined from the position of the fundamental absorption edge using the Tauc equation:

$$(h\nu F(r))^{\frac{1}{n}} = A(h\nu - E_g) \quad (1)$$

where $E_g$ is band gap, $h$ - Planck constant, ν -oscillation frequency of electromagnetic waves, $F(r) = (1 - r_\infty)^2/2r_\infty$ - Kubelka–Munk's function, and $A$ - constant. The exponent $n$ is determined by the nature of interband electronic transitions.

The photocatalytic properties of PEO-coated samples were studied in a model reaction of indigo carmine (IC) degradation under UV irradiation at room temperature. The concentration of the IC aqueous solution was 10 mg/L, and its natural pH was equal 5.9. The volume of the solution was 30 mL, and the sample surface area exposed to UV light was 4 cm$^2$.

An SB-100P irradiator (maximum radiation at a wavelength of 365 nm) was used as source of UV light. The sample immersed in the IC solution was irradiated with UV light for 3 h. The absorbance of the IC solution before ($A_0$) and after reaction time (A) was studied using a UNICO-1200/1201 spectrophotometer at λ=610 nm. The conversion of IC was calculated by formula (2):

$$\chi = \frac{A_0 - A}{A_0} \cdot 100\% \quad (2)$$

## 3. Results and discussions

Table I shows XRD and EDX data for initial and modified PEO coatings. According to EDX, the initial coatings contain C, O, Ti and ~ 10 at.% W. In the composition of the modified PEO coatings, no carbon was found, while ~ 2 at.% Zn appears and the concentration of tungsten increases.

***Table I.*** *Phase and Elemental Composition of the Composites.*

| Sample | Phase | Elemental composition, (at.%) | | | | |
|---|---|---|---|---|---|---|
| | | C | O | Ti | Zn | W |
| Ti/W | $WO_3$ | 13.3 | 69.0 | 7.0 | - | 10.7 |
| Ti/W/Zn-500 | $TiO_2$ (anatase) $WO_3$, ZnO, $ZnWO_4$ | - | 75.7 | 7.4 | 2.6 | 16.3 |
| Ti/W/Zn-700 | $TiO_2$ (anatase), $WO_3$, $ZnWO_4$ | - | 68.8 | 9.7 | 1.6 | 19.9 |

As was established by XRD, the PEO layers formed in the tungstate-borate electrolyte contained only $WO_3$ among the crystalline phases. After their impregnation followed by air annealing at 500°C, the ZnO and $ZnWO_4$ phase were additionally crystallized. After annealing at 700°C, crystalline ZnO was not detected, and the coatings contained only titanium dioxide, tungsten trioxide, and zinc tungstate. Apparently, as a result of high-temperature treatment, zinc oxide, which is deficient in relation to tungsten, completely interacts with tungsten trioxide to form zinc tungstate.

After annealing the Ti/W/Zn sample at 500°C, the numerous elongated nanocrystals about 20 nm thick and no more than 100 nm long cover its surface (Fig. 1a). According to EDX, such nanocrystals contain 3-4 at.% Zn, 15-18 at.% W, and 60-67 at. % O. Raising the annealing temperature to 700°C leads to the deformation of nanocrystals due to their melting and the formation of large crystals, whose composition (25.0 at.% W, 70.0 at.% O, and 0.6 at.% Zn) corresponds to tungsten trioxide (Fig. 1b, c). The melted nanostructures formed after annealing at 700°C (Fig. 1c) are similar in composition to the nanocrystals in Fig. 1a. Thus, the nanostructures formed on the surface of the samples contain elevated concentration of Zn and W compared to their average concentrations. This suggests that such nanostructures are a mixture of zinc tungstate and tungsten oxide.

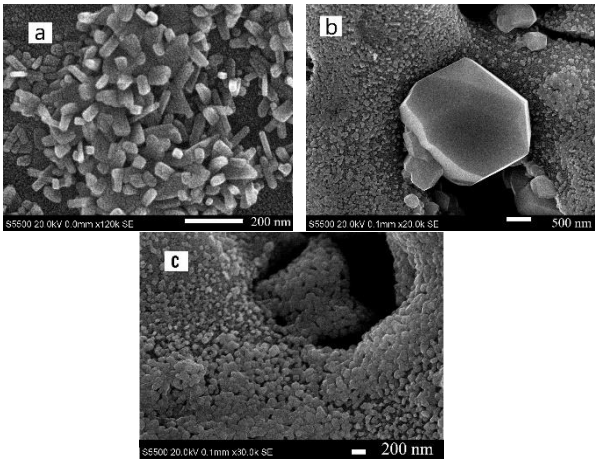


***Fig. 1.*** *SEM images of the Ti/W/Zn annealed at 500°C (a) and 700°C (b, c).*

The $E_g$ values of the formed samples are shown in Table II. Various compounds ($TiO_2$, $WO_3$ and $ZnWO_4$) in the coating composition form the direct and indirect band gaps. There are individual semiconductors having direct transitions with a band gap of 3.2, 3.3 and 3.37 eV, respectively [1-3]. The formation of defect levels within the forbidden band of the semiconductors is able to narrow the energy gap of $TiO_2$-$WO_3$ and $TiO_2$-$WO_3$-$ZnWO_4$ composites [7]. Impregnation and annealing of the Ti/W samples leads to a slight decrease in the band gap of the composites, probably due to an increase in the crystallization of $WO_3$ and $ZnWO_4$.

***Table II.*** *Direct (n=1/2) and Indirect (n=2) Band Gaps $E_g$ and Photocatalytic Activity of the Composites.*

| Sample | $E_g$, (eV) | | IC degradation degree, (%) |
|---|---|---|---|
| | n=1/2 | n=2 | |
| Ti/W | 3.02 | 2.82 | 11 |
| Ti/W/Zn-500 | 2.97 | 2.78 | 25 |
| Ti/W/Zn-700 | 2.98 | 2.74 | 34 |

Under UV irradiation (Table II), unmodified composites exhibit a certain photocatalytic activity, which slightly increases after their impregnation and annealing. An increase in activity after annealing can be associated with an increase in the crystallinity of the films and the formation of mixed nanocrystals, which can contribute to the separation of photogenerated charges.

## 4. Conclusions

The Ti/$TiO_2$-$WO_3$-$ZnWO_4$ composites were formed by combination of plasma electrolytic oxidation and impregnation followed by air annealing at the temperature of 500 and 700°C.

The morphology and phase composition of the modified composites depend on the annealing temperature. Upon annealing at 500°C, the surface is covered with nanocrystals. These nanocrystals are deformed (melted) when the composites are annealed at 700°C. The modification of composites leads to a decrease in the band gap. With an increase in the annealing temperature, the photocatalytic activity of the samples slightly increases, which may be due to the improvement in the separation of electrons and holes in various semiconductors.

## Acknowledgements

The work was carried out within the framework of the State Order of the Institute of Chemistry of FEB RAS, projects No 0205-2021-0003

## References

[1] S.M. Hosseinpour-Mashkani, M. Maddahfar, A. Sobhani-Nasab. J. Electron. Mater. **45**(2016)3612.
[2] M.R. Bayati, A.Z. Moshfegh, F. Golestani-Fard, R. Molaei. Mater. Chem. Phys. **128**(2011)427.
[3] W. Wang, W.F. Bai, B. Shen, J.W. Zhai. Ceram Int. **41**(2015)435.
[4] M. Kaseem, S. Fatimah, N. Nashrah, Y. Gun Ko. Prog. Mater. Sci. **117**(2021)100735.
[5] I.V. Lukiyanchuk, V.S. Rudnev, V.G. Kuryavyi, D.L. Boguta, S.B. Bulanova, P.S. Gordienko. Thin Solid Films **446**(2004)54.
[6] V.S. Rudnev, I.V. Lukiyanchuk, M.S. Vasilyeva, T.A. Kaidalova. Vacuum **167**(2019)397.
[7] J. Huang, W. Li, L.Cao, X. Kong, J. Huang, C. Yao, J. Fei, J. Li. RSC Adv. **6**(2016)23783.

Sixth Asian School-Conference on Physics and
Technology of Nanostructured Materials
Vladivostok, Russia, 25 – 29 April, 2022



# The investigation of the porous silicon powder formed by the Pd-assisted chemical etching with different temperatures

O.V. Volovlikova*, S.A. Gavrilov, G.O. Silakov, E.N. Lazorkina
National Research University of Electronic Technology (MIET), Zelenograd, Moscow, 124498 Russia

*e-mail: 5ilova87@gmail.com

**Abstract.** In this paper, we report the preparation of porous silicon powder by two-step Pd-assisted chemical etching with metallurgical grade polycrystalline silicon powder by varying the etching time and solution temperature with and without thermal stabilization. A high etching time of 90 minutes and a dissolution temperature above 50°C have a negative effect on the formation of porous particles, which leads to the complete dissolution of silicon particles. The positive effect of thermal stabilization in the process of etching on the thickness of the pores walls, reducing the uncontrollably growing rate of silicon etching, as a result, overetching of silicon, is shown.

## 1. Introduction

Metal-assisted chemical etching (MACE) is a promising method for porous Si powder fabrication [1, 2] without an external current source. Various metals have been used for studying the MACE of Si powder [3, 4]. It has been shown that Ag [5, 6] and Fe [7] are among the most cost-effective and efficient. The implementation of MACE to Si powders provides the increasing of the pore diameter range and total porosity. On the other hand, this results in the additional complexity of technology caused by an increased number of process parameters that need to be monitored. For instance, apart from the reactant concentration, etching duration, type, and amount of metal, the formation of pores will also be affected by the powder particle size. Also, the etching of metallurgical-grade Si powder is accompanied by a number of difficulties, in particular, flotation, which prevents the wetting of Si and hence uniform etching. This concern can be successfully remedied by adding an appropriate surfactant. Another general challenge relates to the increase of the solution temperature that leads to a higher etching rate [8]. This allows undesirable effects such as overetching of small particles and underetching of large particles. Furthermore, as has been shown earlier [9], the etching of Si powder with Ag and Fe as a catalyst is accompanied by the formation of silicate sediment. Thermal stabilization of the solution during etching will reduce the uncontrollably growing rate of silicon etching and thus prevent overetching. In order to avoid this phenomenon, we proposed to use the Pd catalyst for etching with and without thermal stabilization [10].

## 2. Experiment

Porous layers were formed at the surface of metallurgical-grade polycrystalline Si powder (MG Si P) with a mean particle diameter of 0.2-5 μm by Pd-assisted chemical etching (Figure 1a). Si powder was treated in a mixture of 0.5 g/L $PdCl_2$ and 0.65 M HC1 aqueous solutions for 30 min at 25 °C. Constant stirring was used to provide the uniform distribution of Pd particles on the surface of Si powder (Figure 1b).

Etching of Si/Pd powder was carried out in a mixture of 40 % aqueous HF solution, 30 % aqueous $H_2O_2$ solution, and deionised water in a volume ratio of 25:10:4 at 25, 50, and 75 °C with and without thermal stabilization. Etching duration was 30-120 minutes. Finally, the powders were rinsed with a mixture of deionized water and ethanol, centrifuged (MPW-351, Advanced Worldwide Technologies, Russia) and dried in room air for 24 h. HF (50 % micropur ULSI solution in water), $H_2O_2$ (37 % solution in water) were purchased from "Russian Chemist" (Moscow, Russia), ethanol (96.3 % solution in water) was purchased from "Russian Chemist" (Moscow, Russia), manufacturer “Konstanta-farm M” (Moscow, Russia), deionized water (18 MΩ·cm). The surface morphology of porous Si powder was analyzed using a scanning electron microscope (SEM; HeliosNanoLab 650, FEI Company, USA). Raman spectroscopy (LabRAM HR UV-VIS-NIR Raman Microscope, Horiba Scientific, Japan) was used to characterize porous silicon structures.

## 3. Results and discussions

Figure 1c shows the micrographs of Si powder etched in $HF/H_2O_2/H_2O$ (volumetric proportions 25/10/4) at 25 °C after 120 min etching.

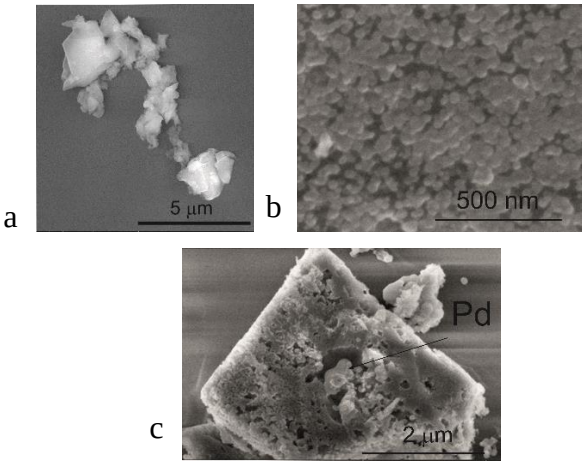


***Fig. 1.*** *SEM images of MG Si P (a), Pd nanoparticles on silicon powder (b), porous silicon powder after 120 min etching (c).*

Figure 2 shows the Raman spectra of porous Si powder formed by MACE with 60 min etching duration at 25, 50 and 75 °C without thermal stabilization. There is a number of spectra to take into account the size distribution of powder particles. Thus, the maximum shift Δω is 17,1$cm^{-1}$ for 25 °C, 9.61 $cm^{-1}$ for 50 °C and 27.7 $cm^{-1}$ for 75 °C. Increasing wavenumber shift indicates that the crystal size decreases, and hence, pore walls become thinner.

For pure Si crystal and powder, a peak appears at 520.9 $cm^{-1}$. We used the equation (1) to calculate the size of the nanoparticles [11]:

$$\Delta\omega(D) = -A \cdot (\alpha/D)^{\gamma}, \quad (1)$$

where $\Delta\omega(D)$ is the Raman shift in nanostructures with diameter $D$, $\alpha$ is the lattice constant of silicon (0.543 nm) and $A = 97.76$ $cm^1$, $\gamma = 1.44$ are fit parameters that describe the phonon confinement in nanometric spheres of diameter $D$.

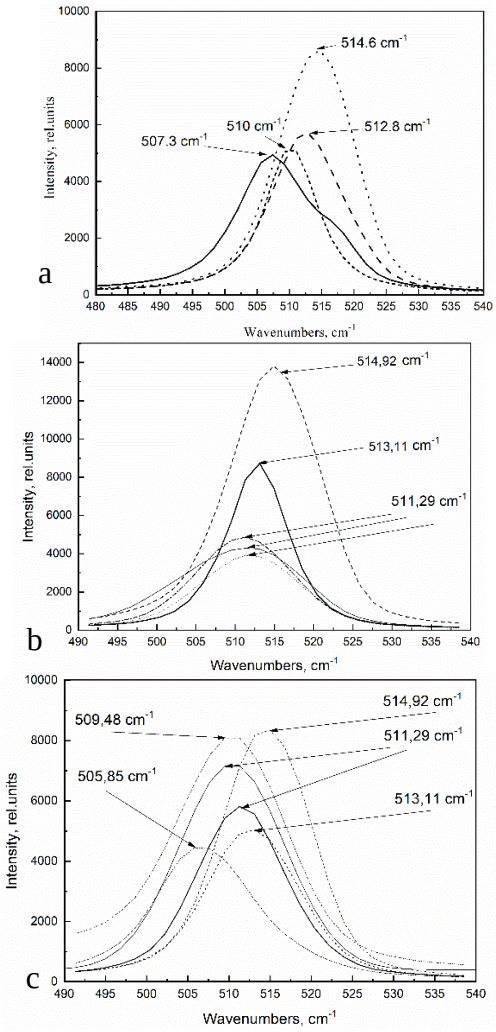


***Fig. 2.*** *Raman spectra obtained for Si powder etched in $HF/H_2O_2/H_2O$ with 60 min etching at 25°C (a), 50°C (b), 75°C (c).*

Table I show crystal size of porous silicon powder after etching with different temperatures and durations without thermal stabilization. It was calculating by data of Raman spectra. Crystal size decreases to 2 nm with increasing temperature of etching up to 50 °C and 75 °C. Silicon powder completely dissolves, irrespective of the powder/etchant ratio at 75 °C and the etching duration of more than 90 min.

According to the results on crystal sizes obtained for the etching with thermal stabilization, crystal size at 25 °C is slightly higher than without thermal stabilization. At 50 °C, crystals having 5-6 times bigger size were detected. Furthermore, there is no complete dissolution of Si powder at 75 °C.

Metal-assisted chemical etching, in particular, Pd-assisted chemical etching is an exothermic process.

***Table I.*** *Crystal size of porous Si powder formed by MACE without thermal stabilization at different temperatures of the solution 25/10/4.*

| Etching duration (*t*), min | Crystal size (*D*), nm | | |
|---|---|---|---|
| | *T*=25°C | *T*=50°C | T = 75 °C |
| Without thermal stabilization | | | |
| 30 | 2-7 | 2 | 2 |
| 60 | 2-4 | 2 | 2 |
| 90 | 2-3 | 2 | full etching |
| 120 | 2-5 | 2 | full etching |
| With thermal stabilization | | | |
| 30 | 6-10 | 2-13 | 2-11 |
| 60 | 2-6 | 3-10 | 3-8 |
| 90 | 2-6 | 2-10 | 2-8 |
| 120 | 4-13 | 2-6 | 2-4 |

The heating of the solution always occurs. The stated temperature of the etching process varies with the surface area of Si particles accessible to the etchant. Therefore, the higher the surface area of Si powder, the higher the etching temperature and, consequently, the etching rate.

Thermal stabilization (cooling) allows to limit the growth rate of temperature, and thereby to prevent overetching of powder particles.

## 4. Conclusions

Thus, it was shown that silicon powder etching for 90 and 120 minutes at T=50 °C and 75 °C without stabilization leads to its complete dissolution. The use of thermal stabilization changes the dissolution rate of the powder, which leads to the formation of a porous layer with a crystal size of 5-6 times higher than without thermal stabilization.

## Funding

This investigation was supported by the Russian Science Foundation (project No. 19-79-00205) in the part associated with samples formation, and by State assignment 2020-2022 № FSMR-2020-0018 in the part associated with porous silicon characterization using a LabRAM HR UV-VIS-NIR Raman Microscope.

## References

[1] O. Volovlikova, S. Gavrilov, A. Sysa, A. Savitskiy, A. Berezkina. 2017 ElConRus 1213.
[2] O. Pyatilova, A. Sysa, S. Gavrilov, L. Yakimova, A. Pavlov, A. Belov, A. Raskin. 2016 *Semiconductors* **50** 1720.
[3] Ch.-L. Lee, K. Tsujino, Yu. Kanda, Sh. Ikeda, and M. Matsumura 2008 *J. Mater. Chem*. **18** 1015.
[4] Z. Huang, N. Geyer, P. Werner, J. de Boor, and U. Gösele 2011 *Adv. Mater*. **23** 285.
[5] T. Nakamura, N. Hosoya, B. Tiwari, and S. Adachi. 2010 *Journal of Applied Physics*. **108** 104315.
[6] R. Ouertani, A. Hamdi, C. Amri, M. Khalifa, H. Ezzaouia. 2014 *Nanoscale Research Letters* **9** 574.
[7] A. Loni, D. Barwick, L. Batchelor, J. Tunbridge, Y. Han, Z. Li and L. Canham. 2011 *Electrochem. Solid-State Lett*. **14** K25.
[8] O. Pyatilova, A. Sysa, S. Gavrilov et al. 2016 *Semiconductors* **50** 1720.
[9] .V.Pyatilova, S.A. Gavrilov, A.A. Dronov, Ya.S. Grishina and A.N. Belov 2014 *Solid State Phenomena* **213** 103.
[10] O. Volovlikova, S. Gavrilov, G. Silakov, A. Zeleznyakova, A. Dudin. 2019 *Russ. Jour. of Electrochem.* **55** 1452.
[11] Periasamy, S et all. 2017 International J. of Res. in Phys. Chem. and Chem. phys. **231** 1585.

# Evolution of tribological properties of the composite coatings on AMg3 aluminum alloy after atmospheric exposure

I.E. Vyaliy*[,1], V.S. Egorkin[1], N.V. Izotov[1], U.V. Kharchenko[1], A.N. Minaev[1,2], S.L. Sinebryukhov[1], S.V. Gnedenkov[1]

[1] Institute of Chemistry, 159 pr. 100-letiya Vladivostoka, Vladivostok 690022, Russia
[2] Far Eastern Federal University, 8 Sukhanova St., Vladivostok 690950, Russia

*e-mail: igorvyal@gmail.com

## 1. Introduction

The formation of wearproof protective surface layers on aluminum and its alloys is an important scientific and practical task [1]. One of the possible ways to solve this problem is the creation of the composite polymer-containing coatings [1, 2]. Plasma electrolytic oxidation (PEO) could be a suitable method for such composite layer formation. The results of our research indicate a high level of protection provided by such coating to aluminum alloy [3, 4], however, it is necessary to verify the obtained parameters under appropriate exploitation conditions. In this regard, studies have been carried out on the evolution of tribological properties of the PEO-coating sealed with fluoropolymers during the one-year atmospheric testing in natural condition.

## 2. Experiment

For the formation of PEO-layers on AMg3 aluminum alloy sheets with size of 50 × 50 × 2 mm, a two-stage bipolar mode was used. At the first stage the voltage during the anode period was increased from 30 to 540 V at a rate of 3.4 V/s, and then the voltage value was maintained at 540 V for 750 s. The electrolyte contained 20 g/L $Na_2SiO_3$ $5H_2O$, 10 g/L $Na_2B_4O_7$ $10H_2O$, 2 g/L NaF and 2 g/L KOH.

15 % suspension of superdispersed polythetrafluoroetylene (SPTFE in isopropyl alcohol) was used to form composite coating on the sample with the PEO-layer by dip-coating method (SPTFE sample). The samples were then heat treated at 315 °C for 15 min to provide the best pores filling with a fluoropolymer material. The PVDF-layer was formed by immersing the sample in a 6 % solution of polyvinylidenefluoride (PVDF) in N-methyl-2-pyrrolidone followed by drying at 70 °C for 2 h. To form PVDF/SPTFE-coatings, SPTFE particles were added to the PVDF solution in various proportions - 1:1, 1:2, 1:3, 1:4, 1:5. Then the samples were dip-coated using respective suspension and dried at 65 °C for 3 h.

The atmospheric corrosion testing of the samples during one year exposure was carried out at the Marine Corrosion Test Station of the Institute of Chemistry of FEB RAS, located on Russkiy Island, Rynda Bay.

Tribological tests were carried out at a load of 10 N and a linear rotation speed of 50 mm/s of corundum ball.

## 3. Results and discussions

The electrochemical studies of the samples with the protective composite coatings previously carried out in [4] established that the layers obtained by applying a mixture of PVDF and SPTFE at a ratio of 1:5 have shown a very good results of the corrosion protection. To assess the impact of the corrosive environment on the tribological properties, the samples with composite coatings were texposed to atmosphere for 3, 6, and 12 months. The results of tribological testing demonstrate that all composite layers have a low wear ($9.7 \cdot 10^{-5}$ - $4.4 \cdot 10^{-4}$ $mm^3/(N\ m)$) and significantly reduce the coefficient of friction, which increases from 0.03-0.06 to 0.54-0.58 due to uniform abrasion of the polymer film to aluminum substrate (Fig. 1).

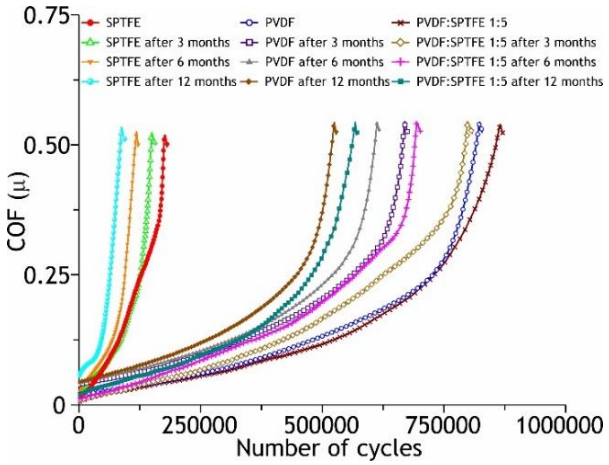


***Fig. 1.*** *Dependences of the friction coefficient on the number of cycles for samples with polymer-containing coatings.*

## 4. Conclusions

It has been established by tribometry that an increase in the duration of climatic tests up to 12 months for all types of composite coatings leads to a decrease in their wear resistance by 1.5–2 times. The largest decrease in the number of cycles is observed in the SPTFE coating (from 174.6 thousand to 86.6 thousand revolutions), which is associated with its thinner thickness compared to PVDF and PVDF/SPTFE coatings. For the last two c of similar thickness, the number of cycles decreased from 823.9 thousand to 525.1 thousand and from 864.9 thousand to 556.6 thousand cycles, respectively.

## Acknowledgements

The reported study was funded by RFBR, project number 19-29-13020.

## References

[1] V.S. Egorkin, I.E. Vyaliy, N.S. Sviridov. Defect and Diffusion Forum **386**(2018)315.
[2] S.V. Gnedenkov, S.L. Sinebrukhov, D.V. Mashtalyar. Protection of metals **44**(2008)704.
[3] S.V. Gnedenkov, S.L. Sinebryukhov, V.S. Egorkin. Russian Journal of Inorganic Chemistry **62**(2017)1.
[4] V.S. Egorkin, D.V. Mashtalyar, A.S. Gnedenkov. Polymers **13**(2021)3827.

# Changes in barrier properties of protective composite coatings on aluminum alloy during climatic testing

I.E. Vyaliy*[,1], V.S. Egorkin[1], N.V. Izotov[1], U.V. Kharchenko[1], A.N. Minaev[1,2], S.L. Sinebryukhov[1], S.V. Gnedenkov[1]

[1] Institute of Chemistry, 159 pr. 100-letiya Vladivostoka, Vladivostok 690022, Russia
[2] Far Eastern Federal University, 8 Sukhanova St., Vladivostok 690950, Russia

*e-mail: igorvyal@gmail.com

## 1. Introduction

Protection of aluminum and its alloys, which are prone to corrosion in halide-containing media, is an important scientific and sought after practical task [1]. The performed studies established a high level of protection provided by a composite coating (CC), where heterogeneous oxide layer is used as a matrix for the polymer layer on aluminum alloy AMg3 [2, 3]. However, the conditions of exploitation and electrochemical express-testing may vary significantly [4]. Therefore, it is necessary to verify the obtained parameters under appropriate exploitation conditions. In this regard, studies have been carried out on the evolution of electrochemical properties of the composite coatings during the 6 months of atmospheric testing.

## 2. Experiment

Plasma electrolytic oxidation (PEO) of aluminum alloy AMg3 samples (30 × 30 × 2 mm) was carried out in bipolar mode for 15 minutes. The voltage during the anode period was equal to 540 V. During the cathodic period current density was maintained at 0.12 A·cm$^{-2}$. The duty cycle was equal to 1. The silicate electrolyte and mode led to formation of the layer with a complex morphology [1].

To form CC, superdispersed polythetrafluoroetylene (SPTFE) particles were added to the 6 % polyvinylidenefluoride (PVDF) solution in N-methyl-2-pyrrolidone in optimal proportions 1:5 [1]. Then the samples were dip-coated and dried at 65 °C for 3 h.

To study the dynamics of changes in electrochemical properties during testing for 6 months atmospheric corrosion, samples were installed at the Marine Corrosion Test Station of the Institute of Chemistry of FEB RAS, located on Russkiy Island, Rynda Bay.

The morphology of the PEO- and composite coatings was investigated by scanning electron microscopy (SEM) using equipment from Carl Zeiss Group. Electrochemical properties were investigated using ModuLab XM ECS.

## 3. Results and discussions

SEM of the CC surface after 6 months of the atmospheric exposure is presented in Fig. 1. It shows that SPTFE particles sealed the pores and defects of the PEO-layer.

The results of electrochemical studies of samples after atmospheric corrosion are presented in Fig. 2. It is shown that the sample with CC has lowest corrosion current density ($2.9\cdot10^{-11}$ A·cm$^{-2}$) compared to both samples bare AMg3 aluminum alloy substrate ($1.7\cdot10^{-5}$ A·cm$^{-2}$) and with PEO-coating ($4.1\cdot10^{-9}$ A·cm$^{-2}$). For sample with PEO-coating the corrosion current density during 6 months exposition is reduced by 20 times due to the sealing of its pores with corrosion products. Also, the corrosion current density for the sample with CC tested for 6 months is 2 orders of magnitude lower in comparison with the sample with PEO-layer and almost 6 orders of magnitude less than for bare AMg3 alloy.

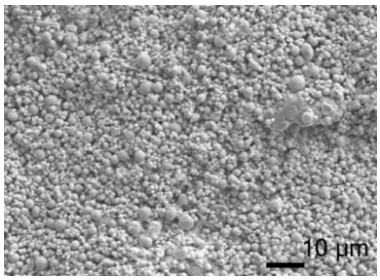


***Fig. 1.*** *SEM image of the composite coating after 6 months of the atmospheric exposure.*

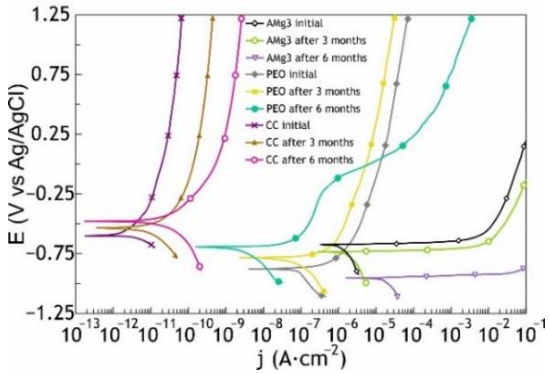


***Fig. 2.*** *Evolution of the electrochemical properties for samples with polymer-containing coatings during atmospheric exposure.*

## 4. Conclusions

It has been established that CC provides reliable protection even after a long-term exposure, the difference in currents is half an order of magnitude. This result is ensured by the high stability of the polymeric materials used and the coating-matrix. The increase in protective parameters for the PEO-coating is explained by the sealing of its pores with corrosion products.

## Acknowledgements

The reported study was funded by RFBR, project number 19-29-13020.

## References

[1] V.S. Egorkin, D.V. Mashtalyar, A.S. Gnedenkov. Polymers **13**(2021)3827.
[2] S.V. Gnedenkov, S.L. Sinebryukhov, V.S. Egorkin. Russian Journal of Inorganic Chemistry **62**(2017)1.

[3] V.S. Egorkin, I.E. Vyaliy, N.S. Sviridov. Defect and Diffusion Forum **386**(2018)315.
[4] V.S. Egorkin, I.E. Vyaliy, A.S. Gnedenkov. Solid State Phenomena **312**(2020)319.

# Electrochemical formation of germanium nanostructures using low-melting-point metal particles

A.N. Zakharov*, I.M. Gavrilin
National Research University of Electronic Technology (MIET), Bld. 1, Shokin Square, Zelenograd, 124498, Moscow, Russia

*e-mail: ee.tv@protonnmail.com

## 1. Introduction

The study of germanium nanostructures, in particular nanowires, has recently attracted significant interest, due to the great potential of their application in lithium- and sodium-ion batteries, photovoltaics, optics, and thermoelectric systems. For the formation of germanium (Ge) nanowires, gas-phase deposition using metal catalysts is mainly used according to the vapor-liquid-crystal (VLC) mechanism, where the size of the metal particles determines the location and geometric parameters of the nanowire (diameter and length) [1]. However, the processes of gas-phase deposition often require the use of complex technological equipment and are carried out at sufficiently high temperatures, as well as toxic and expensive precursors.

From this point of view, the use of electrochemical deposition is a good alternative. However, the cathodic polarization of solid-state electrodes in aqueous solutions of germanium (IV) oxide ensures the formation of films with a thickness of only a few monolayers. At the same time, the use of molten metal particles such as Hg and Ga as crystallization centers makes it possible to obtain both films of sufficient thickness and Ge nanowires [2, 3]. During the electrochemical deposition of Ge, the seed metal dissolves in Ge, and the metal impurity concentration exceeds the theoretical solubility by several orders of magnitude. The presence of this metal will affect the conductivity type of Ge nanowires.

However, when using Hg and Ga, along with the existing technological problems, coalescence and spreading of liquid particles on the substrate are often observed, which make it difficult to control their sizes and, as a result, the sizes of Ge filaments. From this point of view, an alternative is the use of low-melting metals, which can form eutectic alloys with Ge and have a higher melting point than Hg and Ga. The possibility of cathodic deposition of Ge using Indium (a p-type dopant for Ge) nanoparticles has been shown [4].

In this work, it has been demonstrated the features of Ge nanowires growth using Sn (isoelectronic impurities) and BiSn (Bi – fn-type dopant for Ge) nanoparticles.

## 2. Experiment

All samples have been sized 2×3 cm. 50 μm-thickness titanium foil has been used as the substrate.

Arrays of spherical Sn and BiSn nanoparticles have been deposited by the vacuum-thermal evaporation at a residual pressure of $1\times10^{-5}$ Torr of material from a Mo evaporator, placed at 40 cm from the substrate. After depositing the metals, the samples have been annealed in a vacuum at 250°C for 10 min. The electrochemical formation of Ge nanostructures on the obtained Sn and BiSn nanoparticles has been carried out in an electrolyte solution of the following composition: 0.05 M germanium (IV) oxide $GeO_2$, 0.5 M potassium sulphate $K_2SO_4$, and 0.5 M succinic acid. The electrolysis has been carried out in the galvanostatic mode at a current density of 2 mA/cm$^2$. The morphology of the obtained samples has been studied using scanning electron microscopy (SEM).

## 3. Results and discussions

Figure 1 shows the SEM image of the resulting Ge structure with Sn nanoparticles.

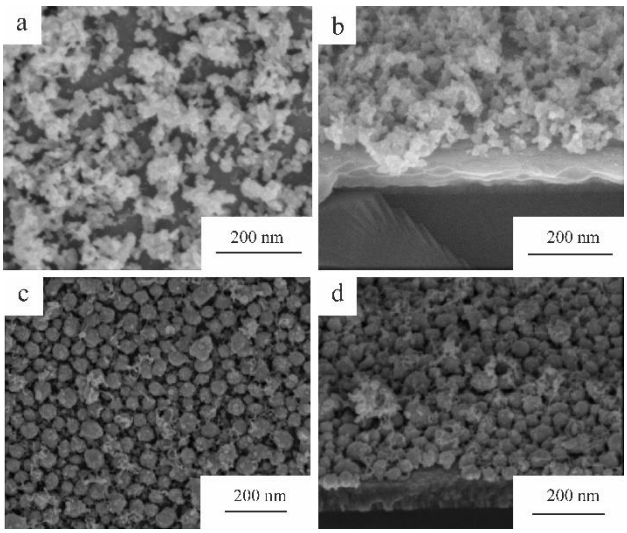


***Fig. 1.*** *SEM images of obtained samples after Ge electrodeposition using Sn nanoparticles.*

As can be seen, the formed samples are filamentous structures with a diameter of ~10 nm (Figure 1 a, b). With an increase in the average size of tin nanoparticles to 40 nm, the morphology of the sample has been changed (Figure 1 c, d). In some places of the surface of Sn nanoparticles, nanowire crystals are forming with a diameter of less than 10 nm. This fact may indicate that the process temperature of 90°C is insufficient for the complete melting of Sn nanoparticles and, as a consequence, for the intensive growth of nanocrystals. Apparently, small liquid droplets up to 10 nm in size are formed on the surface of a large Sn nanoparticle, which ensures the growth of such nanocrystals, as shown in Figure 1 c, d.

In its turn, the use of two-component tin nanoparticles with bismuth makes it possible to obtain Ge nanocrystals with a larger diameter (Fig. 2).

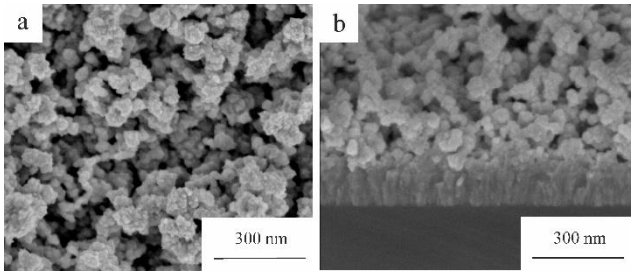


***Fig. 2.*** *SEM images of obtained sample after Ge electrodeposition using Bi-Sn nanoparticles.*

It should be noted that in the case of using two-component Bi-Sn nanoparticles, the nanocrystals have a rough surface in comparison with nanocrystals obtained using In nanoparticles.

The results of the study by the Raman spectroscopy have been showed that the filamentous nanostructures are crystalline Ge (Figure 3).

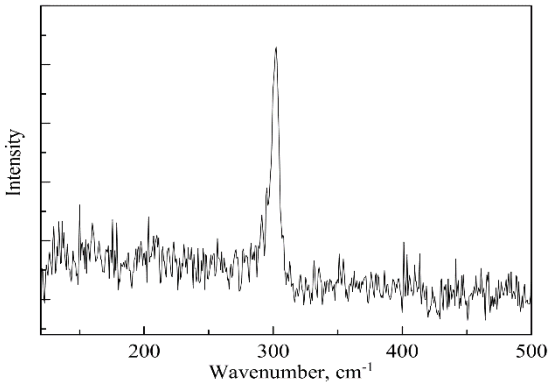


***Fig. 3.*** *Raman spectra of sample.*

This follows from the detected spectral band at 300 $cm^{-1}$, which is characteristic of crystalline Ge [5].

## 4. Conclusions

Thus, Ge nanowires have been obtained by the electrochemical method using Sn and Bi-Sn nanoparticles. The results obtained will expand the range of metal nanoparticles used and control the electrophysical properties of Ge nanowires.

## Acknowledgements

The work is supported by the Grant of the President of the Russian Federation №МК 5839.2021.1.3 and by the State assignment 2020-2022 № FSMR-2020-0018.

## References

[1] O'Regan C., Biswas S., Petkov N., Holmes J.D. Journal of Materials Chemistry **2**(2014) 14-33.
[2] Carim A. I., Collins S. M., Foley J. M., Maldonado S. Journal of the American Chemical Society **133**(2011) 3292–13295.
[3] Ma L., Gu J., Fahrenkrug E., Maldonado S. Journal of The Electrochemical Society **161**(2014) 044–3050.
[4] Gu J., Collins S. M., Carim A. I., Hao X., Bartlett B. M., Maldonado S. NanoLetters **12**(2012) 4617-4623.
[5] Gonzalez de la Cruz I. G., Conteras-Puente G., Castillo-Alvarado F. L., Mejia-Garcia C., Compaan A. Solid State Communications **82**(1992) 927.

# Properties of the solid solution $(Cd_{0.69}Zn_{0.31})_3As_2$

V.S. Zakhvalinskii*[,1], A.V. Borisenko[1], T.B. Nikulicheva[1], A.V. Kochura[2], Aung Zaw Htet[2], E.A. Pilyuk[1]

[1] Belgorod State University, 85 Pobedy St., Belgorod 308015, Russia
[2] South-West State University, Regional Centre of Nanotechnology, 94 50 Let Octjabrja Str., Kursk 305040, Russia

*e-mail: v_zaxvall@mail.ru

**Abstract.** Recent studies of $Cd_3As_2$ have revealed the topological aspect of its electrical properties. At the same time, the attention of researchers is attracted by the study of the properties of solid solutions of the Dirac semimetal $Cd_3As_2$. The modified Bridgeman method was used to obtain single crystals of $(Cd_{0.69}Zn_{0.31})_3As_2$. It has been established that the studied sample crystallizes in space group $P4_2/nmc$ with lattice parameters a = 8.78 Å, b = 12.42 Å. We have investigated the electrical conductivity in the temperature range from 10 to 300 K and in a magnetic field of 1 T, and determined the temperature dependences of the concentration and mobility of charge carriers. It has been established that in the temperature range from 10 to 33 K, hopping conduction with a variable length of the Mott-type hoping takes place, and its micro parameters have been determined.

## 1. Introduction

Among topological materials, the narrow-gap semiconductor cadmium arsenide ($Cd_3As_2$) with an inverted structure of energy bands and the highest carrier mobility among semiconductors and semimetals (largely exceeding $10^4$ $cm^2/(V\cdot s)$ at the room temperature) is distinguished by its chemical stability, low toxicity, and good manufacturability [1,2]. $Cd_3As_2$ was believed to manifest an inverted band structure due to the spin-orbital coupling (SOC) [3]. The 3D Dirac cones of $Cd_3As_2$ have been observed in angle-resolved photoemission spectroscopy (ARPES) [2,4,5]. At low Zn content vapor phase synthesized $(Cd_{1-x}Zn_x)_3As_2$ (CZA) single crystals are demonstrated the Dirac semimetal phase [6 - 8]. Within $0.3\leq x\leq 0.5$ composition region a transition from an inverted band structure is expected, accompanied by a transition from a topological phase to a trivial band semiconductor [7, 8].

## 2. Experiment

The modified Bridgman method was used to obtain CZA single crystals. Stoichiometric amounts of $Cd_3As_2$ and $Zn_3As_2$ binary compounds were placed in a graphitized and evacuated quartz ampoule. The CZA melt was slowly cooled from the melting temperature of 838°C at a rate of 5°C/h in the furnace temperature gradient.

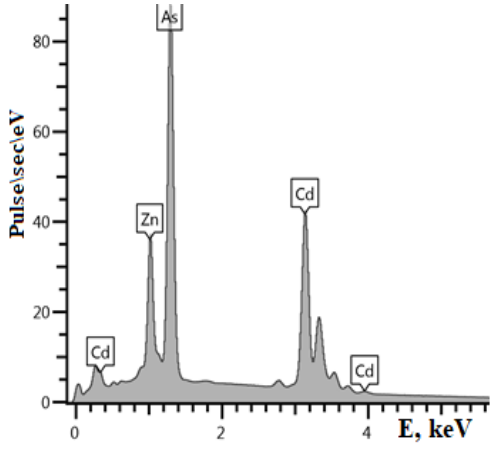


***Fig. 1.*** *The spectrum of EDX from the surface of $(Cd_{1-x}Zn_x)_3As_2$ corresponds to the composition (x=0.31).*

The composition of the samples and their homogeneity were controlled by powder x-ray diffraction and energy dispersive x-ray spectroscopy (EDX). X-ray phase analysis (XPA) of the sample was performed using a GBC EMMA X-ray diffractometer (Cu Kα radiation, λ = 1.5401 Å) at the room temperature. It has been established that the studied sample crystallizes in space group $P4_2/nmc$ with lattice parameters a = 8.78 Å, b = 12.42 Å [9]. To study the composition and distribution of elements on the surface, we used a JSM-6610LV (Jeol) scanning electron microscope (SEM) with an X-Max$^N$ (Oxford Instruments) energy dispersive X-ray spectroscopy (EDX) attachment.

Figure 1 shows the EDX spectrum from the surface of the $(Cd_{1-x}Zn_x)_3As_2$ sample. Figure 2 shows the powder diffraction pattern of the $(Cd_{1-x}Zn_x)_3As_2$ sample.

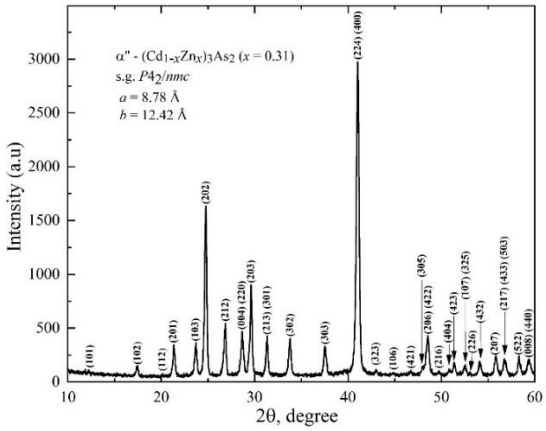


***Fig. 2.*** *Powder diffraction pattern of the $(Cd_{1-x}Zn_x)_3As_2$ sample.*

Samples for the study of electrical conductivity by the six-probe method were parallelepipeds 1.35×0.67×0.50mm. The temperature dependence of electrical conductivity was studied in the temperature range from 10 to 300K, and the Hall effect in a magnetic field 1T.

The results of the study of the temperature dependence of the resistivity of a solid solution single crystal $(Cd_{0.69}Zn_{0.31})_3As_2$ are shown in Figure 3. In the inset to Figure 3, the section corresponding to the variable range of the hopping conductivity according to Mott is highlighted.

## 3. Results and discussions

As the temperature decreases from 320 K, the resistivity decreases from $2 \cdot 10^{-3}$ Ω·cm at 300 K to a minimum of $5 \cdot 10^{-4}$ Ω·cm at 30 K, and then gradually increases. This behavior is typical of the Anderson transition [10]. The study of the Hall Effect in a magnetic field of 1 T made it possible to calculate the Hall coefficient $R_H$, the concentration and mobility of charge carriers. At a temperature of 10 K, the concentration of charge carriers was equal to $2.81 \cdot 10^{17}$ $cm^{-3}$, decreasing with increasing temperature to 30 K corresponding to the metal-insulator

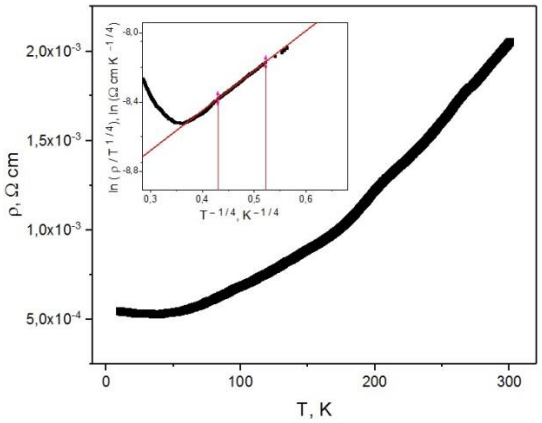


***Fig. 3.*** *Temperature dependence of the resistivity of $(Cd_{0.69}Zn_{0.31})_3As_2$ solid solution single crystal. The temperature range 10-33 K on the Fig. 3. insert corresponding to Mott variable range. hopping conductivity.*

transition. Above 30 K, an activation increase in the concentration of charge carriers was observed, which is typical for impurity semiconductors up to a value of $3.05 \cdot 10^{17}$ $cm^{-3}$. The mobility of charge carriers, μ, exhibits behavior characteristic of semiconductors, increasing with decreasing temperature. The value of mobility is maximum at the metal-dielectric transition point at a temperature of 30 K and is $4.51 \cdot 10^4$ $cm^2$ $V^{-1}$ $s^{-1}$. A further decrease in temperature leads to a decrease in mobility to $4.16 \cdot 10^4$ $cm^2$ $V^{-1}$ $s^{-1}$ at a temperature of 10 K. The mechanisms of charge carrier scattering were evaluated.

At low temperatures, in the temperature range from 10 to 30 K, scattering by ionized impurity atoms and mobility $\mu \sim T^{3/2}$ prevail. In the temperature range from 30 to 300 K, scattering by thermal vibrations of the crystal lattice, $\mu \sim T^{-3/2}$, predominates.

In the inset to Fig.3 a linear section of the temperature dependence of the resistivity in the temperature range from 10 to 33 K, corresponding to the mechanism of hopping conduction by the states of the impurity band, is distinguished. Hopping conductivity is described by the universal equation [10-12]:

$$\rho(T) = DT^m \exp\left(\frac{T_0}{T}\right)^p$$

where D is a constant coefficient, $T_0$ is the characteristic temperature, and the parameters $m$ and $p$ depend on the mechanism of hopping conduction. We have determined the values of the parameters $m$=1/4 and $p$ = 1/4, which indicates the predominance of the mechanism of hopping conduction with a variable range hop according to Mott. Calculating the microparameters, the following obtained values of the coefficients were used: the characteristic temperature of the hopping conductivity $T_0$ = 28.60 K; hopping conduction onset temperature $T_V$ = 28.44; coefficient D = $8.488 \cdot 10^{-5}$. For hopping conduction with a variable hop length, the following values of microparameters were obtained: Coulomb gap width in the density of localized states Δ = 0.43 meV; acceptor zone width W = 2.45 meV; the value of the density of localized states outside the parabolic gap g = $2.93 \cdot 10^{17}$ $cm^{-3}$ $meV^{-1}$; charge carrier localization radius $a$ = 307 Å.

## 4. Conclusions

Single crystals of $(Cd_{0.69}Zn_{0.31})_3As_2$ solid solutions were obtained by the modified Bridgman method. The sample composition and the element distribution was controlled using JSM -6610LV (Jeol) scanning electron microscope (SEM) with an X-Max$^N$ (Oxford Instruments) energy dispersive X-ray spectroscopy (EDX) attachment.

It has been established that the studied sample crystallizes in space group $P4_2/nmc$ with lattice parameters a = 8.78 Å, b = 12.42 Å. We have investigated the electrical conductivity in the temperature range from 10 to 300 K and in a magnetic field of 1 T, and determined the temperature dependences of the concentration and mobility of charge carriers. It has been established that in the temperature range from 10 to 33 K, hopping conduction with a variable range of the Mott-type hop takes place, and its micro parameters have been determined.

## Acknowledgements

This work was supported by the Ministry of Education and Science of the Russian Federation (grant number 0851–2020–0035).

## References

[1] Jeon, S.; Zhou, B. B.; Gyenis, A.; Feldman, B. E.; Kimchi, I.;Potter, A. C.; Gibson, Q. D.; Cava, R. J.; Vishwanath, A.; Yazdani, A.Nature Materials. **13**(2014)851.
[2] Neupane, M.; Xu, S.-Y.; Sankar, R.; Alidoust, N.; Bian, G.; Liu, C.; Belopolski, I.; Chang, T.-R.; Jeng, H.-T.; Lin, H.; Bansil, A.; Chou, F.; Hasan, M. Z. Nature Commun. **5**(2014)3786.
[3] Aubin, M. J., Caron, L. G. & Jay-Gerin, J. P Phys. Rev. B **15**(1977)3872.
[4] Z. K. Liu, J. Jiang, B. Zhou, Z. J. Wang, Y. Zhang, H. M. Weng, D. Prabhakaran, S-K. Mo, H. Peng, P. Dudin, T. Kim, M. Hoesch, Z. Fang, X. Dai, Z. X. Shen, D. L. Feng, Z. Hussain & Y. L. Chen. Nat. Mater. **13**(2014)677.
[5] S. Borisenko, Q. Gibson, D. Evtushinsky, V. Zabolotnyy, B. Büchner, R. J. Cava. Phys. Rev. Lett. 113(2014)027603.
[6] A. V. Kochura, L. N. Oveshnikov, A. P. Kuzmenko, A. B. Davydov, S. Yu. Gavrilkin, V. S. Zakhvalinskii, V. A. Kulbachinskii, N. A. Khokhlov, B. A. Aronzon. JETP Letters. **109**(2019)175.
[7] A.V. Galeeva, I.V. Krylov, K.A. Drozdov, A.F. Knjazev, A.V. Kochura, A.P. Kuzmenko, V.S. Zakhvalinskii, S.N. Danilov, L.I. Ryabova, D.R. Khokhlov. Beilstein Journal of Nanotechnology. **8**(2017)167.
[8] H. Lu, X. Zhang, Y. Bian, Sh. Jia. Scientific Reports **7**(2017)3148.
[9] E.K. Arushanov. Prog. Crystal Growth Charact. **3**(1981)211.
[10] N. F. Mott, Metal–Insulator Transitions, London: Taylor and Francis (1990).
[11] Mott N.F., Davies E.A. Electron Processes in Non-Crystalline Materials. - Oxford: Clarendon, 1979; Shklovskii B.I., Efros A.L. Electronic Propertie of Doped Semiconductors. - Berlin: Springer-Verlag, 1984.

# Nanoscale kinetics of phase transitions in crystalline polyethylene

I.A. Strelnikov, E.A. Zubova*
N.N. Semenov Federal Research Center for Chemical Physics, Russian Academy of Sciences, 4 Kosygina St., Moscow 119991, Russia

*e-mail: zubova@chph.ras.ru

In the simplest polymer, polyethylene (PE), three crystalline phases can be (meta)stable under normal conditions and able to transform one to another by shear-induced (first-order) phase transitions: common orthorhombic (O), monoclinic (M) and triclinic (T). High-symmetry O phase is preferable at high temperatures. The non-O phases are always present in commercial PE. These phases appear under pressure, tension, or shear. Complete or almost complete transitions from the O to the non-O phases are observed on single crystals grown from a solution, extended chain (poly)crystals, or (poly)crystals consisting of stacks of chainfolded lamellas. There are many transformation modes [(almost) simple shears in different directions with different magnitudes] realizing the phase transitions between the crystalline phases of PE. The height of the barriers for actuation of these modes is comparable to the height of the barriers for plastic deformation modes (crystallographic slips or twinning). Therefore, for homogenious crystalline PE samples, the features of the phase transitions between the crystalline phases determine, to a large extent, the character of the deformation process and the composition and the properties of the resulting sample.

Some experimental results regarding the transformations between the crystalline PE phases are unclear. The first puzzle is the appearance of an intermediate M phase between the parent O and the product T phases in an extended chain sample under hydrostatic compression. Besides, the dependence of the final state of the sample on its initial structure and the deformation rate is not properly investigated.

We carry out [1] molecular dynamics simulation of shear-induced martensitic phase transitions between the orthorhombic (O) and nonorthorhombic (triclinic (T) and monoclinic (M)) phases of crystalline polyethylene (PE) in the framework of a realistic all atom model of the polymer. We show that the variation of the shear rate allows observing on a nanosample both a strongly nonequilibrium phase transition occurring by random nucleation and irregular growth of a new phase ("civilian" way) and the coherent, or "military," kinetics (generally considered as usual for martensitic transformations).

We induce transitions from the O to the T phase according to two transformation modes observed in experiment on PE single crystals (O-T T1 and O-T T2 modes). Rapid deformation favors the transition directly to the T phase with expected orientation. Slow deformation causes the transition first to one or two intermediate M phases, and only then - to the expected T phase.

The reason is that the transformation mode to the M phase O-M T1 has a very small magnitude of 0.04 (O-T T1 and T2 modes have magnitudes of 0.18 and 0.35, respectively). There are two nearly perpendicular directions of shear actuating this special mode. Therefore, for any sufficiently slow shear along any direction, this mode will be actuated before any other transformation mode. The resulting M phase can transform into the T phase by the mode M-T T1 directly or after twinning, depending on the direction of the shear. Thus the M phase (through mode O-M T1) naturally emerges in common (slow) experiments as an intermediate in the transition from the O to the T phase.

The molecular dynamics simulation also allows for studying the transition process at the level of individual molecules, unavailable in experiment. In particular, we could observe the process of rotation of half of the chains through 90° around their axes during the transition from the O phase to the T or M phases. The turn proved to occur generally due to generation of a localized twist defect (twiston) at one end of a chain and the subsequent diffusion of the twiston to another end of the chain. The twiston is short (about six $CH_2$ groups), moves at a speed of 250-650 m/s and rotates a chain containing 100 carbon atoms in 20-50 ps. The energy of its generation is 4 kcal/mol for the O-T transition and 2 kcal/mol for the O-M transition. The transition between the M and T phases occurs through half-chain-period translations of the chains along their axes, mostly collectively, as crystallographic slips.

**Acknowledgements**

We appreciate the financial support in the framework of the Program of Fundamental Researches of the Russian Federation (project FFZE-2022-0009, state registration no. 1021051302588-6-1.4.4). The calculations were carried out in the Joint Supercomputer Center of the Russian Academy of Sciences.

**References**

[1] Strelnikov I.A., Zubova E.A. Phys.Rev.B **99**(2019) 134104.

# Synthesis conditions-dependent the wetting properties of porous anodic alumina

A. Bondaruk*[,1,3], D.I. Tishkevich*[,1], A. Vorobjova[2], D. Shimanovich[2], E. Zheleznova[2], T.I. Zubar[1], A.V. Trukhanov[1]

[1] SSPA "Scientific and Practical Materials Research Centre of NAS of Belarus", 220072 Minsk, P. Brovki str. 19, Belarus
[2] Belarusian State University of Informatics and Radioelectronics, 220013 Minsk, P. Brovki str. 6, Belarus
[3] Belarusian State Technological University, 220006 Minsk, Sverdlova str. 13A, Belarus

*e-mail: bondaruk625@gmail.com

**Abstract.** The paper presents the results of preparation and wettability properties studying of porous anodic alumina (PAA) membranes with the thickness of 8±0,5 μm and with a different pore sizes. Fabrication processing features, scanning electron microscopy and wettability characterization results are discribed. The comparative analysis of outer PAA surfaces and effect of morphology of these surfaces on the wettability properties are discussed. Measurements of the interfacial contact angle (ICA) were made on the as-fabricated amorphous PAA membrane and after pore widening with a range of pore diameters from 40 to 120 nm.

## 1. Introduction

Porous anodic alumina (PAA) is a constantly attracting the attention of scientists due to its unique ordered honeycomb cell structure. Such structure allows the formation of many new multifunctional films and micro- and nanoelements by the template-assistant method [1,2]. Recently PAA have been intensively studied for use in medical and biotechnological development: bio-filtration for the separation of proteins and organic molecules; in drug delivery systems and biosensor devices etc. [3,4]. Electrochemical anodization of Al results into a nanoporous structure of alumina with pore size range from 10 to 150 nm and density of about 1×1010 pores cm-2 [5]. This technique is comparatively easier than lithographic methods. In this case, it is desirable to modify the PAA surface in order to obtain a well-wetted surface and pore walls. Optimization of such parameters as pore diameter and length, modification of the PAA surface itself and pore walls make it possible to achieve a further selectivity in bioseparation systems[6].

In our previous work [7] presented the results of preparation and studying of PAA wetting properties with the thickness from 25 to 75 μm and different pore sizes. The analysis of an outer and inner PAA surfaces and morphology effect on the wetting properties are demonstrated. Both alumina surfaces show significant morphology-dependent wettability Here we would like to show that the wettability of PAA changes during the fabrication process and this must be taken into account to receive a template suitable for various membrane applications. For this purpose PAA samples with different morphology parameters were obtained and their wettability properties were investigated.

## 2. Experiment

Samples of the PAA membranes were prepared via two-step anodization of 99.9994 Al foil in 4% C2H2O4 aqueous solution at 15 °C. The fabrication process of the PAA membrnes is described in more detail in [8]. The PAA samples were formed at voltages of 40, 50, 60 V. An outer surface of PAA were chemically modified using 5% H3PO4 aqueous solution at a temperature of (35±2) °C for 5, 10, 15 and 20 min. As a result PAA membranes with an ordered structure of 8 μm thickness with different pore diameter has been obtained. The PAA samples morphology (pore diameter d, interpore distance D and thickness H) were examined using scanning electron microscopy (SEM) Carl Ziess EVO10. Software package "SED (Surface Explorer Document)" was used for the computer processing of the experimental data. This method allows to study the microstructure parameters. The SEM images were also analyzed with graphics editor Image J. The wettability properties of PAA were determined by measuring the interfacial contact angle (θ) using the "recumbent drop" method [9]. A drop of distilled water of the order 15 μl was applied to the PAA surface from the microdoser (Thermo Scientific Finnpipette). The ICA was determined by the goniometric method, in terms of the basic dimensions of the drop and the condition that θ<90° according to the formula:

$$tg\Theta = \frac{2hr}{r^2-h^2} \qquad (1)$$

where, θ is the ICA, r is a contact area radius of the drop with the PAA surface, and h is the drop height.

## 3. Results and discussions

After each main stage of PAA fabrication process the obtained samples were analyzed sing SEM technique. Several types of samples were prepared with different pore sizes, and etching technology of the barrier layer at the bottom of the pores (Table I).

***Table I.*** *The main morphological characteristics of the experimental samples (before etching, as-fabricated amorphous PAA).*

| Sample type | Anodizing voltage *U*, V | Pore diameter *d*, nm | Porosity $\alpha$, % | *d/D* |
|---|---|---|---|---|
| I | 40 | (48)*50 | 17 | 0.44 |
| II | 50 | (60) 65 | 23 | 0.50 |
| III | 60 | (72) 85 | 27 | 0.53 |

**The calculated values (in brackets) and mean values received using SEM images.*

The barrier layer was not etched in as-fabricated samples (I, II, III). For the samples No. 1, 2, 3 and 4 of each type the etching of the barrier layer was carried out by immersing the entire membrane in a 5% H3PO4 aqueous solution at the temperature of (35±2) °C for 5, 10, 15 and

20 min, respectively. Also such important PAA parameter as porosity α depends on pore diameter and channels structure. The alumina porosity with the through pores was determined by formula [10]:

$$\alpha = 0.097(\frac{d}{D})^2 \quad (2)$$

Table 1 presented other important parameters of the PAA microstructure: the thickness of cell walls (W) and the thickness of a barrier layer (B). For highly ordered, densely packed hexagonal cells of PAA membranes with a diameter D the cell walls thickness W can be determined by the formula [10] and is equal to 32.5 nm:

$$W = \frac{D-d}{2} \quad (3)$$

Besides, the thickness of walls is related to thickness of a barrier layer as the following ratio [10] and is equal to 36.4 nm:

$$B=1.12 \cdot W \quad (4)$$

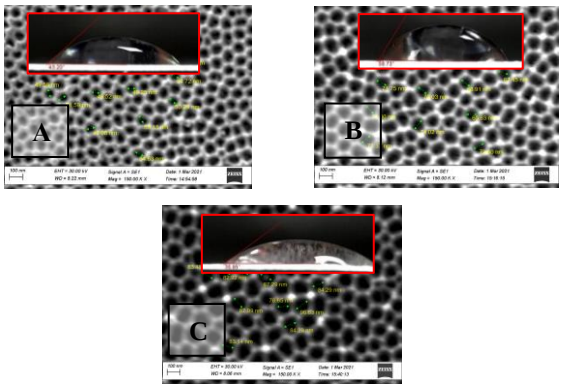


***Fig. 1.*** *Contact angle as a function of surface topology for as-fabricated samples I (A), II (B) and III (C) and corresponding SEM images of outer surfaces.*

In general, SEM images of the PAA samples prepared in the optimal etching mode show high uniformity of PAA topological parameters, both on the surface and in the middle of sample (strictly vertical orientation and nanochannels linearity). The previously presented results [8] show that the topological features of the PAA surface can differ substantially depending on through-pores obtaining process. Therefore, the contact angle was determined on the outer side of the PAA. Figure 1 are

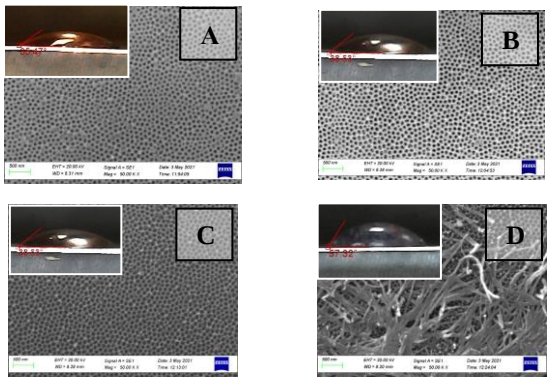


***Fig. 2.*** *Contact angle as a function of surface topology for the PAA sample of the II type after etching in 5% $H_3PO_4$ during 5 min (A), 10 min (B), 15 min (C), 20 min (D) and SEM images of outer surfaces.*

shown the contact angle images and SEM views of outer surface of as-fabricated samples (I, II, III). Figure 2 are shown the contact angle images and SEM views of outer surfaces of PAA sample of the II type after pores opening by etching the barrier layer with different duration. Similar results were obtained for PAA samples I and III after etching and are presented in Figure 3.

Experimental results show that the contact angle depends on such a PAA parameter as porosity. And the porosity is determined by such technological parameters as the anodizing voltage and the barrier layer etching duration. Moreover, the dependence on the anodizing voltage has an extreme character (the ICA has the greatest values for PAA membranes formed at 50 V).

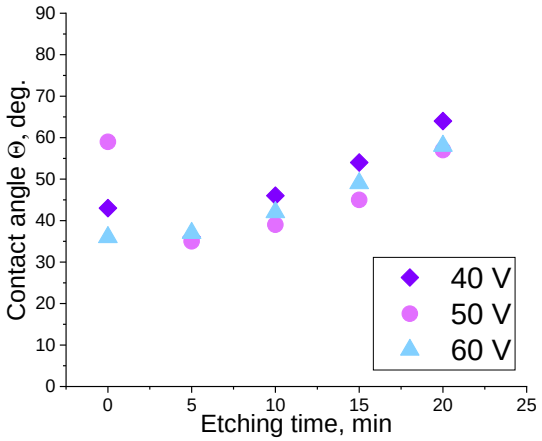


***Fig. 3.*** *Contact angle as a function of etching time of a barrier layer of the PAA outer surfaces.*

## 4. Conclusions

The preparation of PAA membranes by two-step anodization of aluminum foil in oxalic acid electrolyte have been reposted. PAA membranes with a pore diameter in the range from 50 to 85 nm and 8 μm thickness were fabricated. The anodization process was performed in 4% oxalic acid at 40, 50 and 60 V. The surface chemistry of the PAA samples was not specially modified in order to investigate only the effect of own PAA surface morphology on the wettability properties. It was shown that the contact angle depends not only on the pore diameter and anodization voltage but also on the etching time of the barrier layer, that is, it changes during the fabrication process. It was found that with etching duration increasing the pore diameter and contact angle firstly linear rises then this growth more noticeable. These results indicate that it is possible to select the optimal PAA fabrication condition (anodizing voltage, etching duration) depending on the future application of the PAA membranes.

## References

[1] W. Lee [et al.] Chem. Rev. 114 (2014) 7487-7556.
[2] E. Busseron E. [et al.] Nanoscale 5 (2013) 7098-7140.
[3] D. Brüggemann J. Nanomater. 18 (2013) 460870.
[4] C.S. Law [et al.] ACS Appl. Mater. Interfaces 9 (2017) 8929-8940.
[5] A.I. Vorobjova [et al.] Nanomater. 10 (2020) 1-21.
[6] J. Xu [et al.] Nanoscale Res. Lett. 525 (2011) 1-7.
[7] D.L. Shimanovich [et al.] Beilstein J. Nanotechnol. 9 (2018) 1423-1436.
[8] D.I. Tishkevich [et al.] Nanomater. 11 (2021) 1775.
[9] B.D. Summ Chemistry. Moscow, 1976.
[10] G.D. Sulka [et al.] Electrochim. Acta 52 (2007) 1880-1888.

# V. Laser nanofabrication, all-dielectric materials, nanomaterials: fundamentals and applications

Sixth Asian School-Conference on Physics and
Technology of Nanostructured Materials
Vladivostok, Russia, 25 – 29 April, 2022

**V.i.02**

# Highly regular laser-induced periodic surface structures formed on metals and semiconductors

K. Bronnikov*[,1], S. Gladkikh[1], K. Okotrub[1], A. Simanchuk[1], A.Y. Zhizhchenko[2,3], A. Kuchmizhak[2,4] and A. Dostovalov[1]

[1] Institute of Automation and Electrometry of the SB RAS, Novosibirsk, Russia
[2] Institute of Automation and Control Processes FEB RAS, 5 Radio St., 690041 Vladivostok, Russia;
[3] Far Eastern Federal University, 690041 Vladivostok, Russia;
[4] Pacific Quantum Center, Far Eastern Federal University, 690041 Vladivostok, Russia

*e-mail: bronnikovkirill@gmail.com

**Abstract.** The formation of laser-induced periodic surface structures (LIPSS) is an attractive method of surface nanostructuring promising for practical applications, such as surface functionalization, elements of flat optics, sensors, and so on. While interference is a general mechanism of LIPSS formation, structures of different types can form, including ablative LIPSS that represent periodic grooves formed as a result of ablation of the irradiated material, and thermochemical LIPSS, which are periodic oxide protrusions formed due to local oxidation in the interference maxima. As laser-induced surface structuring has practical potential, investigating the regimes of the fabrication of highly regular LIPSS on various materials is an actual task. We report on the formation of ablative and thermochemical LIPSS with high uniformity on metals (Ti, Hf) and semiconductors (Si, Ge) by femtosecond near-IR laser pulses, and study the dependence of the morphology on the laser writing parameters.

## 1. Introduction

Irradiating the surface of metals, semiconductors or their films with ultra-short high energy laser pulses leads to the formation of a periodic relief modulation (grooves or protrusions) called laser-induced periodic surface structures (LIPSS) [1]. They originate from the interference between incident light and scattered waves or surface modes, such as surface plasmons, and form within the focal spot as a grating with a period nearly equal to or less than the laser wavelength. This interference creates a periodic intensity distribution, which regulates consequent physical mechanisms of LIPSS formation, namely, ablation, thermochemical reaction, material reorganization, etc. [2, 3]. Structures formed through each of the mechanisms demonstrate their own distinctive surface morphologies. For example, ablative LIPSS are usually oriented transversely to the linear polarization direction of the incident light and represent an array of valleys or grooves formed in the intensity maxima. In contrast, thermochemical LIPSS (TLIPSS) are protrusions above the surface oriented along the polarization and formed due to thermally stimulated oxidation of the target material. Apart from the main process of interference between incident and scattered light, additional periodicities can arise if the "second-order" effects contribute to the final intensity distribution, such as the interference of the counter-propagating plasmons, thus, further reducing the period.

LIPSS formation is a single-step approach for surface nanostructuring, which is remarkably simple, flexible, and scalable, making it highly attractive for a wide range of practical applications: surface functionalization, flat optics, sensors, and so on [4, 5]. The possibility to obtain periodical patterns with indefinitely large areas by lateral scanning in ambient air distinguishes this method from lithographic techniques or crossing beams interference. Considering these technological prospects, it is important to define the conditions at which highly uniform LIPSS of various types will form.

Here, we report on the formation of highly regular LIPSS on metals and semiconductors by femtosecond near-IR laser pulses. Titanium, hafnium, silicon, and germanium were used in the experiments. Periodic structures of two types were obtained: TLIPSS were fabricated on Ti and Hf films deposited on Si, ablative LIPSS were formed on Si-supported Hf film, and glass-supported Ge film.

## 2. Experiment

Samples used in the experiments were: metal films of Ti and Hf with different thickness (20-400 nm) deposited by magnetron sputtering on a glass or c-Si substrate, semiconductors films of Ge and $\alpha$-Si film deposited onto a glass substrate by magnetron sputtering with the resulting thickness of about 100 nm, crystalline Si (c-Si) wafer with a 20-nm thick Hf layer sputtered on top. A femtosecond laser irradiation with pulse duration of 230 fs and wavelength of 1026 nm focused into the astigmatic spot with an axis ratio of ≈1/10 and a width along the long side of 155 μm was used to form TLIPSS. The pulse repetition rate $f$ and the sample scanning speed υ were varied within the range of 50-200 kHz and 1-2000 μm/s respectively. The pulse energy $E$ was altered to obtain structures with the best regularity.

TLIPSS surface morphology and inner structure were investigated via scanning electron-microscopy (SEM) and focused ion beam (FIB) milling. To analyze the chemical composition, Raman spectroscopy with the laser pumping at 532.1 nm and a 1-μm focal spot was used.

## 3. Results and discussions

The TLIPSS with period of 853±20 nm and high structure regularity was formed on Ti film with thickness of 90 nm upon impact of near-IR laser radiation at the pulse energy of 1.1 μJ and processing speed of 1 μm/s (Fig. 1a). The TLIPSS are oriented along the polarization direction of incident laser radiation. The protrusions are mainly composed of the rutile phase of $TiO_2$ nanocrystallites according to Raman spectroscopy. SEM images of the transverse cross-sectional FIB cuts (Fig. 1c) reveal that $TiO_2$ starts to grow from the Ti film surface as a result of thermochemical reaction of oxidation. Formed protrusion occupies a larger volume in comparison to intact film due

to the porous structure of rutile nanocrystals and a large Pilling and Bedworth ratio $R_{PB}$ = 1.78 for titanium and its oxide.

The highly regular TLIPSS with a period of 990 ± 14 nm are formed on the surface of Hf thin (130 nm) films at pulse energy of 1.75 μJ and processing speed of 75 μm/s (Fig. 1 (b)). The SEM of the cuts shows profile of the structures, having a width of 480 nm and a height of 200 nm (Fig. 1(d)). At low scanning speeds (1–10 μm/s) overexposure is observed in the center of the tracks with the formation of a structure with a period half as long as at the periphery. The height of the oxide protrusions above the surface of the Hf film is about 30 nm, and the penetration depth into the silicon substrate is 50 nm based on the SEM image of the FIB-cut cross section of TLIPSS.

Ablative LIPSS produced on Ge film at low energy and scanning speeds (500 nJ and 1-5 μm/s, respectively) show good uniformity having a period of ~650 nm and orientation perpendicular to the laser polarization. These structures can be referred to as low spatial frequency LIPSS (LSFL) with the period $\Lambda \lesssim \lambda$ formed due to the interference between the SPs excited at surface roughness and the incident pulse [6]. At the same pulse energy and elevated scanning rates, continuous LIPSS cease to form. However, increased pulse energy of 750 nJ allows the fabrication of a uniform periodic structure at the speed of 25 μm/s. With the further increase in scanning rate up to 50 μm/s an interesting new morphology is observed. In contrast to a single "track" with periodic modulation formed within a focal spot, which is usually obtained in other works studying LIPSS, this structure consists of multiple separate grating stripes aligned in parallel (Fig. 2 a). Note that the distance between these small "tracks" is relatively constant suggesting that there is an additional mechanism, which keeps multiple SPs localized and isolated from each other. The generation of one of such separated plasmon modes can be seen at the center of the SEM image in Fig. 2 a, where it branches off the existing mode. An enlarged view of the structures, shown in Fig. 2 b, reveals that they are composed of 450-nm wide grooves with a period of ~880 nm, which is slightly higher than that of LIPSS with continuous morphology.

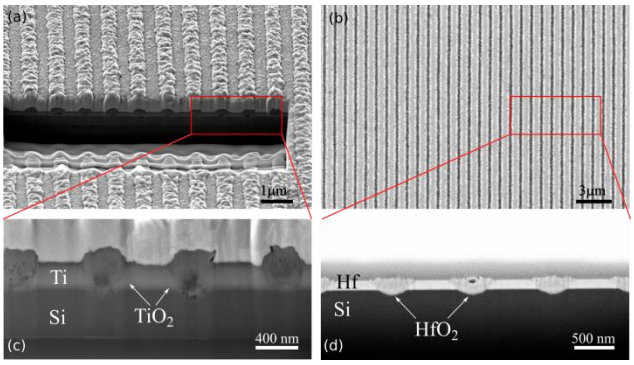


***Fig. 1.*** *SEM images of TLIPSS structures produced on the 90-nm thick Ti film (a) and 130 nm Hf film (b). SEM image of a cross-sectional FIB cut made perpendicularly to the TLIPSS orientation (c, d).*

LIPSS formed on Hf-covered c-Si demonstrate extremely high uniformity having a period of ≈450 nm and can be attributed to high spatial frequency LIPSS (HSFL) with $\Lambda < \lambda/2$. While for structures formed in the air there is some debris which is oxidated Si and Hf material, LIPSS fabricated in a nitrogen atmosphere at 1.75-2.5 μJ and 500-2000 μm/s appear as a clean debris-free structure with a negligible number of defects (Fig. 2 c). The formation of these LIPSS can be explained by the interference of counter-propagating plasmons at the Hf-air/nitrogen interface, where the role of Hf is in facilitating the SP excitation and regulating Si ablation. A magnified part of the SEM image reveals several features: apart from the main periodicity, LIPSS lines have perpendicular periodic modulations of contrast stripes and pits (Fig. 2 d). Although nitrogen environment helps increase the LIPSS quality in the case of c-Si, the laser processing of Ge film at similar conditions leads to the appearance of poorly ordered periodic structure with LIPSS lines oriented in parallel with the polarization and presumably formed due to hydrodynamic instabilities in the molten phase of germanium [7].

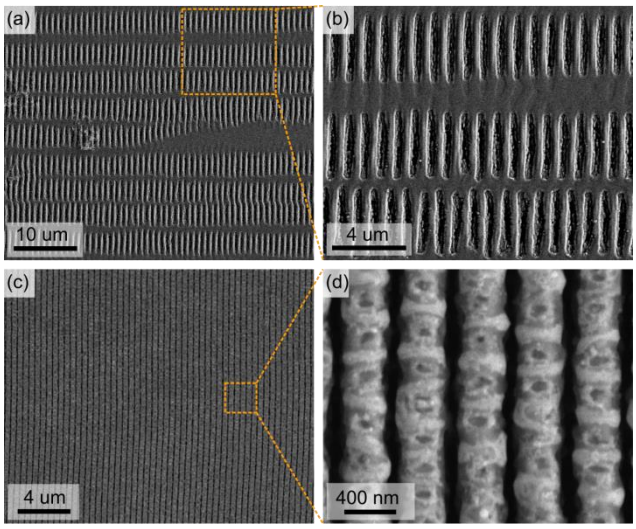


***Fig. 2.*** *SEM images of the LIPSS formed on the 100-nm thick Ge film (a, b) and Hf-covered crystalline Si (c, d) at the following experimental conditions: (a) 750 nJ, 50 μm/s; (c, d) 2.5 μJ, 2000 μm/s.*

## 4. Conclusions

The formation highly regular LIPSS: thermochemical, in the case of metal film due to the thermally stimulated reaction of oxidation resulting in $TiO_2$ or $HfO_2$ protrusion above the initial metal film with orientation parallel to the polarization direction, and ablative, in the case of semiconductors with orientation perpendicular to the polarization direction, were demonstrated. The period of LIPSS depends on the processing conditions and varies in the range of ≈900 nm for fundamental spatial frequency and 450 nm for doubled spatial frequency.

The obtained results open up possibilities for the practical application of the high-throughput formation of high-ordered periodic structures for different possible applications in biomedicine, photovoltaics, improving tribology properties, metal coloration and fabrication of diffraction holograms.

## Acknowledgements

The work was funded by the Russian Science Foundation grant (No. 21-72-20162). In the research, we used the equipment of the following Multiple-Access Centres (MAC): MAC of the Far Eastern Federal University (FEFU), MAC "High-resolution spectroscopy of gases and condensed matters" at IAE SB RAS.

## References


[1] J. Bonse, J. Krüger, S. Höhm, and A. Rosenfeld. Journal of Laser Applications **24**(2012)042006.

[2] Bonse, J. & Gräf, S. Laser & Photonics Reviews 2000215 (2020).

[3] B. Öktem, I. Pavlov, S. Ilday, H. Kalaycıoğlu, A. Rybak, S. Yavaş, M. Erdoğan, and F. Ö. Ilday. Nat. Photon. **7**(2013)897.

[4] A. Dostovalov, K. Bronnikov, V. Korolkov, S. Babin, E. Mitsai, A. Mironenko, M. Tutov, D. Zhang, K. Sugioka, J. Maksimovic, T. Katkus, S. Juodkazis, A. Zhizhchenko, and A. Kuchmizhak. Nanoscale **12**(2020)13431.

[5] J. Bonse, S. V. Kirner, S. Höhm, N. Epperlein, D. Spaltmann, A. Rosenfeld, and J. Krüger. *Laser-Based Micro- and Nanoprocessing XI* **10092** (2017)100920N.

[6] J. Bonse, S. Höhm, S. V. Kirner, A. Rosenfeld, and J. Krüger, "Laser-Induced Periodic Surface Structures - A Scientific Evergreen," IEEE Journal of Selected Topics in Quantum Electronics **23**, (2017).

[7] E. L. Gurevich and S. V. Gurevich, "Laser Induced Periodic Surface Structures induced by surface plasmons coupled via roughness," Applied Surface Science **302**, 118–123 (2014).

Sixth Asian School-Conference on Physics and
Technology of Nanostructured Materials
Vladivostok, Russia, 25 – 29 April, 2022



# Femtosecond laser modification of GST225 thin films: ripples fabrication and reversible phase transitions

S.V. Zabotnov[*,1], A.V. Kolchin[1], D.V. Shuleiko[1], D.E. Presnov[1], M.N. Martyshov[1], P.K. Kashkarov[1], P.I. Lazarenko[2], V.B. Glukhenkaya[2], T.S. Kunkel[3,4], S.A. Kozyukhin[4]

[1] Lomonosov Moscow State University, Faculty of Physics, 1/2 Leninskie Gory, Moscow 119991, Russia
[2] National Research University of Electronic Technology, 1 Shokina Sq., Zelenograd 124498, Russia
[3] Moscow Institute of Physics and Technology, 9 Institutskiy Per., Dolgoprudny141701, Russia
[4] Kurnakov Institute of General and Inorganic Chemistry of RAS, 31 Leninsky Ave., Moscow 119991, Russia

*e-mail: zabotnov@physics.msu.ru

**Abstract.** GST255 based devices attract the attention of researchers due to wide opportunities in designing phase change memory. Herein, we studied a possibility to fabricate periodic micro- and nanorelief at surfaces of GST255 thin films on silicon/silicon oxide substrates under multi-pulse femtosecond laser irradiation with the wavelength of 1250 nm. One-dimensional lattices with periods of about 1250 and 130 nm were obtained depending on the number of acted laser pulses. Emergence of these structures can be explained by plasmon-polariton generation and laser-induced hydrodynamic instabilities, respectively. Additionally, formation of the lattices whose spatial period is close to the impacted laser wavelength can be modelled by considering the free carrier contribution under intensive photoexcitation. The obtained structures demonstrate strong artificial anisotropy of conductivity. Raman spectroscopy revealed both crystallization and re-amorphization of the irradiated films. The obtained results show a possibility to fabricate rewritable all-dielectric data-storage devices based on GST255 with periodic relief.

## 1. Introduction

Chalcogenide alloy GST225 possess a large difference between the optical or electrical properties of the amorphous and crystalline states. Usually, such rapid and reversible phase switching is achieved under optical pumping or resistive heating, which allows for the design of so-called phase change memory devices.

In the case of femtosecond laser treatment, the rate and energy efficiency of triggered crystallization [1] and amorphization [2] might be increased up to several times compared with the impact by nanosecond or longer laser pulses.

Recently, we showed a possibility to fabricate laser-induced periodic surface structures (LIPSS or ripples) in thin GST255 films deposited to multilayer substrates with metal layers [3, 4]. Such structures besides laser-induced phase change transitions seem promising due to their in-plane artificial anisotropy of optical and electrophysical properties.

In the present paper, we perform and theoretically analyse experiments on multi-pulse femtosecond laser irradiation, which lead to LIPPS fabrication, as well as direct and reversible phase transitions in GST225 thin films on an all-dielectric substrate.

## 2. Experiment and calculations

Amorphous GST225 thin films with thicknesses of 130–230 nm were deposited by direct current magnetron sputtering [3] on a thermalized crystalline silicon substrate with silicon oxide of thikness about 1 μm.

The films were irradiated by femtosecond laser pulses from a Cr:Forsterite laser system Avesta (1250 nm, 135 fs, 10 Hz, 0.1–0.2 J/cm$^2$) in air medium at the scanning mode. The pulses were linearly polarized, and the beam incident angle was normal.

The scanning mode during processing was realized by moving the films in the horizontal plane along a meandering trajectory. The number of overlapping laser pulses $N$ on the irradiated area varied from 3 to 750.

Images of irradiated areas were obtained by a scanning electron microscope (SEM) Carl Zeiss Supra 40. Analysis of phase transformations was carried out via Raman spectroscopy using a Horiba Jobin Yvon HR800 spectrometer with excitation at 633 nm.

The electrophysical properties of initial and processed GST225 thin films were studied by a Keithley 6487 picoampermeter and a nitrogen cryostat. For this purpose, 4 square aluminic contacts were deposited by thermal sputtering on initial and irradiated areas, as well as both along and orthogonal to scanlines of the laser beam. It allowed to measure the in-plane conductivity in two orthogonal directions.

In our work, to calculate the orientation and period of LIPSS we used the hybrid so-called Sipe–Drude model which considers photoinduced generation of free carriers at ripples formation [5].

## 3. Results and discussions

Ripples formation was revealed on the irradiated GST225 surface starting with the overlapping pulses number $N$ = 150. The gratings formed at these conditions are directed orthogonally to the polarization and scanlines of the laser beam. The ripples possess the period $\Lambda = 1250 \pm 90$ nm, which is close to the incident laser radiation wavelength (Fig. 1a).

According to our calculations using the Sipe–Drude theory the fabrication of such LIPSS might be modelled by considering the free carrier contribution under intensive photoexcitation [6]. Surface plasmon-polariton generation plays a key role in this process [5].

Additionally, one more type of LIPSS was observed at the center (Fig. 1b) of the irradiated area. It represents elongated clusters possessing a subwavelength period of $\Lambda = 130 \pm 30$ nm. These clusters are directed perpendicularly to the polarization of the laser pulses. The formation of such LIPSS cannot be explained via the Sipe–Drude model but they may be caused because of laser-induced hydrodynamic instabilities associated with Marangoni convection and similar thermo-capillary effects,

which manifest themselves at the times that exceed the laser pulse duration.

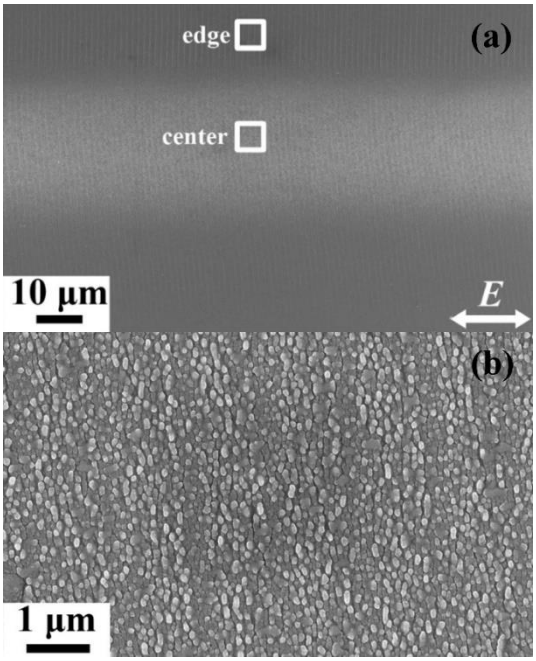


***Fig. 1.*** *SEM images at different magnifications of areas irradiated by N = 750 pulses.*

The laser processing leads to strong electrophysical anisotropy of an irradiated sample as shown in Fig. 2.

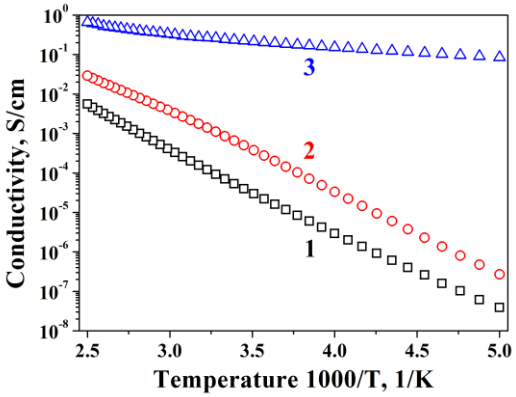


***Fig. 2.*** *Temperature dependencies of conductivity for a nonirradiated sample (1), a sample irradiated by N = 160 pulses when the current is applied in the orthogonal (2) and parallel (3) directions to laser beam scanlines.*

The growth of conductivity up to 4 orders at the room temperature after irradiation explains by crystallization of the amorphous film [3, 4]. The conductivity anisotropy is caused by laser-induced periodic relief formation.

The Raman spectrum of the amorphous GST225 thin film ($N$ = 0) demonstrates a corresponding asymmetric broadband from 110 to 200 $cm^{-1}$ with the maximum near 145 $cm^{-1}$ (Fig. 3). After irradiation an additional Raman line near 125 $cm^{-1}$ appears. It corresponds to the crystalline phase of GST225. The intensity ratio of the 125 $cm^{-1}$ line to the 110–200 $cm^{-1}$ broadband maximum is smaller in the laser spot center than at the scanline periphery area. The inhomogeneous crystallization is also confirmed by SEM analysis (Fig. 1a).

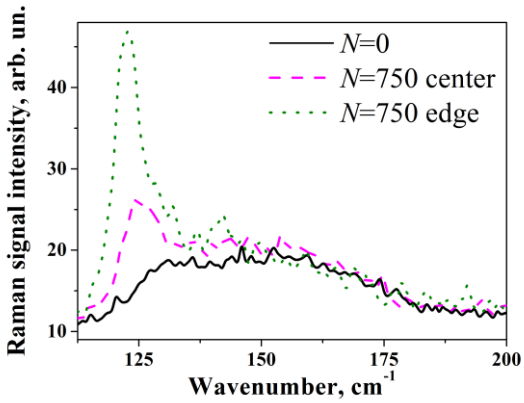


***Fig. 3.*** *Raman spectra of initial sample (N = 0 pulses), central and edge regions of treated area (N = 750 pulses).*

This behavior may indicate a possible re-amorphization occurring in the film exposed by the relatively large number of overlapping laser pulses with an inhomogeneous intensity distribution inside the gaussian laser beam. Such reversible phase transition is possible in GST225 due to the metastability of its face-centered cubic crystalline lattice.

## 4. Conclusions

In conclusion, we observed the formation of two types of ripples during the femtosecond laser treatment of amorphous GST225 thin films on dielectric substrates. The first type of gratings, whose spatial period is close to the laser wavelength, can be induced by surface plasmon-polariton excitation. The structures of the second type have a spatial period noticeably shorter than the laser wavelength and may be explained by the hydrodynamic instabilities in the laser-induced melt and solidification at the times longer than the laser pulse duration. Additionally, the reversible phase transitions and surface inhomogeneous crystallization in the GST225 thin films were achieved because of the laser impact.

The obtained results seem promising for the design of all-dielectric phase change memory devices with artificial anisotropy, which makes these structures sensitive to the direction of applied current in the plane of a sample.

## Acknowledgements

This study was funded by Russian Foundation for Basic Research (projects # 20-32-90111 and # 20-07-01092).

## References

[1] X. Sun, M. Ehrhardt, A. Lotnyk, P. Lorenz, E. Thelander, J.W. Gerlach, T. Smausz, U. Decker, B. Rauschenbach. Sci. Rep. **6**(2016)28246.

[2] J. Siegel, W. Gawelda, D. Puerto, C. Dorronsoro, J. Solis, C.N. Afonso, J.C.G. de Sande, R. Bez, A. Pirovan, C. Wiemer. J. Appl. Phys. **103**(2008)023516.

[3] S. Kozyukhin, P. Lazarenko, Y. Vorobyov, A. Baranchikov, V. Glukhenkaya, M. Smayev, A. Sherchenkov, Y. Sybina, A. Polohin, V. Sigaev. Opt. Laser Technol. **113**(2019)87.

[4] A.V. Kolchin, D.V. Shuleiko, S.V. Zabotnov, L.A. Golovan, D.E. Presnov, T.P. Kaminskaya, P.I. Lazarenko, S.A. Kozyukhin, P.K. Kashkarov. J. Phys. Conf. Ser. **1686**(2020)012006.

[5] J. Bonse, A. Rosenfeld, J. Krüger. J. Appl. Phys. **106**(2009)104910.

[6] S. Zabotnov, A. Kolchin, D. Shuleiko, D. Presnov, T. Kaminskaya, P. Lazarenko, V. Glukhenkaya, T. Kunkel, S. Kozyukhin, P. Kashkarov. Micro **2**(2022)88.

Sixth Asian School-Conference on Physics and
Technology of Nanostructured Materials
Vladivostok, Russia, 25 – 29 April, 2022

**V.i.04**

# Precision laser chemistry for functional metal and hybrid metal-carbon nanostructures

A.A. Vasileva, D.V. Mamonova, A.A. Manshina*
Institute of Chemistry, Saint-Petersburg State University, 26 Universitetskii Prospect, 198504 Saint-Petersburg, Russia

*e-mail: a.manshina@spbu.ru

**Abstract.** The problem of laser-matter interaction in the sense of laser-initiated chemical processes and subsequent formation of solid nanostructured materials will be considered in the talk. The main attention is focused to the effects originated as a result of laser effect on heterogenic systems such as 'solid-liquid' interfaces, and in particular for the case when the chemical activity of the heterogenic system as a whole is mainly determined by the laser-induced effects in liquid phase.

## 1. Introduction

Laser irradiation can provide unique physicochemical conditions in the exposure area, thus initiating diversity of subsequent processes related to phase transitions, structure reorganization and chemical reactions. Fine-tuning of the laser-initiated processes can be easily achieved by precise control of the optical parameters – spectral and energy characteristics, spatial localization, duration of exposure (including different regimes of laser generation – continuous or pulsed). Here the less studied and the most curious processes are connected with laser-initiated chemical reactions that result in generation of materials with diverse chemical structure and compositions. These reactions take place in localized volume determined by laser irradiation zone or laser focus. The focus area of laser radiation can be considered as a local chemical reactor that limits the volume of a chemical reaction and the amount of reagents involved in the process. As a result, the laser-induced reactions and products of reactions can be controlled with high degree of accuracy, and can be called '*precision laser chemistry*'.

Heterogenic systems (solid-liquid interfaces) are extremely promising targets for the laser irradiation because of a variety of chemical processes that can be initiated at interface as a result of laser effect as compared with homogeneous systems (liquids or solids). Well and widely known approach using the highly intense laser irradiation of the interface between solid substrate and liquid phase results in many effects connected with laser ablation in liquids and the subsequent nanostructures formation.

The use of low intense laser irradiation of substrate-solution interfaces is an uncommon approach. However as we found, it opens a novel way of multiphase nanostructures synthesis in a single step process. It is based on laser irradiation of the substrate-solution interface; and we call it Laser-Induced Deposition (LID). As a result of laser-initiated chemical processes, nanostructures are formed in the laser-affected area of the substrate. As a liquid phase, one can use electrolyte solutions traditional for chemical metallization, or solutions of metal salts with some reducing agents, or just solutions of organometallic complexes.

A particularly simple and efficient synthesis of metallic (Ag, Pt, Co, Au, Ru …) and hybrid nanostructures that are multi-metal (Au-Ag, Cu-Ag, Pt-Ag …) nanoclusters incorporated into carbonaceous matrix will be presented in the talk [1-5]. The main competitive advantage of LID over other laser-based methods is its ability to synthesize NPs directly on any given/preselected surface area of the substrate. It allows one-step and 'on-site' functionalization of various types of surfaces with nanostructures active in catalysis and electrocatalysis, surface-enhanced Raman spectroscopy, plasmon-enhanced fluorescence, energy conversion, solar cell technologies, etc**.**

## 2. Experiment

Laser-induced deposition method is based on laser irradiation of substrate-solution interface. As a liquid phase, we use solutions of metal precursor in solvent (water, alcohols, other organic solvents). Precursor can be inorganic, organic salts, or organometallic complexes of different metals (Au, Ag, Pt, Ru, Cu, Co, etc). It can be commercially available organometallic precursors containing single metal, or home-made hetero-metallic supramolecular complexes. As a substrate, one can use structures of various 2D and 3D architecture and various composition – amorphous or crystalline substrates such as microscope cover slips (Menzel cover slip), microscope cover slip coated with an indium–tin oxide (ITO) layer, $Al_2O_3$ and Si crystalline wafers and silicon nanowires (SiNW), etc.

Depending on the optical transparency of the substrate, two different deposition geometries can be used: (1) the solution is above the substrate for nontransparent substrates or (2) the solution is below the substrate for transparent substrates (Fig. 1). This allows for laser-induced deposition on any substrate. The illumination process is stationary—the laser beam is not shifted relatively the substrate. The laser illumination time can be varied in wide limits from minutes to hour. After terminating the laser light exposure, the substrate is removed and washed with isopropyl alcohol.

The choice of laser wavelength is determined by the specific absorption spectrum of chosen precursor. The LID process implies using low-intensity continuous wave (CW) laser that ensures mild illumination conditions preventing thermal side effects such as delocalization of the deposition process and thermal decomposition of the deposits.

The peculiarity of the LID process is the formation of deposits directly on the substrate in the laser-affected area. Thus, LID allows combining synthesis of NPs and their immobilization on the surface in a single-step procedure. The significant advantage of LID is connected with the following features (i) spatial localization of the process in

the laser-affected area, (ii) no destructive effects of mild laser irradiation, as a result no decomposition of deposits or substrate, and (iii) precise control of composition, structure, and morphology of nanostructures that all together provides fine-tuning of deposits functionality.

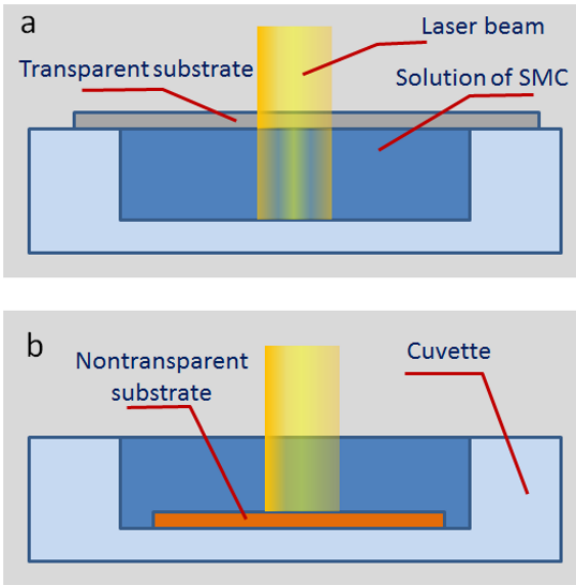


***Fig. 1.*** *The laser-induced deposition scheme for nontransparent (a) and transparent (b) for laser radiation substrate.*

## 3. Results and discussions

*Mono- and multi-metallic nanostructures, hybrid nanostructures*

LID from commercially available organometallic precursors containing single (Au, Ag, Pt, Ru) metal demonstrated possibility of successful formation of mono, bi- and tri-metallic nanoparticles of well-defined composition and morphology [6]. Multimetallic nanostructures were synthesized from mixtures of solutions of monometallic precursors. Nanoparticles form more or less dense and continuous coatings on the surface of the samples. The size of monometallic nanoparticles was found to be dependent on the metal—140–200 nm for Au, 40–60 nm for Ag, 2–3 nm for Pt under the same experimental conditions. While bi- and trimetallic nanoparticles were core-shell structures representing monometallic crystallites surrounded by an alloy of respective metals.

It is interesting to note, that the same approach – LID process – but realized with different precursor allows the creation of a multiphase (carbon/metal) hybrid materials in the single-step process. As a precursor for LID the home-made supramolecular complex $[Au_{13}Ag_{12}(C_2Ph)_{20}(PPh_2(C_6H_4)_3PPh_2)_3][PF_6]_5$ was used. Moreover, we demonstrated that hybrid Au–Ag@C nanoobjects can be synthesized with highly controlled morphology such as nanoparticles, nanoflakes and nanoflowers (Figure 2). The variation of the morphology is achieved by a systematic variation of the deposition parameters, using the same LID method and the same precursor. The variety provided by this method embraces in situ planting of hybrid structures onto the surface of a substrate, which are as different as the previously reported nanoparticles (NP), as well as novel nanoflakes (NFK) and nanoflowers (NFW).

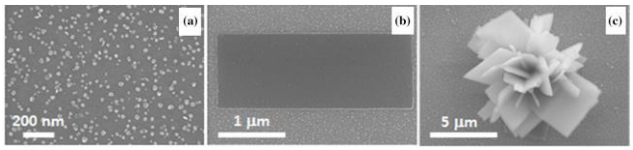


***Fig. 2.*** *Nanostructures (a) nanoparticles, (b) nanoflakes, (c) nanoflowers obtained by LID [1].*

The specific peculiarity of the demonstrated approach is creating a multiphase (carbon/metal) hybrid material in the single-step laser-induced process with simultaneous morphology control.

*Spatial control of LID*

Peculiarity of LID process allows also precise spatial control of the deposition area. One can use laser irradiation of the substrate/solution interface with focused laser beam in scan regime. Figure 3 shows rectangular-shaped patterns of AgAu@C nanoparticles deposited onto a 3D sample (silicon nanowires). The deposited samples were obtained by tight focusing and scanning the laser spot. The deposition density (number of NPs per unit square) was found to be 700 $\mu m^2$ after 30 s (a), 2100 $\mu m^2$ after 5 min (a) and 3500 $\mu m^2$ after 10 min (c).

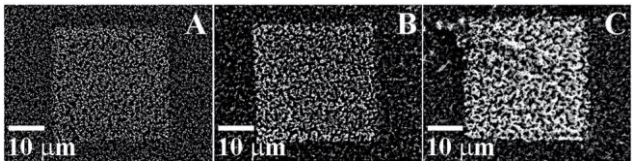


***Fig. 3****. Rectangular-shape patterns of AgAu@C nanoparticles deposited onto a 3D sample (silicon nanowires). Exposure time is varied between 30 s (a), 5 min (b) and 10 min (c) [5].*

Another example of spatial control of the LID process is based on sensitivity of the deposition process to laser irradiation intensity. The peculiarity of the LID presented here is the use of low intensity laser irradiation and laser wavelengths corresponding to the characteristic absorption of the absorption of the precursor, all together proving the photo-induced nature of NPs' formation process. In this case, the deposition process can be sensitive to the spatial variation of laser intensity and promising for the controlled NPs distribution on the substrate surface.

As a proof of concept, the spatially selective deposition of plasmonic Ag NPs in the laser interference pattern was successfully demonstrated (Figure 4) [2]. The result of such spatially selective laser deposition can be diffraction gratings with different parameters (lines/mm) formed of periodically distributed NPs. It is important to note that this is the first demonstration of plasmonic diffraction gratings obtained in a single-step process and consisting of metal NPs only, without other components such as polymers, etc.

*Functionality*

As we have shown, the LID process allows deposition of nanostructures with various chemical composition and morphology; moreover deposits can be formed on any substrate. All together these features open wide application areas for LID and creation structures with wide functionality. One can choose the appropriate precursor for LID in order to obtain required functional properties such as surface-enhanced Raman scattering (SERS), catalysis, electrocatalysis or as possible carriers of drugs, etc.

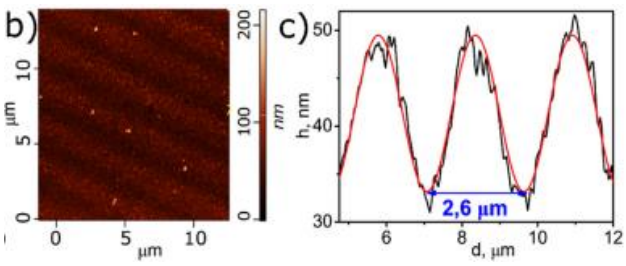


***Fig. 4.*** *(a) AFM image of Ag NPs grating deposited under laser beam with interference pattern 375 lines/mm; (b) average profile (black line) and fitting waveform (red line) of synthesized periodic structure [2].*

The most striking example of plasmon NPs' properties is SERS. Moreover the combination of metal and carbon phases is promising for synergetic effect due to the analyte adsorption by carbonaceous matrix and simultaneous Raman signal enhancement by the metal nanoinclusions. As a test experiment, the substrate with hybrid Au-Ag-C NPs obtained by LID was immersed into highly diluted solution of human blood (2 g of human blood in a liter of deionized water) for different time frames from 0 to 20 min (Fig. 5) [7,8]. The increase in the Raman intensity with longer immersion times indicates an effective adsorption of blood on the carbon shell thus increasing directivity of SERS signal for highly diluted solutions.

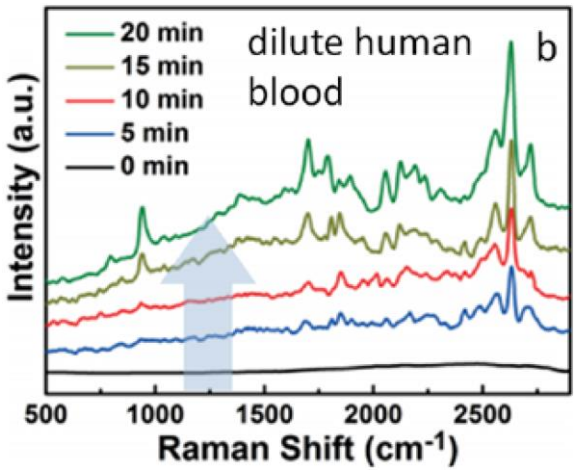


***Fig. 5.*** *Surface-enhanced Raman spectra of dilute human blood (contains blood plasma as well as red blood cells) in deionized water measured on Au-Ag-C NPs at various immersion times (0 to 20 min), arrow shows immersion time increase [8].*

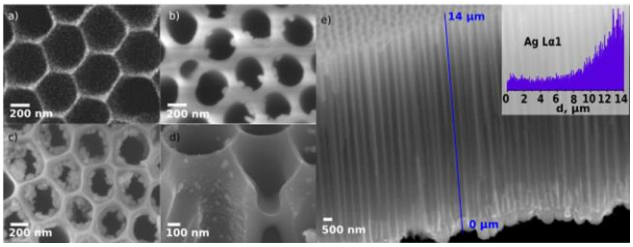


***Fig. 6.*** *Laser-induced deposition on 3D templates: (a) pure AAO template; (b) PtAg@C NPs on AAO; (c) PtAg@C NPs on AAO modified with silanization; (d) PtAg@C NPs on AAO modified with silanization — cross-section view; (e) silver distribution on sample, inset — EDX data across the line [9].*

As example of structure active in electrocatalysis we can show membranes of nanoporous anodic aluminum oxide (AAO) with NPs of AgPt@C deposited by LID not only on surface of the membrane but also inside the pores with high aspect ratio (Figure 6). The obtained nanostructured electrodes demonstrate high electrocatalytic activity in reactions of glucose oxidation [9].

We also successfully demonstrated applicability of LID for creation of a great variety of structures active in metal-enhanced fluorescence, electrocatalysis, other SERS variants etc [10-13].

## 4. Conclusions

Numerous experiments on laser irradiation of the substrate/solution interface opened a new field of research that has great fundamental interest and promising practical importance. These studies have resulted in recommendations for depositing various metal structures with different characteristics (conductivity, adhesion, morphology) on various-type substrates (e.g., ceramics, porous silicon, glasses, crystals, etc.).

In such a way, we offer a well-controlled open-air and room-temperature direct laser-based approach for forming metal and hybrid metal/carbon nanostructures of desired morphology, structure and composition. The deposition process can be easily controlled by the experimental parameters such as the composition of the liquid phase, the concentration of the precursors, the nature of the substrate (crystalline or amorphous), the topology of the substrate (flat or structured), the irradiation dwell time and the deposition geometry.

The attractiveness of the suggested synthetic methodology consists in requiring only a single step for growth of nanostructures, which are complex in composition and well-controlled in morphology. The main list of competitive advantages of precision laser chemistry over other laser-based techniques is the following:

- Synthesis takes place directly on interface of liquid and substrate;
- Mechanism of nanostructures formation is – self-organization process that can be easily affected by variation of experimental parameters;
- Synthesis of multi-phase materials takes place in a single step process;
- Composition, structure, morphology, functionality can be precisely controlled;
- As a precursor wide list of organometallic complexes, organic salts, etc. can be used;
- No thermal effects of mild laser irradiation – no decomposition of deposits or substrate;
- Spatial localization of the process – in the laser-affected area;
- Substrate of any architecture can be functionalized by target nanomaterial.

## Acknowledgements

This work was supported by joint RFBR-DFG project (RFBR project No 20-58-12015, DFG project BA 4277/16-1) Authors are grateful to "Centre for Optical and Laser materials research", "Interdisciplinary Resource Centre for Nanotechnology", "Physics Educational Centre, Centre for Physical Methods of Surface Investigation" and "Centre for X-ray Diffraction Studies" of Research Park of Saint Petersburg State University for technical support.

## References

[1] A. Povolotckaia, D. Pankin, (…) G. Leuchs, and A. Manshina, J Mater Sci **54**, (2019) 8177.

[2] D. Mamonova et al. Materials, **14**, (2021)10.
[3] S. Schlicht, A. Kireev, A. Vasileva et al.Nanotechnology 28:65405(2017).
[4] Bashouti, M.Y., Manshina, A., Povolotckaia, A., (...), Tunik, S., Lab on a Chip, **15**, (2015)1742.
[5] M.Y.Bashouti, A.V.Povolotckaia, A.V.Povolotskiy, G.Leuchs, A.A. Manshina, RSC Advances, **6**(2016)75681.
[6] Mamonova, D.V., Vasileva, A.A., Petrov, Y.V., (...), Bachmann, J., Manshina, A.A, Nanomaterials **12**(2022),146.
[7] Bashouti, M.Y., Manshina, A., Povolotckaia, A., ...Tunik, S., Christiansen, S. Lab on a Chip, **15**(2015), 1742.
[8] Manshina, A. Springer Series in Chemical Physics, **119,** (2019), p. 387.
[9] Vasileva, A., Haschke, S., Mikhailovskii, V., ...Bachmann, J., Manshina, A.Nano-Structures and Nano-Objects, **24**(2020)100547.
[10] I.E.Kolesnikov, T.Y.Ivanova, D.A.Ivanov, ... M.D. Mikhailov, A.A. Manshina, Journal of Solid State Chemistry, **258**(2018)835.
[11] Schlicht, S., Kireev, A., Vasileva, A., Manshina, A.A., Bachmann, J. Nanotechnology, 2017, 28(6), 065405.
[12] Haschke, S., Pankin, D., Mikhailovskii, V., ...Manshina, A., Bachmann, J. Beilstein Journal of Nanotechnology, **10**(2019)157.
[13] Kucherik, A., Arakelian, S., Vartanyan, T., Povolotskii, A., Man'shina, A. Optics and Spectroscopy,**121** (2016), 263.

SixthAsian School-Conference on Physics and
Technologyof Nanostructured Materials
Vladivostok, Russia, 25 – 29April, 2022 **V.o.01**

# Optical properties of transition metal dichalcogenide nanoparticles synthesized by laser ablation

G.I. Tselikov, A.V. Syuy*, D.A. Panova, A.V. Arsenin, V.S. Volkov
Center for Photonics and 2D Materials, Moscow Institute of Physics and Technology, Dolgoprudny 141700, Russia

*e-mail: alsyuy271@gmail.com

**Abstract.**We demonstrate spherical nanoparticles of tungsten and molybdenum disulfides and diselenides produced by femtosecond laser ablation in liquids. Performed analysis reveals that produced nanospheres preserve the crystalline structure, high refractive index, support strong excitons and Mie resonances in spectral range 400-900 nm, resulting in strong light-matter interaction that is favorable for nanophotonic applications.

## 1. Introduction

Two-dimensional (2D) layered transition metal dichalcogenides (TMDCs) have attracted tremendous research interests due to their unique properties for developing new-generation electronic and optoelectronic devices [1]. The well-studied group-6 TMDCs, including $MoS_2$, $WS_2$, $MoSe_2$ and $WSe_2$, have shown excellent performance for compact photodetectors, electro- and photocatalysis, ultrasensitive detectors, and cancer therapies [2].TMDCs exhibit a strong excitonic response, ensuring non-trivial optical phenomena enabled by strong light-matter interactions: exciton-polariton transport, enhanced second and third harmonic generation, high refractive index and giant optical anisotropy [3-5].Thus, nanostructures made from TMDCs represent unique platform for realization of light-matter interaction at the nanoscale. Typical TMDCs nano structuring approaches assume the use of electron beam lithography and reactive ion etching or laser thinning [6-7]. Despite their effectiveness, all these methods cannot provide spherical shape of produced nanoparticles (NPs), while spherical all-dielectric nanoantenna are treated as an elemental basis of modern nanophotonics [8]. This work is dedicated to laser engineering of spherical resonant Mie-excitonic nanoparticles from layered materials, particularly TMDCs.

## 2. Experiment

For the production of $MoS_2$, $WS_2$, $MoSe_2$ and $WSe_2$ NPs from bulk crystal we adopted the methods of ultra-short pulsed laser ablation [9]. We observed anintense coloration of solution within a few minutes of the ablation process, indicating the formation of TMDCs NPs.Concentration of NPs increased linearly at the beginning of the process and then came to a saturation after some time. Saturation concentration and time until saturation depended on pulse energy. In particular, for 100 μJ pulse energy and 10 kHz repetition rate saturation time was 30 min, and the saturation concentration was about 100 μg $mL^{-1}$. TMDCs colloids synthesized by laser ablation in water were very stable with almost no traces of aggregation or precipitation during their storage at ambient conditions for several months. Such a high stability of colloidal solutions was due to an electrostatic stabilization owing to strong charging of NPs surface similar to how it happens for other materials. Once the ablation was completed, the produced colloidal aqueous solutions of TMDCs NPs were subjected to subsequent steps of centrifugation at increasing rotation speed 400-15000 $min^{-1}$ (18-4000g) for 15 minutes to get rid of small (<10nm) NPs and to separate produced nanoparticles by size. After the centrifugation step the extinction spectra of the formed colloidal suspensions were analyzed in the spectral range of 300-1100nm, while the structuraland morphological properties of produced TMDCs NPs were analyzed by SEM, TEM and EDX.

## 3. Results and discussions

The size distributions of synthesized TMDCs NPs were analyzed by SEM. Fig. 1 shows SEM image of the $WS_2$ colloidal nanoparticles separated by centrifugation at 250 rpm. It is seen that $WS_2$ NPs have nearly spherical shape and an average size of 100 nm.Inset shows the corresponding size histogram of $WS_2$ NPs and its approximation by lognormal distribution. Elemental composition analysis was performed by EDX technique. It was found that the value ofMo:X ratio was 1.9-2 where X-chalcogen atom (Se, S). The deviation of stoichiometry index from 2 can be explained by partial oxidation of nanoparticles during the laser ablation in water.

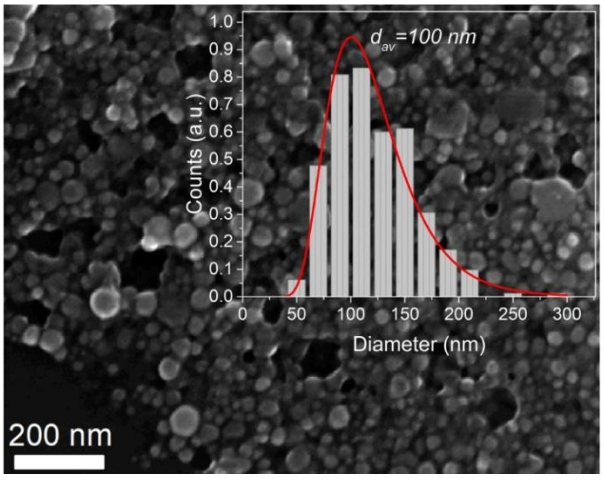


***Fig. 1.*** *SEM image of laser-synthesized$WS_2$NPs selected from a colloidal solution at 250 rpm. Inset shows the corresponding size distribution of $WS_2$ NPs.*

Crystalline structure of synthesized NPs was analyzed by HR-TEM. Fig.2 shows the TEM image of $WS_2$ NPs with the mean size of 30 nm synthesized by pulsed laser ablation of bulk 2H-$MoS_2$ crystal in deionized water. It was found that for all the NPs its structure is formed by polycrystalline inner part covered by fullerene-like outer shell. Such a

complex structure can be explained by a two-step growth of nanoparticles during the relaxation of plasma during the ablation step. First, the polycrystalline core is formedduring the initial growth stage at high temperatures then the outer shell is formingduring the thermodynamically stable growth.It is important to note that thevalues of shell's interlayer distance correspond to those of initial TMDCs crystals.

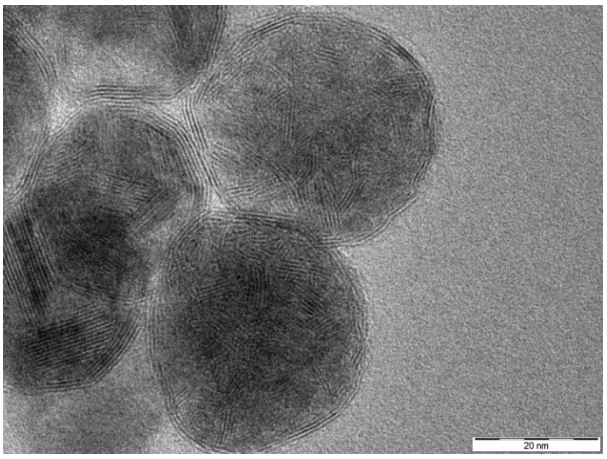


***Fig. 2.*** *TEMimage of $WS_2$ NPs synthesized by pulsed laser ablation of bulk 2H-$MoS_2$ crystal in deionized water.*

As a result, the preserved layered crystalline structure of laser ablated NPs ensures the excitonic behavior of its optical response. The extinction spectra of colloidal $MoS_2$, $WS_2$, $MoSe_2$ and $WSe_2$ NPswith the mean diameter of 100 nm are presented in Fig.3. For all the studied materials the spectra were normalized on the intensity of the extinction peak corresponding to A-exciton transition. Its spectral position was determined as 860, 770, 680 and 630 nm for $MoSe_2$, $WSe_2$, $MoS_2$ and $WS_2$correspondingly. The energies of A-exciton transitions were found to be in good agreement with ones for bulk TMDCs crystals. It is also seen from the Fig.3 that besides the contribution of the A-exciton transitions to the extinction signal, the higher excitonic transitions (B, C and D) are presented in the spectral region 400-600 nm At the same time the long wavelength tales of extinction spectra can be explained by the effective excitation of magnetic dipole (MD) Mie resonances by NPs with the size of 100-150 nm and the refractive index of 4.5-6.

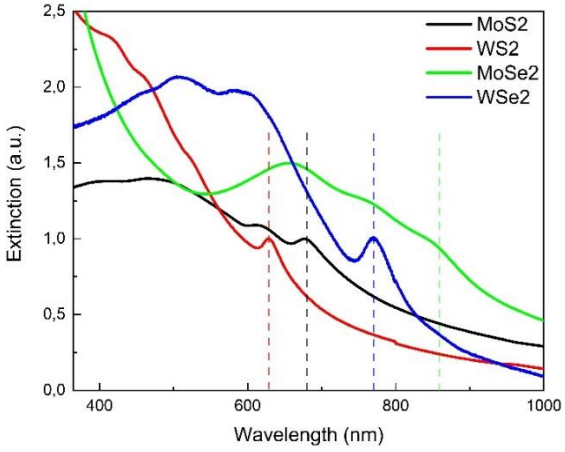


***Fig. 3.*** *Extinction spectra of colloidal $MoS_2$, $WS_2$, $MoSe_2$ and $WSe_2$ NPs. The mean size of NPs is 100 nm. Dashed lines indicate the positions of A exciton transitions on corresponding materials.*

Finally, the coexistence of Mie and excitonic modes in visible and near infrared regions grants the strong light-matter interaction in these spectral regions that is highly demanded for applications in photocatalysis, photothermal therapy and many others.

## 4. Conclusions

We demonstrate the laser-based approach for synthesis of water-dispersed ultra-stable spherical TMDC nanoparticles (NPs) of variable size 10-150 nm. Such nanoparticles demonstrate exciting optical and electronic properties inherited from the TMDC crystals, due to preserved crystalline structure, which offers a unique combination of pronounced excitonic response and high refractive index value, making possible a strong concentration of electromagnetic field in nanoparticles.

## Acknowledgements

The work was supported the Russian Science Foundation (grant № 21-79-00206).

## References

[1] Q.H. Wang, K. Kalantar-Zadeh, A. Kis, J.N. Coleman, M.S. Strano. Nat. Nanotechnol. **7**(2013)699.
[2] K. F.Mak, J. Shan.Nat. Photonics**10**(2013)497.
[3] G.A. Ermolaev, D.V. Grudinin, Y.V. Stebunov et al. Nat. Commun. **12**(2021)854.
[4] G.A. Ermolaev, Y.V. Stebunov, A.A. Vyshnevyy et al.npj 2D Mater. Appl.**4** (2020)21.
[5] I.M.Antropov, A. A. Popkova, G. I. Tselikov et al.Preprint at https://arxiv.org/abs/2105.04985 (2021).
[6] R. Verre, D.G. Baranov, B. Munkhbat, J. Cuadra, M. Käll, T. Shegai. Nat. Nanotechnol.**14**(2019)7.
[7] B. Munkhbat, A.B. Yankovich, D.G. Baranov et al.Nat Commun. **11**(2020)4604.
[8] G.I. Tselikov, G.A. Ermolaev, A.A. Popov et al. Preprint athttps://doi.org/10.48550/arXiv.2111.14004 (2021).
[9] A.A. Popov, G.I. Tselikov, N. Dumas et al. Sci. Rep.**9**,(2019) 1194.

Sixth Asian School-Conference on Physics and
Technology of Nanostructured Materials
Vladivostok, Russia, 25 – 29 April, 2022

**V.o.02**

# Direct laser metallization from deep eutectic solvents: optimization of chemical and physical parameters

E.M. Khairullina[1], D.I. Gordeichuk[1], L. Logunov[2], A.Yu. Shishov[1], A.S. Levshakova[1], I.I. Tumkin*[,1]

[1] Institute of Chemistry, Saint Petersburg University, SPbU, 7/9 Universitetskaya nab., St. Petersburg 199034, Russia
[2] School of Physics and Engineering, ITMO University, Lomonosova, 9, Saint-Petersburg, 191002, Russia

*e-mail: i.i.tumkin@spbu.ru

**Abstract.** The fabrication of conductive metal structures on the surface of various dielectric materials is necessary to create not only standard electrical circuits, but also to create flexible electronics, sensors, and other modern devices [1]. There are many chemical and physical methods and approaches that can be used for this purpose. We propose to significantly improve the LCLD method [2] by using deep eutectic solvents, which made it possible to significantly increase the rate of the process. Here we studied the influence of various physical and chemical parameters on the process of laser-induced metal deposition performed from deep eutectic solvents (DES).

## 1. Introduction

The development of new technologies useful for manufacturing metallic electrically conductive structures on various dielectric substrates is necessary to create not only standard electrical circuits, but also flexible electronics, sensors, and other modern devices. [3] This often necessitates the fabrication of single prototypes or devices with complex surface morphology and sometimes 3D conductive structures. For example, printed electronics technology is a promising alternative to traditional lithographic methods, opening up opportunities for manufacturing flexible and wearable devices, including sensor plat forms for the detection of different biologically significant analytes.

In this regard, one of the promising technologies is “direct laser writing”, which includes a number of methods, including laser-induced deposition of metals from solution (LCLD). This method is simple and does not require expensive equipment. However, despite its simplicity, this method has disadvantages, such as the need to use a large volume of concentrated water-organic solutions, a strong influence of the chemical composition of the solution components on the properties of the resulting metal structures, and a low deposition rate (2.5–5 mm $s^{-1}$).

Our proposed method shows a significant improvement in LCLD by replacing aqueous solutions with a new type of solvent - deep eutectic solvents (DES), which are widely used in many areas of modern science. The use of DES significantly reduces the amount of solvent used and simplifies the entire precipitation procedure. In addition, we have shown that laser deposition of metals from an EDL medium can extremely increase the deposition rate by more than 100 times compared to those observed during deposition from aqueous solutions. These results can become a solid basis for creating a new technology for high-speed direct laser deposition of various metals on dielectric substrates.

## 2. Experiment

For the preparation of eutectic solvents with a high copper content, eutectic solvents of the composition choline chloride/organic acid in the ratio 1/1 were synthesized, since this molar ratio provides the lowest melting temperature of these eutectic mixtures. After that, a given amount of metal chloride or acetate was dissolved in these solvents in a ratio of 1/0.1 to 1/1 (mol/mol) with respect to choline. The precursor mixtures were heated to 120°C. and stirred for half an hour while heating. The synthesized DES solutions containing metal salts were transferred to the substrate by the direct transfer method.

A CW Nd:YAG 532 nm laser was used to carry out the laser synthesis process. The principle of laser synthesis of materials in the DES is illustrated in Figure 1. To optimize the synthesis conditions in the course of the experiments, the laser radiation power (0.1–2 W), the scanning speed (0.15–300 mm/min), and the distance between the laser motion lines (0.025–0.5 mm) were varied. After laser synthesis, the unreacted DES was washed off the glass with water.

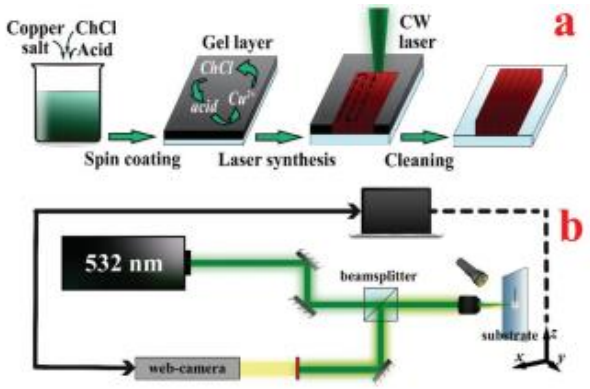


***Fig. 1.*** *The scheme of the procedure (a) and experimental set-up (b) for laser-assisted copper deposition using DESs.*

## 3. Results and discussions

In the course of the work, the conditions for laser synthesis in the DES medium were optimized. At the same time, both physical and chemical parameters that affect the ongoing processes were studied and optimized. As physical parameters, the scanning speed of the laser beam, the radiation power and its type (pulsed/continuous) were studied, it was shown that the above parameters have a significant effect both on the initiation of the deposition process and on the physicochemical and morphological characteristics of the resulting structures. As chemical factors, the following were considered: the qualitative and quantitative composition of DES, as well as additives of functionalizing components (graphene). Mixtures based on choline chloride were used as eutectic solvents, as one of

the most common hydrogen bond acceptors; organic acids, alcohols, urea, etc., acted as donors. It has been shown that DES based on choline chloride as an acceptor and organic acids and/or sugars as donors are the most promising systems for laser-induced synthesis (copper microstructures synthesized from such a composition are shown in Figure 2); these compositions provide the required adhesion of solutions to the substrate surface and have the ability to dissolve metal salts in high concentrations. , and are also characterized by a sufficient reduction ability of the donor to reduce copper under the action of laser radiation.

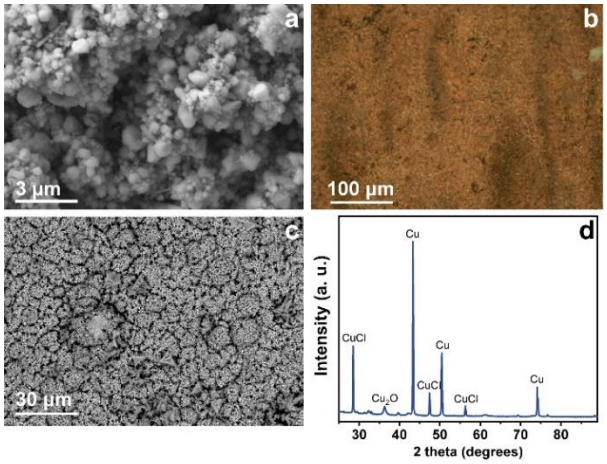


***Fig. 2.*** *SEM images of copper structures obtained from acetate (a, c), micrographs and diffraction patterns of copper structures obtained from acetate (b, d).*

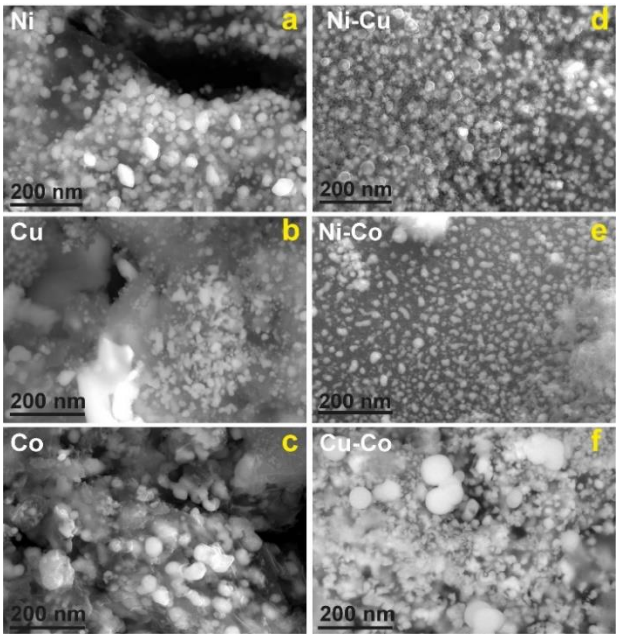


***Fig. 3.*** *SEM images of bimetallic structures synthesized from DESs based on copper, nickel, and cobalt acetates.*

The greatest attention was paid to obtaining materials based on copper and nickel, as the most demanded in terms of creating electronic devices, as well as sensor platforms. The paper also shows the possibility of single-stage laser-induced synthesis in the DES environment of a wide range of materials: monometallic nanostructured deposits (Cu, Ni), bimetallic (Ni/Co/Cu) (Fig. 3) and carbon-containing composites (Ni-graphene). For all systems, the corresponding stable compositions of DES containing oppositely named metal salts and/or target dopant, as well as laser exposure modes, were selected.

Such materials acquire characteristic features and significantly outperform individual components, since in many cases synergistic detection is observed when polymetallic enzyme-free enzymes are used. For the synthesis of bimetallic composites in a Ni-Co-Cu mixture, solvents with citric and tartaric acids based on chlorides and acetates of cobalt, copper and nickel are found (organic acid: choline chloride: metal salt 1: metal salt 2 1:1:0.5:0,5) is synthesized using a continuous laser.

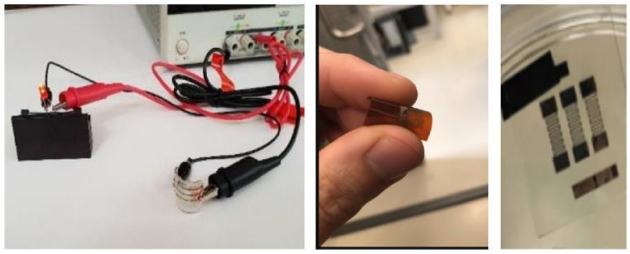

***Fig. 4.*** *Photos of copper deposits on a three-dimensional surface and a demonstration of the performance of structures.*

## 4. Conclusions

In the course of the work, the possibility of laser-induced deposition of metals on dielectric substrates under the action of laser radiation using deep eutectic solvents (DES) was demonstrated. The proposed approach can successfully compete with existing laser micropatterning technologies, such as laser sintering and laser-induced substance transfer (LIFT), since it significantly benefits in ease of implementation, including the laser deposition from DES does not require the use of vacuum systems, pre-synthesis of special precursors or the use of expensive high-precision advances, as well as the speed of the process compared to classical water systems is increased by more than two orders of magnitude.

## Acknowledgements

This work was supported by Russian Science Foundation (grant 20-79-10075). The authors also express their gratitude to the SPbSU Nano-technology Centre, the Centre for Optical and Laser Materials Research and the Centre for X-ray Diffraction Studies.

## References

[1] J. Zhang, J. Feng, L. Jia, H. Zhang, G. Zhang, S. Sun, T. Zhou, Laser-Induced Selective Metallization on Polymer Substrates Using Organocopper for Portable Electronics, ACS Appl. Mater. Interfaces. 11 (2019) 13714–13723.

[2] M. Panov, I. Tumkin, A. Smikhovskaia, E. Khairullina, D. Gordeychuk, V. Kochemirovsky, High rate in situ laser-induced synthesis of copper nanostructures performed from solutions containing potassium bromate and ethanol, Microelectron. Eng. 157 (2016) 13–18.

[3] J. Mater. Chem. C 2017, 5, 6718, Adv. Colloid Interface Sci. 2012, 170, 2, Adv. Eng. Mater. 2014, 16, 1167.

Sixth Asian School-Conference on Physics and
Technology of Nanostructured Materials
Vladivostok, Russia, 25 – 29 April, 2022



# Deep-subwavelength plasmon nanoparticle-embedded laser-induced periodic surface structures on silicon

Yu.M. Borodaenko*,1, S.O. Gurbatov1,2, E.M. Khairullina3, A.A. Kuchmizhak1,2

[1] Institute of Automation and Control Processes FEB RAS , 5 Radio St., Vladivostok 690041, Russia
[2] Far Eastern Federal University, 8 Sukhanova St., Vladivostok 690950, Russia
[3] Saint Petersburg State University, 7/9 Universitetskaya nab., St. Petersburg 199034, Russia

*e-mail: serbm@mail.ru

**Abstract.** Here, direct femtosecond laser processing of crystalline Si wafer in isopropanol/ distilled water containing either $HAuCl_4$ or $AgNO_3$ was demonstrated for fabrication of functional nanotextured morphology decorated by noble-metal nanoparticles. Si laser-induced periodic surface structures (LIPSS) with a periodicity down to 70 nm and embedded plasmon-active nanoparticles were produced and characterized by scanning electron microscopy and energy dispersive X-ray analysis. Formation of the plasmonic nanoparticles was found to be localized within the laser focal spot through the thermal-induced chemical reduction allowing to produce LIPSS locally decorated with dissimilar noble-metal nanoparticles. We envision applicability of the developed structures for molecular sensing and optoelectronics.

## 1. Introduction

Hybrid nanostructures combining low-loss high-index semiconducting materials with noble-metal inclusions supporting collective oscillations of free-electron plasma are highly demanded for optoelectronics, nanophotonics and sensing. Meanwhile, optimal optical response is typically achieved for dissimilar sizes of the semiconductor and metal counterparts within the entire hybrid nanostructures making their fabrication via common lithography-based technologies complicated, time consuming and costly [1]. Laser-based technology utilizing short (femtosecond, fs) pulses provides facile and economically justified way for nanostructure's formation via phase transitions, surface ablation and self-organization driven by interference effect or hydrodynamic instabilities [2]. This allows to produce diverse surface morphologies also referred to as laser-induced periodic surface structures (LIPSS) promising for light-matter interaction and sensing applications [3-6]. Also, the focused laser radiation can be confined within sub-microscale volume to serve as a local chemical reactor for plasmonic nanoparticles formation in liquids by the photo- or thermo-induced reduction processes.

Here, we combined the localized laser-induced chemistry and liquid-phase surface structuring of monocrystalline Si to produce hybrid deep subwavelength LIPSS decorated with plasmonic nanoparticles. By changing the chemical composition of the liquid environment (isopropanol or distilled water with $HAuCl_4$ or $AgNO_3$) we demonstrate possibility of formation of nanoparticle-embedded LIPSS locally decorated with dissimilar metals.

## 2. Experiment

LIPSS embedded with Ag and Au nanoparticles were fabricated on crystalline Si surface second-harmonic (λ=513 nm) 200-fs laser pulses generated at pulse repetition rate of 100 Hz. LIPSS were produced in the form of single-spot surface modifications and lines upon scanning the sample surface with a laser beam at 5 μm/s. Laser processing of the samples was performed at variable pulse energies (between 1.5-4 nJ) and polarization vecor oriented along the scan direction. Laser beam was focused on the sample surface by a dry microscope objective with a numerical aperture (NA) of 0.13, yielding in a focal spot size of ≈5 μm. The samples were processed in a cuvette completely filled with a working solution (distilled water or isopropanol) containing a certain variable amount of $HAuCl_4$ ($C_{M(Au)}$= $5\times10^{-6}$ M) or $AgNO_3$ ($C_{M(Ag)}$=$1\times10^{-3}$ M). The thickness of the liquid layer above the Si surface was 8 mm. After the LIPSS formation, the Si wafer was taken out of the cuvette, rinsed with distilled water and placed in an ultrasound bath for 10 minutes. Fabricated LIPSS were characterized by scanning electron microscopy (SEM), elemental analysis by energy-dispersive X-ray spectroscopy (EDX) and dark-field back-scattering spectroscopy.

## 3. Results and discussions

Figure 1(a,b) shows the LIPSS produced by applying N=3000 laser pulses per each surface spot at pulse energy of ≈2 nJ with and without adding a $AgNO_3$ in the isopropanol. Both morphologies demonstrate ordering with a characteristic period of 70 nm; however, structures produced with $AgNO_3$-contining working solution appear to contain multiple nanoparticles formed upon thermal-induced reduction. Metallic phase of the nanoparticles was confirmed by EDX analysis.

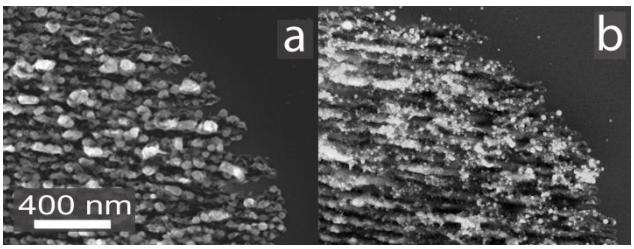


***Fig. 1.*** *SEM images of LIPSS obtained in isopropanol without (a) and with (b) addition of $AgNO_3$ at concentration of $C_{M(Ag)}=1\times10^{-3}$ M (b).*

Experiments showed that N = 1000 pulses per spot is sufficient to form the LIPSS with a periodicity ≈70 nm, but with a larger number of pulses, the gaps between the structures continue to deepen. Longer exposure also increases the amount of the formed nanoparticles.

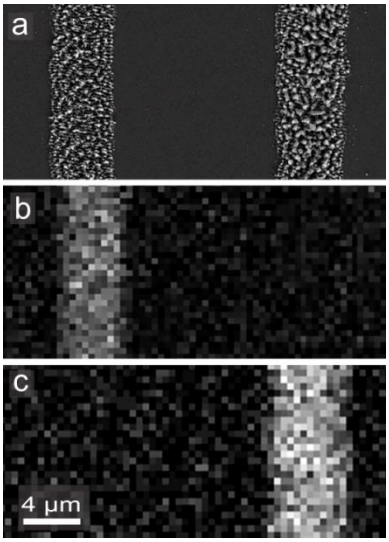


***Fig. 2.*** *(a) Reference SEM image of the Si LIPSS decorated with Ag and Au nanoparticles as well as correlated EDX maps showing distribution of Ag (b) and Au (c). Pulse energy of 3.5 nJ and concentrations of $HAuCl_4$ and $AgNO_3$ in the working solution of $5\times10^{-6}$ M and $1\times10^{-3}$ M were used.*

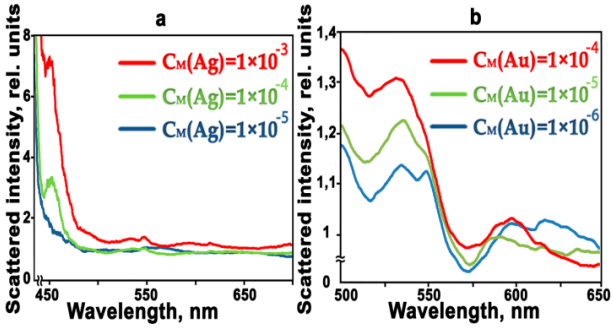


***Fig. 3.*** *Dark-field back-scattering spectra of LIPSS containing Ag (a) and Au (b) nanoparticles generated at various concentrations of $HAuCl_4$ or $AgNO_3$ in the working solutions.*

LIPSS locally decorated with dissimilar nanoparticles were produced upon liquid-phase texturing of the Si surface with a laser beam along the line trajectory. First line was recorded using $HAuCl_4$-containing a working solution containing. Then, the sample was rinsed with distilled water and ultrasonicated for 10 min, while the second line was formed upon surface texturing in the solution containing $AgNO_3$. Such sequence of metal deposition was used due to the chemical potential of the material. SEM image in Figure 2a show the similar morphology of both produced lines. EDX analysis confirmed the presence of the dissimilar (Au and Ag) nanoparticles embedded or capping the LIPSS (Fig. 2(b,c)). Noteworthy, the absence of the metallic phase outside the LIPSS area indicates localization of the nanoparticle synthesis within the laser focal spot, revealing the ability to form dissimilar plasmon-active nanoparticles with micron-scale accuracy.

Dark-field back-scattered spectra of the nanoparticle-embedded LIPSS measured using s-polarized white light demonstrated the characteristic scattering signal matching the localized plasmon resonances of Ag and Au nanoparticles (Figure 3). Increase of the scattering intensity for LIPSS produced at elevating concentrations of the $HAuCl_4$ or $AgNO_3$ in the working solutions indicates the increasing amount of the plasmon-active nanoparticles decorating the surface morphology. We envision applicability of the LIPSS for providing strong SERS signal as a result of the synergetic effect of the generation of hot spots near the sharp edges of deep Si LIPSS and plasmonic nanoparticles presence [7-9].

## 4. Conclusions

Fs-laser ablation of Si surface immersed in solutions with metals showed formation of deep subwavelength plasmon nanoparticle-embedded Si LIPSS with a periodicity down to 70 nm. The point location the LIPSS allows an increase of the metal nanoparticle concentrate directly (by concentration $HAuCl_4$ or $AgNO_3$ of the solution and the number of pulses per each surface spot). The decoration techniques are capable of realizing an homogeneous distribution of nanoparticles over the LIPSS resulting in high reproducibility of the results. In order to exploit and integrate the above capabilities for real sensing devices, fs-laser fabrication techniques are ideally suited for economic, convenience and time considerations. Thus, the hybrid nanostructures could be used for fabricating nanophotonic application with controllable functionalities and biosensing designs for to identify deposited analyte even with a slight concentration.

## Acknowledgements

This work was supported by Russian Science Foundation (grant number 18-79-10091).

## References

[1] A.A. Saleh, A. Rudenko, S. Reynaud, F. Pigeon, F. Garrelie, J.-P. Colombier. Nanoscale **12**(2020) 6609–6616.
[2] J. Bonse, S. Graf. Laser & Phot. Rev. **14**(2020)2000215.
[3] A. Balcytis, Y. Nishijima, S. Krishnamoorthy, A. Kuchmizhak, P.R. Stoddart, R. Petruskevicius, S. Juodkazis. Adv. Opt. Materials **6**(2018)1800292.
[4] A. Pescaglini, D. Iacopino. Journal of Mat. Chem. **3-45**(2015)11785–11800.
[5] A. Dostovalov, K. Bronnikov, V. Korolkov, S. Babin, E. Mitsai, A. Mironenko, M. Tutov, D. Zhang, K. Sugioka, J. Maksimovic. Nanoscale **12**(2020)13431–13441.
[6] O.A. Yeshchenko, S. Golovynskyi, V.Y. Kudrya, A.V. Tomchuk, I.M. Dmitruk, N.I. Berezovska, J. Qu. ACS omega 5-23**(2020)**14030-14039.
[7] R. F. Aroca. Phys. Chem. Chem. Phys. 15**(2013)**5355–5363.
[8] M. Sun, H. Xu,. Small. **8**(2012)2777–2786.
[9] Y. Borodaenko, S. Syubaev, S. Gurbatov, A. Zhizhchenko, A. Porfirev, S. Khonina, E. Mitsai, A.V. Gerasimenko, A. Shevlyagin, E. Modin, S. Juodkazis, E.L. Gurevich, A.A. Kuchmizhak. ACS Appl. Mat. & Int. **13-45**(2021)54551-54560.

Sixth Asian School-Conference on Physics and
Technology of Nanostructured Materials
Vladivostok, Russia, 25 – 29 April, 2022

**V.o.04**

# Photoelectrical characteristics of laser-printed transition metal dichalcogenides alloy

E.V. Zharkova*,[1], A.V. Averchenko[1], I.A. Salimon[1], O.A. Abbas[1], P.J.A. Sazio[2], P.G. Lagoudakis[1], and S. Mailis[1]

[1] Skolkovo Institute of Science and Technology, Moscow, 121205, Russian Federation
[2] Optoelectronics Research Centre, University of Southampton, Southampton, SO17 1BJ, United Kingdom

*e-mail: ekaterina.zharkova@skoltech.ru

**Abstract.** The photoelectric response of $Mo_xW_{1-x}S_2$ alloy films that have been synthesized using a direct laser synthesis method is reported here. The alloys have been produced by laser-induced thermolysis of a composite single-source precursor. The results that are shown here concern a two terminal device, which consist of $Mo_{0.5}W_{0.5}S_2$ laser-synthesized tracks that are connected to metallic contacts. The device acts as a photodetector for visible light.

## 1. Introduction

The isolation of graphene sheets in 2004 has boosted both fundamental and applied interest in electronic systems with reduced dimensionality [1]. Regardless of the high-quality monocrystalline flakes produced by exfoliation, this approach is low yield and it is suitable for prototyping and research solely. Therefore, high-throughput alternatives such as MBE, CVD and PLD have been investigated [2-3]. However, these techniques are budget and time consuming as well as they require controlled environments.

Alternatively, direct laser writing has been suggested recently for synthesizing TMDs by laser irradiating ammonium thiosalts as a simple and cost-effective route that enables fabrication of electronic and optoelectronic devices with minimum lithographic complexities [4].

However, despite the fascinating properties of 2D transition metal dichalcogenides, some of these properties like a bandgap need further engineering to be applied for daily life applications [5]. For example, 2D-TMD based photodetectors suffer from limited spectral responsivity range which can be broadened by tuning the electronic and optical characteristics of 2D-TMD films. Among several methods for tailoring 2D-TMD properties, alloying is the most promising approach due to its simplicity and applicability [6]. Here, we report a direct laser writing method for the synthesis of 2D-TMD alloys, which is based on the process that is outlined in [4]. The composition of the synthesized alloy films is defined by tuning the ratio of partial concentration of precursors ($(NH_4)_2MoS_4$ and $(NH_4)_2MoS_4$)in the starting solution used for laser exposure.

## 2. Experiment

This work is focused on a particular alloy composition ($Mo_{0.5}W_{0.5}S_2$), which has been reported in the literature to have a substantial photo response [7]. An array of multiple laser written alloy tracks have been printed to serve as photodetector channels for the study of photoresponse. Chemical precursors of $MoS_2$ and $WS_2$ consisting of $(NH_4)_2MoS_4$, and $(NH_4)_2WS_4$ respectively were dissolved in a mixture of DMF, butylamine and ethanolamine (for $(NH_4)_2MoS_4$) and in a mixture of NMP, butylamine and ethanolamine (for $(NH_4)_2WS_4$) were mixed to form a composite source precursor solution. The composite precursor solution was then spin-coated onto a $Si/SiO_2$ substrate to obtain a uniform thin film. The composite precursor film was exposed to focused visible laser radiation, which serves as the source of energy that induces thermolysis of the precursor and synthesis of the target TMD alloy.

The synthesis conditions used were the following: laser wavelength = 532nm, irradiation power = 600mW, diameter of the laser spot = 10um, speed of laser beam = 10mm/s. Each device contains 250 linear tracks separated by 10μm from each other, without overlapping. The presence of the alloy was verified with Raman spectroscopy as shown on fig.1(a).

Since the laser beam has a Gaussian intensity profile, the film of the precursor is not irradiated uniformly across the beam diameter. As a result the synthesis of material occurs only in the central area of the track, which is ~5μm wide as shown in fig.1(b).

Gold contacts were deposited through a copper shadow mask to avoid any chemical alteration that might be caused by solvents and photoresists that are normally used in standard photolithography. Gold contacts with a thickness of 60nm were deposited using magnetron sputtering and thermal evaporation to create electrical contacts. A schematic view of a photodetector is shown in fig.1(c). The distance between contacts was set to 30μm. According to the previously described geometry of the tracks of material, the illuminated area of the photodetector is ~$3.75*10^{-4}$ $cm^2$.

The electrical characterization of the sample was conducted with the semiconductor analyzer. Through its leads, the bias voltage was applied to the photodetector and the current flowing through was measured. Values of the applied voltage did not exceed 5V and were swept with 50mV step and 0.5s delay in order to avoid the charging effects.

## 3. Results and discussions

A typical ohmic behavior was observed for both under illumination and dark conditions as shown in fig 1(d) by red and black lines respectively. However, the slight increase in current under illumination compared to dark one indicates that the tracks are photoconductive.

The measurements under the illumination of photodetector were conducted using a broad-band source of the light (LED array). The power of light on the detector was regulated by the use of neutral density filters. The photocurrent ($I_{pc} = I_{light} - I_{dark}$) shows almost linear

dependence on light power (see fig.1(e)). The responsivity of the detector is ~50mA/W.

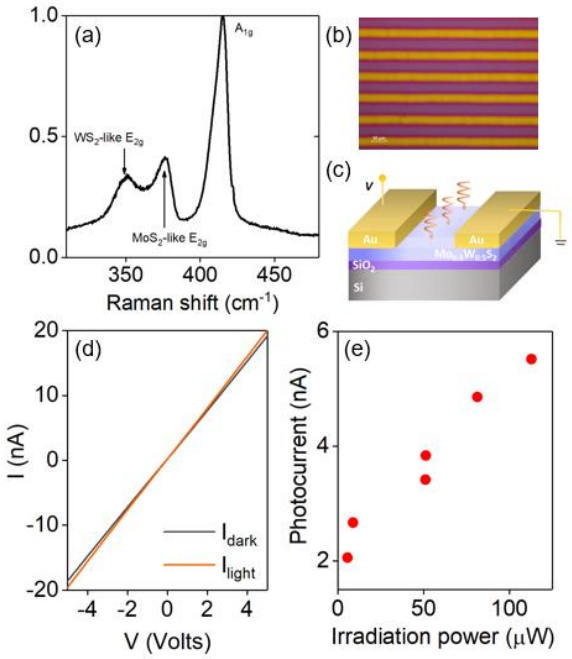


***Fig. 1.*** *(a) Raman spectrum corresponding to a laser synthesized alloy track (b) Optical image of the* $Mo_{0.5}W_{0.5}S_2$ *tracks (c) Schematic representation of the photodetector device (d) Current-Voltage characteristic of the photodetector under 120μW white light illumination (red curve) and in the dark (black curve) (e) Photocurrent at different optical powers at 3V bias voltage.*

Absorption measurements in large area films indicate that there is significant absorption in the visible spectral range, which is responsible for the production of photocarriers. The absorption can also be tuned by the particular composition of the alloy.

It is important to note that the work function of gold is not matched to that of the TMD in question, which in turn results in high resistivity of the device. The photocurrent could be enhanced increased by choosing a low work function metal for contacts such as Indium. Further improvement in the performance of the device could be achieved by optimizing the laser synthesis conditions to achieve better crystallinity and therefore lower defect density in the TMD alloys.

## 4. Conclusions

The photoelectric response of laser synthesized $Mo_{0.5}W_{0.5}S_2$ alloys have been presented. The photoresponse of a device consisting of multiple alloy tracks was investigated using a broadband visible source. A photoresponse of ~50 mA/W was measured. Currently, further work is underway to optimize the electrical contacts and the film synthesis conditions, which is expected to improve the device performance. Furthermore, the photoresponce of other alloy compositions with different ratios of Mo/W is under investigation.

## Acknowledgements

The reported study was financially supported by the Russian Science Foundation (RSF) grant No. 21-79-20208.

## References

[1] Novoselov, K. S. (2004). Science, 306(5696), 666–669.
[2] Zhan, Y., Liu, Z., Najmaei, S., Ajayan, P. M., & Lou, J. (2012). *Small, 8(7), 966–971*.
[3] Ho, Y.-T., Ma, C.-H., Luong, T.-T., Wei, L.-L., Yen, T.-C., Hsu, W.-T, Chang, E. Y. (2015). Physica Status Solidi (RRL) - Rapid Research Letters, 9(3), 187–191.
[4] Abbas, O.A., Lewis, A.H., Aspiotis, N, Sci Rep 11, 5211 (2021).
[5] Yao, J., Zheng, Z., & Yang, G. (2016). ACS Applied Materials & Interfaces, 8(20), 12915–12924.
[6] Xie, L. M. (2015). Nanoscale, 7(44), 18392–18401.
[7] Ruilong Yang, et al (2019) ACS Applied Materials & Interfaces *11* (23), 20979-20986.

Sixth Asian School-Conference on Physics and
Technology of Nanostructured Materials
Vladivostok, Russia, 25 – 29 April, 2022

**V.o.05**

# Effect of laser treatment of $TiO_2$ on optical and photocatalytic properties

Z.P. Fedorovich, O.A. Reutova, E.D. Fakhrutdinova*, V.A. Svetlichnyi
Tomsk State University, 36 Lenin Ave., Tomsk, 634050, Russia

*e-mail: fakfrutdinovaed@gmail.com

**Abstract.** Nanomaterials based on dark titanium dioxide are of considerable interest as promising photocatalysts. In this work, titanium dioxide initially obtained by pulsed laser ablation (Nd:YAG laser with 1064 nm, 7 ns, 20 Hz) was subjected to additional laser treatment. The thus obtained powder materials were annealed and study of the structure by X-ray diffraction, optical properties by diffuse reflection spectroscopy, and photocatalytic properties in the processes of decomposition of the Rhodamine B dye and evolution of hydrogen from an aqueous methanol solution are presented.

## 1. Introduction

The lack of efficient, stable, cheap and environmentally friendly photocatalysts acting in the visible region of the spectrum is currently the main problem in the field of photocatalysis. Recently, a popular object of study is dark titanium dioxide, which has various structural defects and is active in the visible region of the spectrum [1]. Dark titanium dioxide is obtained by various methods: reduction with hydrogen, argon, high or low pressure nitrogen, electrochemical reduction, solvothermal synthesis etc. [1]. A promising way to obtain titanium dioxide in a highly dispersed and highly defective state is the method of pulsed laser ablation (PLA). Previously, by PLA of a metal target in water, we obtained dark defective titanium dioxide, which has absorption in the entire visible range [2]. Additional opportunities for controlling the defectiveness, size and structure are provided by the use of laser treatment of substances at the stage of synthesis. In this work, we show the effect of laser treatment of a colloidal solution of dark $TiO_2$ on the structural optical and photocatalytic properties.

## 2. Experiment

The materials were prepared as follows. Firstly, the colloidal solution was obtained by ablation of metallic Ti target in water for 1 h using Nd:YAG laser (1064 nm, 7 ns, 20 Hz). Then, for an hour, the colloidal solution was subjected to additional laser treatment with the same laser parameters. Colloidal solutions were dried in air at 60 °C to up to a powder and annealed at different temperatures. Thus, a series of powder materials was obtained.

The samples were studied by X-ray diffraction (XRD), the Brunauer–Emmett–Teller (BET) to identify the specific surface area, and UV-vis spectroscopy. Photocatalytic activity was studied during the Rhodamine B dye decomposition under the LED irradiation with $\lambda = 375$ and 410 nm. The materials were tested in the process of hydrogen evolution from the methanol solution under LED irradiation with the same wavelength. Prior to the photocatalytic experiment, a suspension containing 50 mg of catalyst in 100 ml of 20 % methanol solution was purged with an inert gas argon. The amount of generated hydrogen was determined using gas chromatography.

## 3. Results and discussions

The initial powders and the samples annealed at 250 °C are X-ray amorphous. The crystal structure is revealed only after increasing the calcination temperature to 400°C, anatase predominates in samples (96 %). An increase in the annealing temperature does not lead to a complete phase transition of anatase to rutile; at 800 °C the anatase content is 45%. The laser treatment causes fragmentation of large particles, which is supported by the BET data: laser irradiation results in an increase of the specific surface area from 227 to 253 $m^2/g$. All samples absorb in the visible range; however, as the annealing temperature increases, the absorption intensity decreases, but does not disappear completely. The band gap calculated by the Tauc method is approximately 3.07 eV. A decrease in the value of the band gap is associated with the presence of defects in the band gap and thus affects its value.

The data on photocatalytic activity during the decomposition of the dye Rhodamine B show that the samples exhibit high activity both under irradiation at a wavelength of 375 nm and practically do not lose their activity upon irradiation at a wavelength of 410 nm. Complete decomposition of the dye is achieved in 4-4.5 hours. Also, samples annealed at 400 and 600 °C showed good activity in the process of hydrogen evolution from water-methanol solution.

## 4. Conclusions

Thus, additional laser treatment of titanium colloidal solutions after ablation leads to an increase in the anatase content in the samples up to 96%, which is thermally stable. Laser treatment leads to fragmentation of large particles and an increase in the specific surface area, affects the optical and photocatalytic properties. The samples exhibit good photocatalytic activity in the processes of decomposition of the dye Rhodamine B and hydrogen evolution.

## Acknowledgements

This study has been funded from the Russian Science Foundation; Project No. 19-73-30026.

## References

[1] T.S. Rajaraman, S.P. Parikh, V.G. Ghandi. Chem. Eng. **389**(2019)123918.
[2] E.D. Fakhrutdinova, A.V. Shabalina, M.A. Gerasimova, A.L. Nemoykina, O.V. Vodyankina V.A. Svetlichnyi, Materials **13**(2020) 2054.

Sixth Asian School-Conference on Physics and
Technology of Nanostructured Materials
Vladivostok, Russia, 25 – 29 April, 2022

**V.o.06**

# Local crystallization of Bi:YIG thin films by laser annealing in a controlled atmosphere

A.V. Shelaev*[,1], Y.M. Sgibnev[1], S.L. Efremova[1,2], P.N. Tananaev[1] and A.V. Baryshev[1]

[1] Dukhov Automatics Research Institute (VNIIA), 22, ul. Sushchevskaya, Moscow 127055, Russia
[2] Lomonosov Moscow State University, GSP-1, Leninskie Gory, Moscow, 119991, Russia

*e-mail: artem.shelaev@yandex.ru

**Abstract.** In optoelectronic devices (insulators and circulators), it is required to use nonreciprocal elements based on bismuth-substituted yttrium iron garnet (Bi:YIG) bonded or deposited on the surface of silicon waveguiding structures. The limiting factor in the use of Bi:YIG is a high temperature necessary for garnet crystallization. In present work, we demonstrate a solution where local crystallization of an oxide layer having stoichiometric composition is done by a laser beam focused into a spot less than 1 μm. To determine the optimal crystallization conditions, the oxide layer was subjected to laser irradiation in various atmospheres (dry air, oxygen, nitrogen, and argon), and structural, optical and magnetooptical properties were studied.

## 1. Introduction

Optoelectronics and photonics require devices with non-reciprocal elements deposited on $Si/SiO_2$ surface. One of the most common materials is YIG [1]. The main difficulty in production of integrated devices is annealing at a temperature of 600ºC and above, which is necessary for garnet crystallization. An undesirable consequence of such annealing is thermal effects on the semiconductor elements of the device, which leads to a deterioration of characteristics.

We report on a method for local crystallization of Bi:YIG based on laser annealing that can minimize thermal effects on other elements of the device.

## 2. Experiment

Thin oxide film on a $SiO_2$ substrate was prepared by the metal-organic decomposition method [2] and had the stoichiometric composition for $Bi_{0.5}Y_{2.5}Fe_5O_{12}$. Ten 50 nm-thick metal-organic layers were repeatedly deposited by centrifugation and annealed in air at 400ºC for 30 minutes to obtain a 360 nm-thick oxide film for subsequent laser irradiation. Sample was mounted into a gas cell with quartz windows. A 405 nm CW laser was used for local annealing of the oxide film under air, oxygen, nitrogen, and argon ambient conditions. Twenty strips 20 μm long each were irradiated with a laser power range of 8.3–24.6 mW when moving the oxide film at a constant speed of 4 μm/s. Properties of the fabricated microstructures were thoroughly studied.

## 3. Results and discussions

Raman spectroscopy was used to study the local chemical and structural composition of the stripes. According to the Raman spectra, the Bi:YIG phase was grown during laser annealing in all used gas atmospheres. For an oxygen-free atmosphere, the minimum required power was approximately 12 mW, and that of 14 mW were enough in an oxygen-containing atmosphere for formation of Bi:YIG. Overheating caused by laser annealing at the higher power led to the formation of a $Fe_2O_3$ phase in the case of an oxygen atmosphere, $Fe_3O_4$ in the case of oxygen-free atmospheres. In addition, significant bands at 70 $cm^{-1}$ and 97 $cm^{-1}$ were observed after annealing in nitrogen and argon, which corresponded to the metallic bismuth.

Local Faraday rotation measurements showed that laser annealing at the optimal laser power in air, $O_2$, Ar atmospheres resulted in stable Bi:YIG growth, and the polarization rotation was of 0.7-0.8 deg at 500 nm. In a nitrogen atmosphere, the largest rotation did not exceed 0.5 deg at 500 nm. The latter is explained by forming metallic bismuth, i.e., bismuth substitution of yttrium goes less efficiently.

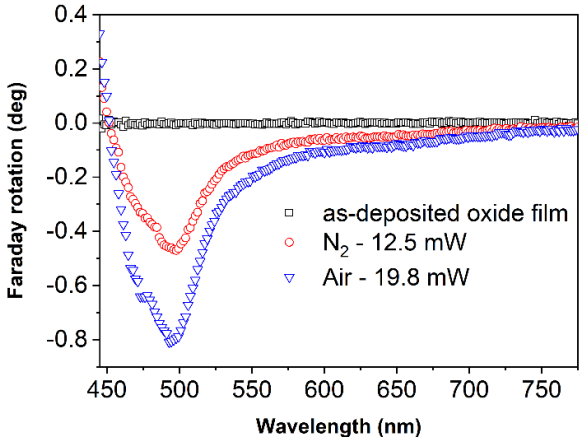


***Fig. 1.*** *Faraday rotation of an initial oxide layer and that of the stripes after laser annealing in $N_2$ and air atmosphere.*

The topography was measured by an atomic force microscope – the width of the crystallized stripes depended on the laser power and was in a range of 2-5 μm. The surface scans showed that Bi:YIG growth was accompanied by a change in thickness–the initial oxide film was compacted by 20%.

## 4. Conclusions

We proposed a method of local Bi:YIG crystallization. Based on the results of measurements, the optimal values of the laser power were determined for various gas atmospheres. Crystallized $Bi_{0.5}Y_{2.5}Fe_5O_{12}$ provided polarization rotation up to 3 deg/μm, and the width of the crystallized Bi:YIG stripes were less than 5 μm. By-products of laser-done crystallization were found, including metallic bismuth and iron oxides.

## References

[1] Stadler, B.J.H., Mizumoto, T. IEEE Photonics J. **6** (2014) 1.
[2] Y. Sgibnev *et al.* Cryst. Growth Des. **22** (2021) 1196.

Sixth Asian School-Conference on Physics and
Technology of Nanostructured Materials
Vladivostok, Russia, 25 – 29 April, 2022



# Laser printing of c-Si hemispherical Mie-nanoresonators toward implicit anti-counterfeit labels

S.A. Syubaev[*,1,2], A.A. Kuchmizhak[1,2]

[1] Institute of Automation and Control Processes FEB RAS , 5 Radio St., Vladivostok 690041, Russia
[2] Far Eastern Federal University, 6 Sukhanova Str., Vladivostok 690950, Russia

*e-mail: trilar@bk.ru

**Abstract.** Laser printing of anti-counterfeiting labels on amorphous Si films is demonstrated. Related security tags are composed of optically undistinguishable laser-drilled micro-holes with/without hemispherical crystalline Si (c-Si) nanoparticles. The nanoparticles exhibit resonant Raman yield at c-Si phonon mode frequency empowered by geometric Mie resonance. This feature allows to realize high-resolution laser encryption scheme with facile Raman mapping optical readout.

## 1. Introduction

All-dielectric resonant nanoscale structures have drawn considerable interest because of their unique features, distinguishing them from plasmonic nanostructures. The excitation of low-loss optical resonances as well as localization of electromagnetic near-field in the subwavelength region provide the utilizing of dielectric nanostructures in various applications, including linear and nonlinear light manipulation [1], metasurfaces design [2], spectroscopic analysis [3] and so forth. Among them, high-index nanostructures are most promising for Raman spectroscopy. Since the Raman scattering is sensitive to vibrational states in molecules or phonon modes in crystalline material, all-dielectric crystalline nanostructures pave the way for controlling and enhancing intrinsic Raman response. This is due to designing the dielectric nanostructures to tune the optical near-field, both inside and outside of nanostructure, supporting electric and magnetic-type Mie resonances.

On the other hand, the phenomenon of counterfeit remains serious and social-threatening worldwide task [4] and there has been limited literature and applications of dielectric nanostructures in the anti-counterfeiting field. Numerous efforts were undertaken to secure legal rights and interests of consumers, using well-established anti-counterfeiting techniques such as inkjet printing-based labels [5], nanoscale barcodes [6], watermarks [7] and holograms [8]. However, owing to their predictable and strictly defined security mechanisms, they are still cloneable. Hence, the development of anti-counterfeiting tags, providing significant data security, has initiated intensive research**.**

Based on our previous work [9] on one-step fabrication of crystalline silicon (c-Si) hemispherical nanoparticles (NPs) of variable size, incorporated in through microhole, via laser-induced dewetting of glass-supported amorphous silicon (α-Si) thin film, herein we introduce a new anti-counterfeit label with security features that can not be identified with the naked eye or using ordinary analytical tools. The proposed label represents array of close-packed 400 nm wide microholes, some of which contain resonant c-Si NPs with diameter of 180 nm. Thus, nanoparticles ordered in a user-defined way indicate encrypted information that can be read using Raman signal intensity mapping at frequency of 519 $cm^{-1}$, corresponding to the main phonon mode of crystalline silicon. Owing to size-dependent Raman scattering, security level can be additionally increased by controllable varying of each NP diameter within the array, resulting in Raman signal variations.

## 2. Experiment

Thin films of α-Si with a thickness of 24 nm were deposited on glass substrate by magnetron sputtering. Linearly-polarized laser pulses, generated by Yb:KGW-based laser system at second-harmonic wavelength of 513 nm and pulse duration of 200 fs, were focused by dry objective lens with numerical aperture (NA) of 0.42 on α-Si film surface. The sample was arranged on computer-controlled 3D nanopositioning platform, permitting to arrange laser pulses in accordance with user-defined design. Morphological changes on the surface on α-Si film after laser irradiation were studied by scanning electron microscopy (SEM). Raman spectroscopy was carried out by automated confocal micro-Raman setup, equipped with CCD-camera. The corresponding Raman signals were excited by CW laser radiation at different wavelengths (473, 532 and 633 nm), collected by the same dry objective lens with NA = 0.7 and detected by 1800 lines/mm grating-type spectrometer. Raman maps were obtained by scanning the area of interest along a snake-like trajectory at 100 nm lateral step in both directions and 0.7 s acquisition time per point. All recorded maps were post-processed by pre-installed software (Image Analysis, NT-MDT).

## 3. Results and discussions

Recently it was shown [9], that ultrafast deposition of laser energy on the surface of thermally-thin α-Si film, supported by glass substrate, allows to produce silicon crystalline hemishperical nanoparticles of variable diameter ($D_{NP}$). The formation process of such nanostructures can be described by successive fluence-depended steps: 1) laser-induced local heating and melting of amorphous silicon; 2) separation of the molten material from the film and its contraction to the center of irradiated area in the shape of hemispherical NP with specific $D_{NP}$, followed by solidification and crystallization; 3) ejection of entire involved material from the substrate and formation of through microhole in the film. It should be noted there that the range of available $D_{NP}$ values is determined by laser focal spot size, defined in its turn by objective lens NA, and thickness of irradiated film. Fixing the latter parameters (0.42 and 24 nm, respectively), Si NPs size can be precisely controlled via variation of adsorbed laser fluence (Fig. 1a).

SEM images of square-shape arrays, containing 400 ordered Si NPs fabricated at increasing laser pulse fluences, demonstrate 97% repeatability of nanostructures within the array. Some dissimilar nanostructures can appear due to film defects and laser system stability.

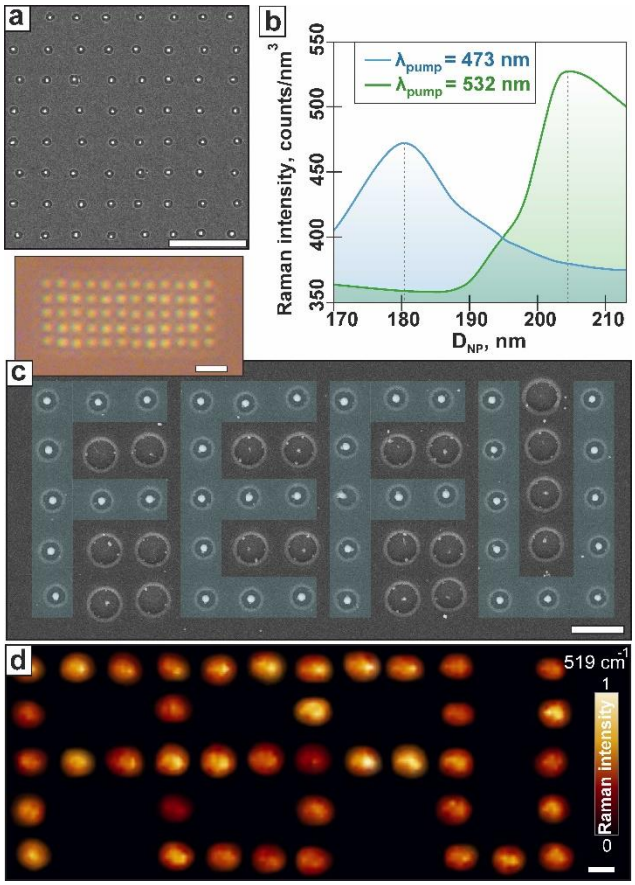


***Fig. 1.*** *(a) SEM image demonstrating repeatability of the NP printing performed at fluence of 45 mJ/cm$^2$. Scale bar corresponds to 5 μm. (b) Averaged Raman yield (at 519 cm$^{-1}$) measured for the isolated c-Si nanoparticles of various diameters at 473 and 532 nm pump wavelength. (c,d) Correlated SEM and Raman (at 519 cm$^{-1}$) images of the security tag, consisting of through micro-holes with/without NPs. Scale bars are 1 μm and 500 nm, respectively. Blue-color areas highlight the encrypted "FEFU" letters. Inset: optical image of the same array, obtained with high-NA objective. Scale bar is 2 μm.*

The phase composition of hemispherical NPs was studied by Raman spectroscopy using various pump wavelengths (473, 532, and 633 nm). The presence of an intense peak at a frequency of 519 cm$^{-1}$ confirmed the nanocrystalline structure of silicon nanoparticles formed in the process of laser-induced melting of amorphous silicon and its rapid crystallization at nanosecond timescale. Systematic studies of the dependence of the intensity of the Raman signal at a frequency of 519 cm$^{-1}$ on the NP diameter made it possible to confirm the presence of resonant optical properties in the fabricated nanoparticles. The maximum intensity of the Raman signal was observed for nanoparticles with a diameter of 180 and 205 nm at Raman laser pumping wavelengths of 473 and 532 nm, respectively (Fig. 1b). This feature is associated with the excitation of geometric Mie resonances of electrical and magnetic nature in nanoparticles [10], which allow, for a fixed ratio of the diameter and pump wavelength, to provide resonant localization of electromagnetic radiation inside the nanoparticle, which justifies an increase of the Raman signal intensity.

The conducted studies open up prospects for realization of controlled laser printing of Mie-resonant hemispherical silicon nanoparticles, which are promising for the fabrication of anti-counterfeiting labels. To demonstrate the applicability of the developed approach for these tasks, we imprinted 2-μm period array of micro-holes, some of which contained Mie-resonant silicon nanoparticles with a diameter of 180 nm (Fig. 1c). Noteworthy, an ordinary optical microscope equipped with a focusing objective NA=0.8 operating either in transmission or reflection mode can not identify the presence/absence of nanoparticle inside certain user-defined micro-holes. Meanwhile, nanoparticles ordered in a special way can contain hidden information, which can be read using Raman signal intensity mapping at frequency of 519 cm$^{-1}$ (Fig. 1d).

## 4. Conclusions

To conclude, we demonstrated high-performing one-step laser printing method, allowing to fabricate resonant crystalline silicon hemispherical nanoparticles of variable diameter, incorporated in through microhole, via laser-induced dewetting of glass-supported amorphous silicon thin film. The fabricated c-Si NPs were shown to demonstrate intrinsic Raman enhancement through the excitation of geometric Mie-resonances. In addition, by combining and mixing the laser-printed through holes with/without Mie-resonant nanoparticles indistinguishable even for high-resolution optical microscopy, we demonstrated security tags with simple Raman mapping readout and printing resolution of 12,500 dpi.

## Acknowledgements

This work was supported by Russian Science Foundation (Grant No. 21-72-20122).

## References

[1] T. X. Hoang, S. T. Ha, Z. Pan, W. K. Phua, R. Paniagua-Domínguez, C. E. Png, H. S. Chu, A. I. Kuznetsov. Nano Lett. **20**(2020)5655.
[2] J. S. Ginsberg, A. C. Overvig, M. M. Jadidi, S. C. Malek, G. N. Patwardhan, N. Swenson, N. Yu, A. L. Gaeta. Nanophoton. **10**(2021)733.
[3] A. Krasnok, M. Caldarola, N. Bonod, A. Alú. Adv. Opt. Mater. **6**(2018)1701094.
[4] R. Arppe, T. J. Sørensen. Nat. Rev. Chem. **1**(2017)1.
[5] Y. Liu, F. Han, F. Li, Y. Zhao, M. Chen, Z. Xu, X. Zheng, H. Hu, J. Yao, T. Guo, W. Lin, Y. Zheng, B. You, P. Liu, Y. Li, L. Qian. Nat. Commun. **10**(2019)1.
[6] S. Shikha, T. Salafi, J. Cheng, Y. Zhang, Chem. Soc. Rev. **46**(2017)7054.
[7] J. Deng, L. Deng, Z. Guan, J. Tao, G. Li, Z. Li, Z. Li, S. Yu, G. Zheng. Nano Lett. **20**(2020)1830.
[8] Y. Blau, O. Bar-On, Y. Hanein, A. Boag, J. Scheuer. Opt. Express **28**(2020)8924.
[9] S. Syubaev, E. Mitsai, S. Starikov, A. Kuchmizhak. Opt. Lett. **46**(2021)2304.
[10] E. Mitsai, M. Naffouti, T. David, M. Abbarchi, L. Hassayoun, D. Storozhenko, A. Mironenko, S. Bratskaya, S. Juodkazis, S. Makarov, A. Kuchmizhak. Nanoscale **11**(2019) 11634.

Sixth Asian School-Conference on Physics and
Technology of Nanostructured Materials
Vladivostok, Russia, 25 – 29 April, 2022

**V.o.08**

# CW laser crystallization of GST thin films in multilayered conductive substrate for reflective display application

V.B. Glukhenkaya*[,1], N.M. Tolkach[1,2], P.I. Lazarenko[1], A.V. Romashkin[1], A.A. Sherchenkov[1], E.A. Lebedev

[1] National Research University of Electronic Technology, 1 Shokin Sq., Moscow 124498, Russia
[2] Ryazan State Radio Engineering University named after V.F. Utkin, 59 Gagarin St, Ryazan 390005, Russia

*e-mail: Kapakycek2009@yandex.ru

**Abstract.** Crystallization process initiated in GST thin film under CW laser irradiation and influence of phase state of GST films on optical properties of multilayered GST/ITO/Al (GIA) structure were investigated. It was shown, that continuous laser exposure leads to significant changes of the optical contrast and Raman spectra of extended areas modifying by CW laser irradiation. Range of changes corresponds to the phase transition of amorphous GST thin film into crystalline state. The energy range of crystallization is in the interval from 0.11 to 0.22 mJ/μm$^2$. The difference in reflectivity change between two phase states is 8 r.u. The threshold energy value of GST material degradation is more than 1.10 mJ/μm$^2$. Based on obtained results recording mode of optically uniform large-size image on the surface of GIA structure was selected, which allowed demonstrating a possibility of formation of different crystalline fractions for tunable multilevel active photonic devices and display application.

## 1. Introduction

Information display systems are currently an important and actively developing area in the field of active photonics. Phase change materials (PCMs) have been widely used for non-volatile tunable optical applications in the visible light range, such as optical switches and modulators [1], light filters [2], metasurfaces and metastructures [3], computer-generated holograms [4], reflective nanopixel display technologies [5] and so on.

PCMs, in particularly $Ge_2Sb_2Te_5$ (GST) thin films, are characterized by rapid reversible structural transformations from amorphous into crystalline states under low-energy thermal, optical or electrical excitation. They have many excellent unique properties, such as high optical contrast (~30%) and low switching time (< 500 ps) between two phase states [6] and non-volatility. These advantages make it possible to develop color multilayer GST/ITO/Al/substrate (GIA) structures for information display systems. In these structures the primary color can be varied in a wide range, according to the thin film interference phenomenon, and is determined by the ITO thickness, and the GST phase state effects on the tint of the GIA structure and its reflectivity.

Dynamic tunability and reversibility in such devices is achieved by laser exposure on GST layer, however the switching modes and operational capabilities of such structures haven't been definitely established. So, the aim of this work is investigation of the crystallization process of the $Ge_2Sb_2Te_5$ thin films by continuous wave (CW) laser crystallization and influence of GST states on the optical properties of GIA structure for tunable multilevel elements for different display application.

## 2. Experiment

The thin films of multylayered GIA structures were deposited on thermally oxidized silicon substrates by the magnetron sputtering. Structural analysis of as-deposited GST films by X-ray diffraction method (Rigaku Smart Lab) shown, that they have an amorphous state.

The layers thicknesses were chosen according to the simulation results so that the color of the GIA structure corresponded to the RGB-colors. The simulation in Mathcad was performed with using of Fresnel's formulas and refractive index n(λ) and extinction coefficient k(λ) obtained by ellipsometry for each layer. In these paper we demonstrate experimental results of red color GIA structure with combination of layers's thiknesses of GST – 10 nm; ITO – 160 nm; Al – 100 nm. The layer thicknesses were controlled by stylus profilometer (KLA Tencor P-7). Reflectivity of formed GIA structure was investigate by spectrofotometry.

CW crystallisation of GST thin film was done by multipurpose equipment (Integra Spectra) including a laser optical system, a scanning electron microscope and a Raman spectrometer. This combination makes it possible to carry out complex research of the surfaces engineering by laser radiation.The formed structures were irradiated by CW laser (λ = 532 nm, $P_{max}$=5 mW, 1 Hz) with energy density in a range from 0.001 to 1.200 mJ/μm$^2$ in a scaning mode. During irradiation, the focus of the laser beam was controlled and checked by focusing on the probe of an atomic force microscope. A focused beam diameter was 1 μm. Structural changes of the modified regions after laser exposure were studied by Raman scattering from the whole area of the irradiated sites. The optical contrast of the modified areas was calculated by changes in reflectivity.

## 3. Results and discussions

Fig. 1 shows the surface of the explored multilayer GIA structure modifying by a CW laser irradiation. The size of formed extended regions corresponds to the scanning area and is 5x5 μm$^2$.

It can be seen that increasing of irradiation energy is accompanied by a monotone change in the surface reflectivity. After CW laser irradiation of the thin film surface all optical changes of the GST films can be divided into 4 different groups (Fig. 2).

The 1$^{st}$ group includes area with no reflectivity changes or with insignificant changes (up to 0.070 mJ/μm$^2$). Raman scattering results for these irradiated areas show that GST thin films are in the initial amorphous state (Fig. 3 (a)).

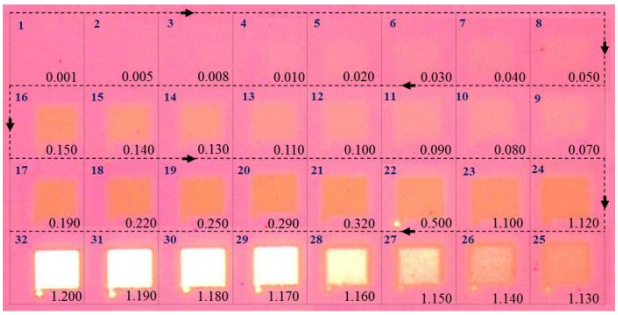


***Fig. 1.*** *The map of formed extended areas on the GIA structure surface after CW laser exposure (point number and energy density (mJ/μm²) marked in the upper left and lower right corners, respectively).*

The 2nd group is extended areas with monotonous decrease of reflectivity (energy density range from 0.07 to 0.22 mJ/μm²). Comparative analysis of the changes in the optical contrast and the differences of the Raman spectra shapes (Fig. 3 (b)) revealed, that these monotonous changes correspond to the phase transition of the GST material from amorphous into crystalline state. The maximum reflectivity changes value during the phase transition is 8 r.u. This difference in optical properties is quite enough to detect states with various crystalline fractions by optical methods which were formed after CW irradiation. It should be noted that the change in optical properties is detected at lower laser fluency than beginning of crystallization process detected by Raman scattering: at 0.07 and 0.11 mJ/μm², respectively. It can be explained by the lower sensitivity of Raman scattering method compared to optical measurements.

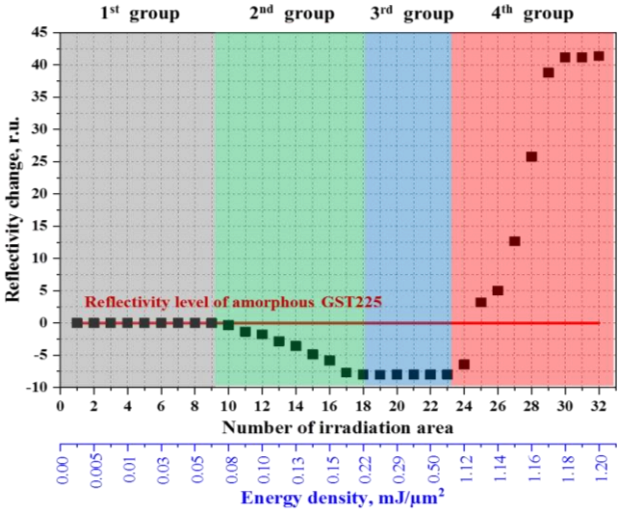


***Fig. 2.*** *Reflectivity of GST thin film after CW laser exposure.*

The 3rd group includes extended regions, the reflectivity within is higher than in the region of the initial amorphous film and doesn't change for energy density in the range from 0.22 to 1.08 mJ/μm². Raman spectra obtained from these areas corresponds to the GST225 spectra in the crystalline state with fcc lattice (Fig. 3 (c), red graph).

In areas exposed to CW irradiation with more than 1.08 mJ/μm² (the 4th group), degradation of the GST material and its partial evaporation are observed. These processes are accompanied by increase in reflectivity. Partial evaporation is confirmed by the decrease of the areas of obtained Raman spectra (Fig. 3 (c), black graph).

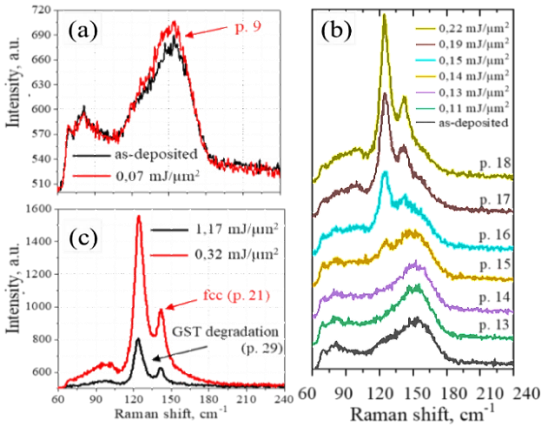


***Fig. 3.*** *Raman spectra of formed extended areas after CW laser irradiation: (a) 1st group is amorphous state; (b) 2nd group is phase transition, (c) 3rd group is fcc state) and 4nd group is degradation of GST material.*

Such complex approach (analysis of changes in optical contrast and Raman spectra) makes it possible to use these multilayer GIA structures for recording of tunable optical images for display application and multilevel optical devices. Optical image in fig. 4 demonstrates the recording a large-size pattern (40x40 μm²) with a maximum contrast after CW laser irradiation with 0.22 mJ/μm².

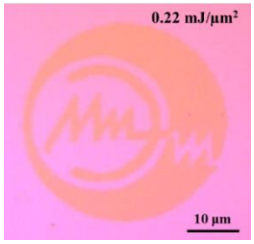


***Fig. 4.*** *The pattern (40x40 μm²) recorded by CW laser.*

## 4. Conclusions

Crystallization processes initiated in GST thin film by CW laser irradiation was investigated. It has been established that the energy range for crystallization of amorphous GST thin film with fcc-structure are in the range from 0.11 to 0.22 mJ/μm². Such laser irradiation leads to the significant changes in the reflectivity and Raman spectra of modified extended areas. Additionally, threshold energy value of GST material degradation was established: degradation begin under irradiation of more than 1.1 mJ/μm². Recording mode accompanied by the formation of optically uniform large-size image on the surface of GIA structure was also determined: the energy density and scanning speed are 0.22 mJ/μm² and 1Hz, respectively. The results of this work demonstrate a possibility of the formation of layers with different crystalline fractions for tunable multilevel active photonic devices and systems of display applications.

## Acknowledgements

This work was supported by Russian Science Foundation (project No. 20-79-10322).

## References

[1] Y. Meng, J.Behera, Y. Ke, L. Chew, Y. Wang, Y. Long, R. Simpson. Appl. Phys. Lett. **113** (2018) 071901.
[2] J. Lee, J. Kim, M. Lee. Nanosc. Adv. **2** (2020) 4930-4937.

[3] C. Galarreta, I. Sinev , A. Alexeev, P. Trofimov, K. Ladutenko, S. Carrillo, E. Gemo, A. Baldycheva, J. Bertolotti, C. Wright. Optica **7** (2020) 476-484.
[4] H. Zhou, Y. Wang, X. Li, Q. Wang, Q. Wei, G. Geng, L. Huang. Nanophotonics **9** (2020) 905-912.
[5] T. Zhou, D. Gao, S. Cao. J. Phys. **1544** (2020) 012034.
[6] A. Lotnyk, I. Hilmi, M. Behrens, B. Rauschenbach. Appl. Surf. Sci. **536** (2021) 147959.

Sixth Asian School-Conference on Physics and
Technology of Nanostructured Materials
Vladivostok, Russia, 25 – 29 April, 2022

**V.o.09**

# Dependence of nanosecond laser damage threshold of metal immersed into water on dynamic of liquid boiling

S.V. Starinskiy*[,1,2], A.A. Rodionov[1,2], Yu.G. Shukhov[1], A.V. Bulgakov[1,3]

[1] S.S. Kutateladze Institute of Thermophysics SB RAS, 1 Lavrentyev Ave, 630090 Novosibirsk, Russia
[2] Novosibirsk State University, Pirogova Str. 2, 630090 Novosibirsk, Russia
[3] HiLASE Centre, Institute of Physics, Czech Academy of Sciences, Za Radnicí 828, 25241 Dolní Břežany, Czech Republic

*e-mail: starikhbz@mail.ru

**Abstract.** Here the nanosecond-laser-induced damage thresholds of tin gold, silver and gold-silver alloys of various compositions in air and water have been measured for single-shot irradiation conditions. The experimental results are analyzed theoretically by solving the heat flow equation for the samples irradiated in air and in water taking into account vapor nucleation at the solid-water interface. The damage thresholds in water for noble metal are found to be considerably higher, by a factor of ~1.5, than the corresponding thresholds in air. While for tin these values are the same. These observations can be explained by the scattering of light by a boiling liquid.

## 1. Introduction

Pulsed laser ablation in liquids (PLAL) is an efficient and flexible technique for colloidal nanoparticles synthesis [1]. The method is universal with respect to particle material and the produced nanoparticles are characterized by high purity when PLAL is performed in water. A variety of complex nanosystems such as alloyed particles with a variable stoichiometric ratio, core–shell nanoparticles, and unique highly active bimetal hydroxide particles, difficult or even impossible to be fabricated by other methods, can be generated by PLAL in a one-step process. Moreover, recent developments of the PLAL technique demonstrate a high productivity of nanoparticle synthesis of industrial-scale production when the method can be more economical than the well-established wet-chemical synthesis [2,3].

Despite widespread use, the many aspects of PLAL are poor understood. The presence of liquid makes the process much more complicated as compared to conventional laser ablation in vacuum or an ambient gas. Apart. Firstly, the liquid medium can participate in the removal of material from the irradiated surface, and secondly, many traditional research methods (mass spectrometry, spectroscopy, etc.) are limitedly applicable. Moreover, many experimental results are controversial. In particular, data on the ratio of damage threshold fluence of materials in air and in water differ in different paper. In present work we compare damage threshold fluence of several metals in air and water. Also modeling of laser heating and vaporization was done to demonstrate the procees taking place in the target and in the water during the laser pulse.

## 2. Experiment & modeling

A five materials were used as the targets, metal tin, gold and silver (both of 99.99% purity) and also two gold-silver alloys with molar gold-silver ratios of 1:1 (AgAu) and 4:1 (AgAu4). The targets was irradiated by pulses of a Nd:YAG laser (1064 nm wavelength, pulse of Gaussian spatial and temporal profiles of 9 ns (FWHM) duration). The peak laser fluence on the target surface was varied in the range 1–13 J/cm2 using a beam attenuator consisting of a half-wave plate and a Glan-Taylor prism. For ablation in water, the sample was immersed into a rectangular glass cuvette (25 ml volume) and irradiated horizontally (through the sidewall and a 10-mm water layer). When calculating laser fluences for PLAL conditions, the attenuation of the laser beam by the cuvette wall and the water layer was taken into account. In order to investigate the water nucleation dynamics under PLAL of metals and, in particular, to evaluate the effect of water vapor on the propagation of the laser beam through the vapor bubble, we have carried out time-resolved pump-probe reflectance measurements for gold irradiation in air and water.

The theoretical analysis of laser-induced heating and melting of the considered metal samples under ambient air and water conditions was performed using a thermal model. The model is based on solving the heat flow equation in its one-dimensional form that allows the time evolution of the temperature profile. In order to estimate the effect of water vaporization in laser induced metal heating, modeling of vapor layer formation near the irradiated surface has been carried out. At the considered extremely high heating rates the dominant bubble generation mechanism is the spontaneous (homogeneous) nucleation due to thermal fluctuations in liquid. Detail of model and experimental setup may be found in [4,5]

## 3. Results and discussions

We systematically measure the damage thresholds of tin, silver, gold, and their alloys in distilled water and in air under nanosecond IR laser irradiation. It was found that the damage thresholds of refractory metals in a liquid is ~ 1.5 times higher than in air. At the same time, the damage thresholds of tin in a liquid is several percent lower than in air. To analyze the obtained results, a numerical simulation was carried out based on the solution of the non-stationary heat conduction equation taking into account heat removal to the liquid, as well as its homogeneous boiling near the target surface.

Good agreement was reached between the experimental values of damage threshold and the calculated values of laser fluence at which materials reach their melting points in air (Fig. 1). The calculated value of damage threshold of refractory metals immersed into liquid were significantly lower than the experimental ones despite of taking into account heat removal from the target and increasing the melting temperature under the influence of water vapor pressure. However, we obtained the good agreement between experimental and calculation result for tin. The observed decrease in the threshold for refused metal in

comparison with the case of irradiation in air was explained by the decrease in the reflection coefficient of immersed in the optical denser medium.

We underline the main difference between tin and noble metals (gold, silver and their alloys) in respect of the ns-PLAL process. The melting temperature of noble metals is higher 1000 K those higher than a water vaporization temperature (~ 600 K) obtained in calculation of ns laser heating of the metal targets immersed in water. So, the refractory metal melting follows after water vaporization which occurs at an early heating stage. Formation liquid-vapor interface near the target surface leads to scattering of a fraction of the incident laser pulse. This assumption are confirmed by a comparison of results probe-beam measurements and calculation data of boiling moment. This results in higher metal damage thresholds than the corresponding values in air. In contrast, the Sn melting temperature is well below 600 K so the laser-induced tin melting occurs before water vapor nucleation and thus before the scattering process starts and leads to energy losses. As a result, the tin damage thresholds in water and air (and in vacuum) are identical. On the other hand, this indicates that, since the water-explosive vaporization under tin ns-PLA usually also occurs early target heating stages, the laser light scattering processes also take place in this case. According to calculation, the energy losses due to the scattering effects can reach up to 30% of the total pulse energy that has to be taken into account when analyzing the PLAL process even for low-melt targets

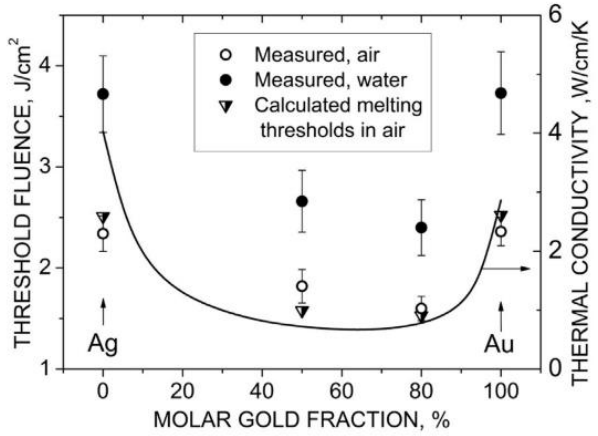


***Fig. 1.*** *The threshold peak fluences for noble metals measured in air and water and calculated for air ambient conditions for all studied samples as a function of gold fraction in the sample. The line shows the data for the thermal conductivity of the gold-silver alloy system.*

## 4. Conclusions

We have systematically investigated the laser-induced single-shot damage thresholds of metals in air and water. The thresholds were determined by measuring the damaged area induced on the surface by a Nd:YAG laser (1064 nm, 9 ns) as a function of laser fluence. The experimental results are analyzed theoretically by solving the heat flow equation for samples irradiated in air and in water taking into account vapor formation at the solid-water interface. The thresholds measured in air agree well with the calculated melting thresholds for all samples implying that metal melting is responsible for the observed surface damage. The damage thresholds of the Au-Ag alloy systems are found to be substantially lower than those for pure metals, both in air and water, explained by lower thermal conductivities of the alloys. For all the investigated metal samples, the thresholds the corresponding values for air. Based on the model calculations for noble obtained in water are considerably, by a factor of ~1.5, higher than it is demonstrated that this difference cannot be explained neither by the conductive heat transfer to water nor by the vapor pressure effect. Scattering of the incident laser light by the vapor-liquid interface is suggested as a possible mechanism responsible for the high damage thresholds in water. This suggestion confirmed by the coincidence of the thresholds for the modification of low-melting tin in water and air. It is shown that the melting of tin occurs before the boiling of the liquid and the scattering of light by vapor does not affect the modification threshold.

**Acknowledgements**

This work was supported by Government of the Russian Federation, State Registration No. 121031800214-7.

**References**

[1] C. Streich, S. Koenen, M. Lelle, K. Peneva, S. Barcikowski, Appl. Surf. Sci. **348**(2015)92.
[2] R. Streubel, S. Barcikowski, B. Gökce, Opt. Lett. **41**(2016)1486.
[3] S. Jendrzej, B. Gökce, M. Epple, S. Barcikowski, ChemPhysChem **18**(2017)1012.
[4] S.V. Starinskiy, A.A. Rodionov, Y.G. Shukhov, E. A. Maximovskiy, A.V. Bulgakov, Appl. Phys. A **125**(2019)734.
[5] S.V. Starinskiy, Y.G. Shukhov, A.V. Bulgakov, Appl. Surf. Sci. **396**(2017)1765.

Sixth Asian School-Conference on Physics and
Technology of Nanostructured Materials
Vladivostok, Russia, 25 – 29 April, 2022 **V.o.10**

# Direct femtosecond-laser imprinting of diffraction-optical elements in $CsPbBr_3$ perovskite microcrystals

A.B. Cherepakhin*[,1], A.Y. Zhizhchenko[1,2], A.P. Porfirev[3], A.P. Pushkarev[4], S.V. Makarov[4], A.A. Kuchmizhak[1]

[1] Institute of Automation and Control Processes FEB RAS , 5 Radio St., Vladivostok 690041, Russia
[2] Far Eastern Federal University, 6 Sukhanova Str., Vladivostok 690950, Russia
[3] Image Processing Systems Institute of the RAS-Branch of FSRC "Crystallography & Photonics" of the RAS, Samara 443001, Russia
[4] ITMO University, St. Petersburg, Russia, 197101

*e-mail: cherepakhinab@yandex.ru

**Abstract.** In this work we demonstrate fabrication of high-quality microscale binary optical elements on surface of chemically synthesized CsPbBr3 perovskite microcrystals using femtosecond-laser projection lithography. We also demonstrate high quality generation of high-order optical vortex beams and nanofocusing capabilities of resulted optical elements. Achieved results shows that CsPbBr3 microcrystals can be used for fabrication of various complex 2D micro-optical elements and holograms by practically relevant and gentle femtosecond-laser direct imprinting.

## 1. Introduction

Halide perovskites recently became a promising class of materials for applications as light-emitting devices and solar cells for their promising combination of optical and optoelectronic properties [1-5]. Inexpensive process of chemical synthesis for fabrication of humidity-robust monocrystalline nanowhiskers and microplates was recently adopted for use in number of applications such as nanoscale coherent light sources and actively tunable micro-optic devices. Tuning ability of the optical properties through vapor-phase anion exchange reaction and ultra-smooth surface of chemically synthesized microcrystals are grate qualities for realization of various micro-optic devises. Common lithography-based fabrication methods such as ion- and electron-beam milling are not only money- and time-consuming for mass production but also cause strong degradation of the perovskite photoluminescence properties if complex modifications in fabrication methods are not being used. Recently, gentle femtosecond (fs)-laser processing appeared as a promising non-destructive approach for perovskite micro- and nano-patterning [6-9]. Additionally, Wang Z et al. recently demonstrated fabrication of Fresnel microlenses in halide perovskite microplates by using direct laser ablation in scanning regime with tightly focused fs-laser pulses [4]. However, the quality of resulted optical elements was not perfect, because typically multi-pulse scanning exposure of the perovskite surface leaving rough deteriorated ablation layer which prevents fabrication of high quality state-of-the-art micro-optical devices.

In this work, we demonstrate fabrication of advanced 2D diffraction-optical elements in chemically synthesized $CsPbBr_3$ perovskite microcrystals via direct imprinting with single-pulse fs-laser projection lithography. In particular, fabrication of micro-scale Fresnel zone plates (FZP) for generation of tightly focused laser beam, as well as binary spiral micro-axicons and binary fork-shaped gratings (FSGs) allowing generation of vortex beams in reflection mode was demonstrated. Ultrafast laser-induced thermalization rate and extremely low conductivity of the $CsPbBr_3$ material resulted in ultra-smooth ablation of perovskite microcrystals. The achieved results highlight the CsPbBr3 microcrystals as a promising material for realization of various complicated 2D micro-optical elements that can be directly imprinted using non-destructive and practically relevant laser technologies.

## 2. Experiment

Synthesized CsPbBr3 microcrystals were patterned by regeneratively amplified Yb:KGW second-harmonic laser system (515 nm central wavelength) with 200-fs laser pulses (Figure 1). By passing laser beam with Gaussian lateral intensity profile through appropriate amplitude mask the complex intensity pattern was generated. Then, this pattern was magnified and placed in focal plane of the dry microscope objective with a numerical aperture (NA) of 0.95 using 4f-optical projection system. The beam shaping amplitude mask were made via direct laser writing in 40 nm-thick Cr films supported by fused silica substrate (CLWS-200). Surface characteristics of resulted perovskite microcrystals with laser patterns was analyzed using optical and scanning electron microscopes (SEM). The focusing performance of the imprinted perovskite micro-optics was studied by irradiating their surface by 515-nm CW collimated beam while the generated intensity profiles were captured in reflection at the corresponding focal plane using the calibrated CCD-camera.

## 3. Results and discussions

We fabricated via fs-laser projection lithography on the surface of CsPbBr3 microcrystals several practically useful designs of binary optical elements such as spiral micro-axicons, FZPs and FSGs (Figure 1). By using corresponding mm-scale Cr amplitude masks and placing them in focal plane of high-NA lens we imprinted all of the optical elements in single-pulse laser regime. First, we made calculations of the mask design for pattering of FZP. Typical FZPs consists of a number of alternating transparent and opaque rings with a specific diameters and widths. The radius of a n-th ring is

$$r_n = \sqrt{n\lambda(f + \frac{n\lambda}{4})} \quad (1)$$

where $n$ is an integer, $\lambda$ is a wavelength of the incident laser radiation. The FZP with10-μm diameter imprinted on the

surface of $CsPbBr_3$ microcrystals is shown in Figure 2(a) revealing smooth geometry of the fabricated radial grooves with typical width of 300 nm and a depth of about 150 nm. Using CW parallel laser beam with wavelength of 515-nm for irradiation of fabricated FZP a tightly focused (1/e-diameter of about 500 nm) laser spot was found few microns above the patterned surface of CsPbBr3 microcrystal showing excellent performance of the imprinted FZP.

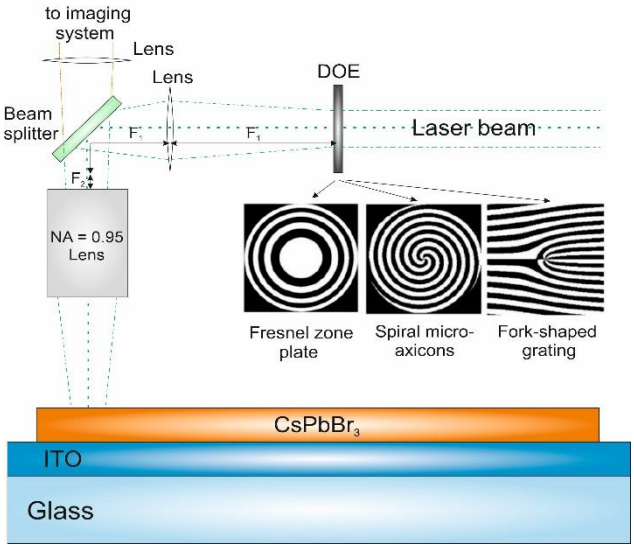


***Fig. 1.*** *Schematic illustration of the setup for fs-laser projection lithography.*

Further, using different amplitude masks we fabricated two types of binary spiral axicons. This type of optical elements can transform Gaussian laser beam into beam with donut-shape intensity profile and a helical wavefront, quasi-non-diffracting optical vortex (OV) or into special type beam with extended focal depth [10]. The main characteristic of the OV beams is their topological charge (TC) *m*, a number of wavefront twists along light propagation axis within a wavelength. In this work, we fabricated two spiral axicons generating the OV beam with the TC *m*=1 and 3. The imprinted micro-optical elements are shown in Figure 2(b,c). Both fabricated optical elements generate OV beam with TC m=1 and 3 above the surface of $CsPbBr_3$ microcrystal at the corresponding focal plane.

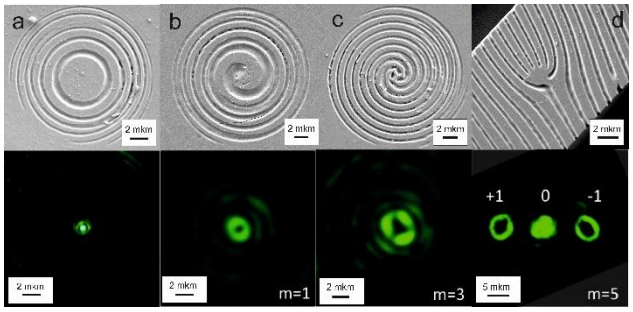


***Fig. 2.*** *Top-view SEM images of the $CsPbBr_3$ microcrystal surfaces imprinted with micro-optical elements including FZP (a), binary spiral axicons (b,c) and binary fork-shape grating (d) as well as there focal-plane intensity distributions at 515 nm punp wavelength showing focusing characteristics of the imprinted 2D perovskite optical elements.*

Finally, we fabricated the FSG. Such optical elements generate OVs with the opposite TCs (±m) in opposite diffraction orders. Theoretical description of Fresnel and Fraunhofer diffraction of a Gaussian laser beam by the FSGs was presented in [11]. We produced the amplitude mask for imprinting of the FSG with such design that resulted pattern allows to generate OV beams with the TCs m=±5. The imprinted perovskite fork-shaped grating is demonstrated in Figure 2d.

## 4. Conclusions

To conclude, we demonstrated high-performing direct fs-laser process for fabricating high-quality reflection-type binary microscale optical elements such as Fresnel zone plates, binary fork-shaped gratings and binary spiral micro-axicons used for generation of tightly focused laser beams and vortex beams generation.

## Acknowledgements

This work was supported by Russian Science Foundation (Grant No. 19-19-00177).

## References

[1] X. Yang, J. Wu, T. Liu, and R. Zhu, 2018 Small Methods 2(10), 1800110.
[2] Fu Y., Zhu H., Chen J., Hautzinger M. P., Zhu X. Y., and Jin S., 2019 Nat. Rev. Mater. 4(3), 169–188.
[3] Wang K., Xing G., Song Q., and Xiao S., 2021 Adv. Mater. 2000306.
[4] Wang Z., Yang T., Zhang Y., Ou Q., Lin H., Zhang Q., Chen H., Hoh H.Y., Jia B., Bao Q., 2020 Adv.Mater. 32, 2001388.
[5] Berestennikov A.S., Voroshilov P. M., Makarov S.V., and Kivshar Y.S., 2019 Appl. Phys. Rev. 6(3), 031307.
[6] Zhou C., Cao G., Gan Z., Ou Q., Chen W., Bao Q., Jia B. and Wen X., 2019 ACS Appl. Mater. Interfaces 11 26017–26023.
[7] Zhizhchenko A, Syubaev S, Berestennikov A, Yulin A V, Porfirev A, Pushkarev A, Shishkin I, Golokhvast K, Bogdanov A A, Zakhidov A A, and Kuchmizhak A A 2019 ACS nano 13(4) 4140-4147Y.
[8] Zhizhchenko A Y, Tonkaev P, Gets D, Larin A, Zuev D, Starikov S, Pustovalov E V, Zakharenko A M, Kulinich S A, Juodkazis S, and Kuchmizhak A A 2020 Small 16(19) 2000410.
[9] Zhizhchenko A.Y., Cherepakhin A.B., Masharin M., Pushkarev A., Kulinich1 S.A., Porfirev A., Kuchmizhak A.A., and Makarov S.V., 2021 Laser Photonics Rev. (accepted manuscript).
[10] Heckenberg N. R., McDuff R., Smith C. P., and White A. G., 1992 Opt. Lett. 17, 221-223.
[11] Janicijevic L. and Topuzoski S., 2008 J. Opt. Soc. Am. A 25, 2659-2669.

Sixth Asian School-Conference on Physics and
Technology of Nanostructured Materials
Vladivostok, Russia, 25 – 29 April, 2022



# Electrically-controlled deposition onto a hybrid superhydrophobic/superhydrophilic surface

G.P. Pavliuk*,[1], A.Y. Zhizhchenko[2], O.B. Vitrik[2]

[1] Far Eastern Federal University, 8 Sukhanova St., Vladivostok 690950, Russia
[2] Institute of Automation and Control Processes FEB RAS , 5 Radio St., Vladivostok 690041, Russia

*e-mail: georgii.23542@gmail.com

**Abstract.** Recently, sensors using surface-enhanced Raman scattering (SERS) detectors combine with superhydrophobic/superhydrophilic analyte concentration systems showed the ability to reach the detection limits less than femto-molar level. However, a further increase in the sensitivity of these sensors is limited by the impossibility of the concentration systems to deposit the analyte on an area of less than 0.01 mm$^2$. This article proposes a fundamentally new approach to the analyte enrichment, based on the effect of non-uniform electrostatic field on the evaporating droplet. This approach, combined with optimized geometry of a superhydrophobic/superhydrophilic concentration system allows more than a six-fold reduction of the deposition area. Potentially, this makes it possible to improve the detection limit of the plasmonic sensors by the same factor bringing it down to the attomolar level.

## 1. Introduction

Various fields of microbiology, biochemistry, medicine require development the techniques that allow to carry out express detection substances in their aqueous solutions at ultra-low concentration [1]. Significant attention in these studies is given plasmonic sensors, mainly due to their, non-invasiveness, and ultra-high sensitivity [2].

Performance plasmonic sensors may be significantly increased by a targeted deposition of analyte molecules on the surface of a sensitive element. One of the effective ways to achieve this is to use superhydrophobic surfaces (SHPS). Due to low adhesion of SHPS, the contact line of a droplet of aqueous solution slides over such surface during evaporation. As a result, the analyte is localized in extremely small area, thereby providing a high deposition density. This makes it possible to increase sensitivity of plasmonic sensors [3].

The highest analyte localization results is demonstrated by hybrid superhydrophobic structures with superhydrophilic central target. Despite the fact that specific implementations of this hybrid superhydrophobic/superhydrophilic structures with a central target may vary considerably in the materials used and in the details of the surface design, they all currently demonstrate a similar limit for minimizing the analyte deposition area, which is about 0.01 *mm*$^2$ [4].

In this work demonstrate more than six-fold reduction in the deposition area achieved by action a non-uniform electrostatic field on evaporating electrically neutral droplet. Geometry modification of the hybrid superhydrophobic/superhydrophilic structures in case of the electrostatic action is also demonstrated.

## 2. Experiment

To create superhydrophobic peripheral part of the hybrid structures we use a single piece substrate of polytetrafluoroethylene (PTFE) on the surface of which superhydrophobic pillars are made by direct femtosecond (fs)-laser printing (Fig. 1a) [5]. Moreover, the surface of these pillars in the process of laser ablation additionally acquires a multimodal roughness. As a result, value of the contact angle at such peripheral part is very large - about $\theta \sim 164^0$. The central target is also formed due to (fs)-laser printing (Fig. 1b) in the form of a larger pillar with a nano-rough surface, which is then covered with thin layers of Ti, Au, and SiO2 (Fig. 1c) to make its sur-face superhydrophilic (Fig. 1d).

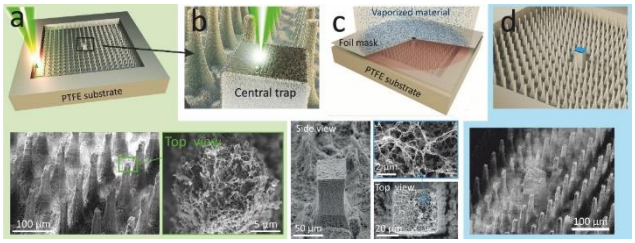


***Fig. 1.*** *Manufacturing process of the initial design LITHS/S-structures. (a) manufacturing of the peripheral superhydrophobic pillars by laser pulses of 0,3 μJ, (b) manufacturing of nano-rough relief of the central target by laser pulses of 0,1 μJ, (c) coating the target in layers Ti, Au, and SiO2 by electron beam sputtering through a mask (d) manufactured LITHS/S- structure.*

We assume that falling of a droplet into the cavity formed on the modified LITHS/S-structure can be avoided when there is an additional vertical force that acts on the droplet, which can compensate for the lack of capillary force. To create such a force, we propose to place an electrically neutral evaporating droplet in a non-uniform electrostatic field (NEF). Due to the polarization of water in the electric field, the drop acquires a dipole moment and subsequently this dipole begins to "pull up" into the region with a higher NEF gradient. The region with a higher NEF gradient is located so that the droplet tends upward, to compensate for the lack of capillary force.

In this work, the NEF is created by applying a potential difference to the upper and lower disc Cu electrodes that are significantly different in diameter (Fig 2a). In this case, the droplet and the substrate are isolated from the electrodes. The droplet is insulated by an air gap, and the PTFE surface is insulated with a polytetrafluoroethylene layer and an additional glass plate (the latter is also needed in order to shift the droplet center slightly upward to the region with a slightly higher NEF gradient). The insulation is needed in order to avoid changing the wetting PTFE surface under the action of the charges flowing into the contact area of the droplet, and substrate. This electrowetting effect, as discussed below, may arrest the process of evaporative reduction of the contact region, which is undesirable for the problems being solved.

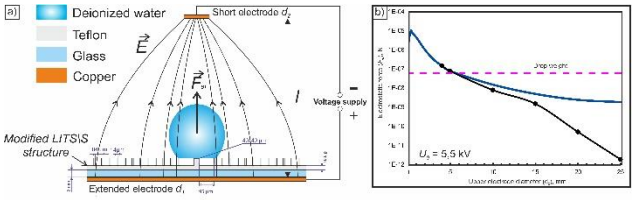


***Fig. 2.*** *A system for droplet evaporation in a non-uniform electrostatic field (a) (for clarity, the scale is not observed) (b) illustrates the dependence of the electrostatic force acting on the droplet by diameter of the upper electrode. Solid curve - analytical results, numerical simulation data are shown by dots.*

If the electric field gradient is constant or changes little within the droplet size, the force of electrostatic action on the droplet can be calculated as

$$\mathbf{F_{el}} = \pi \frac{D_{water}^3}{8} \varepsilon_{air} \frac{\varepsilon_{water} - \varepsilon_{air}}{\varepsilon_{water} + \varepsilon_{air}} \nabla \mathbf{E^2} \qquad (1)$$

where E – field strength; $D_{water}$ – droplet diameter; $\varepsilon_{water}$ – dielectric constant of water; $\varepsilon_{air}$ – dielectric constant of air; $\nabla$ – gradient operator. Analytical calculation of the NEF distribution and the corresponding electrostatic force $F_{el}$ is performed using the method of images.

## 3. Results and discussions

Since the total duration of the formed pulse turns out to be significantly shorter than the total duration of the evaporation final stage (equal to $\approx 300$ *s* at $V_0 = 5$ *μL*), the choice of the pulse timing is of great importance. In order to successfully transfer the contact line to the target, it is necessary to choose the onset of the pulse in such a way that the voltage peak is reached a few seconds prior to than the time of natural separation $\tau_{2\rightarrow}$ of the contact line from the row of pillars $R_{g+2}$. In this case the evaporation of a 5 *μL* droplet with a dissolved Rhodamine 6G (R6G) organic dye used as an analyte at initial concentration $10^{-12}$ *mol/L* illustrated in Fig. 3.

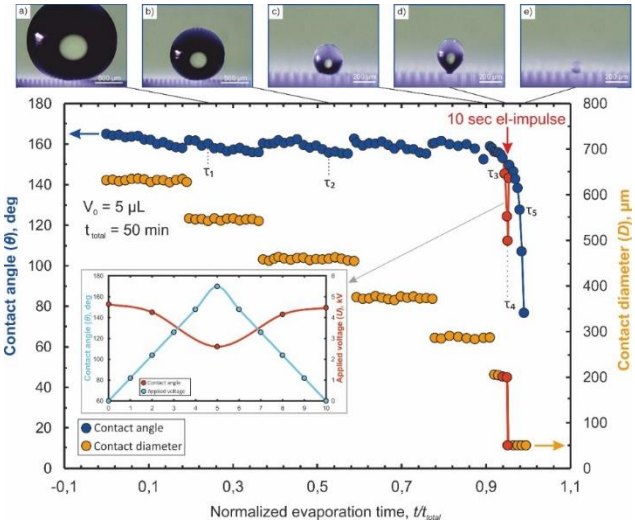


***Fig. 3.*** *Changes in CD and CA depending on the normalized evaporation time on a modified LITHS/S-structure (g = 40 μm, Λ = 84 μm, d = 14 μm) with action a pulse of non-uniform electric field. Insets (a-e) - photomicrographs of a droplet at different evaporation moments. Inset at the bottom - change in CA under electrostatic action, the time on the axis is counted from the moment the interelectrode voltage pulse supply/*

As can be seen from Fig 3, from the moment the NEF is switched on CA decreases as the interelectrode voltage increases, the, which, according to expression (1), leads to an accordingly increase in the depinning force directed to the target. Microscopic observations (inset "c" in Fig 3) show that at this time the droplet is elongated (which is the direct reason for the decrease in CA) and rises upward. At the moment when the maximum voltage is reached, the droplet is detached from the pillars of the $R_{g+2}$ row and the contact line is completely transferred to the surface of the central target (inset "d" in **Ошибка! Источник ссылки не найден.**3). This transition is accompanied by a leap in the CA up to a value close to the initial one, but not yet equal to it, since the droplet still retains its elongated shape under the action of the field. Further, as the voltage decreases, the CA is restored to its initial value, but this happens when the droplet is already entirely on the target surface. The droplet continues to be located on the target even after the field stops acting (inset "e" in Fig 3), as a result of which all the analyte is deposited on the surface of the target

## 4. Conclusions

It is presented a fundamentally new technique that allows control the evaporation of an uncharged liquid droplet on a hybrid superhydrophobic/superhydrophilic surface due to the action of a non-uniform electrostatic field. The analyte enrichment system, obtained by combining this approach with a special design for laser-textured hybrid superhydrophilic-superhydrophobic platforms, outperforms any other analyte enrichment system currently available and allows to realize targeted delivery of molecules of the substance to areas less than 0.0016 $mm^2$. This result is more than six times less than recently achieved of 0.01 $mm^2$ deposition area. It potentially makes possible to reach corresponding additional increase in the sensitivity of plasmonic sensors based on SERS, as well as to significantly increase the reliability and accuracy of the measurements at atto-molar level. We believe that the approach has presented likely to be used for trace chemical detection in many areas.

## References

[1] Deng, Z., et al., *Preparation of hierarchical superhydrophobic melamine-formaldehyde/Ag nanocomposite arrays as surface-enhanced Raman scattering substrates for ultrasensitive and reproducible detection of biomolecules.* Sensors and Actuators B: Chemical, 2019. **288**: p. 20-26.

[2] Kneipp, K., et al., *Single molecule detection using surface-enhanced Raman scattering (SERS).* Physical review letters, 1997. **78**(9): p. 1667.

[3] Luo, X., et al., *Atto-Molar Raman detection on patterned superhydrophilic-superhydrophobic platform via localizable evaporation enrichment.* Sensors and Actuators B: Chemical, 2021. **326**: p. 128826.

[4] Zhizhchenko, A., et al., *On-demand concentration of an analyte on laser-printed polytetrafluoroethylene.* Nanoscale, 2018. **10**(45): p. 21414-21424.

[5] Pavliuk, G., et al., *Ultrasensitive SERS-based plasmonic sensor with analyte enrichment system produced by direct laser writing.* Nanomaterials, 2020. **10**(1): p. 49.

Sixth Asian School-Conference on Physics and
Technology of Nanostructured Materials
Vladivostok, Russia, 25 – 29 April, 2022



# Boosting photoluminescence of infrared-emitting quantum dots coupled to plasmonic nanoarrays

A.A. Sergeev*[,1], D.V. Pavlov[1,2], K.A. Sergeeva[1], A.A. Kuchmizhak[1,2]

[1] Institute of Automation and Control Processes FEB RAS , 5 Radio St., Vladivostok 690041, Russia
[2] Far Eastern Federal University, 8 Sukhanova St., Vladivostok 690950, Russia

*e-mail: sergeev@iacp.dvo.ru

**Abstract.** Control over the radiative and non-radiative channels of the IR-emitting quantum dots (QDs) is crucially important to improve performance of related devices. Here, we study spontaneous photoluminescence (PL) enhancement of mercury telluride QDs coupled to plasmonic nanoantenna arrays supporting collective plasmon mode spectrally matching QD's PL spectrum. Our systematic studies revealed how PL enhancement varies with QDs layer thicknesses as well as laser excitation and emission collection conditions, providing deeper insight into the QD/plasmonic arrays interaction.

## 1. Introduction

To date, near-infrared emitting quantum dots (QDs), namely mercury telluride (HgTe), are considered the most promising candidate for developing novel light-emitting and photodetecting devices covering range from short- to long-waves. However, some factors are reducing the performance of QD-based devices: fundamental limitation on the rate of spontaneous emission; nonradiative recombination centers, arising from the QD's structural and surface defects; nonradiative excitation energy transfer due to resonance energy transfer in the closely packed film once QDs deposited on a substrate.

Previously [1], we have shown that most of these factors can be overcome through combining QDs with plasmonic structures having the resonances spectrally matching with the excitation or emission bands of a QD, leading to noticeable QDs photoluminescence (PL) enhancement. In this work, by varying the QD layer thickness we consequently studied the effect of excitation and emission collection conditions on PL enhancement.

## 2. Experiment

The details for plasmonic metasurfaces fabrication and quantum dots synthesis can be found elsewhere [1, 2]. Briefly, the plasmonic structures were fabricated through direct ablation-free laser nanopatterning of 50 nm-thick gold film on a glass substrate. Once laser pulse shoots gold film, it locally melts and, following processes of dewetting and resolidification, result in bump-like structure formation, which is partially de-attached from the substrate keeping at the same time the film consistency (inset in Fig. 1). The ordered arrays of nanobumps demonstrate complex resonance spectra formed by first-order lattice plasmon resonance (FLPR) in the infra-red region (the peak near 1.5μm, blue curve in Fig. 1) and a superposition of high-order lattice plasmon resonances and localized plasmon resonances of isolated nanobumps in the visible range. The FLPR position depends on the nanobump' size and array' period, while visible-range resonances mostly keep in the same spectral range, probably due to the abovementioned complicated nature.

In its turn, HgTe QDs were synthesized via selective-grow cold injection technique allowing precise control of QDs size and, correspondingly, the PL spectral maximum. As a result, a batch of HgTe QDs with emission, spectrally overlapping FLPR had obtained (Fig. 1).

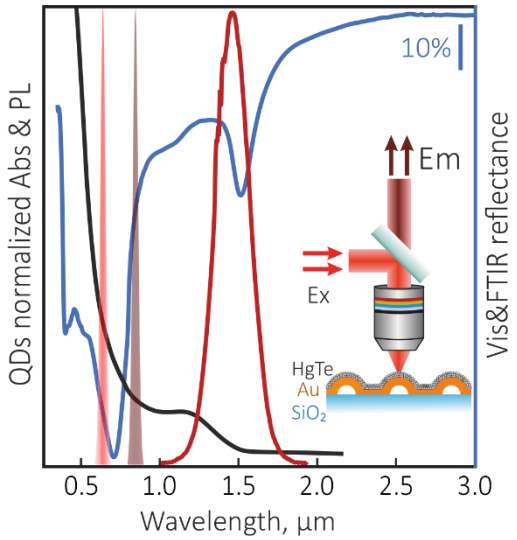


***Fig. 1.*** *Absorption/photoluminescence (black and red curves) spectra of HgTe QDs as well as reflection spectra (blue curve) of plasmonic structures used in this study. HgTe QDs spectra were normalized at maximum value within given spectral range. The scheme of the experiment is shown in the inset.*

To track the PL enhancing phenomena evolution with QDs layer thickness, the as-prepared solution was diluted down to $10^{11}$ dots/ml and deposited on spinning at 1000 rpm substrate. According to atomic-force microscopy, the deposition technique allows to apply a monolayer of the QDs, with an exponential increase of subsequent layer' thickness reaching a 1-μm (that corresponds to the height of the bumps) after the 10-th deposition cycle.

The experimental studies were carried out on F900 (Edinburgh Instruments) spectrometer combined with a home-built micro-PL setup. To estimate the impact of excitation from plasmon resonances in the visible range, the solid-state lasers emitting at 685 and 880nm were used as excitation sources (shaded peaks in Fig. 1). Newport M-series microscope lenses with NAs ranging from 0.1 to 1.2 were used for excitation and emission collection.

## 3. Results and discussions

Owing to strong angular dispersion [3], Q-factor (e.g., ratio of full width at half maximum of the reflection dip and the corresponding wavelength at the dip minimum) of the collective plasmon resonances depends on the range of incident angles of the pump radiation that is defined by the

NA of the focusing lens. Noteworthy, the highest Q-factor (≈10) of as-prepared nanobumps array FLPR was achieved upon measuring the reflection spectra with low-NA optics (NA=0.25), followed by its broadening and decreasing in intensity with NA increasing. At excitation with NA=1.2, the FLPR becomes almost indistinguishable from the reflection spectra of the smooth gold film.

By applying QDs over plasmonic nanostructures the FLPR position linearly redshifts to 2 nm per each 1 nm of the deposited QD layer [4]. Linear dependence is preserved up to 100-nm thick layer, meanwhile for thicker layers the FLPR broadens (starting from 20 nm-thick layer) making detection of its spectral position complicated. For a monolayer of the QDs the PL intensity is comparable to those measured from the same layer capping smooth Au film used as a reference for normalization. This feature indicates plasmon-mediated quenching of the quantum emitter's PL via non-radiative decay in the vicinity of metallic surface. Further increase of the layer thickness leads to a sharp increase of PL enhancement factor to ≈13 achieved for 12-nm thick layer thickness at NA = 1.2. Noteworthy, for the lowest tested NA=0.25 maximal, 5-fold, PL enhancement occurs for 50-nm thick QDs layer. Systematic measurements performed for intermediate NA values give the maximal PL enhancement achieved for QD layer with the thickness ≈ 20-30 nm.

Noteworthy, for the smooth Au film reference once the layer is relatively thin (12-15 nm that corresponds to 4-5 QDs monolayers), PL increases linearly with QD thickness irrespectively of the used NA. Within the 20-70 nm thickness range, PL grows with the lower slope. This indicates that at a given thickness, non-radiative charge transfer between QDs starts to dominate over radiative processes suppressing the "effective" emission from the QDs layer. Increasing layer thickness leads to achieving some equilibrium between radiative and non-radiative processes, resulting in resuming of PL increasing. At the same time, PL intensity of the QDs covering nanostructure array grows monotonically at least up to twice higher thickness (for NA = 1.2), and even after that, no sharp changes in its trend had observed. This behavior allows suggesting the suppression of non-radiative charge carriers' recombination channels once the QD is coupling to a plasmonic structure. On the other side, the absence of PL enhancement for thin QD layers highlights the existence of quenching processes through intrinsic plasmonic losses, which probably decays in a range between 6 to 12-nm layer thickness (2 – 4 QD monolayers), wherein excitation with any NA leads to PL enhancement. The results also highlight that QDs capping smooth Au film emit light predominantly in a vertical direction, resulting in absence of the PL enhancement dependence versus collection angle, in a sharp contrast to the QDs on the plasmonic nanostructure array.

Combining the results obtained, one can conclude that achieving the maximal PL enhancement requires the reduction of non-radiative channels, both plasmonic and QDs intrinsic nature. In this regard, the only way to fulfill these issues is to use a thin, up to 20 nm QDs layer separated from plasmonic structures with a spacer layer no less than 6-nm thickness.

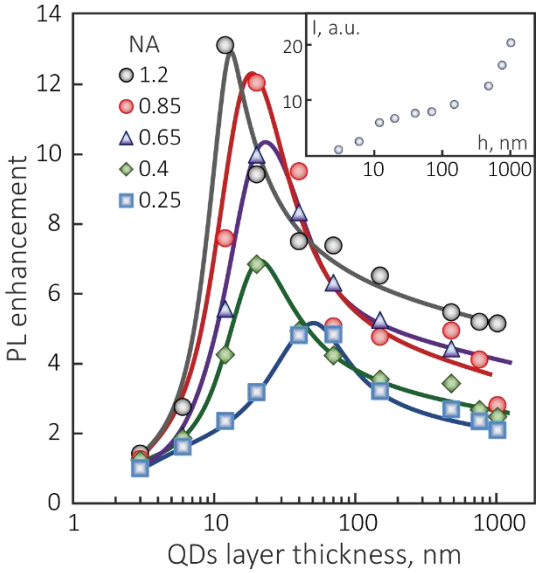


***Fig. 2.*** *PL enhancement factor versus the QDs layer thickness measured for various NAs of the focusing lens used for excitation and emission collection. Insert shows the PL intensity dependence on QDs layer thickness measured from smooth gold film and normalized on thinnest layer PL intensity.*

## 4. Conclusions

We demonstrated that careful adjustment of excitation and emission collection parameters leads to more than an order of magnitude enhancement of spontaneous emission of HgTe QDs coupled with periodical plasmonic arrays with resonances spectrally matched to QDs absorption and emission bands. The region of QDs layer thickness, wherein plasmon-related quenching and dot-to-dot resonance energy transfer have the minimal impact and, hence the PL enhancement has the maximal factor, had been determined.

## Acknowledgements

The financial support from the Russian Science Foundation (#21-79-10197) is gratefully acknowledged.

## References

[1] A.A. Sergeev, D.V. Pavlov, A.A. Kuchmizhak, M.V. Lapine, W.K. Yiu, Y. Dong, N. Ke, S. Juodkazis, N. Zhao, S.V. Kershaw, A.L. Rogach. Light: Sci.&App. **9**(2020)16.

[2] S.V. Kershaw, W.K. Yiu, A. Sergeev, A.L. Rogach. Chem. Mater. **32**(2020)3930.

[3] V. G. Kravets, A.V. Kabashin, W.L. Barnes, A.N. Grigorenko. Chem. Rev. **118**(2018)5912.

[4] D.V. Pavlov, A.Yu. Zhizhchenko, M. Honda, M. Yamanaka, O.B. Vitrik, S.A. Kulinich, S. Juodkazis, S.I. Kudryashov, A.A. Kuchmizhak. Nanomaterials. **9**(2019)1348.

Sixth Asian School-Conference on Physics and
Technology of Nanostructured Materials
Vladivostok, Russia, 25 – 29 April, 2022



# Black silicon with functional luminescent organic monolayer enabled by direct femtosecond-laser printing

Yu.M. Borodaenko*,1, S.O. Gurbatov1,2, A.Yu. Mironenko3, M.V. Tutov3, A.A. Kuchmizhak1,2

[1] Institute of Automation and Control Processes FEB RAS , 5 Radio St., Vladivostok 690041, Russia
[2] Far Eastern Federal University, 8 Sukhanova St., Vladivostok 690950, Russia
[3] Institute of Chemistry of FEB RAS, 159, Prospekt 100-letiya, Vladivostok, 690022, Russia

*e-mail: serbm@mail.com

**Abstract.** Here, we demonstrated fabrication of anti-reflective surface textures on crystalline Si locally functionalized with a photoluminescent molecular nanolayer via single-step femtosecond laser ablation. Laser ablation allows to produce hierarchical surface morphology exhibiting remarkable broadband light-absorbing properties and creates optimal conditions for local morphology functionalization by light-emitting Rhodamine 6G nanolayer. Developed anti-reflecting surface morphology facilitates optical excitation of the Rhodamine 6G resulting in multi-fold enhancement of its spontaneous emission. Our approach holds promise for realization of the multi-purpose photoluminescent chemosensor arrays functionalized with various organic quantum emitters.

## 1. Introduction

Detection of analytes at ultra-low concentrations is an actual problem and important applied task for environmental monitoring, medical diagnostics, microbiology and forensic analysis. The nanostructures attracted great attention due to their extraordinary properties, which offer great promise in the development of chemosensing, facilitating the great improvement of the selectivity and sensitivity of the current methods. In particular, the structures with dimensions smaller than the optical wavelength are capable of sharply amplifying weak electromagnetic fields incident on the surface. The enhancement of electromagnetic radiation amplitude can be observed near the tips of the nanostructures as well as within nano-gaps. This feature allows to use nanotextured surfaces to create compact, efficient and highly sensitive optical sensors [1]. Silicon represents inexpensive earth-abundant material widely used for optoelectronic and photonic applications. Modification of the Si surface using femtosecond laser radiation is an inexpensive high-rate technological process and easy-to-implement scalable fabrication procedure of homogeneous nanotextured surfaces exhibiting feature size below the optical diffraction limit [2]; it is not a multi-step process and not require using masks as for many chemical methods for fabrication of the sensor elements.

Here, we proposed single-step technology allowing to locally bind the organic light-emitting nanolayer in the process of Si surface nanotexturing by fs-laser pulses. Resulting anti-reflecting nanostructures facilitate excitation of the Rhodamine 6G resulting in multi-fold enhancement of its spontaneous emission rate making the developed approach promising for realization of chemosensor arrays.

## 2. Experiment

The structures were fabricated by second-harmonic (λ=513 nm) 200-fs laser pulses generated at pulse repetition rates of 1 KHz. Laser processing of the Si surface was performed at variable pulse energies (tens of nJ), scanning speeds was 100 μm/s at single pass regime, the lateral interval between laser scanning lines was 1 μm); the electric-field polarization vector was oriented parallel to the scan direction [3]. Laser beam was focused on the Si surface by a dry microscope objective with a numerical aperture (NA) of 0.4, yielding in a focal spot size of ≈1.5 μm. Laser-treated surface area was first processed following a snake-like trajectory along one direction and then, the textured area was laser scanned again along the orthogonal direction with the same lateral interval. Laser processing parameters allow to control the features of surface morphology modification and to chose the necessary conditions for obtaining structures with the specified characteristics. The samples were processed in a cuvette completely filled of solution with Rhodamine 6G mixed with 95% methanol. The thickness of the liquid layer above the Si surface was 4 mm. The fabricated sensor elements were investigated by scanning electron microscopy (SEM), correlated reflection amd photoluminescence spectroscopy carried out at 473 nm laser pump.

## 3. Results and discussions

The laser-textured surface structures on Si (Fig. 1(a)) with the of 50×50 μm$^2$ were fabricated in solution containing functional derivative of Rhodamine 6G dye bearing triethoxysilyl anchor groups by 200-fs linearly polarized laser pulses at pulse energy ≈30 nJ and repetition rate 1 KHz. Lateral interval between laser scanning lines was 1 μm, while the scanning speed was fixed at 100 μm/s.

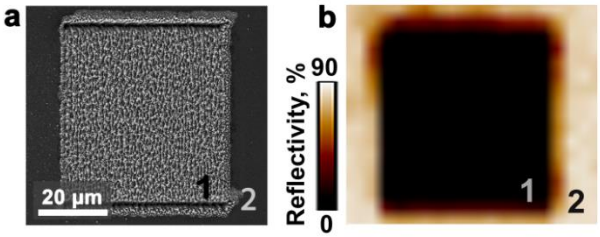


***Fig. 1.*** *Correlated SEM (a) and confocal laser reflection (b) images of the laser-textured area functionalized with Rhodamine 6G nanolayer.*

The fabricated surface textures were found to demonstrate remarkable anti-reflecting properties (Fig. 1(b)). The reflection at 473 nm wavelength used for confocal scanning of the textured area drops from ≈50% for non-textured Si to around 2% upon its texturing with fs-laser in the functionalizing solution. Low reflectivity of the laser-textured Si originates from the enhanced light

absorption by the multi scale surface features as well as gradual decrease of the interface jump of the refractive index by the densely arranged nanoscale surface features. This allows the pump laser radiation to couple the surface features more efficiently resulting in more efficient excitation of the capping Rhodamine 6G nanolayer [4]. This results in averaged 20-fold enhancement of the spontaneous emission (centered at 570 nm) from the Rhodamine 6G nanolayer capping the laser-textured area with respect to noise-like signal observed for surrounding smooth Si area (Fig. 2(a,b)).

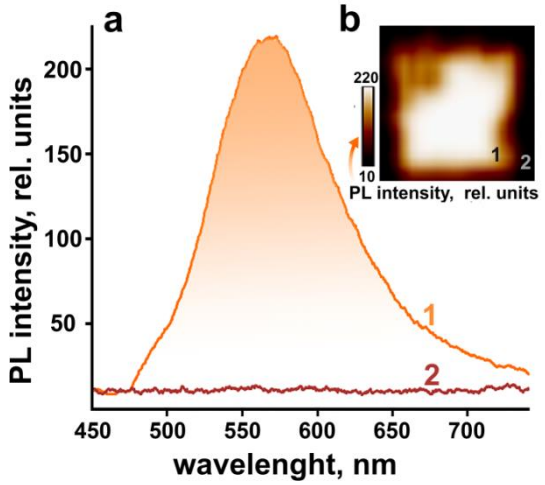


***Fig. 2.*** *Photoluminescence spectra and corresponding photoluminescence map of the Rhodamine 6G capping laser-textured (1) and smooth (2) surface sites. The map size is 80×80 μm². The laser pump at 473 nm was used.*

Characteristic photoluminescence also confirms the local binding of the molecules to the fabricated nanotextured Si surface. The enhanced photoluminescence of the Rhodamine 6G can be related to the improved photoexcitation via decreased Fresnel reflection at the interface, local field enhancement of the pump radiation by nanoscale surface features as well as enlarged surface area increasing density of quantum emitters per surface area. Additionally, non-metal surface morphology structures do not suffer from the photoluminescence quenching as opposed to plasmonic nanostructures [5]. The physical representation of locally attaching a functional compound as shown in [6]: the interacting with a high energy laser pulse, local temperatures reach high values, allowing silicon to actively interact with water in our 95% methanol solvent. After laser processing the surface immediately interacted with water to form surface silanol groups (Si–OH). Then, at still relatively high temperatures, these surface groups condensed with alkoxy (Et–O–Si) and hydroxy (HO–Si) groups of functionalizing compound to form Si–O–Si bonds via either alcohol or water elimination. Such covalent bonding of sensory compounds to substrates provides easier access for the analyte to the sensitive receptors and preventing removing of sensory compound in solutions analysis.

## 4. Conclusions

The surface functionalization of Rhodamine 6G at the process of fs-laser texturing on crystalline Si is demonstrated. The improved optical characteristics of chemosensor, such as low average reflectivity and high refractive index of hierarchical structures, are able to amplify the small signal from thin attached layers of the sensory photoluminescence compound. The presented direct laser nanotexturing technology is promising for the manufacture of a multifunctional "pixelated" chip containing different photoluminescent molecules locally attached to specific nanotextured surface sites ("pixels").

## Acknowledgements

This work was supported by Russian Science Foundation (grant number 18-79-10091).

## References

[1] A. Kuchmizhak, O. Vitrik, Y. Kulchin, D. Storozhenko, A. Mayor, A. Mirochnik, S. Makarov, V. Milichko, S. Kudryashov, V. Zhakhovsky, N. Inogamov. Nanoscale, **8**(2016)12352-12361.

[2] M. Shen, J. E. Carey, C. H. Crouch, M. Kandyla, H.A. Stone, E. Mazur. Nano Lett. **8**(2008)2087–2091.

[3] A. V. Dostovalov, K. A. Okotrub, K. A. Bronnikov, V. S. Terentyev, V. P. Korolkov, S. A. Babin. Las. Phys. Lett. **16**(2019)026003.

[4] S. Dou, H. Xu, J. Zhao, K. Zhang, N. Li, Y. Lin, L. Pan, Y. Li. Adv. Mater. (2020)e2000697.

[5] E. Mitsai, A. Kuchmizhak, E. Pustovalov, A. Sergeev, A. Mironenko, S. Bratskaya, D. Linklater, A. Balcytis, E. Ivanova, S. Juodkazis. Nanoscale **10**(2018)9780–9787.

[6] Yu. Borodaenko, S. Gurbatov, M. Tutov, A. Zhizhchenko, S. A. Kulinich, A. Kuchmizhak, A. Mironenko. Nanomaterials. **11**(2021)401.

Sixth Asian School-Conference on Physics and
Technology of Nanostructured Materials
Vladivostok, Russia, 25 – 29 April, 2022

**V.p.03**

# Influence of femtosecond laser wavelength and ambient environment on morphology and chemical composition of laser-induced periodic structures on metal films

S. Gladkikh[1], K. Bronnikov[*,1], K. Okotrub[1], A. Simanchuk[1], A.Y. Zhizhchenko[2,3], A.A. Kuchmizhak[2,4] and A. Dostovalov[1]

[1] Institute of Automation and Electrometry of the SB RAS, Novosibirsk, Russia
[2] Institute of Automation and Control Processes FEB RAS, 5 Radio St., 690041 Vladivostok, Russia;
[3] Far Eastern Federal University, 690041 Vladivostok, Russia
[4] Pacific Quantum Center, Far Eastern Federal University, 690041 Vladivostok, Russia

*e-mail: bronnikovkirill@gmail.com

**Abstract.** Thermochemical laser-induced periodic surface structures (TLIPSS) have gained significant research interest due to promising applications, where tunable and upscalable periodic surface morphologies are important, such as surface functionalization, diffraction optics, sensors etc. Since TLIPSS form through the thermally stimulated chemical reaction, their morphology and chemical composition are expected to depend on the incident laser radiation wavelength and ambient environment. However, so far uniform TLIPSS were fabricated using near-IR laser pulses in air. We present the results of TLIPSS formation on the surface of titanium (Ti) films by using fs-laser pulses with near-IR (1026 nm), visible (513 nm) and UV (256 nm) wavelengths in the air, vacuum and nitrogen-rich environment. The linear dependence of the TLIPSS period on the laser wavelength is observed. Raman spectroscopy revealed the presence of TiN along with $TiO_2$ (rutile) prevalence for TLIPSS fabricated in the nitrogen-rich atmosphere.

## 1. Introduction

Laser-induced periodic surface structures (LIPSS) are a periodic relief modulation that forms on the surface of solids upon the impact of high-energy laser radiation [1]. In addition to the more investigated LIPSS formed through ablation of irradiated material, there is another type of LIPSS formed due to thermally stimulated chemical reaction of a material with the ambient environment (oxidation, in the case of oxygen-containing media) – thermochemical LIPSS (TLIPSS). Usually, interference between incident light and the wave scattered from surface defects is used to explain the TLIPSS formation [2]. This interference creates the periodic temperature distribution on the surface, which regulates thermochemical reaction.

Owing to extremely high uniformity achievable with fs near-IR laser pulses, possibility to cover indefinitely large areas by lateral scanning, and relative simplicity of a single-step process, TLIPSS are promising in various practical applications, such as surface functionalization, diffraction optics, sensors, and more [2, 3, 4]. From the application point of view, it is important to control the morphology (period, orientation) of the periodic structures, which is possible through the change of the laser wavelength and polarization direction. However, only near-IR spectral range was utilized for the uniform TLIPSS formation so far. In addition, the thermally stimulated chemical process enables regulation of the chemical composition of TLIPSS by the change of the ambient reactive environment.

In this work, thermochemical LIPSS were formed on titanium films upon fs-laser irradiation with near-IR (1026 nm), visible (513 nm), and UV (256 nm) wavelengths. To study the influence of the ambient environment on both morphology and chemical composition, experiments were carried out in the air, vacuum, and nitrogen-rich atmosphere, when using near-IR pulses.

## 2. Experiment

Samples used in the experiments were a two-layer Ti/$\alpha$-Si film with Ti being the top layer with a thickness of 90 or 180 nm produced by magnetron sputtering on a glass substrate. A femtosecond laser with pulse duration of 230 fs was used to form TLIPSS at 1026, 513, 256 nm wavelength at pulse repetition rate $f$ of 50-200 kHz. The sample scanning speed $\upsilon$ was varied within the range of 1-500 μm/s. The laser fluence $F$ was altered to obtain structures with the best regularity.

Different beam shapes were used in the experiments: astigmatic Gaussian beam at $\lambda$ = 1026 nm, flat-top stripe-shaped beam at $\lambda$ = 513 nm and ordinary Gaussian-shaped beam at $\lambda$ = 256 nm. During the TLIPSS fabrication, samples were contained in a vacuum chamber. Laser processing in vacuum ($10^{-2}$ atm) and nitrogen-rich atmosphere (2.5 atm) was performed at $\lambda$ = 1026 nm.

TLIPSS surface morphology and inner structure were investigated via scanning electron-microscopy (SEM) and focused ion beam (FIB) milling. To analyze the chemical composition, Raman spectroscopy with the laser pumping at 532.1 nm and a 1-μm focal spot was used.

## 3. Results and discussions

The highly regular TLIPSS have been formed on 90 nm thick Ti film upon near-IR laser radiation ($\lambda$ = 1026 nm, $F$ = 90 mJ/cm$^2$, $\upsilon$ = 1 μm/s) in air environment (Fig. 1a). The TLIPSS are oriented along the polarization direction of incident laser radiation and have a period of 853±20 nm. Each protrusion has a width of ≈400 nm and consists of $TiO_2$ nanocrystallites with random orientation (Fig. 1d). The protrusions are mainly composed of the rutile phase according to Raman spectroscopy (see more information below). More details about morphology were obtained from SEM visualization of the transverse cross-sectional FIB cuts (Fig. 1e). The $TiO_2$ starts to grow from the Ti film surface as a result of thermochemical interaction with oxygen. Formed protrusion occupies a larger volume in

comparison to intact film due to the porous structure of rutile nanocrystals and a large Pilling and Bedworth ratio $R_{PB}$ = 1.78 for titanium and its oxide.

When utilizing second-harmonic (λ = 513 nm) radiation, highly uniform TLIPSS were formed having a period of 416±17 nm at υ = 3 μm/s and $F$ = 50 mJ/cm$^2$ (Fig. 1b). The rutile protrusions show smoother surface morphology in comparison to the morphology of the TLIPSS produced with near-IR laser pulses. Similar to the case of near-IR wavelength, faster scanning speed worsens the regularity due to the degradation of the positive interference-based feedback.

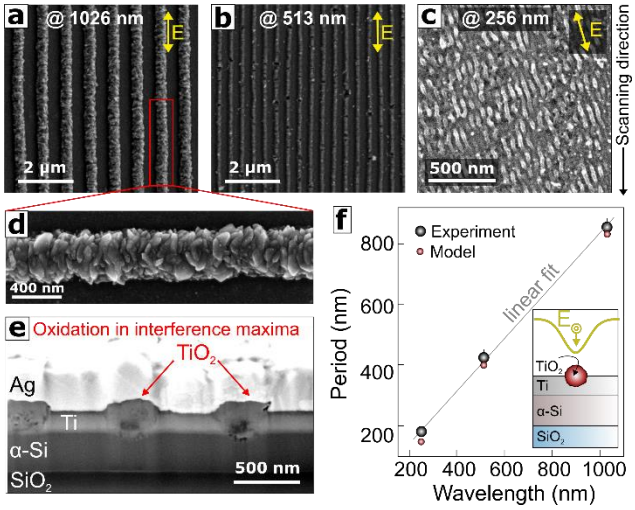


***Fig. 3.*** *Top-view SEM images of TLIPSS structures produced on the 90-nm thick Ti film in air at (a) λ = 1026 nm, (b) λ = 513 nm and (c) λ = 256 nm. A double arrow shows the polarization direction. (d) The enlarged view of the single $TiO_2$ protrusion of structures produced at λ = 1026 nm. (e) SEM image of a cross-sectional FIB cut made perpendicularly to the TLIPSS orientation. (f) Measured and calculated averaged TLIPSS period vs. incident laser wavelength. Inset shows schematic illustration of the modeled geometry.*

Fourth-harmonic (λ = 256 nm) laser pulses were used to further reduce the TLIPSS period. The formation of the structures with the period of 182±22 nm is shown at maximal available laser fluence $F$ = 35 mJ/cm$^2$ and scanning speed of υ = 1 μm/s (Fig. 1c). As in previous cases, the protrusions are oriented along the polarization direction and they have a lesser width of ≈100 nm. In addition, the regularity of the TLIPSS formed at UV wavelength is worse compared to the TLIPSS produced at other harmonics.

The averaged TLIPSS period scales linearly with the wavelength of the incident laser radiation (Fig. 1f). To explain this dependence, we performed finite-element frequency-domain simulations of the scattering of a linearly polarized wave from an isolated $TiO_2$ protrusion as illustrated in the inset in Fig. 1f. The geometry of the protrusion as well as optical properties of $TiO_2$ (including the influence of the porous structure) at different wavelengths were taken into account. The results show a good match with the experimental values confirming the electromagnetic origin of the TLIPSS ordering. To study the influence of the ambient atmosphere on the formation of the TLIPSS protrusions, the following processing parameters have been chosen: $f$ = 200 kHz, $F$ = 70 mJ/cm$^2$, υ = 1 μm/s. The TLIPSS regularity worsens in a vacuum, while additional protrusions are formed between the primary ones, which appears as noise on a 2D-DFT map (inset in **Ошибка! Источник ссылки не найден.**b). The TLIPSS formed in the nitrogen-rich atmosphere have a similar period (≈940 nm) and better ordering (**Ошибка! Источник ссылки не найден.**c).

Raman spectra averaged over multiple surface areas of the produced TLIPSS revealed several bands appearing at 230, 320, 445 and 610 cm$^{-1}$ (**Ошибка! Источник ссылки не найден.**d). They indicate characteristic vibration modes of rutile (except band at 320 cm$^{-1}$). It suggests that oxidation dominates in the formation process even for TLIPSS produced in the nitrogen-rich atmosphere. The line at 320 cm$^{-1}$ is attributed to TiN, which can be seen from the reference Raman spectra of crystalline TiN as well as its amorphous phase. This band is present in the spectrum of TLIPSS formed in the nitrogen-rich atmosphere but undiscerned in the spectra for the TLIPSS formed in air and vacuum.

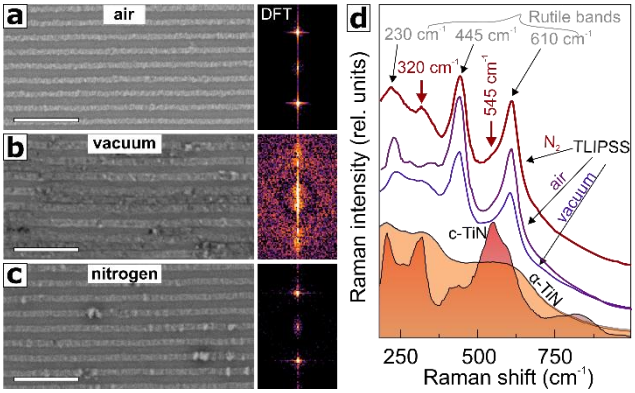


***Fig. 4.*** *SEM images of the TLIPSS formed on the 180-nm thick Ti film in air (a), vacuum (b) and nitrogen-rich atmosphere (c). Insets show 2D-DFT (discrete Fourier transform) images. (d) Averaged Raman spectrum of the TLIPSS produced in the different ambient environments. Raman spectra of amorphous and crystalline TiN are provided for comparison.*

## 4. Conclusions

TLIPSS with periodicity of ≈850, 420 and 180 nm were fabricated on Ti thin films using near-IR (λ = 1026 nm), visible (513 nm) and UV (256 nm) radiation. The linear dependence of the period on irradiating wavelength is demonstrated supported by the numerical simulations. It is shown that the ambient environment influences regularity of the obtained TLIPSS as well as their chemical composition. Raman spectroscopy revealed complex TiN/$TiO_2$ composition with dominating $TiO_2$ (rutile) component for TLIPSS produced in the nitrogen-rich atmosphere.

## Acknowledgements

The work was funded by the Russian Science Foundation grant (No. 21-72-20162). In the research, we used the equipment of the following Multiple-Access Centres (MAC): MAC of the Far Eastern Federal University (FEFU), MAC "High-resolution spectroscopy of gases and condensed matters" at IAE SB RAS.

## References

[1] J. Bonse, J. Krüger, S. Höhm, and A. Rosenfeld. Journal of Laser Applications **24**(2012)042006.
[2] B. Öktem, I. Pavlov, S. Ilday, H. Kalaycıoğlu, A. Rybak, S. Yavaş, M. Erdoğan, and F. Ö. Ilday. Nat. Photon. **7**(2013)897.

[3] A. Dostovalov, K. Bronnikov, V. Korolkov, S. Babin, E. Mitsai, A. Mironenko, M. Tutov, D. Zhang, K. Sugioka, J. Maksimovic, T. Katkus, S. Juodkazis, A. Zhizhchenko, and A. Kuchmizhak. Nanoscale **12**(2020)13431.
[4] J. Bonse, S. V. Kirner, S. Höhm, N. Epperlein, D. Spaltmann, A. Rosenfeld, and J. Krüger. *Laser-Based Micro- and Nanoprocessing XI* **10092** (2017)100920N.

Sixth Asian School-Conference on Physics and
Technology of Nanostructured Materials
Vladivostok, Russia, April 25 - 29, 2022



# Study of the thermal stresses during $TiO_2$ laser annealing on sapphire substrate

Yu.V. Klunnikova[*,1], M.V. Anikeev[1,2], U. Nackenhorst[3], A.V. Filimonov[4]

[1] Southern Federal University, 2 Shevchenko St., Taganrog 347928, Russia
[2] Fraunhofer SIT, Rheinstr. 75, Darmstadt 64295, Germany
[3] Leibniz University of Hanover, Appelstrasse 9a, Hanover 30167, Germany
[4] Peter the Great St. Petersburg Polytechnic University, Politekhnicheskaya St. 29, St. Petersburg 195251, Russia

*e-mail: yvklunnikova@sfedu.ru

Oxide thin films are widely used for the design of functional devices such as photoelectric converters or sensitive elements of gas sensors. Their functionalities depend on the physical properties and on the microscopic interactions at the film/substrate interface [1,2].

The aim of our research is to investigate the thermo-elastic stresses in thin $TiO_2$ films on substrates obtained by laser annealing and to analyze the occurrence and evolution of thermo-elastic stresses and defects in the film-substrate structure and to determine the conditions that prevent cracks formation. It is necessary to find optimal conditions for manufacturing $TiO_2$ films on sapphire substrates for microelectronics application and to improve not only substrate quality but also films characteristics (i.e., reduce defects, improve oxide quality as well as reproducibility and stability of film parameters). The influence of the technological process on thermo-elastic stresses in $TiO_2$ films has been studied experimentally and with computer simulation. We investigate the effects of material properties, thin film structure and processing conditions on the distribution of stresses.

Numerical methods allow us to carry out simulations and determine the optimal parameters and modes of films laser annealing. Two sequential steps have to be performed for the thermo-mechanical stress analysis: (1) a pure thermal analysis which provides temperature and heat flux distributions in space and time, (2) a thermo-elastic analysis to compute the mechanical stresses due to the temperature gradients.

The finite element package ANSYS was used to perform the thermo-mechanical analysis. The temperature history calculation was applied as input for the structural analysis. The transient thermal analysis was performed for the temperature distribution in the titanium dioxide film on the sapphire substrate [3].

For the experimental investigations a thin film of tetraethoxytitanium ($Ti(OC_2H_5)_4$) was brought up onto a sapphire substrate with a thickness of 430 μm by centrifugation (centrifuge SPIN NXG-P1, rotor rotation speed of 2000-3000 rpm, application time of 30 s) [4]. After pre-drying in the oven at 100-120 °C for 15-20 minutes (the solvent and hydrolysis products have been removed from the film before) and laser annealing is carried out using the radiation of a pulsed solid-state Nd:YAG laser with a wavelength of 1064 nm (film temperature of 500-600 ° C, laser beam scanning rate of 1-20 mm/s, laser power of 30-90 W).

The phase composition of the thin film structure was investigated by powder X-ray diffractometry. The material has a phase composition like the rutile modification of titanium oxide.

We calculated the stress distribution in the $TiO_2$ film – sapphire structure caused from laser radiation. The general purpose Finite Element code of ANSYS has been used to simulate $TiO_2$ film – sapphire laser annealing with variation of laser processing parameters such as the scanning speed and laser beam power.

The behavior of stresses in the processed material strongly depends on the temperature gradients. The maximum principal stress indicates the overall stress state of material. When the largest principal stress exceeds the uniaxial tensile strength [5] a crack might be initiated. The tensile strength limit of $TiO_2$ film on sapphire substrate is 333 MPa. If the maximum principal stress is less than the tensile strength limit for titanium dioxide, no cracks formation are expected.

The simulation results indicate that the thickness ratio between the $TiO_2$ film and the sapphire substrate plays an important role in the laser annealing. The capability of the substrate to diffuse the heat from the film enables a proper temperature distribution inside the film, avoiding the overheating of the surface. It has significant influence on defects like cracks formation.

The increase of film thickness from 5 μm to 30 μm decreases the maximum principal stresses. The stress variation induced by the annealing is as much higher as film thickness is low. It is possible to control and vary the value of thermoelastic stresses in the film-substrate structures due to changes of film annealing processing parameters: substrate temperature, laser radiation power, film and substrate thicknesses, pulse duration, sample movement velocity, etc. Thereby one can optimize film properties for the task and device design.

**Acknowledgements**

This work was supported by the Ministry of Science and Higher Education of the Russian Federation and the German Academic Exchange Service (DAAD) within the framework of the joint program “Mikhail Lomonosov”.

**References**

[1] V. Balzano, E. Cavaliere, M. Fanetti, S. Gardonio, L. Gavioli. Nanomaterials **2253**(2021)11.
[2] F. Rubino, A. Astarita, P. Carlone. Coatings **219**(2018)8.
[3] S.P. Malyukov, Yu.V. Klunnikova, A.V. Sayenko. J. of Russian Laser Research **36**(2015)3.
[4] S.P. Malyukov, Yu.V. Klunnikova, A.V. Sayenko, Yu.N. Biyatenko. J. of Civil Engineering and Technology **10**(2019)1.
[5] Y. Wang, Q. Wang, H. Chen, J. Sun, L. He. Materials **794**(2016)9(10).

Sixth Asian School-Conference on Physics and
Technology of Nanostructured Materials
Vladivostok, Russia, 25 – 29 April, 2022



# Electric properties of polarized layer in alkaline silicate glasses

E.Yu. Koroleva*[,1], I. Reshetov[2,3], E. Babich[2,3], S.B. Vakhrushev[1], D. Tagantsev[2,3], A. Lipovskii[2,3]

[1] Ioffe Institute, 26 Politekhnicheskaya, 194021, St. Petersburg, Russia
[2] Alferov University, 8/3 Khlopina, 194021, St. Petersburg, Russia
[3] Peter the Great St. Petersburg Polytechnic University, 29 Politekhnicheskaya, 195251, St. Petersburg, Russia

*e-mail: e.yu.koroleva@mail.ioffe.ru

**Abstract.** Broadband dielectric spectroscopy was applied to study properties and structure of subsurface (anodic) polarized layers in alkaline silicate glasses forming in poling. A model of poled glasses is proposed. It is found that electric properties of the layers essentially depend on the structure of anodic electrode used in glass poling. It is also shown that dielectric response of poled glass samples is mainly determined by the electric properties of the submicron polarized layers and this gives an opportunity to reveal specific properties of the layers rather than ones of the glass sample bulk. Revealed temperature dependence of DC conductivity of the polarized layers obeys Arrhenius's law, and determined activation energy does not depend on the electrode.

## 1. Introduction

Thermal poling of glasses is of interest because of a set of reasons. Poling leads to the breaking of central symmetry of initially isotropic glasses that allows the generation of second harmonic and the Pockels electro-optical phenomenon, as well as to the structuring of glass surface and the formation of optical waveguides and other structures on the surface of poled glasses[1,2]. A powerful technique to study characteristics of materials, including glasses, is the broadband dielectric spectroscopy (BDS), which, basing on impedance measurements in a wide range of frequencies and temperatures, allows getting information about permittivity, conductivity, activation energy and time scale of relaxation processes taking place in materials under study. In this paper, we apply this technique to characterize behavior of differently poled glasses.

## 2. Experiment

In performed experiments, we concentrated on glasses poled in blocking anode configuration[3] with two types of thin-film anodic and cathodic electrodes. For this we deposited 50 nm gold film on both surfaces (25x25 mm$^2$) of 1 mm thick commercial soda-lime glass slides (see glass composition in Table) either onto virgin slide surfaces (AU samples) or onto the surfaces previously covered by 5 nm chromium sublayer (CRAU samples). The samples were thermally poled at 573 K under 400 V DC[4]. After almost complete decay of poling current, poled samples were cooled down to room temperature, and then the applied voltage was switched off. BDS study was performed using Novocontrol BDS80 ultra-broadband dielectric spectrometer (Novocontrol Technologies GmbH und Co. KG, Germany) with a Novotherm-HT furnace in the frequency range 0.2 – 3×10$^5$ Hz and at temperature varying from room temperature to 700 K. The heating rate was 1 K/min.

***Table I.*** *Chemical composition of the Menzel glass.*

| Oxide | $SiO_2$ | $Na_2O$ | $K_2O$ | CaO | MgO | $Al_2O_3$ |
|---|---|---|---|---|---|---|
| *Wt%* | 72.2 | 14.3 | *1.2* | 6.4 | 4.3 | 1.2 |

## 3. Results and discussions

After poling the samples were studied with BDS. The real part and the imaginary part of the complex impedance Z* of the initial and two types of poled glasses in a wide temperature and frequency ranges were measured. It was found that poling resulted in significant changes in the character of temperature dependences, namely: in the appearance of steps and maxima whose positions move with a change in frequency.

In poling with blocking anode, all positive charge carriers are known to leave the subanode layer for the glass bulk. It is obviously that permittivity and conductivity of this layer (known as depleted layer) strongly differ from the ones of the bulk (initial) glass. Thus, any poled glass appears to be a typical bilayer structure. To calculate impedance of such structure one should consider a serial connection of the layers, that is, two parallel RC circuits connected in series. Because the changes in the ion concentration profiles (Na, Ca, etc.) are observed at the thickness of about one (or several) micrometers, we believe that the bulk of the poled glass sample has the same structure and properties as the unpoled glass. Having the complete information about the electrical properties of the initial and poled glasses and about the thickness of depleted layer, one can obtain information about the properties of the layer. Taking a simple two-layer structure of poled glass as the starting point, we can obtain expressions for the components of the complex permittivity (ε*=ε'-iε") of the polarized layer in the form:

$$\varepsilon_l' = \frac{d_l}{d} \cdot \frac{\left(\varepsilon_g''^2 \cdot \varepsilon_c' - \varepsilon_c''^2 \cdot \varepsilon_g'\right)}{\left(\varepsilon_g' - \varepsilon_c'\right)^2 + \left(\varepsilon_g'' - \varepsilon_c''\right)^2},$$

$$\varepsilon_l'' = \frac{d_l}{d} \cdot \frac{\left(\varepsilon_g'^2 \cdot \varepsilon_c'' - \varepsilon_c'^2 \cdot \varepsilon_g''\right)}{\left(\varepsilon_g' - \varepsilon_c'\right)^2 + \left(\varepsilon_g'' - \varepsilon_c''\right)^2}$$

Here, the subscript c refers to the whole structure that is the poled glass sample, l - to the poled layer, and g - to the initial glass. d is the thickness. The thicknesses of the polarized layers was evaluated from the adsorption spectra and were $d_{AU}$=530±60 nm and $d_{CRAU}$=650±25 nm.

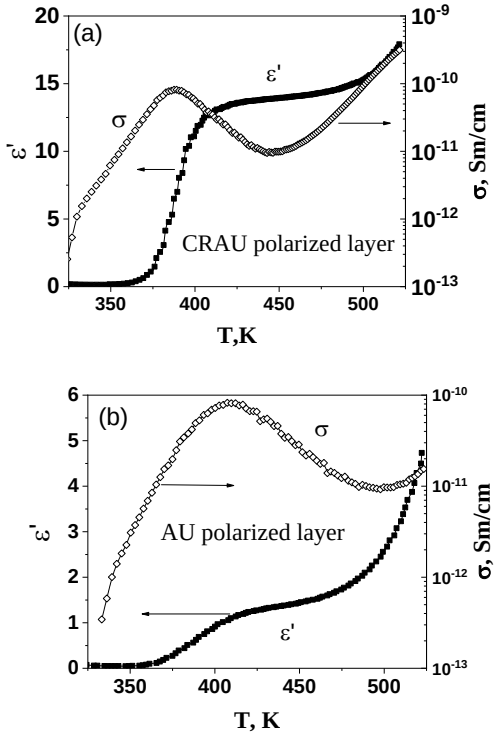


***Fig.*** *Temperature dependences of permittivity and AC-conductivity at 0.2 Hz frequency of 650 nm thick polarized layer in CRAU specimen (a) and 530 nm thick polarized layer in AU specimen (b).*

Using the data for CRAU and AU samples and the evaluated thicknesses of the polarized layers, we calculated the temperature dependences of the permittivity and ac-conductivity of these layers, which are presented in Fig. for 0.2 Hz frequency. The permittivity and ac-conductivity of the polarized layers are very low in comparison with the initial glass, that should be expected, since most of the charge carriers have left these layers. It is interesting that the permittivity and ac-conductivity of the polarized layer in the CRAU sample are several times higher than in the AU sample. Supposedly, this is because trivalent gold atoms effectively occupy non-bridging oxygen bonds remaining after positive ions have left the subanodic layer of the sample. This limits the number of free positions and increases the length of the jump that significantly reduce the value of glass conductivity (presumably, the conductivity is conditioned by some amount of impurities and defects), which has a hopping character. It is essential that the conductivity which is supposedly related to gold ions is low because of their very low mobility in glass. In addition, given the character of the temperature dependences, it can be stated that the polarized layer in the CRAU sample has a complex structure, apparently at least two-layer structure. The polarized layer in the AU sample is also heterogeneous.

We compared the obtained characteristics of the polarized layers with the temperature dependences of the permittivity and ac-conductivity of the AU and CRAU samples used the calculated thicknesses of the polarized layers (650 and 530 nm) but not the thickness of the entire sample (1 mm). We can conclude that the raw data on BDS measurements give dependences just for the polarized layer. This allows one to obtain additional information on the properties of polarized layers by analyzing the frequency dependences of the impedance of poled samples. The behavior of dc-conductivity and static permittivity (ε at zero frequency) of the layers were estimated from the Cole-Cole diagrams. We obtain the temperature dependences of the dc-conductivity of the layers. The conductivity has a thermal activation character with one slope in the temperature range of 400-550 K. The dc-conductivity of the CRAU sample, as we expected, is almost an order of magnitude higher than the AU sample. The activation energies are almost the same and equal to 0.88-0.89 eV. Given the value of the found activation energies, charge carriers could be sodium ions.

## 4. Conclusions

The permittivity and ac-conductivity of polarized subanodic layer are very low compared to the initial glass. This should be expected because the most of the charge carriers have left subanodic region of the poled glass. It is found that electric properties of the layer are essentially conditioned by the structure of anodic electrode used in glass poling. It is also shown that dielectric response of poled glass samples is mainly determined by the electric properties of the cations-depleted subanodic layers. BDS measurements performed at different temperature have shown that the temperature dependence of DC conductivity of the polarized layers obeys Arrhenius's law. The dc conductivity of the depleted (polarized) layer of glass in the case of the anodic electrode with chromium sublayer proves to be about an order of magnitude higher compared to the case of the gold electrode without the sublayer. But the activation energies of the charge carriers in these depleted layers turns out to be about the same and equal to 0.88-0.89 eV. Difference in the absolute values of conductivity when activation energies do not differ can be explained by the presence of gold ions which can penetrate into the glass and block free position for charge carriers' migration. Given the value of the found activation energies, charge carriers could be sodium ions, but, by now, exact their identification is the next challenge of this investigation.

## References

[1] Tanaka K, Kashima K, Hirao K, Soga N, Mito A, Nasu H. Jpn J Appl Phys **32**.(1993) (Part 2, No. 6B)L843.
[2] Russell PSJ, Pannell CN, Kazansky PG, Dong L. Electron Lett. **31**(1) (1995)62.
[3] Carlson DE. J Am Ceram Soc. **57**(7) (1974)291.
[4] Reshetov I V., Kaasik VP, Lipovskii AA, Tagantsev DK. J Phys Conf Ser. 1410(1) (2019) 012148.
[5] J. Chrost, J. J. Hinarejos, E. G. Michel, R. Miranda. Surf. Sci. **330**(1995)34.

Sixth Asian School-Conference on Physics and
Technology of Nanostructured Materials
Vladivostok, Russia, 25 – 29 April, 2022

**V.p.06**

# Optically induced localized spin wave states in all-dielectric nanopillars

D.M. Krichevsky*[,1,2,3], D.O. Ignatyeva[2,3,4], D. Karki[5], A. Kolosvetov[1], A.I. Chernov[1], A.N. Shaposhnikov[3], V.N. Berzhansky[3], M. Levy[5], V.I. Belotelov[2,3,4]

[1] Moscow Institute of Physics and Technology (MIPT), 141700 Dolgoprudny, Russia
[2] Russian Quantum Center, 121353 Moscow, Russia
[3] Physics and Technology Institute, Vernadsky Crimean Federal University, 295007 Simferopol, Russia
[4] Photonic and Quantum Technologies School, Lomonosov Moscow State University, 119991 Moscow, Russia
[5] Physics Department, Michigan Technological University, Houghton, MI, USA

*e-mail: krichevskii.dm@phystech.edu

**Abstract.** We propose an all-dielectric magnetic nanostructure based on periodic array of iron garnet nanopillars for all-optical spin-wave excitation. By choosing proper wavelength of the optical pump pulses corresponding to the resonance in the transmittance spectra of the structure we succeed in excitation several spin-wave modes. The localized nature of the optical modes inside nanopillars was found to be responsible for multimode spin-wave excitation.

## 1. Introduction

The ability to control spin waves (and their quanta - magnons) in magnetic materials opens up opportunities for various applications, such as Boolean logic elements, memory cells, sensors, and elements of quantum computing [1]. Currently, nanophotonics brings a new perspective to light-spin coupling in nanoscale magnetic materials via optical modes excitation [2]. This approach is gaining momentum in current ultrafast nondissipative all-optical control of magnetism. To increase light-matter interaction plasmonic nanostructures made of noble metals are widely utilized [3]. However dissipative nature of the metals decreases the quality factor of the optical resonances and leads to thermal heating. From this perspective, their all-dielectric counterparts are lack of these drawbacks [4].

Here we propose an all-dielectric nanostructure composed of bismuth iron garnet nanopillars (BIG) on $SiO_2$ substrate. The geometric properties of the structure were designed to localize electromagnetic energy inside the nanopillars via specific optical states. It was observed, that such localization induces complex spin-wave behavior excited by the inverse Faraday effect (IFE).

## 2. Experiment

An experimental nanostructure was composed of two-dimensional periodic grating of BIG nanopillars. The period of the structure was 900 nm, the height and diameter of the nanopillars were 500 and 450 nm correspondingly. The structure was produced by electron beam lithography technique. An atomic force microscopy image of the sample is presented in the inset of Fig. 1.

Transmittance spectra of the sample in the 550-1000 nm range consists of several resonant dips. The dips correspond to localized optical modes excitation inside the nanopillar [5]. Such optical modes are characterized by strongly non-uniform electromagnetic field distribution. We investigated an impact of such field inhomogeneities on spin-wave dynamics using optical time-resolved Faraday rotation (TRFR) method (pump-probe technique) [6]. For pump-probe measurements the sample was placed in the static magnetic field generated by electromagnet in Voight configuration. A circularly polarized laser pump pulses falling on the sample excite the system from the ground state via IFE [6] giving rise to spin-wave dynamics. A delayed probe pulse of linear polarization passing through the sample detect magnetization oscillations via Faraday effect. The wavelength of the pump pulses was adjusted to the dips in the transmittance spectra of the sample, while the probe pulses wavelength was set to 525 nm. The pulses duration did not exceed 250 fs. The polar angle of incidence for pump and probe beams were 17 and -17 degrees correspondingly.

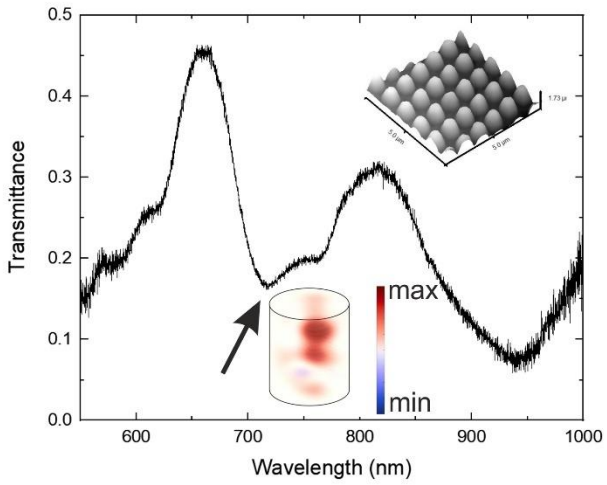


***Fig. 1.*** *Transmittance spectra of the nanostructure at 17 degrees of polar incident angle. Inset – AFM image of the sample and z-component of the IFE distribution.*

## 3. Results and discussions

For the measurements the wavelength of the pump pulse was set to be 730 nm that corresponds to the resonant dip in the transmittance spectra of the sample. At the resonance optical energy is highly concentrated inside nanopillar. As a result, IFE effective magnetic field is also localized and resemble a point source (inset of the Fig. 1). Such a point source-like stimulate sophisticated oscillations in TRFR signal (Fig. 2). The measured TRFR signal is directly connected with magnetization z-component oscillations and corresponds to spin waves. There are distinct beats in the signal of TRFR. To identify the frequencies of the observed oscillations we carried out

Fourier analysis of the TRFR signals. Fig. 3 show fast Fourier transform (FFT) spectra of the magnetization oscillations.

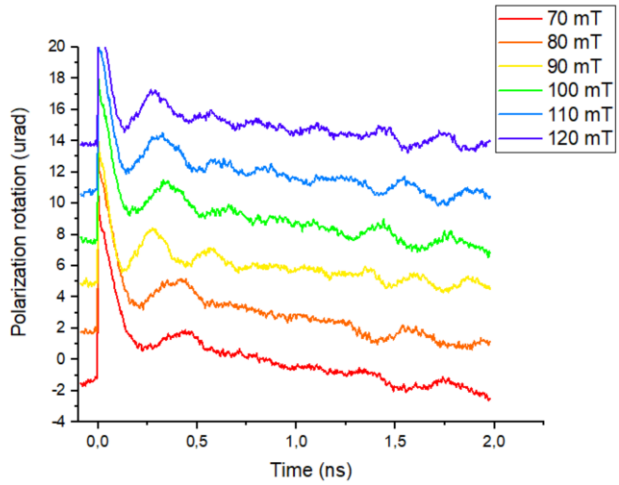


***Fig. 2.*** *TRFR measurements of the sample.*

There are 3 well-defined peaks in the FFT spectra. For the case of 70 mT external field the peaks are located at 1.4, 2.23 and 3.18 GHz. The central one corresponds to backward volume magnetostatic spin wave (BVMSW) of 0-th order, high-frequency satellite corresponds to 1-order BVMSW, while low-frequency one is believed to correspond to so-called "edge" modes. The high-order modes are known to be caused due to standing wave formation inside the nanopillar. The low-frequency mode formation is mainly connected with demagnetization effects in the nanopillar [7]. The frequency of the modes increases with the increase of the external magnetic field amplitude. For instance, the modes observed for 70 mT shifted to 2.67, 3.51 and 4.43 GHz for 120 mT. Notably, in the case of pristine film of the same thickness (~500 nm) only 0-th order BVMSW mode is observed. Consequently, the localized inhomogeneous optical excitation give rise to high- and low-frequency spin-wave modes that can utilized in nanosized multispectral spin-wave based devices.

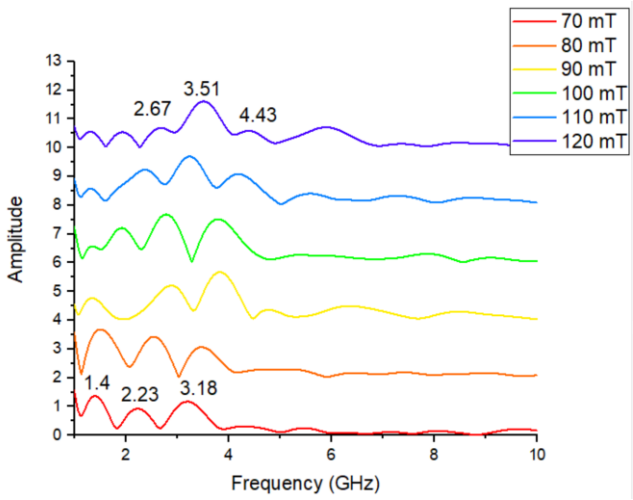


***Fig. 3.*** *The Fourier spectra of the measured oscillations.*

## 4. Conclusions

We investigated peculiarities of the optically exited spin-waves dynamics in the all-dielectric BIG based nanostructure. It was shown that localized nature of optical resonances leads to multimode spin-wave dynamics in a single nanopillar. The observed oscillations were found to be BVMSW mode of different orders and the "edge" modes. The multimode features of spin-wave dynamics in a such all-dielectric magnetic nanopillar can be implemented in multispectral magnon-based computing.

## Acknowledgements

This work was financially supported by Russian Science Foundation, Grant No. 21-72-10020.

## References

[1] A. Chumak et al. Nature Phys 11(2015)453.
[2] A.I Chernov et al. Nano Lett. 20(2020)5259.
[3] A.L. Chekhov et al. Nano Lett. 18(2018)2970.
[4] D.M. Krichevsky et al. Phys. Rev. Appl. 15(2021)034085.
[5] P.E. Zimnyakova et al. Nanophotonics 11(2022)119.
[6] A. Kirilyuk et al. Rev. Mod. Phys. **82**(2010)2731.
[7] O. Klein et al. Phys. Rev. B, 78(2008)144410.

Sixth Asian School-Conference on Physics and
Technology of Nanostructured Materials
Vladivostok, Russia, 25 – 29 April, 2022



# Structural coloring and anti-counterfeiting enabled by direct femtosecond-laser printing

V.S. Lapidas[1,2], A.Y. Zhizhchenko[1,2], A.A. Kuchmizhak[*,1,2]

[1] Institute of Automation and Control Processes FEB RAS , 5 Radio St., Vladivostok 690041, Russia
[2] Far Eastern Federal University, 8 Sukhanova St., Vladivostok 690950, Russia

*e-mail: alex.iacp.dvo@mail.com

**Abstract.** Direct femtosecond laser nanopatterning of metal-insulator-metal (MIM) sandwich designed to support Fabry-Perot mode in the visible spectral range was carried out to demonstrate high-resolution multi-color printing of structural colors in reflection. By varying the applied pulse energy, the type of the surface modification (evolving form hollow nanobumps and nanojets to through holes and spallative craters) can be controlled to tune the local surface reflectivity resulting in variation of the surface color observed in reflection with ordinary optical microscope. Moreover, we demonstrated facile single step printing of multi-color images at resolution up to 25,000 dots per inch justifying the applicability of the developed approach for structural color marking, optical information encryption and anti-counterfeiting.

## 1. Introduction

Structural colors originating from the interaction of broadband visible radiation with optically resonant nanostructures are non-fading and stable against UV radiation and thermal treatment as opposed to chemical dye and pigments [1,2]. Utilization of optically resonant nanostructures paves the way toward high-quality imaging with the lateral resolution up to 100,000 dots per inch (DPI) that overcomes the Abbe diffraction limit and makes the boundaries between neighboring pixels indistinguishable when observed with best dry microscope objectives. Lateral resolution of structural colors technology is two orders of magnitude higher comparing to those for best commercial printers. In the near future, structural colors are expected to revolutionize several technologically relevant areas as optical filters, next-generation displays, color marking and anti-counterfeiting of goods, etc. Moreover, a wide range of available materials for realization of optically resonant nanostructures makes the structural color technology potentially CMOS-compatible.

Despite the well-known physics of structural colors derived from standard bulk optics as prisms, thin films, photonic crystals or diffraction gratings, the interest in structural coloring of surfaces has recently refreshed. In part, this can be attributed to recent advances in such areas as nanophotonics, plasmonics and meta-optics, as well as the spreading of high-resolution planar nanofabrication technologies as electron- and ion- beam lithography that allowed to shrink the size of the structural colored pixel well below optical diffraction limit. Using semiconductor materials with high refractive index and low dissipative losses as well as plasmon-active metals [2,3], it is possible to fabricate sub-wavelength nanostructures with resonant optical response that can be tailored by varying characteristic geometry of nanostructures and their arrangement.

In spite of a new look borrowed from meta-optics, majority of works used rather classical schemes based on thin-film Fabry-Perot filters, percolated films and diffraction gratings [4] being combined with standard planar nano-resonators like nano-disks, and nano-holes, whose planar geometry and arrangement are determined by planar fabrication technologies. Additional functionality and controllability over the single-pixel color and brightness appears to be achieved using 3D optical nanostructures. However, the ability to vary the height of the optically resonant nanostructures in each individual pixel of a color-coded picture cannot be implemented using the time- and money-consuming planar lithographic fabrication technologies.

Pulsed laser radiation is known to drive ultrafast solid-liquid phase transition on the surface of the exposed material that allows its sculpturing and subsequent resolidification in the form of various surface nano-morphologies like nanoparticles, nanoripples and nanobumps and nanoholes. The latter type of structures is of particular interest as the 3D geometry of the nanobumps can be easily controlled by varying only the laser fluence and focusing conditions. Such structures can be imprinted on the surface of all plasmon active metal films without ablation (ejection of the nanoparticles) thus ensuring ultra-clean and reproducible fabrication. Previously, by taking advantage of geometry-dependent resonant scattering of isolated nanobumps we demonstrated the direct laser writing of plasmonic colors that can be observed in the dark-field back-scattering regime [5]. Here, similar femtosecond laser nanopatterning of metal-insulator-metal (MIM) sandwich designed to support Fabry-Perot mode in the visible spectral range was proved usefulness for high-resolution multi-color printing of structural colors in reflection.

## 2. Experiment

The samples for laser nanopatterning were MIM ($Au/Al_2O_3/Ag$) sandwich structure coated above the silica glass substrate via e-beam deposition. The thicknesses of the layers allow to control the reflection spectrum of the resulting MIM structure. In particular, it can be designed in such a way to contain additional reflection dip in the visible spectral range associated with a Fabry-Perot mode (Figure 1). Here, we chose the thicknesses of the $Au/Al_2O_3/Ag$ MIM layers as 40/120/400 nm. Nanopatterning was performed with second-harmonic (515 nm) 200-fs laser pulses coming from regeneratively amplified laser system. Laser pulse were focused onto the sample surface with a dry microscope objective having numerical aperture NA=0.4. The incident pulse energy was varied using motorized attenuator. The reflection spectra were measured

with an optical microscope confocally coupled with the grating-type spectrometer equipped with a CCD camera.

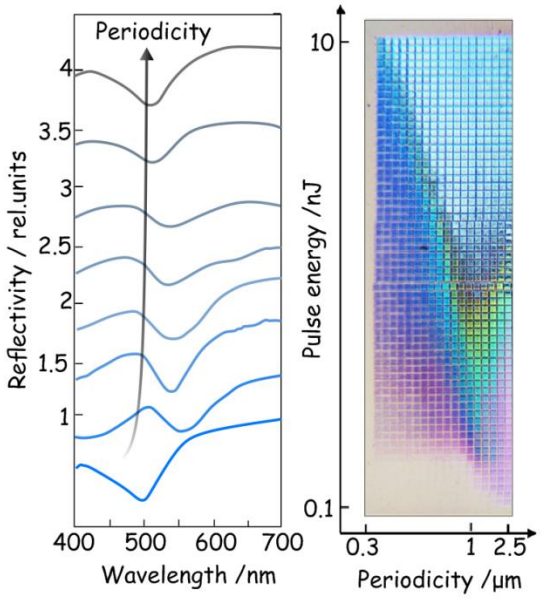


***Fig. 1.*** *(a) Series of reflection spectra of pristine (bottom) and laser-patterned MIM surface. The surface nanotexturing was performed at fixed pulse energy of 3 nJ by varying the periodicity between the neighboring nanostructures. The spectra are vertically offset for better displaying. (b) Corresponding reflection image of the MIM surface patterned by varying the pulse energy and nanostructures periodicity. Each patterned square (pixel) has the size of 30x30 μm². The image was captured with optical microscope at NA=0.3 in reflection mode.*

## 3. Results and discussions

Direct laser nanopatterning of MIM sandwich was carried out by varying only the incident pulse energy from 0.1 to 10 nJ as well as the periodicity of the nanostructures – from 0.3 to 2.5 μm. As can be seen, modulation of both parameters changes local reflectivity of the surface changing its color appearance in the optical microscope (Figure 1). This feature is associated with formation of the nanostructure on the surface of the top Au film of the MIM sandwich via laser-induced melting and ablation.

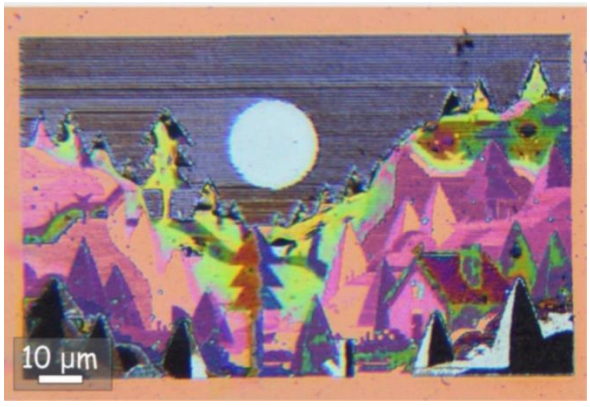


***Fig. 2.*** *Large-scale (120 x 60 μm²) structural color image with the of produced by direct laser printing on MIM sandwich structure. 14 different color tones varied by tuning the applied pulse energy/period were used. The image was captured with optical microscope at NA=0.3 in reflection mode.*

Geometry of the Au surface modification produced by single-pulse exposure varies from hollow parabola-shaped nanobumps to upright-standing nanojets and through micro-holes [6]. Absorption of the nanostructured surface mediated by excitation of surface plasmon-polaritons depends on the shape and geometry of the imprinted nanostructures. Also, modification of the top Au film shifts the spectral position of the Fabry-Perot resonance (with respect to those for the pristine MIM sandwich). Both features allow to tune the reflection spectrum of the surface that renders it to change the color with respect to the pristine surface exhibiting yellowish appearance. By controlling the nanopatterning parameters at microscale, multi-color images with high resolution can be imprinted of the surface of MIM structures via direct laser writing (Figure 2). Noteworthy, complete removal of the top Au film makes the surface to have a white color owing to broadband reflectivity of the bottom Ag film. Further increase of the pulse energy allows to obtain the nanotextured Ag film surface. Such nanotextured surface absorbs light within broad spectral range making it completely black thus enriching the color gamut with pure white/black colors even for highly reflective sample.

## 4. Conclusions

Here, we demonstrated capabilities of direct femtosecond laser nanopatterning for structural coloration. Our approach is based on the designing and pattering the MIM sandwich exhibiting resonant optical properties. We demonstrated facile single step printing of multi-color images at resolution up to 25,000 dots per inch justifying the applicability of the developed approach for structural color marking, optical information encryption and anti-counterfeiting.

## Acknowledgements

This work was supported by Russian Science Foundation (grant number 21-72-20122).

## References

[1] A. Kristensen, J.K.W.Yang, S. Bozhevolnyi, S. Link, P. Nordlander, N.J. Halas, N. A. Mortensen, Plasmonic colour generation. Nat. Rev. Mater. **7**(2016)16088.

[2] Y. Gu, L. Zhang, J. Yang, S. Yeoa, C.-W. Qiu, Color generation via subwavelength plasmonic nanostructures. Nanoscale **7**(2015)6409.

[3] K. Kumar, H. Duan, R. Hegde, S. Koh, J. Wei, J. Yang, Printing colour at the optical diffraction limit. Nat.Nanotechnol. **7**(2012)557.

[4] S. Yokogawa, S. Burgos, H. Atwater, Plasmonic color filters for CMOS image sensor applications. Nano Lett. **12** (2012) 4349.

[5] X. Wang,; Kuchmizhak, D. Storozhenko, S. Makarov, S. Juodkazis, Single-step laser plasmonic coloration of metal films. ACS Appl. Mater. Interfaces. **10**(2018)1422.

[6] S.I. Kudryashov, P.A. Danilov, A.P. Porfirev, I. Saraeva, T. H. T. Nguyen, A. A. Rudenko, O.B. Vitrik,. High-throughput micropatterning of plasmonic surfaces by multiplexed femtosecond laser pulses for advanced IR-sensing applications. Appl. Surf. Sci., **484**(2019) 948.

Sixth Asian School-Conference on Physics and
Technology of Nanostructured Materials
Vladivostok, Russia, 25 – 29 April, 2022



# Laser-assisted fabrication of electrode materials for non-enzymatic sensors using deep eutectic solvents

A.S. Levshakova*, E.M. Khairullina, D.I. Gordeichuk, A.Yu. Shishov, I.I. Tumkin
Institute of Chemistry, Saint Petersburg State University, SPbU, 7/9 Universitetskaya nab., St. Petersburg 199034, Russia

*e-mail: sashkeens@gmail.com

**Abstract.** In this work, we propose a technique for laser-induced deposition of nickel micropatterns from deep eutectic solvents (DES) on the surface of oxide glasses. Solutions of deep eutectic solvents consisting of choline chloride, citric or tartaric acid, and nickel salts were used as solutions for precipitation, and the fundamental possibility of obtaining bimetallic and metal-carbon structures was also demonstrated. It is shown that irradiation with continuous laser radiation at a wavelength of 532 nm makes it possible to significantly increase the rate of metal deposition and create micropatterns with good electrochemical properties, as well as high adhesion to the surface, which makes it possible to use the synthesized patterns in practice, including for creating sensor platforms for electrochemical analysis.

## 1. Introduction

In recent years, the development of simple and fast methods for monitoring various biological analytes, including dopamine, which is a marker of many psychiatric diseases, and paracetamol (AP), (N-(4-hydroxyphenyl-acetamide), a widely used antipyretic and analgesic, has attracted great interest from researchers around the world. unreasonable intake of which can cause acute liver failure and kidney damage in adults. The most attractive method of electrode modification is the use of nanomaterials instead of enzymes as sensor-active elements [1].

In this regard, the development of new sensors based on porous electrically conductive metallic and bimetallic micro- and nanostructures is of great interest.

A worthy alternative to existing technologies for the production of microelectronic components, sensors of other devices, can be direct laser writing methods, among which one can single out the method of laser deposition of metals from a solution, in which metal deposits are formed when laser radiation is applied to the "substrate-solution" interface. When using this method, a metal reduction reaction occurs on the substrate surface at the focus of the laser beam, which leads to the formation of various types of microsized metal structures. In our work devoted to the synthesis of copper on dielectric surfaces, it was shown that when using DES as solutions for deposition, the speed of laser writing can be increased by more than 150 times [3].

## 2. Experiment

The necessary amounts of choline chloride, acid, and copper salt were mixed in vial. The ratio of acid to choline was always kept to 1: 1, whereas the amount of nickel salt was varied. Then, the vials were placed in a drying cabinet at 120 ° C. After the mixtures began to melt, they were placed in a magnetic heating stirrer and mixed at 130 ° C until viscous homogeneous liquids were formed., The resulting eutectic solvents placing on the substrates.

Then, we performed the deposition of nickel on the surface of substrates with LCLD. In this set-up, a continuous wave 532 nm diode-pumped solid state Nd:YAG laser was used. The schematic pictures of the entire procedure of the fabrication of nickel micropatterns using DESs, is shown in Fig. 1. After laser synthesis, the unreacted DES was washed off the glass with water.

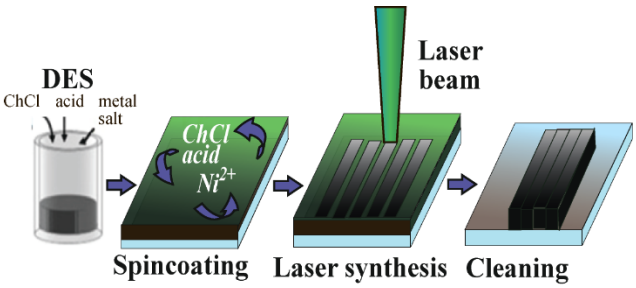


***Fig. 1.*** *Technique of laser synthesis of materials in deep eutectic solvents.*

## 3. Results and discussions

In our previous works, it was demonstrated that LCLD can be successfully used to fabricate enzyme-free sensor platforms suitable for detection of various biologically important analytes [4]. In the current study, we investigated the general electrocatalytic properties of Ni micropatterns deposited from DES with nickel (II) chloride. We tested two quite important for medicine bioanalytes, DA and AP. Fig. 2a demonstrates the CVs of Ni micropatterns recorded in 0.1 M PBS (shown in dark gray) with addition of mixture of 300 μM DA and 500 μM AP. In addition, here one can see the possible electrooxidation reactions of DA and AP that may occure on the surface of this electrode material.

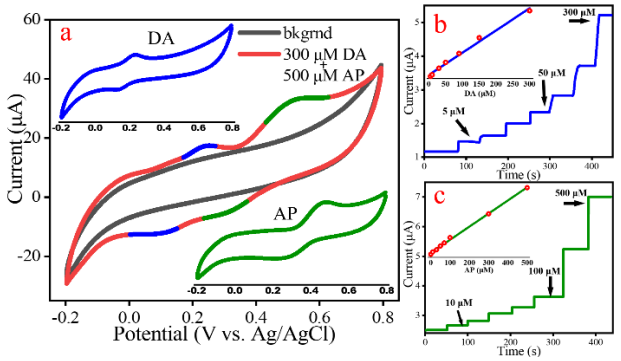


***Fig. 2.*** *(a) The CVs of Ni patterns recorded at a scan rate of 50 mV s− 1 in solutions containing DA (blue) and AP (green) individually and as a mixture (red). The amperometric current of Ni patterns recorded in the presence of different concentration of DA (b) and AP (c) at the potentials of 0.2 and 0.45 V, respectively. Insets in (b) and (c) show the linear ranges of these analytes detection. Possible reactions of the electrooxidation of DA and AP are shown at the bottom.*

Fig. 2b and c illustrates a typical amperometric response of Ni micropatterns. The observed linear ranges of enzymeless detection of DA and AP are 1–300 and 5–500 μM, respectively (insets in Fig. 2b and c). The calculated detection limits (LOD =3S/b, S is the standard deviation from linearity, b is the slope of the calibration curve) are 0.11 and 0.34 μM, respectively. In addition, the estimated sensitivity values are 124 μA $mM^{-1}$ $cm^{-2}$ for DA and 88 μA $mM^{-1}$ $cm^{-2}$ for AP, respectively.

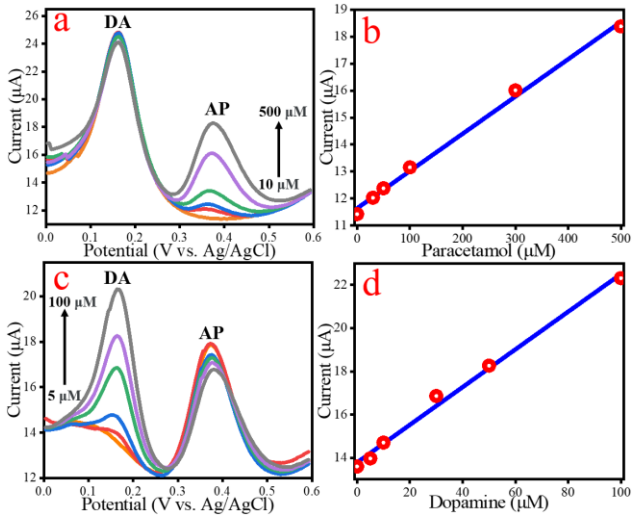


***Fig. 3.*** *DPVs of Ni patterns recorded in solutions containing 300 μM of DA and various concentrations of AP (a) and vice versa (c) recorded at amplitude of 0.05 V, pulse width 0.05 s and pulse period 0.5 s. The linear dependences of the analytical signal on the concentration of AP (b) and DA (d).*

In real biological systems, both DA and AP may coexist together. Differential pulse voltammetry (DPV) may selectively identify one of them in the presence of another avoiding the overlap of their oxidation potentials. According to DPV studies, the linear range of DA detection in the presence of AP is 1–100 μM, whereas for AP detection in the presence of DA this range is equal to 5–500 μM (Fig. 3b and d). Moreover, such an important parameter as adhesion to the substrate and stability were evaluated. As a result, the synthesized nickel-based micropatterns in this regard demonstrated good results during multiple tests.

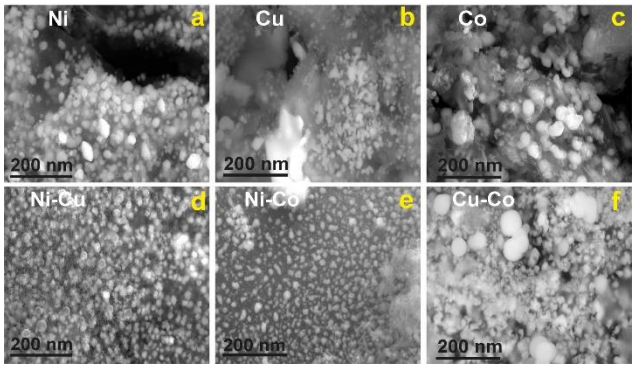


***Fig. 4.*** *SEM images of metal structures made from DES containing chlorides of nickel (a), copper (b), cobalt (c), nickel and copper (e), nickel and cobalt (e), copper and cobalt (f).*

The next stage of research was the synthesis of composite materials in DES; the fundamental possibility of obtaining structural bimetallic particles under the influence of laser radiation on the surface of oxide glass was noted (Fig. 4).

Such materials acquire characteristic features and significantly outperform individual components, since in many cases synergistic detection is observed when polymetallic enzyme-free enzymes are used. For the synthesis of bimetallic composites in a Ni-Co-Cu mixture, solvents with citric and tartaric acids based on chlorides and acetates of cobalt, copper and nickel are found (organic acid: choline chloride: metal salt1: metal salt2 1:1:0.5:0,5) is synthesized using a continuous laser.

## 4. Conclusions

In this work, various physicochemical parameters of the process of laser-induced deposition of nickel micropatterns on a glass surface were studied and optimized using deep eutectic solvents. As a result, the optimal laser power (700–1000 mW) and scanning speed (0.25–0.33 $mm*s^{-1}$) were determined, which can be used to obtain conductive nickel microstructures. Composite microstructures from DES based on nickel, copper and cobalt were also synthesized.

The electrocatalytic properties of nickel microelectrodes have also been studied. The observed linear ranges of enzymeless detection of DA and AP are 1–300 and 5–500 μM, respectively. The calculated detection limits (LOD =3S/b, S is the standard deviation from linearity, b is the slope of the calibration curve) are 0.11 and 0.34 μM, respectively. In addition, the estimated sensitivity values are 124 μA $mM^{-1}$ $cm^{-2}$ for DA and 88 μA $mM^{-1}$ $cm^{-2}$ for AP, respectively.

## Acknowledgements

This work was supported by Russian Science Foundation (grant 20-79-10075). The authors also express their gratitude to the SPbSU Nano-technology Centre, the Centre for Optical and Laser Materials Research and the Centre for X-ray Diffraction Studies.

## References

[1] Gutes A, Carraro C, Maboudian R (2011) Nonenzymatic glucose sensing based on deposited palladium nanoparticles on epoxy-silver electrodes. Electrochim Acta 56(17):5855-5859.

[2] Ilya I. Tumkin, Vladimir A. Kochemirovsky, Mikhail D. Bal'makov et. al. Surface and Coatings Technology, 264, 187–192.

[3] A. Shishov, D. Gordeychuk, L. Logunov, I. Tumkin. High rate laser deposition of conductive copper microstructures from deep eutectic solvents. Chem. Commun., 2019, 55.

[4] A.V. Smikhovskaia, M.S. Panov, I.I. Tumkin, In situ laser-induced codeposition of copper and different metals for fabrication of microcomposite sensor-active materials, Anal. Chim. Acta. 1044 (2018) 138–146.

Sixth Asian School-Conference on Physics and
Technology of Nanostructured Materials
Vladivostok, Russia, 25 – 29 April, 2022



# Band gap and antioxidant properties of cerium dioxide nanoparticles

V.A. Mamontov*, A.Yu. Ryzhenkova, M.A. Pugachevskii
Southwest State University, 50 Let October, 94, Kursk, 305040, Russia

*e-mail: vladimir-mamontov2013@yandex.ru

**Abstract.** Cerium dioxide nanoparticles were obtained by mechanical grinding and laser ablation. The characterization of mechanically ground cerium dioxide nanoparticles was carried out by small-angle X-ray diffractometry. We studied the influence of the size factor on the value of the band gap of cerium dioxide nanoparticles and studied the antioxidant properties of nanodispersed solutions of cerium dioxide particles obtained by various methods in the course of the photocatalytic reaction, depending on their size characteristics. The measurements were carried out in the visible and ultraviolet ranges using an optical spectrophotometer. It was found that an increase in the speed of centrifugation of nanodispersed solutions increases the band gap of cerium dioxide nanoparticles. It was found that ablated cerium dioxide nanoparticles more effectively exhibit antioxidant properties in a photocatalytic reaction than particles obtained by mechanical grinding.

## 1. Introduction

Cerium dioxide has a wide range of applications in various fields of both science and technology, as a catalyst in automobile exhaust systems or solid state energy [1]. It is noted in the works [2-5] that cerium dioxide nanoparticles have the prospect of being used in the biomedical field due to their powerful antioxidant properties. That is, nanosized cerium dioxide inactivates various radicals in biological systems, such as superoxide $O^{2-}$, a highly reactive short-lived hydroxyl radical OH*. The antioxidant properties of cerium dioxide nanoparticles increase due to structural defects on surface of the particles such as an oxygen vacancy. Laser ablation makes it possible to obtain particles with these structural defects [6,7].

## 2. Experiment

Experiments aimed at revealing the difference in the effectiveness of antioxidant properties between ablated nanoparticles and mechanical grinding cerium dioxide particles ground in a mortar in a photocatalytic reaction of methylene blue dye degradation were completed. The photocatalytic reaction was carried out in the presence of zinc oxide, and the oxidation of methylene blue was recorded spectrophotometrically in the wavelength range from 550 to 750 nm. Layers of cerium dioxide nanoparticles were deposited on silicon wafers by laser ablation. This method allows one to obtain $CeO_2$ nanoparticles with surface structural defects of the oxygen vacancy type, which determine their antioxidant properties [7]. The source of laser radiation for the deposition of $CeO_2$ nanoparticles was a pulsed fibre laser activated by diode pumping IPG Photonics, with the "High Contrast" option (radiation wavelength 1.06 μm, laser radiation intensity ~ $10^9$ W/m$^2$, pulse duration 200 μs, pulse repetition rate up to 1 kHz). Pressed cerium dioxide of the class "chemically pure" was used as a target. Also, a mechanical grinding cerium dioxide powder was obtained from the same material that was the target for ablation by grinding in a mortar.

Subsequently, the ablated cerium dioxide nanoparticles, ground cerium dioxide powder and zinc oxide powder were dispersed. The dispersion was 40 minutes for each solution. Then dispersed solutions were centrifuged in a microcentrifuge. For two solutions of cerium dioxide, the time and speed range of the centrifuge were from 10 minutes from 1000 to 5000 rpm, respectively, and for zinc oxide were 5 minutes and 1000 rpm. Centrifugation was carried out to increase the antioxidant properties of the cerium dioxide particles and increase the catalytic zinc oxide particles. In works [2, 4], it was found that in the process of centrifugation it is possible to obtain dispersed solutions, which are more pronounced properties, in particular, antioxidant in comparison with non-centrifuged solutions. This is because, despite the increasing substances in the solution in general, there are several particles with a nanometer range, which exhibit the most pronounced antioxidant properties due to oxygen nonstoichiometry on the surface of these particles. From the upper part of the microtubes, centrifuged solutions were drawn up with a syringe and a volumetric syringe of solutions constituting 80% of the volume of the microtube. Note that, from each microtube, solutions of centrifuged zinc oxide particles were poured into one solution to achieve homogeneity of solid particles. Then the solutions were placed in cuvettes, a solution of methylene blue was added, and the photocatalytic process was carried out, which lasted 100 minutes.

## 3. Results and discussions

The size of mechanical grinding particles of cerium dioxide was also evaluated. The analysis of the sizes of mechanical grinding particles of cerium dioxide, centrifuged at different speeds of the centrifuge, was carried out by the method of small-angle X-ray diffractometry. As a result, it was found that after the process of centrifugation of the dispersed solution at a centrifuge frequency of 1000 rpm, the limiting particle size did not exceed 80 nm, at 5000 rpm – 40 nm, and without centrifugation – 100 nm.

The dependence of the band gap of ablated cerium dioxide nanoparticles on the centrifugation rate of their nanodispersed solutions was studied (Fig. 1).

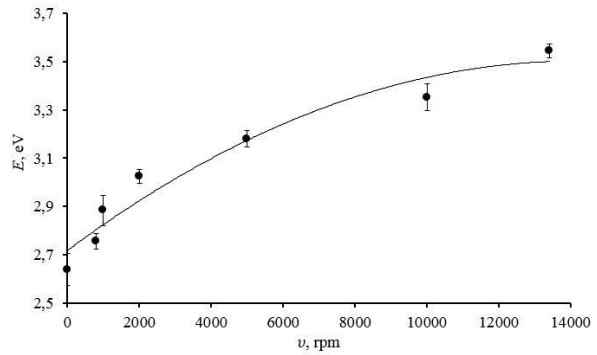


***Fig. 1.*** *Dependence of the band gap on the speed of centrifugation of nanodispersed solutions of cerium dioxide, the solid line is the approximating curve.*

It was determined that with an increase in the speed of centrifugation of nanodispersed aqueous systems of cerium dioxide; the width of the band gap of nanoparticles of cerium dioxide increases.

Figure 2 shows the results of experiments on the antioxidant properties of cerium dioxide nanoparticles obtained by various methods.

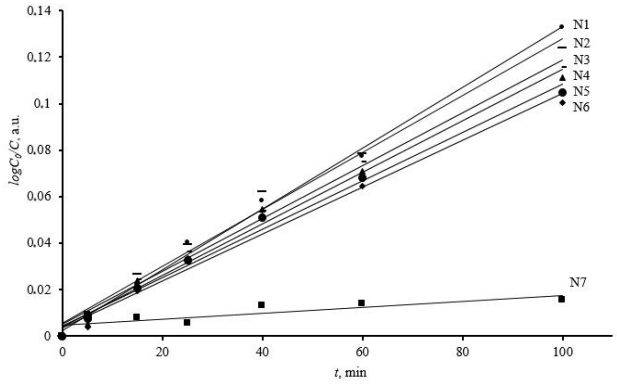


***Fig. 2.*** *Dependence of the logarithm of the residual concentration of methylene blue solution on the time of the photocatalytic reaction with the presence of zinc oxide particles in the systems, the decoding of the designations on the graph is given in the text, solid lines are approximating curves.*

N1 – a system with the presence of non-centrifuged non-centrifuged particles of cerium dioxide; N2 – a system with the presence of mechanical grinding centrifuged particles of cerium dioxide at a speed of 1000 rpm; N3 – a system with the presence of mechanical grinding centrifuged particles of cerium dioxide at a speed of 5000 rpm; N4 – a system with the presence of ablated non-centrifuged particles of cerium dioxide; N5 – a system with the presence of ablated centrifuged particles of cerium dioxide at a speed of 1000 rpm; N6 – a system with the presence of ablated centrifuged particles of cerium dioxide at a speed of 5000 rpm; N7 – a system without the presence of particles of zinc oxide and cerium dioxide.

The graph shows that dispersed solutions with ablated cerium dioxide nanoparticles centrifuged at 5000 rpm exhibit more effective antioxidant properties compared to other solutions. In general, in systems with $CeO_2$ nanoparticles obtained by laser ablation, antioxidant properties are more pronounced than with mechanical grinding cerium dioxide particles. The dependences were approximated by a linear function and the values of the rate constants of reactions in the systems were obtained (Table 1).

***Table I.*** *Values of the rate constants of reactions k in systems in the course of a photocatalytic reaction with the presence of zinc oxide particles.*

| № | N1 | N2 | N3 | N4 | N5 | N6 | N7 |
|---|---|---|---|---|---|---|---|
| k, ($min^{-1}$) | 0.00 13 | 0.00 12 | 0.00 11 | 0.00 11 | 0.00 1 | 0.00 1 | 0.00 01 |

It follows from the tabular data that the rate constant of methylene blue degradation increases in systems with mechanical grinding cerium dioxide nanoparticles, which indicates their weak antioxidant effect in comparison with nanoparticles obtained by laser ablation.

## 4. Conclusions

Evaluation of the size of grinded particles of cerium dioxide by the method of small-angle X-ray scattering diffractometry showed that after the process of centrifugation of the dispersed solution at a centrifuge frequency of 1000 rpm, the limiting particle size did not exceed 80 nm, at 5000 rpm – 40 nm, and without centrifugation – 100 nm. Experimental data showed that ablated $CeO_2$ nanoparticles had more pronounced antioxidant properties than mechanically ground particles.

## Acknowledgements

The work was carried out with the financial support of the Russian Foundation for Basic Research within the framework of scientific project № 20-02-00599. This work was also supported by the Ministry of Education and Science of The Russian Federation (g/z 2020 № 0851-2020-0035), as part of the implementation of the program of strategic academic leadership "Priority-2030" (Agreements No. 075-15-2021-1155 and No. 075-15-2021-1213).

## References

[1] E. Aneggi, C. M. de Leitenburg, Boaro, P. Fornasiero, A. Trovarell Cerium Oxide ($CeO_2$): Synthesis, Prop. and Appl. ed. S. Scirè and L. Palmisano (Amsterdam: Elsevier) (2020)402.
[2] M. A. Pugachevskii, A. N. Chibisov, V. A. Mamontov, A. P. Kuzmenko Phys. Status Solidi **a**(2021)2100355.
[3] A. Filippi et al. RSC Advances **9**(2019)11077.
[4] M. A. Pugachevskii, V. A. Mamontov, N. V. Aung, A. S. Chekadanov, A.P. Kuz'menko, Tech. Phys. Lett. **46**(2020)1032.
[5] M. A. Pugachevskii, Tech. Phys. Lett. **43**(2017)698.
[6] K. RB. Singh, V. Nayak, T. Sarkar, R. P. Singh J. The Royal Society of Chemistry **10**(2020)27194.
[7] M. A. Pugachevskii, A. N. Chibisov, A. P. Kuzmenko, A. S. Fedorov, Solid State Phenom. **312**(2020)68.

Sixth Asian School-Conference on Physics and
Technology of Nanostructured Materials
Vladivostok, Russia, 25 – 29 April, 2022



# Surface enhanced fluorescence on nanostructured dielectric surfaces

A.Yu. Mironenko*,1, M.V. Tutov1,3, A.K. Chepak1, A.A. Kuchmizhak2,3

[1] Institute of Chemistry, 159 Pr. 100-let Vladivostoka, Vladivostok 690022, Russia
[2] Institute of Automation and Control Processes FEB RAS , 5 Radio St., Vladivostok 690041, Russia
[3] Far Eastern Federal University, 8 Sukhanova St., Vladivostok 690950, Russia

*e-mail: almironenko@gmail.com

**Abstract.** Here, we applied direct laser-induced surface structuring to drive phase transition of amorphous silicon (a-Si) into nanocrystalline (nc) Si imprinted as regular arrangement of Si nanopillars passivated with SiO2 layer. Along with surface morphology, nc-Si/SiO2 volume ratio can be also controlled via laser processing parameters allowing to tailor optical properties of the produced textured surfaces to achieve anti-reflection performance or partial transmission in the visible spectral range. By taking advantage of good wettability, enlarged surface area and remarkable light-trapping characteristics of the produced hierarchical morphologies, we demonstrated surface enhanced fluorescent sensor that allowed to identify metal cations providing sub-nM detection limit unachievable by conventional fluorescent measurements in solutions.

## 1. Introduction

Nanostructures and nanotextured surfaces made of low-loss high refractive index (high-n) materials recently emerged as an alternative platform for manipulation of the radiative properties of quantum emitters [1,2]. Such nanostructures allow to produce significantly enhanced electromagnetic fields via excitation of Mie type resonances or light trapping and focusing effects without excessive heating of nanostructure-emitter system. Also, comparing to their plasmonic counterparts, all-dielectric nanostructures do not suffer from luminescence quenching effects and passively cancel electron-driven catalytic reactions [3]. By using mentioned advantages, novel optical sensing platforms with advanced modalities can be realized [4–9].

## 2. Experiment

Amorphous Si (a-Si) films of variable thicknesses were deposited onto a borosilicate glass substrate by magnetron sputtering and used as a sample for direct laser nanotexturing. Laser processing was carried out with 230-fs 1026-nm wavelength laser pulses generated by a regeneративelyamplified Yb:KGW laser system (Pharos, Light Conversion). Laser processing of the sample surface was performed at a fixed pulse repetition rate of 0.2 MHz, variable pulse energies (between 1.15 - 1.85 μJ) and scanning speeds (between 1 to 100 μm/s) under the single pass regime, where the electric-field polarization vector was oriented parallel to the scan direction.

To assess the applicability of designed hierarchical structures for SEF sensing, we developed novel chemosensor with selective fluorescent response to $Hg^{2+}$ cations.

## 3. Results and discussions

Surface morphology and composition of the LIPSS tailored in a facile way by varying laser processing parameters are expected to affect optical and electrical properties of the patterned surface, opening pathways for various sensing and optoelectronic applications. In particular, the revealed geometry containing ordered and isolated nc-Si micropillars explains previously reported anisotropy of electrical conductivity measured for laser patterned a-Si films as well as difference of the Raman signal pumped with laser radiation polarized either along or perpendicular to nc-Si grating. To highlight some potential applications of produced structures, we started by measuring their transmittance and reflectance in the visible and near IR spectral range under normal incidence. Analysis of the results revealed several key features associated with modification of the surface. First of all, by tailoring the laser processing parameters one can achieve remarkable anti-reflection performance for a certain morphology. More specifically, 3D conical arrangements obtained at the slow laser scanning speed (V=1-3 μm/s) provide less than 2% reflection of the normally incident radiation within the probed spectral range of 450-1100 nm. Moreover, 3D conical structures allow to completely suppress the Fabry-Perot modulations in the reflection and transmission spectra of pristine and even laser patterned a-Si films. Secondly, by controlling the content on nc-Si via one can also modify transmission properties of the patterned area in either visible or near-IR part of the spectrum.

Unique hierarchical nano/microscale morphology of 3D conical structures being combined with their remarkable visible light trapping, enlarged surface area and reproducible up-scalable fabrication make these structures useful for realization as various inexpensive sensor platforms for surface enhanced spectroscopy. Such dielectric nanotextures are promising for realization of ultrasensitive devices based on surface-enhanced fluorescence. Noteworthy, all-dielectric resonant structures do not suffer from fluorescence quenching effects or excessive heating inherent to their plasmonic counterparts. Here, to highlight usefulness of produced morphologies for mentioned applications, we demonstrate the ability to increase sensing performance of widespread analytical technique which is based on the use of fluorescent chemosensors for solution analysis. Obtained samples were used as substrates for deposition and analysis of test solutions, containing $Hg^{2+}$ analyte ions and Rhodamine-based probe (d108) with selective fluorescence response. Our experiments validate the conical-shaped structures as an efficient SEF substrate allowing facile analyte deposition and subsequent detection of $Hg^{2+}$ ions at sub-nM concentrations. More specifically, hierarchical nano- and microroughness capped with SiO2 layer renders the surface

superhydrophilic. After removing from the analyte solution, superhydrophilic surface is expected to retain a thin liquid layer of the analyte facilitating its further targeted deposition, while it completely drains from the surrounding smooth a-Si film surface.

Averaged fluorescence intensity versus analyte concentration gives the sensor detection limit of 0.5 nM that can be calculated considering the signal-to-noise ratio of 3. This result substantiates the structure as an efficient SEF substrate that allows to improve the detection limit of solution-based fluorescent approaches by 2 orders of magnitude, without substantial complication of measurement procedure. For demonstration, we realized measurements in transmission geometry, i.e. the incoming laser radiation excited the sensing layer from the substrate side; however, similar measurements can be realized directly in the reflection geometry substantiating flexibility of the measuring procedure.

## 4. Conclusions

Here, laser-induced surface structuring was used to drive phase transition of a-Si into nanocrystalline Si, that was imprinted as regular arrangement of Si nanopillars capped with $SiO_2$ layer. Using unique morphologies with their hierarchical roughness and remarkable light trapping performance, we demonstrated promising SEF sensor that could simplify bio-medical and environmental sensing, where more complicated surface enhanced Raman scattering/spectroscopy is currently used for quantitative measurements at nanomolar concentrations Since fluorescence is proportional to the molecular absorption cross-section $\sigma a/4\pi \approx 10{-}17$ cm$^2$/rad, it is a considerably stronger effect as compared with Raman scattering whose cross section $\sigma R$ is as small as $\approx 10{-}30$ cm$^2$/rad. Excitation of measurable fluorescence requires lower intensity, which, in turn, is favorable for reduction of photo-degradation of analytes.

## Acknowledgements

The work was supported by Russian Science Foundation (project № 18-79-10091).

## References

[1] A. Kuznetsov, A. Miroshnichenko, M. Brongersma, Y. Kivshar, B. Luk'yanchuk, Science. **354**(2016)aag2472.
[2] S. Bidault, M. Mivelle, N. Bonod, J. App. Phys. **126**(2019)094104.
[3] E. Mitsai, A. Kuchmizhak, E. Pustovalov, A. Sergeev, A. Mironenko, S. Bratskaya, D. Linklater, A. Balˇcytis, E. Ivanova, S. Juodkazis. Nanoscale. **10**(2018)9780.
[4] 6 I. Alessandri, J. R. Lombardi. Chem. Rev. **116**(2016)14921.
[5] N. Bontempi, K. E. Chong, H. W. Orton, I. Staude, D.-Y. Choi, I. Alessandri, Y. S. Kivshar, D. N. Neshev. Nanoscale. **9**(2017)4972.
[6] A. Zhizhchenko, A. Kuchmizhak, O. Vitrik, Y. Kulchin, S. Juodkazis. Nanoscale. **10**(2018)21414/.
[7] E. Mitsai, M. Naffouti, T. David, M. Abbarchi, L. Hassayoun, D. Storozhenko, A. Mironenko, S. Bratskaya, S. Juodkazis, S. Makarov et al. Nanoscale. **11**(2019)11634.
[8] V. A. Milichko, D. A. Zuev, D. G. Baranov, G. P. Zograf, K. Volodina, A. A. Krasilin, I. S. Mukhin, P. A. Dmitriev, V. V. Vinogradov, S. V. Makarov et al. Laser Photon. Rev. **12**(2018)1700227.
[9] G. P. Zograf, A. S. Timin, A. R. Muslimov, I. I. Shishkin, A. Nominé, J. Ghanbaja, P. Ghosh, Q. Li, M. V. Zyuzin, S. V. Makarov. Laser Photon. Rev. (2020)1900082.

Sixth Asian School-Conference on Physics and
Technology of Nanostructured Materials
Vladivostok, Russia, 25 – 29 April, 2022



# Hybrid Au@Si microspheres produced via laser irradiation in liquid

V.A. Puzikov*[,1], S.O. Gurbatov[1,2], A.A. Kuchmizhak[1,2]

[1] Institute of Automation and Control Processes FEB RAS , 5 Radio St., Vladivostok 690041, Russia
[2] Far Eastern Federal University, 8 Sukhanova St., Vladivostok 690950, Russia

*e-mail: vladc3010@gmail.com

**Abstract.** Here, we report one-step synthesis of hybrid Au@Si nanomaterial with unique composition and morphology via scalable and high-performing pulsed laser irradiation of isopropanol solution containing commercial Si micropowder and AuCl4- ions. The resulting hybrid nanomaterial represents sub-micron nanocrystalline Si grains embedded into Au surrounding forming micro-spheres (MSs) additionally decorated with Au nanoparticles. Such unique structure and chemical composition of the Au@Si MSs permits to efficiently absorb and enhance incident radiation within rather broad spectral range spanning from visible to near-IR making the nanomaterial promising for plasmon-mediated amplification of linear and nonlinear optical effects.

## 1. Introduction

Hybrid nanostructures containing both high-refractive-index semiconductors with low optical losses and noble metals that support resonant oscillations of free electron plasma (i.e. surface plasmons) are highly demanded for various applications in sensors, optoelectronics and nanophotonics. From this point of view, Si (as widespread commercial semiconductor) and Au (as the most chemically stable metal possessing visible-range surface plasmons) provide an extremely promising combination for the above mentioned applications towards integration of plasmonics and all-dielectric nanophotonics within unified nanostructures. In particular, optically resonant hybrid Au@Si nanostructures were recently employed as efficient nanoscale source of white light and higher harmonics, as well as optical nanoantennas permitting to manipulate electromagnetic waves at the nanoscale and boost photoluminescence (PL) of attached quantum emitters via the Purcell effect.

In this paper, we introduce a one-step synthesis of hybrid Au@Si microspheres (MSs) with unique composition and morphology via scalable and high-performance pulsed laser irradiation of isopropanol dispersion containing commercial Si micro-powder and $AuCl_4$ species. The resulting hybrid nanomaterial is shown to integrate sub-micron nanocrystalline Si grains wrapped by Au nano-mesh forming micronsized Au@Si spheres with their surface decorated with Au NPs. The composition of the Au@Si product as well as the crystalinity of its Si grains were confirmed by energy-dispersive X-ray (EDX), X-ray diffraction (XRD) and micro-Raman spectroscopy.

## 2. Experiment

Au@Si MSs were produced via LIL processing of commercially available crystalline Si micro-powder (Merck KGaA) following a simple experimental procedure. First, to separate relatively large microparticles also available in the as-supplied powder, 20 mg of starting Si material was placed in 15 mL of isopropanol. Then 2 mL of the prepared suspension was centrifuged at 2000 rpm for 1 min which permitted to precipitate larger micro-particles. Then, 1.8 mL of supernatant was removed and placed to a quartz cuvette, while 5 mL of isopropanol and 1 mL of $10^{-3}$ M HAuCl4 were added. The resulting mixture was placed into the quartz cuvette and irradiated for 1 h using second-harmonic (central wavelength of 532 nm) nanosecond laser pulses with pulse duration of 7 ns (Ultra, Quantel). A focusing lens with focal distance of 10 cm was used to shape the laser radiation into a 2-mm diameter focal spot that irradiated the continuously stirred mixture. The pulse energy and repetition rate were fixed at 40 mJ and 20 Hz, respectively.

Fabricated Au@Si MSs were investigated by scanning electron microscopy (SEM), the elemental analysis by energy-dispersive X-ray spectroscopy (EDX), composition and crystal structure by using XRD technique and dark-field back-scattering spectrum were obtained.

## 3. Results and discussions

Fig. 1(a) demonstrates an SEM image of the nanomaterial (drop-cast on Si substrate) produced upon irradiating Si micro-powder dispersed in isopropanol in the presence of HAuCl4. Irradiation of Si suspension in alcohol for 1 h was found to convert all pristine Si micro-particles with irregular geometry into spherically shaped Au@Si micro-particles. A closer look at their morphology provided by high-resolution SEM indicates their complex morphological and chemical composition. More specifically, the MSs are seen in Fig. 1(b) to contain irregularly shaped Si grains, while gold, which appears brighter in SEM contrast, fills in the space between such Si grains forming Au@Si MSs. Separated Au nanoparticles (or nanoclusters) can also be identified on the surface of the prepared Au@Si hybrid structures.

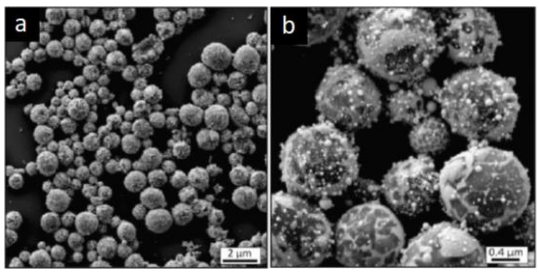


***Fig. 1.*** *SEM images of Au@Si MSs produced via irradiation of precursor microparticles shown in panel.*

To characterize the produced material, first, we probed chemical composition of the obtained Au@Si MSs using EDX spectroscopy. To increase the measurement accuracy, only 1-μm sized micro-spheres were captured by SEM and

then probed by EDX. The measurements showed that for the chosen laser processing conditions the amount of Au detected in Au@Si MSs differed between 16 and 27 wt% (Fig. 2(a)). It is believed that this value can be controlled through the initial concentration of HAuCl4 in the irradiated suspension, as well as through its irradiation time which is also expected to affect the average size of obtained Au@Si MSs.

Fig. 2(b) compares XRD patterns of as-prepared Au@Si MSs (dropcast on crystal Si wafer) with that of a bare Si wafer.

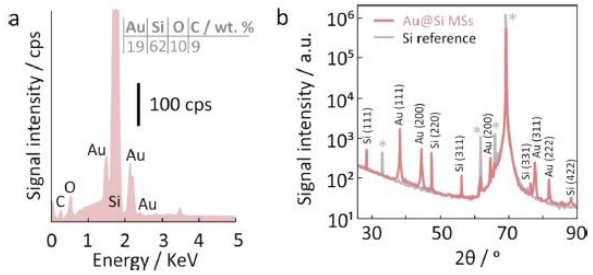


***Fig. 2.*** *Characterization of Au@Si MSs. (a) EDX spectrum of 1-μm-sized Au@Si MS averaged over 50 different MSs with identical diameter. (b) XRD patterns measured from Au@Si MSs (red curve) drop-cast on c-Si wafer (gray curve).*

Crystalline structure of the produced Au@Si MSs was probed using micro-Raman spectroscopy. A representative spectrum of isolated micro-sphere, along with its corresponding SEM and Raman images, are shown in Fig. 3(a), revealing a pronounced spectral shift (Λ) of the main band that corresponds to the phonon mode of crystalline Si. This band is seen to be blueshifted to ≈519.5 $cm^{-1}$ with respect to that of monocrystalline Si reference with its maximum centered at 520.8 $cm^{-1}$. Such a spectral shift was observed for all probed MSs, with a typical value of Λ = 1.3 ± 0.5 $cm^{-1}$ averaged over multiple measurements, and can be attributed to the generally nanocrystalline structure of Si grains inside the Au@Si structures.

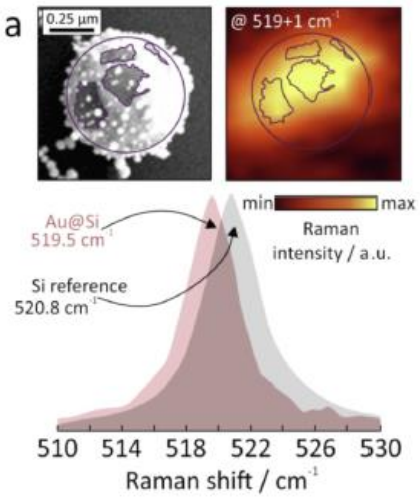


***Fig. 3.*** *Optical characterization of Au@Si MSs. (a) Reference SEM and Raman (at 519 ± 1 $cm^{-1}$) images of isolated 700-nm-sized Au@Si MS (top) and averaged Raman spectra of Au@Si MS and monocrystalline silicon substrate (bottom).*

Altogether, the Au nanoclusters densely arranged on the surface of an Au@Si MS should permit to achieve localization and enhancement of EM-field amplitude of incident waves within a broad spectral range spanning from visible to near-IR. To illustrate this, Fig. 4 provides two maps showing a strong enhancement (up to 102 at certain points) of squared normalized EM-field amplitude (E/E0)2 near the surface of an Au@Si MS pumped at 1000 and 532 nm.

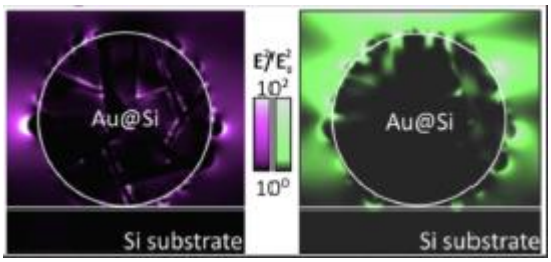


***Fig. 4.*** *Squared normalized electric-field amplitude (E/E0)2 near an isolated Au@Si MS calculated upon its excitation by linearly-polarized plane wave from the top with 532- and 1000-nm pump wavelengths.*

## 4. Conclusions

To conclude, laser irradiation of commercial Si micro-powder suspended in isopropanol containing AuCl4- ions was used to synthesize a novel hybrid nanomaterial, in which sub-micron Si grains were wrapped with Au inclusions to form Si microspheres decorated with Au nanoclusters (Au@Si MSs). The unique structure and composition of the produced Au@Si MSs permits to efficiently absorb and enhance incident radiation within a rather broad spectral range spanning from visible to near-IR, thus making the material promising for amplification of linear and nonlinear optical effects. To prove this, we demonstrated nonlinear generation of broadband "hot" PL in nanocrystalline Si grains stimulated by photoinjection of high-energy carriers from Au surroundings upon excitation with IR fs-laser pulses. Apart from a nonlinear optical response, the produced nanomaterial is expected to be useful for various promising applications where localized plasmon-mediated electromagnetic fields are highly demanded. Among others, one can envision applicability of such Au@Si MSs as single-particle sensors based on surface-enhanced PL/Raman scattering approach, or as photothermal converters of optical radiation operating via volumetric and localized heating. Such research directions are in line with the scalability of laser irradiation in liquid towards inexpensive gram-per-hour yields.

**Acknowledgements**

This work was supported by Russian Science Foundation (grant number 21-79-00302).

Sixth Asian School-Conference on Physics and
Technology of Nanostructured Materials
Vladivostok, Russia, 25 – 29 April, 2022



# Superhydrophilic surfaces obtained by nanosecond laser treatment to enhance nucleate pool boiling heat transfer

S.V. Starinskiy*[,1,2], Yu.G. Shukhov[1], A.A. Rodionov[1,2], A.V. Bulgakov[1,3], A.I. Safonov[1], I. Malakhov[1,2], V.S. Serdykov[1,2], A.S. Surtaev[1,2]

[1] S.S. Kutateladze Institute of Thermophysics SB RAS, 1 Lavrentyev Ave, 630090 Novosibirsk, Russia
[2] Novosibirsk State University, Pirogova Str. 2, 630090 Novosibirsk, Russia
[3] HiLASE Centre, Institute of Physics, Czech Academy of Sciences, Za Radnicí 828, 25241 Dolní Břežany, Czech Republic

*e-mail: starikhbz@mail.ru

**Abstract.** The presented research demonstrates the formation of hierarchical structure of single-crystalline silicon surface in narrow range of nanosecond laser treatment condition. The surface after laser treatment is characterized by superhydrophilic properties ($\theta < 5^\circ$) and retains them for a long time. The results showed that the laser texturing of a surface lead to the heat transfer enhancement during boiling of saturated water over the entire range of heat fluxes. The heat transfer enhancement in the experiments was up to 234% in compare of an ultra-smooth silicon surface.

## 1. Introduction

Fabrication of surfaces with extreme wetting properties, namely, superhydrophilic and superhydrophobic ones, is a hot field in material design engineering. Such materials are very promising for a wide range of applications including self-cleaning fabrics and antifogging surfaces, anticorrosion, separation filters, biosensors and biochips and many others [1] . There are two main approaches to control the wettability, variation of the surface energy by changing its composition and increase of the surface roughness [2]. Laser processing is a very flexible instrument for controlling both of these parameters for different materials [3,4]. To date the laser treatment has already been used by a number of scientific groups to fabricate modified heat transfer surfaces to in- crease heat transfer coefficient (HTC) and critical heat flux (CHF) values during pool boiling [5]. However, studies devoted to the features of boiling on laser-textured silicon surfaces are still rare, which makes it impossible to carry out a detailed analysis and determine the optimal modification configurations of the surface. In present work we demonstrate feature of formation of periodic superhydrophilic microstructures on single-crystal silicon surface by infrared nanosecond laser processing. It is shown that such surfaces allows to increase HTC during boiling process.

## 2. Experiment

The single-crystal silicon (100) wafers were used as irradiation targets. The targets were irradiated by a Nd:YAG laser operating at either fundamental (1064 nm) or second harmonics (532 nm) outputs and providing line-arly polarized Gaussian pulses with duration of 9 and 7 ns (FWHM), respectively. The pulse repetition rate was 7 Hz in all experiments. The laser processing was carried out in a vacuum chamber where the air pressure was varied from the base pressure of 0.01 mbar to 1 bar. To investigate oxidation effects during silicon processing experiments were also performed in pure argon and oxygen at 1 bar. criterion). The average laser fluence at the target surface as varied in the range 1–7 J/cm2. Individual spots were produced by irradiating the same place at the surface with different number of laser pulses N in the range 1–250. To produce large laser-modified areas, several samples were irradiated in the scanning regime. The details of the procedure are described in [6]. Pool boiling experiments were conducted using the setup, which detailed description and the scheme could be found in [7]. As the working fluid, deionized water provided by Milli-Q Synergy purification system was used. The experiments were performed at the saturation conditions under atmospheric pressure. To analyze the dynamics of vapor bubbles during nucleate boiling, the high-speed recording was performed using a Phantom VEO410 video camera. Its maximum frame rate in the experiments was 10,000 fps, the resolution was 0.083 mm per pixel. The temperature field of the ITO film was recorded by a high-speed thermographic camera FLIR Titanium HD 570 M with the frame rate of 1000 fps and resolution of 0.17 mm per pixel

## 3. Results and discussions

The laser treatment of silicon surface at different conditions was done. It was found that the self-organized microstructure on single crystal silicon may be obtained by multipulse nanosecond IR irradiation in very narrow range of condition: laser fluence 3-5 J/cm2, number of pulses 25-75. In this case the morphology of central part of laser spot is mesh of orthogonal cracks (the step is 40-50 mkm) and the microhillocks form on its cross. Formation of cracks weakly depended on laser treatment conditions and surrounding. However, the microhillocks forms only in oxygen content background with pressure around the atmospheric (Fig.1). It was analyzed the dependence of silicon ablated mass on background pressure. It was found that at pressures above 60 Pa the mass of the irradiated target remains unchanged. The increase of oxygen partial pressure lead to formation lager hillocks. The processing of some area at founded regimes for microhillock formation lead to contact angle transition of silicon from $55^o$ to $0^o$. It is found that such bright properties are not achieved when the surface is treated by a green laser or in an inert background.

Using thermographic recording experimental data on the dependence of the heating surface temperature, averaged over time (10 s) and area, on the heat flux density were obtained, and the corresponding boiling curves were plotted for an untreated and laser-textured silicon surface (Fig. 2). Comparison of the obtained data shows that the

treated surface demonstrates the heat transfer enhancement during boiling in the entire range of heat fluxes.

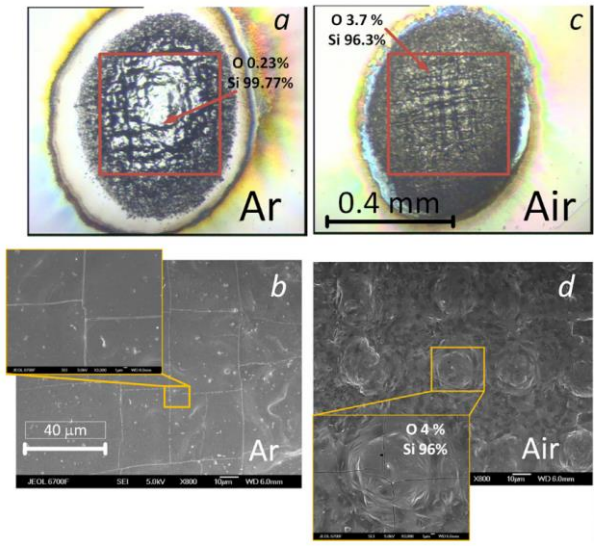


***Fig. 1.*** *Optical (top line) and SEM (bottom line) images of laser spots produced in argon (a,b), air (c,d) background gases at 1 bar. The wavelength is 1064 nm, fluence is 3.3 J/cm2, the number of pulses is 50. The indicated compositions were determined by the EDX method inside the corresponding square regions. For the untreated silicon surface the composition was 0.4% of O and 99.6% of Si.*

To study the heat transfer rate during boiling on the laser-textured surface, at least 4 series of experiments were carried out, both with increasing and decreasing the heat flux density. Comparison of the obtained boiling curves showed that the discrepancy between them is within the measurement error. This indicates the high stability of the obtained microstructures and the preservation of all surface properties (wetting, roughness, capillarity, etc.) during boiling experiments. A detailed analysis of the vapor bubbles dynamics during boiling on the laser-textured silicon surface was carried out to identify the mechanisms and causes of the observed heat transfer enhancement The laser treatment of the heating surface has a significant effect on the boiling behavior. In particular, it can be seen that in the regime of single vapor bubbles (q = 43 kW/m2) boiling on the laser-textured surface is characterized by a significant decrease in the size of vapor bubbles in comparison with the reference surface. Analysis of the video data shows that the waiting time for the appearance of a vapor bubble is about 100 ms for boiling on the untreated surface, while for the modified surface this value is 2 orders of magnitude less (from 1 ms to 3 ms). Therefore, in a number of cases, bubbles growing on a modified surface before their direct detachment can merge with already floated bubbles.

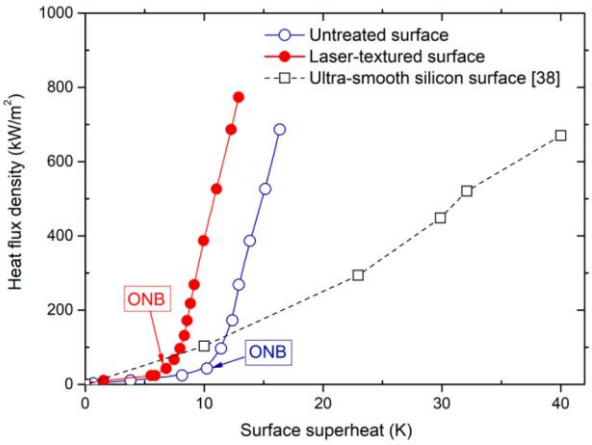


***Fig. 2.*** *Saturated water boiling curves, and during water pool boiling on the untreated and laser-textured silicon surface.*

## 4. Conclusions

The presented research demonstrates the formation of hierarchical structure of single-crystalline silicon surface in narrow range of laser treatment condition. The morphology is periodic hillocks in cracks crossing at microscale and porous surfaces at nanoscale. Analysis of the modified surface showed that laser treatment significantly changes its wettability. In particular, the surface after laser treatment is characterized by superhydrophilic properties ($\theta < 5^\circ$) and retains them for a long time. The results showed that the laser texturing of a surface lead to the heat transfer enhancement during boiling of saturated water over the entire range of heat fluxes. The heat transfer enhancement in the experiments was up to 234% in compare of an ultra-smooth silicon surface. Using the high-speed video recording the effect of the laser texturing on the vapor bubbles dynamics during pool boiling was studied.

## Acknowledgements

The work was supported by the Russian Science Foundation (Grant No. 18–79–10119).

## References

[1] J. Drelich and A. Marmur, Surf. Innov. **2**(2014)**211**.
[2] L. B. Boinovich, A. M. Emelyanenko, Russ. Chem. Rev. **77**(2008)583.
[3] R. Jagdheesh, J. J. Garcia-Ballesteros,J. L. Ocana, Appl. Surf. Sci, **2**(2016)374.
[4] A. Y. Vorobyev and C. Guo, Opt. Express **18**(2010)6455.
[5] G. Udaya Kumar, S. Suresh, C. S. Sujith Kumar, S. Back, B. Kang, H. J. Lee, Appl. Therm. Eng. **174**(2020) 115274.
[6] S.V. Starinskiy, A.A. Rodionov, Y.G. Shukhov, A.I. Safonov, E.A. Maximovskiy, V.S. Sulyaeva, A.V. Bulgakov, Appl. Surf. Sci. **512**(2020) 145753.
[7] V. Serdyukov, S. Starinskiy, I. Malakhov, A. Safonov, A. Surtaev, Appl. Therm. Eng. **194**(2021)117102.

# VI. Photonic and electronic devices: integrated circuits, solar cells, nanophotonics, biophotonics

Sixth Asian School-Conference on Physics and
Technology of Nanostructured Materials
Vladivostok, Russia, 25 – 29 April, 2022



# Chalcogenide thin films for reconfigurable optical waveguide application

P.I. Lazarenko*,1, V. Kovaluyk[2], P. An[2], A. Prokhodtsov[2], V.B. Glukhenkaya[1], T. Kulevoy[3], A.O. Yakubov[1], A.A. Sherchenkov[1], S.A. Kozyukhin[4], G. Goltsman[2]

[1] National Research University of Electronic Technology, Moscow, 124498, Russia
[2] Moscow State Pedagogical University, Moscow, 119992, Russia
[3] National Research Center "Kurchatov Institute"-ITEP, Moscow, 117218, Russia
[4] Kurnakov Institute of General and Inorganic Chemistry, Moscow, 119991, Russia

*e-mail: lpi@org.miet.ru

**Abstract.** The use of phase change materials makes it possible to use nanophotonic devices in different reconfigurable photonic integrated circuits, including fully optical on-chip neural networks. Currently, $Ge_2Sb_2Te_5$ is a functional phase change material which is most commonly used in reconfigurable multilevel devices. However, the operating parameters of the developed reconfigurable nanophotonic devices can be significantly improved by doping $Ge_2Sb_2Te_5$. The effect of tin ion implantation on the amorphous $Ge_2Sb_2Te_5$ thin films is studied, as well as the performance of silicon nitride Mach-Zehnder interferometers and reconfigurable multilevel balanced beam splitters based on them. The effective absorption coefficients for different tin concentrations of Sn-doped $Ge_2Sb_2Te_5$ are experimentally measured on the fabricated on-chip nanophotonic devices: the experiment have illustrated the possibility of reversible recording of 9 logical levels.

## 1. Introduction

Phase change memory materials, in particular Ge-Sb-Te [1,2], are widely used for rewritable optical (DVD, Blu-Ray) and electrical (PCRAM) storage application. This is due to significant changes in the optical and electrical properties during phase transformations between amorphous and crystalline states induced by short and low-energy laser or current pulses. The high rate of phase transformations (less than 16 ns), large optical contrast, and the possibility of the formation of more than ten states with different degrees of crystallization cause an active research interest in searching new photonic areas of their application. The use of phase change materials, in particular, $Ge_2Sb_2Te_5$ (GST225) makes it possible to use nanophotonic devices in different reconfigurable photonic integrated circuits, including fully optical on-chip neural networks. However, the operating parameters of the developed reconfigurable nanophotonic devices can be significantly improved by doping GST225. The present work focuses on the effect of tin ion implantation on the amorphous GST225 thin films, as well as the performance of silicon nitride Mach-Zehnder interferometers and reconfigurable multilevel balanced beam splitters based on them.

## 2. Experiment

The rib waveguide of the resonator was formed the first stage of e-beam lithography and subsequent reactive-ion etching. We used the second stage of e-beam lithography combining with lift-off method for the formation of GST225 active region on the resonator ring surface. Thin films (~20 nm) of the GST225 composition were prepared by DC magnetron sputtering at room temperature. A series of samples with a different concentration of an Sn dopant (5, 2, 1, 0.5 and 0.1%) was prepared on Multipurpose Test Bench. The structure and elemental distribution along the thickness for as-deposited and Sn-doped GST225 thin films were checked by X-Ray diffraction and Auger electron microscopy. Silicia coating layer was used to protect against oxidation of the Sn-doped GST225 during the investigation.

## 3. Results and discussions

The measured transmission spectra for the fabricated devices with amorphous and crystalline GST225 covers in comparison with data for the uncovered O-ring resonator are presented in Fig. 1 e,i. It is seen that the deposition of amorphous GST225 cover on the surface of the waveguide leads to a decrease of the optical power, transmitted through the waveguide (Fig. 1, e), and increase in the optical losses. Comparison of the optical transmittance for O-ring resonators with and without GST225 cover allowed to identify the change in the Q-factor and the wavelength peak shift.

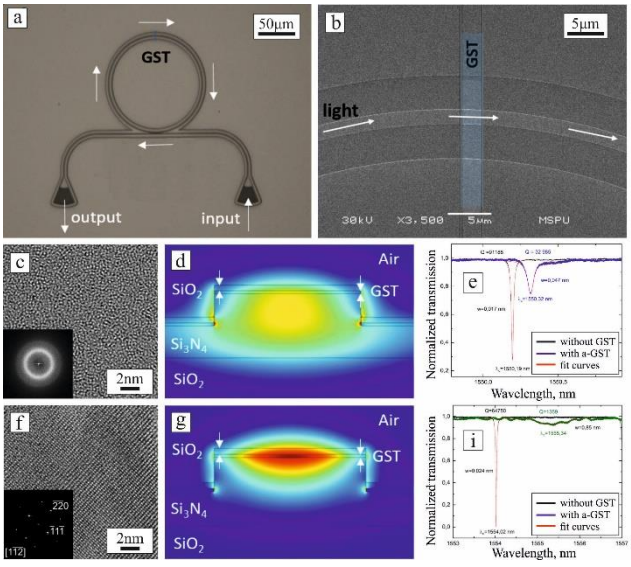


***Fig. 1.*** *The optical micrograph of a fabricated O-ring resonator (a); SEM image of the area with GST cover (b); HRTEM images and Fourier transform patterns (c, f); 2D model cross sections of the resonators (d, g); transmittance spectra for the fabricated resonators (e, i). Images (c,d,e) and (f,g,i) show the results for the a-GST and c-GST cover, respectively.*

Crystallization of the cover leads to a further change in optical transmission. It was observed that crystallization of amorphous GST film lead to a decrease of the transmitted optical power (Fig. 1, i). This can be explained by the differences of the complex refractive indexes of amorphous and crystalline GST225 thin films. From the measurement data, the GST225 effective refractive index was also extracted depending on the ring waveguide width of the resonator for a wavelength of 1550 nm. The influence of the GST225 cover length and the width of the waveguide in the ring part of the microcavity on the optical mode distribution was simulated based on the ellipsometric data and confirmed the experimental results.

XPS and Raman results showed that tin ion implantation in GST225 leads to the effective replacement of the Ge by Sn. Meanwhile, replacement of Ge atoms by Sn is accompanied by the decrease of the binding energies from 420 kJ/mol for the Ge–Te bond to 319,2 kJ/mol for that of Sn–Te. Small amounts of dopants are sufficient to change the properties of thin films. So, the results showed that the Sn incorporation leads to the significant changes in the amorphous GST absorption coefficient of the atop waveguide, which plays a key role for the design of complex tunable and neuromorphic PICs.

To confirm the possibility of using the Sn-doped GST225 thin films to implemented a reversible multi-level phase switching in integrated devices, we investigated switching in a fabricated balance splitter on a chip. The pump-probe experimental setup was used to form a single optical pump pulses for switching the Sn-doped GST225 cell of a nanophotonic device. The time dependence of the probe signal transmission demonstrating the multilevel switching between the logical states for a sample with 2 at. % Sn is shown in Fig. 2.

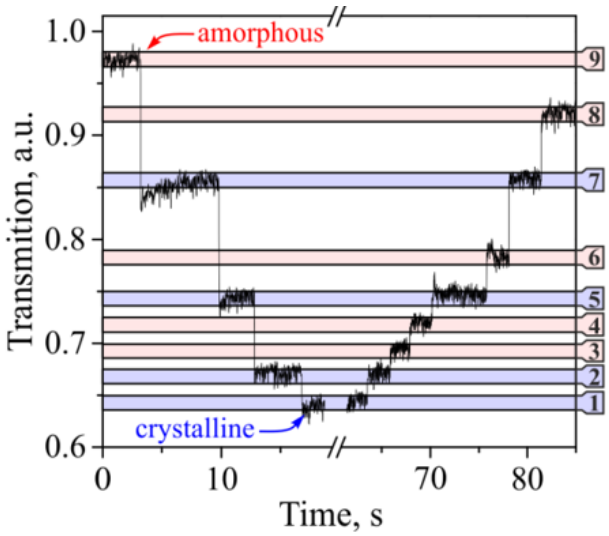


***Fig. 2.*** *Time dependence of a probe signal during 50 ns of the pump pulses absorption for the balance splitter on the basis of GST225 with 2 at.% Sn thin film.*

The 9 nonvolatile different levels (3 bits) for the nanophotonic samples based on the Sn-doped GST225 thin films were demonstrated. It should be noted that switching between levels can be carried out both sequentially and through several levels. This option is required to create neuromorphic computations.

## 4. Conclusions

The effect of tin ion implantation on the properties of amorphous GST225 thin films and influence of using such films on the parameters of silicon nitride nanophotonic circuits have been investigated. The Sn implantation led to the following results having positive complex effect on the energy consumption of laser switching processes. The possibility to use the Sn-doped GST225 thin films for fully optical multilevel reversible recording has been demonstrated by experimental measurements of fabricated on-chip balanced beam splitters. The reversible switching between 9 different levels (3 bits) both sequentially and through several levels without completely erasing the cell was performed. It has the potential to improve the characteristics of reconfigurable multilevel nanophotonic devices using the GST225 thin films and developed on-chip low power all-photonic circuits for post-von Neumann arithmetic processing.

## Acknowledgements

This work was supported by Russian Science Foundation (project No. 20-79-10322).

## References

[1] S. Abdollahramezani, O. Hemmatyar and et al. J. Nanophotonics. **9** (2020) 1189-1241.

[2] N. Youngblood, C. Ríos and et al. Adv. Funct. Mater. **29** (2019) 1807571.

Sixth Asian School-Conference on Physics and
Technology of Nanostructured Materials
Vladivostok, Russia, 25 – 29 April, 2022



# Semimetal $CaSi_2$ thin film: a nontrivial transparent conducting material for VIS-MIR applications

A.V. Shevlyagin*, V.M. Il'yaschenko, A.V. Amosov
Institute of Automation and Control Processes FEB RAS , 5 Radio St., Vladivostok 690041, Russia

*e-mail: shevliagin@mail.ru

**Abstract.** Transparent conducting materials (TCMs) provide low cost, processability and effective solution for the modern optoelectronics. However, despite the progress in band engineering of the transparent conducting metal oxides (TCOs), near-infrared (NIR) and middle-infrared (MIR) spectral ranges are unoccupied niches mainly resulted from the high free-carrier absorption in TCOs. Several works have already reported partial IR transmittance of the thin film semimetals without any idea behind this phenomenon. This study proposes thin film of the calcium disilicide ($CaSi_2$) to fill this application gap for Si-based optical devices. Measured high transparency and conductivity could be easily transferred for Si-based Schottky photodetectors operated in the NIR and MIR spectral ranges and for transparent conducting top electrodes for Si cells owing to demonstrated partial transparency in the visible range as well.

## 1. Introduction

History and commercial application of the transparent conducting materials (TCMs) have started with tin oxide coating on glass substrate in the last century. Since development of the large area deposition techniques, TCMs have a wide variety of applications including energy-conserving smart windows, display panels, electrochromic films and front electrodes for solar cells. However, simultaneous high electrical conductivity and optical transparency within wide spectral range remain challenging. Despite band engineering applied to metal oxides [1] is an effective solution at least for the visible wavelength region (VIS), there is an application gap in the near-infrared (NIR) and middle-infrared (MIR) ones, which are of interest for the Si-based optoelectronics. In this work, we have succeeded in semimetal $CaSi_2$ films growth on $Al_2O_3$ substrates and demonstrated for the first time partial optical transparency in the VIS spectral range in addition to previously reported NIR-MIR optical functions of the $Si/CaSi_2$ and $Si/CaSi_2/Si$ heterostructures [2]. After thickness and annealing temperature optimizations, obtained $CaSi_2$ coatings reached competitive figure of merit in comparison with other widely known TCMs applying as solar cells electrodes and demonstrated ground-breaking NIR-MIR performance suggesting photodetection applications in the frame of Si optoelectronics and sensors.

## 2. Experiment

The $CaSi_2$ films of different thickness were grown on $Al_2O_3(0001)$ substrate by solid phase epitaxy including deposition of the Si/Ca bilayer followed by annealing at ~600°C in vacuum evaporation unit with base pressure of $1\times10^{-6}$ Torr. The chamber is equipped with K-cells for Ca and Si evaporation, quartz crystal microbalance sensor (QCM) and rotating sample's holder with resistive heater. QCM sensor was used for monitoring the deposition rates. A calibration factor was obtained by comparing the thickness inferred from the QCM sensor with that of measured by atomic force microscopy on a specially step-shaped film. Room-temperature optical properties were recorded in the (200-3000) nm range using Cary 5000 spectrophotometer. Sheet resistance of the deposited $CaSi_2$ coatings was calculated from the current-voltage measurements under the known film's geometrical area and thickness.

## 3. Results and discussions

Thickness of the deposited $CaSi_2$ films, room-temperature sheet resistance and optical transmittance at the telecommunication C-band (1550 nm) are summarized in Table I. Next, we have evaluated NIR optical performance of the TCM under consideration by standardized figure of merit (FOM) [3] expressed as follow:

$$FOM = -1/(R_{sheet} \times \ln(T)) \quad (1),$$

where $R_{sheet}$ and $T$ are sheet resistance and optical transmittance both measured at room temperature. Maximal FOM values of 0.59 $\Omega^{-1}$ was calculated for 100 nm-thick $CaSi_2$ film on $Al_2O_3$ substrate, which is superior to that of well-established transparent conducting oxides ($CuScO_2$, ITO, ZnO, SnO and CdO) [4-6], and other semimetals (ErAs and LuAs) [7, 8], whereas it contains neither rare-earth nor toxic elements.

***Table I.*** *Optical and electrical parameters of the grown samples.*

| Sample | Film thickness, (nm) | Sheet resistance, (Ω/□) | Optical transparency @ C-band, (%) | FOM, ($\Omega^{-1}$) |
|---|---|---|---|---|
| *A* | 12 | 70 | 69 | 0.068 |
| *B* | 19 | 29 | 65 | 0.130 |
| *C* | 29 | 68 | 60 | 0.042 |
| *D* | 36 | 238 | 44 | 0.006 |
| *E* | 43 | 14 | 41 | 0.096 |
| *F* | 55 | 15 | 70 | 0.341 |
| ***G*** | **100** | **7** | **67** | **0.594** |
| *H* | 167 | 6 | 50 | 0.290 |

It can be clearly seen that $CaSi_2$ film thickness increase resulted in non-monotonic behavior of the calculated FOM as well as its components being in the denominator. This fact can be tentatively originated from the previously reported phase composition dependence from the total thickness of the grown silicide film [9]. For instance, imbalance in deposited Ca and Si and annealing condition may results in $CaSi_2$ hR3 polymorph growth rather than

hR6 one. Optical and electrical transport properties of the former phase are less well investigated due to the absent of single-phase hR3 films or monocrystals. In addition, Si deficit promotes calcium monosilicide (CaSi) formation being topological insulator. Despite higher overall optical transparency of the CaSi films compared to $CaSi_2$ ones, 10-fold lower electrical conductivity was demonstrated [10], which dramatically drops performance of CaSi as TCM.

For deeper understanding of the obtained FOM values, let us directly compare optical transmittance of the grown $CaSi_2$ coatings in the wide spectral range from 200 to 3000 nm covering UV-VIS-NIR-MIR presented in Fig. 1. $CaSi_2$ films permit from 10 to 75% of sapphire substrate transmittance in visible wavelength. Three distinct features can be pointed out: (i) the thicker $CaSi_2$ film, the lower overall optical transparency is observed; (ii) pronounced interference starts when film thickness exceeded 30 nm; (iii) decrease in film thickness is accompanied by blue shift of the transparency edge.

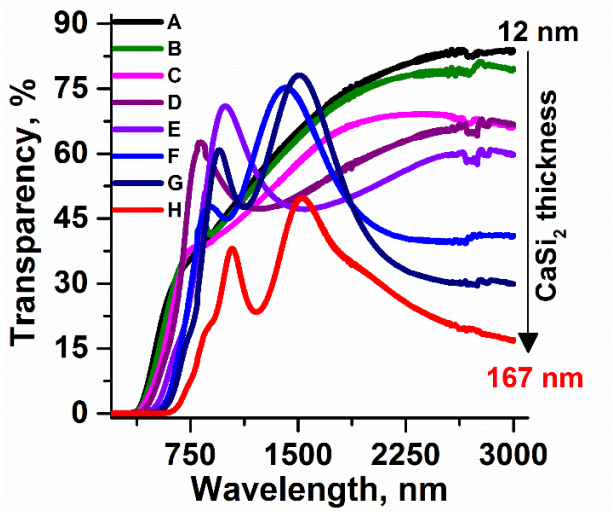


***Fig. 1.*** *Room-temperature optical transmittance spectra for $CaSi_2$ thin film coatings of different thickness deposited on $Al_2O_3$ substrates. Data are normalized on transmittance of the substrate used.*

The first one resulted from increase in optical absorption, as reflectance of the $CaSi_2$ films is thickness independent. The second feature is related to difference in refractive indices of the $Al_2O_3$ and $CaSi_2$. The last one suggests that $CaSi_2$ demonstrates optical properties similar to wide band gap semiconductors or insulators with very high UV absorption. Under this assumption, $CaSi_2$ "band gap" is thickness dependent ranging from 3.8 eV (transparency edge at 325 nm) to 2 eV (transparency edge at 625 nm) for the thinnest and the thickest samples, respectively. This interesting behavior can be applied in UV and solar blind photodetectors alongside with, for example, GaN or $Ga_2O_3$.

Finally, one may make certain of the $CaSi_2$ films VIS transparency paying attention to the photography series shown in Fig. 2. The thinner $CaSi_2$ coatings, the more plainly Institute of Automation and Control Processes logo is seen with its color changing from light yellow to deep brown. Photograph of the optimized in terms of NIR FOM $CaSi_2/Al_2O_3$ sample (Sample **G**) is shown in Fig. 2 as well, demonstrating country house seeing through it. It should be noted that 100-nm thick $CaSi_2$ film remains partial optical transparency in the visible range. Providing one the best room-temperature sheet resistance for the Sample ***G***, the FOM values of 0.05 and 0.15 $\Omega^{-1}$ are calculated separately for VIS (350-800) nm and overall (200-3000) nm ranges, respectively, which leave a room for the further improvements to be competitive with currently used TCMs targeted on VIS region.

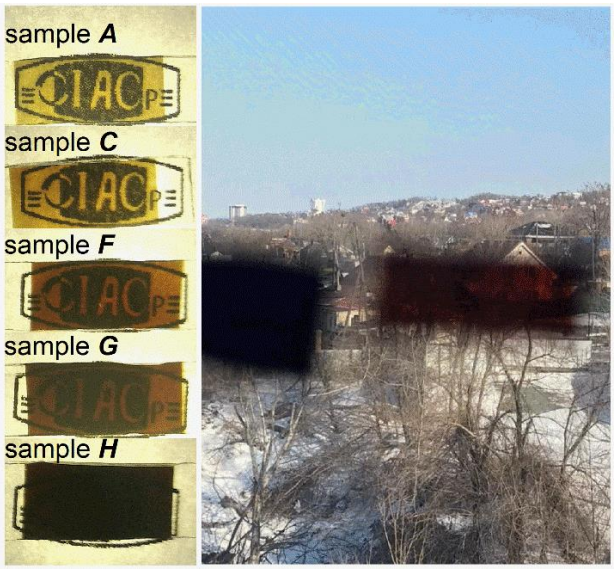


***Fig. 2.*** *Photographs of the $CaSi_2/Al_2O_3$ samples demonstrated partial transparency in the VIS region. Samples are placed from top downward as $CaSi_2$ film thickness increases from the thinnest one (12 nm) to the thickest one (167 nm).*

## 4. Conclusions

In this work, we succeeded in the growth of $CaSi_2$ film on sapphire substrate with neither protective nor stabilization layers. Obtained transparent conducting coatings preserve optical transparency no worse than 20% in the NIR and MIR spectral ranges reaching maximum transmittance of 67% at an important telecommunication wavelength of 1550 nm in addition to low sheet resistance of 7 Ω/□ at room temperature under optimized both $CaSi_2$ thickness and growth conditions. Calculated TCM standardized NIR FOM is superior to other modern materials, while demonstrated for the first time partial VIS transparency suggest $CaSi_2$ to be applied as front electrode for Si-based solar cells.

## Acknowledgements

This research was supported by the Russian Science Foundation under Grant No. 20-72-00006. A.V. Shevlyagin would personally like to thank the Russian President's Young Scientists Scholarship No. СП-1143.2021.1 for financial support.

## References

[1] X. Cai, S. H. Wei. Appl. Phys. Lett. **119** (2021) 070502.
[2] N. G. Galkin *et al.* Jpn. J. Appl. Phys. **59** (2020) SFFA12.
[3] R. G. Gordon. MRS Bull. **25** (2000) 52.
[4] Y.-H. Chuai *et al.* Mater. Res. Express **6** (2019) 126460.
[5] R. A. Maniyara *et al.* APL Mater. **9** (2021) 021121.
[6] Md. F. Hossain *et al.* Mat. Sci. Semicon. Proc. **121** (2021) 105346.
[7] E. M. Krivoy *et al.* Appl. Phys. Lett. **101** (2012) 141910.
[8] M. P. Hanson, A. C. Gossard, E. R. Brown. Appl. Phys. Lett. **89** (2006) 111908.
[9] K. Ito, T. Suemasu, H. Nakano. Jpn. J. Appl. Phys. **57** (2018) 120313.
[10] M. Affronte, O. Laborde, G. L. Olcese, A. Palenzona. J. Alloy Compd. **274** (1998) 68.

Sixth Asian School-Conference on Physics and
Technology of Nanostructured Materials
Vladivostok, Russia, 25 – 29 April, 2022

**VI.o.03**

# CuSCN as hole transport material for perovskite solar cells

D. Sapori*, S.V. Makarov
Department of Physics and Engineering, ITMO University, Lomonosov str 9, Saint Petersburg 191002, Russia

*e-mail: daniel.sapori@metalab.ifmo.ru

**Abstract.** High efficiency perovskite solar cells are usually achieved with expensive hole transport materials (HTM). To bring this technology to industry it is essential to find alternative HTM. Here we use the inorganic semiconductor CuSCN as HTM in inverted device structure. We first studied the interaction between CuSCN and the perovskite solution by performing solubility test and found out that CuSCN can be dissolved in perovskite solution. Then devices were fabricated using single-step deposition technique and sequential deposition technique were first a PbI2 layer is first deposited that could overcome the potential incompatibility of the perovskite solution with the CuSCN. Solar cells with Voc>1000 mV were successfully fabricated with the 2-step process but demonstrated lower efficiencies compared to the 1-step process due to a lower Jsc.

## 1. Introduction

Within the last 10 years, halide perovskites have become one of the most promising materials for photovoltaic application: single-junction perovskite solar cells have seen their conversion efficiency increased from few percent to more than 25% close behind to the record efficiency of reference silicon devices [1,2]. In addition, their combination with silicon absorber in a tandem device have proved to be able to overcome the theoretical limit of efficiency for single junction silicon cell with the certified efficiency approaching 30% [1,3].

Nevertheless, it remains many challenges to bring perovskite materials to industry: upscaling, stability, and choice of materials. For the later, one significant issue is to find alternative hole transport material (HTM) that could replace usual HTM such as PTAA and Spiro-OMeTAD that are costly. Among possibilities, copper(I) thiocyanate (CuSCN) appears as a promising material. Indeed, this inorganic p-type semiconductor has numerous advantages: low-cost, good electrical, optical properties, and thermal stability, well aligned work function with perovskite absorbers and low temperature deposition [4].

Despites these advantages, the use of CuSCN in perovskite devices remains low. First reports highlighted a potential degradation process at the interface between CuSCN and the perovskite [5]. But later Arora et al. showed the instability originated from the CuSCN/Au contact interface and demonstrated an efficiency of 20.8% by adding a reduced graphene oxide spacer at this interface [6]. In inverted structure (i.e., the HTM is first deposited on the substrate, see Fig. 3), there are few reports, but with modest efficiencies ~17% [7].

In this work, we study the use of CuSCN in inverted structure perovskite solar cells. The interaction between this HTM and the perovskite solution is first investigated. Then devices were fabricated using two different deposition techniques of MAPbI3: 1-step antisolvent deposition and 2-step sequential deposition.

## 2. Experiment

*Solubility of CuSCN:* 10 mg of CuSCN were added to 0.5 mL of anhydrous dimethylformamide (DMF) solutions containing eventually PbI2 and MAI materials (see Table I for the details). Solutions were then mixed rigorously and with the help of an ultrasonic bath. The solutions showing low solubility of the CuSCN, were subjected to centrifugation at 4000 rpm during 2 min to highlight the solid phase.

***Table I.*** *Parameters of solutions for solubility test of CuSCN and qualitative results.*

| Samples | Solvent | PbI2 (M) | MAI (M) | Solubility (Qualitive) |
|---|---|---|---|---|
| A | DMF | 0 | 0 | No |
| B | DMF | 1 | 1 | Complete |
| C | DMF | 0 | 1 | Complete |
| D | DMF | 1 | 0 | No |

*Device making:* Fluorine-doped tin oxide (FTO)-glass substrates were first patterned by laser ablation then cleaned by ultrasonication in deionized water, acetone, and then isopropyl alcohol (IPA). Prior the deposition of CuSCN, samples were treated in O2 plasma. The compact layer of CuSCN was deposed by spin-coating at a spin speed of 2000 rpm during 30s, following by an annealing step at 150°C during 10 min.

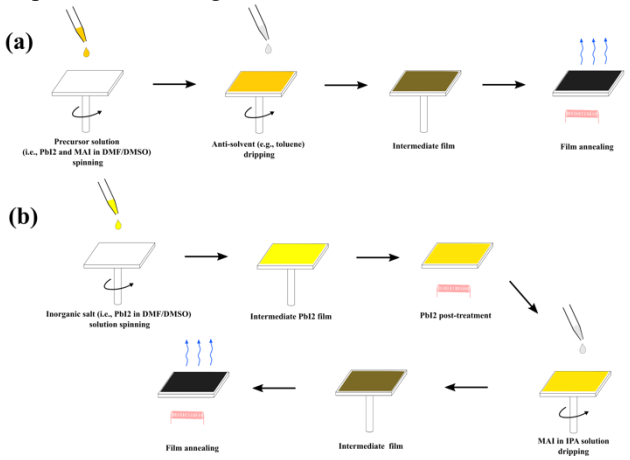


***Fig. 1.*** *Deposition techniques by spin-coating of halide perovskite thin films: 1-step with antisolvent (a) and 2-step sequential deposition (b).*

For the single-step deposition technique (Fig. 1.a), perovskite solution containing PbI2 (1M) and MAI (1M) in 9/1 DMF/ dimethyl sulphoxide (DMSO) was spin-coated at a spin speed of 500 rpm during 15s then 3000 rpm during 25s. 15s before the end of the spin program, 500 µL of diethyl ether was dropped on the sample. The film was then

annealed at 100°C during 10 min. For the sequential deposition method (Fig. 2.b), PbI2 solution (1M) in 9/1 DMF/DMSO was first spin-coated on the substrate at a spin speed of 2000 rpm during 30s. After a waiting time of 2 min, 100 µL of a solution containing 40 mg/mL of MAI in IPA was dropped cast at a spin speed of 5000 rpm during 30s, followed by an annealing at 100°C during 10 min.

After deposition of the perovskite film, subsequently ~25 nm of C60 and ~5 nm of BCP were deposited by thermal evaporation. Finally, the top contact made of 80 nm of Silver was thermally evaporated.

For PEDOT:PSS based devices: instead of the CuSCN deposition step, PEDOT:PSS solution was spin-coated at a spin speed of 3000 rpm during 60s followed by annealing treatment at 140°C during 10 min. For HTM free devices, FTO substrates were subjected first to O2 plasma during 10 min prior the perovskite layer deposition.

## 3. Results and discussions

A first question regarding the use of CuSCN in inverted structure is to understand if the deposition of the perovskite itself would damage the HTM layer. It is known that CuSCN is difficult to dissolve in solvents and usually diethyl sulfide or aqueous ammonia are used. We therefore investigate the solubility of CuSCN in the perovskite solution.

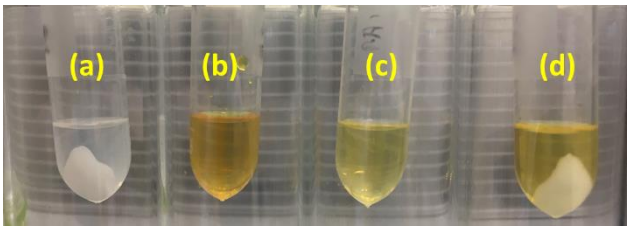


***Fig. 2.*** *Samples of CuSCN powder mixed in different DMF solutions. See the Table 1 for the details.*

As shown in Fig.2.a, CuSCN does not dissolved in DMF. But, interestingly, if the DMF solution contains perovskite precursors (i.e., PbI2 and MAI for MAPbI3 perovskite), CuSCN is completely dissolved (Fig.2.b). This highlights a potential issue when using CuSCN in inverted structure and bring the question if in such condition CuSCN is not damaged during the process if not completely rinsed. To understand better the mechanism, CuSCN solubility was checked in DMF solution containing only MAI or only PbI2. As shown in Fig.2.c, CuSCN is completely dissolved in MAI solution likely by the formation of complexes with $I^-$ and $MA^+$ ions. On the contrary, in PbI2 DMF solution (Fig.2.d), CuSCN is not dissolved, giving a strategy to overcome this potential problem of dissolution of CuSCN: to deposit the perovskite in a sequential deposition. Indeed, in this method, PbI2 is first deposited and then MAI solution in IPA is dropped-cast to form the perovskite (Fig.1).

Devices were then fabricated: the structure is shown in Fig. 3. Two different deposition technics were thus used: one step with antisolvent and the 2-step sequential deposition technic. In addition, PEDOT:PSS was used as a reference device (1-step MAPbI3). The IV characteristics obtained for several samples of different conditions are shown in Fig. 3. CuSCN with 2-step perovskite deposition displayed a remarkable Voc~1010-1020 mV, but a lower FF compared to PEDOT:PSS devices. The best efficiency obtained is 14.4%. Interestingly, devices with CuSCN made with single step deposition of MAPbI3 showed higher efficiency with a record at 15.4% thanks to a much higher current despites a lower Voc. To be noted that additional optimizations are needed for the sequential deposition, a lower current could be explained by an uncomplete formation of the perovskite.

Devices without HTM were made to compare and much lower characteristic values were obtained. It is not clear if CuSCN is still present for the 1-step deposition or if this layer impacts the crystallization of the perovskite and its interface with ITO. Investigations are ongoing.

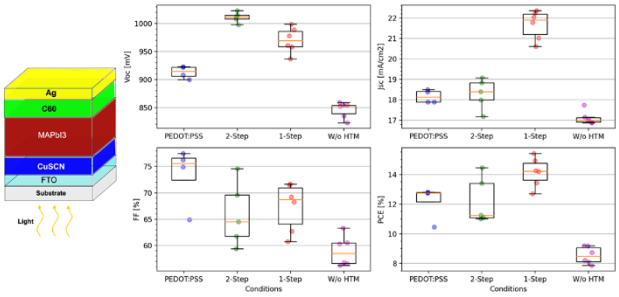


***Fig. 3.*** *Architecture of inverted structure perovskite solar cells fabricated in this work. Solar cells characteristics (i.e., Voc, Jsc, FF and PCE) for different HTM configuration: PEDOT:PSS, CuSCN in 2-Step or 1-Step MAPbI3 deposition, and without HTM.*

## 4. Conclusions

In summary, we have employed CuSCN as HTM in inverted perovskite solar cells. We showed that the deposition of perovskite solution in 1-step was, in principle, problematic as the solution may dissolved CuSCN. Therefore a 2-step technic for the deposition of MAPbI3 was employed to overcome this potential problem: if high Voc>1000mV were obtained, Jsc were quite low compared to the 1-step process which, surprisingly, leads to higher efficiency thanks to this higher Jsc. Optimizations are needed to improve the 2-step deposition technique and additional investigations are required to understand what is happening at the CuSCN interface during the 1-step deposition process.

## Acknowledgements

No specific acknowledgements.

## References

[1] NREL, Best Research-Cell Efficiency Chart, 14/12/2021.
[2] J. Jeong, M. Kim, J. Seo et al. Nature 592, 381–385 (2021).
[3] A. Al-Ashouri et al., Science 370, 1300-1309 (2020).
[4] Singh et al., Appl. Mater. Today 14, 175-200 (2019).
[5] Liu et al., Adv. Funct. Interfaces 3, 1600571 (2016).
[6] Arora et al., Science 358, 768–771 (2017).

Sixth Asian School-Conference on Physics and
Technology of Nanostructured Materials
Vladivostok, Russia, 25 – 29 April, 2022



# Studies on sensor properties of composite CuO/CNPs nanofilms obtained by electrophoretic synthesis

N.W. Aung, M.A. Pugachevskii, A.P. Kuzmenko
Southwest State University, 50 Let October, 94, Kursk, 305040, Russia

*e-mail: naywinaungnano@gmail.com

**Abstract.** Nanocomposite CuO/CNPs films have been synthesized on the glass substrate by the electrophoretic technique. The obtained structures are investigated by Raman spectroscopy, atomic force microscopy, and scanning electron microscopy. A setup for measuring the optoelectronic properties of nanocomposite films has been developed. It was established that with an increase in the irradiation intensity from 10 to 60 mW/m$^2$, the electromotive force (EMF) in the composite CuO/CNPs nanofilm increases from 0.5 to 1.1 mV. The highest sensitivity of CuO/CNPs nanofilms is obtained using colloidal carbon systems centrifuged at a speed of 800-1000 rpm.

## 1. Introduction

Carbon nanomaterials based on carbon nanotubes, graphene oxide, and fullerenes are populated by a great interest in their properties, development of synthesis methods, and industrial devices with advanced applications of these nanomaterials [1]. Carbon nanomaterials are nanosized carbon particles created by using the centrifugation method. The sensory properties of carbon nanoparticles produced from the single-walled carbon nanotube using an electrophoretic method have attracted attention due to their well-defined one-dimensional nanomaterials. This study is interested in the sensory properties of new nanocomposite materials based on carbon nanoparticles with transition metals (copper, titanium, zinc, …). A good method to improve the sensors' applications is coating carbon nanoparticles with metal oxides. Copper oxides are the most extensively studied materials used in many other areas for semiconductors, catalysts, and sensors [2]. Carbon nanoparticles coated with copper oxide (CuO/CNPs) nanocomposite materials based on ultraviolet (UV) sensors by using the electrophoretic method, which has good charge transport and conductivity properties and excellent absorption of light spectrum properties of copper oxide (CuO). The formation of structures of carbon nanoparticles systems with metal oxides using electrophoretic synthesis is widely used for the development of nanocomposite films in the field of nanotechnology [3].

The aims of this work are to obtain carbon nanoparticles depending on concentration and centrifugation method, and to develop nanocomposite structures by controlling the electrophoretic forces. In addition, due to the high transparency in the visible range, as well as the ability to absorb the light as sensory properties, carbon nanoparticles can be used as effective sensors for solar optical radiation.

## 2. Experiment

The CuO/CNPs nanocomposite structures were fabricated on the glass substrate with copper electrodes by controlling the electrophoretic force. Firstly, the original SWCNT (SWCNT TUBALL TM : 0,2%, lignosulfonate vanisperse A: 1%, water: 98%, batch number 19HO05.N1.003) and distilled water (0.2 v/v%) were mixed with an ultrasonic bath (Quick 218) for 30 minutes. The f-SWCNT solution was centrifuged at 800rpm, 1000rpm, 5000rpm, 8000rpm, 10000rpm, and 13400rpm using miniSpin (Eppendorf AG 5452, 22331 Hamburg) and took 80% at the top of the volume. Then the carbon nanoparticles (CNPs) solution was obtained and the 20% of bottom tube was heavy metallic solution. The carbon nanoparticles (CNPs) solution was applied using a pipette (by the drop method) onto the surface of a glass substrate with copper electrodes using the direct electric force for the nanocomposite structures. The copper oxide nanoparticles from the copper electrodes were coated with carbon nanoparticles due to the direct electric current. After evaporation, CuO/CNPs nanocomposite structures were formed onto the glass substrate between the copper electrodes during the electric field [4].

CuO/CNP nanocomposite film on the glass substrate is applied with UV irradiation to the thin film area. The sensitivity of the photocurrent of the nanocomposite structure was measured by using the optoelectric device (ADC L-CARD E2010D). The CuO/CNPs nanocomposite structures are used to improve the ADC's sensitivity to UV irradiation during the process.

The CuO/CNPs nanocomposite structures were analyzed by Confocal microscopy, Raman scattering of light (Omega Scope™ Confocal Raman microscope, 532 nm, 0.8 cm$^{-1}$), the Atomic Force Microscopy (AIST-NT SmartSPM), Scanning Electron Microscopy (JEOL JSM-6610), and optoelectric measurements (ADC L-CARD E2010D).

## 3. Results and discussions

The formation of CuO/CNPs nanocomposite structures was deposited on a glass substrate between the two copper electrodes after the evaporation process by the direct electric force. It can see the formation of nanoparticle structures on the glass substrate in the direction of static electric field strength [5]. The process of electrophoretic structuring of CuO/CNPs nanocomposite in the solution is uniformly opposite to the direction of the electric intensity vector by confocal microscopy. The chemical composition of nanocomposite structures and their properties can be confirmed by using Raman spectroscopy. An Energy-Dispersive Spectroscopy (EDS) data shows that the nanocomposite structures contain carbon (20.39%), oxygen (7.14%), and copper oxide (6.5%). The result is that carbon nanoparticles coated with copper oxide from copper electrodes can stabilize the metal particle solution [6].

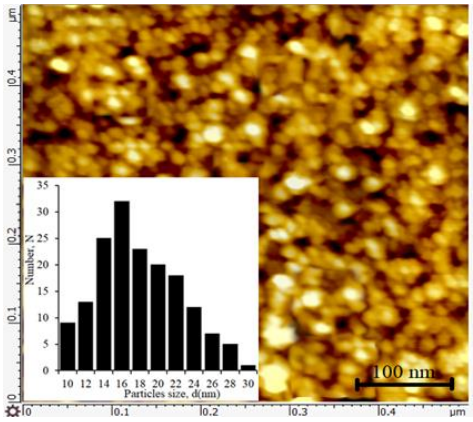


***Fig. 1.*** *AFM images and particle size distribution of CuO/CNPs nanocomposite structures centrifuged at 13400rpm.*

The formation of CuO/CNPs nanoparticle structures and their particle size were characterized by the Atomic Force Microscope. The carbon nanoparticle solution is obtained by the centrifugation method. In this case, the diameter of the nanoparticles decreases as the centrifugation speed increases. The result of particle size dependent on centrifugation speed 13400 rpm was shown in figure 1.

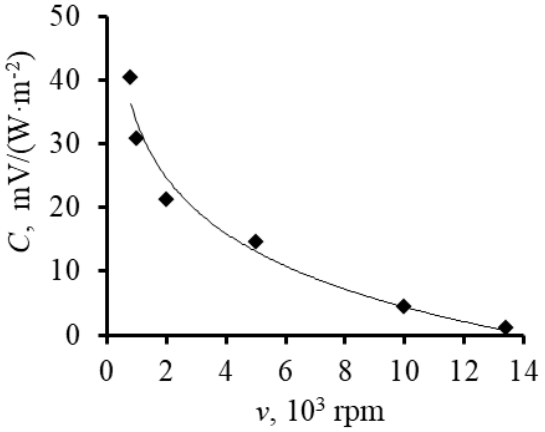


***Fig. 2.*** *Dependence of the centrifuge rate of colloidal carbon solutions on the sensitivity of the grown CuO/CNPs films.*

Studies of the optoelectric properties show that with an increase in the irradiation intensity $I$ from 10 to 60 mW/m$^2$, the excited electromotive force $E$ in the composite CuO/CNPs nanofilm increases from 0.5 to 1.1 mV. The influence of the conditions of obtaining films on their sensory sensitivity $C$ was also determined, which was determined as

$$C = \frac{\Delta E}{\Delta I},$$

where $\Delta E$ and $\Delta I$ are changes of the electromotive force excited in the composite CuO/CNPs nanofilm and the intensity of optical irradiation, respectively.

According to the results of optoelectric measurements, it was found that with an increase in the centrifugation rate of colloidal carbon solutions, the sensitivity of nanocomposite films grown on their basis during the electrophoretic process decreases. This result can be explained as follows. The basis for colloidal solutions of carbon particles were SWCNT TUBALL TM systems, which consist of both carbon nanotubes and carbon nanoparticles of various sizes and morphologies. At high centrifugation speeds (> 5000 rpm), only carbon particles with a limiting size of no more than 30–40 nm were retained in the colloidal system [7], while at low speeds (800–1000 rpm), both particles and carbon nanotubes were present in the system. During the electrophoretic process, carbon tubes were embedded in composite films, oriented in the direction of the electric field from the anode to the cathode. When carrying out optoelectric measurements, carbon tubes could serve as conductors for the drain of the EMF generated in the film upon irradiation with optical photons. In this regard, the number of interphase boundaries defining energy barriers for the flow of conduction currents decreased, which led to a significant increase in the sensitivity of composite CuO/CNPs nanofilms.

## 4. Conclusions

In summary, a CuO/CNPs nanocomposite UV sensor was fabricated on a glass substrate using the electrophoretic method. We have established the effect of the centrifuge velocity on particle size in carbon nanoparticle solution. A setup for measuring the optoelectronic properties of nanocomposite films was developed. It is shown that with an increase in the irradiation intensity $I$ from 10 to 60 mW/m$^2$, the electromotive force $E$ in the composite CuO/CNPs nanofilm increases from 0.5 to 1.1 mV. The highest sensitivity of CuO/CNPs nanofilms was obtained using colloidal carbon systems centrifuged at a speed of 800-1000 rpm. High-performance UV sensors based on composite CuO/CNPs nanofilms can find applications in photovoltaics and biomedicine.

## Acknowledgements

The study was carried out with the financial support of the Russian Foundation for Basic Research within the framework of scientific project No. 20-02-00599, as well as with the support of the Ministry of Education and Science of the Russian Federation (s/o 2020 no. 0851-2020-0035, Prioritet-2030 no. 075-15-2021-1155 and 075-15-2021-1213).

## References

[1] S. Giorgio. Nanomaterials **11**(2021)967.
[2] M. N. Naumih. Journal of Nanomaterials **2020**(2020)8855321.
[3] P. Pawan, P. Sanghoon, J. C. Hyoung. Micromachines **11**(2020)368.
[4] W. A. Nay, M. T. Myo, M. A. Pugachevskii, A. P. Kuzmenko, V. V. Rodionov. Proceedings of the South-west State Uni. Seri.: Engin. and Tech. **10**(2020)86. (in Russian)
[5] W. A. Nay, V. A. Mamontov, M. T. Myo, M. A. Pugachevskii, P. N. Thet. Inter. Conf. Gas Disch. Plas. and Their Appli. – Ekantrinburg **15**(2021)196.
[6] K. S. Khashan, M. S. Jabir, F. A. Abdulameer. IOP Conf. Series: Journal of Physics: Conf. Series **1003**(2018)012100.
[7] M. A. Pugachevskii, V. A. Mamontov, N. V. Aung, A. P. Kuzmenko. Technical Physics Letters. **46**(2020)1032.

Sixth Asian School-Conference on Physics and
Technology of Nanostructured Materials
Vladivostok, Russia, 25 – 29 April, 2022

**VI.o.05**

# Photo-switchable phosphonates with modulated bioactivity

D.V. Pankin[1], I.E. Kolesnikov[1], A.G. Pilip[2], A. Egorova[2], A.A. Manshina[*,3]

[1] Center for Optical and Laser Materials Research, St. Petersburg State University, Uljanovskaya 5, 198504 St. Petersburg, Russia

[2] St. Petersburg Federal Research Center of the Russian Academy of Sciences (SPC RAS), Scientific Research Centre for Ecological Safety of the Russian Academy of Sciences.18, Korpusnaya st., St.Petersburg, 197110, Russia

[3] Institute of Chemistry, Saint-Petersburg State University, 26 Universitetskii Prospect, 198504 Saint-Petersburg, Russia

*e-mail: a.manshina@spbu.ru

**Abstract.** Butyrylcholinesterase inhibition and its change as a result of laser irradiation are demonstrated for the first time for a series of newly synthesized phosphorylated arylaminomalonates and phosphorus functionalized thiazolotriazoles. The effect of compounds structures on butyrylcholinesterase inhibition and its laser-activated change is revealed experimentally and confirmed by molecular dynamics and docking modelling.

## 1. Introduction

Nowadays one can observe high interest of modern fundamental science and medicine in the search for new compounds, promising for the concept of photo-switching of biological activity. Such compounds, which change their bioactivity depending on the conformation that is changed under the influence of light, form the basis of photopharmacology, a rapidly developing interdisciplinary direction that unites the efforts of scientists in the field of biology, medicine, organic chemistry, materials science, and laser chemistry [1].

The concept turned out to be fruitful and has already demonstrated efficiency in photo-switchable antimicrobial, anticancer therapy, ophthalmology, etc [2,3]. In world practice, there are examples of the successful synthesis of a number of new compounds demonstrating photoinduced structural changes and, as a result, modulation of their activity in relation to target tasks; some of these substances are already undergoing preclinical studies [4].

Photopharmacology is based on the control of the biological activity of compounds under the influence of light, and the main advantage of the approach is the ability to fine-tune such a process by controlling the parameters of optical radiation – spectral and energy characteristics, duration of exposure, and spatial localization.

All this opens the way to the creation of "smart drugs" with the possibility of remote, non-invasive and precise control of the area, duration and magnitude of their therapeutic effect. The introduction of "smart drugs" into medical practice will allow in the future to solve the problem of uncontrolled in time and space activity of drugs (including outside the body), which leads to side effects and negative effects on healthy organs, as well as the accumulation of biologically active substances in the environment.

Photopharmacology is based on the design of compounds consisting of two components - a "photo switch" and a biologically active substance - a "pharmacophore". At the same time, one of the main problems that photopharmacology is currently facing, is to ensure the preservation of the required activity of a drug (pharmacophore) when conjugated with a photochromic compound, which is a serious problem requiring the development of independent solutions for each combination of photoswitch-pharmacophore.

The latter circumstance determines the interest in the development of substances that have both biological activity and the ability to change it under the influence of light. However, it should be noted that a limited number of works reporting the successful use of this strategy should be noted, with most of them devoted to the creation of such substances for photodynamic therapy of cancer. In addition, the extremely time-consuming and laborious procedure for searching for compounds with significantly different biological activity in different conformational states is a limiting factor. In this regard, the relevance of the development of compounds with photomodulated bioactivity becomes even more important for the development of photopharmacology**.**

Here we present unique substances demonstrating both characteristics – bioactivity and "photo-switchable" ability. The substances are presenting two different groups in phosphonate family – phosphorus functionalized thiazolotriazole molecules and phosphorylated 2-arylaminomalonate compounds. In spite of different structures, the synthesized compounds possess bioactivity – butyrylcholinesterase (BuChE) inhibition that is changing after compounds illumination with UV light.

## 2. Experiment

The objects of synthesis and investigation in the current research are phosphorus functionalized thiazolotriazole molecules (PFT) and phosphorylated 2-arylaminomalonate compounds (PhAM). The PFT and PhAM compounds (Fig. 1) were prepared according to a reported earlier protocol [5,6].

The choice of phosphonates for our research is conditioned by two aspects – (1) academic interest in the chemistry of halogen and alkyl/phenyl substituents in the design of modern drug-like compounds and (2) prospects of synthetic phosphonates as photopharmacological agents.

Here we present the synthesis, design, the physicochemical characterization, investigation of the light effect to the solutions of PFT and PhAM, study of the biological activity of PFT and PhAM solutions before and after laser irradiation. Biological activity was studied by the example of butyrylcholinesterase (BChE) inhibition.

## 3. Results and discussion

Figure 1 shows structures of PFT and PhAM compounds. Phosphonate groups are marked out with red ellipse.

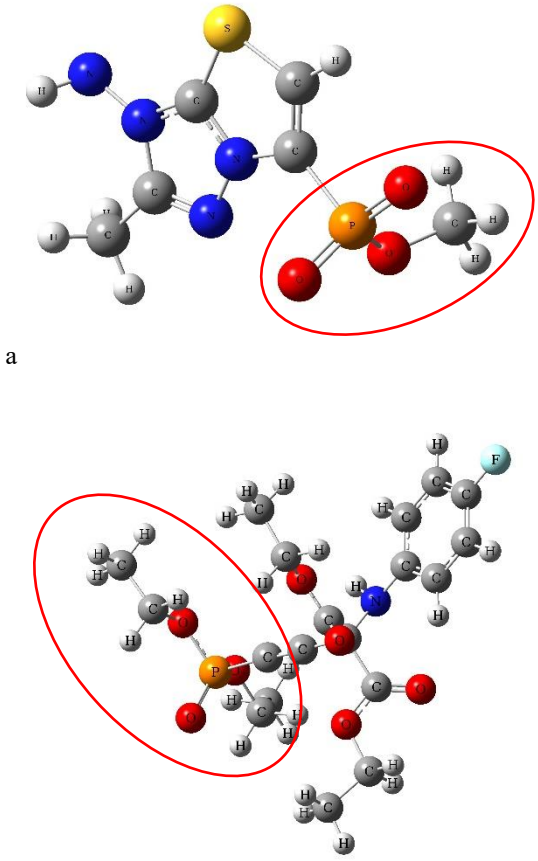

a

B

***Fig. 1.*** *Structures of (a) PFT and (b) PhAM compounds.*

The most surprising result of our research was found to be the demonstration of the laser-induced change of BChE inhibition due to the formation of PFT and PhAM conformers associated with the phosphonate group twisting. Laser-induced 3D geometry reorganization of the PFT and PhAM compounds leads to the fundamental change of the inhibition mechanism and loss of site-specificity due to the change of interaction region, the release of the glycine site, and increased strain energy of protein-ligand complex. It is important to note that PFT and PhAM demonstrate opposite effect to laser irradiation in terms of sign of BChE inhibition change – PFT compounds decrease inhibition, while PhAM increase inhibition as a result of laser irradiation. The uncovered photosensitivity and bioactivity of PFT and PhAM makes them promising compounds for clinical therapy as photopharmacological agents.

The newly synthesized phosphorus functionalized thiazolotriazole molecules and phosphorylated 2-arylaminomalonate compounds demonstrates both features – photoswitch and pharmacophore functions. A combination of "photoswitch – pharmacophore" properties in one molecule is a rarity and makes the suggesting compounds prospective as a molecular basis for the design of photocontrolled pharmacologically active substances based on the mechanism of phosphonate group phototwisting.

**Acknowledgements**

This work was supported by RSF project 22-13-00082. Authors are grateful to "Centre for Optical and Laser materials research", Research Park of Saint Petersburg State University for technical support.

**References**

[1] J. Morstein, D. Trauner, Current Opinion in Chemical Biology. 50 (2019) 145–151.
[2] W.A. Velema, J.P. van der Berg, M.J. Hansen, W. Szymanski, A.J.M. Driessen, B.L.Feringa, Nature Chem. 5 (2013) 924–928.
[3] I. Tochitsky, A. Polosukhina, V.E. Degtyar, N. Gallerani, C.M. Smith, A. Friedman, R.N. Van Gelder, D. Trauner, D. Kaufer, R.H. Kramer, Neuron. 81 (2014) 800–813.
[4] K. Hüll, J. Morstein, D. Trauner, Chem. Rev. 118 (2018) 10710–10747.
[5] D. Pankin, A. Khokhlova, I. Kolesnikov, A. Vasileva, A. Pilip, A. Egorova, E.Erkhitueva, V. Zigel, M. Gureev, A. Manshina, Spectrochimica Acta Part A: Molecular and Biomolecular Spectroscopy. 246 (2021) 118979.
[6] I. Kolesnikov, A. Khokhlova, D. Pankin, A. Pilip, A. Egorova, V. Zigel, M. Gureev, G. Leuchs, A. Manshina, New J. Chem. 45 (2021) 15195–15199.

Sixth Asian School-Conference on Physics and
Technology of Nanostructured Materials
Vladivostok, Russia, April 25 - 29, 2022



# The current-voltage and photoelectric properties of por-Si/Si-p/Si-n diodes with different porous layer's thickness

K.N. Galkin[1], D.T. Yan[*,2], I.M. Chernev[1], A.B. Cherepakhin[1], N.G. Galkin[1]

[1] Institute of Automation and Control Processes FEB RAS , 5 Radio St., Vladivostok 690041, Russia
[2] Far Eastern State Transport University, 47 Serysheva St., Khabarovsk 680021, Russia

*e-mail: dmitry_yan@mail.ru

Works on the creation of LEDs based on porous silicon heterostructures on single-crystal silicon with a built-in p-n junction are well known [1,2]. They focused on two issues: increasing the efficiency of electroluminescence and improving the stability of this type of LEDs. It is known that the formed LED structures based on porous silicon during operation in ambient conditions lose up to 75% of their integrated electroluminescence intensity for half an hour [2], which is associated with a decrease in the injection of carriers from porous silicon due to the rapid oxidation of nanocrystals in an applied electric field even at room temperature. At the same time, the question of the influence of the thickness of the porous silicon layer in a Si wafer with a built-in p-n junction on the current-voltage and photospectral characteristics of diode structures remained unexplored.

In this work, porous silicon layers were created on n-type Si(100) wafers with a resistivity of 0.1 Ω cm with an epitaxial layer of p-type silicon (3 microns) with a resistivity of 7–10 Ω cm by anodizing in a solution of HF:$C_3H_8OH$ = 1:1 at two current densities: 10 and 20 mA/cm$^2$, etching times from 10 to 30 minutes and under illumination with a 150 W tungsten halogen lamp from a distance of 30 cm from the sample. A home-made Teflon attachment with a platinum wire cathode was used for anodizing and a copper anode, which was pressed through a layer of conductive silver paste to the reverse side of the silicon sample with the burnt Au-Sb contact. The edges of the front surface of the sample with an area of up to 1 cm$^2$ were protected with a special varnish. After anodizing, the samples were washed in deionized water and dried in a flow of dry nitrogen. After mechanical removal of varnish residues and wiping with isopropyl alcohol, a layer of aluminum was applied to the PC surface at room temperature in a high vacuum through a square-shaped mask with a square hole in the center. Next, the samples were placed on silver paste in the package of the integrated circuit, and ultrasonic welding of Al wire with a diameter of 20 μm was carried out from Al-plating to the pads of the microcircuit package. At room temperature, the current-voltage characteristics were measured in the dark and under illumination with a tungsten halogen lamp based on a stabilized power source and a microvoltmeter. The spectral characteristics of the photoresponse were studied using a setup based on a monochromator with a radiation source, a modulator, and a differential amplification system.

Studies of the current-voltage (C-V) characteristics of all diodes in the dark and under illumination showed that currents through them are observed only for samples with an anodizing time of 10 to 25 minutes at a current density of 10 mA/cm$^2$, and with an increase in current density to 20 mA/cm$^2$ and times from 15 up to 30 minutes, currents do not flow through the diodes, both in the dark and in the light. This fact is associated primarily with an increase in the thickness of the porous layer and its tree-like structure, which ensures the rapid oxidation of the PS layer. At short anodizing times at both current densities, a single-layer structure of the PC layer with a moderate density is retained [3], which ensures conductivity and retains it for a long time (up to 6 months). An increase in the etching time at a minimum current density from 10 minutes (sample #2-1) to 25 minutes (sample #2-8) led to a decrease in the short-circuit current and, conversely, to an increase in the open circuit voltage (samples #2-5 and #2-7). A diode with a current density of 20 mA/cm$^2$ and an etching time of 10 minutes (sample #2-3) showed the maximum short circuit current density and the minimum open circuit voltage.

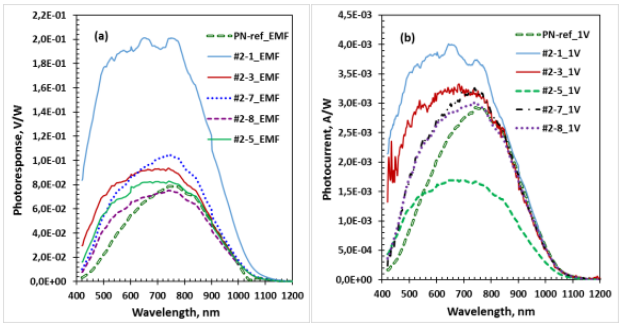


***Fig. 1.*** *Spectral dependences of photoresponse (a) and photocurrent (b) of PS/Si p-n diodes (#2-1, #2-3, #2-5, #2-7, #2-8) and reference Si p-n diode.*

Registration of the spectral characteristics of the photoresponse and photocurrent showed (Fig. 1 a,b) that sample #2-1 with a minimum PC layer thickness of 0.675 μm has the maximum photoresponse and photocurrent [3]. With an increase in the thickness of the PC layer from 0.8 μm to 1.09 μm and 2.7 μm, a decrease in the amplitude of the photoresponse (Fig. 1a) and photocurrent (Fig. 1b) is observed. A characteristic difference between the spectra of working diodes and a reference diode based on a silicon p-n junction is an increase in the short-wavelength contribution and a shift in the maximum of the spectra to the short-wavelength region, which is associated with the generation of electron-hole pairs in the wide-gap PC layer and their separation by the field of the p-n junction. A band model of photodiodes is constructed to explain the dependence of the photoresponse on the PC layer thickness.

## References

[1] P. Stainer, et.al. Apppl. Phys. Lett. **21**(1993)2700.
[2] L. Zhang, et.al. J. Appl. Phys. **77**(1995)5936.
[3] K.N. Galkin, et.al. Abstracts of ASCO-Nanomat 2022, Vladivostok, 2022, p. xx.

Sixth Asian School-Conference on Physics and
Technology of Nanostructured Materials
Vladivostok, Russia, 25 – 29 April, 2022



# Photocatalytic reduction of $CO_2$ over Cu-Rh/$TiO_2$ catalyst in visible spectra

L.I. Sorokina[1], A.I. Savitskiy[1,2], O. Shtyka[3], T. Maniecki[3], M. Szynkowska-Jozwik[3], A. Trifonov[1,4], E. Pershina[5,6], I. Mikhaylov[5], S. Dubkov[*,1], D.G. Gromov[1,7]

[1] Institute of Advanced Materials and Technologies, National Research University of Electronic Technology, 124498 Zelenograd, Russia
[2] Scientific-Manufacturing Complex"Technological Center", Zelenograd 124498, Russia
[3] Institute of General and Ecological Chemistry, Lodz University of Technology, Lodz 90–924, Poland
[4] Scientific Research Institute of Physical Problems Named After F.V.Lukin, Zelenograd 124460, Russia
[5] Institute of Nanotechnology of Microelectronics of the Russian Academy of Sciences, Moscow 119991, Russia
[6] Osipyan Institute of Solid State Physics RAS, Russian Academy of Sciences, Chernogolovka 142432, Russia
[7] I.M. Sechenov First Moscow State Medical University, Moscow 119435, Russia

*e-mail: sv.dubkov@gmail.com

**Abstract.** This work demonstrates an approach to obtaining nanoalloys of the two-component Cu-Rh system by the method of successive vacuum-thermal evaporation of components followed by heat treatment of a thin film. Arrays of Cu-Rh nanoislands with ratios of 25/75, 50/50, 75/25 at.% were formed on the $TiO_2$ layer. The TEM study showed that, at any proportions of the composition, nanoislands are a single-phase solid solution. Arrays of nanoislands were used as photocausalizers in the visible and ultraviolet ranges. It has been established that by changing the proportions of the nanoalloy components it is possible to control the yield of photocatalytic reaction products depending on the spectral range.

## 1. Introduction

In the last two decades, metal nanoparticles (NPs) have attracted the attention of researchers due to their various extraordinary mechanical, physical, physicochemical properties, which differ from the bulk properties of the corresponding materials [1]. Of particular interest are bimetallic NPs, which exhibit a combination of properties associated with the two constituent metals. The alloy of interest to us is the Cu-Rh system, which, according to some studies, is not capable of being in a single-phase state [2].

Also of interest to us is the effect exhibited by nanoparticles, is the enhancement of the photocatalytic effect and the extension of the operating wavelength range for materials such as $TiO_2$. With rising $CO_2$ emissions, the ability of titanium oxide to convert a greenhouse gas into a fuel is of increasing interest, as is the ability to improve the efficiency and spectral work range of this process by adding bi-metallic nanoparticles [3].

## 2. Experiment

The formation of nanoalloys of the Cu-Rh system was carried out by the method of vacuum-thermal evaporation and condensation on an unheated surface, followed by vacuum annealing. For the deposition of Cu, a resistive evaporation method was used. Subsequent deposition of Rh was carried out by the method of electron beam evaporation. The amount of the deposited substance was controlled using a quartz resonator. At the end of the formation the samples were annealed in vacuum at a temperature of 350 °C for 30 minutes. For all vacuum processes, the residual pressure in the chamber was ~ $1 \times 10^{-5}$ Torr. In this way, samples of three different compositions were created: $Cu_{0.25}Rh_{0.75}$; $Cu_{0.50}Rh_{0.50}$ and $Cu_{0.75}Rh_{0.25}$. The required thicknesses of metal films for obtaining alloys with the indicated compositions were obtained on the basis of quartz resonator data (Tab. I).

***Table I.*** *The values of the thicknesses of the metal layers in the studied samples.*

| Alloy composition | Rh (wt. %) | Cu thickness (Å) | Rh thickness (Å) | Total thickness (Å) |
|---|---|---|---|---|
| $Cu_{0.25}Rh_{0.75}$ | 83 | 4 | 14 | 18 |
| $Cu_{0.50}Rh_{0.50}$ | 62 | 7 | 8 | 15 |
| $Cu_{0.75}Rh_{0.25}$ | 35 | 13 | 5 | 18 |

Samples of nanoalloys of the above three compositions for TEM studies were formed on a substrate of a single-crystal KCl salt with 20 nm thick layer of an amorphous carbon, which was previously deposited by magnetron sputtering. Samples of nanoalloys for the study of photocatalytic activity were formed on a stainless steel grid with a cell size of 55 μm and a cross-sectional diameter of 40 μm. Before covering by alloy, grid was etched in $HF:HNO_3:H_2O$ solution and was covered by electrophoretic suspension deposition in a layer of powder photocatalyst $TiO_2$ with a thickness of 6.5 μm.

The microstructure, composition, shape, and size of the obtained Cu-Rh nanoalloys were investigated by high-resolution TEM on a JEOL JEM-2100 Plus electron microscope. The surface morphology of $TiO_2$/Cu-Rh samples was studied using Helios G4 CX two-beam scanning electron microscope. The study of the surface of the samples was also carried out using Jeol Jamp-9510F Auger electron spectrometer.

Photocatalytic measurements were carried out in the visible and ultraviolet light range using a continuous flow reactor equipped with a heating element, quartz window, and optical water filter (to cut IR and UV radiation). The area of the photocatalyst surface exposed to electromagnetic radiation was ~ 10 $cm^2$. The process was carried out under following conditions: the temperature of the reactor 30 °C, the reaction mixture 5% vol. $H_2O$/95% vol. $CO_2$; and total gas flow 1.0 ml/min. The first measurements were taken after at least 2 hours on

stream. The analysis of reaction products was carried out by an on-line gas chromatograph equipped with a flame ionization detector and a capillary HP PLOT/Q column.

### 3. Results and discussions

A TEM study (Fig. 1) of the samples showed that a thin film of the Cu-Rh alloy is an array of nanoislands of various shapes, not exceeding 10 nm in thickness. An XRD sample study of $Cu_{50}Rh_{50}$ showed that the alloy has a cubic crystal lattice with a lattice constant of $a$ = 0,372 nm. This constant is practically the average value between the constants of copper ($a$ = 0,362 nm) and rhodium($a$ = 0,380 nm).

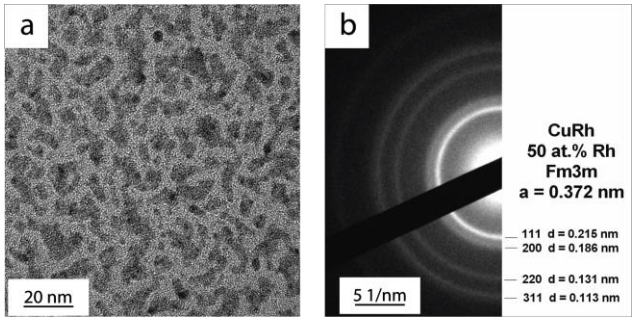


***Fig. 1.*** *Results of investigation of $Cu_{50}Rh_{50}$ alloy samples by transmission electron microscopy: (a) Typical layer image; (b) Selected area diffraction pattern.*

SEM study (Fig. 2) of the morphology of samples for photocatalysis showed that the average thickness of the TiO2 layer on the stainless steel mesh is 6.5 μm. The layer itself is homogeneous and has a developed surface. Due to the small size of nanoislands, they could not be detected by this method.

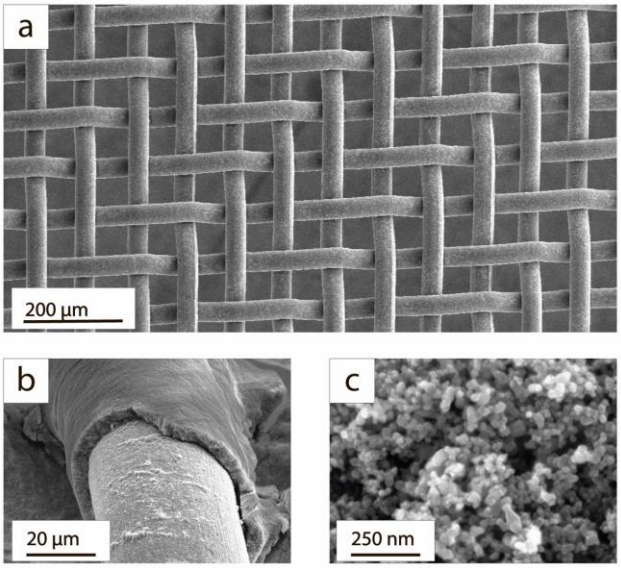


***Fig. 2.*** *SEM images of a TiO2 layer on a stainless steel grid: a) general view of a grid covered with $TiO_2$ layer; b) a section of a grid with $TiO_2$ layer showing the thickness of the deposited layer; c) morphology of a $TiO_2$ layer at high magnification.*

In the course of studying the photocatalytic reduction of $CO_2$ in the presence of water vapor on the surface of the samples, it was found that methanol and acetaldehyde are synthesized in the UV spectrum, and only acetaldehyde is synthesized in the visible spectrum. The best result in methanol production was shown by the $TiO_2/Cu_{0.5}Rh_{0.5}$ sample in the presence of UV radiation, and in the production of acetaldehyde - $TiO_2/Cu_{0.25}Rh_{0.75}$ in the visible range. In the course of research, it was found (Fig. 3) that the synthesis rate increases in the first 1.5 hours, and then drops by 20-25% of the maximum value in 4 hours.

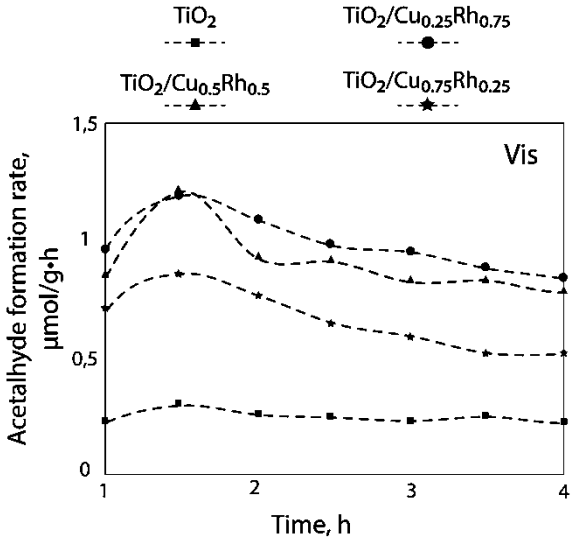


***Fig. 3.*** *The rate of formation of acetaldehyde at visible radiation.*

### 4. Conclusions

Sequential evaporation of metals followed by heat treatment of condensate at a relatively low temperature of 350 °C makes it easy to obtain a Cu-Rh nanoalloy in the form of a single-phase solid solution with a controlled content of components and lattice constant. Controlling the parameters of the Cu-Rh alloy makes it possible to use it for photocatalytic applications, thereby optimizing the composition of the photocatalytic system. The modification of $TiO_2$ with Cu-Rh nanoalloys showed that, under UV irradiation, the highest activity of generating acetaldehyde was demonstrated by a sample with a ratio of components of the Cu-Rh alloy of 75/25 at.%. Highest generation of methanol was observed for Cu-Rh 50/50 at.%. While in the visible range highest generation of acetaldehyde was observed for Cu-Rh 25/75 at.%.

### References

[1] R.A. Andrievskij, A.M. Glezer. Physics of Metals and Metallography **89**(2000)83.
[2] R. Camposeco, M. Hinojosa-Reyes, R. Zanella. Int. J. Hydrogen Energy **46**(2021)26074.
[3] D.J. Chakrabarti, D.E. Laughlin. J. Ph. Equilibria **2**(1982)460.

Sixth Asian School-Conference on Physics and
Technology of Nanostructured Materials
Vladivostok, Russia, 25 – 29 April, 2022



# Spectral sensitivity of photovoltaic cells based on carbon nanotube arrays

Yu.O. Fedorova*, N.N. Schavelev, R.M. Ryazanov, E.P. Kitsyuk
Scientific-Manufacturing Complex "Technological Centre", 1 Shokina Sq., Zelenograd, Moscow 124498, Russia

*e-mail: fedorovauo@mail.ru

**Abstract.** The work on studying spectral sensitivity of photovoltaic cells based on carbon nanotube arrays is presented. It was found that samples with semiconductor nanotubes showed a photoresponse similar to an optical rectenna or a photodiode, depending on the topology design. The samples showed photosensitivity in a wide spectral range from UV to IR.

## 1. Introduction

A significant increase in the performance of solar cells based on a Single-Walled Carbon Nanotubes (SWCNTs) – Silicon (Si) heterojunction was achieved by international researches [1]. It is assumed that at the interface between materials, the main mechanism of charge separation is either a p-n junction, or a Schottky junction, or a metal-insulator-semiconductor (MIS) junction [2]. Mechanisms corresponding to p-i-n-photodiode and optical rectenna were also observed [3]. However, due to the initially different physical characteristics, namely chemical purity, conductivity type, size of the active working area, manufacturing technology, etc., there is no single explanation for the internal processes that occur in photocells. The photocurrent generation in SWCNTs can be caused by the photoelectric effect [4], when the photocurrent is generated due to the electric field, and by the photothermal effect [5], in which the photocurrent is generated due to the difference in the Seebeck coefficients. Photogeneration mechanisms directly describe the properties of individual SWCNTs, but for practical applications, thin films and arrays are more often chosen, since significant differences will be observed between single nanotubes and a bulk sample.

The creation of integrated optical elements based on carbon nanotubes expands the possibilities for using photosensitive elements based on CNTs [6]. This work presents study on spectral sensitivity of photovoltaic cells based on SWCNTs arrays. It is shown that when using the same SWCNTs films, differences in topology affect the spectral response and the photogeneration mechanism.

## 2. Experiment

Substrate KEF 4.5 (100) was choosen as the basis for manufacturing of the “strip” sample. Initially, the substrate was subjected to chemical treatment with further oxidation at a temperature of 1000 °C (thickness of silicon oxide under metallization 200 nm). Next, an Al film (300 nm) was deposited. To form the topology, photolithography was performed followed by etching of Al and $SiO_2$ films to Si. The final operation is cutting the wafers into individual chips. The production of the type “comb” sample was carried out similarly, but with the addition of a gas-phase etching operation of $SiO_2$ (thickness of 100 nm) under the metallization layer, before the final operation. SWCNTs suspensions with a concentration of 0.1 mg/ml (SG65i Sigma-Aldrich catalog no. 773735, ~ 95 % semiconducting tubes with ~ 41 % of (6,5) chirality) were used in the work. SWNTs were deposited by the spray method. The average number of spray passes was 500 times.

To study the spectral sensitivity of experimental photovoltaic cells, current-voltage characteristics (I-V curves) were obtained in the UV–near-IR wavelength range. To clarify the characteristics, similar studies were also carried out for commercial samples: Si pin diode (Hamamatsu S1337-1010BR) and Schottky diode based on Si heterojunction (KEF 4.5 (100)) - Al. When measuring, the probes were placed on the upper metal platform and on the substrate of the structure.

The studies were carried out with setup for measuring the parameters of dye-sensitized solar cells (SCS10-PEC, Zolix). The device uses a 500 W xenon lamp as a radiation source. Each experimental sample was installed as close as possible to the light beam, so that the active area was fully illuminated. In addition, a study was carried out to assess the effect of temperature on the operation of photocells. The purpose of the study was to find patterns of changes in the main parameters of photocells at different temperatures under constant illumination, as well as to establish the effect of elevated temperature on the rate of radiation degradation of devices.

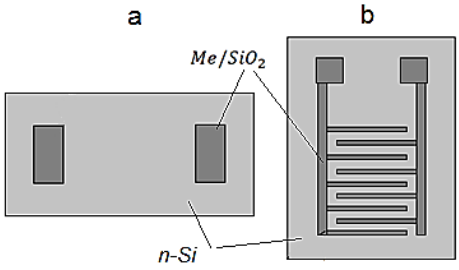


***Fig. 1.*** *Structure of photosensitive elements before SWCNTs film deposition: (a) type “strip”, (b) type “comb”.*

I–V measurements of samples under heating were made using a Cascade Summit 12000 semi-automatic probe setup and a Keysight B1500A semiconductor analyzer. The heating of the table, on which the samples were located, was carried out by activating the control unit of the system and the chiller. Heating was held up to 110 degrees for 4 hours.

## 3. Results and discussions

The I-V curves obtained for the "strip" and "comb" type samples had the same line shape for different wavelengths. The key difference was that for the "strip" type, the I–V curve passed through the second quadrant, and for the

"comb" type – through the fourth quadrant. Both curves also showed rectifying characteristics. The passage of the curve through the second quadrant characterizes the device to operate in a similar way to a rectenna. When light is directed at the "strip" sample, electronic oscillations arise inside the metal–SWCNTs junction similarly to oscillations inside the antenna. This correlates with changing of the Fermi level at the diode barrier, which leads to a shift in the I–V curve. In reverse bias, due to the presence of a wide barrier at the SWCNTs/$SiO_2$/Si interface, the minimum current is observed. It is assumed that since the difference in performance between SWCNTs and the air-resistant metal (Al) is too small to create sufficient asymmetry for optical rectification, further structure optimization will be necessary to control electron tunneling.

The I–V curve of the "comb" sample passes through the IV quadrant, similarly to photodiodes, which indicates that the device generates rather than consumes electricity, i.e. photoelectric effect is observed.

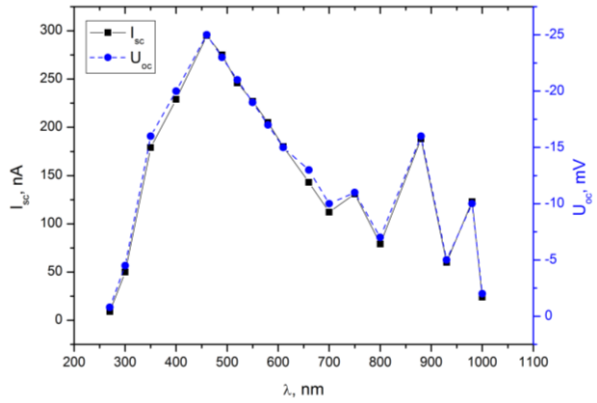


***Fig. 2.*** *Spectral sensitivity of photovoltaic cell of type "strip".*

Figures 2, 3 present the selective spectral sensitivity to different wavelengths of current $I_{sc}$ and voltage $V_{oc}$ for experimental samples. Moreover, the position of the maxima (in absolute value) of the current $I_{sc}$ and voltage $V_{oc}$ by wavelength differs significantly between the samples. It is assumed that the features of the topology of the samples contribute to this difference.

The results obtained for the "strip" sample suggest that the photon-to-current conversion efficiency is higher at those wavelengths where SWCNTs more actively absorb incident radiation. Thus, most of the photons will be "captured" by the nanotubes and will tunnel down into the silicon substrate. For the "comb" sample, the region of maximum current and voltage values coincides with the active operating range of Si photocells, which suggests that the Si substrate makes a significant contribution to the photo-EMF generation. That is, the design for the "comb" makes it possible to enhance the contribution of the silicon substrate to current generation. Similar studies of commercial samples (p-i-n diode and Schottky diode) were performed. The spectral sensitivity of the p-i-n diode corresponded to the sensitivity of Si. For the Schottky diode, a close to linear dependence of the $I_{sc}$ and $V_{oc}$ was observed over the entire wavelength range.

The study of the temperature dependences showed that, when the experimental samples are heated, the absorption edge shifts, which is associated with a narrowing of the crystal band gap, and the number of generated pairs increases.

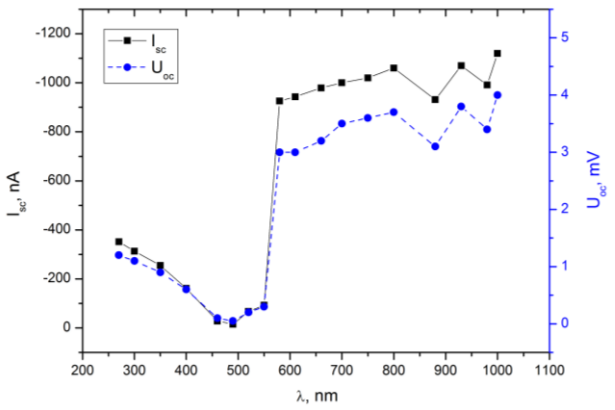


***Fig. 3.*** *Spectral sensitivity of photovoltaic cell of type "comb".*

The narrowing also leads to an increase in dark current and decrease in $V_{oc}$. Long-term heating showed a decrease in resistance, $I_{sc}$ and $V_{oc}$.

## 4. Conclusions

The work presents a study on characterizing photosensitive structures based on SWCNTs – Silicon heterojunctions. Experimental samples with different topologies were selected for analysis. Spectral sensitivity and temperature dependence (degradation with time during heating and illumination) were studied for the samples. Comparison with control samples (p-i-n-diode, Schottky diode) was carried out. It was found that the "strip" design generates power in the II quadrant, which is typical for the photoresponse of an optical rectenna. The "comb" circuit works like photodiodes, but has less usable output power. It was also found that the spectral sensitivity of the "strip" sample has a similar wavelength dependence with a p-i-n diode, but the operating wavelength range is wider and starts from the UV region. Long-term heating of photovoltaic cells showed a decrease in the efficiency of devices. The main difficulty in determining the mechanism of charge separation at the SWCNT film – silicon interface is due to the fact that film comprises semiconductor and metal nanotubes with different diameters and chirality, which affects conductivity type.

## Acknowledgements

This work was supported by the Ministry of Science and Higher Education of the Russian Federation No. FNRM-2021-0002.

## References

[1] P. Rajanna, P. Lund, A. Nasibulin. Wiley Interdiscip. Rev. Energy Environ. **11**(2021)402.
[2] X. Hu, P. Hou, C. Liu, H. Cheng. (2019). Nano Materials Science **1**(2019)156.
[3] M. Sapankaew, W. Dumnernpanich, Y. Jompol. Mater. Res. Express.**8**(2021)066303.
[4] K. Balasubramanian, Y. Fan, M. Burghard, K. Kern, M. Friedrich, U. Wannek, A. Mews. Appl. Phys. Lett. **84**(2004)2400.
[5] A. Tsen, L. Donev, H. Kurt, L. Herman, J. Park. Nat. Nanotechnol. **4**(2009)109.
[6] S. Khasminskaya, F. Pyatkov, B. Flavel, W. Pernice, R. Krupke. Adv. Mater. **26**(2014)3466.

Sixth Asian School-Conference on Physics and
Technology of Nanostructured Materials
Vladivostok, Russia, 25 – 29 April, 2022



# Monte Carlo method and approaches to simulation of radiation transfer in turbid biological tissues

I.V. Krasnikov*[,1,2], A.Y. Seteikin[1,2], B. Roth[3]

[1] Immanuel Kant Baltic Federal University, Kaliningrad, A. Nevskogo st., Kaliningrad 690041, Russia
[2] Amur State University, Ignat'evskoe shosse 21, Blagoveshchensk, 675027, Russia
[3] Hannover Centre for Optical Technologies, Nienburger Str. 17, Hannover 30167, Germany
[4]Cluster of Excellence PhoenixD, Leibniz University Hannover, Welfengarten 1, 30167 Hannover, Germany

*e-mail: ivkrasnikov@gmail.com

**Abstract.** Monte Carlo (MC) simulation for light propagation in scattering and absorbing media is the gold standard for studying the interaction of light with biological tis-sue and has been used for years in a wide variety of cases. The interaction of pho-tons with the medium is simulated based on its optical properties and the original approximation of the scattering phase function. Over the past decade, with the new measurement geometries and recording techniques invented also the corresponding sophisticated methods for the description of the underlying light-tissue interaction taking into account realistic parameters and settings were developed.

From optical imaging, one can now expect the same breakthrough in the field of non-operative diagnostic methods that was provided by X-ray and computed tomography at that time, thanks to the use of non-ionizing radiation and its non-invasiveness [1]. Diffuse reflectance spectroscopy (DRS), near infrared spectroscopy (NIRS), diffractive optical tomography (DOT), Raman tomography, fluorescence tomography, optical microscopy, optical coherence tomography (OCT) and photoacoustic (PA) imaging are among the most widely used in modern times. optical methods in biomedicine, and their potential is far from fully understood [2-3].

The modeling of light propagation in a medium is based on the absorption and scattering characteristics that dominate the propagation of light in biological tissues. The usual approach to modeling the propagation of light in a medium is to use the radiative transfer equation (RTE). Effective solutions or approximations of this equation for a heterogeneous medium (tissue) are still an open question [4].

Modeling the propagation of light in biological tissue based on the MC method has become an important tool for understanding the intricacies of the interaction of light with matter in complex environments. In addition to efficient algorithms, the approximations underlying the model are the key to recent advances in this field. An intensive re-search is currently underway to develop more comprehensive yet effective modeling tools that take into account all aspects of the system itself, as well as take into account all relevant environmental influences [4]. In addition, the trend indicates the use of more anatomically realistic geometries and the development of more user-friendly modeling tools. The further development of biophotonics lies in the ever-increasing processing power of computing systems and artificial intelligence concepts such as the concepts of machine learning, deep learning and data analysis.

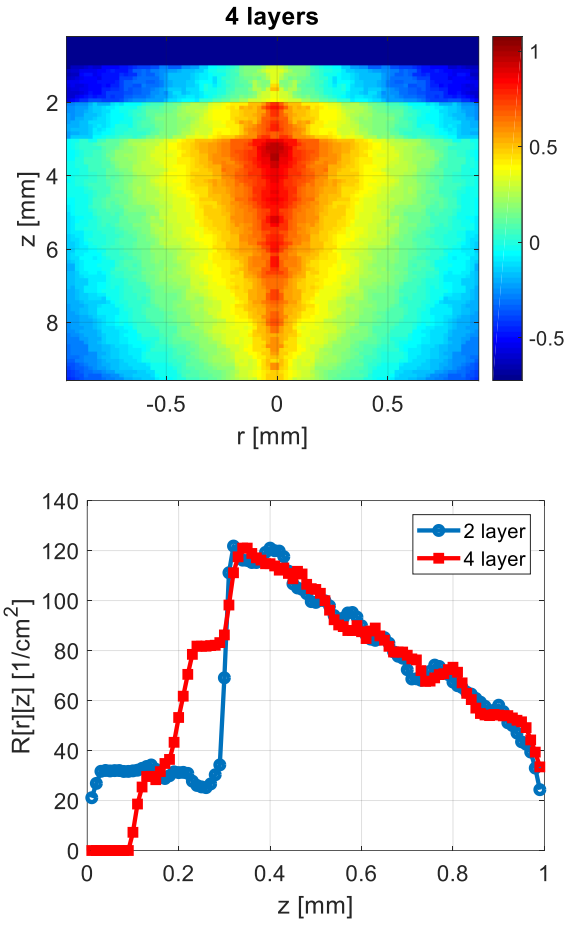


***Fig. 1.*** *Depth-resolved distribution of absorption probability of reemissed Raman photons in the 4-layer bCar+ink solution (top). Simulated Raman photon fluence (bottom).*

## References

[1] V. Tuchin (ed.) Handbook of Optical Biomedical Diagnostics, Vol. PM107, SPIE Press, Washington (2002).
[2] I. Meglinski, A.V. Doronin. Advanced Biophotonics: tissue optical sectioning, V.V. Tuchin, R.K. Wang (Taylor & Francis, 2012).
[3] Yun S. H. and Kwok S.J., Nature Biomed. Eng.V.1 (2017).
[4] I.Krasnikov, A.Seteikin, B.Roth, Biomedical Engineering Letters V. 9(3) (2019) 327.

Sixth Asian School-Conference on Physics and
Technology of Nanostructured Materials
Vladivostok, Russia, 25 – 29 April, 2022



# A comparative study of the transient lateral photovoltaic effect in the hybrid T/$SiO_2$/Si (T = Fe, $Fe_3O_4$, $TiO_2$) structures

T.A. Pisarenko*[,1,2], V.V. Korobtsov[1], A.A. Dimitriev[1,2], V.V. Balashev[1,2]

[1] Institute of Automation and Control Processes FEB RAS, 5 Radio St., Vladivostok 690041, Russia
[2] Far Eastern Federal University, 8 Sukhanova St., Vladivostok 690950, Russia

*e-mail: tata_dvo@iacp.dvo.ru

**Abstract.** In this work, a comparative study of the features of the transient lateral photovoltaic effect (LPE) at pulsed illumination in the hybrid T/$SiO_2$/Si (T = Fe, $Fe_3O_4$, $TiO_2$) structures is represented. The amplitude of the photoresponse signal corresponds to the LPE sensitivity, which is 31, 142, and 477 mV/mm in structures with the top layer of metal, semi-metal, and semiinsulator, respectively. The rise time and the fall time of photoresponse signal are determined by the RC-circuit design induced by the hybrid structure in the near-contact region, depending on the conductivity of the top layer.

## 1. Introduction

Lateral photovoltage in hybrid structures based on $SiO_2$/Si is generated due to the difference of the charge concentration arising as a result of nonuniformly irradiation and of subsequent asymmetric diffusion of the charge, the magnitude of the lateral photovoltage varying linearly with a change of the light spot position [1-3], that may be used, for example, in position-sensitive detectors (PSD) [3, 4]. The operating characteristics of the PSD are the sensitivity of the lateral photoelectric effect (LPE) and LPE nonlinearity [2-4], as well as the rise time and fall time of the photovoltage signal at pulsed illumination [3, 5]. The LPE sensitivity is usually interpreted using the diffusion theory of charge carriers [1-7]. However, in the literature on LPE, there is still a dualism of opinions about the mechanism of lateral conductance in hybrid structures. So in works Ref.[5-7], the current transfer of photocarriers along the inversion layer at the $SiO_2$/Si interface is assumed, while the authors of works Ref.[2, 3] believe that the conductance occurs along the top layer of the hybrid structure. In our opinion, one of the directions in the study of this LPE problem is the investigation of the transient characteristics of the photocurrent in hybrid structures with different conductivity of the top layer. This work presents a study of the transition LPE in hybrid structures T/$SiO_2$/Si (T = Fe, $Fe_3O_4$, $TiO_2$), in which Fe is a metal, $Fe_3O_4$ is a semimetal, and $TiO_2$ is a semiinsulator.

## 2. Experiment

The samples were prepared on n- and p-type single-crystal Si(001) substrates. An ultrathin $SiO_2$ layer ~1.5 nm thick was formed on the Si substrate surface in nitric acid (68% $HNO_3$) at 121°C for 10 minutes at the final stage of cleaning before loading the samples into a vacuum chamber.

Fe and $Fe_3O_4$ films were formed by equipment Katun on an oxidized Si(001) surface by deposition of iron at a rate of 2.5 nm/min in a vacuum and oxygen atmosphere with $P_{O2} = 10^{-6}$ Torr, respectively. $TiO_2$ films were formed by the sol-gel method [8] ex-situ on the oxidized silicon surface. The film thickness was measured by the spectral ellipsometry and the atomic force microscopy.

To measure the photovoltage, aluminum contacts (2-1) mm with a distance of 2 mm between them were deposited on the film surface. Illumination was realized by a He-Ne laser with λ= 633 nm and with a radiation power incident on the sample surface of 0.3 mW. The measurements of the photovoltage dependences U(x) and U(t) were carried out using a Keitly-2000 and an AKIP-4115/5A digital oscilloscope, respectively.

## 3. Results and discussions

For a comparative study, Fig. 1 shows the dependences of the lateral photovoltage on the laser spot position at the optimal thicknesses of the top layer for the T/$SiO_2$/Si (T = Fe, $Fe_3O_4$, $TiO_2$) structures. The optimal thicknesses were determined for an iron film in Ref.[6], for a magnetite film in Ref.[7], and for titanium dioxide it has not been published. The different range of optimal thicknesses is most likely due to the mechanisms of film growth.

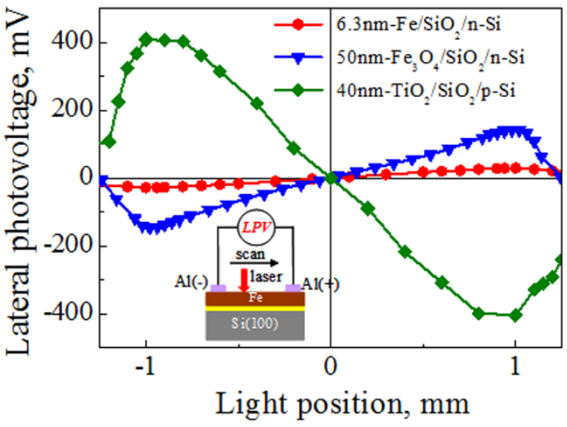


***Fig. 1.*** *LPV on light position in the hybrid T/$SiO_2$/Si (T = Fe, $Fe_3O_4$, $TiO_2$) structures.*

As can see in Fig. 1, an increase of the resistivity of the top layer leads to an increase of the LFE sensitivity. However, we have previously shown in Ref.[6, 7] that an increase of the LPE sensitivity is due to the value of the built-in potential at the $SiO_2$/Si interface, and the highest sensitivity is observed for structures in which an inversion layer is formed at the $SiO_2$/Si interface. In MOS structures such as Fe/$SiO_2$/Si and $Fe_3O_4$/$SiO_2$/Si, this condition is satisfied on n-type substrates [6, 7], while in the $TiO_2$/$SiO_2$/Si heterostructure, an inversion layer is formed

at the $SiO_2$/p-Si interface. It can also be seen in Fig. 1 that the polarity of the lateral photovoltage changes when the type of substrate conductivity is changed.

In our previous works [6, 7], we proposed a two-channel model of lateral current transport along the inversion layer at the $SiO_2$/Si interface by analogy with work Ref.[9]. However, in the $TiO_2/SiO_2$/p-Si structure, the resistance of the titanium oxide film is orders of magnitude higher than the resistance of transition metal films; therefore, the decrease of the LPE sensitivity with an increase of the $TiO_2$ film thickness is due not to a decrease in its resistance, but to voltage losses at the contacts because of the high film resistance in the transverse direction. The study of transient LPE can also provide important data for determining the mechanism of current transfer of nonequilibrium photocarriers in hybrid structures.

The time profiles of the laser pulse at room temperature for the Fe/$SiO_2$/n-Si, $Fe_3O_4/SiO_2$/n-Si and $TiO_2/SiO_2$/p-Si structures are shown in Fig. 2, from which it can be seen that an increase of the top layer resistivity leads to both an increase of the photovoltage signal amplitude and a change of the photoresponse signal shape. It is easy to see in Fig. 2 that the amplitude of the photoresponse pulses corresponds to the LPE sensitivity in the investigated structures, that is, it is determined by the value of the built-in potential. Whereas an increase of the rise time and fall time in the $Fe_3O_4/SiO_2$/n-Si and $TiO_2/SiO_2$/p-Si structures is associated with an increase of the multilayer system resistance.

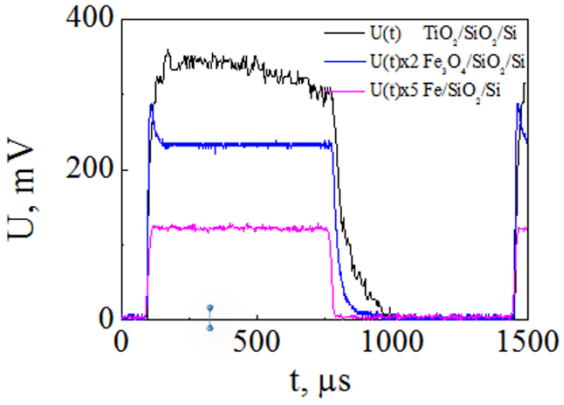


***Fig. 2.*** *LPE photoresponse in the hybrid T/$SiO_2$/Si (T = Fe, $Fe_3O_4$, $TiO_2$) structures.*

In this work, the rise time is defined as the time required to increase the photovoltage from 10% to 90% of the peak photovoltage ($U_{max}$), and the fall time is defined as the time required to reduce the photovoltage from 90% to 10% of $U_{max}$. The rise time in the $Fe_3O_4/SiO_2$/n-Si structure is 8 μs, which is ~ 2 times longer than in the Fe/$SiO_2$/n-Si structure, where it is 3.9 μs, and ~ 7.6 times shorter than the rise time in the $TiO_2/SiO_2$/p-Si structure. A significantly large difference is observed for the fall time. From the analysis of the falling edges of the photovoltage signal, the fall times are 3.8, 53, and 240 μs in the structures Fe/$SiO_2$/n-Si, $Fe_3O_4/SiO_2$/n-Si, and $TiO_2/SiO_2$/p-Si, respectively.

To explain the obtained results, we considered three versions of the equivalent circuit for three types of the top layer conductivity. For the Fe/$SiO_2$/n-Si structure, the transient characteristics will be determined only by the RC filter, which consists of the distributed characteristics of the silicon near-surface layer and the silicon oxide layer. For the $Fe_3O_4/SiO_2$/n-Si structure, the active resistance of the film in the transverse direction is successively added to the above mentioned RC filter of the $SiO_2$/Si interface. In the case of a $TiO_2/SiO_2$/p-Si heterostructure, an complementary RC filter of the film is added to the RC filter of the $SiO_2$/Si interface, which takes into account the impedance characteristics of the $TiO_2$ film.

Thus, the generality of studying the transition LPE in structures with different conductivity of the top layer can be achieved using the equivalent circuits of the hybrid structure.

## 4. Conclusions

It was found that the slowing down of the photoresponse process in the $Fe_3O_4/SiO_2$/n-Si and $TiO_2/SiO_2$/p-Si structures is associated with a change of the RC characteristics of the electrical contact. From the point of view of transient LPE, the most promising candidates for LPE-based PSDs should be considered hybrid $Fe_3O_4/SiO_2$/n-Si structure with a semimetallic top layer, which have the high LPE sensitivity and the relatively short photoresponse time and relaxation time.

## References

[1] J.T. Wallmark. Proceedings of the IRE.45.4 (1957) 474.
[2] C. Yu, H. Wang. Sensors. 10.11 (2010) 10155.
[3] C. Hu, X. Wang, B. Song. Light: Science & Applications 9 (2020) 1.
[4] J. Henry, J. Livingstone. Journal of Physics D: Applied Physics 37.22 (2004): 3180.
[5] X. Wang, B. Song, M. Huo, Y. Song, Z. Lv, Y. Zhang, ... & J. Tang. RSC Advances 5.80 (2015): 65048-65051.
[6] T.A. Pisarenko, V.V. Balashev, V.V. Korobtsov, A.A. Dimitriev, V.A. Vikulov. Defect and Diffusion Forum. 386 (2018) 137.
[7] T.A. Pisarenko, V.V. Balashev, V.A. Vikulov, A.A. Dimitriev, V.V. Korobtsov. Physics of the Solid State. 60.7 (2018) 1316.
[8] D.P. Opra, S.V. Gnedenkov, S.L. Sinebryukhov, A.B. Podgorbunsky, A.A. Sokolov, A.Y. Ustinov, ... & V.V. Zheleznov. Chemical Physics, 538 (2020) 110864.
[9] J. Dai, L. Spinu, K.Y. Wang, L., Malkinski, J.Tang. Journal of Physics D: Applied Physics. 33. 11 (2000) L65.

Sixth Asian School-Conference on Physics and
Technology of Nanostructured Materials
Vladivostok, Russia, 25 – 29 April, 2022



# Giant lateral photovoltaic effect in the $TiO_2/SiO_2$/p-Si heterostructure

T.A. Pisarenko*[,1,2], V.V. Korobtsov[1,2], A.A. Dimitriev[1,2], V.V. Balashev[1,2], V.V. Zheleznov[3]

[1] Institute of Automation and Control Processes FEB RAS, 5 Radio St., Vladivostok 690041, Russia
[2] Far Eastern Federal University, 8 Sukhanova St., Vladivostok 690950, Russia
[3] Institute of Chemistry of FEB RAS, 159, 100 years to Vladivostok Av., Vladivostok 690022, Russia

*e-mail: tata_dvo@iacp.dvo.ru

**Abstract.** In this work, we study the lateral photovoltaic effect in the $TiO_2/SiO_2$/p-Si structure. It was found a giant lateral photoeffect was observed in the $TiO_2/SiO_2$/p-Si heterostructure due to the formation of high built-in barrier at the $SiO_2$/p-Si interface ($\varphi_i$=0.62 eV). Optimum relationship of the LPE sensitivity and nonlinearity is 477 mV/mm and 9%, respectively. It was found that both the thickness dependences of the sensitivity and the timing data of the photoresponse under pulsed illumination are associated with a change in the parameters of the equivalent electrical circuit. The reason for the significant rise time and fall time is the impedance characteristics of the $TiO_2/SiO_2$/p-Si structure in the near-contact region.

## 1. Introduction

The lateral photoelectric effect (LPE) is a characteristic feature of semiconductor structures and serves as an effective method for studying the properties of nanomaterials and nanostructures [1]. It is known [1, 2] that LPE occurs when a laser beam nonuniformly irradiates the surface of a pn-junction or a heterojunction, and a large number of electron-hole pairs are excited and then separated by this pn junction in the illuminated region by means of a built-in field. Thus, the difference in electrical potentials is created due to the carrier concentration gradient between the illuminated and non-illuminated regions, which leads to lateral diffusion of nonequilibrium photocarriers from the illuminated region to the contacts [2, 3]. Interest to this effect is due to the linear dependence of the lateral photovoltage (LPV) on the laser spot position between the electrodes, which can be used, for example, in position-sensitive detectors (PSD) [1]. One of the ways to improve the characteristics of LPE-based PSD, which are the LPE sensitivity and LPE nonlinearity [1, 3] as well as response times under pulsed illumination [4], is a select of the top layer material with high resistivity [4, 7] and with large work function [1, 3-5]. The large work function provides significant band bending at the $SiO_2$/Si interface (preferably with inversion layer [4, 5]), and the low conductivity shifts the optimal film thickness to the range guarantying the formation of a homogeneous built-in barrier [6, 7].

## 2. Experiment

$TiO_2$ films were formed on the oxidized silicon surface by the sol-gel method [8]. To measure the photovoltage, aluminum contacts (2×1) mm with a distance of 2 mm between them were deposited on the film surface. Illumination was occurred by a He-Ne laser with $\lambda$= 633 nm and with a radiation power incident on the sample surface of 0.3 mW. The measurements of the photovoltage dependences of U(x) and of U(t) were carried out using a multimeter Keitly-2000 and an digital oscilloscope AKIP-4115/5A, respectively.

## 3. Results and discussions

Previously, we studied the Fe/$SiO_2$/n-Si [5] and $Fe_3O_4/SiO_2$/n-Si [9] structures, in which LPE was observed, and an increase in the resistivity of the top layer led both to an increase in the LPE sensitivity by 4.7 times and to a decrease in nonlinearity from 6 to 5%. In both cases, there was a dependence of the LPE parameters on the top layer thickness. In this work, low-conductivity $TiO_2$ films doped with manganese [8] were chosen by us as the top layer material that satisfies the above properties [1, 3, 7, 9].

The band diagrams were preliminarily constructed for the $TiO_2/SiO_2$/Si structure. Taking into account that $TiO_2$ films are a semi-insulator with a band gap of 3.1 eV and a work function of 5.87 eV [10, 11], it was found that a large built-in potential $\varphi_i$=0.62 eV at the $SiO_2$/p-Si interface is formed in the $TiO_2/SiO_2$/p-Si heterostructure, whereas in the $TiO_2/SiO_2$/n-Si structure $\varphi_i$=0.16 eV. Thus, it was found that high value of the LPE sensitivity should be expected in the $TiO_2/SiO_2$/p-Si structure, in which an inversion layer is formed at the $SiO_2$/p-Si interface, as well as in the structures previously investigated by us [5, 9].

The dependences of the lateral photovoltage on the laser spot position in the $TiO_2/SiO_2$/p-Si structure at different thicknesses of the top layer are linear these were parameterized by the LPE sensitivity and the LPE nonlinearity. The LPE characteristics in the $TiO_2/SiO_2$/p-Si structure at different thicknesses of the top layer are presented in Table. 1, from which it can be seen that the optimal thickness of the top layer exists for the LPE sensitivity, as well as for the previously studied structures [5, 9], while the dependences of the LPE nonlinearity decrease nonlinearly with an increase of the top layer thickness.

***Table I.*** *LPE Parameters of Samples*

| Sample | Deposition time, min | Sensitivity, mV/mm | Non-linearity, % | Rise time, μs | Fall time, μs |
|---|---|---|---|---|---|
| *A* | 40 | 45 | 17.4 | 13 | 35 |
| *B* | 45 | 605 | 21 | 53 | 252 |
| *C* | 50 | 477 | 9 | 30 | 240 |
| *D* | 55 | 217 | 10 | 20 | 46 |

The maximum LPE sensitivity equal to 605 mV/mm is achieved when a titanium dioxide film is deposited for 45 min (sample B). However, at this film thickness the LPE

nonlinearity is 21%, which exceeds the threshold of 15% [3]. Based on the requirements to the performance characteristics for the PSD, in this case, sample C with the LPE sensitivity of 477 mV/mm and nonlinearity of 9% should be chosen as the optimal thickness.

Usually, the change in the dependence of the LPE sensitivity on the top layer thickness is explained from two points of view [6]. On the one hand, a decrease of the LPE sensitivity in the range of small thicknesses is associated with a film discontinuity and, accordingly, a decrease in the height of the built-in barrier [7]. The LPE maximum is achieved when the film becomes continuous, and the height of the built-in barrier becomes homogeneous [7, 9]. On the other hand, a decrease of the LPE sensitivity with a further increase in the film thickness results in a decrease in its resistance, which leads to short-circuiting of two measuring electrodes. However, in the $TiO_2/SiO_2$/p-Si structure, the resistance of a titanium oxide film is orders of magnitude higher than the resistance of transition metal films [3, 5, 6]; therefore, a decrease in the LPE sensitivity with an increase of the $TiO_2$ film thickness, in our opinion, is due not to a decrease of its resistance, but due to voltage losses at the contacts because of high film resistance in the transverse direction.

The high value of the LPE nonlinearity in the $TiO_2/SiO_2$/p-Si heterostructure, in our opinion, is due to the strong morphological roughness of the film since it is known [12] the morphological roughness of $TiO_2$ films can reach 30-50% of the film thickness, and the nonlinear I–V characteristic of heterostructure.

The time dependences of LPV at a pulsed illumination were also investigated. It was noted that the photovoltage signal in the $TiO_2/SiO_2$/p-Si structure is characterized not only by a high pulse amplitude, corresponding to the LPE sensitivity, but also by rather long rise time and fall time, Table 1. In this work, the rise time is defined as the time required to increase the photovoltage from 10% to 90% of the peak photovoltage ($U_{max}$), and the fall time is defined as the time required to reduce the photovoltage from 90% to 10% $U_{max}$.

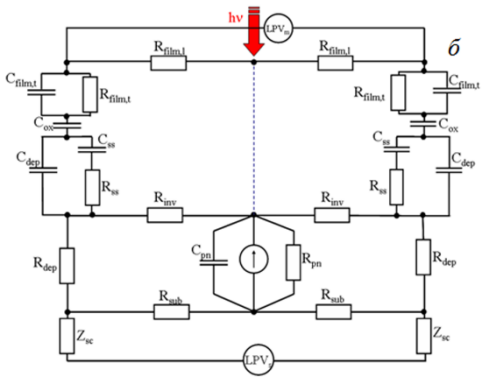


***Fig. 1.*** *Equivalent circuit of the lateral conductivity in the $TiO_2/SiO_2$/p-Si structure.*

Large value of time parameters in the $TiO_2/SiO_2$/p-Si heterostructure, in comparison with the previously studied structures [5, 13], can be explained on the basis of the equivalent circuit, Fig. 1. Since the top layer in the $TiO_2/SiO_2$/p-Si heterostructure is a semi-insulator, current transfer through it does not occur, and this conduction channel is shunted by the inversion layer and the transverse conductivity in the near-contact region.

As can see in Fig. 1, in contrast to conventional MOS structures, in this case, in the transverse direction, a complementary RC filter for the $TiO_2$ film is added to the RC filter of the $SiO_2$/p-Si interface, taking into account its impedance characteristics, which slow down the photoresponse.

## 4. Conclusions

Thus, the choice of a semi-insulator as the top layer allows us to conclude that lateral photoconductivity in the $TiO_2/SiO_2$/p-Si heterostructure occurs along the inversion layer and the near-contact regions, while the titanium dioxide film serves only to generate a built-in potential at the $SiO_2$/p-Si interface. The LPE characteristics obtained during the study of the $TiO_2/SiO_2$/p-Si structure make it possible to consider this structure as a promising candidate for optoelectronics.

## References

[1] C. Hu, X. Wang, B. Song. Light: Science & Applications **9** (2020) 1-9.
[2] J.T. Wallmark. Proceedings of the IRE.**45**.*4* (1957) 474-483.
[3] C. Yu, H. Wang. Sensors. **10**.*11* (2010) 10155-10180.
[4] X. Wang, B. Song, M. Huo, et.al. RSC Advances **5**.*80* (2015) 65048-65051.
[5] T.A. Pisarenko, V.V. Balashev, V.V. Korobtsov, A.A. Dimitriev, V.A. Vikulov. Defect and Diffusion Forum **386** (2018) 137-142.
[6] X. Huang, C. Mei, J. Hu, D. Zheng, Z. Gan, P. Zhou, H. Wang. IEEE Electron Device Letters **37** (2016) 1018-1021.
[7] S. Rahmatallahpur, M. Yegane. Physica B: Condensed Matter **406**.*8* (2011) 1351-1356.
[8] D.P. Opra, S.V. Gnedenkov, S.L. Sinebryukhov, A.B. Podgorbunsky, A.A. Sokolov, A.U. Ustinov, … V.V. Zheleznov. Chemical Physics **538** (2020) 110864.
[9] T.A. Pisarenko, V.V. Balashev, V.A. Vikulov, A.A. Dimitriev, V.V. Korobtsov. Physics of the Solid State **60**.*7* (2018) 1316-1322.
[10] A. Kiejna, T. Pabisiak, S.W. Gao. Journal of Physics: Condensed Matter **18**.*17* (2006) 4207.
[11] G. Xiong, R. Shao, T.C. Droubay, A.G. Joly, K.M. Beck, S.A. Chambers, W.P. Hess, Advanced Functional Materials **17**.*13* (2007) 2133-2138.
[12] J. Lias, S.A. Shahadan, M.S.A. Rahim, N. Nayan, M.K. Ahmad, M.Z. Sahdan. Jurnal Teknologi. **78** (2016) 10-3.
[13] T.A. Pisarenko, V.V. Korobtsov, V.V. Balashev, A.A. Dimitriev. Solid State Phenomena. – Trans Tech Publications Ltd, **312** (2020) 92-97.

Sixth Asian School-Conference on Physics and
Technology of Nanostructured Materials
Vladivostok, Russia, 25 – 29 April, 2022



# Numerical simulations and experimental observation of photonic nanojets generated by $TiO_2$ microparticles

K.A. Sergeeva*, A.A. Sergeev
Institute of Automation and Control Processes FEB RAS , 5 Radio St., Vladivostok 690041, Russia

*e-mail: kspetrovykh@gmail.com

**Abstract.** Here we present a combination of numerical and experimental methods to investigate the parameters of the photonic nanojets generated by titanium dioxide truncated cones. The technological approach to create uniform ordered arrays of the microparticles was successfully developed. Depending on the microparticle spatial ordering and propagating media the effective length of the photonic nanojet can reach from 4 to 8λ. It was found that the sensitive layer (chitosan polymer/luminescent dye) shows up to 3.5-fold photoluminescence enhancement under photonic nanojets excitation. The abovementioned parameters of the photonic nanojets provide promising results in the field of optical sensorics both in gaseous and aqueous media.

## 1. Introduction

At present, the photonic nanojet (PNJ) effect is considered as an alternative to plasmon structures for transmitting light at the nanoscale, that is the basis for creating new fully optical computing devices [1, 2]. The possibility of overcoming the diffraction limit causes the development of additional fields of PJ application to create systems of high-resolution optical microscopy (so-called nanoscopy [3]), submicron optical waveguides [4], and optical integrated circuits [5], as well as various kinds of sensor systems [6-8].

In turn, the strong dependence of the PNJ cross-section, effective length, and maximum intensity on the geometry and material of the microparticle, the refractive index of the environment, the wavelength, and the polarization of the exciting radiation, requires choosing the optimal kind of particle for specific tasks. Many theoretical studies of the photonic nanojets are carried out for optical contrast values (the ratio of the refractive indices of a parental microstructure and the environment) that are difficult to achieve in practice, and particles of complex geometry, for example, combinations of several cylinders separated by hemispheres. Obviously, for all the advantages of photonic nanojets formed by such structures, the experimental implementation of even one of them is an extremely difficult task, and creating an array is practically impossible.

In this regard, our work was aimed on the one hand to accurate numerical simulations of PNJ parameters varying the parental microstructure geometry. And, on the other hand, we did develop a technology to obtain the photonic nanojet generating titanium dioxide microparticles ordered in arrays using generally available methods and standard technological approaches of silicon microelectronics.

## 2. Numerical simulations and experimental technique

The interaction of incident radiation (λ = 0.535 μm) with $TiO_2$ (refractive index (RI) is 2.445) microparticles was simulated by the finite-difference in the time domain method. The intensity of the plane monochromatic radiation source was 1 a.u. The size of the uniform cell was 1 $nm^3$. The boundary conditions were set as a perfectly matched layer in all x, y, and z dimensions for the case of one microparticle, while for the ordered particle array the boundary conditions were periodic (x, y axes) and perfectly matched layer (z, that is light propagation direction). The modeling was performed for truncated cones with a base diameter D equal to 2 μm, height h = 0.65 μm, and base angle α 60°. The PNJ propagation media was the air with RI=1 or optically active layer with a RI=1.545 (chitosan polymer at 40% relative humidity).

The ordered arrays of titania truncated cones were obtained by the following steps: (I) An electronic resist layer (2 mass % of polymethyl methacrylate (PMMA) in chloroform) was spin-coated on the preliminarily prepared glass substrate. (II) The PMMA coating was further annealed in a muffle furnace at 120 °C for three hours. (III) Writing of microparticle array templates by electron beam lithography. (IV) After writing, the templates were developed in an isopropyl alcohol/water solution (9:1) to etch the resist. (V) Vacuum deposition of titanium dioxide at a rate of 0.01 Å/s. (VI) After deposition, the sample was washed with acetone in an ultrasonic bath for a minute to completely remove the PMMA film. (VII) Covering of fabricated structures by sensitive layer via spin-coating of chitosan polymer/dye solution. The Nile red or rhodamine 6G dyes were used depending on the analyte type during sensor response studies. The technique developed allows creation of ordered arrays of microparticles placed in the corners of the squares or hexagons with a period (a distance between the microparticles) of 2.5 or 4 μm. The square area of each array was 200x200 μm.

The images of the titania truncated cone ordered arrays were obtained by scanning electron microscopy (SEM). We directly observed the photonic nanojets using a home-built experimental setup described in detail in [9]. The sample is illuminated (λ = 532 nm) from the bottom side, while the images of the PNJs were captured by the CCD device via scanning in a plane perpendicular to the Z-axis with a step of 0.1 or 0.2 μm for air and sensitive layer covering the arrays, respectively. The optical signal from the sample is collimated by a 0.9 NA microscope lens and then split for two equal paths. One path was directed to the CCD camera, and the other part went to a fiber-optic spectrometer with a fiber input adjusted to the center of the image.

## 3. Results and discussions

Numerical simulations show that in the air single titania truncated cone demonstrates two light localization maxima inside the microparticle (Fig. 1a). Outside the microstructure, low intensity photonic nanojet decays fast and becomes undistinguishable at 2.5 μm apart from the

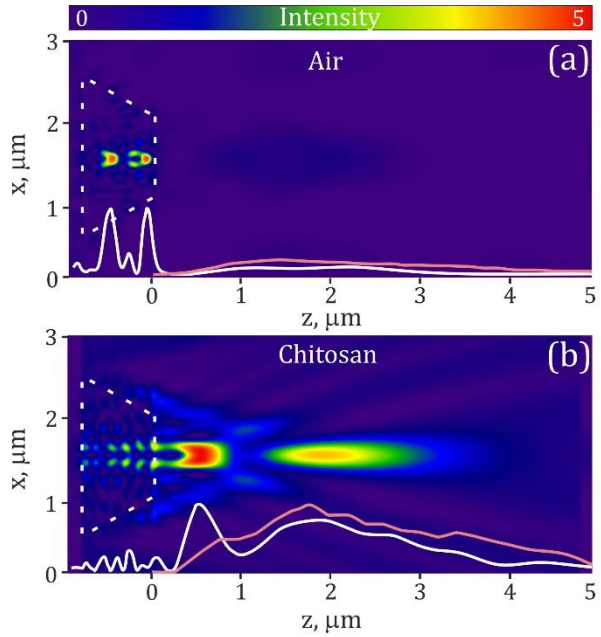


***Fig. 1.*** *Numerically simulated profile of PNJ generated by single $TiO_2$ microparticle propagating in air (a) and dry chitosan (b). White solid lines are calculated intensity distribution along Z-axis; salmon solid lines correspond the data obtained experimentally. White dashed line shows the position of the TiO2 truncated cone.*

surface. In its turn, in a dry chitosan film PNJ propagates up to 4 μm from the parental truncated cone. (Fig. 1b). In addition, the intensity of the photonic nanojet in its maximum in the chitosan polymer is 5-times higher compared with the air environment.

For the arrays of microparticles, the constructive interference of light beams diffracted by the neighboring particles was observed. In the case of the dense square packing of truncated cones (the period is 2.5 μm), the effective length of the PNJ can reach up to 10 μm. Further increase of the period to 4 μm leads to PNJ characteristics similar to the single microparticle (Fig. 2a). On the other hand, hexagonal ordering with the period 2.5 μm leads to the quenching of the PNJ at 3.5 μm apart from the cone surface (Fig. 2b).

One can note that the characteristics of the PNJs obtained by direct experimental observations are in good agreement with the numerical simulations. This fact indicates that the technology developed is effective for the formation of the arrays of microparticles generating the photonic nanojets with the required parameters.

It is important to add that up to a 3.5-fold increase in photoluminescence intensity of the active layer (chitosan polymer with rhodamine 6G or Nile red dyes) was observed under PNJ excitation compared with the reference area (i.e., the area without the $TiO_2$ microstructures). In addition, preliminary studies of the possibility of sensor response enhancement of the sensitive layer via PNJ excitation have been conducted. It was obtained that square packed arrays of titanium dioxide truncated cones exhibit the sensor response to ethanol vapors with an estimated limit of detection (LOD) equal to 0.04 ppm. That is more than an order of magnitude lower than the LOD for free-propagating light excitation (0.6 ppm). As to the metal ion presence the studies in swollen chitosan media has shown 0.1 ppm LOD compared with 1 ppm from the reference area.

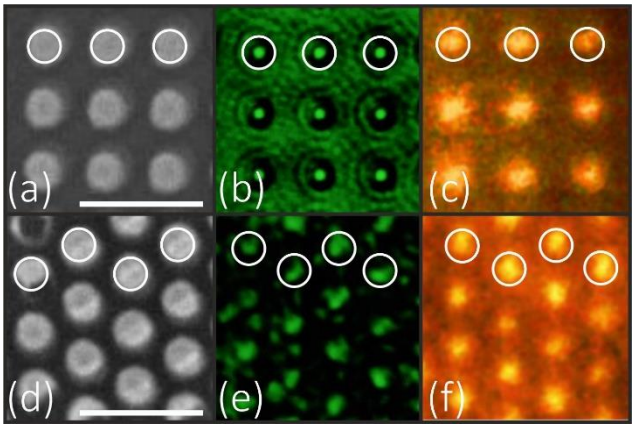


***Fig. 2.*** *SEM images of the $TiO_2$ microparticles ordered in squares (a) and hexagons (d). As well as the images of PNJs obtained by direct experimental observations: at the maximum of PNJ intensity (b and e); enhancement of the photoluminescence of the sensitive layer (c and f) for square and hexagonal packaging respectively. The sensitive layer is chitosan containing rhodamine 6G. The scale bar on SEM images is 10 μm, all images are on the same scale.*

The obtained results confirmed the perspectivity of the chosen approach to excite the sensitive layer by PNJs to increase its sensor performance.

## 4. Conclusions

The parameters of the photonic nanojets generated by $TiO_2$ truncated cones had been characterized by numerical simulation, followed by direct experimental observations. The technology based on the common approaches of silicon microelectronics to obtain uniform microparticle arrays different spatial symmetry was developed. Photonic nanojets generated by titania truncated cones demonstrate 3.5-fold enhancement of the photoluminescence of the sensitive layer, and high sensor response.

## Acknowledgements

This work was financially supported by the Russian Science Foundation (project 20-72-00066).

## References

[1] D. K. Gramotnev and S. I. Bozhevolnyi. Nat. Photonicics **4** (2010) 83.
[2] B. Born et al. Nat. Commun. **6** (2015) 8097.
[3] H. Yang et al. Nano Lett.**16** (2016) 4862.
[4] S. Yang and V. N. Astratov, Appl. Phys. Lett. **92** (2008) 261111.
[5] Luk'yanchuk B.S. et al. Opt. Mat. Exp. **7** (2017) 1820.
[6] Y.-C. Li. Light: Sci. Appl. **5** (2016) e16176.
[7] Ghenuche P. App. Phys. Let. **105** (2014) 131102.
[8] H. Yang et al. Nano Lett. **15** (2015) 1730–1735.
[9] K.A. Sergeeva et al. Sens. and Actuat. B: Chem. **305** (2020) 127354.

Sixth Asian School-Conference on Physics and
Technology of Nanostructured Materials
Vladivostok, Russia, 25 – 29 April, 2022



# Facile fabrication of a $TiO_2$ NW-based glucose sensor by direct ink writing

A. Tarasov*[,1], S. Dubkov[1], D. Gromov[1], R.M. Ryazanov[2], L. Volkova[3]

[1] National Research University of Electronic Technology "MIET", 124498 Moscow, Russia
[2] Scientific-Manufacturing Complex «Technological Centre», 124498 Moscow, Russia
[3] Institute of Nanotechnology of Microelectronics of the Russian Academy of Sciences, 119991 Moscow, Russia,

*e-mail: bloggger4@gmail.com

**Abstract.** This paper presents the results on the synthesis of titanium dioxide nanowires and the formation of sensitive elements of glucose biosensors on their basis by direct ink writing (DIW). Nanowires were synthesized by the hydrothermal method in an alkali solution. Results were obtained on the morphology of nanowires at different temperatures and times of synthesis. The effect of thermal treatment on the crystal structure of $TiO_2$ nanowires was also studied. Printing ink was prepared on the basis of suspensions of various compositions. The resulting structures showed sensitivity to a glucose solution at a micromolar concentration.

## 1. Introduction

Currently, biosensors are an attractive object of study due to their high sensitivity and high detection rate of substances with low concentrations. The structure of a biosensor based on the measurement of the current-voltage characteristic can detect many organic substances such as antibodies, dyes, etc. One-dimensional semiconductor materials are used as a sensitive element in such sensors. [1]. The use of one-dimensional nanoobjects opens up new possibilities for creating biosensors with a lower sensitivity threshold. However, such biosensors are disposable, since cleaning the sensitive element of the sensor is practically impossible. The solution to this problem can be the use of $TiO_2$ nanowires as a sensitive element of a biosensor [2]. $TiO_2$ is a material with photocatalytic properties that allow surface cleaning under ultraviolet light. In nanowires, in comparison with films, there is no depletion and accumulation of charge carriers on the surface and in the bulk of the structure, which contributes to the detection of a small amount of a substance. One of the promising methods for forming sensitive elements of a sensor is robocasting, which makes it possible to form structures directly from suspensions.

## 2. Experiment

Synthesis of nanowires.

Titanium dioxide nanowires were obtained using the hydrothermal synthesis method. For synthesis, 0.3 g of commercial $TiO_2$ powder (Degussa P25) and 50 mL of 10 M NaOH aqueous solution were putted into a Teflon-lined stainless autoclave. Fill factor 1/2. Then the autoclave was heated in a muffle furnace and kept for a specified time. The autoclave together with the muffle furnace was cooled down to room temperature. After synthesis, the nanowires were washed in a 0.1 M HCl solution to neutralize alkali residues and Na ions. Then it is necessary to remove the remaining acid by washing in deionized water with constant stirring and heating. The nanofilaments were filtered and added to water again. Washing was carried out up to normal pH = 7. Then, the nanowires were dried at 100 °C in air.

At the beginning, the dependence of the morphology of nanowires was studied at different synthesis times. The synthesis temperature was constant and amounted to 250 °C. Synthesis time 3, 6, 9 and 12 hours. Then, the dependence of the synthesis temperature on the nanowire morphology was studied. The synthesis was carried out for 12 hours at temperatures of 150 and 200 °C.

Annealing of nanowires.

To study the effect of thermal post-treatment on the crystal structure of titanium dioxide nanowires, annealing was carried out. Annealing was carried out in air for 4 hours at temperatures of 500, 700, and 900 °C.

Ink preparation.

For the formation of sensitive elements of the glucose sensor by direct printing, two inks were prepared. The first option was based on an aqueous suspension. 20 mg of TiO2 nanowires were added to 20 ml of deionized water, and ultrasonic treatment was carried out. The second version of the ink was based on an aqueous solution of polyvinyl alcohol (PVA). PVA (20 g) was added to 20 ml of deionized water, stirred until complete dissolution, 20 mg of $TiO_2$ nanowires were added, and the ink was sonicated.

Drawing contacts.

Silicon with an oxide layer 100 nm thick was used as a substrate for the glucose sensor. It was deposited with gold contacts 100 nm thick with a step of 5 mm using vacuum-tremic evaporation.

Printing of sensitive elements of sensors.

The formation of sensitive elements of the sensor by the DIW method was carried out on a modified 3D printer with a specially designed print head, inside which a syringe with ink is fixed. Nozzle diameter 0.4 mm, heated table temperature 100°C. When using inks with polymer, subsequent heat treatment is necessary to burn out the polymer. Burning was carried out in air at a temperature of 600 °C for 10 minutes.

Measurement of the current-voltage characteristic.

The study of the sensory properties of titanium dioxide nanowires was carried out by measuring the current-voltage characteristics of the sensitive layer coated with 10 μl of 5, 10, and 100 μM glucose solution. An Agilent e3647a power supply, a Keithley 6485 picoampimeter, a Keithley 2700 multimeter, and a probe station were used for measurements.

## 3. Results and discussions

The obtained nanowires were studied by SEM. After three hours of synthesis, single nanowires formations and large agglomerates are observed. As the synthesis time

increases, the number of agglomerates decreases. Minimum number of agglomerates is observed after 12 hours of synthesis (Fig. 1). The average length of the nanowires was 6, 7 and 8 μm for 6, 9, and 12 hours of synthesis, respectively. Therefore, a 12-hour synthesis was chosen as the most optimal one.

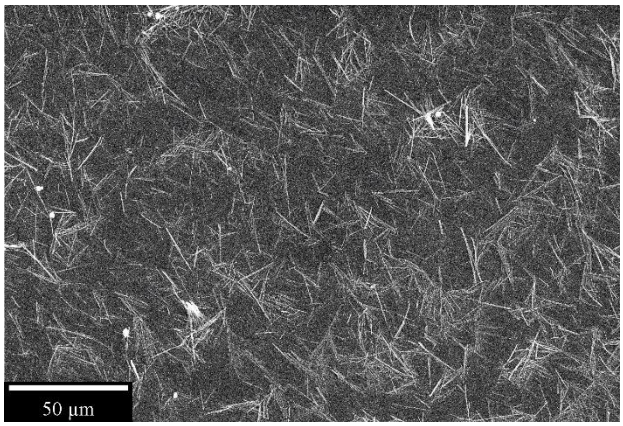


***Fig. 1.*** *SEM images of nanowires after (a) 3, (b) 6, (c) 9 and (d) 12 hours synthesis at 250 °C.*

After that, the temperature dependence of synthesis of nanowires was studied. At 150 °C, no growth of nanowires is observed. At 200 °C, the average length of nanowires was 4 μm, which is two times less than in synthesis at 250 °C. Therefore, a synthesis mode of 250 °C and 12 hours was chosen.

At 500 °C annealing, mainly anatase and TiO2-B peaks are observed. After annealing at 700 °C, peaks characteristic of rutile appears. Rutile peaks dominate after annealing at 900 °C. It is believed that the highest catalytic activity is observed in samples that are an anatase-rutile mixture. Therefore, annealing at 700 °C was chosen for further work.

When printing with water-based ink, a non-continuous layer is formed. This can be explained by the low viscosity of such inks. The use of ink based on PVA water solution gives the best result.

After annealing, only nanowires remain on the silicon wafer surface. These nanofilaments have a preferred direction. The direction is the same as the movement of the print head. This effect can affect the sensitivity of the sensor.

The obtained current-voltage characteristics (Fig. 2) demonstrate the sensitivity of the sensor to low concentrations of glucose. With an increase in glucose concentration, the conductivity of the sensitive layer increases.

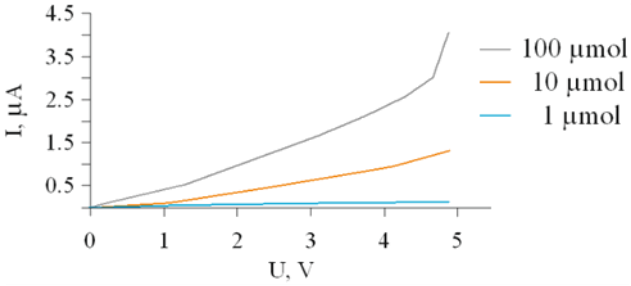


***Fig. 2.*** *Volt-ampere characteristic as a function of glucose concentration.*

## 4. Conclusions

In this work, a facile synthesis of $TiO_2$ nanowires was demonstrated. The average length of nanowires was 6, 7 and 8 μm for 6, 9 and 12 hours of synthesis for 250 °C. The dependences of the crystal structure on the annealing temperature were obtained. Anatase is formed after annealing at 500 °C, a mixture of rutile anatase at 700 °C and rutile at 900 °C. The obtained ink showed that viscosity is an important parameter for DIW printing. This was demonstrated using two suspensions as an example. A more viscous PVA aqueous solution showed better layer morphology. Based on such ink, a glucose sensor was created. The sensor showed sensitivity to micromolar concentrations of glucose solution.

## Acknowledgements

This work was financially supported by the grant of President of the Russian Federation (project MK-2201.2021.4).

## References

[1] F. Patolsky, G. Zheng, C. M. Lieber. Nanowire-based biosensors. 78(2006)4260.
[2] H. Jeong, J. Yoo, S. Park, J. Lu, J. Lee. Biosensors. 11(2021) 149.

Sixth Asian School-Conference on Physics and
Technology of Nanostructured Materials
Vladivostok, Russia, April 25 - 29, 2022



# Influence of current density, anodization time and illumination on the thickness of porous silicon in wafers with built-in p-n junction and its photoluminescence

K.N. Galkin[1], D.T. Yan[*,2], A.V. Nepomnyashchiy[1], N.G. Galkin[1]

[1] Institute of Automation and Control Processes FEB RAS , 5 Radio St., Vladivostok 690041, Russia
[2] Far Eastern State Transport University, 47 Serysheva St., Khabarovsk 680021, Russia

*e-mail: dmitry_yan@mail.ru

For anodizing n-type silicon wafers, regardless of its electrical conductivity, it is necessary to ensure the generation of holes, which are minority carriers. This can be done in two ways [1]: (1) by applying a critical electric field to effect electrical breakdown, and (2) by illuminating with radiation sufficient to generate holes due to the photoelectric effect. It is known that IR illumination from the reverse side of the substrate provides the generation of electron-hole phases, their separation, and the diffusion of holes to the front side of the substrate, which is under the action of a negative potential, which leads to the formation of macroporous structures during anodization [1,2]. However, under conditions of illumination from the front side of the silicon substrate [3], depending on the parameters of anodization and the degree of its doping, the formation of a two-layer structure was observed, consisting of a thin nanoporous layer and a thicker macroporous layer. However, complex studies of anodization in silicon with a built-in p-n junction, to our knowledge, have not been previously carried out.

In this work, the formation of a porous layer in a thin n-type layer epitaxially grown on p-type silicon at two anodizing current densities and different anodizing currents is studied and a comparison is made of transverse cleavages, surface morphology, reflection spectra, and photoluminescence spectra.

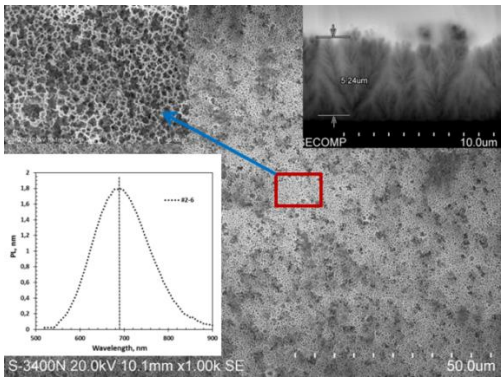


***Fig. 1.*** *SEM image of the morphology of sample #2_6 anodized at 10 mA/cm$^2$ and 25 min. The upper left inset shows an enlarged image of the red rectangle. The upper right insert shows cross-section SEM image. The bottom left insert shows PL spectrum at room temperature.*

For anodizing, single-crystal silicon Si(100) wafers of p-type conductivity with an epitaxial layer of n-type conductivity were used. Layers of porous silicon (PS) were formed at two anodizing current densities (10 and 20 mA/cm$^2$) and etching durations from 10 to 30 minutes, as well as using illumination with a 150 W tungsten lamp during the anodizing process. After washing in deionized water and drying in a flow of dry nitrogen, the samples were examined by optical reflectance and photoluminescent (PL) spectroscopy, as well as by scanning electron microscopy (SEM).

When anodizing with a current density of 10 mA/cm$^2$ for up to 15 minutes, the formation of a relatively homogeneous PS layer with a low density of punctures is observed, which has a high PL intensity at a laser wavelength λ=405 nm and a very low one at λ=532 nm. This indicates its high porosity [3] and the generation of the PL signal only in a thin PS layer. With an increase in the duration of etching to 25 minutes, a network surface structure is formed (Fig. 1), which grows deeper into a tree-like structure (Fig. 1, upper right inset) with a thickness of about 5.24 μm. The high PL intensity at λ=405 nm (Fig. 1, bottom left inset) quickly drops to almost zero at λ=532 nm, which confirms the localization of PL in a thin PS surface layer (Fig. 1, upper right inset). An increase in the etching time to 30 minutes led to an increase in the PS thickness to 7.2 μm. At the same time, a relatively smooth layer up to 2 μm thick, but with microcracks and punctures, is observed on the surface, which then passes into a tree-like structure. The PL spectra at 405 nm and 532 nm also confirmed the localization of the PL signal in the thin upper PS layer. Registration of reflectance spectra in the UV-VIS range showed that in layers with a tree-like structure, a sharp decrease in reflection is observed over the entire range, which indicates an increase in irretrievable light losses in such layers. The latter are associated with the loss of PL intensity upon localization of light (532 nm) in them.

An increase in the anodization current density to 20 mA/cm$^2$ led to the formation of a two-layer PS structure, which includes a thin homogeneous PS layer and then a tree-like structure. The thickness of the entire PS layer increased with the etching time (10, 15, 30 min) from 4.5 μm to 17.4 μm. The position of the maximum in the PL spectrum practically did not depend on the etching time, and the intensity of the PL peak decreased with increasing etching time, which is confirmed by a decrease in the PL intensity upon going from λ=405 nm to λ=532 nm and PL localization mainly in the upper PS layer, but with variable porosity. It turned out to be maximum for the minimum etching time.

## References

[1] V. Lehmann. J. Electrochem. Soc. **140**(1993)2836.
[2] P. Kleimann, J. Linnros, S. Peterson. Mat. Sci. & Engineer. B **69**(2000)29.
[3] C. Levy-Clement, A. Logoubi, M. Parameters. J. Electrochem. Soc. **141**(1994)958.

# Author Index

## H



## I



## J



## K



## L



## M



## N

## O



## P



## R



## S



## T

## U



## V



## X



## Y



## Z

# Sixth Asian School-Conference on Physics and Technology of Nanostructured Materials (ASCO-NANOMAT 2022)

International School-Conference
Vladivostok, Russia, April 25 – 29, 2022

## PROCEEDINGS

In charge of publication: N.G. Galkin

Design and layout: S.V. Chusovitina

# Шестая азиатская школа-конференция по физике и технологии наноструктурированных материалов

Международная школа-конференция
Владивосток, Россия, 25 – 29 апреля 2022

Редактор: Н.Г. Галкин

Дизайн и вёрстка: С.В. Чусовитина

## СБОРНИК ТРУДОВ

**(на англ. яз.)**

Отпечатано с оригинал-макета,
подготовленного в Институте автоматики и процессов управления ДВО РАН,
минуя редподготовку в издательстве «Дальнаука»

Подписано к печати 05.04.2022 г.

Отпечатано в ООО “Дальнаука”
690106, г. Владивосток, пр-т Красного знамени, 10